



Lecture Notes in Mechanical Engineering

Hung Nguyen-Xuan
Phuc Phung-Van
Timon Rabczuk *Editors*

Proceedings of the International Conference on Advances in Computational Mechanics 2017

ACOME 2017, 2 to 4 August 2017,
Phu Quoc Island, Vietnam

 Springer

Lecture Notes in Mechanical Engineering

Lecture Notes in Mechanical Engineering (LNME) publishes the latest developments in Mechanical Engineering—quickly, informally and with high quality. Original research reported in proceedings and post-proceedings represents the core of LNME. Also considered for publication are monographs, contributed volumes and lecture notes of exceptionally high quality and interest. Volumes published in LNME embrace all aspects, subfields and new challenges of mechanical engineering. Topics in the series include:

- Engineering Design
- Machinery and Machine Elements
- Mechanical Structures and Stress Analysis
- Automotive Engineering
- Engine Technology
- Aerospace Technology and Astronautics
- Nanotechnology and Microengineering
- Control, Robotics, Mechatronics
- MEMS
- Theoretical and Applied Mechanics
- Dynamical Systems, Control
- Fluid Mechanics
- Engineering Thermodynamics, Heat and Mass Transfer
- Manufacturing
- Precision Engineering, Instrumentation, Measurement
- Materials Engineering
- Tribology and Surface Technology

More information about this series at <http://www.springer.com/series/11236>

Hung Nguyen-Xuan · Phuc Phung-Van
Timon Rabczuk
Editors

Proceedings of the International Conference on Advances in Computational Mechanics 2017

ACOME 2017, 2 to 4 August 2017, Phu Quoc
Island, Vietnam

 Springer

Editors

Hung Nguyen-Xuan
CIR Technology
Ho Chi Minh City University
of Technology
Ho Chi Minh
Vietnam

Timon Rabczuk
Computational Mechanics
Bauhaus-University Weimar
Weimar
Germany

Phuc Phung-Van
Faculty of Engineering and Architecture
Ghent University
Ghent
Belgium

ISSN 2195-4356 ISSN 2195-4364 (electronic)
Lecture Notes in Mechanical Engineering
ISBN 978-981-10-7148-5 ISBN 978-981-10-7149-2 (eBook)
<https://doi.org/10.1007/978-981-10-7149-2>

Library of Congress Control Number: 2017957662

© Springer Nature Singapore Pte Ltd. 2018

This work is subject to copyright. All rights are reserved by the Publisher, whether the whole or part of the material is concerned, specifically the rights of translation, reprinting, reuse of illustrations, recitation, broadcasting, reproduction on microfilms or in any other physical way, and transmission or information storage and retrieval, electronic adaptation, computer software, or by similar or dissimilar methodology now known or hereafter developed.

The use of general descriptive names, registered names, trademarks, service marks, etc. in this publication does not imply, even in the absence of a specific statement, that such names are exempt from the relevant protective laws and regulations and therefore free for general use.

The publisher, the authors and the editors are safe to assume that the advice and information in this book are believed to be true and accurate at the date of publication. Neither the publisher nor the authors or the editors give a warranty, express or implied, with respect to the material contained herein or for any errors or omissions that may have been made. The publisher remains neutral with regard to jurisdictional claims in published maps and institutional affiliations.

Printed on acid-free paper

This Springer imprint is published by the registered company Springer Nature Singapore Pte Ltd. part of Springer Nature
The registered company address is: 152 Beach Road, #21-01/04 Gateway East, Singapore 189721, Singapore



Preface

This book contains selected papers from the second International Conference on Advances in Computational Mechanics (ACOME 2017), held at Phu Quoc Island, Vietnam, from 2 August to 4 August 2017. The conference provides an international forum for scholars and researchers to exchange knowledge and expertise in the development of modern numerical methods and their applications to challenging engineering problems. The ACOME conference in 2017 received over 140 submissions from different universities and research institutes of 20 countries. They were allocated into 6 parallel technical sessions, including eight plenary talks and several keynote talks. This book contains 75 selected papers from the conference that cover “Biological Systems”, “Computational Fracture and Damage Mechanics”, “Catastrophic Destruction Mechanics and Numerical Modelling”, “Computational Mechatronics”, “Composites and Hybrid Structures”, “Flow Problems”, “Multiscale Multiphysics Problems”, “Numerical Methods and High-Performance Computing”, “Optimisation and Inverse Problems”, “Reinforced Concrete, Steel and Steel-Concrete Composite Structures”. These papers were selected in a peer-reviewing process by at least two independent reviewers that are recognised experts in the topical field.

The editors would like to thank all the authors for their contributions to this conference. We also express our sincere gratitude to the dedicated reviewers for their time and contribution to enhance the scientific quality of the manuscripts.

The conference was jointly hosted by the Vietnam Association of Computational Mechanics (VACOM) and Ho Chi Minh City University of Technology (HUTECH). We gratefully acknowledge the financial support from the sponsors: National Foundation for Science and Technology Development (NAFOSTED), SAKI Corporation, Duy Tan University (DTU) and China Medical University Taiwan (CMU).

Ho Chi Minh, Vietnam
Ghent, Belgium
Weimar, Germany

Hung Nguyen-Xuan
Phuc Phung-Van
Timon Rabczuk

Organising Committee

Chairman

Hung Nguyen-Xuan, Hutech University, Ho Chi Minh City, Vietnam

Co-chairman

Timon Rabczuk, Bauhaus University Weimar, Germany

Antonio J. M. Ferreira, University of Porto, Portugal

Finance Division

Duc Ngoc Nguyen, Hutech University, Vietnam

Conference Secretariat

Phuc Phung-Van, Ghent University, Belgium

Tu Le-Van, The University of Melbourne, Australia

Khanh Chau-Nguyen, Hutech University, Vietnam

Khai Chau-Nguyen, Hutech University, Vietnam

Chi Kim Nguyen, Hutech University, Vietnam

Local Organising Committee

Son Hoai Nguyen, HCMC University of Technology and Education, Vietnam

Quy Minh Le, Hanoi University of Science and Technology, Vietnam

Hung Quoc Nguyen, Vietnam-German University, Vietnam

Canh Van Le, HCMC International University, VNU-HCMC, Vietnam

Thanh Dinh Chau, HCMC University of Technology and Education, Vietnam

Long Minh Nguyen, HCMC University of Technology, Vietnam



Contents

Part I Computational Fracture and Damage Mechanics

Truss Damage Detection Using Modified Differential Evolution Algorithm with Comparative Studies	3
Sumin Kim, Nam Il Kim, Hyunjoo Kim, T. N. Nguyen, Q. X. Lieu and Jaehong Lee	
Finite Element Simulation on Small Punch Test for an Evaluation of J-integral for TRIP Steel	17
H. T. Pham and T. Iwamoto	
On the Buckling Behavior of Multi-cracked FGM Plates	29
Nguyen Dinh Duc, Truong Duc Trinh, Thom Van Do and Duc Hong Doan	
Using a Non-local Elastic Damage Model to Predict the Fatigue Life of Asphalt Pavement Structure	47
H. T. Tai Nguyen and N. Hung Nguyen	
Failure of Building Structural Members During the Cooling Phase of a Fire	65
Q. V. Truong, T. H. Pham and T. B. Chu	
Numerical Studies of Some Modified Polarization Saturation Models in 2-D Semipermeable Piezoelectric Media Using Distributed Dislocation Method	79
Kuldeep Sharma and Sandeep Singh	
Stress Analysis of Silicon-Based Anode in Li-Ion Battery	95
T. Nguyen-Huu and Q. Le-Minh	
Modeling of 3D Inflatable Large Deformation Air Plug in Contact With Concrete Lining	105
Anan Liao, Hui Shang, Xiaoyong Kou, Jun Huang and Xiaoying Zhuang	

Upper Bound Limit Analysis of Circular Tunnel in Cohesive-Frictional Soils Using the Node-Based Smoothed Finite Element Method	123
T. Vo-Minh, T. Nguyen-Minh and A. Chau-Ngoc	
Numerical Studies on Contact Problem of Inter-locking Concrete Blocks Forming Revetment Structure	143
L. Dang-Bao, P. Truong-Thi, M. A. Wahab and Hung Nguyen-Xuan	
Part II Multiscale Multiphysics Problems	
Orientation-Dependent Response of Pure Zinc Grains Under Instrumented Indentation: Micromechanical Modeling	157
N. P. T. Nguyen, F. Abbès, B. Abbès and Y. Li	
Atomistic Simulation of Boron Nitride Nanotubes Under Bending	171
T. Nguyen-Van, T. Nguyen-Danh and Q. Le-Minh	
Part III Optimization and Inverse Problems	
A Quick Computational Method for Improving Aerodynamic Shape of UAV Wing	183
D. Tran-Duy, C. Nguyen-Duc, K. Mai and T. Nguyen-Duc	
Engineering Optimization Using an Improved Epsilon Differential Evolution with Directional Mutation and Nearest Neighbor Comparison	201
A. H. Pham, C. T. Vu, D. B. Nguyen and D. T. Tran	
Optimization of the Longitudinal Cooling Fin by Levenberg–Marquardt Method	217
Q. Nguyen, S. Nguyen-Hoai, T. Chuong-Thiet and T. Lam-Phat	
An Artificial Neural Network-Based Optimization of Stiffened Composite Plate Using A New Adjusted Differential Evolution Algorithm	229
T. Lam-Phat, S. Nguyen-Hoai, V. Ho-Huu, Q. Nguyen and T. Nguyen-Thoi	
Part IV Reinforced Concrete, Steel and Steel-Concrete Composite Structures	
Theoretical and Experimental Studies on Hybrid Steel-RC Walls	245
Nguyen Quang-Huy, Hjjaj Mohammed and Tran Van Toan	
Numerical Study on a New Through-Column-Type Joint for RCS Frame	261
D. D. Le, X. H. Nguyen and Q. H. Nguyen	

Flexural Behavior of Unbonded Post-Tensioned Concrete T-Beams Externally Bonded With CFRP Sheets Under Static Loading 273
 Q. P. T. Truong, P. Phan-Vu, D. Tran-Thanh, T. D. Dang and L. Nguyen-Minh

Numerical Analysis of the Behaviors of End-Plate Beam-to-Column Steel Joints Subjected to Cyclic Loading 291
 A. T. Le and H. Pham

Experimental and Numerical Research on the Fire Behaviour of Steel Column Protected by Gypsum Plasterboard Under Fire Condition 307
 T. Nguyen-Vo, V. Nguyen-Duc and H. Tran

Part V Composites and Hybrid Structures

Comparison Between Numerical and Experimental Results of the Hybrid Members Subjected to Bending and Shear 327
 T. V. Tran and H. Q. Nguyen

Analytical Behavior of Rectangular Plates Under in-Plane and Lateral Dynamic Loads 345
 Sofia W. Alisjahbana, Wiratman Wangsadinata and Irene Alisjahbana

Static Analysis of FG-CNTRC Plates Using C0-HSDT 357
 T. Nguyen-Quoc, S. Nguyen-Hoai and D. Mai-Duc

Finite Element Simulation of the Strength of Corrugated Board Boxes Under Impact Dynamics 369
 V. Dung Luong, Fazilay Abbès, Boussad Abbès, P. T. Minh Duong, Jean-Baptiste Nolot, Damien Erre and Ying-Qiao Guo

Static and Free Vibration Analysis of Functionally Graded Shells Using a Cell-Based Smoothed Discrete Shear Gap Method and Triangular Elements 381
 D. Le-Xuan, H. Pham-Quoc, V. Tran-The and N. Nguyen-Van

Optimal Volume Fraction of Functionally Graded Beams with Various Shear Deformation Theories Using Social Group Optimization 395
 A. H. Pham, T. V. Vu and T. M. Tran

A Node-Based MITC3 Element for Analyses of Laminated Composite Plates Using the Higher-Order Shear Deformation Theory 409
 T. Chau-Dinh, T. Truong-Duc, K. Nguyen-Trung and H. Nguyen-Van

Equivalent Inclusion Approach and Approximations for Thermal Conductivity of Composites with Fibrous Fillers 431
 Nguyen Trung Kien, Nguyen Thi Hai Duyen and Pham Duc Chinh

Crack Detection in a Beam on Elastic Foundation Using Differential Quadrature Method and the Bees Algorithm Optimization 439
R. Khademi Zahedi, P. Alimouri, Hung Nguyen-Xuan and Timon Rabczuk

Nonlinear Static Bending Analysis of Functionally Graded Plates Using MISQ24 Elements with Drilling Rotations 461
H. Nguyen-Van, H. L. Ton-That, T. Chau-Dinh and N. D. Dao

A Pull-Out Test to Characterize the Fiber/Matrix Interfaces Aging of Hemp Fiber Reinforced Polypropylene Composites 477
C. Nguyen-Duy, A. Makke and G. Montay

A Modified Moving Kriging Interpolation-Based Meshfree Method with Refined Sinusoidal Shear Deformation Theory for Analysis of Functionally Graded Plates 485
V. Vu-Tan and S. Phan-Van

Bending Analysis of Laminated Composite Beams Using Hybrid Shape Functions 503
Ngoc-Duong Nguyen, Trung-Kien Nguyen, Thien-Nhan Nguyen and Thuc P. Vo

Part VI Numerical Methods and High Performance Computing

Numerical Analysis of Hybrid Members Using FEM 521
T. V. Tran

Effect of Hyper-Parameters on Deep Learning Networks in Structural Engineering 537
Seunghye Lee, Mehriniso Zokhirova, Tan Tien Nguyen and Jaehong Lee

DOF Condensation of Thick Curved Beam Element Formulated by Isogeometric Approach. 545
Buntara S. Gan, Dinh-Kien Nguyen, Aylie Han and Sofia W. Alisjahbana

Optimal Airplanes’ Paths For Minimizing Airline Company’s Cost Subjected to Passengers’ Demand: Formulation and Verification 561
V. H. Nguyen, M. Ehsaei, J. Creedon, G. Sanjabi and D. T. Nguyen

A New Beam Theory Considering Horizontal Shear Strain 579
T. Vu-Thanh

Analytical Study on In-plane and Out-of-plane Responses of a Curved Floating Bridge 591
B. K. Lim, J. Dai, K. K. Ang and G. C. Yap

Establishment of Artificial Accelerogram for Shaking Table Test 605
T. Nguyen-Vo, T. Do-Tien and K. Nguyen-Trung

A Naturally Stabilized Nodal Integration Meshfree Formulation for Thermo-Mechanical Analysis of Functionally Graded Material Plates 615
 Chien H. Thai, Dung T. Tran and Hung Nguyen-Xuan

Nondestructive Vibrational Tests and Analytical Solutions to Determine the Young’s Modulus of Rammed Earth Material 631
 Quoc-Bao Bui

Investigation of A5052 Aluminum Alloy to SS400 Steel by MIG Welding Process 645
 Quoc Manh Nguyen, Huong Thao Dang Thi, Van Thinh Nguyen, Minh Hue Pham Thi, Khac Thong Nguyen, Shyh-Chour Huang and Van Nhat Nguyen

Behaviour of Two Chamber Aluminium Profiles Under Axial Crushing: An Experimental and Numerical Study 657
 Nguyen-Hieu Hoang, Magnus Langseth, Gaute Gruben and Terence Coudert

Part VII Flow Problems

Evaluating the Saltwater Intrusion to Aquifer Upper-Middle Pleistocene (qp₂₋₃) in Coastal Area of Tra Vinh Province Due to Groundwater Exploitation 675
 Huynh Van Hiep, Nguyen The Hung and Pham Van Long

Study the Hull Form and Propeller-Rudder System of the Fishing Vessel for Vietnam 691
 Victor G. Bugaev, Dam Van Tung and Yana R. Domashevskaya

Research the Strength of the Decking Overlap of the Fishing Vessel for Vietnam 701
 Victor G. Bugaev, Dam Van Tung and Yana R. Domashevskaya

Analysis and Evaluation of the Ground Wave Propagation Due to Blasting Activities of the Road Construction by Numerical Models and Experiments 709
 Lan Nguyen, Huy Hung Pham and Phuong Hoa Hoang

Fluid–Structure Interaction Analysis of Revetment Structures—An Overview 723
 T. Vu-Huu, C. Le-Thanh, Phuc Phung-Van, Hung Nguyen-Xuan and M. Abdel-Wahab

Building the Empirical Formula Defining Parameters of Blast Wave in Coral Environment 733
 L. Vu-Dinh and T. Nguyen-Huu

A CFD Modeling of Subcooled Pool Boiling	741
T. T. Nguyen, H. N. Duong, V. T. Tran and H. Kikura	
Optimization of Precision Die Design on High-Pressure Die Casting of $AlSi_9Cu_3$	759
T. A. Do and V. T. Tran	
Flow and Performance Analysis of a Valveless Micropump	773
P. K. Das and A. B. M. T. Hasan	
Aeroelastic Analysis on Wing Structure Using Immersed Boundary Method	783
D. T. K. Hoang, S. V. Pham, K. N. Tran, C. D. Nguyen and K. P. Nguyen	
Development of a 3-DOF Haptic Tele-manipulator System Using Magnetorheological Brakes	793
Nguyen Ngoc Diep, Hung Nguyen-Xuan, Nguyen Ngoc Tuyen and Nguyen Quoc Hung	
Studying Convective Flow in a Vertical Solar Chimney at Low Rayleigh Number by Lattice Boltzmann Method: A Simple Method to Suppress the Reverse Flow at Outlet	807
Y. Q. Nguyen	
A Dual Approach to Modeling Solute Transport	821
H. Nguyen-The	
A Nonlocal Formulation for Weakly Compressible Fluid	835
Huילong Ren and Xiaoying Zhuang	
CFD Simulations of the Natural Cavitating Flow Around High-Speed Submerged Bodies	851
T. T. Nguyen, H. N. Duong, T. Q. Nguyen and H. Kikura	
Effect of Low-Frequency Flow on Cable Dry-State Galloping	875
H. Vo-Duy, L. Hoang-Trong, M. Nguyen-Van and V. Nguyen-Hoang	
Investigation on Turbulence Effects on Flutter Derivatives of Suspended Truss Bridge Section	891
L. Hoang-Trong, V. Nguyen-Hoang and H. Vo-Duy	
Numerical Modelling of the Aeroelastic Response of Irregular Slender Structures	903
Cung H. Nguyen	
Analysis of Fluid–Structures Interaction Problem of Revetment Slope Thin-Walled Structure Using Abaqus	917
P. Truong-Thi, L. Dang-Bao, M. Abdel Wahab, H. Duong-Ngoc, T. Hoang-Duc and Hung Nguyen-Xuan	

Influence of Swelling Pressure on Pore Water in Embankment Core with Swelling Clay Soil 927
 Tuong Nguyen Ke, Hung Nguyen Pham Khanh, Hung Nguyen Minh, Hung Nguyen Viet and Thi Nguyen Minh

Part VIII Catastrophic Destruction Mechanics and Numerical Modelling

Concrete Mesoscopic Model and Numerical Simulation Based on Quadtree Mesh Refinement Technology 941
 Guojian Shao and Shengyong Ding

A Coupling of Three-Dimensional Finite Element Method and Discontinuous Deformation Analysis Based on Complementary Theory 955
 C. Su, Z. M. Ren, V. H. Dao and Y. J. Dong

Part IX Computational Mechatronics

Analysis and Summarization of a Mechanism Featuring Variable Stiffness 977
 Do Xuan Phu, Nguyen Quoc Hung and Ta Duc Huy

Dynamic Analysis of Hydraulic–Mechanical System Using Proportional Valve 991
 D. T. Luan, L. Q. Ngoc and P. H. Hoang

A Tooth Profile Design for Roots Rotors of Vacuum Pump 1003
 V. Tran-The and T. Do-Anh

Cascade Training Multilayer Fuzzy Model for Identifying Nonlinear MIMO System 1017
 Cao Van Kien and Ho Pham Huy Anh

Enhanced Adaptive Fuzzy Sliding Mode Control for Nonlinear Uncertain Serial Pneumatic Artificial Muscle (PAM) Robot System 1033
 Cao Van Kien and Ho Pham Huy Anh

Performance Evaluation of a 2D-Haptic Joystick Featuring Bidirectional Magneto-Rheological Actuators 1051
 Tri Bao Diep, Hiep Dai Le, Cuong Van Vo and Hung Quoc Nguyen

Design and Evaluation of a Shear-Mode MR Damper for Suspension System of Front-Loading Washing Machines 1061
 D. Q. Bui, V. L. Hoang, H. D. Le and H. Q. Nguyen

Part X Computational Dynamics

Transient Analysis of Laminated Composite Shells Using an Edge-Based Smoothed Finite Element Method 1075

D. Pham-Tien, H. Pham-Quoc, V. Tran-The, T. Vu-Khac and N. Nguyen-Van

Estimating Modal Parameters of Structures Using Arduino Platform 1095

Tuan Ta Duc, Tuan Le Anh and Huong Vu Dinh

Analysis of Dynamic Impact Factors of Bridge Due to Moving Vehicles Using Finite Element Method 1105

T. Nguyen-Xuan, Y. Kuriyama and T. Nguyen-Duy

Stationary Random Vibration Analysis of Dynamic Vehicle-Bridge Interaction Due to Road Unevenness 1121

T. Nguyen-Xuan, Y. Kuriyama and T. Nguyen-Duy

Dynamic Analysis of Beams on Two-Parameter Viscoelastic Pasternak Foundation Subjected to the Moving Load and Considering Effects of Beam Roughness 1139

T. Tran-Quoc, H. Nguyen-Trong and T. Khong-Trong

Part XI Biological Systems

The Prevention of Pressure Ulcers: Biomechanical Modelization and Simulation of Human Seat Cushion Contributions 1157

T. H. Bui, P. Lestriez, D. Pradon, K. Debray and R. Taiar

Part I
Computational Fracture and Damage
Mechanics

Truss Damage Detection Using Modified Differential Evolution Algorithm with Comparative Studies



Sumin Kim, Nam Il Kim, Hyunjoo Kim, T. N. Nguyen, Q. X. Lieu and Jaehong Lee

Abstract In this paper, an efficient numerical algorithm is developed for the damage detection of planar and space truss structures based on the modified differential evolution algorithm (mDE) and vibration data. For this purpose, the mathematical programming of the finite element based on the force method and the singular value decomposition technique is presented. The general equilibrium equations in which unknown member forces and reaction forces are taken into account are formulated. The compatibility equations in terms of forces are explicitly presented by using the singular value decomposition method. The modified differential evolution algorithm (mDE) is used as an optimization algorithm of damage detection. The objective function for damage detection is based on vibration data such as natural frequencies and mode shapes. The feasibility and efficiency of the present method are compared with a genetic algorithm (GA) and a particle swarm optimization (PSO) for example. The numerical results show that the proposed strategy based on force method using mDE and vibration data can provide a reliable tool on determining the sites and extents of multiple damages of truss structures.

Keywords Damage detection · Force method · Free vibration analysis
Modified differential evolution algorithm (mDE)

1 Introduction

The identification of structural damage is an important part of the monitoring and repairing of structural systems during their functional age. In order to improve the safety and life expectancy of structures, it is necessary to detect the damage extents and sites. The damage assessment technique has drawn wide attention from various

S. Kim · N. I. Kim · H. Kim · T. N. Nguyen · Q. X. Lieu · J. Lee (✉)
Department of Architectural Engineering, Sejong University, Seoul, Republic of Korea
e-mail: jhlee@sejong.ac.kr

S. Kim
e-mail: sumkim9355@gmail.com

© Springer Nature Singapore Pte Ltd. 2018
H. Nguyen-Xuan et al. (eds.), *Proceedings of the International Conference on Advances in Computational Engineering Mechanics 2017*, Lecture Notes in Mechanical Engineering, https://doi.org/10.1007/978-981-10-7149-2_1

engineering fields such as aerospace, mechanical, and civil engineering applications. The proposed identification of structural damage prevents the deterioration in a structural system from the impact loads and the responses of the structure. For damage detection and structural health monitoring, techniques based on vibration data have been extensively used. Thus, the damage evaluation of structures has derived wide consideration from engineering fields.

The various computational techniques have been used to solve the damage detection problem such as genetic algorithm (GA), differential evolution algorithm (DE), and particle swarm optimization (PSO). Among non-gradient-based methods, GA has been used widely from damage detection field. The GA is a well-known global optimizer based on the Darwin's theory of evolution and survival of the fittest and the natural process through reproduction [1]. It makes the mechanisms of biological evolution to perform optimization without information regarding the objective function. Generally, the GA has been shown to be solved various optimization problems through some basic concepts and operators. However, some research work has appeared that it is complex for the simple GA to solve the damage quantification problems properly. To achieve a better detection result, the various optimization algorithms were improved [2–4]. Krishnakumar [5] proposed the micro-genetic algorithm based on serial genetic algorithms [6], and Koh and Dyke [2] proposed the use of correlation-based damage detection methods for long-span cable-stayed bridge. Nobahari and Seyedpoor [7] proposed a modified genetic algorithm (MGA) to identify multiple damage and two new tools to recognize the actual damage correctly and rapidly. Also, he used the DE algorithm to solve the optimization problem for detecting actual sites and elements which was demonstrated by truss structures. The GA has discrete design variables, and new attempts based on continuous domain have been proposed such as PSO, DE, and ant colony optimization (ACO).

Turning to the problems of global optimization method, Storn and Price [8] proposed the differential evolution (DE) algorithm as a simple and powerful population-based stochastic method, which has an operation process similar to GA. In order to overcome the shortcomings of the non-gradient-based methods regarding computational time as well as of the gradient-based methods concerning solution accuracy, several variations of DE algorithm have been suggested. Pampara et al. [9] suggested a binary DE using trigonometric functions, in which experimental results indicate the effectiveness of the technique and the viability for the DE to operate in binary space. Zou et al. [10] proposed to solve constrained optimization problems using a modified differential evolution algorithm. Its own crossover rate and scale factor were adjusted using uniform distribution, and mutation phase was modified to enhance the convergence for unconstrained optimization problems. Concerning the damage detection, Vo-Duy et al. [11] used a strain energy-based method and an improved differential evolution algorithm to locate and quantify damage on the laminated composite plate. Also, Dinh-Cong et al. [12] proposed a two-stage damage identification method to identify the location and extent of multiple damages at individual layers in laminated composite beams using DE algorithm. Jena et al. [13] presented a damage detection technique combining analytical and experimental investigations on a cantilever aluminum alloy beam with a transverse surface crack. The damage location and assess-

ment is the third stage and is formulated as a constrained optimization problem and solved using the proposed differential evolution algorithm.

Based on the mentioned researches, the mDE has not yet been used as optimizer for 2D and 3D truss structures based on force method and vibration data until now. In this study, a mDE combined with the free vibration analysis is proposed as a highly efficient algorithm for performing the damage identification of truss structures. The introduced algorithm resolves efficiently the limitation of GA by randomly continuous design variables instead of discrete domain as in the GA. In order to solve the problem, the number of design variables and member types of truss structures are first defined. Design variables are randomly created in the range of lower and upper bounds based on the number of design variables. Consequently, based on the force method with the present mDE in the damage detection process, the results satisfying the required deficiencies of the force method and equilibrium matrices are selected.

2 Theoretical Modeling

In order to build a model for truss structure, the general equations and relations are briefly presented. Several approaches that are similar to those can be found in the literature [14, 15]. For a d -dimensional ($d = 2$ or 3) truss structure with m members, n free nodes, and n_c constrained nodes, its topology can be expressed by a connectivity matrix \mathbf{C}_s [16]. Let r_c be the unknown vector of reaction forces employed to remove all boundary constraints. Therefore, the constrained nodes can now be treated as free nodes. In the context, the general equilibrium equations for all nodes (including constrained nodes) of the discrete truss can be written as follows:

$$\bar{\mathbf{A}}\bar{\mathbf{f}} = \bar{\mathbf{p}} \quad (1)$$

where $\bar{\mathbf{A}}$ is called the general equilibrium matrix of all nodes, which transforms the vector of member and reaction forces $\bar{\mathbf{f}}$ to the vector of external loads $\bar{\mathbf{p}}$, $\bar{\mathbf{f}}$ is the unknown member and reaction force vector, and $\bar{\mathbf{p}}$ is the external load vector of all nodes.

In this study, the SVD method is used as an effective and numerically stable algorithm in order to extract r compatibility conditions. The SVD is performed on the general equilibrium matrix $\bar{\mathbf{A}}$ instead of the kinematic matrix \mathbf{B} (i.e., the transpose of the general equilibrium matrix $\bar{\mathbf{A}}$). The compatibility equations expressed in terms of forces are obtained as follows:

$$\mathbf{D}\bar{\mathbf{f}} = \mathbf{p}_{e_o} \quad (2)$$

where \mathbf{D} is the compatibility matrix in terms of forces of all members and \mathbf{p}_{e_o} is the virtual force vector in the indeterminate truss caused by member initial elongations \mathbf{e}_o .

For the free vibration analysis, the extended equation of motion based on the force method can be written as

$$\bar{\mathbf{M}}\ddot{\bar{\mathbf{d}}} + \tilde{\mathbf{A}}\bar{\mathbf{f}} = 0 \quad (3)$$

where $\bar{\mathbf{M}}$ is the extended mass matrix, $\ddot{\bar{\mathbf{d}}}$ is the extended acceleration vector, and $\tilde{\mathbf{A}}$ is the square full-rank matrix coupling the general equilibrium matrix and the compatibility matrix. For this analysis case, it is assumed that element forces are harmonics in time, $\bar{\mathbf{f}} = \bar{\mathbf{F}}\sin(\omega t)$, where ω and $\bar{\mathbf{F}}$ are the circular frequency and corresponding force mode shape, respectively. Therefore, equation [14] can be written as the following eigenvalue problem

$$(\tilde{\mathbf{A}} + \omega^2\mathbf{B})\bar{\mathbf{F}} = 0 \quad (4)$$

where

$$\mathbf{B} = \bar{\mathbf{M}}\tilde{\mathbf{A}}^{-T}\mathbf{G} \quad (5)$$

and $\bar{\mathbf{M}}$ is the extended mass matrix.

3 Structural Damage Detection

To determine the location and extent of the damages more accurately, the natural frequency and the mode shape changes are demanded *messina_s,structural_1998, wang_s,structural_2001*. In this study, the objective function based on the sum of two formulations is given as follows:

$$f(\mathbf{X}) = f_1(\mathbf{X}) + f_2(\mathbf{X}) \quad (6)$$

where

$$f_1(\mathbf{X}) = \sum_{i=1}^n \frac{|\omega_{di} - \omega_i(\mathbf{X})|}{\omega_{di}} \quad (7)$$

and

$$f_2(\mathbf{X}) = \sum_{i=1}^n \sum_{j=1}^m \left\| \frac{\Phi_{dj} - \Phi_j(\mathbf{X})}{\Phi_{dj}} \right\| \quad (8)$$

where ω_i is the corresponding hypothesis natural frequency which is can be expected from analytic model and ω_{di} is the i th natural frequency of the damaged truss. Φ_{dj} and $\Phi_j(\mathbf{X})$ are the j th component of the i th damaged force eigenvector and the j th component of the i th hypothesis force eigenvector, respectively, in $f_2(\mathbf{X})$. Then, the optimal design problem for damage identification of the truss structure is formulated

as follows:

$$\text{Minimize } f(X) + \gamma g(X) \quad (9)$$

in which

$$g(X) = (n_d - n_h)^2 \quad \text{for } n_d > n_h \quad (10)$$

where x_i is the damaged elastic modulus of the i th member, γ is the penalty parameter, n_d and n_h are the number of the damaged elements and the number of the healthy elements, respectively. In real life, the healthy members are more than the damaged members in structures. Thus, both algorithms in this study can be accelerated to find better solution using the penalty function $g(X)$. In many researches related to the damage detection problem, the damage has been simulated by decreasing one of the stiffness parameters of the element. In this study, the damage of truss structures is simulated by the reduction in the elasticity modulus in each element as

$$x_i = \frac{E - E_i}{E}, \quad i = 1, \dots, n \quad (11)$$

where E is the initial elastic modulus and E_i is the final elastic modulus of n th element.

4 Optimization Algorithm

4.1 Differential Evolution Algorithm

Differential evolution (DE) has been first proposed by Storn and Price [8] as a vector-based metaheuristic algorithm. The DE has similarity to genetic algorithms, its use of selection, crossover, and mutation. The DE is a stochastic search algorithm with self-organizing tendency and does not use the information of derivatives [17]. Thus, it is a population-based, derivative-free method. In addition, DE uses real numbers as solution strings, so no encoding and decoding is needed. The main procedure of DE includes mutation, crossover, selection, and initialization of design variables.

4.1.1 Initialization

In the DE algorithm, d -dimensional real number of design variable vectors is randomly generated as much as population size for global optimum point. The i th vector of the population at any iteration can be expressed by conventional notation as

$$X_i = \{x_{i,1}, x_{i,2}, \dots, x_{i,d}\} \quad (12)$$

where X_i is a vector at i th population and d is a number of design variables in X_i vector. It is noted that this vector, called target vector, can be considered as chromosomes. A d -dimensional vector represents a candidate result to the problem and is randomly made in the domain as follows:

$$x_{i,j} = x_{\min,j} + \text{rand} \times (x_{\max,j} - x_{\min,j}), \quad i = 1, \overline{\text{NP}}, \quad j = 1, \bar{n} \quad (13)$$

where NP is the population size, n is the number of design variables or dimensions, rand is a uniformly distributed random number in the interval $[0,1]$, $x_{i,j}$ is the j th component of individual \mathbf{x}_i , and $x_{\min,j}$ and $x_{\max,j}$ are the lower and upper bounds of x_j , respectively.

4.1.2 Mutation

In the mutation step, DE generates a mutant vector \mathbf{v}_i based on the target vector \mathbf{x}_{r_1} by using mutation operation at the current iteration. The frequently used some mutation schemes are introduced as below:

$$\mathbf{v}_i = \mathbf{x}_{r_1} + F \times (\mathbf{x}_{r_2} - \mathbf{x}_{r_3}) \quad (14)$$

where \mathbf{v}_i is a mutation vector and known as a new candidate solution; \mathbf{x}_{r_1} , \mathbf{x}_{r_2} , and \mathbf{x}_{r_3} are candidate solutions; r_1 , r_2 , and r_3 are randomly determined from $[1, \overline{\text{NP}}]$ to satisfy the constraints as $r_1 \neq r_2 \neq r_3 \neq i$; the scale factor F can be selected within the range $F \in [0, 2]$.

4.1.3 Crossover

In the crossover process, trial vector \mathbf{u}_i is created by combining the target vector \mathbf{x}_i and the mutant vector \mathbf{v}_i . The combination of these vectors in this process is controlled by a crossover ratio (CR) chosen in the range $[0,1]$. The CR controls how likely it is that each component of \mathbf{u}_i comes from the mutant vector \mathbf{v}_i and is defined by user. The range $[0.1,0.8]$ or 0.5 can get good result at the beginning.

The crossover phase is generally performed two schemes: binomial and exponential. Due to its simplicity, the binomial crossover is employed and defined as follows:

$$u_{i,j} = \begin{cases} v_{i,j}, & \text{if } (\text{rand}_{i,j} < CR) \text{ or } (j = j_{\text{rand}}) \\ x_{i,j}, & \text{otherwise} \end{cases} \quad (15)$$

in which $\text{rand}_{i,j}$ is a uniformly distributed random number $[0,1]$ and j_{rand} is the integer chosen from $[0,1]$.

4.1.4 Selection

Finally, the \mathbf{u}_i and \mathbf{x}_i vectors are compared so that the most fit vector in each pair is kept for the next generation and the least fit is discarded. This selection process is essentially the same as that used in GA and expressed as

$$\mathbf{x}_i^{new} = \begin{cases} \mathbf{u}_i, & \text{if } f(\mathbf{u}_i) \leq f(\mathbf{x}_i) \\ \mathbf{x}_i, & \text{otherwise} \end{cases} \quad (16)$$

where $f(\mathbf{u}_i)$ and $f(\mathbf{x}_i)$ are the objective functions.

4.2 A Modified Differential Evolution Algorithm

In this section, mutation and selection phases are modified to overcome the drawbacks of the non-gradient- and gradient-based algorithms.

4.2.1 Modification of the Mutation Phase

Two mutation operators are adaptively chosen based on the absolute value of deviation of objective function between the best individual and the entire population in the previous generation (denoted as δ). More specifically, the value of δ is defined by

$$\delta = \left| \frac{f_{mean} - f_{best}}{f_{best}} \right| \quad (17)$$

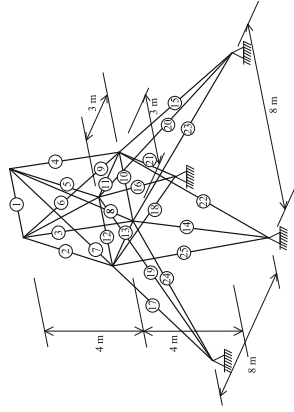
where f_{mean} is the mean objective function value of the whole population and f_{best} is the objective function value of the best individual. The new mutation scheme is described as follows:

$$\mathbf{v}_i = \begin{cases} \mathbf{x}_{best} + F^k \times (\mathbf{x}_{r_1} - \mathbf{x}_{r_2}), & \text{if } \delta > \text{threshold} \\ \mathbf{x}_{r_1} + F^k \times (\mathbf{x}_{r_2} - \mathbf{x}_{r_3}), & \text{otherwise} \end{cases} \quad (18)$$

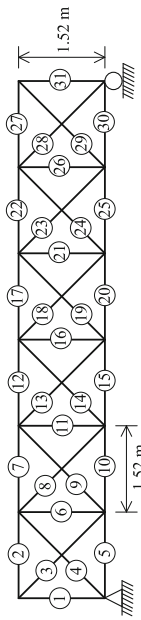
where F^k is a number randomly chosen in $[0,1]$ at the k th iteration; threshold is a criterion value which is chosen based on the stopping criterion of the algorithm.

4.2.2 Modification of the Selection Phase

In the DE's selection, the vectors are compared and unselected individual is worse than its target individual in the pair, but it can be still better than other individuals in the entire population. Consequently, several good information of unselected indi-



(b) The 25-bar space truss



(a) The 31-bar planar truss

Fig. 1 Two- and three-dimensional truss structures

viduals can be omitted and the convergence speed of the DE algorithm is slow. The good individuals are kept for the next iteration as follows:

$$Q = P \cup U \tag{19}$$

Table 1 Induced elastic modulus for 31-bar planar truss

Member	x_i	GA (dq)				PSO	This study
		0.1	0.05	0.01	0.001		
1	0	0.0	0.00	0.00	0.008	0.027	0.073
2	0	0.0	0.00	0.00	0.000	0.050	0.034
3	0	0.0	0.00	0.02	0.152	0.065	0
4	0	0.0	0.00	0.00	0.000	0.040	0.006
5	0	0.0	0.00	0.00	0.078	0.060	0.022
6	0	0.0	0.00	0.15	0.000	0.062	0.01
7	0	0.0	0.00	0.00	0.000	0.008	0.006
8	0.475	0.5	0.50	0.42	0.407	0.475	0.475
9	0	0.0	0.00	0.00	0.000	0.009	0.016
10	0	0.0	0.00	0.00	0.000	0.011	0
11	0	0.2	0.00	0.11	0.011	0.021	0.099
12	0	0.0	0.00	0.00	0.000	0.018	0.085
13	0	0.0	0.00	0.05	0.038	0.033	0.088
14	0	0.0	0.00	0.00	0.047	0.065	0.076
15	0	0.0	0.00	0.00	0.012	0.006	0.048
16	0.319	0.1	0.30	0.17	0.000	0.319	0.319
17	0	0.0	0.00	0.00	0.008	0.045	0.058
18	0	0.0	0.00	0.06	0.000	0.073	0.021
19	0	0.0	0.00	0.04	0.000	0.081	0.01
20	0	0.0	0.00	0.00	0.088	0.010	0.005
21	0	0.2	0.00	0.06	0.000	0.008	0.036
22	0	0.0	0.00	0.00	0.002	0.078	0
23	0	0.0	0.00	0.00	0.148	0.035	0.013
24	0	0.0	0.00	0.07	0.000	0.015	0.002
25	0	0.0	0.00	0.00	0.000	0.005	0.018
26	0	0.0	0.00	0.05	0.096	0.019	0.03
27	0	0.0	0.00	0.00	0.000	0.026	0.029
28	0	0.0	0.00	0.00	0.010	0.048	0.003
29	0	0.0	0.00	0.00	0.082	0.022	0.013
30	0	0.0	0.00	0.00	0.000	0.050	0.088
31	0	0.0	0.00	0.00	0.000	0.024	0
$f(X)$		1.86E-2	6.62E-3	4.19E-2	1.41E-1	4.37E-8	3.86E-11

where \mathbf{P} and \mathbf{U} are populations consisting of NP individuals \mathbf{x}_i and \mathbf{u}_i with $i = 1, \overline{\text{NP}}$, respectively; \mathbf{Q} includes all individuals of \mathbf{P} and \mathbf{U} . Then, NP best individuals in \mathbf{Q} are chosen to create a new population for the next iteration. Thus, the best solutions of the whole population are always stored for the next generation and the convergence rate is significantly improved.

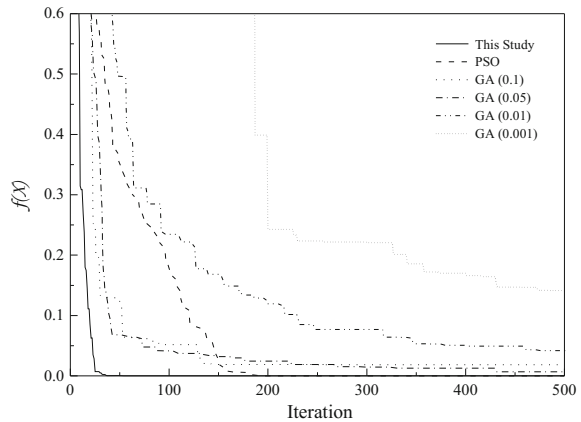
5 Numerical Examples

In this section, two- and three-dimensional truss structures are investigated using GA, PSO, and proposed mDE algorithm. The searching process of these algorithms will be stopped when the maximum number of iterations is reached. In all examples, the crossover ratio (CR) for the proposed mDE and GA is set to be 0.6 and 1.0, respectively. Accordingly, all populations have to perform a crossover operation at all generation and there is no use of mutation process. The first three natural frequencies and mode shapes are used for detection. mDE algorithm and PSO find solution in a continuous domain, while results gained by GA are done in a discrete domain. The numerical results obtained by mDE are compared to GA and PSO to illustrate the accuracy and effectiveness of the proposed algorithm.

5.1 31-Bar Planar Truss

The first example is a 31-bar planar truss as shown in Fig. 1 and is modeled using 28 consistent finite elements without internal nodes leading to 25 degrees of freedom. The elasticity modulus $E = 70$ GPa, the mass density $\rho = 2,770$ kg/m³, and the area of cross section $A = 0.01$ m². For every algorithms, the maximum number of

Fig. 2 Convergence history of the 31-bar planar truss



iterations and population size are respectively set to be 500 and 300. In damage case, as damage ratios, the stiffness reduction in elasticity modulus 0.475 and 0.319 is induced at elements 8 and 16, respectively. The detected damages are shown by comparing the ratios of elasticity modulus reduction in GA, PSO, and mDE. Here, GA is considered with four different step points $dq = 0.1, 0.05, 0.01, \text{ and } 0.001$. The obtained results are expressed in Table 1 in comparison with each step points of GA and PSO. From this table, the damage location and extent of proposed algorithm were successfully determined than other cases of GA and agree well with this acquired by PSO. In a narrow discrete domain of search space, GA cannot find exact damage. Thus, GA have some difficulties about the accuracy of the solution if real solutions have many digits after the decimal point. Figure 2 shows the comparison

Table 2 Induced elastic modulus for 25-bar space truss

Member	x_i	GA (dq)				PSO	This study
		0.1	0.05	0.01	0.001		
1	0	0.0	0.40	0.00	0.596	0.022	0
2	0	0.0	0.00	0.00	0.006	0.011	0.008
3	0	0.0	0.00	0.03	0.022	0.008	0.006
4	0	0.0	0.05	0.00	0.066	0.029	0.052
5	0	0.0	0.00	0.00	0.276	0.064	0.056
6	0.383	0.4	0.40	0.45	0.328	0.383	0.383
7	0	0.0	0.00	0.04	0.194	0.048	0.061
8	0	0.0	0.15	0.00	0.004	0.069	0.02
9	0	0.0	0.00	0.00	0.069	0.040	0
10	0	0.1	0.25	0.24	0.055	0.052	0.01
11	0	0.1	0.00	0.08	0.295	0.092	0
12	0	0.0	0.00	0.27	0.089	0.077	0.064
13	0	0.0	0.00	0.00	0.232	0.041	0
14	0	0.0	0.00	0.00	0.137	0.030	0.024
15	0	0.0	0.00	0.00	0.047	0.071	0.039
16	0.294	0.3	0.40	0.32	0.522	0.294	0.294
17	0	0.0	0.05	0.01	0.002	0.019	0.04
18	0	0.0	0.00	0.00	0.097	0.051	0.022
19	0	0.0	0.05	0.00	0.019	0.087	0.058
20	0	0.0	0.00	0.03	0.070	0.047	0.066
21	0	0.0	0.00	0.00	0.006	0.085	0.055
22	0	0.0	0.00	0.00	0.045	0.062	0.02
23	0	0.0	0.00	0.04	0.018	0.082	0.001
24	0	0.0	0.05	0.00	0.165	0.088	0.025
25	0	0.0	0.00	0.00	0.106	0.063	0.096
$f(X)$		3.37E-02	2.05E-01	1.34E-01	8.65E-01	9.76E-7	2.80E-11

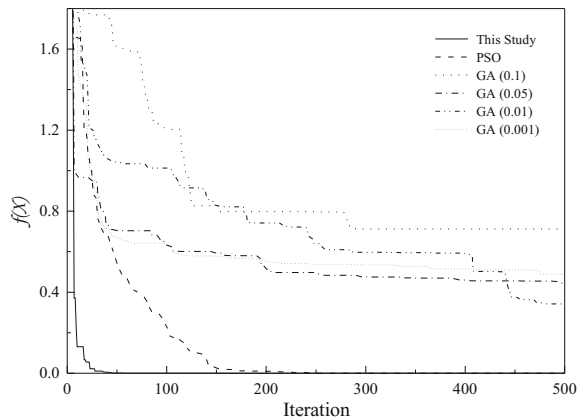
of the convergence of each cases of GA, PSO and mDE at the whole iterations. As shown in the figure, mDE converges faster and lower than GA. For more detail, the mDE converges in 00 iterations with an objective function $f(X) = 3.86 \times 10^{-11}$ in the first damage case, while each step point of GA converges 1.86×10^{-2} , 6.62×10^{-3} , 4.19×10^{-2} , and 1.41×10^{-1} corresponding step points 0.1, 0.05, 0.01 and 0.001, respectively.

5.2 25-Bar Space Truss

The 25-bar space truss is shown in Fig. 1, with 10 nodes leading to 18 degrees of freedom. The area of cross section $A = 0.25 \text{ m}^2$, the material density $\rho = 7,830 \text{ kg/m}^3$, and the modulus of elasticity $E = 210 \text{ GPa}$. Likewise, the maximum number of iterations and population size are, respectively, set to be 500 and 300.

As a case of damage, the stiffness reductions in elasticity modulus 0.383 and 0.294 are induced at elements 6 and 16, respectively. The results gained by this example in comparison with the GA and PSO are presented in Table. 2. It can be seen that the present algorithm has shown excellent performance for damage detection than all step points of GA and agrees well with the result of PSO. When the step point increases, the gained results of GA are less accurate. Moreover, the convergence history of GA, PSO, and mDE are shown in Fig. 3. It demonstrates that mDE converges even faster than GA. Specially, mDE converges as 2.80×10^{-11} , while each step point of GA converges as 3.37×10^{-2} , 2.05×10^{-1} , 1.34×10^{-1} , and 8.65×10^{-1} corresponding to step points $dq = 0.1, 0.05, 0.01, \text{ and } 0.001$, respectively, and the value of converged objective function from PSO is 9.76×10^{-7} .

Fig. 3 Convergence history of the 25-bar space truss



6 Conclusion

This study proposed the optimization technique which properly determines the locations and extents of multiple damages of planar and space trusses based on the modified differential evolution (mDE) algorithm with comparative studies. To generate the compatibility conditions for indeterminate trusses, the singular value decomposition technique is employed on the general equilibrium equations. The force mode vectors are introduced as eigenvectors in the objective function. The optimization problem has been solved using mDE which has continuous design variables to identify the actual damages. Three illustrated test examples such as planar and space trusses are considered in order to assess the performance of the proposed method. Throughout the numerical examples, the relative performance of mDE, GA, and PSO in the damage detection of trusses is studied. Numerical results show that the combination of the present force method and mDE is far more efficient than PSO and GA with discrete design variables for identifying multiple damages of trusses.

References

1. Michalewicz Z (1994) GAs: What are they? In: Genetic algorithms + data structures = evolution programs. Springer, Heidelberg, p. 13–30. https://doi.org/10.1007/978-3-662-07418-3_2
2. Bertalmio M, Sapiro G, Caselles V, Ballester C (2000) Image inpainting. In: Proceedings of the 27th annual conference computer graphics and interactive techniques. ACM Press/Addison-Wesley Publishing Co., New York, NY, USA, pp 417–424
3. Chan T, Vese L (2001) Active contours without edges. *IEEE Trans Image Process* 10(2):266–277
4. Criminisi A, Pérez P, Toyama K (2004) Region filling and object removal by exemplar-based image inpainting. *IEEE Trans Image Process* 13:1200–1212
5. Emerson C, Lam N, Quattrochi D (1999) Multi-scale fractal analysis of image texture and patterns. *Photogramm Eng Remote Sens* 65(1):51–62
6. Farias M, Mitra S (2005) No-reference video quality metric based on artifact measurements. In: Proceedings of the international conference on image processing, vol 3, pp III–141–4
7. Faugeras O, Lustman F (1988) Motion and structure from motion in a piecewise planar environment. Technical report RR-0856, INRIA
8. Fischler MA, Bolles RC (1981) Random sample consensus: a paradigm for model fitting with applications to image analysis and automated cartography. *Commun ACM* 24(6):381–395
9. Google images (2012). <http://www.images.google.com>
10. Guillemot C, Meur OL (2014) Image inpainting: overview and recent advances. *IEEE Signal Process Mag* 31(1):127–144
11. Hartley R, Zisserman A (2003) Multiple view geometry in computer vision, 2nd edn. Cambridge University Press, New York, NY, USA
12. Jobson DJ, Rahman Z, Woodell GA (1997) Properties and performance of a center/surround retinex. *IEEE Trans Image Process* 6(3):451–462
13. Katahara S, Aoki M (1999) Face parts extraction windows based on bilateral symmetry of gradient direction. *Computer analysis of images and patterns*, vol 1689. Springer, Heidelberg, pp 834–834
14. Kenney JF (1954) *Mathematical statistics*. Van Nostrand

15. Kovesi PD (2005) MATLAB and Octave: functions for computer vision and image processing. Centre for Exploration Targeting, School of Earth and Environment, The University of Western Australia. <http://www.csse.uwa.edu.au/pk/research/matlabfns/robust/ransacfithomography.m>
16. Legrand P (2009) Local regularity and multifractal methods for image and signal analysis. In: Scaling, fractals and wavelets. Wiley
17. Lowe DG (2004) Distinctive image features from scale-invariant keypoints. *Int J Comput Vis* 60(2):91–110

Finite Element Simulation on Small Punch Test for an Evaluation of J -integral for TRIP Steel



H. T. Pham and T. Iwamoto

Abstract The small punch test (SPT) has been recently successfully developed for the purpose of evaluating the fracture toughness in not only brittle but also ductile materials. It is considered that fracture toughness of materials can be estimated by means of the SPT based on the measurement of equivalent fracture strain in the SPT and its correlation with fracture toughness. Moreover, fracture toughness of TRIP (transformation-induced plasticity) steel was evaluated by J -integral by using pre-cracked specimen under three-point bending test in the past study. However, the value of J -integral is determined at a limited range of deformation rate in three-point bending test. Thus, fracture toughness of TRIP steel needs to be evaluated by means of the SPT, especially at a relatively high deformation rate. Additionally, since the effect of strain-induced martensitic transformation during plastic deformation of TRIP steel coupled with a high increase of temperature is quite complicated, a computational work is indispensable. In this study, finite element simulations are performed for the SPT at various deflection rates and different sizes of specimen and puncher by an application of damage model for type-304 austenitic stainless steel, a kind of TRIP steel. The rate-sensitivity of fracture-mechanical characteristics is examined for different sizes of specimen and puncher. Furthermore, a relationship between equivalent fracture strain in the SPT and J -integral obtained from three-point bending test is challenged to be correlated.

Keywords TRIP steel • J -integral • Small punch test • Finite element simulation

H. T. Pham (✉)

Faculty of Engineering, Vietnam National University of Agriculture, Hanoi, Vietnam
e-mail: pthang@vnua.edu.vn

T. Iwamoto

Academy of Science and Technology, Hiroshima University, Higashihiroshima, Japan
e-mail: iwamoto@mec.hiroshima-u.ac.jp

© Springer Nature Singapore Pte Ltd. 2018

H. Nguyen-Xuan et al. (eds.), *Proceedings of the International Conference on Advances in Computational Mechanics 2017*, Lecture Notes in Mechanical Engineering, https://doi.org/10.1007/978-981-10-7149-2_2

1 Introduction

The small punch test (SPT), a kind of test for bending deformation using very small disc specimens, has become widespread over last decades. It has been widely applied to evaluate mechanical properties [1] due to a simple testing methodology as well as a reduction of machining costs. Also, the SPT is successfully developed for the purpose of evaluating the fracture toughness in not only brittle but also ductile materials [2–5]. It is considered that fracture toughness of materials can be estimated by means of the SPT based on the measurement of equivalent fracture strain in the SPT and its correlation with fracture toughness [4].

On the other hand, TRIP (transformation-induced plasticity) steel has been nowadays wide application in automotive industries to keep the safe upon to a collision of vehicle because of its high energy absorption capacity [6, 7]. In order to utilize its application in impact condition, the fracture-mechanical characteristics of TRIP steel, which are subjected to high deformation rate, need to be investigated. In the previous study [8], fracture toughness of TRIP steel was evaluated by J -integral by using pre-cracked specimen under three-point bending test. However, the value of J -integral is determined at a limited range of deformation rate because a conventional impact test based on the Split Hopkinson pressure bar method cannot be applied for a large dimension specimen. From the point of view mentioned above, fracture toughness of TRIP steel can be evaluated by means of the SPT, especially at a relatively high deformation rate and an investigation on SPT for TRIP steel is necessary. Additionally, since the effect of strain-induced martensitic transformation during plastic deformation of TRIP steel coupled with a high increase of temperature is quite complicated [9, 10], a finite element simulation is indispensable.

The relationship between fracture toughness of materials and equivalent fracture strain obtained from SPT in austenitic stainless steel, a kind of TRIP steel, was investigated by some researchers. Mao et al. [4] reported that equivalent fracture strain can be directly related to the fracture toughness, and an empirical formulation was proposed for this relationship. Then, Shindo et al. [11] introduced an equation for the correlation of J -integral and equivalent fracture strain in SPT only under the condition of low deformation rate and cryogenic temperature for some austenitic stainless steels. More recently, computational on SPT of type-304 austenitic stainless steel was conducted by Ling et al. [12]. The size effect of specimen and puncher in SPT for this material was examined by Yang et al. [13] by means of a finite element simulation with an application of a damage model. Although numerous investigations on SPT can be found, standardization of this method is still in progress [14]. As a result, an examination of the size effect as well as an evaluation of J -integral by means of SPT needs to be conducted for TRIP steel.

In this study, finite element simulations are performed for the SPT at various deflection rates and different sizes of specimen and puncher by an application of damage model for type-304 austenitic stainless steel, a kind of TRIP steel. Then, a comparison of computational results with experimental result as well as other

publication is given to confirm the validity of computation. The rate-sensitivity of fracture-mechanical characteristics is examined for different sizes of specimen and puncher. Furthermore, based on the conventional method, a relationship between equivalent fracture strain in the SPT and J -integral obtained from three-point bending test on pre-cracked specimen in the previous study [8] is challenged to be correlated.

2 Methodology

2.1 Conventional Method for Estimation of Fracture Toughness from the SPT

Figure 1 shows a schematic illustration of the SPT. In the actual situation, a disc specimen is placed in the center of the lower die. The upper and lower dies of the fixture are clamped together by the screws. During the test, the load is applied to the specimen through a puncher which consists of a pusher rod and a hard ball made of steel or ceramic.

Figure 2 shows a typical plot of the force-deflection curve obtained from the SPT [5]. The force-deflection curve can be divided into several parts [5]. Part I mainly indicates the purely elastic properties of the materials. Part II describes the transition between the elastic and elasto-plastic deformation behavior. Part III corresponds to membrane stretching behavior due to plastic bending up to part IV where the first necking is produced and then damage occurs.

Furthermore, it is reported that equivalent fracture strain is one of the most important fracture parameter of the SPT for an evaluation of fracture toughness of materials [3–5]. In order to obtain equivalent fracture strain, the values of the thickness in the specimen at the thinnest section, t_f , are necessary to measure. A measurement of t_f is indicated in Fig. 3 which shows a photograph of the

Fig. 1 A schematic illustration of the SPT apparatus

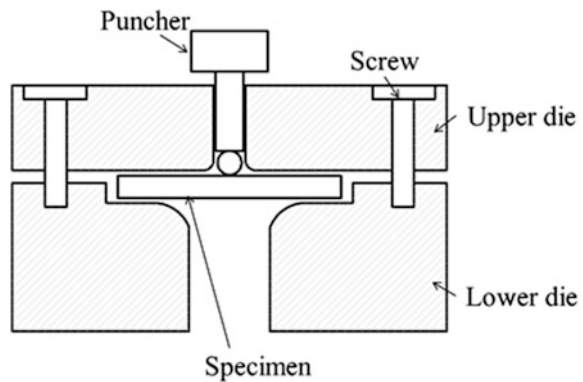


Fig. 2 A typical force-deflection curve obtained from the SPT [5]

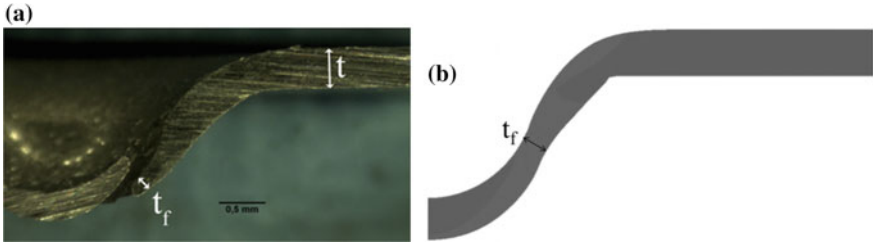
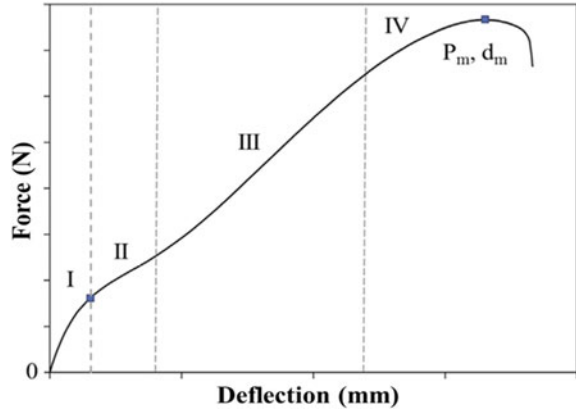


Fig. 3 A method for measurement of thickness of deformed specimen at the thinnest section in **a** experiment [5] and **b** simulation

deformed specimen after failure in experiment [5] and simulation. The profile of deformed specimen obtained from the simulation is examined at the level of deformation at maximum force, d_m . Since t_f cannot be measured by the same method to that in Fig. 3a, it is determined by the thickness of specimen at the thinnest section at this level of deformation as shown in Fig. 3b. Then, the equivalent fracture strain, $\bar{\epsilon}_{qf}$, is determined by using the following equation under an assumption that the volume of specimen during plastic deformation is constant [4].

$$\bar{\epsilon}_{qf} = \ln\left(\frac{t_o}{t_f}\right) \tag{1}$$

where t_o is the initial thickness of the specimen. At the same time, $\bar{\epsilon}_{qf}$ can also be calculated from the value of deflection at the initial fracture, d_f . However, the determination of initial fracture of specimen in the SPT is quite complicated. Therefore, the value of deflection at the maximum force, d_m as shown in Fig. 2,

is usually used instead of d_f in some past studies [4, 5] for a calculation of $\bar{\epsilon}_{qf}$ in the SPT as,

$$\bar{\epsilon}_{qf} = \alpha \left(\frac{d_m}{t_o} \right)^n \quad (2)$$

Value of α and n can be identified from a correlation between $\ln(t_o/t_f)$ and d_m/t_o in a logarithmic plot. Finally, a correlation of equivalent fracture strain in the SPT and fracture toughness of the material is challenged to obtain.

2.2 Computational Method

2.2.1 Damage Model Applied for Finite Element Simulation

The kinetics model of SIMT proposed by Iwamoto et al. [9] and the multiaxial constitutive equations [10] including the heat conduction equation [15] for TRIP steel are employed. In addition, in order to describe the damage and fracture process of material, a modified version of the Johnson-Cook (JC) damage model [16] is applied. In the paper by Yoon et al. [17], the damage variable at a material element, ω , can be incorporated into the constitutive relation when the value of ω is less than 1.

It is assumed that the failure is occurred only in the parent phase and it is only included into the stress-strain relationship of parent phase as,

$$\bar{\sigma}_{0(\gamma)} = (1 - \omega) \left\{ \sigma_{y(\gamma)} + C_1 \left[1 - \exp \left(-C_2 \bar{\epsilon}_{(\gamma)}^{pslip} \right) \right]^{C_3} \right\} \quad (3)$$

The damage variable is determined by Dey et al. [18] based on the JC damage model as,

$$\omega = \int \frac{\dot{\bar{\epsilon}}_{(\gamma)}^{pslip}}{\bar{\epsilon}_f} dt, \quad (4)$$

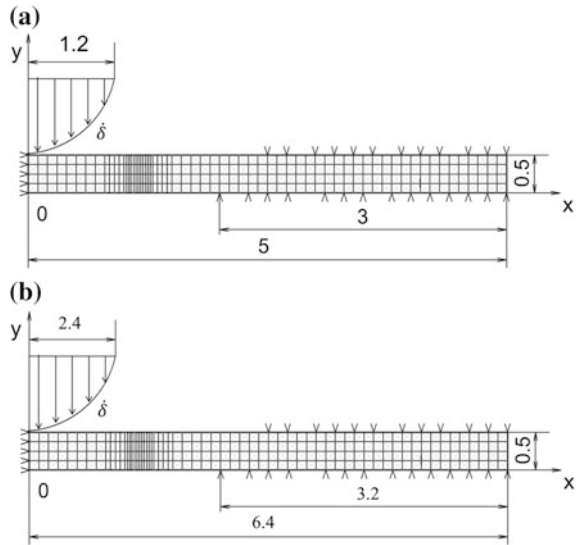
$$\bar{\epsilon}_f = \{D_1 + D_2 \exp(D_3 \Sigma)\} \left(1 + \frac{\dot{\bar{\epsilon}}_{(\gamma)}^{pslip}}{\dot{\epsilon}_0} \right)^{D_4} \left(1 + D_5 \frac{T - T_r}{T_m - T_r} \right),$$

where t is the time, $\bar{\epsilon}_f$ is the equivalent fracture strain of one material element, T is absolute temperature and $D_1 \sim D_5$ are material parameters. Table 1 shows the newly identified parameters for type-304 austenitic stainless steel.

Table 1 Material parameters of damage model for type-304 austenitic stainless steel

D_1	D_2	D_3	D_4	D_5	T_r (K)	T_m (K)
2.0	1.936	-2.969	-0.06	1.014	293	1673

Fig. 4 A finite element model for an axisymmetric computational simulation in the case of puncher with diameter of **a** 2.4 and **b** 4.8 mm



2.2.2 Finite Element Model and Boundary Conditions

In this study, a disc specimen with 10 mm in diameter and 0.5 mm in thickness is used. The diameter of the puncher is 2.4 mm, and the span length is set to be 4 mm. In order to investigate the influence of dimension of specimen as well as puncher on rate-sensitivity of fracture-mechanical characteristics, another bigger specimen with 12.8 mm in diameter and 0.5 mm in thickness is also used. The diameter of the puncher is 4.8 mm, and the span length is 6.4 mm in this case. Figure 4 shows a finite element model for an axisymmetric computational simulation in the case of puncher with diameter of (a) 2.4 and (b) 4.8 mm. The simulation is performed at 293 K for both cases of the puncher. Due to a symmetry on the shape of the specimen and boundary condition, the deformation of the specimen in an entire region is simulated with the finite element discretization by a crossed-triangular axisymmetric element. Partial areas of the lower and upper surfaces of the specimen are fixed as similar to the paper by Ling et al. [12]. The nodal displacement rates, δ , at the axisymmetric boundary in the horizontal direction and the fixed surfaces in the vertical direction are set to be zero.

3 Results and Discussion

3.1 Validity of Computation and the Size Effect on the Rate-Sensitivity of Mechanical-Fracture Characteristics

Figure 5 shows a force-deflection curve obtained from experiment and simulation at deflection rate of 0.033 mm/s for the cases of puncher with diameter of 2.4 and 4.8 mm. The shape of the curves is quite similar to a typical shape of force-deflection curve in SPT as shown in Fig. 2. In both cases of puncher, a fairly good agreement between experiment and computation can be seen. From this figure, the deflection at the maximum force is determined to be 1.8 and 2.5 mm for the puncher with diameter of 2.4 and 4.8 mm, respectively.

Moreover, Fig. 6 shows the shape of deformed specimen in the simulation with the distribution of the damage variable at deflection rate of 0.033 mm/s and deflection at the maximum force for the case of puncher having 2.4 mm in diameter. The value of damage variable is concentrated in a small region where a necking may appear. The profile of deformed specimen in the simulation as well as position of fracture point is quite similar to that in Fig. 3a and observation of Ling et al. [12]. From Figs. 5 and 6, the validity of computational results can be confirmed sufficiently.

Figure 7 shows the force-deflection relationship at different deflection rates for two cases of the puncher. In general, the case of larger puncher shows higher value of maximum force and deflection at the maximum force. Therefore, it can be considered that the total consumption energy, which is calculated by the area under the force-deflection curve until the maximum force, increases with an increase in the diameter of the puncher and specimen. From this figure, a bigger specimen with larger puncher is fractured at larger deformation compared to a smaller one.

Fig. 5 Force-deflection curves obtained from experiment and simulation for two cases of puncher

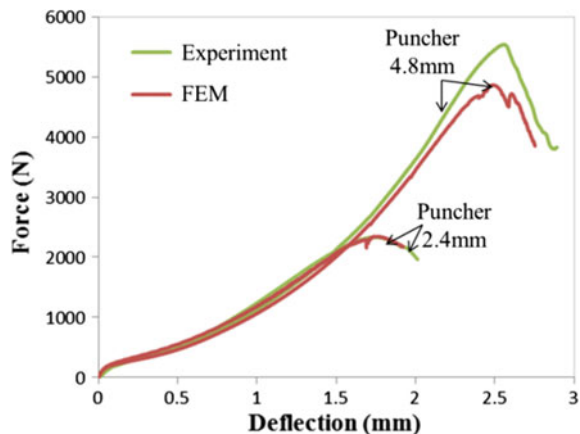


Fig. 6 Shape of deformed specimen with the distribution of damage variable at deflection rate of 0.03 mm/s and deflection of 1.8 mm (puncher 2.4 mm)

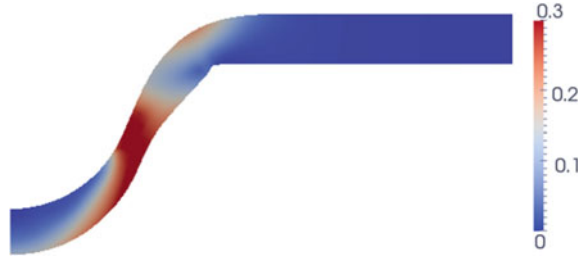


Fig. 7 Force-deflection curve obtained from simulation for two cases of puncher at various deflection rate

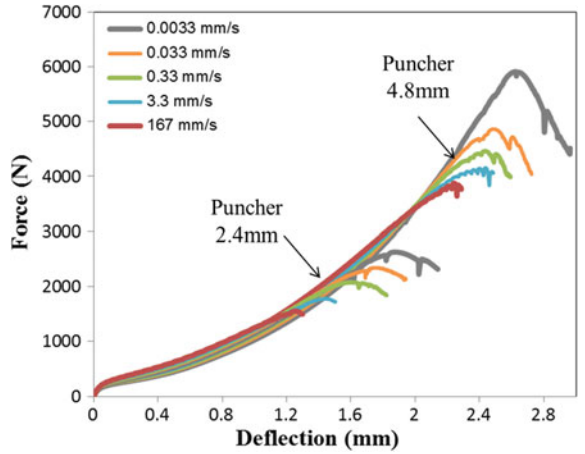
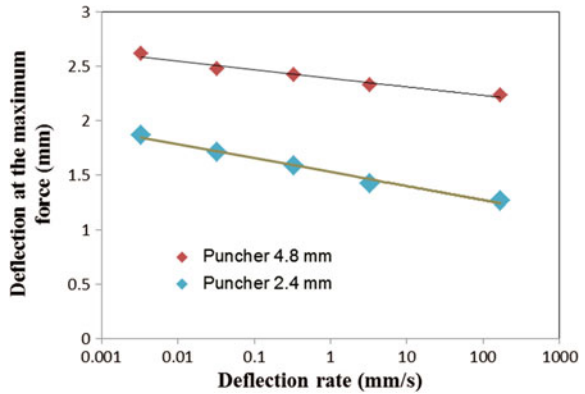


Fig. 8 Rate-sensitivity of deflection at maximum force in a semi-logarithmic plot for two cases of puncher



Additionally, a negative rate-sensitivity of maximum force as well as the deflection at the maximum force can be seen in cases of the puncher with 2.4 and 4.8 mm in diameter.

Figure 8 shows the relationship between deflection at the maximum force and deflection rate in a semi-logarithmic plot for two cases of the puncher. The value of

deflection at the maximum force slightly decreases with an increase in the deflection rate and shows a linear relationship. A similar tendency can be observed from two cases of the puncher. Thus, it can be considered that the equivalent fracture strain is lower at higher rate of deformation.

3.2 An Evaluation of J-integral Based on the Conventional Method

The conventional method described in the above section is applied to calculate equivalent fracture strain computationally. Values of deflection at the maximum force and thickness of deformed specimen at the thinnest section are presented in Table 2 for different deflection rates.

Figure 9 shows the plotted relationship between $\ln(\ln(t_o/t_f))$ and $\ln(d_m/t_o)$. From this figure, the relationship between $\ln(\ln(t_o/t_f))$ and $\ln(d_m/t_o)$ is approximately linear. Therefore, the value of α and n in Eq. (2) is determined as 0.19 and 0.67, respectively. Equation (5) for a calculation of equivalent fracture strain of the SPT can be obtained.

Table 2 Values of deflection at the maximum force and thickness of deformed specimen at the thinnest section

Deflection rate (mm/s)	0.0033	0.033	0.33	3.3	167	1667	3333
d_m (mm)	1.87	1.71	1.581	1.4241	1.2671	1.071	1.049
t_f (mm)	0.30	0.33	0.34	0.347	0.349	0.361	0.364

Fig. 9 Relationship between $\ln(\ln(t_o/t_f))$ and $\ln(d_m/t_o)$

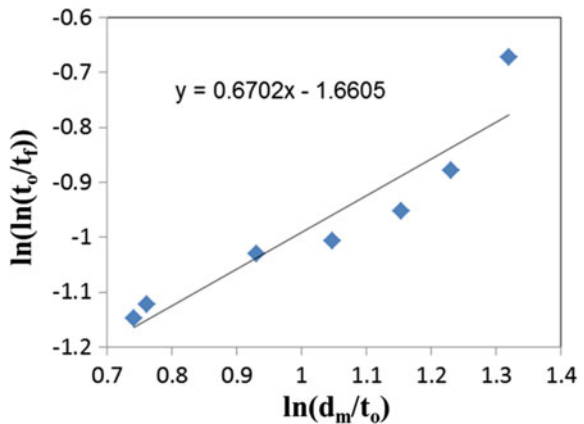


Fig. 10 Relationship between equivalent fracture strain and deflection rate in a semi-logarithmic plot

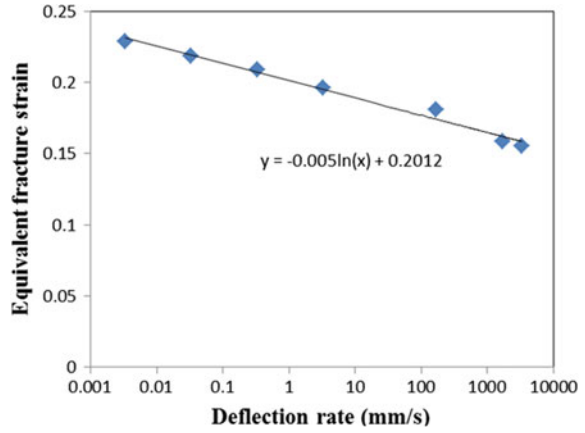
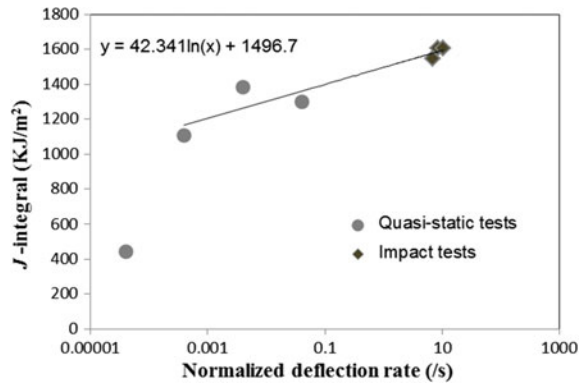


Fig. 11 Relationship between J -integral and normalized deflection rate in a semi-logarithmic plot obtained from three-point bending test [8]



$$\bar{\epsilon}_{qf} = 0.19 \left(\frac{d_m}{t_o} \right)^{0.67} \tag{5}$$

Finally, the relationship between equivalent fracture strain and deflection rate in a semi-logarithmic plot is shown in Fig. 10. From this figure, a negative rate-sensitivity of equivalent fracture strain of the SPT with almost linear relationship can be observed. Otherwise, in previous study [8], TRIP steel shows a positive rate-sensitivity of J -integral as shown in Fig. 11. An opposite in rate-sensitivity of equivalent fracture strain of the SPT and J -integral can be seen. This result might come from several reasons. One of them is that value of J -integral at high deformation rate might have a limitation because of some problems due to its weakness. Moreover, the deformation mode of the SPT and three-point bending test on pre-cracked specimen is totally different. Furthermore, to obtain a correlation between equivalent fracture strain in Fig. 10 and J -integral obtained from three-point bending test, the method for normalization of deflection rate of these

testing methods should have a correlation. Due to a difference in the shape and dimension of the specimen in the SPT and three-point bending test, the correlation of the method for normalization is quite difficult to obtain. Consequently, the correlation between the equivalent fracture strain of the SPT and J -integral could not be achieved for rate-sensitivity based on the conventional methodology. In order to obtain the correlation, it is necessary to propose a new method.

4 Concluding Remarks

In this study, finite element simulation was performed for the SPT for TRIP steel at different deflection rates for the cases of puncher having 2.4 and 4.8 mm in diameter. The validity of computation was confirmed by a comparison of computational result with experimental result for both two cases of puncher. The investigated steel indicates a negative rate-sensitivity of maximum force as well as deflection at the maximum force in the SPT. At higher deflection rate, the damage occurs when deflection is lower level. Although the total consumption energy is considerably higher in case of larger puncher and bigger specimen, a similar tendency of deflection at the maximum force can be obtained for different sizes of the puncher and specimen. Furthermore, a correlation between equivalent fracture strain and fracture toughness of the steel cannot be obtained based on the conventional method because of an opposite in rate-sensitivity and a different method for normalization of deflection rate in the SPT and three-point bending test. In order to obtain a correlation, it is necessary to propose a new method.

Acknowledgements This research is funded by Vietnam National Foundation for Science and Technology Development (NAFOSTED) under Grant no. 107.02-2017.17. The support is gratefully acknowledged.

References

1. Zhou X, Pan W, Mackenzie D (2013) Material plastic properties characterization by coupling experimental and numerical analysis of small punch beam tests. *Comput Struct* 118:59–65
2. Guan K, Xu T, Zhang X, Wang Z (2013) Effect of microdefects on load-deflection of small punch test by experimental investigation and finite element analysis. *Int J Press Vessels Pip* 110:14–16
3. Wang Z, Shi HJ, Lu J, Shi P, Ma X (2008) Small punch testing for assessing the failure properties of the reactor vessel steel with different thicknesses. *Nucl Eng Des* 238:3186–3193
4. Mao X, Shoji T, Takahashi H (1987) Characterization of fracture behavior in small punch test by combined recrystallization-etch method and rigid plastic analysis. *J Test Eval* 15:30–37
5. García TE, Rodríguez C, Belzunce FJ, Suárez C (2014) Estimation of the mechanical properties of metallic materials by means of the small punch test. *J Alloy Compd* 582: 708–717

6. Iwamoto T, Pham HT (2015) Review on spatio-temporal multiscale phenomena in TRIP steels and enhancement of its energy absorption. In: Altenbach H, Matsuda T, Okumura D (eds) From creep damage mechanics to homogenization methods—a liber amicorum to celebrate the birthday of Nobutada Ohno. Springer, pp 143–161
7. Pham HT, Iwamoto T (2016) A computational investigation on bending deformation behavior at various deflection rates for enhancement of absorbable energy in TRIP steel. *Metall Mater Trans A* 47A(8):3897–3911
8. Pham HT, Iwamoto T (2015) An experimental investigation on rate sensitivity of fracture-mechanical characteristics in 304 austenitic stainless steel under bending deformation. *ISIJ Int* 55(12):2661–2666
9. Iwamoto T, Tsuta T, Tomita Y (1998) Investigation on deformation mode dependence of strain-induced martensitic transformation in TRIP steels and modeling of transformation kinetics. *Int J Mech Sci* 40:173–182
10. Iwamoto T, Tsuta T (2002) Computational simulation on deformation behavior of CT specimens of TRIP steels under mode I loading for valuation of fracture toughness. *Int J Plast* 18(11):1583–1606
11. Shindo Y, Horiguchi K, Sugo T, Mano Y (2000) Finite element analysis and small punch testing for determining the cryogenic fracture toughness of austenitic stainless welds. *J Test Eval* 28:431–437
12. Ling X, Zheng Y, You Y, Chen Y (2007) Creep damage in small punch creeps specimens of type 304 stainless steel. *Int J Press Vessels Pip* 84(15):304–309
13. Yang S, Zhou J, Ling X, Yang Z (2012) Effect of geometric factors and processing parameters on plastic damage of SUS304 stainless steel by small punch test. *Mater Des* 41:447–452
14. Janca A, Siegl J, Hausild P (2016) Small punch test evaluation methods for material characterisation. *J Nucl Mater* 481:201–213
15. Tomita Y, Iwamoto T (1995) Constitutive modeling of TRIP steel and its application to the improvement of mechanical properties. *Int J Mech Sci* 37:1295–1305
16. Johnson GR, Cook WH (1985) Fracture characteristics of three metals subjected to various strains, strain rates, temperatures, and pressures. *Eng Fract Mech* 21:31–48
17. Yoon SW, Lee CS, Park WS, Kim MH, Lee JM (2011) Temperature and strain rate dependent constitutive model of TRIP steels for low-temperature applications. *Comput Mater Sci* 50:2014–2027
18. Dey S, Borvik T, Hopperstad OS, Langseth M (2007) On the influence of constitutive relation in projectile impact of steel plates. *Int J Impact Eng* 34:464–486

On the Buckling Behavior of Multi-cracked FGM Plates



Nguyen Dinh Duc, Truong Duc Trinh, Thom Van Do
and Duc Hong Doan

Abstract In this paper, a model of statically stability plate with crack-based finite element analysis will be introduced by numerical simulation computation. The simulation model was built based on phase field theory in mechanics of fracture; the case study of plate was significantly computed with the new third-order shear deformation plate theory (TSDT), which is derived from an elasticity formulation, rather by the hypothesis of displacements [1]. Importantly, to verify of reliability of the modeling computation theory, the simulation result was compared to the experiment of Seifi and Nafiseh [2] to ensure the essential reliability for the paper. After that, the authors also propose and test the effects due to the size, the declination of cracks as well as the thickness of the plate to the stability, additionally, the relation between number of cracks and buckling load involved to instability of plate will be discussed. Lastly, visual configurations about forms of instability of plate with cracks will be presented.

Keywords Buckling · TSDT · Phase field method · Multi-crack

1 Introduction

Nowadays, the structures of composite with functionally graded material (FGM) plate are applied in use of technical reality and engineering applications widely [3]. However, there are appearances of defects such cracks caused by many

N. D. Duc (✉) · D. H. Doan

Advanced Materials and Structures Laboratory, VNU Hanoi, University
of Engineering and Technology, 144 - Xuan Thuy - Cau Giay, Hanoi, Vietnam
e-mail: ducnd@vnu.edu.vn

N. D. Duc · T. D. Trinh (✉)

Infrastructure Engineering Program, VNU Hanoi, Vietnam-Japan University,
Luu Huu Phuoc Street - My Dinh 1, Hanoi, Vietnam
e-mail: truongtrinhduc.tnut@gmail.com

T. Van Do

Department of Mechanics, Le Quy Don Technical University,
236 Hoang Quoc Viet-Bac Tu Liem, Hanoi, Vietnam

© Springer Nature Singapore Pte Ltd. 2018

H. Nguyen-Xuan et al. (eds.), *Proceedings of the International Conference on Advances in Computational Mechanics 2017*, Lecture Notes in Mechanical Engineering, https://doi.org/10.1007/978-981-10-7149-2_3

unexpected reasons due to the working conditions, from manufacturing processes to working conditions in use that make cracks. These appearances of crack will weaken the hardness of the structure as well as durability significantly. When the plate is under pressure load on the surface, it is easier to make the plate be unstable comparing to the case of plate that do not have fractures, especially size and position of cracks also affect differently to the possibility of unstable in structures of plates. Therefore, research about instability of plate with internal cracks has the great meaning in real construction [4, 5], becomes a basement for studying which factors of crack affects majorly to stable ability of plate, and a step to the computation in expanding of crack in structures.

Recent years, the influence of crack to the stable possibility of the FGMs plate form has been studying in both numerical theory and experiment, especially some kinds of the FGMs plates such as ceramic-metal FGM have been manufactured successfully and further developed as well as designed in many engineering applications of extremely severe working conditions such as high-temperature working environment due to its gradually various changes of material property characteristics. Since their superior features and great characteristics of ceramic could resist against heat and corrosion, and the high toughness of metal also attracts energy and plastic deformation. The FGMs have significantly abilities of withstanding intense high-temperature gradient and maintaining the structural integrity, even eliminating interface problems or thermal stress concentration [6]. During the working processing period, the plate could normally have the in-plane compressible forces because of thermal or mechanic loads, these forces easily make the structure of plate to be in buckling phenomenon before reaching to the yield stress state, then the structure will take on a great deformation behavior, obviously the capacity of load carrying is totally reduced at this buckling state, furthermore, this phenomenon also becomes more seriously with the appearances of defects. As a consequence, the critical buckling issue with fracture in this FGMs plate plays a very important role in both plate structure study and practical application. This paper will focus specifically on the study of critical buckling load phenomena of FGMs plate with internal flaws under the variation of number cracks.

There are several studies in the exploration of buckling behaviors in FGPs. Shariat and Eslami [7] built a new closed-form computation for thermal buckling of FGPs which is a thick plate based on the first-order shear deformation theory, also by using this theory, the circular deformation of FGPs under thermal loading with temperature dependent properties was studied by Golmakani and Kadkhodayan [8]. On the other hand, Najafizadeh and Haydari [9] already investigated the critical buckling temperature rise of circular FGPs based on the third-order shear deformation theory. In Talha and Singh [10] study, an analysis of static behavior and free vibration with various boundary conditions using high-order theory-based finite element methods (FEM) presented. Additionally, studies on fracture got many concentrations recently. While Dolbow et al. [11] applied extend finite element method (XFEM) to modeling the mix mode of the deflection of the Mindlin-Reissner plate theory, then explored the strength of the stress concentration in crack plates. Moreover, the effect of boundary conditions, defect size, the gradient volume

fraction index, are studied using FEM in the purpose of analyzing the critical buckling temperature rise in a composite plate with a circular cutout by Shaterzadeh et al. [12]. Especially, among the studies which analyzed the buckling with internal crack, Yu et al. [13] already investigated thermal buckling impacts using extended isogeometric analysis of FGPs with cracks, Baiz and Natarajan [14, 15] used XFEM and SFEM to attempt linear plate buckling analysis with crack based on Mindlin-Reissner plate theory; furthermore by using XFEM and first-order shear deformation theory, Baiz P. and Natarajan S. also figured out the influence of crack's geometric impact in FGMs plate. It can see that cracked plate get many interests in buckling problems. Phase field method is a new method applied in fracture study in structure in representing the geometry and approximations with high accuracy; this method shows advantages when analyzing and modeling internal fracture in structure for both static and dynamic problems [16, 17]. For instance as remarkable in strong point of phase field method, Areias et al. [18] applied phase field method in finite strain plates to represent bending with fracture; the advantages in fracture and crack modeling by phase field method are shown more by Amiri et al. [19] in which the author built crack model for thin shell; obviously, parameters needed in phase field method will bring the level of computation become much harder. Nonetheless, the analysis of critical buckling load with multiple defects in FGPs also plays an important role in understanding the behaviors of plate with internal cracks, but there are still quite rare studies on this kind of problem.

In this paper, an investigation of critical buckling behaviors of FGPs with multiple fractures using phase field method for modeling the defects in design based on the new third-order shear deformation theory is proposed by Shi [1]. The calculated numerical results are taken to compare with the reference [13, 14] to show the accuracy of the analysis. Then, the effects and impacts of multiple cracks on buckling values in FGPs also are represented and analysis in the following section. The rest of the paper is represented as following sections. In the Sect. 2, the theory to build numerical formulation is reported in Sects. 2.1 and 2.2. While Sect. 3 is presented for critical buckling analysis for cracks based on phase field method for the numerical results with analysis and discussion for different cases of cracks on plate, firstly is two cracks, secondly is three and lastly is three cracks concentrated together at central position of plate. The conclusion is summarized in Sect. 4.

2 Formulation for Third-Order Shear Deformation Theory

2.1 Functionally Graded Plates

Functionally graded plates are normally considered to be changed by the material properties according to the vary in the plate thickness due to the volume fractions (n). In this study, the functionally graded plate (FGP) type is chosen as

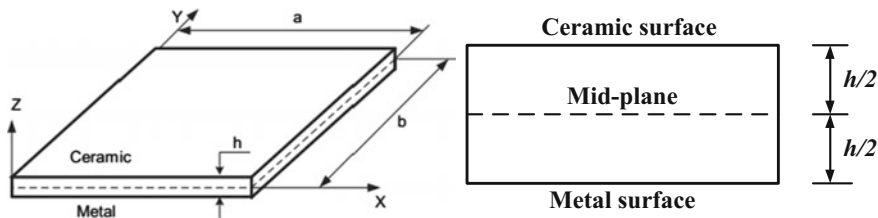


Fig. 1 Geometry of a functionally graded plate

ceramic-metal FGP with a thickness h as described in Fig. 1, supposing that its bottom and top surfaces are being fully composed by metallic and ceramic, respectively. To make the integral computation be easier, the xy -plane is chosen to be in the mid-plane of the plate, whereas the positive z -axis is upward from the xy -plane. There are several explanations for the variation of the volume fractions; however, in this study, the common simple power-law assumption for describing the volume fraction of the ceramic (V_c) and the metal (V_m) [13, 20] is being used:

$$V_c = \left(\frac{z}{h} + \frac{1}{2} \right)^n ; V_m = 1 - V_c \text{ with } n \geq 0 \quad (1)$$

where z is the thickness coordinate variable with $-h/2 \leq z \leq h/2$, the subscripts c and m represent the ceramic and metal material components, respectively. In this paper, the variable n is signified as non-negative volume fraction gradient index. The Young's modulus E , the Poisson's ratio ν with a power-law distribution as below [20]:

$$E(z) = E_m + (E_c - E_m) \left(\frac{z}{h} + \frac{1}{2} \right)^n, \quad \nu(z) = \nu_m + (\nu_c - \nu_m) \left(\frac{z}{h} + \frac{1}{2} \right)^n \quad (2)$$

2.2 Kinematic Equations of Plates

This part introduces a finite element formulation for functionally graded plate which uses a new simple third-order shear deformation plate theory. This theory is originally proposed by Shi [1] based on rigorous kinematic assumption on displacements. Previous effort presented in reference [6] has made to reveal the advantages of this new theory as it substantially provides more accuracy than other higher-order shear deformation plate theories. It may be due to the fact that the kinematic of displacements is derived from an elasticity formulation rather than the hypothesis of displacements. The three-dimensional displacements (u , v , w) at a point (x, y, z) in the plate can be expressed in terms of five unknown variables as follows:

$$\begin{aligned}
 u(x, y, z) &= u_0(x, y) + \frac{5}{4} \left(z - \frac{4}{3h^2} z^3 \right) \phi_x(x, y) + \left(\frac{1}{4} z - \frac{5}{3h^2} z^3 \right) w_{0,x} \\
 v(x, y, z) &= v_0(x, y) + \frac{5}{4} \left(z - \frac{4}{3h^2} z^3 \right) \phi_y(x, y) + \left(\frac{1}{4} z - \frac{5}{3h^2} z^3 \right) w_{0,y} \\
 w(x, y, z) &= w_0(x, y)
 \end{aligned} \tag{3}$$

$$\begin{Bmatrix} \boldsymbol{\varepsilon}_x \\ \boldsymbol{\varepsilon}_y \\ \boldsymbol{\varepsilon}_{xy} \\ \boldsymbol{\gamma}_{yz} \\ \boldsymbol{\gamma}_{xz} \end{Bmatrix} = \begin{Bmatrix} u_{0,x} + z \frac{1}{4} (5\phi_{x,x} + w_{,xx}) + z^3 \left(\frac{-5}{3h^2} \right) (\phi_{x,x} + w_{,xx}) \\ v_{0,y} + z \frac{1}{4} (5\phi_{y,y} + w_{,yy}) + z^3 \left(\frac{-5}{3h^2} \right) (\phi_{y,y} + w_{,yy}) \\ u_{0,y} + v_{0,x} + z \frac{1}{4} (5\phi_{x,y} + 2w_{,xy} + 5\phi_{y,x}) + z^3 \left(\frac{-5}{3h^2} \right) (\phi_{x,y} + 2w_{,xy} + \phi_{y,x}) \\ \frac{5}{4} (\phi_y + w_{,y}) + z^2 \left(\frac{-5}{h^2} \right) (\phi_y + w_{,y}) \\ \frac{5}{4} (\phi_x + w_{,x}) + z^2 \left(\frac{-5}{h^2} \right) (\phi_x + w_{,x}) \end{Bmatrix} \tag{4}$$

where u, v, w define the displacements at the mid-plane of a plate in the x, y, z directions, respectively. While ϕ_x, ϕ_y represent the transverse normal rotations of the x - and y -axes. In Eqs. (3) and (4), the comma describes the differentiation against x and y coordinates.

From the Hooke' law, the constitutive relations of normal and shear stress are following equations:

$$\begin{aligned}
 \sigma &= D_m(z) (\boldsymbol{\varepsilon}^{(0)} + z\boldsymbol{\varepsilon}^{(1)} + z^3\boldsymbol{\varepsilon}^{(3)}) \\
 \tau &= D_s(z) (\boldsymbol{\gamma}^{(0)} + z^2\boldsymbol{\gamma}^{(2)})
 \end{aligned} \tag{5}$$

$$\text{With } \boldsymbol{\sigma} = [\sigma_x \ \sigma_y \ \sigma_{xy}]^T; \boldsymbol{\tau} = [\tau_{yz} \ \tau_{xz}]^T$$

$$D_s(z) = \frac{E(z)}{2(1+\nu)} \begin{bmatrix} 1 & 0 \\ 0 & 1 \end{bmatrix}; D_m(z) = \frac{E(z)}{1-\nu^2} \begin{bmatrix} 1 & \nu & 0 \\ \nu & 1 & 0 \\ 0 & 0 & \frac{1}{2}(1-\nu) \end{bmatrix} \tag{6}$$

It is necessary to notice that Eq. (5) are denoted $\boldsymbol{\varepsilon}^{(0)}; \boldsymbol{\varepsilon}^{(1)}; \boldsymbol{\varepsilon}^{(3)}; \boldsymbol{\gamma}^{(0)}; \boldsymbol{\gamma}^{(2)}$ for the strain and shear components induced from Eq. (4) of displacements in the plate [21].

So that, according to the third-order shear deformation theory proposed by Shi [1], the normal forces, bending moments, higher-order moments and shear forces can be computed and written in matrix form as following:

$$\begin{Bmatrix} \tilde{N} \\ \tilde{M} \\ \tilde{P} \\ \tilde{Q} \\ \tilde{R} \end{Bmatrix} = \begin{bmatrix} A & B & E & 0 & 0 \\ B & D & F & 0 & 0 \\ E & F & H & 0 & 0 \\ 0 & 0 & 0 & \hat{A} & \hat{B} \\ 0 & 0 & 0 & \hat{B} & \hat{D} \end{bmatrix} \begin{Bmatrix} \boldsymbol{\varepsilon}^{(0)} \\ \boldsymbol{\varepsilon}^{(1)} \\ \boldsymbol{\varepsilon}^{(3)} \\ \boldsymbol{\gamma}^{(0)} \\ \boldsymbol{\gamma}^{(2)} \end{Bmatrix} \tag{7}$$

$$\begin{aligned} \text{With } (A, B, D, E, F, H) &= \int_{-h/2}^{h/2} (1, z, z^2, z^3, z^4, z^6) D_m(z) dz; (\hat{A}, \hat{B}, \hat{D}) \\ &= \int_{-h/2}^{h/2} (1, z^2, z^4) D_s(z) dz \end{aligned} \quad (8)$$

$$U(\delta) = \frac{1}{2} q_e^T \int_{\Omega} \begin{pmatrix} B_1^T A B_1 + B_1^T B B_2 + B_1^T E B_3 + B_2^T B B_1 \\ + B_2^T D B_2 + B_2^T F B_3 + B_3^T E B_1 + B_3^T F B_2 \\ + B_3^T H B_3 + B_4^T \hat{A} B_4 + B_4^T \hat{B} B_5 + B_5^T \hat{B} B_4 \\ + B_5^T \hat{D} B_5 \end{pmatrix} d\Omega q_e \quad (9)$$

2.3 Phase Field Theory and Crack Modeling

Phase field theory provides a parameter s which is varying continuously in the interval of $(0,1)$. When s equal to 0, then there is a fracture in the considering phase of material plate, oppositely with s equal to 1. If s varies in the interval of $(0,1)$, it means the plate begins to be softer and at the onset of bending. Therefore, it can be said that phase field theory helps crack modeling become easily to control by varying the state of normal-softening-fracture by solving the phase field parameter s from 0 to 1. This parameter s is considered as a variable in strain energy formula by s^2 function, thus the crack in plate could happen as strain energy reduces to 0.

From the kinematic equation derived above, the total strain energy of plate due to the normal forces, bending moments, higher-order moments and shear forces could be represented by:

$$\begin{aligned} U(\delta, s) &= \left\{ \begin{aligned} &\frac{1}{2} q_e^T \int_{\Omega} s^2 \begin{pmatrix} B_1^T A B_1 + B_1^T B B_2 + B_1^T E B_3 + B_2^T B B_1 \\ + B_2^T D B_2 + B_2^T F B_3 + B_3^T E B_1 + B_3^T F B_2 \\ + B_3^T H B_3 + B_4^T \hat{A} B_4 + B_4^T \hat{B} B_5 + B_5^T \hat{B} B_4 \\ + B_5^T \hat{D} B_5 \end{pmatrix} d\Omega q_e \\ &+ \frac{1}{2} \int_{\Omega} s^2 [w_{,x} \quad w_{,y}] \delta^0 [w_{,x} \quad w_{,y}]^T h d\Omega + \frac{1}{2} \int_{\Omega} s^2 [\phi_{,x,x} \quad \phi_{,x,y}] \delta^0 [\phi_{,x,x} \quad \phi_{,x,y}]^T \frac{h^3}{12} d\Omega \\ &+ \frac{1}{2} \int_{\Omega} s^2 [\phi_{,y,x} \quad \phi_{,y,y}] \delta^0 [\phi_{,y,x} \quad \phi_{,y,y}]^T \frac{h^3}{12} d\Omega + \int_{\Omega} G_C h \left[\frac{(1-\nu)^2}{4l} + l |\nabla s|^2 \right] d\Omega \end{aligned} \right\} \\ &= \left\{ \int_{\Omega} s^2 \Psi(\delta) d\Omega + \int_{\Omega} G_C h \left[\frac{(1-\nu)^2}{4l} + l |\nabla s|^2 \right] d\Omega \right\} \end{aligned} \quad (10)$$

where q_e is used to denote the element displacement vector, and G_C is used for the critical energy release rate in Griffith's theory, and l is a positive regularization constant to adjust the size of the fracture zone.

$$\delta^0 = \begin{bmatrix} \sigma_x^0 & \tau_{xy}^0 \\ \tau_{xy}^0 & \sigma_y^0 \end{bmatrix} \quad (11)$$

The first variation of the functional $U(\delta, s)$ is particularly computed by

$$\begin{cases} \delta U(\delta, s, \delta\delta) = 0 \\ \delta U(\delta, s, \delta s) = 0 \end{cases} \quad (12)$$

Continuously, the formulations for pre-buckling analyzes of cracked plate could be described as functions below:

$$\{ (\sum \mathbf{K}^e + \lambda_{cr} \sum \mathbf{K}_G^e) \delta = 0 \quad (13)$$

$$\left\{ \int_{\Omega} 2s\Psi(\delta)\delta s d\Omega + \int_{\Omega} 2G_C h \left[-\frac{(1-\nu)}{4l} + l\nabla s \nabla(\delta s) \right] d\Omega = 0 \quad (14)$$

Once computed the value δ of from Eq. (14), it could be easily computed for eigenvalue λ_{cr} in Eq. (13) which is considered as the critical buckling load.

3 Numerical Results and Discussion

In this section, the critical buckling analysis of FGPs with multiple internal cracks using phase field method coupled with finite element method is presented. In all the numerical calculation, a square of Al/ZrO₂ plate with cracks which is meshed by 10 × 10 element scheme is assigned. All the plates being studied are considered under uniaxial load. The critical buckling load, which is being solved directly from the eigenvalue equation of buckling plates by the development of the third-order shear deformation theory, is numerically analyzed. The value of buckling load is presented as a non-dimensionalized value $k_c = (10^2 \lambda_{cr} a_0) / (Eh_0)$ (with $a_0 = 10h_0$). For convenience in representing the results, different boundary conditions at each edge of the plate are namely set up as simply supported (S), clamped (C), and free (F). The analyzed square plate has length and wide to be $H = L = 0.2$ m, while the thickness of plate is set as $h = H/100$ or $h = 0.002$ m for analyzing, due to the variation of change of the volume fraction index, the length of the cracks as well as the distance among cracks.

3.1 Convergence and Accuracy Studies

There is still rarely numerical result in critical buckling load investigated with internal crack; in this part specifically, the critical buckling temperature rise

Fig. 2 Model geometry of a square Al/ZrO₂ with an inclined central crack

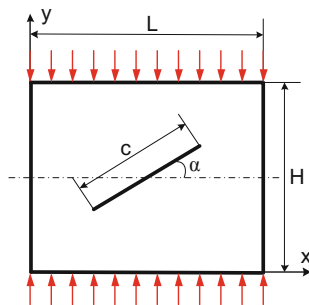


Table 1 Comparison of the critical buckling of a fully simple supported square Al/ZrO₂ with the effect of the inclined angle of crack ($c/H = 0.6$) altered by volume fraction exponent

n		Inclined angle (degree)						
		0	15	30	50	60	75	90
0	Ref. [13]	8.894	8.797	8.608	8.506	8.608	8.797	8.894
	Computed	12.0379	11.9206	11.4213	11.4219	11.4213	11.9206	12.0379
0.5	Ref. [13]	6.114	6.047	5.918	5.848	5.918	6.047	6.114
	Computed	6.76757	6.70251	6.42222	6.4243	6.42222	6.70251	6.76757
1	Ref. [13]	5.412	5.353	5.238	5.176	5.238	5.353	5.412
	Computed	5.56817	5.48895	5.34501	5.28711	5.34501	5.48895	5.56817
2	Ref. [13]	5.012	4.958	4.851	4.794	4.851	4.958	5.012
	Computed	4.94782	4.8761	4.74779	4.69783	4.74779	4.8761	4.94782
5	Ref. [13]	4.771	4.718	4.616	4.561	4.616	4.718	4.771
	Computed	5.08094	5.00445	4.87055	4.82002	4.87055	5.00445	5.08094

(CBTR) of a square plate with length and wide to be $H = L = 0.2$ m, subjected to a uniform temperature rise is considered to verify the convergence property and accuracy of the developed phase field based on third-order shear deformation theory in order to compare to the reference solutions [13].

Considering a plate with an inclined central crack subjected to a temperature rise as showed in Fig. 2 is studied with the change of inclined angles and vary of the values gradient volume facture index. As the results described in Table 1, the CBTR computed by the third-order shear deformation theory with various inclined angles converges well to the reference solutions [13]. The reference solutions [13] were derived based on the present XIGA with the first-order shear deformation theory. The results also reveal one interesting point that when the plate exhibits much more metallic behavior, or the larger gradient volume fraction index, the more convergence CBTR could reach, though with the gradient volume fraction index is 0, the CBTR is a little higher than the reference solutions [13], and the decrease of CBTR as the volume fraction index from 0 to 5 is significant, in about twice.

Table 2 Comparison of critical buckling of simply supported square plate with thickness ratio $h/H = 0.01$ and longitudinal central crack $c/H = 0.2$

Mesh density	Computed	MITC [14]	MISC2 [14]	MISC2_b [14]
31×31	4.2742	4.0229	4.0325	4.0394

Table 3 Comparison of critical buckling of simply supported square plate with thickness ratio $h/H = 0.01$ and no crack

Mesh density	Computed	Q4R [14]	MITC [14]	MISC2 [14]	MISC2_b [14]
11×11	4.4793	4.0715	4.0437	4.0320	4.0389
15×15	4.3216	4.0371	4.0223	4.0161	4.0198
19×19	4.2232	4.0222	4.013	4.0092	4.0115

This phenomenon can also be found the same for the reference solutions [13]. It can be observed in the numerical results that both solutions show the same behavior as the CBTR values decrease with increasing the volume fraction exponent and become converge as increasing of n .

On the other hand, the reference solutions [14] provided the investigation of a square plate with the same characteristics of the analysis in this study. Tables 2 and 3 describe the numerical solution comparisons with the reference [14]. Since the reference solutions are considered with the Mindlin-Reissner plate theory with different types of plate elements, this analysis has been changed the modeling into the homogeneous plate, and make the comparison with the results in which the mesh distortion is 0 [14]. All of the results are very close to each other in both cases that having crack or no crack; this shows the clearly reliability for the modeling in this study. Furthermore, according to the reference [14], the solutions also reveal that the convergence and the influence of crack size impacts to the critical buckling load which is the same with the results in this study represented in the detail analysis in the next parts.

3.2 Critical Buckling with Two Cracks Equidistant Analysis

A square of Al/ZrO_2 plate with two cracks equidistant from the central as described in Fig. 3 has been studied. Figure 4 presents the gained numerical results of the critical buckling load of a fully simple supported Al/ZrO_2 plate as the length of cracks is set to increase from 10 to 90% of the total length of the plate. The numerical analysis is significantly computed based on the change of volume fraction index, the cracks size, and the distance between two cracks set in the plate interface. The presented numerical results show that when the distance between two cracks is kept equilateral on the surface of the plate and increasing the volume fraction index, it makes a decrease of the critical load, no matter how increasing

Fig. 3 Functionally graded plate with two cracks equidistant geometric

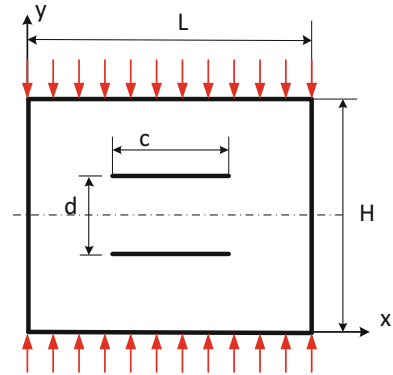
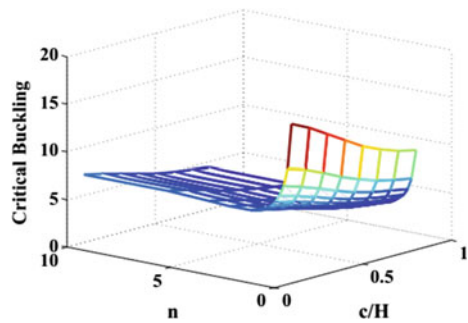


Fig. 4 Critical buckling values with the change of volume fraction index (n) and crack's length (c/H)



changes of cracks sizes, however, as increasing the length of crack, it also induces a gradual decrease of the critical buckling load as described in Fig. 4.

On the other hand, in the second analysis as shown in Fig. 5, if keeping the crack size as half of the length of the plate and make an increasingly change in the volume fraction index, it can be found that similarly to the case of previous test when the crack sizes in length increases, the numerical results of critical load decrease.

Especially, as making increasing the distance between two cracks from 10 to 90% of the total length of the plate, contrary to the first test, the critical load values are also increasing measurably, notice that at the beginning when increasing the distance of two cracks, there is a little diminish of the critical load at first, the reason is as the distance between two cracks is too small and the buckling phenomena happen from the center at first, thus it easily to release the energy of buckling load than when the position of cracks is far from the central positions.

In the next analysis in Fig. 6, the influence and relationship between the size of cracks and distance between two cracks are presented. Obviously, according to two previous numerical results, it is reasonable to predict that the critical buckling will be reducing as spreading the size of cracks, and be rising as expanding the distance between of the crack. By Fig. 6, the numerical results reveal that the analysis is reliable to each other. Figure 7 shows the first five buckling mode shapes of cracked

Fig. 5 Critical buckling values with the change of volume fraction index (n) and distance between cracks (d/H) when keeping the crack's size as 0.5 of plate's length

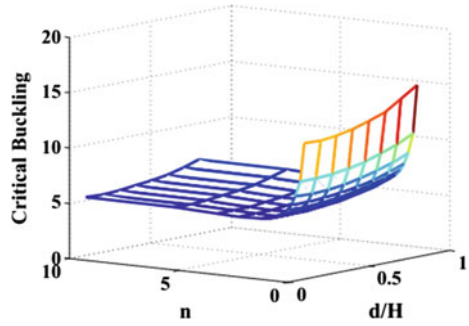


Fig. 6 Critical buckling values with the change of cracks' length (c/H) and distance between cracks (d/H) when keeping the volume fraction index as 0.5

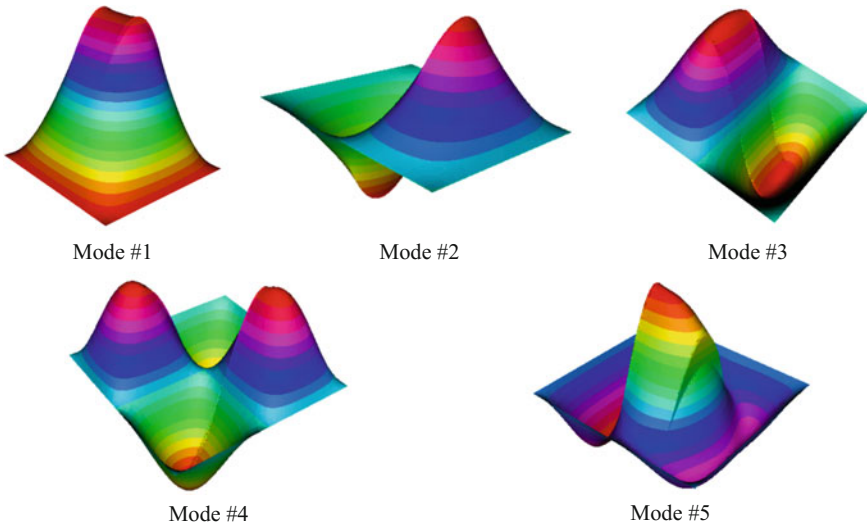
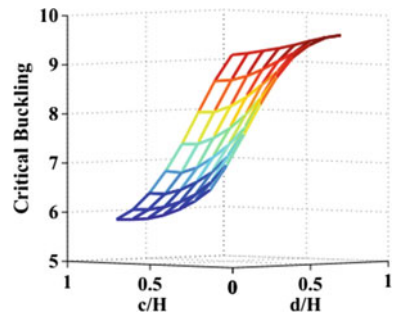
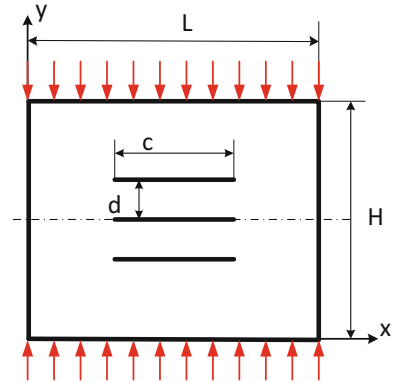


Fig. 7 First five buckling modes of CFCF plate with two cracks ($L = H = 0.2$ m, $h = 0.002$ m, $c/H = 0.5$)

Fig. 8 Functionally graded plate with three cracks equidistant geometric



plates with two cracks equidistant, obviously, the numbers of cracks affects much in the shape of plate at buckling state.

3.3 Critical Buckling with Three Cracks Equidistant Analysis

This section is devoted for the next numerical example by considering the same characteristics of Al/ZrO_2 plate with three cracks equidistant from the central as described in Fig. 8 has been studied. In this analysis, when progressively increasing the length of cracks or growing the gradient volume fraction, it is easy to see that the critical buckling decreases as showed in Fig. 9. However, in the test of keeping the equal length of cracks as half of the plate's length and making change in distance among cracks as Fig. 10 presented, as the distance among crack is small, there is a little reduce of buckling load, but when the distance of two out side cracks becomes larger compared to the position of the central cracks, the load increases back; especially, it can be seen that the critical load is changed not much due to the

Fig. 9 Critical buckling values with the change of volume fraction index (n) and crack's length (c/H)

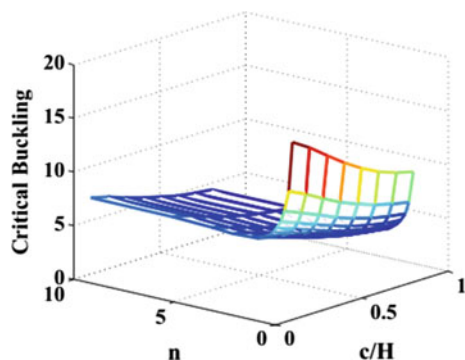


Fig. 10 Critical buckling values with the change of volume fraction index (n) and distance between cracks (d/H) when keeping the crack's size as 0.5 of plate's length

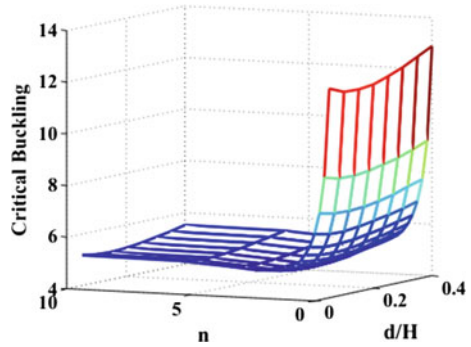
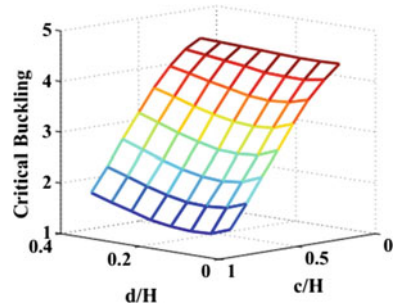


Fig. 11 Critical buckling values with the change of cracks' length (c/H) and distance between cracks (d/H) when keeping the volume fraction index as 0.5



change of crack's length, the reasons are that the energy loss from the central crack position also compensate for the energy of buckling state from two out side cracks.

In the next test, the model is set up by keeping the constant of the volume fraction index and making change in both the length of cracks and the distance among cracks as shown in Fig. 11, the impacts from numbers of cracks show clearly in this part since compare to the plate having only two cracks. The critical load in this test is only half comparing to that of plate having two cracks, furthermore, one of three cracks are at the central, so it is easy to release the buckling energy, similarly to previous test, the critical buckling is not changed much when increasing the distance among cracks, but as the crack's lengths become larger, the buckling state get easier to release energy and that is why the critical load is also smaller.

The further observation on the numerical critical buckling results is presented in Table 4; it shows a strong influence of the boundary conditions on the buckling load. The cracks affect the critical buckling load as it is found to be decreased for the CCCC, SCSC, SSSS, and SFSF boundary conditions. The load of the CCCC is much greater than that of a SSSS as well as the other boundary conditions. The forces or constrains make the critical load decrease when enlarging the volume fraction index from ceramic to metal material as well as when changing the boundary conditions. However, as the volume fraction index becomes larger than 1, even increasing the length of crack, the critical buckling load is not changed much, but become converge (Table 4). Figure 12 describes the first five buckling mode shapes cracked plates with three cracks equidistant.

Table 4 Critical buckling load of plate with two cracks for different boundary conditions ($h/H = 0.01$, $c/H = 0.5$) altered by volume fracture exponent

n	CCCC	SCSC	SSSS	SFSF
0	27.7015	24.7433	12.0902	4.87837
0.5	15.6317	13.9517	6.79643	2.74525
1	12.936	11.4476	5.57393	2.25181
5	11.795	10.442	5.07708	2.0529
10	11.9537	10.5941	5.17638	2.08977

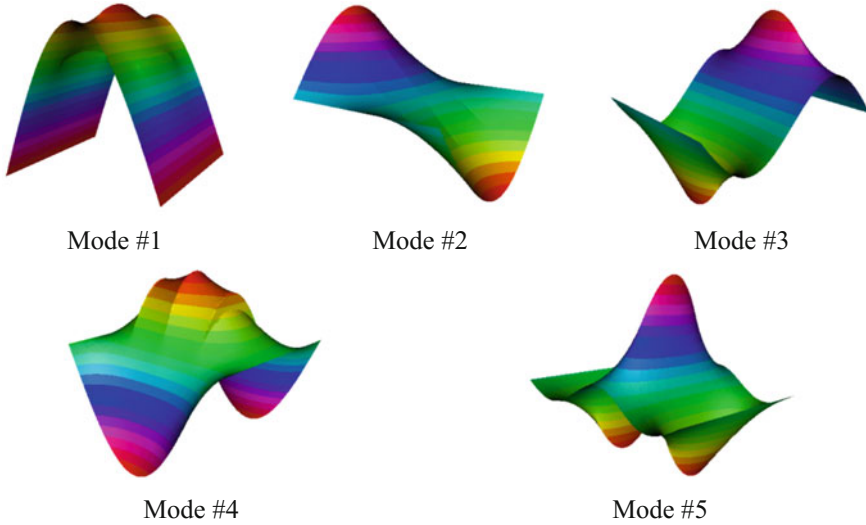


Fig. 12 First five buckling modes of CFCF plate with three cracks ($L = H = 0.2$ m, $h = 0.002$ m, $c/H = 0.5$)

3.4 Critical Buckling of Three Cracks Concentrated at Central of Plate

The development of dynamics cracks is an important study in the future, thus in this part, the impact of multiple cracks which are connected to each other in the central of plate that will be presented. The square plate with the same characteristics as two previous sections is chosen. Three cracks with the equal length are changed from $c/H = 0.1-0.4$ and the crack angle α is 45° as Fig. 13. Figure 14 represents the behaviors of buckling state in this case; obviously, as cracks concentrate at the central with the increasing progressively, the critical buckling load will be reduced much. The length of cracks is proportional to the buckling load. It can be said that avoiding central cracks as well as the numbers of cracks affects significantly to the buckling fail of plates. Figure 15 also presents the first five buckling mode shapes

Fig. 13 Functionally graded plate with three cracks concentrated at central geometric

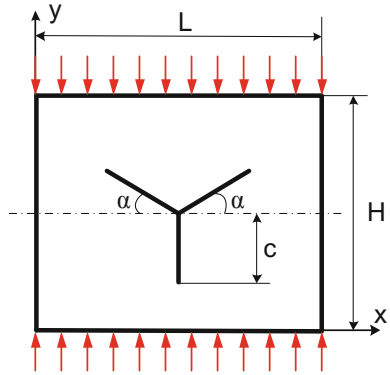
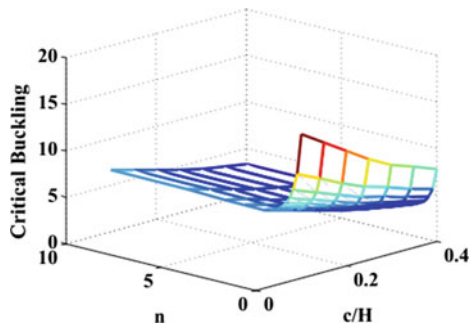
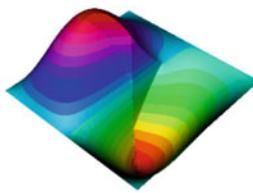


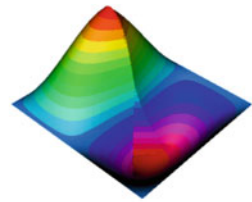
Fig. 14 Critical buckling values with the change of volume fraction index (n) and crack's length (c/H)



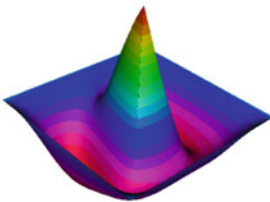
Mode #1



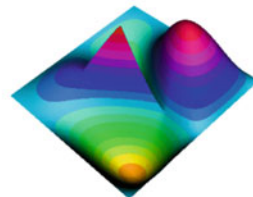
Mode #2



Mode #3



Mode #4



Mode #5

Fig. 15 First five buckling modes of CFCF plate with three concentrated cracks ($L = H = 0.2$ m, $h = 0.002$ m, $c/H = 0.5$)

of cracked plates with three cracks which are concentrated to each other at the central position of the plate, obviously, comparing to the two equidistant cracks and three equidistant cracks, from the five mode shapes, it can be said that not only the numbers of cracks but also the distribution or shapes of cracks in the plate also have significantly large impacts in the shape of plate at buckling state.

4 Conclusions

Based on the third-order shear deformation theory promoted by Shi [1] as well as phase field theory, the paper has analyzed the critical buckling behaviors of functionally graded plates with multiple internal defects such as cracks. In this cracked plate buckling problem, plate is compressed in two opposite clamped edges while free the other two edges. The influences of the gradient volume fraction index, the number of cracks as well as their positions, the length of cracks, and boundary conditions on the critical buckling load are investigated. When raising the gradient volume fraction index or in increasing the length of cracks, the critical buckling load is decreased, and the plate is prone for buckling; it is contrary that when increasing the distance between cracks, the critical load is increasing. The boundary conditions, on the other hand, have the significantly important affects to the buckling state indeed. The study also points out that the impacts of cracks when they are at the central also influence the critical buckling load since the central position is where buckling happens at first. The accuracy of the buckling load obtained has high reliability and good agreements with the reference solutions for thin plates with internal defects. Nevertheless, the present numerical study opens new potentials and further extension to other promising problems such as dynamics cracks progress leads to develop multiple cracks, especially thermal buckling problems which have thermal factor impact.

Acknowledgements This research is funded by Vietnam National University, Hanoi under grant number QG.17.45. The authors are grateful for this support.

References

1. Shi G (2007) A new simple third-order shear deformation theory of plates. *Int J Solids Struct* 44:4399–4417
2. Seifi R, Nafiseh K-Y (2011) Experimental and numerical studies on buckling of cracked thin plates under full and partial compression edge loading. *Thin Walled Struct* 19:1504–1516
3. Jha DK, Kant T, Singh RK (2013) A critical review of recent research on functionally graded plates. *Compos Struct* 96:833–849
4. Fantuzzi N, Tornabene F, Viola E (2016) Four-parameter functionally graded cracked plates of arbitrary shape: a GDQFEM solution for free vibrations. *Mech Adv Mater Struct* 23(1): 89–107

5. Huang CS, McGee OG III, Chang MJ (2011) Vibrations of cracked rectangular FGM thick plates. *Compos Struct* 93(7):1747–1764
6. Wattanasakulpong N, Prusty GB, Kelly DW (2013) Free and forced vibration analysis using improved third-order shear deformation theory for functionally graded plates under high temperature loading. *J Sandwich Struct Mater* 15:583–606
7. Shariat BAS, Eslami MR (2007) Buckling of thick functionally graded plates under mechanical and thermal loads. *Compos Struct* 78(3):433–439
8. Golmakani ME, Kadhodayan M (2011) Large deformation analysis of circular and annular FGM plates under thermo-mechanical loadings with temperature dependent properties. *Composite Part B* 42:614–625
9. Najafizadeh MM, Heydari HR (2004) Thermal buckling of functionally graded circular plates based on higher order shear deformation plate theory. *Eur J Mech* 23(6):1085–1100
10. Talha M, Singh BN (2010) Static response and free vibration analysis of FGM plates using higher order shear deformation theory. *Appl Math Model* 34:3991e4011
11. Dolbow J, Moës N, Belytschko T (2000) Modeling fracture in Mindlin-Reissner plates with the extended finite element method. *Int J Solids Struct* 37:7161–7183
12. Shaterzadeh A, Abolghasemi S, Rezaei R (2014) Finite element analysis of thermal buckling of rectangular laminated composite plates with circular cutout. *J Therm Stress* 37(5):604–623
13. Yu T, Bui TQ, Yin S, Doan DH, Wu CT, Van Do T, Tanaka S (2016) On the thermal buckling analysis of functionally graded plates with internal defects using extended isogeometric analysis. *Compos Struct* 136:684–695
14. Baiz PM, Bordas S, Kerfriden P, Rabczuk T (2011) Linear buckling analysis of cracked plates by SFEM and XFEM (SmXFEM). *J Mech Mater Struct* 6(9–10):1213–1238
15. Natarajan S, Baiz PM, Bordas S, Rabczuk T, Kerfriden P (2011) Natural frequencies of cracked functionally graded material plates by the extended finite element method. *Compos Struct* 93(11):3082–3092
16. Kuhn C, Muller R (2010) A continuum phase field model for fracture. *Eng Fract Mech* 77:3625–3634
17. Borden MJ, Verhoosel CV, Scott MA, Hughes TJR, Landis CM (2012) A phase-field description of dynamic brittle fracture. *Comput Methods Appl Mech Eng* 217–220:77–95
18. Areias P, Rabczuk T, Msek M (2016) Phase-field analysis of finite-strain plates and shells including element subdivision. *Comput Methods Appl Mech Eng* 312(C):322–350
19. Amiri F, Milan D, Shen Y, Rabczuk T, Arroyo M (2014) Phase-field modeling of fracture in linear thin shells. *Theoret Appl Fract Mech* 69:102–109
20. Reddy JN (2000) Analysis of functionally graded plates. *Int J Numer Methods Eng* 47:663–684
21. Bui TQ, Van Do T, Ton LHT, Doan DH, Tanaka S, Pham DT, Nguyen-Van T-A, Yu T, Hirose S (2016) On the high temperature mechanical behaviors analysis of heated functionally graded plates using FEM and a new third-order shear deformation plate theory. *Compos Part B* 92:218–241

Using a Non-local Elastic Damage Model to Predict the Fatigue Life of Asphalt Pavement Structure



H. T. Tai Nguyen and N. Hung Nguyen

Abstract Asphalt concrete is a composite material comprising aggregate, sand, mineral filler and bitumen as a binder. Although good compaction is performed during the construction, there is still relatively large discontinuity inside the material, and this will favour the appearance of micro-cracks, which decreases the performance of the material. Structural cracking resulted from repeated loading, or fatigue cracking, is a common failure mode of asphalt pavement structure, reducing the serviceability of the pavement. Owing to the present of micro-cracking, the fatigue cracking of asphalt pavement is generally modelled by using damage theory. In this paper, the authors aim to illustrate the application of an isotropic non-local elastic damage model in predicting the fatigue life of a pavement structure. A scalar D , called damage variable, is used to define the damage state at a point of the material, and the evolution of this variable at a point depends on the historic damage state as well as the present strain tensor at that point. The model parameters are determined on the basis of fatigue test results—namely, 4-point bending test. Numerical examples are presented to illustrate the ability of using damage theory to predict the damage evolution of a pavement structure as well as its service life.

Keywords Non-local elastic damage • Damage law • Fatigue life
Pavement structure • Finite element method

H. T. T. Nguyen (✉) · N. H. Nguyen

Department of Architecture and Civil Engineering, Thu Dau Mot University, Binh Duong, Vietnam

e-mail: tainht@tdmu.edu.vn

N. H. Nguyen

e-mail: hungnn@tdmu.edu.vn

H. T. T. Nguyen

Department of R&D, BMT Investment Construction J.S.C., Ho Chi Minh City, Vietnam

© Springer Nature Singapore Pte Ltd. 2018

H. Nguyen-Xuan et al. (eds.), *Proceedings of the International Conference on Advances in Computational Mechanics 2017*, Lecture Notes in Mechanical Engineering, https://doi.org/10.1007/978-981-10-7149-2_4

1 Introduction

Asphalt concrete is a widely used material for pavement surface because of its advantages, such as good workability, ease of repair and smoothness for vehicles travelling on it. Rutting and fatigue cracking are two common distresses of asphalt pavement. While rutting distress generally occurs relatively early after opening to traffic, fatigue cracking can be observed only after millions of load passes. The appearance of fatigue cracks does not reduce traffic safety as soon as it appears, yet it will facilitate the penetration of water, which will accelerate the degradation of the pavement structure. Therefore, the prediction of resistance to fatigue cracking, or fatigue life, is an important aspect in pavement structure design.

The fatigue life of a pavement structure can be estimated by using a simple prediction model of the tensile strain at the bottom of the asphalt layers due to the bending effect of traffic loading (bottom-up cracking). In many design guides for pavement structures [1, 2], prediction models, or transfer functions, have been specified to estimate the fatigue life. The model parameters in these design guides have been determined in advance based on laboratory test results of asphalt concrete beams [3, 4], fatigue testing of test-tracks [5] and field observations of pavements constructed in the past.

Along with the development of computational method, the modelling of fatigue behaviour of asphalt pavement structure under the exertion of repeated loading using numerical method is more and more favoured, including that using the theory of fracture [6–8] and damage [9–14]. Owing to the present of micro-cracking inside the material, the fatigue cracking of asphalt pavement is more frequently modelled by using damage theory. Because spurious localisation of strain and damage into a zone of vanishing volume commonly arises from the calculation using the classical continuum local damage theory, the non-local damage theory of Cabot and Bazant [15] is the most appropriate choice to overcome this issue. The evolution of fatigue cracking can be represented by the loss of stiffness in the structure, which is modelled by a damage law depending on the historic damage state and the strain tensor within the non-viscous behaviour assumption [10, 11, 16] or by a more sophisticated and versatile constitutive law when viscous behaviour is fully considered [17].

The purpose of this paper is to illustrate the use of a non-local elastic damage model to predict the fatigue life of asphalt pavement structure. Based on our observations on fatigue test results of several asphalt concretes in Vietnam and inspired by the idea of [10, 11], a modified damage model is also proposed.

2 Theoretical Formulation

Let Σ denote the second Piola–Kirchhoff stress tensor, which describes the stress state of a solid body in equilibrium under exterior loads and effects, and \mathbf{F} denotes

the deformation gradient tensor. Unless otherwise stated, Einstein's summation convention is used throughout. The local equilibrium equation of a solid body at any point is expressed by Eq. (1):

$$\mathbf{Div}(\mathbf{F} \cdot \boldsymbol{\Sigma}) + \rho_0 \mathbf{f} = 0 \quad (1)$$

where ρ_0 is the density body, \mathbf{f} is the prescribed body force of unit mass, and the \mathbf{Div} operator is defined as $(\mathbf{Div}(\mathbf{F} \cdot \boldsymbol{\Sigma}))_i = \frac{\partial(\mathbf{F} \cdot \boldsymbol{\Sigma})_{ij}}{\partial X_j}$. Let \mathbf{E} denote the Green–Lagrange strain tensor, which is related to the displacement field \mathbf{U} by

$$\mathbf{E} = \frac{1}{2} (\mathbf{Grad}(\mathbf{U}) + \mathbf{Grad}^T(\mathbf{U}) + \mathbf{Grad}^T(\mathbf{U}) \cdot \mathbf{Grad}(\mathbf{U})) \quad (2)$$

where the \mathbf{Grad} operator is defined as $(\mathbf{Grad}(\mathbf{U}))_{ij} = \frac{\partial U_i}{\partial X_j}$.

Under the effect of repeated loading, micro-cracking presents in the material, which decreases the effective resisting area of the material. Consequently, the true stress is higher than the macroscopic stress while the true strain remains unchanged. The relationship between the true and macroscopic stresses can be expressed as Eq. (3):

$$\boldsymbol{\Sigma}' = \frac{\boldsymbol{\Sigma}}{1 - D} \quad (3)$$

where D is a scalar describing the damage state at a point of the material. The value of D is in the range of $[0, 1]$, where $D = 0$ corresponds to no damage occurring and $D = 1$ represents a total failure of the material at that point.

For the sake of simplicity, let us assume that there is not plastic deformation in the asphalt pavement, and the behaviour of material is time-independent. The true stress is therefore assumed to be related to the elastic strain by means of Saint–Venant Kirchhoff's law:

$$\boldsymbol{\Sigma}' = 2\mu \mathbf{E} + \lambda \cdot \text{tr}(\mathbf{E}) \cdot \mathbf{I} \quad (4)$$

where \mathbf{I} is the second-order tensor of unity, μ is the shear modulus, λ is the Lamé constant, and the trace of tensor \mathbf{E} is defined as $\text{tr}(\mathbf{E}) = E_{ii}$. The shear modulus and Lamé constant are related to the Young modulus E and the Poisson ratio ν by $\mu = E/[2(1 + \nu)]$, $\lambda = E\nu/[(1 + \nu)(1 - 2\nu)]$. Substituting Eq. (3) in Eq. (4) gives rise to Eq. (5)

$$\boldsymbol{\Sigma} = (1 - D)[2\mu \mathbf{E} + \lambda \cdot \text{tr}(\mathbf{E}) \cdot \mathbf{I}] \quad (5)$$

In other words, the stiffness of the material at a point decreases by a factor of $(1 - D)$. The reduction of material stiffness can be expressed by the evolution of internal variable D . In case of modelling the fatigue behaviour of asphalt concrete,

the development of D can be expressed as a function of historic damage state and strain tensor as follows:

$$\frac{\Delta D}{\Delta N} = f(D, \mathbf{E}) \quad (6)$$

where N is the number of load cycles.

2.1 Damage Model for Predicting the Fatigue Life of Asphalt Concrete

Under cyclic loading, the material gets damage and loses its initial stiffness. Because the material is much stronger in compression than in tension, only tensile strain is considered in the damage model. The equivalent tensile strain is normally used and is defined using Mazar's definition [18]

$$E^{eq} = \sqrt{\langle E_i \rangle^2} \quad (7)$$

where $\langle E_i \rangle$ is the positive part of i th principal value of strain tensor. Inspired by the idea of [10, 11], the damage growth used in this work is modified as follows:

$$f(D, \mathbf{E}) = \left[\frac{A}{1 + \exp\left[\left(\frac{\alpha}{E^{eq}} D\right)^m\right]} + B \right] (E^{eq})^n \quad (8)$$

where A, B, α, m, n are model parameters to be identified based on laboratory test results.

2.2 The Need of Non-local Elastic Damage Theory

Many authors have demonstrated that the damage obtained with the local damage theory often localise into a zone of vanishing volume [15]. There are several techniques to ignore this spurious solution but the most general and effective one is to use the non-local damage theory.

A non-local damage treatment can be performed by replacing the local value of equivalent strain in Eq. (7) at a point \mathbf{X} by its average value over a certain volume, defined by

$$\tilde{E}^{eq}(\mathbf{X}) = \frac{1}{V_r} \int_{V_r} \varphi(R) E^{eq} dV \quad (9)$$

where V_r is the representative volume in which the value of equivalent strain at a point is averaged by those at other points on that volume, $\varphi(R)$ is a weight function of R being the distance from a point to \mathbf{X} . A bell shape function is used for $\varphi(R)$ in this work, defined by

$$\varphi(R) = \begin{cases} 1 - \frac{R^2}{R_c^2} & \text{if } R \leq R_c \\ 0 & \text{if } R > R_c \end{cases} \quad (10)$$

where R_c is the characteristic radius of the representative volume. Interested authors are also invited to consult the works of Jirasek [19, 20] and Belaidi Chabane Chaouche et al. [21] for a more detailed discussion on choosing weight function and the computational aspects of non-local damage theory.

2.3 Tangent Stiffness Matrix

Because of nonlinearity, discrete equilibrium equation system resulting from finite element discretisation can be solved with the Newton–Raphson method, and tangent stiffness matrix must be determined. From Eq. (5), the tangent stiffness can be expressed as follows:

$$\frac{\partial \Sigma}{\partial \mathbf{E}} = (1 - D) \left(2\mu \tilde{\mathbf{I}} + \lambda \tilde{\mathbf{J}} \right) - \frac{\partial D}{\partial \mathbf{E}} \otimes [2\mu \mathbf{E} + \lambda \cdot \text{tr}(\mathbf{E}) \cdot \mathbf{I}] \quad (11)$$

where the fourth-order tensor of unity is defined as $(\tilde{\mathbf{I}})_{ijkl} = \delta_{ik} \cdot \delta_{jl}$, $(\tilde{\mathbf{J}})_{ijkl} = \delta_{ij} \cdot \delta_{kl}$ and δ is Kronecker delta. Because the damage variable D is evaluated using the non-local equivalent strain, its derivative with respect to strain tensor \mathbf{E} is non-local and very complicated. If enough small time steps are applied, \tilde{E}_{n-1}^{eq} at the previous step can be used in place of \tilde{E}^{eq} and the non-local term related to the derivative of D does not remain. Thus, the only non-local term is the equivalent strain. The remaining terms are local as they are in a usual local finite element implementation.

3 Numerical Examples

This section shows the calculation results carried out on the basis of the previous formulation. All numerical results have been obtained using a home-made finite element programme developed under the Intel Visual Fortran environment.

3.1 An Elastic Bar Subjected to Cyclic Tensile Strain

This example addresses an elastic bar prescribed by a cyclic tensile strain of constant amplitude. The existence of exact solution to the problems allows the author to assess the efficiency of the formulation proposed. Because the strain has the same value at all point, the damage is therefore constant in space. The evolution of damage variable obeys the damage law presented in Eq. (8). Moreover, the non-local equivalent strain is also constant in space because of the uniform distribution of the local one.

Let us consider an elastic damage circular bar of 0.38 m in length and 0.1 m in diameter, which is excited by a cyclic strain of constant amplitude at two extremities. Because of axisymmetry, the problem can be treated in two dimensions, and just a half of the bar is discretised by 256 8-node rectangular elements as shown in Fig. 1a. The boundary conditions are as follows. The displacements along the z -axis are restrained for all nodes at the left boundary, and the displacements along the r -axis are restrained for all nodes on the symmetric axis. All nodes on the right extremity are prescribed by a cyclic displacement of constant amplitude such that the tensile strain amplitude is $E_{\max} = 10^{-4}$ m/m. The model parameters are assumed to be as follows: $E = 5$ GPa, $\nu = 0.35$, $A = 1.2 \times 10^2$, $B = 5.0$, $\alpha = 1.67 \times 10^{-3}$, $m = 2$, $n = 2$, and the characteristic radius of representative volume is chosen $R_c = 0$ or 0.03 m. The calculation results show that the damage is uniformly distributed in the bar, and the damage value calculated using non-local theory coincides that resulted from a local damage calculation (Fig. 1b). The numerical results match well with the analytical solution obtained using the explicit Euler method as can be observed in Fig. 1b.

A limited numerical parametric study has also been conducted to investigate the influence of the model parameters on the calculation result. It can be seen in Fig. 2 that the value of A, B, α has a different effect on the reduction in stiffness of the bar. Both parameters A and B have an influence on the rate of stiffness reduction. The larger the value of A and B is, the larger the rate of damage will be. While the effect

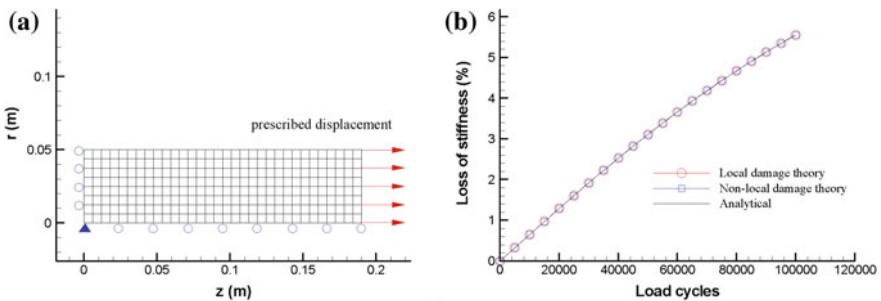


Fig. 1 Simple cyclic traction test. **a** Finite element modelling. **b** Evolution of damage (or loss of stiffness). Solid line: analytical solution, line with symbols: numerical solutions

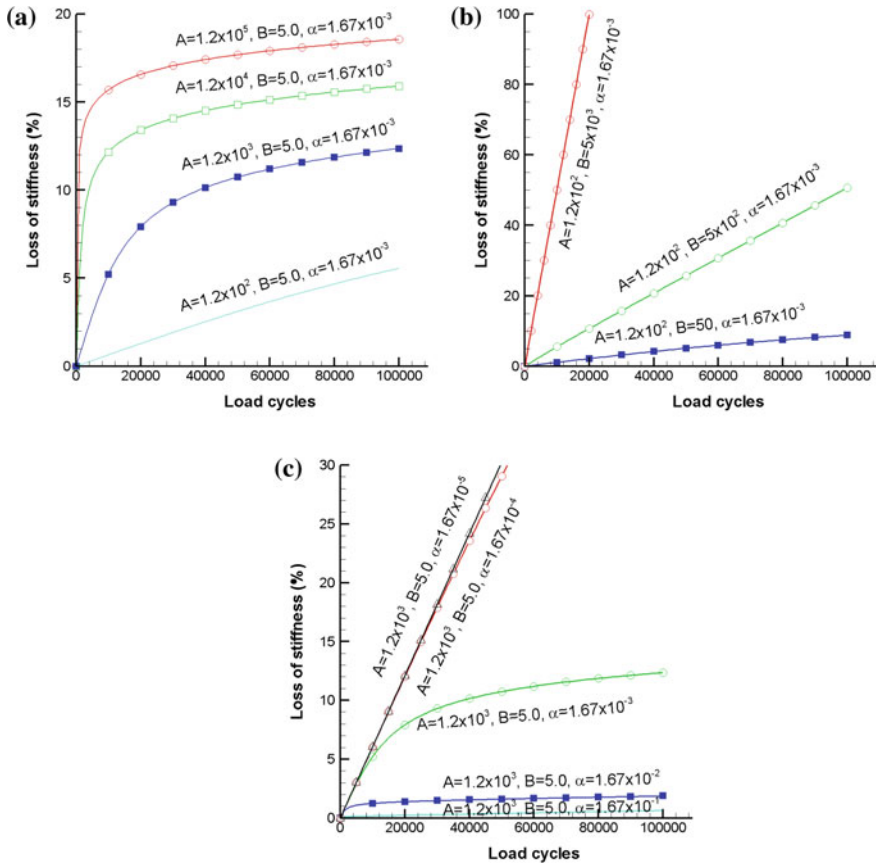


Fig. 2 Influence of the model parameters on the calculation result

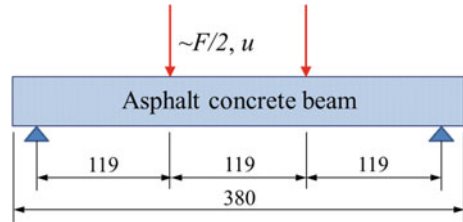
of B is almost unchanged, the effect of A can be attenuated by changing the parameters α and m . The value of n represents the sensitivity of damage in the material to the stress level. By choosing these model parameters, one can represent the fatigue behaviour of asphalt concrete as will be presented in the next example.

3.2 4-point Bending Test

3.2.1 Description of the Test

The 4-point bending test is normalised in many standards, such as AASHTO-T321 [3] and EN 12697-24 [4] and is widely used for evaluating the resistance of asphalt concrete to fatigue cracking when it is excited by a cyclic loading (Fig. 3). The

Fig. 3 4-point bending test



sample used has a form of a beam with dimensions $380 \times 50 \times 63 \text{ mm}^3$, which is prepared by sawing a slab cut from onsite pavement or prepared by a roller sector compactor. During the test, the asphalt concrete beam is held at a constant temperature by air conditioning. The applying forces have a form of a haversine function whose amplitudes are controlled to maintain a maximum stress or strain of constant amplitude in the beam. The corresponding displacement of the beam is also recorded.

The maximum tensile stress is located at the lower edge of the beam and is given by $\Sigma_{\max} = 3Fa/(bh^2)$, in which a is the equal distance between the supports and the acting points of applied forces and b, h are the width and height of the beam, respectively. The corresponding maximum tensile strain is a function of the displacement u , distance a , and the length of span L by $E_{\max} = 12uh/(3L^2 - 4a^2)$. The stiffness of the beam is defined as the ratio of stress to strain $S = \Sigma_{\max}/E_{\max}$, and therefore, the stiffness is a function of force and displacement.

There are two types of test including the constant stress and constant strain testing. In a constant stress testing, the applied forced is controlled to maintain a maximum stress of constant amplitude while the displacement is recorded to calculate the stiffness of the beam. The test usually ends up with the total failure of the beam. In contrast, the beam is normally considered failure if the reduction in stiffness reaches 50% in a constant strain testing.

3.2.2 Finite Element Modelling

The problem can be solved in two dimensions, and just a half of the beam is discretised using 256 8-node rectangular elements as shown in Fig. 4a. The total number of nodes in the problem is 849. The boundary conditions of the problem are as follows. Horizontal displacements are restrained for all nodes on the right side of the beam. The node at the location $x=0.011875 \text{ m}, y=-0.05 \text{ m}$ is fixed for all displacements, and the node at the location $x=0.130625 \text{ m}, y=0$ is prescribed by a cyclic force or displacement of constant amplitude. The model parameters are the same as those in the previous example, and the characteristic radius of representative volume is chosen $R_c=0.03 \text{ m}$.

- Constant strain testing

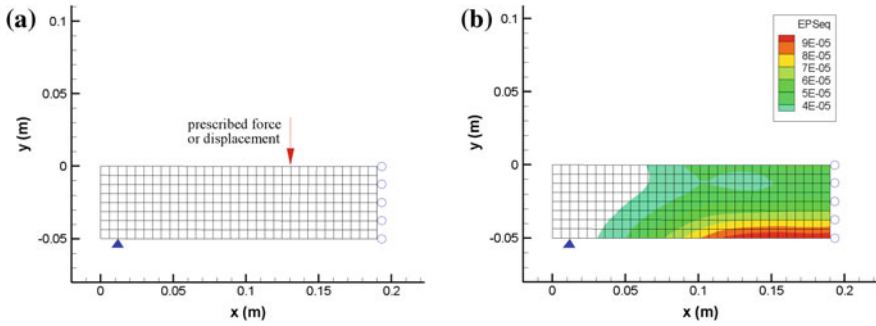


Fig. 4 Modelling the 4-point bending test. **a** Finite element modelling. **b** Distribution of the equivalent strain in the beam (only values of greater than or equal to 4×10^{-5} are shown)

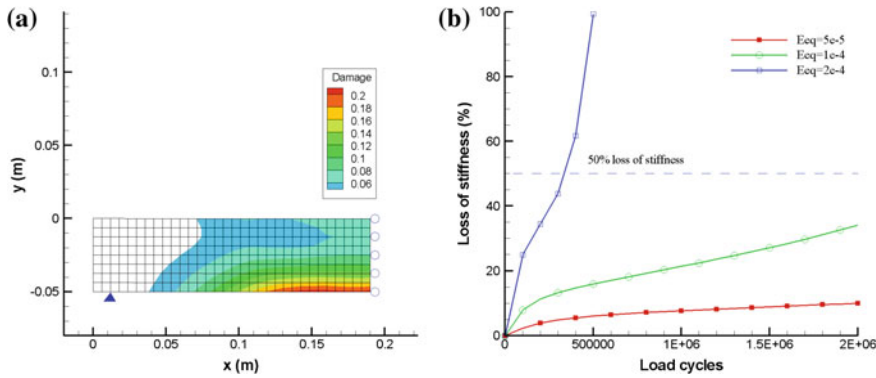
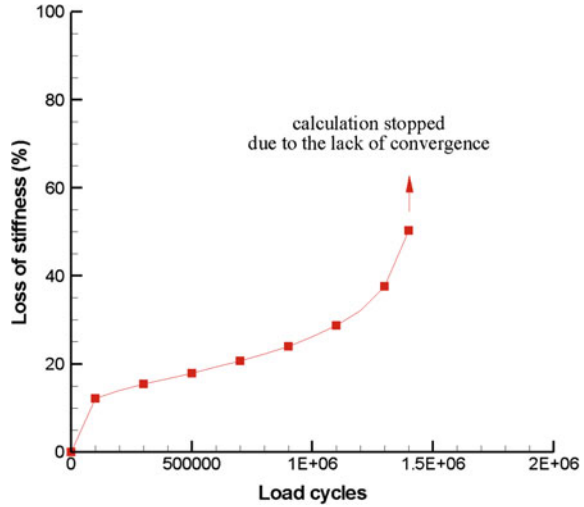


Fig. 5 Calculation results. **a** Distribution of damage in the beam (only values of greater than or equal to 0.06 are shown). **b** Reduction in stiffness of the beam—constant strain testing

The prescribed displacement amplitude is constant and its value is such that the amplitude of the maximum equivalent tensile strain in the beam is equal to $\tilde{E}_{max}^{eq} = 10^{-4}$ m/m (see Fig. 4b). Such displacement was found to have an amplitude of $u = -0.848 \times 10^{-4}$ m. The convergence was achieved in only 1–2 iterations on average, and the programme took approximately 2 min to complete 2,000 increments with an Intel Core i5 personal computer, in which 1000 load cycles were considered per increment.

The calculated results are summarised as follows. After 2,000,000 load cycles, the stiffness of the beam loses 10% of its initial value, and the distribution of damage in the beam is similar to that of equivalent strain (Fig. 5a). Damage almost occurs at the lower edge of the beam located between the two acting points of applied force where the equivalent strain amplitude is the highest. The loss of beam stiffness increases with an increase of load cycles, and strain amplitude is also presented in Fig. 5b.

Fig. 6 Reduction in stiffness of the beam—constant stress testing



- Constant stress testing

The prescribed force amplitude is constant during the test and its value is such that the maximum equivalent tensile strain amplitude in the beam is initially equal to that in the constant strain testing $\tilde{E}_{\max}^{eq} = 10^{-4}$ m/m, giving rise to $F/2 = -0.335747 \times 10^4$ N. The calculated results are summarised as follows. After 1,400,000 load cycles, the beam decreases 50.3% of its initial stiffness. Therefore, the number of load cycles needed for the beam to fail in constant stress testing condition is much smaller than that in constant strain testing condition. The stiffness of the beam decreases rapidly in the last load cycles (see Fig. 6), resulting in lack of numerical convergence.

3.2.3 Choosing the Characteristic Radius

In this section, the effect of characteristic radius changes on the numerical solution, especially the strain localisation is considered. The problem used in this section is the same as that in the previous section excepted that the value of the characteristic radius varies in the range of $[0, h]$ —namely, $0, h/5, 2 h/5, 3 h/5, 4 h/5$, and h . The calculation results show that there are spurious strain localisations into a zone of vanishing volume in case of $R_c \in [0, 2h/5]$ as illustrated in Fig. 7, and the characteristic radius has a strong influence on the maximum equivalent strain amplitude as demonstrated in Table 1. The larger the representative volume is, the lower the maximum equivalent strain amplitude will be because of the average effect. Consequently, the value of R_c affects the evolution of damage in the beam in a way that the loss of stiffness always decreases with an increase of the characteristic radius. Thus, the characteristic radius should have the lowest value such that there is not

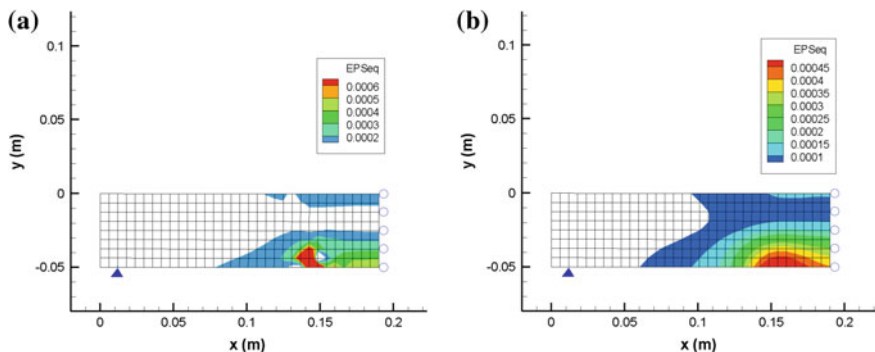


Fig. 7 Strain localisation in case of: **a** $R_c=0$ (values of less than 0.0002 are not shown), **b** $R_c=2h/5$ (values of less than 0.0001 are not shown)

Table 1 Effect of characteristic radius on the maximal equivalent tensile strain

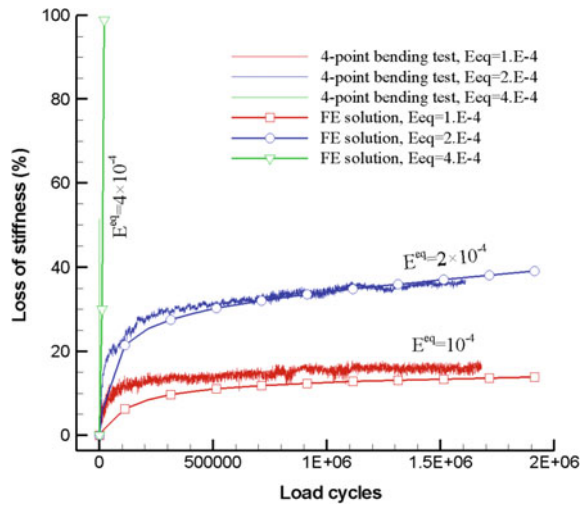
Characteristic radius R_c	$\tilde{E}_{\max}^{eq} (\times 10^{-6} \text{ m/m})$ $u = -0.848 \times 10^{-4} \text{ m}$	$\tilde{E}_{\max}^{eq} (\times 10^{-6} \text{ m/m})$ $u = -1.696 \times 10^{-4} \text{ m}$	$\tilde{E}_{\max}^{eq} (\times 10^{-6} \text{ m/m})$ $u = -3.392 \times 10^{-4} \text{ m}$
0	170.5	340.7	681.5
$h/5$	146.1	292.2	583.4
$2h/5$	122.9	245.8	491.2
$3h/5$	100.3	200.3	400.5
$4h/5$	82.6	165.3	330.5
h	73.5	144.8	296.0

spurious strain localisation, and the relevant value of R_c in this example is $R_c=3h/5$, or $R_c=0.03 \text{ m}$. This value verifies well the suggestion of Bazant and Cabot [22] that the characteristic radius should be 2.7 times the size of maximum aggregate size, ranging from 0.025 to 0.051 m for asphalt concrete.

3.2.4 Model Parameters Identification

In this section, we make use of the 4-point bending test results for the back-calculation of model parameters. The process of identifying model parameters is as follows. After the laboratory test results were obtained; the 4-point bending test problem was solved with different ranges of input model parameters. The model parameters to be determined are the input parameters that reproduce the stiffness loss curve, which well fit those obtained from the laboratory tests. Let us consider a set of 4-point bending test results of a specific asphalt concrete at three specific strain amplitude—namely, 10^{-4} m/m , $2 \times 10^{-4} \text{ m/m}$, and $4 \times 10^{-4} \text{ m/m}$ as shown in Fig. 8 (the continuous lines). The following input data reproduces the stiffness loss curve and well fit the results obtained from the 4-point bending test: $E = 5 \text{ GPa}$,

Fig. 8 Model parameters identification



$\nu = 0.35$, $A = 4.42 \times 10^4$, $B = 44.2$, $\alpha = 10^{-3}$, $m = 2$, $n = 2.5$. In other words, these parameters can be considered as material constants and will be used in the next example to predict the fatigue life of a realistic pavement structure made of this material.

3.3 Predicting the Fatigue Life of a Pavement Structure

Let us consider two typical pavement structures that are commonly used for national road and expressway in Vietnam. The first one is a 2-asphalt layer structure hereafter denoted as thin structure, and the second one is a 3-asphalt layer structure hereafter denoted as thick structure. The thin structure is widely used for national highway because of its low cost while the thick structure is almost only used for expressway where high level of evenness and longer service life are required. The thickness of the first, the second, and the third asphalt layer is generally 5 cm, 7 cm, and 9 cm, respectively. According to the Vietnam Standard for calculating pavement structure 22TCN: 211-06 [23], the wheel load is represented by a uniformly distributed force of 100 kN acting upon a circular area of 33 cm in diameter, corresponding to a pressure of 0.6 MPa.

Because of axisymmetry, the pavement structure can be treated in two dimensions, and just a half of the pavement structure is discretised by 735 8-node rectangular elements as shown in Figs. 9a and 10a. The total number of nodes in the problem is 2318. The boundary conditions of the problem are as follows. Horizontal displacements are restrained for all the leftmost nodes and for those on the symmetric line. All nodes on the bottom of the structure are fixed for all displacements.

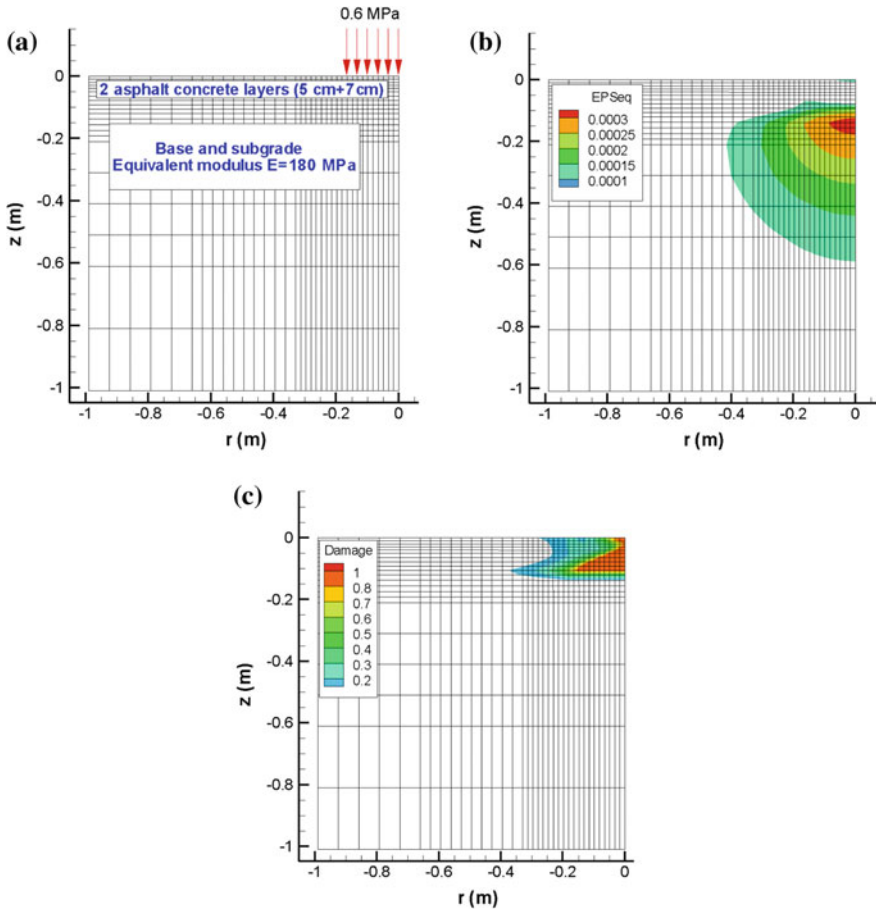


Fig. 9 2-asphalt layer structure. **a** Finite element discretisation. **b** Distribution of equivalent tensile strain amplitude (values of less than 10^{-4} are not shown). **c** Distribution of damage after 292,100 load cycles (values of less than 0.2 are not shown)

The asphalt layers are assumed to be an elastic damage material while the base and subgrade are assumed to be purely elastic. The bonds between asphalt layers and between an asphalt layer and the base are perfect to simplify the problem. The programme took 1–2 iterations on average for one increment, and the total computational time for a problem was approximately 22 min. The calculation results are summarised as follows. The maximum equivalent tensile strain at initial configuration for the thin structure is 3.19×10^{-4} m/m and located at the bottom of the second asphalt layers as can be seen in Fig. 9b. After 272,500 load cycles, the stiffness of the thin structure decreases 72.4% of its initial value (Fig. 11, the curve in blue). The damage is concentrated at the lower edge of the asphalt layer at the beginning and gradually develops to surface of the pavement as can be seen in

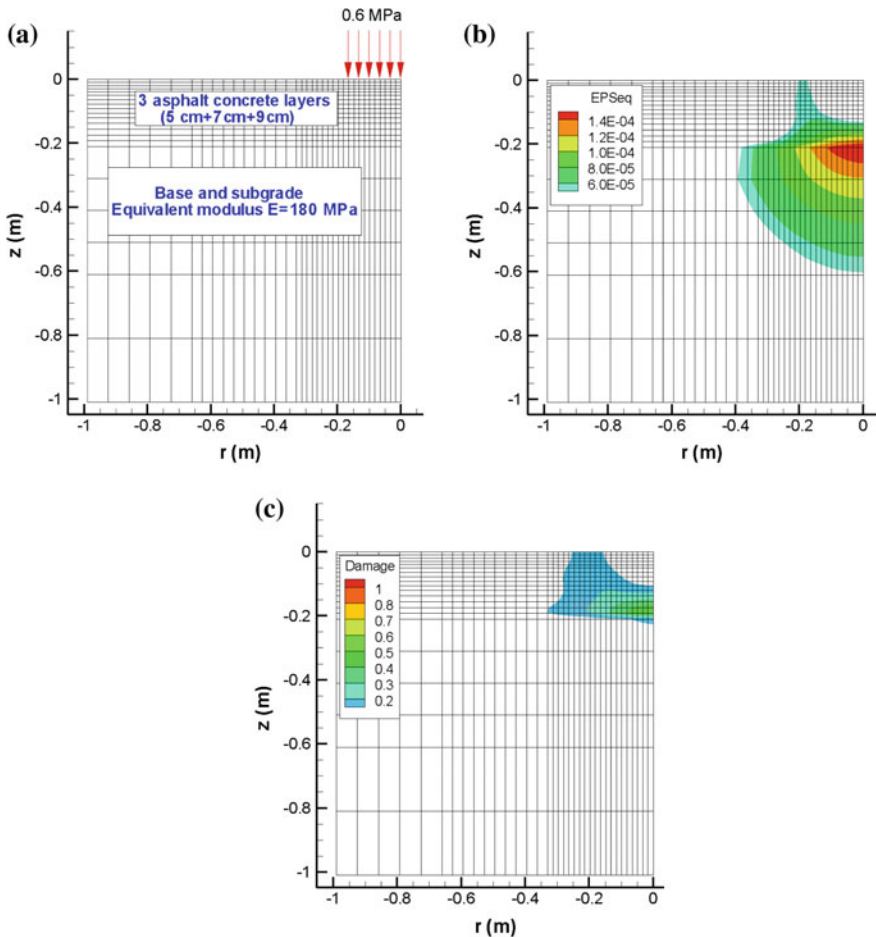
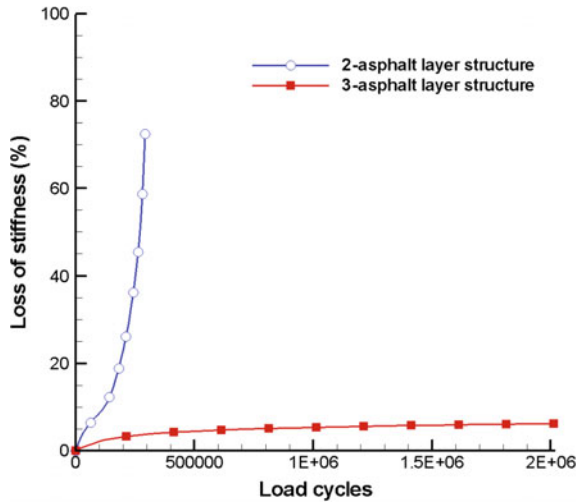


Fig. 10 3-asphalt layer structure. **a** Finite element discretisation. **b** Distribution of equivalent tensile strain amplitude (values of less than 5×10^{-5} are not shown). **c** Distribution of damage after 9,915,000 load cycles (values of less than 0.2 are not shown)

Fig. 9c. If the failure of a pavement structure is defined as the state at which the reduction of stiffness reaches 50%, the number of load cycles to failure, or the fatigue life, of the thin structure is only 292,100 cycles.

This value is too much lower compared to the fatigue life of a realistic pavement whose value is generally millions of load cycles. The reason is that the pavement is subjected to healing phenomenon that occurs between vehicle passes and during the high temperature periods and the wheel loads on realistic pavement do not apply at the same location, which increase the fatigue life [24]. Moreover, the stiffness reduction in the 4-point bending test is influenced by other effects, such as nonlinear effect, self-heating, and thixotropy during the test, which increase artificially the

Fig. 11 Reduction in stiffness of pavement structure. The curve in blue corresponds to 2-asphalt layer structure and that in red corresponds to 3-asphalt layer structure



reduction in stiffness of the beam [25–27]. Therefore, the predicted fatigue life based on laboratory 4-point bending test result should be multiplied by a factor, called shift factor, to account for the differences between laboratory and field conditions. By using a shift factor of 18.4 proposed by the Asphalt Institute [24], the fatigue life of this pavement will be 5,374,640 load cycles, which is a reasonable value.

The same calculation is performed for the thick structure. The results show that the maximum equivalent tensile strain is two times smaller (1.61×10^{-4} m/m) compared to that of the thin structure, giving rise to a much longer fatigue life (1.5×10^8 cycles). This value is extrapolated from the curve of loss of stiffness presented in Fig. 11 (the curve in red). The distribution of maximum equivalent tensile strain amplitude at initial configuration and the damage state in the thick structure are also presented in Fig. 10b, c. It is clear that the fatigue life of a 3-asphalt layer structure is much longer than that of a 2-asphalt layer structure. The excess cost for adding the third asphalt layer in the structure is compensated by a much longer fatigue life and therefore a reduction in the maintenance cost.

4 Conclusions

The non-local damage theory is successfully applied to predict the fatigue life of asphalt pavement structure, and the proposed damage model is capable to reproduce the reduction in stiffness of asphalt concrete structures. The issue of spurious localisation of strain and damage into a zone of vanishing volume is properly addressed if an enough large characteristic radius is used. By using the damage value computed at the previous step instead of the actual one in the damage law, the

evaluation of tangent stiffness becomes local, which simplifies the calculation while enough accuracy can be attained if enough small calculation steps are applied. The formulation is nearly local, which is illustrated and validated by means of specific calculation examples. The first example is devoted to validating the formulation via a simple example of a one-dimensional elastic damage bar for which an analytical solution exists, whereas the last two examples relate to simulating the fatigue behaviour and evaluating the fatigue life of an asphalt concrete structure. It can be observed from the calculation results that the fatigue life of the pavement structures in these examples has reasonable value compared to that of a realistic pavement.

References

1. Setra-LCPC (1994) Conception et dimensionnement de structures de chaussée-Guide technique, Service d'études techniques des routes et autoroutes – Laboratoire central des ponts et chaussées
2. AASHTO (2008) Mechanistic-empirical pavement design guide—a manual of practice. American Association of State Highway and Transportation Officials
3. AASHTO T-321 (2004) Standard method of test for determining the fatigue life of compacted asphalt mixtures subjected to repeated flexural bending, Washington
4. EN 12697-22 (2007) Bituminous mixtures: test method for hot mix asphalts-Part 24: Resistance to fatigue, Brussels
5. IFSTTAR. Le manège de fatigue des structures routières. http://www.lames.ifsttar.fr/fileadmin/redaction/1_institut/1.20_sites_integres/MAST/LAMES/Grands_%C3%A9quipements/plaquette_manege_fr.pdf
6. Kuai H, Le H, Zi G, Mun S (2009) Application of generalized J -integral to crack propagation modeling of asphalt concrete under repeated loading. *Transp Res Rec* 2127:72–81
7. Luo X, Luo R, Lytton RL (2013) A modified Paris' law to predict entire crack growth in asphalt mixtures. *Transp Res Rec* 2373:54–62
8. Luo X, Zhang Y, Lytton RL (2016) Implementation of pseudo J -integral based Paris' law for fatigue cracking in asphalt mixtures and pavements. *Mater Struct* 49(9):3713–3732
9. Alimami M (1987) PhD thesis: Contribution à l'étude de l'endommagement par fatigue des enrobés bitumineux, University of Paris 6, Paris
10. Bodin NB (2002) PhD thesis: Modèle d'endommagement cyclique: Application à la fatigue des enrobés bitumineux, Ecole Centrale de Nantes, Nantes
11. Bodin ND, Pijaudier-Cabot G, De la Roche C, Piau JM, Chabot A (2004) Continuum damage approach to asphalt concrete fatigue modeling. *J Eng Mech (ASCE)* 130(6):700–708
12. Christensen DW, Bonaquist R (2005) Practical application of continuum damage theory to fatigue phenomena in asphalt concrete mixtures. *J Assoc Asphalt Paving Technol* 74:963–1002
13. Underwood BS, Baek C, Kim YR (2012) Simplified viscoelastic continuum damage model as platform for asphalt concrete fatigue analysis. *Transp Res Rec* 2296:36–45
14. Arsenie IM, Chazallon C, Duchez JL, Mouhoubi S (2017) Modelling of the fatigue damage of a geogridreinforced asphalt concrete. *Road Mater Pavement Des* 18(1):250–262
15. Pijaudier-Cabot G, Bazant ZP (1987) Nonlocal damage theory. *J Eng Mech* 113(10):1512–1533
16. Di Benedetto H, Ashayer Soltani MA, Chaverot P (1996) Fatigue damage for bituminous mixtures: a pertinent approach. *J Assoc Asphalt Paving Technol* 65:142–158
17. Neifar M, Di Benedetto H (2001) Thermo-viscoplastic law for bituminous mixes. *Road Mater Pavement Des* 2(1):71–95

18. Mazars J (1984) PhD thesis. Application de la mécanique de l'endommagement au comportement non linéaire et à la rupture de béton de structure, Université Pierre et Marie Curie, Paris
19. Jirasek M (2004) Non-local damage mechanics with application to concrete. *Revue Française de Génie Civil* 8(5–6):683–707
20. Jirasek M. Lecture note. Nonlocal damage models. <http://mech.fsv.cvut.cz/~milan/sample.pdf>
21. Belaidi Chabane Chaouche O, Almansba M, Frarah D, Hannachi NE (2013) Theoretical and computational aspects of non local damage coupling with elastic behaviour. *UPB Sci Bull Ser D Mech Eng* 75(1):57–72
22. Bazant ZP, Pijaudier-Cabot G (1989) Measurement of characteristic length of nonlocal continuum. *J Eng Mech* 115(4):755–767
23. TCN: 211-06 (2006) Flexible pavement. Specifications and requirements for pavement structure design. Vietnamese Standard, Hanoi
24. Huang YH (2004) Pavement analysis and design, 2nd edn. Pearson Prentice Hall, Upper Saddle River
25. Di Benedetto H, Nguyen QT, Sauzéat C (2011) Nonlinearity, heating, fatigue and thixotropy during cyclic loading of asphalt mixtures. *Road Mater Pavement Des* 12(1):129–158
26. Mangiafico S et al (2015) Quantification of biasing effects during fatigue tests on asphalt mixes: non-linearity, self-heating and thixotropy. *Road Mater Pavement Des* 16(S2):73–99
27. Riahi E et al (2017) Modelling self-heating and thixotropy phenomena under the cyclic loading of asphalt. *Road Mater Pavement Des* 18(S2):155–163

Failure of Building Structural Members During the Cooling Phase of a Fire



Q. V. Truong, T. H. Pham and T. B. Chu

Abstract Fires in buildings are characterized by a heating phase followed by a cooling phase, but the effects of the cooling phase on structures are not well researched. This work presents an analysis of the behavior of different structural members under natural fires, with the aim to characterize their delayed failure in the cooling phase of a natural fire. Thermo-mechanical numerical simulations based on the nonlinear finite element method (SAFIR code) are conducted. Results show that, for all the studied members (column, beam) and materials (reinforced concrete, steel, steel-concrete composite), structural failure during the cooling phase of a fire is a possible event. The time structures fail can be up to 250 min later than the time maximum temperature in room reaches. The major factors that affect delayed failure time of structural members are the duration of heating phase of the fire, the applied load ratio, and the thickness of thermal insulation material (including concrete material). This work enhances the understanding of the structural behavior in the cooling phase of a fire and gives information for the safety of the fire fighters and people in a natural fire.

Keywords Natural fire · Cooling phase · Building structures
Delayed failure

Q. V. Truong (✉)

The University of Fire Fighting and Prevention, Hanoi, Vietnam
e-mail: tqvinhduy@gmail.com

T. H. Pham · T. B. Chu (✉)

Hanoi Architectural University, Hanoi, Vietnam
e-mail: chuthibinh.hau@gmail.com

T. H. Pham

e-mail: phamthanhhung.hau@gmail.com

© Springer Nature Singapore Pte Ltd. 2018

H. Nguyen-Xuan et al. (eds.), *Proceedings of the International Conference on Advances in Computational Mechanics 2017*, Lecture Notes in Mechanical Engineering, https://doi.org/10.1007/978-981-10-7149-2_5

1 Introduction

In a performance-based approach, natural fire models include the heating phase and the cooling phase, while standard fires consist in heating phase only such as the standard ISO 834 and ASTM E119 fires [1, 2] (Fig. 1). In literature, most researches on building structures in fire conditions focus on the behavior of structures in the heating phase only [3–5]. Recently, the possibility of structural collapse during or after the cooling phase has been examined by some authors, [6–8] but they focus mainly on the possibility of structural collapse and the minimum value of heating time that the structures fail. This research focuses on the analysis of delayed failure time of building structural members in the cooling phase of a natural fire. The moment structures may fail is important to fire fighters who need to know the failure time to avoid danger during fire fighting operation.

To allow for comparative analyses and quantification of the response, following definitions are introduced:

- Load ratio: the ratio of applied load acting on the structural element in fire conditions to the load-carrying capacity of the element at room temperature. In

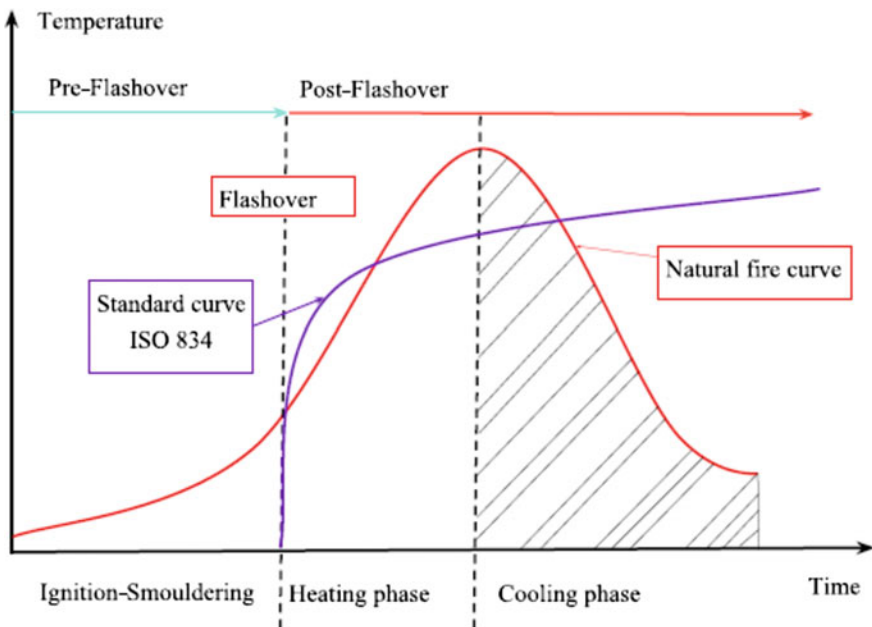


Fig. 1 Natural fire curve and standard fire curve

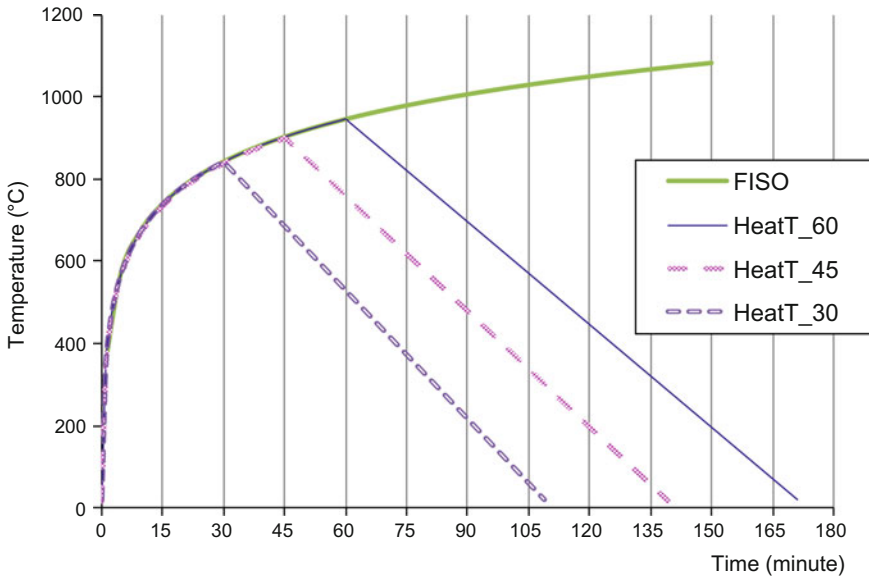


Fig. 2 Eurocode parametric fire model for natural fire

the event of a fire, the applied loads are much lower than the maximum design loads specified for normal temperature conditions because load combination factors are smaller under fire conditions compared to normal conditions. Load ratio is recommended less than 0.65 in EN1991-1-2 [9] and not greater than 0.6 as calculated in the thesis of Chu Thi Binh [10]

- Fire resistance rating (R): the fire resistance time (in minute) of structures exposed to a standard fire until failure. R relates closely to the applied load ratio.
- Heating time (HeatT): The duration of heating phase (in minute) of a natural fire (Fig. 2).
- Time of failure (Tfail): The duration (in minute) from the beginning of the fire to the moment structures fail.
- Delayed failure time (DelayT): The duration (in minute) from the end of heating phase to the moment structures fail: $DelayT = T_{fail} - HeatT$

The objective of this research is to do numerical analyses of various structural elements subjected to natural fires in order to identify which parameters affect the delayed failure time (DelayT). The studied structural elements are columns and beams made of reinforced concrete, steel, and steel-concrete composite.

2 Computational Models of Structural Members Exposed to Natural Fire

The analysis of structural members subjected to fire has been done using SAFIR code. SAFIR is a nonlinear finite element software developed at the University of Liege, Belgium for the simulation of thermal and structural behavior under ordinary and fire. More information about SAFIR program is given in [11]. The validation of SAFIR code has been done in some studies [12, 13].

2.1 Fire Model

The adopted model for the natural fires is the parametric fire model from EN 1991-1-2 [9]. The value of the factor Γ is 1.0 in the model, which makes the heating phase of the time–temperature curve of this natural fire model approximates the standard ISO curve. Figure 2 shows the time–temperature curves for different values of HeatT. Curve HeatT_60 expresses the natural fire with 60 min of heating phase. FISO is the standard fire curve ISO 834.

2.2 Heat Transfer Analysis

A uniform temperature is assumed over the height of the element. Thus, thermal analysis can be reduced to a two-dimensional problem. The cross section is discretized using triangular and quadrilateral elements. Figure 3 represents one of the composite sections analyzed in this study.

The thermal properties of steel and concrete are taken from Eurocodes [14]. Where concrete is used, siliceous concrete is chosen, with a density of 2400 kg/m^3 and a water content of 48 kg/m^3 .

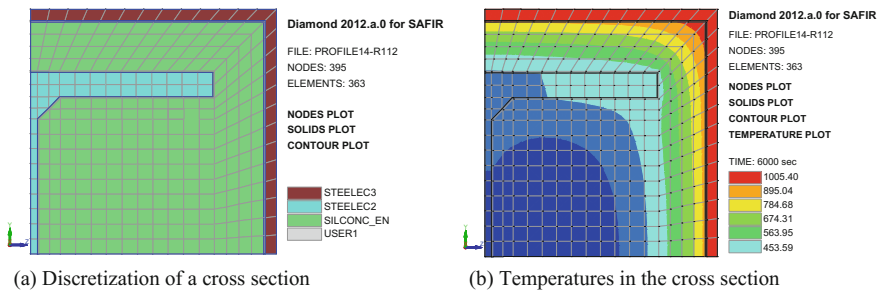


Fig. 3 Column cross section (1/4 of the section by symmetry)

2.3 *Structural Analysis*

In the model, the structural elements are built up by means of several 2-D Bernoulli beam elements. The cross section is divided into fibers that match the discretization used for the thermal analysis.

In this research, all the mechanical properties of the steel and concrete follow the recommendations of the Eurocodes. The mechanical behavior of steel follows the model of Eurocode [15]. For concrete material, the Explicit Transient Creep Eurocode model added to SAFIR code by Gernay T. [16] is used.

3 **Analysis of the Failure of Building Structural Members in the Natural Fire**

3.1 *Temperature Evolutions in Cross-Section of Structural Elements*

Figure 4 shows the temperature evolution in a section of steel-composite element. The furnace temperature is a natural fire with 60 min of heating phase. The temperatures of external steel hollow section (node 6), the internal steel profile (node 7), and the concrete core (node 3) are shown. The furnace and the external steel profile reach maximum temperature at time 60 min while the internal steel profile reaches maximum temperature after 120 min. The temperatures of concrete in center zone keep on increasing even after 180 min. The column may not fail after 60 min exposed to heating phase (if the fire resistance R is greater than 60 min) but it possibly fails after more than 60 min, during the cooling phase of the fire.

3.2 *Delayed Failure Time (DelayT) of Structural Element*

It is defined that $\text{DelayT} = T_{\text{fail}} - \text{HeatT}$. An example of steel-concrete composite column in Fig. 4 is used to explain. The columns expose to natural fire $\text{HeatT} = 60$ min. It is calculated that the column fails at time $T_{\text{fail}} = 120$ min, so $\text{DelayT} = 120 - 60 = 60$ min. It means that the column fails 60 min later than the moment the fire starts decreasing its temperature. It is important to know the delayed time to let the fire fighters keep off the failure of the buildings. One of the objectives of this study is to give an insight into the parameters that affect the delayed failure time DelayT of structural elements made of steel, concrete, and steel-concrete composite.

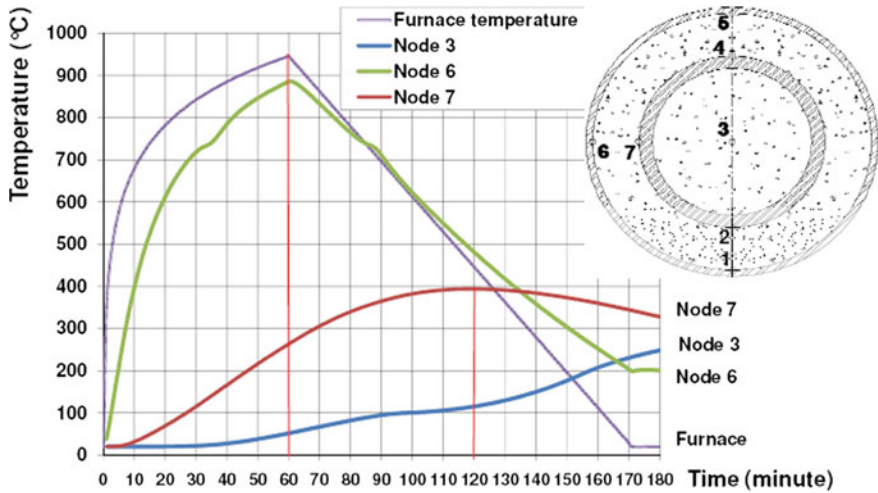


Fig. 4 Temperature evolution in steel-composite sections in the natural fire with 60 min of heating phase

3.3 Parametric Studies of Delayed Failure Time (DelayT)

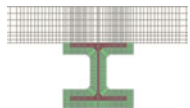
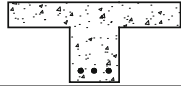
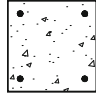


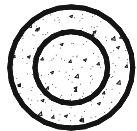
Twenty-four cross sections have been studied. This article shows six typical cross sections (Table 1). The other cross sections are similar to the cross-sectional types of the profiles in Table 1 but different dimensions and different steel profiles. The steel profiles are accordant with European standards.

The structural element (beam or column) is divided into 10 beam elements to take into account deformed geometry. Columns are hinged at both ends and subjected to a compression load which is constant during the fire (Fig. 5). Beams are simply supported beams subjected two point loads (Fig. 6).

The fire resistance R and the time of failure T_{fail} are calculated for columns with various fire curve, cross-section, column length, concrete grade, and load ratio. Column length is from 2 to 8 m. Beam length is from 4 to 6 m. Concrete strength 30, 40, and 50 MPa is used. Applied load ratios from 0.2 to 0.6 are studied.

The simulations aim at assessing the failure of the structural member during the course of the natural fire. For a given structural member, numerical simulations are run under different natural fire exposures (see Fig. 2). The objective is to find the relationship between some parameters such as heating time $HeatT$, load ratio, concrete cove thickness on $DelayT$ of structural members. Moreover, the study finds how great $DelayT$ could be for calculated structural members.

Table 1 Cross-sections of studied structural elements

Cross-section name	Image	Description
Profile 22		Steel beam covered by fire insulations Steel profile: HE160B Supports concrete slab
Profile 20		RC beam Section dimension: 300 × 600 mm Containing 3 steel bars of 20 mm diameter
Profile 21		RC column Section dimension: 300 × 300 mm Containing 4 steel bars of 20 mm diameter
Profile 14		Composite section External steel profile: S 350 × 8 Internal steel profile: HE260B
Profile 11		Composite section External steel profile: C 355.5 × 6 Internal steel profile: HE200B
Profile 15		Composite section External steel profile: C 355.5 × 6 External steel profile: C 273 × 12

3.3.1 Effect of Heating Time HeatT

T_{fail} and Delay_T are calculated with different fire curves (different Heat_T). Table 2 shows the results of beam profile 20 and column profile 14 under a defined load. In beam profile 20, the fire resistance of the beam is 115 min. Therefore, under the fire curve with Heat_T = 115, the beam fails at time 115 (=R), of course. Under the fire curve with Heat_T = 95, the beam fails at time 120. Under the fire curve with Heat_T = 100, the beam fails at time 116, and so on with Heat_T = 91 the beam does not fail. The note “NO” in Table 2 expresses the element does not fail in this fire exposure. Results show that the smaller Heat_T is, the greater Delay_T is.

3.3.2 Effect of Load Ratio

The parameter “load ratio,” defined as the ratio of axial load acting on the column to the load-carrying capacity of the column at room temperature, is of more important than the applied load value acting on the column, as the load ratio represents the extent to which the column is stressed.

Fig. 5 Column model

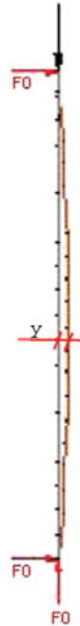


Fig. 6 Beam model and bending moment

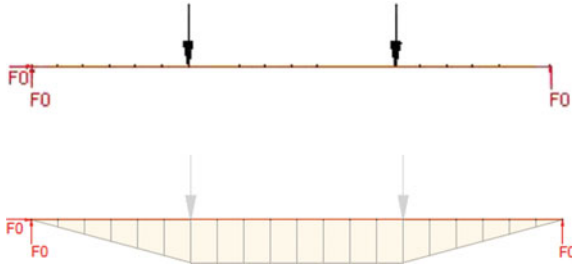


Table 2 Results of beams profile 20 and columns profile 14 with various HeatT and load ratio

Element	R (min)	HeatT (min)	Tfail (min)	DelayT (min)	R-HeatT (min)
Beam Profile 20	115	115	115	0	0
		105	115	10	10
		100	116	16	15
		95	120	25	20
		92	126	34	23
		91	NO		
Column profile 14	164	164	164	0	0
		159	164	5	5
		154	165	11	10
		144	169	25	20
		139	172	33	25
		129	186	57	35
		126	208	82	38
		125	NO		39

Table 3 Results of columns profile 15, column profile 11, and beam profile 20 with various load ratios

Element	Load ratio	R (min)	HeatT (min)	Tfail (min)	DelayT (min)
Column Profile 15	0.3	140	111	167	56
	0.4	104	85	126	41
	0.5	64	57	76	19
	0.6	41	36	47	11
Column Profile 11	0.3	97	77	114	37
	0.4	69	56	80	24
	0.5	51	34	118	84
	0.6	37	27	83.5	57
Beam Profile 20	0.3	115	92	126	34
	0.4	102	80	113	33
	0.5	91	70	102	32
	0.6	81	62	87	25

The structural elements were analyzed with the load ratio from 0.3 to 0.6. Results with R lower than 30 min are ignored because they are not useful in practice. Table 3 shows results of columns profile 15, column profile 11, and beam profile 20. Column height is 3 m, concrete grade is C50, and eccentricity of axial load is 1 cm. Beam length is 6 m, and concrete grade is C30. For each value of load ratio, DelayT is calculated with various values of HeatT but Table 3 notes only the case that gives the greatest DelayT. As shown in Table 2, for a defined member the smallest HeatT gives the greatest DelayT. In some other publications [6, 17], the minimum value of HeatT that results in a failure of structures is noted DHP (duration of heating phase). Calculating DHP requires an iterative process, which may be computationally expensive.

Results show that load ratio affects much Tfail and DelayT.

In most cases, DelayT decreases when load ratio increases but in some cases it does not follow this correlation (see columns profile 11 in Table 3). Some composite elements of external steel tube embeds another internal steel profile have unusual great DelayT. The load resistance of the element first decreases then raises then decreases during the fire. It can be explained that after the heating phase of the fire the external steel tube is cooler while the internal steel profile is continuously hotter, so the external steel profile is recovering its strength while the internal steel profile is losing its strength. It results in the load resistance of the members sometimes decreases sometimes raises with fire time, leading to unusual great value of DelayT. This phenomenon often appears in composite columns consist of a hollow steel section embed another steel profile. It rarely appears in reinforced concrete elements and steel elements. The reason may be the cooler zone of the elements during cooling phase plays more important role in composite columns than in reinforced concrete or steel members.

Table 4 R, Tfail, and DelayT with various thickness of fire protection layer

Element	Insulation thickness (mm)	Load ratio	R (min)	HeatT (min)	Tfail (min)	DelayT (min)
Beam profile 22	24	0.5	175	175	175	0
	24	0.5		150	179	29
	24	0.5		132	205	73
	24	0.5		131	NO	
Beam profile 22	18	0.5	132	132	132	0
	18	0.5		122	133	11
	18	0.5		102	153	51
	18	0.5		101	NO	
Beam profile 22	15	0.5	112	112	112	0
	15	0.5		91	118	27
	15	0.5		88	127	39
	15	0.5		87	NO	
Beam profile 22	12	0.5	91	91	91	0
	12	0.5		86	91	5
	12	0.5		73	102	29
	12	0.5		72	NO	

3.3.3 Effects of Insulation Cover Thickness

The failure time Tfail of beam profile 22 with various values of insulation cover thickness is calculated. The insulation is CAFCO300 spay applied fireproofing. The thickness of the insulation layer is 12, 15, 18, and 24 mm. For each value of insulation cover thickness, the element has each value of fire resistance R so we calculated with different HeatT for different values of insulation cover thickness. It cannot compare DelayT of the elements under different fire curves so we compare the greatest value DelayT could be for each of the values of the insulation cover thickness. It is the value of DelayT corresponding to the minimum value of HeatT that makes elements fail. Results show that the thicker insulation layer gives the greater DelayT (Table 4).

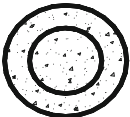
3.3.4 Effect of Concrete Cover Thickness

The fire resistance R and Tfail of column profile 21 with various values of concrete cover thickness are calculated. Because concrete acts as an insulation layer for steel bar in reinforced concrete structures so the greater concrete cover thickness is, the greater DelayT can be (Table 5).

Table 5 R, Tfail, and DelayT with various concrete cover thickness

Element	Concrete cover thickness (mm)	HP (min)	Load ratio	R (min)	HeatT (min)	Tfail (min)	DelayT (min)
Column profile 22	27	FISO	0.4	60	60	60	0
	27	55	0.4		55	61	6
	27	49	0.4		49	66	17
	27	48	0.4		48	68	20
	27	47	0.4		47	NO	
Column profile 22	31	FISO	0.4	64	64	64	0
	31	59	0.4		59	65	6
	31	53	0.4		53	68	15
	31	50	0.4		50	73	23
	31	49	0.4		49	NO	
Column profile 22	45	FISO	0.4	74	744	74	0
	45	59	0.4		69	75	6
	45	53	0.4		54	87	33
	45	50	0.4		53	94	41
	45	49	0.4		52	NO	

Table 6 DelayT of column profile 17

Cross-section	Height (m)	Load ratio	R (min)	HeatT (min)	Tfail (min)	DelayT (min)
 Composite section C 406.4 × 6 C 273 × 12	7	0.3	266	178	284	106
	7	0.4	109	123	375	252
	7	0.5	158	73	222	149
	7	0.6	123	45	183	138

3.3.5 Finding the Great Value of DelayT

The value of DelayT is important with fire fighters who need to know to keep off the failure of the buildings. Therefore, one objective of this study is to know how great the value of DelayT could be for studied structural elements. With results of parametric studies of various structural elements, it is recognized that DelayT trends to be greater with composite columns, high concrete cover thickness, and small HeatT. Therefore, steel-concrete composite columns are calculated to find the great value of DelayT. Column profile 17 with parameter in Table 6 gives the great

values of DelayT. Profile 17 has the same cross-section type with Profile 15 but the external steel tube is C406.4 × 6. As can be seen, DelayT can be up to 252 min.

4 Conclusion

- Delayed failure time (DelayT) of structures during the cooling phase of the fire is important to fire fighters. Therefore, it should be brought more attention to the value of DelayT.
- Parametric studies have been done for various structural elements consist of steel, concrete, and steel-concrete composite materials. The type of cross-section, dimensions, concrete grade, and load ratio is varied widely in practical range. For all calculated elements, the delayed time of failure DelayT can be up to 252 min. Steel-concrete composite columns often have greater DelayT because external steel tube can recover its strength much during the cooling of the fire.
- Load ratio affects mainly the value of DelayT. In most cases, DelayT decreases when load ratio increases but in some composite columns, it does not follow this correlation. This manner can be explained logically.
- Insulation cover thickness and concrete cover thickness have moderate effect on the value of T_{fail} and DelayT. The greater insulation material thickness is, the greater DelayT could be.
- More numerical studies should be done to find the correlation between DelayT and main parameters such as load ratio, slenderness of column, eccentricity of load, and concrete strength.

References

1. ISO 834-1. Fire resistance test—elements of building construction
2. E119-15 standard test methods for fire tests of building construction and materials
3. Kodur VKR, Dwaikat MB (2011) Design equation for predicting fire resistance of reinforced concrete beams. *Eng Struct* 33(2):602–614
4. Rodrigues JPC, Laím L (2017) Fire resistance of restrained composite columns made of concrete filled hollow sections. *J Constr Steel Res* 133:65–76
5. Porcari GLF, Zalok E, Mekky W (2015) Fire induced progressive collapse of steel building structures: a review of the mechanisms. *Eng Struct* 82(1):261–267
6. Gernay T, Franssen JM (2015) A performance indicator for structures under natural fire. *Eng Struct* 100:94–103
7. Dimia MS, Guenfoud M, Gernay T, Franssen J-M (2011) Collapse of concrete columns during and after the cooling phase of a fire. *J Fire Prot Eng* 245–263
8. Gernay T (2015) Sensitivity of structures to fire decay phases. In: Proceedings of the international conference on applications of structural fire engineering, Dubrovnik, Croatia

9. EN 1991-1-2 (2002) Eurocode 1: Actions on structures—Part 1–2: General actions—actions on structures exposed to fire. European Committee for Standardization, Brussels
10. Binh CT (2009) Hollow steel section columns filled with self-compacting concrete under ordinary and fire conditions. PhD thesis, University of Liege, Belgium
11. Franssen JM (2005) SAFIR. A thermal/structural program modelling structures under fire. *Eng J AISC* 42(3):143–158
12. Talamona D, Lim L, Franssen JM (2003) Validation of a shell finite element for concrete and steel structures subjected to fire. In: Proceedings of the international seminar on fire and explosion hazards, Londonderry, University of Ulster, Northern Ireland
13. Binh CT, Dotreppe JC, Franssen JM (2010) Numerical modeling of building structures in fire conditions. In: Proceedings of the construction under exceptional condition, Hanoi, Vietnam
14. EN 1994-1-2 (2005) Eurocode 4—design of composite steel and concrete structures. Part 1–2: General rules—STRUCTURAL fire design. European Committee for Standardization, Brussels
15. EN 1993-1-2 (2005) Eurocode 3—design of steel structures—Part 1–2: General rules—structural fire design. European Committee for Standardization, Brussels
16. Gernay T, Franssen JM (2012) A formulation of the Eurocode 2 concrete model at elevated temperature that includes an explicit term for transient creep. *Fire Saf J* 51:1–9
17. Gernay T, Salah Dimia M (2013) Structural behaviour of concrete columns under natural fires. *Eng Comput* 30(6):854–872

Numerical Studies of Some Modified Polarization Saturation Models in 2-D Semipermeable Piezoelectric Media Using Distributed Dislocation Method



Kuldeep Sharma and Sandeep Singh

Abstract In this paper, some modified polarization saturation models are proposed and studied numerically in 2-D semipermeable piezoelectric media using distributed dislocation technique (DDT). The polarization saturation (PS) model is modified here by varying the saturated condition imposed on the electrically saturated strip, i.e. a constant saturated condition to linear, quadratic and cubic varying electric displacement saturated condition. Numerical studies for these proposed models are simulated by considering their equivalent forms based on the principle of superposition. A centre-cracked problem in 2-D semipermeable piezoelectric media under arbitrary poling direction and in-plane electromechanical loadings is considered for these analyzes. To validate the developed numerical codes and iterative numerical approach for finding the unknown saturated zone length, the obtained results for PS model are compared with the analytical results available in literature. Thereafter, the results are presented for modified PS models, they show the effect of variation in saturation condition on saturated zone length, critical applied electric displacement loading and crack opening potential (COP), whereas no significant effect has been observed on local intensity factor (LIF) and crack opening displacement (COD). Further, saturated zone length increases with respect to increase in degree of variation of saturation condition, i.e. from constant to cubic. Moreover, the variation shows the effect on implication of applied electric loading and defines the critical applied electric loading corresponding to each model. It is observed that the critical value of applied electric loading significantly decreases with the increase in degree of variation of saturation condition. Here, a significant effect of poling direction is also found in all the parameters such as saturated zone length, LIF, COD and COP.

K. Sharma (✉) · S. Singh

Department of Sciences & Humanities, National Institute of Technology Uttarakhand,
Srinagar (Garhwal), Uttarakhand, India
e-mail: kuldeppurc@gmail.com

S. Singh

e-mail: sbisht402357@gmail.com

© Springer Nature Singapore Pte Ltd. 2018

H. Nguyen-Xuan et al. (eds.), *Proceedings of the International Conference on Advances in Computational Mechanics 2017*, Lecture Notes in Mechanical Engineering, https://doi.org/10.1007/978-981-10-7149-2_6

Keywords Distributed dislocation method • Local intensity factor
Piezoelectric • Polarization saturation • Semipermeable

1 Introduction

Piezoelectric materials due to their electromechanical coupling properties are considered as one of the important smart materials and have been extensively used as an actuator and transducer in smart embedded structures. However, these materials are highly brittle but have low fracture toughness in nature. Therefore, they are always susceptible to fracture/failure under high electromechanical loadings in the presence of defects such as cracks, voids or inhomogeneities. Moreover, under high electric fields, piezoelectric ceramics showing a reduction of the ionic movement and so it creates a limitation on the amount of polarization and hence the saturation in the electric displacement. In addition to this, the presence of defects causing a drastic amplification in stresses and in the electric quantities, and therefore, considered these regions as possible areas where electric displacement saturation might reach and play a key role in defining the fracture parameters. Gao and his co-researcher [1] were the first who considered the role of electric displacement saturation in studying the fracture mechanics of piezoelectric materials and proposed a polarization saturation model. They justified this model by considering piezoelectric materials as mechanically brittle and electrically ductile and proposed the same in analogous to Dugdale's model [2]. In this model, they considered an electrical yielding zone in front of the crack-tip in the form of a strip which is bounded by the normal saturated electric displacement value. Even to explain the discrepancies between the experimental obtained results and theoretical predicted values (on the basis of linear theory piezoelectricity) under the influence of electric loading, they proposed the new fracture parameters, i.e. local energy release rate and global energy release rate. Their predictions on the basis of local energy release rate subjected to electric loadings were found in broad agreement with the experimental evidences. Moreover, the obtained local energy release rate was independent of the size and strength of the saturated zone. Thereafter, several researchers [3–12] worked on PS model and studied various types of fracture mechanics problems in piezoelectric and magnetoelastoelectric materials using PS model. Considering the unknown saturated electric displacement distribution over the saturated strip, Ru [3] derived a generalized solution using complex variable technique and presented the effect of electrical polarization saturation on the stress intensity factor in piezoelectric materials. Wang [4] presented a fully anisotropic analysis of strip electric saturation model by demonstrating the crack perpendicular and parallel to the poling axis. Similar to PS model, Zhang et al. [5] proposed a dielectric breakdown (DB) model in 2-D piezoelectric media. In DB model,

the electric field in a strip ahead of the crack-tip was assumed to be equal to the dielectric breakdown strength, which was considered in analogy with the classical Dugdale model for plastic yielding. Using the Stroh formalism and the dislocation modelling of a crack, they derived the relationship between the DB strip size and applied mechanical and electrical loads, the intensity factors of stresses and electric displacement and the local energy release rate. Fan et al. [6] applied the non-linear hybrid extended displacement discontinuity-fundamental solution method (NLHEDD-FSM) to obtain the numerical solution of PS/DB models in 2-D finite piezoelectric media.

In most of the literature till date on PS/DB models, researchers studied the cracks problems based on PS/DB models using impermeable crack-face conditions. To attempt this paucity, Fan et al. [7] presented an analytical study of a semipermeable crack in 2-D piezoelectric media based on PS model using distributed dislocation/semi-analytical technique. Numerical results were demonstrated which showed the effect of different boundary conditions on the electric yielding zone and the local stress intensity factor. Loboda et al. [8] extended PS model to limited permeable crack in an interlayer between piezoelectric materials with different zones of electrical saturation and mechanical yielding. Later, Zhao et al. [9] extended the 2-D PS model to derive the fundamental solutions and numerical modelling of polarization saturated elliptical crack in a 3-D transversely isotropic piezoelectric medium. Fan et al. [10] presented the numerical solution of PS model in 3-D piezoelectric medium using extended displacement discontinuity boundary integral equation and the boundary element method. Bhargava and Jangid [11] extended PS model to study the semipermeable two collinear cracks in an infinite 2-D piezoelectric media. They applied the complex variable technique to obtain the analytical expressions for saturated zone length, COD, COP and local intensity factor. Apart from extension of non-linear (PS/DB and Dugdale) models in 2-D to 3-D or multiple cracks or bimetals, etc., Dugdale model was also modified by various researchers [13, 14] after varying the condition of normal cohesive stress. Bhargava and Hasan [14] modified the Dugdale model for multiple collinear cracks by quadratically varying normal cohesive stress distribution over the rims of yield zones. Even in piezoelectric media, similar modifications were made by Ru [3] who derived an analytical solution of generalized impermeable PS model by considering the unspecified normal electrical displacement distributed over the electrical yielding zone in place of constant saturated value. Bhargava and Setia [12] proposed and studied the impermeable crack-arrest models in 2-D piezoelectric strip by linearly varying the saturation condition. But till date, no modified PS model (varying the saturated condition) is reported in 2-D semipermeable piezoelectric media by considering the arbitrary polarized direction. Therefore, to attempt this paucity, authors proposed modified PS models by varying polarization saturation condition from constant to linear, quadratic and cubic types of varying polarization

saturation condition. Numerical studies of these modified models along with PS model are presented here for an arbitrary polarized semipermeable centre crack in an infinite 2-D piezoelectric media by using DDT and Gauss-Chebyshev quadrature method. In addition to this, authors simulate the PS model/modified PS models by solving their equivalent forms numerically using DDT derived on the basis of principle of superposition. Results are obtained for saturated zone length, COD, COP and local intensity factor w.r.t electrical loading for all the modified models subjected to electromechanical loadings and for different set of crack-face conditions.

2 Equivalent Form of PS Models/Modified PS Models Using Principle of Superposition

According to PS model [1], an electric yielding zone near the crack-tip was considered and approximated to a line segment in front of the crack-tip along with a constant normal electric displacement equal to its saturated value imposed on the strip. Figure 1a represents the geometrical representation of the PS model in an infinite 2-D piezoelectric media. It shows a centre crack with centre at origin along with saturated zone length $c - a$ lying on both sides of crack. As per the model, the cracked domain is considered as mechanically defective with crack length equal to $2a$ ($-a \leq x \leq a$) and electrically defective with effective crack length of $2c$ ($-c \leq x \leq c$) and additionally the rims of the strips are bounded by normal electric displacement equal to its saturated value, i.e. D_s .

In this paper, employing the principle of superposition, authors considered its equivalent form by considering a crack length equal to $2c$ ($-c \leq x \leq c$) which is considered both mechanically and electrically defective of the same length. But the rims of the zones are arrested by applying not only the saturated normal electric displacement, i.e. D_s but also by external applied mechanical loading, i.e. σ_{22}^∞ as it is the same mechanical loading responsible for opening the crack mechanically. The geometry of this equivalent form of PS model is shown in Fig. 1b.

The main advantage of considering this approach is that cracks problems in 2-D piezoelectric media based on PS models can be easily studied numerically. It would be also helpful to study those problems where analytical solutions are difficult to obtain on the basis of PS/DB models such as study of multiple cracks, cracks in multilayered piezoelectric media, etc. Geometrical representation of the modified PS models and their equivalent forms are shown in Fig. 1c, d.

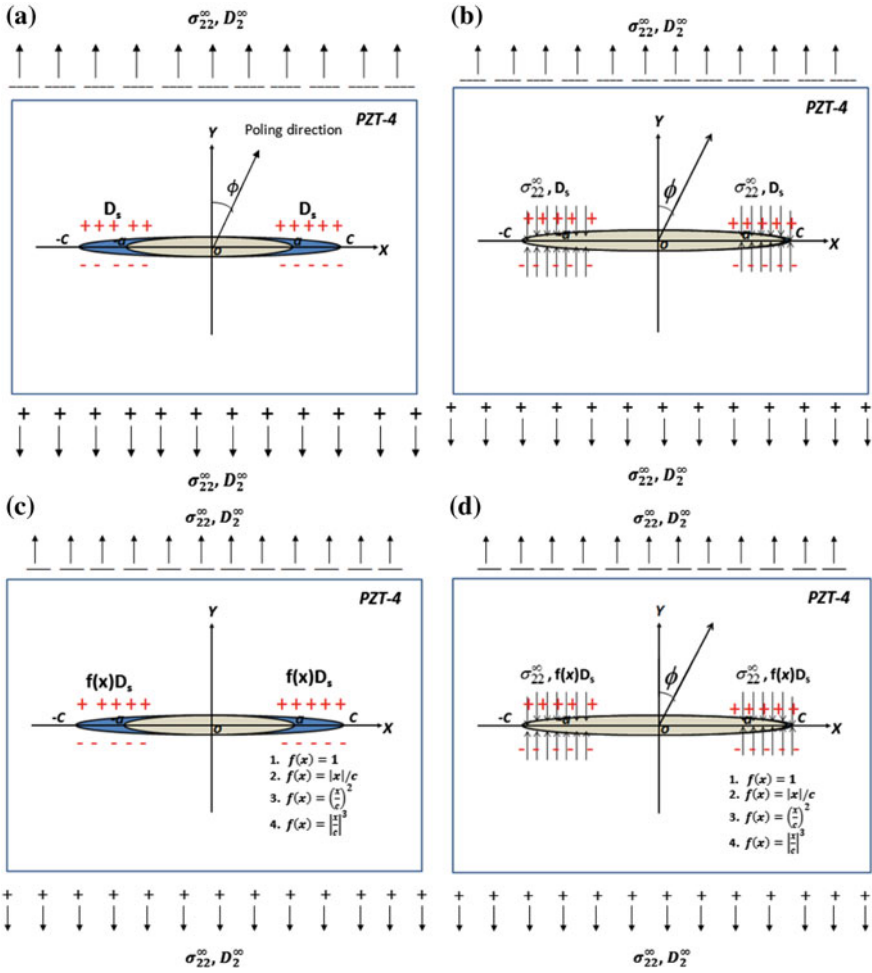


Fig. 1 a Model geometry of the PS model b equivalent form of PS model c generalized modified PS model d equivalent form of generalized PS model

3 Basic Equations of Piezoelectricity and Generalized Stroh Formulation

The basic equations and the boundary conditions for 2-D linear piezoelectric materials in a fixed rectangular coordinate system $x_j(j = 1, 2, 3)$ can be expressed as

3.1 Field Equations

$$\text{Constitutive equations: } \sigma_{ij} = C_{ijks}\varepsilon_{ks} - e_{sij}E_s; D_i = e_{iks}\varepsilon_{ks} + \kappa_{is}E_s \quad (1)$$

$$\text{Kinematic equations: } \varepsilon_{ij} = \frac{1}{2}(u_{i,j} + u_{j,i}); E_i = -\varphi_{,i} \quad (2)$$

Equilibrium equations: In the absence of body forces and charges, the equilibrium equations for the stresses and electric displacements can be described as

$$\sigma_{ij,j} = 0; D_{i,i} = 0 \quad (3)$$

where C_{ijks} and e_{iks} are the elastic and piezoelectric constants, respectively; σ_{ij} , ε_{ij} , D_i and E_i are the components of the stress, strain, electric displacement and electric field, respectively; while κ_{is} defines the dielectric permittivity. The comma denoted in Eqs. (2) and (3) represents the partial differentiation against the argument following it; u_i is the component of the elastic displacement vector u ; while φ is the electric potential; where i, j, k and $s = 1, 2, 3$.

3.2 Boundary Conditions

The boundary conditions in the form of resultant of stresses and electric displacements applied on the boundary of the domain are given by

$$\sigma_{ij}n_j = t_j \text{ and } D_jn_j = -\omega \quad (4)$$

where t_j and ω represent the prescribed traction value and charge defined on surface while n being the outward drawn unit normal vector on S .

3.3 Crack-Face Boundary Conditions

There are mainly three boundary conditions on crack faces taken in literature [7, 15], namely impermeable, permeable and semipermeable. The impermeable and semipermeable crack-face boundary conditions are represented mathematically as

Impermeable boundary conditions: Crack faces Γ_c are assumed to be traction-free and electrically impermeable, i.e.

$$\sigma_{ij}n_j = 0 \text{ and } D_jn_j = 0 \text{ on } \Gamma_c \quad (5)$$

Semipermeable boundary conditions: Semipermeable boundary conditions proposed by Hao and Shen [16] for piezoelectric ceramics are more realistic boundary conditions and are given by

$$\sigma_{ij}n_j = 0 \text{ and } D_2^+ = D_2^- = D_2^c = -\kappa_c \frac{\Delta\varphi(x)}{\Delta u_2(x)} \tag{6}$$

where “+” and “-” represent the upper and lower crack surfaces, $\Delta\varphi(x)$ is the electrical potential jump and $\Delta u_2(x)$ is the crack opening displacement; while κ_c is the permittivity of medium between crack faces.

It is interesting to see that one can reduce semipermeable boundary conditions to impermeable one when the term κ_c in Eq. (6) is set to be equal to zero. For semipermeable conditions, the permittivity constant of the air is taken, i.e. $\kappa_c = 8.85 \times 10^{-12} \text{ F m}^{-1}$.

3.4 Generalized Stroh Formulation

For two-dimensional deformations, the generalized displacement vector $U = [u_1, u_2, u_3, \xi]^T$, and the generalized stress vector $\psi = [\psi_1, \psi_2, \psi_3, \psi_4]^T$ which depend on the coordinate system (x, y) can be expressed as

$$U = 2\text{Re}(Af(z)) \text{ and } \psi = 2\text{Re}(Bf(z)) \tag{7}$$

where $z = x + py$. The eigenvalues p and eigenvectors A are obtained after solving the following characteristic equation

$$\left(\begin{bmatrix} C_{i1k1} & e_{i11} \\ e_{1k1} & -\kappa_{11} \end{bmatrix} + \begin{bmatrix} C_{i2k1} + C_{i1k2} & e_{i21} + e_{i12} \\ e_{2k1} + e_{1k2} & -\kappa_{12} - \kappa_{21} \end{bmatrix} p + \begin{bmatrix} C_{i2k2} & e_{i22} \\ e_{2k2} & -\kappa_{22} \end{bmatrix} p^2 \right) \begin{bmatrix} A_i \\ A_4 \end{bmatrix} = 0 \tag{8}$$

whereas the eigenvectors B are determined by the following relation:

$$\begin{bmatrix} B_i \\ B_4 \end{bmatrix} = \left\{ \begin{bmatrix} C_{i1k2} & e_{i12} \\ e_{1k2} & -\kappa_{21} \end{bmatrix} + p \begin{bmatrix} C_{i2k2} & e_{i22} \\ e_{2k2} & -\kappa_{22} \end{bmatrix} \right\} \begin{bmatrix} A_i \\ A_4 \end{bmatrix}. \tag{9}$$

The stress and electric displacement can be evaluated by using the following relations as

$$\begin{bmatrix} t_1 \\ t_2 \end{bmatrix} = \begin{bmatrix} -\psi_{,2} \\ \psi_{,1} \end{bmatrix} = \begin{bmatrix} \{\sigma_{11}, \sigma_{12}, \sigma_{13}, D_1\} \\ \{\sigma_{21}, \sigma_{22}, \sigma_{23}, D_2\} \end{bmatrix} \tag{10}$$

For a piezoelectric dislocation located at z_0 in an infinite piezoelectric medium, the analytic function in the vector form is given as

$$f(z) = \langle \ln(z - z_0) \rangle q, \tag{11}$$

where $q = \frac{1}{2\pi i}(A^T F + B^T b)$ represents the generalized piezoelectric dislocation in the form of generalized Burgers vector, $b = [b_1, b_2, b_3, b_4]^T$ and the generalized

force vector $F = [F_1, F_2, F_3, -\omega]$. Here, $b_i (i = 1, 2, 3)$ and b_4 are mechanical displacement jump and an electric potential jump in the plane, respectively. Also, F_i denotes a line force per unit length along the x_i direction and ω stands for a line charge per unit length.

Further, if a conventional dislocation is located at a point x_d on the x -axis in an infinite body without any crack, the dislocation induces a generalized stress, $\Sigma_{2,k}$ and an electric displacement component, $D_{2,k}$ along the x -axis as:

$$\Sigma_{2,k} = \frac{1}{\pi(x-x_d)} \begin{bmatrix} G_1 \\ G_2 \end{bmatrix} \begin{Bmatrix} b_1 \\ b_2 \\ b_3 \end{Bmatrix} \text{ and } D_{2,k} = \frac{1}{\pi(x-x_d)} [G_2^T] b_4 \quad (12)$$

where $H = 2Re(iAB^{-1})$ and $H^{-1} = \begin{bmatrix} G_1 & G_2^T \\ G_2 & G_4 \end{bmatrix}$.

Also, if an electric dislocation is located at a point x_d on the x -axis without any crack, then the generalized stress, $\Sigma_{2,k}$ and an electric displacement component, $D_{2,k}$ along the x -axis induced by this dislocation are defined as:

$$\Sigma_{2,k} = \frac{1}{\pi(x-x_d)} \begin{bmatrix} G_2^T \\ G_4 \end{bmatrix} \begin{Bmatrix} b_1 \\ b_2 \\ b_3 \end{Bmatrix} \text{ and } D_{2,k} = \frac{1}{\pi(x-x_d)} G_4 b_4. \quad (13)$$

4 Distributed Dislocation Technique (DDT) and Mathematical Formulation of the Problem

DDT [17] is based on the concept of expressing the crack in a material as a continuous distribution of dislocations. By doing this, the problem of crack(s) in the specimen is reduced into simultaneous singular integral equations in terms of dislocation density variable(s) at the crack. After solving these integral equations, one can obtain the dislocation density variable(s) at the crack-tip, and hence the fracture parameters which are in terms of dislocation densities at the crack-tip. Bilbey et al. [18] analyzed the problem of strip plastic yielding model using DDT. Both the crack and the strip plastic zones are simulated by an array of dislocations. Sharma et al. [15] applied the DDT to study the array of equidistant semipermeable inclined cracks in 2-D piezoelectric media. Zhang et al. [5] and Fan et al. [7] applied the DDT to study the impermeable DB model and semipermeable PS model, respectively. In their approach, they reduced the problem into system of integral equations and then obtained the analytical solution of the field variables. This approach could be useful to those problems where analytical expressions are easy to obtain but for multiple cracks problems, crack with inclusion and bimetals problem, etc., the kernel function involved in the integral equations are not in the simple form $\frac{1}{x-x_d} [L]$, L is a material matrix, so it is difficult to obtain the analytic form of solution in those cases. Therefore, in this manuscript, authors proposed an equivalent form of

the PS/DB model using principle of superposition, reduced it in terms of simultaneous integral equations and then solved the same by using numerical quadrature scheme, i.e. Gauss-Chebyshev quadrature scheme. The obtained numerical results of PS model are found in good agreement with the established results [1, 7] or analytical results, and hence show the accuracy and efficacy of this approach and method for studying the PS models in 2-D piezoelectric media.

Similar to the approach followed by Zhang et al. [5] and Fan et al. [7], equivalent form of PS model (i.e. a crack in piezoelectric media of length equal to effective crack length, i.e. crack with saturated zone lengths, $-c \leq x \leq c$) is modelled as a continuous distribution of array of dislocation with generalized Burger vectors, $b = [b_1, b_2, b_3, b_4]^T$ with corresponding density functions $m_i (i = 1, 2, 3 \text{ and } 4)$ at point x_0 along the effective crack. Geometrical representation of the problem is shown in Fig. 1.

After employing the continuous distribution of dislocation and applied surface traction charge conditions as defined in Eq. (12), a system of singular integral equations for dislocation density, $m_i b_i$, is obtained as

$$\int_{-c}^c \frac{1}{\pi(x-x_0)} G_1 \langle m_i \rangle \begin{bmatrix} b_1 \\ b_2 \\ b_3 \end{bmatrix} dx_0 + \int_{-c}^c \frac{1}{\pi(x-x_0)} G_2^T m_4 b_4 dx_0 + \left\{ \begin{array}{l} \sigma_{21}^\infty \\ \sigma_{22}^\infty \\ \sigma_{23}^\infty \end{array} \right\} = 0, |x| \leq a, \quad (14)$$

$$\int_{-c}^c \frac{1}{\pi(x-x_0)} G_2 \langle m_i \rangle \begin{bmatrix} b_1 \\ b_2 \\ b_3 \end{bmatrix} dx_0 + \int_{-c}^c \frac{1}{\pi(x-x_0)} G_4 m_4 b_4 dx_0 + D_2^\infty - D_2^c = 0, |x| \leq a, \quad (15)$$

$$\int_{-c}^c \frac{1}{\pi(x-x_0)} G_1 \langle m_i \rangle \begin{bmatrix} b_1 \\ b_2 \\ b_3 \end{bmatrix} dx_0 + \int_{-c}^c \frac{1}{\pi(x-x_0)} G_2^T m_4 b_4 dx_0 + \left\{ \begin{array}{l} \sigma_{21}^\infty \\ \sigma_{22}^\infty \\ \sigma_{23}^\infty \end{array} \right\} = \left\{ \begin{array}{l} \sigma_{21}^\infty \\ \sigma_{22}^\infty \\ \sigma_{23}^\infty \end{array} \right\}, a \leq |x| \leq c, \quad (16)$$

$$\int_{-c}^c \frac{1}{\pi(x-x_0)} G_2 \langle m_i \rangle \begin{bmatrix} b_1 \\ b_2 \\ b_3 \end{bmatrix} dx_0 + \int_{-c}^c \frac{1}{\pi(x-x_0)} G_4 m_4 b_4 dx_0 + D_2^\infty - D_2^c = f(x) D_S - D_2^c, a \leq |x| \leq c, \quad (17)$$

where $D_2^c = -\kappa_c \frac{H_{41}\sigma_{yx} + H_{42}\sigma_{yy} + H_{43}\sigma_{yz} + H_{44}(D_y - D_2^c)}{H_{21}\sigma_{yx} + H_{22}\sigma_{yy} + H_{23}\sigma_{yz} + H_{24}(D_y - D_2^c)}$ is obtained by solving the non-linear equation in D_2^c and $H = 2\text{Re}(AB^{-1})$.

Moreover, by varying the function $f(x)$ as follows, authors presented numerical studies for some modified PS models.

$$\text{Case 1: } f(x) = 1, \text{ Case 2: } f(x) = \frac{|x|}{c}, \text{ Case 3: } f(x) = \left(\frac{x}{c}\right)^2, \text{ Case 4: } f(x) = \left|\frac{x}{c}\right|^3.$$

Further, for single-valued displacements and electric potential, the following conditions must also be satisfied

$$\int_{-c}^c m_i b_i dx_0 = 0 \text{ for } i = 1, 2, 3 \text{ and } 4. \quad (18)$$

To obtain the solution of the aforementioned singular integral equations, authors employed the numerical approach, i.e. Gauss-Chebyshev quadrature method [17].

As per this scheme, the discretized form of any singular integral equation of the form

$$\int_{-1}^1 \frac{L v(\xi)}{\pi(\xi - \eta)} d\eta = -t^*(\eta) \quad (19)$$

can be written as

$$\sum_{k=1}^m \frac{1}{m} \left[\frac{L}{(s_{r0} - s_k)} \right] v(s_k) = -t^*(s_{r0})$$

and single-valued condition reduces to

$$\sum_{k=1}^m v(s_k) = 0, \quad (20)$$

where

$$v(\xi) = \frac{\sum_{k=1}^m w_k v(s_k)}{\sqrt{(1 - s_k^2)}}, s_k = \cos\left(\frac{(2k-1)\pi}{2m}\right), k = 1, 2, \dots, m \text{ and } s_{r0} = \cos\left(\frac{r\pi}{m}\right), r = 1, 2, \dots, m-1..$$

Once the generalized dislocation densities $m\mathbf{b}$ have been obtained, the intensity factors (IFs) at the crack-tips ($\pm a$) and effective crack-tips ($\pm c$) are given by

$$[K_{II}^a K_I^a K_{III}^a K_{IV}^a]^T = \sqrt{\frac{\pi}{4c_i}} H^{-1} [v_1(\pm a/c) v_2(\pm a/c) v_3(\pm a/c) v_4(\pm a/c)]^T \quad (21)$$

and

$$[K_{II}^c K_I^c K_{III}^c K_{IV}^c]^T = \sqrt{\frac{\pi}{4c_i}} H^{-1} [v_1(\pm 1) v_2(\pm 1) v_3(\pm 1) v_4(\pm 1)]^T, \quad (22)$$

respectively.

Using Fan et al. [7], the local intensity factor is evaluated as

$$K_I^l = K_I^a - \frac{G_{42}}{G_{22}} K_{IV}^a G_{42}, \quad \text{where } = H^{-1}(4, 2) \text{ and } G_{22} = H^{-1}(2, 2). \quad (23)$$

5 Evaluation of Unknown Saturated Zone Length

Since, the approach proposed by the authors is a numerical one, so evaluation of saturated zone length is one of the important tasks, considering other parameters fixed such as crack length and loadings, etc. Moreover, it is an unknown quantity prior to get numerical solution. Therefore, it is obtained here by applying an iterative approach in which saturated zone length is varied alongwith imposing a supplementary condition of finite electric displacement at the outer tips of the zone. Further, the zone length is varying arbitrarily from zero to a suitable finite value and correspondingly obtained the normalized electric displacement intensity factor (K_{IV}^*) at each varying tip of the zone. Hence, an interval is obtained where the K_{IV}^* changes its sign. To find the accuracy of the solution up to three decimal places, authors vary the arbitrary zone length by considering a small step size, i.e., 0.001 units and further applied the bisection method to get the accuracy up to three decimal places. By doing this way, approximated saturated zone length is evaluated where the K_{IV}^* is zero. Figures 2a, b validate the aforementioned approach with established results [1, 7] of PS model considering both impermeable and semipermeable crack conditions and subjected to $D_2^\infty/D_s = 0.5$ and $\sigma_{yy}^\infty = 10$ MPa loading. Validation accords this technique and approach, and hence the same is also applied on other modified PS models.

6 Numerical Studies

In this section, numerical studies of PS and modified PS models are presented w.r.t electrical loading, polarization angle and crack-face conditions by considering centre-cracked problem in 2-D piezoelectric media. The study is presented for

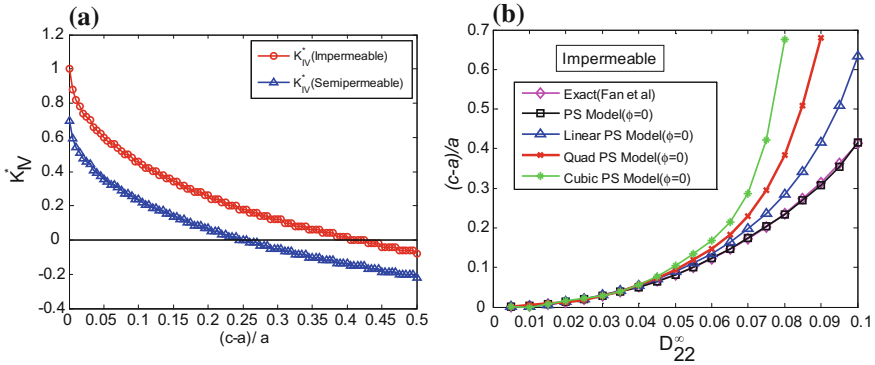


Fig. 2 **a** Numerical approach to find the saturated zone length for PS model **b** numerical validation of the modelling and technique

PZT-4 material with electromechanical loadings $\sigma_{22}^{\infty} = 10$ MPa and electric displacement loading $D_2^{\infty} = 0.08$ C/m² (if not specified). Throughout the analysis, saturated electric displacement loading is considered equal to $D_s = 0.2$ C/m².

To verify the accuracy of the numerical solution and proposed modelling, results of normalized saturated zone length are obtained for PS model w.r.t electric displacement loading under both crack-face conditions and also compared with the reference solutions of Fan et al. [7]. A good agreement of results are obtained and shown in Figs. 2b and 3a.

Also, the variations in normalized saturated zone length w.r.t electric displacement loading are presented in Fig. 3 for modified PS models. The study is presented for semipermeable crack-face conditions and considering different polarization angles, i.e. $0^{\circ}, 30^{\circ}, 50^{\circ}$ and 80° . Figure 3 shows that the saturated zone length increases w.r.t electric displacement loading for all the PS models. But for a particular electrical loading, saturated zone has higher values as saturated condition varies from constant to cubic and this difference increases with the increase in electrical loading. Moreover, the behaviour of saturated zone length and modified PS models w.r.t electric displacement loading are found same for all the polarization angle. However, a significant effect of poling direction is observed on the saturated zone lengths. At a particular electrical loading, the value of saturated zone length decreases w.r.t increase in polarization angle and even at higher polarization angle no significant effect of saturation condition is observed on it.

Further, to understand the effect of polarization angle and variation in saturation condition on PS models, analyzes of normalized local intensity factor is presented w.r.t electric displacement loading under the impermeable and semipermeable crack-face conditions. It is found that local intensity factor increases w.r.t electrical loading for all polarization angles which is in agreement to the experimental evidences. Further, the obtained results under $\phi = 0^{\circ}$ are in agreement with the established results [1, 7]. Also, local intensity factor decreases w.r.t to increase in polarization angle whereas no effect of saturated condition is observed on the local intensity factor.

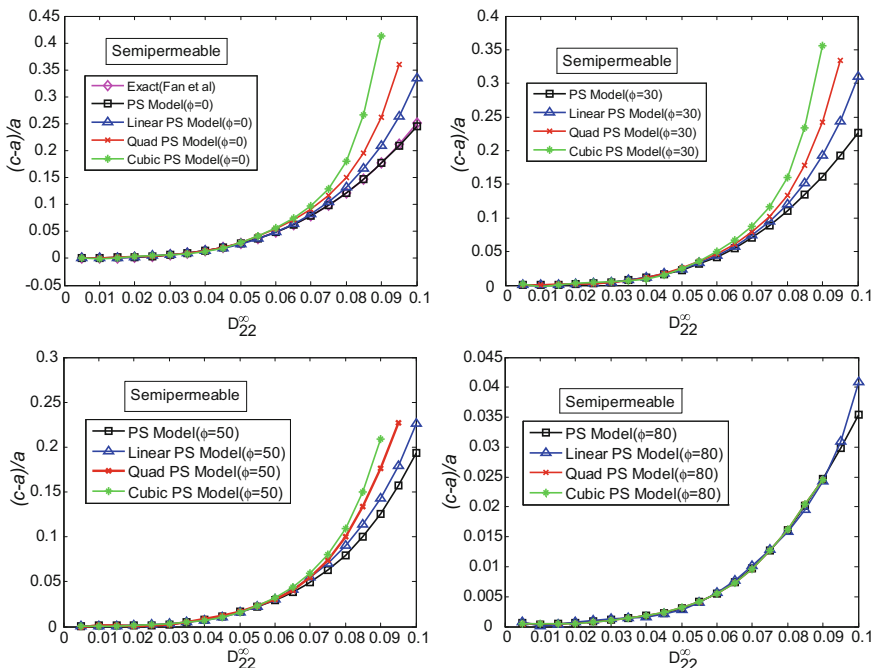


Fig. 3 Variations in normalized saturated zone length w.r.t electric displacement loadings for different polarization angles $\phi = 0^\circ, 30^\circ, 50^\circ$ and 80°

In addition to this, COD and COP are also obtained for PS/modified PS models subjected to different polarization angle and semipermeable crack-face conditions. No significant effect has been obtained in case of COD w.r.t variation in saturated normal electric displacement condition (or modified PS models) whereas its effect has been observed on COP. Its values obtained along the saturated zone increases in magnitude w.r.t constant to cubic saturated varying conditions whereas it is almost same along the cracklength. Also, a significant effect of poling direction is observed on both COD and COP (Figs. 4 and 5).

The effect of saturation condition is also observed on the applied electrical loading. Figure 6 shows the variation in K_{IV}^* w.r.t arbitrarily varying normalized saturated zone length subjected to different electrical loading, i.e. $D_2^\infty/D_s = 0.75, 0.65$ and 0.62 and considering linearly varying PS model. It shows that maximum applied electric displacement loading is approximately 0.62 times the saturated value. Moreover, the critical applied electric loading is slightly higher for semipermeable conditions than the impermeable conditions. Similar types of behaviour are observed for PS model, quadratic PS model and cubic PS model. Analysis based on aforementioned iterative approach shows that critical applied loading for PS model, quadratic and cubic varying PS models are approximately equal to $D_s, 0.5D_s$ and $0.4D_s$, respectively.

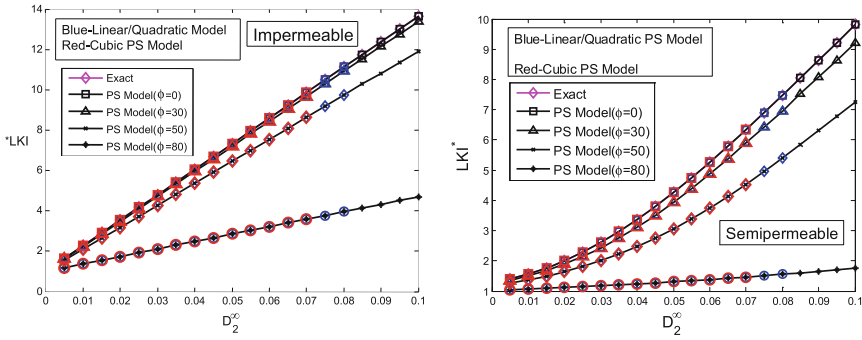


Fig. 4 Variations in normalized local intensity factor w.r.t electric displacement loadings for different polarization angles $\phi = 0^\circ, 30^\circ, 50^\circ$ and 80°

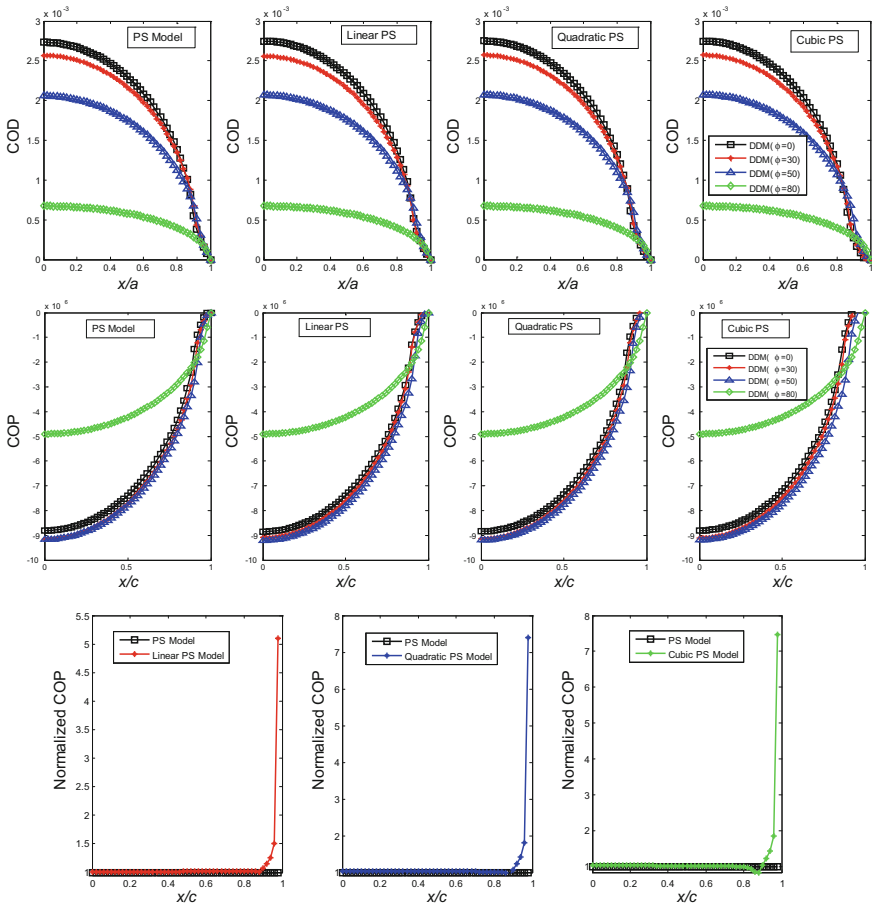


Fig. 5 Variations in COD, COP and normalized COP w.r.t x/a , x/c and x/c , respectively for different polarization angle

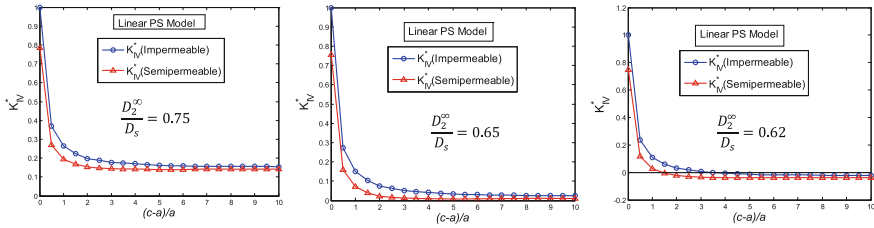


Fig. 6 Evaluation of critical applied electric displacement loading for linearly varying PS model

7 Conclusions

Authors present a detailed numerical study of some modified polarization saturation models in a cracked 2-D piezoelectric media subjected to semipermeable crack-face conditions and arbitrary polarization direction. The results of fracture parameters for PS/modified PS models are obtained after considering their proposed equivalent form numerically using DDT. This approach can be extended to study the PS models/modified PS models to study multiple cracks problems, cracks in a finite piezoelectric media and multilayered piezoelectric composite, etc. Some conclusions derived from the present work are as follows:

- Equivalent form of PS model is proposed and studied using DDT. Obtained results of saturation zone length and local intensity factors using proposed equivalent model are found in good agreement with the established results [1, 7].
- Modified PS models are proposed and studied here successfully using DDT. Proposed models have shown the effect of saturation condition imposed over the strip on the saturation zone length, COP and critical applied electric loading. Saturation zone length increases w.r.t increase in the degree of variation of saturation condition whereas critical applied electrical loading shows the reverse behaviour, i.e. decreases w.r.t increase in degree of variation of saturation condition. No effect of variation in saturation condition is observed on the local intensity factor.
- Effects of poling direction and crack-face conditions are observed on saturation zone length, local intensity factors, COD and COP (Figs. 4 and 5).
- Accuracy of the obtained numerical results shows the efficiency and efficacy of the proposed modelling of PS/modified PS models using DDT.

Acknowledgements Authors gratefully acknowledge NIT Uttarakhand, Srinagar (Garhwal), India, for providing the research facilities during the course of this work.

References

1. Gao H, Zhang TY, Tong P (1997) Local and global energy release rate for an electrically yielded crack in a piezoelectric ceramic. *J Mech Phys Solids* 45(4):491–510
2. Dugdale DS (1960) Yielding of steel sheets containing slits. *J Mech Phys Solids* 8:100–104
3. Ru CQ (1999) Effect of electrical polarization saturation on stress intensity factors in a piezoelectric ceramic. *Int J Solids Struct* 36:869–883
4. Wang TC (2000) Analysis of strip electric saturation model of crack problem in piezoelectric materials. *Int J Solids Struct* 37:6031–6049
5. Zhang TY, Zhao MH, Gao CF (2005) The strip dielectric breakdown model. *Int J Fract* 132:311–327
6. Fan CY, Zhao MH, Zhou YH (2009) Numerical solution of polarization saturation/dielectric breakdown model in 2D finite piezoelectric media. *J Mech Phys Solids* 57:1527–1544
7. Fan CY, Zhao YF, Zhao MH, Pan E (2012) Analytical solution of a semi-permeable crack in a 2D piezoelectric medium based on the PS model. *Mech Res Commun* 40:34–40
8. Loboda V, Laputsa Y, Sheveleva A (2010) Limited permeable crack in an interlayer between piezoelectric materials with different zones of electrical saturation and mechanical yielding. *Int J Solids Struct* 47:1795–1806
9. Zhao MH, Zhang QY, Pan E, Fan CY (2014) Fundamental solutions and numerical modeling of an elliptical crack with polarization saturation in a transversely piezoelectric medium. *Eng Fract Mech* 131:627–642
10. Fan CY, Dang HY, Zhao MH (2014) Nonlinear solution of the PS model for a semipermeable crack in 3-D piezoelectric medium. *Eng Anal Boundary Elem* 46:23–29
11. Bhargava RR, Jangid K (2013) Strip-saturation model for piezoelectric plane weakened by two collinear cracks with coalesced interior zones. *Appl Math Model* 37:4093–4102
12. Bhargava RR, Setia A (2008) Modified strip saturation model for a cracked piezoelectric strip. *Arch Mater Sci Eng* 30(1):33–36
13. Hasan S, Akhtar N (2015) Dugdale model for three equal collinear straight cracks: an analytical approach. *Theoret Appl Fract Mech* 78:40–50
14. Bhargava RR, Hasan S (2011) Crack opening displacement for two unequal straight cracks with coalesced plastic zones—a modified Dugdale model. *Appl Math Model* 35:3788–3796
15. Sharma K, Bui TQ, Bhargava RR, Yu T, Lei J, Hiroshi S (2016) Numerical studies of an array of equi-distant semi-permeable inclined cracks in 2-D piezoelectric strip using distributed dislocation method. *Int J Solids Struct* 80:137–145
16. Hao TH, Shen ZY (1994) A new electric boundary condition of electric fracture mechanics and its applications. *Eng Fract Mech* 47:793–802
17. Hills DA, Kelly PA, Dai DN, Korsunsky AM (1996) *Solution of crack problems—the distributed dislocation*. Kluwer Academic Publishers, Dordrecht
18. Bilby BA, Cottrell AH, Swinden KH (1963) The spread of plastic yield from a notch. *Proc R Soc A* 272:304–314

Stress Analysis of Silicon-Based Anode in Li-Ion Battery



T. Nguyen-Huu and Q. Le-Minh

Abstract We analyze during charging the stress evolution in silicon-based anodes of lithium-ion batteries by using an extensive finite element simulation. Effects of charge rates and geometric parameters of the anodes are considered. Results are useful for the design of new architectures of anodes for lithium-ion batteries.

Keywords Diffusion · Finite element analysis · Li-ion battery
Stress

1 Introduction

The lithium (Li) storage capacity of silicon (Si) has been theoretically estimated at 4200 and 3579 mAh/g, when $\text{Li}_{22}\text{Si}_5$ and $\text{Li}_{15}\text{Si}_4$ lithium alloys are formed, respectively [1–4]. This Li storage capacity of Si is much higher than that of graphite (372 mAh/g) [5, 6], which is the most common anode material in commercial Li-ion batteries. While the maximum volume expansion in graphite anode is about 10% due to the insertion of Li, the volume expansion of the anode can reach up to about 400% for Si-based anodes [2, 3, 7, 8]. During the charge/discharge, the huge volume variation of the metal- or alloy-based anodes causes high stresses, cracking, pulverization, voids of the anode, and loss of electrical contact, which results in poor cycling stability and battery fading [9–15]. Therefore, the commercialization of the alloy-based anode materials is still limited. Among various new architectures and structures of anodes, which have been proposed to

T. Nguyen-Huu · Q. Le-Minh (✉)

Department of Mechanics of Materials and Structures, School of Mechanical Engineering, Hanoi University of Science and Technology, No. 1 Dai Co Viet Road, Ha Noi, Vietnam
e-mail: quy.leminh@hust.edu.vn

T. Nguyen-Huu
e-mail: huutu123456@gmail.com

T. Nguyen-Huu
Faculty of Fundamental Science, Military Academy of Logistics, Ha Noi, Vietnam

© Springer Nature Singapore Pte Ltd. 2018

H. Nguyen-Xuan et al. (eds.), *Proceedings of the International Conference on Advances in Computational Mechanics 2017*, Lecture Notes in Mechanical Engineering, https://doi.org/10.1007/978-981-10-7149-2_7

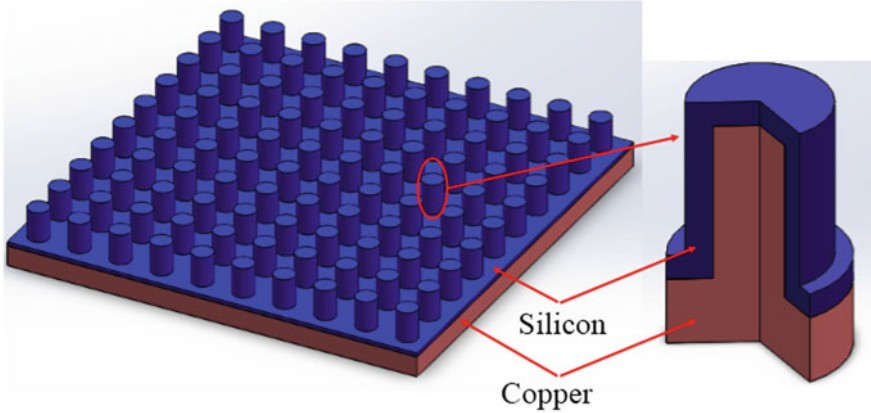


Fig. 1 Schematic illustration of silicon on nanopillar copper for anode in Li-ion batteries [16]

overcome these limitations, we focus here a new structure with silicon on nanopillar copper recently proposed by [16] as schematically shown in Fig. 1. Previous computational studies, see e.g. [17–21], have shown that stress-strain state of anodes and the performance of Li-ion batteries depend on the detailed structures of anodes as well as of the batteries, therefore stress analyzes should be simulated before their fabrications to reduce the cost. The new structure with silicon on nanopillar copper indicated in Fig. 1 has been recently fabricated [16]. Simulation of the stress-strain state in Si anode during charging is much needed to better understand its performance and helps the improvement of this new structure. Therefore, the present study investigates through an extensive FEA, stress, and deformation during charging of this new silicon/copper structure for anode in Li-ion batteries.

2 Numerical Procedure

Due to the periodicity of the nanopillar structures as depicted in Fig. 1, only a representative volume is studied. We adopt here the axisymmetric model for this representative volume as shown in Fig. 1. Hence, only one half of the model is used in FEA as shown in Fig. 2. We note that our model excludes the end cap of silicon for simplicity with $D = 1 \mu\text{m}$, $d = 500 \text{ nm}$, $H_1 = 1 \mu\text{m}$, $H_2 = 2 \mu\text{m}$, and $h = 150 \text{ nm}$. Four-node bilinear axisymmetric elements are used. The copper substrate and silicon anode consist of 3222 and 9600 elements, respectively. Elastic perfectly plastic model is adopted here for copper. The Young's modulus, Poisson's ratio, and yield stress of copper are here taken as 90 GPa, 0.28, and 330 MPa, respectively [18].

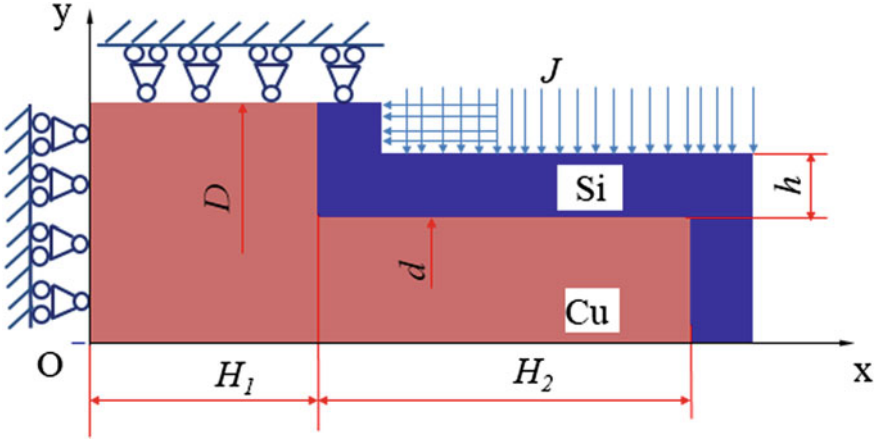


Fig. 2 A half of the representative volume used in FEA ($D = 1000$ nm, $d = 500$ nm, $H_1 = 1000$ nm, $H_2 = 2000$ nm, $h = 150$ nm)

Due to Li insertion, Si anode undergoes softening. The mechanical properties of Si are taken as follows [22]:

$$E_{Si}(\bar{C}) = E_0 + \bar{C}(E_1 + E_0), \quad (1a)$$

$$\nu_{Si}(\bar{C}) = \nu_0 + \bar{C}(\nu_1 + \nu_0), \quad (1b)$$

$$\sigma_{Si}^y(\bar{C}) = \sigma_0^y + \bar{C}(\sigma_1^y + \sigma_0^y). \quad (1c)$$

C is the concentration of Li-ion in Si anode. We denote $\bar{C} = C/C_{max}$. $C = 0$ ($\bar{C} = 0$) and $C_{max} = 3.75$ ($\bar{C} = 1$) correspond to the initial state (uncharging with pure silicon) and final state (fully charging with alloy $Li_{15}Si_4$), respectively.

$E_{Si}(\bar{C})$, $\nu_{Si}(\bar{C})$, and $\sigma_{Si}^y(\bar{C})$ are the Young's modulus, Poisson's ratio, and yield stress of the Si anode at the Li-ion concentration \bar{C} . The Young's modulus E_0 , Poisson's ratio ν_0 , and yield stress σ_0^y of the Si anode without Li-ion ($\bar{C} = 0$) are $E_0 = 150$ GPa, $\nu_0 = 0.21$, and $\sigma_0^y = 1.5$ GPa, respectively. The Young's modulus E_1 , Poisson's ratio ν_1 , and yield stress σ_1^y of the Si anode with $\bar{C} = 1$ are $E_1 = 50$ GPa, $\nu_1 = 0.21$, $\sigma_1^y = 0.6$ GPa, respectively.

The expansion coefficient of Si anode due to the Li-ion insertion is written as follows [22]:

$$\alpha = \frac{Ln(1 + \Omega\bar{C})}{3\bar{C}}, \quad (2)$$

where $\Omega = 2.7$, because the volume expansion of Si anode is about 270% when it contains fully Li-ion ($\text{Li}_{15}\text{Si}_4$ alloy is formed).

The diffusion coefficient of Li-ion into Si anode is taken as $D = 10^{-16} \text{ m}^2/\text{s}$ [23]. Cohesive zone is used to model the imperfect interface between Si and Cu with a moderate interfacial fracture toughness $G_c = 20 \text{ J/m}^2$ [18]. The flux of Li-ion is taken as $J = 1 \text{ nm}^{-2} \text{ s}^{-1}$ [24].

3 Results and Discussion

First, we show that simulation results are independent of the discretization of our finite element model (FEM). We have used two FEMs. Si anode is discretized by 9600 and 38400 (four times larger) elements in the first and second FEM, respectively. Computed results of the stress in Si anode are almost similar with two FEMs as indicated in Fig. 3. To save computational cost, we use the first FEM as described in the Sect. 2. Figures 4, 5, and 6 show the distribution of Li-ion, equivalent Von Mises stress, and total equivalent plastic strain in Si anode at different stages of the charging process, respectively. During charging, the Li-ion concentration in the outer surface of Si anode is higher than that inside the anode. This phenomenon has been previously observed in other structures of Si anodes [19, 20]. The Li-ion concentration is highest at the corner and outer surface of the anode. The normalized concentration of Li-ion at the corner is estimated at about 0.13, 0.32, 0.48, and 0.77 at the charging time $t/t_{\max} = 0.01, 0.05, 0.1, \text{ and } 0.2$,

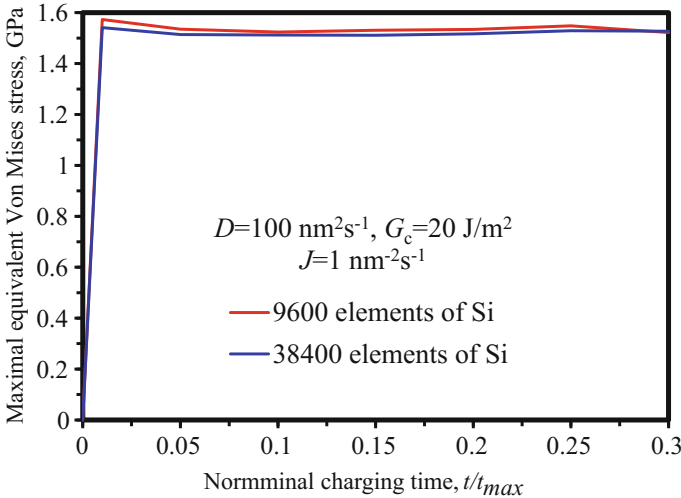


Fig. 3 Variation of the maximal equivalent Von Mises stress in the anode versus the normalized charging time

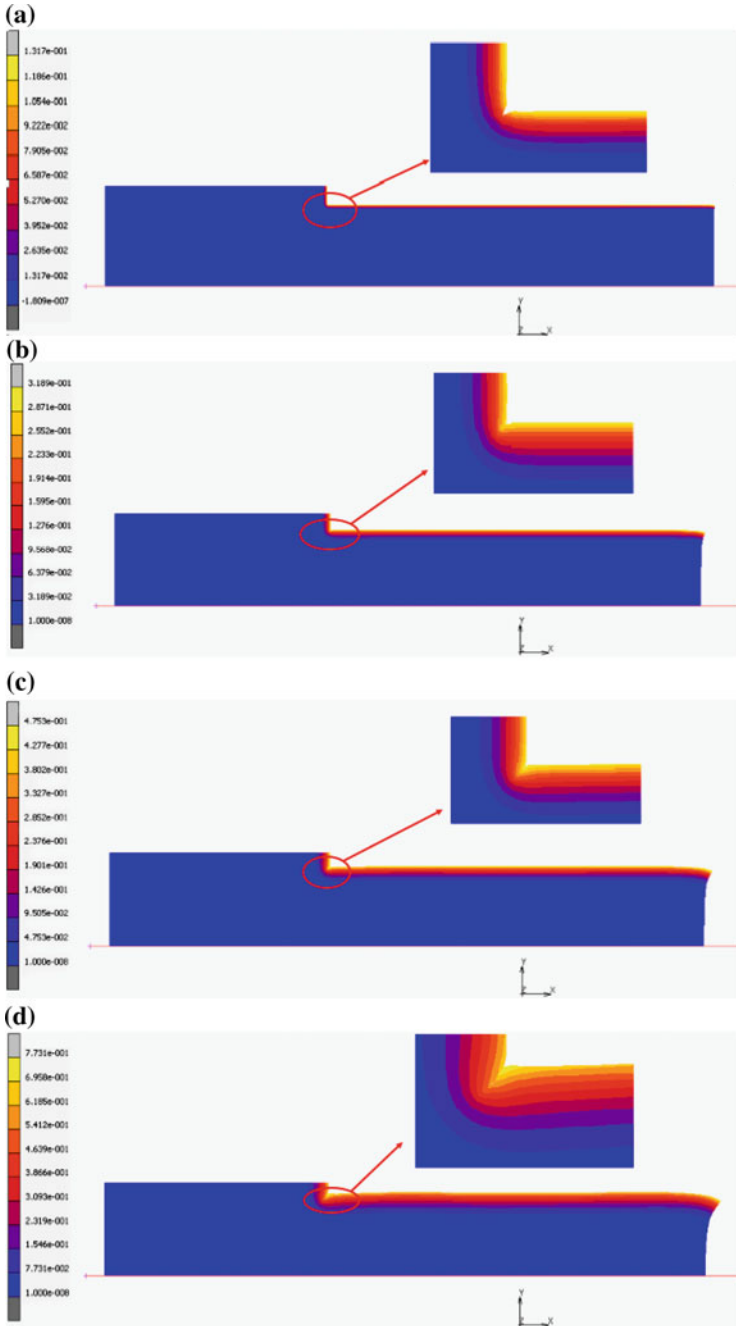


Fig. 4 Distribution of normalized concentration of Li-ion \bar{C} in the anode at normalized charging time (t is the charging time, t_{\max} is the total charging time for full insertion of Li-ion in anode): **a** $t/t_{\max} = 0.01$; **b** $t/t_{\max} = 0.05$; **c** $t/t_{\max} = 0.1$; and **d** $t/t_{\max} = 0.2$

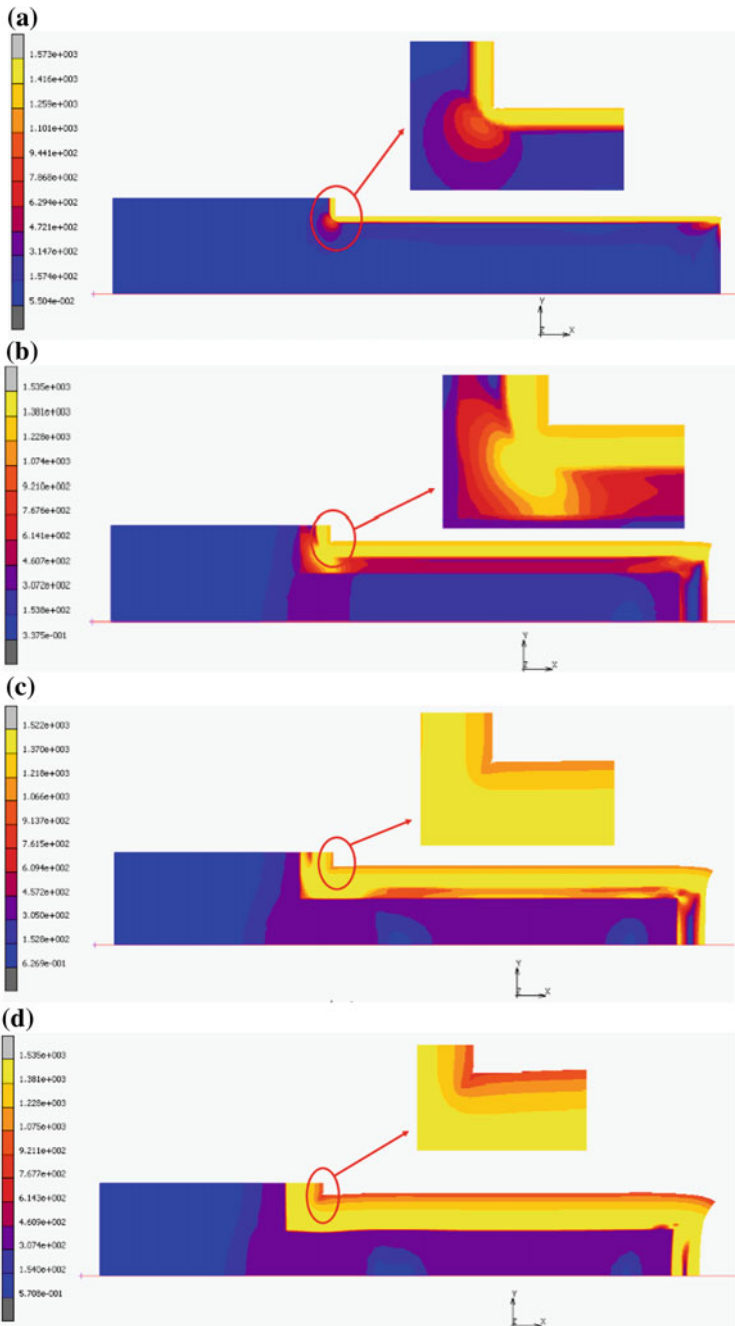


Fig. 5 Distribution of equivalent Von Mises stress in the anode at normalized charging time: **a** $t/t_{\max} = 0.01$; **b** $t/t_{\max} = 0.05$; **c** $t/t_{\max} = 0.1$; and **d** $t/t_{\max} = 0.2$

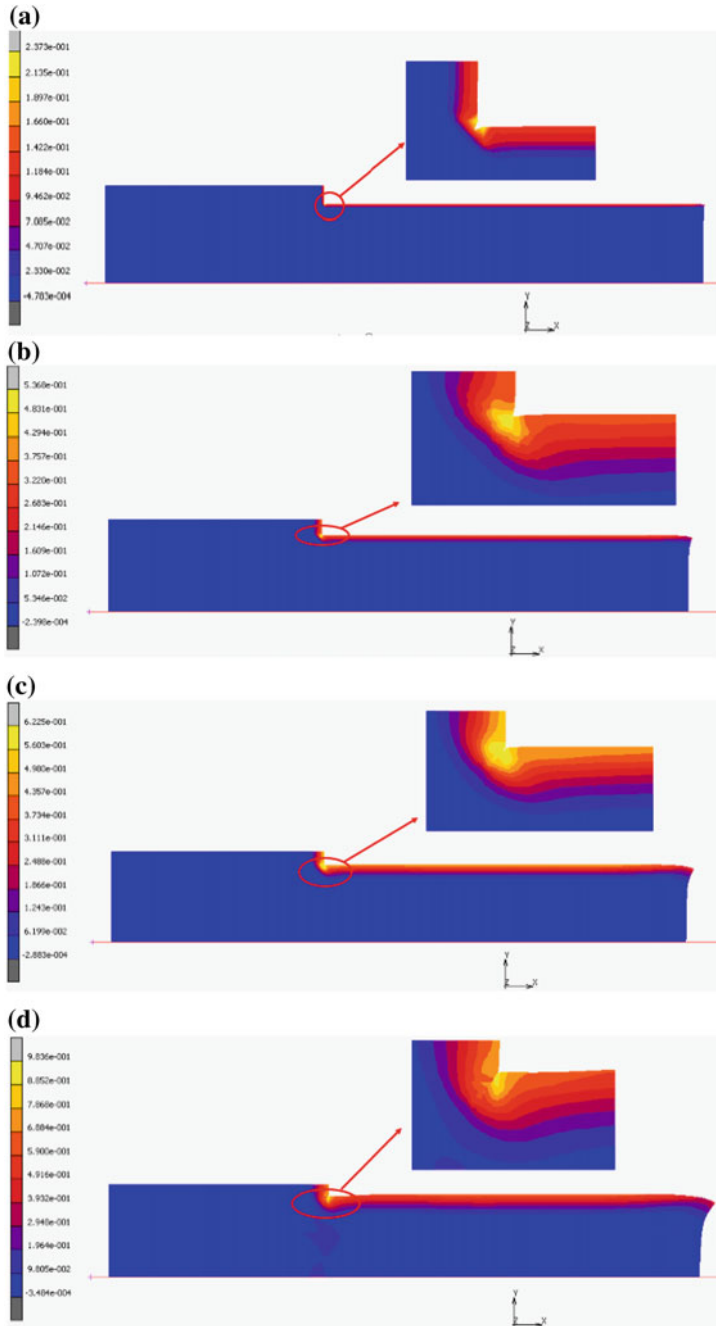


Fig. 6 Distribution of the total equivalent plastic strain at normalized charging time: **a** $t/t_{max} = 0.01$; **b** $t/t_{max} = 0.05$; **c** $t/t_{max} = 0.1$; and **d** $t/t_{max} = 0.2$

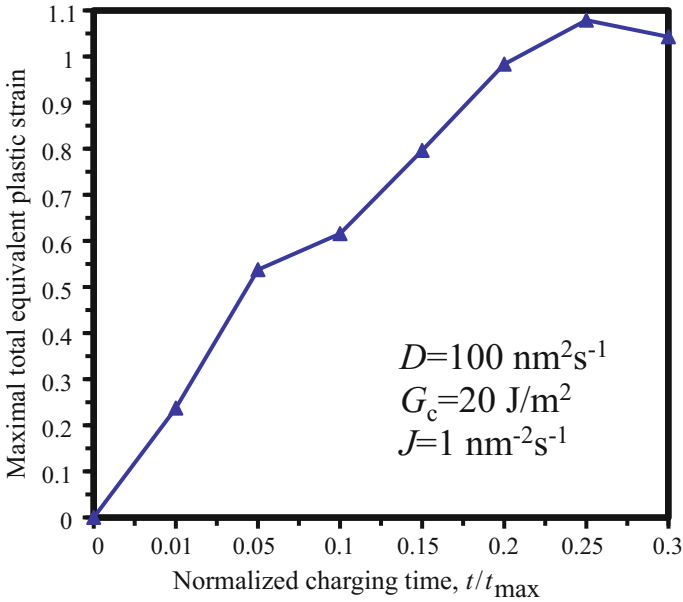


Fig. 7 Variation of the maximal total equivalent plastic strain versus the normalized charging time

respectively. Just after short charging time ($t/t_{\max} \sim 0.01$, t is the charging time and t_{\max} is the charging time with the full concentration of Li-ion in Si anode), the equivalent Von Mises stress reaches a peak value of ~ 1535 MPa and remains a constant during the charging as shown in Fig. 3. This value of stress exceeds well the yield stress of Si. Consequently, the plastic deformation occurs just after short charging time at the corner of Si anode as shown in Fig. 6. During charging, the plastic deformation accumulates and enlarges in Figs. 6 and 7. The total equivalent plastic strain increases almost monotonously with an increase of the charging time as indicated in Fig. 7. The maximum total equivalent plastic strain is estimated at about 25, 54, 62 and 100% at the charging time $t/t_{\max} = 0.01, 0.05, 0.1$, and 0.2 , respectively. At the corner of Si anode, the Li-ion concentration, equivalent Von Mises stress, and total equivalent plastic strain are highest.

4 Summary

The stress and deformation during charging of the anode made by silicon on nanopillar copper for anode in Li-ion batteries have been studied through an extensive FEA. It is found that stress and plastic strain increase rapidly during charging. Charging parameters should be carefully chosen to decrease the stress and

plastic deformation of the Si anode. More investigation should be done to analyze in details these issues.

Acknowledgements This work was supported by Vietnam National Foundation for Science and Technology Development (NAFOSTED) under the grant number: 107-02-2017-02.

References

1. Li, X Chen Y, Huang H, Mai Y-W, Zhou L (2016) Electrospun carbon-based nanostructured electrodes for advanced energy storage—a review. *Energy Storage Mater* (2016)
2. Obrovac M, Christensen L, Le DB, Dahn J (2007) Alloy design for lithium-ion battery anodes. *J Electrochem Soc* 154(9):A849–A855
3. Obrovac M, Christensen L (2004) Structural changes in silicon anodes during lithium insertion/extraction. *Electrochem Solid-State Lett* 7(5):A93–A96
4. Nitta N, Wu F, Lee JT, Yushin G (2015) Li-ion battery materials: present and future. *Mater Today* 18(5):252–264
5. Noel M, Suryanarayanan V (2002) Role of carbon host lattices in Li-ion intercalation/de-intercalation processes. *J Power Sour* 111(2):193–209
6. Dahn JR, Zheng T, Liu Y, Xue J (1995) Mechanisms for lithium insertion in carbonaceous materials. *Science* 270(5236):590
7. Chou C-Y, Kim H, Hwang GS (2011) A comparative first-principles study of the structure, energetics, and properties of Li–M (M = Si, Ge, Sn) alloys. *J Phys Chem C* 115(40):20018–20026
8. Beaulieu L, Hatchard T, Bonakdarpour A, Fleischauer M, Dahn J (2003) Reaction of Li with alloy thin films studied by in situ AFM. *J Electrochem Soc* 150(11):A1457–A1464
9. Chen Z, Christensen L, Dahn J (2003) Large-volume-change electrodes for Li-ion batteries of amorphous alloy particles held by elastomeric tethers. *Electrochem Commun* 5(11):919–923
10. Beattie SD, Larcher D, Morcrette M, Simon B, Tarascon J-M (2008) Si electrodes for Li-ion batteries—a new way to look at an old problem. *J Electrochem Soc* 155(2):A158–A163
11. Zhang Z, Zhang SS (2015) Challenges of key materials for rechargeable batteries, in rechargeable batteries. Springer, pp 1–24
12. Glaize C, Genies S (2013) Lithium batteries and other electrochemical storage systems. Wiley, New York
13. Bagotsky VS, Skundin AM, Volkovich YM (2015) Electrochemical power sources: batteries, fuel cells, and supercapacitors. Wiley, New York
14. McDowell MT, Xia S, Zhu T (2016) The mechanics of large-volume-change transformations in high-capacity battery materials. *Extrem Mech Lett* 9(Part 3):480–494
15. Zhao K, Cui Y (2016) Understanding the role of mechanics in energy materials: a perspective. *Extrem Mech Lett* 9(Part 3):347–352
16. Kim G, Jeong S, Shin J-H, Cho J, Lee H (2014) 3D amorphous silicon on nanopillar copper electrodes as anodes for high-rate lithium-ion batteries. *ACS Nano* 8(2):1907–1912
17. Grazioli D, Magri M, Salvadori A (2016) Computational modeling of Li-ion batteries. *Comput Mech* 58(6):889–909
18. Pal S, Damle SS, Kumta PN, Maiti S (2013) Modeling of lithium segregation induced delamination of a-Si thin film anode in Li-ion batteries. *Comput Mater Sci* 79:877–887
19. Liu M (2015) Finite element analysis of lithiation-induced decohesion of a silicon thin film adhesively bonded to a rigid substrate under potentiostatic operation. *Int J Solids Struct* 67:263–271
20. Xu R, Zhao K (2015) Mechanical interactions regulated kinetics and morphology of composite electrodes in Li-ion batteries. *Extrem Mech Lett*

21. Shirazi A, Mohebbi F, Azadi Kakavand M, He B, Rabczuk T (2016) Paraffin nanocomposites for heat management of lithium-ion batteries. *J Nanomater* 59
22. Wang H, Nadimpalli SP, Shenoy VB (2016) Inelastic shape changes of silicon particles and stress evolution at binder/particle interface in a composite electrode during lithiation/delithiation cycling. *Extrem Mech Lett*
23. Ding N, Xu J, Yao Y, Wegner G, Fang X, Chen C, Lieberwirth I (2009) Determination of the diffusion coefficient of lithium ions in nano-Si. *Solid State Ionics* 180(2):222–225
24. Chew HB, Hou B, Wang X, Xia S (2014) Cracking mechanisms in lithiated silicon thin film electrodes. *Int J Solids Struct* 51(23):4176–4187

Modeling of 3D Inflatable Large Deformation Air Plug in Contact With Concrete Lining



Anan Liao, Hui Shang, Xiaoyong Kou, Jun Huang and Xiaoying Zhuang

Abstract Resilient tunnel plug is a recently developed technique for the block of flood in tunnel by using an inflatable cylindrical airbag with air concealed. The plug, i.e., air bag surface, itself is made of textile composite with high strength, lightweight and easily foldable. The air plug can be inflated in a short amount of time and aligns with the internal surface of the tunnel tightly so that the fluid will be stopped at the required position. The use of air plug provides new solutions to the response of emergencies and accidents in tunnel operation such as the screening of smoke from fire and flood from precipitation. Recently, the possibility of using the air plug for the rescue of accidents in tunneling construction is being explored. In this paper, the feasibility of utilizing air plug to screen the soil and water flow in case of boring face failure is investigated. Membrane element is used to model the plug, and surface-based fluid modeling based on the Uniform Pressure Method (UPM) is used to model the coupling between the deformation and the pressure of the plug. Surface-to-surface contact interaction is used to model the frictional contact between the tunnel lining and the air plug surface. It is revealed that for embedded depth up to 20 m, the air plug can provide sufficient friction to resist the flow of water and soil

The International Conference On Advances In Computational Mechanics Acome 2017 August 02–04, Phu Quoc, Vietnam

A. Liao · H. Shang · X. Zhuang (✉)
Department of Geotechnical Engineering, College of Civil Engineering, Tongji University,
Shanghai 200092, China
e-mail: zhuang@ikm.uni-hannover.de

A. Liao
e-mail: ananliao@tongji.edu.cn

X. Kou · J. Huang
Shanghai Tunnel Engineering Co., Ltd., Shanghai 200232, China
e-mail: kxyyxk@126.com

X. Zhuang
Institute of Continuum Mechanics, Leibniz University Hannover, 30167 Hannover, Germany

without inducing excessive deformation of the tunnel structure. However, the careful choice of the pressure is important to avoid excessive deformation of the tunnel lining.

Keywords Large deformation · Inflatable plug · Membrane Structure · UPM Contact · Tunnel

1 Introduction

In recent years, tunnels and underground structures have been rapidly developed in China, meanwhile quite a number of accidents and disasters took place during excavation, and safety issues arise with increasing complexities in geological conditions in urban areas. Especially, the collapse and the inrush of water and mud that can result in earth movement of surrounding buildings and destruction of entire tunnels. In general, these accidents caused by both natural conditions and human errors are recognized to occur suddenly, spread easily, develop rapidly, and leave short time to reaction. Once the accident happens, two measures, namely blocking and supporting, are commonly used to control the spreading of damage and hazard. With blocking, which uses rapid hardening cement or polyurethane to form waterproof shield, it is possible to partly seal the leakage point, reduce the amount of water pouring-in and improve the stress condition. On the other hand, supporting, by definition, means using steel supports to increase the stiffness and strength of underground structure and control the surface settlement. However, these traditional approaches are often proved to be inefficient, often not in time and not mobile enough since the site of accident is unknown in advance. Therefore, new approaches for mitigating threats should be considered and developed.

With the development of modern construction technology, membrane structures started to be widely used from the middle of the twentieth century [1]. Modeling of thin structures still poses challenges to computational methods which are urgently needed to support the design of protection underground systems; see for instance, the contributions in [2–15] of efficient thin shell/membrane formulations. Another challenge is modeling the complex behavior of reinforced concrete structures which are dominated by several different fracture mechanisms including bending, anchorage, and shear failure to name a few. Efficient formulations for reinforced concrete structures can be found for instance in [16–22].

Two types of membrane structures are the most commonly used, i.e., air-supported membrane structure and inflatable membrane structure. For air-supported membrane structures, membrane is tensioned to resist external loads and cover large span by inflating air or using cables as well as other rigid supports. And inflatable membrane structure is usually an inflatable plug with a particular shape which has been already applied to numerous fields, e.g., automobile airbags, the airbags used for the Mars pathfinder, as well as other industrial applications [23]. The development of textile composite materials and membrane structures presents new solutions for

sealing gas, fire, flood, and mud. An inflatable membrane structure, i.e., inflatable plug, filled with air or other medium can provide flexible block at a certain position in a pipeline or even a tunnel, by the friction provided through the contact pressure developed between the membrane surface and structure surface [24]. Compared with traditional sealing methods, the advantages are obvious as reflected in light weight, quick response, low maintenance costs, convenient operation, and minimal influence on existing facilities [25]. Recently, many inflatable pipe plugs with diameters ranging from 50 to 2700 mm are used in underground pipes, e.g., water supply and drainage. These plugs with small sizes turn out to be economic and efficient in stopping oil spilling, water and smoke leakage, etc.

Meanwhile, large inflatable plugs have been proposed to protect underground subway tunnels that are susceptible to extreme climate induced hazards and terrorist attacks [26]. It is recognized that inflatable plug for large-scale tunnel are firstly implemented by the US Department of Homeland Security Science and Technology Directorates Resilient Tunnel Project [27]. The project is aimed at restraining flood-water in the event of flooding to a certain area in the transportation subways. Sosa et al. [28] designed and manufactured a full-scale prototype that is composed of a cylindrical region closed by two end caps and made of three-layer Vectran material to study the deployment and sealing characteristics of the system. The results showed that the plug sealed the test tunnel and resisted the simulated flood successfully. Apparently, damages can be substantially minimized by narrowing down the area affected by the event, buying as much time as possible for evacuating workers, grouting reinforcement as well as deploying inner support system, etc. By partitioning off the tunnel, dangers can be controlled within certain areas; meanwhile, adjacent ones will not be influenced or be slightly affected only. Inflatable large deformation air plugs are supposed as a flexible strategy to achieve this goal.

However, most of the existing air plug applications and researches focus on the blocking of low pressure fluid in small pipelines. For large-sized sections with high pressure fluid, air plug sealing technology is still in its early stage, and there are only few studies existing so far which are however focused on shape, packing, as well as material characteristics without considering the deformation of tunnel lining [29]. The possibility of using air plug for disaster reduction in tunneling construction remains to be explored. This paper investigates the feasibility of utilizing air plug to screen the soil and water flow in case of boring face failure in tunnels under construction, and close attention is also paid to the deformation of tunnel lining under high internal pressure.

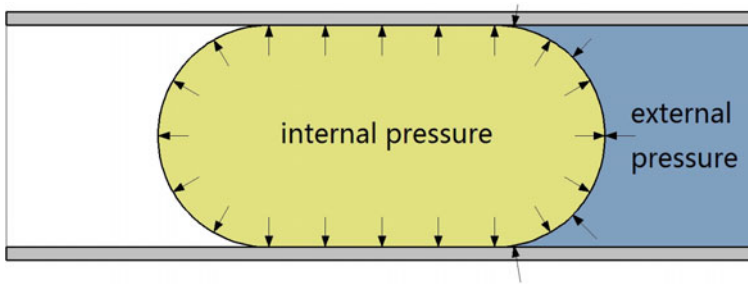


Fig. 1 The inflatable tunnel plug and the block of water inflow on right face

2 Working Conditions of Inflatable Air Plug for Tunnel Under Construction

The basic working principle of inflatable tunnel plug is shown in Fig. 1. In order to achieve the best effect of blocking the tunnel section, the following conditions should be satisfied:

(1) The air plug should be placed in a section behind the boring face where deformation tends to be stable as soon as there are signs of disaster, making sure that there will be enough time for the plug to reach the required shape and pressure.

(2) Compared with operating tunnels, there are less cables and pipes inside tunnels under construction, and the majority of them can be pretreated or removed. However, the friction coefficient may decrease significantly if there is mud attached to the plug, and there is often much mud in unfinished tunnels. So during the deployment, large-scale facilities such as rails that may cause gaps and leakage should be removed, and mud in the tunnel section should be cleaned as much as possible.

(3) The methods that can be used to inflate the plug depend on the hazard to be contained and have obvious difference in inflation times [25]. To make inflation as quickly as possible, methods such as releasing compressed gas, using controlled chemical reactions, or using phase-change systems can be applied. However, a fast inflating rate can mean high risks of burst and other dangers. To stand high external pressure, the plug can be inflated with liquid, but the self-weight of liquid may cause large settlement. In short, pumping air is a safe and suitable method in this case.

(4) To maintain axial stability of plug, there are two possible methods, i.e., fully relying on friction between plug and tunnel lining or using additional mechanical anchors to assist [30]. Of these two choices, the former method is less harmful to the tunnel and the inflatable plug, while there are concentrated loads at the anchorage region.

The numerical model in the next section is developed basing on these working conditions.

3 The Numerical Model

The numerical simulation of this paper is performed by using Abaqus/Explicit. Two main components are considered in the numerical modeling, one is the inflatable air plug for tunnel under construction, and the other is the tunnel in which the plug will be installed. Other components include auxiliary planes which help to fold and move the plug [31].

The plug is composed of a middle cylindrical region and two semi-spherical end caps, ignoring the fill ports. The cylindrical region is the fundamental part which is in contact with the tunnel lining and responsible for sealing the tunnel. The upstream one of the two end caps is in direct contact with mud and water, and the downstream one is rather free. According to the research by Barbero [25], the size of the cylinder must be slightly larger than the tunnel section to ensure that the plug adapts to pipes and cables and fits the tunnel section perfectly. The plug is modeled with membrane elements, which are surface elements transmitting in-plane forces only and have no bending stiffness, with an equivalent single-layer membrane thickness of 8 mm. The material of the plug is linear elastic with a density of 1300 kg/m³ and a Young's modulus of 2000 MPa.

The tunnel, according to the Shanghai metro tunnel, is a single-layer lining shield tunnel under straight joint assembling with an outside diameter of 6.6 m, an inside diameter of 5.9 m, a segment thickness of 0.35 m, and a ring width of 1.2 m. Each lining ring consists of a key block, two adjacent blocks, two standard blocks, and one arch block. Two rings are connected using 17 M30 longitudinal bolts, and blocks in one ring are connected using 12 M30 circular bolts. The segment-joint model, illustrated in Fig. 2, is utilized to model the action of the tunnel lining [32]. The steel bars (black parts in Fig. 2) are embedded in the segment so that there will not be any relative displacement between the steel bars and the concrete. The nuts of the bolts (red parts in Fig. 2) are also embedded in the corresponding positions of the segments, but the screws (blue parts in Fig. 2) are independent of the segments. The water stops, hand holes, other embedded parts, tunnel facilities, etc., are ignored. The segments and the bolts are modeled using solid elements, while the steel bars are modeled using beam elements. When the analyses emphasize on the plug itself, e.g., the study of axial stability of the plug, the tunnel lining can be then simplified as a rigid shell and modeled with rigid elements.

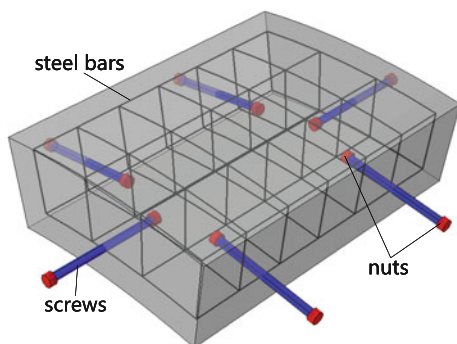
The material of segments, i.e., C55 concrete, is elastic-plastic, and the parameters are set according to the average strength for nonlinear analysis. The relationship of stress and strain can be written as

$$\sigma = (1 - d_t) \sigma_t$$

$$d_t = \begin{cases} 1 - (1.2x - 0.2x^6) & x \leq 1 \\ 1 - \frac{x}{\alpha_t(x-1)^{1.7} + x} & x > 1 \end{cases} \quad (1)$$

$$x = \epsilon / \epsilon_t$$

Fig. 2 Part of the segment–joint model



under tension, and

$$\sigma = (1 - d_c) \sigma_c$$

$$d_t = \begin{cases} 1 - [\alpha_a x + (3 - 2\alpha_a) x^2 + (\alpha_a - 2) x^3] & x \leq 1 \\ 1 - \frac{x}{\alpha_d(x-1)^2 + x} & x > 1 \end{cases} \quad (2)$$

$$x = \epsilon / \epsilon_c$$

under compression, where α_t , α_a , and α_d are parameters depended on the strength of the concrete. Some important parameters of the concrete and their values are listed in Table 1, and the stress-strain curve of the concrete is illustrated in Fig. 3. HRB400 steel bar and grade 6.8 bolt are both ideal elastic-plastic.

The contact between segment and segment as well as segment and plug is modeled using surface-to-surface contact interaction. The normal behavior of the contact relationship is defined as hard contact using penalty contact enforcement, and when surfaces are in contact, any contact pressure can be transmitted between them. The tangential behavior is achieved using the basic Coulomb friction model with different friction coefficients. The friction coefficient between different segment surfaces is 0.4, and between segment and plug is 0.3. Additionally, the self-contact of differ-

Table 1 Values of parameters of C55 concrete

Parameter	Value
Youngs modulus E_c	35.5 GPa
Tensile strength f_t	3.35 MPa
Peak tensile strain ϵ_t	125×10^{-6} GPa
Compressive strength f_c	43.3 MPa
Peak compressive strain ϵ_c	1832×10^{-6}
Density ρ_c	2500 kg/m ³

ent parts of the plug is modeled using the same contact relationship with a friction coefficient of 0.3.

To take into account the coupling between the deformation of the plug and the pressure exerted by the contained fluid inside the plug, the Uniform Pressure Method based on the control volume algorithm is used. Thus, the gas inside the plug is modeled using the surface-based fluid modeling technique in Abaqus, which is an improvement of the UPM. The basic assumption of the surface-based fluid modeling is that the fluid inside the structure is homogeneous and the pressure within

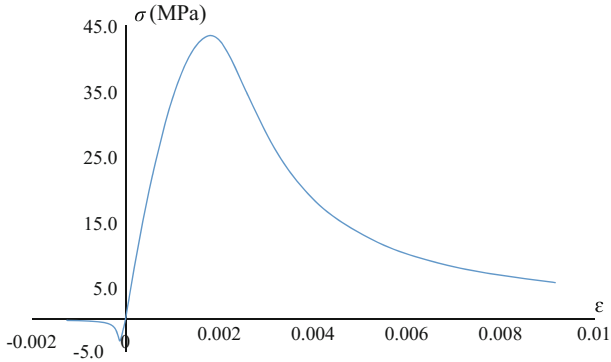


Fig. 3 Stress-strain curve of C55 concrete

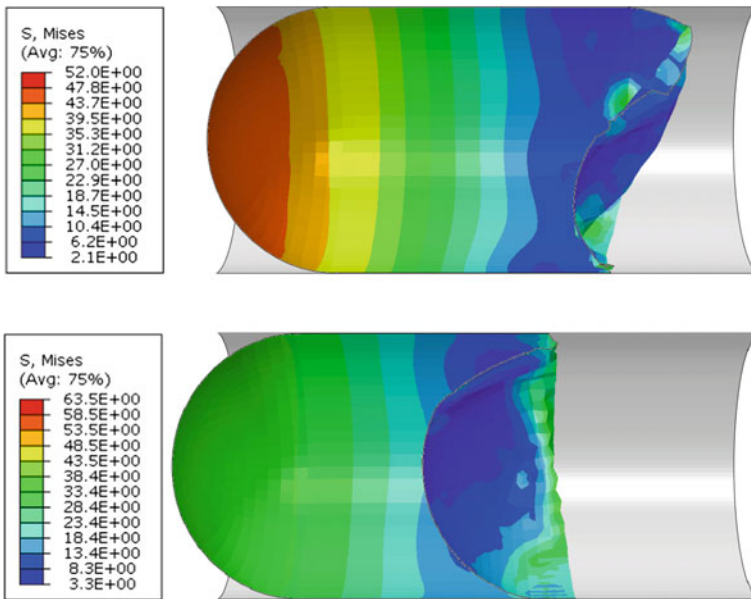
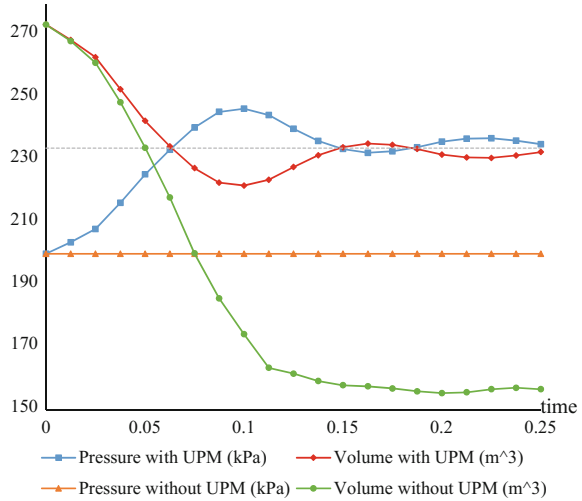


Fig. 4 Mises stress of plug with and without using UPM (MPa)

Fig. 5 Pressure and volume of plug with and without using UPM



the structure is spatially uniform during the whole process. The modeling requires the definition of the closed surface-based cavity inside the structure using the fluid–structure interface, the nature of the fluid, the reference point of the cavity, etc. And the finite element calculations are performed using volume elements created internally and automatically. Results show that when the internal air pressure is bigger than the external water pressure, the differences between using and not using the surface-based fluid modeling are negligible. However, when the internal pressure is smaller, the differences can be very obvious as shown in Figs. 4 and 5. Figure 5 also shows that by using the UMP, the gas in the plug satisfies the ideal gas equation when there is no gas exchange and the isothermal condition is satisfied.

4 Analysis of Axial Stability of the Plug

4.1 Analysis Of Axial Stability Under Normal Condition

The axial stability of the plug is controlled by the external water pressure and the friction provided by the contact pressure between the plug surface and the tunnel lining. Based on the working conditions of inflatable air plug, the facilities inside the tunnel are ignored, and the tunnel lining is simplified as a rigid shell. According to Martinez’ study, the length of the cylindrical region should be close to its diameter, thus it is set to 6.0 m while the inner diameter of the tunnel is 5.9 m. The diameter of the cylindrical region and the end caps is set to 5.900, 5.959, and 6.018 m, respectively, (i.e., 0, 1 and 2% larger than the tunnel) to analyze and compare the axial stability of plugs with different sizes. Under the normal condition in which the internal air pres-

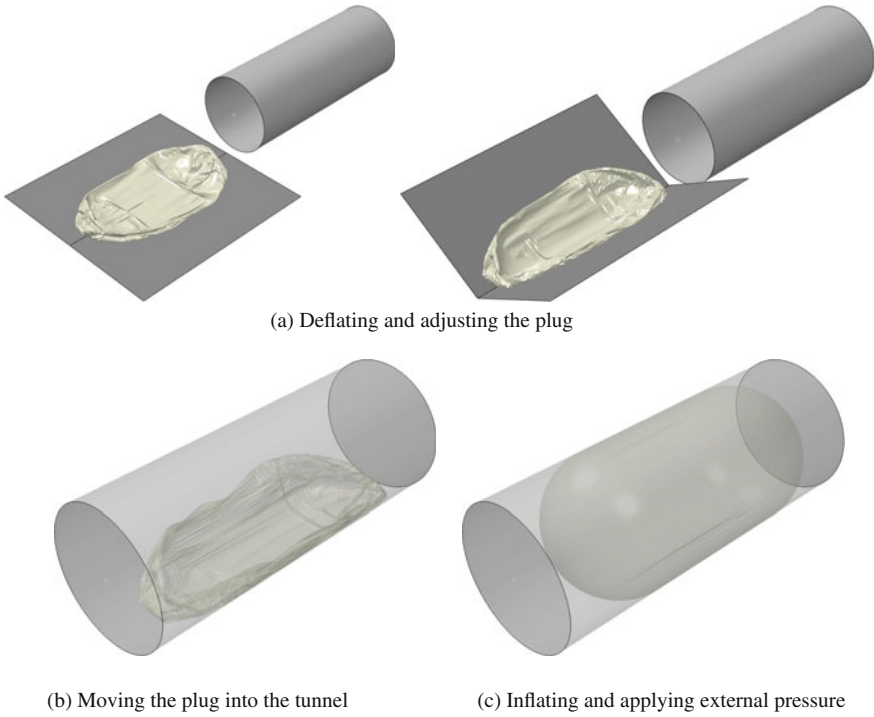


Fig. 6 Numerical simulation process for axial stability analyses

Table 2 Simulation results of axial stability under normal condition

Plug diameter D/m	Total normal contact forces $N_{in}/10^3 kN$	Total external axial forces $F_{ex}/10^3 kN$	Safety factor η_a
5.900	25.00	4.99	1.50
5.959	27.63	5.06	1.64
6.018	28.95	5.10	1.70

sure and the external water pressure are stable, the total normal contact forces N_{in} and the total external axial forces F_{ex} are calculated with the numerical simulation process as shown in Fig. 6, assuming that the air pressure is 220 kPa and the average water pressure is 183 kPa. Defining the axial stability safety factor η_a as:

$$\eta_a = \frac{\mu N_{in}}{F_{ex}} \tag{3}$$

where μ is the friction coefficient between the tunnel lining and the plug which is 0.3 in these cases; the results are listed in Table 2.

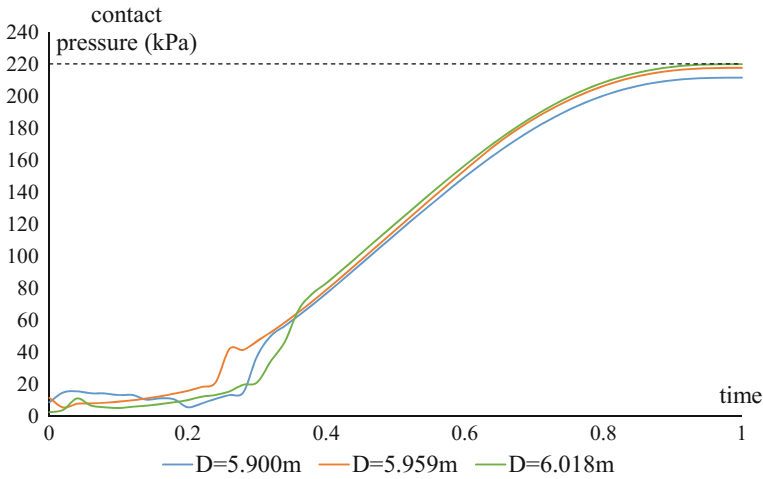


Fig. 7 Development of contact pressure of plugs with different sizes during inflation

As it is shown in Table 2, even for the most critical case, the safety factor is larger than 1, indicating that with suitable air pressure, the air plug is able to resist the water pressure and block the tunnel section. As plug diameter increases, the total contact forces increase significantly while the changes in total external forces are relatively small, resulting in larger safety factor, which coincides with the research by Barbero et al. [25]. Development of average contact pressure of the bottom area during the inflating process illustrated in Fig. 7 further explains these results, as a larger plug size comes with a higher final contact pressure. However, a larger plug size may also lead to more wrinkles developing during the inflation, which could be natural channels for leaking and are against the axial stability of the plug.

4.2 Analysis Of Axial Stability With Sudden Change In Water Pressure

After being deployed and fully inflated, the plug starts to block the water and the pressure is relatively low at this stage. Right at the moment that the section is full, the water head should be recalculated according to the groundwater level, resulting in a sudden increase in external water pressure. The axial stabilities of the plug before, at, and after the sudden pressure change are analyzed. The numerical simulation is simplified by setting up a plug of nominal size firstly inside the tunnel shell and inflating as well as applying external pressure afterward. A plug diameter of 5.900 m and a total plug length of 11.9 m are set, which can be seen from the previous section is the most critical case. The initial air pressure of the plug is 270 kPa. The average water pressure is 29.5 kPa at first and changes to 233 kPa instantaneously

Fig. 8 Mises stress of the plug before, at, and after the sudden pressure change (MPa)

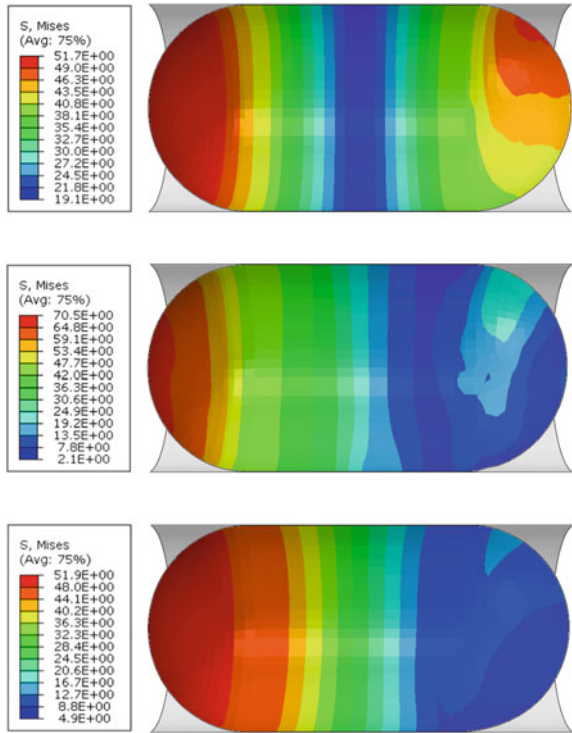
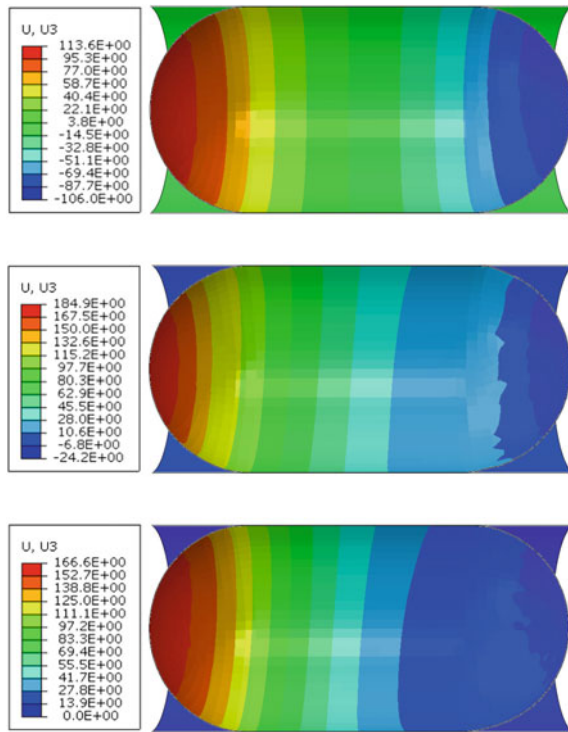


Table 3 Simulation results of axial stability under normal condition

Stage	Total normal contact forces $N_{in}/10^3$ kN	Total external axial forces $F_{ex}/10^3$ kN	Safety factor η_a
Before the change	28.98	0.68	12.79
At the change	30.40	8.68	1.05
After the change	28.95	6.32	1.37

(corresponding to a tunnel embedded depth of 20 m). The von Mises stress and the axial displacement in each stage are illustrated in Figs. 8 and 9, respectively, with the total normal contact forces, etc., listed in Table 3. The results show the plug suffered sudden changes in stress condition and axial displacement as it is impacted. The safety factor decreases when the increase of pressure happens and recovers afterward. During the whole process, the safety factor remains being larger than 1, indicating that the inflatable plug is able to withstand sudden changes in water pressure to some extent.

Fig. 9 Axial displacement of the plug before, at, and after the sudden pressure change (mm)



5 Analysis of Deformation of Tunnel

The deformation of tunnel lining interacted with plug is the result of both external earth pressure and internal plug pressure, so the key of this section is to study the variations of stress and deformation of tunnel lining subject to internal pressure. Since the lining contacts only with the cylindrical part of the air plug, a half-model is taken regardless of the influence of the external water pressure. The numerical model is also simplified by setting up a plug of nominal size inside the tunnel as shown in Fig. 10.

The simulation is conducted using loading structure method. The earth pressure at the top of the tunnel lining is 303 kPa/m and at the bottom is 428.4 kPa/m, corresponding to a tunnel embedded depth of 15 m, and the coefficient of earth pressure is set to 0.65. The subgrade reaction is considered with a coefficient of 8000 kN/m³. The pretightening force of each bolt is about 100 kN. Two major steps of the simulation are (1) applying earth pressure, dead loads, and pretightening forces and (2) applying pressure on the inner surface of the plug, which is 225 kPa in this case.

Fig. 10 Numerical model for deformation of tunnel (in half-view)

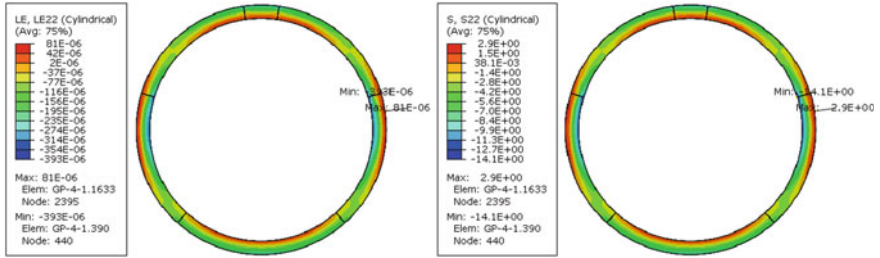
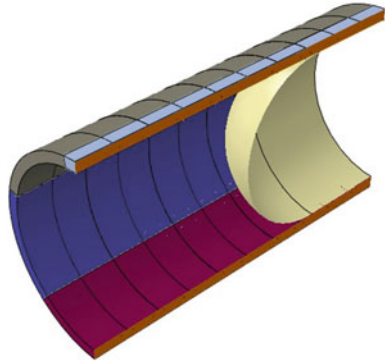


Fig. 11 Circumferential strain and stress (MPa) before applying internal pressure

5.1 Deformation Of The Tunnel Before Applying Internal Pressure

After the earth pressure and other boundary conditions have been applied, the tunnel lining changes form circular to oval with radius increased in the horizontal direction and decreased in the vertical direction. The maximum horizontal relative displacement is 9.2 mm (1.4 of D_{ex} , and D_{ex} is the outer diameter of the tunnel lining), and the minimum vertical relative displacement is -9.6 mm (-1.5 of D_{ex}), both of which satisfy the requirement of the shield tunnel design. The deformation of the lining is relatively small, and the largest longitudinal joint open is less than 0.1 mm.

As shown in Fig. 11, the maximum circumferential tensile strain is 81×10^{-6} at the outer side of the haunch, and the corresponding maximum tensile stress is 2.9 MPa. The minimum circumferential compressive strain is -393×10^{-6} at the inner side of the joint in the haunch, and the corresponding minimum compressive stress is of -14.1 MPa. Both tensile and compressive strains have not exceeded the corresponding peak value. In addition, the maximum tensile stress of the bolts is 153.9 MPa, and the maximum tensile stress of the steels is 71.3 MPa. Both of them are still in elastic state.

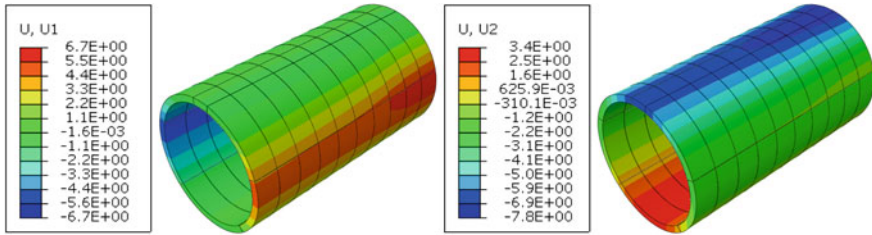


Fig. 12 Horizontal and vertical displacement after applying internal pressure (mm)

5.2 Deformation Of The Tunnel After Applying Internal Pressure

As shown in Fig. 12, the tunnel lining deforms unevenly after applying the plug pressure, and the lining ring corresponding to the middle of the plug deforms the most. The maximum horizontal relative displacement reaches 13.4 mm (2.0 of D_{ex}), and the minimum vertical relative displacement reaches -11.2 mm (-1.7 of D_{ex}). Instead of supporting the tunnel vertically, the internal plug pressure causes the section to be more oval, yet the threshold of the shield tunnel deformation according to design code is still satisfied. This can be explained as that the lining suffers larger loads vertically than laterally, in another word, the lateral constraint is weaker. Since the deformation increases, the longitudinal joints open much more with a maximum value of 0.8 mm at the outer side of haunch and a value of 0.4 mm at the inner side of the arch crown.

As shown in Fig. 13, for the most deformed lining ring, the tensile strain of the concrete at the inner side of the joint in the haunch is very large, which may be attributed to the constructional reinforcement is not modeled in these areas. Besides, the minimum circumferential compressive strain is -336×10^{-6} at the inner side of the joint in the haunch and the corresponding minimum compressive stress of -11.1 MPa. The circumferential tensile strain is 87×10^{-6} at the inner side of the arc crown, and the corresponding maximum tensile stress is 3.2 MPa. In addition, the maximum tensile stress of the bolts is 251.4 MPa, the maximum tensile stress of the steels is 158.2 MPa, and both remain within elastic stage.

6 Conclusion

This paper presented the numerical models to simulate an inflatable large deformation air plug in contact with concrete lining. The axial stability of plug under different conditions and the deformation of tunnel interacting with plug were studied. With an appropriate pressure, the inflatable plug is able to remain stable in the axial direction, even in cases of accidents, e.g., a sudden change in external water pressure.

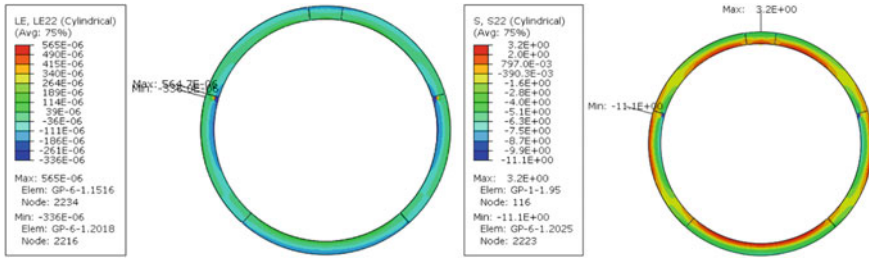


Fig. 13 Circumferential strain and stress (MPa) after applying internal pressure

When the size of the plug is close to the tunnel, the larger the diameter of the plug, the greater the total normal contact forces. However, more wrinkles are likely to appear on plug with a larger size. In conclusion, the inflatable plug is feasible to seal large-sectional tunnels. With the internal plug pressure, the tunnel lining deforms unevenly and appears more oval, resulting in larger joint opens which weakens the waterproof of the joints, yet the threshold of the shield tunnel deformation according to design code is still satisfied. The internal plug pressure and external earth pressure counteract with each other. So the internal pressure should be carefully chosen and controlled according to both the axial slippage of plug and the deformation of tunnel lining on site. With the application of the Uniform Pressure Method and other modeling techniques, the numerical models provide a reasonably accurate predicting tool, which allows further parametric studies of designing and deploying inflatable tunnel plugs. In the future, we intend to quantify uncertainties in the input parameters as in [33–35, 35–38] to finally optimize tunnel air plug systems accounting for uncertainties as has been done in other applications by [39–45].

References

1. Pons J, Oñate E, Flores F, García J, Ribó R, Marcipar J (2005) Numerical and experimental values comparison for an inflatable structure. In: *Textile Composites and Inflatable Structures II*
2. Chen L, Nguyen-Thanh N, Nguyen-Xuan H, Rabczuk T, Bordas S, Limbert G (2014) Explicit finite deformation analysis of isogeometric membranes. *Comput Methods Appl Mech Eng*, 277:104–130
3. Areias P, Rabczuk T, Reinoso J, Csar de SJ (2017) Finite-strain low order shell using least-squares strains and two-parameter thickness extensibility. *Eur J Mech, A/Solids* 61:293–314
4. Areias P, Rabczuk T, Msek M (2016) Phase-field analysis of finite-strain plates and shells including element subdivision. *Comput Methods Appl Mech Eng* 312:322–350
5. Areias P, Soares C, Rabczuk T, Garo J (2016) A finite-strain solidshell using local lw din frames and least-squares strains. *Comput Methods Appl Mech Eng* 311:112–133
6. Nguyen-Thanh N, Zhou K, Zhuang X, Areias P, Nguyen-Xuan H, Bazilevs Y, Rabczuk T (2016) Isogeometric analysis of large-deformation thin shells using rht-splines for multiple-patch coupling. In: *Computer methods in applied mechanics and engineering*. (Article in Press)

7. Areias P, Rabczuk T, deS J, NatalJorge R (2015) A semi-implicit finite strain shell algorithm using in-plane strains based on least-squares. *Comput Mech* 55(4):673–696
8. Nguyen-Thanh N, Valizadeh N, Nguyen M, Nguyen-Xuan H, Zhuang X, Areias P, Zi G, Bazilevs Y, De Lorenzis L, Rabczuk T (2015) An extended isogeometric thin shell analysis based on kirchhoff-love theory. *Comput Methods Appl Mech Eng* 284:265–291
9. Amiri F, Milln D, Shen Y, Rabczuk T, Arroyo M (2014) Phase-field modeling of fracture in linear thin shells. *Theor Appl Fract Mech*, 69:102–109
10. Areias P, Rabczuk T (2013) Finite strain fracture of plates and shells with configurational forces and edge rotations. *Int J Numer Methods Eng* 94(12):1099–1122
11. Chau-Dinh T, Zi G, Lee P.-S, Rabczuk T, Song J.-H (2012) Phantom-node method for shell models with arbitrary cracks. *Comput Struct* 92–93:242–246
12. Nguyen-Thanh N, Kiendl J, Nguyen-Xuan H, Wchner R, Bletzinger K, Bazilevs Y, Rabczuk T(2011) Rotation free isogeometric thin shell analysis using pht-splines. *Comput Methods Appl Mech Eng* 200(47–48):3410–3424
13. Rabczuk T, Areias P, Belytschko T (2007) A meshfree thin shell method for non-linear dynamic fracture. *Int J Numer Methods Eng* 72(5):524–548
14. Rabczuk T, Areias P (2006) A meshfree thin shell for arbitrary evolving cracks based on an extrinsic basis. *CMES-Comput Model Eng Sci* 16(2):115–130
15. Rabczuk T, Gracie R, Song J.-H, Belytschko T (2010) Immersed particle method for fluid-structure interaction. *Int J Numer Methods Eng* 81(1):48–71
16. Rabczuk T, Eibl J (2004) Numerical analysis of prestressed concrete beams using a coupled element free galerkin/finite element approach. *Int J Solids Struct* 41(3–4):1061–1080
17. Rabczuk T, Belytschko T (2004) Cracking particles: A simplified meshfree method for arbitrary evolving cracks. *Int J Numer Methods Eng* 61(13):2316–2343
18. Rabczuk T, Akkermann J, Eibl J (2005) A numerical model for reinforced concrete structures. *Int J Solids Struct* 42(5–6):1327–1354
19. Rabczuk T, Belytschko T (2006) Application of particle methods to static fracture of reinforced concrete structures. *Int J Fract* 137(1–4):19–49
20. Rabczuk T, Belytschko T (2007) A three-dimensional large deformation meshfree method for arbitrary evolving cracks. *Comput Methods Appl Mech Eng* 196(29–30):2777–2799
21. Rabczuk T, Zi G, Bordas S, Nguyen-Xuan H (2008) A geometrically non-linear three-dimensional cohesive crack method for reinforced concrete structures. *Eng Fract Mech* 75(16):4740–4758
22. Rabczuk T, Zi G, Bordas S, Nguyen-Xuan H (2010) A simple and robust three-dimensional cracking-particle method without enrichment. *Comput Methods Appl Mech Eng* 199(37–40):2437–2455
23. H. Verakis, “Technology developments and mine safety engineering evaluations,” *M UTMAN-SKY JM, RAMANI R V. Proceedings and Monographs in Engineering: Water and Earth Sciences. London: Taylor and Francis Group*, pp. 565–568, 2006
24. Hinkle JM, Cadogan DP, Roushey JL, Cook RJ (2012) Design and testing of an expandable structure using multi-layer softgoods technology. In: *Proceedings of the AIAA/ASME/ASCE structures, dynamics, and materials*
25. Barbero E, Sosa E, Martinez X, Gutierrez J (2013) Reliability design methodology for confined high pressure inflatable structures. *Eng Struc* 51:1–9
26. Martinez X, Davalos J, Barbero E, Sosa E, Huebsch W, Means K, Banta L, Thompson G (2012) Inflatable plug for threat mitigation in transportation tunnels. In: *Proceedings of the society for the advancement of material and process engineering (SAMPE) 2012 conference*, pp 21–24
27. “35,000 gallons of protection: Containing a tunnel flood with an inflatable stopper,” Technical report, U.S. Department of Homeland Security’s Science and Technology Directorates (2012). <https://www.dhs.gov/science-and-technology/35000-gallons-prevention>
28. Sosa E, Thompson G, Barbero E (2014) Testing of full-scale inflatable plug for flood mitigation in tunnels. *Transp Res Rec J Transp Res Board* 2407:59–67
29. Sosa EM, Thompson GJ, Barbero EJ, Ghosh S, Peil KL (2014) Friction characteristics of confined inflatable structures. *Friction* 2:365

30. Sill JJ (2011) Friction and leakage characteristics of water-filled structures in tunnels. Master's thesis, West Virginia University
31. Sosa EM, Wong JC-S, Adumitroaie A, Barbero EJ, Thompson GJ (2016) Finite element simulation of deployment of large-scale confined inflatable structures. *Thin-Walled Struct* 104:152–167
32. Zhuang X, Zhang X, Zhu H (2015) 3-d finite element model for destruction process of segment joints of shield tunnel using elastoplastic and damage constitutive methods. *Chin J Geotech Eng* 37:1826–1834
33. Vu-Bac N, Lahmer T, Zhuang X, Nguyen-Thoi T, Rabczuk T (2016) A software framework for probabilistic sensitivity analysis for computationally expensive models. *Adv Eng Softw* 100, pp 19–31
34. Hamdia K, Msekh M, Silani M, Vu-Bac N, Zhuang X, Nguyen-Thoi T, Rabczuk T (2015) Uncertainty quantification of the fracture properties of polymeric nanocomposites based on phase field modeling. *Compos Struct* 133:1177–1190
35. Vu-Bac N, Lahmer T, Keitel H, Zhao J, Zhuang X, Rabczuk T (2014) Stochastic predictions of bulk properties of amorphous polyethylene based on molecular dynamics simulations. *Mech Mater* 68:70–84
36. Vu-Bac N, Rafiee R, Zhuang X, Lahmer T, Rabczuk T (2015) Uncertainty quantification for multiscale modeling of polymer nanocomposites with correlated parameters. *Compos Part B: Eng* 68:446–464
37. Vu-Bac N, Silani M, Lahmer T, Zhuang X, Rabczuk T (2015) A unified framework for stochastic predictions of mechanical properties of polymeric nanocomposites. *Comput Mater Sci* 96(PB):520–535
38. Vu-Bac N, Lahmer T, Zhang Y, Zhuang X, Rabczuk T (2014) Stochastic predictions of interfacial characteristic of polymeric nanocomposites (pnCs). *Compos Part B Eng* 59:80–95
39. Ghasemi H, Park H, Rabczuk T (2017) A level-set based iga formulation for topology optimization of flexoelectric materials. *Comput Methods Appl Mech Eng* 313:239–258
40. Ghasemi H, Brighenti R, Zhuang X, Muthu J, Rabczuk T (2015) Optimal fiber content and distribution in fiber-reinforced solids using a reliability and nurbs based sequential optimization approach. *Struct Multidiscip Optim* 51(1):99–112
41. Ghasemi H, Rafiee R, Zhuang X, Muthu J, Rabczuk T (2014) Uncertainties propagation in metamodel-based probabilistic optimization of cnt/polymer composite structure using stochastic multi-scale modeling. *Comput Mater Sci* 85:295–305
42. Ghasemi H, Brighenti R, Zhuang X, Muthu J, Rabczuk T (2014) Optimization of fiber distribution in fiber reinforced composite by using nurbs functions. *Comput Mater Sci* 83:463–473
43. Nanthakumar S, Lahmer T, Zhuang X, Park H, Rabczuk T (2016) Topology optimization of piezoelectric nanostructures. *J Mech Phys Solids* 94:316–335
44. Nanthakumar S, Valizadeh N, Park H, Rabczuk T (2015) Surface effects on shape and topology optimization of nanostructures. *Comput Mech* 56(1):97–112
45. Nanthakumar S, Lahmer T, Zhuang X, Zi G, Rabczuk T (2015) Detection of material interfaces using a regularized level set method in piezoelectric structures. *Inverse Probl Sci Eng (Article in Press)*

Upper Bound Limit Analysis of Circular Tunnel in Cohesive-Frictional Soils Using the Node-Based Smoothed Finite Element Method



T. Vo-Minh, T. Nguyen-Minh and A. Chau-Ngoc

Abstract In this paper, a numerical procedure using the node-based smoothed finite element method (NS-FEM) is proposed to evaluate the stability of a plane strain circular tunnel in cohesive-frictional soils subjected to continuous loading on the ground surface. In the NS-FEM, the strain smoothing is calculated over smoothing domains associated with the nodes of the elements. The soil is described as a uniform Mohr–Coulomb material and it obeys an associated flow rule. The limit load and failure mechanisms of circular tunnel are calculated from solving the optimization problems. In this study, the influence of the soil weight ($\gamma D/c'$), the ratio of tunnel diameter to its depth (H/D) on the stability numbers (σ_s/c') and collapse mechanisms are investigated. The results obtained from the present analysis are compared with the available literature for tunnels located below the horizontal ground surface.

Keywords Limit analysis · Circular tunnel · Stability · SOCP
NS-FEM

1 Introduction

In recent years, underground systems have become essential for the rapid development of many major cities. In fact, such underground infrastructures as underground railway and gas pipeline have become increasingly popular in many

T. Vo-Minh · T. Nguyen-Minh (✉) · A. Chau-Ngoc (✉)
Faculty of Civil Engineering, Ho Chi Minh City University of Technology,
Ho Chi Minh City, Vietnam
e-mail: nmtam@hcmut.edu.vn

A. Chau-Ngoc
e-mail: cnan@hcmut.edu.vn

T. Vo-Minh
e-mail: thienk94@gmail.com

T. Vo-Minh
Faculty of Civil Engineering, HUTECH University, Ho Chi Minh City, Vietnam

metropolises to meet the demand of citizens. During the construction of such underground networks, the depth of tunnels need to be investigated carefully because this plays an important role in constructing process and may help to reduce the cost of constructions. Moreover, in order to construct the tunnel systems in highly populous cities, engineers need to determine the limit load and failure mechanism of tunnels subjected to continuous loading on the ground surface.

The stability of circular tunnel was first studied at Cambridge University in the 1970s. A series of centrifuge model tests of tunnels in dry sand were described by Atkinson and Pott [1]. Atkinson and Cairncross [2] investigated the failure mechanism of circular tunnels when considering soil behaviour as a uniform Mohr–Coulomb material. In the study of Cairncross [3], experiment approach was used to determine the deformation around a circular tunnel in stiff clay. In 1979, Seneviratne [4] investigated the influence of pore-pressure on the stability of circular tunnels in soft clay. Mair [5] also conducted some centrifugal model tests to estimate the stability of circular tunnels in soft clay for plane strain. In 1994, Chambon and Corte [6] conducted a series of centrifuge tests to evaluate the tunnel face stability in sand. Recently, Kirsch [7] and Idinger et al. [8] performed small-scale tunnel model in geotechnical centrifuge to investigate the face stability of shallow tunnel in dry sand.

The stability of a tunnel in cohesive material using the upper and lower bound theorems has been studied by several researchers, for example, the works of Davis et al. [9], Mühlhaus [10], Leca and Dormieux [11]. Recently, Zhang et al. [12] proposed a new 3D failure mechanism using the upper bound limit analysis theory to determine the limit support pressure of the tunnel face.

In recent decades, the finite element method using triangular element (FEM-T3) has been rapidly developed to solve important geotechnical problems. A finite element procedure for linear analysis was first given by Sloan and Assadi [13] to evaluate the undrained stability of a square tunnel in a soil whose shear strength increases linearly with depth. Lyamin and Sloan [14], Lyamin et al. [15] and Yamamoto et al. [16, 17] developed FEM-based nonlinear analysis methods to calculate the failure mechanisms of circular and square tunnels in cohesive-frictional soils. However, one of the marked drawbacks of FEM-T3 elements is volumetric locking phenomenon, which is often occurred in the nearly incompressible materials. To overcome this, Chen et al. [18, 19] proposed a stabilized conforming nodal integration using the strain smoothing technique. Liu et al. [20–31] applied this technique to standard FEM and proposed a class of smoothed finite element method (S-FEM). Typical S-FEM models include the cell-based S-FEM (CS-FEM) [21], node-based S-FEM (NS-FEM) [22], face-based S-FEM (FS-FEM) [23], and edge-based S-FEM (ES-FEM) [24]. Several further developments of S-FEMs for limit and dynamic analysis have been investigated in [32–36].

In this study, the node-based smoothed finite element method (NS-FEM) has been employed for upper bound limit problems due to following advantages: (i) total degrees-of-freedom significantly decreased, leading to a fast convergence

for solutions, (ii) volumetric locking phenomenon is prevented by using NS-FEM method in solving undrained geotechnical analysis, (iii) by using of smoothed strains in NS-FEM, the integration is conducted in the edges of smoothed cells, as a results, there is no need to calculate the derivatives of the shape function. Studies demonstrate that the NS-FEM performs well in heat transfer analysis [37, 38], fracture analysis [39], acoustic problems [40, 41], axisymmetric shell structures [42], static and dynamic analysis [43–45]. Recently, Vo et al. [46, 47] applied an upper bound limit analysis using NS-FEM and second order cone programming (SOCP) to determine the stability of dual circular and dual square tunnels in cohesive-frictional soils.

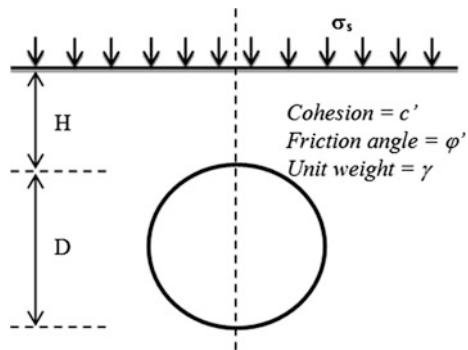
This paper presents the stability analysis of circular tunnel in cohesive-frictional soils subjected to surcharge loading using NS-FEM. In this study, the influence of the soil weight, internal friction angle and the ratio of tunnel diameter to its depth on the stability numbers and collapse mechanisms are investigated. To evaluate the accuracy of this suggested procedure, the obtained results are compared with those of Yamamoto et al. [17].

2 Problem Definition

The circular tunnel is considered to have diameter D and depth H as illustrated in Fig. 1. The soil behavior is described as a uniform Mohr–Coulomb material with value of cohesion c' , friction angle ϕ' and unit weight γ . Drained loading conditions are considered, and continuous loading is applied to the ground surface. The stability of the tunnel is described by the dimensionless stability number σ_s/c' which is a function of ϕ' , $\gamma D/c'$ and H/D as shown in the following equation:

$$\frac{\sigma_s}{c'} = f(\phi', \frac{\gamma D}{c'}, \frac{H}{D}) \tag{1}$$

Fig. 1 Circular tunnel subjected to surcharge loading



In order to calculate the stability numbers σ_s/c' , the variation of the soil weight $\gamma D/c' = 0-3$, internal friction angle $\phi' = 0^\circ-35^\circ$ and the ratio $H/D = 1-5$ are investigated. To describe the rough or smooth interface condition between the loading and the soil, the lateral displacement are fix to zero ($u = 0$) or free ($u \neq 0$) along the ground surface.

3 Brief on the Node-Based Smoothed Finite Element Method

In the NS-FEM, the problem domain Ω is discretized by N_e triangular elements with totally N_n nodes and N_n smoothing domains $\Omega^{(k)}$ associated with the node k such that $\Omega = \sum_{k=1}^{N_n} \Omega^{(k)}$ and $\Omega^i \cap \Omega^j = \emptyset, i \neq j$. Smoothing domain of the node k in NS-FEM is constructed based on the elements connected to the nodes k , as illustrated in Fig. 2. The requirement of the smoothing domain is non-overlap and not required to be convex. Therefore, the smoothing domain is created by connecting sequentially the mid-edge-points to the centroids of the surrounding triangles.

The matrix form of the smoothed strain associated with the node k can be calculated by

$$\tilde{\epsilon}_k = \sum_{I \in N^{(k)}} \tilde{\mathbf{B}}_I(\mathbf{x}_k) \mathbf{d}_I \tag{2}$$

where $N^{(k)}$ is a group of nodes associated with smoothing domain $\Omega^{(k)}$, \mathbf{d}_I is the nodal displacement vector and $\tilde{\mathbf{B}}_I(\mathbf{x}_k)$ is the smoothed strain-displacement matrix on the smoothing domain $\Omega^{(k)}$ that can be expressed as

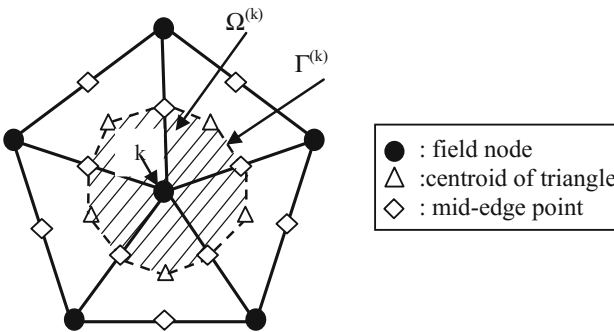


Fig. 2 Triangular elements and smoothing cells associated with the nodes in the NS-FEM

$$\tilde{\mathbf{B}}_I(\mathbf{x}_k) = \begin{bmatrix} \tilde{b}_{Ix}(\mathbf{x}_k) & 0 \\ 0 & \tilde{b}_{Iy}(\mathbf{x}_k) \\ \tilde{b}_{Iy}(\mathbf{x}_k) & \tilde{b}_{Ix}(\mathbf{x}_k) \end{bmatrix} \quad (3)$$

$$\tilde{b}_{Im}(\mathbf{x}_k) = \frac{1}{A^{(k)}} \int_{\Gamma^{(k)}} \mathbf{n}_m^{(k)}(\mathbf{x}) \mathbf{N}_I(\mathbf{x}) d\Gamma, \quad (m = x, y) \quad (4)$$

where $A^{(k)} = \int_{\Omega^{(k)}} d\Omega$ is the area of the cell $\Omega^{(k)}$, $\mathbf{n}_m^{(k)}(\mathbf{x})$ is a matrix with components of the outward normal vector on the boundary $\Gamma^{(k)}$, $\mathbf{N}_I(\mathbf{x})$ is the FEM shape function for node I .

Implementing Gauss integration over each sub-boundary $\Gamma^{(k)}$ of $\Omega^{(k)}$, the Eq. (4) can be rewritten as

$$\tilde{b}_{Im}(\mathbf{x}_k) = \frac{1}{A^{(k)}} \sum_{j=1}^{n_{eg}} \mathbf{N}_I(\mathbf{x}_j^{GP}) n_{jm}^{(k)} l_j^{(k)}, \quad (m = x, y) \quad (5)$$

where n_{eg} is the total number of the sub-boundary segment of $\Gamma^{(k)}$, \mathbf{x}_j^{GP} is the Gauss point of the sub-boundary segment of $\Gamma^{(k)}$ which has length $l_j^{(k)}$ and outward unit normal $n_{jm}^{(k)}$.

4 NS-FEM Formulation for Plane Strain with Mohr-Coulomb Yield Criterion

The Mohr-Coulomb yield criterion is assumed to be applicable for the soil mass. It is also considered that the soil mass follows an associated flow rule. Therefore, the power of plastic dissipation can be calculated by [48]

$$D(\boldsymbol{\varepsilon}) = \int_{\Omega} c' \mathbf{t} \cos \phi' d\Omega \quad (6)$$

where \mathbf{t} is a vector of additional variables defined by

$$\|\boldsymbol{\rho}\| \leq \mathbf{t}$$

$$\boldsymbol{\rho} = \begin{bmatrix} \rho_1 \\ \rho_2 \end{bmatrix} = \begin{bmatrix} \varepsilon_{xx} - \varepsilon_{yy} \\ \gamma_{xy} \end{bmatrix} \quad (7)$$

The changed volume after deformation in cohesive-frictional soil can be calculated from

$$\varepsilon_{xx} + \varepsilon_{yy} = \mathbf{t} \cdot \sin \phi' \quad (8)$$

The problem domain is discretized using NS-FEM, the smoothed strains can be calculated from Eq. (2). The upper bound limit analysis for plane strain can be determined by minimizing the objective function

$$\frac{\sigma_s}{c'} = \alpha^+ = \min \left(\sum_{i=1}^{N_n} c' \cdot A_i \cdot t_i \cdot \cos \phi' - W_{ext}^0(\mathbf{u}) \right)$$

$$st \begin{cases} u = 0 & \text{on } \Gamma_u \\ W_{ext}(\mathbf{u}) = 1 \\ \tilde{\varepsilon}_{xx}^i + \tilde{\varepsilon}_{yy}^i = t_i \sin \phi', i = 1, 2, \dots, N_n \\ \|\boldsymbol{\rho}\|_i \leq t_i, i = 1, 2, \dots, N_n \end{cases} \quad (9)$$

where α^+ is a stability number, A_i is the area of the element of node i , N_n is the total number of nodes in domain, ϕ' is the internal friction angle, $W_{ext}^0(\mathbf{u})$ is the external work of loads not subjected to α^+ .

The computations were performed on a Dell Optiplex 990 (Intel Core™ i5, 1.6 GHz CPU, 8 GB RAM) in Window XP environment using the conic interior-point optimizer of the Mosek package [49].

5 Numerical Examples

Due to symmetry, only half of the problem is considered. In this paper, GiD [50] was used to generate three node triangular elements with reduced element size close to the periphery of the tunnel. The size of domain is chosen sufficiently large enough to ensure that the failure mechanism only taking place inside the considered domain. For the case of $H/D = 1$, the typical finite element meshes of 5280 triangular elements are employed in numerical analysis as shown in Fig. 3.

In order to find the collapse load, the details of the rigid-block mechanism were presented by Chen [51]. And then, Yamamoto et al. [17] applied the upper bound rigid-block mechanism to calculate the stability numbers of circular tunnel subjected to surcharge loading.

In this paper, the results obtained when analyzing a variety of tunnels depth using NS-FEM and SOCP were plotted in Figs. 4, 5, 6 and 7. It is noticeable that

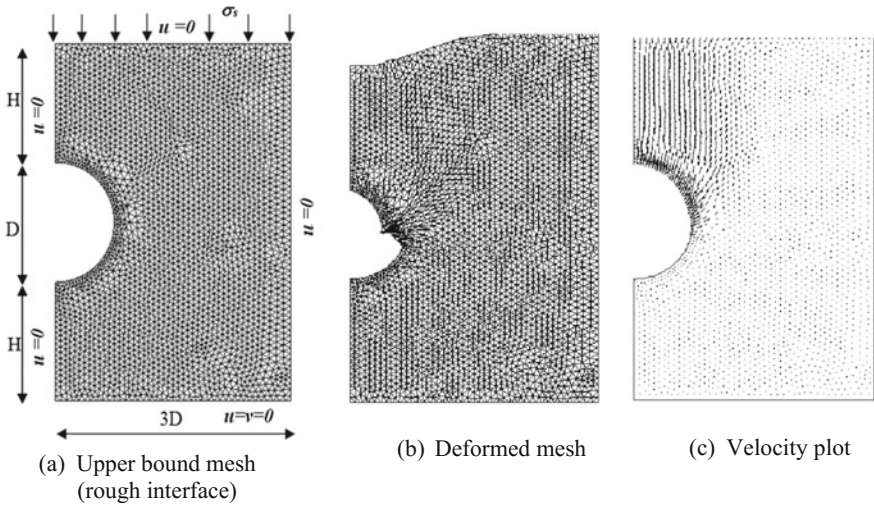
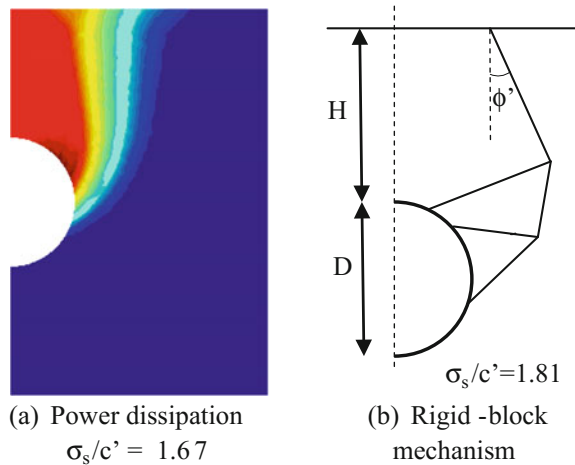


Fig. 3 Typical NS-FEM meshes for a circular tunnel ($H/D = 1$, $\gamma D/c' = 1$, $\phi' = 5^\circ$)

Fig. 4 Comparison of rigid-block mechanism with NS-FEM limit analysis ($H/D = 1$, $\gamma D/c' = 1$, $\phi' = 5^\circ$, smooth interface)



the failure mechanisms obtained by this proposed procedure are identical to those derived from rigid blocks and the results of Yamamoto et al. [17].

Figure 4 shows the power dissipation of circular tunnel for shallow tunnel in the case that small friction angle ϕ' . In this figure, a failure surface originates around the middle part of the tunnel and extends up to the ground surface. When friction angle ϕ' increases, as shown in Fig. 5, the failure plane is moved close to the

Fig. 5 Comparison of rigid-block mechanism with NS-FEM limit analysis ($H/D = 1$, $\gamma D/c' = 1$, $\phi' = 20^\circ$, smooth interface)

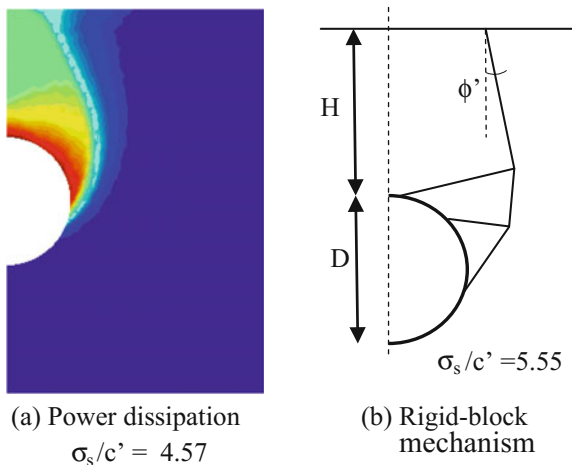
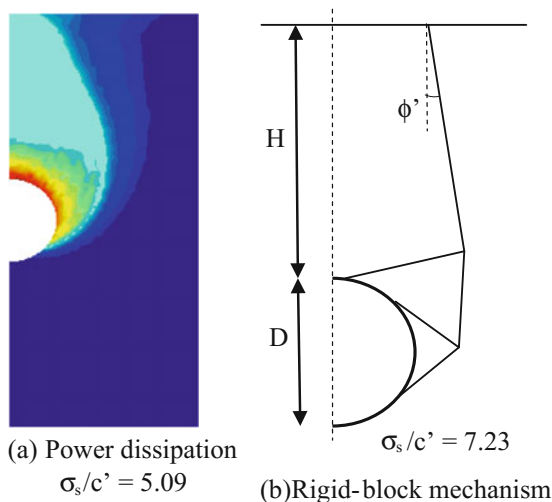


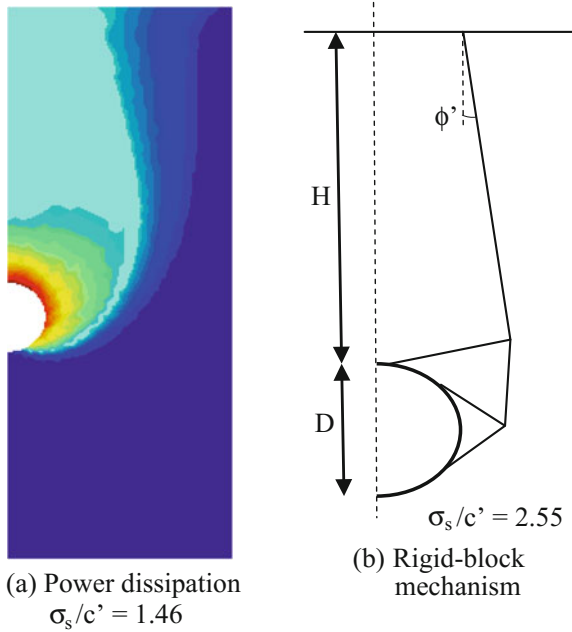
Fig. 6 Comparison of rigid-block mechanism with NS-FEM limit analysis ($H/D = 2$, $\gamma D/c' = 1$, $\phi' = 15^\circ$, smooth interface)



symmetrical plane of the tunnel. As expected, the failure mechanism obtained from this suggested method is almost identical to rigid blocks results.

The stability of deep tunnels was also considered in this study. When H/D increases, as shown in Figs. 6 and 7, the failure mechanism originates the bottom of the tunnel and extends up to the ground surface. It is clear that the figure of failure mechanism obtained is quite the same that of rigid-block approach. However, the stability numbers obtained from assuming rigid-block mechanism are greater than

Fig. 7 Comparison of rigid-block mechanism with NS-FEM limit analysis ($H/D = 4$, $\gamma D/c' = 1$, $\phi' = 5^\circ$, smooth interface)



those of this proposed numerical procedure. The obtained results are in well agreement with the average values of the lower bound and upper bound reported by Yamamoto et al. [17]. The errors stability numbers calculated from NS-FEM limit analysis and Yamamoto et al. [17] in the cases are shown in Figs. 4, 5, 6, 7 are 0.59%, 0.4%, 0% and 1.35%, respectively.

To investigate the influence of number of elements in simulated model, the stability numbers σ_s/c' of both FEM-T3 and NS-FEM are demonstrated in Table 1 (for the case $H/D = 1$, $\gamma D/c' = 1$, $\phi' = 5^\circ$). For a coarse mesh, the stability number

Table 1 The comparison of stability numbers using NS-FEM and FEM (For the case: $H/D = 1$, $\gamma D/c' = 1$, $\phi' = 5^\circ$, smooth interface)

σ_s/c'	FEM-T3 (UB)	3.5997	3.5460	2.7074	2.6139	2.2906	2.2888	2.1169
	NS-FEM (UB)	1.6725	1.6714	1.6682	1.6652	1.6637	1.6636	1.6620
N_e		791	969	1320	1603	2072	3646	5280
N_n		444	538	723	871	1115	1928	2765
N_{var}	FEM-T3	3261	3983	5406	6551	8446	14794	21370
	NS-FEM	2220	2690	3615	4355	5575	9640	13825

UB = Upper bound, LB = Lower bound, N_e = no. of elements, N_n = no. of nodes, N_{var} = no. of variables, $N_{var}(\text{FEM-T3}) = 2N_n + 3N_e$, $N_{var}(\text{NS-FEM}) = 5N_n$

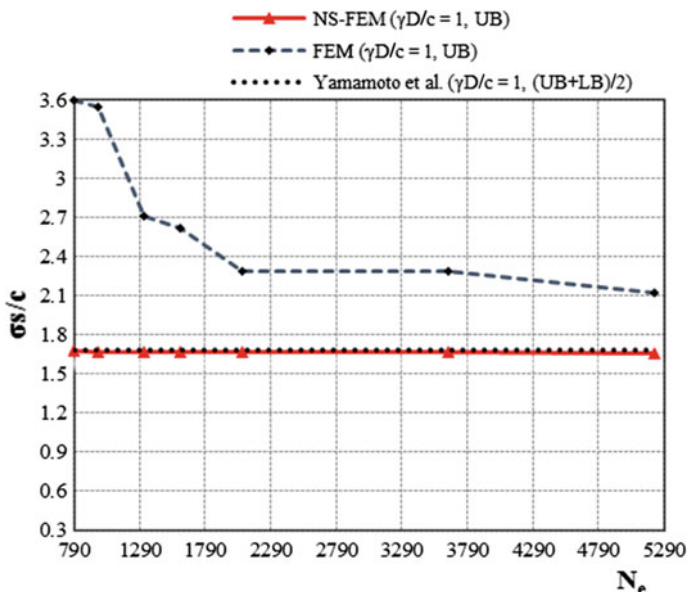


Fig. 8 Comparison of convergence rate between NS-FEM and FEM-T3 (for the case: $H/D = 1$, $\gamma D/c' = 1$, $\phi' = 5^\circ$)

using NS-FEM is more accurate than FEM-T3. When the meshes are refined, the accuracy of FEM-T3 increases, but the convergence rate is very slowly. In comparison with those of Yamamoto et al. [17], it is recognized that the numerical procedure using NS-FEM and SOCP not only reduces a appreciable amount of variables in optimization problem, but also helps to reduce time for solving optimization problems. The convergence rate is illustrated by Fig. 8.

The values of stability numbers obtained by using NS-FEM and SOCP are summarized in Tables 2 and 3. It can be noted that irrespective of the value of ϕ' , the stability number decreases with an increase in $\gamma D/c'$, its mean that the soil weight effects to the failure mechanism of circular tunnel. In some cases of $H/D = 4$, $H/D = 5$ and $\gamma D/c' = 3$, the stability numbers that approximate zero are indicated by “-”, its mean that the tunnels collapse under the weight of the soil.

It is important to note that the meaning of the stability. The negative results imply that a tensile normal stress can be applied to the ground surface to ensure that there is no collapse occurred, but this can not be seen in engineering practice. The positive one means that the tunnel will be collapsed when it is subjected a compressive stress on the ground surface as this value.

Table 2 Results of stability numbers $\sigma_{\phi}c'$ (smooth interface)

ϕ	H/D	$\gamma D/c' = 0$		$\gamma D/c' = 1$		$\gamma D/c' = 2$		$\gamma D/c' = 3$	
		NS-FEM	Yamamoto et al. [17]	NS-FEM	Yamamoto et al. [17]	NS-FEM	Yamamoto et al. [17]	NS-FEM	Yamamoto et al. [17]
0	1	2.44	2.44	1.26	1.26	0.02	0.02	-1.29	-1.28
	2	3.46	3.46	1.18	1.18	-1.15	-1.16	-3.57	-3.59
	3	4.13	4.13	0.80	0.80	-2.60	-2.60	-6.08	-6.08
	4	4.64	4.64	0.28	0.27	-4.15	-4.17	-8.65	-8.68
	5	5.04	5.04	-0.33	-0.35	-5.79	-5.81	-11.31	-11.34
5	1	2.94	2.94	1.67	1.68	0.38	0.38	-0.95	-0.95
	2	4.42	4.42	1.94	1.94	-0.57	-0.57	-3.12	-3.12
	3	5.47	5.47	1.81	1.81	-1.88	-1.88	-5.62	-5.62
	4	6.29	6.30	1.46	1.48	-3.41	-3.39	-8.34	-8.33
	5	6.99	6.99	1.00	1.01	-5.06	-5.04	-11.23	-11.21
10	1	3.65	3.66	2.26	2.27	0.87	0.87	-0.55	-0.55
	2	5.88	5.89	3.10	3.11	0.30	0.30	-2.55	-2.55
	3	7.64	7.64	3.48	3.48	-0.76	-0.76	-5.13	-5.13
	4	9.10	9.12	3.55	3.58	-2.16	-2.13	-	-
	5	10.40	10.42	3.46	3.49	-3.79	-3.76	-	-
15	1	4.69	4.70	3.15	3.15	1.59	1.60	0.02	0.02
	2	8.31	8.32	5.09	5.09	1.80	1.81	-1.58	-1.57
	3	11.50	11.51	6.58	6.58	1.44	1.44	-	-
	4	14.38	14.44	7.70	7.77	0.59	0.66	-	-
	5	17.09	17.18	8.65	8.74	-0.58	-0.48	-	-
20	1	6.36	6.38	4.57	4.59	2.77	2.79	0.95	0.96

(continued)

Table 2 (continued)

ϕ'	H/D	$\gamma D/c' = 0$		$\gamma D/c' = 1$		$\gamma D/c' = 2$		$\gamma D/c' = 3$	
		NS-FEM	Yamamoto et al. [17]	NS-FEM	Yamamoto et al. [17]	NS-FEM	Yamamoto et al. [17]	NS-FEM	Yamamoto et al. [17]
	2	12.77	12.77	8.83	8.84	4.76	4.78	0.48	0.49
	3	19.25	19.26	13.05	13.06	6.42	6.42	-0.95	-0.96
	4	25.65	25.84	17.09	17.27	7.63	7.80	-	-
	5	32.21	32.50	21.20	21.48	8.70	8.95	-	-
	25	9.26	9.28	7.09	7.11	4.89	4.91	2.66	2.68
	2	21.97	22.01	16.82	16.86	11.39	11.41	5.55	5.58
	3	37.34	37.45	28.81	28.89	19.40	19.47	8.81	8.85
	4	54.33	55.15	42.14	42.92	28.23	28.91	11.82	12.47
	5	73.50	74.93	57.41	58.79	38.44	39.71	15.29	16.52
	30	14.91	14.98	12.09	12.15	9.21	9.27	6.25	6.30
	2	44.59	44.73	37.03	37.14	28.64	28.96	19.93	20.05
	3	89.47	89.58	75.92	75.91	60.42	60.37	42.65	42.59
	4	146.15	150.65	125.60	129.01	101.20	105.14	72.18	75.00
	5	218.76	228.03	190.30	197.16	155.12	161.85	112.11	118.46
	35	27.87	28.04	23.73	23.91	19.48	19.66	15.20	15.26
	2	114.91	115.57	101.47	101.99	86.50	86.99	69.98	70.42
	3	290.04	289.34	261.98	261.33	229.38	228.42	191.18	190.11
	4	551.96	581.10	505.28	533.68	447.58	474.96	377.71	398.03
	5	946.26	1013.81	875.14	942.38	783.95	853.55	670.19	739.79

Table 3 Results of stability numbers σ_{ϕ}/c (rough interface)

ϕ	H/D	$\gamma D/c = 0$		$\gamma D/c = 1$		$\gamma D/c = 2$		$\gamma D/c = 3$	
		NS-FEM	Yamamoto et al. [17]	NS-FEM	Yamamoto et al. [17]	NS-FEM	Yamamoto et al. [17]	NS-FEM	Yamamoto et al. [17]
0	1	2.51	2.51	1.33	1.33	0.10	0.10	-1.22	-1.22
	2	3.53	3.53	1.25	1.26	-1.09	-1.09	-3.53	-3.53
	3	4.20	4.21	0.87	0.88	-2.54	-2.53	-6.03	-6.01
	4	4.70	4.71	0.33	0.35	-4.11	-4.09	-8.63	-8.61
	5	5.10	5.11	-0.29	-0.28	-5.75	-5.74	-11.29	-11.27
5	1	3.03	3.04	1.76	1.77	0.46	0.46	-0.89	-0.88
	2	4.51	4.52	2.02	2.03	-0.51	-0.50	-3.07	-3.07
	3	5.57	5.58	1.89	1.90	-1.83	-1.82	-5.59	-5.57
	4	6.40	6.42	1.54	1.56	-3.35	-3.34	-8.31	-8.30
	5	7.09	7.12	1.07	1.10	-5.02	-4.99	-11.23	-11.20
10	1	3.78	3.79	2.38	2.39	0.96	0.97	-0.48	-0.48
	2	6.04	6.05	3.22	3.23	0.38	0.39	-2.51	-2.50
	3	7.80	7.83	3.59	3.62	-0.69	-0.68	-5.10	-5.11
	4	9.28	9.34	3.68	3.72	-2.09	-2.07	-	-
	5	10.59	10.66	3.58	3.63	-3.75	-3.71	-	-
15	1	4.89	4.90	3.31	3.31	1.71	1.72	0.11	0.11
	2	8.58	8.60	5.28	5.30	1.93	1.94	-1.52	-1.51
	3	11.79	11.87	6.77	6.82	1.55	1.58	-	-
	4	14.72	14.87	7.94	8.05	0.70	0.78	-	-
	5	17.49	17.68	8.89	9.05	-0.49	-0.38	-	-
20	1	6.66	6.69	4.82	4.83	2.96	2.98	1.08	1.09

(continued)

Table 3 (continued)

ϕ'	H/D	$\gamma D/c' = 0$		$\gamma D/c' = 1$		$\gamma D/c' = 2$		$\gamma D/c' = 3$	
		NS-FEM	Yamamoto et al. [17]	NS-FEM	Yamamoto et al. [17]	NS-FEM	Yamamoto et al. [17]	NS-FEM	Yamamoto et al. [17]
	2	13.24	13.31	9.18	9.23	5.00	5.03	0.61	0.62
	3	19.80	20.02	13.44	13.60	6.65	6.57	-0.83	-0.86
	4	26.39	26.84	17.61	17.97	7.94	8.19	-	-
	5	33.15	33.74	21.89	22.34	9.00	9.39	-	-
	25	1	9.76	9.78	7.52	7.52	5.23	5.23	2.91
	2	22.95	23.09	17.58	17.70	11.93	12.03	5.91	5.96
	3	38.59	39.27	29.81	30.31	20.13	20.46	9.26	9.39
	4	56.16	57.84	43.56	45.02	29.17	30.37	12.18	13.19
	5	76.22	78.60	59.59	61.67	39.84	41.69	15.91	17.43
	30	1	15.87	15.92	12.92	12.94	9.92	9.90	6.81
	2	46.90	47.43	38.99	39.41	30.43	30.72	21.13	21.28
	3	93.45	95.21	79.52	80.67	63.67	64.14	45.53	45.29
	4	151.97	159.33	130.44	137.23	105.10	110.96	74.69	79.78
	5	230.82	240.57	201.32	209.98	164.66	172.28	119.64	125.96
	35	1	30.01	30.06	25.66	25.61	21.16	21.11	16.49
	2	122.01	123.85	107.88	109.31	92.42	93.36	75.30	75.73
	3	309.29	312.86	281.07	282.38	248.11	246.78	209.79	205.33
	4	581.11	622.25	532.05	571.22	471.31	508.04	398.22	431.13
	5	1038.50	1076.84	964.58	999.53	871.60	903.00	757.44	781.57

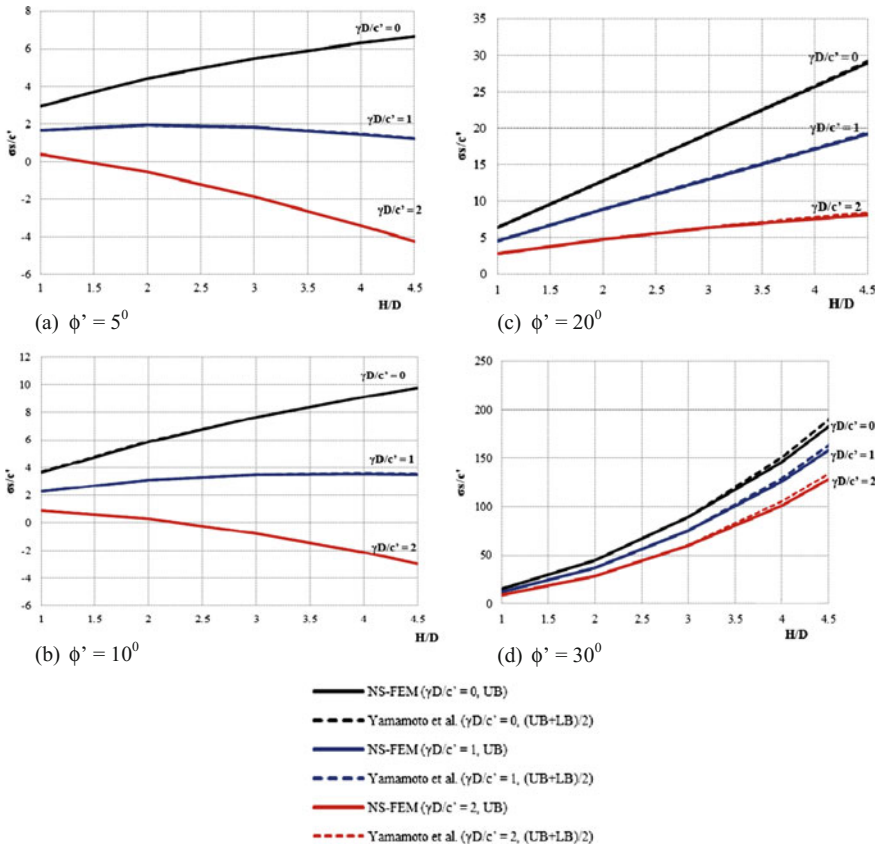


Fig. 9 The variation of stability numbers σ_s/c' for different values of H/D **a** $\phi' = 5^\circ$, **b** $\phi' = 10^\circ$, **c** $\phi' = 20^\circ$, **d** $\phi' = 30^\circ$ smooth interface

Figures 9, and 10 illustrate the stability numbers obtained using NS-FEM and those of Yamamoto et al. [17] in the case smooth interface and rough interface. These figures show that the results derived from this proposed method are in well agreement with the average values of the lower bound and upper bound reported by Yamamoto et al. [17]. It is worth noting that the number of elements in the meshes used in NS-FEM ranged from 3650 to 5280 triangular elements, while there were a significantly larger number elements employed in Yamamoto’s model (28800 triangular elements and 43020 stress/velocity discontinuities).

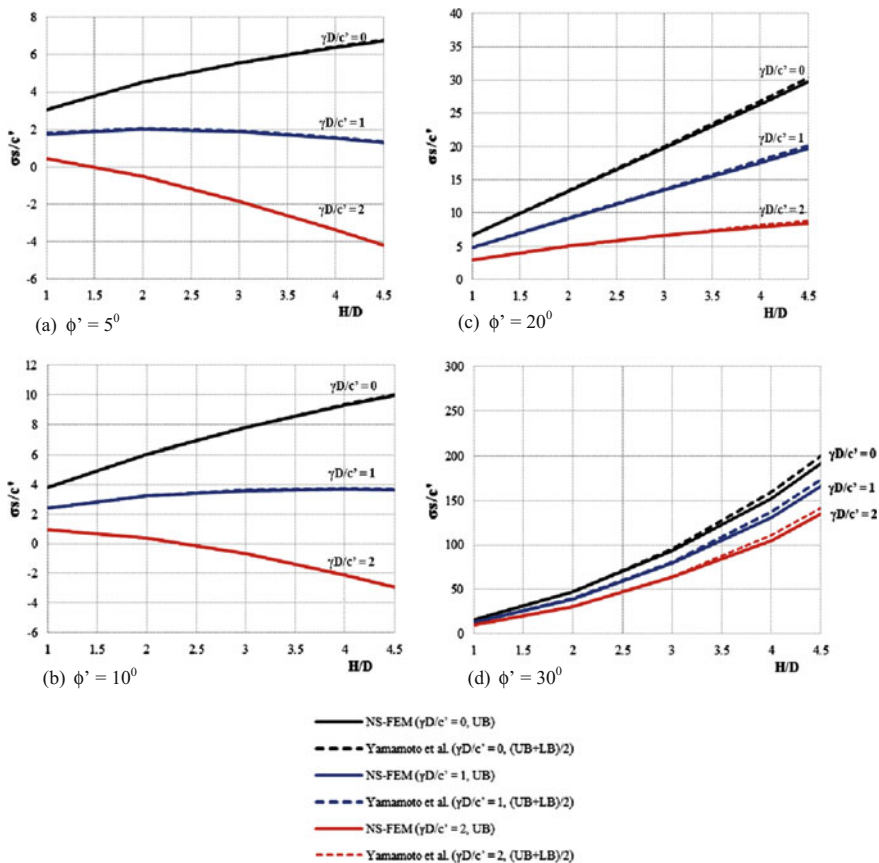


Fig. 10 The variation of stability numbers σ_s/c' for different values of H/D **a** $\phi' = 5^\circ$, **b** $\phi' = 10^\circ$, **c** $\phi' = 20^\circ$, **d** $\phi' = 30^\circ$ rough interface

6 Conclusions

This paper has presented a new method for upper bound limit analysis of cohesive-frictional soils using the node-based smoothed finite element method (NS-FEM) and second-order cone programming (SOCP). Stability numbers are provided in charts as a function of H/D , ϕ' and $\gamma D/c'$. The stability numbers are found to increase with ϕ' and H/D and decrease with $\gamma D/c'$. Various numerical examples for circular tunnel problems have been carried out showing that the presented method is able to provide accurate and stable solutions with minimal computational effort. The obtained results are in well agreement with the average values of the lower bound and upper bound reported by Yamamoto et al. [17]. It is promising to develop the proposed method for more complex and large scale problems.

References

1. Atkinson JH, Potts DM (1977) Stability of a shallow circular tunnel in cohesionless soils. *Geotechnique* 27(2):203–215
2. Atkinson JH, Cairncross AM (1973) Collapse of a shallow tunnel in a Mohr–Coulomb material. In: *Role of plasticity in soil mechanics*, Cambridge
3. Cairncross AM (1973) Deformation around model tunnels in stiff clay. PhD thesis, University of Cambridge
4. Seneviratne HN (1979) Deformations and pore-pressures around model tunnels in soft clay. PhD thesis, University of Cambridge
5. Mair RJ (1979) Centrifugal modelling of tunnel construction in soft clay. PhD thesis, University of Cambridge
6. Chambon P, Corté JF (1994) Shallow tunnels in cohesionless soil: stability of tunnel face. *J Geotech Eng* 120(7):1148–1165
7. Kirsch A (2010) Experimental investigation of the face stability of shallow tunnels in sand. *Acta Geotech* 5:43–62
8. Idiger G, Aklik P, Wei W, Borja RI (2011) Centrifuge model test on the face stability of shallow tunnel. *Acta Geotech* 6:105–117
9. Davis EH, Gunn MJ, Mair RJ, Seneviratne HN (1980) The stability of shallow tunnels and underground openings in cohesive material. *Geotechnique* 30(4):397–416
10. Mühlhaus HB (1985) Lower bound solutions for circular tunnels in two and three dimensions. *Rock Mech Rock Eng* 18:37–52
11. Leca E, Dormieux L (1990) Upper and lower bound solutions for the face stability of shallow circular tunnels in frictional material. *Geotechnique* 40(4):581–606
12. Zhang C, Han K, Zhang D (2015) Face stability analysis of shallow circular tunnels in cohesive–frictional soils. *Tunn Undergr Space Technol* 50:345–357
13. Sloan SW, Assadi A (1991) Undrained stability of a square tunnel in a soil whose strength increases linearly with depth. *Comput Geotech* 12(4):321–346
14. Lyamin AV, Sloan SW (2000) Stability of a plane strain circular tunnel in a cohesive frictional soil. In: *Proceedings of the J.R. Booker memorial symposium*, Sydney, Australia, pp 139–153
15. Lyamin AV, Jack DL, Sloan SW (2001) Collapse analysis of square tunnels in cohesive–frictional soils. In: *Proceedings of the first Asian-Pacific congress on computational mechanics*, Sydney, Australia, pp 405–414
16. Yamamoto K, Lyamin AV, Wilson DW, Sloan SW, Abbo AJ (2011) Stability of a single tunnel in cohesive–frictional soil subjected to surcharge loading. *Can Geotech J* 48(12):1841–1854
17. Yamamoto K, Lyamin AV, Wilson DW, Sloan SW, Abbo AJ (2011) Stability of a circular tunnel in cohesive–frictional soil subjected to surcharge loading. *Comput Geotech* 38(4):504–514
18. Chen JS, Wu CT, Yoon S (2001) A stabilized conforming nodal integration for Galerkin meshfree method. *Int J Numer Methods Eng* 50:435–466
19. Yoo JW, Moran B, Chen JS (2004) Stabilized conforming nodal integration in the natural-element method. *Int J Numer Methods Eng* 60:861–890
20. Liu GR, Nguyen-Thoi T (2010) *Smoothed finite element methods*. CRC Press, New York
21. Liu GR, Dai KY, Nguyen-Thoi T (2007) A smoothed finite element for mechanics problems. *Comput Mech* 39:859–877
22. Liu GR, Nguyen-Thoi T, Nguyen-Xuan H, Lam KY (2009) A node based smoothed finite element method (NS-FEM) for upper bound solution to solid mechanics problems. *Comput Struct* 87:14–26
23. Nguyen-Thoi T, Liu GR, Lam KY, Zhang GY (2009) A face-based smoothed finite element method (FS-FEM) for 3D linear and nonlinear solid mechanics problems using 4-node tetrahedral elements. *Int J Numer Methods Eng* 78:324–353

24. Liu GR, Nguyen-Thoi T, Lam KY (2009) An edge-based smoothed finite element method (ES-FEM) for static, free and forced vibration analyses of solids. *J Sound Vib* 320:1100–1130
25. Liu GR, Nguyen-Thoi T, Dai KY, Lam KY (2007) Theoretical aspects of the smoothed finite element method (SFEM). *Int J Numer Methods Eng* 71:902–930
26. Liu GR, Nguyen-Xuan H, Nguyen-Thoi T (2010) A theoretical study of S-FEM models: properties, accuracy and convergence rates. *Int J Numer Methods Eng* 84:1222–1256
27. Nguyen-Xuan H, Rabczuk T, Nguyen-Thoi T, Tran TN, Nguyen-Thanh N (2012) Computation of limit and shakedown loads using a node-based smoothed finite element method. *Int J Numer Methods Eng* 90:287–310
28. Le CV, Nguyen-Xuan H, Askes H, Bordas S, Rabczuk T, Nguyen-Vinh H (2010) A cell-based smoothed finite element method for kinematic limit analysis. *Int J Numer Methods Eng* 83:1651–1674
29. Nguyen-Xuan H, Liu GR (2015) An edge-based finite element method (ES-FEM) with adaptive scaled-bubble functions for plane strain limit analysis. *Comput Methods Appl Mech Eng* 285:877–905
30. Nguyen-Xuan H, Rabczuk T (2015) Adaptive selective ES-FEM limit analysis of cracked plane-strain structures. *Frontiers Struct Civil Eng* 9:478–490
31. Nguyen-Xuan H, Wu CT, Liu GR (2016) An adaptive selective ES-FEM for plastic collapse analysis. *Eur J Mech A/Solid*. <https://doi.org/10.1016/j.euromechsol.2016.02.005>
32. Nguyen-Thoi T, Rabczuk T, Lam-Phat T, Ho-Huu V, Phung-Van P (2014) Free vibration analysis of cracked Mindlin plate using an extended cell-based smoothed discrete shear gap method (XCS-DSG3). *Theoret Appl Fract Mech* 72:150–163
33. Nguyen-Thoi T, Luong-Van H, Phung-Van P, Rabczuk T, Tran-Trung D (2013) Dynamic responses of composite plates on the Pasternak foundation subjected to a moving mass by a cell-based smoothed discrete shear gap (CS-FEM-DSG3) method. *Int J Compos Mater* 3 (A):19–27
34. Nguyen-Thoi T, Phung-Van P, Nguyen-Thoi MH, Dang-Trung H (2015) An upper-bound limit analysis of Mindlin plates using CS-DSG3 method and second-order cone programming. *J Comput Appl Math* 281:32–48
35. Nguyen-Hoang S, Phung-Van P, Natarajan S, Kim H-G (2016) A combined scheme of edge-based and node-based smoothed finite element methods for Reissner-Mindlin flat shells. *Eng Comput* 32(2):267–284
36. Nguyen-Thoi T, Phung-Van P, Nguyen-Hoang S, Lieu-Xuan Q (2014) A coupled alpha-FEM for dynamic analyses of 2D fluid–solid interaction problems. *J Comput Appl Math* 271:130–149
37. Wu SC, Liu GR, Zhang HO, Xu X, Li ZR (2009) A node-based smoothed point interpolation method (NS-PIM) for three-dimensional heat transfer problems. *Int J Therm Sci* 48:1367–1376
38. Cui XY, Li ZC, Feng H, Feng SZ (2016) Steady and transient heat transfer analysis using a stable node-based smoothed finite element method. *Int J Therm Sci* 110:12–25
39. Liu GR, Chen L, Nguyen-Thoi T, Zeng KY, Zhang GY (2010) A novel singular node-based smoothed finite element method (NS-FEM) for upper bound solutions of fracture problems. *Int J Numer Methods Eng* 83:1466–1497
40. Wang G, Cui XY, Liang ZM, Li GY (2015) A coupled smoothed finite element method (S-FEM) for structural-acoustic analysis of shells. *Eng Anal Boundary Elem* 61:207–217
41. Wang G, Cui XY, Feng H, Li GY (2015) A stable node-based smoothed finite element method for acoustic problems. *Comput Methods Appl Mech Eng* 297:348–370
42. Cui XY, Wang G, Li GY (2016) A nodal integration axisymmetric thin shell model using linear interpolation. *Appl Math Model* 40:2720–2742
43. Feng H, Cui XY, Li GY (2016) A stable nodal integration method with strain gradient for static and dynamic analysis of solid mechanics. *Eng Anal Boundary Elem* 62:78–92
44. Wang G, Cui XY, Li GY (2016) A rotation-free shell formulation using nodal integration for static and dynamic analyses of structures. *Int J Numer Methods Eng* 105:532–560

45. Wang G, Cui XY, Li GY (2015) Temporal stabilization nodal integration method for static and dynamic analyses of Reissner-Mindlin plates. *Comput Struct* 152:124–141
46. Vo TM, Nguyen TM, Chau AN, Nguyen HC (2017) Stability of twin circular tunnels in cohesive-frictional soil using the node-based smoothed finite element method (NS-FEM). *J VibroEng* 19(1):520–538
47. Vo TM, Chau AN, Nguyen TM, Nguyen HC. A node-based smoothed finite element method for stability analysis of dual square tunnels in cohesive-frictional soils. *Scientia Iranica* (in press)
48. Makrodimopoulos A, Martin CM (2006) Upper bound limit analysis using simplex strain elements and second-order cone programming. *Int J Numer Anal Methods Geomech* 31:835–865
49. Mosek. The MOSEK optimization toolbox for MATLAB manual. <http://www.mosek.com>
50. GiD 11.0.4. International Center for Numerical Methods in Engineering (CIMNE), Reference manual. <http://www.cimne.com>
51. Chen WF (1975) *Limit analysis and soil plasticity*. Elsevier, Amsterdam

Numerical Studies on Contact Problem of Inter-locking Concrete Blocks Forming Revetment Structure



L. Dang-Bao, P. Truong-Thi, M. A. Wahab and Hung Nguyen-Xuan

Abstract The importance of revetment slope (RS) structures for protecting coastal is indisputable. RS structures not only can maintain stability of embankment, but also can reduce sea wave energy by its optimized geometric features. For years, civil engineers have developed numerous solutions of RS structures based on theoretical aspects, experiments, and numerical analysis. Due to the lack of analysis criterion, design codes, and experimental facilities, numerical analysis methods significantly become of interest. One of the most challenges is that to perform the interactions between concrete blocks, which form RS structure, and water, i.e. dynamic fluid–structure interaction (FSI). Also, interaction between RS structures and embankment or foundation slope stability must be investigated carefully. Analysis of inter-locking block interactions is one of our missions in the VLIR-OUS TEAM 2017 project that we are running. In addition, due to the limitation of existing RS structures, e.g., heavy and dense materials, optimizations of RS structure are concerned. This paper is to overview the development of RS structures and approaches for analyzing contact problems. Theoretical aspects and computational modeling procedures are mentioned. ABAQUS commercial software is adopted. Hence, novel efficient RS structures could be developed and applied in the real world.

Keywords Revetment slope structure · Inter-locking · Interactions
Finite element method

L. Dang-Bao (✉) · P. Truong-Thi · H. Nguyen-Xuan
Center for Interdisciplinary Research in Technology, HUTECH University,
Ho Chi Minh City, Vietnam
e-mail: dangbaoloi@muce.edu.vn

L. Dang-Bao · P. Truong-Thi · M. A. Wahab
Laboratory Soete, Faculty of Engineering and Architecture, Ghent University,
Ghent, Belgium

L. Dang-Bao
Mien Trung University of Civil Engineering, Tuy Hoa City, Vietnam

P. Truong-Thi
Institute of Mechanics, VAST, Hanoi, Vietnam

1 Introduction

Nowadays, climate change affects human life worldwide. Extreme events such as droughts, desertification, melting ice sheets, heavy precipitation, flooding, typhoon, high sea level rise, take place frequently more than ever [1]. One of them, extreme sea level rise has been seriously taken into account, especially in nations adjacent to the sea, e.g., Vietnam. For decades, it can be seen that sea level gradually increases due to melting ice sheets at the poles as shown in Fig. 1 [2]. Several countries which have coastline are vulnerable due to extreme sea level rise causing coastal hazards as shown in Fig. 2. Many efforts have been made to decrease the influence of that phenomenon. Numerous solutions for protecting hinterland have been applied. RS structures are known as one of effective solutions, which can be implemented in various structural formations and materials as well. An overview of development of RS structures is presented in Sect. 2.

As a part of the project, we attempt to analyze the interactions between inter-locking blocks forming RS structures under dynamic load, e.g., sea wave. This kind of contact between solid bodies under loading is a nonlinear problem, although stresses in solid bodies still in elastic regime. Due to the complication of contact problem, finite element method (FEM) is adopted [3–5]. Contact problem concept will be discussed in Sect. 3. Computational aspect with illustrated models will be presented in Sect. 4. Appropriate modeling techniques are proposed for researchers in order to achieve more accurate results.

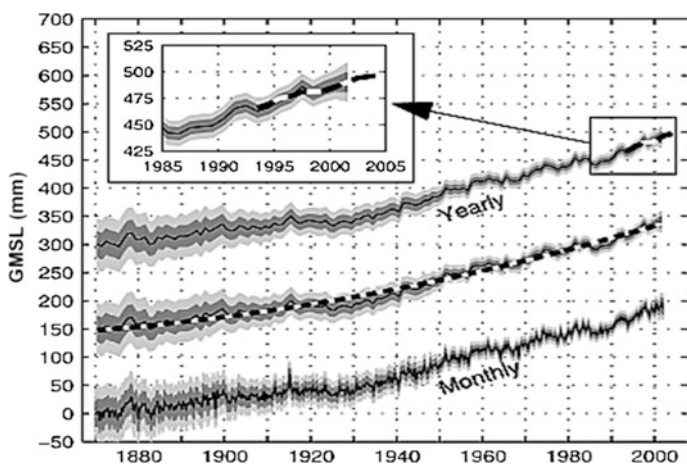


Fig. 1 Global mean sea level [2]



Fig. 2 Coastal erosion in Australia, *Photograph by John Grainger*



Fig. 3 **a** Inter-locking blocks forming RS structure, **b** RS structure failure, and **c** illustration of thin-wall RS structure from BUSADCO, *Internet*

2 Revetment Slope Structures Consideration

For long time ago, people have attempted to apply dozens of coastal protecting solutions. In this article, RS structures are prior considered. Classical revetments can be classified into following categories: natural material (sand, clay, and grass), protected by loose units (gravel and riprap), protected by inter-locking units (concrete block and mats), protected by concrete and asphalt slabs [6]. In this order, the resistance of RS structures is derived from friction, cohesion, self-weight of the units, and mechanical strength. Each type of revetments owns certain advantages and disadvantages. In addition, they can be combined with other protecting structures such as breakwater in order to efficiently mitigate the influence of extreme sea level rise. For a permanent solution, RS structures formed by inter-locking concrete blocks are of interest as shown in Fig. 3a, b.

The main drawback of traditional concrete material is its weight. In some case, however, there are regions where geotechnical conditions are not good enough particularly low soil strength, which is unsuitable to employ such heavy structures

at those regions. Therefore, in an attempt to vanish that disadvantage, alternate materials, e.g., foam concrete, fiber-reinforced concrete are used. Using eco-friendly and recycling materials receives massive support from society. Recently, a construction company named BUSADCO, located in Vietnam, has developed novel RS thin-wall structures that can reduce weight of components as shown in Fig. 3c [7]. However, due to the lack of analyzing criterion and design code, such structures are only examined in laboratory. This led to high cost of experimental process. Therefore, numerical analysis method is adopted that can help designer to eliminate undesired structures. Our work in this project is to supply an effective tool to validate BUSADCO's patents.

3 Contact Problem Concept

Basically, there are two theories of numerical contact problem in term of the difference in their approaches: the penalty function method and the Lagrange multipliers method. The main distinct between them is in the way they involve in their formulations the potential energy of contacting surfaces [3, 5]. The penalty function method is useful for solving frictional contact problems while the Lagrange method, based on multipliers, known for its accuracy. The main drawback of the Lagrange method is that it may lead to ill-converging solutions, while the penalty method may lead to inaccurate ones. In the following, the penalty and Lagrange methods will be presented in detail.

The penalty method includes adding a penalty term to enhance the computing process. In contact problems, the penalty term involves the stiffness matrix of the contact surface. The matrix results from the concept that one body imaginary penetrates another. The stiffness matrix of the contact surface is added to the stiffness matrix of the contacting body, hence the incremental equation of the finite element becomes:

$$[K_b + K_c]u = F, \quad (1)$$

where K_b is the stiffness matrix of contacting body; K_c is stiffness matrix of contact surface which is a nonlinear term; u is displacement; F is force. The total load and displacement values are:

$$F^{tot} = \sum \Delta F, \quad (2)$$

$$u^{tot} = \sum \Delta u, \quad (3)$$

where F^{tot} is the force vector and u^{tot} is displacement vector.

To derive the stiffness matrix, the contact region (enclose the contact surface) is divided into a series of contact elements. The element represents the interaction

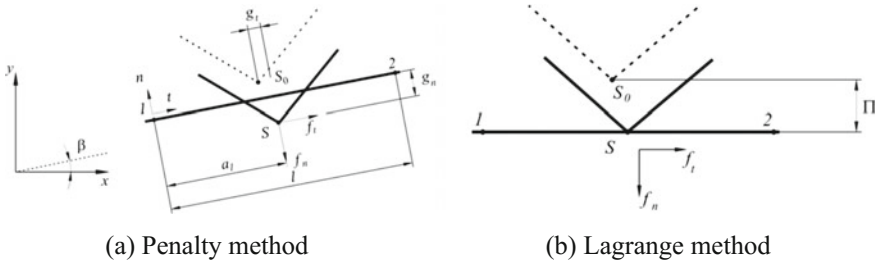


Fig. 4 Illustrations of finite element formulations of contact problems

between the surface nodes of one body with the respective element face of another. Figure 4a shows a contact element in a two-dimensional application. It consists of a slave node (point S) and a master line, connecting nodes 1 and 2. S_0 marks the slave node before the application of the load increment, and S marks the node after loading.

Given the nature of the numerical simulations presented afterward, only the sliding mode of friction will be presented. In this case, the tangential force acting at the contact surface equals to the magnitude of the friction force, hence the first variation of the potential energy of a contact element is:

$$\delta\Pi_c = f_n\delta g_n + f_t\delta g_t = k_n g_n\delta g_t + \text{sgn}(g_t)\mu_d k_n g_n\delta g_t, \tag{4}$$

where k_n represents penalty terms used to express the relationship between the contact force and the penetrations along the normal direction; k_t —penalty terms used to express the relationship between the contact force and the penetrations along the tangential direction; g_n —penetration along the normal direction; g_t —penetration along the tangential direction;

$$f_n = k_n g_n, \tag{5}$$

$$f_t = -\text{sgn}(g_t)\mu_d(k_n g_n). \tag{6}$$

In the case of classical Lagrange multiplier method, the contact forces are expressed by Lagrange multipliers. The augmented Lagrange method includes the regularization of classical Lagrange method by adding a penalty function from the penalty method [8]. This method does not allow any relative motion between two closed surfaces until resultant shear stress is equivalent to the critical shear stress as shown in Fig. 4b. Unlike the classical one, augmented Lagrange method can be applied to sticking friction, sliding friction, and frictionless contact.

The contact problem includes the minimization of potential Π by equating to zero the following expression:

$$\Pi(u, \Lambda) = \Pi_b(u) + \Lambda^T g + \frac{1}{2} g^T k g, \quad (7)$$

where

$$\Lambda^T = \left[\left\{ \begin{matrix} \lambda_n^1 \\ \lambda_t^1 \end{matrix} \right\}, \left\{ \begin{matrix} \lambda_n^2 \\ \lambda_t^2 \end{matrix} \right\}, \dots, \left\{ \begin{matrix} \lambda_n^k \\ \lambda_t^k \end{matrix} \right\} \right], \quad (8)$$

with λ_n —Lagrange multiplier for the normal direction; λ_t —Lagrange multiplier for the tangential direction;

$$g = \left[\left\{ \begin{matrix} g_n^1 \\ g_t^1 \end{matrix} \right\}, \left\{ \begin{matrix} g_n^2 \\ g_t^2 \end{matrix} \right\}, \dots, \left\{ \begin{matrix} g_n^k \\ g_t^k \end{matrix} \right\} \right]. \quad (9)$$

4 Contact Constraint Enforcement Methods and Application

In this section, contact constraint enforcement methods for normal contact are taken into account throughout a validated RS structure simulated by ABAQUS/Standard software. Additionally, the contact pressure–overclosure relationships are also important relationships for contact problems. The most common one, which is used in these simulations under considering contact conditions, is “hard” contact criterion.

There are three contact constraint enforcement methods available in ABAQUS/Standard: penalty method, augmented Lagrange method, and directly method. The first one is a stiff approximation of hard contact. The second one uses the same kind of stiff approximation as the penalty method, but also uses augmentation iterations to improve the accuracy of the approximation. The last one attempts to strictly enforce a given pressure–overclosure behavior per constraint, without approximation or use of augmentation iterations. Each method owns certain advantages and disadvantages. For the below RS structure, in terms of hard contact simulation, the directly method is susceptible to over constraint issues. Hence, only two methods, penalty method and augmented Lagrange method, will be applied for such interactions. The results are used for comparison in order to propose appropriate method for certain problem. In addition, ABAQUS/Standard offers linear and nonlinear variations of the penalty method. With the linear penalty method, the so-called penalty stiffness is constant, so the pressure–overclosure relationship is linear. With the nonlinear penalty method, the penalty stiffness increases linearly between regions of constant low initial stiffness and constant high final stiffness, resulting in a nonlinear pressure–overclosure relationship as shown in Fig. 5.

For tangential contact, ABAQUS uses a penalty scheme to impose friction constraints. The penalty scheme allows some relative motion of the surfaces when it

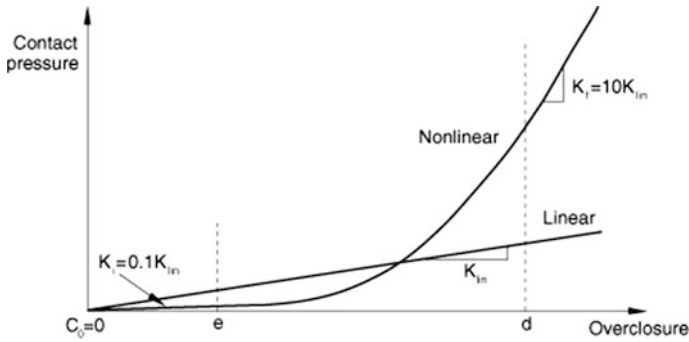


Fig. 5 Comparison of linear and nonlinear pressure–overclosure relationships [9]

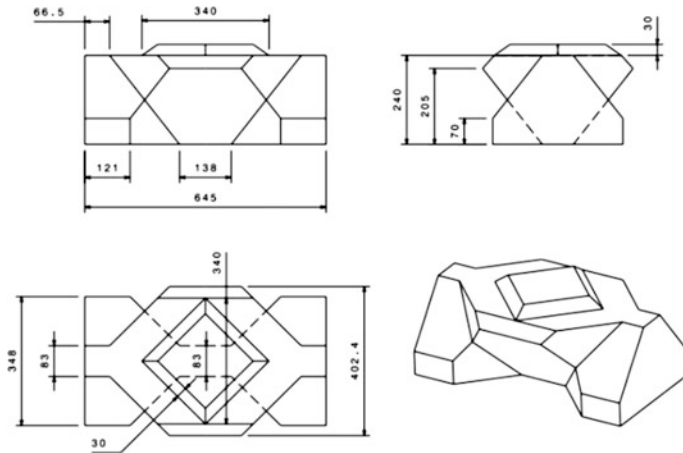


Fig. 6 Shape of concrete block [10]

should be sticking. The magnitude of sliding is limited to an elastic slip, which is characterized by slip tolerance and contact surface length. Another method that can enforce the sticking and sliding constraints more precisely is Lagrange multipliers scheme. To reduce computational load and convergence issues, penalty method is recommended for tangential interaction of such inter-locking blocks forming RS structures (Fig. 6).

In this section, comparison between two contact constraint enforcement methods are made in terms of displacement of structures, contact pressure, and stress in the same certain area. In doing so, validated model is employed. The procedure of modeling is illustrated in Fig. 8 in detail. A RS structure formed by above inter-locking blocks and a pressure load is applied, representing sea wave load as shown in Fig. 9 [10, 11]. Only a part involving 6×12 blocks is considered for reducing computation load as shown in Fig. 7. Slope of roof is 1:4. The lower and

Fig. 7 Forming RS structure by 6×12 blocks in ABAQUS software

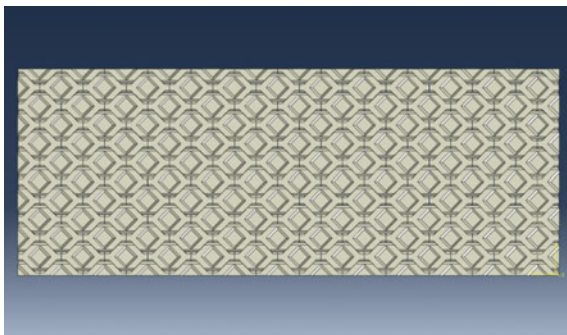


Fig. 8 Schematic of modeling procedure

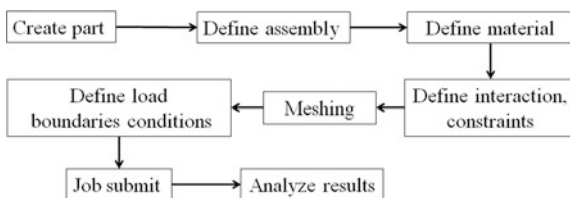
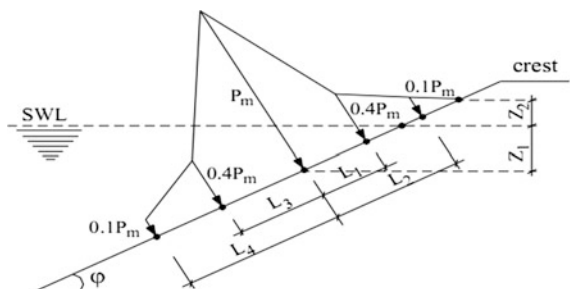


Fig. 9 Distribution of pressure wave load on the roof of revetment slope



upper edges of rectangular mat are defined as symmetric boundaries. The remaining edges are clamped. The coefficient of friction between the blocks is 0.3. Value of Young's modulus, Poisson's ratio, and density of concrete used in the simulation are 2.5×10^{10} N/m², 0.2, and 2500 kg/m³, respectively. Mesh density is high enough to ensure the accuracy. The pressure distribution on area of mat when strongest wave hitting the RS structure is determined by Djunkovski's formula as follows [12]:

$$P_m = K\bar{P}\gamma h_s, \tag{10}$$

where

\bar{P}_m is relative pressure exerted on the wave slope depending on the height of wave h_s ,

K is coefficient depends on ratio λ/h_s and angle of slope,

γ is density of seawater.

In this simulation, value of P_m corresponding typhoon level 9 is equal to 95 kPa.

Foundation beneath cover layer is simplified by springs connecting blocks to earth. Spring stiffness is calculated by formula as follows:

$$K^{str} = k_z A_i, \tag{11}$$

where

A_i is contact area between block and foundation,

k_z is foundation coefficient determined by expression:

$$k_z = \frac{P}{S} \tag{12}$$

S is final stable settlement value; p is applied pressure load in experimental measurement.

Here, we assume k_z , then calculate K^{str} for each spring depend on different A_i .

In simulations, general contact and contact pair algorithms for modeling contact are chosen. Other contact algorithms in ABAQUS/Standard that are contact elements are not considered. For general contact algorithm, interactions typically include all bodies in the model with single interaction property. Default surfaces are defined automatically but can include/exclude surface pairs. Whereas, contact pairs algorithm describes contact between two individual specified surfaces. Each algorithm owns certain advantages and disadvantages (Figs. 10, 11, 12, and 13).

The simulation results for comparing two contact constraint enforcement methods are presented in Tables 1 and 2 in case of general contact and contact pair, respectively.

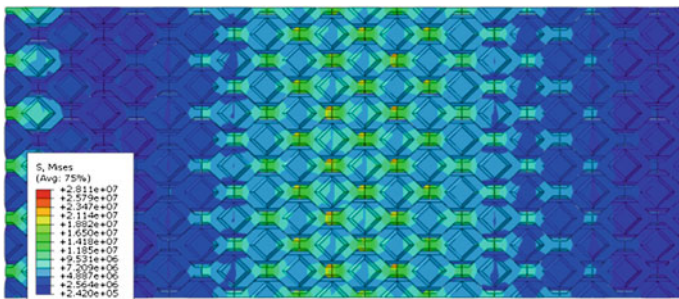


Fig. 10 von Mises stress

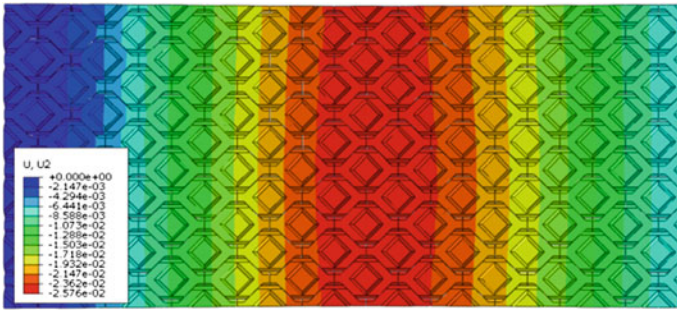


Fig. 11 Displacement perpendicular to roof of embankment

Fig. 12 Tetrahedral mesh density

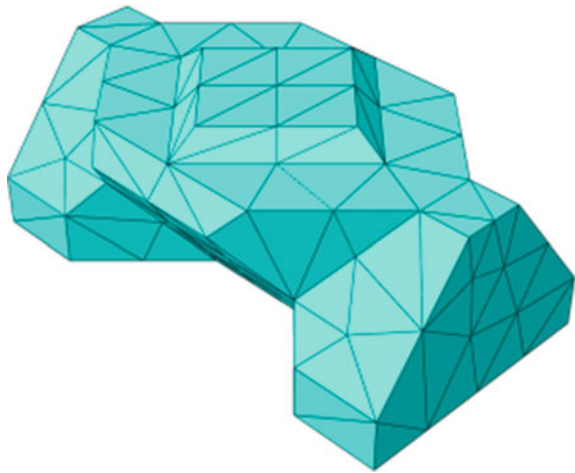


Fig. 13 von Mises stress on single block

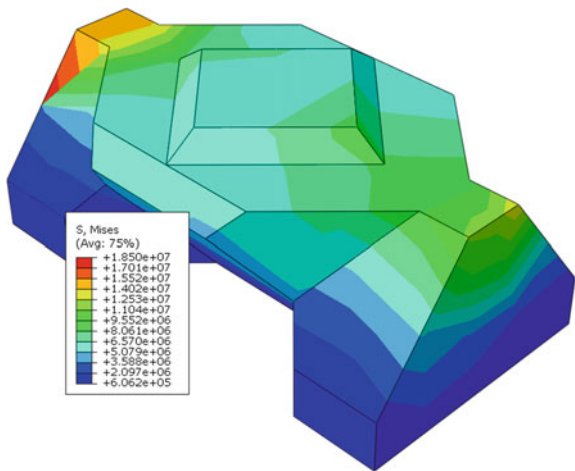


Table 1 Comparison of two contact constraint enforcement methods (general contact algm.)

Classification	Penalty method		Augmented Lagrange method
	Linear	Nonlinear	
Max. disp. of roof (mm)	22.43	25.76	22.22
Max. von Mises stress (N/m ²)	2.879E7	2.811E7	2.884E7
Max. contact pressure (N/m ²)	4.356E7	2.870E7	5.128E7



Table 2 Comparison of two contact constraint enforcement methods (contact pairs algm.)

Classification	Penalty method		Augmented Lagrange method
	Linear	Nonlinear	
Max. disp. of roof, mm	21.39	23.05	21.16
Max. von Mises stress (N/m ²)	2.796E7	2.820E7	2.786E7
Max. contact pressure (N/m ²)	4.271E7	2.900E7	5.012E7

It is seen that the results of two contact algorithm are slightly identical. However, it is observed that contact pairs algorithm consume more time for calculation than other because it has more restrictions on type of surfaces involved. For comparison of two contact constraint enforcement methods, simulation results are not much different in terms of von Mises stress. However, in terms of displacement of cover layer, penalty method in case of nonlinear consideration results in the highest value, but maximum contact pressure resulting from this method is smallest. The reason is that in nonlinear penalty method, the initial penalty stiffness is less than linear one ten times. Moreover, in the contact stiffening regime, the contact pressure varies quadratically for penetrations, and in our simulation, the nonlinear penalty stiffness still less than linear penalty stiffness constant that results in smaller contact pressure. It is recommended that nonlinear penalty method should be applied for such inter-locking blocks forming RS structures.

5 Conclusion

Overview of RS structures and contact problem concept was revealed. Contact constraint enforcement methods and illustrated computational result are presented, so that researchers can obtain a better approach for inter-locking interaction problem. Many factors such as interactions, meshing, constraints must be considered carefully for improving the accuracy. Hence, an innovative tool for designing revetment structures can be proposed.

Acknowledgements The authors acknowledge the financial support of VLIR-OUS TEAM Project, VLIRUOS2017-2021-75900, funded by the Flemish Government. Authors would like to thank Prof. Hung Nguyen-Dang and Mr. Huy Phan-Tan for their helps in relevant research materials.  

References

1. Herring SC, Hoell A, Hoerling MP, Kossin JP, Schreck III CJ, Stott PA (eds) (2016) Explaining extreme events of 2015 from a climate perspective. *Bull Am Meteor Soc* 97(12): SI-SI45
2. Church JL, White NJ (2006) A 20th-century acceleration in global sea-level rise. *Geophys Res Lett*
3. Popov VL (2010) *Contact mechanics and friction: physical principles and application*. Springer, Berlin
4. Zienkiewicz OC, Taylor RL, Zhu JZ (2013) *The finite element method: its basis and fundamentals*, 7th ed. Butterworth-Heinemann, 2013
5. Wriggers P, Laursen TA (2002) *Computational contact and impact mechanics*. Springer, Berlin and Heidelberg
6. Silvester R (1974) *Coastal engineering*. Elsevier, Amsterdam
7. BUSADCO Construction Joint Stock Company, Vietnam. <http://busadco.com.vn>
8. Simo JC, Laursen TA (1992) An augmented Lagrangian treatment of contact problems involving friction. *Comput Struct* 42(1):97–116
9. ABAQUS 6.13 Documentation
10. Nguyen HD, Phan TD, Phan HT (2015) Analysis of inter-locking blocks structure for coastal revetment using non-linear finite element analysis. In: National fluid mechanics conference, Vietnam
11. Nguyen HD, Nguyen VM (2007) New structure for coastal protection realized in the Ham Tien, Mui Ne, Vietnam. In: Proceedings of Japan-Vietnam Estuary workshop, August/2007, WREE Journal, Hanoi
12. Pilarczyk KW (1998) *Dikes and revetments: design, maintenance and safety assessment*. Balkema, Rotterdam

Part II
Multiscale Multiphysics Problems

Orientation-Dependent Response of Pure Zinc Grains Under Instrumented Indentation: Micromechanical Modeling



N. P. T. Nguyen, F. Abbès, B. Abbès and Y. Li

Abstract This chapter concerns the micromechanical behavior modeling of a pure zinc polycrystal. An inverse optimization strategy was developed to determine plastic deformation properties from instrumented indentation tests performed on individual grains of cold-rolled polycrystalline sheets. Nanoindentation tests have been performed on grains using a spherical–conical diamond indenter, providing load–penetration depth curves. The crystalline orientation of those grains has been determined using an EBSD analysis. Furthermore, a crystal plasticity model has been implemented in the finite element code Abaqus using a user material subroutine. To identify the constitutive model parameters, the inverse identification problem has been solved using the MOGA-II genetic algorithm coupled with a finite element analysis of the nanoindentation test. In a first approach, the identification procedure used the load–displacement curves issued from the indentation performed on a grain of given crystalline orientation. A good agreement is achieved between experimental and numerical results. This constitutive model has been validated by simulating the indentation response of grains of distinct crystalline orientations, involving different slip systems activity rates.

Keywords HCP • Crystal plasticity • Inverse identification
Nanoindentation • Finite element analysis

N. P. T. Nguyen • F. Abbès (✉) • B. Abbès • Y. Li
GRESPI, University of Reims Champagne-Ardenne, Campus Moulin de la Housse,
BP 1039, 51687 Reims Cedex 2, France
e-mail: fazilay.abbes@univ-reims.fr

N. P. T. Nguyen
e-mail: pham-the-nhan.nguyen@etudiant.univ-reims.fr

B. Abbès
e-mail: boussad.abbes@univ-reims.fr

Y. Li
e-mail: yuming.li@univ-reims.fr

1 Introduction

Zinc metal has a number of characteristics that make it a well-suited corrosion protective coating for iron and steel products. Its high corrosion resistance in most environments accounts for its successful use as a protective coating on a variety of products and in many exposure conditions, especially in automotive and building applications [1].

In automotive industry, hot-dip galvanized sheets, with 100% of zinc, or GALFAN (with 95% zinc and 5% Al) are the most used products. The mechanical resistance is not the only matter of interest but corrosion resistance and aesthetics are also important. An efficient coating then requires a good forming ability and adhesive bonding, with no crack or flaking during forming process.

Zinc has a hexagonal close-packed (hcp) crystalline structure. Compared to other hcp metals like titanium or magnesium, zinc is characterized by a high c/a lattice ratio ($\frac{c}{a}|_{Zn} = 1.856$, $\frac{c}{a}|_{Mg} = 1.624$, $\frac{c}{a}|_{Ti} = 1.588$) and then exhibits a strong anisotropic behavior.

Due to the lack of adequate constitutive laws, hcp sheet forming finite element simulations have been generally performed using classical macroscopic anisotropic criteria for cubic metals [2, 3]. Recent advances in the formulation, numerical implementation, and validation of macroscopic plasticity models for hcp materials have allowed a better capture of specific features like the anisotropy and the tension–compression asymmetry in yielding of hcp metals [4–9].

A physically based approach requires a good understanding of the deformation mechanisms, namely dislocation slip at the individual grain scale in the polycrystalline sample. Moreover, depending on its orientation, the grain response involves different slip systems' activity rates. Indeed, an accurate determination of slip resistance and its evolution, that is hardening, is of prime importance to well predict the macroscopic response of a polycrystalline specimen.

In practice, the first possibility consists in carrying out *in situ* SEM microtensile tests. Electron backscatter diffraction (EBSD) maps are taken before and after testing on selected areas of the specimen. Then slip trace analysis is conducted to identify the active deformation modes based on the obtained SEM images and EBSD data. Correlating those data with available and possible deformation systems then enables the determination of the corresponding critical resolved shear stress (CRSS).

Another way concerns instrumented indentation tests performed on grains of distinct crystallographic orientations. Then, combining crystal plasticity finite element method (CPFEM) with an inverse identification, one can determine the unknown CRSS. This chapter details such approach in the case of a pure polycrystalline zinc sheet.

This chapter is organized as follows: Sect. 2 presents the crystal plasticity model and the governing equations implemented in the finite element code Abaqus using a user material subroutine. In Sect. 3, we present the material under study, the sample preparation and the experimental protocol for instrumented indentation tests. The

identification strategy for the optimization of the slip resistance and slip hardening parameters is described in Sect. 4. In Sect. 5, the numerical results are discussed along with experimental data.

2 Crystal Plasticity Model

The crystal plasticity theory postulates that the plastic deformation results from the cumulative effect of crystalline glide in all activated slip systems. The deformation rate is then given by the sum over all the shear rates contributed by all activated systems. Obeying Schmid's law, the shear strain rate $\dot{\gamma}^{(\alpha)}$ on the α th slip system is given by the following power law:

$$\dot{\gamma}^{(\alpha)} = \dot{\gamma}_0^{(\alpha)} \left| \frac{\tau^{(\alpha)}}{\tau_c^{(\alpha)}} \right|^n \text{sgn}(\tau^{(\alpha)}) \quad (1)$$

where $\dot{\gamma}_0^{(\alpha)}$ is the reference shear strain rate on slip system α , $\tau_c^{(\alpha)}$ is the slip resistance, that is the critical resolved shear stress of the slip system α , and n is the strain-rate sensitivity exponent.

For multiple slips, the evolution of the slip resistance $g^{(\alpha)}$ is governed by the hardening law expressed through a linear incremental relation:

$$\dot{g}^{(\alpha)} = \sum_{\beta} h_{\alpha\beta} \dot{\gamma}^{(\beta)} \quad (2)$$

where $h_{\alpha\beta}$ stands for the slip hardening moduli, the sum ranges over all activated slip systems. Here $h_{\alpha\alpha}$ and $h_{\alpha\beta}$ ($\alpha \neq \beta$) are called self and latent hardening moduli, respectively.

Peirce et al. [10] have expressed the relation between self and latent hardening moduli as follows:

$$\begin{cases} h_{\alpha\alpha} = h(\gamma) = h_0 \sec h^2 \left| \frac{h_0 \gamma}{\tau_s - \tau_0} \right| \\ h_{\alpha\beta} = qh(\gamma) \quad (\alpha \neq \beta) \end{cases} \quad (3)$$

where h_0 denotes the initial hardening modulus, τ_0 is the critical resolved shear stress and τ_s is the saturation strength. γ is the Taylor cumulative shear strain on all slip systems:

$$\gamma = \sum_{\alpha} \int_0^t |\dot{\gamma}^{(\alpha)}| dt \quad (4)$$

The parameter q characterizes the hardening behavior. It is defined as the ratio of latent over self-hardening moduli, taken equal to unity in our simulations.

Because of zinc's high c/a axial ratio, the basal glide is the primary slip system ($B\langle a \rangle\{0001\}\langle 11\bar{2}0 \rangle$). To achieve the Taylor criterion [11] requiring five independent slip systems for the ductility of polycrystalline metals, deformation is accommodated by prismatic glide ($P\langle a \rangle\{10\bar{1}0\}\langle 11\bar{2}0 \rangle$) and/or 2nd-order pyramidal glide ($\Pi_2\langle c+a \rangle\{11\bar{2}2\}\langle 11\bar{2}3 \rangle$).

It is worth mentioning here that we have not considered 1st-order pyramidal slip systems ($\Pi_1\langle a \rangle$), following the analysis of Yoo and Wei [12], who have stated that basal and prismatic slip systems are crystallographically equivalent to $\Pi_1\langle a \rangle$ glide.

Finally, following the work of Yoo and Lee [13], given its c/a axial ratio, zinc exhibits compression twins $\{10\bar{1}2\}\langle 10\bar{1}\bar{1} \rangle$ causing a contraction along the c -axis.

The afore-mentioned deformation systems are illustrated in Fig. 1.

The crystal plasticity model for cubic systems was initially implemented into the implicit finite element (FE) code ABAQUS/Standard through a user material subroutine (UMAT) by Huang [14] and modified by Kysar and Hall [15]. We have adapted this UMAT for crystal plasticity modeling of zinc hcp crystal. The FE formulation includes elastic-plastic and viscoplastic deformation. The plastic deformation is assumed due solely to the crystallographic dislocation glide, deformation by diffusion, twinning, and grain-boundary sliding not being considered here.


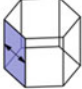


Primary slip system			Secondary slip systems			Compression twin system
Name	Number of slip systems	Independent slip systems	Name	Number of slip systems	Independent slip systems	
Basal $\{0001\}\langle 11\bar{2}0 \rangle$ $B\langle a \rangle$ 	3	2	Prismatic $\{10\bar{1}0\}\langle 11\bar{2}0 \rangle$ $P\langle a \rangle$ 	3	2	$\{10\bar{1}2\}\langle 10\bar{1}\bar{1} \rangle$ 
			2 nd order Pyramidal $\{11\bar{2}2\}\langle 11\bar{2}3 \rangle$ $\Pi_2\langle c+a \rangle$ 	6	5	

Fig. 1 Deformation modes in zinc

3 Experimental Procedure

3.1 Sample Preparation

The material under study is an annealed cold-rolled sheet (1-mm thickness) of high-purity polycrystalline zinc ($Zn > 99.99 + \text{wt}\%$). The chemical composition is given in Table 1.

The as-received sheets have been plastically deformed (thickness reduction rate of 50%) and annealed at a temperature of 100 °C for a period of 2 h to trigger the recrystallization of new grains.

Microstructure characterization was evaluated by electron backscatter diffraction (EBSD) using a JEOL65 field emission gun-scanning (FEG) electron microscope (SEM) equipped with OIM EBSD system. Samples preparations for EBSD examination were first ground with sand paper, and then they were polished with 1- μm diamond paste to mirror finish. In order to achieve the surface quality required for nanoindentation tests and EBSD examination (i.e, deformation-free and scratch-free surface), a chemo-mechanical polishing with colloidal silica suspension ($\sim 40 \text{ nm}$) on porous neoprene polishing cloth for about 35 mn was used.

3.2 Instrumented Indentation Tests

Instrumented indentation tests were performed using a 90° cono-spherical diamond indenter (tip radius of 1 μm) mounted in a NHT-2 nanoindenter (CSM Instruments). Indentations were carried out in load-control mode, at a constant loading rate $\dot{F} = 50 \mu\text{N s}^{-1}$, following a trapezoidal loading curve, with loading up to a maximum load F_{max} , then holding for a duration equal to the loading one to test creep behavior, and finally complete unloading.

The selected grains for nanoindentation tests are shown on the following EBSD maps (Fig. 2a, b), along with their location in the standard stereographic triangle (Fig. 2c). The size and the crystalline orientation using the Euler-Bunge angles of those grains are listed in Table 2 [16]. In what follows, grains for which the $\langle c \rangle$ axis (i.e., $\langle 0001 \rangle$) is parallel to the normal direction of the sheet are called basal grains. Grains for which the $\langle 12\bar{1}0 \rangle$ direction is parallel to the normal direction of the sheet are called pyramidal grains. Finally, grains for which the $\langle 01\bar{1}0 \rangle$ direction is along the normal direction of the sheet are called prismatic grains.

To avoid grain-boundary influence, indents were located in the mid-zone of individual grains. To get the local crystal orientation at the indentation site, the

Table 1 Chemical analysis (ppm) of as-cast high-purity (99.99 + %) polycrystalline zinc

Ag	Cd	Ca	Cr	Cu	Cs	Fe	Mn	Ni	Pd	Pb	Rh	Ta	T	Ti
0.36	3.4	<0.1	0.55	4.0	<0.1	4.9	0.18	0.66	<1	12	<0.5	<10	5.1	4.5

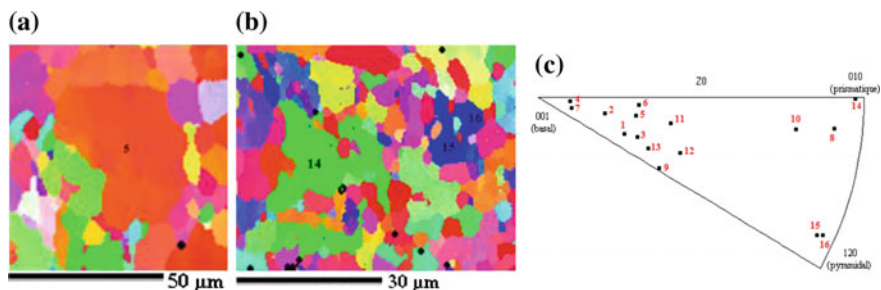


Fig. 2 Selected grains for nanoindentation tests

Table 2 Average diameter and crystalline orientation of the selected grains

Grain number	Average diameter (μm)	Euler-Bunge angles ($^{\circ}$)			Crystalline orientation
		φ_1	Φ	φ_2	
5	24.138	3.4	24.6	49.6	Basal
14	19.292	15.1	87.1	0.1	Prismatic
15	10.943	50.3	83.8	24.7	Pyramidal

precise locations of the indents were checked a posteriori by EBSD and secondary electron imaging in the scanning electron microscope (SEM). It is worth mentioning that no twinning was observed [16].

4 Identification Process

Three-dimensional finite element simulations of the nanoindentation tests were performed using the commercial software ABAQUS/Standard 6.13. Assuming a single-crystal-like behavior, each grain has been modeled as a cylinder of 60- μm diameter and 60- μm height to avoid grain-boundary effects. The selection of the mesh size is generally a compromise between the computational cost and the solution accuracy. The sample was discretized using 26624 eight-node linear hexahedral elements with reduced integration scheme (C3D8R) to ensure that the mesh was fine enough, especially the area that makes contact with the indenter. Away from the tip, the mesh density was progressively coarsened to keep the simulations computationally tractable. The total number of elements is about 10 times more than those used in published papers by Liu et al. [17, 18] for similar depth of indentation (200–300 nm), and of same order than those used by Liu et al. [19] for depth of indentation of 2000 nm. In terms of boundary conditions, the bottom face of the specimen was fully constrained. The indenter was only allowed to move in the z-direction. The FE model is illustrated in Fig. 3.

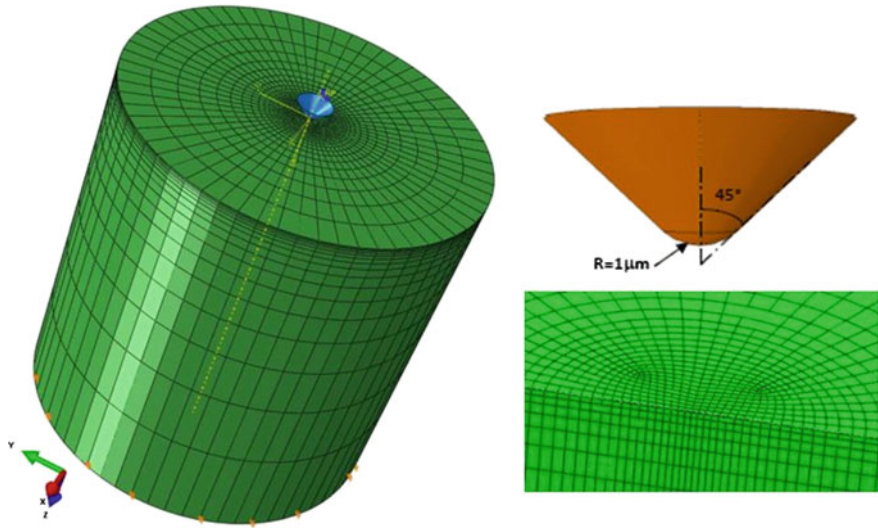


Fig. 3 3D finite element model

The cono-spherical indenter was modeled as a fully rigid body, with a tip radius of 1 μm and a half-included angle of 45°.

A friction coefficient of 0.1 was assumed between the indenter and the zinc substrate. Even if friction is known to play a minor role on the load versus displacement response during indentation [20], the use of a friction coefficient enhances convergence by limiting mesh elements distortion in the contact area. The effect of coefficient of friction on the nanoindentation behavior of single-crystal copper has been investigated by Liu et al. [17] and it was found that while the introduction of friction does not change the nanoindentation load–displacement relationship, it changes the indent surface pileup profiles.

Furthermore, like experimental conditions, all simulations were performed under quasi-static, isothermal load-controlled conditions. In addition, nonlinearity option was used to account for both material and geometric (finite strains and rotations) nonlinearities.

The stiffness tensor C was considered to model the single-crystal elastic response, which is composed of six terms, listed in Table 3 [21].

Since plastic deformation is obtained by crystallographic dislocation slips, a total of 12 slip systems were considered: basal slip systems (3), prismatic slip systems (3), and $\Pi_2\langle c + a \rangle$ slip systems. According to the proposed crystal plasticity model, and in addition to the strain-rate sensitivity exponent “ n ,” 4 material parameters ($h_0^{(\alpha)}$, $\tau_0^{(\alpha)}$, $\tau_s^{(\alpha)}$, and $\dot{\gamma}_0^{(\alpha)}$) should be identified for each family of slip systems.

Table 3 Elastic constants (GPa) of the zinc single crystal

$C_{11}=C_{22}$	C_{12}	$C_{13}=C_{23}$	C_{33}	$C_{44}=C_{55}$	C_{66}
165	31.1	50	61.8	39.6	66.95

To keep the inverse identification problem more tractable, we assumed first similar values of reference shear strain rate on each slip system α , that is $\dot{\gamma}_0^{(\alpha)} = \dot{\gamma}_0 = 1.25 \times 10^{-2}$ [1].

Furthermore, the basal glide being the easy slip system for zinc, we assumed a constant ratio between basal and prismatic glide initial yield stresses on the one hand, and between basal and pyramidal glide initial yield stresses on the other hand. Namely, $\tau_0^{Prism} / \tau_0^{Basal} = 15$ and $\tau_0^{Pyr(c+a)} / \tau_0^{Basal} = 10$, as suggested by Philippe et al. [22] and Fundenberger et al. [23].

Besides, we supposed a correlation between the initial yield stress and the saturation strength of each slip family, considered as constant, that is $\tau_s^{(\alpha)} / \tau_0^{(\alpha)} = sat > 1$.

Hence, determining the “*sat*” parameter allows getting the saturation strengths of the considered slip systems ($\tau_s^{Basal}, \tau_s^{Prism}, \tau_s^{Pyr(c+a)}$).

Finally, this identification strategy allowed the reduction of the parameter vector to a 6-component vector only ($h_0^{Basal}, h_0^{Prism}, h_0^{Pyr(c+a)}, \tau_0^{Basal}, sat, n$) instead of the initial set of thirteen parameters.

Those material parameters are obtained through an inverse identification procedure, by iterative adjusting to match numerical and experimental load-penetration depth curves. The optimization loop combines the FE analysis (ABAQUS code) and the optimization procedure. In practice, we used the genetic algorithm MOGA-II to minimize the objective function defined as follows:

$$F_{obj} = \frac{1}{N} \sum_{i=1}^N (h_{num}(P, t_i) - h_{exp}(t_i))^2 \quad (5)$$

where P stands for the vector of unknown parameters, N is the number of data set, t_i denotes the time of the corresponding experimental point “ i ,” and $h_{num}(P, t_i)$ and $h_{exp}(t_i)$ are the indenter displacements numerically computed and experimentally measured, respectively.

The workflow of the optimization process is shown in Fig. 4.

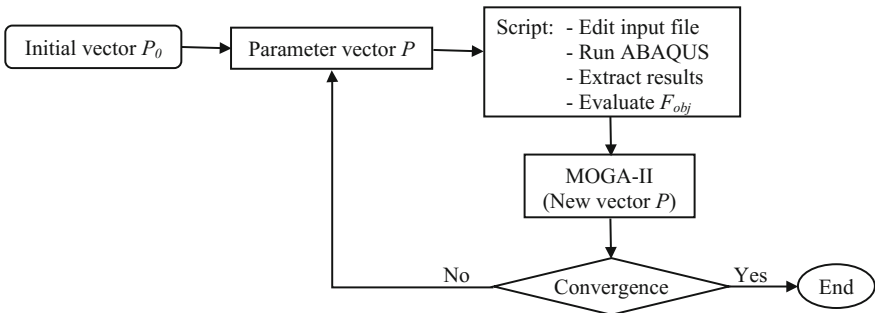


Fig. 4 Flowchart of the optimization process for material parameter identification

5 Results and Discussion

5.1 Identification of the Crystal Plasticity Model Parameters

Given the identification strategy described in Sect. 4, we have selected Grain #14 for the identification of the crystal plasticity model parameters. As summarized in Table 2 and plotted in Fig. 2c, this grain is close to the $\langle 01\bar{1}0 \rangle$ corner and therefore has the $\langle 01\bar{1}0 \rangle$ crystal direction almost parallel to the indentation direction.

The data set used is the load-penetration depth measured in load-control mode at a maximum load of 1 mN. The loading conditions are similar to the experimental ones, including the loading, holding, and unloading stages.

Figure 5 depicts the experimental load-penetration depth curve, and the numerical one issued from the identification procedure. The identified parameters are summarized in Table 4.

One can notice the good agreement between the experimental data and the simulated response of Grain #14. An analysis of the onset of slip systems activity in the area underneath and around the indenter is shown in Fig. 6. Point I which is located underneath the tip is the point where first signs of yield are observed. As penetration depth increases, Points II and III, respectively, located around and far from the indenter, undergo plastic deformation at a lower rate.

Fig. 5 Experimental and simulated load-penetration depth curves for Grain #14

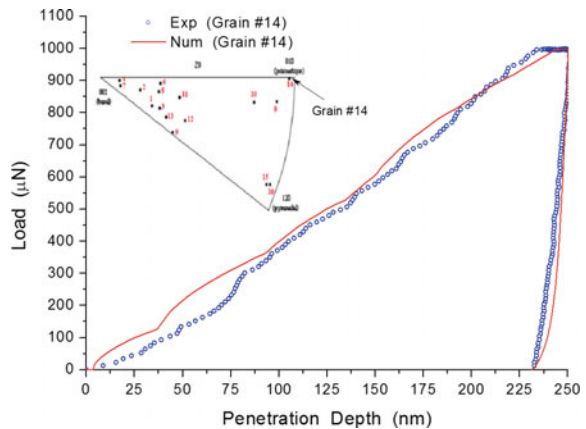


Table 4 Crystal plasticity model parameters identified for pure zinc

$\dot{\gamma}_0 (s^{-1})$	n	h_0^{Basal} (MPa)	h_0^{Prism} (MPa)	$h_0^{Pyr(c+a)}$ (MPa)	τ_0^{Basal} (MPa)	sat
0.0125	58	104	595	845	3	3.5

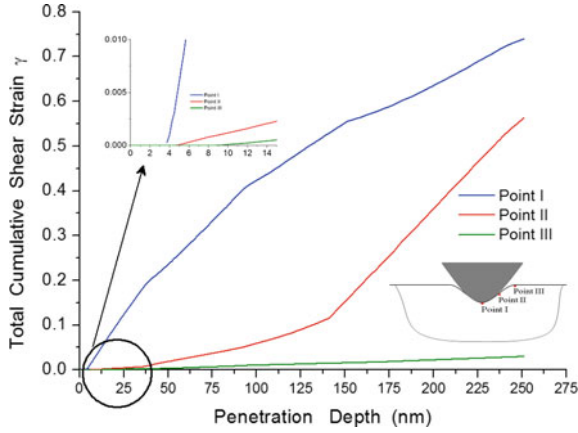


Fig. 6 Total cumulative shear strain versus penetration depth at three selected points (Grain #14)

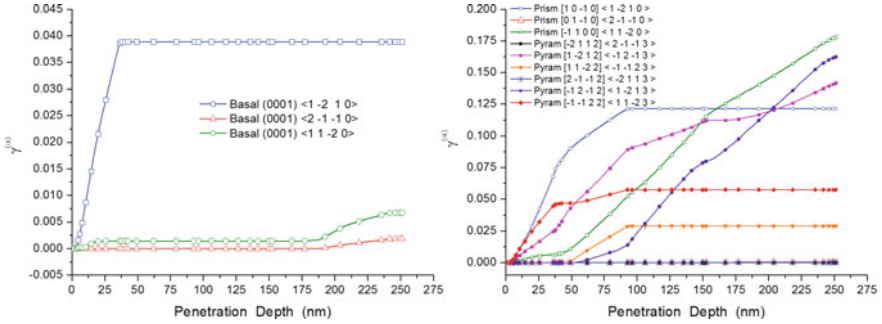
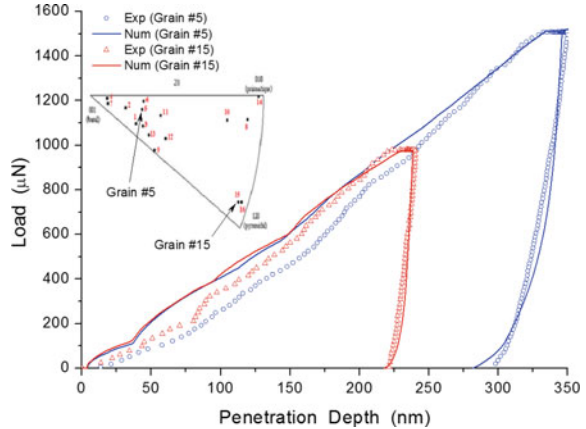


Fig. 7 Evolution of $\gamma^{(\alpha)}$ at Point I for all slip systems (Grain #14)

Figure 7 illustrates the corresponding evolution of shear strain ($\gamma^{(\alpha)}$) on all slip systems at Point I location. The onset of plasticity occurs at 3.5 nm and is initiated by activation of the easy glide (0001) \langle 1210 \rangle basal slip system, consistent with experimental observations [23]. It is followed by the early activation of the (0001) \langle 1120 \rangle basal slip system, [1010] \langle 1210 \rangle and [1100] \langle 1120 \rangle prismatic slip systems, and [1212] \langle 1213 \rangle and [1122] \langle 1123 \rangle pyramidal slip systems, between 4 nm and 6 nm penetration depth. Indeed, the contribution of [0110]2110 prismatic slip system, [2112] \langle 2113 \rangle and [2112] \langle 2113 \rangle pyramidal slip systems to the total cumulative shear strain over the entire loading stage is not observed. Moreover, the remaining slip systems are activated progressively with increasing penetration depth to accommodate the plastic deformation.

Fig. 8 Prediction of Grain #5 and Grain #15 nanoindentation responses using the identified model



5.2 Validation of the Crystal Plasticity Model

To assess the validity of the proposed model, indentation tests performed on grains of different crystalline orientations were simulated using the CPFEM model with the identified parameters given in Table 4. Grain #5 and Grain #15 have been selected given their quite distinct location in the standard stereographic triangle. Therefore, such distinct crystalline orientations should involve different slip systems activity rates.

The comparison between experimental data and numerical simulations is depicted on Fig. 8. It is worth noting that the mechanical behavior of such grains under heterogeneous loading conditions is fairly good predicted by our model. Those results validate the identified model for pure zinc.

6 Conclusion

In this chapter, we studied the orientation-dependent response of pure zinc grains. Nanoindentation experiments were performed on grains of different crystalline orientations. A crystal plasticity model was implemented in the FE code Abaqus through a user subroutine. The model parameters were identified by solving an inverse problem. Experimental data and numerical results are in good agreement. The analysis of the slip systems activity in the area underneath the indenter highlights that the basal glide is activated as primary slip system, followed by secondary slip systems provided by pyramidal $\langle c + a \rangle$ and/or prismatic glide to accommodate the deformation. The model thus identified can be used, for example, in deep drawing of zinc sheet finite element analysis for further experimental validations [24].

References

1. American Galvanizers Association website. <https://www.galvanizeit.org>
2. Takuda H, Yoshii T, Hatta N (1999) Finite-element analysis of the formability of a magnesium-based alloy AZ31 sheet. *J Mater Process Technol* 89–90:135–140
3. Kuwabara T, Katami C, Kikuchi M, Shindo T, Ohwue T (2001) Cup drawing of pure titanium sheet-finite element analysis and experimental validation. In: Proceedings of the seventh international conference on numerical methods in industrial forming processes, Toyohashi, Japan, 18–20 June 2001, p 781
4. Cazacu O, Barlat F (2004) A criterion for description of anisotropy and yield differential effects in pressure-insensitive metals. *Int J Plast* 20:2027–2045
5. Cazacu O, Plunkett B, Barlat F (2006) Orthotropic yield criterion for hexagonal closed packed metals. *Int J Plast* 22:1171–1194
6. Plunkett B, Lebensohn RA, Cazacu O, Barlat F (2006) Anisotropic yield function of hexagonal materials taking into account texture development and anisotropic hardening. *Acta Mater* 54:4159–4169
7. Nixon ME, Cazacu O, Lebensohn RA (2010) Anisotropic response of high-purity-titanium: experimental characterization and constitutive modeling. *Int J Plast* 26:516–532
8. Khan SK, Yu S, Liu H (2012) Deformation induced anisotropic responses of Ti–6Al–4V alloy. Part II: A strain rate and temperature dependent anisotropic yield function. *Int J Plast* 38:14–26
9. Yoon JH, Cazacu O, Mishra RK (2014) Constitutive modeling of AZ31 sheet alloy with application to axial crushing. *Mater Sci Eng A* 565:203–212
10. Peirce D, Asaro RJ, Needleman A (1983) Material rate dependence and localized deformation in crystalline solids. *Acta Metall* 31:1951–1976
11. Taylor GI (1938) Plastic strains in metals. *J Inst Metals* 62:307–324
12. Yoo MH, Wei CT (1966) Application of anisotropic elasticity theory to the plastic deformation in hexagonal zinc. *Phil Mag* 13:759–775
13. Yoo MH, Lee JK (1991) Deformation twinning in HCP metals and alloys. *Phil Mag* 63:987–1000
14. Huang Y (1991) A user-material subroutine incorporating single crystal plasticity in the Abaqus finite element program. Mech report 178, Harvard University
15. Kysar JW, Hall P (1991) Addendum to “a user-material subroutine incorporating single crystal plasticity in the Abaqus finite element program, Y. Huang, Mech. Report 178, Harvard University
16. Nguyen LT (2014) Contribution à l'étude des mécanismes de plasticité dans les hexagonaux compacts lors de l'essai de nanoindentation: Application au Zinc. PhD thesis, University of Reims Champagne-Ardenne
17. Liu Y, Wang B, Yoshino M, Roy S, Lu H, Komanduri R (2005) Combined numerical simulation and nanoindentation for determining mechanical properties of single crystal copper at mesoscale. *J Mech Phys Solids* 53:2718–2741
18. Liu Y, Varghese S, Ma J, Yoshino M, Lu H, Komanduri R (2008) Orientation effects in nanoindentation of single crystal copper. *Int J Plast* 24:1990–2015
19. Liu M, Lu C, Tieu AK (2015) Crystal plasticity finite element method modelling of indentation size effect. *Int J Solids Struct* 54:42–49
20. Bhattacharya AK, Nix WD (1988) Finite element simulation of indentation experiments. *Int J Solids Struct* 24:881–891
21. Tromans D (2011) Elastic anisotropy of HCP metal crystals and polycrystals. *Int J Res Rev Appl Sci* 6:462–483
22. Philippe MJ, Serghat M, Houtte PV, Esling C (1994) Modelling of texture evolution for materials of hexagonal symmetry: I—Application to zinc alloys. *Acta Metall Mater* 42:239–250

23. Fundenberger JJ, Philippe MJ, Wagner F, Esling C (1997) Modelling and prediction properties for materials with hexagonal symmetry (zinc, titanium and zirconium alloys). *Acta Mater* 45:4041–4055
24. Van TP, Jöchen K, Böhlke T (2012) Simulation of sheet metal forming incorporating EBSD data. *J Mater Process Technol* 212:2659–2668

Atomistic Simulation of Boron Nitride Nanotubes Under Bending



T. Nguyen-Van, T. Nguyen-Danh and Q. Le-Minh

Abstract We investigate the bending buckling behavior of boron nitride (BN) nanotubes through molecular dynamics finite element method with Tersoff potential. Effects of the tube length on the critical bending buckling angle and moment are examined for (5, 5) BN armchair and (9, 0) BN zigzag tubes, which exhibit approximately identical diameters. The buckling and fracture mechanisms of the tubes under bending are considered and discussed with respect to various tube length–diameter ratios $L/D = 10\text{--}40$. Simulation results will help to design and use BN nanotube-based nanocomposites and nanodevices.

Keywords Atomistic simulation bending • Boron nitride nanotube Buckling

1 Introduction

A boron nitride nanotube (BN-NT) can be geometrically formed by rolling up a hexagonal boron nitride (BN) layer or a carbon nanotube (CNT) [1] in which alternating B and N atoms entirely substitute for C atoms as shown in Fig. 1.

Various techniques have been used to synthesize BN-NTs, including arc-discharge, chemical vapor deposition, laser ablation, ball-milling methods (see,

T. Nguyen-Van · T. Nguyen-Danh · Q. Le-Minh (✉)

Department of Mechanics of Materials and Structures, School of Mechanical Engineering,
Hanoi University of Science and Technology, Hanoi, Vietnam
e-mail: quy.leminh@hust.edu.vn

T. Nguyen-Van
e-mail: shachootrang@gmail.com

T. Nguyen-Danh
e-mail: tuong.nguyendanh@hust.edu.vn

T. Nguyen-Van
Faculty of Mechanical Engineering, Thai Nguyen University of Technology, Thai Nguyen,
Vietnam

© Springer Nature Singapore Pte Ltd. 2018

H. Nguyen-Xuan et al. (eds.), *Proceedings of the International Conference on Advances in Computational Mechanics 2017*, Lecture Notes in Mechanical Engineering, https://doi.org/10.1007/978-981-10-7149-2_12

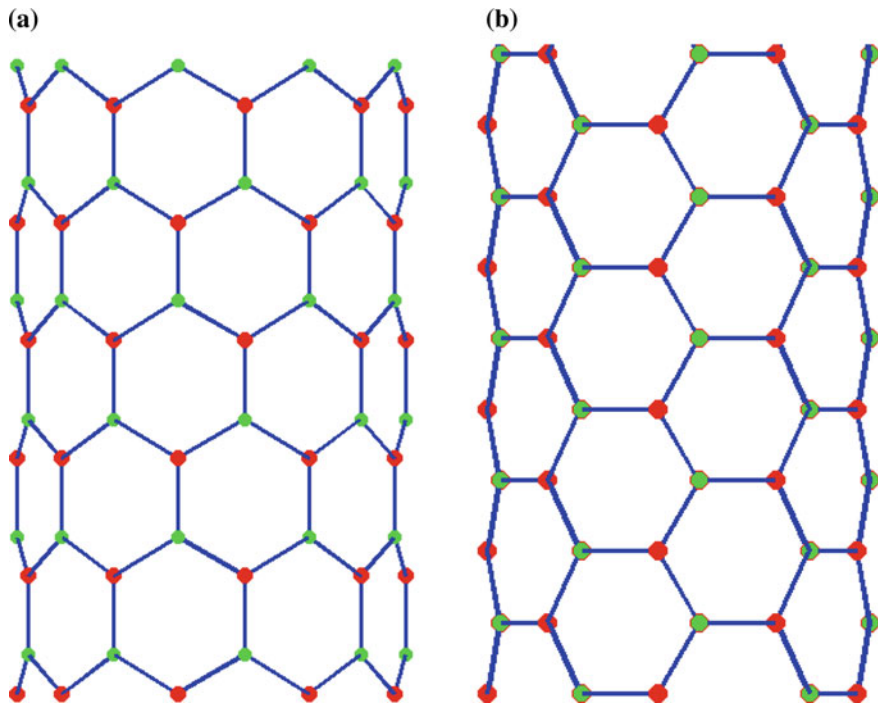


Fig. 1 Schematic illustration of: **a** (9, 0) BN zigzag tube; **b** (5, 5) BN armchair tube

e.g., the review by [2]). BN-NTs exhibit good mechanical properties with high elastic modulus of $\sim 0.5\text{--}1$ TPa and tensile strength of ~ 61 GPa [3]. They possess distinguishable chemical and thermal stability with high oxidation resistance up to 900°C in air [4], wide bandgaps independent of tube structures [5, 6], excellent thermal conductivity [7]. BN-NTs are also an effective violet and ultra-violet light emission material [8, 9]. Potential applications of BN-NTs include nanofillers in polymeric [10] and metallic [11] composites, optoelectronic fields [8], radiation shielding in space vehicles [12]. Potential applications of BN-NTs need a comprehension of the mechanical properties and performance of BN-NTs under various loading conditions. BN-NTs under compression [13–15], tension [16, 17], torsion [16, 18–20], and bending with two fixed or simple supports [21, 22] have been investigated. So far, theoretical studies of the buckling behavior under bending of BN-NTs seem unexplored. It should be noted that the buckling behavior of CNTs under bending has been investigated by continuum methods, atomistic simulations, and multi-scale approach; see, for example, [23, 24] and references therein.

The present work investigates through molecular dynamics finite element method (MDFEM) the buckling behavior of BN-NTs under bending. The critical bending buckling angle and moment are studied with respect to the length–diameter ratios of BN-NTs.

2 Framework for Analysis

Tersoff potential is used to model the B-N interatomic interactions [25]. The potential energy E of the atomic structure is a function of atomic coordinates as below:

$$E = \sum_i E_i = \frac{1}{2} \sum_{i \neq j} V_{ij}, V_{ij} = f_C(r_{ij}) [f_R(r_{ij}) + b_{ij} f_A(r_{ij})]; \quad (1a)$$

$$f_R(r_{ij}) = A_{ij} \exp(-\lambda_{ij}^I r_{ij}), f_A(r_{ij}) = -B_{ij} \exp(-\lambda_{ij}^H r_{ij}); \quad (1b)$$

$$f_C(r_{ij}) = \begin{cases} 1, & r_{ij} \leq R_{ij}; \\ \frac{1}{2} + \frac{1}{2} \cos\left(\pi \frac{r_{ij} - R_{ij}}{S_{ij} - R_{ij}}\right), & R_{ij} \leq r_{ij} \leq S_{ij}; \\ 0, & r_{ij} \geq S_{ij}; \end{cases} \quad (1c)$$

$$b_{ij} = \chi_{ij} \left(1 + \beta_i^{n_i} \zeta_{ij}^{n_i}\right)^{-1/2n_i}, \zeta_{ij} = \sum_{k \neq i, j} f_C(r_{ik}) \omega_{ik} g(\theta_{ijk}), g(\theta_{ijk}) \\ = 1 + c_i^2/d_i^2 - c_i^2 / \left[d_i^2 + (h_i - \cos \theta_{ijk})^2\right] \quad (1d)$$

$$\lambda_{ij}^I = (\lambda_i^I + \lambda_j^I)/2, \lambda_{ij}^H = (\lambda_i^H + \lambda_j^H)/2, A_{ij} = \sqrt{A_i A_j}, B_{ij} = \sqrt{B_i B_j}, R_{ij} \\ = \sqrt{R_i R_j}, S_{ij} = \sqrt{S_i S_j} \quad (1e)$$

Here, the lower indices i, j , and k label the atoms of the system, where interaction between atoms i and j is modified by a third atom k . r_{ij} is the distance between atoms i and j ; f_A and f_R are the attractive and repulsive pairwise terms; f_C is a cutoff function to ensure the nearest-neighbor interactions; R_{ij} and S_{ij} denote the small cutoff distance and the large one, respectively; b_{ij} is a bond-order parameter, depending on the local coordination of atoms around atom i . Further detail of the Tersoff potential is given in [25]. Force field parameters are taken from the work by Sevik et al. [26] for B-N interactions.

While the density functional theory (DFT) calculations and molecular dynamics (MD) simulations are time-consuming, molecular dynamic finite element methods (MDFEMs), sometimes known as atomic-scale finite element methods or atomistic finite element methods, have been developed to analyze nanostructured materials in a computationally efficient way; see, for example, [27, 28]. To achieve the atomic positions of the BN-NT under specific boundary conditions, molecular dynamic finite element method (MDFEM) is here adopted. In MDFEM, atoms and atomic displacements are considered as nodes and translational degrees of freedom (nodal displacements), respectively. Both first and second derivatives of system energy are used in the energy minimization computation, hence it is faster than the standard conjugate gradient method which uses only the first-order derivative of system energy as

discussed in [27]. The stiffness matrices of these elements are established based upon interatomic potentials. Similar to conventional finite element method, global stiffness matrix is assembled from element stiffness matrices. Hence, relations between atomic displacement and force can be derived by solving a system of equations. Further detailed numerical procedure of MDFEM and our specific development for Tersoff potentials are available in our previous work [29] and references therein. Initial positions of atoms are generated by using the B-N bond length of 1.444 Å taken from previous MD simulations [30] at optimized structure at 0 K with the same force field. (5, 5) BN armchair and (9, 0) BN zigzag tubes are considered. Difference in diameters of these two tubes is less than 4%. The diameter is about 0.717 and 0.689 nm for (9, 0) BN armchair and (5, 0) BN zigzag tubes, respectively.

3 Results and Discussion

Figure 2 shows the variations of the bending moment versus the bending angle of (9, 0) and (5, 0) BN tubes with the length–diameter ratio $L/D = 30$. The bending angle θ is here defined as the angle between two planes containing the two ends of the tube under bending. It can be seen from Fig. 2 that the bending moment increases monotonously with an increase of the bending angle up to a critical value, and then the bending moment drops suddenly, demonstrating a brittle fracture. The critical bending angle of the (9, 0) BN zigzag tube is approximately 66.6°, 136.6°, 210.6°, and 278.0° for $L/D = 10, 20, 30,$ and $39,$ respectively. The critical bending angle of the (5, 5) BN armchair tube is about approximately 121.7°, 142.9°, 176.7°, and 181.0° for $L/D = 10, 20, 30,$ and $40,$ respectively.

Figure 3 shows the effects of tube's length on the variations of the critical bending moments, critical bending angle, and critical bending curvature of these

Fig. 2 Variations of the bending moment versus the bending angle of the (9, 0) and (5, 0) BN tubes with $L = 30D$

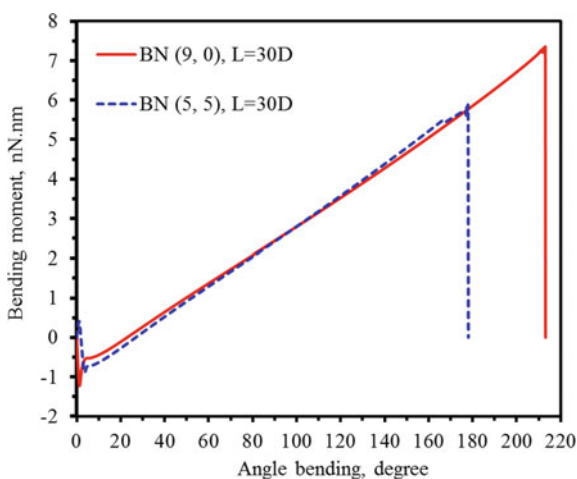
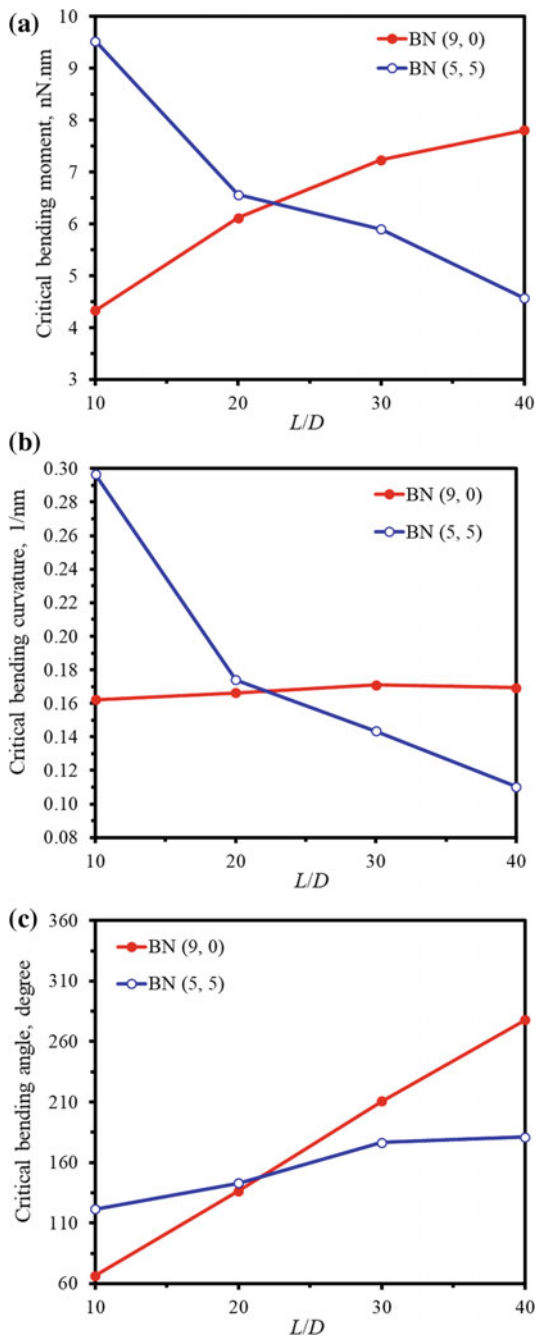


Fig. 3 Variations versus the tube length of: **a** the critical bending angle; **b** critical bending curvature; and **c** critical bending moment



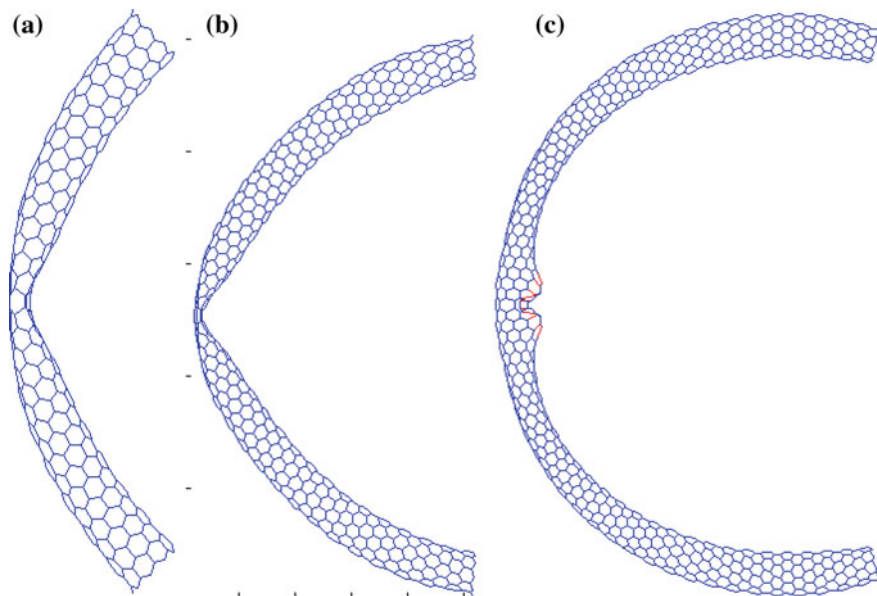


Fig. 4 Post-buckling shapes of (9, 0) BN zigzag tubes: **a** $L/D = 10$, $\theta = 91.67^\circ$; **b** $L/D = 20$, $\theta = 171.89^\circ$; and **c** $L/D = 30$, $\theta = 213.37^\circ$

two tubes. The critical bending moment and the critical bending curvature of (9, 0) BN tubes increase with an increase of the tube's length in the range $L/D = 10$ –40, whereas the critical bending moment and the critical bending curvature decrease when increasing the length of the (5, 5) BN tube. The critical bending angles of these two tubes increase with increasing the tube's length.

The critical bending moment, the critical bending curvature, and critical bending angle of (5, 5) tubes are higher than those of (9, 0) tubes when $L/D = 10$, hence short (5, 5) tubes resist better than short (9, 0) tubes under bending. Whereas long (9, 0) tubes undergo bending better than long (5, 5) tubes; the critical bending moment, the critical bending curvature, and critical bending angle of (9, 0) tubes are higher than those of (5, 5) tubes at $L/D = 30$ and 40 as indicated in Fig. 3. Figure 4 shows the post-buckling shapes of (9, 0) BN zigzag tubes with $L/D = 10$, 20, and 30. Snapshots under progressive bending are depicted in Figs. 5 and 6 for (9, 0) BN zigzag tube with $L/D = 39$ and (5, 5) BN armchair tube with $L/D = 20$, respectively.

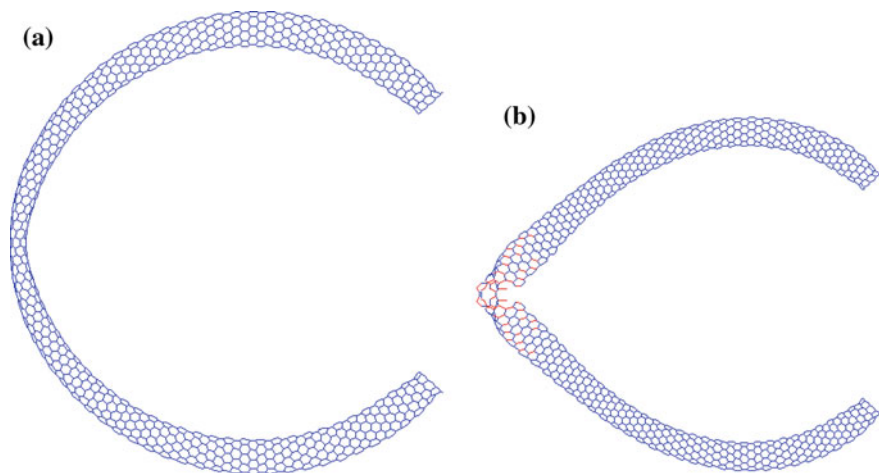


Fig. 5 Snapshots of a (9, 0) BN zigzag tube with $L/D = 39$ under a bending angle of: **a** 279.37°; and **b** 279.49°

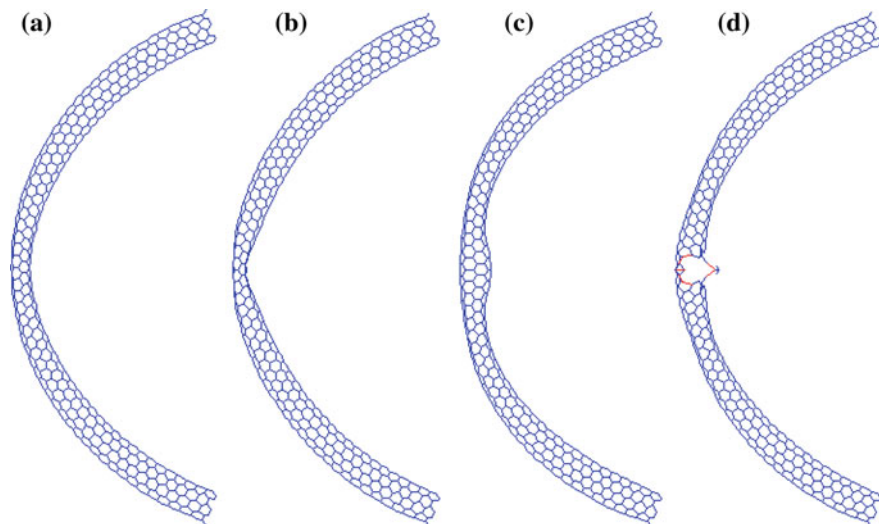


Fig. 6 Snapshots of a (5, 5) BN armchair tube with $L/D = 20$ under a bending angle of: **a** 143.35°; **b** 143.58°; **c** 143.70°; and **d** 143.81°

4 Conclusions

We present the simulation results of the buckling behavior of BN nanotubes under bending with the use of MDFEM. We have found that the tube length affects significantly the bending behavior of the tube. All tubes exhibit brittle fracture under bending. The buckling takes place in the middle of the compressive side of the tube. More investigation should be done to analyze in details the buckling behavior of the BN tubes.

Acknowledgements Danh-Truong Nguyen's work was funded by Vietnam National Foundation for Science and Technology Development (NAFOSTED) under grant number 107.02-2016.13.

References

1. Iijima S (1991) Helical microtubules of graphitic carbon. *Nature* 354(6348):56
2. Zhi C, Bando Y, Tang C, Golberg D (2010) Boron nitride nanotubes. *Mater Sci Eng R Rep* 70(3):92–111
3. Arenal R, Wang M-S, Xu Z, Loiseau A, Golberg D (2011) Young modulus, mechanical and electrical properties of isolated individual and bundled single-walled boron nitride nanotubes. *Nanotechnology* 22(26):265704
4. Chen Y, Zou J, Campbell SJ, Le Caer G (2004) Boron nitride nanotubes: pronounced resistance to oxidation. *Appl Phys Lett* 84(13):2430–2432
5. Baumeier B, Krüger P, Pollmann J (2007) Structural, elastic, and electronic properties of SiC, BN, and BeO nanotubes. *Phys Rev B* 76(8):085407
6. Guo G, Ishibashi S, Tamura T, Terakura K (2007) Static dielectric response and Born effective charge of BN nanotubes from ab initio finite electric field calculations. *Phys Rev B* 75(24):245403
7. Chang C, Fennimore A, Afanasiev A, Okawa D, Ikuno T, Garcia H, Li D, Majumdar A, Zettl A (2006) Isotope effect on the thermal conductivity of boron nitride nanotubes. *Phys Rev Lett* 97(8):085901
8. Attacalite C, Wirtz L, Marini A, Rubio A (2013) Efficient Gate-tunable light-emitting device made of defective boron nitride nanotubes: from ultraviolet to the visible. *Sci Rep* 3
9. Li LH, Chen Y, Lin M-Y, Glushenkov AM, Cheng B-M, Yu J (2010) Single deep ultraviolet light emission from boron nitride nanotube film. *Appl Phys Lett* 97(14):141104
10. Meng W, Huang Y, Fu Y, Wang Z, Zhi C (2014) Polymer composites of boron nitride nanotubes and nanosheets. *J Mater Chem C* 2(47):10049–10061
11. Nautiyal P, Gupta A, Seal S, Boesl B, Agarwal A (2017) Reactive wetting and filling of boron nitride nanotubes by molten aluminum during equilibrium solidification. *Acta Mater* 126:124–131
12. Kang JH, Sauti G, Park C, Yamakov VI, Wise KE, Lowther SE, Fay CC, Thibeault SA, Bryant RG (2015) Multifunctional electroactive nanocomposites based on piezoelectric boron nitride nanotubes. *ACS Nano* 9(12):11942–11950
13. Chandra A, Patra PK, Bhattacharya B (2016) Thermomechanical buckling of boron nitride nanotubes using molecular dynamics. *Mater Res Express* 3(2):025005
14. Huang Y, Lin J, Zou J, Wang M-S, Faerstein K, Tang C, Bando Y, Golberg D (2013) Thin boron nitride nanotubes with exceptionally high strength and toughness. *Nanoscale* 5(11):4840–4846

15. Li T, Tang Z, Huang Z, Yu J (2017) A comparison between the mechanical and thermal properties of single-walled carbon nanotubes and boron nitride nanotubes. *Physica E* 85:137–142
16. Kinoshita Y, Ohno N (2010) Electronic structures of boron nitride nanotubes subjected to tension, torsion, and flattening: a first-principles DFT study. *Phys Rev B* 82(8):085433
17. Anoop Krishnan N, Ghosh D (2014) Defect induced plasticity and failure mechanism of boron nitride nanotubes under tension. *J Appl Phys* 116(4):044313
18. Anoop Krishnan N, Ghosh D (2014) Chirality dependent elastic properties of single-walled boron nitride nanotubes under uniaxial and torsional loading. *J Appl Phys* 115(6):064303
19. Xiong Q-L, Tian XG (2015) Torsional properties of hexagonal boron nitride nanotubes, carbon nanotubes and their hybrid structures: a molecular dynamics study. *AIP Adv* 5(10):107215
20. Garel J, Leven I, Zhi C, Nagapriya K, Popovitz-Biro R, Golberg D, Bando Y, Hod O, Joselevich E (2012) Ultrahigh torsional stiffness and strength of boron nitride nanotubes. *Nano Lett* 12(12):6347–6352
21. Tanur AE, Wang J, Reddy AL, Lamont DN, Yap YK, Walker GC (2013) Diameter-dependent bending modulus of individual multiwall boron nitride nanotubes. *J Phys Chem B* 117(16):4618–4625
22. Zhang J (2016) Size-dependent bending modulus of nanotubes induced by the imperfect boundary conditions. *Sci Rep* 6
23. Hollerer S (2014) Numerical validation of a concurrent atomistic-continuum multiscale method and its application to the buckling analysis of carbon nanotubes. *Comput Methods Appl Mech Eng* 270:220–246
24. Wang C, Liu Y, Al-Ghalith J, Dumitrică T, Wadee MK, Tan H (2016) Buckling behavior of carbon nanotubes under bending: from ripple to kink. *Carbon* 102:224–235
25. Tersoff J (1989) Modeling solid-state chemistry: Interatomic potentials for multicomponent systems. *Phys Rev B* 39(8):5566
26. Sevik C, Kinaci A, Haskins JB, Çağın T (2011) Characterization of thermal transport in low-dimensional boron nitride nanostructures. *Phys Rev B* 84(8):085409
27. Liu B, Huang Y, Jiang H, Qu S, Hwang KC (2004) The atomic-scale finite element method. *Comput Methods Appl Mech Eng* 193:1849–1864
28. Wackerfuß J (2009) Molecular mechanics in the context of the finite element method. *Int J Numer Meth Eng* 77:969–997
29. Le MQ, Nguyen DT (2014) Atomistic simulations of pristine and defective hexagonal BN and SiC sheets under uniaxial tension. *Mater Sci Eng, A* 615(2014):481–488
30. Le M-Q (2014) Atomistic study on the tensile properties of hexagonal AlN, BN, GaN, InN and SiC sheets. *J Comput Theor Nanosci* 11(6):1458–1464

Part III
Optimization and Inverse Problems

A Quick Computational Method for Improving Aerodynamic Shape of UAV Wing



D. Tran-Duy, C. Nguyen-Duc, K. Mai and T. Nguyen-Duc

Abstract To obtain an optimal aerodynamic 3D shape of small-sized UAV wing at small flight speed and high lift coefficient, the optimization problem is set to minimize drag coefficient with fixed plane form and constant lift coefficient. The thickness of chordwise function is assumed to be given. The direct optimization problem must be solved by CFD methods with viscosity consideration in 3D flow that involves a great volume of computations which is feasible only to super computers [1, 6]. This chapter presents a combined direct inverse method that makes the optimization problem be feasible to ordinary PC.

Keywords Computational mechanics • Wing shape optimization
CFD • Vortex lattice method

1 Introduction

Unmanned aerial vehicle (UAV) with surveillance mission and flight time is mainly in cruise mode. At this time, the lifting force and weight of the UAV are equal, and lift coefficient C_L is calculated according to the formula:

$$C_L = \frac{\frac{G}{S}}{0.5\rho V^2}$$

where V —speed of cruise flights; ρ —density of air; S —area of wing; G —weight of the UAV.

D. Tran-Duy (✉) · K. Mai · T. Nguyen-Duc
Institute for Military Science and Technology, Hanoi, Vietnam
e-mail: duyduyen85@gmail.com

C. Nguyen-Duc
Vietnam Aerospace Association, Hanoi, Vietnam
e-mail: cuongnd45@gmail.com

To provide the necessary quality of surveillance in *UAV*, its flight speed is not required to be large. And in order to increase the width of visibility swarth, it is necessary to fly at high altitude, so the air density is small. To reduce the impact of wind disturbance on complex terrain, the specific load on the wing (ratio $\frac{G}{S}$) should be also designed to be large. Therefore, the above-mentioned formula shows that the *UAV* cruise flights must be implemented at high lift coefficient.

Optimizing the wing shape plays an important role in reducing the drag of the whole aircraft, and there are many works on this subject. However, almost all works focus on solving the *2D* problem at high speed (small lift coefficient) with the effect of viscosity and the *3D* problem with compressible flow but without viscosity (potential flow). Some works were implemented in *3D* flow and with compressibility and viscosity, but because of very large computational volume, the problem solutions are feasible only to super computers [1, 2]. For the case of high lift coefficient, it is necessary to solve the *3D* problem, the computation volume is huge even without the compressibility, so it is often solved without viscosity. However, since most *UAVs* are small in size with small flight speed, the numbers Re are small, and the viscosity of the flow can not be ignored when the considering problem is set to minimize drag coefficient. So that involves a great of computation volume which is feasible only to super computers even without compressibility because of necessity to consider many wing shapes in the optimization process.

To reduce the volume of calculation and to make the optimization problem feasible to ordinary *PC*, the paper presents a combined direct-inverse method to solve the optimization problem. The inverse problem is based on the elliptical spanwise distribution of aerodynamic loads (that is optimal according to linear lifting surface theory) with a smooth entry on leading edge [3]. The solution by the vortex lattice method will give us some curved surface [4]. The curved surface is considered as a mean surface and is added with the given thickness function, for example, according to aerofoil NACA 0012, to obtain so-called quasi-optimal wing shape. The quasi-optimal wing shape will be the initial shape for further optimization. The last one is solved by gradient method using commercial *CFD* software *ANSYS/CFX*. The parametrization of the quasi-optimal wing geometry is made by only two design variables: (i) the given lift coefficient C_L^* for inverse linear problem to obtain the mean surface and (ii) the added twist angle φ of the wing tip section relative to the wing root section assuming the twist angles are changed spanwise as a linear function. The lift coefficient C_L^* given for inverse linear problem is a representative parameter for both chordwise curvature and the spanwise twist/curvature of the mean surface. Thus, the direct optimization problem is solved with only three parameters: angle of attack α , C_L^* , and φ instead of using dozens of parameters as other authors do [2, 5, 6].

The significant effect of wing shape optimization was demonstrated for the wings with one and the same rectangular plan form and relative thickness. The comparison of the optimized wing at $C_L = 0.3$ with the wing with symmetrical

airfoil *NACA 0012* showed the essential improvements in lift-to-drag ratio at cruise flights with increased lift coefficients, as well as the comparison with the wing with a curved airfoil showed the apparent improvements at flights with small lift coefficients. Thus, the proposed wings allow to “reconcile” the drag coefficient C_D of classic wings with different curvatures. It leads to less fuel consumptions, which allows to get more payload for a given flight time when the *UAV* flies at different lift coefficients.

2 A Solution Method and Results

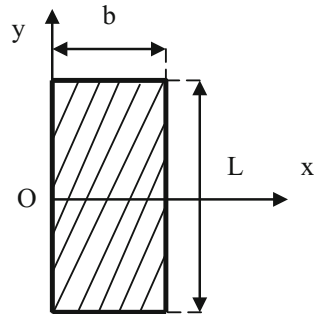
2.1 Method and Algorithms for Determination of Quasi-Optimal Wing Shape

2.1.1 A Proposed Distribution of Aerodynamic Loads Function to Ensure Smooth Entry on Leading Edge and Elliptical Spanwise Distribution on a Rectangular Plane Form

We will consider a rectangular wing with the size of the chord is b and the span L , the reference system of Oxy is chosen as shown in Fig. 1. To ensure the elliptical spanwise distribution of aerodynamic loads (according to linear lifting surface theory) with smooth entry on leading edge, moreover chordwise distribution of aerodynamic loads function is continuous and with limited the slope of this function (to limit the positive pressure gradient to delay the flow separation), at the same time aerodynamic loads at the rear edge of wing is zero (Kutte—Zhoucovsky’s postulate). One of the distributions of aerodynamic loads function that fits all the said condition may be as following:

$$\Delta\bar{p} = A \cdot x(x - b)^2 \sqrt{1 - \left(\frac{y}{\frac{L}{2}}\right)^2} \tag{2.1}$$

Fig. 1 Reference system on the plane form of a rectangular wing



Determination of the coefficient A:

$$\text{Formula for aerodynamic lift: } Z = 0.5C_L^*\rho V^2S = C_L^*q_\infty S \tag{2.2}$$

Where $q_\infty = 0.5\rho V^2$ is the speed pressure of the undisturbed flow, $S = bl$ —area of the wing.

Aerodynamic lift is also calculated according to the formula:

$$Z = \iint \Delta p dS = q_\infty \iint \Delta \bar{p} dS = q_\infty \int_0^b \int_{-\frac{L}{2}}^{\frac{L}{2}} A \cdot x(x-b)^2 \sqrt{1 - \left(\frac{y}{L}\right)^2} dx dy = Aq_\infty \frac{\pi Lb^4}{48} \tag{2.3}$$

Comparing (2.2) and (2.3) \Rightarrow

$$A = \frac{48C_L^*S}{\pi Lb^4} \tag{2.4}$$

Finally, we will have a desired distribution of aerodynamic loads on the plane form of a rectangular wing:

$$\Delta \bar{p} = \frac{48C_L^*S}{\pi Lb^4} x(x-b)^2 \sqrt{1 - \left(\frac{y}{L}\right)^2} \tag{2.5}$$

2.1.2 A Method to Determine the Mean Surface Satisfying a Given Distribution of Aerodynamic Loads on the Wing

The essence of determining the mean surface satisfying given distribution of aerodynamic loads on the wing is to find the local slope of mean curved line at different cross sections (the derivatives of the mean curved line). By integrating these local slopes with initial conditions on the leading edge of the base plane, the curved surface will satisfy the given distribution of aerodynamic loads. The details of the method are presented as follows.

A curved surface with relatively small slope and set to coming flow under a small enough angle of attack. In the linear consideration, the “superimposed” rule of solutions can be applied to the aerodynamic loads, namely “*The aerodynamic loads on the curved surface at a certain angle of attack α is equivalent to the aerodynamic loads on the flat plate at angle of attack α and plus the aerodynamic loads on the curved surface at zero angle of attack*” (Fig. 2).

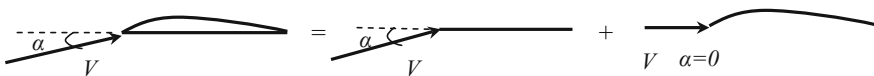


Fig. 2 Equivalent flows in linear consideration

Symbols:

$\Delta\bar{p}_{ij}^2$: Dimensionless aerodynamic loads in ij -th cell on curved surface at an angle of attack α ;

$\Delta\bar{p}_{ij}^1$: Dimensionless aerodynamic loads in ij -th cell on flat plate (the base plane) at the angle of attack α ;

$\Delta\bar{p}_{ij}^2$: Dimensionless aerodynamic loads in ij -th cell on curved surface at zero angle of attack.

Due to the imposition of aerodynamic loads on the curved surface at an angle of attack α , or $\Delta\bar{p}_{ij}^1$, has been determined. $\Delta\bar{p}_{ij}^1$ determined by the vortex lattice method [3]. Then, aerodynamic loads in ij -th cell on curved surface at angle of attack $\alpha = 0$ is:

$$\Delta\bar{p}_{ij}^2 = \Delta\bar{p}_{ij} - \Delta\bar{p}_{ij}^1. \tag{2.6}$$

Assuming that only the ij -th cell of the curved surface inclined relatively to a base plane at an angle of α_{ij} , the inclination of the cell $i^*j^*(i = i^*, j = j^*)$ will be found independently, while the remaining cells remain not inclined ($\alpha_{i^*j^*} = 0$ when $i \neq i^*, j \neq j^*$). Then, the aerodynamic loads in ij -th cell are calculated by the formula [3]:

$$\Delta\bar{p}_{ij}^{i^*j^*} = 2(n-1)\alpha_{i^*j^*}\bar{\Gamma}_{ij}^{\alpha_{i^*j^*}} \tag{2.7}$$

where n, N is the number of strips divided spanwise and chordwise of the wing; i, j is the index that characterizes the position of the vortex spanwise and chordwise ($i = \overline{1, n}, j = \overline{1, N}$); $\bar{\Gamma}_{ij}^{\alpha_{i^*j^*}}$ is the derivative of vortex dimensionless strength on the ij -th cell at the angle of $\alpha_{i^*j^*}$ [3].

In the linear consideration, the angles of $\alpha_{i^*j^*}$ are small: when all the ij -th cells are tilted to the corresponding angle of $\alpha_{i^*j^*}$ ($i^* = \overline{1, n}, j^* = \overline{1, N}$) then aerodynamic loads in ij -th cell on curved surface at angle of attack $\alpha = 0$:

$$\Delta\bar{p}_{ij}^2 = \sum_{i^*=1}^n \sum_{j^*=1}^N \Delta\bar{p}_{ij}^{i^*j^*} \tag{2.8}$$

From (2.6), (2.7), and (2.8) \Rightarrow linear algebraic systems (2.9) to find local angles of $\alpha_{i^*j^*}$:

$$2(n-1) \sum_{i^*=1}^n \sum_{j^*=1}^N \alpha_{i^*j^*}\bar{\Gamma}_{ij}^{\alpha_{i^*j^*}} = \Delta\bar{p}_{ij} - \Delta\bar{p}_{ij}^1 \tag{2.9}$$

Integrating (getting a sum of Δz) angles of $\alpha_{i^*j^*}$ ($\approx \frac{dz}{dx}$) with initial condition is the leading edge of curved surface on the base plane ($z_{1j} = 0, j = \overline{1, N}$) \Rightarrow the formula for determining the z_{ij} coordinate corresponding to the x_{ij} coordinate of the curved surface:

$$\begin{cases} z_{1j} = 0, j = \overline{1, N} \\ z_{ij} = \sum_{k=2}^{k=i} (x_{kj} - x_{(k-1)j}) \operatorname{tg} \alpha_{(k-1)j^*}, i = \overline{2, n}, j = \overline{1, N} \end{cases} \quad (2.10)$$

The set of points (x_{ij}, z_{ij}) determines the mean surface of the wing satisfying the given distribution of aerodynamic loads. The result is more accurate when the number of dividing lines n (the spanwise direction) and N (the chordwise directions) is greater.

2.1.3 Determination of the Shape of the Wing According to the Mean Surface

Assuming that the mean surface of the wing was defined and function of mean line of the j -th section will be as follows:

$$z_{cj} = f_j(x_c), j = \overline{1, N} \quad (2.11)$$

The thickness chordwise function may be taken according to the symmetric NACA aerofoil [7]:

$$z_t = \frac{b \bar{c}_{max}}{0.2} \left(a_0 \left(\frac{x}{b} \right)^{0.5} + a_1 \left(\frac{x}{b} \right) + a_2 \left(\frac{x}{b} \right)^2 + a_3 \left(\frac{x}{b} \right)^3 + a_4 \left(\frac{x}{b} \right)^4 \right) \quad (2.12)$$

where $a_0 = 0.2969$, $a_1 = -0.126$, $a_2 = -0.3516$, $a_3 = 0.2843$, and $a_4 = -0.1036$; b : the chord length; $\bar{c}_{max} = \frac{c_{max}}{b}$: the largest relative thickness, and c_{max} is the largest thickness of aerofoil.

The symbols (x_{uj}, z_{uj}) , (x_{lj}, z_{lj}) are the coordinates of the points defining the upper and under lines of the aerofoil of the j -th section of the wing. Equations defining the deformation of j -th section of the wing [7]:

$$\begin{cases} x_{uj} = x_{cj} - z_t \sin \theta_j \\ z_{uj} = z_{cj} + z_t \cos \theta_j \end{cases}, \begin{cases} x_{lj} = x_{cj} + z_t \sin \theta_j \\ z_{lj} = z_{cj} - z_t \cos \theta_j \end{cases}, \theta_j = \operatorname{atan} \left(\frac{dz_{cj}}{dx} \right) \quad (2.13)$$

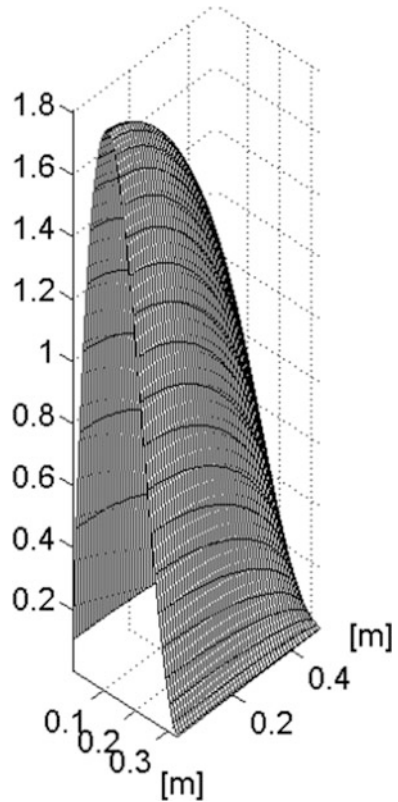
2.1.4 The Results of Determination of Quasi-Optimal Wing Shape and Its CFD Simulation

The received quasi-optimal wing shape with input data:

+ Lift coefficient of wing $C_L^* = 0.8$ (determining the mean curved surface as solution of linear inverse problem);

+ Chord $b = 0.337$ [m]; span of wing $L = 1$ [m]; the largest (relative) thickness $\bar{c}_{max} = 12\%$;

Fig. 3 Given distribution of aerodynamic loads on the half wing corresponding to the lift coefficient $C_L^* = 0.8$



+ Number of strips divided spanwise and chordwise: $n = 41, N = 21$.

The distribution of aerodynamic loads on a half wing is presented in Fig. 3. The results of computation program of the quasi-optimal wing shape are shown in Fig. 4.

On the other hand, the authors implemented *CFD* simulation of the quasi-optimal wing shape by the *ANSYS/CFX* commercial software and at the angle of attack $\alpha = 8^\circ$, flight altitude $H = 0[m]$ ($\rho = 1.225[kg/m^3]$). The simulation results calculate the lift coefficient of the quasi-optimal wing: $C_L = 0.85$, the difference from the linear vortex lattice method ($C_L^* = 0.8$) is 7%. The error is acceptable and the suitability of the results of programs confirms the reliability of the computational program for inverse problem solution.

Fig. 5 shows the graph $C_D = f(C_L)$ of the quasi-optimal wing $C_L^* = 0.8$ and some equivalent classic wings (with the same plane form $b = 0.337[m]$, $L = 1[m]$, and the same relative thickness $\bar{c}_{max} = 12\%$) at the high lift coefficient range. The results were obtained by the *ANSYS/CFX* software.

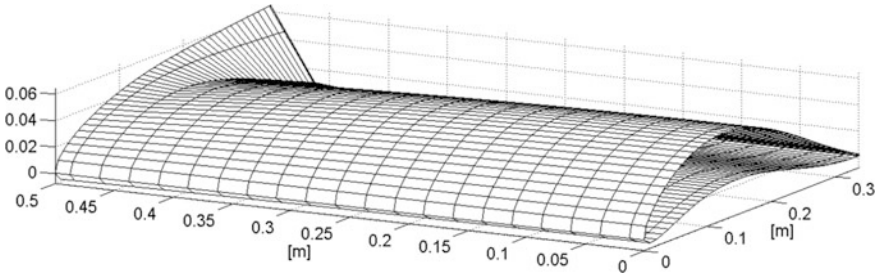


Fig. 4 Half-wing shape of quasi-optimal wing corresponds to the lift coefficient of wing $C_L^* = 0.8$

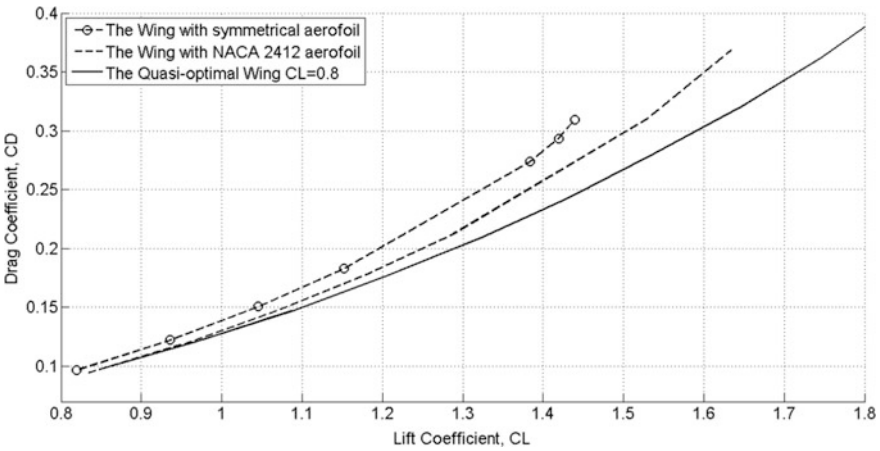


Fig. 5 Graph $C_D = f(C_L)$ of the quasi-optimal wing $C_L^* = 0.8$ and some equivalent classic wings at high lift coefficient range

Based on the results some comments may be made. They are as follows:

+ At $C_L = 0.85$ (corresponding to the calculation point determining the quasi-optimal wing shape $C_L^* = 0.8$): the quasi-optimal wing has not reduced the drag coefficient C_D in comparison with the classic wings.

+ At increased lift coefficients C_L , the drag coefficient C_D is reduced significantly. For example, at $C_L = 1.2$, the drag coefficient C_D of the quasi-optimal wing $C_L^* = 0.8$ was reduced by 13% compared to the wing with symmetrical aerofoil (*NACA 0012*) was reduced by 5% compared to wing have curvature of the aerofoil is 2% (*NACA 2412*).

So the quasi-optimal wing is not optimal at the angle of attack α^* according to the thin-wing theory, which is optimal at angles of attack α greater than α^* . This is why wing shapes are found from a computational program called *the quasi-optimal wing*.

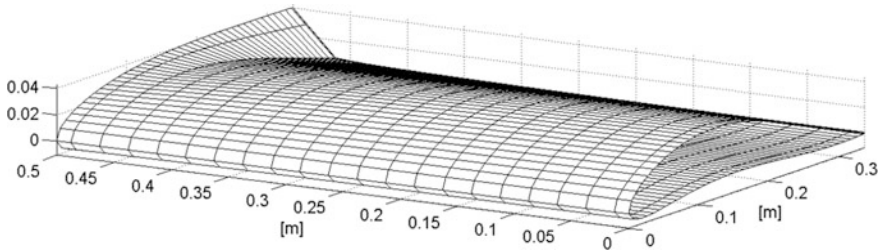


Fig. 6 Half-wing shape of quasi-optimal wing corresponding to the lift coefficient of wing $C_L^* = 0.5$

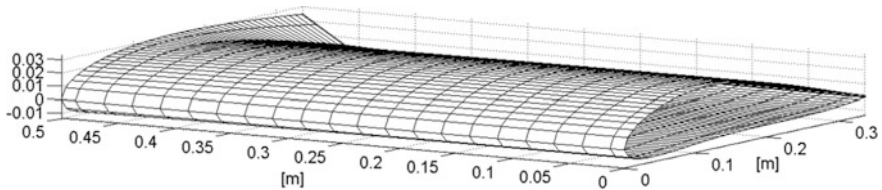


Fig. 7 Half-wing shape of quasi-optimal wing corresponding to the lift coefficient of wing $C_L^* = 0.3$

The program results of the quasi-optimal wing shape corresponding to $C_L^* = 0.5$, $C_L^* = 0.3$ were shown in Figs. 6 and 7. Comparing Figs. 4, 6 and 7 one may see the quasi-optimal wing with the greater C_L^* , then its mean surface has the greater curvature. At the same time, the geometric twist angle φ_0 (which is the angle of the wing tip section relative to the wing root section) is also greater.

The graphs $C_D = f(C_L)$ of some quasi-optimal wings were shown in Fig. 8:

- + The quasi-optimal wing with the greater C_L^* the drag coefficient C_D reduction is more significant at higher lift coefficients C_L (corresponding to the lift coefficient range $C_L^* > 1.1$).

- + In contrast, the quasi-optimal wing with the smaller C_L^* the drag coefficient C_D reduction is as much at smaller lift coefficients C_L (corresponding to the lift coefficient range $C_L^* < 0.9$).

2.2 Optimization of Quasi-Optimal Wing Shape

2.2.1 Construction of the Optimization Problem of Drag Coefficient C_D

If one selects a large number of parameters to optimize, then the computation volume drastically increases and the optimization process may be impossible to ordinary PC.

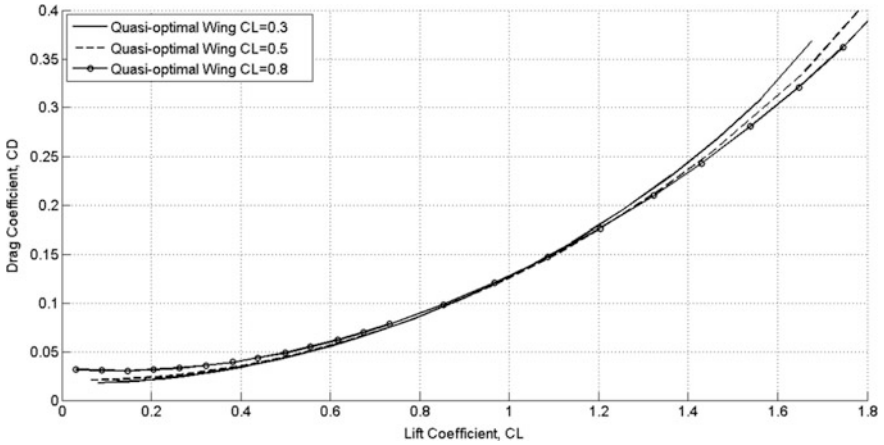


Fig. 8 Graph $C_D = f(C_L)$ of the some quasi-optimal wings

Hence, it is necessary to select a small set of parameters but those which have a strong influence on the coefficients C_D , C_L to optimize the wing shape.

Obviously, the parameter angle of attack α (defined as angle of attack of the chord of wing root section of the wing) and the parameter C_L^* (represents the whole mean surface shape of quasi-optimal wing, both the curvature of every section and the twist angles between themselves) are the most influential among the coefficients C_D , C_L . Also, the quasi-optimal wing has geometry twist φ_0 is significantly, so one can choose as a third design parameter the added twist angle φ of the wing tip section relative to the wing root section assuming the twist angles are changed spanwise as a linear function:

$$\varphi(|y|) = \frac{|y|}{\frac{L}{2}} \varphi \tag{2.14}$$

where $\varphi > 0$ when angle of attack of chord of the wing tip section is greater than of attack of chord of the wing root section of the quasi-optimal wing and vice versa.

Thus, the problem is set out as follows:

Give $C_L = const$, find three parameters $(\alpha, \varphi, C_L^*)_{opt}$ so as to:

$$C_D = C_D(\alpha, \varphi, C_L^*) \rightarrow C_{Dmin} \text{ with the constraint } C_L(\alpha, \varphi, C_L^*) = C_L^{ht} = const \tag{2.15}$$

where the constraint conditions are made in a cruise flights mode with lift coefficient $C_L = C_L^{ht}$.

The following presents an algorithm for solving optimization problem (2.15) using a gradient method, although the optimum has been found by this method only numerically (it is not strictly proved).

2.2.2 Optimization Algorithm the Drag Coefficient C_D with Constraint Conditions the Lift Coefficient $C_L = \text{const}$ by Gradient Method

Considering the optimization problem (2.15), Fig. 9 shows how to determine the “fastest direction of decreasing” the coefficient C_D and ensure the coefficient C_L to satisfy the constraint surface $C_L = C_L^{ht} = \text{const}$. This step length must be chosen appropriately and play a very important role in the speed of convergence of the optimization process and this issue will be considered later. There are some definitions:

+ Surfaces $C_L = \text{const}$ is the constraint surface of equation:

$$C_L(\alpha, \varphi, C_L^*) = C_L^{ht} = \text{const} \tag{2.16}$$

+ Contour line $C_D = \text{const}$ is the curve of equation:

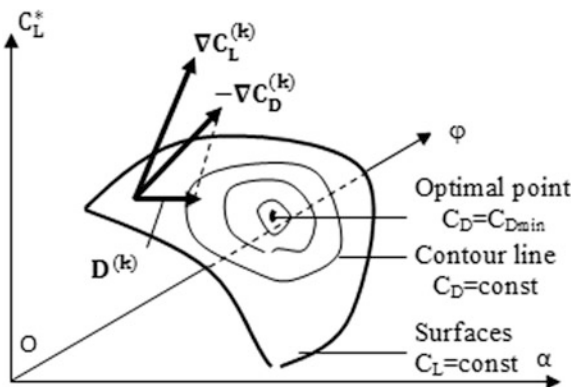
$$\begin{cases} C_D(\alpha, \varphi, C_L^*) = \text{const} \\ C_L(\alpha, \varphi, C_L^*) = \text{const} \end{cases} \tag{2.17}$$

+ $\nabla C_D^{(k)}$, $\nabla C_L^{(k)}$, respectively, is gradient vector of drag coefficient C_D , lift coefficient C_L at the point k of calculation on the constraint surface $C_L = \text{const}$, and the formula determines the gradient vector $\nabla C_D^{(k)}$, $\nabla C_L^{(k)}$:

$$\begin{aligned} \nabla C_D^{(k)} &= \left(\frac{\partial C_D^{(k)}}{\partial \alpha^{(k)}}, \frac{\partial C_D^{(k)}}{\partial \varphi^{(k)}}, \frac{\partial C_D^{(k)}}{\partial C_L^{*(k)}} \right); \\ \nabla C_L^{(k)} &= \left(\frac{\partial C_L^{(k)}}{\partial \alpha^{(k)}}, \frac{\partial C_L^{(k)}}{\partial \varphi^{(k)}}, \frac{\partial C_L^{(k)}}{\partial C_L^{*(k)}} \right) \end{aligned} \tag{2.18}$$

As well known in numerical methods, the partial derivatives of the coefficient C_D , C_L by some variable are replaced by the ratio of their increments (when changing only that variable) and the increment of that variable.

Fig. 9 Determining the direction of fastest decreasing the coefficient C_D while providing the coefficient C_L closest asymptotically to the constraint surface in 3D space by the numerical gradient method



$$\nabla C_D^{(k)} \approx \left(\frac{\Delta C_D^{(k)}(\alpha)}{\Delta \alpha^{(k)}}, \frac{\Delta C_D^{(k)}(\varphi)}{\Delta \varphi^{(k)}}, \frac{\Delta C_D^{(k)}(C_y^*)}{\Delta C_L^{*(k)}} \right); \Delta C_L^{(k)} \approx \left(\frac{\Delta C_L^{(k)}(\alpha)}{\Delta \alpha^{(k)}}, \frac{\Delta C_L^{(k)}(\varphi)}{\Delta \varphi^{(k)}}, \frac{\Delta C_L^{(k)}(C_L^*)}{\Delta C_L^{*(k)}} \right) \quad (2.19)$$

To find the gradient information $\nabla C_D^{(k)}$, $\nabla C_L^{(k)}$ relatively accurate by numerical method, the choice the increments $\Delta \alpha^{(k)}$, $\Delta \varphi^{(k)}$, $\Delta C_L^{*(k)}$ at the k -th calculation point must be reasonable. They must be selected several times in the computer to find the appropriate increments for accurately determining the gradient information $\nabla C_D^{(k)}$, $\nabla C_L^{(k)}$. This information is considered accurate when giving the increments $\Delta \alpha^{(k)}$, $\Delta \varphi^{(k)}$, $\Delta C_L^{*(k)}$ change smaller, at the same time with each change the calculated ratios $\frac{\Delta C_D^{(k)}}{\Delta \alpha^{(k)}}$; $\frac{\Delta C_D^{(k)}}{\Delta \varphi^{(k)}}$; $\frac{\Delta C_D^{(k)}}{\Delta C_L^{*(k)}}$; $\frac{\Delta C_L^{(k)}}{\Delta \alpha^{(k)}}$; $\frac{\Delta C_L^{(k)}}{\Delta \varphi^{(k)}}$; $\frac{\Delta C_L^{(k)}}{\Delta C_L^{*(k)}}$ are relatively stable.

+ $\mathbf{D}^{(k)}$ is projection vector of vector $-\nabla C_D^{(k)}$ on a plane perpendicular to the vector $\nabla C_L^{(k)}$ at the k -th calculation point.

+ C_{Dmin} is coefficient C_D achieve the smallest value corresponding to the solution of the constrained optimization problem $C_L = const$. Call α_{opt} , φ_{opt} , C_{Lopt}^* is the solution of the problem (2.15). Then:

$$C_{Dmin} = C_D(\alpha_{opt}, \varphi_{opt}, C_{Lopt}^*) \quad (2.20)$$

According to the work [8]: the fastest approach to the optimum $C_{Dmin} = f(\alpha_{opt}, \varphi_{opt}, C_{Lopt}^*)$ must be in the direction of the vector $\mathbf{D}^{(k)}$ at the k -th calculation point, while the vector \mathbf{D} is determined as the projection of the anti-gradient $-\nabla C_D$ to the surface $C_L = const$.

Formula determines the vector $\mathbf{D}^{(k)}$ (in matrix form):

$$\mathbf{D}^{(k)} = -\mathbf{P}^{(k)} \nabla C_D^{(k)}; \mathbf{P}^{(k)} = \mathbf{I} - \nabla C_L^{(k)} \frac{\nabla C_L^{T(k)}}{|\nabla C_L^{(k)}|^2} \quad (2.21)$$

Here: \mathbf{I} , \mathbf{P} , respectively, is unit matrix and projection matrix size 3×3 ;

$\nabla C_L^{T(k)}$ is the transpose matrix of the matrix $\nabla C_L^{(k)}$;

$|\nabla C_L^{(k)}|^2$ is square of the modulus of vector $\nabla C_L^{(k)}$.

The numerical optimization algorithm for the coefficient C_D with the constraint $C_L = const$ is shown in Fig. 10:

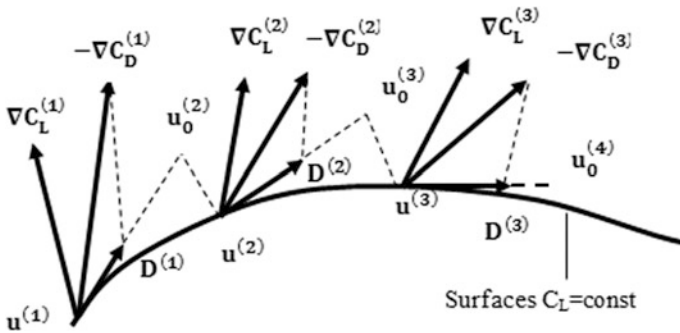


Fig. 10 Numerical algorithm for optimizing coefficient CD have the constraint CL = const

Accordingly, the steps to perform the numerical optimization process are explained as follows: assuming that the initial point is the point 1: $u^{(1)}$; at this point, one computes the gradient vectors $\nabla C_L^{(1)}$, $\nabla C_D^{(1)}$ and the projection vector $D^{(1)}$. Then to make a step $h^{(1)}$ toward the vector $D^{(1)}$ to the point $u_0^{(2)}$. In common case, the point $u_0^{(2)}$ is not on constraint surface, so at this point, one has to adjust the variable (for this problem, it is most convenient to adjust only the angle of attack α) to set the point 2: $u^{(2)}$ on the constraint surface $C_L = const$. The calculation process is repeated with convergent condition when the following signs appear simultaneously:

- Coefficient C_D begins to increase or lift-to-drag ratio K begins to decrease.
- Module of projection vector $|D^{(k)}| \ll |D^{(1)}|$ (much smaller than the value in the first step).
- If the number of iterations is n , then $C_{Dmin} = C_D^{(n-1)}$, $K_{max} = K^{(n-1)}$.

Some notes to choose the step length $|h^{(k)}|$ by numerical method: the step length $|h^{(k)}|$ decides the speed of convergence of optimization process (if selection is not suitable, the algorithm even may not convergence). In particular, each of the points computed by ANSYS software takes time from some dozens of minutes. If the step length is too large, then the coefficients C_D , C_L will go far beyond the optimal point and the constraint surface $C_L = const$; this slows down the convergence speed or even makes the optimization process not to converge. If the step length is too small, of course, the speed of convergence is very slow.

2.2.3 Optimization Results and Comments

The results of optimization of the wing shape are illustrated with the input data as follows:

+ Chord: $b = 0.337$ [m]; span of wing: $L = 1$ [m]; the largest (relative) thickness: $\bar{c}_{max} = 12\%$;

+ Constraint condition: $C_L = C_L^{ht} = 0.3$ (cruise flights with lift coefficient $C_L = 0.3$);

+ Flight speed $V = 30$ [m/s], altitude $H = 0$ [m] ($\rho = 1.225$ [kg/m³]).

Optimization results:

+ $C_{Dmin} = 0.0265$ at the point: $(\alpha, \varphi, C_L^*)_{opt} = (2.8^\circ, 0.4^\circ, 0.3)$;

+ The optimal wing with constraints $C_L = C_L^{ht} = 0.3$ is called *the optimal wing* $C_{Lopt} = 0.3$; (Fig. 11).

Comments:

* The graph $C_D = f(C_L)$ of the optimal wing $C_{Lopt} = 0.3$ and some equivalent classic wings are shown in Figs. 12 and 13:

+ At the high lift coefficients, coefficient C_D of optimal wing $C_{Lopt} = 0.3$ is basically equivalent to the wing have curvature of aerofoil is 4% and were significantly reduces in comparison with the wing with symmetrical aerofoil (Fig. 12). For example, when $C_L = 1.2$: coefficient C_D of optimal wing $C_{Lopt} = 0.3$ and wing with 4% curvature were decreased 12% in comparison with the wing with symmetrical aerofoil.

+ At the small lift coefficients, coefficient C_D of optimal wing $C_{Lopt} = 0.3$ was lower than the wing have curvature of the aerofoil is 4% and higher in comparison with the wing with symmetrical aerofoil (Fig. 13). For example, when $C_L = 0.1$, the coefficient C_D of optimal wing $C_{Lopt} = 0.3$ was reduced by 5% in comparison with the wing with 4% curvature and 4% higher in comparison with the wing with symmetrical aerofoil.

* At the optimal point, added twist angle $\varphi_{opt} = 0.4^\circ$ is not significant. Therefore, the mean surface of the quasi-optimal wing with geometrically twist angle is essentially optimal (that means no need to optimize this parameter) and the optimal

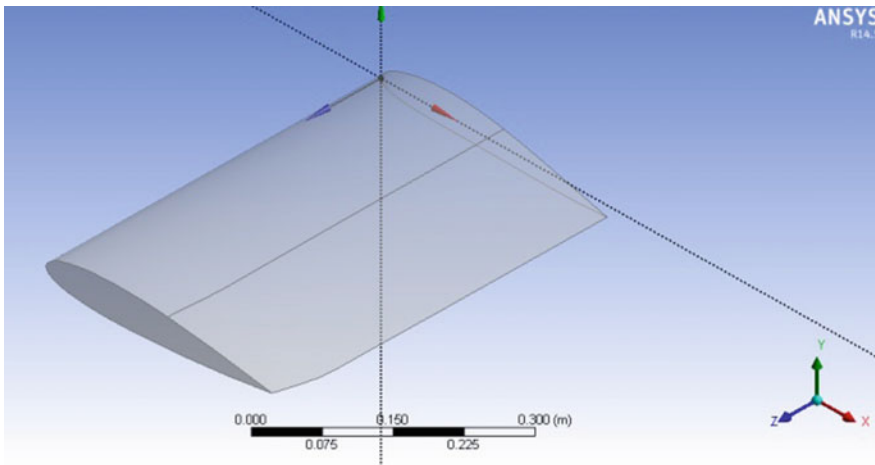


Fig. 11 Optimal half-wing shape $C_{Lopt} = 0.3$

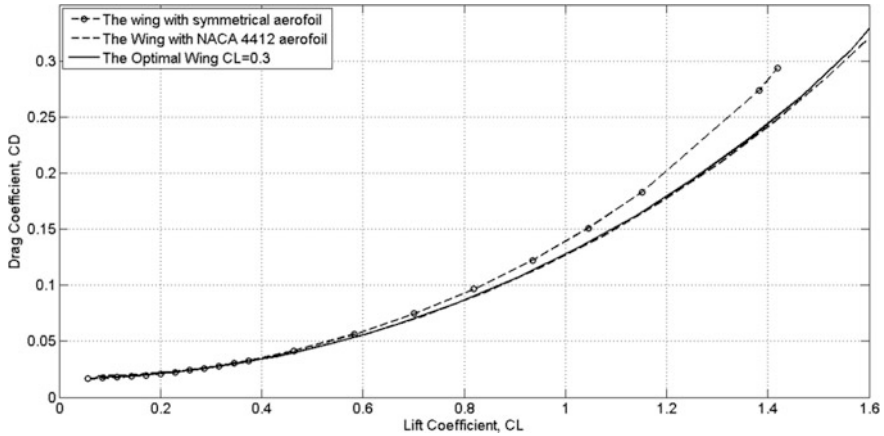


Fig. 12 Graph $K = f(Cy)$ optimal wing $C_{Lopt} = 0.3$ and some equivalent classic wings

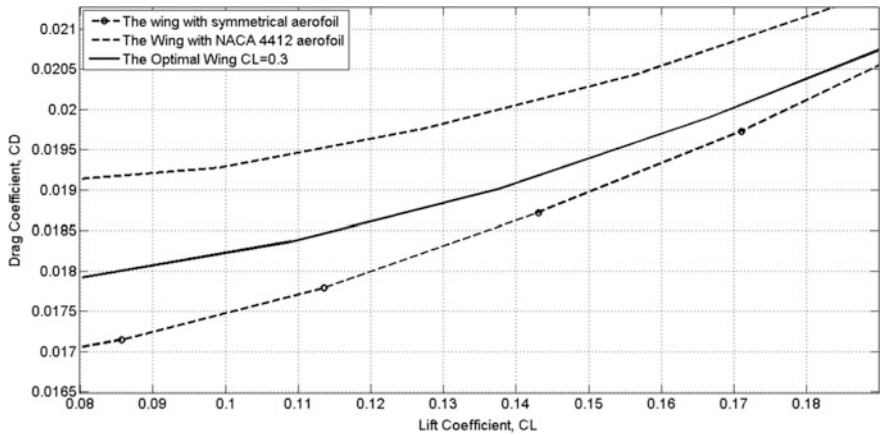


Fig. 13 Graph $K = f(Cy)$ optimal wing $C_{Lopt} = 0.3$ and some equivalent class wings small lift coefficient region

wing shape at cruise flights mode with certain lift coefficient C_L is, in fact, the quasi-optimal wing shape. However, this quasi-optimal wing must have lift coefficient determining mean surface $C_L^* = C_{Lopt}^*$ and to fly at angle of attack $\alpha = \alpha_{opt}$, where C_{Lopt}^* and α_{opt} are the solutions of the optimization problem $C_D \rightarrow C_{Dmin}$, $C_L = C_L^{ht} = const$.

* As well known, a wing with a symmetrical aerofoil have the smallest coefficient C_D when flying with lift coefficient $C_L \rightarrow 0$. Figure 14 shows the quasi-optimal wing shape with lift coefficient determining mean surface $C_L^* = 0$ shows the quasi-optimal wing has “degenerated” into a wing with a symmetrical aerofoil.

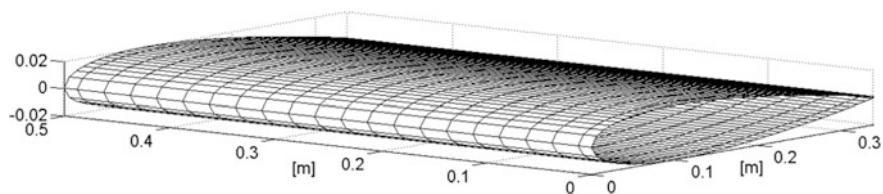


Fig. 14 Quasi-optimal half-wing shape $C_L^* = 0$ is “degenerated” into a wing with symmetrical aerofoil

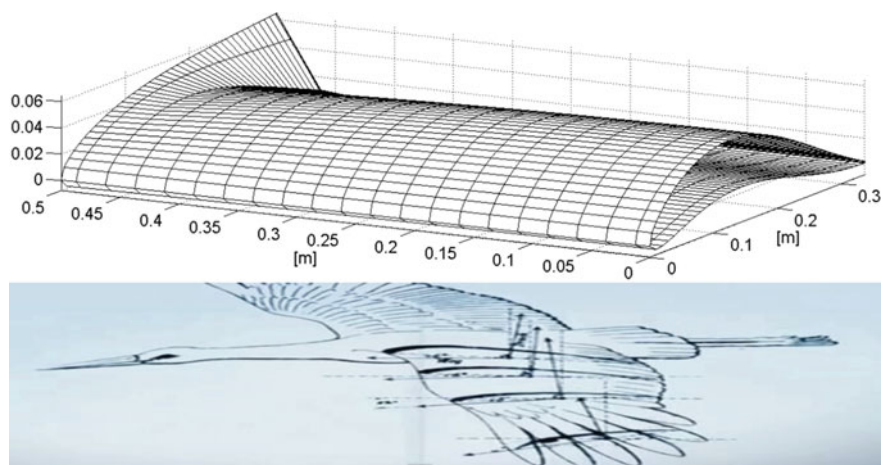


Fig. 15 Comparison of optimal wing and the bird’s wings

* The similarity between the optimal wing and the bird’s wings is as follows (Fig. 15):

- + The mean line of aerofoil at different cross sections (parallel to the symmetry plane) has an increasing curvature from the root to the tip of the wing;
- + The chords of the sections are “twisted” in the direction to decrease the local angle of attack also from the root to the tip of the wing.

During flight at different speeds and altitudes (corresponding to the different lift coefficients), the bird’s wings will change their shape (mostly changes in the mean surface) to adapt to the flight parameters. Thus, the optimal wing partly explains the bird’s wings—the optimization of the nature.

3 Conclusions

The optimal wing allows to “reconcile” the drag coefficient C_D of classic wings with different curvatures or the optimal wing were decreased the drag coefficient at high lift coefficient range but no significant increase the drag coefficient at small lift coefficient range. It leads to less fuel consumptions that allows to get more payload for a given flight time when the *UAV* flies at different lift coefficients.

For *UAV* performing multiple missions (cruise flights with different lift coefficient C_L), the above selection of the optimal wing shape is a suitable choice.

References

1. Lyu Z, Kenway GKW, Martins JRR (2014). Aerodynamic shape optimization investigations of the common research model wing benchmark. Department of Aerospace Engineering, University of Michigan, Ann Arbor, MIAIAA J
2. <http://www.optimenga777.com/en/category/mainpage/>
3. Белоцерковский СМ, Скрипач БК (1975) Аэродинамические производные летательного аппарата и крыла при дозвуковых скоростях. Москва, Наука
4. Прысев Б.Ф. Расчет аэродинамических характеристик неплоского крыла с механизацией и его срединной поверхностью под заданную нагрузку при дозвуковых скоростях. Труды ЦАГИ, вып. 2237, 1984
5. Popovich C, Shapiro N, Epstein B, Peigin S (2013) Massively parallel industry-strength design of aerodynamic wings. Elsevier Procedia Eng 61:292–297
6. Gagnon H, Zingg DW (2016) Euler-equation-based drag minimization of unconventional aircraft configurations. J Aircr 53(5):361–1371
7. Jacobs Eastman N, Ward Kenneth E, Pinkerton Robert M (1933) The Characteristics of 78 related airfoil sections from tests in the variable-Density Wind Tunnel. Langlay Memorial Aeronautical Laboratory, New York
8. Snyman JA (2005) Practical mathematical optimization: an introduction to basic optimization theory and classical and new gradient-based algorithms. Springer Publishing. ISBN 0-387-24348-8
9. Belytschko T, Guo Y, Liu WK, Xiao SP (2000) A unified stability analysis of meshless particle methods. Int J Numer Meth Eng 48:1359–1400

Engineering Optimization Using an Improved Epsilon Differential Evolution with Directional Mutation and Nearest Neighbor Comparison



A. H. Pham, C. T. Vu, D. B. Nguyen and D. T. Tran

Abstract In this paper, an efficient differential evolution (DE) algorithm is presented to solve constrained optimization problem. To skip unnecessary function evaluations, a simple mechanism called nearest neighbor comparison (NNC) is applied. The NNC is a method to prejudge a solution by its nearest point in the search population, so that unpromising solution will be skipped without evaluation. The NNC has been proposed to reduce the number of function evaluations effectively in unconstrained optimization. In this study, the NNC method is proposed for constrained optimization by combining with the ϵ constrained method. Moreover, a simple directional mutation rule is introduced to increase the possibility of creating improved solutions. Both the NNC method and the directional mutation rule do not require additional control parameter for DE, as often found in several modified DE variants. The effectiveness of the proposed constrained DE algorithm, named as ϵ DEdn, is illustrated by solving five benchmark engineering design problems. The results show that the NNC combined with the ϵ constrained method can omit up to fifty percents function evaluations. It is also shown that the direction mutation can increase the convergence rate of the optimization. Comparing with other state-of-the-art DE variants reported in the literature, the proposed DE often gives equal or better results with considerably smaller number of function calls.

Keywords Engineering optimization · Differential evolution · Directional mutation · Nearest neighbor comparison · Epsilon constrained method

A. H. Pham (✉) · C. T. Vu · D. B. Nguyen · D. T. Tran
Department of Structural Mechanics, National University of Civil Engineering,
Hanoi, Vietnam
e-mail: anhph2@nuce.edu.vn

© Springer Nature Singapore Pte Ltd. 2018
H. Nguyen-Xuan et al. (eds.), *Proceedings of the International Conference on Advances in Computational Mechanics 2017*, Lecture Notes in Mechanical Engineering, https://doi.org/10.1007/978-981-10-7149-2_14

201

1 Introduction

Engineering optimization problems arising from modern engineering design process often involve inequality and/or equality constraints. Most of these constrained optimization problems (COPs) are complex and difficult to solve by traditional gradient-based techniques. Meta-heuristic algorithms have received considerable attention and have been successfully applied in many real applications in recent years.

Among different meta-heuristics (MH), differential evolution (DE) [1], a population-based MH, is considered as one of the most efficient algorithms, suitable for various optimization problems from diverse domains of science and technology. The advantage of DE is that it has simple structure, requires few control parameters and highly supports parallel computation. Together with the constraint-handling techniques, DE has been applied to the COPs [2]. However, like many population-based MH, one of the main issues in applying DE is its expensive computation requirement, since DE often needs to evaluate objective function as well as constraints thousand times to get a well acceptable solution.

A simple method, the nearest neighbor comparison, has been proposed to reduce the number of function evaluations effectively [3]. This method uses a nearest neighbor in the search population to judge a new point whether it is worth evaluating, i.e., the function evaluation of a solution is omitted when the fitness of its nearest point in the search population is worse than that of the compared point. The nearest neighbor comparison (NNC) method has been proposed for unconstrained optimization [3].

In this study, the NNC method is proposed to constrained optimization. In order to use the nature of NNC, the ϵ constrained method [4] is applied to handle constraints. The ϵ constrained method can transform algorithms for unconstrained problems into algorithms for constrained problems using the ϵ level comparison that compares search points based on their pair of fitness value and their constraint violation. It has been shown that the application of ϵ constrained method to DE (ϵ DE) could solve constrained problems successfully and stably [5, 6]. The proposed constrained DE in this paper is defined by applying the NNC method to the ϵ level comparison. Thus, it is expected that both the number of fitness evaluations and the number of constraint evaluations can be reduced. Moreover, a simple directional mutation rule based on the order relation of two different points is introduced to increase the possibility of creating improved solutions. The effectiveness of the proposed constrained DE, named as ϵ DE_{dn}, is shown by solving five well-known benchmark engineering design problems and comparing the results with those of ϵ DE and other state-of-the-art DE algorithms.

2 The Epsilon Constrained Method

2.1 Constrained Optimization Problem

We consider the following optimization problem with equality constraints, inequality constraints, and boundary constraints:

$$\begin{aligned}
 &\text{minimize} && f(\mathbf{x}) \\
 &\text{subject to} && g_j(\mathbf{x}) \leq 0, \quad j = 1, \dots, q \\
 & && h_j(\mathbf{x}) = 0, \quad j = 1 + q, \dots, m \\
 & && x_i^l \leq x_i \leq x_i^u, \quad i = 1, \dots, D
 \end{aligned} \tag{1}$$

where \mathbf{x} is a D -dimension vector, x_i is the i -th decision variable of \mathbf{x} , $f(\mathbf{x})$ is an objective function, $g_j(\mathbf{x}) \leq 0$ and $h_j(\mathbf{x}) = 0$ are q inequality constraints and $m - q$ equality constraints, respectively. The functions f , g_i , and h_i are real-valued functions, can be linear or nonlinear. Values x_i^l and x_i^u are the lower bound and upper bound of x_i , respectively.

2.2 The ϵ Constrained Method

In the ϵ constrained method, the constraint violation is defined by the maximum of all constraints (Eq. (2)) or the sum of all constraints (Eq. (3)):

$$\phi(\mathbf{x}) = \max \left\{ \max_j \{0, g_j(\mathbf{x})\}, \max_j |h_j(\mathbf{x})| \right\} \tag{2}$$

$$\phi(\mathbf{x}) = \sum_j \|\max\{0, g_j(\mathbf{x})\}\|^p + \sum_j \|h_j(\mathbf{x})\|^p \tag{3}$$

where p is a positive number. The ϵ constrained method uses the ϵ level comparison that is defined as an order relation on a pair of objective function value and constraint violation $(f(\mathbf{x}), \phi(\mathbf{x}))$. Let f_1 (f_2) and ϕ_1 (ϕ_2) be the function value and the constraint violation at a point \mathbf{x}_1 (\mathbf{x}_2), respectively. Then, for any $\epsilon \geq 0$, ϵ level comparisons $<_\epsilon$ and \leq_ϵ between (f_1, ϕ_1) and (f_2, ϕ_2) are defined as follows:

$$(f_1, \phi_1) <_\epsilon (f_2, \phi_2) \Leftrightarrow \begin{cases} f_1 < f_2, & \text{if } \phi_1, \phi_2 < \epsilon \text{ or } \phi_1 = \phi_2 \\ \phi_1 < \phi_2, & \text{otherwise} \end{cases} \tag{4}$$

$$(f_1, \phi_1) \leq_\epsilon (f_2, \phi_2) \Leftrightarrow \begin{cases} f_1 \leq f_2, & \text{if } \phi_1, \phi_2 \leq \epsilon \text{ or } \phi_1 = \phi_2 \\ \phi_1 < \phi_2, & \text{otherwise} \end{cases} \tag{5}$$

When $\varepsilon = \infty$, the ε level comparisons $<_\varepsilon$ and \leq_ε become the ordinary comparisons $<$ and \leq between function values. When $\varepsilon = 0$, $<_\varepsilon$ and \leq_ε are equivalent to the lexicographic orders in which the constraint violation $\phi(\mathbf{x})$ precedes the function value $f(\mathbf{x})$. Using the ε constrained method, a constrained optimization problem is converted into an unconstrained one by replacing the ordinary comparison in direct search methods with the ε level comparison.

3 Improved Epsilon Differential Evolution

3.1 Basic Differential Evolution

Differential evolution (DE), which was introduced by Storn and Price [1], is a population-based optimizer. DE uses a population of NP candidate vectors $\mathbf{x}_k (k = 1, 2, \dots, NP)$ (called individuals) of the design variables. The population is then restructured by survival individuals evolutionally. The basic steps of DE are as follows: initialization, mutation, crossover, and selection.

Initialization

First, an initial population is randomly sampled from the solution space as Eq. (6),

$$x_{k,i} = x_i^l + \text{rand}[0, 1] \times (x_i^u - x_i^l), \quad i = 1, 2, \dots, D \quad (6)$$

where x_i^l and x_i^u are the lower and the upper bounds of x_i , respectively; D is the number of design variables of the optimization problem; $\text{rand}[0, 1]$ is a uniformly distributed random real value in the range $[0, 1]$.

Mutation

For each target vector \mathbf{x}_k , a mutant vector \mathbf{y} is first generated. Various mutation strategies can be employed to create the mutant vector. The most popular one in classical DE is the so-called ‘DE/rand/1,’ where the mutant vector is determined as:

$$\mathbf{y} = \mathbf{x}_{r_1} + F(\mathbf{x}_{r_2} - \mathbf{x}_{r_3}) \quad (7)$$

where \mathbf{x}_{r_1} , \mathbf{x}_{r_2} , \mathbf{x}_{r_3} are three mutually different individuals randomly selected from the current population, i.e., $r_1 \neq r_2 \neq r_3 \neq k$; F is a scaling factor, a real and constant factor usually chosen in the interval $[0, 1]$ which controls the amplification of the differential variation. In Eq. (7), \mathbf{x}_{r_1} is called the base vector, while the others are called the difference vectors.

Crossover

Crossover is introduced to exchange the information of the mutant vector with the target vector \mathbf{x}_k , creating a trial vector \mathbf{z} with its elements determined by:

$$z_i = \begin{cases} y_i, & \text{if } (\text{rand}[0, 1] \leq Cr) \text{ or } (r = i) \\ x_{k,i}, & \text{otherwise} \end{cases} \quad (8)$$

where $i = 1, 2, \dots, D$, $\text{rand}[0, 1]$ is a uniformly distributed random number in $[0, 1]$; r is a randomly chosen integer in the interval $[1, D]$ to ensure that the trial vector has at least one element from the mutant vector; Cr is the crossover rate predefined in $[0, 1]$, which control the fraction of elements copied from the mutant vector.

Selection

The trial vector \mathbf{z} is compared with the target vector \mathbf{x}_k of the current population, and the better one will be selected as member for the population of next generation.

3.2 Directional Mutation Rule

In the mutation operators of Eq. (7), a random variation is derived from the difference of two randomly selected different vectors. Consequently, it has no bias to any special search directions. To take advantage of guiding information of the population, the scaled differential variation is multiplied by a ‘directed’ factor d , i.e.,

$$\mathbf{y} = \mathbf{x}_{r_1} + d \times F(\mathbf{x}_{r_2} - \mathbf{x}_{r_3}) \quad (9)$$

where d takes either value 1 or -1 depending on the order relation between the difference vectors \mathbf{x}_{r_2} and \mathbf{x}_{r_3} . Specifically, d is determined as

$$d = \begin{cases} 1, & \text{if } \mathbf{x}_{r_2} \text{ is better than } \mathbf{x}_{r_3} \\ -1, & \text{otherwise} \end{cases} \quad (10)$$

This kind of directional mutation has the same concept of the well-known opposition-based method presented for improving DE performance in the literature [7]. This rule guarantees that the differential variation is oriented toward a better vector, thus increasing the possibility of creating an improved solution.

3.3 Nearest Neighbor Comparison

Basic DE calls for function evaluation for all trial vectors and many of them do not survive in the selection phase. Thus, many evaluations are useless. It is desirable that trial vectors that might produce no better fitness should not be evaluated. It is particularly important in problems where function evaluation is costly. A method

called ‘Nearest neighbor comparison’ (NNC) is a recently developed method by Pham [3], which can effectively reduce the number of function evaluations for various unconstrained benchmark optimization problems. In this study, the NNC method is incorporated to the ε constrained method to reduce unnecessary function evaluations in solving constrained optimization problem. The method is briefly described as follows. For more details of NNC, readers can refer to Ref. [3].

Firstly, for each trial vector \mathbf{z} created, a vector \mathbf{x}_n ($n \in [1, NP]$) in the current population which is closest to \mathbf{z} is sought using normalized Euclidean distance measure:

$$d(\mathbf{x}, \mathbf{z}) = \sqrt{\sum_{i=1}^D \left(\frac{x_i - z_i}{x_i^{\max} - x_i^{\min}} \right)^2} \quad (11)$$

where $d(\mathbf{x}, \mathbf{z})$ is the distance measure between two vectors \mathbf{x} and \mathbf{z} ; x_i^{\max} and x_i^{\min} are the current maximum and minimum values of the corresponding design variable x_i of all solutions in the population. Thus, \mathbf{x}_n is the vector in the current population with smallest distance to the trial vector \mathbf{z} .

Secondly, \mathbf{x}_n is compared with the target vector \mathbf{x}_k . If \mathbf{x}_n is worse than \mathbf{x}_k , the trial vector is likely worse than the target vector and it will be skipped. Otherwise, the trial vector is evaluated for further selection decision. In this way, several unpromising trial vectors are omitted, and useless function evaluations can be reduced during the searching process.

3.4 The Proposed ε Constrained DE

The proposed ε constrained DE has the same steps as the classical DE, i.e., it consists the initialization, mutation, crossover, and selection. The modifications are made in the mutation step with the use of ‘directed’ value d (Eq. (9)), and in the selection step with the application of NNC method using the ε level comparison. The NNC selection can be written as follows:

If $(f_n, \phi_n) \leq_\varepsilon (f_k, \phi_k)$
Then Calculate $f(\mathbf{z}), \phi(\mathbf{z})$;
If $(f(\mathbf{z}), \phi(\mathbf{z})) \leq_\varepsilon (f_k, \phi_k)$
Then $\mathbf{x}_k = \mathbf{z}; f_k = f(\mathbf{z}); \phi_k = \phi(\mathbf{z})$;
End
End

It is noted that both \mathbf{x}_n and \mathbf{x}_k are known vectors in the current population, i.e., the objective values and constraint violations (f_n, ϕ_n) and (f_k, ϕ_k) are already calculated and stored in the previous generation.

Obviously, the NNC method requires computational cost for searching nearest vectors. Nevertheless, this additional cost is normally negligible compared with the overall computational cost taken to solve the optimization problem. It is assumed that the computational cost for function evaluation is so large, and the size of the population is so small that the time taken for the detection of nearest vectors will be comparatively small.

In addition, the judgment becomes less reasonable if the trial solution and its nearest neighbor are not close enough, especially when the search space is large. If the nearest neighbor comparison is not efficient, the algorithm may reject good trial solutions (solutions those are actually better than the target one). Thus, the size of the population plays an important role on the effectiveness of the NNC. A big population can help reducing wrong judgments, however, lowers the convergence speed. For the considered examples in this study, the population size of 40 is found to be adequate for balancing between efficiency and velocity of the algorithm.

The proposed DE algorithm, named as ϵ DEdn, requires no additional parameter setting. The pseudo-code of ϵ DEdn is shown in Algorithm 1. In the Algorithm 1, two termination criteria are employed, which are the number of function evaluations (FE) and the deviation (δ) of the objective function value. Here, δ is determined as in [8].

$$\delta = |f_{\text{mean}}/f_{\text{min}} - 1| \quad (12)$$

where f_{min} is the objective function value of the best individual, and f_{mean} is the mean objective function value of the whole population.

The optimization process will stop when FE exceeds a maximum number of evaluations, FE_{max} (assume that we have a computational budget of FE_{max} function evaluations), or when δ is less than a tolerance value Tol .

Algorithm 1: The pseudo-code of ϵ DEdn

```

Define NP, F, Cr, FEmax, Tol, fitness function, constraints, and design variable bounds;
Generate initial population and evaluate fitness f and constraint violation ϕ for each individual;
FE=NP; t=1;
while (FE < FEmax) and (delta > Tol) do
  for k = 1 to NP do
    Choose random index r from {1,2,...,D};
    Select randomly three indices r1≠r2≠r3≠k;
    Set directed value d according to Eq. (10)
    for i = 1 to D do
      Mutation and Crossover according to Eqs. (9) and (8)
    end for
    Search for the nearest neighbor xn of z;
    Apply the NNC selection;
  end for
  delta = |fmean/fmin - 1|
  t = t+1;
end while

```

4 Solving Engineering Optimization Problems

4.1 Test Problems and Experimental Conditions

In this section, five benchmark engineering design problems are solved to test the performance of ϵ DEdn. The problems are as follows: the welded beam design [9], the tension/compression spring design [10], the pressure vessel design [11], speed reducer design [12], and the three-bar plane truss sizing [9]. Due to space limitation, the formulations of these problems are omitted here.

The parameter setting for the ϵ level comparison is as follows. The constraint violation ϕ is given by the sum of all constraints ($p = 1$) in Eq. (3). The ϵ level is controlled according to Eq. (13) [5]. The ϵ level is updated until the number of iterations reaches the control generation T_c . After the number of iterations exceeds T_c , the ϵ level is set to 0 to obtain feasible solutions.

$$\epsilon(t) = \begin{cases} \epsilon(0) \left(1 - \frac{t}{T_c}\right)^p & \text{for } t \leq T_c \\ 0 & \text{for } t > T_c \end{cases} \quad (13)$$

where $\epsilon(0) = \phi(\mathbf{x}_\theta)$, \mathbf{x}_θ is top θ -individual in the initial population and $\theta = 0.2NP$, p is a parameter to control the speed of reducing relaxation of constraints and $p = 5$.

For each test problem, three algorithms are first examined, which are the epsilon constrained differential evolution (ϵ DE), the epsilon constrained differential evolution with directional mutation (ϵ DEd), and the epsilon constrained differential evolution with directional mutation, and NNC method (ϵ DEdn). Then, the proposed ϵ DEdn is compared with some state-of-the-art DE variants found in the literature. To obtain statistical results, 50 independent runs are carried out for each test case.

To evaluate the performance of different algorithms, beside the accuracy of the search results, the number of function evaluation (FE) is also used as a performance measure. The number of function evaluations is a reasonable measurement criterion for measuring different algorithms as different algorithms often have different computational complexity. Thus, the following measurements are employed to evaluate the performance:

- Best function value (Best);
- Mean of function values (Mean);
- Standard deviations of function values (SD);
- Worst function value (Worst); and
- Average function evaluations (FE).

In the first set of experiments, the algorithms ϵ DE, ϵ DEd, and ϵ DEdn are compared based on the same stop condition $\delta \geq Tol = 10^{-6}$. In the second set of experiments, the termination criterion for ϵ DEdn is as follows: $FE \geq FE_{\max}$, in which $FE_{\max} = 10,000$ for the welded beam problem, the tension/compression spring problem, the pressure vessel problem; $FE_{\max} = 15,000$ for the speed reducer problem; and $FE_{\max} = 2000$ for the three-bar truss sizing problem. These values of

Table 1 Parameter setting for DE

	Welded beam	Spring	Pressure vessel	Speed reducer	Three-bar truss
NP	40	40	40	40	20
F	0.5	0.8	0.8	0.5	0.8
Cr	0.9	0.9	0.9	0.7	0.9

FE_{max} are chosen to be equal or less than those of the other compared algorithm reported in the literature.

The binary crossover and random mutation with one pair of individuals (DE/rand/1/bin) are adopted as the base algorithm. The parameters of DE are given in Table 1. All codes are implemented in MATLAB R2012a and executed on a personal computer with an Intel CPU Core i3 2.3 GHz and 2 GB RAM.

4.2 Experimental Results and Discussion

4.2.1 The Welded Beam Design Problem

Figure 1 plots the average convergence curves of best objective function values over the number of function evaluations obtained by ϵ DE, ϵ DEd, and ϵ DEdn. Clearly, the ϵ DEdn converges faster than ϵ DE and ϵ DEd. The ϵ DEd is faster than ϵ DE in the early iterations.

The statistical results in 50 runs for ϵ DE, ϵ DEd, and ϵ DEdn, are given in Table 2. It is shown that the results of ϵ DEdn and ϵ DEd are similar, and better than those of ϵ DE in terms of the mean, the worst and the standard deviation values. Especially, on average ϵ DEdn can reduce about half of the number of function evaluations in comparison with ϵ DE and ϵ DEd.

Fig. 1 Convergence graphs of welded beam problem

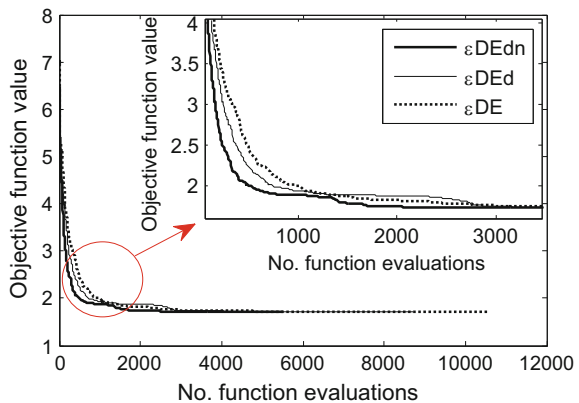


Table 2 Optimization results for welded beam problem

	ϵ DE	ϵ DEd	ϵ DEdn
Best	1.724852784	1.724852702	1.724852958
Mean	1.724854486	1.724853617	1.724853991
Worst	1.724857335	1.724854977	1.724856338
SD	1.1363E-06	5.6288E-07	8.2970E-07
Average FE	8893	7903	4507

Table 3 Comparison with other DE algorithms on welded beam problem

Method	Best	Mean	Worst	SD	FE
ϵ DEdn	1.724852309	1.724852309	1.724852309	6.04E-15	10,000
ϵ DEdn	1.724852309	1.724852309	1.724852309	3.21E-12	8000
COMDE [13]	1.724852309	1.724852309	1.724852309	1.60E-12	20,000
rank-iMDDE [14]	1.724852309	1.724852309	1.724852309	7.71E-11	15,000
NDE [15]	1.724852309	1.724852309	1.724852309	3.73E-12	8000

Table 3 compares the results obtained by the proposed ϵ DEdn with those of some state-of-the-art DE variants found in literature, including constrained modified differential evolution (COMDE) [13], improved constrained differential evolution (rank-iMDDE) [14] and novel differential evolution (NDE) [15]. A result in boldface means a better (or best) solution obtained. From the results in Table 3, we can see that ϵ DEdn obtains the optimal solution in all runs. Moreover, ϵ DEdn gives smallest standard deviation values compared with other DE algorithms. The number of actual function evaluations by ϵ DEdn is even much smaller than the other algorithms, except NDE.

4.2.2 The Tension/Compression Spring Design Problem

Figure 2 shows the best function values corresponding to ϵ DE, ϵ DEd, and ϵ DEdn over the number of function evaluations. The figure shows that ϵ DEd is faster than ϵ DE, and ϵ DEdn is the fastest algorithm. The statistical results in Table 4 indicate that, with about one-half of function calls, ϵ DEdn can obtained solution with similar quality as those obtained by ϵ DE.

The optimization results of ϵ DEdn are compared with the results obtained by other DE algorithms in Table 5. We can observe that ϵ DEdn with about one-half of function evaluations provides as good results as other algorithms, such as ϵ DE-LS (improved local search based epsilon differential evolution) [16] and ϵ DE-PCGA (ϵ constrained differential evolution with pre-estimated comparison using gradient-based approximation) [17], and it is better than rank-iMDDE, COMDE, and NDE in terms of both solution quality and number of function calls. It should be noted that ϵ DE-PCGA is an algorithm which applied the same function reduction

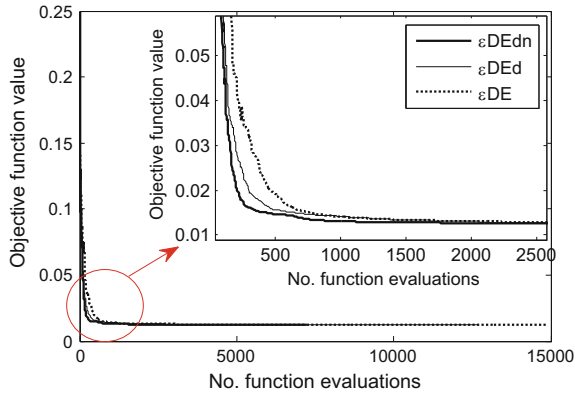


Fig. 2 Convergence graphs of tension/compression problem

Table 4 Optimization results for tension/compression spring problem

	εDE	εDEd	εDEdn
Best	0.012665233	0.012665233	0.012665233
Mean	0.012665238	0.012665236	0.012665239
Worst	0.012665247	0.012665244	0.012665284
SD	2.6793E-09	2.1439E-09	8.0297E-09
Average FE	12664	10561	6057

Table 5 Comparison with other DE algorithms on tension/compression spring problem

Method	Best	Mean	Worst	SD	FE
εDEdn	0.012665233	0.012665233	0.012665233	3.01E-11	10,000
COMDE [13]	0.012665233	0.012667168	0.012676809	3.09E-06	24,000
rank-iMDDE [14]	0.012665233	0.012665264	0.01266765	2.45E-07	19,565
εDE-LS [16]	0.012665233	0.012665233	0.012665233	5.01E-14	20,000
εDE-PCGA [17]	0.012665233	0.012665233	0.012665235	4.43E-10	20,000
NDE [15]	0.012665232	0.012668899	0.012687092	5.38E-06	24,000

strategy, i.e., using prejudgement of a trial solution before evaluating it. However, εDE-PCGA employed gradient-based approximation to estimate a trial solution, while the proposed εDEdn used the nearest neighbor solution to approximate a trial solution.

4.2.3 Pressure Vessel Design Problem

For this problem, εDEdn is the fastest algorithm, and εDEd is faster than εDE, as clearly seen from Fig. 3. Experimental results on the problem are shown in Table 6. Clearly, εDEdn requires less function evaluations than εDE and εDEd. Comparing

Fig. 3 Convergence graphs of pressure vessel problem

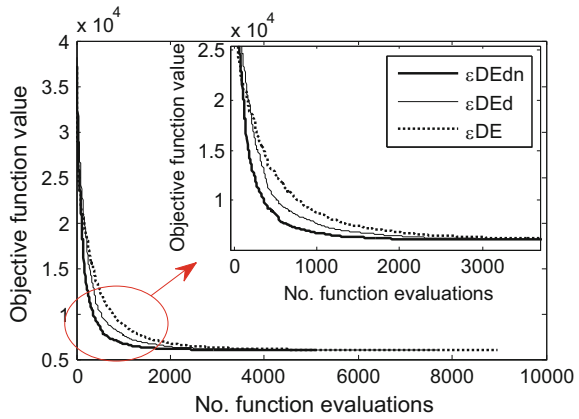


Table 6 Optimization results for pressure vessel problem

	ϵ DE	ϵ DEd	ϵ DEdn
Best	6059.714468	6059.714388	6059.714629
Mean	6060.332153	6059.715170	6059.715958
Worst	6090.527144	6059.716300	6059.717720
SD	4.357363963	0.000495493	0.000788475
Average FE	7982	6932	4478

with ϵ DE, ϵ DEdn can omit more than 40% evaluations. It also found that ϵ DE converges to a local minimum once. Comparing with other DE algorithms (Table 7), ϵ DEdn provides equal or better results. With respect to the number of function evaluations, ϵ DEdn is superior to the other algorithms.

Table 7 Comparison with other state-of-the-art algorithms on pressure vessel problem

Method	Best	Mean	Worst	SD	FE
ϵ DEdn	6059.714335	6059.714335	6059.714335	9.46E-13	10,000
COMDE [13]	6059.714335	6059.714335	6059.714335	3.62E-10	30,000
rank-iMDDE [14]	6059.714335	6059.714335	6059.714335	7.57E-07	15,000
ϵ DE-LS [16]	6059.7143	6059.7143	6059.7143	3.4030E-13	20,000
ϵ DE-PCGA [17]	6059.714335	6059.714335	6059.714335	3.96E-09	20,000
NDE [15]	6059.714335	6059.714335	6059.714335	4.56E-07	20,000

4.2.4 Speed Reducer Design Problem

Figure 4 illustrates the convergence histories of the best objective function. Clearly, ϵ DEd is much faster than ϵ DE, and ϵ DEdn is fastest. The statistical results are given in Table 8. The results show that ϵ DEdn can omit more than 30% function evaluations. Comparing with other DE variants, the ϵ DEdn gives equal or better results with considerably smaller number of function calls (see in Table 9).

Fig. 4 Convergence graphs of speed reducer problem

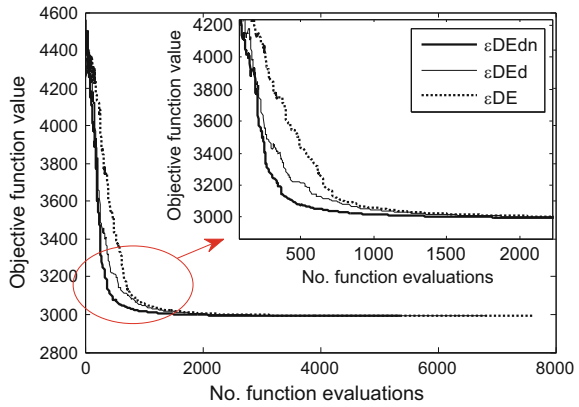


Table 8 Optimization results for speed reducer design problem

	ϵ DE	ϵ DEd	ϵ DEdn
Best	2994.472198	2994.472482	2994.473424
Mean	2994.475645	2994.474308	2994.475647
Worst	2994.480189	2994.477360	2994.478818
SD	0.001615587	0.001278890	0.001266380
Average FE	7100	6311	4917

Table 9 Comparison with other state-of-the-art algorithms on speed reducer problem

Method	Best	Mean	Worst	SD	FE
ϵ DEdn	2994.4710661	2994.4710661	2994.4710661	3.87E-12	15,000
COMDE [13]	2994.4710661	2994.4710661	2994.4710661	1.54E-12	21,000
rank-iMDDE [14]	2994.471066	2994.471066	2994.471066	7.93E-13	19,920
ϵ DE-LS [16]	2994.471071	2994.471098	2994.471137	1.70E-05	21,000
ϵ DE-PCGA [17]	2994.4710661	2994.471066	2994.4710661	1.16E-10	20,000
NDE [15]	2994.4710661	2994.4710661	2994.4710661	4.17E-12	18,000

4.2.5 Three-Bar Truss Sizing Problem

The convergence curves of the best objective function over the function evaluations are depicted in Fig. 5. We can see from Fig. 5 that ϵ DDEd is faster than ϵ DE, and ϵ DDEdn is the fastest algorithm. The optimization results given in Table 10 show that all ϵ DE, ϵ DDEd, and ϵ DDEdn provide equally good results. However, ϵ DDEdn uses only about 50% function evaluations comparing with ϵ DE. For this problem, ϵ DDEdn is superior to the other DE variants in term of function evaluations required to obtain an optimal solution (Table 11).

Fig. 5 Convergence graphs of three-bar truss problem

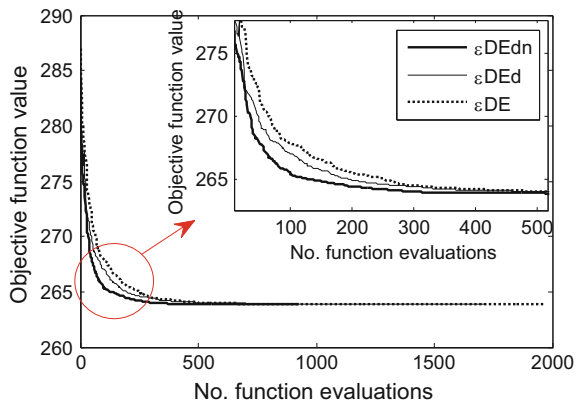


Table 10 Optimization results for three-bar truss problem

	ϵ DE	ϵ DDEd	ϵ DDEdn
Best	263.8958444	263.8958453	263.8958456
Mean	263.8959041	263.8958743	263.8958901
Worst	263.8961593	263.8959373	263.8960654
SD	6.8847E-05	1.9603E-05	4.1248E-05
Average FE	1524	1377	773

Table 11 Comparison with other state-of-the-art algorithms on three-bar truss problem

Method	Best	Mean	Worst	SD	FE
ϵ DDEdn	263.8958434	263.8958434	263.8958434	2.44E-13	2000
COMDE [13]	263.8958434	263.8958434	263.8958434	5.34E-13	7000
rank-iMDDE [14]	263.8958434	263.8958434	263.8958434	0.00E + 00	4920
ϵ DE-LS [16]	263.8958434	263.8958434	263.8958434	2.3206E-14	15,000
ϵ DE-PCGA [17]	263.89584	263.89584	263.89584	2.1268E-14	15,000
NDE [15]	263.8958434	263.8958434	263.8958434	0.00E + 00	4000

5 Conclusion

This paper presented a new constrained differential evolution, ϵ DEdn, for solving engineering optimization problems. The new algorithm combines differential evolution, the nearest neighbor comparison, and the ϵ constrained method. It is enhanced further with a simple directional mutation rule. The performance of ϵ DEdn was evaluated by five widely used benchmark engineering design problems. It was observed that ϵ DEdn reduced the evaluations of the constraints and objective function up to 50% comparing with ϵ DE. With lower function evaluation requirement, ϵ DEdn is also very competitive when comparing with other DE algorithms. Therefore, the ϵ DEdn can solve constrained engineering optimization problems very effectively, especially for the problems with expensive function evaluation.

References

1. Storn R, Price K (1997) Differential evolution—a simple and efficient heuristic for global optimization over continuous spaces. *J Glob Optim* 11(4):341–359
2. Storn R (1999) System design by constraint adaptation and differential evolution. *IEEE Trans Evol Comput* 3(1):22–34
3. Pham HA (2015) Reduction of function evaluation in differential evolution using nearest neighbor comparison. *Vietnam J Comput Sci* 2(2):121–131
4. Takahama T, Sakai S, Iwane N (2006) Solving nonlinear constrained optimization problems by the ϵ constrained differential evolution. In: *Proceedings of the 2006 IEEE conference on systems, man, and cybernetics*, vol 3, 2322–2327
5. Takahama T, Sakai S (2006) Constrained optimization by the ϵ constrained differential evolution with gradient-based mutation and feasible elites. In: *Proceedings of the 2006 IEEE congress on evolutionary computation*, pp 308–315
6. Takahama T, Sakai S (2010) Constrained optimization by the ϵ constrained differential evolution with an archive and gradient-based mutation. In: *Proceedings of the 2010 IEEE world congress on evolutionary computation*, pp 1680–1688
7. Rahnamayan S, Tizhoosh HR, Salama MM (2008) Opposition-based differential evolution. *IEEE Trans Evol Comput* 12(1):64–79
8. Ho-Huu V, Nguyen-Thoi T, Vo-Duy T, Nguyen-Trang T (2016) An adaptive elitist differential evolution for optimization of truss structures with discrete design variables. *Comput Struct* 165:59–75
9. Rao SS (1996) *Engineering optimization*, 3rd edn. Wiley, New York
10. Arora J (1989) *Introduction to optimum design*. McGrawHill
11. Sandgren E (1990) Nonlinear integer and discrete programming in mechanical design optimization. *J Mech Des* 112(2):223–229
12. Golinski J (1974) An adaptive optimization system applied to machine synthesis. *Mech Mach Theory* 8(4):419–436
13. Mohamed AW, Sabry HZ (2012) Constrained optimization based on modified differential evolution algorithm. *Inf Sci* 194:171–208
14. Gong W, Cai Z, Liang D (2014) Engineering optimization by means of an improved constrained differential evolution. *Comput Methods Appl Mech Eng* 268:884–904

15. Mohamed AW (2017) A novel differential evolution algorithm for solving constrained engineering optimization problems. *J Intell Manuf* 1–34
16. Yi W, Zhou Y, Gao L, Li X, Zhang C (2016) Engineering design optimization using an improved local search based epsilon differential evolution algorithm. *J Intell Manuf* 1–22
17. Yi W, Li X, Gao L, Zhou Y, Huang J (2016) ϵ constrained differential evolution with pre-estimated comparison using gradient-based approximation for constrained optimization problems. *Expert Syst Appl* 44:37–49

Optimization of the Longitudinal Cooling Fin by Levenberg–Marquardt Method



Q. Nguyen, S. Nguyen-Hoai, T. Chuong-Thiet and T. Lam-Phat

Abstract The optimization of longitudinal cooling fin by using Levenberg–Marquardt method (LMM) is implemented in this paper. The fin profile is constructed by Bezier curve, and the control points of the Bezier curve are considered the optimization variables. Furthermore, a “volume updating” mechanism was introduced into LMM to obtain the minimum volume of the optimal fin. To demonstrate the proposed method, two cases with the various conditions of the longitudinal cooling fin design problems are examined and the geometry parameters of optimal fin from the proposed method will be compared with the published optimal results. From the obtained results, it can be declared that LMM can be utilized efficiently to determine the minimum volume of the longitudinal cooling fin.

Keywords Shape optimization • Levenberg–Marquardt method
Fin problem

1 Introduction

In automobile engine, heat devices, and electronics devices, fins are important equipment to enhance the rate of the heat transfer between the devices and the surrounding air. However, in many practical applications, the volume (mass) of the

Q. Nguyen (✉)

Department of Engineering Technology, Pham Van Dong University, Quảng Ngãi, Vietnam
e-mail: nquan@pdu.edu.vn

S. Nguyen-Hoai (✉) · T. Chuong-Thiet · T. Lam-Phat

GACES, HCMC University of Technology and Education, Ho Chi Minh City, Vietnam
e-mail: sonnh@hcmute.edu.vn

T. Chuong-Thiet

e-mail: chuongthiettu@gmail.com

T. Lam-Phat

e-mail: thuanlp@hcmute.edu.vn

© Springer Nature Singapore Pte Ltd. 2018

H. Nguyen-Xuan et al. (eds.), *Proceedings of the International Conference on Advances in Computational Mechanics 2017*, Lecture Notes in Mechanical Engineering, https://doi.org/10.1007/978-981-10-7149-2_15

system can be increased when the fins are used. Thus, the optimization of the fin is essential and is interested by many researchers in the past few years [1].

One of the approaches for the fin optimization is that the fin shape needs to be obtained to minimize its volume for a known transfer rate. In this approach, the optimization fin with the minimum volume is a parabolic profile and this was proven firstly by Schmidt [2]. After that, Duffin [3] evaluated again this result by performing some powerful formulations. In another research, Natarajan and Shenoy [4] optimized the profiles of the convection pin fin with an assumption of the variable convection heat transfer coefficient, $h = 1/D^n$. The results archived from Ref. [4] presented that Schmidt's results still correct for the optimal fin with the variable convection heat transfer coefficient. Nevertheless, these optimum results by analytical analysis are only obtained under the assumptions of the constant thermal parameters and the power law of the convection heat transfer coefficient.

For the optimization of the nonlinear fin problem with non-constant thermal properties, some scientists utilized the numerical method and an optimization algorithm to deal with. For instance, the finite element method and Genetic algorithm (GA) were used in Fabbri [5] and Copiello and Fabbri [6] to optimize the longitudinal fin with polynomial shape. Azarkish et al. [7] optimized the longitudinal fin with a given volume to find out the maximum heat loss in one-dimensional model by using the finite volume method and GA. The obtained results in [5–7] showed that GA can be utilized for solving the nonlinear fin optimization problems. However, GA is adaptive heuristic search algorithm known as non-gradient-based method and thus has the high computational cost. To save the computational cost, some researchers used the gradient-based method to deal with the fin optimization problem. For example, Bobaru and Rachakonda [8] used sequential quadratic programming to optimize the two-dimensional fin profile and Huang and Hsiao [9] used conjugate gradient method to find out the optimal shape of the spine and longitudinal fins. Recently, Nguyen and Yang [10] used the modified Newton–Raphson method to minimize the volume of the longitudinal fin with the parabolic shape which built by B-spline and Bezier curve. The results in [10] also showed that Bezier curve with three control points can be used to determine the minimum volume of longitudinal fin for the linear or nonlinear fin design problems.

In this work, we continue to examine the problem in Ref. [10] by another method. In particularly, we use Levenberg–Marquardt method (LMM) to determine the minimum volume of the general fin design problems. LMM is known as the damped least-squares method and is more robust than Newton–Raphson method for solving the nonlinear problem as the general longitudinal cooling fin design problem as in Ref. [10]. In this work, the governed heat transfer equation of the fin problem is nonlinear with the presence of temperature-dependent convective heat transfer coefficient and emissivity coefficient. Thus, the finite element method is applied to solve this equation. On the other hand, the fin shape is constructed by Bezier curve with three control points as [10]. LMM is used to find the optimal locations of these control points by minimizing an appropriate function representation. Furthermore, to obtain the minimum volume of the fin, a mechanism “volume updating” is also introduced to LMM algorithm.

2 Problem Statement

In general, a longitudinal fin model with the symmetric profile built by Bezier curve is considered as Fig. 1. In the steady state condition, the general heat transfer equation of the two-dimensional fin problem without internal heat source takes on the following forms:

$$\frac{\partial}{\partial x} \left(k \frac{\partial T}{\partial x} \right) + \frac{\partial}{\partial y} \left(k \frac{\partial T}{\partial y} \right) = 0 \text{ in domain of fin } (\Omega) \tag{1}$$

$$-kA_b \frac{\partial T}{\partial x} = q_{flow} \text{ at fin base } (\Gamma_0) \tag{2}$$

$$-k \left(\frac{\partial T}{\partial x} + \frac{\partial T}{\partial y} \right) \cdot \mathbf{n} = h(T - T_\infty) + \varepsilon\sigma(T^4 - T_{sur}^4) \text{ at convective surface } (\Gamma_1) \tag{3}$$

$$k \frac{\partial T}{\partial y} = 0 \text{ at symmetric of fin } (\Gamma_2) \tag{4}$$

where T is the temperature field over the domain of fin (domain Ω), with the fin cross-sectional area, A_b , at the base and the inward total heat loss at the base (boundary Γ_0) denoted by q_{flow} , k is the thermal conductivity, h is the convection heat transfer coefficient (boundary Γ_1), ε is emissivity coefficient, σ is Stefan-Boltzmann constant, T_∞ and T_{sur} are the ambient and surrounding temperature, respectively, and \mathbf{n} is the exterior normal vector of the convective surface (boundary Γ_2). In general, the coefficients k , h , ε are constant or functions of temperature.

When the shape of fin and all boundary condition are given, the temperature field of the fin and the base temperature could be obtained by solving the forward fin

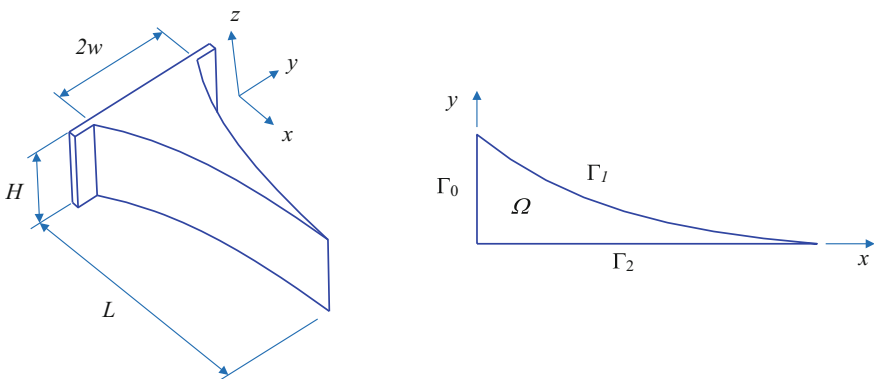


Fig. 1 Single longitudinal fin with variable cross-sectional area

problem by Eqs. (1–4). In this work, the finite element method (FEM) [11] is applied to solve this forward problem.

3 Bezier Curve for Fin Shape Design

Bezier curve is commonly used in the geometry design and the optimization [12]. In this research, Bezier curve is considered to create the shape of longitudinal cooling fin. In general, a Bezier curve $B(t)$ is defined as a polynomial spline function of p -th degree given by:

$$B(u) = \sum_{i=0}^m P_i N_{i,p}(u) \tag{5}$$

where P_i is the set of m control points, and $N_{i,p}(t)$ are the basis functions of degree p which are defined as:

$$N_{i,0}(u) = \begin{cases} 1 & \text{if } u_i \leq t \leq u_{i+1} \\ 0 & \text{otherwise} \end{cases} \tag{6}$$

$$N_{i,p}(u) = \frac{(u - u_i)N_{i,p-1}(u)}{u_{i+p} - u_i} + \frac{(u_{i+p} - u)N_{i+1,p-1}(u)}{u_{i+p+1} - u_{i+1}} \tag{7}$$

and u is independent value, U is a monotonically increasing knot vector with $m + p + 1$ elements expressed in the by:

$$U = \{ \underbrace{0, \dots, 0}_{p+1}, 1, \dots, m - p - 1, \underbrace{n - p, \dots, n - p}_{p+1} \} \tag{8}$$

The requirement of any Bezier curve is given as:

$$p = m - 1 \tag{9}$$

The characteristic and detailed information of Bezier curves are presented by Rogers [12] and Piegl and Tiller [13].

In this paper, the location of the control points of Bezier curve is considered as design variable and directly updated during the fin shape optimization process.

4 Levenberg–Marquardt Method

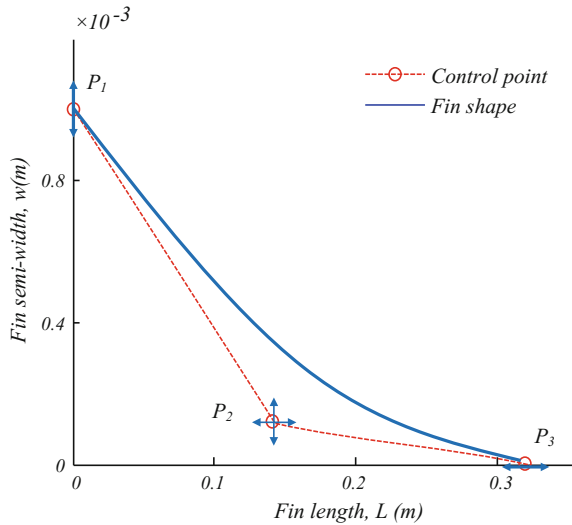
In this paper, the aim of the problem is to determine the optimum position of the control points to obtain the minimum volume of the longitudinal cooling fin for the known heat loss and base temperature. Consequently, the location of the control points is considered as the optimization variable. The number of variables depends upon the number of the degree of freedom of the control points. In this work, we use Bezier curve with three control points ($m = 3$). Thus, there are $2m - 2 = 4$ optimization variables including two variables for the first and last control point and two variables for the middle control point as Fig. 2.

Furthermore, to ensure that the unphysical fin profile is not occurred and keep on the continuity during the optimization process, the location of the control points must fulfill the conditions as following:

$$\begin{cases} x_{P1} = 0 \leq x_{P2} \leq \dots \leq x_{Pm} \\ y_{P1} \geq y_{P2} \geq \dots \geq y_{Pm} = 0 \end{cases} \quad (10)$$

LMM is used to optimize the fin profile with the minimum volume by finding out the optimum location of the control points. To do that, the expected base temperature T_{xpcd} and the expected fin volume V_{xpcd} are necessary to be given first; the calculated temperature Φ_c^i and the calculated volume of fin V_c are evaluated from the direct problem. Then, the estimation of the optimal shape of the fin can be archive by minimizing the following sum of squares function:

Fig. 2 Order of freedom of control points



$$\begin{aligned}
 J(\boldsymbol{\chi}) &= \sum_{i=1}^N (\Phi_c^i - T_{xpcd})^2 + (\hat{V}_c - T_{xpcd})^2 \\
 &= \sum_{i=1}^{N+1} (\mathbf{Y}_i - T_{xpcd})^2
 \end{aligned} \tag{11}$$

where N is the number of the temperature equation obtained from the base, \mathbf{Y} includes Φ_c^i and \hat{V}_c ; T_{xpcd} is the expected temperature at the base, \hat{V}_c is the converted volume given by:

$$\hat{V}_c = \frac{V_c}{V_{xpcd}} \cdot T_{xpcd} \tag{12}$$

and the optimization variables are set as following:

$$\boldsymbol{\chi} = \{x_{P_1}, x_{P_2}, \dots, x_{P_N} | y_{P_1}, y_{P_2}, \dots, y_{P_N}\}^T \tag{13}$$

To minimize the function J in Eq. (11), the position of the control points satisfies the following set of nonlinear equations:

$$\sum \frac{\partial \mathbf{Y}}{\partial \boldsymbol{\chi}} (\mathbf{Y} - T_{xpcd}) = 0 \tag{14}$$

In the other word, the value of unknown position of the control points can be obtained by solving the system of Eq. (14). Due to the nonlinearity of Eq. (14), LMM is chosen. This method uses the parameter μ to guarantee the iterative convergence. In general, the formula to compute the search direction for the parameters $\boldsymbol{\chi}$ in LMM can be expressed as following:

$$\boldsymbol{\chi}^{k+1} = \boldsymbol{\chi}^k - (\mathbf{B}^T \mathbf{B} + \mu \boldsymbol{\Omega})^{-1} \mathbf{B}^T (\mathbf{Y} - T_{xpcd}) \tag{15}$$

where $\mathbf{B} = \partial \mathbf{Y} / \partial \boldsymbol{\chi}$ is the sensitivity matrix, $\boldsymbol{\Omega}$ is the diagonal matrix, and k is the iteration index.

Equation (15) shows that the solution can be achieved when the appropriate volume of the longitudinal cooling fin and its base temperature is specified. Nevertheless, the minimum volume of the fin is undetermined prior and is the goal obtained. To deal with this problem, a mechanism called “volume updating” is introduced into LMM. This mechanism is based on “curve fitting” mechanism of LMM. In this mechanism, the obtained solution is the best approximation which is defined as that which minimizes the sum of squared differences between the computed and expected value. Thus, the value of N is larger in Eq. (15), the solution to the expected temperature compared to the expected volume is closer. Consequently, “volume updating” approach is expressed as following:

- Step 1: Set N with a big value and guess an initial fin volume with small value.
- Step 2: Find the best solution by using Eqs. (11–15).
- Step 3: Update the new fin volume archived from the best solution of step 2 and return to step 1.
- Step 4: Stop the process if the stopping criterion is fulfilled.

In this work, the solution of the problem stops when the stopping criterion is satisfied. Two stopping criteria are used in the proposed method. One is for updating the fin volume, and another is for LMM.

From the literature [14], the volume of the longitudinal cooling fin would be updated when both of two criteria are satisfied as following:

$$\begin{cases} \mathbf{Y} - T_{xpcd} \geq 0 \\ \|\mathbf{J}(\chi_{k+1}) - \mathbf{J}(\chi_k)\| \leq \delta \|\mathbf{J}(\chi_{k+1})\| \end{cases} \quad (16)$$

and the stopping criterion of LMM iteration is given by:

$$\|\Phi - T_{xpcd}\| \leq e \|T_{xpcd}\| \quad (17)$$

or

$$\|\mathbf{J}(\chi_{k+1}) - \mathbf{J}(\chi_k)\| \leq \delta \|\mathbf{J}(\chi_{k+1})\| \quad (18)$$

where e and δ are the convergence tolerances.

Finally, the computational algorithm of the proposed method can be illustrated as following:

Set the initial control point χ_0 , the initial volume of fin V_{xpcd}^0 , the adjusting factor μ (say $\mu = 1$ in the present work), and the convergence tolerance e and δ . The value χ_k is determined at the iteration k as following:

- Step 1: Compute the calculated temperature Φ_c^i by solving the direct problem Eq. (1)
- Step 2: Calculate χ_{k+1} through Eq. (15) and determine new \mathbf{J} from Eq. (11).
- Step 3: If $\mathbf{J}(\chi^{k+1}) > \mathbf{J}(\chi^k)$ or the condition of Eq. (10) is not satisfied, replace $\mu^k = 10\mu^k$, and return step 3. Otherwise, accept the new χ_{k+1} .
- Step 4: Update the fin volume if the updating criterion Eq. (16) is satisfied and replace k by $k + 1$, set $\mu^{k+1} = 0.1\mu^k$, and return to Step 1.
- Step 5: Terminate the process if the stopping criteria in Eqs. (17) and (18) are satisfied. Otherwise, replace k by $k + 1$ and return to Step 1.

5 Results and Discussions

To validate the proposed method, two cases with the various conditions of the longitudinal fin design problems are adopted in this section. Besides, the optimal results are compared with Schmidt [2], Nguyen and Yang [10], and Azarkish et al. [15] results.

For case 1, a linear longitudinal cooling fin design problem is investigated with the constant convective heat transfer coefficient of $h = 5.24 \text{ [W/m}^2\text{K]}$ and the thermal conductivity of $k = 210 \text{ [W/mK]}$. The expected base temperature $T_a = 500 \text{ [K]}$ and the ambient temperature are $T_b = 300 \text{ [K]}$. The height of the longitudinal cooling fin is $H = 0.4 \text{ [m]}$ with the given heat loss $q_{flow} = 152.6 \text{ [W]}$. Bezier curve with three control point, $m = 3$, is used in this case. The value of both updating and stopping criteria are set 10^{-5} , and the initial volume is $V_{xpcd}^0 = 8 \times 10^{-5} \text{ [m}^3\text{]}$.

The semi-shape of the optimal fin obtained by using LMM in case 1 is illustrated in Fig. 3a, and the temperature distribution along the longitudinal cooling fin length is shown in Fig. 3b. The profile of the optimal longitudinal cooling fin and the temperature distribution along the fin length archived by Schmidt [2] are also presented in Fig. 3. Table 1 shows the geometry parameters of the optimal fin. The relative deviation of the optimal fin geometry parameters between the proposed method and Schmidt [2] results is also illustrated in Table 1. From the obtained results, the optimal longitudinal cooling fin by the proposed method is in good agreement with Schmidt's. In Fig. 3, we see that these optimal shapes are coincident. Furthermore, the relative deviation of the optimal geometric parameters between the proposed method and the method in Schmidt [2] is very small (as Table 1). This can be declared that LMM determine accurately the minimum

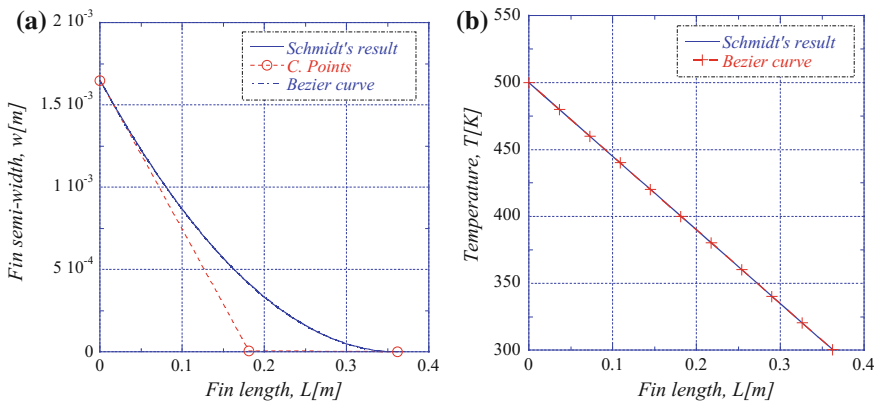


Fig. 3 **a** Optimal shape with the control points of Bezier curve and **b** Temperature distribution along with the fin length

Table 1 Optimal fin dimensions and their relative deviation in case 1

Geometry parameter	The proposed method	Schmidt [2]	Deviation (%)
Volume (m ³)	15.987e-05	15.988e-5	0.003
Length, L(m)	0.3620	0.3633	0.4
Semi-width, w(x)	1.65e-03	1.65e-3	0.000

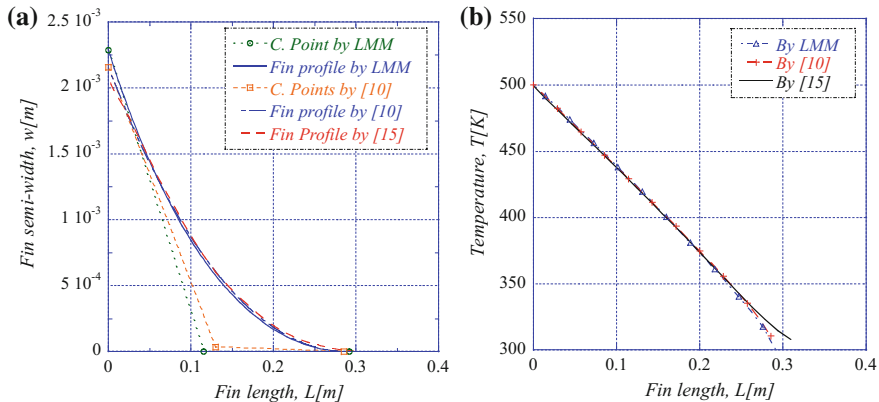


Fig. 4 **a** Optimal shape with the control points of Bezier curve and **b** Temperature distribution along with the fin length

volume of the optimal longitudinal cooling fin for the specified base temperature and the given heat flow in the linear fin design problems.

For case 2, a nonlinear longitudinal cooling fin design problem is considered with the variable convective heat transfer, the constant emissivity coefficient of $\epsilon = 0.3$, and the constant thermal conductivity of $k = 210$ [W/mK]. The variable convective heat transfer coefficient is defined as following [8]:

$$h = \frac{8k \text{Pr}^{1/2}}{3H \left[336 \left(\text{Pr} + \frac{9}{5} \right) \right]} \left(\frac{g\beta [T(x) - T_\infty] H^3}{\nu^2} \right)^{1/4} \tag{19}$$

where all the fluid properties are calculated by $T_m = (T_b + T_\infty)/2$. The given heat loss in this case is $q_{flow} = 224.1$ [W].

By using the proposed method, the fin shape and temperature distribution along the fin length of the optimal fin built by Bezier curve are illustrated in Fig. 4. The Nguyen and Yang [10] and Azarkish et al. [15] results are also shown in this figure. Moreover, the geometric parameters of optimal fin and the relative discrepancy of optimal geometric parameters between the obtained results with Nguyen and Yang [10] results and between the obtained results with Azarkish et al. [15] results are presented in Table 2 and Table 3, respectively. From obtained results, the obtained minimum volume by the proposed method is in good agreement with that by

Table 2 Optimal fin dimensions and their relative deviation between the proposed method and Nguyen and Yang [10] result in case 2

Geometry parameter	The proposed method (LMM)	Nguyen and Yang [10]	Deviation (%)
Volume (m ³)	15.903e-5	15.952e-5	0.3
Length, L(m)	0.2905	0.2854	1.7
Semi-width, w(x)	2.28e-03	2.16e-03	5

Table 3 Optimal fin dimensions and their relative deviation in case 2

Geometry parameter	The proposed method (LMM)	Azarkish [15]	Deviation (%)
Volume (m ³)	15.903e-5	16.190e-5	1.8
Length, L(m)	0.2905	0.3100	6
Semi-width, w(x)	2.28e-03	2.10e-03	8

Nguyen and Yang [10] results. However, we can see that the obtained minimum volume by the proposed method is quite different with that by Azarkish et al. [15]. For particularly, the relative difference of the optimal volume between the proposed and Nguyen and Yang [10] method is 0.3%, and that between the proposed and Azarkish et al. [15] method is 1.8%. The relative differences of the length and width of the optimal fin are also shown in Tables 2 and 3. In general, this deviation is small and is due to the errors of the numerical solutions in solving the direct problems and the optimization algorithm.

From the obtained results in two cases above, it can be claimed that LMM can be applied efficiently to find out the minimum volume of the optimal longitudinal fin for the general fin design problems.

6 Conclusions

In this work, the minimum volume of the general longitudinal cooling fin design problems was presented by using LMM combining with Bezier curve. A mechanism “volume updating” was presented in LMM to achieve the minimum volume of the optimum longitudinal cooling fin for the given heat loss and the expected temperature at the fin base. Two cases with the various conditions of the longitudinal cooling fin design problems are adopted. The obtained results by LMM have been compared with the results of Schmidt [2], Nguyen and Yang [10], and Azarkish et al. [15]. The results showed that the values of the minimum volume of the optimal fin are in good agreement with that of Schmidt [2], Nguyen and Yang [10], and Azarkish et al. [15] in two cases. In the other words, it can be declared that LMM can determine efficiently and accurately the minimum volume of the optimal longitudinal cooling fin with the shape built by Bezier curve for the given heat loss

and the expected temperature at the base. Furthermore, the proposed method in this work does not depend on the type of the direct problem and can be thus applied for any linear or nonlinear fin design problem.

References

1. Kraus AD, Aziz A, Welty J (2001) Extended surface heat transfer
2. Schmidt E (1926) Die Wärmeübertragung durch Rippen
3. Duffin RJ (1959) A variational problem related to cooling fins. *J Math Mech* 8(47–56)
4. Natarajan U, Shenoy UV (1990) Optimum shapes of convective pin fins with variable heat transfer coefficient. *J Franklin Inst* 327(6):965–982
5. Fabbri G (1997) A genetic algorithm for fin profile optimization. *Int J Heat Mass Transf* 40(9):2165–2172
6. Copiello D, Fabbri G (2009) Multi-objective genetic optimization of the heat transfer from longitudinal wavy fins. *Int J Heat Mass Transf* 52(5–6):1167–1176
7. Azarkish H, Sarvari SMH, Behzadmehr A (2010) Optimum geometry design of a longitudinal fin with volumetric heat generation under the influences of natural convection and radiation. *Energy Convers Manag* 51(10):1938–1946
8. Bobaru F, Rachakonda S (2004) Boundary layer in shape optimization of convective fins using a meshfree approach. *Int J Numer Meth Eng* 60(7):1215–1236
9. Huang C-H, Hsiao J-H (2002) A non-linear fin design problem in determining the optimum shape of spine and longitudinal fins. *Commun Numer Methods Eng* 19(2):111–124
10. Nguyen Q, Yang C-Y (2016) Design of a longitudinal cooling fin with minimum volume by a modified Newton-Raphson method. *Appl Therm Eng* 98:169–178
11. Baskharone EA (2013) The finite element method with heat transfer and fluid mechanics applications
12. Rogers DF (2001) Introduce on NURBS with historical perspective
13. Piegl L, Tiller W (1997) The NURBS book
14. Beck JV, Blackwell B, St.Clair CR (1985) Inverse heat conduction ill-posed problems
15. Azarkish H, Sarvari SMH, Behzadmehr A (2010) Optimum design of a longitudinal fin array with convection and radiation heat transfer using a genetic algorithm. *Int J Therm Sci* 49(11):2222–2229

An Artificial Neural Network-Based Optimization of Stiffened Composite Plate Using A New Adjusted Differential Evolution Algorithm



T. Lam-Phat, S. Nguyen-Hoai, V. Ho-Huu, Q. Nguyen
and T. Nguyen-Thoi

Abstract Stiffened composite plates have been widely used in many engineering areas including construction, shipbuilding, and aircraft. And so, the demand of optimizing the design of stiffened composite plate has also been rising. In this paper, a so-called ABDE (ANN-based differential evolution) algorithm is introduced to search for the optimal design of stiffened composite plates. The new algorithm is the combination of the artificial neural network (ANN) and an improved differential evolution (DE) algorithm in solving optimization problems. In this technique, the ANN helps to quickly compute the respond of the structure, which is used in constraint handling step or finding the value of an objective function of DE algorithm. This helps to decrease the cost and increase the speed of convergence effectively.

Keywords Differential Evolution (DE) • Artificial Neural Network (ANN) Optimization algorithm • Stiffened composite plate • Composite structures

T. Lam-Phat (✉) · S. Nguyen-Hoai

GACES, HCMC University of Technology and Education, Ho Chi Minh City, Vietnam
e-mail: thuanlp@hcmute.edu.vn; lamphatthuan@gmail.com

S. Nguyen-Hoai

e-mail: sonvn55@yahoo.com

V. Ho-Huu · T. Nguyen-Thoi

Division of Computational Mathematics and Engineering, Institute for Computational Science, Ton Duc Thang University, Ho Chi Minh City, Vietnam
e-mail: hohuuvinh@tdt.edu.vn

T. Nguyen-Thoi

e-mail: thoitrong76@gmail.com

Q. Nguyen

Department of Engineering Technology, Pham Van Dong University,
Quang Ngai, Vietnam
e-mail: nquan@pdu.edu.vn

© Springer Nature Singapore Pte Ltd. 2018

H. Nguyen-Xuan et al. (eds.), *Proceedings of the International Conference on Advances in Computational Mechanics 2017*, Lecture Notes in Mechanical Engineering, https://doi.org/10.1007/978-981-10-7149-2_16

229

1 Introduction

Structural optimization is a potential field and has attracted the attention of many researchers around the world. During the past decades, many optimization techniques have been proposed and applied to solve a wide range of various problems. The algorithms can be classified into two main groups: gradient-based and popular-based approach. Some of the gradient-based optimization methods can be named here as sequential linear programming (SLP) [1, 2], sequential quadratic programming (SQP) [3, 4], steepest descent method, conjugate gradient method, and Newton's method [5]. Most of them are applied to continuous design variables. The population-based techniques can be listed such as genetic algorithm (GA), differential evolution (DE), particle swarm optimization (PSO), cuckoo search (CS), and firefly algorithm (FA) [6]. These methods are used extensively in structural problems because of their flexibility and efficiency in handling both continuous and discontinuous design variables. In addition, the solutions obtained from population-based algorithms in most cases are global ones. Among the methods mentioned above, the differential evolution is one of the most widely used methods. Since it was first introduced by Storn and Price [7], many studies have been carried out to improve and apply DE in solving structural optimization problems. The results have proven the great effectiveness of the method [8–12]. However, like many other population-based optimizations, one of the disadvantages of DE is that the optimal computational time is much slower than the gradient-based optimization methods. This is because DE takes a lot of time in evaluating the fitness of individuals in the population. Specifically, in the structural optimization problem, the calculation of the objective function or constraint function values is usually done by using the finite element to analyze the structural response. To overcome this disadvantage, artificial neuron networks (ANN) are proposed to combine with the DE algorithm. Based on the idea of imitation of the brain structure, ANN is capable of approximating an output corresponding to a set of input data quickly after the network has been trained, also known as a learning process. Thanks to this remarkable advantage, the computation of objective function or constraint function values in the DE algorithm will be done quickly. As a result, ANN will help significantly improve the efficiency of DE calculations. The effectiveness and applicability of ANN since the early groundwork ideas put forward by Warren McCulloch and Walter Pitts [13] in 1943 have so far proved to be very convincing through numerous studies. Application areas include system identification and control, pattern recognition, sequence recognition (gesture, speech, and handwritten text recognition), data mining, visualization, machine translation, social networking filtering, and email spam filtering [14–19].

The next issue is the development of optimal algorithms integrated ANN with DE and applying the proposed algorithms to a practical structure to examine the effectiveness of the method. At present, the structures made from the composite material are widely used in almost all fields such as construction, mechanical engineering, marine, and aviation. In particular, stiffened composite plates made of

composite material are an outstanding form and are used increasingly by its superior advantages. By combining the advantages of composite materials and the reinforced beams structure, the reinforced composite plates have very high bending strength with very lightweight. Due to its high practical applicability, the need to optimize the design of the structure to save costs and increase the efficiency of use is also high. However, because of the complexity of computing the behavior of this particular type of structure, finding a good algorithm for optimizing design parameters is essential to ensure computational efficiency.

In this paper, the ANN-based differential evolution (ABDE) algorithm is proposed to optimize the fiber angles of the stiffened composite plate. In the ABDE algorithm, ANN was used to approximate the objective function value from the set of different design variables instead of using the finite element analysis as in the previous DE algorithm. Thanks to the remarkable performance in terms of calculating the value of the objective function of ANN, the optimal performance of the problem also increased significantly. The numerical results presented in this paper demonstrate the effectiveness and accuracy of the proposed method.

2 Fundamental Theory

2.1 Brief on the Behavior Equation of Stiffened Composite Plate

Stiffened composite plate is formed by a composite plate combining with a stiffening Timoshenko composite beam, as illustrated in Fig. 1. The beam is considered as a stiffener and is set parallel with the axes in the surface of the plate. The centroid of the beam has a distance e from the middle plane of the plate. The plate-beam system is discretized by a set of node. The degree of freedom (DOF) of each node of the plate is $\mathbf{d} = [u, v, w, \beta_x, \beta_y]^T$, in which u, v, w are the displacements at the middle

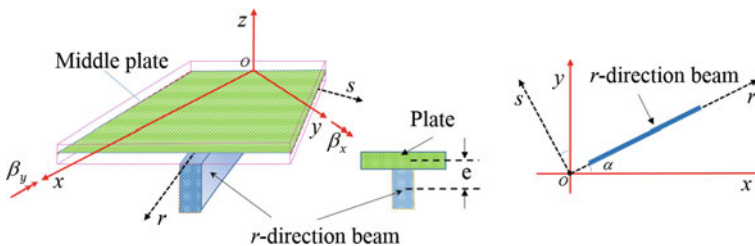


Fig. 1 Plate composite stiffened by an r -direction stiffener

of the plate and β_x, β_y are the rotations around the y-axis and x-axis. Each node of the beam has the DOF of $\mathbf{d}_{st} = [u_r, u_s, u_z, \beta_r, \beta_s]^T$, where u_r, u_s, u_z are, respectively, centroid displacements of the beam and β_r, β_s are the rotations of beam around r -axis and s -axis.

The displacement compatibility between plate and beam is ensured by:

$$u = u_r(r) + z\beta_r(r); \quad v = z\beta_s(r); \quad w = u_z(r) \quad (1)$$

The strain energy of composite plate is given by:

$$U_P = \frac{1}{2} \iint_A (\boldsymbol{\epsilon}_0^T \mathbf{D}^m \boldsymbol{\epsilon}_0 + \boldsymbol{\epsilon}_0^T \mathbf{D}^{mb} \boldsymbol{\kappa}_b + \boldsymbol{\kappa}_b^T \mathbf{D}^{mb} \boldsymbol{\epsilon}_0 + \boldsymbol{\kappa}_b^T \mathbf{D}^b \boldsymbol{\kappa}_b + \boldsymbol{\gamma}^T \mathbf{D}^s \boldsymbol{\gamma}) dA \quad (2)$$

where $\boldsymbol{\epsilon}_0, \boldsymbol{\kappa}_b, \boldsymbol{\gamma}$ are, respectively, membrane, bending, and shear strains of composite plate and are expressed as follows

$$\boldsymbol{\epsilon}_0 = [u_{,x}, v_{,y}, u_{,y} + v_{,x}]^T; \quad \boldsymbol{\kappa}_b = [\beta_{x,x}, \beta_{y,y}, \beta_{x,y} + \beta_{y,x}]^T; \quad \boldsymbol{\gamma} = [w_{,x} + \beta_x, w_{,y} + \beta_y]^T. \quad (3)$$

$\mathbf{D}^m, \mathbf{D}^{mb}, \mathbf{D}^b, \mathbf{D}^s$ are material matrices of plate.

The strain energy of composite stiffener is given by

$$U_{st} = \frac{1}{2} \int_l ((\boldsymbol{\epsilon}_{st}^b)^T \mathbf{D}_{st}^b \boldsymbol{\epsilon}_{st}^b + (\boldsymbol{\epsilon}_{st}^s)^T \mathbf{D}_{st}^s \boldsymbol{\epsilon}_{st}^s) dx \quad (4)$$

where $\boldsymbol{\epsilon}_{st}^b, \boldsymbol{\epsilon}_{st}^s$ are, respectively, bending, the shear strain of beam and are expressed as follows

$$\boldsymbol{\epsilon}_{st}^b = [u_{r,r} + z_0 \beta_{r,r}, \beta_{r,r}, \beta_{s,r}]^T; \quad \boldsymbol{\epsilon}_{st}^s = [u_{z,r} + \beta_r]^T \quad (5)$$

$\mathbf{D}_{st}^b, \mathbf{D}_{st}^s$ are material matrices of the composite beam.

Using the superposition principle, total energy strain of stiffened composite plate is obtained:

$$U = U_P + \sum_{i=1}^{N_{st}} U_{st} \quad (6)$$

where N_{st} is the number of stiffeners.

For static analysis, the global equations for the stiffened composite plate $[\mathbf{K}]\{\Delta\} = \{\mathbf{F}\}$ can found in [20] for detail.

2.2 Brief on the ANN-Base Differential Evolution Algorithm

a. Differential Evolution Algorithm

The original differential evolution algorithm firstly proposed by Storn and Price consists of four main phases: initialization, mutation, crossover, and selection. In the initialization phase, the population is created by randomly sampling from the search space. Each individual x_i of the population is then used to generate a new mutant vector v_i in the next phase of mutation. After that, at the crossover step, a trial vector u_i is created by replacing some elements of the mutant vector v_i via crossover operation. And finally, a comparison between the objective function values of the trial vector u_i with the target vector x_i is made to select a new set of population for the next generation. To improve the effectiveness of the algorithm, Ho-Huu et al. [9–12] have recently proposed some modifications on the *mutation phase*, and the *selection phase* of the original algorithm and the new version of DE were proved to be more effective than the original one. Specifically, in the *mutation phase*, the individuals participating in mutation are chosen following a priority based on their fitness instead of being chosen randomly. In the *selection phase*, the children population C consisting of trial vectors is combined with parent population P of target vectors to create a combined population Q. Then, best individuals are chosen from the combined population Q to construct the population for the next generation. By doing so, the best individuals of the whole population are always saved for the next generation and significantly improve the speed of convergence of the solution.

The modified algorithm is then expressed as below [21]:

1:	Generate the initial population
2:	Evaluate the fitness for each individual in the population using FEM
3:	while <the stop criterion is not met> do
4:	Calculate the selection probability for each individual
5:	for i =1 to NP do {NP: Size of population}
6:	Do mutation phase based on Roulette wheel selection
7:	$j_{rand} = \text{randi}(1,D)$ {D: number of design variables}
8:	for j =1 to D do
9:	if $\text{rand}[0,1] < CR$ or $j == j_{rand}$ then {CR: crossover control parameter}
10:	$u_{i,j} = x_{r1,j} + Fx(x_{r2,j} - x_{r3,j})$ {F:randomly chosen within [0,1] interval}
11:	else
12:	$u_{i,j} = x_{i,j}$
13:	end if
14:	end for
15:	Evaluate the trial vector u_i using FEM
16:	end for
17:	Do selection phase based on Elitist selection operator
18:	end while

Fig. 2 MLP network model

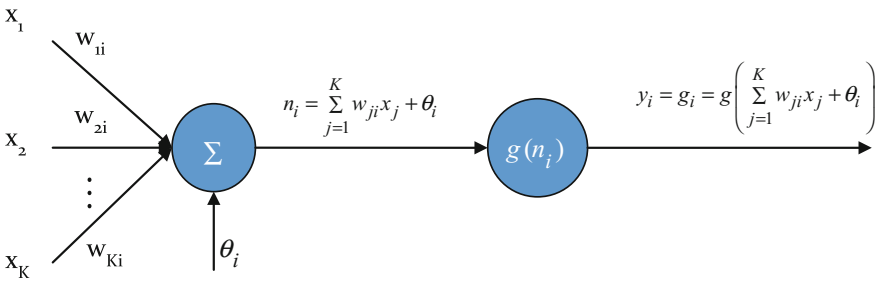
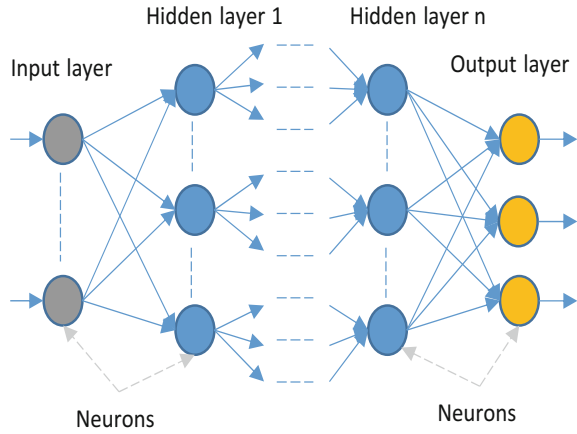


Fig. 3 Single node in a MLP network

b. Artificial Neural Network

Neural networks consist of a large class of different architectures. In this paper, one of the most useful neural networks in function approximation, multilayer perceptron (MLP), is used. An MLP consists of an input layer, several hidden layers, and an output layer as in Fig. 2.

In an MLP network, a single node i , also called a neuron, includes a summer and a nonlinear activation function g is shown in Fig. 3.

The inputs $x_k, k = 1, \dots, K$ to the neuron are multiplied by weights w_{ki} and summed up together with the constant bias term θ_i . The resulting n_i is the input to the activation function g . The activation function was originally chosen to be a relay function, but for mathematical convenience, a hyperbolic tangent (tanh) or a sigmoid function are most commonly used. The output of node i becomes

$$y_i = g_i = g\left(\sum_{j=1}^K w_{ji}x_j + \theta_i\right) \tag{7}$$

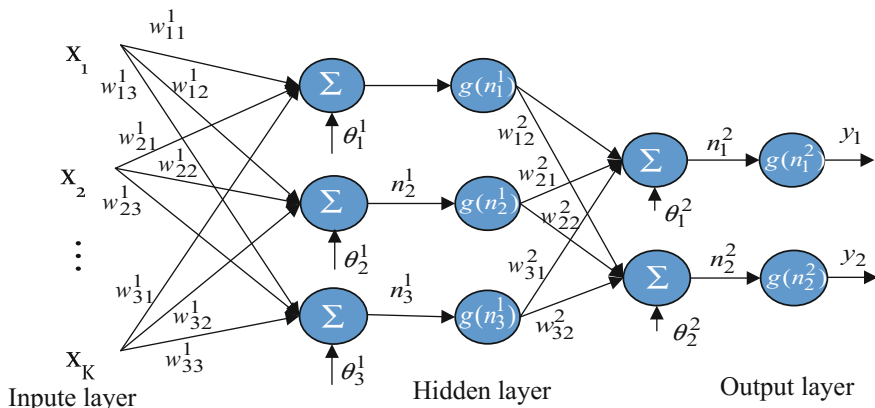


Fig. 4 Multilayer perceptron network with one hidden layer

Connecting several nodes in parallel and series, an MLP network is formed. A typical network is shown in Fig. 4.

The output y_i , $i = 1, 2$ of the MLP network becomes

$$y_i = g \left(\sum_{j=1}^3 w_{ji}^2 g(n_j^1) + \theta_j^2 \right) = g \left(\sum_{j=1}^3 w_{ji}^2 g \left(\sum_{k=1}^K w_{kj}^1 x_k + \theta_j^1 \right) + \theta_j^2 \right) \quad (8)$$

To find the best MLP network with a set of given input-output data (x_i, y_i) , $i = 1, \dots, N$, the parameters (w_{ji}^k, θ_j^k) need to be determined. The algorithms for determining the network parameters are called learning or teaching algorithms. There are many teaching algorithms. In this paper, the Levenberg-Marquardt algorithm is used. The procedure of teaching algorithms for multilayer perceptron networks is summarized below:

- The structure of the network is first defined. In the network, activation functions are chosen, and the network parameters, weights, and biases are initialized.
- The parameters associated with the training algorithm like error goal, the maximum number of epochs (iterations) is defined.
- The training algorithm is called.
- After the neural network has been determined, the result is first tested by simulating the output of the neural network with the measured input data. This is compared with the measured outputs. Final validation must be carried out with independent data.

The advantage of ANN is that the network after being determined can be used to approximate the output immediately from any given set of input data. And this is

really helpful in evaluating fitness functions or objective functions in many optimization algorithm.

c. The ANN-Based Differential Evolution Algorithm

By combining the above advantages of ANN and the DE algorithm, the ANN-based differential evolution optimization algorithm is proposed. Specifically, the calculation of the objective function values of individuals in the population at each generation and the evaluation of the trial vectors in the crossover step carried out by finite element analysis as in the original DE algorithm are replaced by the approximation of the ANN as illustrated in Fig. 5. In Fig. 5, the process of building an ANN model usually consists of three main parts: sampling, training, and verifying the net as illustrated in the block of “ANN Building steps.” In this paper, the samples used for ANN training are created by the FEM, and the algorithm used to train the net is Levenberg-Marquardt.

Thanks to the advantage of being able to immediately evaluate the fitness of all individuals in the population by just a single command “*net(popular)*” rather than using the *for/end* loop and finite analysis for each individual value, the

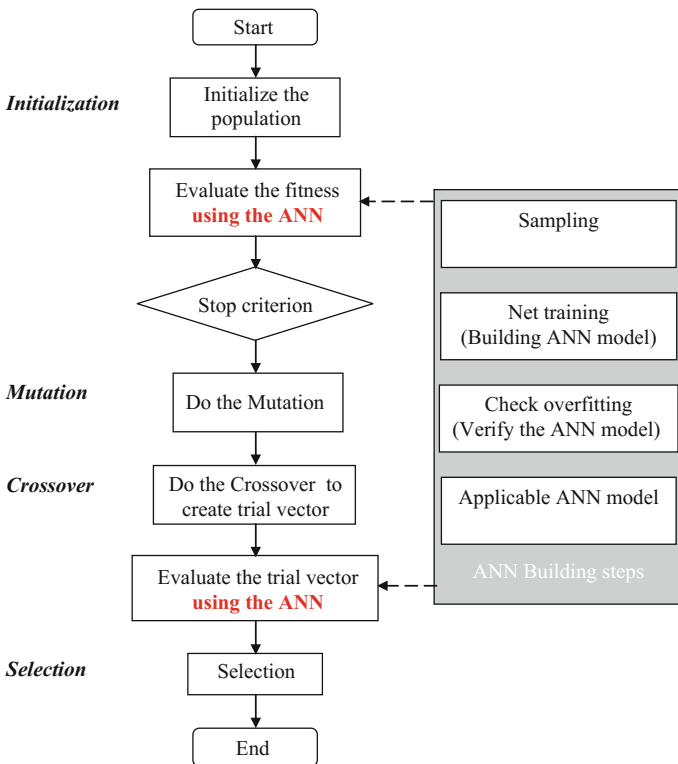


Fig. 5 Optimization process of the ABDE algorithm

computational speed of the ABDE optimization algorithm is increased significantly. Although the approximation of the structural response of stiffened composite plate based on the training network “*train(net,input,output)*” is erroneous; however, this error is small and the accuracy is acceptable. This is demonstrated in the numerical results of the paper.

In addition, the proposed ABDE algorithm has the great advantages that the original DE algorithm based on finite element analysis is impossible or difficult to do, such as the ability to solve optimization problems that does not have the behavior equation of the object or providing a good support in studying the effect of the optimal parameters on the result of the problem.

3 Numerical Results

3.1 Static Analysis of the Stiffened Composite Plate

Finite element analysis of static structural response will be used to generate the set of input samples for the network training model of ANN. Therefore, it is important to ensure the accuracy of the static analysis. In this section, the static response analysis of stiffened composite plate was performed by finite element method using the triangle element CS-DSG3 [22]. The results were compared with the available results of other authors to ensure the accuracy of the method. The square plate model under simply supported condition is reinforced in the X-direction and has the dimensions as shown in Fig. 6. The plate has thickness t , and dimensions in x and y directions are $l_x = 254$ mm and $l_y = 254$ mm, respectively.

Both plate and beam have four symmetric layers. The fiber orientation for layers of the plate is a set $[\theta_1 \theta_2 \theta_2 \theta_1]$, and for the layers of the beam is $[\theta_3 \theta_4 \theta_4 \theta_3]$. The plate and beam are made of the same materials with $E_1 = 144.8$ GPa, $E_2 = E_3 = 9.65$ GPa, $G_{12} = G_{13} = 4.14$ GPa, $G_{23} = 3.45$ GPa, $\nu_{12} = \nu_{13} = \nu_{23} = 0.3$. The plate is subject to a uniform load $f = 0.6895$ (N/mm²).

Fig. 6 Model of a stiffened composite plate

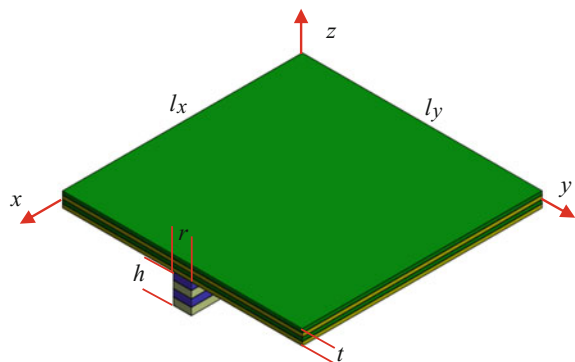


Table 1 Comparison of central deflection (mm) of the simply supported square stiffened composite plates

Fiber angle for both beam and plate	[0°/90°/90°/0°]			[45°/−45°/−45°/45°]	
Method	CS-DSG3	[20]	[23]	CS-DSG3	[23]
Central deflection	1.0917	1.0396	1.0892	2.5049	2.4912

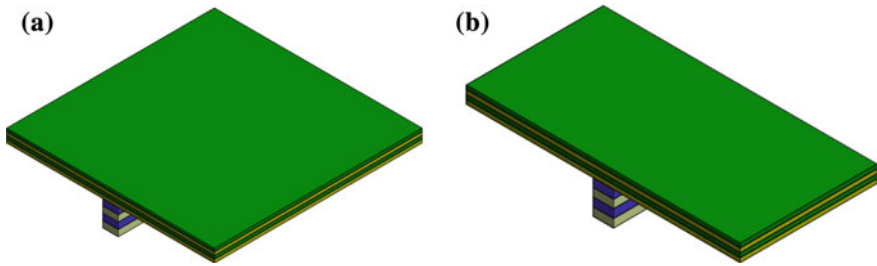


Fig. 7 Optimization analysis of stiffened composite plate **a** square plate—**b** rectangular plate

The static analysis is carried out for two cases of fiber angle of [0°/90°/90°/0°] and [45°/−45°/−45°/45°]. The central deflection of the stiffened composite plate obtained from FEM is shown in Table 1. The results are compared with those by Li and Kolli and show good agreement. The maximum error is just 0.55%.

3.2 The Effective of the Differential Evolution Algorithm

To verify the accuracy of the DE algorithm, the fiber-angle optimization of two models of square and rectangular stiffened composite plate is considered in this section. The stiffeners in both cases are in X-direction as shown in Fig. 7. The objective function in this problem is the strain energy of the plate.

The optimization problem is expressed as:

$$\begin{cases} \min_{\theta} & U = \frac{1}{2} \mathbf{d}^T \mathbf{K} \mathbf{d} \\ \text{subject to} & 0 \leq \theta_i \leq 180, \quad i = 1, \dots, 4 \end{cases}$$

where U is strain energy and θ_i is fiber orientation of *i*th layer.

In order to save the time of computation but still ensure accuracy, the integer values of design variables were used in this analysis.

The optimization parameters of differential evolution algorithm used in this stage are given here:

Initial population size (NP): 20 individuals each generation

Table 2 Optimal results of two problems

Type of stiffened plate	Method	Optimal angle (°)				Strain energy (Nm)	Computational time (s)
		θ_1	θ_2	θ_3	θ_4		
Square	DE	135	48	0	180	6183.2	2065
	GA	135	48	0	180	6183.1	2253
Rectangular	DE	160	37	0	180	30366	2851
	GA	159	37	0	180	30300	4995

Total generation: 200

The crossover control parameter (Cr): 0.9

The scaling factor (Fx): 0.8

Tolerance: 1e-6

The optimal results of fiber orientations for both cases are presented in Table 2. The results from the Table 2 show that the solutions by the DE agree very well with those by the GA. The errors of strain energy in both cases are very low. The maximum one is just about 0.2% for the case of a rectangular plate. However, the computational time of the DE algorithm is much better. Especially, in the case of a rectangular plate, the time of computation from the GA method is nearly double in comparison with the one from DE, 4995 s and 2851 s, respectively. This proves the accuracy and the effectiveness of the DE method.

The results of Table 2 also show that the geometric parameters of the structures also have influence to the optimal values of the problems. This is explained by the fact that the optimal fiber orientations of the square and rectangular plate are quite different under the same conditions.

3.3 The ANN-Based Differential Evolution

In this section, the ABDE optimization algorithms were applied to three problem models: rectangular plate with X-directional stiffener (R-X), rectangular plate with Y-directional stiffener (R-Y), and square plate reinforced in two directions X and Y (S-XY). The results in this section obtained by the computer with the following configuration:

Processor Intel® Core™ i5-2430M CPU @ 2.4 GHZ
 Installed Memory (RAM) 4.00 GB (3.90 GB usable)
 System type 64-bit Operating System, x64-based processor

Firstly, the samples for net training were created with 10,000 samples for each case. The net after training will be checked for “overfitting phenomenon” with other 1,296 samples to ensure the accuracy and the applicability of the net. The time for sampling and the average errors of overfitting checking process are presented in the below Table 3.

Table 3 Sampling and overfitting checking error

Samples	Case	Total time (s)	Avg. error (%)
10000	R-X	38535	2.55
10000	R-Y	39188	3.55
10000	S-XY	19434	3.01

Table 4 Comparison of accuracy and computational time between DE and ABDE

Type of stiffened plate	Method	Optimal angle (°)				Strain energy (Nm)	Error (%)	Cost (s)
		θ_1	θ_2	θ_3	θ_4			
R-X	DE	160	37	0	180	30366	0.86	2851
	ABDE	160	38	0	180	30104		8
R-Y	DE	178	12	0	180	33039	1.57	2903
	ABDE	177	11	0	180	32520		13
S-XY	DE	135	45	0	0	4223	1.99	1497
	ABDE	134	42	0	0	4307		5

The average errors for three cases are small, so the ANN model can ensure the accuracy in approximating the objective function of the stiffener composite plate in the optimization process of the DE algorithm.

The optimal results are shown in Table 4. Compared to the optimal results obtained from the DE algorithm, the values of the design variable computed from ABDE are very similar. The errors of objective function values obtained for the three models were 0.86%, 1.57%, 1.99%, respectively. These errors are most influenced by the training model of ANN. However, with a maximum error of 1.99%, it is perfectly acceptable. Besides, a superior advantage in terms of computational time, which is also the strongest advantage of the ABDE algorithm, was very well expressed. The cost for the R-X model computed by ABDE is only 8 s compared to 2851 s of DE, which is 356 times faster. The remaining two cases of R-Y and S-XY models, the cost are, respectively, 13 s and 5 s compared to 2903 s and 1497 s of the DE algorithm. This superiority is due to the fact that the objective function can be approximated from the ANN model by a single command: *net (popular)*, which is independent of the population of each generation, instead of using *for/end* loop as in the original DE algorithm. In three cases above, the lowest computational time with the highest error is of S-XY case. This is because the square plate has a smaller dimension in comparison with the rectangular one, so the computational time is faster. Meanwhile, the error may be caused by the error in the approximation of ANN model and the accuracy of the FEM procedure in creating the sample for neural network training. Therefore, to ensure the accuracy and the effectiveness of the proposed method, the ANN training and sampling step must be considered carefully.

The results in Table 4 can prove the ABDE algorithm’s superior accuracy and efficiency in comparison with the independent DE algorithm. This is especially

useful for solving problems with a large quantity of loops and high-cost objective functions.

Additionally, this algorithm can also be applicable for many types of problems including linear and nonlinear ones because the idea here is just alternating the approach of evaluating the objective function by using ANN instead of using FEM. Therefore, the computational time is saved. Moreover, the ANN model can well approximate both linear and nonlinear response. So, this technique will be applied for both linear and nonlinear optimization problems.

4 Conclusions

The ANN algorithm combined with the DE algorithm in the optimization of the fiber direction of stiffened composite plate gives a good result in accuracy, with the maximum error being 1.99%. This error is due to the influence of the evaluation of the objective function from the ANN algorithm. However, the computational time is superior due to the fact that the time taken to calculate the objective function from ANN is much faster than calculating the objective function value from the numerical method such as FEM. This will be very useful in calculating large problems with many loops.

In addition, integrating ANN with an optimal population-based approach has several benefits:

- The problem not having clear behavioral equation can still be resolved, just need the data set of input and output.
- Changing the values of the parameters of the optimization methods (tol, population size, ...) for checking the sensitivity (the influence of the optimization parameters) may take a lot of time. ANN will help resolve this problem quickly thanks to the superior advantage in terms of saving time.
- Saving a lot of time when experimenting a variety of optimization methods with the same structure. After the ANN model has been built, the process of evaluating objective functions or constraint functions in population-based optimization methods can be quickly done by ANN. This helps to quickly check the effectiveness of many optimization methods and is very useful in research work.

References

1. Lamberti L, Pappalettere C (2000) Comparison of the numerical efficiency of different sequential linear programming based algorithms for structural optimisation problems. *Comput Struct* 76:713–728
2. Lamberti L, Pappalettere C (2004) Improved sequential linear programming formulation for structural weight minimization. *Comput Methods Appl Mech Eng* 193:3493–3521

3. Sedaghati R (2005) Benchmark case studies in structural design optimization using the force method. *Int J Solids Struct* 42:5848–5871
4. Nguyen-Thoi T, Ho-Huu V, Dang-Trung H, Bui-Xuan T, Lam-Phat T (2013) Optimization analysis of stiffened composite plate by sequential quadratic programming. *J Sci Technol* 51:156–165
5. Singiresu SR (2009) *Engineering optimization theory and practice*. Wiley
6. Yang X-S, Bekdas G, Nigdeli SM (2016) *Metaheuristics and optimization in civil engineering*. Springer
7. Storn R, Price K (1997) Differential evolution—a simple and efficient heuristic for global optimization over continuous spaces. *J Glob Optim* 341–359. <https://doi.org/10.1023/A:1008202821328>
8. Wang ZWZ, Tang HTH, Li PLP (2009) Optimum design of truss structures based on differential evolution strategy. In: 2009 International conference on information engineering and computer science, pp 0–4. <https://doi.org/10.1109/ICIECS.2009.5365996>
9. Le-Anh L, Nguyen-Thoi T, Ho-Huu V, Dang-Trung H, Bui-Xuan T (2015) Static and frequency optimization of folded laminated composite plates using an adjusted differential evolution algorithm and a smoothed triangular plate element. *Compos Struct* 127:382–394. <https://doi.org/10.1016/j.compstruct.2015.02.069>
10. Ho-Huu V, Nguyen-Thoi T, Nguyen-Thoi MH, Le-Anh L (2015) An improved constrained differential evolution using discrete variables (D-ICDE) for layout optimization of truss structures. *Expert Syst Appl*. <https://doi.org/10.1016/j.eswa.2015.04.072>
11. Ho-Huu V, Nguyen-Thoi T, Khac-Truong T, Le-Anh L, Nguyen-Thoi MH (2015) A fast efficient differential evolution based on roulette wheel selection for shape and sizing optimization of truss with frequency constraints
12. Ho-Huu V, Nguyen-Thoi T, Vo-Duy T, Nguyen-Trang T (2016) An adaptive elitist differential evolution for optimization of truss structures with discrete design variables. *Comput Struct* 165:59–75
13. McCulloch W, Pitts W (1943) A logical calculus of ideas immanent in nervous activity. *Bull Math Biophys* 5(4):113–115
14. Engelbrecht AP (2002) *Computational intelligence*. Wiley
15. Rutkowski L (2008) *Computational intelligence—methods and techniques*. Springer
16. Marin L, Trias D, Badallo P, Rus G, Mayugo JA (2012) Optimization of composite stiffened panels under mechanical and hygrothermal loads using neural networks and genetic algorithms. *Compos Struct* 94:3321–3326
17. Zissis D (2015) A cloud based architecture capable of perceiving and predicting multiple vessel behaviour. *Appl Soft Comput* 35:652–661
18. Sengupta N, Sahidullah M, Saha G (2016) Lung sound classification using cepstral-based statistical features. *Comput Biol Med* 75(1):118–129
19. Schechner S (2017) Facebook boosts A.I. to block terrorist propaganda. *Wall Street J*. ISSN 0099-9660
20. Kolli M, Chandrashekhara K (1996) Finite element analysis of stiffened laminated plates under transverse loading. *Compos Sci Technol* 56:1355–1361
21. Lam-Phat T, Nguyen-Hoai S, Ho-Huu V, Nguyen-Thoi T (2016) Optimization of stiffened composite plate using adjusted differential evolution. In: ICCM2016, 1–4 Aug 2016, Berkeley, CA, USA
22. Liu GR, Trung NT (2010) *Smoothed finite element methods*. CRC Press, Taylor and Francis Group, New York
23. Li L, Ren X (2010) Stiffened plate bending analysis in terms of refined triangular laminated plate element. *Compos Struct* 2936–2945

Part IV
Reinforced Concrete, Steel
and Steel-Concrete Composite Structures

Theoretical and Experimental Studies on Hybrid Steel-RC Walls



Nguyen Quang-Huy, Hjiyaj Mohammed and Tran Van Toan

Abstract Hybrid RCS frames consisting of reinforced concrete (RC) column and steel (S) are used frequently in practice for mid- to high-rise buildings. RCS frames possess several advantages from structural, economical and construction view points compared to either traditional RC or steel frames. One of the key elements in RCS frames is the composite shear wall consisting of several steel sections encased in reinforced concrete. Regarding the RC walls reinforced by more than one steel profile, namely hybrid steel-RC wall, although a number of researchers have focused on its various aspects, they are currently not covered by standards because they are neither reinforced concrete structures in the sense of Eurocode 2 or ACI318, nor composite steel-concrete structures in the sense of Eurocode 4 or AISC 2010. This paper deals with theoretical and experimental study on hybrid walls with several embedded steel profiles. The first part of this paper is dedicated to present a tentative design model for hybrid elements (walls and columns) subjected to combined axial force, bending and shear. Particular attention will be paid to shear (longitudinal and transversal) resistances because preventing shear failure is one of the major concerns when designing a composite structural member. Next, an experimental study on the static behavior of hybrid walls subjected to combined shear and bending is presented. Six hybrid walls with different types of the structural steel-concrete connection and reinforcement detailing are tested. The specimens exhibited ductility behavior. The specimens with shear connectors (i.e. headed studs, stiffeners) were more ductile in terms of displacement ductility than the ones without connectors. Finally, to assess the validity of the developed design model a comparison between the experimental results and design predictions is presented.

N. Quang-Huy (✉) · H. Mohammed
Structural Engineering Research Group, INSA de Rennes,
20 Avenue des Buttes de Coësmes, 35043 Rennes, France
e-mail: qnguyen@insa-rennes.fr

H. Mohammed
e-mail: mhjiyaj@insa-rennes.fr

T. Van Toan
Thuyloi University, 175 Tay son, Hanoi, Vietnam
e-mail: tranvantoan@wru.vn

Keywords Steel • Concrete hybrid shear walls • Shear connection • Design method • Static test

1 Introduction

The design of a framing system that combines structural steel and reinforced concrete produces a building having the advantages of each material, stiffness, damping, and economy of reinforced concrete, and the speed of construction, strength, long-span capability, and light weight of structural steel. One of the key elements is the composite wall, where the practice of encasing structural steel shapes encased in reinforced concrete is common. The use of encased composite walls is actually more or less limited to the simple encased steel profile because this kind of composite walls is covered by standard rules of [1]. Regarding the concrete walls reinforced by more than one steel profile, namely “hybrid” wall, although a number of researchers have focused on its various aspects [2–4], they are currently not covered by standards because they are neither reinforced concrete structures in the sense of Eurocode 2 [5] or ACI-318 [6], nor composite steel-concrete structures in the sense of Eurocode 4 [1] or AISC [7]. Gaps in knowledge are mostly related to the problem of force transfer between concrete and embedded steel profiles, a situation in which it is neither known how to combine the resistances provided by bond, by stud connectors and by plate bearings, nor how to reinforce the transition zones between classical reinforced concrete and concrete reinforced by steel profiles.

Various types of composite walls have been developed, investigated and used for core walls of high-rise buildings in seismic zones. Zhao and Astaneh-Asl (2004) [8] attached RC panels to the steel plate walls using bolts, resulting in highly ductile behavior and stable cyclic post-yielding performance. Saari et al. (2004) [9] studied the behavior of headed shear stud connectors for use in steel frames with partially restrained connections and reinforced concrete infill walls, attached compositely to the steel frame around the perimeter of each wall panel. Zhou et al. (2010) [10] performed experimental and numerical studies of composite shear with multi-embedded steel sections at wall boundaries as well as wall middles. They indicated that composite shear walls with multi-embedded steel sections had better energy dissipation capacity than that with steel sections only at boundaries. The presence of multi-embedded steel sections did not affect the final failure mode of the composite shear walls, but they would restrain the development of cracks and prevent the concrete from serious spalling. Similar kind of composite shear walls was experimentally and numerically studied by Dan et al. (2011) [4]. They encased vertical steel profiles into RC walls and demonstrated the effectiveness of the steel profiles in improving the seismic performance of RC shear walls. Rafiei et al. (2015) and Hossain et al. (2016) [11, 12] studied the behavior of composite shear walls consisting of two skins of profiled steel sheeting and an infill of concrete under in-plane monotonic and cyclic loading respectively, demonstrating more ductile behavior and higher energy absorbing capacity. Zhang et al. (2016) [13] proposed and investigated a novel structural

shear wall consisting of bundled lipped channels seam-welded together and in-filled concrete. They pointed out that that the level of axial force ratio and the configuration detail significantly affect the entire hysteresis performance, while the presence of shear studs delays the occurrence of fracture and failure.

This paper deals with design method and experimental study of hybrid walls with several embedded steel profiles. The first part of this paper is dedicated to present a tentative design model for hybrid elements (walls and columns) subjected to combined axial force, bending and shear. This model is based principally on the design rules of [5] and [1]. Particular attention will be paid to shear (longitudinal and transversal) resistances. Next, an experimental study on the static behavior of hybrid walls subjected to combined shear and bending is presented. Six hybrid walls with different types of the structural steel-concrete connection and reinforcement detailing are tested. Finally, to assess the validity of the developed design model a comparison between the experimental results and design predictions is presented.

2 Design Method

As already mentioned in the introduction, the studied hybrid walls are not yet covered by design standards. The present study aims to develop a tentative design method for such element subjected to combined axial force, bending and shear. Let consider a hybrid steel-concrete element subjected to axial force, bending and shear as shown in Fig. 1. The cross-section consists of a rectangular RC section reinforced by several steel profiles.

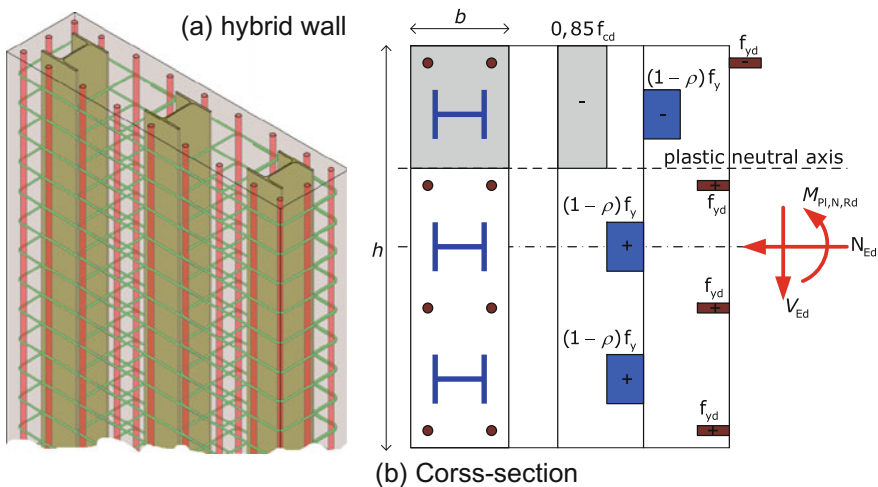


Fig. 1 Description of studied hybrid walls

In the proposed design method, particular attention will be paid to shear (longitudinal and transversal) resistances because preventing shear failure is one of the major concerns when designing a such composite structural member. Experiments conducted with simple encased steel profile shown that the shear failure generally involves three possible failure modes:

- (1) the diagonal shear failure, which closely resembles the shear failure of an ordinary reinforced concrete structural member;
- (2) the longitudinal shear failure, which results in cracks along the interface of the steel flange and concrete.
- (3) the flexural failure, which results in vertical cracks at mid-span.

A method for the calculation of the number of connector to ensure the full interaction between steel profiles and concrete around is firstly developed. The bending resistance will be determined using the M-N interaction curve which is build using the method of stress distribution of Eurocode 4 [1]. Regarding the shear resistance, a strut-and-tie model is developed taking into account the contribution of the steel profiles. For the sake of simplicity, in this work, we consider only the case of three encased steel profiles. The three steel profiles are oriented such that they are submitted to weak axis bending. The second order effect is not treated in this paper. All details of the design model related to the second effect of hybrid members can be found in [15].

Design Resistance of Cross-Section to Combined Compression and Bending

There is nowadays no design standard providing the guidance on how to determine properly the plastic resistances of composite section with more than one encased steel profile. However, once the steel profiles are fully embedded in concrete, the resistance of hybrid cross-sections to combined compression and bending and the corresponding interaction curve may be calculated assuming rectangular stress blocks as shown in Fig. 1. This method is inspired from the simplified method of design of Eurocode 4 [1]. In this method, the tensile strength of the concrete is neglected.

If the shear force $V_{a,Ed}$ acting on one steel section exceeds 50% of the design shear resistance of the steel section $V_{pl,a,Rd}$, the influence of the transverse shear on the resistance in combined bending and compression should be taken into account by a reduced design steel strength $(1 - \rho)f_y$ where

$$\rho = \left(\frac{2V_{a,Ed}}{V_{pl,a,Rd}} - 1 \right)^2 \quad (1)$$

The shear force $V_{a,Ed}$ acting on one steel section is assumed to be determined by:

$$V_{a,Ed} = \frac{V_{Ed}}{n_a} \frac{M_{pl,a,Rd}}{M_{pl,Rd}} \quad (2)$$

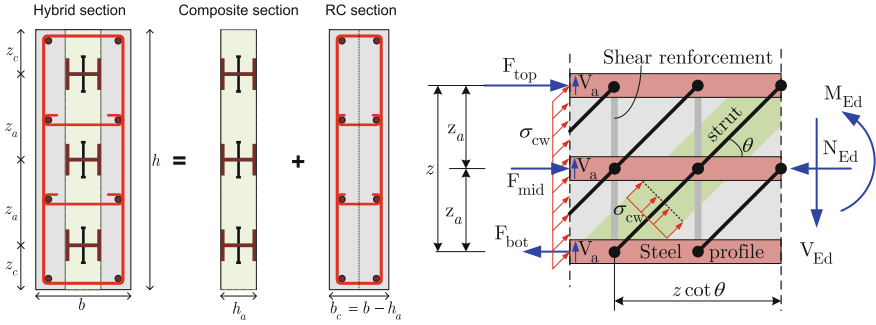


Fig. 2 Decomposition of hybrid section; and strut-and-tie model fore shear resistance

where $M_{pl,a,Rd}$ is the plastic resistance moment of n_a steel sections and $M_{pl,Rd}$ is the plastic resistance moment of the hybrid section.

Design Transverse Shear Resistance

If the encased steel profiles are considered as reinforcing bars, the shear resistance can be evaluated using the strut-and-tie model proposed in Eurocode 2 [5]. However it is obvious that the shear resistance provided by the steel profiles must be not negligible for such hybrid section. In our design approach it is assumed that the shear resistance of the hybrid section is given by adding up the shear resistances of RC section and composite steel-concrete section. As shown in Fig. 2, the composite section has a width limited to the width of the steel shape h_a and the RC section has a width $b_c = b - h_a$ where b being the width of hybrid section.

$$V_{Rd} = V_{Rd,RC} + V_{Rd,a} \tag{3}$$

where:

- $V_{Rd,RC}$ is the design shear resistance of RC section which is determined in accordance with Eurocode 2:

$$V_{Rd,RC} = \min \left[\begin{array}{l} V_{Rd,s} = \frac{A_{sw}}{s} z f_{ywd} \cot \theta \\ V_{Rd,max} = \frac{\alpha_{cw} b_c z v_1 f_c}{\cot \theta + \tan \theta} \end{array} \right] \tag{4}$$

- $V_{Rd,a}$ is the design shear resistance of composite section which is given by:

$$V_{Rd,a} = n_a (1 - \eta) V_{pl,a,Rd} \tag{5}$$

with n_a being the number of steel profiles; $V_{pl,a,Rd}$ being the design shear resistance of one steel section determined in accordance with Eurocode 3; The coefficient η represents the influence of normal stress on the shear resistance of steel profile when

the design axial force exceeds 50% of the plastic resistance to compression $N_{pl,Rd}$:

$$\eta = \left(\frac{2N_{Ed}}{N_{pl,Rd}} - 1 \right)^2 \quad (6)$$

Design Longitudinal Shear Resistance

Vertical force equilibrium:

$$V_{Ed} = b z \sigma_{cw} \sin^2 \theta + n_a V_{a,Ed} \quad (7)$$

where σ_{cw} is the compression stress in struts; z is the distance between the compression and tension chords. In wall with huge embedded steel sections, it is proposed to consider z as the distance between the center of top and bottom embedded profiles. θ is the inclination of the compression struts.

The longitudinal shear force acting on the bottom (or top) embedded profile can be obtained by

$$g_{Ed} = \frac{h_a \sigma_{cw} \sin \theta (\cos \theta - \mu \sin \theta)}{\chi_a} \quad (8)$$

where χ_a is the perimeter of the steel profile section. If the longitudinal shear force g_{Ed} is greater than the design shear strength τ_{Rd} given in [1], shear connectors are therefore needed to ensure the full interaction between steel profiles and concrete. In this case, the longitudinal shear force, namely V_L , acting on the shear connectors from the cross-section where the full plastic bending moment is reached to the cross-section where the bending moment vanishes is

$$V_L = A_a (1 - \rho) f_y \quad (9)$$

where A_a is area of one steel profile. The minimum number of shear stud needed for one steel profile to ensure the full interaction is $n_{min} = V_L / P_{Rd}$ where P_{Rd} is design shear resistance of one shear connector.

3 Experimental Program

Description of Test Specimens

The experimental program consists of seven 2:3 scale wall specimens whose one is RC wall (served as reference specimen) and six others are composite wall with three encased steel profiles. They have been designed using the design model presented above. All specimens had the same size, geometry and longitudinal reinforcing bar arrangements. The primary differences between seven specimens were the type of the structural steel-concrete connection and the stirrup spacing. Details evaluated in

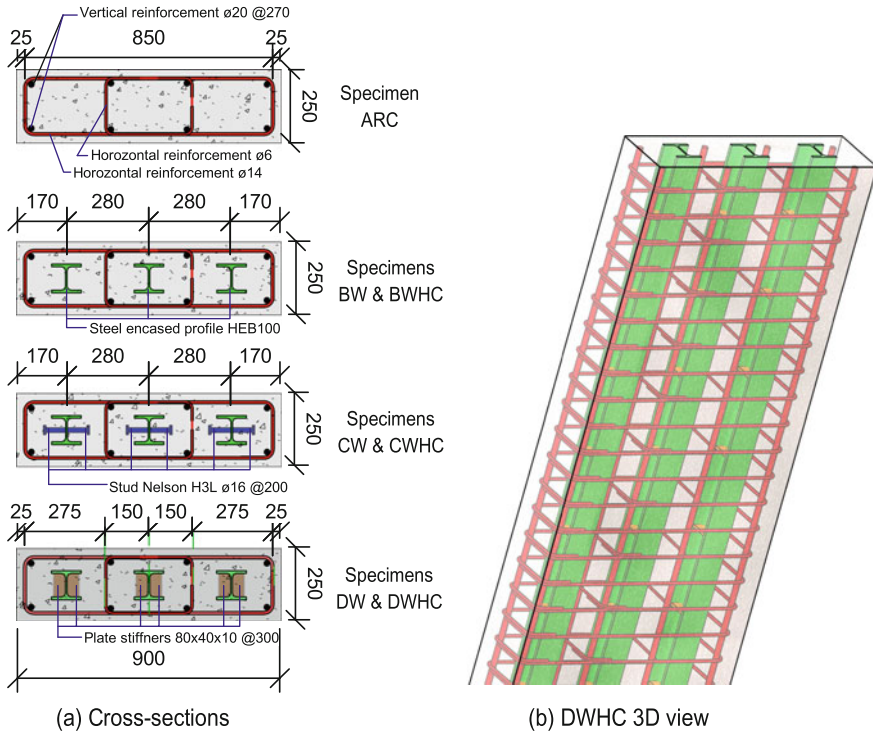


Fig. 3 Details of the test specimens

the test include the contributions of the steel profiles, shear studs, stiffeners, bond and stirrup spacing to the bending and shear resistance. Figure 3 shows the design details of all the seven specimens of hybrid walls.

Test Setup

The test setup is shown in Fig. 4. The third-point flexural beam test configuration was adopted to evaluate the resistance of specimens to combined bending and shear without axial force. Specimens were loaded at the mid-length by two hydraulic actuators (1500 kN capacity each). Pinned boundary conditions at the each end of the specimens were simulated by two supports as shown in Fig. 4. A transverse brace system was used in order to avoid out-of-plan displacement of the specimens.

Instrumentation

Several different instruments were used in the testing of the specimens. The arrangement of the instrumentation is presented in Fig. 5. During the loading, the test results were recorded every second.

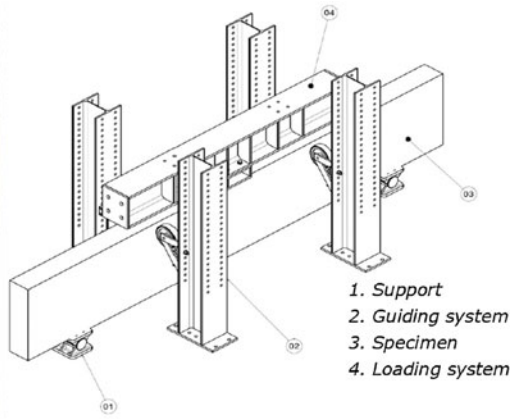


Fig. 4 Test setup

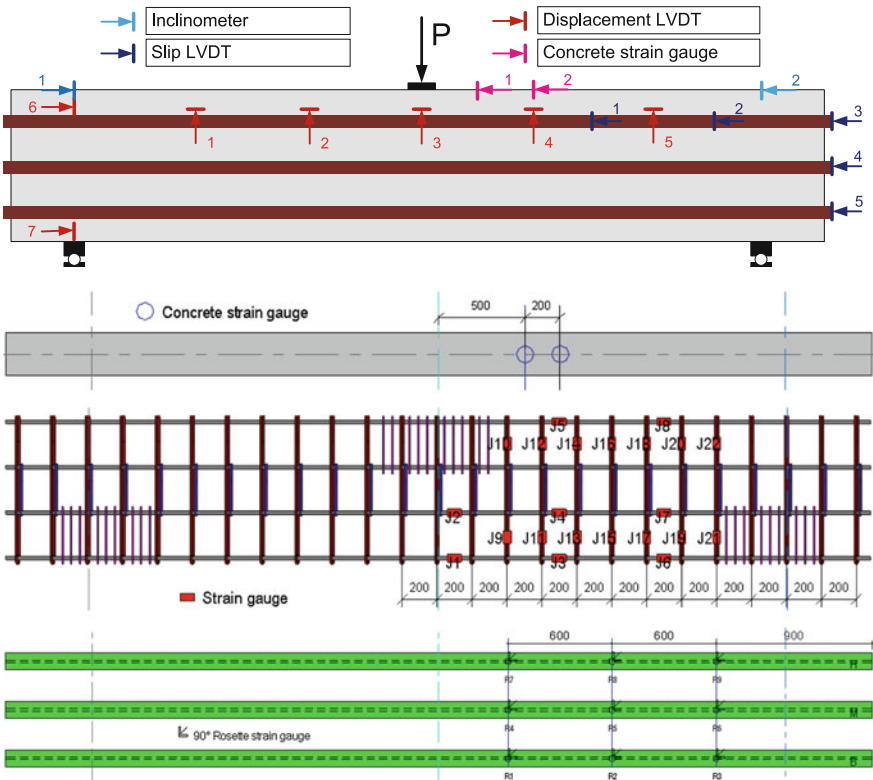


Fig. 5 Detailed arrangement of measuring devices

4 Experimental Results

A stable applied load versus displacement behaviour was observed in all seven specimens. Figure 6 presents the load versus displacement at mid-span curves for all specimens. It was observed that ductile failure took place gradually with the widening of the critical flexural cracks. It can be seen that the specimens with shear connectors had more ductile behavior than the ones without connectors. Table 1 presents the correspondence between the forces and the displacements at different characteristic points from the tests, which are: As yielding point of the first longitudinal reinforcement layer; Bs yielding point of the second longitudinal reinforcement layer; Cs yielding point of stirrups; Ds yielding point of the lower encased steel profile; Fs ultimate load capacity of the specimen; and Ys yielding of the specimen [16].

The strength of the specimens was defined in terms of load bearing capacity and represents the maximum applied vertical force. The absolute values of the load bearing capacity are presented in Table 1. The maximum load bearing capacity of the hybrid specimens was attained by CWHC and DWHC specimens, whilst the minimum is attained by BWHC specimen. The differences between these values must be due to the different concrete strengths, due to the type of the structural steel-concrete connection (i.e. bond, shear stud and stiffener) and due to the stirrup spacing of the specimens. The normalized load bearing capacity is defined as the ratio between the load bearing capacity of hybrid specimens and the load bearing capacity of the reference A-RC specimen. Figure 7 shows the normalized values of the load bearing capacity also with reference to the normalized concrete compressive strength of the specimens. It can be noticed that for BWHC specimen, although the concrete compressive strength is almost the same with A-RC specimen, the difference in load bearing capacity is about 2 times. For BW, CW and DW specimens, which were realized using a concrete of 1.3 times compressive strength from the compressive

Fig. 6 Load-displacement at mid-span curves for all specimens

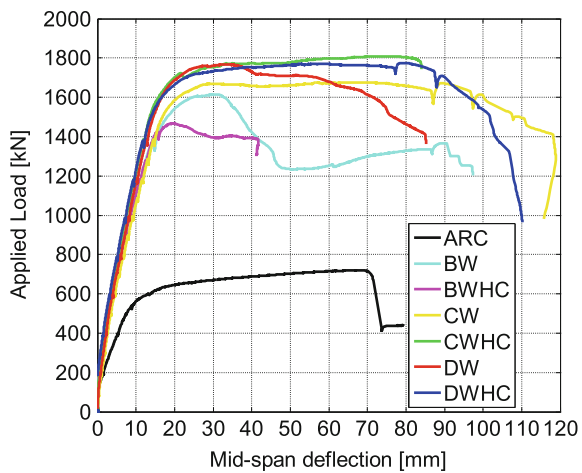
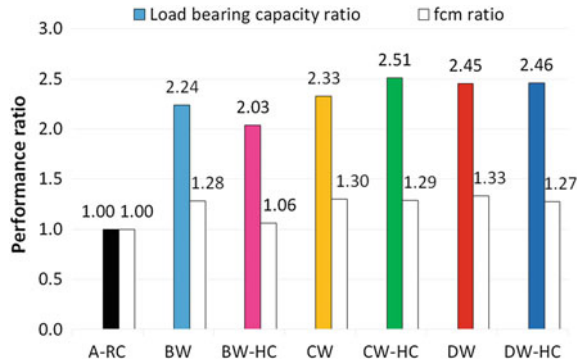


Table 1 Forces and displacements at different characteristic points

Specimen	Yielding point As		Yielding point Bs		Yielding point Cs		Yielding point Ds		Yielding point Fs		Yielding point Ys		Failure mode
	F_{As} KN	Δ_{As} mm	F_{Bs} KN	Δ_{Bs} mm	F_{Cs} KN	Δ_{Cs} mm	F_{Ds} KN	Δ_{Ds} mm	F_{Fs} KN	Δ_{Fs} mm	F_{Ys} KN	Δ_{Ys} mm	
ARC	352	4.3	519	8.2	-	-	-	-	721	66.9	557	7.94	Flexural
BW	820	6.1	1226	11.8	1302	12.9	1409	15.7	1613	30.0	1241	12.51	Flexural and shear
BWHC	880	7.0	1281	12.6	-	-	1423	15.4	1467	19.6	1173	11.26	Flexural and shear
CW	898	7.9	1402	15.1	-	-	1455	15.9	1678	57.2	1428	16.39	Flexural and shear
CWHC	977	7.3	1526	14.0	-	-	-	-	1809	76.6	1490	14.63	Flexural and shear
DW	824	7.4	1610	16.9	-	-	1435	13.5	1768	33.6	1467	15.30	Flexural and shear
DWHC	778	5.6	1299	11.1	-	-	1363	12.0	1774	78.8	1459	14.50	Flexural and shear

Fig. 7 The normalized load bearing capacity of the specimens



strength of A-RC specimen, the difference in load bearing capacity is about between 2.2 and 2.4 times. This highlights the important contribution of three encased steel profiles on the load bearing capacity. Moreover, for CWHC and DWHC specimens, which were realized using a concrete of 1.3 times compressive strength from the compressive strength of A-RC specimen, the difference in load bearing capacity is 2.5 times for the hybrid specimens. This means that the double number of stirrups did not improve significantly the load bearing capacity of hybrid specimens. This small increasing may be explained as the concrete strength became a little bit higher due to the confinement making by the stirrups. This is to say that the failure of CW and DW specimens was not caused by the yielding of the stirrups.

5 Assessment of the Proposed Design Model

Assessment of the Design Resistances

To compare the accuracy of the proposed design model to predict the bending and shear resistances of hybrid walls, a comparison between ultimate experimental and predicted strength was carried out. For the comparison purposes, the evaluation of flexural and shear resistances is made for the maximal applied load recorded on each test. The design-experimental comparisons are summarized in Table 2. Regarding the bending resistance, the $M_{pl,Rd}/M_{Ed}$ ratio varied from 0.88 to 1.08 with a mean value of 0.94 and a standard deviation of 0.075. This is to say that the proposed design model provides fairly consistent and conservative bending strengths of the tested hybrid walls.

The V_{Rd}/V_{Ed} ratio varied from 1.83 to 2.94. It is noted that due to the contribution of the shear resistance of the steel profiles the transverse shear strength V_{Rd} is largely greater than V_{Ed} . Therefore, the observed ultimate state of all hybrid specimens is ductile bending. If the contribution of the steel profiles to the transverse shear strength would be neglected, the resistance of specimen CW and DW would be conditioned by the shear resistance $V_{Rd,s}$ which represents the yielding of stirrups. How-

Table 2 Predicted versus experimental strengths

Specimen	Experimental values			Design calculation					EC4
	F_{\max} (kN)	V_{Ed} (kN)	M_{Ed} (kNm)	$V_{a,Ed}$ (kN)	σ_{cW} (Mpa)	$^a g_{Ed}$ (MPs)	$M_{pl,Rd}$ (kNm)	V_{Rd} (kN)	
BW	1613	807	1512	130	5.96	0.75	11446	1614	
BWHC	1467	734	1375	114	5.57	0.70	1490	2160	
CW	1678	839	1573	131	6.39	0.81	1493	1614	
CWHC	1809	905	1696	141	6.88	0.87	1491	2160	0.51
DW	1768	884	1658	137	6.75	0.85	1498	1614	
DWHC	1774	887	1663	139	6.74	0.85	1489	2160	

^aThe coefficient of friction is taken as 0.5 (see Eurocode 4 part 1 Sect. 6.7.4.2(4))

^b τ_{Rd} including β factor of Eurocode 4 for concrete cover greater than 40 mm; $\beta = 1.7$

ever, no yielding stress of stirrups was detected from the tests resulting in the non-negligible contribution of the steel profiles to shear resistance. Indeed, the proposed design model predicts that about 47% of the total shear force V_{Ed} acts on the steel profiles (the $n_a V_{a,Ed}/V_{Ed}$ ratio varied from 0.468 to 0.482). In order to evaluate the validity of the evaluation of the shear force in the steel profiles by the design model, we consider the case of $V_{Ed} = 600$ kN which corresponds to a total applied load of 1200 kN. Shear force in the profiles is calculated from the measurements at rosettes. As can be seen from Fig. 5, only the rosettes R2, R5 and R8 which are at a distance greater than the section height from the side forces can be considered as being outside of the disturbance zone and is used for the comparison purposes. The design-experimental comparison of the shear force in steel profiles is presented in Table 3. It can be observed that the measured shear forces are not equal in the three embedded profiles. There seem to be some regularity in the differences, with the lower profile being more stressed. The shear force in steel profiles is calculated as the sum of the individual shear force measured in each profile. The $V_{a,Ed}^{design}/V_{a,Ed}^{exp}$ ratio varied from 0.922 to 1.027 with a mean value of 0.81 and a standard deviation of 0.054. This is to say that the design predictions fits very well with the measured values. Furthermore, it is noted that the shear force in the lower steel profile $V_{a,Ed}^{rosette2}$ is much lower than the shear resistance of one steel profile $V_{pl,a,Rd} = 1.333 \times 462.62/\sqrt{3} = 1068$ kN. Therefore, for the tested specimens the influence of the transverse shear on the bending resistance can be neglected.

The prediction of the longitudinal shear stress at concrete-steel profile interface is presented in Table 2. As can be seen, at the maximum applied load the predicted shear stress g_{Ed} is greater than the design shear strength τ_{Rd} which is taken equal to 0.51 MPa according to Eurocode 4 part 1 Sect. 6.7.4.3(4). This points out that in all specimen for design conditions the shear connectors are always required to provide at least a shear resistance equal to 0.51 MPa. This is correct since the observation is that the specimens without shear connector (BW and BWHC) have significant strength loss after reaching the maximum load and a less ductile behaviour than specimens with connectors. Note that according to the design prediction the applied

Table 3 Shear force in the steel profiles at applied load of 1200 kN

Specimen	$V_{a,Ed}^{Rosette2}$ (kN)	$V_{a,Ed}^{Rosette5}$ (kN)	$V_{a,Ed}^{Rosette8}$ R8 (kN)	$V_{a,Ed}^{exp}$ (kN)	$V_{a,Ed}^{design}$ (kN)	$\frac{V_{a,Ed}^{design}}{V_{a,Ed}^{exp}}$
BW	175.50	40.87	74.24	290.61	289.47	0.996
BWHC	166.80	62.08	44.69	273.57	280.83	1.027
CW	N/A	N/A	45.53	N/A	280.21	N/A
CWHC	162.90	N/A	41.96	N/A	280.67	N/A
DW	181.20	37.01	84.92	303.13	279.34	0.922
DWHC	191.50	N/A	96.90	N/A	281.09	N/A

Note N/A stands for “not available” due to some deficient rosettes

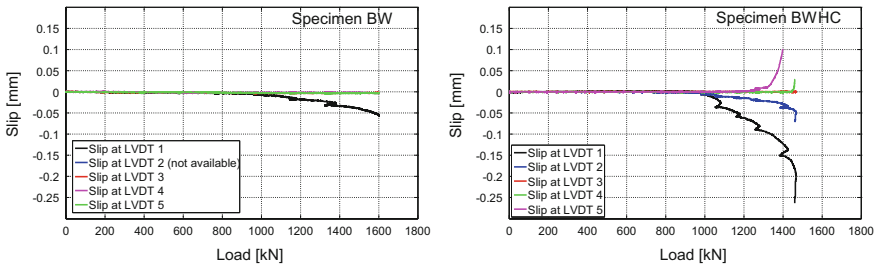


Fig. 8 Applied load versus slips in specimens without shear connector

load corresponding to a shear stress of 0.51 MPa is about 1100 kN. It indicates that below this load level the bond and friction can ensure the full interaction between steel profiles and concrete and the specimens without shear connector must have the same global behaviour as the ones with connectors. This is indeed in good agreement with what can be seen in Fig. 8.

6 Conclusions

In this paper, analytical and experimental aspects for hybrid steel-concrete walls with several steel encased profiles have been described. Firstly, a design model for hybrid walls subjected to combined compression, bending and shear has been proposed. Particular attention has been paid to transverse shear resistance for which a strut-and-tie model has been developed taking into account the contribution of the steel profiles. Furthermore, the proposed design model provides a method to evaluate longitudinal shear the concrete-steel profile interface, which is necessary to design an adequate shear connection of the profile to concrete. Secondly, an experimental study on the behavior of hybrid walls subjected to combined shear and bending has been presented. The hybrid walls consists of three steel profiles HEB100 totally encased into reinforced concrete. Seven 2:3 scale specimens were tested at Structures Labo-

ratory of INSA Rennes. Three point bending test configuration was adopted because the main objective is to evaluate the resistance to combined bending and shear of the composite walls. The wall behavior was examined by considering the load versus stress response at various points in the longitudinal rebars, in the steel profiles, in the stirrups and in the concrete. Based on the results described in this paper, the following conclusions can be drawn:

- For six hybrid specimens, the load bearing capacity was very close. The load-displacement experimental curves indicates that they had almost the same behaviour until the applied reached about 70% of the load bearing capacity. The specimens with shear connectors were more ductile in terms of displacement ductility than the ones without connectors;
- The concrete confinement made by mean of stirrups in specimens BWHC, CWHC and DWHC does not significantly increases the specimen's load bearing capacity. In other words, the concrete may be already well confined with the number of stirrups placed in specimens BW, CW and DW;
- The proposed design model provides a fairly consistent and conservative bending strength of the tested hybrid walls;
- The proposed design model provides a fair estimation of the part of applied shear which is applied to the embedded steel profiles; this allows to take into account the influence of transverse shear on the combined axial force and bending resistance.
- When used with design values of bond and friction shear strength of Eurocode 4, the proposed design model gives a fair estimation of the longitudinal shear stress at the concrete-steel profile interface.

Acknowledgements The authors gratefully acknowledge financial support by the European Commission (Research Fund for Coal and Steel) through the project SMARTCOCO (SMART COmposite COmponents: concrete structures reinforced by steel profiles) under grant agreement RFSRCT-2012-00031.

References

1. Eurocode 4. EN1994-1-1 Design of composite steel and concrete structures—Part 1: General rules and rules for buildings
2. Echigo S, Tachibana Y, Kitajima A (1998) New type hybrid structure and practical analysis method of creep and shrinkage. *Constr Build Mater* 12(2–3):93–103
3. Morino S (1998) Recent developments in hybrid structures in Japan—research, design and construction. *Eng Struct* 20(4–6):336–346
4. Dan D, Fabian A, Stoian V (2011) Theoretical and experimental study on composite steel-concrete shear walls with vertical steel encased profiles. *J Constrl Steel Res* 67(5):800–813
5. Eurocode 2. EN1992-1-1 Design of concrete structures—Part 1: General rules and rules for buildings
6. American Concrete Institute (2005) Building code requirements for reinforced concrete. ACI-318
7. American Institute for Steel Construction (2010) Specifications for structural steel buildings. ANSI/AISC 360-05, AISC

8. Zhao Q, Astaneh-Asl A (2004) Cyclic behavior of traditional and innovative composite shear walls. *J Struct Eng* 130(2):271–284
9. Saari WK, Hajjar JF, Schultz AE, Shield CK (2004) Behavior of shear studs in steel frames with reinforced concrete infill walls. *J Constr Steel Res* 60(10):1453–1480
10. Zhou Y, Lu X, Dong Y (2010) Seismic behaviour of composite shear walls with multi-embedded steel sections. Part I: Experiment. *Struct Des Tall Spec Build* 19(6):618–636
11. Rafiei S, Hossain KMA, Lachemi M, Behdinan K (2015) Profiled sandwich composite wall with high performance concrete subjected to monotonic shear. *J Constr Steel Res* 107:124–136
12. Hossain KMA, Rafiei S, Lachemi M, Behdinan K (2016) Structural performance of profiled composite wall under in-plane cyclic loading. *Eng Struct* 110:88–104
13. Zhang X, Qin Y, Chen Z (2016) Experimental seismic behavior of innovative composite shear walls. *J Constr Steel Res* 116:218–232
14. Plumier A, Dragan D, Nguyen Q-H, Dege H (2017) An analytical design method for steel-concrete hybrid walls. *Structures* 9:185–199
15. Keo P, Somja H, Nguyen Q-H, Hjjaj M (2015) Simplified design method for slender hybrid columns. *J Constr Steel Res* 110:101–120
16. Li B, Lam ES, Wu B, Wang Y (2013) Experimental investigation on reinforced concrete interior beam-column joints rehabilitated by ferrocement jackets. *Eng Struct* 56:897–909

Numerical Study on a New Through-Column-Type Joint for RCS Frame



D. D. Le, X. H. Nguyen and Q. H. Nguyen

Abstract Hybrid RCS frames consisting of reinforced concrete (RC) column and steel (S) are used frequently in practice for mid- to high-rise buildings. RCS frames possess several advantages from structural, economical, and constructional view points compared to either traditional RC or steel frames. One of the key elements in RCS frames is the beam–column joints. This paper deals with numerical study on static response of a new reinforce concrete–steel (RCS) exterior beam–column joint. The studied beam–column joint detail is a through-column type in which an H steel profile totally embedded inside RC column is directly welded to the steel beam. The H steel profile was covered by two supplementary plates in the joint area. This detail provides two main advantages: The column is continuous, and no stirrups in the joint area are needed. The nonlinear behavior of the new joint is studied numerically and showed that this proposed joint is suitable as a special moment connection. In addition, the parametric studies are carried out to investigate the influences of the stirrups, the encased profile length, and supplementary plate length on the behavior of the joint.

Keywords Beam · Column connection · RCS joint · FE modeling

D. D. Le · X. H. Nguyen (✉)
University of Transport and Communications, 3 Cau Giay Street, Hanoi, Vietnam
e-mail: nguyensexuanhuy@utc.edu.vn

D. D. Le
e-mail: ledangdung@utc.edu.vn

Q. H. Nguyen
INSA de Rennes, 20 avenue des Buttes de Coësmes, CS 70839,
35708 Rennes Cedex 7, France
e-mail: qnguyen@insa-rennes.fr

1 Introduction

Hybrid RCS frames consisting of reinforced concrete (RC) column and steel (S) are used frequently in practice because of their advantages such as reduction in structure's weight, covering large spans, increasing the lateral stiffness, convenience in adoption of strong column-weak beam criterion in tall buildings, and enhanced ductility and energy dissipation capacities [1]. One of the key elements in RCS frames is the beam-column joints. The connections between the column and beam can be divided into two types: continuous beam through (CBT) and continuous column through (CCT). In CBT connections, the beam runs through the joints continuously and the column envelopes the beams at the connection. On the contrary, with the CCT connection, the column runs continuously through the joint. FBPs, cover plate, or shear studs are placed in the joint area. The beams are connected directly to the plates by penetration weld.

The CBT joints are primarily problematic due to possible congestion of vertical rebars passing through the continuous beam and difficulties in pouring and compacting concrete in such location, especially for the middle CBT connection [1]. Kanno and Deierlein (2000) [2] suggested different types of CBT such as face bearing plate (FBP), extended face bearing plate (E-FBP), transverse beam, small column. Other types of through-column joints have also been suggested by Nishiyama et al. (2004) [3]. In the suggested configurations, steel beams are split by the continuous RC column and connected directly to the cover plate or face bearing plates, confined by horizontal stiffener, vertical stiffener, diagram. In 2013, a new through-column-type joint for composite reinforced concrete and steel frames was proposed by Mirghaderi and Eghbali (2013). In 2016, several new configurations for composite steel-concrete connections were proposed for a continuous column and a steel beam by Zibasokhan et al. (2016) [1]. The continuous column is confined by the cover plates in all of column faces. The steel beam is connected directly to the column by shear studs or the steel U-channels. Recently, European RCFS SMARTCOCO (2017) [4] project investigated the design of the new type beam-column joint to connect a steel beam and a reinforced concrete (RC) column. The steel profile is totally embedded into a RC column which is used to connect the beam through the steelwork part of composite section.

Despite the extensive research conducted on RCS connections, research methods are mainly through experiments and analyses of RCS connections using finite element method still remain in the beginning stage. Compared to the experiment, finite element method is more effective from an economical viewpoint and can also gain important data that could not be measured in experiment. [5] have presented the formulation for a plasticity-based distributed beam-column element that can be used for the seismic analysis of three-dimensional mixed frame structures comprised of steel, reinforced concrete, and composite members. Cheng and Chen (2005) [6] have simulated the force-deformation behavior of RCS joint sub-assemblages by a nonlinear analysis program, DRAIN-2DX, with consideration of composite effects of the beam and slab as well as shear distortion in the panel zone. Noguchi and Uchida (2004)

[7] utilized the nonlinear three-dimensional finite element method (FEM) to analyze two frame specimens with reinforced concrete columns and steel beams, which had different beam–column joint detailing. Li et al. (2012) [8] studied the influence of different parameters on the behavior of composite frame structures by finite element software ABAQUS.

A novel through-column-type joint, in which an H steel profile covered by two supplementary plates totally embedded inside RC column is directly welded to the steel beam (Fig. 1), is recently proposed within INSAR-UTC Nafosted project (2016–2019) [9]. Compared to the RCS joint studied within European RCFS SMARTCOCO (2017) [4], the main advantage of this joint is that the problematic due to congestion of stirrups passing through the continuous beam can be avoided because the stirrups at the joint region are omitted. Unfortunately, this kind of joint detail is not covered yet by the existing design guidelines. Indeed, Eurocodes 2, 3, and 4 give some provisions that can partly be used for the design of such a joint. There remains however a real lack of knowledge relatively to the issue of the force transmission from the embedded steel profile to the surrounding concrete of the column. Questions that can rise when designing such a connection are about the optimal anchorage length to embed the H steel profile or the optimal length of the supplementary plates. Therefore, experimental tests and numerical simulations need to be conducted to answer to these questions. In this paper, the main objective is to develop a reliable nonlinear three-dimensional finite element model to investigate the behavior of the new RCS joint detail illustrated in Fig. 1. The finite element ABAQUS software is employed. Extensive parametric studies are carried out to investigate the influences of the stirrups, the encased profile length, and supplementary plate length on the behavior of the joint.

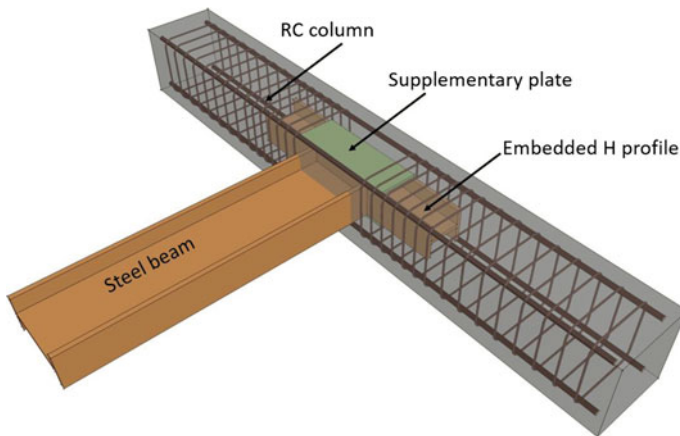


Fig. 1 Novel through-column-type joint detail proposed within INSAR-UTC Nafosted project (2016–2019) [9]

2 Finite Element Model

Advances in computational features and software have brought the finite element method within reach of both academic research and engineers in practice by means of general-purpose nonlinear finite element analysis packages, with one of the most used nowadays being [10] software. The program offers a wide range of options regarding element types, material behavior, and numerical solution controls, as well as graphical user interfaces, auto-meshers, and sophisticated post-processors and graphics to speed the analyses. In this paper, this commercial software is employed to develop reliable three-dimensional finite element model for the RCS joint specimen.

Due to the symmetry of the specimen geometry and loading, in order to save the calculation time, only half of the specimen was modeled. A full view of specimen is shown in Fig. 1 for reference. Five components of specimen (concrete column, rebars, steel beam, embedded steel profile, and headed studs) are modeled separately and assembled to make a complete specimen model. In addition, the interaction between components influences greatly the analysis results. Thus, the interface and contact between the concrete in joint region and the structural steel, the headed studs and concrete, the interaction of reinforcement and concrete need also to be modeled. Furthermore, the choice of element types, mesh sizes, boundary conditions, and load applications that provide accurate and reasonable results are also important in simulating the behavior of the RCS joint. Displacements are assumed to be small; therefore, the nonlinear geometric effect is not considered. However, the material nonlinearity is included in the finite element analysis.

Selection of Element Type and Meshing

The concrete column, steel beam, and headed stud are modeled with solid C3D8R element available in ABAQUS library. The C3D8R element is an 8-node linear brick element with reduced integration stiffness and with hour-glass enhanced. Note that compared to the quadratic brick C3D20R element (20-node element), the accuracy of this element is slightly lower, but using this element leads to a significant reduction of degree of freedom therefore computational cost. Furthermore, according to ABAQUS manual, this element is suitable for nonlinear analysis including contact, large deformation, plasticity, and failure. The reinforcement bars can be modeled using solid, beam, or truss elements. The use of solid elements is computationally expensive and therefore not chosen. Because the reinforcing bars do not provide a very high bending stiffness, the 2-node linear 3-D truss elements, namely T3D2, are used.

Figure 2 shows the meshing of the FE model for the concrete column, rebars, steel beam, embedded steel profile. In order to achieve the reliable results, the fine mesh was used in the connection zone. Reasonable convergence was achieved with such a mesh size, and refinement of the mesh was studied only up to the point where the change in the mesh size did not have an impact on the results.

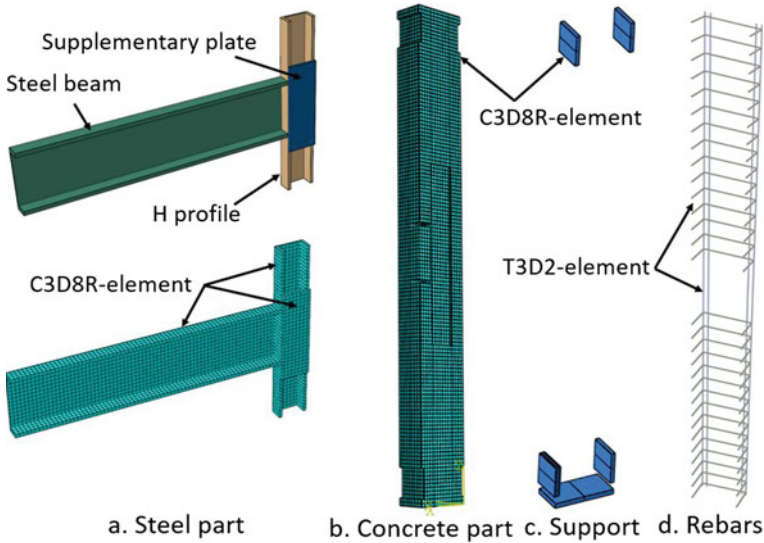


Fig. 2 FE type and mesh of components of the exterior RSC joint specimen

Interaction Conditions Between Components

Contact interactions between components may significantly affect the complete specimen behavior and need to be carefully conditioned. Improper definition of contact interactions may introduce nonphysical into the simulation. In fact, the reinforcing bars are fully anchored in concrete so that embedded constraint can be used for the interaction between rebars and concrete surrounding. This constraint implies an infinite bond strength at the interface between the concrete and the reinforcement. In the present case, the truss elements representing the reinforcement are the embedded region while the concrete slab is the host region. Surface-to-surface contact elements (available in ABAQUS library) are used to model the interaction between concrete column and steel profile. The interaction properties are defined by the behavior normal and tangential to the surfaces. For the normal behavior, surface “hard” contact constraint is assumed. This type of normal behavior implies that no penetration is allowed at each constraint location. For the tangential behavior, the penalty frictional formulation is used, and the coefficient of friction between the steel profile and the concrete column is assumed to be 0.5.

Loading and Boundary Conditions

One of the objectives of this numerical study is to estimate the strength of the test specimens in the future experimental study. Therefore, the loading and boundary conditions are taken as in the experimental test setup which is illustrated in Fig. 3. The loading is applied continuously in the form of the displacement control manner. The displacement of 75 mm is imposed on the whole cross section at the beam end in horizontal direction.

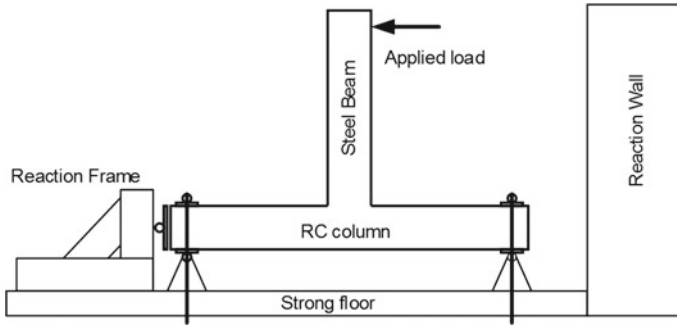


Fig. 3 Test setup

Material Modeling of Steel

The von Mises yield criterion with isotropic hardening rule is used for the structural steel, reinforcing steel, and steel plate. An elastic-linear-work-hardening material, available in ABAQUS material library, is considered with tangent-hardening modulus being equal to 1/10000 of elastic modulus, in order to avoid numerical problems. The yielding stress and elastic modulus are taken equal to 280 MPa and 210000 MPa for structural steel, respectively, while 360 MPa and 200000 MPa for reinforcing steel and headed stud.

Material Modeling of Concrete

The concrete damaged plasticity (CDP) model, developed by Lee and Fenves [11], available in ABAQUS material library is used to model the concrete material. This model consists of the combination of nonassociated multi-hardening plasticity and scalar damaged elasticity to describe the irreversible damage that occurs during the fracturing process. In the CDP model, five parameters control the evolution and the shape of the yield surface and the flow potential. The first parameter is the dilation angle which is measured at high confining pressure in the plan of hydrostatic pressure stress p and Mises equivalent stress q . The second parameter is the eccentricity of the plastic potential surface. The third parameter is the ratio of initial equibiaxial compressive yield stress fb_0 to initial compressive yield stress fc_0 . The next parameter is named K which allows to determine the shape of loading surface in the deviatoric plane. The last one is the viscosity parameter which allows to slightly exceed the plastic potential surface area in certain sufficiently small problem steps to overcome convergence problems. Therefore, a very small value (0.0001) is chosen for simulation in this study.

For compressive behavior, the uniaxial stress–strain curve of [12] is selected for the determination of yield stress and inelastic strain. The compressive stress is assumed to increase linearly with respect to the total strain until the initial yield/damage stress which is taken equal to $0.4f_{cm}$ where f_{cm} is the mean compressive cylinder strength. The initial Young's modulus is calculated according to [12]. The Poisson's ratio is taken as 0.2. Then, the compressive stress grows until failure strength

Table 1 Material parameter of CDP model for concrete of $f_{cm} = 40$ MPa

Density			Parameters of CDP model		
ρ (tonne/mm ³)	2.4×10^{-9}		Dilation angle	36°	
Elasticity			Eccentricity	0.1	
E (MPa)	33346		fb0/fc0	1.15	
ν	0.2		K	0.6667	
			Viscosity parameter	0.001	
Compressive behavior			Tensile behavior		
Yield stress (MPa)	Inelastic strain	Damage	Yield (MPa)	Displacement (mm)	Damage
16.00	0.00000	0.000	2.90	0.000	0.000
27.68	0.00017	0.039	1.94	0.066	0.381
35.73	0.00043	0.088	1.30	0.123	0.617
40.00	0.00100	0.181	0.87	0.173	0.763
39.19	0.00132	0.234	0.59	0.220	0.853
36.71	0.00170	0.298	0.39	0.265	0.909
32.52	0.00212	0.376	0.26	0.308	0.944
24.16	0.00278	0.516	0.18	0.351	0.965

f_{cm} . The strain (ϵ_{c1}) associated with f_{cm} is equal to 0.0022, given by [12]. After exceeding the compression strain ϵ_{c1} , localization of damage occurs and the compressive stress decreases with the softening strain. For tensile behavior of concrete, the effects of the reinforcement interaction with concrete is considered and the tension stiffening is specified by means of a post-failure stress–displacement relationship. The damage parameters in compression as in tension are determined by assuming that the split of inelastic strains into plastic and damaging parts by the scalar parameter as proposed by [13]. The material properties assigned in CDP model are summarized in Table 1.

3 Parametric Studies

Parameter Sets

In our parametric studies, the geometrical properties of the beam and the RC column (as shown in Fig. 4) are unchanged. The parameter sets are the embedded H profile, the thickness of supplementary plates, and the length of supplementary plates. Table 2 summarizes the values of the parameter sets used in the parametric studies.

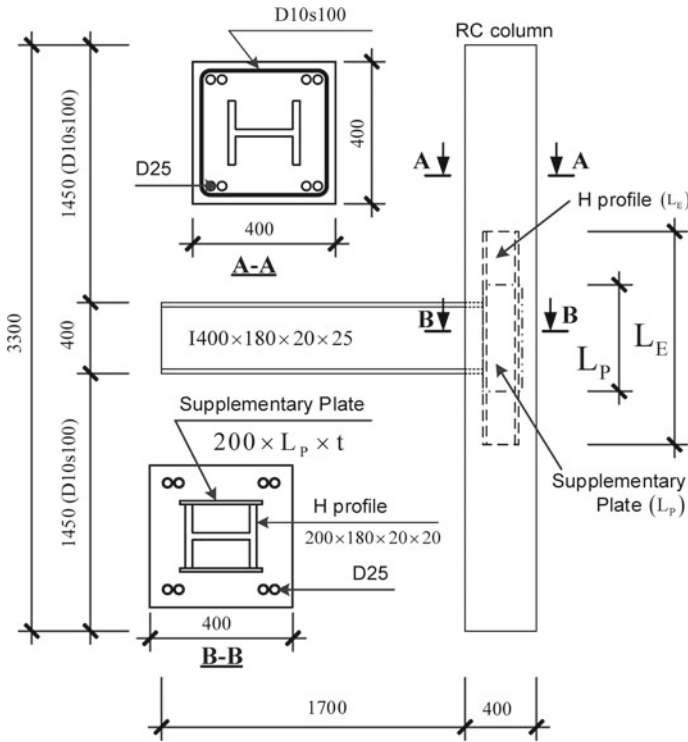


Fig. 4 Description of the test specimen modeled by FE model

Influence of Length of Embedded H Profile

The influence of length of embedded H profile on the global behavior of the hybrid joint is presented in Fig. 5 in terms of load-displacement curves. The length of embedded H profile, namely L_e , was taken from 40 to 330 cm. It can be observed that, for L smaller than 80 cm, the stiffness and resistance of the joint increase with increasing of L_e . However, the load-displacement curves obtained with $L \geq 120$ cm remain almost unchanged. It can be pointed out from this numerical study that the joint behavior is not affected by the length of embedded H profile when the latter exceeds three times of the beam height. Further, experimental research needs to be conducted to confirm this.

Influence of Thickness of Supplementary Plates

The main advantage of the proposed joint detail compared to the one proposed in European RCFS SMARTCOCO (2017) [4] project is that the stirrups in the beam-column connection region can be omitted because of the presence of supplementary plates. Therefore, in this parametric study the influence of the supplementary plates on the behavior of the proposed joint is carried out. Figure 6 presents the load-displacement curves obtained with different thickness of supplementary plates. Note

Table 2 Parameter sets for parametric studies

Parameter sets Name of Model	Length of embedded H profile (L_E) mm	Supplementary Plate (200x L_P x t)			Stirrups in joint region
		Length L_P mm	With 200 mm	Thickness t mm	
L40	400	/	/	/	5 ϕ 10
L60	600				5 ϕ 10
L80	800				5 ϕ 10
L120	1200				5 ϕ 10
L160	1600				5 ϕ 10
L200	2000				5 ϕ 10
L300	3300				5 ϕ 10
L120P15x40	1200				400
L120P15x60	1200	600	200	15	
L120P15x80	1200	800	200	15	
L120P15x100	1200	1000	200	15	
L120P15x120	1200	1200	200	15	
L120P3x60	1200	600	200	3	/
L120P5x60	1200	600	200	5	
L120P10x60	1200	600	200	10	
L120P15x60	1200	600	200	15	
L120P20x60	1200	600	200	20	
L80P5x60	800	600	200	5	/
L80P10x60	800	600	200	10	
L80P15x60	800	600	200	15	
L80P20x60	800	600	200	20	

that the length of embedded H profile is taken equal to 120 cm in order to avoid the influence of length of the embedded H profile (see paragraph above). The black line in Fig. 6 corresponds to the case with out supplementary plate but five stirrups $\phi 5$ are present in the joint region. The other curves correspond to the cases where the stirrups are removed and replaced by the plates of 60 cm length. It can be seen from Fig. 6 that the supplementary plates can play the role of stirrups in the joint region. Regarding the influence of the thickness of supplementary plates, more the thickness increases more the stiffness and resistance of the joint increase. The load-displacement curves remain almost unchanged when the thickness exceeds 15 mm.

Fig. 5 Influence of the length of embedded H profile

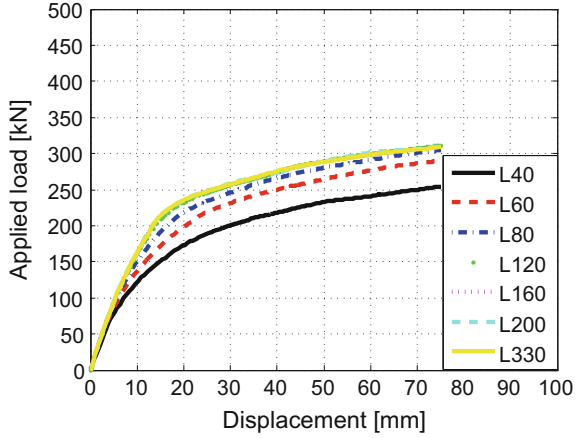
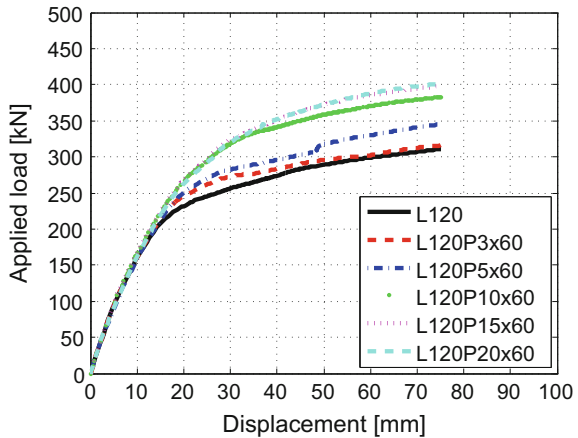


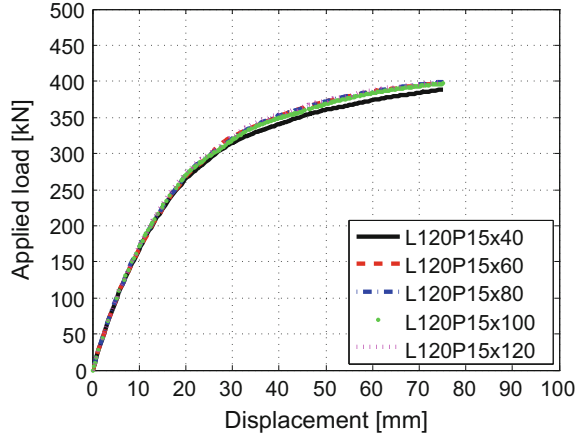
Fig. 6 Influence of the thickness of supplementary plates



Influence of Length of the Supplementary Plates

The numerical results shown in Fig. 6 indicated that by adding the supplementary plates, the stirrups in the joint region can be omitted. However, the curves in Fig. 6 correspond to the cases where the length of supplementary plates, namely L_p , is equal to the height of the steel beam. Question can be raised is what is the influence of length of supplementary plates on the global behavior of the joint. Therefore, five values of the plate length are considered in this parametric study. Figure 7 presents the load-displacement curves obtained with different lengths of the supplementary plates. As can be seen, the load-displacement curves remain almost unchanged when the length L_p is greater than the height of the steel beam. This is to say that the supplementary plates are needed only in the beam–column connection area.

Fig. 7 Influence of the length of supplementary plates



4 Conclusion

In this paper, a numerical analysis of the behavior of a novel type of exterior RCS joint subjected to static loading has been presented. The considered exterior RCS connection consists of an H steel profile covered by two supplementary plates totally embedded inside RC column directly welded to the steel beam. This type of beam-to-column joint has been recently proposed within INSAR-UTC Nafosted project (2016–2019) [9] because it seems to present some advantages compared to the existing RCS joint in terms of resistance and construction methods. A 3-D finite element model has been created using ABAQUS software. This model takes into account the material nonlinearities, interaction, and the contact between steel and concrete. Extensive parametric studies have been carried out to investigate the influences of the stirrups, the encased profile length, and the supplementary plate length on the behavior of the joint. The numerical results indicated that the effect of length of embedded H profile on the joint behavior is no longer significant when it exceeds about three times of the steel beam height. This is to say that the optimal anchorage length to embed the H steel profile is $L_e = 3H_{beam}$. It has been observed that the presence of the supplementary plates in the joint region can allow to remove the stirrups in this region. Furthermore, parametric study performed with different lengths of the supplementary plates pointed out that the supplementary plates are needed only in the beam–column connection area. However, future experimental research needs to be conducted to confirm this.

Acknowledgements This research is funded by Vietnam National Foundation for Science and Technology Development (NAFOSTED) under grant number 107.01-2016.06.

References

1. Zibasokhan H, Behnamfar F, Behfarnia K (2016) The new proposed details for moment resisting connections of steel beam to continuous concrete column. *Adv Struct Eng* 19(1):156–169
2. Kanno R, Deierlein G (2000) Design model of joints for RCS frames, composite construction in steel and concrete IV, pp 947–958
3. Nishiyama I, Kuramoto H, Noguchi H (2004) Guidelines: seismic design of composite reinforced concrete and steel buildings. *J Struct Eng ASCE* 130(2):336–342
4. SMARTCOCO (2017) Smart composite components: concrete structures reinforced by steel profiles SmartCoCo—Final report: European Committee: Research Programme of the Research Fund for Coal and Steel
5. El-Tawil S, Deierlein GG (2001) Nonlinear analysis of mixed steel-concrete frames. I: Element formulation. *J Struct Eng ASCE* 127(6):647–655
6. Cheng CT, Chen CC (2005) Seismic behavior of steel beam and reinforced concrete column connections. *J Constr Steel Res* 61:587–606
7. Noguchi H, Uchida K (2004) Finite element method analysis of hybrid structural frames with reinforced concrete columns and steel beams. *J Struct Eng ASCE* 130:328–335
8. Li W, Li QN, Jiang WS (2012) Parameter study on composite frames consisting of steel beams and reinforced concrete columns. *J Constr Steel Res* 77:145–162
9. NAFOSTED (2016). Experimental and numerical investigation on seismic behavior of composite reinforced concrete and steel joints. The National Foundation for Science and Technology Development, Vietnam
10. ABAQUS User's Manual V.6.13 (2013) Dassault Systems Simula Corp
11. Lee J, Fenves GL (1998) Plastic-damage model for cyclic loading of concrete structures. *J Eng Mech* 124:892–900
12. Eurocode 2 (2004) EN1992-1-1 Design of concrete structures—Part 1: General rules and rules for buildings
13. Krätzig WB, Pölling R (2004) An elasto-plastic damage model for reinforced concrete with minimum number of material parameters. *Comput Struct* 82:1201–1215

Flexural Behavior of Unbonded Post-Tensioned Concrete T-Beams Externally Bonded With CFRP Sheets Under Static Loading



Q. P. T. Truong, P. Phan-Vu, D. Tran-Thanh, T. D. Dang
and L. Nguyen-Minh

Abstract This paper presents a study on flexural behavior of unbonded post-tensioned concrete T-beams (UPC) externally strengthened by CFRP sheets under static loading with or without the presence of U-strip CFRP anchorage systems. A total of nine UPC T-beams in large size including one control unstrengthened beam and eight beams externally strengthened with varied number of CFRP sheets (2, 4, and 6 plies) were tested. Two types of transverse CFRP U-strip anchorage system were also retrofitted in the shear span. The results showed that CFRP sheets significantly increased the flexural capacity (up to 37%), decreased deflection in serviceability state, improved ductility, and reduced crack width (up to 48%) of the tested beams. The maximum strain in CFRP sheets in strengthened UPC T-beams ranged from 38.7 to 69.3% of the rupture strain of the CFRP sheets and tended to decrease with a large number of CFRP sheets. Strain in tendons of strengthened beams was significantly affected by the CFRP sheets and transverse U-strip anchorage system.

Keywords CFRP sheet · Flexural strengthening · Number of CFRP layer · U-strip CFRP anchorage · Post-tensioned concrete T-beams
Cracking behavior · Flexural capacity · Formula

Q. P. T. Truong

Faculty of Civil Engineering, Van Lang University, Ho Chi Minh City, Vietnam
e-mail: truongthiphuongquynh@vanlanguni.edu.vn

P. Phan-Vu

Faculty of Civil & Electrical Engineering, Open University, Ho Chi Minh City, Vietnam
e-mail: phuong.pv@ou.edu.vn

D. Tran-Thanh · T. D. Dang · L. Nguyen-Minh (✉)

Faculty of Civil Engineering, HCMC University of Technology, Ho Chi Minh City, Vietnam
e-mail: nguyenminhlong@hcmut.edu.vn

D. Tran-Thanh

e-mail: tranthanhduong31@gmail.com

T. D. Dang

e-mail: ddtung@hcmut.edu.vn

© Springer Nature Singapore Pte Ltd. 2018

H. Nguyen-Xuan et al. (eds.), *Proceedings of the International Conference on Advances in Computational Mechanics 2017*, Lecture Notes in Mechanical Engineering, https://doi.org/10.1007/978-981-10-7149-2_19

List of Symbols

AN1	U-strip anchorage system with one 300-mm-wide strip and three 100-mm-wide strips installed within the distance of $L/4 = 1350$ mm from each end of CFRP sheet
AN2	U-strip anchorage system with six 100-mm-wide strips evenly spaced within the distance of $L/4 = 1350$ mm from each end of CFRP sheet
an	number of CFRP U-strip 100-mm-wide anchorage
$a_{cr,exp}$	crack width of tested beam, mm
$a_{cr,u,CFRP}$	maximum crack width of FRP-strengthened beam, mm
$a_{cr,u,0}$	maximum crack width of the control beam, mm
t_f	thickness of one ply of the CFRP sheet, mm
$a_{cr,CFRP}$	crack width of FRP-strengthened beam, mm
a_f	width of the CFRP reinforcing plies, mm
n	number of plies of CFRP sheet
s_f	spacing of CFRP U-strip, mm
w_f	width of CFRP U-strip anchors, mm
$P_{cr,exp}$	cracking load of test beam, kN
P_{exp}	test load, kN
$P_{u,0,exp}$	ultimate load of the control beam, kN
$P_{u,exp}$	ultimate load of test beam, kN
$\delta_{u,exp}$	maximum displacement at midspan of test beam, mm
$\delta_{exp,mid}$	displacement at midspan of test beam, mm
$\epsilon_{ten,u,mid}$	maximum tensile strain in unbonded tendon at midspan, ‰
$\delta_{u,0}$	maximum displacement at midspan of the control beam, mm
ϵ_{cu}	maximum concrete strain, ‰
ϵ_{CFRP}	tensile strain in CFRP sheets, ‰
ϵ_{su}	maximum tensile strain in non-prestressed reinforcement at the ultimate load, ‰
$\epsilon_{fu,end}$	maximum tensile strain in CFRP sheets at the ends of the bond length, ‰
$\epsilon_{fu,L/3}$	maximum tensile strain in CFRP sheets of test beam at the loading locations, ‰
$\epsilon_{fu,mid}$	maximum tensile strain in CFRP sheets of test beam at midspan, ‰

1 Introduction

Recently, most of the studies relating to the repair and retrofit of prestressed members using CFRP materials have mainly focused on pretensioned concrete (PC) beams, particularly on degraded or damaged PC beams due to overloading or impact of overweight vehicles or construction equipment [1–6]. All experimental results have pointed out that using of CFRP strengthening systems helped increase the stiffness and flexural capacity of specimens, reduce crack spacing and crack width, as well as delay

the debonding of FRP sheets and consequently improved the ductility of strengthened beams. Although pretensioned members have constituted a fair proportion of structure members, there have been very few researches about FRP-strengthening on such type of members, especially on unbonded post-tensioned ones (UPC) [7–10]. This lack of experimental results has deemed as a main reason why existing guidelines for the design and construction of CFRP systems have not yet proposed any terms for this case of UPC beams. Differing from bonded ones, the behavior of unbonded tendons is really complicated due to not working together with surrounding concrete and CFRP reinforcing plies. As a result, the interaction between unbonded strands and the surrounding concrete as well as FRP sheets in UPC beams becomes weaker as compared to that in bonded PC beams in which FRP sheets, tendons and nearby concrete maintain the integrity and thus the strain compatibility condition in these components is satisfied. This difference might result in the decrease in the flexural FRP-strengthening effectiveness in the case of UPC beams. It is, therefore, crucial to thoroughly understand the tendon's behavior and its interaction with CFRP reinforcement in order to support the evaluation and calculation of the efficiency of FRP-strengthening more complete and reliable under the existing guidelines [11–13] in the absence of design instruction of CFRP materials for UPC beams.

This paper deals with flexural behavior of UPC T-beams externally strengthened by CFRP sheets with or without the usage of U-wrap CFRP anchorage systems. The experimental program was conducted on nine post-tensioned concrete T-beams in large size encompassing one control beam and eight beams strengthened with 0, 2, 4, and 6 CFRP plies, respectively. All specimens were monotonically tested under four-point loading. Main purposes of this study are: (1) assess flexural capacity of CFRP-strengthened UPC T-beams with or without CFRP anchorage systems under static loading; (2) evaluate interaction between unbonded tendons and CFRP sheets as well as the influence of the CFRP sheets upon strain in tendons.

2 Experimental Program

2.1 Material Properties

The concrete for casting specimens was produced with graded aggregates as follows: cement PC40 (410 kg/m³); crushing stone 1 × 2 (22 mm, 1028 kg/m³); river sand (0 ÷ 4 mm, 550 kg/m³); crushed sand (0 ÷ 2 mm, 247 kg/m³); and plasticizing admixture (5.5 l/m³). The average 28-day cube compressive strength is determined by the compression test on six cubes of size 150 × 150 × 150 mm, $f_{c,cube} = 47.2$ MPa and the splitting tensile strength of concrete $f_{sp,cube} = 5.8$ MPa. The concrete slump approximates 12 ± 2 cm. Each beam was prestressed with seven-wire unbonded strands of which the nominal diameter = 12.7 mm, the nominal yield strength f_{py} and nominal ultimate strength f_{pu} were 1675 MPa, 1860 MPa, respectively. Modulus of elasticity of strand is $E_p = 195$ GPa. The average yield strength and ultimate tensile strength of non-prestressed

reinforcement and stirrup were determined by tensile testing on three reinforcing steel specimens as follows: $f_y = 430$ MPa and $f_u = 600$ MPa; $f_{yw} = 342$ MPa and $f_{uw} = 463$ MPa. Modulus of elasticity of reinforcement is $E_s = 200$ GPa. Hand layup was used as the method of constructing CFRP composite system. The mechanical properties of the carbon fiber fabric were given as follows: thickness $t_f = 0.166$ mm; ultimate tensile strength $f_{fu} = 4900$ MPa; tensile modulus $E_f = 240$ GPa; rupture strain $\epsilon_{fu} = 2.1\%$. The resin has the ultimate tensile strength $f_{epoxy,u} = 60$ MPa and tensile modulus = 3000–3500 MPa.

2.2 Test Beams

The experimental program was carried out on nine UPC T-beams, including one unstrengthened control beams (M0) and eight beams externally bonded with different layers of CFRP sheets (2, 4, and 6 layers). The dimensions of the test beams were illustrated in Fig. 1 with 360 mm depth, 200 mm flange width, 6000 mm length, and 5600 mm span length. The specimen size was selected as one-half scale of the actual size of reinforced concrete bridges in Dong Thap, Viet Nam. Specifications of the cross section are designed in accordance with ACI 318-14 for Class U-uncracked members. All beams were prestressed with two unbonded low-relaxation seven-wire 12.7 mm diameter draped strands. Non-prestressed reinforcement is provided by two 12 mm diameter mild steel bars at the tension fibers of the beam web and four 10 mm diameter bars at the compression zone of the flange. The stirrups with diameter of 6 mm were set with a spacing of 175 mm along the span and a spacing of 50 mm at beam ends. The specimen geometry was illustrated in Fig. 1 and summarized in Table 1.

The bottom concrete surface of the strengthened beams was applied the unidirectional CFRP sheets, of which fibers were parallel to the beam longitudinal axis. Among these strengthened beams, five beams were retrofitted with two types of CFRP U-strip anchorage system for debonding mitigation. Details of the CFRP

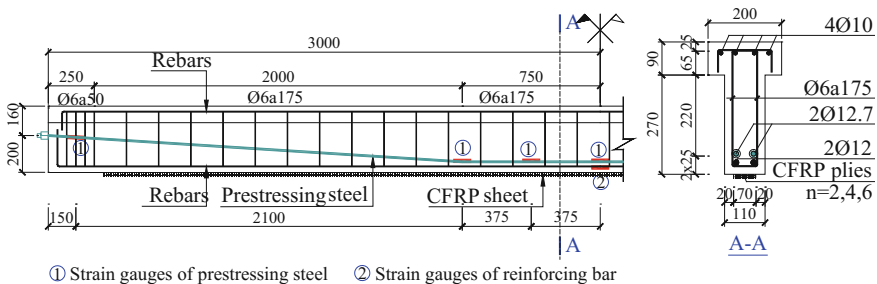


Fig. 1 Details of internal reinforcement with the arrangement of strain gauges (dimensions in mm)

Table 1 Specimen specifications

Sign. of beams	$f_{c,cube}$ (MPa)	$b \times h \times b_t \times h_t \times L$ (mm)	n	an	a_f (mm)	t_f (mm)	w_f (mm)	s_f (mm)	Type of U anchorage
M0	47.2	$110 \times 360 \times 200 \times 90 \times 6000$	–	–	–	–	–	–	–
M2CB			2	–	70	0.127	–	–	–
M4CB			4	–	70	0.127	–	–	–
M6CB			6	–	70	0.127	–	–	–
M2CBAN1			2	12	70	0.127	300;100	250	AN1
M4CBAN1			4	12	70	0.127	300;100	250	
M6CBAN1			6	12	70	0.127	300;100	250	
M2CBAN2			2	12	70	0.127	100	150	AN2
M4CBAN2			4	12	70	0.127	100	150	

strengthening configuration and two types of U-strip anchorage system were shown in Fig. 3 and summarized in Table 1.

2.3 Test Setup and Instrumentation

The specimens were tested in a four-point flexural loading configuration (Fig. 2). The load provided by one hydraulic jack was transferred to the beam specimen as two-point loads via a distribution steel girder. The distance between the loading points and the nearest support approximates one-third of span $L/3 = 1870$ mm.

Four strain gauges (SGs) were installed on the bottom surface of strengthened beams along the CFRP bonding length to record strain of CFRP sheet at four positions: one at the midspan, two at loading points, and one at a distance of 650 mm from the support. The strain of prestressing strands was determined by four SGs: one at the distance of 150 mm from the anchor head; one at the midspan; and two at the draped positions of the strand profile. One strain gauge was installed on the longitudinal reinforcement at midspan to measure their strain. Another four SGs were bonded on the concrete surface along the beam height at midspan to record the concrete strain. Beam deflection was measured by five linear variable differential transformer (LVDT) located at different positions: one at the midspan, two at the loading points, and the remaining two at the support locations. The specimens were subjected to static loading. The beams were initially loaded with an incremental load of 15 kN prior to the predicted cracking load. After first crack appeared, the specimens were loaded up to failure with an incremental load of 30 kN. Each incremental loading was maintained for approximately 3 min to record displacement, deformation, crack width, fracture formation, and development. All displacement and deformation measurements are automatically recorded via a data

Fig. 2 Test beam in laboratory



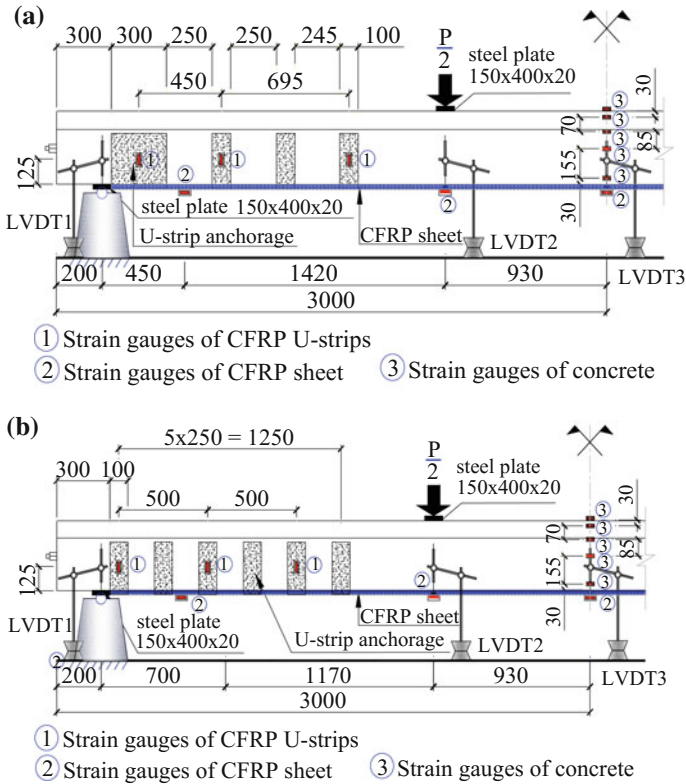


Fig. 3 CFRP strengthening layout and the arrangement of strain gauges with two types of CFRP U-wrap anchorage system: **a** Type AN1; **b** Type AN2

acquisition system with multiple channels. The arrangement of measuring devices is shown in Fig. 3.

3 Experimental Results

3.1 Failure Mode

The experimental results of all beams are summarized in Table 2. The flexural failure of the control unstrengthened beam occurred along with crushing of compression concrete. In eight strengthened beams, flexural failure was accompanied by cover delamination and debonding of CFRP sheets without damage of compression concrete (Fig. 5). Concrete flexural cracks began to form within the flexural span at a load level of approximately 35% of the failure load $P_{u,exp}$, originated at the tension zone perpendicular to the beam longitudinal axis then propagated upward to

Table 2 Summary of test results

Specimen	$P_{cr,exp}$	$P_{u,exp}$	$\delta_{u,mid}$	c_u	$f_{u,end}$	$f_{u,L/3}$	$f_{u,mid}$	$t_{en,u,mid}$	s_u	G_F
	kN	kN	mm	% $_{e}$	% $_{e}$	% $_{e}$	% $_{e}$	% $_{e}$	% $_{e}$	N/mm
M0	50	145	75.12	3.50	–	–	–	8.94	33.53	150
M2CB	50	156	81.68	1.91	0.21	12.39	5.93	8.95	11.60	185
M4CB	50	165	90.20	2.18	0.26	11.39	11.53	9.35	29.15	219
M6CB	68	190	105.11	2.65	0.33	8.13	5.78	9.87	32.09	291
M2CB-AN1	60	176	100.02	2.57	0.13	14.56	10.98	10.31	27.40	246
M4CB-AN1	60	189	115.79	2.79	2.78	12.98	11.51	11.03	20.83	314
M6CB-AN1	69	199	124.01	2.95	0.39	9.56	7.64	11.51	19.44	366
M2CB-AN2	60	169	90.00	2.37	0.43	13.93	11.53	10.13	27.64	211
M4CB-AN2	60	189	115.00	2.51	1.77	11.54	13.25	10.85	–	315

the compression flange. At the subsequent load levels, together with the growth of existing cracks, new cracks appeared and propagated progressively toward the two supports. At the load level of approximately 70% of the failure load $P_{u,exp}$, some inclined cracks started to be visible in the shear span. At the load level of approximately 90% $P_{u,exp}$, cover delamination initiated within the constant moment region then debonding at curtailment of externally bonded CFRP reinforcement accompanying with rupture of the U-strip anchorage occurred at failure (Fig. 4).

At failure of non-anchorage strengthened beams, cover delamination occurred at the loading region whereas debonding of the CFRP reinforcing sheet initiated at the loading region then propagated toward the other side support. At failure of U-strip anchorage beams, debonding and delamination occurred at the non-anchorage region, and the rupture of U-shaped anchorage strips along with debonding of CFRP sheet may happen at one side of the beam (Fig. 5). This clearly shows the considerable effect of the U-strip anchorage system on debonding of the externally bonded CFRP sheet. Overall, the U-strip anchorage system most likely delayed the debonding failure thereby improved the flexural strength and deformation capacity of strengthened beams [2, 5]. Cracking in U-strip anchorage beams was delayed with their smaller crack width as compared to that of non-anchorage strengthened

**Fig. 4** Cover delamination at the constant moment region of strengthened beams



Fig. 5 Crack patterns of test beams

beams. The failure crack width of the strengthened beams was 1.3–3.5 times less than that of the control beam.

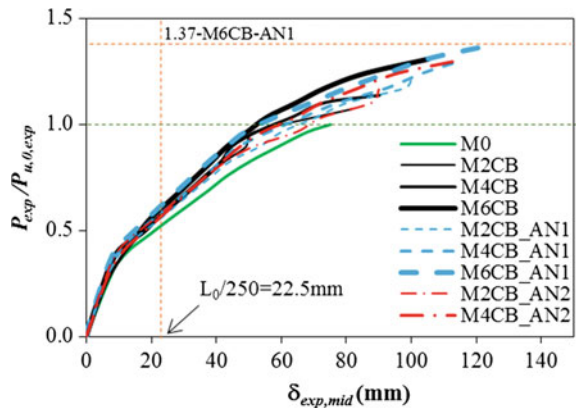
Based on the empirical observations presented above, it can be seen that the failure mechanism of CFRP-strengthened UPC beams with and without CFRP U-strip anchorage systems under flexural loading is quite complicated. Multiple failure modes may occur at the same time in the beam, where two main mechanisms are delamination and debonding. In this study, cover delamination almost exclusively occurred in the flexural span, or within the constant moment region, while the CFRP debonding appeared in the shear span, or in the region from one loading point to the nearest support. In the flexural span, the very high tensile stresses cause the early flexural cracks and gradually reduce the adhesion of the longitudinal steel reinforcement to the concrete cover. At a sufficiently large loading, the width of these cracks rises rapidly, causing the relative slipping between the longitudinal reinforcement and the concrete cover, resulting in splitting cracks and propagating along the longitudinal reinforcement axis on the concrete surface within the flexural span. At the loading close to the failure load level, the splitting cracks were large enough to connect to each other, result in the separation of the bottom cover concrete from the rest of the beam section, hence leading to delamination. Besides, in the shear span, the tensile stress in the tensile region of beam was slight, the crack

width of this region was smaller, the decrease rate in the adhesion strength of steel reinforcement with the surrounding concrete was slower, and the slipping of steel reinforcement was less than that in the flexural span. At a sufficiently large loading, the tensile stress in the shear span, which may have exceeded the adhesion between the resin and the concrete substrate, was not large enough to cause the significant slipping of the steel reinforcement, hence the thin mortar-rich layer was damaged, causing the debonding of the CFRP sheet in the shear span prior to crack occurrence. These findings may provide valuable database for future study on FRP-strengthened UPC beams in the field of numerical simulation.

3.2 Flexural Behavior of Specimens

From the commencement of loading up to approximately 35% of the failure load of the control beam (M0), the load-deflection curves of all specimens initially exhibited linear relationship without significant difference in flexural behavior (Fig. 6). It can be seen that the initial visible cracks occurred in the tension zone of 9 specimens at the load level from 35 to 38% of the failure load of the control beam. As previously known, in the RC or PC beams prior to the occurrence of crack formation, reinforcing steel and prestressing tendons slightly contribute to carrying load and their deformation was very small, therefore, the increase or decrease in their reinforcement ratio as well as in CFRP external reinforcement ratio has no significant effect on flexural behavior. However, from the load level of 35% of the control beam’s failure load up to the rupture load of strengthened beams, the occurrence and expansion of the flexural cracks weakened the beam stiffness, and the beam displacement began to increase rapidly with continued loading. In this stage, CFRP reinforcing sheet reduced the beams’ displacements by limiting the expansion of the flexural cracks, thereby resulting in the displacements of strengthened beams smaller than that of the control beam at a same load level.

Fig. 6 Relative load and midspan-displacement relationship of test beams



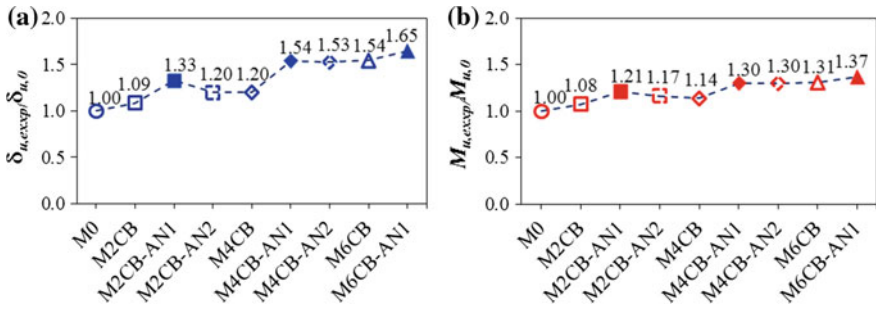


Fig. 7 a Increase in ultimate midspan displacement. b Increase in ultimate flexural resistance

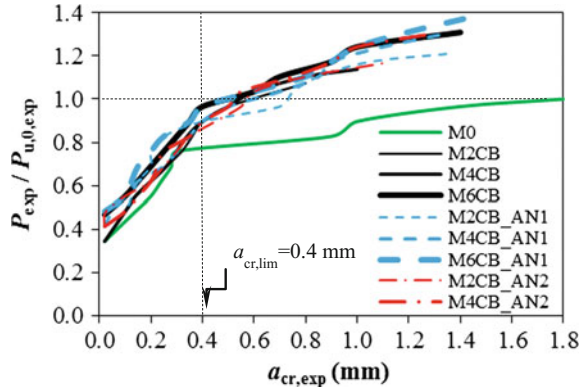
Furthermore, the deformation capacity (the experimental ultimate deflection) of non-anchorage strengthened beams and that of U-strip anchorage beams increased from 9% to 54%, from 20% to 65%, respectively, compared to that of the control beam. This result shows that the increase in the number of CFRP externally reinforcing layers has significantly improved the ductility of the beams, and the deformation capacity of U-strip anchorage beams was better than that of non-anchorage strengthened beams with the same CFRP flexural reinforcement ratio (Fig. 7a).

The CFRP external reinforcing sheet significantly enhanced the flexural capacity of the beams. The increase in the experimental ultimate flexural resistance of strengthened beams, ranging from 8 to 31% for non-anchorage strengthened beams and from 17 to 37% for U-strip anchorage beams, was in line with the increase in the number of CFRP reinforcing plies (Fig. 7b). For this reason, the two types of anchorage system AN1 and AN2 considerably contributed to the flexural strengthening effectiveness of the CFRP external reinforcing sheet. However, there are no significant differences in flexural strength between the beams retrofitted with these two types of anchorage system.

3.3 Cracking Behavior and Fracture Energy of Test Beams

The CFRP external reinforcing sheet exhibited its effectiveness in crack control and crack width reduction (Fig. 8). The fracture behaviors of strengthened beams were similar but the cracking growth rate in non-anchorage strengthened beams was higher than that in U-strip anchorage beams. Flexural cracks in strengthened beams occurred later than that in the control beam. The cracking load $P_{cr,exp}$ of the strengthened beams was from 20 to 38% higher than that of the control beam (Table 2). At the failure load of the control beam $P_{u,0,exp}$, the crack width of the strengthened beams was 2.5–3.5 times smaller than that of the control beam. Figure 9a shows that the crack width in strengthened beams decreased with the increase in the number of CFRP reinforcing layers. The reason is that the CFRP

Fig. 8 Relative load and crack width relationship of test beams



axial rigidity ($E_f A_f$) was improved as the number of CFRP reinforcing plies increased (E_f and A_f are the elastic modulus and the area of CFRP external reinforcement, respectively), resulting in the tensile stress reduction in CFRP sheet and the decline of crack width. For that reason, at the failure load of each beam, the maximum crack width in strengthened beams was 1.3–3.5 times smaller than that of the control beam (Fig. 9b). The crack width reduction in U-strip anchorage beams is considerably greater than that in non-anchorage strengthened beams.

Together with the empirical method of analyzing structural behavior, numerical analysis method, such as FEM, is commonly used thanks to its advantages in cost and time savings, flexibility and multivariable analysis capabilities. In comparison with steel structures, cracking analysis is really complicated in the case of concrete or RC structures. Comprehensive understanding of the behavior of concrete structures before and after the occurrence of cracks is extremely significant in prediction of load-bearing capacity, deformation, and, most importantly, lifetime of structures. Some recent researches, such as Rabczuk et al. (2005, 2008, 2010) [14–16] and Rabczuk and Belytschko (2004, 2006, 2007) [17–19], have proposed several analytical methods and models for crack simulation in RC structures and the

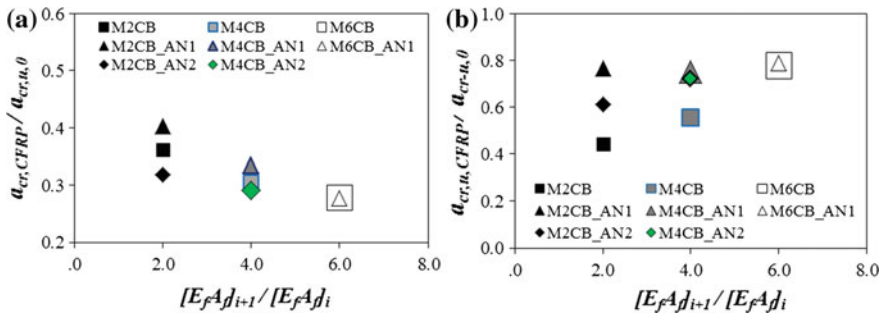


Fig. 9 Crack width reduction versus axial stiffness of CFRP sheets: **a** at the failure load of the control beam— $P_{u,0,exp}$; **b** at the failure load of the strengthened beams— $P_{u,exp}$

results are very promising. In most of recent methods and models of crack analysis, the fracture energy, G_F , is considered as an important material parameter. In order to provide the basis parameter for the next potential study relating to the numerical analysis of the flexural behavior of CFRP-strengthened UPC beams, in this research, the parameter G_F was determined according to the guidelines of RILEM (1985) [20]. G_F is the ratio of the area under load–displacement curve to the corresponding cross section area. The results presented in Table 2 indicated that the fracture energy of the control beam was about 150 N/mm, however, in the case of strengthened beams, CFRP sheets considerably increased the fracture energy of these beams. As compared to the control beam, the fracture energy of CFRP-strengthened beams without U-wraps increased by 1.23, 1.46, and 1.94 times, corresponding to 2, 4, and 6 FRP layers strengthening. When it comes to strengthened beams with U-wraps, there were increases of 1.64, 2.09, and 2.44 times in fracture energy for AN1 anchorage beams retrofitted with 2, 4, and 6 FRP layers, respectively, and of 1.41 and 2.1 times for AN2 anchorage beams retrofitted with 2 and 4 FRP layers, respectively.

3.4 Strain in CFRP External Reinforcing Sheet

The relation between load levels and strain in CFRP sheets of test beams is shown in Fig. 10. From the first load level up to the load level of 40% of the failure load of the control beam— $P_{u,0,exp}$, the deformations of CFRP reinforcing sheet were inconsiderable and hardly dependent on CFRP external reinforcement ratio or anchorage types. When the loading level reached approximately 40% $P_{u,0,exp}$, the CFRP sheet with its remarkably increasing deformation began to considerably contribute to the beam flexural behavior. During this stage, the CFRP sheets of the non-anchorage strengthened beams have deformed more than that of the U-strip anchorage beams. The strain in the CFRP sheets at the loading locations tended to be greater than that at midspan. Non-anchorage strengthened beams retrofitted with 2, 4, and 6 CFRP reinforcing plies exhibited the maximum strain in CFRP sheets of 12.39%, 11.53%,

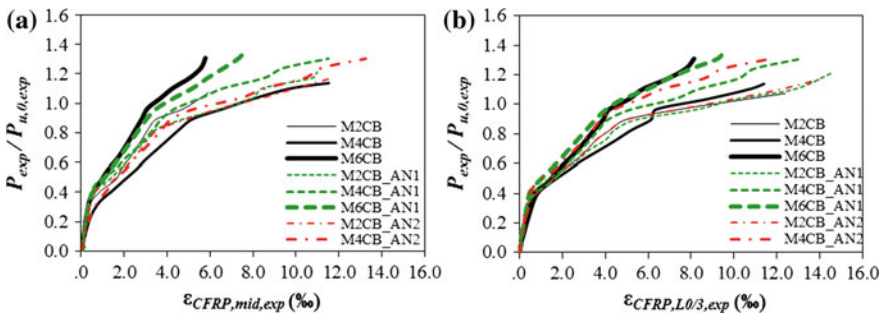


Fig. 10 Relative load and strain in CFRP sheets: a at midspan; b at loading points

and 8.13‰, respectively. Similarly, for the U-strip anchorage strengthened beams, CFRP strain was ranged from 9.56‰ (for beams bonded with 6 CFRP reinforcing layers) to 14.56‰ (for beams bonded with 2 CFRP reinforcing layers), thereby it can be seen that the maximum strain in CFRP sheet tended to decrease with the increase in the number of CFRP sheets. It can be explained that debonding of CFRP sheets tended to occur quickly as the increase in the number of CFRP reinforcing layers reduced the force transmission from the concrete substrate to the CFRP reinforcing sheet (this is evident at the slope reduction exhibited in the curves of load—strain in CFRP sheets). The U-strip anchorage systems improved the ductility of strengthened beams, therefore, the CFRP sheets of U-strip anchorage strengthened beams have attained its higher deformation as well as withstanding greater load than that of non-anchorage beams; however, debonding of CFRP sheets was not mitigated in the beams externally bonded with multiple layers of CFRP sheets. The deformation of CFRP reinforcing sheet distributed along the bond length is shown in Fig. 11. These CFRP deformation charts of tested beams, except for that of the beam M4CB-AN2, represent an unequal distribution along the CFRP sheet length with high density at midspan, greatest strain at the loading points and deformation decreasing toward the support locations. By observing the failure modes of the beams presented above, it can be seen that this uneven distribution of CFRP sheet deformation was governed by the cover delamination or debonding of external reinforcement. The regions in CFRP sheets significantly affected by debonding or delamination exhibited large deformation. It should be noted that the deformation of CFRP sheets at the loading points was up to 52.5% greater than that at midspan. This phenomenon can be explained by the local effect in the material behavior. In addition, the strain distribution in CFRP sheets of non-anchorage beams inconsiderably differed from that of U-strip anchorage beams.

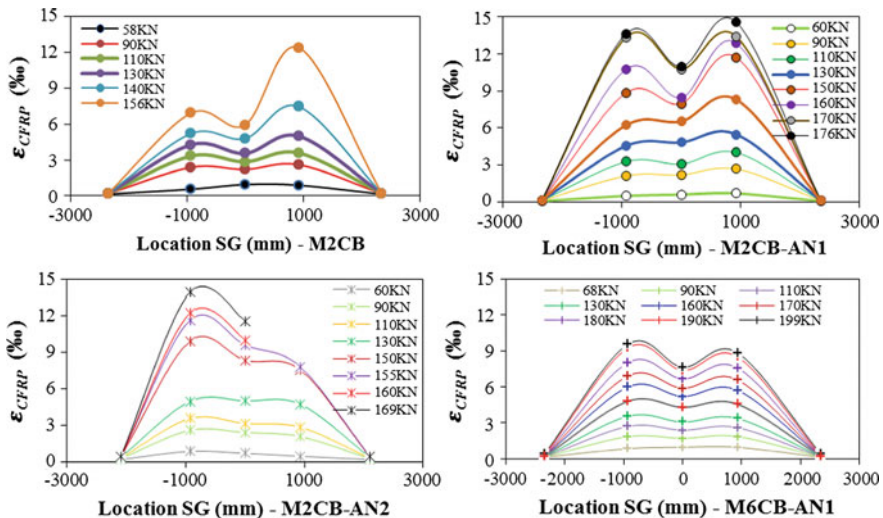


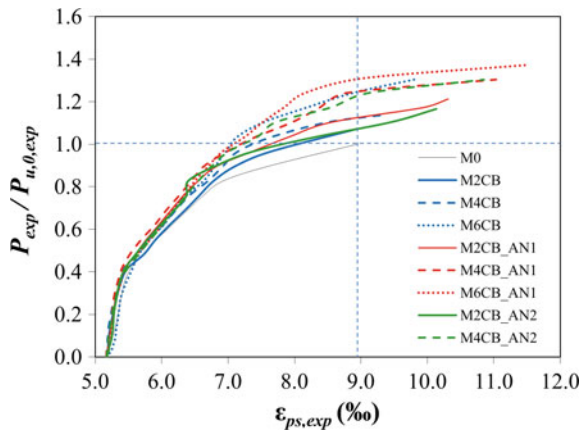
Fig. 11 Typical strain distribution of CFRP sheets along the bond length

3.5 Strain in Tendons

The relation between load and deformation of the tendon at midspan is shown in Fig. 12. Prior to the occurrence of cracks, strain in unbonded tendons $\Delta\epsilon_{ps,exp}$ was inconsiderable. After visible cracking appeared, the tendon deformation increased rapidly, and strain in prestressing tendon of strengthened beams tended to be smaller than that of the control beam at the same load level (Fig. 12). Under the load level $P_{cr,lim,0}$ at which the control beam reached the limited crack width of $a_{cr,lim} = 0.4$ mm ($P_{cr,lim,0}$ is equivalent to 77% $P_{u,exp,0}$), the increment in the maximum tendon strain of the control beams was 1.51‰ while that of the strengthened beams M2CB, M4CB and M6CB attained 1.43‰, 1.29‰, and 1.24‰, respectively. It can be seen that the strain increment in unbonded prestressing tendons at $P_{cr,lim,0}$ tended to decline with the large number of CFRP sheets, and the load level at which strengthened beams reached the allowable crack width $a_{cr,lim}$ (from 0.9 to 0.97 times of $P_{u,exp,0}$) was considerably greater than $P_{cr,lim,0}$.

The deformation reduction in prestressing tendon was more apparent at the load level equivalent to the failure load of the control beam. At the failure load level of the control beam, with the increase in the number of CFRP reinforcing plies (ranging from 2 to 6 layers), the reduction in tendon strain in non-anchorage strengthened beams, AN1 anchorage beams, AN2 anchorage beam was ranged from 23 to 50%, from 35 to 49%, and from 29 to 46%, respectively. However, at the failure load of strengthened beams, the CFRP reinforcing sheet increased the deformability of the tendon from 4.6 to 10.4% (in non-anchorage beams), from 15.3 to 28.7% (in AN1 anchorage beams), and from 15.2 to 21.4% (in AN2 anchorage beams). For that reason, it can be seen that the CFRP reinforcing sheet and transverse U-strip anchorage had a significant effect on the performance of tendon. The U-strip anchorage systems were sufficient to regulate the deformation of CFRP external reinforcement and prestressing tendons in tested beams. In addition, the maximum strain of prestressing tendons exceeded the yielding strain value (= 8.6‰).

Fig. 12 Relative load and strain in tendons at midspan



4 Conclusions

Based on the findings obtained from this study, the following conclusions can be drawn:

1. The CFRP sheets have shown some of the following benefits for the unbonded post-tensioned concrete beams:
 - The CFRP sheets enhance considerably the flexural resistance of tested beams (up to 31% for non-anchorage strengthened beams and 37% for U-strip anchorage beams);
 - The CFRP sheets showed its efficiency in reducing beam deflection (up to 30% for non-anchorage strengthened beams and 29% U-strip anchorage beams) and strongly improved the beam ductility and deformability (up to 54% for non-anchorage strengthened beams and 65% for U-strip anchorage beams);
 - Crack width was significantly reduced (up to 48%);
 - Maximum strain in tendon increased (10.4% for non-anchorage strengthened beams and 28.7% for U-strip anchorage beams). In other words, the CFRP sheets improved the performance of the tendons.
2. With the usage of CFRP U-strip anchorage system, the strain of CFRP sheets was significantly increased (approx. 18%); however, there were slight differences in flexural resistance between the beams retrofitted with these two types of U-strip anchorage system.
3. The maximum strain in CFRP sheets of non-anchorage strengthened beams ranged from 8.13 to 12.4‰ (equivalent of 39 to 59% of the CFRP sheet's rupture strain), from 9.56 to 14.56‰ for that of U-strip anchorage beams (equivalent of 46 to 69% of the CFRP sheet's rupture strain). The maximum strain in CFRP sheets tended to decrease with the increase in the number of CFRP sheets.

Acknowledgements This research was funded by Dong Thap province's Department of Science and Technology and Department of Transport.

References

1. Reed CE, Peterman RJ (2004) Evaluation of prestressed concrete girders strengthened with carbon fiber reinforced polymer sheets. *J Bridge Eng* 9:185–192
2. Rosenboom O, Hassan TK, Rizkalla S (2006) Flexural behavior of aged prestressed concrete girders strengthened with various FRP systems. *Constr Build Mater* 21(4):764–776
3. Ludovico MD, Prota A, Manfredi G, Cosenza E (2010) FRP strengthening of full-scale PC girders. *J Compos Constr* 14(5):510–520

4. Kasan JL, Harries KA, Miller R, Brinkman RJ (2012) Limits of application of externally bonded CFRP repairs for impact-damaged prestressed concrete girders. *J Compos Constr* 18 (3):A4013013
5. Afefy HM, Sennah K, Cofini A (2015) Retrofitting actual-size precracked precast prestressed concrete double-Tee girders using externally bonded CFRP sheets. *J Perform Constr Facil* 30 (2):04015020
6. Pino V, Nanni A, Arboleda D, Roberts-Wollmann C, Cousins T (2016) Repair of damaged prestressed concrete girders with FRP and FRCM composites. *J Compos Constr* 21 (3):04016111
7. Chakrabari PR (2005) Behavior of un-bonded post-tensioned beams repaired and retrofitted with composite materials. In: *ASCE structures congress: metropolis and beyond*, pp 1–11
8. Meski FE, Harajli M (2013) Flexural behavior of unbonded posttensioned concrete members strengthened using external FRP composites. *J Compos Constr* 17(2):197–207
9. Meski FE, Harajli M (2014) Evaluation of the flexural response of CFRP-strengthened unbonded posttensioned members. *J Compos Constr* 19(3):04014052
10. Ghasemi S, Maghsoudi AA, Bengar HA, Ronagh HR (2015) Sagging and hogging strengthening of continuous unbonded posttensioned HSC beams by NSM and EBR. *J Compos Constr* 20(2):04015056
11. ACI Committee 440 (2008) Guide for the design and construction of externally bonded FRP systems for strengthening of concrete structures (ACI 440.2R-08). American Concrete Institute, Farmington Hills, Michigan, USA
12. Concrete Society Committee (2012) Design guidance for strengthening concrete structures using fibre composite materials. Technical report No. 55, 3rd edn. Camberley, Surrey
13. Advisory Committee on Technical Recommendations for Construction (2013) Guide for the Design and Construction of externally bonded FRP systems for strengthening existing structures (CNR-DT 200R1/2004). National Research Council, Rome
14. Rabczuk T, Akkermann J, Eibl J (2005) A numerical model for reinforced concrete structures. *Int J Solids Struct* 42(5–6):1327–1354
15. Rabczuk T, Zi G, Bordas S, Nguyen-Xuan H (2008) A geometrically non-linear three dimensional cohesive crack method for reinforced concrete structures. *Eng Fract Mech* 75 (16):4740–4758
16. Rabczuk T, Zi G, Bordas S, Nguyen-Xuan H (2010) A simple and robust threedimensional cracking-particle method without enrichment. *Comput Methods Appl Mech Eng* 199 (37–40):2437–2455
17. Rabczuk T, Belytschko T (2004) Cracking particles: a simplified meshfree method for arbitrary evolving cracks. *Int J Numer Meth Eng* 61(13):2316–2343
18. Rabczuk T, Belytschko T (2006) Application of particle methods to static fracture of reinforced concrete structures. *Int J Fract* 137(1–4):19–49
19. Rabczuk T, Belytschko T (2007) A three dimensional large deformation meshfree method for arbitrary evolving cracks. *Comput Methods Appl Mech Eng* 196(29–30):2777–2799
20. RILEM Technical Committee 50 (Draft Recommendation) (1985) Determination of the fracture energy of mortar and concrete by means of three-point bend tests on notched beams. *Mater Struct* 18:287–290

Numerical Analysis of the Behaviors of End-Plate Beam-to-Column Steel Joints Subjected to Cyclic Loading



A. T. Le and H. Pham

Abstract This chapter presents the implementation of the modified Richard-Abbott model for the response of the extended end-plate composite joints subjected to cyclic loading. The combination of finite element models simulated in ABAQUS and the Richard-Abbott mathematical expression is the method to construct the hysteretic moment–rotation curves of the joint. The joint’s parameters are found based upon the comparison between the analysis and the experimental results. After that, the behavior of the joint is analyzed subjected to various cyclical loads. The dissipated energy of the joint within a load cycle is estimated and discussed. Relationship between dissipated energy and stiffness degradation of a joint is found as the joint subjected to the arbitrary cyclic loading.

Keywords Dissipated energy • The steel–concrete composite joints
The hysteretic moment–rotation curve • Partial-strength composite joint
The rigidity degradation of the joint

1 Introduction

The behavior of a composite structure of steel and concrete under seismic load depends on the composite behavior of connection joints. The behavior of connections greatly influences the horizontal deformation of a frame structure [1]. For example, if the joint’s stiffness reduces 50–60%, the frame stiffness will reduce 20–30%. Some researcher approved that the composite joints are represented by mechanical characteristic as strength, ductility, and energy dissipation. A cyclic loading will lead to the possibility of continuous reduce in strength and stiffness of the connection until it is destroyed.

A. T. Le (✉) · H. Pham
Civil Engineering Department, HCMUTE University, Ho Chi Minh City, Vietnam
e-mail: thangla@hcmute.edu.vn

H. Pham
e-mail: phamhoang10114@gmail.com

Behavior predictions of a composite connection joint under cyclic loads are very difficult. It is combined of many members with difference material behaviors. They include plasticity behavior of materials, nonlinear deformation, nonlinear loading, cracking of concrete, slip, and other nonlinear parameters. In addition, it is difficult to determine the behavior of the connection due to the presence of pinching under cyclic loading.

In the past, two mathematical models were proposed to determine the behavior of the joint. The expression of Ramberg–Osgood (1943) [2] described the deformation or displacement as a nonlinear function of stress or force. Popov and Pinkey (1968) [3] applied the Ramberg–Osgood model for a symmetry welded steel–concrete composite joints. After that, Popov and Bertero (1973) [4] used the Ramberg–Osgood model for end-plate steel–concrete composite joints. On the other hand, the mathematical expression proposed by Richard-Abbott (1975) [5, 6] described the force or stress as a nonlinear function of deformation or displacement. In 1984, the expression of Richard-Abbott was first applied by De Martino to determine the behavior of the joint. However, the model did not simulate the pinching coefficient. In 2000, Della Corte proposed a new model based on the expression of Richard-Abbott with some improvement of the limit of this expression, simulate the pinching effect. The model can simulate more accurately the hysteretic moment–rotation curve of a joint.

Moreover, previous researches concentrated to the joint behavior subjected to several certain cyclic loads. They concentrated on matching the modeled moment–rotation curves to their experiment results. Besides, they did compare the dissipated energy of joints between experiment results and those from mathematical models. However, seismic load is commonly complex, and they might be composed of various load patterns. The behavior of a certain joint should be considered subjected to the arbitrary load patterns. For exploring behavior of a composite joint subjected to the more complex load patterns, this chapter focuses on determining the mechanical characteristics of an extended end-plate composite joint. The considered characteristics are hysteretic moment–rotation curves, stiffness, and energy dissipation capacity.

The chapter simulated the steel–concrete composite joints in ABAQUS environment subjected to different loads proposed by European Convention for Constructional Steel work (ECCS). The Richard-Abbott models with parameters determined from experiment results are utilized for the study.

2 Characteristic Behaviors of a Joint

In case of joint subjected to static load, the main properties required for the analysis behaviors of a joint are the moment resistance $M_{j,Rd}$, the rotation stiffness $S_{j,ini}$, and the rotation capacity ϕ_{cd} . The joint's behavior is assumed fully rigid under torsion or shear forces, and it is semi-rigid subjected to bend or axial forces.

Figure 1 shows a steel joint subjected to monotonic loading. As small load, the internal moment and rotation are increased linearly. The relationship is a linear line presented in Fig. 1b. Rotation stiffness $S_{j,ini}$ could be determined as in Fig. 1b. As load keeps increasing, the moment–rotation relationship becomes a curve. There are some components of the joint started yield. After that, the component stiffness is reduced continuously until the joint failures. Moment–rotation relationship becomes a horizontal line.

Difference between the behavior of the joint subjected to static load, the joint subjected to cyclic load has the relationship between strength and deformation presented as the hysteretic moment–rotation curve. Figure 2 shows the hysteretic moment–rotation curve of a joint under cyclical loading. In the experiments, the acting on a joint often is the displacement control instead of the force control. The acting on a joint with the displacement control is called as load. As the joints reaching the hardening state, the hysteretic curve does not get the same as the original curve as the load is changed from push to pull, Fig. 2a. After a cycle of push and pull acting on the joint, there are nearly closed curves of moment–rotation relationship, called as hysteretic curves. On the hysteretic curve, there are pinching, friction, stiffness and strength degradation. They are illustrated in Fig. 2a. The Fig. 2a also shows the changing in peak of internal moment with height. There is degradation of both stiffness and strength following every loop of load. The friction force occurs when the internal components are slipped together. Besides, the pinching behavior illustrated in Fig. 2b, which is controlled by the parameter P , is defined in Eq. 1 [7] based upon the moment–rotation relationship of experiment.

$$P = \frac{M_{ap}^{lo}}{M_{ap}} \tag{1}$$

where M_{ap}^{lo} and M_{ap} could be determined geometrically as illustrated in Fig. 2b.

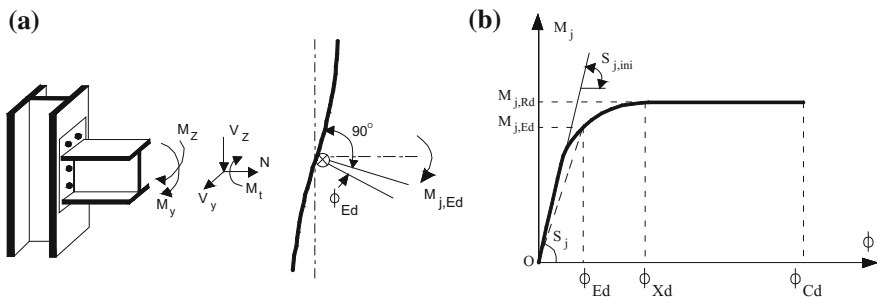


Fig. 1 Joint subjected to static load [1]. a Bolted end-plate joint, and b moment–rotation curve

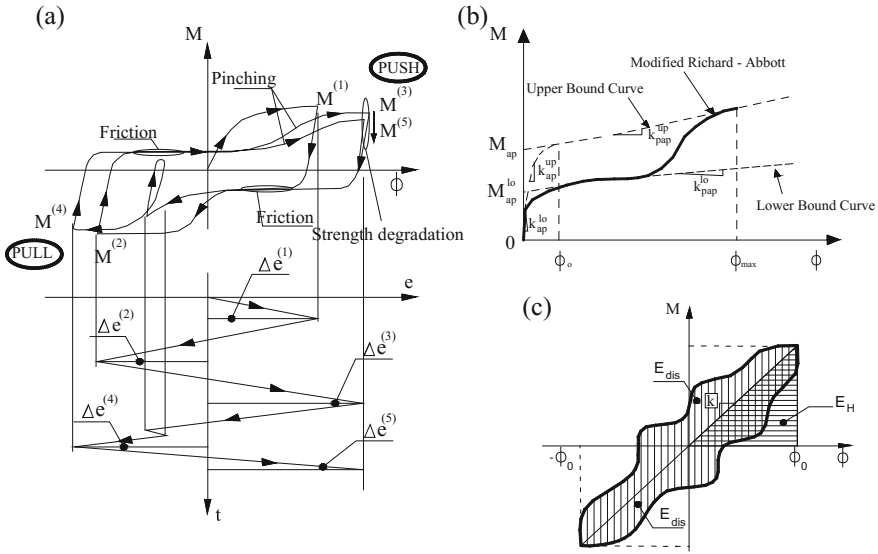


Fig. 2 Behavior of a joint under cyclical loading. **a** Hysteretic moment–rotation curves [8], **b** Loading branch with pinching, [7] and **c** Dissipated energy capacity of a joint in a cyclic load [1]

The area inside the closed curve in Fig. 2c, called as E_{dis} , represents the dissipated energy capacity of a joint. Besides, Fig. 2c also illustrates the cumulative energy E_H corresponding to the stiffness k of the joint in a branch of the hysteretic moment–rotation curve. The cumulative energy is known as the greatest deformation energy and defined as follows

$$E_h = \frac{k \times \phi_o^2}{2} \tag{2}$$

where ϕ_o is defined in Fig. 2c.

Because of the stiffness degradation, stiffness degradation of joint (k_j) should be estimated in every cycle of load and defined as follows [9] :

$$k_i = \frac{|M_{imax}^+| + |M_{imin}^-|}{|\phi_{imax}^+| + |\phi_{imin}^-|} \tag{3}$$

where M_{max}^+ and ϕ_{max}^+ are the biggest values of moment and rotation of the push branch; M_{min}^- and ϕ_{min}^- are the highest values of moment and rotation of the pull branch; the abbreviation “ i ” indicates the i th loading cycle.

3 Loading Controlled Displacement Test Protocols

Loading protocols provided by the European Convention for Constructional Steel work (ECCS 1986) for carrying out tests of characteristic of structural components under cyclic loading [10]. Four patterns controlled displacement are selected in the study based on the loading protocols of ECCS, which are illustrated in Fig. 3.

In the Fig. 3, the amplitude patterns of various loads depend on the yield displacement (e_y^+ or e_y^-). The yield displacements are defined as $e_y^+ = \frac{F_y^+}{tg\alpha_y^+}$ and $e_y^- = \frac{F_y^-}{tg\alpha_y^-}$. Where F^\pm is the yield load in the positive/negative force, and $tg\alpha^\pm$ is slope of the tangent at the origin of the ($F-e$) curve.

For LOAD 1, the amplitude increases every cycle as follow: $e_y^\pm/4$, $2 e_y^\pm/4$, $3 e_y^\pm/4$, e_y^\pm , $2e_y^\pm$, and then, the amplitude increases every three cycles as $(2 + 2n)e_y^\pm$. For LOAD 2, the displacement amplitude varies from $e_y^\pm/e_u^\pm = 0.25$ to $e_y^\pm/e_u^\pm = 6$, and then, it is kept unchanged. For LOAD 3, the displacement amplitude increases suddenly from $e_y^\pm/e_u^\pm = 0.25$ to $e_y^\pm/e_u^\pm = 6$, and then, it is kept unchanged. Finally, the displacement amplitude varies cyclic from $e_y^\pm/e_u^\pm = 3$ to $e_y^\pm/e_u^\pm = 9$ in the pattern of LOAD 4.

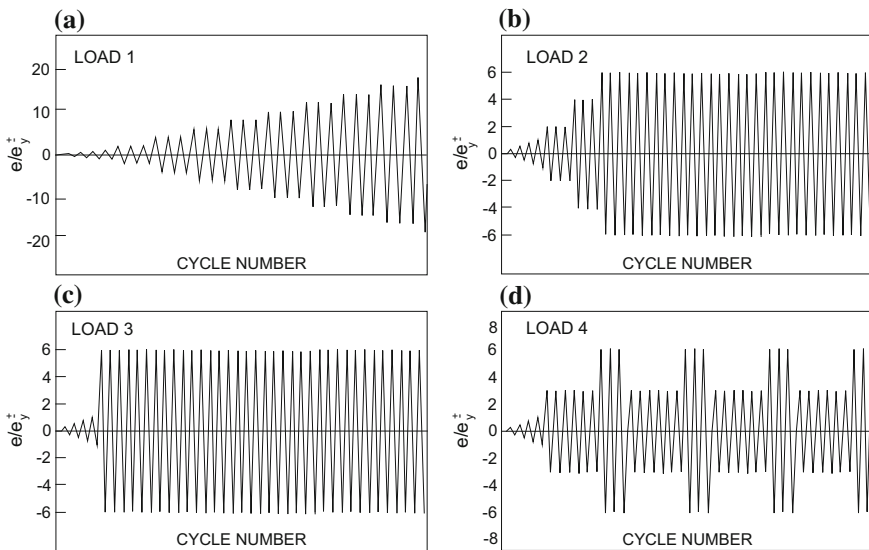


Fig. 3 Controlled displacement test protocols [10]

4 Modified Richard-Abbott Model

Richard-Abbott’s model is the model based on a formula developed by Richard in 1975 to reproduce the elastic–plastic behavior of several materials [6]. It was initially used to simulate the static response of joints. After that, the moment–rotation curve produced from the analysis of static response of joints is based to simulate the cyclic response of joints. The initial branch of the moment–rotation curve, Fig. 4a, is described in Eq. 4.

$$M = \frac{(k_{ap}^{up} - k_{pap}^{up})\phi}{\left[1 + \left(1 + \frac{(k_{ap}^{up} - k_{pap}^{up})\phi}{M_{ap}}\right)^N\right]^{1/N}} - k_{pap}^{up}\phi \tag{4}$$

The generic push branch of a moment–rotation curve was proposed by Della Corte [7]. It is given by Eqs. 5 and 6 and illustrated in Fig. 4.

$$M = M_n - \frac{(k_{ap}^{up} - k_{pap}^{up})(\phi_n - \phi)}{\left[1 + \left(1 + \frac{(k_{ap}^{up} - k_{pap}^{up})(\phi_n - \phi)}{M_{oa}}\right)^N\right]^{1/N}} - (k_{ap}^{up} - k_{pap}^{up})(\phi_n - \phi) \tag{5}$$

$$N = \frac{\ln 2}{\ln\left(\frac{M_1}{M_{ap}} - \frac{k_{pap}}{k_{ap} - k_{pap}}\right)} \tag{6}$$

The pinching is considered by smoothing hysteretic curve [11] illustrated in Fig. 2b. The push branch is interpolated between the upper and lower bound curve. The upper bound curve is the curve determined by Eqs. 5 and 6, while the lower curve is constructed by pinching parameters and determined so that the branch considering pinching is fit to the experiment curve. The modified push branch could be described by the equations below.

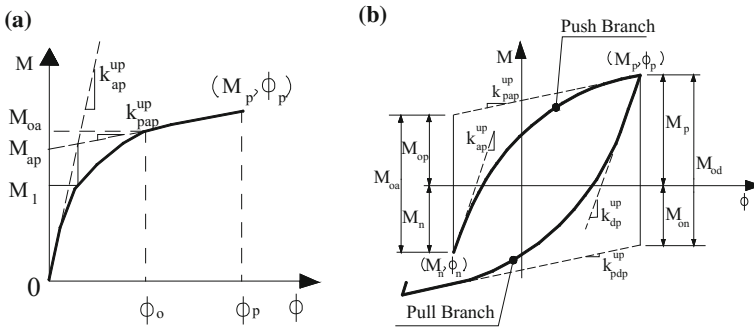


Fig. 4 Branch of the hysteretic moment–rotation curves. **a** initial push branch, and **b** generic branch [6]

$$M = \frac{(k_{ap}^t + k_{pap}^t)\phi}{\left[1 + \left(\frac{(k_{ap}^t + k_{pap}^t)\phi}{M_a^t}\right)^{n_a}\right]^{1/n_a}} - k_{pap}^t\phi \quad (7)$$

$$k_{ap}^t = k_{ap}^{up} + (k_{ap}^{lo} - k_{ap}^{up})t \quad (8)$$

$$M_a^t = M_{ap}^{lo} + (M_{ap} - M_{ap}^{lo})t \quad (9)$$

$$k_{pap}^t = k_{pap}^{up} + (k_{pap}^{lo} - k_{pap}^{up})t \quad (10)$$

$$n_a^t = n_{ap} + (n_a - n_{ap})t \quad (11)$$

$$t = \left[\frac{(\phi/\phi_{lim})^{t_{1a}}}{(\phi/\phi_{lim})^{t_1} + 1} \right]^{t_{2a}} \quad (12)$$

$$\phi_{lim} = |\phi_o| + |\phi_{max}| \quad (13)$$

where k_{ap}^{up} and k_{ap}^{lo} are the initial stiffness of upper and lower bound curves; k_{pap}^{up} and k_{pap}^{lo} are the post-limit stiffness of upper and lower bound curves; M_{ap}^{lo} , k_{ap}^{up} , k_{pap}^{up} , k_{ap}^{lo} , k_{pap}^{lo} , and M_{ap} are the values illustrated in Fig. 2b; n_{ap} and n_a are the shape parameters. The parameter “ t ” is in the range [0, 1] defining the transition law from the lower bound to the upper bound curve. $|\phi_o|$ is the absolute value of the rotation corresponding to the starting point of the current excursion (Fig. 4a); $|\phi_{max}|$ is the maximum absolute value of the rotation experienced in the previous loading history; t_{1a} and t_{2a} are the two parameters related to the pinching.

The cyclic loading is accompanied by degradation of the structure response because of deterioration of joint's components. This can be taken into consideration both for strength and stiffness by the following equations.

$$M_{p,red} = M_p \left(1 - i_M \times \frac{E_h}{M_{oa} \times \phi_o} \right) \quad (14)$$

$$K_{p,red} = k_{ap} \left(1 - i_K \times \frac{E_h}{M_{oa} \times \phi_o} \right) \quad (15)$$

where i_M and i_K are experiment parameters; E_h is the cumulative energy determined by Eq. 2.

Cyclic action in the inelastic range produces plastic deformation. Plastic deformation is accumulated until ductility of the system locally exhausted, and failure occurs due to fracture. Hardening due to cyclic plastic deformation is considered to be isotropic. Besides, the experimental results of constant deformation amplitude tests show that the cyclic hardening grows up in few cycles and then

becomes stable if joints are not exhibiting strength. The following equations are proposed for hardening consideration.

$$M_{p,inc} = M_p \quad \text{If } \phi_p^{\max} \leq \phi_o \quad (16)$$

$$M_{p,inc} = M_p \left(1 + H_h \frac{\phi_p^{\max} - \phi_o}{\phi_o} \right) \quad \text{If } \phi_p^{\max} > \phi_o \quad (17)$$

where M_p and $M_{p,inc}$ are the initial and the increase value of moment considering hardening; ϕ_p^{\max} is the greatest rotation; ϕ_o is the value of the plastic rotation. H_h is an empirical coefficient defining the level of the isotropic hardening.

The pull branch is obtained in the same way, replacing M_p, ϕ_p by M_n, ϕ_n and the parameters of M_{oa}, k_a, k_{pa} are replaced by the parameters at unloading M_{od}, k_d, k_{pd} .

5 An Application of Modified Richard-Abbott Model

In the study, two steel–concrete composite joints are simulated in ABAQUS environment. One is the external joint, and the other is the internal joint of a frame. The joint models are verified by the experiment performed by Ferrario [10]. In the experiment, each joint is subjected to both monotonic and cyclical loading. The cyclical loading pattern is LOAD 1 of ECCS.

The experiment joints are shown in detail in Fig. 5. The beams are made of IPE300 section that acted compositely with the 150 mm thick concrete slab poured on a 55 mm deep trapezoidal composite steel deck. The steel wires $\phi 6$ mm of the deck are spaced at 150 mm and oriented perpendiculars to the direction of the moment frames. Shear studs of 19 mm arranged in pairs are placed at every rib. The beam-to-column joint has been designed with a thin end plate of 15 mm thickness and 6 $\phi 24$ bolts, illustrated in Fig. 5. Column is encased in concrete with longitudinal ($\phi 12$) and transversal ($\phi 8$) reinforcing steel provided in the concrete portions of the columns. The materials include the concrete class of C25/30, the structural steel class of S235, and reinforcing steel class of B450-C. The horizontal displacement-controlled load was established by a hydraulic jack at top column. Measurement results based on the linear variable differential transformers (LVDTs) are utilized to construct the moment–rotation curve in case the joint subjected to static loading and to construct the hysteretic moment–rotation curves in case the joint subjected to cyclic loading. Figure 5 also shows the finite element models of joints after they are analyzed. The boundary condition and loading direction are presented in Fig. 5b, d corresponding to the internal and external joint.

In the study, the element type of C3D8R is used for solid parts. They include concrete, stud, bolt, and steel section. C3D8R could be suitable for nonlinear analysis. The rebar is assigned by the element type of T3D2, which could be utilized for plasticity model. The profile steel sheet is considered as shell element. S4R is

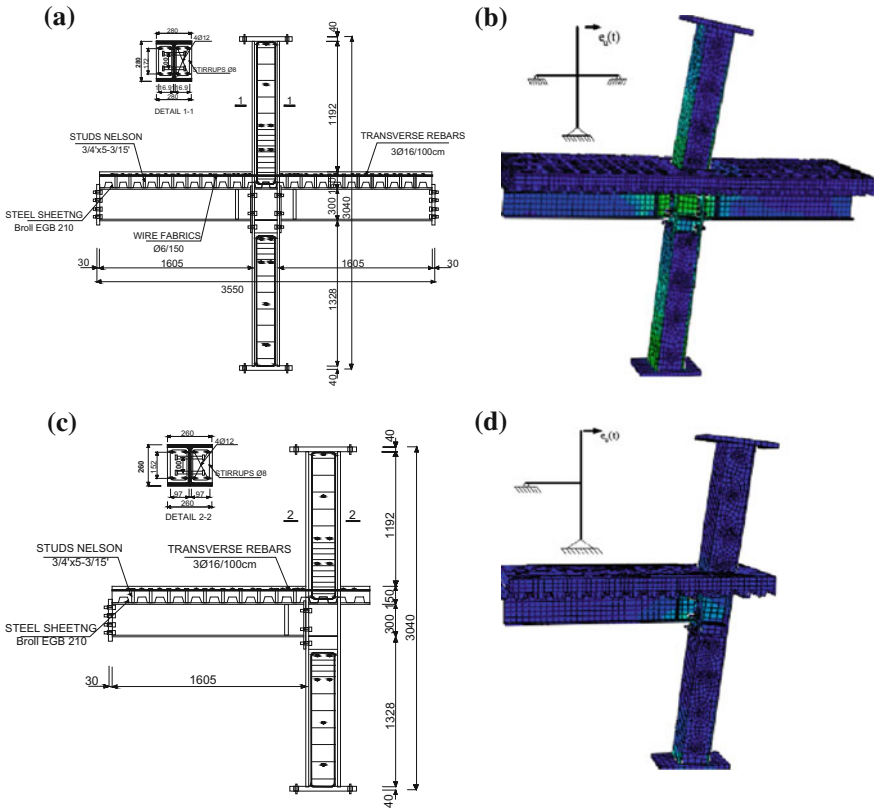


Fig. 5 Composite joint illustration. **a** Internal joint in experiment [10]. **b** Internal joint in ABAQUS. **c** External joint in experiment [10]. **d** External joint in ABAQUS

assigned to the profile steel sheet. Individual elements are connected together by interaction type of master–slave. The concrete damaged plasticity model is selected for concrete material. The parameters of the model are proposed by ABAQUS [12]. The parameters include deviator stress invariant ratio $K = 0.667$, potential eccentricity $\epsilon = 0.1$, Biaxial/uniaxial compressive strength ratio $\sigma_{bo}/\sigma_{co} = 1, 16$, dilation angle $\psi = 5^\circ$, and viscosity parameter $\mu = 0, 1$. The von Mises yield criterion is utilized for steel material. The elastic modulus of steel E_s is 210000 MPa. The Poisson’s ratio is 0.3. The mass density of the steel is 7850 kg/m^3 .

Figure 6 presents the comparison of the moment–rotation curve subjected to the monotonic load of both internal and external joints described above. In the figure, the curves established from the ABAQUS model could reach to the critical point. The critical point (cr) illustrated in the figure is the point corresponding to maximum values of both moment and rotation. It could be seen that the gaps between experiment and simulation curves are not great. The error values of moment are ranged from 4.3 to 12.5%, while error values of rotation are ranged from 2.4 to

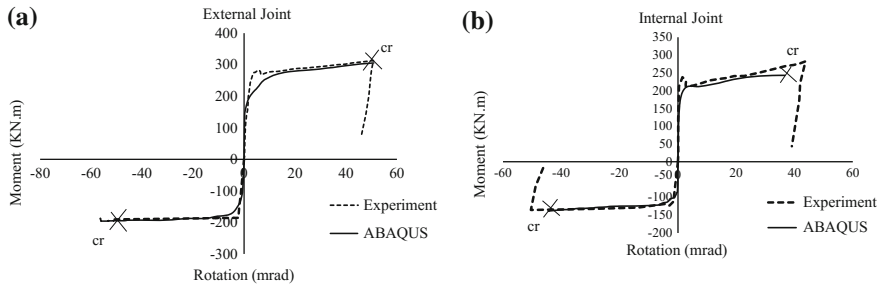


Fig. 6 Joint subjected to monotonic load **a** Moment–rotation curve of the external joint, and **b** Moment–rotation curve of the internal joint

11.2%. Small errors between measure and calculated values demonstrate that the finite element model of joints is reliable.

The modified Richard-Abbott (2000) mathematical expression with pinching parameters is applied to determine behavior of the above composite joints. Two consecutive steps are performed.

First, necessary parameters of a composite joint are determined based upon the moment–rotation curve as the joint is subjected to monotonic load. The parameters illustrated in Fig. 4a include the initial stiffness, the moment resistance, and the post-limit stiffness. They are evaluated so that the curve of Richard-Abbott model fits the experiment curve.

Second, the other parameters of the model are determined to simulate the behavior of the composite joint subjected to cyclic load. They are utilized to control the shape of push or pull branch. Those parameters, including pinching parameters, are estimated so that the hysteretic moment–rotation curves obtained from the model are fit completely those of experiment. Table 1 summarizes the obtained parameters of both internal and external joints. They are described in the Sect. 4 and illustrated in Fig. 4b. In the table, abbreviation “a” is represented for the push branch, and abbreviation “d” is represented for the pull branch of the moment–rotation curve. Based on the obtained parameters, the hysteretic moment–rotation curves and the dissipated energy calculated by each of load cycles are plotted in comparison with those obtained from the experiment.

The load pattern of LOAD 1 is considered with the displacement amplitude increased up to $e_y^\pm/e_u = 10$. It is the displacement amplitude of 21st loading cycle. This is also the displacement amplitude causing the failure of the external joint. The values of moment and rotation reach to their maximum values, the “cr” point in Fig. 6a.

Figure 7 shows the comparison results of both internal and external composite joints. It could be observed that the hysteretic moment–rotation curves fitting to experimental curves. Besides, the dissipated energy results are approximately equal to experimental results. It is noticed that the dissipated energy is not considered as the behavior of joints is elastic. The dissipated energy values of the several initial

Table 1 Modified Richard-Abbott model parameters

Model parameters	Internal joint	External joint
$k_{ap}^{up} = k_{ap}^{lo}, k_{pd}^{up} = k_{pd}^{lo}$ (kN m/mrad)	73000, 369800	59259.3, 238000
M_{oa}, M_{od} (kN m)	240, 200	200, 120
M_{oa}^{lo}, M_{od}^{lo} (kN m)	156, 130	130, 75
$k_{pap}^{up} = k_{pap}^{lo}, k_{pdp}^{up} = k_{pdp}^{lo}$ (kN m/mrad)	1650, 1950	750, 500
n_{ap}^1, n_{dp}^1	2, 2	2, 2
n_{ap}^2, n_{dp}^2	1, 1	1, 1
t_{1a}, t_{1d}	6, 6	6, 6
t_{2a}, t_{2d}	0.15, 0.15	0.15, 0.15
C_a, C_d	1, 1	1, 1
i_{ka}, i_{kd}	0.01, 0.01	0.01, 0.01
i_{Ma}, i_{Md}	15, 15	15, 15
H_a, H_d	1E-7, 1E-7	1E-7, 1E-7
E_{max}^a, E_{max}^d (rad)	0.1, 0.1	0.1, 0.1

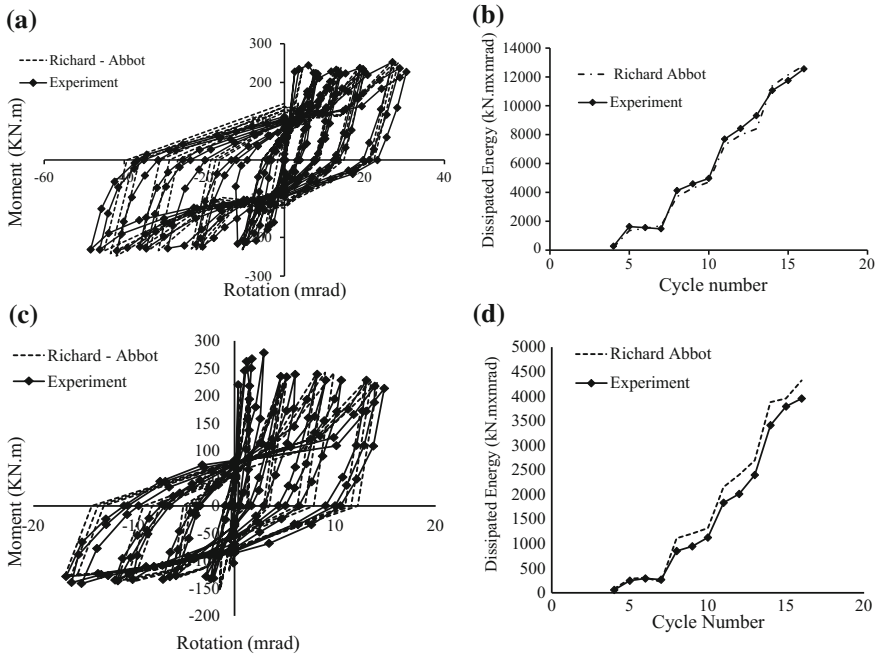


Fig. 7 Joint subjected to cyclical load. **a** Hysteretic moment–rotation curves of the external joint. **b** Dissipated energy in each cycle of the external joint. **c** Hysteretic moment–rotation curves of the internal joint. **d** Dissipated energy in each cycle of the internal joint

load cycles are ignored in the chart. In this case, dissipated energy is determined from $e_y^\pm/e_u = 1$, the 4th loading cycle. The experiment results are presented up to the 16th loading cycle, the displacement amplitude of $e_y^\pm/e_u = 8$. Thus, the comparison of dissipated energy between experiment and modeling in Fig. 7b, d is only presented up to the 16th loading cycle.

For the external joint, the biggest error of dissipated energy is 27.9% at the 13th cycle load, and the smallest is 1.9% at the 4th cycle load. In case of the internal joint, the biggest error of dissipated energy is 28.6% at the 12th cycle load, and the smallest error is 4.02% at the 4th cycle load. Those small errors indicate that the combination of finite element models and Richard-Abbott mathematical model could exactly simulate the behavior of steel–concrete composite joints subjected to cyclical loading. They are utilized to explore the behavior of the joint subjected to four cyclical load patterns described above.

6 The Behaviors of the Joints Subjected to the Cyclic Loading Patterns of ECCS

The behaviors of the composite joints subjected to an arbitrary load pattern are analyzed in this section. The hysteretic moment–rotation curves are conducted by the combination of finite element model and modified Richard-Abbott mathematical expression. The pinching parameters are included into the analysis process. Load patterns of ECCS described in the Sect. 3 are selected for the study. The numbers of load cycles reaching the “cr” point, the failure point of a composite joint, vary depending on load pattern and amplitude of load. For exploring the failure point of the joint subjected different loading patterns, the number of load cycles in case of LOAD 1, 2, 3 and 4 is selected as 33, 36, 36, and 39, respectively. The different behavior of joints could be observed as there are the differences of hysteretic moment–rotation curves in Figs. 8 and 9. Through the hysteretic moment–rotation curves, the degradation of stiffness could be observed. However, the degradation of a joint subjected to the arbitrary load patterns could not be seen obviously.

Figures 8e and 9e show the dissipated energy accumulated through every cycle load. It could be observed that there is an intersection point of different accumulated energy curves. The intersection point is located around the 16th loading cycle. The 16th loading cycle is also the final loading cycle reported in the experiment with the joint subjected to the LOAD 1 pattern. This intersection point could be used to determine the failure point of the joint [8].

Figures 8f and 9f show the relationship of the stiffness degradation (k_j) and the dissipated energy E_{dis} in a loading cycle. The power-law equations could fit the relationship between the rigidity degradation and the dissipated energy. The relation equations are proposed as follows:

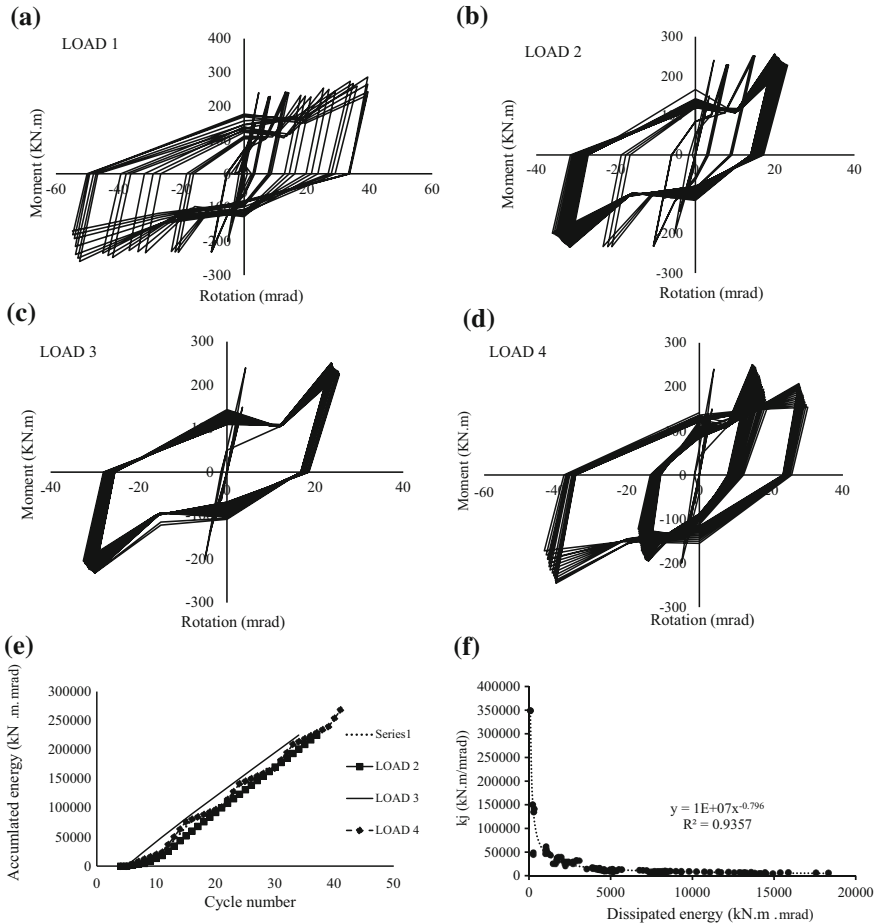


Fig. 8 External joint. **a** Hysteretic moment–rotation curves corresponding to LOAD 1. **b** LOAD 2. **c** LOAD 3. **d** LOAD 4. **e** Accumulated dissipated energy, and **f** stiffness degradation (k_j) and dissipated energy in a cyclic load

$$k_j = 10^7 \times E_{dis}^{-0.791} \text{ (kN m/mrad)}, R^2 = 0,9357 \quad (18)$$

The fitting rate is measured by R-squared values. It could be seen in Figs. 8f and 9f. The R-squared values reaching to one indicate that the dissipated energy over a load cycle could be predicted based on the rigidity degradation of the joint as the joint subjected to the arbitrary load patterns. On the other hand, the rigidity degradation of the joint may be determined based upon the curves of monotonic load. Thus, the dissipated energy of the arbitrary cyclic load could be predicted based on the curves of monotonic load.

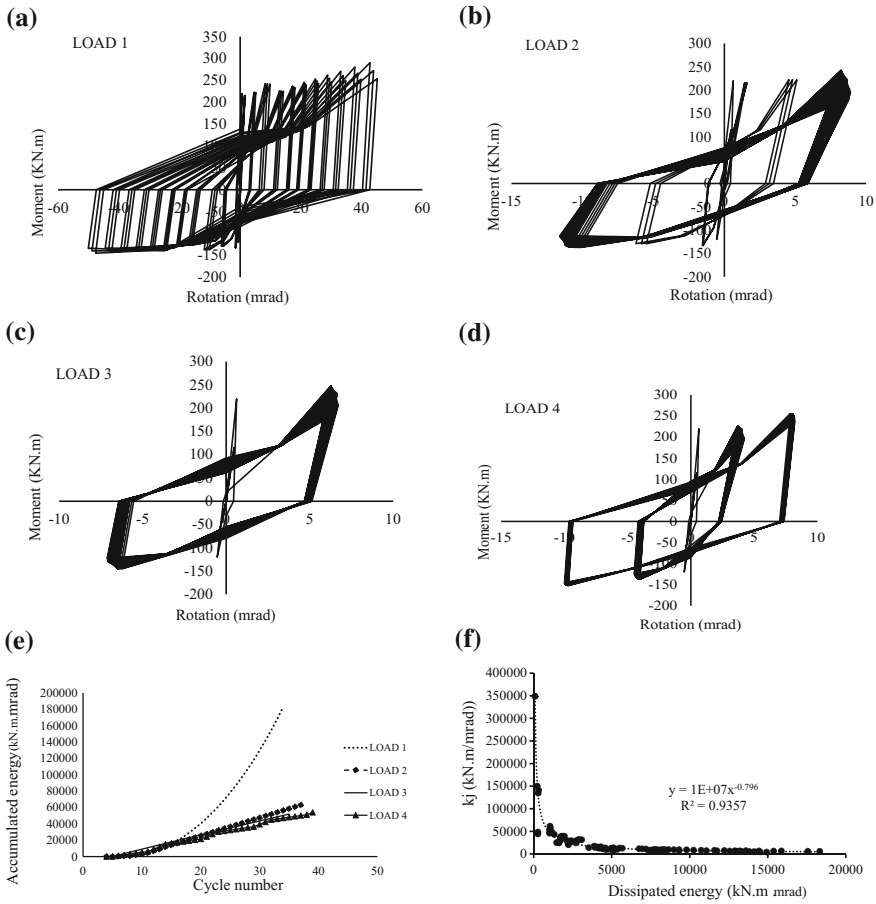


Fig. 9 Internal joint. **a** Hysteretic moment–rotation curves corresponding to LOAD 1. **b** LOAD 2. **c** LOAD 3. **d** LOAD 4. **e** Accumulated dissipated energy, and **f** stiffness degradation (k_j) and dissipated energy in a cyclic load

7 Conclusions

The finite element model of an internal joint and the other of an external joint are established in ABAQUS environment for exploring the behavior of a certain steel–concrete composite joint subjected to the arbitrary load patterns. They are verified by the experiment of Ferrario [10] in cases of the joint subjected to both monotonic and cyclic loads. The moment–rotation curves obtained from the finite element models as joint subjected to the monotonic loading are combined with the modified Richard-Abbott model to erect the hysteretic moment–rotation curves. The current approach could produce the small errors between modeling and testing results. Then, the models are utilized for exploring the effect of the arbitrary load

patterns subjected to a certain composite joint. Four different load patterns proposed by ECCS are selected for the exploration. As a result, the failure point of joint could be determined easily from the intersection of various accumulated dissipated energy curves. Besides, the dissipated energy over a load cycle could be estimated from the rigidity degradation of joint based upon the regression equations as the steel-concrete composite joints are subjected to the arbitrary load patterns.

References

1. Nguyen LN (2011) Theory calculation building subjected earthquake. Science and Technician Publishing House
2. Ramberg W, Osgood WR (1943) Description of stress-strain curves by three parameters. Monograph No. 4, Pubblicazione Italsider, Nuova Italsider, Genova
3. Popov EP, Pinkney RB (1968) Behavior of steel building connections subjected to inelastic strain reversals. Bulletin No.13, American Iron and Steel Institute
4. Bertero VV, Krawinkler H, Popov EP (1973) Further studies on seismic behavior of steel beam-column subassemblages. EERC report 73-27, Earthquake engineering research center, University of California
5. Richard RM, Abbott BJ (1975) Versatile elasto-plastic stress-strain formula. J Eng Mech Div, ASCE 101, EM4:511-515
6. Nogueiro P, Simões da Silva L, Bento R, Simões R (2009) Calibration of model parameters for the cyclic response of end-plate beam-to-column steel-concrete composite joints. Int J Steel Compos Struct 9(1):39-58
7. Málaga-Chuquitaype C, Elghazouli AY (2012) Inelastic displacement demands in steel structures and their relationship with earthquake frequency content parameters. J Int Assoc Earthq Eng 41(5):831-852
8. Ericher S (2003) Hysteretic degrading models for the low-cycle fatigue behaviour of structural elements: theory, numerical aspects and applications
9. Liao FY, Han LH, Tao Z (2004) Behavior of composite joints with concrete encased CFST columns under cyclic loading: experiment. Eng Struct 26:745-764
10. Ferrario F (2004) Analysis and modeling of the seismic behavior of high ductility steel-concrete composite structure
11. Ray T, Reinhorn AM (2012) Enhanced smooth hysteretic model with degrading properties. Am Soc Civ Eng
12. Tambusay A, Suprobo P, Arwin Amiruddin A, Faimun F (2016) Analyses behaviour of slab-column connections using ECC material based on finite element approach. In: Proceedings of the fourteenth East Asia-Pacific conference on structural engineering and construction

Experimental and Numerical Research on the Fire Behaviour of Steel Column Protected by Gypsum Plasterboard Under Fire Condition



T. Nguyen-Vo, V. Nguyen-Duc and H. Tran

Abstract In Vietnam, the fire problem in steel structures is relatively much, thus the study of fire protection solutions for the load-bearing steel structures (beams, columns) is very important. One of the solutions is the use of gypsum plasterboard. This paper presents firstly an experimental identification of the thermal conductivity of gypsum plasterboard used in Vietnam and then a full-scale experimental investigation relative to the fire resistance of steel column protected by gypsum plasterboard. In parallel, a numerical model is also developed in order to simulate the thermal transfer and mechanical behaviour of steel column protected by gypsum plasterboard under fire conditions. This model is used to compare with the experimental results and to analyse the influence of different parameters on the fire behaviour of steel column protected by gypsum plasterboard in Vietnam conditions.

Keywords Steel column · Fire resistance · Gypsum plasterboard
Fire test · Numerical model

1 Introduction

Steel structures have been popularly used in the world and increasingly used in many projects in Vietnam. Besides many advantages of steel structures, one of its inconveniences is the low fire resistance. Thus, the study of fire protection solutions for the load-bearing steel structures (beams, columns) is very important. One of the solutions is the use of gypsum plasterboard.

T. Nguyen-Vo (✉) · H. Tran

Vietnam Institute for Building Science and Technology—IBST, Hanoi, Vietnam

e-mail: thongnguyenvo@gmail.com

V. Nguyen-Duc

University of Fire Prevention and Firefighting, Ho Chi Minh City, Vietnam

e-mail: vietpccc@gmail.com

© Springer Nature Singapore Pte Ltd. 2018

H. Nguyen-Xuan et al. (eds.), *Proceedings of the International Conference on Advances in Computational Mechanics 2017*, Lecture Notes in Mechanical Engineering, https://doi.org/10.1007/978-981-10-7149-2_21

307

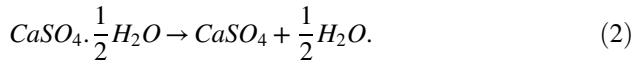
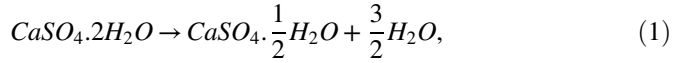
The studies on the behaviour of steel structures protected by gypsum plasterboard have also been mentioned in a number of studies in the world. However, these research works have not yet mentioned the impact of the actual moisture in the gypsum on its insulation capacity when the fire occurs. The thermal calculation used the thermal conductivity of gypsum plasterboard as a constant with a dehydrated gypsum plasterboard provided by the manufacturer, while at the moment of a fire occurring, there still exists an amount of free and chemical water in gypsum plasterboard. Impacts of heat during fire will make these water dehydrated, causing the thermal conductivity coefficient to change. Therefore, the fire resistance for the protected structures when using the values of the changing thermal conductivity coefficient mentioning the effects of dehydration process will create results close to the reality, ensuring the safety for the structures.

This paper presents firstly an experimental identification of the thermal conductivity of gypsum plasterboard heated in one side in fire condition. Based on the results, a full-scale experimental investigation relative to the fire resistance of steel column protected and unprotected by gypsum plasterboard was conducted in order to analyse the behaviour of steel column protected and unprotected in standard fire test. In parallel, a numerical model is also developed in ANSYS in order to simulate the thermal transfer and mechanical behaviour of steel column protected and unprotected by gypsum plasterboard under fire conditions. This model is used to compare with the experimental results and to analyse the influence of different parameters on the fire behaviour of steel column protected by gypsum plasterboard in Vietnam conditions.

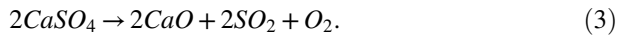
2 Experimental Identification for Thermal Conductivity Coefficient of Gypsum Plasterboard in Fire Condition

Plasterboard is made mainly of plaster with the chemical formula $\text{CaSO}_4 \cdot 2\text{H}_2\text{O}$. The composition of gypsum plasterboard consists of gypsum covered by two thin layers of cardboard paper, about 0.3 mm, on either side of the face. In some special cases, such as fire gypsum plasterboard, the gypsum core is reinforced with fibreglass, vermiculite and clay. Fibreglass helps keep the mechanical stabilizer while vermiculite and clay are added to help reduce the shrinkage of the plasterboard when subjected to high temperatures [1]. The characteristics of gypsum plasterboard under elevated temperature are described below:

- In the temperature range from 30 to 200 °C: When heating the whole face of the panel, over 70 °C the water separation starts occurring and destroyed the crystal lattice structure. At the temperature of approximately 200 °C, the chemical water in the gypsum is completely separated. At the temperature of 200 °C, the weight loss of sample is the largest (approximately 21%) due to the complete dehydration of gypsum. The dehydration reactions follow Eqs. (1) and (2).



- In the temperature range of 400–700 °C: Because in the previous period, the panel has been completely dehydrated so at these temperatures the weight of the sample does not change.
- From 900 °C: Chemical reaction will occur as follows in Eq. (3).



To determine the thermal conductivity coefficient of the gypsum plasterboard, in the paper, the determination of the thermal conductivity coefficient was done by heating on one side in an electric furnace. The temperature at hot side is heated (in the furnace) as the heating curve in ISO 834 [2]. The experiment samples were placed in front of the furnace and the inner side of the panel directly contacting the heat source (hot side). This heat source can be adjusted to maintain a certain stable heating temperature. The location of contact between the sample and the furnace was inserted with a sealed insulation material, ensuring the heat in the furnace not to escape. The heat transfer in the panel was assumed to be unidirectional, stable at the cross section of the panel and considered as homogeneous isotropic material. The temperature at the surface of the panel exposed to heat (the hot side) and the outer surface (cold side) was measured with the temperature probes. Temperatures at the cold side were monitored until stabilized and thereby determining the necessary values and calculating the corresponding thermal conductivity coefficient as follows in Eq. (4). Electric furnace was located in the air-conditioned room with temperature outside the furnace kept stable. The thermal conductivity coefficient was determined as the following formula:

$$\lambda = \frac{U \cdot I \cdot \delta}{A \cdot (T_1 - T_2)} \quad (4)$$

Of which:

- I intensity of electricity provided for the furnace, A
- U voltage provided for the furnace, V
- A contact area of the sample with the furnace
- δ Thickness of the sample, m
- T1 temperature contacting heat, °C
- T2 temperature contacting the environment, °C

In the above formula, heat transferring from hot surface to cold surface was assumed to be linear allocation based on the thickness of panels

2.1 Test Results for Thermal Conductivity

The values of the thermal conductivity coefficient calculated from the experimental measurements of two types of Boral Firebloc and Gyproc gypsum plasterboard were given in the following table: Tables 1 and 2

The comparisons of the thermal conductivity are presented in Fig. 1 (for Gyproc gypsum plasterboard) and Fig. 2 (for Boral gypsum plasterboard). The comparisons show that (1) from the heating degree to temperatures of 200 °C or higher, the value of the thermal conductivity coefficient of two panels virtually unchanged and was regarded as constant, (2) The law of the influence of the moisture loss to the thermal conductivity coefficient as for two gypsum plasterboard with two different thicknesses was similar. At the same heat level, the value of the thermal conductivity

Table 1 Thermal conductivity of Gyproc (12.7 mm and 15.8 mm thickness)

12.7 mm Gyproc panel		15.8 mm Gyproc panel	
Temperature (°C)	Thermal conductivity coefficient (W/m°C)	Temperature (°C)	Thermal conductivity coefficient (W/m°C)
50	0.41	50	0.53
100	0.28	100	0.35
120	0.24	120	0.29
200	0.19	200	0.25
400	0.18	400	0.22
600	0.18	600	0.21
800	0.19	800	0.21
1000	0.19	1000	0.23

Table 2 Thermal conductivity of Boral (12.5 mm and 15 mm thickness)

12.5 mm BORAL panel		15 mm BORAL panel	
Temperature (°C)	Thermal conductivity coefficient (W/m°C)	Temperature (°C)	Thermal conductivity coefficient (W/m°C)
50	0.39	50	0.43
120	0.19	120	0.25
200	0.15	200	0.2
400	0.16	400	0.18
600	0.18	600	0.18
800	0.22	800	0.23
1000	0.22	1000	0.23

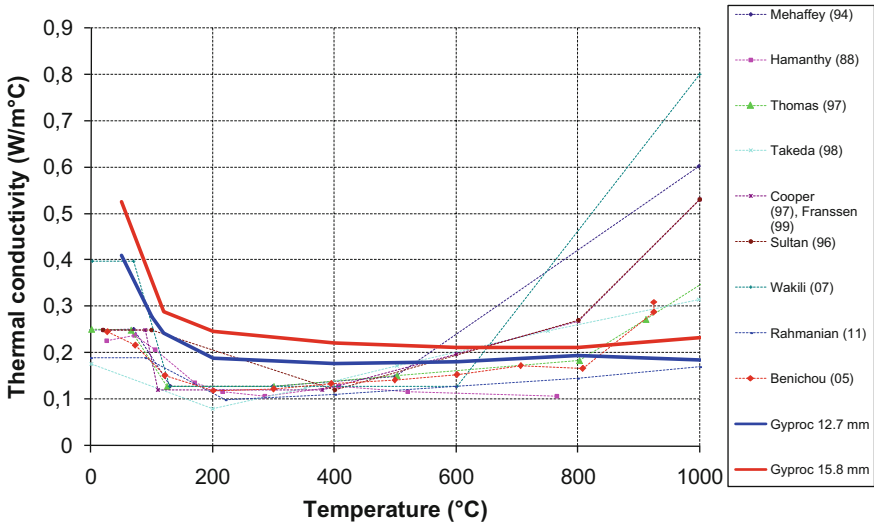


Fig. 1 Comparison of the thermal conductivity coefficient of the two types of Gyproc gypsum plasterboard with the reference values [3–5]

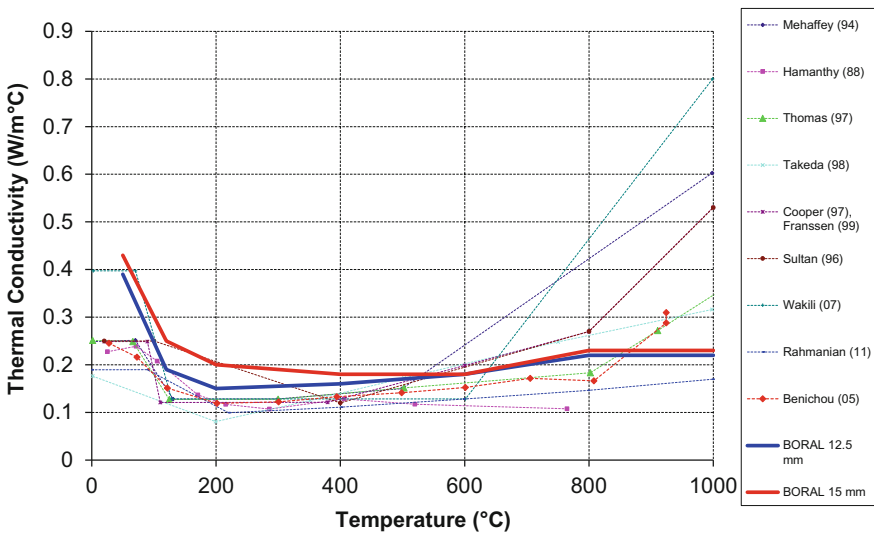


Fig. 2 Comparison of the thermal conductivity coefficient of the two types of Boral Firebloc gypsum plasterboard with the reference values [3–5]

coefficient of the thin panel is smaller than the thick one. This can be interpreted as thinner gypsum plasterboard will dehydrate much more, and therefore, it has a smaller thermal conductivity coefficient. Thus, with a certain thickness, the use of

many thin panels will be more effective than the use of one panel with a thickness equivalent.

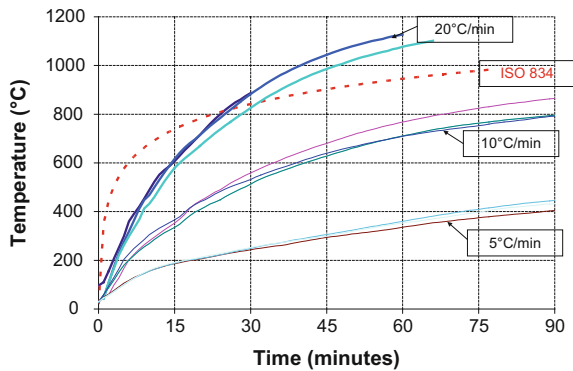
2.2 Influence of Heating Rate

For each type of fires, heating rate usually follows a certain law. To examine the impact of this parameter, the experiments to determine the thermal conductivity coefficient were conducted in the condition that the furnace temperature was continuously increased as in three heating curves, at the rate of 20 °C/min, 10 °C/min and 5 °C/min, respectively (Fig. 3). At each heating rate, three specimens were taken.

The experimental results in Fig. 4 show that (1) effect of heating rate on the thermal conductivity coefficient of thin panels was smaller than that of thicker ones; (2) effect of heating rate on the thermal conductivity coefficient of the experimental panels of different thickness mainly ranging from 30 to 200 °C, and within this temperature range, high heating rate (20 °C/min) had a greater impact on the thermal conductivity coefficient in comparison with lower heating rate; (3) with the two experimental panels, the largest heating rate (20 °C/min) will give the largest thermal conductivity coefficient.

The above results show the need to determine the thermal conductivity coefficient for each specific type of panel. In the case of safety, experiments can be conducted for the largest panels and heat transfer 20 °C/min to obtain the thermal conductivity and calculate the most unfavourable results.

Fig. 3 Comparison of temperature of Gyproc gypsum plasterboard with different heating rate and standard fire curve ISO 834



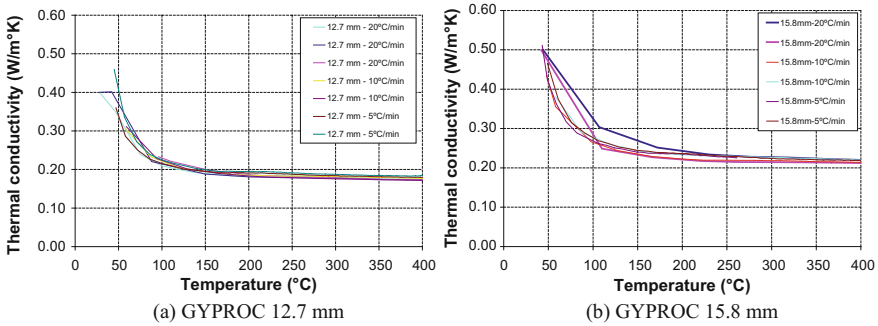
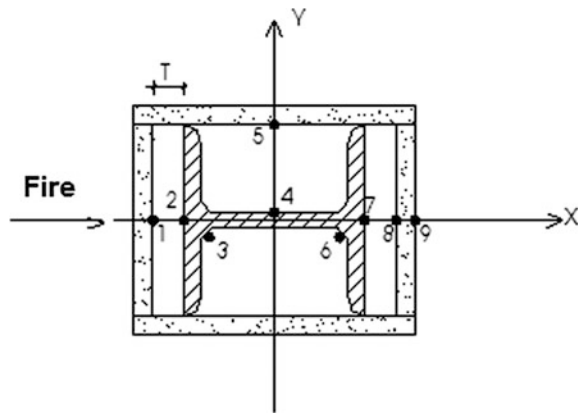


Fig. 4 Comparison of thermal conductivity of Gyproc gypsum plasterboard with different heating rate (20 °C/min, 10 °C/min, 5 °C/min)

Fig. 5 Locations of temperature probes in the section of steel columns protected by gypsum plasterboard (9 points)



3 Full-Scale Fire Test of Steel Column Protected and Unprotected by Gypsum Plasterboard

3.1 Test Description

The full-scale fire test was conducted at fire prevention laboratory—Vietnam Institute for Building Science and Technology—IBST with four specimens of 2,4 m steel column H150 (one protected by gypsum plasterboard 12.7 mm, one protected by gypsum plasterboard 15.8 mm, two unprotected). These specimens were subjected to compression load (25 tons/column) and heated on one side according to the standard fire curve ISO 834 [2]. The objective of the test was to determine the two main parameters: (1) determining the temperature at different points on the height of the steel columns (Figs. 5 and 6); (2) identifying the displacement in two directions of x and y at 04 locations along the height of the steel columns (Figs. 7 and 8).

Fig. 6 Locations of temperature probes in the section of steel columns unprotected (8 points)

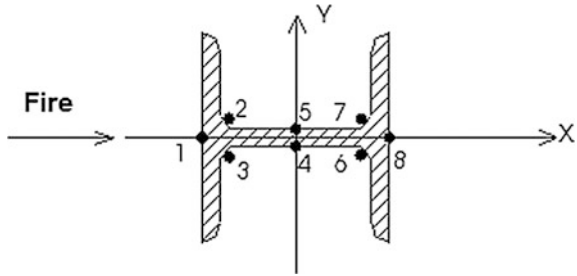


Fig. 7 02 steel column protected by gypsum plasterboard 12.7 and 15.8 mm



a. *Temperature:*

For the temperature, temperature probes arranged at three longitudinal sections along with the height of the columns.

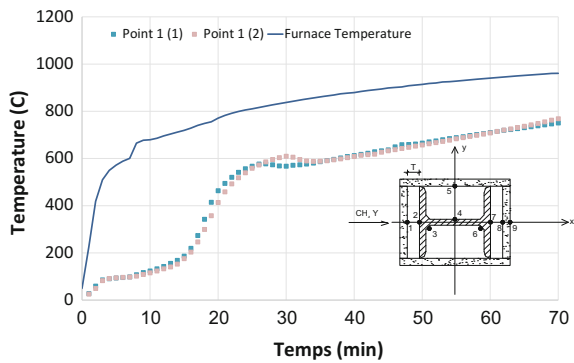
b. *Displacement:*

Displacement measuring was set up at four locations along the height of the columns. The following figures present some photograph of test specimen of steel column protected by gypsum plasterboard.



Fig. 8 02 steel column protected by gypsum plasterboard 12.7 and 15.8 mm (2)

Fig. 9 Temperature at measuring locations on the gypsum plasterboard contacting fire (column H150 protected by Gyproc 12.7 mm)



3.2 Test Results

a. Temperature:

Measured temperatures for steel columns H150 protected by Gyproc plasterboard 12.7 mm are shown in Figs. 9, 10, 11, 12 and 13. From the measured results, temperature distribution of steel column H150 protected by gypsum plasterboard can be characterized by:

- For the temperature in gypsum plasterboard exposed to fire: in the first 15 min, the temperature in the gypsum plasterboard slowly increases in the vicinity of 100 °C. This is explained by the fact that dehydration reaction is occurring and decreases the rate of thermal expansion in the gypsum plasterboard. From the

Fig. 10 Temperature at measuring locations on the steel column (column H150 protected by Gyproc 12.7 mm)

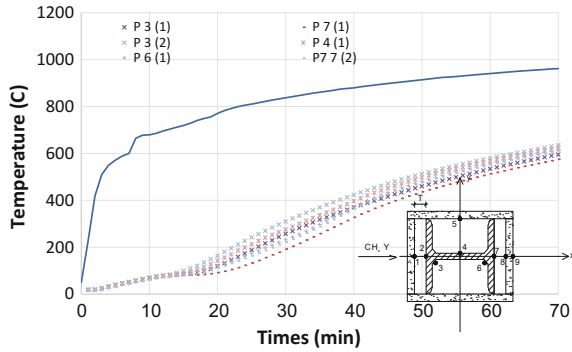


Fig. 11 Temperature at measuring locations on the gypsum plasterboard contacting the environment (column H150 protected by Gyproc 12.7 mm)

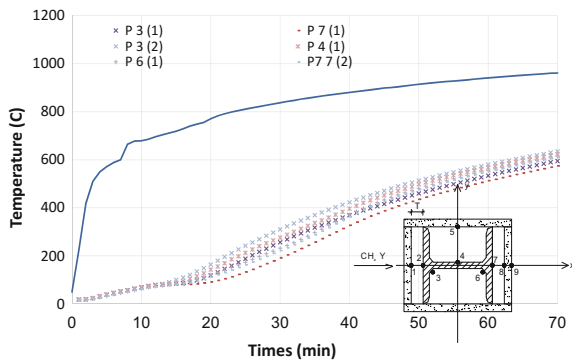
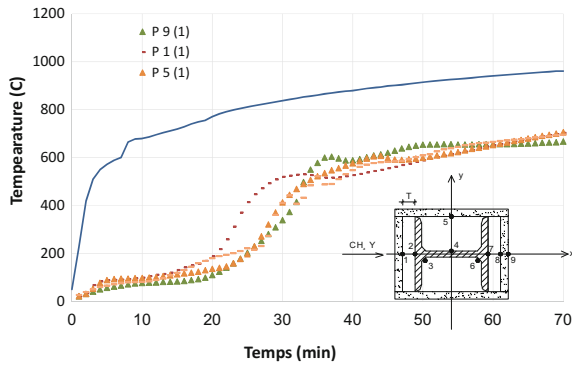


Fig. 12 Temperature at measuring locations (column H150 protected by Gyproc 15.8 mm)



15th min onwards, the temperature in the gypsum plasterboard increased rapidly and the plate lost its insulating capacity due to the dehydration of gypsum plasterboard;

Fig. 13 Temperature at measuring locations on steel column (column H150 unprotected)

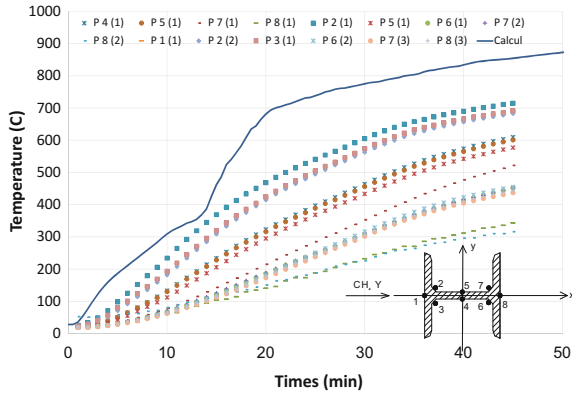
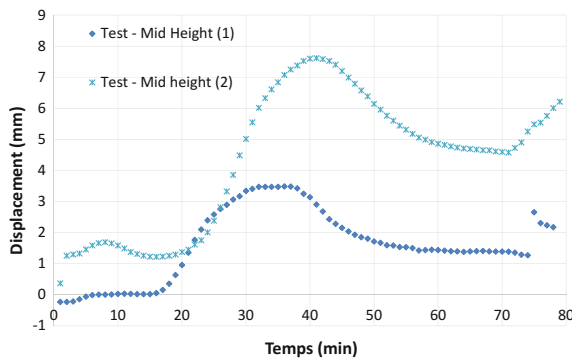


Fig. 14 Displacement of steel column H150 protected by gypsum plasterboard 12.7 mm



- For the temperature in steel column: due to gypsum plasterboard, temperature in steel increased slowly during the first 20 min. Then, the temperature of the steel column increases rapidly due to the dehydration of gypsum plasterboard;
- For the temperature in the plasterboard exposed to the environment: the temperature in the plate increased slowly in the first 25 min. This time is longer due to the influence of gypsum plasterboard exposed to fire, which reduces the overall temperature of the structural system. From the 25th min onwards, the temperature increased with a constant rate to 45 min, and from the 45th min, the plate’s temperature increased slowly until the end of the test;

From 60 min, temperatures in steel column were approximately 550 °C, the integrity of gypsum plasterboard was preserved and the connect elements (screws, bolts) remain in place. Thus, the fire resistance 60 min for steel column protected by gypsum plasterboard is achieved.

b. *Displacement:*

The displacement measurements of the steel columns H150 protected by 12.7 mm and 15.8 mm gypsum plasterboards are shown in Figs. 14, 15 and 16.

Fig. 15 Displacement of steel column H150 protected by gypsum plasterboard 15.8 mm

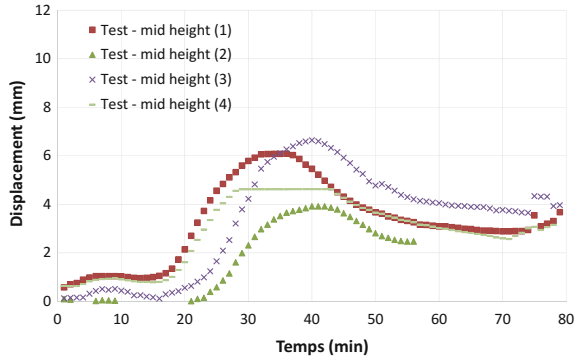
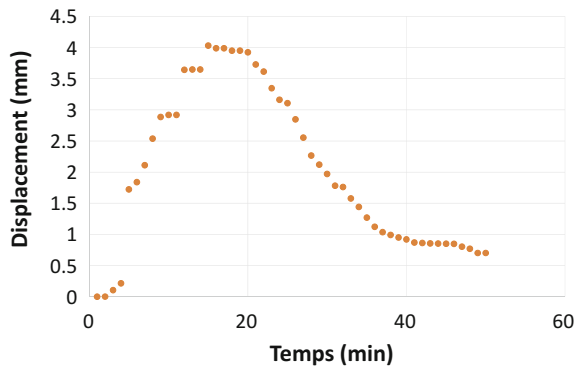


Fig. 16 Displacement of steel column H150 unprotected



For the displacement measurement, the number of measurement points remains active until the end of the test was not much, since the probes were separated during the fire test.

3.3 Comparing with Calculation Results

ANSYS software was utilized in order to model the fire behaviour of steel column protected by gypsum plasterboard. The first step was the development of a thermal model in order to determine accurately the temperature distributions through the section. These temperatures were used as input data for the thermo-mechanical model. One assumed a weak coupling of the two models [6].

- Thermal analysis was conducted on a 2D model using 4-node linear elements. The facings were subdivided into several layers depending on the thickness of

the facing. The thermo-physical properties of steel are those given in Eurocode 3 (Part 1–2) [7], while those of the plasterboards were identified versus temperature by a characterization programme and shown in Sect. 2 and reference [8].

- For the thermo-mechanical analysis, the gypsum plasterboard was assumed negligible from the model and only the steel column was modelled by nonlinear shell elements. The thermal expansion, geometric and material nonlinearity were taken into account for all elements. The Eurocode 3 [7, 9] steel properties were used.

The boundary conditions for thermal and thermo-mechanical analysis are presented in Figs. 17, 18, 19 and 20.

Fig. 17 Calculation model and boundary conditions in case the steel column unprotected

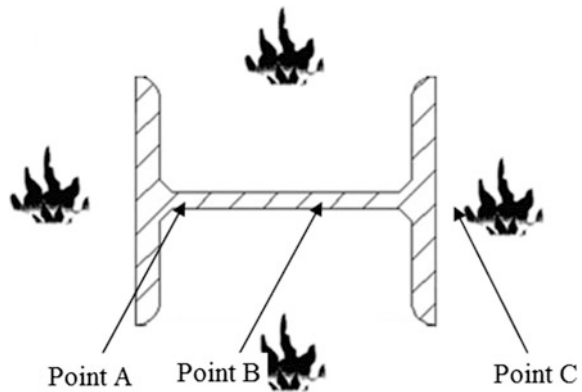


Fig. 18 Calculation model and boundary conditions in case the steel column protected by the gypsum plasterboard

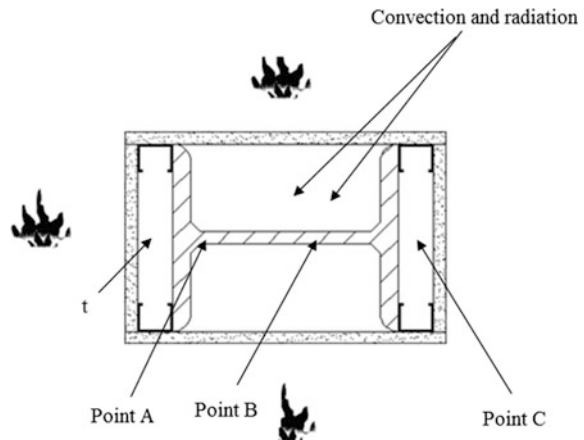


Fig. 19 Boundary condition for the thermo-mechanical analysis

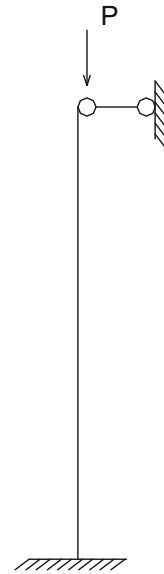
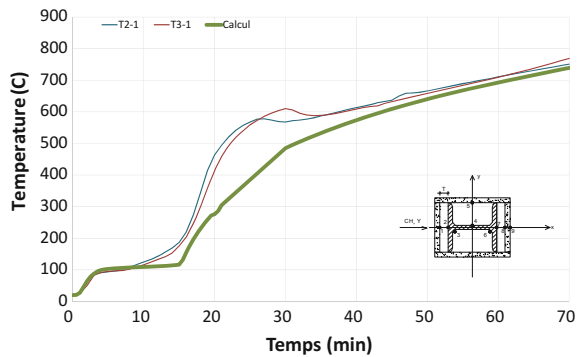


Fig. 20 Comparing temperatures at gypsum plasterboard contacting fire



The temperature comparisons in Figs. 20, 21, 22 and 23 show that the calculated temperature values from the model are relatively close to the experimental results in the first 20–25 min. From the 25th min, the temperature curve derived from the calculation has the same trend as the experimental temperature curve, but the calculated value is less than the measured value from 30 to 100 °C.

For the displacement comparison, the results show that the horizontal displacement curve of the calculated steel column is the same as the experimental horizontal displacement curve. However, in terms of value, the measured value is greater than the calculated value about 25%. This difference can be explained by a number of boundary conditions such as the steel plates kept in oven, the influence of insulating glass wool. These effects are not included in the calculation model.

Fig. 21 Comparing temperatures at different locations on steel column

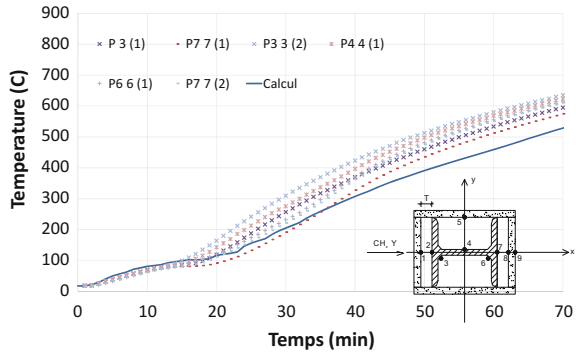


Fig. 22 Comparing temperatures at gypsum plasterboard contacting the environment

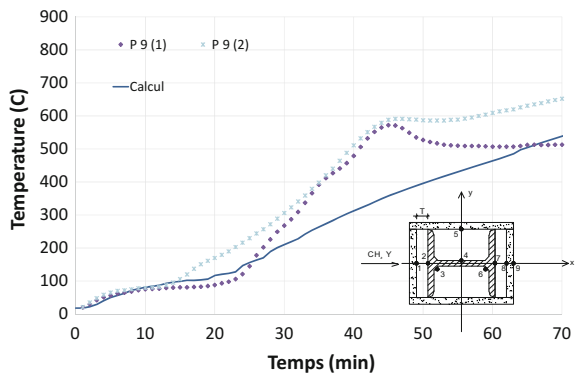


Fig. 23 Comparing horizontal displacement of steel column protected with panel 12.7 mm between calculation and experiment

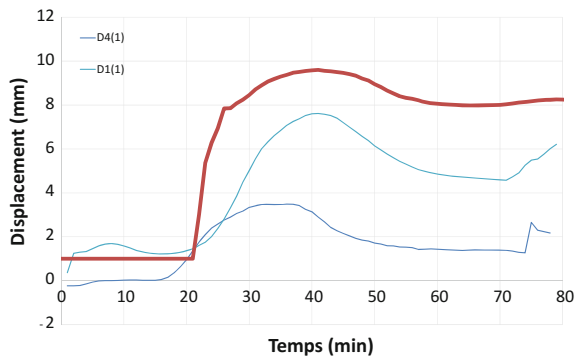


Table 3 shows the comparisons of temperature, displacement and fire resistance of the steel column between calculation and test. For the fire resistance, when the temperature limit of the steel column is 550 °C, the comparison shows that the predicted fire resistance by the model is close to the actual measured value with a difference less than 5%.

Figures 24, 25, 26 and 27 show the comparison of the temperature and displacement values of the unprotected steel column between the calculated value and the measured value. Table 4 shows the comparison of temperature, displacement and fire resistance of the steel column unprotected between calculation and test. The comparisons show that the calculated results are relatively close to the test results for the first 15 min. For the fire resistance, when the temperature limit of the steel column is 550 °C, the fire resistance of steel column is equivalent to 37 min. From Table 4, it can be seen that the calculated fire resistance was relatively large compared to the experimental value. This difference may be due to the influence of insulating glass wool which affects the area exposed to the fire of the steel column, and then the measured temperature of steel columns is smaller than calculated

Table 3 Comparing temperature, displacement and fire resistance of steel columns protected with Gyproc 12.7 mm

Temperature of steel column at 70 min (°C)		Maximum horizontal displacement (mm)		Fire resistance (minutes)	
Calculation	Experiment	Calculation	Experiment	Calculation	Experiment
550	580	10	8	70	60

Fig. 24 Comparing temperature of steel column protected with gypsum panel 15.8 mm between calculation and experiment

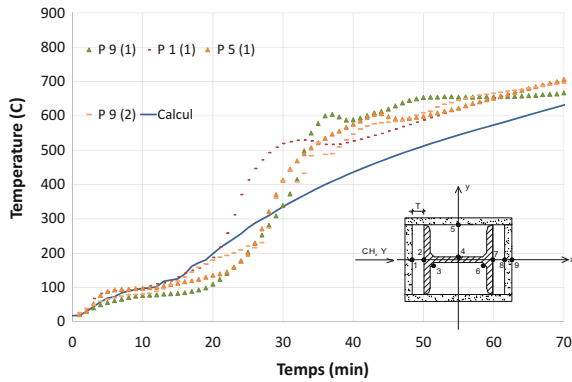


Fig. 25 Comparing horizontal displacement of steel column protected with gypsum panel 15.8 mm between calculation and experiment

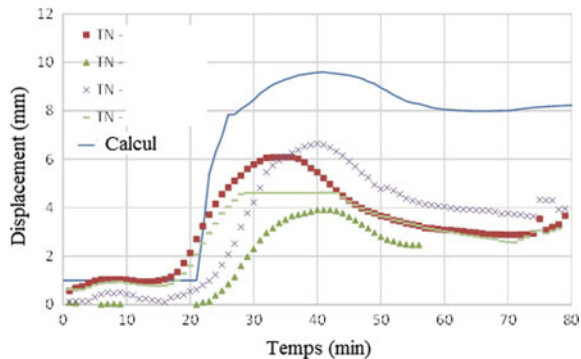


Fig. 26 Comparing temperature of steel column H150 unprotected between calculation and experiment

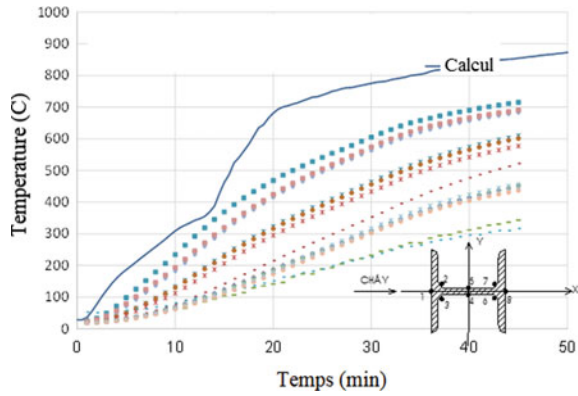


Fig. 27 Comparing horizontal displacement of steel column unprotected with gypsum panel 15.8 mm between calculation and experiment

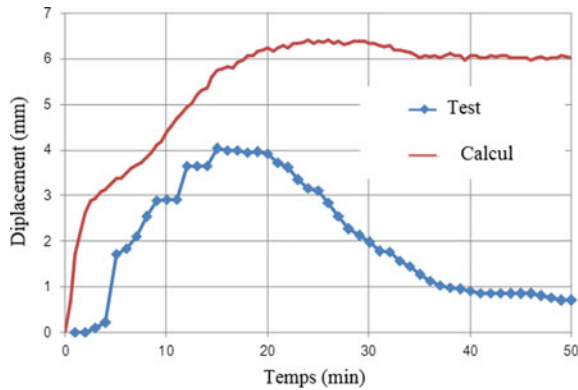


Table 4 Comparing temperature, displacement and fire resistance of steel columns unprotected between calculation and experimental value

Temperature of steel column at 45 min (°C)		Maximum horizontal displacement (mm)		Fire resistance (minutes)	
Calculation	Experiment	Calculation	Experiment	Calculation	Experiment
850	600	6,4	4	17	37

value. Relative to the horizontal displacement of the column, comparing the maximum horizontal displacement value in the middle of the column shows that the calculated value is greater than the experimental value for the first 20 min. From the 20th min, the experimental value diminishes while the calculated values remain constant.

4 Conclusion

This paper presents firstly an experimental identification of the thermal conductivity of gypsum plasterboard used in Vietnam. The experimental procedure has been developed to define the thermal conductivity coefficient of gypsum plasterboard matching the hot and humid climate conditions of Vietnam and the actual impact of the fire.

Then, a full-scale experimental investigation relative to the fire resistance of 04 steel columns protected and unprotected by gypsum plasterboard was conducted in order to analyse the fire behaviour of steel column in temperature and displacement. In parallel, a numerical model is also developed in order to simulate the thermal transfer and mechanical behaviour of steel column protected by gypsum plasterboard under fire conditions. This model uses the thermal conductivity obtained from the experimental identification programme. Comparison between the experimental results and the calculated results of displacements and temperature in steel columns with some cases full of measurement results shows that the difference of temperature and of fire resistance is more or less 5% while the displacement deviation is relatively large, which is the basis to be able to apply thermal conductivity coefficient by experimental and algorithms described in the paper when designing the fire protection for steel structures.

References

1. Thomas G (2010) Modelling thermal performance of gypsum plasterboard-lined light timber frame walls using SAFIR and TASEF. *Fire Mater* 34(8):385–406
2. BS ISO 834-11:2014 Fire resistance tests. Elements of building construction. Specific requirements for the assessment of fire protection to structural steel elements
3. Mehaffey JR, Cuerrier P, Carisse G (1994) A model for predicting heat transfer through gypsum-board/wood-stud walls exposed to fire. *Fire Mater* 18(5):297–305
4. Ang C (2004) The effect of water movement on specific heat of gypsum plasterboard in heat transfer analysis under natural fire exposure. *Constr Build Mater* 18(7):505–515
5. Thomas G (2002) Thermal properties of gypsum plasterboard at high temperatures. *Fire Mater* 26(1):37–45
6. Zienkiewicz OC, Taylor RL, Zhu JZ (2013) *The finite element method: its basis and fundamentals*, 7th edn. Butterworth-Heinemann
7. BS EN 1993-1-2 General rules. Structural fire design
8. Tran H (2012). Numerical and experimental study of behavior of gypsum plasterboard separating elements under fire conditions. Paper (in French). Ecole normal superior Cachan
9. BS EN 1993-1-1 General rules and rules for buildings

Part V
Composites and Hybrid Structures

Comparison Between Numerical and Experimental Results of the Hybrid Members Subjected to Bending and Shear



T. V. Tran and H. Q. Nguyen

Abstract This paper presents experimental and numerical results of the hybrid members with several encased steel profiles subjected to bending and shear. These results are compared with each other on the load-bearing capacity, the strain distribution, the stress distribution, the slip distribution, the crack pattern, the failure modes. These steel-concrete composite structural elements belong to the so-called “hybrid” structures which are neither reinforced concrete structure in the sense of Eurocode 2, nor steel-concrete composite structures in the sense of Eurocode 4. Currently, there is no design calculation guide of the resistance for this type of structure in international standards. Therefore, the comparison between numerical and experimental results is performed to point out the mechanism of the load transfer and failure taking place within the hybrid members subjected to bending and shear. It is the basis for calibrating the proposed design method for hybrid members reinforced by several steel profiles. The six hybrid member specimens were prepared and tested at the Structures Laboratory of INSA Rennes, France. The structural response of all hybrid members specimens were simulated by a full 3D finite element model using the Abaqus software.

Keywords Numerical simulation · Experimental results · Hybrid member
Static test · 3D Fe model

T. V. Tran (✉)

Faculty of Construction Engineering, Thuy Loi University, Hanoi, Vietnam
e-mail: tranvantoan@wru.vn

H. Q. Nguyen (✉)

Laboratory of Civil and Mechanical Engineering INSA Rennes,
Department of Civil Engineering and Urban, Rennes, France
e-mail: Quang-huy.nguyen@insa-rennes.fr

© Springer Nature Singapore Pte Ltd. 2018

H. Nguyen-Xuan et al. (eds.), *Proceedings of the International Conference on Advances in Computational Mechanics 2017*, Lecture Notes in Mechanical Engineering, https://doi.org/10.1007/978-981-10-7149-2_22

1 Introduction

For many years, the traditionally reinforced concrete shear members have been used as the primary lateral load-resisting system in multistory buildings. Although reinforced concrete shear members have many structural and economical advantages, some disadvantages appear when using this structural system in buildings subjected to seismic action. One of the main disadvantages is the development of tension cracks in tension zones and compressive crushing in localized compression areas during large cyclic excursions. Such cracks and crushing failures can result in splitting and spalling failure of the member with serious deterioration of stiffness and reduction in strength. Steel-concrete composite shear members can mitigate most disadvantages of reinforced concrete (RC) shear members and take advantage of the best characteristics the RC and the steel can. Today, reinforced concrete reinforced by more than one steel profile is used extensively for high load-bearing structures, especially for the rigid structures of high-rise buildings by their outstanding advantages. The RC members reinforced by more than one steel profile, namely hybrid member, although a number of researchers have focused on its various aspects, they are currently not covered by standards because they are neither reinforced concrete structures in the sense of Eurocode 2 [1] or ACI-318 [2]), nor composite steel-concrete structures in the sense of Eurocode 4 [3] or AISC [4]. Gaps in knowledge are mostly related to the problem of force transfer between concrete and embedded steel profiles, a situation in which it is neither known how to combine the resistances provided by bond, by stud connectors, and by plate bearings, nor how to reinforce the transition zones between classical reinforced concrete and concrete reinforced by steel profiles. This paper is dedicated to present a tentative design model for hybrid members with several embedded steel profiles subjected to combined axial force, bending, and shear. This model is based principally on the design rules of Eurocode 2 [1] and Eurocode 4 [3]. Particular attention will be paid to shear (longitudinal and transversal) resistances because preventing shear failure is one of the major concerns when designing a composite structural member. Experiments conducted with steel-concrete composite columns (simple encased steel profile) showed that the shear failure generally involves two possible failure modes: (1) the diagonal shear failure, which closely resembles the shear failure of an ordinary reinforced concrete structural member and (2) the shear bond failure, which results in cracks along the interface of the steel profile and concrete. For this reason, an experimental program was conducted on the hybrid member with three steel profiles to evaluate the load-bearing capacity and the maximum resistance values. Furthermore, the experimental program also shows the diagonal shear failure and the shear bond failure principle. Simultaneously, a numerical model was also performed to compare the results with the experimental results. So that we have a basis for calibrating the proposed design method developed by Nguyen et al. [5] and by Plumier et al. [6, 7] for estimating the transverse shear resistance taking into account the contribution of the steel profiles of this type of structure.

2 Description of the Experimental Program on Hybrid Members

The experimental program consists of six 2:3 scale member specimens which are composite member with three encased steel profiles (hybrid member). All specimens had the same size, geometry, and longitudinal reinforcing bar arrangements. The primary differences between six specimens were the type of the structural steel-concrete connection and the stirrup spacing. Details evaluated in the test include the contributions of the steel profiles, shear studs, stiffeners, bond, and stirrup spacing to the bending and shear resistance. Figure 1 shows the design details of all the six specimens of hybrid members. Component size is selected at minimum in working condition between concrete and reinforcement (minimum profile steel is *HEB100*). All specimens consisted of RC member that had 5 m length, 25 × 90 cm rectangular cross section, and were reinforced with eight 20-mm-diameter vertical reinforcing bars (Grade B). The horizontal reinforcement consisting of 14 and 6 mm reinforcing bars was made in form of stirrups. The reinforcing bar arrangement is the same in all specimens except the stirrup spacing which was 200 mm in BW, CW, and DW

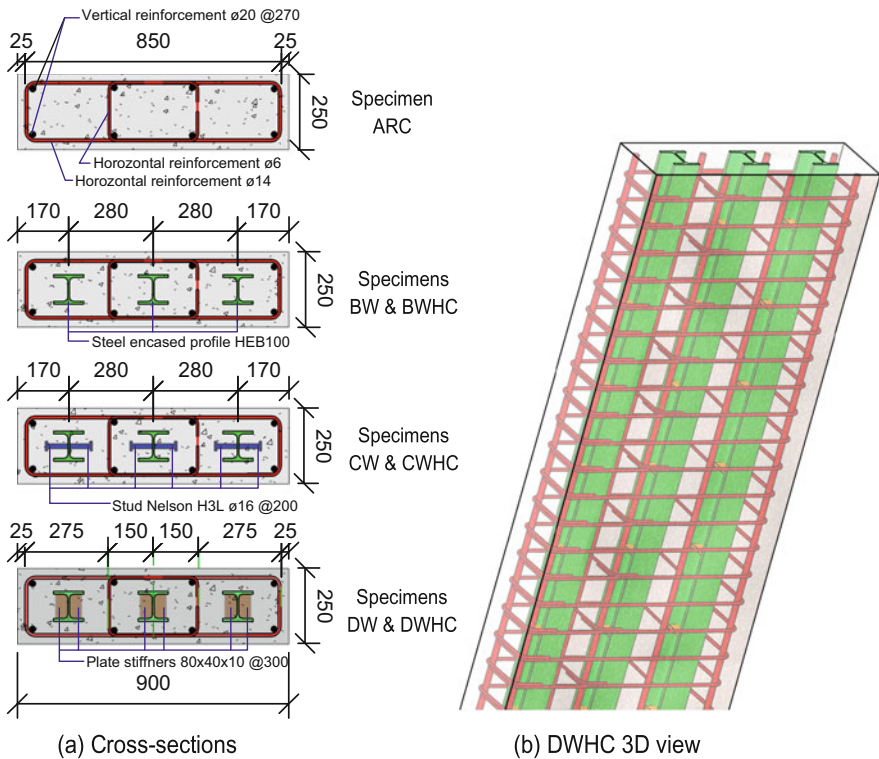


Fig. 1 Details of the test specimens

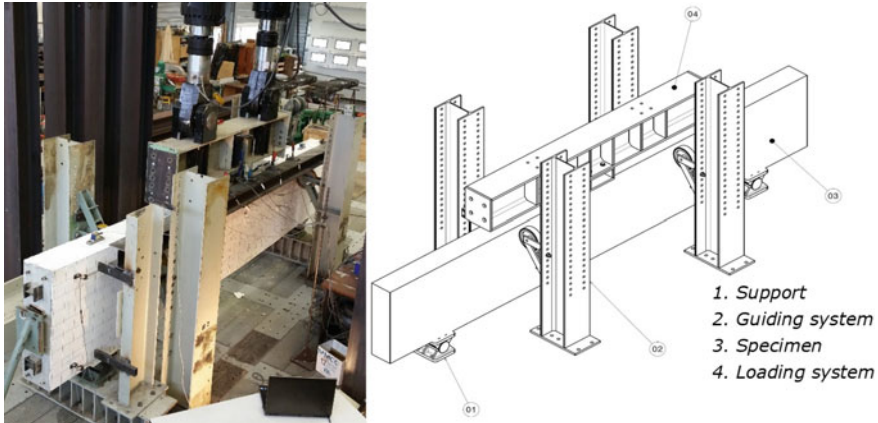


Fig. 2 Test setup

specimens and 100 mm in BW-HC, CW-HC, and DW-HC specimens. Moreover, they had additional three *HEB100* which were totally encased into the concrete with shear stud connectors between the concrete and the steel profiles for the CW and CW-HC specimens (50×3 Nelson *S3L16* – 75 mm, 200 mm spacing), with stiff connectors between the concrete and the steel profiles for the DW and DW-HC specimens (30×3 plate stiffeners, 10 mm thickness, 300 mm spacing) and without connectors for the BW and BW-HC specimens.

In the test, the solution of keeping the members in simple cantilever form is not possible for the test setup to be shown in Fig. 2. The third-point flexural beam test configuration was adopted to evaluate the resistance of specimens to combined bending and shear without axial force. Specimens were loaded at the mid-length by two hydraulic actuators (1500 kN capacity each). The actuators were operated in displacement control, with each actuator having the same displacement at any instant of time. Pinned boundary conditions at each end of the specimens were simulated by two supports. No restraint was provided against rotation along any axis.

Table 1 Structural and reinforcing steel strenghts

Item	f_y (MPa)	f_u (MPa)	$\frac{f_u}{f_y}$	E (GPa)	Applying
HEB 100	462.7	583.5	1.26	214.45	Profiles, plate stiffener
$\phi 20$ mm bars	383.91	542.62	1.41	210.74	Longitudinal rebar
$\phi 14$ mm bars	633.26	656.34	1.04	207.46	Stirrups class, shear stud

Table 2 Concrete properties

Specimen	No of sample	f_{cm} (MPa)	E (cm)
A-RC	3	24.61	30179
BW	3	31.50	31341
BW-HC	3	26.04	30862
CW	3	32.00	31328
CW-HC	3	31.63	31194
DW	3	32.73	31563
DW-HC	3	31.30	31149

The designed material quality was C30 for the concrete, S500 for the reinforcement, and S460 for the profile steel and the structural steel according to Eurocode 2. The experimental results related to the steel properties are given in Table 1, and the

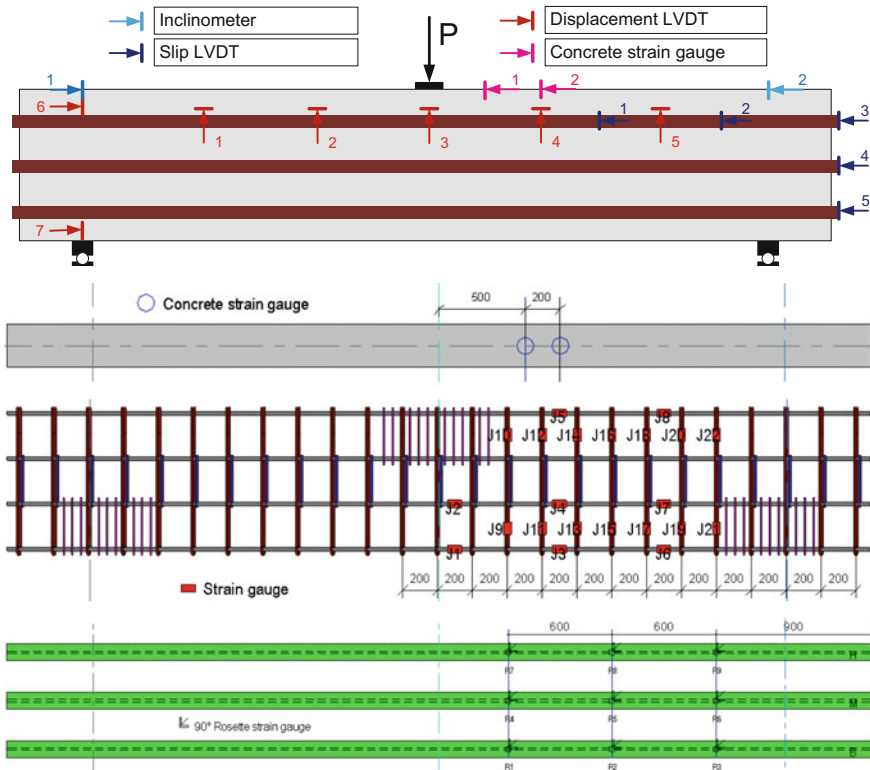


Fig. 3 Detailed arrangement of measuring devices

average cube strength and Young's modulus of concrete at age of the tests had the values presented in Table 2.

Several different instruments were used in the testing of the specimens. The arrangement of the instrumentation is presented in Fig. 3. The data acquisition devices include: Five LVDT placed along the specimen length (two at middle), measuring the deflection shape, five LVDT measuring the slips at the interface concrete-steel profile, two LVDT measuring the horizontal displacements at the specimen end, two inclinometers (devices that measure changes in angle) measuring the rotations at specimen's ends, two concrete strain gauges pasted to the top concrete surface, 22 strain gauges pasted to the reinforcement steel, and nine strain gauge rosettes 0° – 45° – 90° pasted to steel profiles.

3 3D Finite Element Model Using the ABAQUS Software

The test hybrid member specimens are simulated by 3D finite element model in the Abaqus software. Due to the symmetry of the specimen geometry and loading, in order to save the calculation time, only half of the specimen was modeled as shown in Fig. 4. Four components of specimen (concrete, rebars, steel profile, and connector) are modeled separately and assembled to make a complete specimen model.

The hybrid members proposed for finite element modeling embody situations of material discontinuity, yielding, stress concentration, contact, and composite behavior. These complex 3D phenomena are reproduced by adopting hexahedra solid elements [8], which are used to model majority of the parts of the specimens. Exception is the ordinary reinforcement in the concrete members, where truss elements are used. In ABAQUS, the finite elements C3D8 (eight nodes) and C3D20 (20

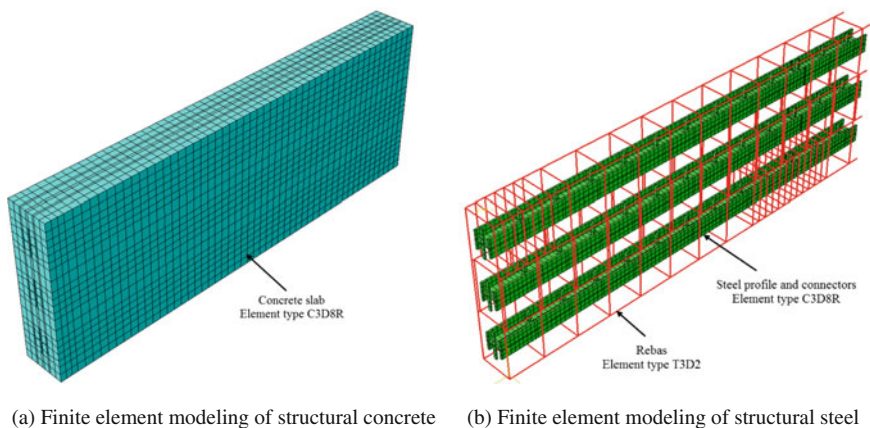


Fig. 4 Finite element type and mesh

Table 3 Material parameter of concrete damage plasticity model for concrete of $f_{cm} = 30$ MPa

Density		Parameters of concrete damaged plasticity model		
$P(\text{tonne/mm}^3)$	2.4×10^{-9}	Dilation angle	38°	
Elasticity		Eccentricity	0.1	
$E(\text{MPa})$	33346	f_{co}/f_{co}	1.16	
ν	0.2	K	0.67	
		Viscosity parameter	0.0001	
Compressive behavior		Tensile behavior		
Yield stress (MPa)	Inelastic strain	Yield stress (MPa)	Displacement (mm)	Damage
12.80	0	2.870	0	0
19.40	0.00016	2.428	0.0225	0.492
24.37	0.00037	1.706	0.0662	0.802
28.86	0.00066	1.192	0.1084	0.904
30.00	0.00102			
28.41	0.00156			
23.77	0.00219			
16.27	0.00291			

nodes) are continuum stress/displacement 3D solid finite elements of first and second order, respectively, either with reduced or full integration. The 8-node element with reduced integration is chosen for the general numerical simulations. A sensitivity analysis is performed with respect to the element type to check the required mesh density for application. For this purpose, the second-order element (C3D20R) with reduced integration is used to obtain the “correct” solution. The truss element (T3D2) used to model the ordinary reinforcement is a two-node linear 3D truss element that can only transmit axial forces.

Figure 4 shows the meshing of the FE model for the concrete member, rebar, steel member, and headed studs. The element size is 0.025 m for the elements of concrete member, steel profiles, reinforcement bars, and shanks of the shear connectors, plate stiffeners, and 0.005 m for a head of the shear connectors. The head and the stud of the connectors are approximated by a hexagon.

The stress–displacement curve is defined by Lubliner et al. (1989) and by Lee and Fenves (1988) [8]. Finally, for the five constitutive parameters (ψ —dilatation angle; ϵ —flow potential eccentricity; f_{bo}/f_{co} ratio of initial equibiaxial compressive yield stress to initial compressive yield stress; k —ratio of second stress invariant on the tensile meridian; μ —viscosity parameter) required to complete the definition of the constitutive model, no information was available from the experimental tests and therefore default values [8, 9] were used (see Table 3). Design concrete class is the C30 [1, 3].

To model the behavior of structural steel and reinforcement, the classical isotropic material law that implements the von Mises plasticity model (isotropic yielding) is used. For the generality of the steel parts, an elasto-plastic behavior with hardening is assumed. For the steel profiles and rebars, the true stress–strain ($\sigma_{true} - \epsilon_{true}$) material curve available from the experimental tests is considered. The latter properties are calculated as expressed in Eqs. (1) and (2) [9, 10] using the nominal properties (ϵ, σ) obtained in the tests.

$$\sigma_{true} = \sigma(1 + \epsilon) \quad (1)$$

$$\epsilon_{true} = \ln(1 + \epsilon) \quad (2)$$

The steel profile and the steel plate stiffener grade are S460. The steel longitudinal rebar class, the steel stirrups class, and the steel shear stud class are S500B [1–4]. The material behavior was considered as bilinear stress–strain diagram with hardening until $\epsilon_{lim} = 0.05$. And their detailed values are presented in Table 1.

In ABAQUS, the 3D modeling of reinforced concrete may be performed using steel rebar (truss element (two nodes)), steel profile, steel shear stud, steel plate stiffener (solid (continuum) element (eight nodes)) and all ordinary reinforcement embedded or not in the concrete. Due to the importance of the steel profiles and connectors reinforced in the hybrid member, they are modeled with 3D solid elements. For this type of element, bond behavior may be defined to model the interaction with the concrete, whereby the bond between concrete and steel profiles is modeled by an approximation of the bond-slip response (this model proposed by Eligehausen et al. [3, 11] and the typical traction-separation response available in ABAQUS [8]. Modeling the interaction with perfect bond leads to excessive stresses in concrete and stiffer response of the reinforcement. Contact with cohesive behavior may be considered to model the bond behavior in the reinforcement-concrete interface. The contact and interface stresses are treated using the “hard” contact model with frictional behavior.

For the application of the support conditions, all the nodes at the support location (concrete reaction surface) in the opposite direction of loading are restricted from moving in the Y direction to resist the flexion load. All the nodes of the concrete member, steel profile flanges, and the rebar web, that lie on the opposite symmetry surface are restricted due to symmetry from moving in the Z direction and rotating in the Y and Z direction. All the concrete nodes and steel profile flange nodes that lie perpendicular to symmetry surface are restricted from moving in the X direction and rotating in the Y and Z direction.

A deformation-controlled load is applied at the mid-span of the hybrid member, i.e., above the concrete load surface on the symmetrical surface (on the left side) as shown in Fig. 4.

4 Comparison Between Numerical and Experimental Results

The simulation results are compared with the experimental results. The load-bearing capacity, stress and strain analysis, and failure modes have been investigated.

4.1 Load-Deflection Response

The load-displacement curves obtained from the FE model for all test hybrid member specimens are compared to the experimental ones in Fig. 5. It can be observed that the numerical load-deflection behavior resembles the experimental behavior reasonably well. The numerical response is the load up to failure. It can be noticed that the stiffness of the elements obtained in the numerical simulations is higher than the stiffness obtained in the experimental tests. This difference appears firstly to the different material pattern (homogeneous in case of numerical simulations and inhomogeneous in the experimental tests) and secondly due to the different way in simulating the connection between steel profiles and concrete surrounding.

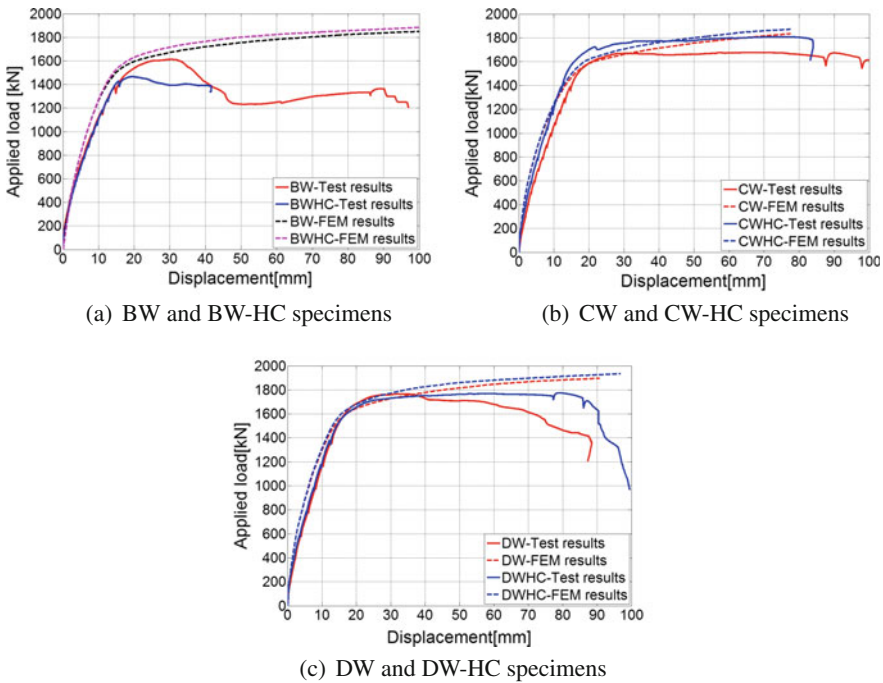
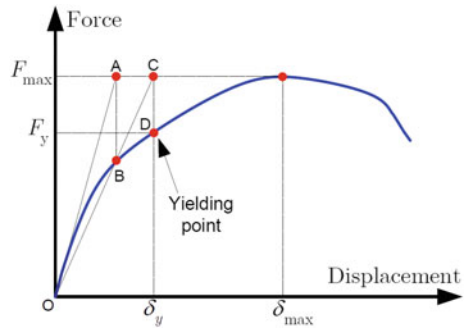


Fig. 5 Numerical-experimental comparison of load-displacement curves

Table 4 Comparative study of the load bearing capacity

Specimen	ΔF_s (mm)	Experimental F_{max}^{Exp} (kN)	Numerical F_{max}^{Num} (kN)	$\frac{F_{max}^{Num}}{F_{max}^{Exp}}$
BW	30.0	1613.4	1730.5	1.07
BW-HC	19.6	1567.5	1690.4	1.08
CW	57.2	1677.9	1780.8	1.06
CW-HC	76.6	1809.2	1870.7	1.03
DW	33.6	1767.6	1747.2	0.99
DW-HC	78.8	1774.2	1910.7	1.08

Fig. 6 General yielding point method



Nevertheless, the values of the load-bearing capacities of the elements obtained in the experimental tests [12] and those obtained in the numerical simulations are very close (1 ÷ 8% difference). Table 4 shows the load-bearing capacities of the test specimens predicted by the FE model in comparison with those from the experiment. The load-bearing capacity is maximum load obtained in the experimental or is load obtained in the numerical corresponding to the displacement of the experimental.

Likewise, the yielding point F_y is determined based on the general yielding method developed by Li [13] as shown in Fig. 6 [13]. The specimen yielding points F_y obtained in the experimental tests and obtained in the numerical simulations are shown in Table 5. The load values at the yielding point F_y of the elements obtained in the experimental tests and those obtained in the numerical simulations are also very close (0 ÷ 9% difference) except for the BW-HC specimen because the compressive strength values of the concrete are different (see the Table 2). These load values at the yielding point F_y correspond to the displacement of the experimental.

Table 5 Comparative study of the specimen yielding points F_y

Specimen	Experimental		Numerical		$\frac{F_y^{Num}}{F_y^{Exp}}$
	$\Delta_{F_y}^{Exp}$ (mm)	F_y^{Exp} (kN)	$\Delta_{F_y}^{Num}$ (mm)	F_y^{Num} (kN)	
BW	12.5	1241.2	12.5	1357.0	1.09
BW-HC	11.3	1173.6	11.3	1366.9	1.16
CW	16.4	1428.1	16.4	1509.2	1.06
CW-HC	14.6	1490.5	14.6	1485.2	1.00
DW	15.3	1466.6	15.3	1560.9	1.06
DW-HC	14.5	1458.8	14.5	1562.5	1.07

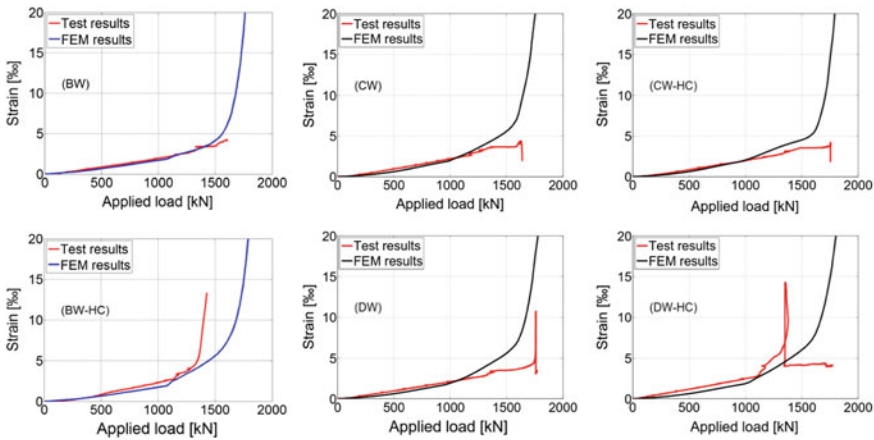


Fig. 7 Numerical–experimental comparison of strain at strain gauge J_1 location versus applied load

4.2 Strain Comparison

The strains of the longitudinal rebars versus applied load from the FE model for six test hybrid member specimens are compared to the experimental ones in Fig. 7. The strains of the steel profiles versus applied load from the FE model for six test hybrid member specimens are compared to the experimental ones in Fig. 8. Good agreement can be observed from the beginning of the test until the measurement of the strain gauge is failed.

Figure 9 shows the numerical–experimental comparison of the strain in stirrup (at strain gauge J14) versus applied load. It can be observed that for all specimens, there is a good agreement at the beginning of loading (for instance, up to about 600 kN for CW specimen). Then, the strains predicted by FE model are smaller than the experimental ones. It can be explained by the fact that in the numerical model, the

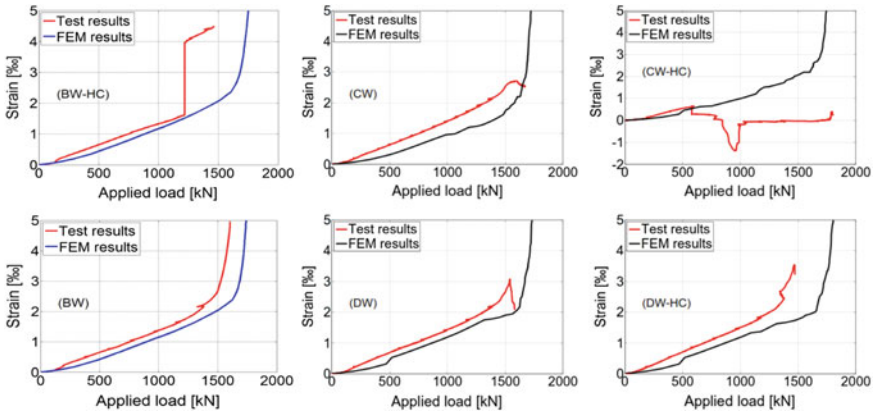


Fig. 8 Numerical–experimental comparison of strain at rosette $R_1 - 0^\circ$ location versus applied load (Note Rosette R_1 of specimen BW-HC was failed from 1240 kN and Rosette R_1 of specimen CW-HC was failed from 580 kN)

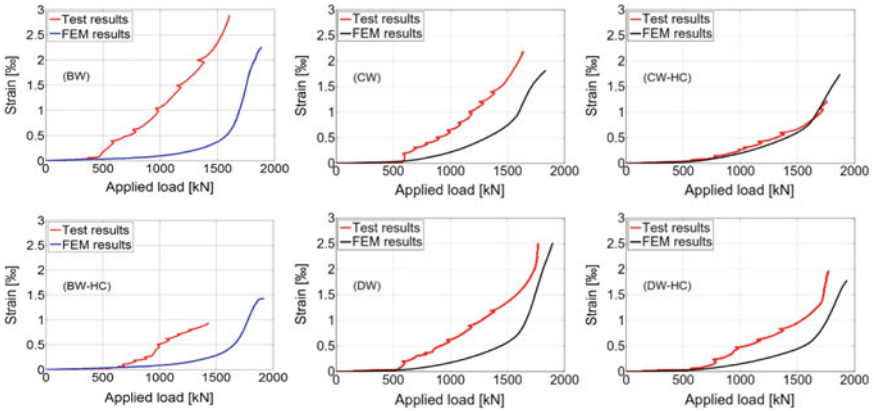


Fig. 9 Numerical–experimental comparison of strain at strain gauge J_{14} location versus applied load

concrete cracking is modeled by a continuous plasticity approach and the stirrup is embedded in the concrete. Therefore, the obtained strains are more or less the mean strains of certain region. However, the experimental tests the strain in stirrup depends strongly on location of shear crack. After certain load level, shear crack appears in the compression zone starting from the application load point. Indeed, the strains of stirrup are maximums at the crack point and decrease at the other points by tension-stiffening effect.

4.3 Stress Comparison

The stresses of the longitudinal, vertical reinforcement, and the steel profile versus applied load from the FE model for six test hybrid member specimens are compared to the experimental ones in Figs. 10, 11 and 12. Good agreement between numerical and experimental results can be observed. Again the fact that the reinforcement and the steel profile are embedded in concrete (full interaction) in the FE model leads to higher stresses in reinforcement compared to the experimental ones. This observation highlights indeed the tension stiffening-effect which takes place in reinforced concrete elements in tension. As can be seen from the Figs. 10 and 11 for all specimens, the first layer of longitudinal rebars and the first layer of steel profiles were yielded. However, the stirrups are still in the elastic range as indicated in Fig. 12. As a result, the load-bearing capacities of the specimens did not significantly improve when a double number of stirrup were used. In other words, the specimens were yielded first by flexion.

4.4 Crack Pattern

Figure 13 illustrates the tensile damage distribution in the concrete at deflection level 60 mm. Note that the concrete model adopted for FEM is a continuous model therefore the cracking cannot be reproduced in the discrete way as can be seen in the experiment. However, by analyzing the distribution of the tensile damage variable, one can have an idea about the crack pattern at different load level. It can be observed that initial the specimens were principally damaged by flexion effect at mid-span region,

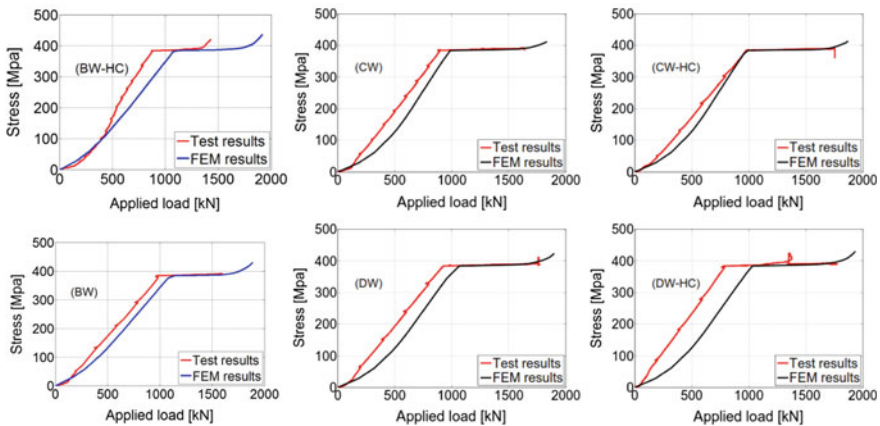


Fig. 10 Numerical–experimental comparison of stress at strain gauge J_1 location versus applied load

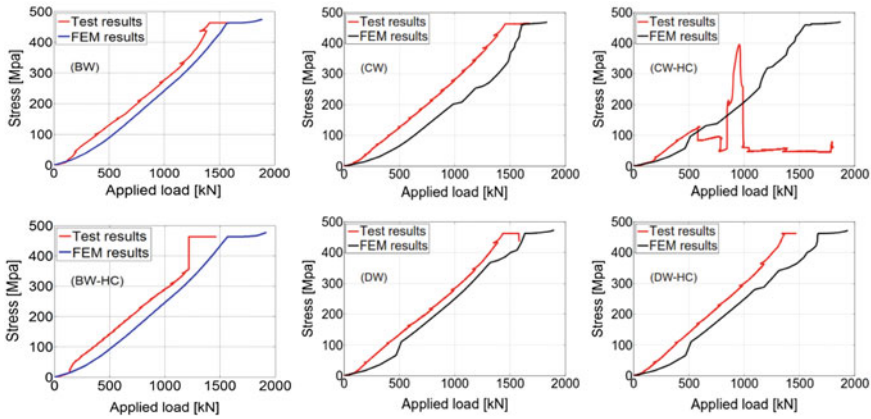


Fig. 11 Numerical–experimental comparison of stress at rosette R_1 location versus applied load (note: Rosette R_1 of specimen CW-HC was failed from 580 kN)

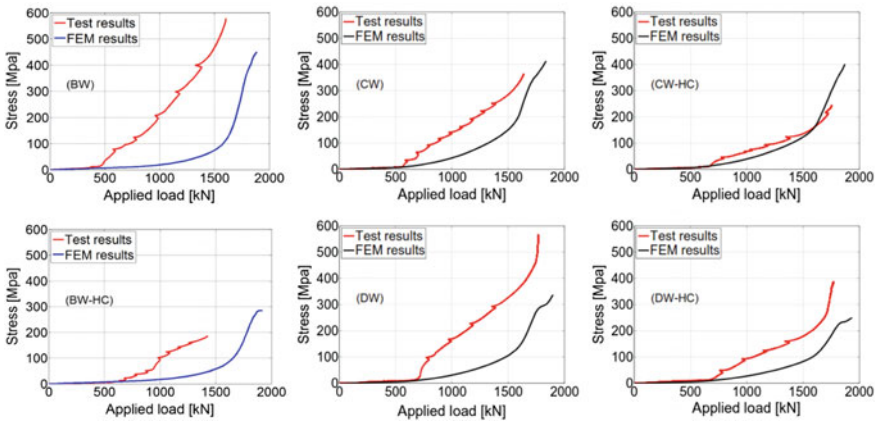


Fig. 12 Numerical–experimental comparison of stress at strain gauge J_{14} location versus applied load

after that the concrete “struts” were formed in the regions in between steel profiles. The concrete struts between upper and middle profiles were more pronounced in BW and BW-HC specimens than the other specimens. It should be noted that in the FE model of BW and BW-HC specimens, the steel profiles were embedded in concrete. That means the full interaction between steel profile and concrete was assumed. Therefore, the slip is prevented in BW and BW-HC specimens and that explains why the concrete between upper and middle profiles was more mobilized in tension. In other words, by preventing the slip, the concrete struts are totally anchored therefore the shear effect is more active. It also explains the fact that in BW and BW-HC specimens, the concrete region after the support is not damaged. In contrast, in other specimens, the slip is not prevented therefore one can see the effect of the longitudi-

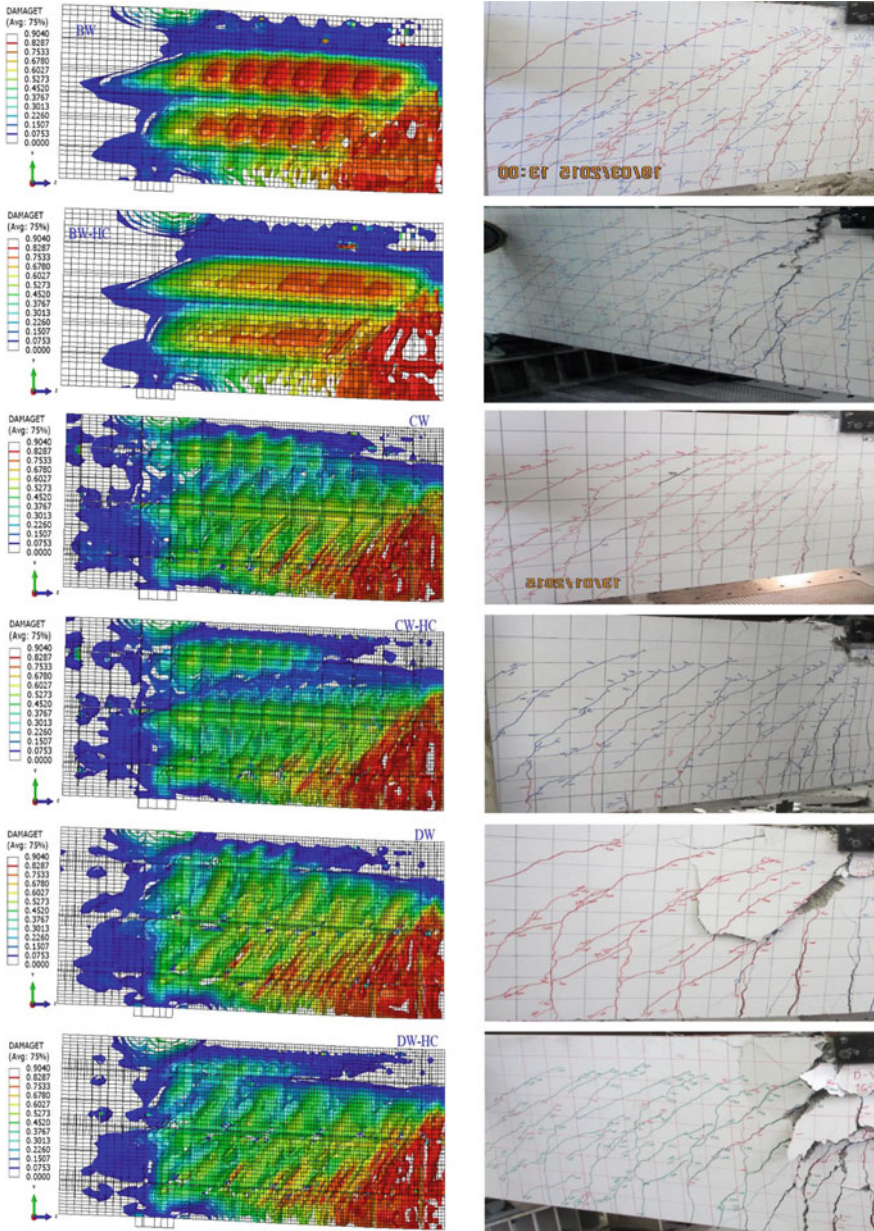


Fig. 13 Comparative of crack pattern in the concrete at deflection level 60 mm

nal shear which is locally active at the connector location and that makes the concrete region after the support damaged as can be seen in Fig. 13.

It can be observed in the right part of Fig. 13 and that at 60 mm of deflection, the concrete damaged by shear is more pronounced, especially in BW specimen. One can see clearly the concrete struts in the region at the middle between load point and support. By regarding the direction of the tensile-damaged zone, one can say that the angle of the concrete struts is about 45° . The cracking analysis pointed out that the angle of concrete strut observed in the test was from 41° to 51° . It was also entirely consistent with the experimental results.

The concrete confinement effect can be noticed by comparing the damage zone of BW specimen with the one of BW-HC specimen. As can be seen, the concrete is indeed less damaged in the specimens where a double number of stirrups were placed to make the concrete confinement.

5 Conclusion

In this paper, the results obtained from the experimental and numerical modelings on the static behavior of hybrid members subjected to combined shear and bending have been compared with each other. The results of the numerical model show that some main behaviors of the studied hybrid member specimens such as load-bearing capacity, relation of load and displacement predicted by FE model are in good agreement with test results.

The strain analysis has identified the yielding of the components as well as the failure mode of each specimen. It has been found that for all specimens, the yielding of the first longitudinal reinforcement and the yielding of the second longitudinal reinforcement were reached first followed by the yielding of lower steel profile and then by the concrete crushing by shear effect.

The angle of concrete strut between the profiles steel was 45° . It was also entirely consistent with the previous studies.

The developed FE model can be eventually used in the future works to perform a parametric study or to calibrate the design method on hybrid members. So that it is the basis for proposing a tentative design model for hybrid members with several embedded steel profiles subjected to combined axial force, bending, and shear. This model is based principally on the design rules of Eurocode 2 (Eurocode 2, 2004) and Eurocode 4 (Eurocode 4, 2004). In addition, it is also the basis for calibrating the strut-and-tie model developed to evaluate the transverse shear resistance taking into account the contribution of the steel profile by authors themselves.

Acknowledgements The authors gratefully acknowledge financial support by the European Commission (Research Fund for Coal and Steel) through the project SMARTCOCO (SMART COmposite COmponents: concrete structures reinforced by steel profiles) under grant agreement RFSRCT-2012-00031.

References

1. Eurocode 2 (2004) EN 1992-1-1. Design of concrete structures—Part 1: General rules and rules for buildings. European Commission, Brussels
2. ACI-318 (2005) Building code requirements for reinforced concrete. American Concrete Institute, USA
3. Eurocode 4 (2005) EN 1994-1-1. Design of composite steel and concrete structures—Part 1.1: General rules and rules for buildings. European Commission, Brussels
4. ACI-2010 (2010) Specification for structural steel buildings. American Concrete Institute, USA
5. Nguyen QH, Tran VT, Mohammed H (2016) Design model for hybrid steel-RC walls. In: Proceedings of the 11th joint Canada-Japan workshop on composites/first joint Canada-Japan-Vietnam workshop on composites
6. Plumier A, Dragan D, Nguyen QH (2016) A design method for walls with encased steel profiles. Where Technology and Engineering Meet, HighTech Concrete, pp 1067–1076
7. Plumier A, Dragan D, Nguyen QH, Degee H (2017) Design method for steel—concrete hybrid walls. Structures 9:185–189
8. David H et al (2012) ABAQUS standard user's manual (Version 6.12.1). USA
9. José H, Luís S, Isabel B (2013) Numerical modeling of composite beam to reinforced concrete member joints—Part I: calibration of joint components. Eng Struct 52:747–761
10. Girao Coelho A, Simoes da Silva L, Bijlaard F (2006) Numerical evaluation of the behaviour of the T-Stub. J Struct Eng 132(6):918–928
11. Eligehausen R, Popov E, Bertero V (1983) Local bond stress-slip relationship of deformed bars under generalized excitation. Report No. UCB/EERC-83/23, Earthquake Engineering Center, University of California, Berkeley
12. Tran VT, Nguyen QH (2016) Experimental study of hybrid members with several fully encased steel sections. The 7th international conference of Asian Concrete Federation ACF 2016, Hanoi, Vietnam
13. Li B, Lam ES-S, Wu B, Wang Y-Y (2013) Experimental investigation on reinforced concrete interior beam-column joints rehabilitated by ferrocement jackets. Eng Struct 56:897–909

Analytical Behavior of Rectangular Plates Under in-Plane and Lateral Dynamic Loads



Sofia W. Alisjahbana, Wiratman Wangsadinata
and Irene Alisjahbana

Abstract Analytical behavior of rectangular plates with semi-rigid boundary conditions under in-plane and lateral dynamic loads of constant thickness resting on the Winkler foundation is analyzed using a modified Bolotin method. The presentation of the semi-rigid isotropic plate's frequency in a form analogous to the corresponding frequency of a simply supported plate is postulated, considering the wave numbers as unknown quantities. These two equations are determined from a system of two transcendental equations, obtained from the solution of two auxiliary Levy-type problems. The method was shown to be remarkably accurate when used to determine the natural frequencies of plates with non-simply supported boundary conditions. A natural extension of this research is related to the buckling and lateral vibration of isotropic plates subjected to in-plane forces which are time invariant and constant over the area of the plate, with their principal directions parallel to the plate edges and the dynamic lateral force. It is the purpose of this paper to illustrate this extension and to demonstrate its applicability by the presentation of numerical results for a particular plate.

Keywords Modified Bolotin method • Transcendental equation
Auxiliary • In-plane forces • Lateral force

Wiratman Wangsadinata—Deceased.

S. W. Alisjahbana (✉)

Faculty of Engineering and Informatics, Bakrie University, Jakarta, Indonesia
e-mail: sofia.alisjahbana@bakrie.ac.id

W. Wangsadinata

Wiratman and Associates, Jakarta, Indonesia
e-mail: wiratman@wiratman.co.id

I. Alisjahbana

Civil Engineering Department, Stanford University, Palo Alto 94025, CA, USA
e-mail: irenealisjahbana@gmail.com

© Springer Nature Singapore Pte Ltd. 2018

H. Nguyen-Xuan et al. (eds.), *Proceedings of the International Conference on Advances in Computational Mechanics 2017*, Lecture Notes in Mechanical Engineering, https://doi.org/10.1007/978-981-10-7149-2_23

1 Introduction

The instability characteristics of isotropic rectangular concrete plate subjected to in-plane and lateral loads are utilized in many areas including engineering design and earthquake-resistant structures. Significant studies have been made by Viswanathan et al. in 2006 on buckling analysis of rectangular plates with variable thickness resting on elastic foundations [1]. The plate was homogeneous with the plate thickness varying using spline function approximation techniques. The plate is fully attached to the foundation. A pair of the rectangular plate's opposite edges is subjected to compressive uniform load. Two cases of boundary conditions are considered for these edges: clamped-clamped and clamped-simply supported. The deflection equation yields an eigenvalue problem solving in which the critical loads and the mode shapes of buckling are obtained.

In the present work, the buckling of thin isotropic rectangular plates of constant thickness resting on elastic foundation is studied. The boundary condition that is considered for these edges is semi-rigid. The eigenvalue and eigenvector problems are solved by using the modified Bolotin method. The mode shapes of buckling are obtained from the transcendental equation.

Parametric studies of the variation of the critical load with respect to the aspect ratio, foundation stiffness, and variation of thickness of the plate are made. Selected mode shapes of buckling are also presented.

2 Formulation of the Problem

Consider a thin isotropic rectangular plate bounded by $x = 0$, $x = a$, $y = 0$, and $y = b$ as shown in Fig. 1. The isotropic plate is subjected to the in-plane forces N_x and N_y , acting on and normal to the edge $x = 0$; $x = a$; $y = 0$; and $y = b$. Its transverse deflection $w(x, y, t)$ by using the classical plate theory is governed by the fourth-order partial differential equation as follows:

$$D \left(\frac{\partial^4 w(x, y, t)}{\partial x^4} + 2 \frac{\partial^4 w(x, y, t)}{\partial x^2 \partial y^2} + \frac{\partial^4 w(x, y, t)}{\partial y^4} \right) - N_x \frac{\partial^2 w(x, y, t)}{\partial x^2} - N_y \frac{\partial^2 w(x, y, t)}{\partial y^2} + k_f w(x, y, t) + \rho h \frac{\partial^2 w(x, y, t)}{\partial t^2} = p(x, y, t) \quad (1)$$

where $w(x, y, t)$ is the transverse displacement of the plate; D is the flexural rigidity of the plate defined by

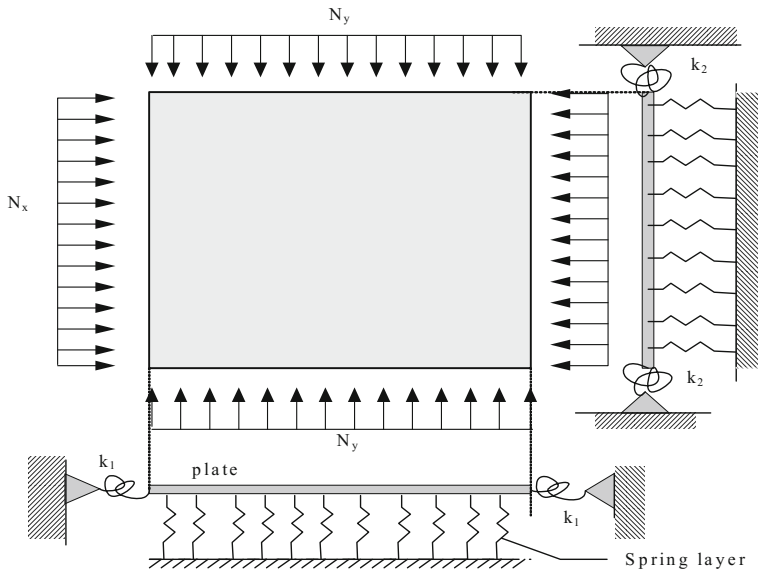


Fig. 1 Isotropic rectangular plate of thin plate on elastic foundation subjected to the in-plane forces

$$D = \frac{Eh^3}{12(1-\nu^2)}, \tag{2}$$

E is Young's modulus; h is the plate thickness; k_f is the foundation stiffness; ν is Poisson's ratio; N_x and N_y are normal forces per unit length of plate in the x - and y -directions, respectively, positive if in tension; and $p(x, y, t)$ is the lateral dynamic load. The forces per unit length are related to the in-plane stresses ($\sigma_x, \sigma_y, \tau_{xy}$) by $N_x = \sigma_x h$; $N_y = \sigma_y h$ and $N_{xy} = \tau_{xy} h$. Let us assume $N_y = \alpha N_x$ and $N_{xy} = 0$ [2].

The isotropic plate is fully attached to the elastic foundation of elastic coefficient k_f . Let the edges $x = 0$; $x = a$; $y = 0$; and $y = b$ be semi-rigid supported, then the boundary conditions can be expressed as follows.

At $x = 0$ and $x = a$:

$$w(x, y, t) = 0 \text{ and } D \left(\frac{\partial^2 w(x, y, t)}{\partial x^2} + \nu \frac{\partial^2 w(x, y, t)}{\partial y^2} \right) = k_1 \frac{\partial w(x, y, t)}{\partial x} \tag{3}$$

At $y = 0$ and $y = b$:

$$w(x, y, t) = 0 \text{ and } D \left(\frac{\partial^2 w(x, y, t)}{\partial y^2} + \nu \frac{\partial^2 w(x, y, t)}{\partial x^2} \right) = k_2 \frac{\partial w(x, y, t)}{\partial y} \tag{4}$$

Adopting the non-dimensional coordinates $\xi = x/a$; $\eta = y/b$, Eq. (1) becomes

$$\frac{\partial^4 w}{\partial \xi^4} + 2s^2 \frac{\partial^4 w}{\partial \xi^2 \partial \eta^2} + s^4 \frac{\partial^4 w}{\partial \eta^4} + \frac{a^4 \rho h}{D} \frac{\partial^2 w}{\partial t^2} + \frac{a^2 N_x}{D} \left(\frac{\partial^2 w}{\partial \xi^2} + \alpha s^2 \frac{\partial^2 w}{\partial \eta^2} \right) + \frac{a^4 k_f}{D} w = 0 \tag{5}$$

where s is the aspect ratio defined by a/b ; α is the ratio between N_x/N_y .

A solution for the displacement $w(\xi, \eta, t)$ can be expressed by:

$$w(\xi, \eta, t) = W_{mn}(\xi, \eta) \cos(\omega_{mnt}) = X_m(\xi) Y_n(\eta) \cos(\omega_{mnt}) \tag{6}$$

where ω_{mn} is the natural frequency of the plate and $W_{mn}(\xi, \eta)$ is the function of position coordinates determined for the mode numbers m and n in the ξ -direction and η -direction, respectively, which can be determined from the first and second auxiliary Levy-type problem [3].

3 Determination of the Eigenfrequencies

In order to solve the non-dimensional Eq. (5) of the problem, the free vibration solution of the problem is set as shown in Eq. (6) above.

3.1 First Auxiliary Levy-Type Problem

Based on the modified Bolotin method, the solution of Eq. (5) for the first auxiliary problem can be expressed in non-dimensional form as:

$$W_{mn}(\xi, \eta) = \sum_{m=1}^m \sum_{n=1}^n X_{mn}(\xi) \sin(\pi q \eta) \tag{7}$$

Satisfying the semi-rigid boundary conditions along $\xi = 0$ and $\xi = 1$:

$$X_{mn}(\xi) = 0; \left(\frac{\partial^2 W(\xi, \eta)}{\partial \xi^2} + \nu s^2 \frac{\partial^2 W(\xi, \eta)}{\partial \eta^2} \right) = -\bar{k}_1 s \frac{\partial W(\xi, \eta)}{\partial \xi} \tag{8}$$

where $\bar{k}_1 = \frac{k_1 b}{D}$ is the non-dimensional rotational stiffness coefficient that varies from 0 to 1.

Substituting Eq. (7) into Eq. (5) and satisfying the boundary conditions according to Eq. (8), the non-dimensional eigenvector in ξ -direction can be expressed as

$$X_{mn}(\xi) = \sum_{m=1}^m \sum_{n=1}^n \cos(p\pi\xi) + F_1 \sin(p\pi\xi) - \cosh(\beta\pi\xi) + F_2 \sinh(\beta\pi\xi) \quad (9)$$

where

$$\beta = \sqrt{-\frac{s^2 N_0}{\pi^2} + p^2 + 2s^2 q^2} \quad (10)$$

$$F_1 = -\frac{\beta \cos(p\pi)}{\beta \sin(p\pi) - p \sinh(\pi\beta)} + \frac{\beta \cosh(\pi\beta)}{\beta \sin(p\pi) - p \sinh(\pi\beta)} - \frac{p^2 \pi \sinh(\pi\beta)}{s\overline{k}_1(\beta \sin(p\pi) - p \sinh(\pi\beta))} - \frac{\beta^2 \pi \sinh(\pi\beta)}{s\overline{k}_1(\beta \sin(p\pi) - p \sinh(\pi\beta))} \quad (11)$$

$$F_2 = \frac{p \cos(p\pi)}{\beta \sin(p\pi) - p \sinh(\pi\beta)} - \frac{p \cosh(\pi\beta)}{\beta \sin(p\pi) - p \sinh(\pi\beta)} + \frac{p^2 \pi \sin(p\pi)}{s\overline{k}_1(\beta \sin(p\pi) - p \sinh(\pi\beta))} + \frac{\beta^2 \pi \sin(p\pi)}{s\overline{k}_1(\beta \sin(p\pi) - p \sinh(\pi\beta))} \quad (12)$$

$$N_0 = \frac{b^2 N_x}{D} \quad (13)$$

3.2 Second Auxiliary Levy-Type Problem

The solution of Eq. (5) for the second auxiliary problem in non-dimensional form can be expressed as:

$$W_{mn}(\xi, \eta) = \sum_{m=1}^m \sum_{n=1}^n \sin(\pi p \xi) Y_{mn}(\eta) \quad (14)$$

Satisfying the semi-rigid boundary conditions along $\eta = 0$ and $\eta = 1$:

$$Y_{mn}(\eta) = 0; \left(\frac{\partial^2 W(\xi, \eta)}{\partial \eta^2} + \frac{\nu}{s^2} \frac{\partial^2 W(\xi, \eta)}{\partial \xi^2} \right) = -\frac{\overline{k}_2}{s} \frac{\partial W(\xi, \eta)}{\partial \eta} \quad (15)$$

where $\overline{k}_2 = \frac{k_2 a}{D}$ is the non-dimensional rotational stiffness coefficient that its value varies from 0 to 1.

Substituting Eq. (3) into Eq. (5) and satisfying the boundary conditions according to Eq. (15), the non-dimensional eigenvector in η -direction can be expressed as:

$$Y_{mn}(\eta) = \sum_{m=1}^m \sum_{n=1}^n \cos(q\pi\eta) + F_3 \sin(q\pi\eta) - \cosh(\theta\pi\eta) + F_4 \sinh(\theta\pi\eta) \quad (16)$$

where

$$\theta = \frac{1}{s} \sqrt{2p^2 + s^2q^2 - \frac{s^2N_0\alpha}{\pi^2}} \quad (17)$$

$$F_3 = - \frac{\bar{k}_2\theta \cos(\pi q) - \bar{k}_2 \cosh(\pi\theta) + s\pi(q^2 + \theta^2) \sinh(\pi\theta)}{\bar{k}_2(\theta \sin(\pi q) - q \sinh(\pi\theta))} \quad (18)$$

$$F_4 = \frac{\bar{k}_2q \cos(\pi q) - \bar{k}_2 \cosh(\pi\theta) + s\pi(q^2 + \theta^2) \sinh(\pi q)}{\bar{k}_2(\theta \sin(\pi q) - q \sinh(\pi\theta))} \quad (19)$$

The unknown quantities p and q which are the number of modes in the x - and y -directions for non-simply supported conditions are calculated from the transcendental equations:

$$-2s^2\bar{k}_1^2p\beta + 2s^2\bar{k}_1^2p\beta \cos(p\pi) \cosh(\pi\beta) + \left(s^2\bar{k}_1^2(p^2 - \beta^2) + \pi^2(p^2 + \beta^2)^2 \right) \sin(p\pi) \sinh(\pi\beta) = 0 \quad (20)$$

$$-2\bar{k}_2^2q\theta + 2\bar{k}_2^2q\theta \cos(q\pi) \cosh(\pi\theta) + \left(\bar{k}_2^2(q^2 - \theta^2) + s^2\pi^2(q^2 + \theta^2)^2 \right) \sin(q\pi) \sinh(\pi\theta) = 0 \quad (21)$$

Once the value of p and q are determined from Eqs. (20)–(21), the non-dimensional critical in-plane stresses for statics condition and the eigenvalues of the system can be expressed as

$$N_0 = \frac{p^4\pi^4 + 2s^2p^2\pi^4q^2 + s^4(\bar{k}_f + \pi^4q^4)}{s^2\pi^2(p^2 + s^2q^2\alpha)} \quad (22)$$

$$\bar{\omega}_{mn} = \sqrt{p^4\pi^4 + s^2p^2\pi^2(-N_0 + 2\pi^2q^2) + s^4(\bar{k}_f + \pi^4q^4 - N_0\pi^2q^2\alpha)} \quad (23)$$

where $\bar{k}_f = \frac{k_f a^4}{\pi^4 D}$ is non-dimensional Winkler foundation stiffness.

The eigenmodes of the system are determined as the product of Eqs. (9)–(16).

3.3 Determination of the Time Function

The time function for the system can be solved by using the Duhamel integration. It can be expressed as:

$$\ddot{T}_{mn}(t) + 2\xi\omega_{mn}\dot{T}(t) + \omega_{mn}^2 T(t) = \frac{\int_0^a X_{mn}(x)dx \int_0^b Y_{mn}(y)dy}{\rho h Q_{mn}} P(t) \delta[x - (x_0 - \Delta x H(t - t_0))] \delta[y - y_0] \quad (24)$$

where Q_{mn} is the normalization factor of the eigenmodes that can be expressed as:

$$Q_{mn} = \int_0^a (X_{mn}(x))^2 dx \int_0^b (Y_{mn}(y))^2 dy \quad (25)$$

The lateral load, $p(x, y, t)$, that moves suddenly from the initial position at $x = x_0$ to the new position at $x = x_1$ at time $t = t_0$ can be expressed by using the Heaviside unit step function, $H[.]$ [4].

Finally, the generalized dynamic deflection of the system can be solved by multiplying the spatial functions with the temporal function which is the solution of Eq. (24).

4 Numerical Applications, Results, and Discussion

Using the procedure described above, the concrete plate on the Winkler foundation subjected to the in-plane stresses in the x - and y -directions and the lateral load $P(t)$ is analyzed. The plate is suddenly moved from the initial position at $x = x_0$ to the new position at $x = x_1$ at time $t = t_0$. The structural properties of the plate are $a = 3$ m; $s = a/b$ is varied from 1 to 2; the thickness, h is 0.12 m. The physical characteristics of the plate are $\rho = 2400$ kg/m³; $E = 30.10^9$ N/m²; $\nu = 0.3$; $\bar{k}_f = 1$, $\bar{k}_1 = 0.5$; and $\bar{k}_2 = 0.5$. The non-dimensional in-plane stresses in the x -direction, $N_0 = 1$; $\alpha = 1$; the lateral load amplitude $P_0 = 10^5$ Nm/m². The initial position of the load at $x_0 = 0.3a$, $y_0 = b/2$, and $t_0 = 2$ s.

4.1 Variation of Aspect Ratio Versus the Critical in-Plane Stress

Figure 2 shows the variation of aspect ratio as the function of the non-dimensional in-plane stresses for the rectangular plate with semi-rigid conditions at all edges.

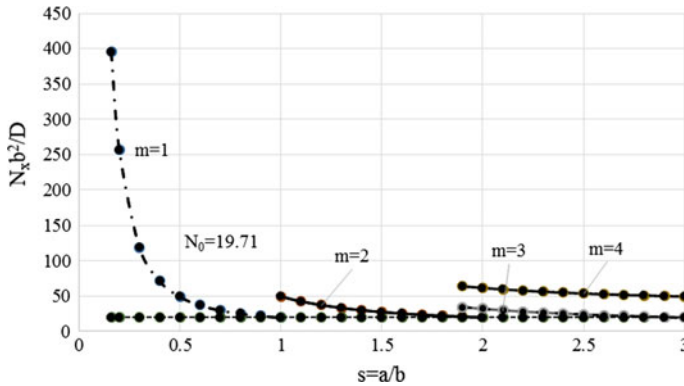


Fig. 2 Non-dimensional critical buckling loads $N_0 = N_x b^2 / D$ as a function of $s = a/b$ for plate with semi-rigid conditions, $\bar{k}_1 = \bar{k}_2 = 0.5$

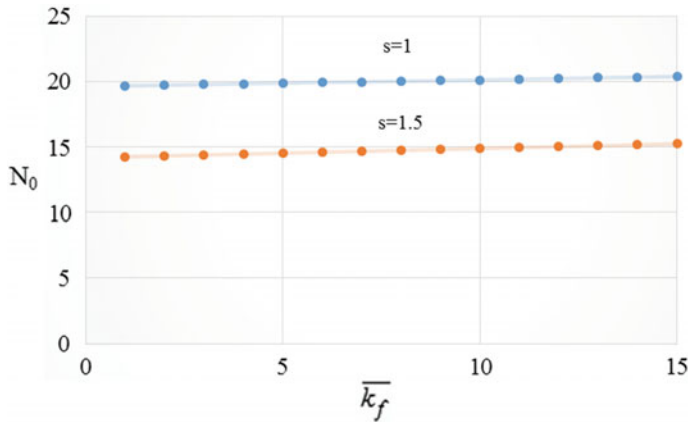


Fig. 3 Non-dimensional value of N_0 as a function of non-dimensional value of the foundation stiffness \bar{k}_f for 2 values of s

A rectangular plate as shown in Fig. 1 is compressed by in-plane stresses N_0 along all of the four edges ($\alpha = 1$). The smallest critical load is obtained for $m = 1$ and $n = 1$. Results from Eq. (22) are shown in Fig. 2, which shows that $N_0 = 19.7176$.

The buckling loads displayed in Fig. 2 are critical values. That is, they are the lowest of the doubly infinite set of bucking eigenvalues that arise for each a/b . For $0.16 \leq s \leq 1$, then $m = 1$; for $1 \leq s \leq 2$, then $m = 2$; and for $s > 2$, then $m = 3$. The critical loads listed in Fig. 2 are only for the range of plate aspect ratios $0.16 \leq s \leq 3$.

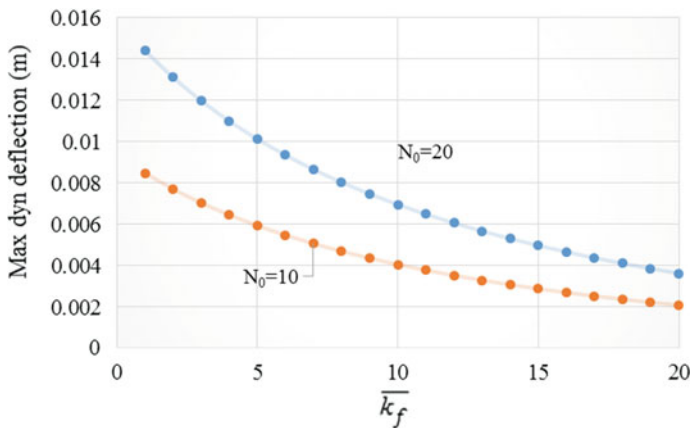


Fig. 4 Graph of non-dimensional foundation stiffness versus maximum dynamic deflection for the value of $s = 1$; $\overline{k}_1 = \overline{k}_2 = 0.5$; $N_0 = 10$

Increasing the aspect ratio s from $s = 1$ to $s = 1.5$ results in lowering the non-dimensional value of N_0 as shown in Fig. 3. The foundation stiffness also plays a very important factor in increasing the value of the critical in-plane stresses.

4.2 Variation of Foundation Stiffness Versus the Maximum Dynamic Deflection

Figure 4 shows the non-dimensional foundation stiffness coefficient versus the maximum dynamic deflection computed using the value of $N_0 = 10$ and $\overline{\omega} = 10$ and 20. It can be seen from Fig. 3 that by increasing the foundation stiffness coefficient, the maximum dynamic deflection decreases for the value of load's frequency $\overline{\omega} = 10$; 20. It is also shown from Fig. 3 that the closer the value of load's frequency to the value of the first natural frequency of the system, the higher the value of the maximum dynamic deflection.

4.3 Effect of in-Plane Stress and Lateral Load on Dynamic Deflection

Figure 5 shows the response spectra of the plate subjected to in-plane stresses in x - and y -directions and lateral load $p(x, y, t)$. The lateral load is positioned initially at $x = x_0$ and at time $t = t_0$ before suddenly moved into a new position at $x = x_2$. It can

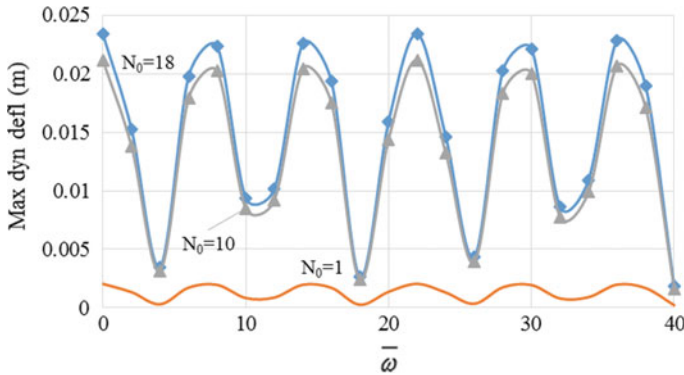


Fig. 5 Response spectra of the plate subjected to in-plane stresses and lateral load

be seen that the maximum dynamic deflection is influenced by the value of N_0 . When the value of N_0 approaches N_{cr} , the dynamic deflection will reach maximum value.

Figures 5 and 6 show the various dynamic response of the plate subjected to in-plane stresses and lateral dynamic load that are suddenly moved to its new position for two different values of N_0 . It can be seen that the dynamic response of the system is higher when the N_0 is close to the value of N_{cr} . By increasing the value of in-plane stresses by 10 times for $\bar{\omega} = 20$, the dynamic response of the system increased by 90.5% for the dynamic deflection. The dynamic response of the system also increased drastically when the frequency of the lateral load approaches the fundamental frequency of the system as shown in Fig. 4.

5 Conclusion

The foregoing work has shown how the modified Bolotin method is used to analyze the buckling and the forced vibrations of rectangular plate sitting on the elastic foundation having two opposite edges in semi-rigid conditions. The procedure may be applied to all possible combination of fixed, simply supported, semi-rigid, or free-edge conditions applied continuously along the edges of the plate.

Analytical solutions of the mode number in the x and in the y direction is solved by using two transcendental equations. The whole formulation in this work is based on the assumption that the boundary supports of the plate are semi-rigid with rotational restraint. This is a very realistic assumption, particularly for concrete plates, because one may find that rotational deformations exist along the joints.

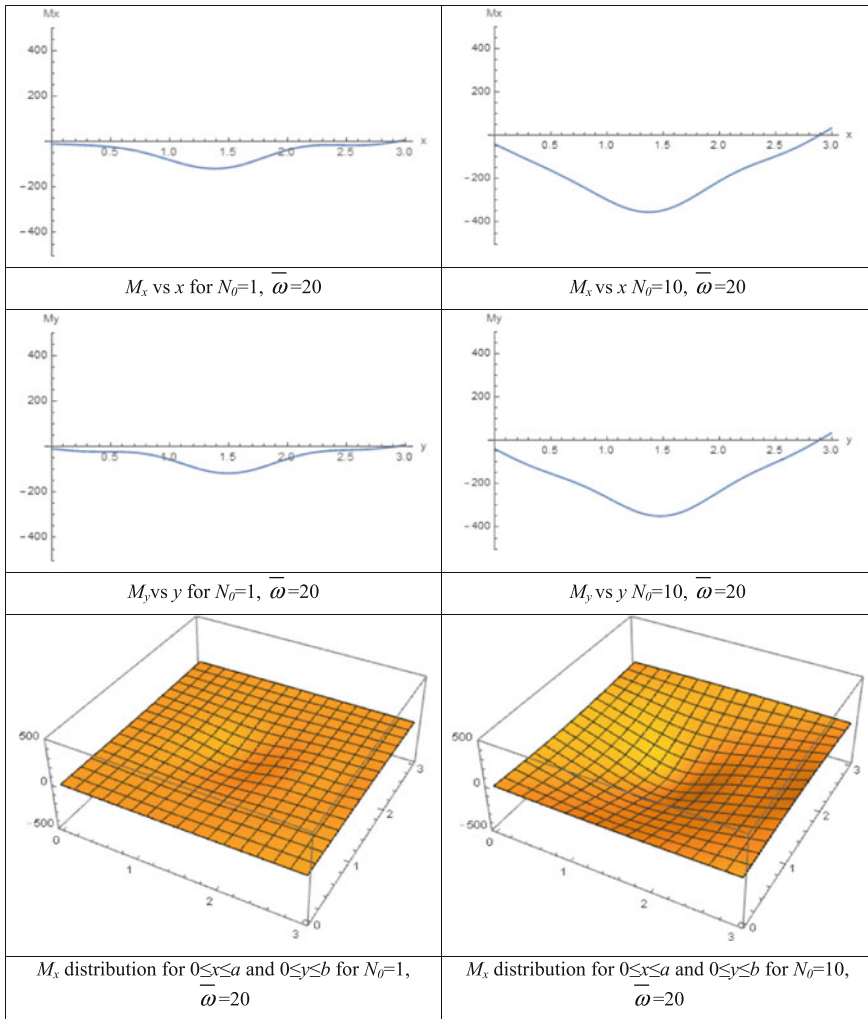


Fig. 6 Various dynamic response of plate subjected to in-plane stresses and lateral load for the value of $s = 1$; $\bar{k}_1 = \bar{k}_2 = 0.5$; $\alpha = 1$ and $\bar{k}_f = 1$

Critical in-plane stresses for plates on the Winkler foundation increase linearly with the value of foundation parameter k_f . The load combination of the in-plane compressive stresses in the x - and y -directions as well as the transversal load drastically effects the maximum dynamic deflection of the system, especially when the value of the in-plane stresses converges to the critical value and when the frequency value of the load converges to the fundamental frequency of the system.

The stability and the dynamic analysis presented here would be quite useful for plate structural elements such as concrete plate pavements.

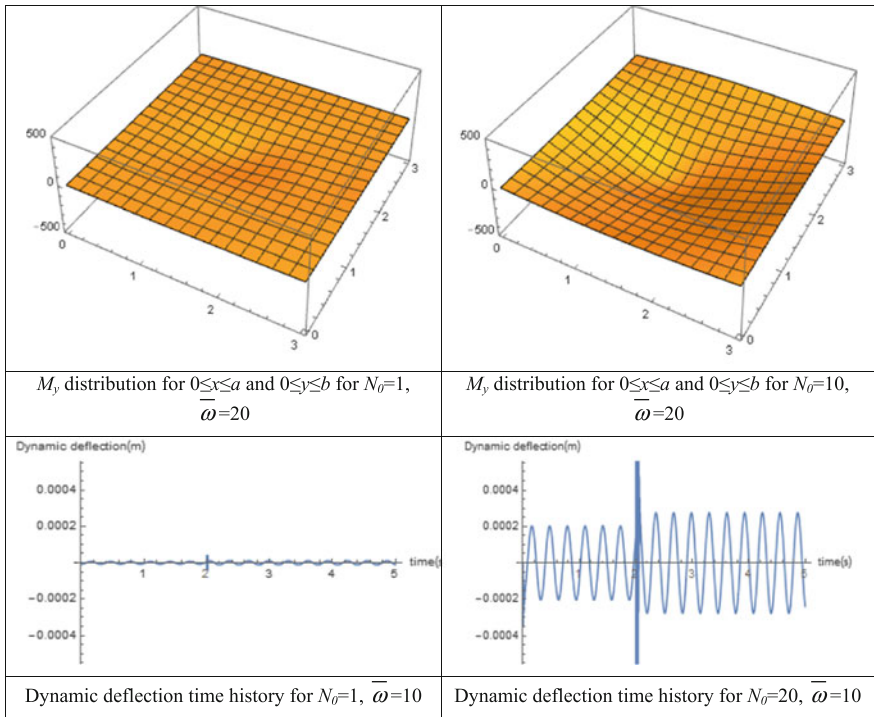


Fig. 6 (continued)

References

1. Arthur J-HK, Leissa W (2002) Exact solutions for vibration and buckling of an SS-C-SS-C rectangular plate loaded by linearly varying in-plane stresses. *Int J Mech Sci* 44:1925–1945
2. Alisjahbana SW, Wangsadinata W, Alisjahbana I (2016) Numerical studies of concrete plates under localized blast loads. In: *Integrated solutions for infrastructure development*, Sarawak
3. Viswanathan K, Navaneethakrishnan P, Aziz Z (2015) Buckling analysis of rectangular plates with variable thickness resting on elastic foundation. *Earth Environ Sci* 23
4. Alisjahbana SW, Wangsadinata W (2000) Response of large space building floors to dynamic moving load which suddenly move to its new position. In: *The 7th international symposium on structural failure and plasticity, implast 2000*, Melbourne

Static Analysis of FG-CNTRC Plates Using C0-HSDT



T. Nguyen-Quoc, S. Nguyen-Hoai and D. Mai-Duc

Abstract Recently, an edge-based smoothed discrete shear gap method (ES-DSG) based on the first-order shear deformation theory (FSDT) was developed to investigate static and free vibration analyses of Reissner–Mindlin plates [1]. In this paper, we extend ES-DSG to the C0-type higher-order shear deformation theory (C0-HSDT) to study static analysis of functionally graded carbon nanoreinforced composite (FG-CNTRC) plates. Four distributions of volume fractions of carbon nanotubes (CNTs) including UD, FG-V, FG-O, FG-X are considered. The governing equations are approximated according to a combination between ES-DSG and HSDT model. Hence, this does not require shear correction factors and improves the accuracy of the present method. Numerical examples are performed to show the reliability and accuracy of the present method.

Keywords FG-CNTRC · Carbon nanotubes (CNTs) · Higher-order shear deformation theory (HSDT) · Static analysis

1 Introduction

Carbon nanotubes (CNTs) are considered “material for this century—twenty-first” [2] that have attracted much attention of researchers, introduced by Iijima [3]. With special properties, CNTs are considered as a potential material for reinforcement of composites [4]. Zhu et al. [5] using FSDT and finite element method (FEM) reported static and free vibration analyses of thick composite plates reinforced by single-walled carbon nanotubes (SWCNTs). By using Ritz method, Ke et al. [6]

T. Nguyen-Quoc (✉) · S. Nguyen-Hoai

Faculty of Civil Engineering, Ho Chi Minh City University of Technology and Education,
1 Vo van Ngan Street, Thu Duc District, Ho Chi Minh City, Vietnam
e-mail: 1621002@student.hcmute.edu.vn; tuannnguyenquoc074@gmail.com

D. Mai-Duc

Faculty of Mechanical Engineering, Ho Chi Minh City University of Technology
and Education, 1 Vo van Ngan Street, Thu Duc District, Ho Chi Minh City, Vietnam

© Springer Nature Singapore Pte Ltd. 2018

H. Nguyen-Xuan et al. (eds.), *Proceedings of the International Conference on Advances in Computational Mechanics 2017*, Lecture Notes in Mechanical Engineering, https://doi.org/10.1007/978-981-10-7149-2_24

357

examined nonlinear vibration of FG-CNTRC Timoshenko beams. Alibeigloo and Liew [7] used elasticity theory to study thermo-elastic analysis of FG-CNTRC plates. Nonlinear behavior of FG-CNTRC plates using analytical method and asymptotic solutions was indicated by Shen [8]. Recently, Phung-Van et al. [9, 10] used isogeometric approach (IGA) integrated with HSDT to examine behaviors of FG-CNTRC plates [9] and nanoplates [10]. Further, the study of dynamic responses of plate elements was performed in Refs. [11–14]. Available studies have concentrated on FG-CNTRC plates using mesh-free methods, FEM, IGA, or theory of elasticity. In addition, we can see that the literature related to study responses of FG-CNTRC plates based on C0-HSDT is somewhat limited. So, in this research, we try to fill this gap by developing smoothed finite element method (S-FEM) using a three-node triangular plate element.

S-FEM was introduced by Liu and Trung [15] which has combined the strain smoothing technique [16] and FEM. Moreover, the S-FEM models have also been studied and applied to many physical problems including plate and shell structures [17–23], piezoelectricity [24], crack plates [25], and fluid–structure interaction [26–28]. In S-FEM models, ES-FEM [29] shows good properties in structures/solid mechanics. This paper develops combination between the advantages of ES-FEM and discrete shear gap method (DSG) [30] using C0-HSDT for static analysis of FG-CNTRC plates. Four distributions of the volume fraction of carbon nanotubes including UD, FG-X, FG-O, FG-V are performed. According to a combination between ES-DSG and HSDT model, governing equations are approximated. Hence, this does not require shear correction factors and improves the accuracy of the proposed method. Numerical results are investigated and verified to show the reliability of the proposed method.

2 FG-CNTRC Plates

A FG-CNTRC plate with four distributions, shown in Fig. 1, is considered in this research. Four distributions of CNTs are described as follows [8]

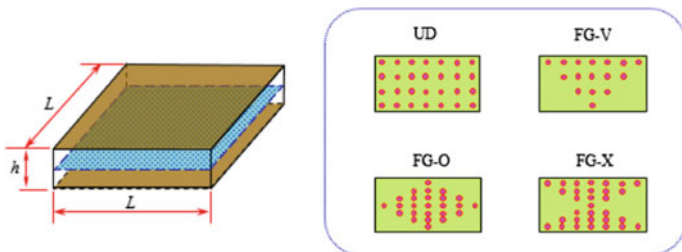


Fig. 1 Configuration of the FG-CNTRC plate

$$V_{CNT} = \begin{cases} V_{CNT}^* & \text{(UD)} \\ (1 + \frac{2|z|}{h})V_{CNT}^* & \text{(FG - V)} \\ 2(1 - \frac{2|z|}{h})V_{CNT}^* & \text{(FG - O)} \\ 2(\frac{2|z|}{h})V_{CNT}^* & \text{(FG - X)} \end{cases} \quad (1)$$

By using rule of mixtures, material properties of FG-CNTRC are expressed

$$E_{11} = \eta_1 V_{CNT} E_{11}^{CNT} + V_m E^m, \quad \frac{\eta_2}{E_{22}} = \frac{V_{CNT}}{E_{22}^{CNT}} + \frac{V_m}{E^m}; \quad \frac{\eta_3}{G_{12}} = \frac{V_{CNT}}{G_{12}^{CNT}} + \frac{V_m}{G^m} \quad (2)$$

where G^m and E^m are the shear modulus and Young’s modulus of the isotropic matrix, respectively; G_{12}^{CNT} and $E_{11}^{CNT}, E_{22}^{CNT}$ are the shear and Young’s modulus of CNT, respectively. η_1, η_2 and η_3 were defined in Ref. [8].

3 Mathematical Equations

Based on C0-type HSDT model [31], the displacement fields of plates are defined

$$\begin{aligned} u(x, y, z) &= u_0 + \left(z - \frac{4z^3}{3t^2} \right) \beta_x - \frac{4z^3}{3h^2} \phi_x \quad (-h/2 \leq z \leq h/2) \\ v(x, y, z) &= v_0 + \left(z - \frac{4z^3}{3t^2} \right) \beta_y - \frac{4z^3}{3h^2} \phi_y \\ w(x, y) &= w_0 \end{aligned} \quad (3)$$

where $\boldsymbol{\beta} = \{\beta_x \beta_y\}^T$ are the rotations around y-axis and x-axis, respectively; h is thickness of plate; w_0 and $\mathbf{u}_0 = \{u_0 \ v_0\}^T$ are the transverse displacement and the membrane displacements, respectively. $\boldsymbol{\Phi} = \{\phi_x \ \phi_y\}^T$ is warped function defined in Ref. [32]

The in-plane strains are expressed as follows:

$$\boldsymbol{\varepsilon}_p = [\varepsilon_{xx} \ \varepsilon_{yy} \ \gamma_{xy}]^T = \boldsymbol{\varepsilon}_0 + z\boldsymbol{\kappa}_1 + z^3\boldsymbol{\kappa}_2 \quad (4)$$

where

$$\begin{aligned} \boldsymbol{\varepsilon}_0 &= \left\{ \frac{\partial u_0}{\partial x} \quad \frac{\partial v_0}{\partial y} \quad \frac{\partial u_0}{\partial y} + \frac{\partial v_0}{\partial x} \right\}^T = \nabla_s \mathbf{u}_0; \quad \boldsymbol{\kappa}_1 = \frac{1}{2} \{ \nabla \boldsymbol{\beta} + (\nabla \boldsymbol{\beta})^T \} \\ \boldsymbol{\kappa}_2 &= \frac{c}{6} \{ (\nabla \boldsymbol{\Phi} + (\nabla \boldsymbol{\Phi})^T) + (\nabla \boldsymbol{\beta} + (\nabla \boldsymbol{\beta})^T) \} \end{aligned} \quad (5)$$

in which $\nabla = [\partial/\partial x \quad \partial/\partial y]^T$ and shear strains are written

$$\boldsymbol{\gamma} = \begin{bmatrix} \gamma_{xz} \\ \gamma_{yz} \end{bmatrix} = \begin{bmatrix} w_{,x} + \beta_x \\ w_{,y} + \beta_y \end{bmatrix} + c \begin{bmatrix} \phi_x + \beta_x \\ \phi_y + \beta_y \end{bmatrix} z^2 = \boldsymbol{\varepsilon}_s + z^2 \boldsymbol{\kappa}_s \tag{6}$$

where $c = -4/h$. It can be seen that the shear strains in C0-HSDT shown in Eq. (6) are quadratic functions, so the shear stress is represented parabolically. This improves the accuracy of shear stresses when compared those in FSDT.

For static analysis, a weak form for FG-CNTRC plates under uniform loading q_0 is written:

$$\int_{\Omega} \delta \boldsymbol{\varepsilon}_p^T \mathbf{D}^* \boldsymbol{\varepsilon}_p d\Omega + \int_{\Omega} \delta \boldsymbol{\gamma}^T \mathbf{D}_s^* \boldsymbol{\gamma} d\Omega = \int_{\Omega} \delta w q_0 d\Omega \tag{7}$$

and material constant matrices \mathbf{D}^* and \mathbf{D}_s^* have the forms of

$$\mathbf{D}^* = \begin{bmatrix} \mathbf{A} & \mathbf{B} & \mathbf{E} \\ \mathbf{B} & \mathbf{D} & \mathbf{F} \\ \mathbf{E} & \mathbf{F} & \mathbf{H} \end{bmatrix}; \mathbf{D}_s^* = \begin{bmatrix} \mathbf{A}^s & \mathbf{B}^s \\ \mathbf{B}^s & \mathbf{D}^s \end{bmatrix} \tag{8}$$

where

$$\begin{aligned} (\mathbf{A}_{ij}, \mathbf{B}_{ij}, \mathbf{D}_{ij}, \mathbf{E}_{ij}, \mathbf{F}_{ij}, \mathbf{H}_{ij}) &= \int_{-h/2}^{h/2} (1, z, z^2, z^3, z^4, z^6) \bar{Q}_{ij} dz \quad i, j = 1, 2, 6 \\ (\mathbf{A}_{ij}^s, \mathbf{B}_{ij}^s, \mathbf{D}_{ij}^s) &= \int_{-h/2}^{h/2} (1, z^2, z^4) \bar{Q}_{ij} dz \quad i, j = 4, 5 \end{aligned} \tag{9}$$

where the material constants are given by

$$\begin{aligned} Q_{11} &= \frac{E_{11}}{1 - \nu_{12}\nu_{21}}, Q_{12} = \frac{\nu_{12}E_{22}}{1 - \nu_{12}\nu_{21}}, Q_{22} = \frac{E_{22}}{1 - \nu_{12}\nu_{21}} \\ Q_{66} &= G_{12}, Q_{55} = G_{13}, Q_{44} = G_{23} \end{aligned} \tag{10}$$

4 An ES-DSG Formulations for FG-CNTRC Plates

In ES-FEM [29], the 2D problem is discretized into a mesh of triangular elements. The ES-FEM stiffness matrix is calculated according to the edge-based smoothing domains. In this research, we apply ES-FEM [29] to discrete shear gap method (DSG) [30], which is so-called ES-DSG. For triangular elements, by connecting two end nodes of the edge to centroids of adjacent elements, the smoothing domain associated with the edge k is created, as indicated in Fig. 2.

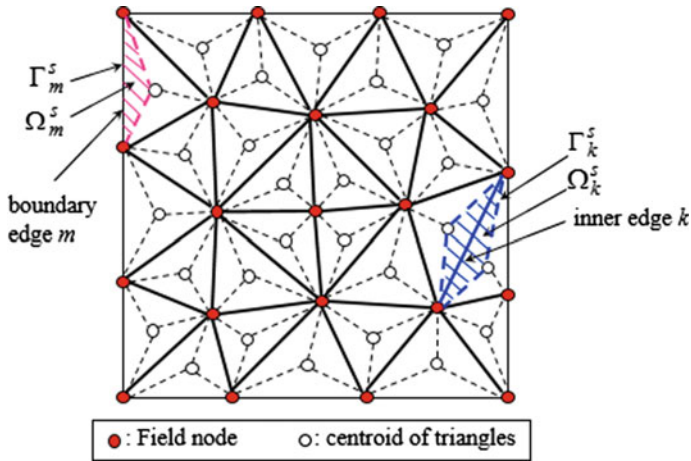


Fig. 2 Smoothing cells Ω_k^s

Applying ES-FEM technique [29], the strains ϵ^h in Eqs. (4)–(6) are used to create a smoothed strains $\tilde{\epsilon}^h$ on the smoothing cell Ω_k^s associated with the edge k , such as:

$$\tilde{\epsilon}^h = \int_{\Omega_k^s} [\epsilon_p \quad \gamma]^T \Phi^k(\mathbf{x}) d\Omega \tag{11}$$

where a smoothing function, $\Phi^k(\mathbf{x})$, satisfies at least unity property and can be expressed as

$$\Phi^k(\mathbf{x}) = \begin{cases} 1/A^k & \mathbf{x} \in \Omega_k^s \\ 0 & \mathbf{x} \notin \Omega_k^s \end{cases} \tag{12}$$

where the area, A^k , of the smoothing domain Ω_k^s computed by

$$A^k = \int_{\Omega_k^s} d\Omega = \frac{1}{3} \sum_{i=1}^{N_e^k} A_i \tag{13}$$

where N_e^k is the number of elements attached to the edge k ($N_e^k = 1$ for the boundary edges and $N_e^k = 2$ for inner edges as depicted in Fig. 2), and A_i is the area of the i th element attached to the edge k .

Based on three-node triangular elements, the displacement field for FG-CNTRC plates can be defined

$$\mathbf{u}^e(\mathbf{x}) = \sum_{i=1}^3 \text{diag}(N_i^e(\mathbf{x}), N_i^e(\mathbf{x}), N_i^e(\mathbf{x}), N_i^e(\mathbf{x}), N_i^e(\mathbf{x}), N_i^e(\mathbf{x}), N_i^e(\mathbf{x})) \mathbf{d}_i^e = \sum_{i=1}^3 \mathbf{N}_i^e(\mathbf{x}) \mathbf{d}_i^e \tag{14}$$

The smoothed strains at edge k are defined:

$$\tilde{\boldsymbol{\epsilon}}^h = \sum_{l=1}^{N_n^k} \tilde{\mathbf{B}}_l \mathbf{d}_l \tag{15}$$

where N_n^k is the number of nodes belonging to elements connected to edge k ($N_n^k=3$ for the boundary edges and $N_n^k=4$ for inner edges depicted in Fig. 2); $\tilde{\mathbf{B}}_l$ are given by

$$\tilde{\mathbf{B}}_l^k = [\tilde{\mathbf{B}} \quad \tilde{\mathbf{S}}] = \frac{1}{A^k} \sum_{i=1}^{N_n^k} \frac{1}{3} A_i \mathbf{B}_i \tag{16}$$

where \mathbf{B}_i is obtained from

$$\mathbf{B}_i = [(\mathbf{B}_i^m)^T (\mathbf{B}_i^{b_1})^T (\mathbf{B}_i^{b_2})^T (\mathbf{B}_i^{s_0})^T (\mathbf{B}_i^{s_1})^T] \tag{17}$$

in which

$$\mathbf{B}^m = \frac{1}{2A_e} \begin{bmatrix} b-c & 0 & 00000 & c & 0 & 00000 & -b & 0 & 00000 \\ 0 & d-a & 00000 & 0 & -d & 00000 & 0 & a & 00000 \\ d-1 & b-c & 00000 & -d & c & 00000 & a & -b & 00000 \end{bmatrix} \tag{18}$$

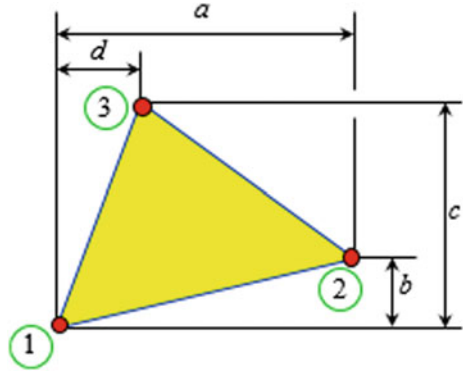
$$\mathbf{B}^{b_1} = \frac{1}{2A_e} \begin{bmatrix} 000 & b-c & 0 & 00 & 000 & c & 0 & 00 & 000 & -b & 0 & 00 \\ 000 & 0 & d-a & 00 & 000 & 0 & -d & 00 & 000 & 0 & a & 00 \\ 000 & d-a & b-c & 00 & 000 & -d & c & 00 & 000 & a & -b & 00 \end{bmatrix} \tag{19}$$

$$\mathbf{B}^{b_2} = \frac{1}{2A_e} \begin{bmatrix} 000 & b-c & 0 & b-c & 0 & 000 & c & 0 & c & 0 & 000 & -b & 0 & -b & 0 \\ 000 & 0 & d-a & 0 & d-a & 000 & 0 & -d & 0 & -d & 000 & 0 & a & 0 & a \\ 000 & d-a & b-c & d-a & b-c & 000 & -d & c & -d & c & 000 & a & -b & a & -b \end{bmatrix} \tag{20}$$

$$\mathbf{B}^{s_0} = \frac{1}{2A_e} \begin{bmatrix} 00b-c & A_e & 000 & 00 & c & ac/2 & bc/2 & 00 & 00 & -b & bd/2 & -bc/2 & 00 \\ 00d-a & 0 & A_e & 00 & -d & -ad/2 & -bd/2 & 00 & 00 & a & ad/2 & ac/2 & 00 \end{bmatrix} \tag{21}$$

$$\mathbf{B}^{s_1} = \frac{1}{2A_e} \begin{bmatrix} 000 & 1 & 010 & 000 & 1 & 010 & 000 & 1 & 0 & 1 & 0 \\ 000 & 0 & 101 & 000 & 0 & 101 & 000 & 0 & 1 & 0 & 1 \end{bmatrix} \tag{22}$$

Fig. 3 DSG triangular element [30]



here A_e is the area of the element; a, b, c, d are calculated as indicated in Fig. 3. Hence, the stiffness of the ES-DSG element is expressed:

$$\begin{aligned} \tilde{\mathbf{K}} &= \int_{\Omega_k^i} \tilde{\mathbf{B}}_i^T \mathbf{D}^* \tilde{\mathbf{B}}_j d\Omega + \int_{\Omega_k^i} \tilde{\mathbf{S}}_i^T \mathbf{D}_s^* \tilde{\mathbf{S}}_j d\Omega \\ &= \tilde{\mathbf{B}}_i^T \mathbf{D}^* \tilde{\mathbf{B}}_j A_e + \tilde{\mathbf{S}}_i^T \mathbf{D}_s^* \tilde{\mathbf{S}}_j A_e \end{aligned} \tag{23}$$

5 Numerical Results

In this study, some numerical examples are studied to show the accuracy and stability of the present method. Material properties of matrix, PmPV, are given as $E^m = 2.1 \text{ GPa}$, $\rho^m = 1.16 \text{ g/cm}^2$, $\nu^m = 0.34$ and material properties of the reinforcements, the (10, 10) SWCNTs, are $E_{11}^{CNT} = 5.6466 \text{ (TPa)}$, $E_{22}^{CNT} = 7.08 \text{ (TPa)}$, $G_{12}^{CNT} = 1.9445 \text{ (TPa)}$, $\alpha_{11}^{CNT} = 3.4584 (10^{-6}/\text{K})$, $\alpha_{22}^{CNT} = 5.1682(10^{-6}/\text{K})$. Moreover, we assume $\eta_3 = \eta_2$ and $G_{23} = G_{13} = G_{12}$. The FG-CNTRC plate may have clamped (C) edges or simply supported (S). The symbol, CCCC or SSSS, for instance, indicates clamped or simply supported boundary conditions, respectively.

Now a square SSSS and CCCC FG-CNTRC plate under a uniform load $q = 0.1 \text{ MPa}$ is considered. A deflection $\bar{w} = w/h$ is considered.

Firstly, UD plates with five meshes index $n = 4, 8, 12, 16, 20$ are analyzed. The convergence of the deflection of the FG-CNTRC plate is plotted in Fig. 4. And the reference solution was reported in Ref. [5]. We can observe that the ES-DSG is much better than the DSG with the same degree of freedoms (DOFs). Next, Table 1 shows the effect of length-to-thickness ratios L/h on the central deflection of the FG-CNTRC with $V_{CNT}^* = 0.11$ and meshing 8×8 . We can see that the proposed results are much better than the DSG and match very well with those of reference solutions [5] with all ratios $L/h = 10, 20,$ and 50 . Besides, we recognize that the central deflections of the FG-O and FG-V plate are larger than those of the UD and

Fig. 4 Convergence of results of the SSSS UD plate with $a/h = 10$ and $V_{CNT}^* = 0.17$

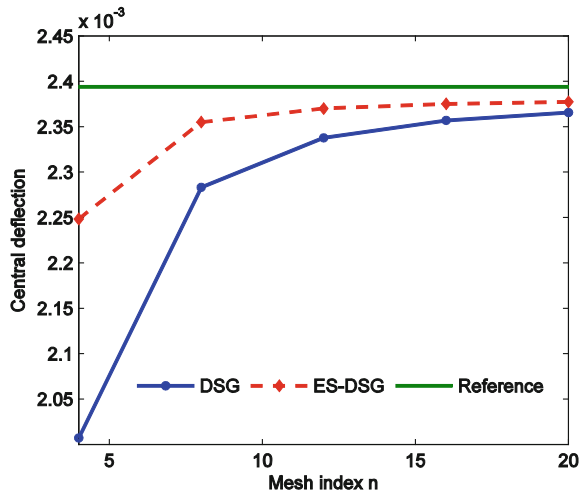


Table 1 Central deflection of the plate with $V_{CNT}^* = 0.11$

a/h	Types	SSSS			CCCC		
		DSG	ES-DSG	Ref [4]	DSG	ES-DSG	Ref [4]
10	UD	3.57E-03	3.68E-03	3.74E-03	2.05E-03	2.14E-03	2.23E-03
	FG-V	4.24E-03	4.38E-03	4.46E-03	2.16E-03	2.27E-03	2.35E-03
	FG-O	5.16E-03	5.33E-03	5.22E-03	2.48E-03	2.61E-03	2.51E-03
	FG-X	3.03E-03	3.12E-03	3.18E-03	1.93E-03	2.02E-03	2.10E-03
20	UD	3.46E-02	3.56E-02	3.63E-02	1.26E-02	1.32E-02	1.34E-02
	FG-V	4.61E-02	4.76E-02	4.88E-02	1.48E-02	1.57E-02	1.59E-02
	FG-O	5.86E-02	6.07E-02	6.14E-02	1.80E-02	1.92E-02	1.86E-02
	FG-X	2.59E-02	2.66E-02	2.70E-02	1.08E-02	1.13E-02	1.15E-02
50	UD	1.09	1.13	1.16	2.44E-01	2.62E-01	2.62E-01
	FG-V	1.52	1.61	1.65	3.31E-01	3.60E-01	3.65E-01
	FG-O	1.95	2.09	2.15	4.23E-01	4.68E-01	4.71E-01
	FG-X	0.76	0.78	0.79	1.80E-01	1.90E-01	1.90E-01

FG-X plate. This means that distributions of CNTs effect on the stiffness of the FG-CNTRC plate. And UD and FG-X plates depicted in Fig. 1 have more CNTs at the bottom and the top layer and as a result the plate becomes stiffer.

Effects of the volume fractions $V_{CNT}^* = 0.14$ and $V_{CNT}^* = 0.17$ on the deflection for the plate are listed in Tables 2 and 3, respectively. Again, it can be observed that the results of the proposed method match well to those of Ref. [5] and are much better than the DSG.

Table 2 Deflection of the plate with $V_{CNT}^* = 0.14$

a/h	Types	SSSS			CCCC		
		DSG	ES-DSG	Ref [4]	DSG	ES-DSG	Ref [4]
10	UD	3.14E-03	3.25E-03	3.306 e-3	1.91E-03	1.99E-03	2.09E-03
	FG-V	3.70E-03	3.82E-03	3.894 e-3	2.00E-03	2.09E-03	2.18E-03
	FG-O	4.46E-03	4.61E-03	4.525 e-3	2.26E-03	2.38E-03	2.31E-03
	FG-X	2.73E-03	2.82E-03	2.842 e-3	1.81E-03	1.89E-03	1.98E-03
20	UD	2.86E-02	2.95E-02	3.00E-02	1.12E-02	1.17E-02	1.19E-02
	FG-V	3.81E-02	3.93E-02	4.03E-02	1.30E-02	1.37E-02	1.39E-02
	FG-O	4.84E-02	5.00E-02	5.07E-02	1.56E-02	1.65E-02	1.60E-02
	FG-X	2.18E-02	2.23E-02	2.26E-02	9.81E-03	1.03E-02	1.04E-02
50	UD	0.87	0.90	0.918	2.01E-01	2.13E-01	2.13E-01
	FG-V	1.23	1.29	1.326	2.71E-01	2.93E-01	2.96E-01
	FG-O	1.59	1.69	1.738	3.47E-01	3.79E-01	3.80E-01
	FG-X	0.60	0.62	0.628	1.50E-01	1.57E-01	1.57E-01

Table 3 Central deflection of the plate with $V_{CNT}^* = 0.17$

a/h	Types	SSSS			CCCC		
		DSG	ES-DSG	Ref [4]	DSG	ES-DSG	Ref [4]
10	UD	2.28E-03	2.36E-03	2.39E-03	1.30E-03	1.36E-03	1.41E-03
	FG-V	2.73E-03	2.81E-03	2.86E-03	1.37E-03	1.44E-03	1.48E-03
	FG-O	3.29E-03	3.40E-03	3.37E-03	1.55E-03	1.63E-03	1.59E-03
	FG-X	1.95E-03	2.02E-03	2.01E-03	1.23E-03	1.29E-03	1.32E-03
20	UD	2.24E-02	2.30E-02	2.35E-02	8.04E-03	8.45E-03	8.56E-03
	FG-V	3.00E-02	3.10E-02	3.17E-02	9.52E-03	1.01E-02	1.02E-02
	FG-O	3.81E-02	3.95E-02	4.01E-02	1.15E-02	1.22E-02	1.20E-02
	FG-X	1.68E-02	1.73E-02	1.74E-02	6.97E-03	7.31E-03	7.29E-03
50	UD	0.71	0.74	0.75	1.58E-01	1.70E-01	1.70E-01
	FG-V	0.99	1.05	1.08	2.15E-01	2.35E-01	2.39E-01
	FG-O	1.27	1.37	1.41	2.74E-01	3.05E-01	3.08E-01
	FG-X	0.49	0.51	0.51	1.17E-01	1.24E-01	1.23E-01

6 Conclusions

In this research, we reported a simple approach based on ES-DSG and C0-HSDT for static analysis of FG-CNTRC plates. The stiffness formulation of the ES-DSG based on C0-HSDT is performed by using the smoothing domains associated with edges of elements. So, this does not require shear correction factors and can improve the accuracy of the present method. The material properties of FG-CNTRC are assumed to be graded through the thickness direction according to several distributions of CNTs. The distributions of CNTs have a large impact on the

deflection of the plate. UD and FG-X plates become stiffer than those of FG-O and FG-V. The numerical results displayed high accuracy of the ES-DSG for the thin to thick plates.

References

1. Nguyen-Xuan H, Liu GR, Thai-Hoang C, Nguyen-Thoi T (2010) An edge-based smoothed finite element method (ES-FEM) with stabilized discrete shear gap technique for analysis of Reissner-Mindlin plates. *Comput Methods Appl Mech Eng* 199(9):471–489
2. P. Harris (2001) *Carbon nanotubes and related structures: new materials for the twenty-first century*. Cambridge University Press
3. Iijima S (1991) Helical Microtubules of Graphitic Carbon. *Nature* 354:56–58
4. Fiedler B, Gojny FH, Wichmann MHG, Nolte MCM, Schulte K (2006) Fundamental aspects of nano-reinforced composites. *Compos Sci Technol* 66(2006):3115–25
5. Zhu P, Lei ZX, Liew KM (2012) Static and free vibration analyses of carbon nanotube-reinforced composite plates using finite element method with first order shear deformation plate theory. *Compos Struct* 94:1450–1460
6. Ke LL, Yang J, Kitipornchai S (2010) Nonlinear free vibration of functionally graded carbon nanotube-reinforced composite beams. *Compos Struct* 92:676–683
7. Alibeigloo A, Liew KM (2013) Thermoelastic analysis of functionally graded carbon nanotube-reinforced composite plate using theory of elasticity. *Compos Struct* 106:873–881
8. Shen HS (2009) Nonlinear bending of functionally graded carbon nanotube-reinforced composite plates in thermal environments. *Compos Struct* 91:9–19
9. Phung-Van P, Abdel-Wahab M, Liew KM, Bordas SPA, Nguyen-Xuan H (2015) Isogeometric analysis of functionally graded carbon nanotube-reinforced composite plates using higher-order shear deformation theory. *Compos Struct* 123:137–149
10. Phung-Van P, Lieu QX, Nguyen-Xuan H, Abdel-Wahab M (2017) Size-dependent isogeometric analysis of functionally graded carbon nanotube-reinforced composite nanoplates. *Compos Struct* 166:120–135
11. Phung-Van P, De Lorenzis L, Thai CH, Abdel-Wahab M, Nguyen-Xuan H (2015) Analysis of laminated composite plates integrated with piezoelectric sensors and actuators using higher-order shear deformation theory and isogeometric finite elements. *Comput Mater Sci* 96:495–505
12. Phung-Van P, Tran LV, Ferreira AJM, Nguyen-Xuan H, Abdel-Wahab M (2017) Nonlinear transient isogeometric analysis of smart piezoelectric functionally graded material plates based on generalized shear deformation theory under thermo-electro-mechanical loads. *Nonlinear Dyn* 87:879–894
13. Phung-Van P, Nguyen LB, Tran LV, Dinh TD, Thai CH, Bordas SPA, Abdel-Wahab M, Nguyen-Xuan H (2015) An efficient computational approach for control of nonlinear transient responses of smart piezoelectric composite plates. *Int J Nonlinear Mech* 76:190–202
14. Phung-Van P, Ferreira AJM, Nguyen-Xuan H, Abdel-Wahab M (2017) An isogeometric approach for size-dependent geometrically nonlinear transient analysis of functionally graded nanoplates. *Compos Part B-Eng* 118:125–134
15. Liu GR, Trung NT (2010) *Smoothed finite element methods*. CRC Press, Taylor and Francis Group, New York
16. Chen JS, Wu CT, Yoon S, You Y (2001) A stabilized conforming nodal integration for Galerkin mesh-free methods. *Int J Numer Meth Eng* 50:435–466
17. Nguyen-Thoi T, Bui-Xuan T, Phung-Van P, Nguyen-Hoang S, Nguyen-Xuan H (2014) An edge-based smoothed three-node mindlin plate element (ES-MIN3) for static and free vibration analyses of plates. *Ksce J Civ Eng* 18:1072–1082

18. Phung-Van P, Nguyen-Thoi T, Luong-Van C, Thai-Hoang H, Nguyen-Xuan H (2014) A cell-based smoothed discrete shear gap method (CS-FEM-DSG3) using layerwise deformation theory for dynamic response of composite plates resting on viscoelastic foundation. *Comput Method Appl M* 272(2014):138–59
19. Nguyen-Hoang S, Phung-Van P, Natarajan S, Kim HG (2016) A combined scheme of edge-based and node-based smoothed finite element methods for Reissner-Mindlin flat shells. *Eng Comput* 32:267–284
20. Phung-Van P, Luong-Van H, Nguyen-Thoi T, Nguyen-Xuan H (2014) A cell-based smoothed discrete shear gap method (CS-FEM-DSG3) based on the C0-type higher-order shear deformation theory for dynamic responses of Mindlin plates on viscoelastic foundations subjected to a moving sprung vehicle. *Int J Numer Meth Eng* 98:988–1014
21. Phung-Van P, Nguyen-Thoi T, Luong-Van H, Lieu-Xuan Q (2014) Geometrically nonlinear analysis of functionally graded plates using a cell-based smoothed three-node plate element (CS-MIN3) based on the C-0-HSDT. *Comput Method Appl M* 270:15–36
22. Phung-Van P, Nguyen-Thoi T, Tran LV, Nguyen-Xuan H (2013) A cell-based smoothed discrete shear gap method (CS-DSG3) based on the C-0-type higher-order shear deformation theory for static and free vibration analyses of functionally graded plates. *Comput Mater Sci* 79:857–872
23. Phung-Van P, Thai CH, Nguyen-Thoi T, Nguyen-Xuan H (2014) Static and free vibration analyses of composite and sandwich plates by an edge-based smoothed discrete shear gap method (ES-DSG3) using triangular elements based on layerwise theory. *Compos Part B-Eng* 60:227–238
24. Phung-Van P, Nguyen-Thoi T, Le-Dinh T, H. Nguyen-Xuan H (2013) Static and free vibration analyses and dynamic control of composite plates integrated with piezoelectric sensors and actuators by the cell-based smoothed discrete shear gap method (CS-FEM-DSG3). *Smart Mater Struct* 22
25. Nguyen-Thoi T, Rabczuk T, Lam-Phat T, Ho-Huu V, Phung-Van P (2014) Free vibration analysis of cracked Mindlin plate using an extended cell-based smoothed discrete shear gap method (XCS-DSG3). *Theor Appl Fract Mec* 72:150–163
26. Nguyen-Thoi T, Phung-Van P, Ho-Huu V, Le-Anh L (2015) An edge-based smoothed finite element method (ES-FEM) for dynamic analysis of 2D Fluid-Solid interaction problems. *Ksce J Civ Eng*. 19:641–650
27. Nguyen-Thoi T, Phung-Van P, Rabczuk T, Nguyen-Xuan H, Le-Van C (2013) An application of the ES-FEM in solid domain for dynamic analysis of 2D fluid–solid interaction problems. *Int J Comput Methods* 10(1):1340003
28. Nguyen-Thoi T, Phung-Van P, Nguyen-Hoang S, Lieu-Xuan Q (2014) A smoothed coupled NS/nES-FEM for dynamic analysis of 2D fluid-solid interaction problems. *Appl Math Comput* 232:324–346
29. Liu GR, Nguyen-Thoi T, Lam KY (2009) An edge-based smoothed finite element method (ES-FEM) for static and dynamic problems of solid mechanics. *J Sound Vib* 320:1100–1130
30. Bletzinger KU, Bischoff M, Ramm E (2000) A unified approach for shear-locking free triangular and rectangular shell finite elements. *Comput Struct* 75:321–334
31. Shankara CA, Iyengar NGR (1996) A C0 element for the free vibration analysis of laminated composite plates. *J Sound Vib* 191:721–738
32. Reddy JN (1984) A simple higher-order theory for laminated composite plates. *J Appl Mech* 51:745–752

Finite Element Simulation of the Strength of Corrugated Board Boxes Under Impact Dynamics



V. Dung Luong, Fazilay Abbès, Boussad Abbès, P. T. Minh Duong,
Jean-Baptiste Nolot, Damien Erre and Ying-Qiao Guo

Abstract In this study, we propose a model based on the finite element method to study the behavior of corrugated cardboard boxes subjected to shocks. To reduce the preparation of the CAD model and the computational times, we have developed an elastoplastic homogenization model for the corrugated cardboard. The homogenization consists in representing a corrugated cardboard panel by a homogeneous plate. A through-thickness integration on a periodic unit cell containing a flute and two flat linerboards is proposed. Each constituent is considered as an orthotropic elastoplastic material with specific hypotheses for the corrugated medium. The model was implemented in the finite element software ABAQUS. Damage boundary curve (DBC) for corrugated cardboard boxes are defined by experimental testing and finite element simulations using the proposed model. The numerical results obtained are in good agreement with the experimental results.

V. D. Luong · F. Abbès · B. Abbès (✉) · D. Erre · Y.-Q. Guo
GRESPI, University of Reims Champagne-Ardenne, Campus Moulin de La Housse, BP
1039, 51687 Reims Cedex 2, France
e-mail: boussad.abbes@univ-reims.fr

V. D. Luong
e-mail: vietdung2282@gmail.com

F. Abbès
e-mail: fazilay.abbes@univ-reims.fr

D. Erre
e-mail: damien.erre@univ-reims.fr

Y.-Q. Guo
e-mail: yq.guo@univ-reims.fr

J.-B. Nolot · D. Erre
ESiReims, 3 Esplanade Roland Garros, 51100 Reims, France
e-mail: jb.nolot@univ-reims.fr

P. T. M. Duong
Thai Nguyen University of Technology, Thai Nguyen, Vietnam
e-mail: tuongminh80@gmail.com

© Springer Nature Singapore Pte Ltd. 2018

H. Nguyen-Xuan et al. (eds.), *Proceedings of the International Conference
on Advances in Computational Mechanics 2017*, Lecture Notes in Mechanical
Engineering, https://doi.org/10.1007/978-981-10-7149-2_25

Keywords Corrugated cardboard • Finite element • Homogenization
Impact dynamics

1 Introduction

Corrugated shipping containers are designed to protect the product from hazards of the distribution, transportation, and storage environment so that the product can be shipped to consumers without damage. Consumer products usually encounter shocks in two conditions in the lifespan: One is bumps and bounces caused by vehicle on bumpy roads during the transportation, and the other is drops caused by human negligence in handling the goods. Mechanical shock test, which offers prompt verification of structural strength in the product design stage for deciding whether proper buffering is required in the packing design, is one of crucial items for validating the design.

In recent years, many researchers used measurement method of the vibration levels in truck shipments to study effects on the products. These studies measured the vibration levels in two of the most commonly used truck types to ship packaged goods as a function of road condition and vehicle speed [1–3]. Newton [4] used the damage boundary curve to define the fragility of a product based on its sensitivity to acceleration and the velocity change that occurs during impact. The theoretical basis for the widely accepted damage boundary curve (DBC) approach to product fragility and the applicability of its associated ASTM D3332 fragility assessment test procedure is discussed by Burgess [5].

Using finite element simulations allows avoiding numerous experimental tests and predicting possible failures during the early design stage. However, a computer-aided design of corrugated cardboard box is fastidious, and its meshing generates heavy models which increases CPU time. An alternative is to develop a homogenization model for the corrugated cardboard. Some authors [6–10] have developed analytical homogenization models for linear elastic behavior of corrugated cardboard. However, for corrugated cardboard undergoing large deformations, a nonlinear behavior is more suitable. Mäkelä and Östlund [11] proposed an orthotropic elastoplastic model in plane stresses (IPE-Isotropic Plasticity Equivalent model) to accurately describe the behavior of paperboard with only few parameters that are easily determined from simple tensile tests. Based on this model, we have developed an elastoplastic homogenization model for the corrugated cardboard. The homogenization consists in representing a corrugated cardboard panel by a homogeneous plate. A through-thickness integration on a periodic unit cell containing a flute and two flat linerboards is proposed. Each constituent is considered as an orthotropic elastoplastic material with specific hypotheses for the corrugated medium. The model was implemented in the finite element software ABAQUS. This model is then applied to define the damage boundary curve (DBC) to assess the fragility of corrugated cardboard boxes. The proposed model was successfully validated by comparing the experimental results with the simulation ones.

2 Materials and Methods

2.1 Material

Corrugated cardboard is one of the most used packaging material to make boxes or interlayers for goods transport. The manufacturing process gives three characteristic directions: the machine direction (MD), the cross direction (CD), and the thickness direction (ZD). In this study, we used corrugated cardboard with the properties shown in Fig. 1 and given in Table 1.

2.2 Experiment

The test procedure requires the use of a programmable shock machine, such as the one depicted in Fig. 2, which can vary the acceleration amplitude, duration, and

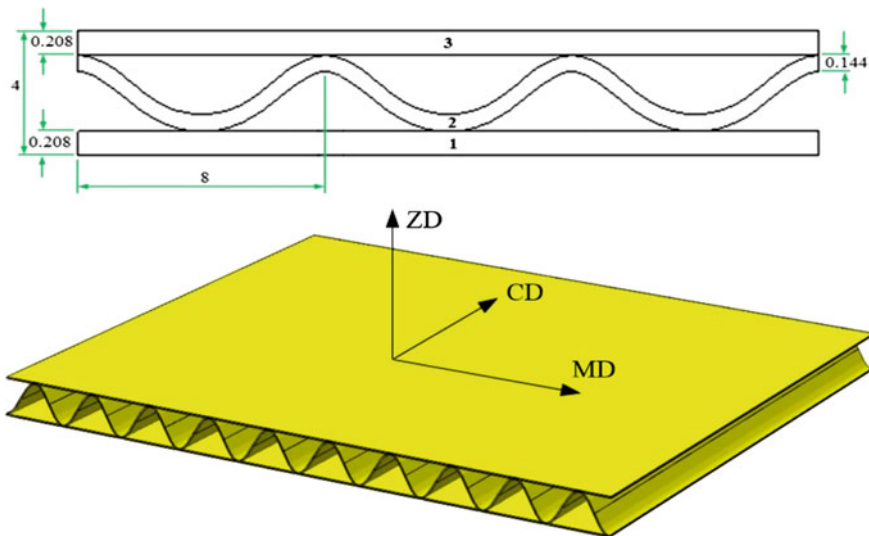


Fig. 1 Geometric structure and the directions of corrugated cardboard plate

Table 1 Properties of the papers

Paperboard	Grammage (g/mm ²)	Thickness (mm)
1	140	0.208 ± 0.004
2	92	0.144 ± 0.008
3	140	0.208 ± 0.004

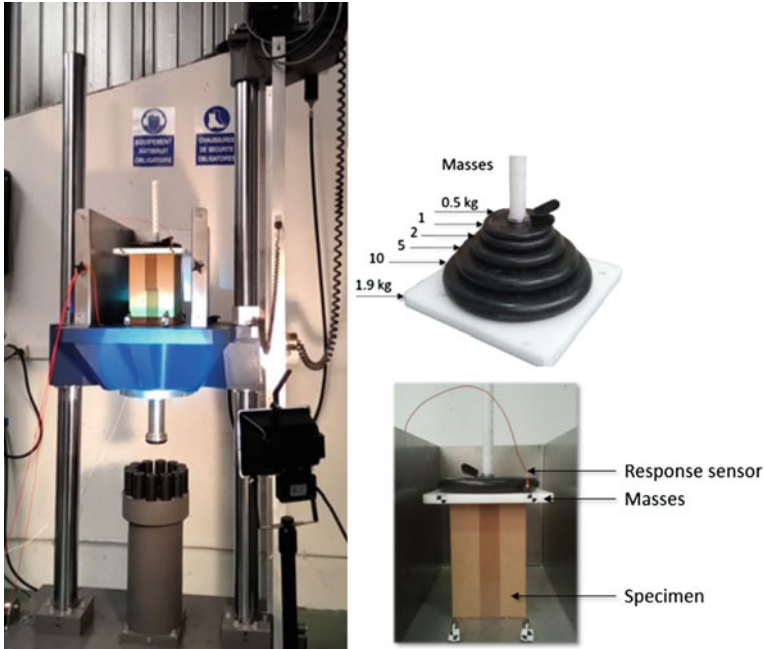


Fig. 2 Shock machine and experimental setup

velocity change parameters of repeated impacts. The acceleration and velocity change are the two parameters recorded and plotted in the testing procedure.

In our study, all shock tests were carried out under standard conditions: 23 °C and 50% relative humidity (RH). Cardboard boxes having the following dimensions length = 222 mm, width = 185 mm, height = 295 mm were obtained using a cutting table (ZÜND M-1600). Different masses are stacked on the top of the packaging as shown in Fig. 2.

The damage boundary curve is generated by two steps: velocity step (short impact) and acceleration step (long impact). The velocity step allows to define the critical velocity change, ΔV_C , for the critical component of the packaging. Half-sine impact shock pulses are programmed for a short duration. The packaging is attached to the shock machine carriage and dropped from a series of increasing drop heights until the critical element is damaged. Every shock pulse is recorded and plotted as acceleration, in g, versus velocity change. The point where damage occurs ends the step velocity portion of the test. The critical velocity change is defined by drawing a vertical line through the last point prior to damage.

Experimentally, the damage is performed by inspection of the box after completion of each impact test. No permanent deformation should be seen on the box. The test continues with until the product is damaged.

The acceleration step allows to define the critical acceleration, A_C , for the critical component of the packaging. The shock machine programmer is set to produce a

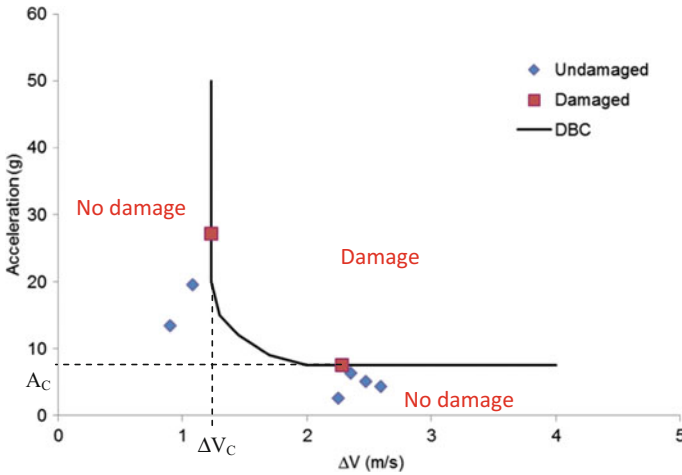


Fig. 3 Damage boundary curve obtained for corrugated cardboard box preloaded with $M = 21.9 \text{ kg}$

trapezoidal shock pulse. The drop height is fixed and only the acceleration is increased, in order to increase the severity of the series of impacts. As before, the test continues until damage to the critical component is observed. A horizontal line is drawn through the last point prior to damage. The final step in the development of the damage boundary curve is to include the rounded corner. An ellipse is fitted between the points $(\Delta V_C, 2A_C)$ and $(\pi/2)\Delta V_C, A_C)$. An example of an experimental damage boundary curve obtained for corrugated cardboard box preloaded with 21.9 kg is shown in Fig. 3. In this figure, the diamonds represent the experimentally undamaged boxes, while the squares represent the damaged ones. The solid line represents the DBC obtained by the method aforementioned.

3 Finite Element Model

3.1 Anisotropic Elastoplastic Behavior Model of Paperboard

Paperboard consists mainly of wood fibers with three components: cellulose, hemicellulose, and lignin. Because of the continuous paper manufacturing process, the wood fibers are oriented more in the machine direction. Paperboard is an anisotropic material; it is two to four times stiffer in the machine direction (MD) than the cross direction (CD).

The in-plane properties of paperboard are relatively easy to determine by tensile tests. Due to its low thickness, out-of-plane properties are more difficult to obtain. Stenberg [12] showed that the Young's modulus along normal direction (ZD) is about 200 times lower than that of MD. Stenberg et al. [13] observed that the deformation in the plane is negligible during the compression according to the thickness. The Poisson coefficients ν_{xz} and ν_{yz} consequently are close to zero.

In this study, we used the IPE model [11] to describe the behavior of corrugated cardboard components. The orthotropic elasticity behavior in plane stresses is defined by:

$$\{\sigma\} = \begin{Bmatrix} \sigma_x \\ \sigma_y \\ \sigma_{xy} \end{Bmatrix} = [H]\{\varepsilon^e\} = \frac{1}{(1-\nu_{xy}\nu_{yx})} \begin{bmatrix} E_x & \nu_{yx}E_x & 0 \\ \nu_{xy}E_y & E_y & 0 \\ 0 & 0 & G_{xy}(1-\nu_{xy}\nu_{yx}) \end{bmatrix} \begin{Bmatrix} \varepsilon_x^e \\ \varepsilon_y^e \\ \gamma_{xy}^e \end{Bmatrix} \quad (1)$$

The deviatoric stresses vector and the IPE plasticity criterion are given by:

$$\{s\} = \begin{Bmatrix} s_x \\ s_y \\ s_z \\ s_{xy} \end{Bmatrix} = [L]\{\sigma\} = \frac{1}{3} \begin{bmatrix} 2A & C-A-B & 0 \\ C-A-B & 2B & 0 \\ B-C-A & A-B-C & 0 \\ 0 & 0 & 3D \end{bmatrix} \begin{Bmatrix} \sigma_x \\ \sigma_y \\ \sigma_{xy} \end{Bmatrix} \quad (2)$$

$$f = \sigma_{eq} - Y = \left(\frac{3}{2}\langle s \rangle \{s\}\right)^{1/2} - E_0(\varepsilon_0 + \varepsilon_{eq}^p)^{1/n} = 0 \quad (3)$$

where Y is the yield stress, $A, B, C, D, E_0, \varepsilon_0, \varepsilon_{eq}^p, n$ are the parameters of the IPE model that can be determined using experimental tests.

3.2 Identification of the IPE Model

For each corrugated cardboard constituent (skins and flute), experimental tensile tests were carried out for three directions (MD, CD, and 45°) at a crosshead speed of 10 mm/min under standard conditions (23 °C and 50% relative humidity). Table 2 summarizes the model parameters identified for the two skins and the flute.

3.3 Homogenization Method for Corrugated Cardboard

Using the full 3D model for corrugated cardboard boxes consumes a lot of time. To reduce the preparation of the model and the computational times, we have developed a homogenization model for the corrugated cardboard. The homogenization

Table 2 Parameters of the IPE model for corrugated cardboard constituent

Skins (E_x, E_y, G_{xy} and E_0 in MPa)										
E_x	E_y	ν_{xy}	G_{xy}	E_0	n	A	B	C	D	ϵ_0
2433.2	859.91	0.0829	1077.2	96.45	4.97	1.0	2.498	2.498	1.622	0.486E-3
Flute (E_x, E_y, G_{xy} and E_0 in MPa)										
E_x	E_y	ν_{xy}	G_{xy}	E_0	n	A	B	C	D	ϵ_0
1130.4	625.85	0.0717	303.05	87.31	4.247	1.0	2.178	2.178	1.871	0.923E-3

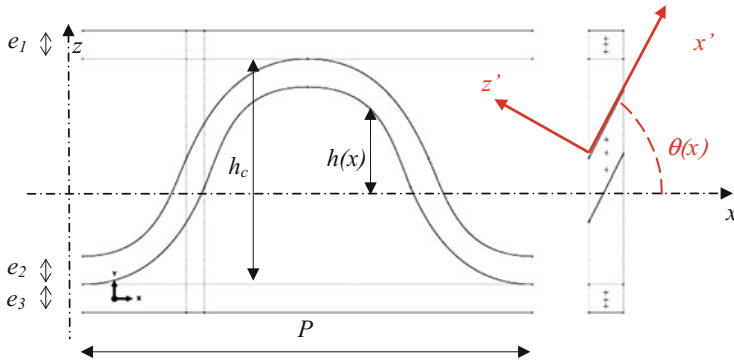


Fig. 4 Periodic unit cell of a corrugated cardboard and numerical integration points through the thickness

consists in representing a sandwich panel by a homogeneous plate. We consider a periodic unit cell in Fig. 4.

The plane strains are decomposed into membrane and bending parts as follows:

$$\{\epsilon\} = \{\epsilon_m\} + z\{\kappa\} \tag{4}$$

where $\{\epsilon_m\}$ is the membrane strains vector and $\{\kappa\}$ is the curvatures vector.

The membrane forces, the bending, and torsion moments are obtained by integrating the stresses through the thickness of the corrugated cardboard:

$$\{N\} = \int_{-\frac{h}{2}}^{\frac{h}{2}} \begin{bmatrix} \sigma_x \\ \sigma_y \\ \sigma_{xy} \end{bmatrix} dz; \{M\} = \int_{-\frac{h}{2}}^{\frac{h}{2}} z \begin{bmatrix} \sigma_x \\ \sigma_y \\ \sigma_{xy} \end{bmatrix} dz \tag{5}$$

For each layer of the corrugated cardboard (skins and flute), we use three integration points through thickness. The plasticity algorithm is applied at each integration point to determine the stress state and the elastoplasticity matrix in the local coordinate system of each layer. It should be noted that the local coordinate system of the flute is defined by the angle $\theta(x)$ (Fig. 4) as follows:

$$\theta(x) = \tan^{-1}\left(\frac{dh(x)}{dx}\right); h(x) = \left(\frac{h_c}{2} - \frac{e_2}{2}\right) \sin\left(2\pi\frac{x}{P}\right) \tag{6}$$

The stress vector and the elastoplasticity matrix of the flute are defined in the local frame (x', z') and then transformed into the global frame (MD- x , CD- y , ZD- z) to achieve the integration through the thickness of the corrugated cardboard. On the other hand, the flute cannot support the normal stress along x -axis (N_x) and the bending moment M_x on MD- x section. This allows to neglect the normal stress along the x -direction as well as the first line and the first column of the elastoplasticity matrix.

Finally, the homogenized membrane forces, bending, and torsion moments for the corrugated cardboard are given by the following expressions:

$$\left\{ \begin{aligned} N_x &= \frac{e_1}{2} \sum_{i=1}^3 \sigma_{xi}^{(1)} \omega_i + \frac{e_3}{2} \sum_{i=1}^3 \sigma_{xi}^{(3)} \omega_i \\ N_y &= \frac{e_1}{2} \sum_{i=1}^3 \sigma_{yi}^{(1)} \omega_i + \frac{e_2}{2 \cos(\theta)} \sum_{i=1}^3 \sigma_{yi}^{(2)} \omega_i + \frac{e_3}{2} \sum_{i=1}^3 \sigma_{yi}^{(3)} \omega_i \\ N_{xy} &= \frac{e_1}{2} \sum_{i=1}^3 \sigma_{xyi}^{(1)} \omega_i + \frac{e_2}{2 \cos(\theta)} \sum_{i=1}^3 \sigma_{xyi}^{(2)} \omega_i + \frac{e_3}{2} \sum_{i=1}^3 \sigma_{xyi}^{(3)} \omega_i \end{aligned} \right. \tag{7}$$

$$\left\{ \begin{aligned} M_x &= \frac{e_1}{2} \sum_{i=1}^3 \sigma_{xi}^{(1)} z_i \omega_i + \frac{e_3}{2} \sum_{i=1}^3 \sigma_{xi}^{(3)} z_i \omega_i \\ M_y &= \frac{e_1}{2} \sum_{i=1}^3 \sigma_{yi}^{(1)} z_i \omega_i + \frac{e_2}{2 \cos(\theta)} \sum_{i=1}^3 \sigma_{yi}^{(2)} z_i \omega_i + \frac{e_3}{2} \sum_{i=1}^3 \sigma_{yi}^{(3)} z_i \omega_i \\ M_{xy} &= \frac{e_1}{2} \sum_{i=1}^3 \sigma_{xyi}^{(1)} z_i \omega_i + \frac{e_2}{2 \cos(\theta)} \sum_{i=1}^3 \sigma_{xyi}^{(2)} z_i \omega_i + \frac{e_3}{2} \sum_{i=1}^3 \sigma_{xyi}^{(3)} z_i \omega_i \end{aligned} \right. \tag{8}$$

where $e_1, e_2,$ and e_3 represent the thicknesses of the three layers, ω_i represents the numerical integration weight corresponding to the integration point i . The elastoplastic homogenization model was implemented in the finite element software ABAQUS using UGENS user subroutine [14].

4 Results

4.1 Numerical Validation of the H-Model on the Impact Test

To validate our elastoplastic H-model, impact tests finite element simulations are run with the full 3D structure of the box and the homogenized 3D box (Fig. 5). The dimensions of the box are similar to the experimental ones. The elastoplastic

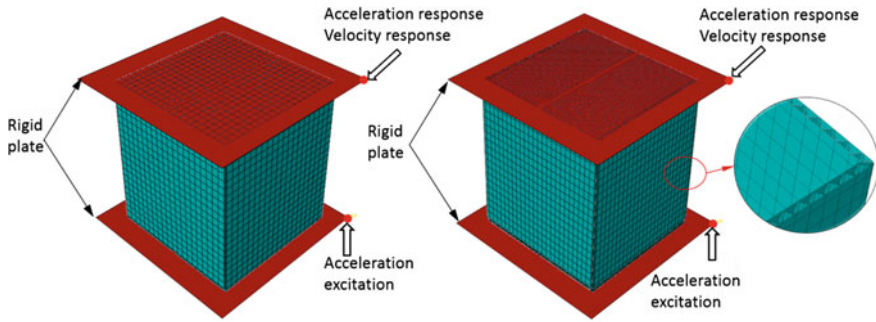


Fig. 5 Full 3D and the homogenized box used for the simulations

Table 3 Comparison between 3D model and H-model

Model	3D model	H-model	Relative difference (%)
A excitation (g)	10	10	–
A response (g)	20.8	19.1	–8.2
ΔV response (m/s)	2.1	1.9	–9.0
CPU time (s)	14163	551	–96.1

properties of the three layers are those given in Table 3. The full 3D corrugated cardboard box and the homogenized one are meshed with reduced-integration four node shell elements (S4R) with 10 mm element size. The box is placed between two rigid plates which are tied to the latter. In the proposed example, a mass of 6 kg is attached to the top plate. A trapezoidal shock pulse is applied to the bottom plate for a short duration. The acceleration amplitude and the velocity change are recorded on the top plate during the simulations.

Several simulations were carried out with different acceleration amplitudes and durations. As an example, the results for an excitation with an amplitude $A = 10$ g and a duration $t = 14$ ms are given in Table 3. This was the case in all the simulations. The relative difference between the full 3D model and the H-model is less than 10% for the acceleration and velocity difference responses. However, the CPU time is reduced by more than 96% for all the simulations. Therefore, the H-model can be used to determine quickly by finite element simulations the damage boundary curves of corrugated cardboard boxes.

4.2 Evaluation of DBC Using H-Model Numerical Simulations

This section is devoted to the evaluation of damage boundary curves by numerical simulations using the developed H-model. As for the experimental tests, we run

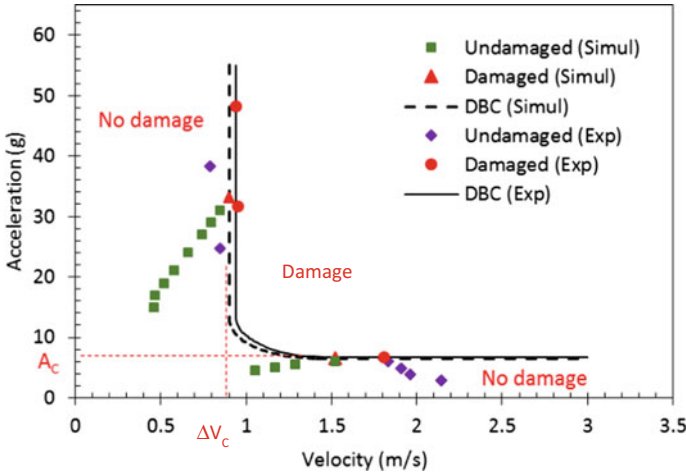


Fig. 6 Experimental and numerical DBC for a box preload with $M = 16.9$ kg

successive simulations for velocity step (half-sine impact shocks) and acceleration step (trapezoidal impact shocks). For each simulation, the acceleration response amplitude versus the velocity change is plotted. The step stops when the box undergoes a damage. The box is considered damaged when the equivalent plastic strain exceeds 5% at any point in the box. This value corresponds to the experimental value beyond which the constituents of the corrugated cardboard are damaged. Figure 6 shows the results obtained for a box preload with $M = 16.9$ kg. In this figure, the diamonds and the squares represent the undamaged boxes for experiments and simulations, respectively, while the bullets and the triangles represent the damaged ones for experiments and simulations, respectively. The solid and dotted lines represent the experimental and numerical DBC, respectively. We can notice that the experimental and numerical DBC are in good agreement. This is confirmed by the results reported in Table 4, where the relative difference between experimental and numerical for the critical A_C and ΔV_C is less than 6%. The critical acceleration (A_C) and velocity change (ΔV_C) levels are very important for design decisions [15].

Table 4 Comparison of A_C and ΔV_C between H-model and experiment with preload $M = 16.9$ kg

	Simulation	Experiment	Relative difference (%)
A_C (g)	6.5	6.7	-3.1
ΔV_C (m/s)	0.85	0.9	-5.8

5 Conclusion

In this paper, we have proposed a finite element methodology to define the damage boundary curve (DBC) for corrugated cardboard boxes. To run the needed impact dynamic simulations, we have developed an elastoplastic homogenization model for the corrugated cardboard. We have shown that this model can reduce the preparation of the CAD model and the computational time. The comparison of the results obtained by the homogenization model simulations and by the experiments has proved the precision and effectiveness of the model. By using our H-model, we have defined DBC for a preloaded box with a good agreement with the experimental results. The present model allows to predict the mechanical behavior of corrugated cardboard boxes under impact dynamics in early stage of design development. DBC can be applied to several distribution package development decisions. One can use the critical acceleration level (A_C) to assign a G fragility for cushioning decisions and design. The damage is prevented if the critical G level is not exceeded. An appropriate cushion design can then be determined by using cushion performance information. The critical velocity change level (ΔV_C) is also used for package design decisions. The drop height of the packaged product is strongly related to the velocity change that products will receive in transportation and handling. Thus, if the package's drop height is controlled, then damage can be avoided.

References

1. Huart V, Nolot JB, Candore JC, Pellot J, Krajka N, Odof S, Erre D (2016) A damage estimation method for packaging systems based on power spectrum densities using spectral moments. *Packag Technol Sci* 29(6):303–321
2. Huart V, Candore JC, Nolot JB, Krajka N, Pellot J, Odof S, Erre D (2015) Proposition of a new severity analysis based on 'shake' detection: example of the vetry airport tarmac. *Packag Technol Sci* 28(6):529–544
3. Nolot JB, Delloque P, Candore JC, Huart V, Pellot J, Copinet A, Odof S, Erre D (2014) How to choose the resistance to vertical crushing of stacked cardboard box suitable for your trip. In: *Proceedings of the 19th IAPRI world conference on packaging*, Melbourne, Australia, 15–18 June, p 237–242
4. Newton R (1968) *Fragility assessment: theory and test procedure*. Monterey Research Laboratory Inc, Monterey, CA
5. Burgess GJ (1988) Product fragility and damage boundary theory. *Packag Technol Sci* 1:5–10
6. Duong PTM, Abbès B, Li YM, Hammou AD, Makhlof M, Guo YQ (2013) An analytic homogenization model for shear torsion coupling problems of double corrugated core sandwich plates. *J Compos Mater* 47:1327–1341
7. Hammou AD, Duong PTM, Abbès B, Makhlof M, Guo YQ (2012) Finite element simulation with a homogenization model and experimental study of free drop tests of corrugated cardboard packaging. *Mech Ind* 13(3):175–184
8. Abbès B, Guo YQ (2010) Analytic homogenization for torsion of orthotropic sandwich plates: application to corrugated cardboard. *Compos Struct* 92:699–706

9. Talbi N, Batti A, Ayad R, Guo YQ (2009) An analytical homogenization model for finite element modeling of corrugated cardboard. *Compos Struct* 88:280–289
10. Nordstrand T, Carlsson LA, Allen HG (1994) Transverse shear stiffness of structural core sandwich. *Compos Struct* 27:317–329
11. Mäkelä P, Östlund S (2003) Orthotropic elastic-plastic material model for paper materials. *Int J Solids Struct* 40:5599–5620
12. Stenberg N (2003) A model for the through-thickness elastic-plastic behavior of paper. *Int J Solids Struct* 40:7483–7498
13. Stenberg N, Fellers C, Östlund S (2003) Plasticity in the thickness direction of paperboard under combined shear and normal loading. *J Eng Mater Technol* 123(4):184–190
14. ABAQUS (2016) ABAQUS documentation, Dassault Systèmes, Providence, RI, USA
15. Goodwin D, Young D (2011) Protective packaging for distribution: design and development. DESTech Publications Inc., Lancaster, USA

Static and Free Vibration Analysis of Functionally Graded Shells Using a Cell-Based Smoothed Discrete Shear Gap Method and Triangular Elements



D. Le-Xuan, H. Pham-Quoc, V. Tran-The and N. Nguyen-Van

Abstract A cell-based smoothed discrete shear gap method (CS-DSG3) using three-node triangular element was recently proposed to improve the effectiveness of the discrete shear gap method (DSG3) for static and vibration analyses of isotropic Mindlin plates and shells. In this study, the CS-DSG3 is further extended for static and free vibration responses of functionally graded shells. In the present method, the first-order shear deformation theory is used in the formulation owing to the simplicity and computational efficiency. Several numerical examples are provided to validate high reliability of the CS-DSG3 in comparison with other numerical methods.

Keywords Cell-based smoothed discrete shear gap method (CS-DSG3) Functionally graded shell • First-order shear deformation theory (FSDT)

1 Introduction

Functionally graded materials (FGMs) obtained significant consideration due to outstanding properties, such as high stiffness and strength-to-weight ratios, light-weight, heat-resisting material. On the other hand, FGMs shells have been widely used in aerospace, defense, electronics and nuclear reactors. Therefore, the static and free vibration analysis of FG shells has been receiving considerable concern by researchers. Loy et al. [1] and Pradhan et al. [2] studied the vibration of FG cylindrical shells using the Love's shell theory. The eigenvalue governing equations

D. Le-Xuan (✉) · V. Tran-The
Tran Dai Nghia University, Ho Chi Minh City, Vietnam
e-mail: xuandoan1085@gmail.com

H. Pham-Quoc
Le Qui Don University, Hanoi, Vietnam

N. Nguyen-Van
Faculty of Mechanical Technology, Industrial University of Ho Chi Minh City,
Ho Chi Minh City, Vietnam

are solved by using Rayleigh-Ritz method. However, as the Love's shell theory neglects the effects of transverse shear, this theory only provides good results for an analysis of the thin shells case. To overcome the drawbacks, the first-order shear deformation theory (FSDT), which accounts for the transverse shear effects, was used to analyze FG shells. Aghdam et al. [3] proposed the extended Kantorovich method (EKM) to solve bending of moderately thick doubly curved FG shells. In this study, they used FSDT and five highly coupled partial differential equation to obtain in term of five displacement components. Su et al. [4] investigated the free vibration of FG cylindrical, conical shells with general boundary conditions using Rayleigh-Ritz method. Using the element-free kp -Ritz method, Zhao et al. [5] investigated the static and vibration of FG shells subjected to mechanical and thermomechanical load based on Sander's FSDT. Recently, in order to improve the quality of the numerical results, various theories have been developed to analyze FG shell such as the higher-order shear deformation theory (HSDT) [6], layer-wise theory [7]. However, these theories have a high computationally cost which causes the limit of their practical applications. Therefore, from the engineering point of view, the FSDT is still the most attractive and widely used approach due to its simplicity and computational efficiency.

For the purpose of improving the quality of numerical results, Liu and Nguyen [8] proposed a smoothed finite element method (S-FEM), which is based on the stabilized conforming nodal integration (SCNI) of mesh-free method, including the cell-based smoothed finite element (CS-FEM) [9–13], the node-based smoothed finite element [14–16], the edge-based smooth finite element method [17, 18] and the face-based smoothed finite element [19]. Each of these S-FEM has different properties and has been successfully introduced for the analysis of practical mechanics problems, especially for various problems plates and shells [20–22].

Among these S-FEM models, the CS-FEM shows some interesting properties in the solid mechanics problems. Extending the idea of the CS-FEM to plate structures, Nguyen-Thoi et al. [23] have recently formulated a cell-based smoothed stabilized discrete shear gap element (CS-DSG3) for static and free vibration analyses of isotropic shell structures by combining the CS-FEM with the original DSG3 [24]. In the CS-DSG3, each triangular element will be divided into three sub-triangles, and in each sub-triangle, the stabilized DSG3 is used to compute the strains. Then the strain smoothing technique on whole triangular element is used to smooth the strains on three sub-triangles. The numerical results showed that the CS-DSG3 is free of shear locking and achieves a high accuracy compared with the exact solutions. Recently, the CS-DSG3 has been extended to analyze various plate and shell problems such as flat shells [23], stiffened plates [25], FGM plates [26], piezoelectricity plates [27] and composite plates [28]. However, as far as authors are aware, static and free vibration analysis of FG shells using a CS-DSG3 has not been found yet. Therefore, this paper aims to extend further the CS-DSG3 to static and free vibration analyses of FG shells based on FSDT. The accuracy and reliability of the proposed method are verified by comparing its numerical solutions with those of others available numerical results.

2 Theoretical Formulation

2.1 Functionally Graded (FG) Shells

A FG shell made from a mixture of ceramic and metal is shown in Fig. 1. In this study, the material properties are assumed to be graded through the thickness by the power distribution given by

$$P(z) = (P_c - P_m)V_c + P_m; V_c = \left(\frac{1}{2} + \frac{z}{t}\right)^n \quad (n \geq 0) \tag{1}$$

where P is the effective material properties, including the modulus of elasticity E , density ρ , Poisson’s ratio ν . P_c and P_m are the properties of the ceramic and metal, respectively; V_c is the volume fraction of the ceramic; t is the thickness of shell and z is the distance from its middle surface; n is the volume fraction exponent which controls the variation of volume fraction through the thickness shown in Fig. 1b.

2.2 Weak Form of FG Shell

According to the first-order shear deformation theory, the displacement field at any point in the shell can be expressed as follows

$$\begin{cases} u(x, y, z) = u_0(x, y) + z\theta_x(x, y), \\ v(x, y, z) = v_0(x, y) + z\theta_y(x, y), \\ w(x, y, z) = w_0(x, y), \end{cases} \tag{2}$$

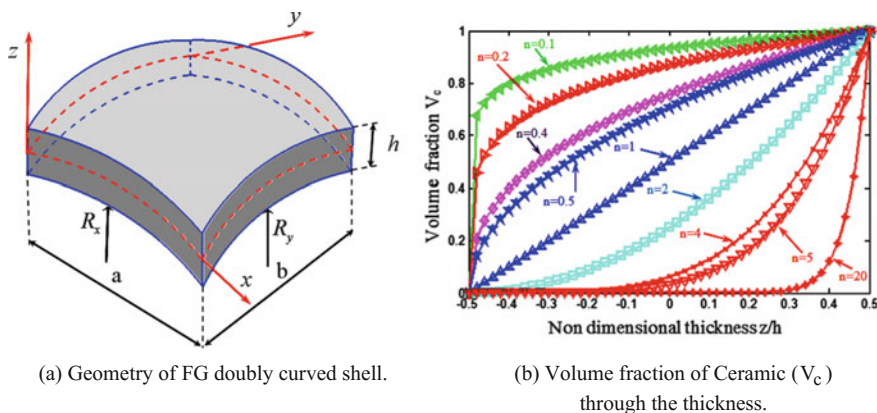


Fig. 1 a Geometry of FG doubly curved shell. b Volume fraction of Ceramic (V_c) through the thickness

where u_0, v_0 and w_0 are the displacements of the mid-plane of shell in x, y and z directions, θ_x and θ_y donate the rotations around the y - and x -axes, respectively, as shown in Fig. 1a. The generalized strains can be written in terms of the mid-plane deformations, which give

$$\boldsymbol{\varepsilon} = \{ \varepsilon_{xx}, \varepsilon_{yy}, \gamma_{xy}, \gamma_{xz}, \gamma_{yz} \}^T = \left\{ \begin{matrix} \boldsymbol{\varepsilon}^m \\ 0 \end{matrix} \right\} + z \left\{ \begin{matrix} \boldsymbol{\kappa} \\ 0 \end{matrix} \right\} + \left\{ \begin{matrix} 0 \\ \boldsymbol{\gamma} \end{matrix} \right\}, \tag{3}$$

where the membrane strain $\boldsymbol{\varepsilon}^m$, bending strain $\boldsymbol{\kappa}$ and shear strain $\boldsymbol{\gamma}$ are, respectively, given by

$$\boldsymbol{\varepsilon}^m = \left\{ \frac{\partial u_0}{\partial x}, \frac{\partial v_0}{\partial y}, \frac{\partial u_0}{\partial y} + \frac{\partial v_0}{\partial x} \right\}^T; \boldsymbol{\kappa} = \left\{ \frac{\partial \theta_x}{\partial x}, \frac{\partial \theta_y}{\partial y}, \frac{\partial \theta_x}{\partial y} + \frac{\partial \theta_y}{\partial x} \right\}^T; \boldsymbol{\gamma} = \left\{ \gamma_{xz}, \gamma_{yz} \right\} = \left\{ \frac{\partial w}{\partial x} + \theta_x, \frac{\partial w}{\partial y} + \theta_y \right\}^T. \tag{4}$$

The linear stress–strain relations are expressed as

$$\left\{ \begin{matrix} \sigma_{xx} \\ \sigma_{yy} \\ \sigma_{xy} \end{matrix} \right\} = \begin{bmatrix} Q_{11} & Q_{12} & 0 \\ Q_{21} & Q_{22} & 0 \\ 0 & 0 & Q_{66} \end{bmatrix} \left\{ \begin{matrix} \varepsilon_{xx} \\ \varepsilon_{yy} \\ \gamma_{xy} \end{matrix} \right\}; \left\{ \begin{matrix} \sigma_{xz} \\ \sigma_{yz} \end{matrix} \right\} = \begin{bmatrix} Q_{55} & 0 \\ 0 & Q_{44} \end{bmatrix} \left\{ \begin{matrix} \gamma_{xz} \\ \gamma_{yz} \end{matrix} \right\}, \tag{5}$$

where

$$Q_{11}(z) = Q_{22}(z) = \frac{E(z)}{1 - \nu(z)^2}; \quad Q_{12}(z) = \nu(z)Q_{11}(z); \quad Q_{44}(z) = Q_{55}(z) = Q_{66}(z) = \frac{E(z)}{2(1 + \nu(z))}. \tag{6}$$

The standard Galerkin weak form of the static equilibrium equations for the Reissner-Mindlin shell can be written follow as

$$\int_{\Omega} \delta \left\{ \begin{matrix} \boldsymbol{\varepsilon}^m \\ \boldsymbol{\kappa} \\ \boldsymbol{\gamma} \end{matrix} \right\}^T \begin{bmatrix} \mathbf{A} & \mathbf{B} & \mathbf{0} \\ \mathbf{B} & \mathbf{D} & \mathbf{0} \\ \mathbf{0} & \mathbf{0} & \mathbf{D}^s \end{bmatrix} \left\{ \begin{matrix} \boldsymbol{\varepsilon}_0 \\ \boldsymbol{\kappa} \\ \boldsymbol{\gamma} \end{matrix} \right\} d\Omega = \int_{\Omega} \delta \mathbf{u}^T \mathbf{b} d\Omega, \tag{7}$$

where the matrices $\mathbf{A}, \mathbf{B}, \mathbf{D}$ and \mathbf{D}^s are the extensional, coupling, bending and the transverse shear stiffness, respectively, which are given by

$$(A_{ij}, B_{ij}, D_{ij}) = \int_{-h/2}^{h/2} (1, z, z^2) Q_{ij} dz, \quad (i, j = 1, 2, 6); \quad D^s = \int_{-h/2}^{h/2} Q_{ij}^* dz, \quad (i, j = 4, 5), \tag{8}$$

And $\mathbf{b} = \{0, 0, p(x, y, z), 0, 0, 0\}^T$ is the distributed load applied on the shell.

For the free vibration problems, the standard Galerkin weak form can be expressed by

$$\int_{\Omega} \delta \begin{Bmatrix} \boldsymbol{\varepsilon}^m \\ \boldsymbol{\kappa} \\ \boldsymbol{\gamma} \end{Bmatrix}^T \begin{bmatrix} \mathbf{A} & \mathbf{B} & \mathbf{0} \\ \mathbf{B} & \mathbf{D} & \mathbf{0} \\ \mathbf{0} & \mathbf{0} & \mathbf{D}^s \end{bmatrix} \begin{Bmatrix} \boldsymbol{\varepsilon}_0 \\ \boldsymbol{\kappa} \\ \boldsymbol{\gamma} \end{Bmatrix} d\Omega = \int_{\Omega} \delta \mathbf{u}^T \mathbf{m} \dot{\mathbf{u}} d\Omega, \tag{9}$$

where \mathbf{m} is the mass matrix containing the mass density of the material ρ .

2.3 The General FEM Formulation of FG Shells

In FEM, the problem domain is discretized using a mesh of n^e three-node finite elements such that $\Omega = \bigcup_{e=1}^{n^e} \Omega^e$ and $\Omega^i \cap \Omega^j = \emptyset$ for $i \neq j$.

The finite element approximation $\mathbf{u}^h = \{u, v, w, \beta_x, \beta_y, \beta_z\}^T$ of a displacement model for FG shell elements can be expressed as

$$\mathbf{u}^h = \sum_{I=1}^{N_n} N_I(\mathbf{x}) \mathbf{I}_6 \mathbf{d}_I = \sum_{I=1}^{N_n} \mathbf{N}_I \mathbf{d}_I, \tag{10}$$

where \mathbf{I}_6 is the unit matrix of sixth rank; N_n is the total number of nodes of problem domain discretized; $\mathbf{d}_I = \{u_I, v_I, w_I, \beta_{xI}, \beta_{yI}, \beta_{zI}\}^T$ denotes the displacement vector of the nodal degrees of freedom of \mathbf{u}^h associated with the I th node; $N_I(\mathbf{x})$ is the shape function at the I th node. According to Eq. (4), the approximation of the membrane, bending and shear strains can be expressed in matrix forms as

$$\boldsymbol{\varepsilon}_0 = \sum_I \mathbf{R}_I \mathbf{d}_I; \boldsymbol{\kappa} = \sum_I \mathbf{B}_I \mathbf{d}_I; \boldsymbol{\gamma} = \sum_I \mathbf{S}_I \mathbf{d}_I, \tag{11}$$

where

$$\mathbf{R}_I = \begin{bmatrix} N_{I,x} & 0 & 0 & 0 & 0 & 0 \\ 0 & N_{I,y} & 0 & 0 & 0 & 0 \\ N_{I,y} & N_{I,x} & 0 & 0 & 0 & 0 \end{bmatrix}; \mathbf{B}_I = \begin{bmatrix} 0 & 0 & 0 & N_{I,x} & 0 & 0 \\ 0 & 0 & 0 & 0 & N_{I,y} & 0 \\ 0 & 0 & 0 & N_{I,y} & N_{I,x} & 0 \end{bmatrix}; \tag{12}$$

$$\mathbf{S}_I = \begin{bmatrix} 0 & 0 & N_{I,x} & N_I & 0 & 0 \\ 0 & 0 & N_{I,y} & 0 & N_I & 0 \end{bmatrix}.$$

The discretized system of equations of the FG shell for static analysis can be given by

$$\mathbf{Kd} = \mathbf{F}, \tag{13}$$

In which \mathbf{K} is the global stiffness matrix which can be computed as

$$\mathbf{K} = \int_{\Omega} \begin{Bmatrix} \mathbf{R} \\ \mathbf{B} \\ \mathbf{S} \end{Bmatrix}^T \begin{bmatrix} \mathbf{A} & \mathbf{B} & \mathbf{0} \\ \mathbf{B} & \mathbf{D} & \mathbf{0} \\ \mathbf{0} & \mathbf{0} & \mathbf{D}^s \end{bmatrix} \begin{Bmatrix} \mathbf{R} \\ \mathbf{B} \\ \mathbf{S} \end{Bmatrix} d\Omega, \quad (14)$$

and \mathbf{F} is the global load vector expressed by:

$$\mathbf{F} = \int_{\Omega} p \mathbf{N} d\Omega + \mathbf{f}^b, \quad (14)$$

In which \mathbf{f}^b is the remaining term of \mathbf{F} subjected to prescribed boundary loads. For the free vibration analysis problem, we obtained

$$(\mathbf{K} - \omega^2 \mathbf{M}) \mathbf{d} = \mathbf{0}, \quad (15)$$

where ω is the natural frequency and \mathbf{M} is the global mass matrix

$$\mathbf{M} = \int_{\Omega} \mathbf{N}^T \mathbf{m} \mathbf{N} d\Omega. \quad (16)$$

2.4 Brief on the CS-DSG3 Formulation

In the DSG3 [24], the shear strain is linear interpolated based on the concept “shear gap” of displacement along the sides of the elements by using the standard element shape functions. Accordingly, the approximation \mathbf{u}_e^h of a three-node triangular shell element can be written as

$$\mathbf{u}_e^h = \sum_{I=1}^3 N_I(\mathbf{x}) \mathbf{I}_6 \mathbf{d}_{eI} = \sum_{I=1}^3 \mathbf{N}_I \mathbf{d}_{eI}, \quad (17)$$

where $\mathbf{d}_{eI}^h = \{u_I, v_I, w_I, \beta_{xI}, \beta_{yI}, \beta_{zI}\}^T$ is the nodal degrees of freedom of \mathbf{u}_e^h associated with the I th node and $N_I(\mathbf{x})$ is linear shape functions in a natural coordinate defined by

$$N_1 = 1 - \xi - \eta; N_2 = \xi; N_3 = \eta. \quad (18)$$

Then, the membrane, bending and shear strains in the element are then obtained by

$$\boldsymbol{\varepsilon}_0^h = [\mathbf{R}_1, \mathbf{R}_2, \mathbf{R}_3] \mathbf{d}_e = \mathbf{R} \mathbf{d}_e; \boldsymbol{\kappa}^h = [\mathbf{B}_1, \mathbf{B}_2, \mathbf{B}_3] \mathbf{d}_e = \mathbf{R} \mathbf{d}_e; \boldsymbol{\gamma}^h = [\mathbf{S}_1, \mathbf{S}_2, \mathbf{S}_3] \mathbf{d}_e = \mathbf{S} \mathbf{d}_e, \quad (19)$$

where

$$\mathbf{R}_1 = \begin{bmatrix} b-c & 0 & 0000 \\ 0 & d-a & 0000 \\ d-a & b-c & 0000 \end{bmatrix}; \mathbf{R}_2 = \begin{bmatrix} c & 0 & 0000 \\ 0 & -d & 0000 \\ -d & c & 0000 \end{bmatrix}; \tag{20}$$

$$\mathbf{R}_3 = \begin{bmatrix} -b & 0 & 0000 \\ 0 & a & 0000 \\ a & -b & 0000 \end{bmatrix},$$

$$\mathbf{B}_1 = \begin{bmatrix} 000 & b-c & 0 & 0 \\ 000 & 0 & d-a & 0 \\ 000 & d-a & b-c & 0 \end{bmatrix}; \mathbf{B}_2 = \begin{bmatrix} 000 & c & 0 & 0 \\ 000 & 0 & -d & 0 \\ 000 & -d & c & 0 \end{bmatrix}; \tag{21}$$

$$\mathbf{B}_3 = \begin{bmatrix} 000 & -b & 0 & 0 \\ 000 & 0 & a & 0 \\ 000 & a & -b & 0 \end{bmatrix},$$

$$\mathbf{S}_1 = \frac{1}{2A_e} \begin{bmatrix} 00 & b-c & A_e & 0 & 0 \\ 00 & d-a & 0 & A_e & 0 \end{bmatrix}; \mathbf{S}_2 = \frac{1}{2A_e} \begin{bmatrix} 00 & c & ac/2 & bc/2 & 0 \\ 00 & -d & -ad/2 & -bd/2 & 0 \end{bmatrix};$$

$$\mathbf{S}_3 = \frac{1}{2A_e} \begin{bmatrix} 00 & -b & -bd/2 & -bc/2 & 0 \\ 00 & a & ad/2 & ac/2 & 0 \end{bmatrix}, \tag{22}$$

In which $a = x_2 - x_1, b = y_2 - y_1, c = y_3 - y_1, d = x_3 - x_1$ with $\mathbf{x}_i = \{x_i, y_i\}, i = 1, 2, 3$ are coordinates of three nodes in the local coordinate system, respectively, as shown in Fig. 2a and A_e denote the area of the triangular element. The global stiffness matrix in Eq. (14) now can be written by:

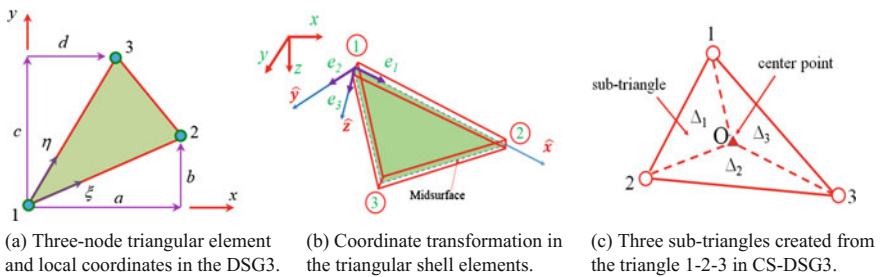


Fig. 2 a Three-node triangular element and local coordinates in the DSG3. b Coordinate transformation in the triangular shell elements. c Three sub-triangles created from the triangle 1-2-3 in CS-DSG3

$$\mathbf{K}^{DSG3} = \sum_{e=1}^{N_m} \mathbf{K}_e^{DSG3} \tag{23}$$

where \mathbf{K}_e^{DSG3} is the element stiffness matrix of the DSG3 element and is given by:

$$\mathbf{K}_e^{DSG3} = \mathbf{T}^T \left(\int_{\Omega_e} \begin{Bmatrix} \mathbf{R} \\ \mathbf{B} \\ \mathbf{S} \end{Bmatrix}^T \begin{bmatrix} \mathbf{A} & \mathbf{B} & \mathbf{0} \\ \mathbf{B} & \mathbf{D} & \mathbf{0} \\ \mathbf{0} & \mathbf{0} & \mathbf{D}^s \end{bmatrix} \begin{Bmatrix} \mathbf{R} \\ \mathbf{B} \\ \mathbf{S} \end{Bmatrix} d\Omega \right) \mathbf{T}, \tag{24}$$

with \mathbf{T} is the transformation matrix of coordinate from global coordinate xyz to the local coordinate system $\hat{x}\hat{y}\hat{z}$ [29], as shown in Fig. 2b.

In the formulation of the CS-DSG3 [23, 30], each triangular element is further divided into three sub-triangles by connecting the central point of the element to three field nodes, as shown in Fig. 2c. Then, the displacement vector at central point is assumed to be the simple average of three displacement vectors of three field nodes. In each sub-triangles, the stabilized DSG3 has computed the strains and to avoid the transverse shear locking. Accordingly, the smoothed element membrane strain $\tilde{\boldsymbol{\epsilon}}_e^m$, the smoothed element bending strain $\tilde{\boldsymbol{\kappa}}$ and the smoothed element shear strain $\tilde{\boldsymbol{\gamma}}$ are written follow as

$$\tilde{\boldsymbol{\epsilon}}_e^m = \tilde{\mathbf{R}}_e \mathbf{d}_e; \quad \tilde{\boldsymbol{\kappa}} = \tilde{\mathbf{B}}_e \mathbf{d}_e; \quad \tilde{\boldsymbol{\gamma}} = \tilde{\mathbf{S}}_e \mathbf{d}_e \tag{26}$$

where $\tilde{\mathbf{R}}_e$, $\tilde{\mathbf{B}}_e$ and $\tilde{\mathbf{S}}_e$ are the smoothed membrane gradient matrix, smoothed bending gradient matrix and smoothed shear gradient matrix, respectively, given by

$$\tilde{\mathbf{R}}_e = \frac{1}{A_e} \sum_{i=1}^3 A_{\Delta_i} \mathbf{R}_e^{\Delta_i}; \quad \tilde{\mathbf{B}}_e = \frac{1}{A_e} \sum_{i=1}^3 A_{\Delta_i} \mathbf{B}_e^{\Delta_i}; \quad \tilde{\mathbf{S}}_e = \frac{1}{A_e} \sum_{i=1}^3 A_{\Delta_i} \mathbf{S}_e^{\Delta_i}, \tag{25}$$

where A_{Δ_i} is the area of sub-triangle Δ_i ; $\mathbf{R}_e^{\Delta_i}$, $\mathbf{B}_e^{\Delta_i}$ and $\mathbf{S}_e^{\Delta_i}$ are, respectively, the membrane, bending and shear strain gradient matrices of sub-triangle Δ_i . Substituting matrix $\tilde{\mathbf{R}}_e$, $\tilde{\mathbf{B}}_e$ and $\tilde{\mathbf{S}}_e$ in Eq. (26) into Eq. (14), the global stiffness matrix of CS-DSG3 element is obtained by

$$\mathbf{K}_e^{CS-DSG3} = \mathbf{T}^T \left(\int_{\Omega_e} \begin{Bmatrix} \tilde{\mathbf{R}}_e \\ \tilde{\mathbf{B}}_e \\ \tilde{\mathbf{S}}_e \end{Bmatrix}^T \begin{bmatrix} \mathbf{A} & \mathbf{B} & \mathbf{0} \\ \mathbf{B} & \mathbf{D} & \mathbf{0} \\ \mathbf{0} & \mathbf{0} & \mathbf{D}^s \end{bmatrix} \begin{Bmatrix} \tilde{\mathbf{R}}_e \\ \tilde{\mathbf{B}}_e \\ \tilde{\mathbf{S}}_e \end{Bmatrix} d\Omega \right) \mathbf{T}, \tag{27}$$

From Eqs. (26) and (27), we can see that the values of element stiffness matrix at the drilling degree of freedom β_z equal zero which can cause the singularity in the global stiffness matrix when all the element meeting at node are coplanar. To solve this problem, the null values of the stiffness corresponding to the drilling degree of freedom are replaced by approximate values. This approximate value is taken to be equal to 10^{-3} times the maximum diagonal value in the element stiffness matrix [23].

3 Numerical Results

In this section, various numerical examples are presented to show the accuracy and stability of the CS-DSG3 for static and free vibration responses of FG shells. The results are compared to the other existing numerical solutions. The central normalized deflection and non-dimensional fundamental frequencies is given by

$$\bar{w} = \frac{E_c h^3}{q a^4} w; \Omega = \omega h \sqrt{\rho_c / E_c}. \tag{26}$$

The first example, consider a fully clamped spherical FG shell under uniformly distributed load. Geometrical parameters for spherical shell are: $a/b = 1, R_x = R_y = R$, length-to-thickness ratio $a/h = 10$ and radius-to-length ratios $R/a = 5, 10$. Mechanical properties of metal (SUS-304): $E_m = 207.79$ GPa, $\nu_m = 0.32$ and ceramic (Si_3N_4): $E_c = 322.27$ GPa, $\nu_c = 0.24$. The volume fraction exponent (n) is variable. The results of the central normalized deflection are presented and compared with Aghdam et al. [3]. It is found that the results presented in Table 1 are in excellent agreement with above-published results.

This example is further extended for static analysis of FG spherical shell when the change in volume fraction exponent and the radius-to-length ratios are shown in Table 2.

The next example, consider a fully clamped cylindrical FG shell subjected to uniformly distributed load. Geometrical parameters for cylindrical shell are: $a/b = 1, R_x = R, R_y = \infty$, radius-to-length ratio $R/a = 2$ and length-to-thickness ratio $a/h = 10$. Mechanical properties are metal (Aluminum): $E_m = 70$ GPa, $\nu_m = 0.3$ and Ceramic (SiC): $E_c = 427$ GPa, $\nu_c = 0.17$. The volume fraction exponent n is equal to 2. The results for the central normalized deflection along the x -axis are shown in Table 3 and compared with Aghdam et al. [3] and ABAQUS. The present results are in close agreement with EKM and ABAQUS.

Table 1 Comparison of the central normalized deflection of FG spherical shell

R/a	Method	n		
		0	2	∞
5	EKM [3]	–	0.0204	–
	Present (8 × 8)	0.0150	0.0194	0.0229
	Present (12 × 12)	0.0156	0.0203	0.0239
	Present (24 × 24)	0.0160	0.0208	0.0245
10	EKM [3]	0.0165	–	0.0248
	Present (8 × 8)	0.0156	0.0203	0.0242
	Present (12 × 12)	0.0164	0.0212	0.0254
	Present (24 × 24)	0.0168	0.0217	0.0260

Table 2 Central normalized deflections \bar{w} of FG spherical shell with various radius-to-length ratio (R/a) and the volume fraction exponent (n)

R/a		n					
		0	0.5	1	2	4	10
2	Present (8×8)	0.0110	0.0127	0.0135	0.0143	0.0150	0.0158
	Present (12×12)	0.0114	0.0132	0.0140	0.0149	0.0156	0.0164
	Present (20×20)	0.0116	0.0134	0.0143	0.0151	0.0159	0.0167
5	Present (8×8)	0.0150	0.0173	0.0185	0.0194	0.0202	0.0212
	Present (12×12)	0.0156	0.0181	0.0193	0.0203	0.0211	0.0222
	Present (20×20)	0.0160	0.0185	0.0197	0.0208	0.0216	0.0227
10	Present (8×8)	0.0156	0.0181	0.0193	0.0203	0.0211	0.0222
	Present (12×12)	0.0164	0.0190	0.0202	0.0212	0.0221	0.0232
	Present (20×20)	0.0168	0.0194	0.0207	0.0217	0.0226	0.0237
20	Present (8×8)	0.0158	0.0183	0.0195	0.0205	0.0213	0.0224
	Present (12×12)	0.0166	0.0192	0.0204	0.0215	0.0223	0.0235
	Present (20×20)	0.0170	0.0197	0.0209	0.0220	0.0228	0.0240

Table 3 Comparison of the central normalized deflection (27) of cylindrical FG shell along x -axis

x/a	Present	EKM [3]	ABAQUS
0	0	0	0
0.1	0.0628	0.0712	0.0783
0.2	0.1739	0.1795	0.1847
0.3	0.2789	0.2771	0.2799
0.4	0.3498	0.3414	0.3426
0.5	0.3746	0.3636	0.3643

Table 4 presents the responses of FG cylindrical shell with different volume fraction exponent and radius-to-length ratios. From Tables 3 and 4, it is found that the behavior of FG shallow shells become softening when the volume fraction exponent (n) increase from ceramic to metal. Furthermore, the increase of curvature ratio leads to increasing displacement of FG shallow shells.

Finally, the vibration of simply supported FG plate and three types of shallow shell include spherical, cylindrical and hyperbolic paraboloid is investigated. Geometrical parameters for plate are $a/b = 1$, length-to-thickness ratio $a/h = 10$ and shallow shell are $a/b = 1$, radius-to-length ratio $R/a = 2$, length-to-thickness ratio $a/h = 10$. The volume fraction exponents $n = 0, 0.5, 1, 4$ and 10 are considered. Mechanical properties are metal (Aluminum): $E_m = 70$ GPa, $\nu_m = 0.3$, $\rho = 2700$ kg/m³ and Ceramic (Alumina): $E_c = 380$ GPa, $\nu_c = 0.3$, $\rho = 3800$ kg/m³. Table 5 shows results with coarse mesh size 8×8 . It is found that numerical results are in excellent agreement with results available of Alijani et al. [31], Matsunaga [32] and Chorfi and Houmat [33].

Table 4 Non-dimensional center deflections $10 \bar{w}$ of FG cylindrical shell with various radius-to-length ratio (R/a) and the volume fraction exponent (n)

R/a		n					
		0	0.5	1	2	4	10
2	Present (8 × 8)	0.1470	0.2213	0.2861	0.3746	0.4551	0.5484
	Present (12 × 12)	0.1512	0.2269	0.2927	0.3827	0.4652	0.5618
	Present (20 × 20)	0.1612	0.2399	0.3076	0.4001	0.4863	0.5907
5	Present (8 × 8)	0.1723	0.2636	0.3436	0.4495	0.5365	0.6324
	Present (12 × 12)	0.1780	0.2717	0.3536	0.4619	0.5512	0.6509
	Present (20 × 20)	0.1917	0.2911	0.3768	0.4895	0.5836	0.6920
10	Present (8 × 8)	0.1766	0.2709	0.3538	0.4627	0.5505	0.6466
	Present (12 × 12)	0.1825	0.2796	0.3645	0.4761	0.5664	0.6662
	Present (20 × 20)	0.1969	0.3005	0.3898	0.5065	0.6016	0.7101
20	Present (8 × 8)	0.1777	0.2729	0.3564	0.4661	0.5549	0.6503
	Present (12 × 12)	0.1837	0.2817	0.3675	0.4799	0.5705	0.6703
	Present (20 × 20)	0.1983	0.3031	0.3935	0.5113	0.6068	0.7152

Table 5 Non-dimensional fundamental frequencies of FG plate and three types FG shallow shells

	n	Present	Alijani et al. [31]	Chorfi and Houmat [33]	Matsunaga [32]
Plate	0	0.0591	0.0597	0.0577	0.0588
	0.5	0.0506	0.0506	0.0490	0.0492
	1	0.0462	0.0456	0.0442	0.043
	4	0.0405	0.0396	0.0383	0.0381
	10	0.0381	0.0380	0.0366	0.0364
Spherical shell	0	0.0779	0.0779	0.0762	0.0751
	0.5	0.0670	0.0676	0.0664	0.0657
	1	0.0611	0.0617	0.0607	0.0601
	4	0.0514	0.0519	0.0509	0.0503
	10	0.0475	0.0482	0.0471	0.0464
Cylindrical shell	0	0.0642	0.0648	0.0629	0.0622
	0.5	0.0548	0.0553	0.0540	0.0535
	1	0.0500	0.0501	0.0490	0.0485
	4	0.0431	0.0430	0.0419	0.0413
	10	0.0403	0.0408	0.0395	0.0390
Hyperbolic paraboloid shell	0	0.0581	0.0597	0.0580	0.0563
	0.5	0.0498	0.0506	0.0493	0.0479
	1	0.0455	0.0456	0.0445	0.0432
	4	0.0399	0.0396	0.0385	0.0372
	10	0.0375	0.0380	0.0368	0.0355

4 Conclusions

In the present study, a combination of the cell based on smoothed discrete shear gap method with three-node triangular elements is proposed to investigate the static responses and free vibration of FG shells include spherical, cylindrical and hyperboloid paraboloid shells. The first-order shear deformation theory is used in the formulation due to the simplicity and computational efficiency. The effects of several parameters such as the radius-to-length ratios and the volume fraction exponent are examined. Present results are in good agreement in most of the cases which are compared with reference solutions.

References

1. Loy C, Lam K, Reddy J (1999) Vibration of functionally graded cylindrical shells. *Int J Mech Sci* 41:309–324
2. Pradhan S, Loy C, Lam K, Reddy J (2000) Vibration characteristics of functionally graded cylindrical shells under various boundary conditions. *Appl Acoust* 61:111–129
3. Aghdam M, Bigdeli K, Shahmansouri N (2010) A semi-analytical solution for bending of moderately thick doubly curved functionally graded panels. *Mech Adv Mater Struct* 17:320–327
4. Su Z, Jin G, Shi S, Ye T, Jia X (2014) A unified solution for vibration analysis of functionally graded cylindrical, conical shells and annular plates with general boundary conditions. *Int J Mech Sci* 80(3/2014):62–80
5. Zhao X, Lee YY, Liew KM (2009) Thermoelastic and vibration analysis of functionally graded cylindrical shells. *Int J Mech Sci* 51(9/2009):694–707
6. Oktem A, Mantari J, Soares CG (2012) Static response of functionally graded plates and doubly-curved shells based on a higher order shear deformation theory. *Eur J Mech A Solids* 36:163–172
7. Liu B, Ferreira AJM, Xing YF, Neves AMA (2016) Analysis of functionally graded sandwich and laminated shells using a layerwise theory and a differential quadrature finite element method. *Compos Struct* 136(2016/02/01/2016):546–553
8. Liu G, Nguyen T (2010) *Smoothed finite element methods*. CRC Press, Taylor and Francis Group, NewYork
9. Liu G, Dai K, Nguyen T (2007) A smoothed finite element method for mechanics problems. *Comput Mech* 39:859–877
10. Liu G, Nguyen T, Dai K, Lam K (2007) Theoretical aspects of the smoothed finite element method (SFEM). *Int J Numer Methods Eng* 71:902–930
11. Liu G, Nguyen-Xuan H, Nguyen-Thoi T (2010) A theoretical study on the smoothed FEM (S-FEM) models: Properties, accuracy and convergence rates. *Int J Numer Methods Eng* 84:1222–1256
12. Liu GR, Nguyen-Thoi T, Nguyen-Xuan H, Dai KY, Lam KY (2009) On the essence and the evaluation of the shape functions for the smoothed finite element method (SFEM). *Int J Numer Methods Eng* 77:1863–1869
13. Nguyen T, Liu G, Dai K, Lam K (2007) Selective smoothed finite element method. *Tsinghua Sci Technol* 12:497–508

14. Liu GR, Nguyen-Thoi T, Nguyen-Xuan H, Lam KY (2009) A node-based smoothed finite element method (NS-FEM) for upper bound solutions to solid mechanics problems. *Comput Struct* 87(1/2009):14–26
15. Nguyen-Thoi T, Liu G, Nguyen-Xuan H (2009) Additional properties of the node-based smoothed finite element method (NS-FEM) for solid mechanics problems. *Int J Comput Methods* 6:633–666
16. Nguyen-Thoi T, Liu G, Nguyen-Xuan H, Nguyen-Tran C (2011) Adaptive analysis using the node-based smoothed finite element method (NS-FEM). *Inte J Numer Methods Biomed Eng* 27:198–218
17. Liu GR, Nguyen-Thoi T, Lam KY (2009) An edge-based smoothed finite element method (ES-FEM) for static, free and forced vibration analyses of solids. *J Sound Vib* 320(3/6/2009):1100–1130
18. Nguyen-Thoi T, Liu G, Nguyen-Xuan H (2011) An n-sided polygonal edge-based smoothed finite element method (nES-FEM) for solid mechanics. *Inte J Numer Methods Biomed Eng* 27:1446–1472
19. Nguyen-Thoi T, Liu G, Lam K, Zhang G (2009) A face-based smoothed finite element method (FS-FEM) for 3D linear and geometrically non-linear solid mechanics problems using 4-node tetrahedral elements. *Int J Numer Methods Eng* 78:324–353
20. Cui X, Liu G, Li G, Zhao X, Nguyen-Thoi T, Sun G (2008) A smoothed finite element method (SFEM) for linear and geometrically nonlinear analysis of plates and shells. *Comput Model Eng Sci* 28:109–125
21. Nguyen-Thoi T, Phung-Van P, Luong-Van H, Nguyen-Van H, Nguyen-Xuan H (2012) A cell-based smoothed three-node Mindlin plate element (CS-MIN3) for static and free vibration analyses of plates. *Comput Mech*:1–17
22. Nguyen-Xuan H, Liu G, Thai-Hoang CA, Nguyen-Thoi T (2010) An edge-based smoothed finite element method (ES-FEM) with stabilized discrete shear gap technique for analysis of Reissner–Mindlin plates *Comput Methods Appl Mech Eng* 199:471–489
23. Nguyen-Thoi T, Phung-Van P, Thai-Hoang C, Nguyen-Xuan H (2013). A cell-based smoothed discrete shear gap method (CS-DSG3) using triangular elements for static and free vibration analyses of shell structures. *Int J Mech Sci* 74(9/2013):32–45
24. Bletzinger K-U, Bischoff M, Ramm E (2000) A unified approach for shear-locking-free triangular and rectangular shell finite elements. *Comput Struct* 75(4/2000):321–334
25. Nguyen-Thoi T, Bui-Xuan T, Phung-Van P, Nguyen-Xuan H, Ngo-Thanh P (2013) Static, free vibration and buckling analyses of stiffened plates by CS-FEM-DSG3 using triangular elements. *Comput Struct* 125:100–113
26. Phung-Van P, Nguyen-Thoi T, Tran LV, Nguyen-Xuan H (2013) A cell-based smoothed discrete shear gap method (CS-DSG3) based on the C 0-type higher-order shear deformation theory for static and free vibration analyses of functionally graded plates. *Comput Mater Sci* 79:857–872
27. Phung-Van P, Nguyen-Thoi T, Le-Dinh T, Nguyen-Xuan H (2013) Static and free vibration analyses and dynamic control of composite plates integrated with piezoelectric sensors and actuators by the cell-based smoothed discrete shear gap method (CS-FEM-DSG3). *Smart Mater Struct* 22:095026
28. Phung-Van P, Nguyen-Thoi T, Luong-Van H, Thai-Hoang C, Nguyen-Xuan H (2014) A cell-based smoothed discrete shear gap method (CS-FEM-DSG3) using layerwise deformation theory for dynamic response of composite plates resting on viscoelastic foundation. *Comput Methods Appl Mech Eng* 272:138–159
29. Nguyen-Hoang S, Phung-Van P, Natarajan S, Kim H-G (2016) A combined scheme of edge-based and node-based smoothed finite element methods for Reissner–Mindlin flat shells. *Eng Comput* 32:267–284 (SCIE-Springer)
30. Nguyen-Thoi T, Phung-Van P, Nguyen-Xuan H, Thai-Hoang C (2012) A cell-based smoothed discrete shear gap method using triangular elements for static and free vibration analyses of Reissner–Mindlin plates. *Int J Numer Methods Eng* 91:705–741

31. Alijani F, Amabili M, Karagiozis K, Bakhtiari-Nejad F (2011) Nonlinear vibrations of functionally graded doubly curved shallow shells. *J Sound Vib* 330:1432–1454
32. Matsunaga H (2008) Free vibration and stability of functionally graded shallow shells according to a 2D higher-order deformation theory. *Compos Struct* 84:132–146
33. Chorfi S, Houmat A (2010) Non-linear free vibration of a functionally graded doubly-curved shallow shell of elliptical plan-form. *Compos Struct* 92:2573–2581

Optimal Volume Fraction of Functionally Graded Beams with Various Shear Deformation Theories Using Social Group Optimization



A. H. Pham, T. V. Vu and T. M. Tran

Abstract In this paper, the optimization of the volume fraction of functionally graded (FG) beams for maximizing the first natural frequency is investigated. Distribution laws using three, four and five parameters are used to describe volume fraction. Navier-type solutions based on various shear deformation theories are developed to compute the natural frequencies. A new metaheuristic algorithm called Social Group Optimization (SGO) is employed for the first time to solve the functionally graded beam optimization problem. Optimal volume fractions for beams with different material properties are then obtained. It is found that the five-parameter distributions give the highest first natural frequency for all cases. Moreover, the results show the consistency of the optimal volume fractions obtained by different shear deformation theories. It is also confirmed that SGO is an efficient tool for this complicated optimization problem.

Keywords Functionally graded beam · Shear deformation theory
Volume fraction · Free vibration · Social Group Optimization

1 Introduction

Functionally graded (FG) materials are increasingly and widely used in different fields such as aerospace, marine, mechanical and structural engineering. FG materials are made of two or more constituents that have a continuous and smooth variation of the relative volume fraction and microstructure [1]. It is well known that the performance

A. H. Pham (✉)

Department of Structural Mechanics, National University of Civil Engineering,
Hanoi, Vietnam
e-mail: anhph2@nuce.edu.vn

T. V. Vu · T. M. Tran

Department of Strength of Materials, National University of Civil Engineering,
Hanoi, Vietnam

© Springer Nature Singapore Pte Ltd. 2018

H. Nguyen-Xuan et al. (eds.), *Proceedings of the International Conference on Advances in Computational Mechanics 2017*, Lecture Notes in Mechanical Engineering, https://doi.org/10.1007/978-981-10-7149-2_27

395

of a FG composite depends not only on the material properties and quantity of its constituent materials but also on the distribution of these constituents. Often, the volume fractions of the constituents are tailored to obtain an optimal material composition satisfying design needs. This paper focuses on tailoring the material distribution to maximize the first natural frequency of FG beams. The maximization of natural frequencies of structures is a common optimization objective since an increase in fundamental frequencies can provide an improvement in structural stiffness [2].

The optimal design of volume fraction for maximizing the natural frequencies of FG beams has been a research interest in recent years. Goupee and Vel [3] used the two-dimensional spatial distribution of volume fractions represented by piecewise cubic interpolation of volume fraction values determined at a finite number of grid points to optimize the natural frequencies of functionally graded beams. In the work by Yas et al. [4, 5] and Kamarian et al. [6], the volume fraction optimization in the thickness direction of a FG beam resting on elastic foundation was studied using three-parameter power law distribution. The three-parameter power law distribution of volume fraction has been also employed in recent works by Roque and Martins [7] and Roque et al. [8]. Some researchers tailored the material distribution through the longitudinal direction for maximizing the fundamental frequency of four-parameter or five-parameter FG beams [9] and arches [10].

On the other hand, the determination of the natural frequencies requires the solution of the free vibration problem. There have been many published works on the analysis of the free vibration of FG beams using different shear deformation theories (e.g. see [11–15]). High-order shear deformation theories can be used to obtain precise results in the case of thick beams. Nevertheless, the past works on optimization of FG beams have mostly based on classical beam theory or first-order shear deformation theory.

In this study, various shear deformation theories are employed in the free vibration analysis of FG beams. Navier-type solution method is used to obtain the natural frequencies. Four-parameter power law distribution and five-parameter trigonometric distribution are introduced to describe the volume fraction in beam thickness direction. These distribution formulations are supposed to permit more diverse material distributions when compared with the simple power law or three-parameter power law. The objective is to find optimal parameter values so as the first natural frequency is maximized. Since the optimization problem is highly nonlinear and complex that is not easily solved by traditional gradient-based techniques, a novel population-based metaheuristic algorithm, called Social Group Optimization (SGO), is applied for the first time to optimize the volume fraction of FG beams. Beams with different material properties are examined.

2 Free Vibration of Functionally Graded Beam

Consider a functionally graded (FG) beam composed of two materials with length L and rectangular cross section $b \times h$, where b is the width and h is the height. The x , y and z coordinates are taken along the length, width and height of the beam, respectively. The study is limited to linear elastic material behaviour.

2.1 Formulations of Volume Fraction

The material properties of a FG beam are assumed to vary continuously along the thickness of the beam (in the z direction) and governed by the volume fraction of its constituents according to the rule of mixtures:

$$P(z) = P_1 V_1(z) + P_2 V_2(z); \quad V_2(z) = 1 - V_1(z) \tag{1}$$

where P represents the effective material property such as Young’s modulus E and mass density ρ ; V is the volume fraction; subscripts 1 and 2 represent the constituent 1 and constituent 2, respectively.

Possible distribution laws for volume fraction are the power law [16], the sigmoid law [17], the exponential law [18] and the three-parameter law [19]. In this study, to spatially tailor the material properties, it is proposed that the volume fraction of constituent 1 follows four-parameter power law distribution formulations or five-parameter trigonometric distribution as given in Table 1.

The parameters a, b, c, d and p are the control parameters, or the design variables of the optimization problem. The proposed equations allow more diverse material distributions when compared with the simple power law. As shown later in this paper, these distributions are also more advantageous than the three-parameter power law distribution (Eq. 2), which was used in the previous work by Roque and Martins [7] to optimize the volume fraction of the same FG beams.

$$V_1 = \left[\frac{1}{2} + \frac{z}{h} + b \left(\frac{1}{2} - \frac{z}{h} \right)^c \right]^p \tag{2}$$

2.2 Analytical Solution for Free Vibration of FG Beams

Based on the higher-order shear deformation theory, the displacement field for the beam is assumed in the following form

$$\begin{aligned} u(x, z, t) &= u_0(x, t) - z \frac{\partial w(x, z, t)}{\partial x} + f(z)\phi(x, t) \\ v(x, z, t) &= 0 \\ w(x, z, t) &= w_0(x, t) \end{aligned} \tag{3}$$

where u, v and w are the displacements at a point of the beam along x, y and z directions; u_0 and w_0 are the axial and transverse displacement of a point on the

Table 1 Volume fraction of constituent 1

Four-parameter power law distribution	Five-parameter trigonometric distribution
$V_1 = a \left[\frac{1}{2} + \frac{z}{h} + b \left(\frac{1}{2} - \frac{z}{h} \right)^c \right]^p$	$V_1 = a \left[\frac{1}{2} - \frac{z}{h} \sin \left(c\pi \left(\frac{1}{2} - \frac{z}{h} \right) + d \right) \right]^p$

mid-surface, respectively; ϕ is the rotation of the cross section about the y -axis; and $f(z)$ is a shape function characterizing the distribution of the transverse shear strain and shear stress through the thickness of the beam.

With Eq. (3), different shear deformation theories can be introduced to obtain the displacements of the beam by using different shape functions $f(z)$. In this study, the Euler–Bernoulli beam theory (CBT), the exponential beam theory (EBT) of Karama et al. [20], the hyperbolic beam theory (HBT) of Soldatos [21], the sinusoidal beam theory (SBT) of Touratier [22] and the third-order beam theory (TBT) of Reddy [23] are employed with the corresponding shape functions $f(z)$ given in Table 2. The Timoshenko beam theory (TMT) is not considered for the analysis since it has been already used in [7].

The strain–displacement relationships are obtained from:

$$\begin{aligned} \epsilon_x &= \frac{\partial u}{\partial x} = \frac{\partial u_0}{\partial x} - z \frac{\partial^2 w}{\partial x^2} + f(z) \frac{\partial \phi}{\partial x} \\ \gamma_{xz} &= \frac{\partial u}{\partial z} + \frac{\partial w}{\partial x} = f'(z) \phi \end{aligned} \tag{4}$$

The stresses are of the form:

$$\begin{aligned} \sigma_x &= E(z) \epsilon_x \\ \tau_{xz} &= \frac{E(z)}{2(1 + \nu)} \gamma_{xz} = G(z) \gamma_{xz}; \quad G(z) = \frac{E(z)}{2(1 + \nu)} \end{aligned} \tag{5}$$

Applying the principle of virtual work to the free vibration problem of the beam leads to:

$$b \int_0^L \int_{-h/2}^{h/2} (\sigma_x \delta \epsilon_x + \tau_{xz} \delta \gamma_{xz}) dz dx + b \int_0^L \int_{-h/2}^{h/2} \rho(z) \left(\frac{\partial^2 u}{\partial t^2} \delta u + \frac{\partial^2 w}{\partial t^2} \delta w \right) dz dx = 0 \tag{6}$$

where the symbol δ denotes the variation operator. By substituting Eqs. (4) and (5) into Eq. (6), integrating by parts and noting that the variation δu_0 , δw_0 and $\delta \phi$ can be arbitrary, the following governing equations can be derived:

$$\begin{aligned} -A \frac{\partial^2 u_0}{\partial x^2} + B \frac{\partial^3 w_0}{\partial x^3} - C \frac{\partial^2 \phi}{\partial x^2} + I_1 \frac{\partial^2 u_0}{\partial t^2} - I_2 \frac{\partial^3 w_0}{\partial x \partial t^2} + I_3 \frac{\partial^2 \phi}{\partial t^2} &= 0 \\ -B \frac{\partial^3 u_0}{\partial x^3} + D \frac{\partial^4 w_0}{\partial x^4} - F \frac{\partial^3 \phi}{\partial x^3} + I_2 \frac{\partial^3 u_0}{\partial x \partial t^2} - I_4 \frac{\partial^4 w_0}{\partial x \partial t^2} + I_5 \frac{\partial^3 \phi}{\partial x \partial t^2} + I_1 \frac{\partial^2 w_0}{\partial t^2} &= 0 \\ -C \frac{\partial^2 u_0}{\partial x^2} + F \frac{\partial^3 w_0}{\partial x^3} - G_1 \frac{\partial^2 \phi}{\partial x^2} + H_1 \phi + I_3 \frac{\partial^2 u_0}{\partial t^2} - I_5 \frac{\partial^3 w_0}{\partial x \partial t^2} + I_6 \frac{\partial^2 \phi}{\partial t^2} &= 0 \end{aligned} \tag{7}$$

Table 2 Shape functions

Beam theory	Euler–Bernoulli (CBT)	Karama et al. (EBT)	Soldatos (HBT)	Touratier (SBT)	Reddy (TBT)
$f(z)$	0	$z \exp^{-2(\frac{z}{h})^2}$	$z \cos h(\frac{1}{2}) - h \sin h(\frac{z}{h})$	$\frac{h}{\pi} \sin(\frac{\pi z}{h})$	$z \left(1 - \frac{4}{3} \frac{z^2}{h^2} \right)$

where the coefficients $A, B, C, D, F, G_1, H_1, I_1, I_2, I_3, I_4, I_5$ and I_6 are given by:

$$\begin{aligned}
 (A, B, C, D, F, G_1) &= \int_{-h/2}^{h/2} E(z)(1, z, f, z^2, zf, f^2) dz; \\
 H_1 &= \int_{-h/2}^{h/2} G(z)(f')^2 dz \\
 (I_1, I_2, I_3, I_4, I_5, I_6) &= \int_{-h/2}^{h/2} \rho(z)(1, z, f, z^2, zf, f^2) dz
 \end{aligned}
 \tag{8}$$

For simply supported beams with length L , the analytical solution can be derived by considering the following expansions for displacements $u_0(x, t)$, $w_0(x, t)$ and $\phi(x, t)$:

$$\begin{aligned}
 u_0(x, t) &= \sum_{m=1}^{\infty} u_m \cos\left(\frac{m\pi x}{L}\right) \sin \omega_m t \\
 w_0(x, t) &= \sum_{m=1}^{\infty} w_m \sin\left(\frac{m\pi x}{L}\right) \sin \omega_m t \\
 \phi(x, t) &= \sum_{m=1}^{\infty} \phi_m \cos\left(\frac{m\pi x}{L}\right) \sin \omega_m t
 \end{aligned}
 \tag{9}$$

where ω_m is the m th natural frequency. In this study, only the first natural frequency is optimized and therefore $m = 1$. Substituting Eq. (9) in Eq. (7), the following set of equations is obtained:

$$\begin{aligned}
 &\left[\left(A \frac{m^2 \pi^2}{L^2} \right) u_m - \left(B \frac{m^3 \pi^3}{L^3} \right) w_m + \left(C \frac{m^2 \pi^2}{L^2} \right) \phi_m \right] - \omega^2 [I_1 u_m - I_2 \frac{m\pi}{L} w_m + I_3 \phi_m] = 0 \\
 &\left[- \left(B \frac{m^3 \pi^3}{L^3} \right) u_m + \left(D \frac{m^4 \pi^4}{L^4} \right) w_m - \left(F \frac{m^3 \pi^3}{L^3} \right) \phi_m \right] - \omega^2 \left[- I_2 \frac{m\pi}{L} u_m + \left(I_1 + I_4 \frac{m^2 \pi^2}{L^2} \right) w_m - I_5 \frac{m\pi}{L} \phi_m \right] = 0 \\
 &\left[\left(C \frac{m^2 \pi^2}{L^2} \right) u_m - \left(F \frac{m^3 \pi^3}{L^3} \right) w_m + \left(H_1 + G_1 \frac{m\pi}{L} \right) \phi_m \right] - \omega^2 [I_3 u_m - I_5 \frac{m\pi}{L} w_m + I_6 \phi_m] = 0
 \end{aligned}
 \tag{10}$$

The system is an eigenproblem of type $[K - \omega^2 M]\{\Delta\} = \{0\}$, where ω is a natural frequency.

3 Optimization Problem

The optimal design of a FG beam is based on the optimization of material distribution throughout beam height, i.e. optimizing the volume fractions of the material constituents. The optimization problem considered in this study is the maximization of the fundamental frequency. The problem is formulated as Eq. (11).

$$\text{Maximize } \bar{\omega} = \frac{\omega L^2}{h} \sqrt{\frac{\rho_2}{E_2}}
 \tag{11}$$

$$\begin{aligned}
 \text{Subject to} \quad & 0 \leq V_1 \leq 1 \\
 & a_{\min} \leq a \leq a_{\max} \\
 & b_{\min} \leq b \leq b_{\max} \\
 & c_{\min} \leq c \leq c_{\max} \\
 & d_{\min} \leq d \leq d_{\max} \\
 & p_{\min} \leq p \leq p_{\max}
 \end{aligned}$$

where $\bar{\omega}$ is the normalized fundamental frequency, with ρ_2 and E_2 are the density and modulus of elasticity of constituent 1, respectively.

In the above optimization problem, the design variables a, b, c, d and p are subjected to bound constraints and they must be chosen such that the volume fraction at any point along the height will stay within the permissible physical limits, i.e. $0 \leq V_1 \leq 1$. To assure that, a set of constraints is introduced as:

$$\begin{aligned}
 0 \leq V_{1, \text{top}}, V_{1, \text{bottom}} \leq 1 \\
 0 \leq V_{1, \text{min}}; V_{1, \text{max}} \leq 1
 \end{aligned} \tag{12}$$

where $V_{1, \text{top}}, V_{1, \text{bottom}}$ are the volume fractions at the boundaries (at the top and the bottom); and $V_{1, \text{min}}, V_{1, \text{max}}$ are the minima and maxima within the structure domain. The maxima/minima point z_{opt} can be obtained by solving:

$$V_1'(z) = 0 \tag{13}$$

For four-parameter power law distribution, we obtained:

$$z_{\text{opt}} = \frac{h}{2} \left(1 - 2e^{\frac{-\log[b] - \log[c]}{c-1}} \right) \tag{14}$$

For five-parameter trigonometric distribution, we obtained:

$$z_{\text{opt}} = \left[\begin{array}{c} \frac{h(2d - \pi + c\pi)}{2c\pi} \\ \frac{h(2d + \pi + c\pi)}{2c\pi} \\ h \left(\frac{2d + c\pi - 2 \arcsin \left[\frac{1 - 2b^{\frac{-1+p}{c}}}{b} \right]}{2c\pi} \right) \end{array} \right] \tag{15}$$

After solving for maxima or minima, then the values of the volume fraction at all the points in the structure domain corresponding to these maxima or minima should satisfy the permissible limits.

4 Social Group Optimization

The SGO is one of the most recent optimization techniques, developed by Satapathy and Naik for global optimization [24]. SGO is based on the concept of social behaviour of human towards solving a complex problem, i.e. a problem/task which is too difficult to solve by a single person can be solved by a group of persons. It has been shown in [24] that SGO outperforms several advanced optimization techniques in solving different unconstrained benchmark functions. The technique is quite simple and straightforward to implement. Details of the concept and the mathematical formulation of SGO can be found in [24].

4.1 Basic Procedure of SGO

SGO is a population-based optimizer, where the population of candidate solutions is considered as a group of N persons $X_k (k=1, 2, \dots, N)$ and each person is defined by $X_k = (x_{k1}, x_{k2}, \dots, x_{kD})$, where $x_{ki} (i=1, 2, \dots, D)$ is the traits (design variables) assigned to a person and D is the dimension of the optimization problem. Each person in the group gets knowledge and has a certain level of capacity for solving the problem, which is corresponding to the ‘fitness’, f_k . The best person X_{gbest} is the one with best fitness. The best person intends to propagate knowledge to the other person, which will improve the knowledge level of the whole group.

The procedure of SGO consists of two phases: the ‘improving phase’ and the ‘acquiring phase’. At the ‘improving phase’, each person is influenced by the best person and his/her knowledge level is enhanced. At the ‘acquiring phase’, the knowledge level of each person is improved through mutual interaction with another person and the best person in the group at that time. The basic steps of SGO are given in the following.

Initialization

An initial population is randomly sampled from the solution space as Eq. (16),

$$x_{ki} = x_i^l + \text{rand}[0, 1] \times (x_i^u - x_i^l), \quad i = 1, 2, \dots, D \quad (16)$$

where x_i^l and x_i^u are the lower and the upper bounds of the i th design variable, respectively; $\text{rand}[0, 1]$ is a uniformly distributed random real value in the range $[0, 1]$. Then, calculate the fitness of each person in the population f_k .

Improving Phase

In this phase, each person X_k acquires knowledge from the group’s best person X_{gbest} . The updating of each person is given as follows:

$$X_k^{new} = c * X_k^{old} + \mathbf{r} * (X_{gbest} - X_k^{old}), \quad k = 1, 2, \dots, N \quad (17)$$

where c is a self-introspection parameter and $0 < c < 1$; \mathbf{r} is a vector of D uniformly distributed random numbers within the range $[0, 1]$. Accept X_k^{new} if it provides a better fitness than X_k^{old} does; otherwise, the X_k^{old} is retained in the group.

Acquiring phase

In this phase, each person interacts with other person of the group for acquiring knowledge. The best knowledgeable person (here known as the person with the best fitness at the end of the improving phase) has the greatest influence on others. A person will also get new information from others if they have more knowledge than he/she has. The updating of each person is as follows.

For each person X_k , randomly select another person in the current group X_r , where $r \neq k$:

If X_k is better than X_r :

$$X_k^{new} = X_k^{old} + \mathbf{r}_1 * (X_k - X_r) + \mathbf{r}_2 * (X_{gbest} - X_k) \quad (18)$$

Otherwise,

$$X_k^{new} = X_k^{old} + \mathbf{r}_1 * (X_r - X_k) + \mathbf{r}_2 * (X_{gbest} - X_k) \quad (19)$$

where \mathbf{r}_1 and \mathbf{r}_2 are two vectors of D uniformly distributed random numbers in $[0, 1]$. Accept X_k^{new} if it gives a better fitness than X_k^{old} does.

The improving and acquiring phases are repeated until a termination criterion is reached.

4.2 Constraint Handling

The SGO has been developed originally for unconstrained optimization problem. In order to adapt SGO to the optimization of FG beams discussed in Sect. 3, constrained handling is required. In the optimization of FG beams, there are two types of constraints: bound constraints and inequality constraints.

Handling of bound constraints

If the value of a design variable x_{kj}^{new} violates the bound(s) b_j , its value is recomputed as:

$$x_{kj}^{new} = \frac{x_{kj}^{old} + b_j}{2} \quad (20)$$

Handling of inequality constraints

Consider the inequality constraint of the form:

$$c_j(X_k) \leq 0, \quad j = 1, 2, \dots, N_C \quad (21)$$

where N_C is the number of constraints of the optimization problem; $c_j(X_k)$ is the j th constraint function. For the FG beam problem, the constraints are the requirement on the volume fraction as given in Eq. (12).

The constraint violation of a solution X_k is then determined by:

$$C_k = \max \left\{ \max_j \{0, c_j(X_k)\} \right\}, \quad j = 1, 2, \dots, N_C \tag{22}$$

Deb’s rules [25] are employed in this study to handle inequality constraints:

- (1) A feasible solution is better than any infeasible one.
- (2) Of two feasible solutions or two solutions with equal constraint violation, the one with better fitness is the better.
- (3) Of two infeasible solutions, the one with a smaller constraint violation is the better.

Deb’s constraint rules have been successfully applied for genetic algorithm and several metaheuristics.

5 Optimization Results

The FG beam considered in the optimization is composed of two materials. Material properties for material 1, Young’s modulus and mass density are the same as those of aluminium. Material properties for material 2 are obtained by considering different material property ratios $s = E_2/E_1$. The choice of these material properties is purely for the illustration of the optimization problem. The properties of the FG beam are the same as those in [7] and listed in Table 3.

Two optimization problems are considered. In the first problem (Problem 1), volume fraction is followed by the four-parameter power law distribution, and in the second problem (Problem 2), the five-parameter trigonometric distribution is applied. For both problems, the fundamental natural frequencies are obtained for the beam using the shear deformation theories mentioned in Sect. 2. The ranges of the design variables for each problem are given in Table 4. These ranges are chosen based on a preliminary investigation of the proposed models of volume fraction given in Table 1, which ensure a wide range of possibilities for material distribution.

Table 3 Data for the FG beam

L	h	E_1, ρ_1	E_2, ρ_2	ν	s
1 m	0.1 m	70 GPa; 2702 kg/m ³	$E_2 = sE_1; \rho_2 = s\rho_1$	0.3	(0.1, 0.2, 0.5, 0.8, 2, 5)

Table 4 Design variable ranges

Design variable	a	b	c	d	p
Problem 1	[0, 1]	[0, 20]	[0, 20]	NA	[0, 20]
Problem 2	[0, 1]	[0, 1]	[-2, 2]	$[-\pi, \pi]$	[0, 20]

Table 5 Best optimization results with four-parameter volume fraction model

E_2/E_1	Method	$\bar{\omega}$	a	b	c	p
0.1	CBT	3.6676	1.0000	1.0000	2.1842	16.3418
	EBT	3.5567	1.0000	1.0000	2.1598	17.1856
	HBT	3.5571	1.0000	1.0000	2.1639	16.9524
	SBT	3.5565	1.0000	1.0000	2.1619	17.0732
	TBT	3.5570	1.0000	1.0000	2.1637	16.9624
	TMT [7]	3.761	–	1	2.2	16.2
0.2	CBT	3.3958	1.0000	1.0000	2.3178	11.9999
	EBT	3.3212	1.0000	1.0000	2.2993	12.3127
	HBT	3.3212	1.0000	1.0000	2.3028	12.2362
	SBT	3.3211	1.0000	1.0000	2.3012	12.2794
	TBT	3.3212	1.0000	1.0000	2.3027	12.2397
	TMT [7]	3.493	–	1	2.3	12.1
0.5	CBT	3.0572	1.0000	1.0000	2.6036	7.6126
	EBT	3.0103	1.0000	1.0000	2.5929	7.7061
	HBT	3.0101	1.0000	1.0000	2.5951	7.6820
	SBT	3.0102	1.0000	1.0000	2.5939	7.6948
	TBT	3.0101	1.0000	1.0000	2.5950	7.6831
	TMT [7]	3.155	–	1	2.6	7.6
0.8	CBT	2.9041	1.0000	1.0000	2.8120	5.9198
	EBT	2.8660	1.0000	1.0000	2.8053	5.9681
	HBT	2.8658	1.0000	1.0000	2.8071	5.9549
	SBT	2.8658	1.0000	1.0000	2.8062	5.9639
	TBT	2.8658	1.0000	1.0000	2.8069	5.9558
	TMT [7]	3.002	–	1	2.8	5.9
2	CBT	3.0877	0.0003523	1.3825	0.4749	19.7312
	EBT	3.0354	0.0001241	1.4638	0.4332	19.4969
	HBT	3.0358	0.0009587	1.3192	0.5106	19.5211
	SBT	3.0363	0.0001419	1.4537	0.4464	19.7027
	TBT	3.0362	0.0009676	1.3161	0.5113	19.5959
	TMT [7]	2.963	–	0	0	0.2
5	CBT	3.3513	0.0006794	1.4369	0.4375	16.3266
	EBT	3.2691	0.0014563	1.3211	0.5038	18.1318
	HBT	3.2736	0.0028439	1.3018	0.5239	17.1733
	SBT	3.2717	0.0095000	1.2608	0.5450	14.9335
	TBT	3.2734	0.0064380	1.2827	0.5350	15.4265
	TMT [7]	2.970	–	0	0	0.1

The parameter setting for SGO is the group size $N = 50$, the maximum iteration $T_{\max} = 300$ and the self-introspection $c = 0.2$. The computation program is implemented in MATLAB R2012a and executed on a personal computer with an

Table 6 Best optimization results with five-parameter volume fraction model

E_2/E_1	Method	$\bar{\omega}$	a	b	c	d	P
0.1	CBT	3.8488	1.0000	1.0000	-2.0000	-1.5708	10.1284
	EBT	3.6925	1.0000	1.0000	-2.0000	-1.5708	13.0317
	HBT	3.6942	1.0000	1.0000	-2.0000	-1.5708	12.0928
	SBT	3.6927	1.0000	1.0000	-2.0000	-1.5708	12.6138
	TBT	3.6940	1.0000	1.0000	-2.0000	-1.5708	12.1375
0.2	CBT	3.5690	1.0000	1.0000	2.0000	-1.5708	5.9319
	EBT	3.4675	1.0000	1.0000	2.0000	-1.5708	6.6279
	HBT	3.4689	1.0000	1.0000	2.0000	-1.5708	6.3766
	SBT	3.4679	1.0000	1.0000	2.0000	-1.5708	6.5085
	TBT	3.4688	1.0000	1.0000	-2.0000	-1.5708	6.3874
0.5	CBT	3.1572	1.0000	1.0000	-2.0000	-1.5708	3.0738
	EBT	3.1018	1.0000	1.0000	-2.0000	-1.5708	3.1935
	HBT	3.1020	1.0000	1.0000	2.0000	-1.5708	3.1508
	SBT	3.1018	1.0000	1.0000	-2.0000	-1.5708	3.1727
	TBT	3.1020	1.0000	1.0000	-2.0000	-1.5708	3.1526
0.8	CBT	2.9396	1.0000	1.0000	2.0000	-1.5708	2.2412
	EBT	2.8991	1.0000	1.0000	-2.0000	-1.5708	2.2933
	HBT	2.8990	1.0000	1.0000	2.0000	-1.5708	2.2754
	SBT	2.8990	1.0000	1.0000	-2.0000	-1.5709	2.2849
	TBT	2.8990	1.0000	1.0000	2.0000	-1.5708	2.2761
2	CBT	3.1140	1.0000	1.0000	-2.0000	1.5708	0.7186
	EBT	3.0606	1.0000	1.0000	-2.0000	1.5708	0.7023
	HBT	3.0613	1.0000	1.0000	-2.0000	1.5708	0.7080
	SBT	3.0609	1.0000	1.0000	2.0000	1.5708	0.7051
	TBT	3.0613	1.0000	1.0000	2.0000	1.5708	0.7078
5	CBT	3.4097	1.0000	1.0000	2.0000	1.5708	0.4391
	EBT	3.3240	1.0000	1.0000	2.0000	1.5708	0.4211
	HBT	3.3275	1.0000	1.0000	-2.0000	1.5708	0.4281
	SBT	3.3255	1.0000	1.0000	2.0000	1.5708	0.4246
	TBT	3.3273	1.0000	1.0000	-2.0000	1.5709	0.4278

Intel CPU Core i3 2.3 GHz and 2 GB RAM. For each case, the optimization is performed with 25 independent runs.

For Problem 1, the best solutions for each ratio E_2/E_1 are presented in Table 5. Optimization results show that the volume fraction can be tailored with respect to the ratio E_2/E_1 in order to achieve maximum fundamental frequencies. It is found that, for ratios $E_2/E_1 < 1$, the results obtained with different shear deformation theories are quite consistent. The material profiles obtained by the proposed four-parameter distribution model are similar to those given by the three-parameter power law distribution in [7]. However, the maximum fundamental frequencies by this study are slightly smaller than those obtained by Timoshenko beam theory in

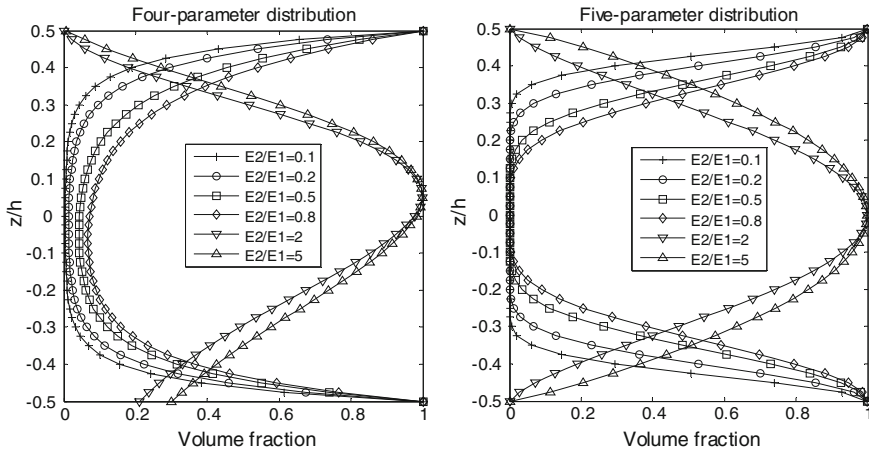


Fig. 1 Best optimal material profiles, V_1 , after 25 runs

[7]. For ratios $E_2/E_1 > 1$, the optimal solutions given by different shear deformation theories are slightly different from each other. The maximum fundamental frequencies found in this study are higher than those in [7], which implies that the optimal results of four-parameter distribution are better than those of the three-parameter power law distribution.

For Problem 2, the best solutions for each ratio E_2/E_1 are presented in Table 6. For all ratios E_2/E_1 , the maximum fundamental frequencies are higher than the corresponding results obtained in Problem 1, as shown in Table 6. That means the proposed trigonometric volume fraction can provide better material distribution for maximizing the natural frequencies of FG beams. In this problem, quite consistent material profiles are obtained with different beam theories. It is found that the parameters a and b become unity regardless of ratios E_2/E_1 .

The material profiles, V_1 , along the beam thickness based on the third-order beam theory (TBT) are shown in Fig. 1. The optimized profiles found for different E_2/E_1 correspond to ‘a sandwich-structured composite, with a smooth transition between face and core properties’. It is noted that these profiles are similar with the finding in [7] for the case $E_2/E_1 < 1$. For $E_2/E_1 > 1$, optimal solutions found in [7] using three-parameter volume fraction are closer to simple power law distribution.

6 Conclusion

In this study, the optimization of volume fraction for maximizing the fundamental frequency of FG beam using various shear deformation theories and different distribution laws for volume fraction is investigated. Different ratios of material properties were tested.

For the cases considered, the optimized material profile was found quite consistent for different shear deformation theories. Using the proposed four-parameter and five-parameter formulations for volume fraction, it is able to tailor the material distribution for different design of FG beam. For different ratios of material properties, the optimized solutions correspond to ‘a sandwich-structured composite, with a smooth transition between face and core properties’. Moreover, the five-parameter formulation for volume fraction can provide better material distribution for maximizing the natural frequencies of FG beams.

The recent Social Group Optimization algorithm, which was originally developed for unconstrained optimization, has been adapted to effectively solve highly nonlinear, complex constrained optimization problem like the FG beam design.

References

1. Miyamoto Y, Kaysser WA, Rabin BH, Kawasaki A, Ford RG (1999) Functionally graded materials: design, processing and applications. Chapman & Hall, London
2. Save WPM, Warner WH (eds) (1990) Structural optimization. Springer
3. Goupee AJ, Vel SS (2006) Optimization of natural frequencies of bidirectional functionally graded beams. *Struct Multidiscip Optim* 32(6):473–484
4. Yas MH, Kamarian S, Eskandari J, Pourasghar A (2011) Optimization of functionally graded beams resting on elastic foundations. *J Solid Mech* 3(4):365–378
5. Yas MH, Kamarian S, Pourasghar A (2014) Application of imperialist competitive algorithm and neural networks to optimise the volume fraction of three-parameter functionally graded beams. *J Exp Theor Artif Intell* 26(1):1–12
6. Kamarian S, Yas M, Pourasghar A, Daghigh M (2014) Application of firefly algorithm and anfis for optimisation of functionally graded beams. *J Exp Theor Artif Intell* 26(2):197–209
7. Roque CMC, Martins PALS (2015) Differential evolution for optimization of functionally graded beams. *Compos Struct* 133:1191–1197
8. Roque CMC, Martins PALS, Ferreira AJM, Jorge RMN (2016) Differential evolution for free vibration optimization of functionally graded nano beams. *Compos Struct* 156:29–34
9. Alshabatat NT, Naghshineh K (2014) Optimization of natural frequencies and sound power of beams using functionally graded material. *Adv Acoust Vib* 2014
10. Tsiatas GC, Charalampakis AE (2017) Optimizing the natural frequencies of axially functionally graded beams and arches. *Compos Struct* 160:256–266
11. Aydogdu M, Taskin V (2007) Free vibration analysis of functionally graded beams with simply supported edges. *Mater Des* 28(5):1651–1656
12. Şimşek M (2010) Fundamental frequency analysis of functionally graded beams by using different higher-order beam theories. *Nucl Eng Des* 240(4):697–705
13. Thai HT, VO TP (2012) Bending and free vibration of functionally graded beams using various higher-order shear deformation beam theories. *Int J Mech Sci* 62(1):57–66
14. Mashat DS, Carrera E, Zenkour AM, Al Khateeb SA, Filippi M (2014) Free vibration of FGM layered beams by various theories and finite elements. *Compos Part B: Eng* 59(2014) 269–278
15. Hadji L, Khelifa Z, Daouadji TH, Bedia EA (2015) Static bending and free vibration of FGM beam using an exponential shear deformation theory. *Coupled Syst Mech* 4(1):99–114
16. Bao G, Wang L (1995) Multiple cracking in functionally graded ceramic/metal coatings. *Int J Solids Struct* 32(19):2853–2871

17. Chi S-H, Chung Y-L (2006) Mechanical behavior of functionally graded material plates under transverse loadpart I: analysis. *Int J Solids Struct* 43(13):3657–3674
18. Ait Atmane H, Tounsi A, Meftah SA, Belhadj HA (2011) Free vibration behavior of exponential functionally graded beams with varying crosssection. *J Vib Control* 17(2):311–318
19. Viola E, Tornabene F (2009) Free vibrations of three parameter functionally graded parabolic panels of revolution. *Mech Res Commun* 36(5):587–594
20. Karama M, Afaq KS, Mistou S (2003) Mechanical behaviour of laminated composite beam by the new multi-layered laminated composite structures model with transverse shear stress continuity. *Int J Solids Struct* 40(6):1525–1546
21. Soldatos KP (1992) A transverse shear deformation theory for homogeneous monoclinic plates. *Acta Mech* 94(3):195–220
22. Touratier M (1991) An efficient standard plate theory. *Int J Eng Sci* 29(8):901–916
23. Reddy JN (1984) A simple higher-order theory for laminated composite plates. *J Appl Mech* 51(4):745–752
24. Satapathy S, Naik A (2016) Social group optimization (SGO): a new population evolutionary optimization technique. *Complex Intell Syst* 2(3):173–203
25. Deb K (2000) An efficient constraint handling method for genetic algorithms. *Comput Methods Appl Mech Eng* 186(2):311–338

A Node-Based MITC3 Element for Analyses of Laminated Composite Plates Using the Higher-Order Shear Deformation Theory



T. Chau-Dinh, T. Truong-Duc, K. Nguyen-Trung and H. Nguyen-Van

Abstract In this paper, the node-based smoothed finite element method is developed for three-node triangular plate elements using the mixed interpolation of tensorial components (MITC) technique to remove the shear locking. The C^0 -type continuous plate elements represent the higher-order shear deformation theory of laminated composite plates by adding two degree of freedoms related to derivatives of deflection. Based on the MITC3 technique for three-node triangular degenerated shell elements, an explicit formulation of gradients of the transverse shear strains is derived. The constant strain fields within the C^0 -type continuous plate elements are averaged over node-based domains defined by connecting the centroids and edges' middle points of elements having common nodes. The proposed elements, namely NS-MITC3, show good accuracy and convergence as compared to other plate elements when employed to analyze laminated composite plates.

Keywords Node-based smoothed finite element method (NS-FEM) • Mixed interpolation of tensorial components (MITC) • Higher-order shear deformation theory (HSDT) • Laminated composite plates

T. Chau-Dinh (✉) · K. Nguyen-Trung
Faculty of Civil Engineering, Ho Chi Minh City University of Technology and Education,
Thu Duc District, Ho Chi Minh City, Vietnam
e-mail: chdthanh@hcmute.edu.vn

T. Truong-Duc
Economy and Infrastructure Office, Chau Thanh District, An Giang Province, Vietnam

H. Nguyen-Van
Faculty of Civil Engineering, Ho Chi Minh City University of Architecture, District 3,
Ho Chi Minh City, Vietnam

1 Introduction

Behaviors of laminated composite plates currently attract many researches in computational mechanics because the structures gain an increasing popularity among many manufacturing industries. The behaviors of the laminated composite plates can be analyzed by models of three dimensions, quasi-three dimensions, layerwise, or equivalent single layer (ESL). In which, the ESL model is simple and efficient due to low computational cost and high accuracy. Compared with the classical plate theory or the first-order shear deformation theory, many higher-order shear deformation theories (HSDT) have been suggested and successfully applied to the ESL model to capture the behaviors of the laminated composite plate, especially the stresses and strains through the thickness, with more accuracy [1].

The HSDT for the ESL model of the laminated composite plates can be solved by analytical or numerical approaches. Under the circumstances of laminated composite plates with arbitrary geometry, boundary, and loadings, the numerical methods and particularly the finite element method (FEM) are preferred. The simplest plate finite elements are three-node triangular elements using C^0 -displacement approximation using the shear deformation theory or Mindlin plate theory. However, these pure C^0 -displacement plate elements overestimate the transverse shear strain energy when the plate thickness becomes thin. This phenomenon is called the shear locking. To be used for analyzing both thin and thick plates, or to overcome the shear locking, such approaches as reduced integration (RI) [2], selective reduced integration (SRI) [3], or independent interpolation of the transverse shear strains [4–8] are employed to the C^0 -displacement elements. The RI and SRI methods are simple but make the elements have spurious zero-energy modes. Therefore, the independent interpolations of the transverse shear strains based on the assumed natural strains (ANS) [4], the enhanced assumed strains (EAS) [5], the discrete shear gap (DSG) [6], or the mixed interpolation tensorial components (MITC) [7, 8] have been developed and managed to remove the shear locking and spurious zero modes. Among the shear locking removing approaches, the MITC3 technique developed for three-node triangular continuum mechanics-based shell finite elements also satisfies the spatially isotropic property [8], meaning the behavior of the elements independent from the order of nodal numbering. In addition, the conventional C^0 -displacement plate elements cannot reasonably approximate the derivatives of deflection in the HSDT. However, the drawback has been successfully solved by considering the derivatives of deflection as independent variables named “warping” and approximated by standard C^0 -shape functions [9, 10].

In an effort to improve accuracy of the three-node triangular plate finite elements, the smoothed FEM [11] have been developed for these elements using the DSG3 technique for removing the shear locking. These smoothed DSG3 plate elements gave the numerical results more accurately than those provided by the standard DSG3 elements in cases of isotropic, laminated composite or functionally

graded material plates using the first-order or higher-order shear deformation theories [12–19], just cited some references. Similarly, the smoothed FEM have also been used to enhance the plate finite elements attenuating the shear locking by the MITC3 technique. To do this, the MITC3 technique developed for three-node triangular degenerated shell elements [8] has been implicitly derived for the transverse shear strains of the plates. Using only one Gaussian quadrature point, the formulation of the gradient matrix related between the transverse shear strains and the nodal displacements is dependent on the nodal coordinates or constant over the elements. Therefore, the MITC3-type transverse shear strains are easily smoothed over domains between elements defined by common the element edges or nodes equivalent to edge-based smoothed (ES) or node-based smoothed (NS) methods [11], respectively. Numerical results shown that the ES-MITC3 or NS-MITC3 plate elements are good competitors as compared to other similar three-node plate elements when analyzing both thin and thick isotropic or laminated composite plates using the first-order shear deformation theory [20, 21]. In this paper, the NS-MITC3 plate elements are extended to analyze the laminated composite plates using the HSDT.

The paper is organized as follows. In the next section, the third-order shear deformation theory [1] for the laminated composite plates is briefly presented, and the corresponding NS-MITC3 plate elements are derived. Then, numerical results of the popular laminated composite and sandwich plates are provided to compare and discuss the accuracy of the present elements with other elements. In the last section, some conclusions are summarized.

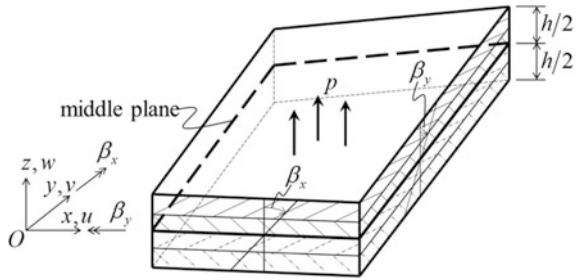
2 Formulation of NS-MITC3 Elements for HSDT-Type Laminated Composite Plates

2.1 HSDT for the ESL Model of Laminated Composite Plates

Give a laminated composite plate having n layers with total thickness h and subjected to transverse loads p as shown in Fig. 1. The third-order shear deformation theory [1] for the ESL model of the laminated composite plate defines the displacements u , v , w , respectively, corresponding to x -, y -, z -directions as follows

$$\begin{aligned} u(x, y, z) &= u_0 + \left(z - \frac{4z^3}{3h^2} \right) \beta_x - \frac{4z^3}{3h^2} \frac{\partial w}{\partial x} \\ v(x, y, z) &= v_0 + \left(z - \frac{4z^3}{3h^2} \right) \beta_y - \frac{4z^3}{3h^2} \frac{\partial w}{\partial y}. \\ w(x, y, z) &= w_0 \end{aligned} \tag{1}$$

Fig. 1 Laminated composite plate and positive directions of the displacements



In which, u_0, v_0, w_0 are the translational displacements of the middle plane in x -, y -, z -directions, respectively; β_x and β_y are, respectively, the rotational displacements of the middle plane about y - and x - axis with positive directions defined in Fig. 1.

To use C^0 -type approximations for the displacements of the HSDT given by Eq. (1), the derivatives of deflection w with respect to x and y are replaced by independent “warping” functions ϕ_x, ϕ_y [9, 10]. As a result, the displacement fields in Eq. (1) can be rewritten as

$$\begin{aligned} u(x, y, z) &= u_0 + \left(z - \frac{4z^3}{3h^2} \right) \beta_x - \frac{4z^3}{3h^2} \phi_x \\ v(x, y, z) &= v_0 + \left(z - \frac{4z^3}{3h^2} \right) \beta_y - \frac{4z^3}{3h^2} \phi_y. \\ w(x, y, z) &= w_0 \end{aligned} \tag{2}$$

From the displacement fields in Eq. (2), we obtain the in-plane and transverse shear strain fields

$$[\epsilon_{xx} \ \epsilon_{yy} \ \gamma_{xy}]^T = \boldsymbol{\epsilon}_0 + z\boldsymbol{\kappa}_1 + z^3\boldsymbol{\kappa}_2 \tag{3}$$

$$[\gamma_{xz} \ \gamma_{yz}]^T = \boldsymbol{\gamma}_s + z^2\boldsymbol{\kappa}_s \tag{4}$$

Here,

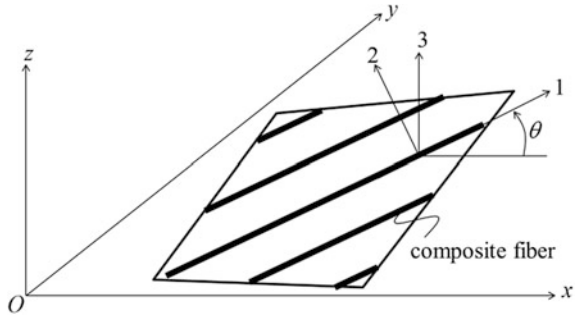
$$\boldsymbol{\epsilon}_0 = \begin{Bmatrix} u_{0,x} \\ v_{0,y} \\ u_{0,y} + v_{0,x} \end{Bmatrix}; \boldsymbol{\kappa}_1 = \begin{Bmatrix} \beta_{x,x} \\ \beta_{y,y} \\ \beta_{x,y} + \beta_{y,x} \end{Bmatrix}; \boldsymbol{\kappa}_2 = -\frac{4}{3h^2} \begin{Bmatrix} \beta_{x,x} + \phi_{x,x} \\ \beta_{y,y} + \phi_{y,y} \\ \beta_{x,y} + \phi_{x,y} + \beta_{y,x} + \phi_{y,x} \end{Bmatrix} \tag{5}$$

$$\boldsymbol{\gamma}_s = \begin{Bmatrix} w_{0,x} + \beta_x \\ w_{0,y} + \beta_y \end{Bmatrix}; \boldsymbol{\kappa}_s = -\frac{4}{h^2} \begin{Bmatrix} \beta_x + \phi_x \\ \beta_y + \phi_y \end{Bmatrix} \tag{6}$$

In these equations, the comma denotes derivatives.

Consider a layer k having the composite fibers inclined at an angle of $\theta^{(k)}$ to the x -direction with positive definition shown in Fig. 2. The layer k is laid parallel to

Fig. 2 Direction of composite fibers in the layer k



the Oxy plane at the elevation z^k and z^{k+1} measured from its lower and upper surfaces, respectively. The material properties are the Young's moduli $E_1^{(k)}, E_2^{(k)}$, the shear moduli $G_{12}^{(k)}, G_{23}^{(k)}, G_{13}^{(k)}$, and the Poisson's ratios $\nu_{21}^{(k)} = \nu_{12}^{(k)} (E_1^{(k)} / E_2^{(k)})$, where subscripts 1, 2, 3, respectively, describe the material properties in directions along the composite fibers, perpendicular to the composite fibers and on the layer k and normal to the layer k (see Fig. 2). The relationship between the stresses and strains of the layer k is [1]

$$\begin{Bmatrix} \sigma_x \\ \sigma_y \\ \tau_{xy} \\ \tau_{xz} \\ \tau_{yz} \end{Bmatrix}^{(k)} = \begin{bmatrix} \bar{Q}_{11} & \bar{Q}_{12} & \bar{Q}_{16} & 0 & 0 \\ \bar{Q}_{12} & \bar{Q}_{22} & \bar{Q}_{26} & 0 & 0 \\ \bar{Q}_{16} & \bar{Q}_{26} & \bar{Q}_{66} & 0 & 0 \\ 0 & 0 & 0 & \bar{Q}_{55} & \bar{Q}_{45} \\ 0 & 0 & 0 & \bar{Q}_{45} & \bar{Q}_{44} \end{bmatrix}^{(k)} \begin{Bmatrix} \varepsilon_x \\ \varepsilon_y \\ \gamma_{xy} \\ \gamma_{xz} \\ \gamma_{yz} \end{Bmatrix}^{(k)} \quad (7)$$

In which,

$$\begin{aligned} \bar{Q}_{11} &= Q_{11}^{(k)} \cos^4 \theta^{(k)} + Q_{22}^{(k)} \sin^4 \theta^{(k)} + 2(Q_{12}^{(k)} + 2Q_{66}^{(k)}) \sin^2 \theta^{(k)} \cos^2 \theta^{(k)} \\ \bar{Q}_{22} &= Q_{11}^{(k)} \sin^4 \theta^{(k)} + Q_{22}^{(k)} \cos^4 \theta^{(k)} + 2(Q_{12}^{(k)} + 2Q_{66}^{(k)}) \sin^2 \theta^{(k)} \cos^2 \theta^{(k)} \\ \bar{Q}_{66} &= (Q_{11}^{(k)} + Q_{22}^{(k)} - 2Q_{12}^{(k)} - 2Q_{66}^{(k)}) \sin^2 \theta^{(k)} \cos^2 \theta^{(k)} + Q_{66}^{(k)} (\sin^4 \theta^{(k)} + \cos^4 \theta^{(k)}) \\ \bar{Q}_{12} &= (Q_{11}^{(k)} + Q_{22}^{(k)} - 4Q_{66}^{(k)}) \sin^2 \theta^{(k)} \cos^2 \theta^{(k)} + Q_{12}^{(k)} (\sin^4 \theta^{(k)} + \cos^4 \theta^{(k)}) \\ \bar{Q}_{16} &= (Q_{11}^{(k)} - Q_{12}^{(k)} - 2Q_{66}^{(k)}) \sin \theta^{(k)} \cos^3 \theta^{(k)} + (Q_{12}^{(k)} - Q_{22}^{(k)} + 2Q_{66}^{(k)}) \sin^3 \theta^{(k)} \cos \theta^{(k)} \\ \bar{Q}_{26} &= (Q_{11}^{(k)} - Q_{12}^{(k)} - 2Q_{66}^{(k)}) \sin^3 \theta^{(k)} \cos \theta^{(k)} + (Q_{12}^{(k)} - Q_{22}^{(k)} + 2Q_{66}^{(k)}) \sin \theta^{(k)} \cos^3 \theta^{(k)} \\ \bar{Q}_{44} &= Q_{44}^{(k)} \cos^2 \theta^{(k)} + Q_{55}^{(k)} \sin^2 \theta^{(k)} \\ \bar{Q}_{55} &= Q_{55}^{(k)} \cos^2 \theta^{(k)} + Q_{44}^{(k)} \sin^2 \theta^{(k)} \\ \bar{Q}_{45} &= (Q_{55}^{(k)} - Q_{44}^{(k)}) \sin \theta^{(k)} \cos \theta^{(k)} \end{aligned} \quad (8)$$

With

$$Q_{11}^{(k)} = \frac{E_1^{(k)}}{1 - \nu_{12}^{(k)} \nu_{21}^{(k)}}; Q_{22}^{(k)} = \frac{E_2^{(k)}}{1 - \nu_{12}^{(k)} \nu_{21}^{(k)}}; Q_{12}^{(k)} = \frac{\nu_{12}^{(k)} E_2^{(k)}}{1 - \nu_{12}^{(k)} \nu_{21}^{(k)}}; Q_{66}^{(k)} = G_{12}^{(k)}; Q_{44}^{(k)} = G_{23}^{(k)}; Q_{55}^{(k)} = G_{13}^{(k)} \quad (9)$$

Substituting the stresses computed from Eq. (7) into the weak form of the laminated composite plate under the applied loads p and then integrating the constitutive matrices through the thickness, the weak form written on the middle plane Ω is

$$\int_{\Omega} \delta \boldsymbol{\varepsilon}^T \mathbf{D}_b^* \boldsymbol{\varepsilon} d\Omega + \int_{\Omega} \delta \boldsymbol{\gamma}^T \mathbf{D}_s^* \boldsymbol{\gamma} d\Omega + \int_{\Omega} \delta \mathbf{u}^T \mathbf{m} \ddot{\mathbf{u}} d\Omega = \int_{\Omega} \delta w_0 p d\Omega \quad (10)$$

where $\mathbf{u} = [u_0 \ v_0 \ w_0 \ \beta_x \ \beta_y \ \phi_x \ \phi_y]^T$, $\ddot{\mathbf{u}} = [\ddot{u}_0 \ \ddot{v}_0 \ \ddot{w}_0 \ \ddot{\beta}_x \ \ddot{\beta}_y \ \ddot{\phi}_x \ \ddot{\phi}_y]^T$, \mathbf{m} is the lumped mass matrix [16]

$$\mathbf{m} = \begin{bmatrix} I_1 & 0 & 0 & I_2 & 0 & \frac{-4}{3h^2} I_4 & 0 \\ 0 & I_1 & 0 & 0 & I_2 & 0 & \frac{-4}{3h^2} I_4 \\ 0 & 0 & I_1 & 0 & 0 & 0 & 0 \\ I_2 & 0 & 0 & I_3 & 0 & \frac{-4}{3h^2} I_5 & 0 \\ 0 & I_2 & 0 & 0 & I_3 & 0 & \frac{-4}{3h^2} I_5 \\ \frac{-4}{3h^2} I_4 & 0 & 0 & \frac{-4}{3h^2} I_5 & 0 & \frac{16}{9h^3} I_7 & 0 \\ 0 & \frac{-4}{3h^2} I_4 & 0 & 0 & \frac{-4}{3h^2} I_5 & 0 & \frac{16}{9h^3} I_7 \end{bmatrix} \quad (11)$$

with

$$(I_1, I_2, I_3, I_4, I_5, I_7) = \int_{-h/2}^{h/2} \rho (1, z, z^2, z^3, z^4, z^6) dz, \quad (12)$$

where ρ is the mass density,

$$\mathbf{D}_b^* = \begin{bmatrix} \mathbf{A} & \mathbf{B} & \mathbf{E} \\ \mathbf{B} & \mathbf{D} & \mathbf{F} \\ \mathbf{E} & \mathbf{F} & \mathbf{H} \end{bmatrix}; \mathbf{D}_s^* = \begin{bmatrix} \mathbf{A}_s & \mathbf{B}_s \\ \mathbf{B}_s & \mathbf{D}_s \end{bmatrix} \quad (13)$$

with

$$(A_{ij}, B_{ij}, D_{ij}, E_{ij}, F_{ij}, H_{ij}) = \sum_{k=1}^n \int_{z_k}^{z_{k+1}} (1, z, z^2, z^3, z^4, z^6) \overline{Q}_{ij}^{(k)} dz \quad i, j = 1, 2, 6 \quad (14)$$

$$(A_{ij}^s, B_{ij}^s, D_{ij}^s) = \sum_{k=1}^n \int_{z_k}^{z_{k+1}} (1, z^2, z^4) \bar{Q}_{ij}^{(k)} dz \quad i, j = 4, 5 \quad (15)$$

and

$$\boldsymbol{\varepsilon} = [\boldsymbol{\varepsilon}_0^T \boldsymbol{\kappa}_1^T \boldsymbol{\kappa}_2^T]^T; \boldsymbol{\gamma} = [\boldsymbol{\gamma}_s^T \boldsymbol{\kappa}_s^T]^T \quad (16)$$

2.2 Formulation of NS-MITC3 Elements for the HSDT-Type Laminated Composite Plates

Discretize the middle plane of the laminated composite plate by three-node triangular elements with the area Ω^e . The displacements and warping functions of the middle plane in Eq. (2) are approximated by the C^0 -shape functions and nodal values as follows

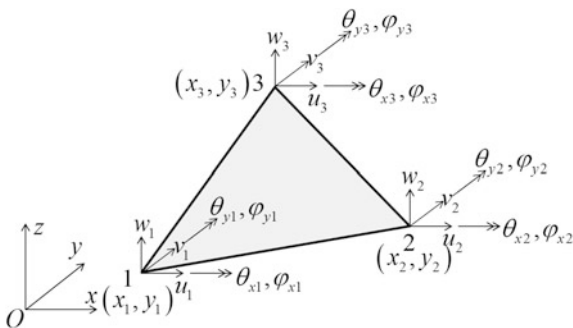
$$\begin{aligned} u_0 &= \sum_{I=1}^3 N_I u_I; v_0 = \sum_{I=1}^3 N_I v_I; w_0 = \sum_{I=1}^3 N_I w_I; \\ \beta_x &= \sum_{I=1}^3 N_I \theta_{yI}; \beta_y = - \sum_{I=1}^3 N_I \theta_{xI}; \phi_x = \sum_{I=1}^3 N_I \varphi_{yI}; \phi_y = - \sum_{I=1}^3 N_I \varphi_{xI} \end{aligned} \quad (17)$$

In which, $u_I, v_I, w_I, \theta_{xI}, \theta_{yI}, \varphi_{xI}$, and φ_{yI} are the translational, rotational displacements and warping of node I with definition of positive directions illustrated in Fig. 3, and $N_1 = 1 - \xi - \eta, N_2 = \xi, N_3 = \eta$ are the C^0 -shape functions in the natural coordinates (ξ, η) .

The approximations in Eq. (17) are substituted into Eqs. (5) and (6), and the relationships between the strains and nodal displacements \mathbf{d}_e are obtained as

$$\boldsymbol{\varepsilon}_0 = \mathbf{B}_m \mathbf{d}^e; \boldsymbol{\kappa}_1 = \mathbf{B}_{b1} \mathbf{d}^e; \boldsymbol{\kappa}_2 = \mathbf{B}_{b2} \mathbf{d}^e; \boldsymbol{\kappa}_s = \mathbf{B}_{s1} \mathbf{d}^e \quad (18)$$

Fig. 3 A three-node triangular plate element with positive directions of nodal values



$$\boldsymbol{\gamma}_s = \mathbf{B}_s \mathbf{d}^e \tag{19}$$

where $\mathbf{d}^e = [u_1 \ v_1 \ w_1 \ \theta_{x1} \ \theta_{y1} \ \varphi_{x1} \ \varphi_{y1} \ u_2 \ v_2 \ w_2 \ \theta_{x2} \ \theta_{y2} \ \varphi_{x2} \ \varphi_{y2} \ u_3 \ v_3 \ w_3 \ \theta_{x3} \ \theta_{y3} \ \varphi_{x3} \ \varphi_{y3}]^T$

$$\mathbf{B}_m = \frac{1}{2A^e} \begin{bmatrix} b-c & 0 & 0 & 0 & 0 & 0 & 0 & c & 0 & 0 & 0 & 0 & 0 & -b & 0 & 0 & 0 & 0 & 0 & 0 \\ 0 & d-a & 0 & 0 & 0 & 0 & 0 & 0 & -d & 0 & 0 & 0 & 0 & 0 & a & 0 & 0 & 0 & 0 & 0 \\ d-a & b-c & 0 & 0 & 0 & 0 & 0 & -d & c & 0 & 0 & 0 & 0 & a & -b & 0 & 0 & 0 & 0 & 0 \end{bmatrix} \tag{20}$$

$$\mathbf{B}_{b1} = \frac{1}{2A^e} \begin{bmatrix} 0 & 0 & 0 & 0 & b-c & 0 & 0 & 0 & 0 & 0 & 0 & c & 0 & 0 & 0 & 0 & 0 & -b & 0 & 0 \\ 0 & 0 & 0 & -d+a & 0 & 0 & 0 & 0 & 0 & d & 0 & 0 & 0 & 0 & 0 & 0 & -a & 0 & 0 & 0 \\ 0 & 0 & 0 & -b+c & d-a & 0 & 0 & 0 & 0 & -c & -d & 0 & 0 & 0 & 0 & 0 & b & a & 0 & 0 \end{bmatrix} \tag{21}$$

$$\mathbf{B}_{b2} = -\frac{4}{3h^2} \frac{1}{2A^e} \begin{bmatrix} 0 & 0 & 0 & 0 & b-c & 0 & 0 & 0 & 0 & c & 0 & c & 0 & 0 & 0 & 0 & -b & 0 & -b \\ 0 & 0 & 0 & -d+a & 0 & -d+a & 0 & 0 & 0 & 0 & d & 0 & 0 & 0 & 0 & -a & 0 & -a & 0 \\ 0 & 0 & 0 & -b+c & d-a & -b+c & 0 & 0 & 0 & -c & -d & -c & 0 & 0 & 0 & b & a & b & a \end{bmatrix} \tag{22}$$

$$\mathbf{B}_{s1} = -\frac{4}{h^2} \frac{1}{2A^e} \begin{bmatrix} 0 & 0 & 0 & 0 & \frac{1}{3} & 0 & \frac{1}{3} & 0 & 0 & 0 & 0 & \frac{1}{3} & 0 & \frac{1}{3} & 0 & 0 & 0 & 0 & \frac{1}{3} & 0 & \frac{1}{3} \\ 0 & 0 & 0 & -\frac{1}{3} & 0 & -\frac{1}{3} & 0 & 0 & 0 & 0 & -\frac{1}{3} & 0 & -\frac{1}{3} & 0 & 0 & 0 & 0 & -\frac{1}{3} & 0 & -\frac{1}{3} & 0 \end{bmatrix} \tag{23}$$

$$\mathbf{B}_s = \begin{bmatrix} 0 & 0 & b-c & 0 & N_1 & 0 & 0 & 0 & 0 & c & 0 & N_2 & 0 & 0 & 0 & 0 & -b & 0 & N_3 & 0 & 0 \\ 0 & 0 & d-a & -N_1 & 0 & 0 & 0 & 0 & 0 & -d & -N_2 & 0 & 0 & 0 & 0 & 0 & a & -N_3 & 0 & 0 & 0 \end{bmatrix} \tag{24}$$

Here, a , b , c , and d are computed from nodal coordinates as defined in Fig. 4, and A^e is the area of the element.

The transverse shear strains $\boldsymbol{\gamma}_s$ in Eq. (19) will not approach zero and overestimate the transverse shear energy when the plate thickness becomes thin. This shear locking of the bending plate elements is removed by separately interpolating the transverse shear strains through their values evaluated at the tying points. Lee and Bathe [8] have derived the interpolation functions of the transverse shear strains and the position of tying points in the natural coordinates, shown in Fig. 5, for three-node triangular degenerated shell elements of isotropic materials, namely MITC3. In this paper, these interpolations are explicitly formulated for the transverse shear strains of the three-node plate elements in the $Oxyz$ coordinates, which

Fig. 4 Nodal coordinates of a three-node triangular plate element

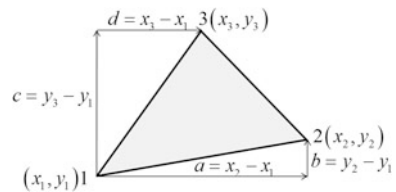
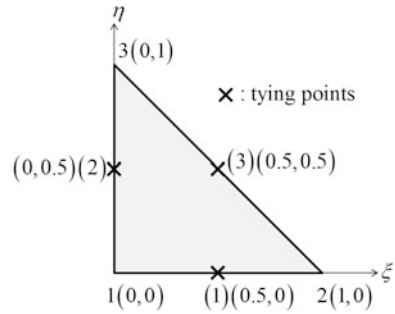


Fig. 5 Coordinates of the tying points in the natural coordinates



are used for the HSDT-type laminated composite plates. The constant MITC3 transverse shear strains within the element are related to the nodal displacements by

$$\boldsymbol{\gamma}_s^{MITC3} = \mathbf{B}_s^{MITC3} \mathbf{d}^e \tag{25}$$

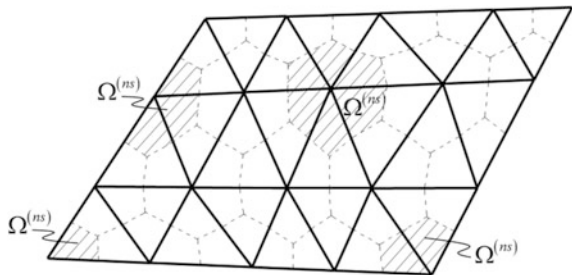
With

$$\mathbf{B}_s^{MITC3} = \frac{1}{2A^e} \begin{bmatrix} 0 & 0 & b-c & \frac{(b-c)(b+c)}{6} & A^e + \frac{(d-a)(b+c)}{6} & 0 & 0 & 0 & 0 & c & -\frac{bc}{2} + \frac{c(b+c)}{6} & \frac{ac}{2} - \frac{d(b+c)}{6} & 0 & 0 \\ 0 & 0 & d-a & -A^e - \frac{(b-c)(a+d)}{6} & -\frac{(d-a)(a+d)}{6} & 0 & 0 & 0 & 0 & -d & \frac{bd}{2} - \frac{c(a+d)}{6} & -\frac{ad}{2} + \frac{d(a+d)}{6} & 0 & 0 \\ 0 & 0 & -b & \frac{bc}{2} - \frac{b(b+c)}{6} & -\frac{bd}{2} + \frac{a(b+c)}{6} & 0 & 0 & 0 & 0 & 0 & 0 & 0 & 0 & 0 \\ 0 & 0 & a & -\frac{ac}{2} + \frac{b(a+d)}{6} & \frac{ad}{2} - \frac{a(a+d)}{6} & 0 & 0 & 0 & 0 & 0 & 0 & 0 & 0 & 0 \end{bmatrix} \tag{26}$$

To attenuate the stepped constant strains between elements, the node-based smooth FEM [11, 16] is employed. Based on this approach, the strains are averaged over domains $\Omega^{(ns)}$ defined by segments connecting the centroid(s) and centers of edges of element(s) around a common node as illustrated in Fig. 6. As a result, the strains are smoothed

$$\tilde{\boldsymbol{\epsilon}}_0 = \frac{1}{A^{(ns)}} \int_{\Omega^{(ns)}} \boldsymbol{\epsilon}_0 d\Omega; \tilde{\boldsymbol{\kappa}}_1 = \frac{1}{A^{(ns)}} \int_{\Omega^{(ns)}} \boldsymbol{\kappa}_1 d\Omega; \tilde{\boldsymbol{\kappa}}_2 = \frac{1}{A^{(ns)}} \int_{\Omega^{(ns)}} \boldsymbol{\kappa}_2 d\Omega \tag{27}$$

Fig. 6 Node-smoothed domains of a plate discretized by the three-node triangular elements



$$\tilde{\gamma}_s^{MITC3} = \frac{1}{A^{(ns)}} \int_{\Omega^{(ns)}} \boldsymbol{\gamma}_s^{MITC3} d\Omega; \tilde{\kappa}_s = \frac{1}{A^{(ns)}} \int_{\Omega^{(ns)}} \boldsymbol{\kappa}_s d\Omega \quad (28)$$

where $A^{(ns)}$ is the area of the node-based smooth domain $\Omega^{(ns)}$.

Replacing the constant strains over elements given in Eqs. (18) and (25) into the smoothed strains, we have

$$\tilde{\boldsymbol{\epsilon}}_0 = \tilde{\mathbf{B}}_m^{(ns)} \mathbf{d}^{(ns)}; \tilde{\boldsymbol{\kappa}}_1 = \tilde{\mathbf{B}}_{b1}^{(ns)} \mathbf{d}^{(ns)}; \tilde{\boldsymbol{\kappa}}_2 = \tilde{\mathbf{B}}_{b2}^{(ns)} \mathbf{d}^{(ns)} \quad (29)$$

$$\tilde{\boldsymbol{\gamma}}_s^{MITC3} = \tilde{\mathbf{B}}_s^{(ns)MITC3} \mathbf{d}^{(ns)}; \tilde{\boldsymbol{\kappa}}_s = \tilde{\mathbf{B}}_{s1}^{(ns)} \mathbf{d}^{(ns)} \quad (30)$$

Here, $\mathbf{d}^{(ns)}$ is the nodal displacements of the domain $\Omega^{(ns)}$ and

$$\tilde{\mathbf{B}}_m^{(ns)} = \frac{1}{A^{(ns)}} \sum_{e=1}^{N_e^{(ns)}} \frac{A_e}{3} \mathbf{B}_m^e; \tilde{\mathbf{B}}_{b1}^{(ns)} = \frac{1}{A^{(ns)}} \sum_{e=1}^{N_e^{(ns)}} \frac{A_e}{3} \mathbf{B}_{b1}^e; \tilde{\mathbf{B}}_{b2}^{(ns)} = \frac{1}{A^{(ns)}} \sum_{e=1}^{N_e^{(ns)}} \frac{A_e}{3} \mathbf{B}_{b2}^e \quad (31)$$

$$\tilde{\mathbf{B}}_s^{(ns)MITC3} = \frac{1}{A^{(ns)}} \sum_{e=1}^{N_e^{(ns)}} \frac{A_e}{3} \mathbf{B}_s^{MITC3,e}; \tilde{\mathbf{B}}_{s1}^{(ns)} = \frac{1}{A^{(ns)}} \sum_{e=1}^{N_e^{(ns)}} \frac{A_e}{3} \mathbf{B}_{s1}^e \quad (32)$$

In which, $N_e^{(ns)}$ is number of the elements e belonging to the node-based smoothed domain $\Omega^{(ns)}$, and $\mathbf{B}_m^e, \mathbf{B}_{b1}^e, \mathbf{B}_{b2}^e, \mathbf{B}_s^{MITC3,e}, \mathbf{B}_{s1}^e$ are, respectively, computed from Eqs. (20), (21), (22), (26), and (23) for the element e .

Therefore, the weak form in Eq. (10) can be derived to discretized equilibrium equations by the standard FEM as follows

$$\mathbf{M}\ddot{\mathbf{d}} + \mathbf{K}\mathbf{d} = \mathbf{F} \quad (33)$$

where, \mathbf{d} is the nodal displacements of the plate, \mathbf{K} is the global stiffness matrix assembled from stiffness matrices $\tilde{\mathbf{K}}^{(ns)}$ of the node-based domains $\Omega^{(ns)}$ given by

$$\tilde{\mathbf{K}}^{(ns)} = \begin{bmatrix} \tilde{\mathbf{B}}_m^{(ns)} \\ \tilde{\mathbf{B}}_{b1}^{(ns)} \\ \tilde{\mathbf{B}}_{b2}^{(ns)} \end{bmatrix}^T \mathbf{D}_b^* \begin{bmatrix} \tilde{\mathbf{B}}_m^{(ns)} \\ \tilde{\mathbf{B}}_{b1}^{(ns)} \\ \tilde{\mathbf{B}}_{b2}^{(ns)} \end{bmatrix} A^{(ns)} + \begin{bmatrix} \tilde{\mathbf{B}}_s^{(ns)MITC3} \\ \tilde{\mathbf{B}}_{s1}^{(ns)} \end{bmatrix}^T \mathbf{D}_s^* \begin{bmatrix} \tilde{\mathbf{B}}_s^{(ns)MITC3} \\ \tilde{\mathbf{B}}_{s1}^{(ns)} \end{bmatrix} A^{(ns)} \quad (34)$$

\mathbf{F} is the global force vector assembled from the element force vectors

$$\mathbf{F}_I^e = \int_{\Omega^e} p[00N_I0000]^T d\Omega \quad (35)$$

and \mathbf{M} is the global mass matrix assembled from the element mass matrices

$$\mathbf{M}_{IJ}^e = \int_{\Omega^e} \mathbf{N}_I^T \mathbf{m} \mathbf{N}_J d\Omega \tag{36}$$

with

$$\mathbf{N}_I = \begin{bmatrix} N_I & 0 & 0 & 0 & 0 & 0 & 0 \\ 0 & N_I & 0 & 0 & 0 & 0 & 0 \\ 0 & 0 & N_I & 0 & 0 & 0 & 0 \\ 0 & 0 & 0 & 0 & -N_I & 0 & 0 \\ 0 & 0 & 0 & N_I & 0 & 0 & 0 \\ 0 & 0 & 0 & 0 & 0 & 0 & -N_I \\ 0 & 0 & 0 & 0 & 0 & N_I & 0 \end{bmatrix} \tag{37}$$

We solve $\mathbf{Kd} = \mathbf{F}$ for static analysis and determinant of $(\mathbf{K} - \omega_i^2 \mathbf{M})$ equal to 0 for natural frequencies ω_i .

3 Numerical Examples

3.1 Static Analysis of Laminated Composite Plates

In these examples, simply supported square laminated composite plates of the a -length and the h -thickness are considered. The plates are subjected to uniformly distributed load p in Fig. 7 or sinusoidal distributed load $p \sin(\pi x/a) \sin(\pi y/a)$ in

Fig. 7 The $[0^\circ/90^\circ/90^\circ/0^\circ]$ laminated composite plate under uniformly distributed load

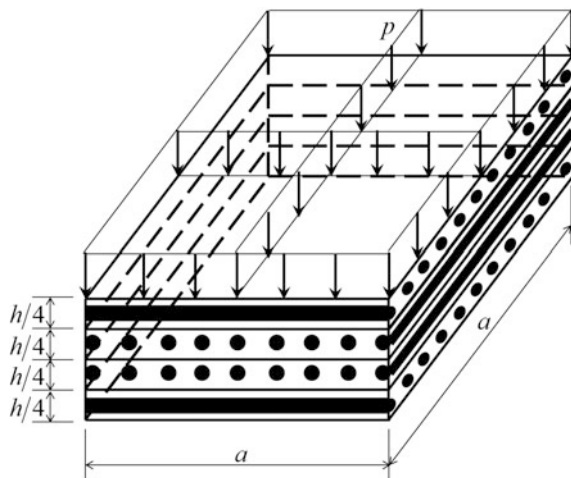


Fig. 8 The $[0^\circ/90^\circ]$ laminated composite plate under sinusoidal distributed load

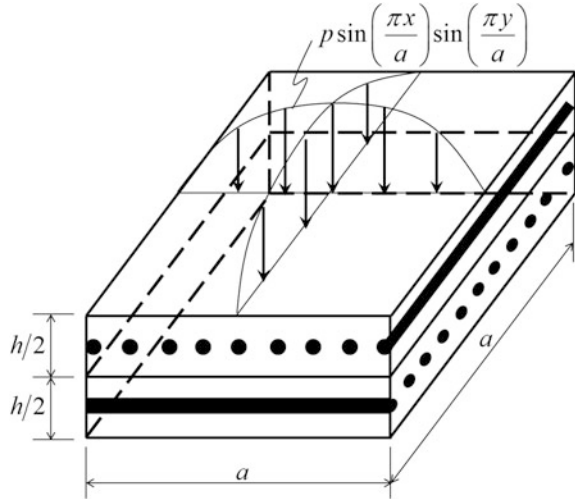


Fig. 8. The h -thick plate is made of layers that have the identical thicknesses. The material properties of each layer are $E_2 = 1$, $E_1 = 25E_2$, $G_{12} = G_{13} = 0.5E_2$, $G_{23} = 0.2E_2$, and $\nu_{12} = 0.25$.

To compare with other reference results, the behaviors of the plates are normalized as follows

$$\begin{aligned} \bar{w} &= \frac{100E_2h^3}{pa^4} w\left(\frac{a}{2}, \frac{a}{2}, 0\right); \bar{\sigma}_x = \frac{h^2}{pa^2} \sigma_x\left(\frac{a}{2}, \frac{a}{2}, \frac{h}{2}\right); \bar{\sigma}_y = \frac{h^2}{pa^2} \sigma_y\left(\frac{a}{2}, \frac{a}{2}, \frac{h}{4}\right); \\ \bar{\tau}_{xy} &= \frac{h^2}{pa^2} \tau_{xy}\left(0, 0, \frac{h}{2}\right); \bar{\tau}_{xz} = \frac{h}{pa} \tau_{xz}\left(0, \frac{a}{2}, 0\right); \bar{\tau}_{yz} = \frac{h}{pa} \tau_{yz}\left(\frac{a}{2}, 0, 0\right) \end{aligned}$$

3.1.1 Four-Layer $[0^\circ/90^\circ/90^\circ/0^\circ]$ Square Composite Plate Under Uniform or Sinusoidal Load

Consider a four symmetric crossply layer $[0^\circ/90^\circ/90^\circ/0^\circ]$ composite plate subjected by the uniformly distributed load p or sinusoidal distributed load $p \sin(\pi x/a) \sin(\pi y/a)$. The length-to-thickness ratio a/h is 5 or 20 for the uniform load case and 4, 20, or 100 for the sinusoidal load case.

To investigate the convergent rate, the displacements at the center of the plate under the sinusoidal load are computed by using variously regular mesh of $N \times N \times 2$ NS-MITC3 elements, in which $N = 8, 12, 16,$ and 20 are the number of elements on each edge of the plate. The reference value analytically solved by Reddy [22] is chosen to calculate the relative errors of the central displacements given by the NS-MITC3, NS-DSG3 [16], and ES-DSG3 [18]. Figure 9a, b shows the convergent rates of the NS-MITC3, NS-DSG3, and ES-DSG3 in the case of $a/h = 4$ and

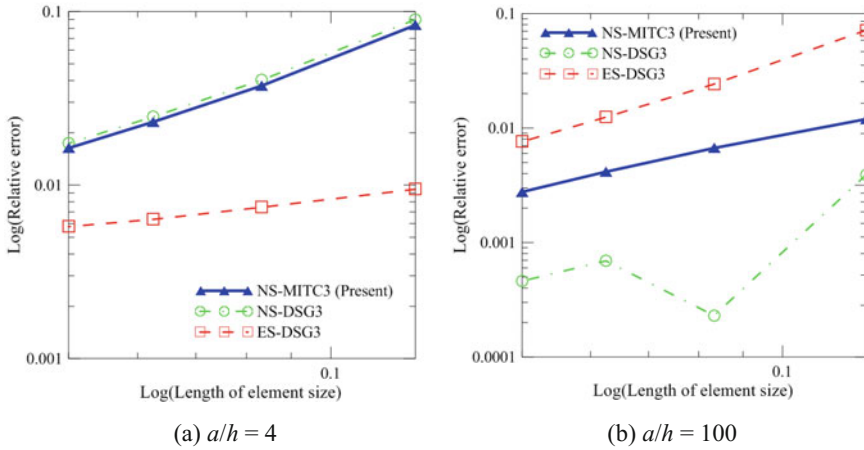


Fig. 9 Convergent rates of the $[0^\circ/90^\circ/90^\circ/0^\circ]$ square plate under sinusoidal load

$a/h = 100$, respectively. In the both thick and thin plates, the convergent rate of NS-MITC3 is similar to those of NS-DSG3 and ES-DSG3. In the thick plate, the NS-MITC3 is more accurate than NS-DSG3 but less accurate than ES-DSG3. In contrast, the NS-MITC3 is more accurate than ES-DSG3 but less accurate than NS-DSG3 in the case of thin plate.

Due to the reasonable results provided by the mesh of $20 \times 20 \times 2$ elements, this mesh is employed to compute results of the NS-MITC3 elements in all examples of this paper. Numerical results given by the NS-MITC3 elements are shown in Table 1 for the uniform load and Table 2 for the sinusoidal load. Tables 1 and 2 also present reference results provided by the NS-DSG3 elements [16], the

Table 1 Normalized deflection and stresses of the four-layer composite plate under uniform load

a/h	Method	\bar{w}	$\bar{\sigma}_x$	$\bar{\sigma}_y$	$\bar{\tau}_{xy}$	$\bar{\tau}_{xz}$	$\bar{\tau}_{yz}$
5	3D-FEM [23]	2.1044	0.8995	0.7386	0.0991	0.5340	0.4240
	HSDT-MQ [23]	1.8736	0.8640	0.6720	0.0740	0.7320	0.6860
	HSDT-NS-DSG3 [16]	2.1936	0.9202	0.8287	0.0900	0.5846	0.5086
	HSDT-NS-MITC3	2.1932	0.9204	0.8310	0.0816	0.4376	0.5142
20	3D-FEM [23]	0.7794	0.8207	0.4870	0.0444	0.6040	0.4545
	HSDT-MQ [23]	0.7538	0.8100	0.4750	0.0408	0.8250	0.6950
	HSDT-NS-DSG3 [16]	0.7966	0.8251	0.4144	0.0469	0.6940	0.3934
	HSDT-NS-MITC3	0.7982	0.8260	0.4151	0.0433	0.5812	0.3945

Table 2 Normalized deflection and stresses of the four-layer composite plate under sinusoidal load

a/h	Method	\bar{w}	$\bar{\sigma}_x$	$\bar{\sigma}_y$	$\bar{\tau}_{xy}$	$\bar{\tau}_{xz}$	$\bar{\tau}_{yz}$
4	3D-Elasticity [24]	1.9540	0.7200	0.6660	0.0467	0.2700	–
	HSDT-Elasticity [22]	1.8937	0.6651	0.6322	0.0440	0.2064	0.2390
	HSDT-ES-DSG3 [18]	1.9046	0.7005	0.6236	0.0476	0.2071	0.2387
	HSDT-NS-DSG3 [16]	1.9266	0.7076	0.6303	0.0475	0.2084	0.2404
	HSDT-NS-MITC3	1.9246	0.7076	0.6320	0.0449	0.2139	0.2461
20	3D-Elasticity [24]	0.5170	0.5430	0.3090	0.0230	0.3280	–
	HSDT-Elasticity [22]	0.5060	0.5393	0.3043	0.0228	0.2825	0.1230
	HSDT-ES-DSG3 [18]	0.5047	0.5380	0.3019	0.0236	0.3033	0.1273
	HSDT-NS-DSG3 [16]	0.5089	0.5433	0.3050	0.0234	0.3051	0.1266
	HSDT-NS-MITC3	0.5099	0.5438	0.3055	0.0224	0.3069	0.1276
100	3D-Elasticity [24]	0.4347	0.5390	0.2710	0.0214	0.3390	–
	HSDT-Elasticity [22]	0.4343	0.5387	0.2708	0.0213	0.2897	0.139
	HSDT-ES-DSG3 [18]	0.4310	0.5331	0.2680	0.0213	0.3222	0.1365
	HSDT-NS-DSG3 [16]	0.4345	0.5384	0.2706	0.0211	0.3183	0.1183
	HSDT-NS-MITC3	0.4355	0.5390	0.2710	0.0210	0.3167	0.1146

meshless local Petrov–Galerkin method (MLPG) with the multiquadric (MQ) radial basis functions [23], the FEM using 20-node brick elements of the commercial package ABAQUS [23], the exact closed-form solutions of the three-dimensional model of Pagano [24] and the HSDT of Reddy [22]. Compared to the three-dimensional solutions, the NS-MITC3 elements can give more accurate results of the deflection and stresses than those given by the MLPG and the closed-form solutions suggested by Reddy in the cases of uniform or sinusoidal loads. The similar results provided by the NS-MITC3 and NS-DSG3 elements show that the NS-MITC3 elements are also reasonable competitor used for static analyses of HSDT-type laminated composite plates.

The distributions of the normalized normal stress $\bar{\sigma}_x$ at point $(a/2, a/2)$ and the transverse shear strain $\bar{\tau}_{xz}$ at point $(0, a/2)$ through the thickness of the 4-layer composite laminated plate under the uniform load are illustrated in Fig. 10 and Fig. 11, respectively.

Fig. 10 $\bar{\sigma}_x$ through the thickness of the 4-layer plate under the uniform load at point $(a/2, a/2)$ given by the NS-MITC3 elements

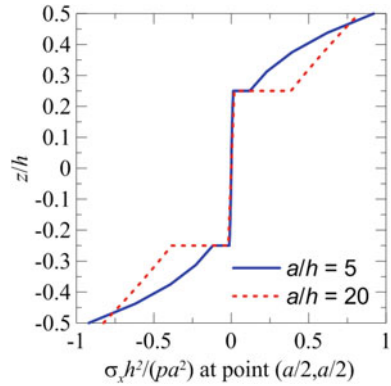
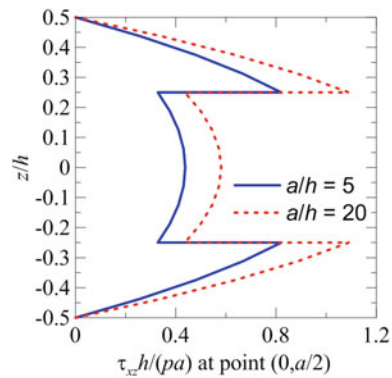


Fig. 11 $\bar{\tau}_{xz}$ through the thickness of the 4-layer plate under the uniform load at point $(0, a/2)$ given by the NS-MITC3 elements



3.1.2 Two-Layer $[0^\circ/90^\circ]$ Square Composite Plate Under Sinusoidal Load

Give an antisymmetric crossply laminated plate consisting of 0° and 90° layers. The plate is applied a sinusoidal distributed load $p \sin(\pi x/a) \sin(\pi y/a)$. The length-to-thickness ratio a/h is 4, 10, or 100.

Table 3 shows the normalized deflection and stresses provided by the NS-MITC3 elements, the closed-form solutions of the three-dimensional elasticity [24] and the HSDT elasticity [22, 25], and the FEM solutions using four-node quadrilateral elements with reduced integration for the transverse shear strain energy [26]. Except for the deflection of the thick laminated composite plate with $a/h = 4$, the present elements, NS-MITC3, gave the numerical results in good agreements with the closed-form solutions of three-dimensional elasticity [24] and lightly better than those of the HSDT solutions [22] and even the four-node quadrilateral elements [26].

Table 3 Normalized deflection and stresses of the two-layer composite plate under sinusoidal load

a/h	Method	\bar{w}	$\bar{\sigma}_x$	$\bar{\tau}_{xy}$	$\bar{\tau}_{xz}$
4	3D-Elasticity [24]	1.7287	-0.7807	-0.0591	0.1353
	HSDT-Elasticity [22, 25]	1.6760	-0.8385	-0.0558	-
	HSDT-RQ4 [26]	1.9563	-1.0181	-0.0600	0.1327
	HSDT-NS-MITC3	2.0513	-0.8323	-0.0553	0.1163
10	3D-Elasticity [24]	1.2318	-0.7300	-0.0538	0.1250
	HSDT-Elasticity [22, 25]	1.2161	-0.7468	-0.0533	-
	HSDT-RQ4 [26]	1.2125	-0.7644	-0.0542	0.1324
	HSDT-NS-MITC3	1.2249	-0.7368	-0.0525	0.1193
100	3D-Elasticity [24, 25]	1.0742	-0.7219	-0.0529	-
	HSDT-Elasticity [22, 25]	1.0651	-0.7161	-0.0525	-
	HSDT-RQ4 [26]	1.0656	-0.7229	-0.0530	0.1319
	HSDT-NS-MITC3	1.0677	-0.7161	-0.0518	0.1205

Fig. 12 $\bar{\sigma}_x$ through the thickness of the $[0^\circ/90^\circ]$ plate under the sinusoidal load at point $(a/2, a/2)$ given by the NS-MITC3 elements

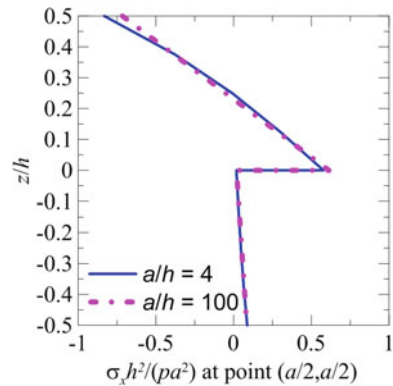


Figure 12 and Fig. 13, respectively, show the distributions of $\bar{\sigma}_x$ at $(a/2, a/2)$ and $\bar{\tau}_{xz}$ at $(0, a/2)$ through the antisymmetric crossply laminated plate under the sinusoidal load for the length-to-thickness $a/h = 4$ and 100.

3.2 Static Analysis of Sandwich Plate

A square sandwich plate of length a and thickness h is made of 3 layers including a core and 2 skins as shown in Fig. 14. The plate is simply supported and subjected to a sinusoidal distributed load $p \sin(\pi x/a) \sin(\pi y/a)$. The thickness of core is $0.8 h$, and the thickness of each skin is $0.1 h$. The material properties of the core are $E_{1c} = 0.04$, $E_{2c} = 0.04$, $G_{12c} = 0.016$, $G_{13c} = G_{23c} = 0.06$, $\nu_{12c} = \nu_{23c} = \nu_{13c} = 0.25$ and those

Fig. 13 $\bar{\tau}_{xz}$ through the thickness of the $[0^\circ/90^\circ]$ plate under the sinusoidal load at point $(0, a/2)$ given by the NS-MITC3 elements

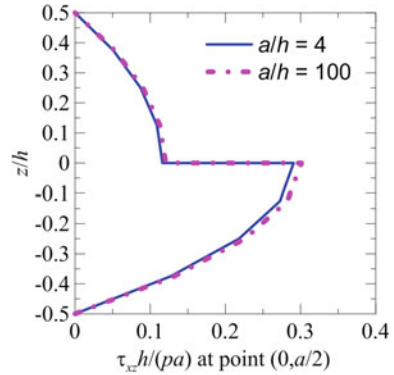
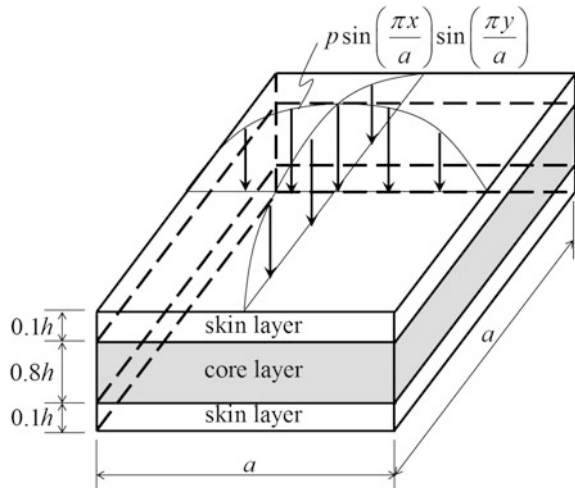


Fig. 14 Simply supported 3-layer sandwich plate under sinusoidal distributed load



of skins are $E_{1s} = 25$, $E_{2s} = 1$, $G_{12s} = 0.5$, $G_{13s} = G_{23s} = 0.2$, $\nu_{12s} = \nu_{23s} = \nu_{13s} = 0.25$.

For comparison, the following nondimensional deflection and stresses are used

$$\begin{aligned} \bar{w} &= \frac{100h^3}{pa^4} w\left(\frac{a}{2}, \frac{a}{2}, 0\right); \bar{\sigma}_x = \frac{h^2}{pa^2} \sigma_x\left(\frac{a}{2}, \frac{a}{2}, \frac{h}{2}\right); \bar{\sigma}_y = \frac{h^2}{pa^2} \sigma_y\left(\frac{a}{2}, \frac{a}{2}, \frac{h}{2}\right); \\ \bar{\tau}_{xz} &= \frac{h}{pa} \tau_{xz}\left(0, \frac{a}{2}, 0\right); \bar{\tau}_{yz} = \frac{h}{pa} \tau_{yz}\left(\frac{a}{2}, 0, 0\right) \end{aligned}$$

The nondimensional deflection and stresses given by the NS-MITC3 elements for different length-to-thickness ratio $a/h = 4, 10, 20, 100$ of the sandwich plate are shown in Table 4. The results of the present elements are not as good as those of the three-dimensional elasticity [24], the 9-node quadrilateral elements are based on higher-order zigzag plate theory (HOZT) [27], and the ES-DSG3 elements are

Table 4 Nondimensional deflection and stresses of the sandwich plate under sinusoidal load

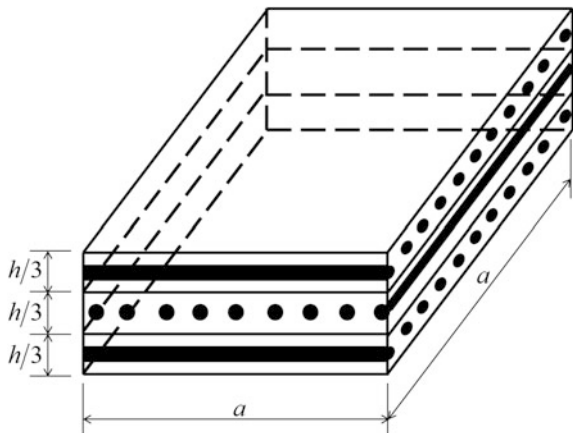
a/h	Method	\bar{w}	$\bar{\sigma}_x$	$\bar{\sigma}_y$	$\bar{\tau}_{xz}$	$\bar{\tau}_{yz}$
4	3D-Elasticity [24]	7.5962	1.5560	0.2595	0.2390	0.1072
	HOZT-FEMQ9 [27]	7.5822	1.5306	0.2581	0.2436	0.1147
	Layerwise-ES-DSG3 [28]	7.6613	1.4600	0.2477	0.2343	0.1021
	HSDT-NS-MITC3	7.2323	1.5068	0.2395	0.2834	0.1172
10	3D-Elasticity [24]	2.2004	1.1153	0.1104	0.3000	0.0527
	HOZT-FEMQ9 [27]	2.1775	1.1528	0.1143	0.3058	0.0575
	Layerwise-ES-DSG3 [28]	2.1980	1.1378	0.1079	0.2957	0.0504
	HSDT-NS-MITC3	2.0991	1.1500	0.1044	0.3504	0.0583
20	3D-Elasticity [24]	1.2264	1.1100	0.0700	0.3170	0.0361
	HOZT-FEMQ9 [27]	1.2121	1.1103	0.0742	0.3272	0.0399
	Layerwise-ES-DSG3 [28]	1.2212	1.0987	0.0690	0.3140	0.0352
	HSDT-NS-MITC3	1.1990	1.1096	0.0683	0.3689	0.0413
100	3D-Elasticity [24]	0.8923	1.0980	0.0550	0.3240	0.0297
	HOZT-FEMQ9 [27]	0.8814	1.0982	0.0592	0.3426	0.0322
	Layerwise-ES-DSG3 [28]	0.8867	1.0872	0.0544	0.3244	0.0326
	HSDT-NS-MITC3	0.8934	1.0980	0.0549	0.3764	0.0352

based on the first-order layerwise plate theory [28], especially in the cases of thick sandwich plates. It can be explained by the ESL model used in this paper.

3.3 Frequency Analysis of Laminated Composite Plate

Consider a clamped $[0^\circ/90^\circ/0^\circ]$ square plate with the length-to-thickness ratios $a/h = 10$ or 100 , see Fig. 15. Each layer has the identical thickness and properties of

Fig. 15 Clamped $[0^\circ/90^\circ/0^\circ]$ laminated composite plate for frequency analysis



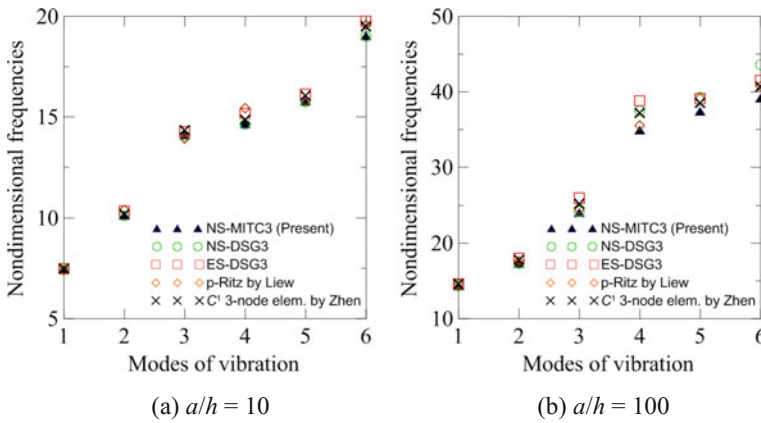


Fig. 16 First 6 nondimensional frequencies of a clamped [0°/90°/0°] squared plate

$E_2 = 1$, $E_1 = 40E_2$, $G_{12} = G_{13} = 0.6E_2$, $G_{23} = 0.5E_2$, $\nu_{12} = 0.25$, and $\rho = 1$. In order to easily compare with other references, the nondimensional natural frequency $\bar{\omega}_i = (\omega_i a^2 / \pi^2) \sqrt{\rho h / D_0}$ with $D_0 = E_2 h^3 / 12 / (1 - \nu_{12} \nu_{21})$ is used. The first 6 nondimensional frequencies given by the mesh of $20 \times 20 \times 2$ NS-MITC3 elements are shown in Fig. 16a for $a/h = 10$ and Fig. 16b for $a/h = 100$ and similar to those provided by p-Ritz solution [29], C^1 -type three-node triangular elements [30], and smoothed FEM combined with DSG3 technique as NS-DSG3 [16], ES-DSG3 [18]. It can be commented that the NS-MITC3 elements are good competitor for the analysis of free vibration.

4 Conclusions

The node-based smoothed three-node triangular plate elements, NS-MITC3, were studied for static and frequency analyses of laminated composite plates using the HSDT based on ESL model. Based on the MITC3 technique, the gradient transverse shear strains are explicitly formulated to be dependent on nodal coordinates of elements. All the constant strains within elements are averaged over the domains defined by elements shearing common nodes. The numerical results given by the present elements are in good agreements with the references in static analyses of symmetric, antisymmetric laminated composite, and sandwich plates with various thicknesses. The suggested elements also give reasonable natural frequencies of thin and thick laminated composite plates. The NS-MITC3 elements are competitor against other C^0 -type HSDT laminated plate elements.

References

1. Reddy JN (2004) Mechanics of laminated composite plates and shells—theory and analysis, 2nd edn. CRC Press
2. Zienkiewicz OC, Taylor RL, Too JM (1971) Reduced integration technique in general analysis of plates and shells. *Int J Numer Methods Eng* 3:275–290
3. Hughes TJR, Cohen M, Haroun M (1978) Reduced and selective integration techniques in the finite element analysis of plates. *Nucl Eng Des* 46:203–222
4. Kim JH, Kim YH (2002) Three-node macro triangular shell element based on the assumed natural strains. *Comput Mech* 29:441–458
5. Andelfinger U, Ramm E (1993) EAS-elements for two-dimensional, three-dimensional, plate and shell structures and their equivalence to HR-elements. *Int J Numer Methods Eng* 36:1311–1337
6. Bletzinger K-U, Bischoff M, Ramm E (2000) A unified approach for shear-locking-free triangular and rectangular shell finite elements. *Comput Struct* 75:321–334
7. Bathe K-J, Dvorkin EN (1985) A four-node plate bending element based on Mindlin/Reissner plate theory and a mixed interpolation. *Int J Numer Meth Eng* 21:367–383
8. Lee P-S, Bathe K-J (2004) Development of MITC isotropic triangular shell finite elements. *Comput Struct* 82:945–962
9. Shankara CA, Iyengar NGR (1996) A C^0 element for the free vibration analysis of laminated composite plates. *J Sound Vib* 191:721–738
10. Nguyen TN, Thai CH, Nguyen-Xuan H (2016) On the general framework of high order shear deformation theories for laminated composite plate structures: A novel unified approach. *Int J Mech Sci* 110:242–255
11. Liu GR, Nguyen-Thoi T (2010) Smoothed finite element methods. CRC Press
12. Liu GR, Nguyen-Thoi T, Lam KY (2009) An edge-based smoothed finite element method (ES-FEM) for static, free and forced vibration analyses of solids. *J Sound Vib* 320:1100–1130
13. Nguyen-Xuan H, Rabczuk T, Nguyen-Thanh N, Nguyen-Thoi T, Bordas S (2010) A node-based smoothed finite element method with stabilized discrete shear gap technique for analysis of Reissner-Mindlin plates. *Comput Mech* 46:679–701
14. Nguyen-Thoi T, Phung-Van P, Luong-Van H, Nguyen-Van H, Nguyen-Xuan H (2012) A cell-based smoothed three-node Mindlin plate element (CS-MIN3) for static and free vibration analyses of plates. *Comput Mech* 51:65–81
15. Nguyen-Thoi T, Phung-Van P, Nguyen-Xuan H, Thai-Hoang C (2012) A cell-based smoothed discrete shear gap method using triangular elements for static and free vibration analyses of Reissner-Mindlin plates. *Int J Numer Methods Eng* 91:705–741
16. Thai CH, Tran LV, Tran DT, Nguyen-Thoi T, Nguyen-Xuan H (2012) Analysis of laminated composite plates using higher-order shear deformation plate theory and node-based smoothed discrete shear gap method. *Appl Math Model* 36:5657–5677
17. Phung-Van P, Nguyen-Thoi T, Bui-Xuan T, Lieu-Xuan Q (2015) A cell-based smoothed three-node Mindlin plate element (CS-FEM-MIN3) based on the C^0 -type higher-order shear deformation for geometrically nonlinear analysis of laminated composite plates. *Comput Mater Sci Part B* 96:549–558
18. Tran LV, Nguyen-Thoi T, Thai CH, Nguyen-Xuan H (2015) An edge-based smoothed discrete shear gap method using the c^0 -type higher-order shear deformation theory for analysis of laminated composite plates. *Mech Adv Mater Struct* 22:248–268
19. Nguyen-Xuan H, Tran LV, Thai CH, Nguyen-Thoi T (2012) Analysis of functionally graded plates by an efficient finite element method with node-based strain smoothing. *Thin-Walled Struct* 54:1–18
20. Chau-Dinh T, Nguyen-Duy Q, Nguyen-Xuan H (2017) Improvement on MITC3 plate finite element using edge-based strain smoothing enhancement for plate analysis. *Acta Mech* 228:2141–2163

21. Châu Đình T, Nguyễn Văn D (2016) Static and vibration analyses of laminated composite plates using MITC3 elements having strains averaged on node-based domains (NS-MITC3). In: National conference on composite materials and structures. Construction Publishing House, Nha Trang, Vietnam, (in Vietnamese)
22. Reddy JN (1984) A simple higher-order theory for laminated composite plates. *J Appl Mech* 51:745–752
23. Xiao JR, Gilhooley DF, Batra RC, Gillespie JW, McCarthy MA (2008) Analysis of thick composite laminates using a higher-order shear and normal deformable plate theory (HOSNDPT) and a meshless method. *Compos B Eng* 39:414–427
24. Pagano NJ (1970) Exact Solutions for Rectangular Bidirectional Composites and Sandwich Plates. *J Compos Mater* 4:20–34
25. Lee SJ, Kim HR (2013) FE analysis of laminated composite plates using a higher order shear deformation theory with assumed strains. *Lat Am J Solids Struct* 10:523–547
26. Kant T, Pandya BN (1988) A simple finite element formulation of a higher-order theory for unsymmetrically laminated composite plates. *Compos Struct* 9:215–246
27. Chalak HD, Chakrabarti A, Iqbal MA, Hamid A (2012) Sheikh. An improved C0 FE model for the analysis of laminated sandwich plate with soft core. *Finite Elem Anal Des* 56:20–31
28. Phung-Van P, Thai CH, Nguyen-Thoi T, Nguyen-Xuan H (2014) Static and free vibration analyses of composite and sandwich plates by an edge-based smoothed discrete shear gap method (ES-DSG3) using triangular elements based on layerwise theory. *Compos B Eng* 60:227–238
29. Liew KM (1996) Solving the vibration of thick symmetric laminates by Reissner/Mindlin plate theory and the p-Ritz method. *J Sound Vib* 198:343–360
30. Zhen W, Wanji C (2006) Free vibration of laminated composite and sandwich plates using global–local higher-order theory. *J Sound Vib* 298:333–349

Equivalent Inclusion Approach and Approximations for Thermal Conductivity of Composites with Fibrous Fillers



Nguyen Trung Kien, Nguyen Thi Hai Duyen and Pham Duc Chinh

Abstract Based on the polarization approximations, the expression for the thermal conductivity of composites with randomly oriented inclusions of fiber forms is firstly derived. Equivalent inclusion approach is then developed to account for possible diversions such as non-idealistic geometric forms of the inhomogeneities, or the fact that the conductivity of the fibers is unknown, using reference conductivity data. Applications involving experimental data from the literature show the usefulness of the approach.

Keywords Effective conductivity · Polarization approximations · Fibrous fillers

1 Introduction

A macroscopic transport property of many practical composites, such as the thermal conductivity, is difficult to be determined analytically. Many effective medium approximations (EMA) and micro-mechanic schemes have been developed to estimate the effective properties [1–5]. Most effective medium approximations use analytical dilute solution results for an ellipsoidal inclusion embedded in an infinite matrix as the references, and they converge at those dilute limits. Though in many practical cases the inhomogeneities may have the forms close to the extreme spherical, circular cylinder (fiber), platelet ones, they often do not have those exact ideal-

N. Trung Kien (✉)

Research and Application Center for Technology in Civil Engineering,
University of Transport and Communications, 3 Cau Giay, Dong Da Hanoi, Vietnam
e-mail: ntkien@utc.edu.vn

N. T. Hai Duyen

Division of Engineering Mechanics, Faculty of Mechanical Engineering,
Thuy loi University, Hanoi, Vietnam
e-mail: duyennt@tlu.edu.vn

P. D. Chinh

VAST Institute of Mechanics, 264 Doi Can, Hanoi, Vietnam
e-mail: pdchinh@imech.vast.vn

© Springer Nature Singapore Pte Ltd. 2018

H. Nguyen-Xuan et al. (eds.), *Proceedings of the International Conference on Advances in Computational Mechanics 2017*, Lecture Notes in Mechanical Engineering, https://doi.org/10.1007/978-981-10-7149-2_29

istic forms. The sizes of the inhomogeneities may be down to the nanosizes (such as nanotubes and nanoplates), and it may be not easy to give them the appropriate exact conductivity values for use in calculating the conductivity of a composite. Instead, empirical and semiempirical formulae are developed and used widely by the practitioners in the field to estimate macroscopic conductivities of the composites over a range of components' proportions [6–11].

In [12], from the minimum energy principles, the polarization approximations have been constructed for effective conductivity of isotropic multicomponent materials, which can use dilute solution reference or reference at components' finite volume proportions, that always lie within Hashin–Shtrikman (HS) bounds over all the ranges of volume proportions of the component materials. In the case of two-component matrix composites with inclusions of ellipsoidal forms, the approximation using dilute solution reference coincides with the well-known Mori–Tanaka approximation. In this paper, those approximations with equivalent inclusion approach shall be used in conjunction with experimental data to estimate the effective conductivity of matrix composites from literature with fibrous fillers.

2 Polarization Approximation and Equivalent Inclusion Approach

Let us consider an isotropic multicomponent material that consists of n components of volume proportions v_i having conductivities c_i ($i = 1, \dots, n$). The polarization approximation for the effective conductivity c^{eff} of the composite constructed from the minimum energy principles, under condition of perfect contact between the component materials, has the particular form [12]

$$c^{eff} = P_c(c_0) = \left(\sum_{i=1}^n \frac{v_i}{c_i + 2c_0} \right)^{-1} - 2c_0 \quad (1)$$

where the reference parameter c_0 should be determined from a reference dilute solution result or reference effective conductivity of the composite at certain finite volume proportions of the components. Note that, function $P_c(c_0)$ has the remarkable property that it is a positive monotonous-increasing function of the positive parameter c_0 . With the reference parameter c_0 lying within the limits

$$c_{min} = \min\{c_1, \dots, c_n\} \leq c_0 \leq c_{max} = \max\{c_1, \dots, c_n\}, \quad (2)$$

the function $P_c(c_0)$ increases from Hashin–Shtrikmans lower (HSL) to upper (HSU) bounds, which read

$$P_c(c_{min}) \leq c^{eff} \leq P_c(c_{max}) \quad (3)$$

In the case of two-component matrix composites, Eq. (1) simplifies to

$$c^{eff} = P_c(c_0) = \left(\frac{v_M}{c_M + 2c_0} + \frac{v_I}{c_I + 2c_0} \right)^{-1} - 2c_0, \quad (4)$$

while the respective dilute solution result has the form

$$c^{eff} = c_M + v_I(c_I - c_M)D(c_I, c_M) + O(v_I^2) \quad (5)$$

Equalizing (4) and (5) at $v_I \ll 1$, one finds

$$c_0 = \frac{D(c_I, c_M)c_I - c_M}{2(1 - D(c_I, c_M))} \quad (6)$$

where $D(c_I, c_M)$ is some inclusion function, which is specific for inclusion component's geometry. For the circular fiber inclusion, one has

$$D(c_I, c_M) = \frac{c_I + 5c_M}{3(c_I + c_M)}. \quad (7)$$

Substituting (7) into (6), one obtains

$$c_0 = \frac{c_I + 3c_M}{4}. \quad (8)$$

The approximation from (4) and (8) for matrix composites with fibrous inclusions is called the polarization approximation using fibrous inclusion dilute solution reference (FIPA). It satisfies HS bounds over all the ranges of volume proportion v_I of the inclusion phase.

In practice, the inhomogeneities may not have exact idealistic geometries but those more or less close to them. Equivalent inclusion approach is a practical way to modify the approximations. The idea of the equivalent inclusion is that one uses a modified value \bar{c}_I in the place of the inclusion conductivity c_I in the approximation formulae [13]. The equivalent inclusion conductivity value \bar{c}_I is derived from the experimental value of the reference effective conductivity c_{ref}^{eff} at some volume proportion v_I^{ref} of the inclusion. For fiber inclusion composite, one uses the fibrous inclusion polarization approximation from (4), (8)

$$c_{ref}^{eff} = \left(\frac{2v_I^{ref}}{3(\bar{c}_I + c_M)} + \frac{2v_M^{ref}}{\bar{c}_I + 5c_M} \right)^{-1} - \frac{\bar{c}_I + 3c_M}{2} \quad (9)$$

which yields

$$\bar{c}_I = \frac{1}{2v_I^{ref}} \left\{ c_{ref}^{eff} (1 + 2v_M^{ref}) - 3c_M - 2v_I^{ref} c_M + \left[\left(c_{ref}^{eff} (1 + 2v_M^{ref}) - 3c_M - 2v_I^{ref} c_M \right)^2 - 4v_I^{ref} c_M (3v_M^{ref} c_M - 2v_I^{ref} c_{ref}^{eff} - 3c_{ref}^{eff}) \right]^{1/2} \right\}. \quad (10)$$

Then the fibrous equivalent inclusion polarization approximation (FEIPA) for the effective conductivity of the composite would have the particular expression

$$c_{FEIPA}^{eff} = \left(\frac{2v_I}{3(\bar{c}_I + c_M)} + \frac{2v_M}{\bar{c}_I + 5c_M} \right)^{-1} - \frac{\bar{c}_I + 3c_M}{2} \quad (11)$$

in which, \bar{c}_I is determined from (10). A particular feature of equivalent inclusion polarization approximations (10) and (11) is that the exact value c_I of the inclusions is not required, while the respective equivalent inclusion conductivity \bar{c}_I is found from the reference experimental effective conductivity c_{ref}^{eff} at v_I^{ref} , and then the approximation is used to predict c^{eff} at a range of v_I beyond v_I^{ref} . That is practical, because in many practical cases involving nanosize inclusions such as nanotubes, the information about exact conductivity values of those nanoparticles as well as contact conditions with surrounding matrix may not be available and specified quantitatively.

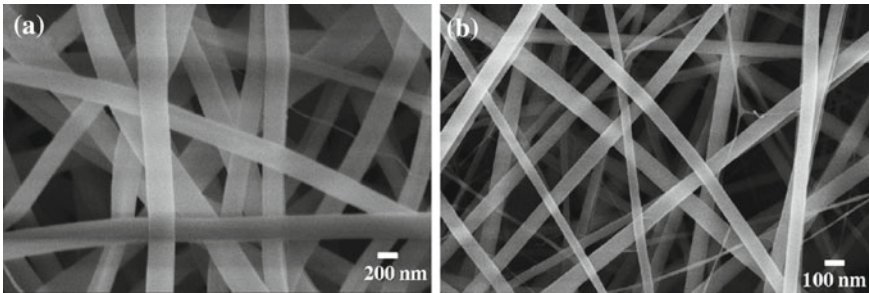


Fig. 1 SEM image of silica-PVP nanofibers (Liyun Ren et al. [14])

Table 1 Experimental values from [14] on thermal conductivity of epoxy matrix composite filled with silica fibers and polarization approximations

$v_I(\%)$	EXP	FEIPA0.005	FEIPA0.02	FEIPA0.03	FEIPA0.06	FEIPA0.09	FIPA
0.563	0.1982	0.1982	0.1966	0.1983	0.2019	0.2010	0.1933
1.704	0.21	0.2150	0.21	0.2153	0.2262	0.2235	0.2001
2.8	0.2319	0.2313	0.2231	0.2319	0.2499	0.2455	0.2067
5.704	0.3143	0.2757	0.2586	0.2769	0.3143	0.3052	0.2246
8.74	0.37	0.3239	0.2971	0.3257	0.3843	0.37	0.2438

3 Experimental Reference and Results

Figure 1 presents the scanning electron microscope (SEM) image of the polymer composite with randomly oriented silica nanofibers [14]. Conductivities of the epoxy matrix and silica fibers are $0.19 \text{ Wm}^{-1}\text{K}^{-1}$ and $1.38 \text{ Wm}^{-1}\text{K}^{-1}$, respectively. The experimental measured values (EXP) of c^{eff} at different volume fractions of the fillers and the polarization approximations are presented in Table 1. Figure 2 compares the experimental data and fibrous equivalent inclusion polarization approximation (FEIPA) from (10) and (11). FEIPA (0.06) is constructed using the reference experimental conductivity at the concentration point close to $v_I^{ref} \approx 0.06$. The equivalent inclusion conductivity $\bar{c}_I = 5.78 \text{ Wm}^{-1}\text{K}^{-1}$ is found according to (10) while $c_I = 1.38 \text{ Wm}^{-1}\text{K}^{-1}$ according to the source. The fibrous inclusion polariza-

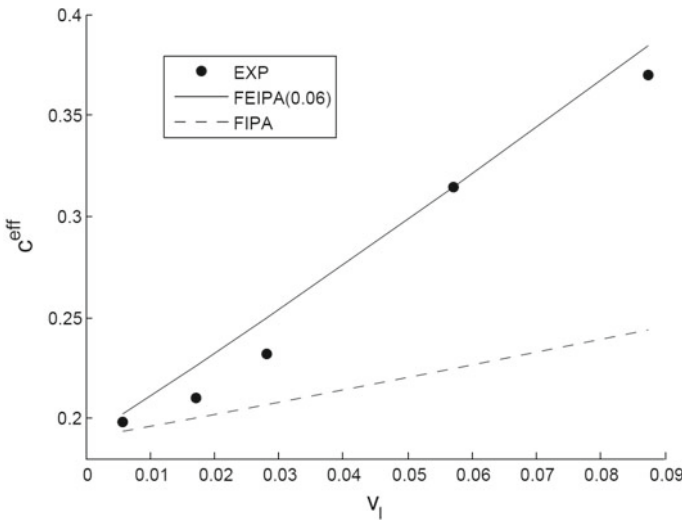


Fig. 2 Fibrous polarization approximation compared with experimental data: epoxy matrix (thermal conductivity $c_M = 0.19 \text{ Wm}^{-1}\text{K}^{-1}$) filled with silica nanofibers, FEIPA (0.06) uses the reference at $v_I^{ref} \approx 0.06$ and FIPA without equivalent inclusion modification

Table 2 Experimental values from [15] on thermal conductivity of polytetrafluoroethylene matrix composite filled with carbon nanotubes and polarization approximations

$v_I(\%)$	EXP	FEIPA0.05	FEIPA0.1	FEIPA0.2	FEIPA0.3
5	0.079	0.079	0.091	0.087	0.088
10	0.114	0.088	0.114	0.104	0.108
20	0.143	0.109	0.164	0.143	0.151
30	0.2	0.131	0.221	0.187	0.2

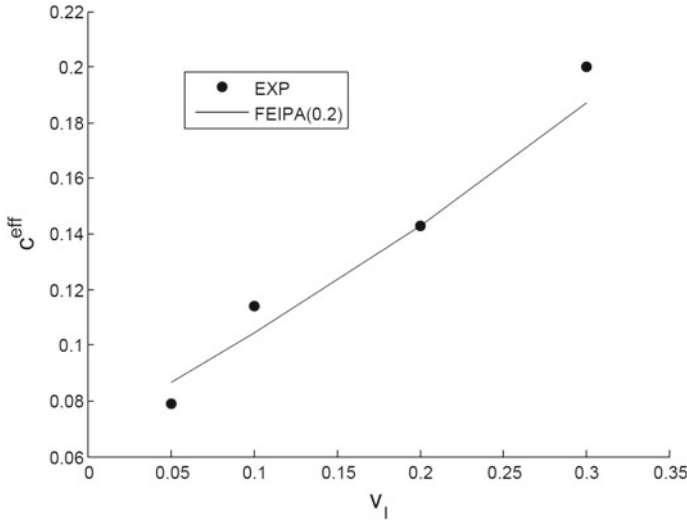


Fig. 3 Fibrous polarization approximation compared with experimental data: polytetrafluoroethylene matrix (thermal conductivity $c_M = 0.07 \text{ Wm}^{-1}\text{K}^{-1}$) filled with carbon nanotubes, FEIPA (0.2) uses the reference at $v_I^{ref} = 0.2$

tion approximation (FIPA) from (4) and (8) without equivalent inclusion is also included for comparison which diverges from EXP and FEIPA.

Similarly, Table 2 presents the experimental thermal property measurements of polytetrafluoroethylene (PTFE) as a base matrix ($c_M = 0.07 \text{ Wm}^{-1}\text{K}^{-1}$) combined with carbon nanotubes fillers (CNT) [15] and the results obtained from fibrous equivalent inclusion polarization approximation. In Fig. 3, the experimental data are plotted, FEIPA (0.2) is constructed using the reference experimental conductivity at the concentration point $v_I^{ref} = 0.2$. The equivalent inclusion conductivity $\bar{c}_I = 0.807 \text{ Wm}^{-1}\text{K}^{-1}$ is found while c_I not yet known.

4 Conclusion

Equivalent inclusion polarization approximations have been proposed to estimate the effective conductivity of isotropic matrix composites with randomly oriented inclusions of close to fiber forms. The approximation from (4) and (8) for the circular cylinder fiber inclusion ones, which satisfies HS bounds over all the volume proportions of the components, under perfect interface condition. To account for possible non-idealistic forms of the inclusions and unspecified conductivity values of nanofillers, the equivalent inclusion polarization approximations using the reference experimental macroscopic conductivity of the composite at certain volume proportion of component materials have been developed for fibrous filler like

inclusion composites (9)–(11). In this approximation, the equivalent inclusion conductivity is found from a reference experimental value of the macroscopic conductivity, not requiring knowledge about specific conductivity of the fillers—that is of practical interest, especially for composites with fillers in nanoscales. Comparison of the approximations with experimental data illustrates promising capacity of the approach.

Acknowledgements This research is supported by Vietnam National Foundation for Science and Technology Development (NAFOSTED) under grant number 107.02-2015.05.

References

1. Mori T, Tanaka K (1973) Average stress in matrix and average elastic energy of materials with misfitting inclusions. *Acta Metall* 21:571–574
2. Christensen RM (1979) *Mechanics of composite materials*. Wiley, New York
3. Pham DC, Torquato S (2003) Strong-contrast expansions and approximations for the effective conductivity of isotropic multiphase composites. *J Appl Phys* 94:6591–6602
4. Pham DC (2008) Weighted effective medium approximations for conductivity of random composites. *Int J Heat Mass Transf* 51:3355–3361
5. Kushch VI, Sevostianov I (2016) Maxwell homogenization scheme as a rigorous method of micromechanics: Application to effective conductivity of a composite with spheroidal particles. *Int J Eng Sci* 98:36–50
6. Nielsen LE (1974) The thermal and electrical conductivity of two-phase systems. ACS Publications, *Industrial & engineering chemistry fundamentals*
7. Zimmerman RW (1989) Thermal conductivity of fluid-saturated rocks. *J Petrol Sci Eng* 3:219–227
8. Ashby MF, Evans AG, Fleck NA, Gibson LJ, Hutchinson J, Wadley HNG (2000) *Metal foams: a design guide*. Butterworth Heinemann, Oxford
9. Pham DC (2000) Electrical properties of sedimentary rocks having interconnected water-saturated pore spaces. *Geophysics* 65:1093–1097
10. Ordonez-Miranda J, Alvarado-Gil JJ (2012) Thermal conductivity of nanocomposites with high volume fractions of particles. *Compos Sci Technol* 72:853–857
11. Mendes MAA, Ray S, Trimis D (2014) An improved model for the effective thermal conductivity of open-cell porous foams. *Int J Heat Mass Transf* 75:224–230
12. Pham DC, Nguyen TK (2015) Polarization approximations for macroscopic conductivity of isotropic multicomponent materials. *Int J Eng Sci* 97:26–39
13. Do QH, Tran AB, Pham DC (2016) Equivalent-inclusion approach and effective medium approximations for the effective conductivity of isotropic multicomponent materials. *Acta Mech* 227:387–398
14. Ren L, Pashayi K, Fard HR, Kotha SP, Tasciuc TB, Ozisik R (2014) Engineering the coefficient of thermal expansion and thermal conductivity of polymers filled with high aspect ratio silica nanofibers. *Compos Part B Eng* 58:228–234
15. Smith DK, Pantoya ML (2015) Effect of nanofiller shape on effective thermal conductivity of fluoropolymer composites. *Compos Sci Technol* 118:251–256

Crack Detection in a Beam on Elastic Foundation Using Differential Quadrature Method and the Bees Algorithm Optimization



**R. Khademi Zahedi, P. Alimouri, Hung Nguyen-Xuan
and Timon Rabczuk**

Abstract In the present contribution, a practical and non-destructive method for the identification of a single crack in a beam resting on elastic foundation is presented. The beam is modelled by differential quadrature method, and the location and depth of crack are predicted by bees algorithm. The crack is assumed to be open and is simulated by torsional spring which divides all parts through cracked beam into two segments. Then, the differential quadrature method is applied to the governing differential equation of motion of each segment and the corresponding boundary and continuity conditions. An eigenvalue analysis is performed on the resulting system of algebraic equations to obtain the natural frequencies of the cracked beam on elastic foundation. Then, the location and depth of cracks are

R. Khademi Zahedi (✉) · T. Rabczuk

Institute of Structural Mechanics, Bauhaus-Universität Weimar, Mariensstraße 15,
99423 Weimar, Germany
e-mail: reza.khademi.zahedi@nui-weimar.de

T. Rabczuk

e-mail: Timon.rabczuk@nui-weimar.de; timon.rabczuk@tdt.edu.vn

P. Alimouri

Department of Mechanical Engineering, Shahid Chamran University of Ahvaz, Blv.
Golestan, Ahvaz City, Iran
e-mail: alimouri_P@yahoo.com

H. Nguyen-Xuan

Center for Interdisciplinary Research in Technology, HUTECH University,
Ho Chi Minh City, Vietnam
e-mail: ngx.hung@hutech.edu.vn

H. Nguyen-Xuan

Department of Physical Therapy, Graduate Institute of Rehabilitation Science,
China Medical University, Taichung 40402, Taiwan

T. Rabczuk

Faculty of Civil Engineering, Ton Duc Thang University, Ho Chi Minh City, Vietnam

T. Rabczuk

Division of Computational mechanics, Ton Duc Thang University, Ho Chi Minh City,
Vietnam

© Springer Nature Singapore Pte Ltd. 2018

H. Nguyen-Xuan et al. (eds.), *Proceedings of the International Conference
on Advances in Computational Mechanics 2017*, Lecture Notes in Mechanical
Engineering, https://doi.org/10.1007/978-981-10-7149-2_30

determined by bees algorithm optimization technique. The formulation of thin-walled beams theory is used for the crack detection in this research. To insure the integrity and robustness of the presented algorithm, the finite element analysis is performed on the set of cantilever beams, with different crack lengths and locations. The results show that the presented algorithm predicts location and depth of crack well and can be effectively employed for crack detection in other structures.

Keywords Vibration analysis • Crack detection • Differential quadrature method • Bees algorithm

1 Introduction

Industrial development can be achieved through the production of improved machinery and equipment. One of the major goals that is often followed by manufacturing and production industries is the reliability of their products [1]. The existence of defects in some produced parts will cause the catastrophic failure of whole structure which will result in loss of life and property. Crack is one of the major defects which may appear in a structure.

As the final failure in parts and structures usually happens by the initiation and propagation of the crack, the investigation and research in these fields will be effective and appropriate [2]. The increasing daily need for the detection of flaws and defects in overall parts of a complicated structure leads to the chasing of some methods by researchers in which the variation in the specification of whole structure to be investigated. The most applicable methods are the inspection based on the vibration behaviour of the structure. The main idea behind these methods is the investigation of the modal parameters before and after the occurrence of the defect in structure. Swamidas et al. [3] used the energy approach to estimate bending stiffness of the cracked beam, and by implementing it in the beam differential equation, they estimated natural frequencies of the cracked beam with different crack sizes and locations. Then, the crack size and location were investigated by solving the inversed problem. Qian et al. [4] derived an element stiffness matrix of a beam hoisting an open-edge crack by integrating over the stress intensity factors. They established the finite element model of a cracked beam, and for a cantilever cracked beam, they determined eigenfrequencies of different crack lengths and locations. Narkis et al. [5] investigated the bending and axial vibrations of a cracked simply supported uniform beam. By simulating the crack with an equivalent torsional spring, they derived algebraic equations with respect to the natural frequencies of the beam and crack length and location. Then, the inverse problem was applied to identify the crack length and location. Nanthakumar et al. [6] presented an iterative method to treat the inverse problem of detecting cracks and voids in piezoelectric structures. Extended finite element was employed for solving forward problem. Then, the minimization of cost function was performed by multilevel coordinate search method. In addition, they [7] proposed a strategy to detect

multiple voids in piezoelectric structures by using XFEM and combining shape derivative and level sets as employed in structural optimization problems. Dems and Meroz [8] utilized the difference between natural frequencies of intact and cracked states of structures and applied the solution of the related constrained optimization problem to investigate damage or fault in structure. The relation between stiffness and frequency is defined as the problem constraint. Chang and Chen [9] estimated the positions and depths of cracks in Timoshenko beam from spatial wavelet transform-based method. First, they obtained the mode shapes of free vibration and natural frequencies of the cracked beam by analytical method. The crack was assumed to be open and was represented as a torsional spring. Then, the mode shapes were analysed by wavelet transformation to get the positions of the cracks, and natural frequencies were used to predict the depths of the cracks through the characteristic equations.

In this research, the crack is modelled based on the presented method by Vakili Baghmisheh [10], and then, the differential quadrature (DQ) method is employed to compute the natural frequencies of the cracked beam. Finally, the weighted sum of the squared errors between the measured and computed natural frequencies by finite element analysis and DQ method, respectively, is used as the objective function and minimized by the bees algorithm (BA) to predict the location and depth of the crack. The formulation developed in this study is applied to the cracked cantilever beams on elastic foundation, but it can be extended to other types of boundary conditions.

2 Theory

2.1 Differential Quadrature Technique

Differential quadrature technique is based on the Gaussian differentiation of a function to calculate function derivative which is based on the function values in limited points of the domain. This approximate solution for estimating the derivative of a function at a point located in the related domain is based on the weighted linear sum of the function values at all discrete points chosen inside the domain. The DQM first proposed in early seventies by Bellman [11]. The following equation is the mathematical representation of the definition stated by Bellman for the DQ expansion:

$$\left. \frac{df}{dx} \right|_{x=x_i} = \sum_{j=1}^N C_{ij}^{(1)} f_j \quad i, j = 1, 2, \dots, N \quad (1)$$

In this equation, N is the number of discrete sampling points, x_i is the coordinate of i th discrete sampling point in the computational domain, f_j is the functional value

at x_j , and $C_{ij}^{(j)}$ is weighting coefficient related to the first-order derivative of the function at point x_j .

2.2 Modelling the Vibration Behaviour of the Damaged Beam

Figure 1 shows an elastic cantilever beam of length L , height H and width b , having an open-edge full width crack of depth a , perpendicular to the beam's longitudinal axis which is resting on the elastic foundation (L_C).

To investigate the mechanical behaviour of the system, the elasticity of the foundation is modelled by springs of k_f spring stiffness. As the presence of the crack in beam changes the beam stiffness at the crack location, the simplest cracked beam modelling method is to model it as two separate uniform segments connected with a torsional spring. Therefore, as shown in Fig. 2, the crack with finite length divides the beam into two segments and the segments are connected with a massless torsional spring. The spring stiffness, k_t , used to model the crack can be calculated from the following equation:

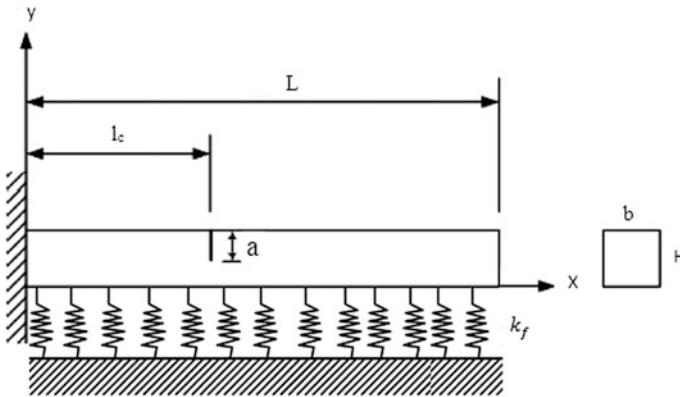


Fig. 1 Geometry of a cracked cantilever beam on elastic foundation

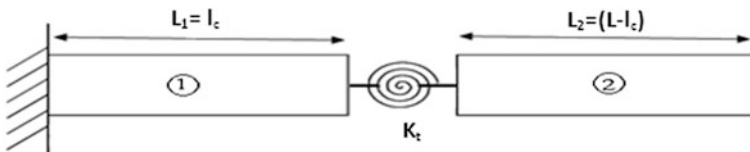


Fig. 2 Crack modelling in beam

$$k_t = \frac{EI}{6H(1-\nu^2)Q\left(\frac{a}{H}\right)} \quad (2)$$

where EI , ν and a are the bending rigidity of the beam, the poisson's ratio of the beam material and the crack depth, respectively. The geometrical factor Q can be expressed by [12, 13]:

$$f\left(\frac{a}{H}\right) = 1.8224\left(\frac{a}{H}\right)^2 - 3.95\left(\frac{a}{H}\right)^3 + 16.375\left(\frac{a}{H}\right)^4 - 37.226\left(\frac{a}{H}\right)^5 \\ + 76.81\left(\frac{a}{H}\right)^6 - 126.9\left(\frac{a}{H}\right)^7 + 172\left(\frac{a}{H}\right)^8 - 143\left(\frac{a}{H}\right)^9 + 66.56\left(\frac{a}{H}\right)^{10} \quad (3)$$

The differential equation of motion is described for bending vibration of each segment. These equations along with equations related to the boundary conditions and compatibility equations of the cracked section are transformed to an eigenvalue problem by means of differential quadrature method, which will be used to extract the natural frequencies of the proposed system. Compatibility conditions consist of the discontinuity of slope and continuity of deflection, bending moment and shear force at the crack location. The mathematical model applied to describe the motion of a beam with finite crack consists of two separate functions. These functions $W_1(x, t)$ and $W_2(x, t)$ describe beam's transverse vibration of the two segments illustrated in Fig. 2. Equation of motion of a cracked beam can be stated as:

$$\frac{d^4 W_k}{dx^4} - \alpha^4 W_k = 0 \quad k = 1, 2 \quad (4)$$

In the above equation, k is the beam number. Also, α is the dimensionless frequency of the beam which can be expressed by the following equation:

$$\alpha^4 = \left(\frac{-k_f}{EI} + \frac{\omega^2}{c^2} \right) \quad c = \sqrt{\frac{EI}{\rho A}} \quad (5)$$

where ω , ρ and A are natural frequency, density and cross-sectional area of the beam, respectively. The beam considered here is a cantilever beam. The boundary conditions of a cantilever beam are assumed to be as below:

$$W_1|_{x=0} = 0, \quad \frac{dW_1}{dx}|_{x=0} = 0 \quad (6)$$

due to the deflection and rotation both being zero at the clamped end. Also due to the bending moment and shear force both vanishing at the beam-free end, these boundary conditions can be stated as Eqs. (5) and (6):

$$\frac{d^2 W_2}{dx^2} \Big|_{x=l} = 0 \tag{7}$$

$$\frac{d^3 W_2}{dx^3} \Big|_{x=l} = 0 \tag{8}$$

Besides, Eq. (9) satisfies the compatibility of the displacements, bending moments and shear forces of two segments at the crack location:

$$W_1 \Big|_{x=l_c} = W_2 \Big|_{x=l_c} \quad \frac{d^2 W_1}{dx^2} \Big|_{x=l_c} = \frac{d^2 W_2}{dx^2} \Big|_{x=l_c} \quad \frac{d^3 W_1}{dx^3} \Big|_{x=l_c} = \frac{d^3 W_2}{dx^3} \Big|_{x=l_c} \quad \frac{d^3 W_2}{dx^3} \Big|_{x=l} = 0 \tag{9}$$

Subsequently, as shown in Eq. (10), the difference in the slopes of the two segments at the crack location can be related to the bending moment exerted by the torsional spring [12]:

$$\left(\frac{dW_1}{dx} + \frac{EI}{k_t} \frac{d^2 W_2}{dx^2} \right) \Big|_{x=l_c} = \frac{dW_2}{dx} \Big|_{x=l_c} \tag{10}$$

The lengths of beam number 1 and 2 are specified by l_1 and l_2 , respectively. Using sampling point distribution equation, here each domain is divided into N discrete points located at right and left side of the spring. By using the variable change $X = \frac{x}{L}$ and applying DQ on the beams differential equation, one can obtain:

$$\frac{1}{l_k^4} \sum_{j=1}^N C_{ijk}^{(4)} W_{jk} + \alpha^4 W_{ik} = 0 \quad k = 1, 2 \tag{11}$$

In the above equation, $C_{ijk}^{(4)}$ is the weighting coefficient of the fourth-order derivative at the i th sampling point of the k th region of the beam, W_{ik} is lateral deflection at the i th point of the beam number k , and l_k is the length of the beam k . In each boundary node, located on $X = 0$ ($x = 0$) in Eq. 6 and $X = 1$ ($x = L$) in Eqs. 7 and 8 are two boundary conditions and at $X = l_c/L$ ($x = l_c$) at both sides of spring, four compatibility conditions should be satisfied. Degree of freedom of each node is assumed to be one, but the solution of the problem at the mentioned nodes will lead to the increase of equations which are independent of unknown variables defined at these nodes and also mathematical contradiction. As stated previously, different solutions have been proposed to eliminate the mentioned problem which will be discussed as below.

2.3 The δ -Method

The δ -technique was proposed by Jang et al. [14, 15] to eliminate the difficulties in implementing two conditions at a single boundary point. In this method, some adjacent points located at very small distances δ from boundary point are chosen (Fig. 3). One of the boundary conditions is applied at boundary point itself, and the other boundary condition is applied at its adjacent point which is at the distance δ which forms the boundary point. To obtain an accurate numerical solution, the values of δ should be chosen to be very small and possibly not greater than 10^{-5} compared to unity. In this method, one of the boundary conditions is applied correctly, while the other boundary condition is applied approximately.

$$W_1 = 0 \quad ; \quad \sum_{j=1}^N C_{2j1}^{(1)} W_{j1} = 0 \tag{12}$$

$$W_{N1} = W_{12}$$

$$\frac{1}{l_1^2} \sum_{j=1}^N C_{N-1j1}^{(2)} W_{j1} = \frac{1}{l_2^2} \sum_{j=1}^N C_{1j2}^{(2)} W_{j2}$$

$$\frac{1}{l_1^3} \sum_{j=1}^N C_{Nj1}^{(3)} W_{j1} = \frac{1}{l_2^3} \sum_{j=1}^N C_{2j2}^{(3)} W_{j2} \tag{13}$$

$$\frac{1}{l_1} \sum_{j=1}^N C_{N-1j1}^{(1)} W_{j1} + \frac{1}{l_2} \frac{EI}{k_t} \sum_{j=1}^N C_{2j2}^{(2)} W_{j2} = \frac{1}{l_2} \sum_{j=1}^N C_{2j2}^{(1)} W_{j2}$$

$$\frac{1}{l_2^2} \sum_{j=1}^N C_{N-1j2}^{(2)} W_{j2} = 0 \quad ; \quad \frac{1}{l_2^3} \sum_{j=1}^N C_{Nj2}^{(3)} W_{j2} = 0 \tag{14}$$

Beam differential Eq. (14) is applied at internal points ($3 \leq i \leq N - 2$). The combination of Eqs. (12)–(14) forms an eigenvalue problem with the dimension of $(2N) \times (2N)$ which can be represented by a system of linear equations, as follows:

$$\begin{bmatrix} [A_{bb}] & [A_{bi}] \\ [A_{ib}] & [A_{ii}] \end{bmatrix} \begin{Bmatrix} W_b \\ W_i \end{Bmatrix} = \lambda \begin{bmatrix} 0 & 0 \\ B_{ib} & B_{ii} \end{bmatrix} \begin{Bmatrix} W_b \\ W_i \end{Bmatrix} \tag{15}$$

where the subscripts b and i denote for the boundary and interior points used for writing the differential quadrature, respectively. The vectors $\{W_b\}$ and $\{W_i\}$ contain



Fig. 3 Representation of δ nodes in the beam problem

the deflections corresponding to the boundary and interior points. Also in the above equation, λ is a function of ω which is defined as below:

$$\omega = c\lambda^2 \sqrt{1 + \frac{k_f}{EI\lambda^2}} \quad (16)$$

Transforming Eq. (15) into a general eigenvalue form in terms of $\{W_i\}$ results in Eq. (17):

$$[A^*] \{W_i\} = \lambda [B^*] \{W_i\} \quad (17)$$

where

$$\begin{aligned} [A^*] &= [A_{ii} - A_{ib} \cdot A_{bb}^{-1} \cdot A_{bi}] \\ [B^*] &= [B_{ii} - B_{ib} \cdot A_{bb}^{-1} \cdot A_{bi}] \end{aligned} \quad (18)$$

Solution of the above eigenvalue problem by a standard eigensolver provides the natural frequencies of the cracked beam.

2.4 Crack Detection Procedure

In the previous section, the computation of beam natural frequencies with assumed crack location and depth is investigated (direct method). In this section, the inverse solution using finite element natural frequencies is applied to identify the location and depth of the crack.

2.4.1 The Bees Algorithm

As specified earlier to locate the crack and simulate the crack depth, it is required that the intelligent optimization algorithms to be used. For these purposes, the bees algorithm has been employed. In the following, the bees algorithm will be discussed briefly. Honey bees swarm optimization algorithm could be regarded as belonging to the category of evolutionary algorithms. An organized social behaviour has been observed in honey bee swarms which can be used for solving social optimization problems. Each bees swarm has some scout bees that explore randomly for food sources. When they return to the hive, those scout bees that found a patch which is related above a certain quality threshold deposit their nectar or pollen and perform a dance known as the “waggle dance” [16]. This mysterious dance is essential for colony communication and contains three pieces of information regarding a flower patch: the direction in which it will be found, its distance from the hive and its

quality rating [16, 17]. In the next step, the follower bees fly to the located site of flower patch. More follower bees are sent to more promising patches.

Among a set of random solutions N_r , a few solutions N_{l1} with the highest fitness values are chosen as the best ones. Among the best answers, N_{l2} solutions with highest reliability will be selected as elite solutions. In hope to find better solutions, neighbourhood searching around the best and elite solutions is performed. Following each iteration, the new population has two parts: representative from neighbourhood searches having the best fitness value in their neighbourhood space and randomly selected solutions. The iteration continues, and at the end, there are a series of optimum fitness values; the best of them would represent the global optimum.

2.4.2 Crack Detection Using the Bees Algorithm Optimization Problem

In this method, crack detection procedure is considered as an optimization problem to find the optimum location and depth of the crack by error function minimization which is based on the difference between natural frequencies obtained by finite element solution and differential quadrature method. Optimization algorithm defines an array of variables which must be optimized. In this research, these arrays are dimensionless location and depth of the crack. The objective function, F , to be minimized is defined as:

$$F = \sum_{j=1}^s w_j (\Omega_j^m - \Omega_j^c)^2 \quad (19)$$

In Eq. (19), s is the number of implemented natural frequencies, Ω_j^c is the j th numerical dimensionless bending natural frequency of the cracked beam calculated by DQM, Ω_j^m is the j th measured dimensionless bending natural frequency of the cracked beam calculated with finite element method, and w_j is the j th weighting factor.

3 Results and Discussion

3.1 Accuracy of the Natural Frequencies Calculated by DQ Solution

To insure for the appropriate modelling of supports and measurement accuracy, in Table 2, corresponding numerical natural frequencies that are calculated by the DQ method for an intact cantilever beam on an elastic foundation are compared to the natural frequencies calculated by ANSYS. Also, the dimension and mechanical properties of the mentioned beam are presented in Table 1.

Table 1 Dimensions and mechanical properties of the beam on elastic foundation

Spring constant $\frac{N}{M}$	Poisson's ratio	Young's modulus (Gpa)	Density (kg/m^3)	Beam thickness (cm)	Beam width (cm)	Beam length (m)
100000	0.3	200	7800	2	2	1

Table 2 Natural frequencies of the intact beam on elastic foundation

Method	ω_1 (Hz)	Error (%)	ω_2 (Hz)	Error (%)	ω_3 (Hz)	Error (%)
ANSYS	9.97	–	51.62	–	143.93	–
DQ	9.96	0.1	51.59	0.06	143.82	0.08

As can be observed from Table 2, the delivered errors from the results of DQ method are very small compared to the ANSYS results. The maximum error value is 0.1%. DQ method calculations have been performed repeatedly, and the results were identical for each iteration. Based on the appropriate agreement between DQ and ANSYS methods, it was implied that the modelling of cantilever beam on elastic foundation has been performed properly.

3.2 The Effect of Various Sampling Points on Estimating the Natural Frequencies

As stated, sampling points distribution relations play an important role in computing natural frequencies. The curves on Fig. 4 represent the effect of various relations for the choice of sampling points on the determination of the first natural frequency. In the mentioned curves, equally spaced sampling points distribution, the roots of Chebyshev sampling points determination, Gauss–Lobatto–Chebyshev and Lagrange polynomials are used to evaluate the convergence of the first frequency. As can be observed from the curves, the choice of sampling points based on Lagrange polynomials delivers smaller errors and faster convergence in comparison with the other sampling points. Therefore, in this research, the roots of Lagrange polynomials have been chosen as sampling points. Please find the data in the below table.

Number of sampling points	6	7	8	9	10	11	12	13	14	15	16
Gauss-Lobatto-Chebyshev	8.43	8.49	8.91	9.38	9.93	9.94	9.94	9.94	9.94	9.94	9.94
Chebyshev	11.89	8.23	8.55	9.48	9.98	9.98	9.98	9.98	9.97	9.95	9.98
Legendre	8.91	11.31	8.99	9.96	9.96	9.96	9.96	9.96	9.95	9.96	9.96
Equal displacement	6.23	7.23	7.98	8.03	9.89	9.87	9.87	9.77	9.87	10.07	9.87

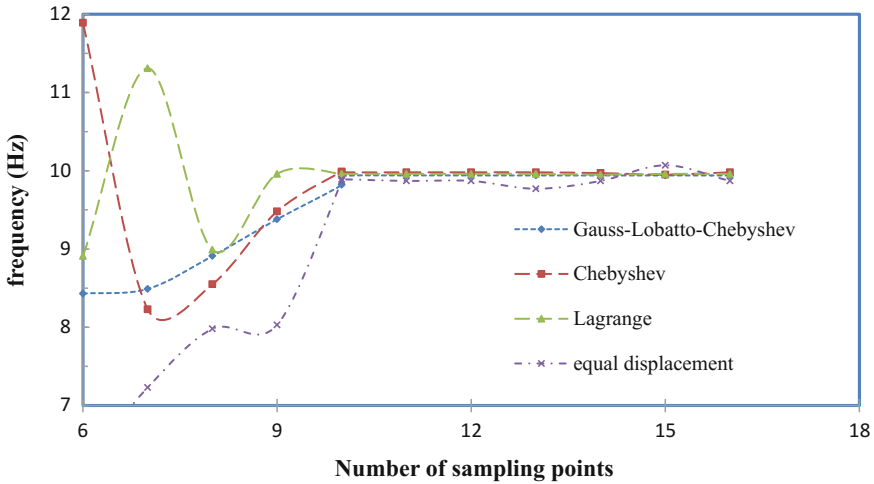


Fig. 4 Effect of sampling points relation on calculating the first frequency by delta method

As can be seen for each mentioned relationship choosing minimum number of 10 sampling points, delivers a good convergence for the first natural frequency and also the same process occurs in higher natural frequencies. In the following, this method is employed to calculate the frequencies of a beam on an elastic foundation. Also, it is required to be mentioned that this method has the capability of producing highly accurate solutions with implementing a limited number of points, when compared to the other conventional numerical solution techniques such as finite element and boundary value methods.

3.3 The Investigation of Convergence of DQ Method Using Different Sampling Points

To assess the overall convergence efficiency of the DQ method in computing natural frequencies of a beam on elastic foundation, the natural frequencies of the cracked beam obtained by DQ are compared with the finite element results of ANSYS commercial software. In this section, firstly the results obtained for the first to the third natural frequencies at different crack locations and depths are compared. The simulated cracks are considered to be perpendicular to the beam’s longitudinal axis at different positions, namely $X_c = (lc/L) = 0.25, 0.50, 0.75$ from the clamped edge. The Figs. 5, 6 and 7 represent relative errors of the first, second and third natural frequencies compared to the results obtained by ANSYS. As illustrated,

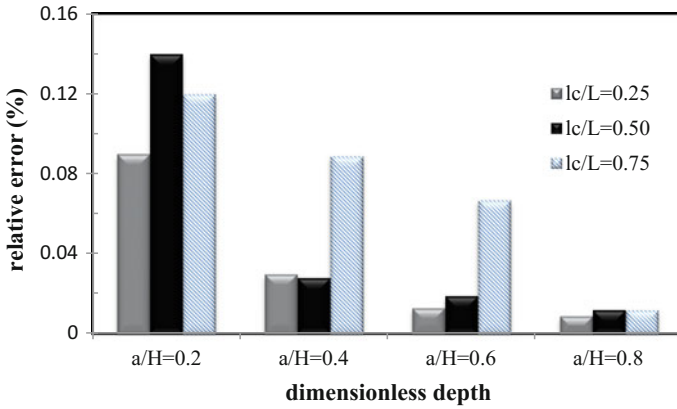


Fig. 5 Relative error in beam’s first natural frequency based on ANSYS and DQ methods in different relative lengths and locations

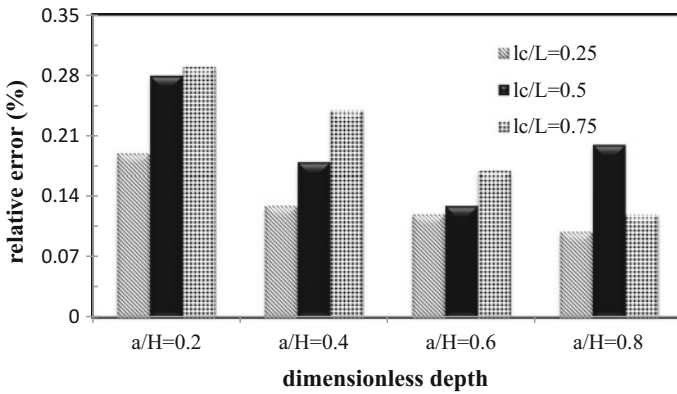


Fig. 6 Relative error in beam’s second natural frequency based on ANSYS and DQ methods in different relative lengths and locations

relative crack depth and relative crack location errors are calculated. In all cases, the resulting errors are very small and sufficiently below 0.5%. Figures 5, 6 and 7 show smaller errors in lower frequencies relative to higher ones. As the relative depth of the crack increases, the error decreases.

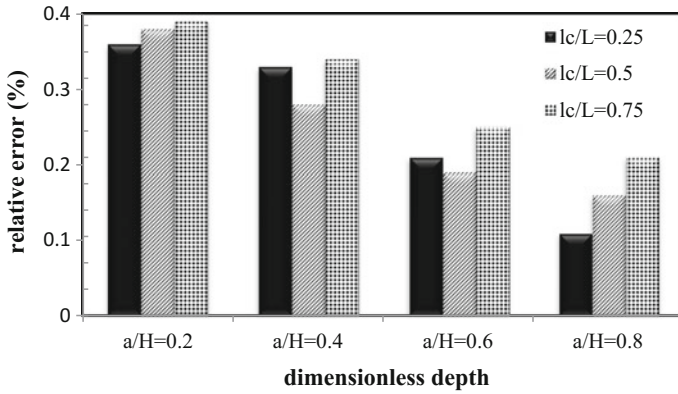


Fig. 7 Relative error in beam’s third natural frequency based on ANSYS and DQ methods in different relative lengths and locations

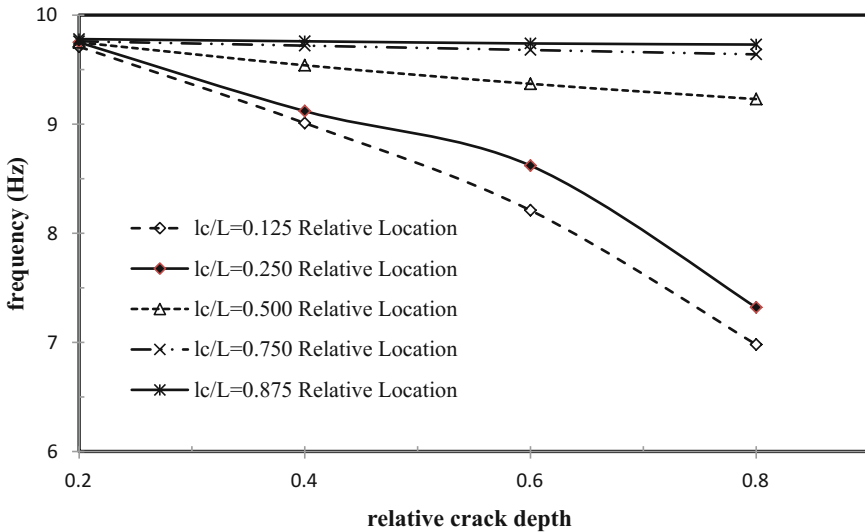


Fig. 8 Effect of relative crack depth on the first natural frequency

3.4 The Effect of Crack Depth on the Variation of the Natural Frequencies

In this section, the effect of the crack depth on natural frequencies of cantilever beam on the elastic foundation is investigated for different crack locations which are based on the DQM results. The related curves are shown in Figs. 8, 9 and 10.

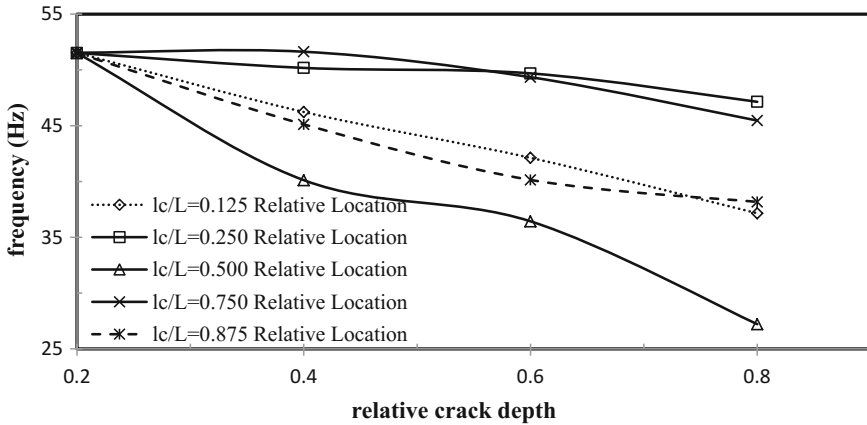


Fig. 9 Effect of relative crack depth on the second natural frequency

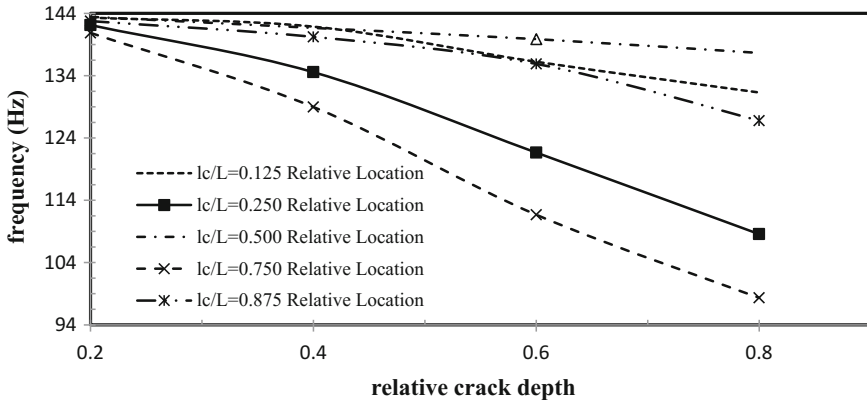


Fig. 10 Effect of relative crack depth on the third natural frequency

As can be seen from the figures, increasing crack depth would result in a decrease in the natural frequencies of the beam. Furthermore Eq. (10) shows that increasing the crack depth would result in a decrease in the beam stiffness which this issue will decrease natural frequencies of the beam on elastic foundation. As there is a direct relation between natural frequencies and beam stiffness, the reduction in stiffness will result in the reduction of natural frequencies. Figure 8 shows that as the crack position reaches the free end of the cracked beam on the elastic foundation, the change in first natural frequency decreases. In fact, closed to the free end of the beam, the crack losses influence on the value of the first natural frequency of the beam on elastic foundation.

3.5 The Effect of Crack Location on the Variation of the Natural Frequencies

In Figs. 11, 12 and 13, the influence of relative location of the crack on natural frequencies for different crack depths of a beam on elastic foundation is investigated. As shown in figures, when the crack is placed at the beam modal nodes, there

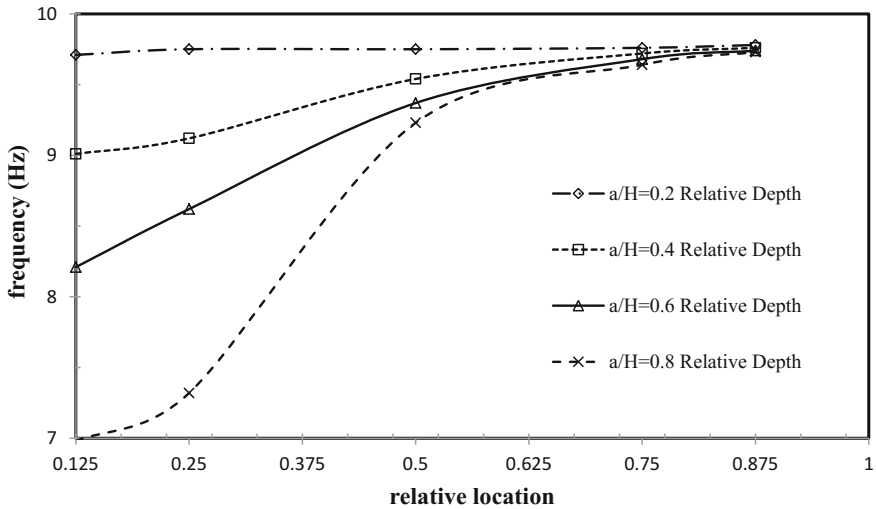


Fig. 11 Effect of relative crack location on the first natural frequency

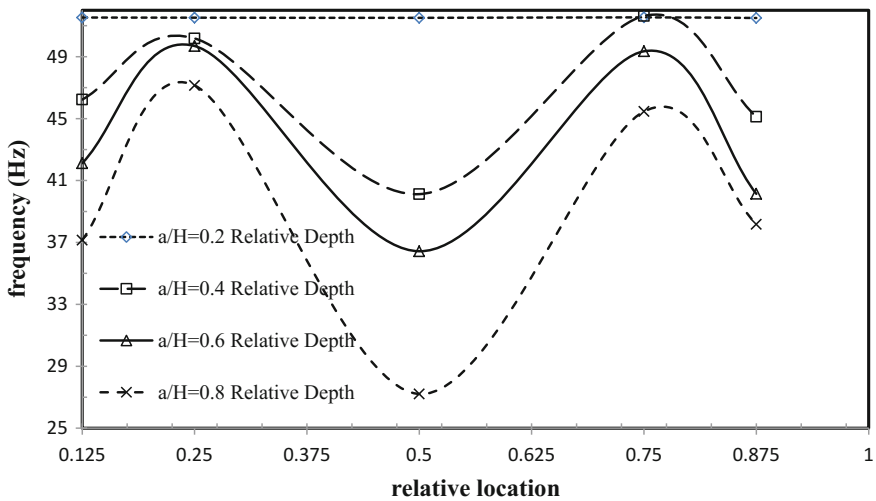


Fig. 12 Effect of relative crack location on the second natural frequency

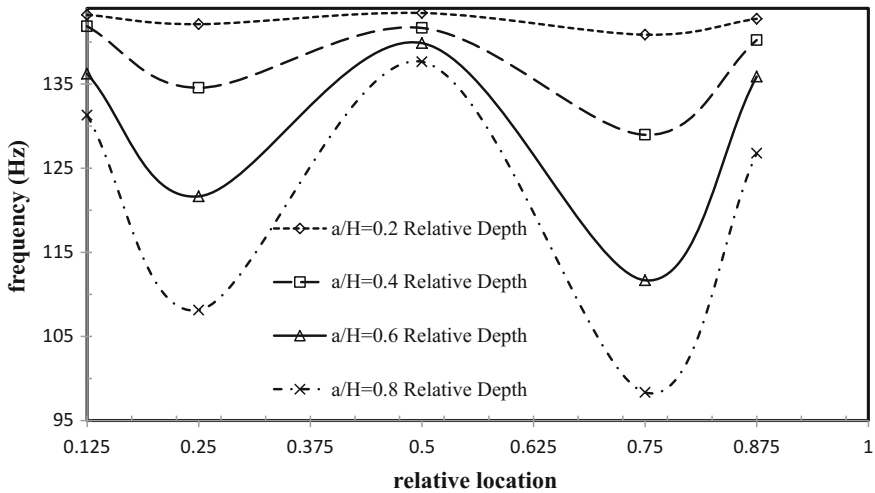


Fig. 13 Effect of relative crack location on the third natural frequency

is no change in natural frequencies of the beam. These locations will change for different boundary conditions and vibration modes. Moreover, the change in natural frequencies is in direct relation with the beam modal curvature so that the maximum changes in natural frequencies take place when the cracks are located in the places with highest modal curvature.

It also can be stated from the figures that increasing crack depth would result in a decrease in the natural frequencies of the beam. Moreover, Eq. (10) shows that increasing the crack depth would result in an increase in the slope and cause a reduction in the beam stiffness and subsequently natural frequencies of the beam on elastic foundation.

3.6 Identification of the Location and Depth of the Crack

After investigating the effect of the location and the depth of the crack on changes in the natural frequencies of a beam, in this section, natural frequencies for different cracks are computed by DQ, finite element and bees algorithm methods. Finally, to ensure the integrity and robustness of the presented method, estimated values of crack location and depth are compared with finite element results. It is required to note that in order to verify the effectiveness of the bees algorithm optimization, this process will be done in four stages. In the first stage, the length and depth of the cracks will be examined using the first three natural frequencies. In this stage, all three frequencies have the same influence on estimating the location and the depth of the crack. In the second stage, three natural frequencies will be used again, but the lower frequencies have more effect and influence rather than higher frequencies.

In the third stage, four first natural frequencies will be used to examine the length and depth of the crack. Then, in the last stage same as the previous section, higher values of weighting coefficients will be used for lower frequencies. In the following, the outcome of four above-mentioned methods is compared.

3.6.1 The Investigation of Bees Algorithm Optimization Control Parameters

As stated in Sect. 2.4, the application of optimization techniques to minimize function (19) will result in corresponding increase in the accuracy of the results for the crack location and length. In relation (19), objective function is considered as error function which is based on the difference between natural frequencies of the cracked beam on the elastic foundation computed by finite element method and the numerical results obtained by DQ method and should be minimized. As the convergence in bees algorithm in this research, occurred after 40 iterations, for all cases solved by bees algorithm, in this research, 40 iteration is chosen to proceed. To consider the random nature effects of the bees algorithm optimization method, the average of 15 run is accepted as the final result. The control parameters applied for the bees algorithm in this research are presented in Table 3. These data have been obtained based on a lot of experimental investigation.

3.6.2 The Results of the Crack Location and Depth Detection by Bees Algorithm Optimization

The frequencies computed by differential quadrature numerical method for different cracks are used to compute the location and depth of a crack by bees algorithm. Table 4 represents the results obtained for different crack cases using the first three natural frequencies with the same influence. Also to investigate the crack prediction accuracy, the crack location and depth relative error are calculated, respectively.

$$l_e = \frac{\Delta x}{L} \times 100 \tag{20}$$

$$S_e = \frac{\Delta a}{H} \times 100 \tag{21}$$

Table 3 Number of control parameters for the bees algorithm optimization

Number of calculated functions	Negh	m	e	Nsp	Nep	N	Number of iteration
12450	0.02	15	5	15	25	50	40

Table 4 Prediction of crack results and accuracy investigation

Crack case number	Exact value		Predicted crack		Prediction accuracy (%)	
	Depth ($\frac{a}{H}$)	Location ($\frac{L}{L}$)	Depth ($\frac{a}{H}$)	Location ($\frac{L}{L}$)	Depth	Location
1	0.25	0.2	0.241	0.209	4.1	4.0
2	0.4	0.25	0.439	0.213	3.9	3.7
3	0.6	0.25	0.632	0.219	3.2	3.1
4	0.8	0.25	0.789	0.227	1.1	2.3
5	0.2	0.50	0.166	0.409	3.4	9.1
6	0.4	0.50	0.323	0.421	7.7	7.9
7	0.6	0.50	0.539	0.428	6.1	7.2
8	0.8	0.50	0.756	0.439	4.4	6.1
9	0.2	0.75	0.146	0.681	5.4	6.9
10	0.4	0.75	0.308	0.693	9.2	5.7
11	0.6	0.75	0.543	0.710	5.7	4.0
12	0.8	0.75	0.732	0.722	6.8	2.8

As shown in this table, the minimum crack location error (l_e) is 2.3% for the case study 4 and the maximum crack location error is 9.1%. With respect to the defined error (l_e), the error value 9.1% means that the predicted crack (crack case 5) is located 9.1 cm far from the exact position of the crack (the beam length is assumed to be 100 cm). Also, Table 4 presents the errors in the crack depth prediction (s_e) for different crack cases. As shown in this table, the maximum crack depth error is 9.2% (for the case study 10) and the minimum crack depth error is 1.1% (for the case study 4). Regarding the defined errors (s_e), the error value 9.2% means that the predicted crack depth (crack number 10) is 1.84 mm different from the exact depth of the crack (the beam depth is assumed to be 20.2 mm).

As stated in the beginning of the Sect. 3.6, the second optimization case is investigated for the first three natural frequencies by applying coefficients. In this section, higher values of weighting coefficients will be used as the lower frequencies are close to each other. For example, weighting coefficients 1, 0.5 and 0.33 are used for the first, second and third frequencies, respectively. In this section, the control parameters will be same as the previous method. Table 5 presents the results of the mentioned method. As can be concluded from Table 5, this method delivers more accurate results compared to the previous method. The cause is that corresponding errors in computing lower frequencies by both finite element method and differential quadrature method are smaller. Therefore, as lower frequencies have more influence on optimization method, obtained results will be more accurate.

To investigate the third case of optimization method, first four natural frequencies without weighting coefficients are used. For this method also control parameters of the previous method have been used. Table 6 represents the results of this method.

Table 5 Prediction of crack results and accuracy investigation

Crack case number	Exact value		Predicted crack		Prediction accuracy (%)	
	Depth ($\frac{a}{H}$)	Location ($\frac{L}{L}$)	Depth ($\frac{a}{H}$)	Location ($\frac{L}{L}$)	Depth	Location
1	0.2	0.25	0.214	0.229	1.4	2.1
2	0.4	0.25	0.417	0.239	1.7	1.1
3	0.6	0.25	0.604	0.248	0.4	0.2
4	0.8	0.25	0.797	0.251	0.3	0.1
5	0.2	0.50	0.118	0.447	1.8	5.3
6	0.4	0.50	0.384	0.466	1.6	3.4
7	0.6	0.50	0.579	0.484	2.1	1.6
8	0.8	0.50	0.786	0.495	1.4	0.5
9	0.2	0.75	0.163	0.712	3.7	6.9
10	0.4	0.75	0.378	0.721	2.2	3.8
11	0.6	0.75	0.581	0.736	1.9	1.4
12	0.8	0.75	0.789	0.741	1.1	0.9

Table 6 Prediction of crack results and accuracy investigation

Crack case number	Exact value		Predicted crack		Prediction accuracy (%)	
	Depth ($\frac{a}{H}$)	Location ($\frac{L}{L}$)	Depth ($\frac{a}{H}$)	Location ($\frac{L}{L}$)	Depth	Location
1	0.2	0.25	0.212	0.231	1.2	1.9
2	0.4	0.25	0.418	0.240	1.8	1.0
3	0.6	0.25	0.602	0.249	0.2	0.1
4	0.8	0.25	0.798	0.250	0.2	0.0
5	0.2	0.50	0.214	0.448	1.4	5.2
6	0.4	0.50	0.389	0.474	1.1	2.6
7	0.6	0.50	0.586	0.491	1.4	0.9
8	0.8	0.50	0.788	0.493	1.2	0.7
9	0.2	0.75	0.175	0.723	2.5	3.7
10	0.4	0.75	0.384	0.725	1.6	3.5
11	0.6	0.75	0.587	0.738	1.3	1.2
12	0.8	0.75	0.792	0.744	0.8	0.6

To investigate the last case of optimization method, first four natural frequencies with weighting coefficients are used. Weighting coefficients 1, 0.5, 0.33 and 0.25 are used for the first, second third and fourth natural frequencies, respectively. For this method also control parameters of the previous method have been used. Table 7 presents the results of the mentioned method.

Table 7 Prediction of crack results and accuracy investigation

Crack case number	Exact value		Predicted crack		Prediction accuracy (%)	
	Depth ($\frac{a}{H}$)	Location ($\frac{L}{L}$)	Depth ($\frac{a}{H}$)	Location ($\frac{L}{L}$)	Depth	Location
1	0.2	0.25	0.209	0.234	0.9	1.6
2	0.4	0.25	0.413	0.243	1.3	0.7
3	0.6	0.25	0.601	0.250	0.1	0.0
4	0.8	0.25	0.800	0.250	0.0	0.0
5	0.2	0.50	0.213	0.455	1.3	4.5
6	0.4	0.50	0.393	0.479	0.7	2.1
7	0.6	0.50	0.591	0.495	0.9	0.5
8	0.8	0.50	0.792	0.494	0.8	0.6
9	0.2	0.75	0.179	0.731	2.1	1.9
10	0.4	0.75	0.388	0.739	1.2	1.1
11	0.6	0.75	0.591	0.742	0.9	0.8
12	0.8	0.75	0.795	0.747	0.5	0.3

3.6.3 The Results Verification

In Figs. 14 and 15, all the charts of the four mentioned stages are plotted together. As can be seen, the error values in the fourth case are less than the other cases. But the time consumed in this case is more than the other cases.

In order to evaluate the solution quality of the random bees algorithm, a practical reliability indicator is defined as the possibility of the solutions to reach a practical optimum. It should be noted that a practical optimum is defined as an optimum solution within 0.1% of the global optimum [18]. In this study, the best solution for

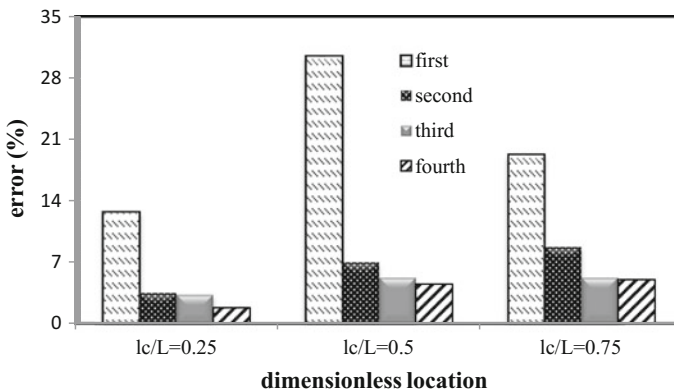


Fig. 14 Comparison of the mean error values at different crack locations by four mentioned optimization method

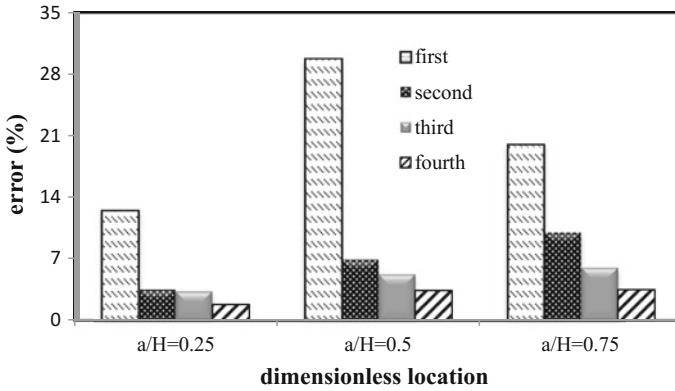


Fig. 15 Comparison of the mean error values at different crack depths by four mentioned optimization method

Table 8 Effectiveness of the bees algorithm optimization method

Practical reliability	Objective function average	Normalized price	The best objective function value
0.8	1.345×10^{-3}	15562.5	0.136×10^{-4}
0.9	1.212×10^{-3}	13833.33	7.809×10^{-4}
0.6	4.231×10^{-3}	20750	6.641×10^{-3}
0.7	6.264×10^{-3}	17785.71	9.864×10^{-3}

objective function was found after 100 iterations. Therefore, this value is used to define the practical reliability. Another indicator which has been used in this research is called normalized price and is defined as the average number of the function evaluations by the practical reliability. In this section, 4 cases have been chosen from Table 5, and normalized prices and practical reliabilities of these cases are presented in Table 8. It is necessary to mention that the values presented in this table validate the effectiveness of the bees algorithm results.

As can be seen from Table 8, the lowest normalized price belongs to crack case 2 and it shows that an acceptable result has been obtained with the minimum cost.

4 Conclusions

In this study, the crack identification problem of a beam on elastic foundation was investigated by applying a non-destructive method. After modelling the crack with torsional spring and performing DQ method on the differential equation of a beam on elastic foundation and applying continuity equations and boundary conditions, natural frequencies of a cracked beam were obtained. The computed numerical natural frequencies by DQ were in good agreement with those of finite element analysis. Also, in

this study, bees algorithm has been applied to the inverse solution. Therefore, the cracks with different depths and locations were created in a beam on elastic foundation, and the related natural frequencies were calculated for each case of beam on the elastic foundation. Then, computed natural frequencies of a beam on elastic foundation by finite element analysis were considered as the input data for the crack identification algorithm, and also the depths and locations of the cracks were determined. The proposed method predicted crack depths and locations with a very good accuracy so that the maximum error was under 10%. The worst cases were corresponding to the cracks with small depths which were near the free end of the beam.

References

1. Hull JB, John VB (1972) Non destructive testing, 1st ed. McMillan Education Ltd
2. Lee YS, Myung JC (2000) A study on crack detection using eigen frequency test data. *J Comput Struct* 77:327–342
3. Swamidas ASJ, Yang XF, Seshadri R (2004) Identification of cracking in beam structures using timoshenko and euler formulations. *J Eng Mech* 130(11):1297–1308
4. Qian GL, Gu SN, Jiang JS (1990) The dynamic behavior and crack detection of a beam with a crack. *J Sound Vib* 138(2):233–243
5. Narkis Y (1994) Identification of crack location in vibrating simply supported beams. *J Sound Vib* 172(4):549–558
6. Nanthakumar SS, Lahmer T, Rabczuk T (2013) Detection of flaws in piezoelectric structures using extended FEM. *Int J Numer Methods Eng* 96:373–389
7. Nanthakumar SS, Lahmer T, Rabczuk T (2014) Detection of multiple flaws in piezoelectric structures using XFEM and level sets. *Comput Methods Appl Mech Eng* 275:98–112
8. Dems K, Meroz Z (2001) Identification of damage in beam and plate structures using parameters dependent frequency changes. *J Eng Comput* 18(1/2):96–120
9. Chang CC, Chen LW (2005) Detection of the location and size of cracks in the multiple cracked beam by spatial wavelet transform based approach. *Mech Syst Signal Process* 19:139–155
10. Baghmisheh M, Peimani M, Sadeghi M, Ettefagh M (2008) Crack detection in beam- like structures using genetic algorithms. *J Appl Soft Comput* 8:1150–1160
11. Bellman R, Kashef BG, Casti J (1972) Differential quadrature: a technique for the rapid solution of nonlinear partial differential equations. *J Comput Phys* 10:40–51
12. Moradi S, Razi P, Fathi L (2011) On the application of bees algorithm to the problem of crack detection of beam-type structures. *Comput Struct* 89:2169–2175
13. Rizos PF, Aspragathos N, Dimargonas AD (2002) Identification of crack location and magnitude in a cantil ver beam from the vibration modes. *J Sound Vib* 257(3):559–583
14. Jang SK, Bert CW, Striz AG (1989) Application of differential quadrature to static analysis of structural components. *Int J Numer Method Eng* 28(3):561–577
15. Shu C (2000) *Differential quadrature and its application in engineering*. ISBN 1-85233-209-3 (2000)
16. Von Frisch K (1976) *Bees: their vision, chemical senses and language*, Revised edn. Cornell University Press, NY, Ithaca
17. Camazine S, Deneubourg J, Franks NR, Sneyd J, Theraula G, Bonabeau E (2013) *self-organization in Biological Systems*. Princeton University Press, Princeton
18. Kogiso N, Watson LT, Gurdal Z, Haftka RT (1994) Genetic algorithms with local improvement for composite laminate design. *Struct Optim* 7(4):207–218

Nonlinear Static Bending Analysis of Functionally Graded Plates Using MISQ24 Elements with Drilling Rotations



H. Nguyen-Van, H. L. Ton-That, T. Chau-Dinh and N. D. Dao

Abstract This paper develops a computational model for nonlinear static bending analysis of functionally graded (FG) plates using a smoothed four-node quadrilateral element MISQ24 [1, 2] within the context of the first-order shear deformation theory (FSDT). In particular, the construction of the nonlinear geometric equations is based on Total Lagrangian approach in which motion at the present state compared with the initial state is considered large. Small strain–large displacement theory of von Karman will be used in nonlinear formulations of the smoothed quadrilateral element MISQ24 with drilling rotations. The drilling rotations are introduced to improve the coarse mesh accuracy of the MISQ24 element. The solution of the nonlinear equilibrium equations is obtained by the iterative method of Newton–Raphson with the appropriate convergence criteria. The present numerical results are compared with the other numerical results available in the literature in order to demonstrate the effectiveness of the developed element. These results also contribute a better knowledge and understanding of nonlinear bending behaviors of these structures.

Keywords Functionally graded plates • Nonlinear static bending analysis
First-order shear deformation theory (FSDT) • Drilling rotations

H. Nguyen-Van (✉) · H. L. Ton-That · N. D. Dao
Faculty of Civil Engineering, Ho Chi Minh City University of Architecture,
District 3, Ho Chi Minh City, Vietnam
e-mail: hieu.nguyenvan@uah.edu.vn

H. L. Ton-That
Faculty of Civil Engineering, Ho Chi Minh City University of Technology
and Education, Thu Duc District, Ho Chi Minh City, Vietnam

T. Chau-Dinh
GACES, Faculty of Civil Engineering, Ho Chi Minh City University of Technology
and Education, Thu Duc District, Ho Chi Minh City, Vietnam

© Springer Nature Singapore Pte Ltd. 2018

H. Nguyen-Xuan et al. (eds.), *Proceedings of the International Conference on Advances in Computational Mechanics 2017*, Lecture Notes in Mechanical Engineering, https://doi.org/10.1007/978-981-10-7149-2_31

1 Introduction

To date, composite materials play an important role in many manufacturing industries such as space shuttles, airplanes, ships, and cars because of their high strength-to-weight, stiffness-to-weight ratios, excellent resistance to corrosive substances, and potentially high overall durability. Laminated composite materials, however, often suffer from the delaminated phenomenon that occurs due to the weak bonds and stress concentration between laminas and causes to reduce lifetime of the materials. To overcome the delamination, the concept of functionally graded materials (FGMs) was firstly proposed by Japanese scholars in 1984 [3]. The FGMs are constituted by two different materials, which are usually ceramic and metal, with the material properties continuously changed in one direction. This makes the FGMs free-stress concentration, toughness, and high-temperature resistance and be widely applied in many structures.

The rapid growth of FGM structures has required deep research on behavior of these structures, especially FGM plates. Many analytical and numerical methods have been developed to simulate and analyze the behavior of FGM plates under various loading conditions. The analytical methods [4–8] limit on the FGM plates with simple geometry and boundary conditions. In contrast, the numerical methods such as finite element methods, mesh-free methods, and isogeometric methods [9–13] can effectively compute the behavior of the FGM plates having arbitrary shape, loadings, and boundaries. More researches on the analysis of FGM plates can be found in a recent critical review of Jha et al. [14].

Within these above numerical methods, the finite element methods (FEMs) employed for FGM plates using the first-order shear deformation theory (FSDT) give reasonable results and easy implementation in the standard FEM codes. Although triangular finite elements are most efficient for discretizing arbitrary shell geometries, quadrilateral elements are usually used owing to their better performance with respect to convergence rates than that of triangular elements. The difficulty in the development of the four-node element is that such elements are too stiff when simulating thin plates. This phenomenon is called shear locking and can be treated by many techniques such as assumed natural strain (ANS), enhanced assumed strain (EAS), mixed interpolation of tensorial components (MITC), or discrete shear gap (DSG). Recently, modification of the standard FEM, the so-called smoothed FEM (SFEM), has been suggested by Liu et al. [15], and given excellent results when applied to different types of plate problems made of laminated composite [16–18] or FG materials [19, 20]. Some latest numerical methods such as isogeometric methods have been also developed for composite and FG materials [21–23].

The main objective of this work is to further develop the flat four-node MISQ24 element (Mixed Interpolation Smoothing Quadrilateral element with 24 DOFs), whose performances in linear analysis have already been verified and demonstrated in References [1, 2] for geometric nonlinear bending analysis of functionally graded plates. The von Karman's large deflection theory and the Total Lagrangian

(TL) approach are utilized in the small strain–large deformation formulation, and then, the solution of nonlinear equilibrium equations is obtained by the Newton–Raphson method with the automatic incremental algorithm. With the aid of the assumed strain smoothing technique, the evaluations of the membrane, bending, and geometric stiffness matrices are built by the integration on smoothing cells’ boundaries. This technique incorporated with the drilling degrees of freedom contributes to the high accuracy of the proposed method using the MISQ24 element even with coarse meshes.

In the next section, a brief review of the FSDT finite element formulations for geometrically nonlinear analysis of FGM plates is first introduced. Then, the description of assumed strain smoothing approach for the generalized strain and the tangent stiffness matrix of the MISQ24 element are developed. Numerical examples of FGM plates are analyzed to verify the robustness and accuracy of the MISQ24 elements. Finally, some concluding remarks are withdrawn.

2 Nonlinear Bending Formulation of the MISQ24 Element

2.1 The First-Order Shear Deformation Theory (FSDT) for Geometric Nonlinear Bending Analysis

Consider an FGM plate made of metal and ceramic constituents as shown in Fig. 1. The FGM material continuously changes through the plate thickness h from the metal at the bottom to the ceramic at the top of the plate. Assume that through the FGM plate thickness, the Poisson’s ratio $\nu(z)$ and the Young’s modulus $E(z)$ are characterized by the following power law

$$E(z) = (E_c - E_m) \left(\frac{1}{2} + \frac{z}{h} \right)^n + E_m \tag{1}$$

$$\nu(z) = (\nu_c - \nu_m) \left(\frac{1}{2} + \frac{z}{h} \right)^n + \nu_m \tag{2}$$

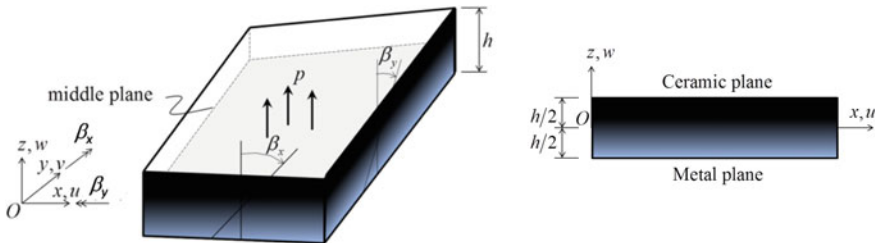


Fig. 1 Functionally graded plate and positive definition of displacements, rotations

in which E_c, ν_c and E_m, ν_m are Young’s moduli and Poisson’s ratios of the ceramic and metal constituents, respectively; $n \geq 0$ is the power law index; and z is the coordinates in the direction normal to the middle plane Oxy of the plate (see Fig. 1).

When the FGM plate is applied by loads p normal to the top, displacements in the plate can be expressed by the first-order shear deformation theory [24] as follows

$$\begin{aligned} u(x, y, z) &= u_0 + z\beta_x \\ v(x, y, z) &= v_0 + z\beta_y \\ w(x, y, z) &= w_0 \end{aligned} \tag{3}$$

Here u, v , and w are the translational displacements in the x -, y -, and z -directions, respectively; u_0, v_0 , and w_0 correspond to the displacements of the middle plane; and β_x and β_y are, respectively, the rotation of the mid-plane about y - and x -axis with positive directions defined in Fig. 1.

For large deformation analysis, the in-plane vector of Green-Lagrangian strain in a plate element is

$$\boldsymbol{\varepsilon} = \begin{Bmatrix} \varepsilon_x \\ \varepsilon_y \\ \varepsilon_{xy} \end{Bmatrix} = \begin{Bmatrix} u_{,x} + \frac{1}{2}(u_{,x}^2 + v_{,x}^2 + w_{,x}^2) \\ v_{,y} + \frac{1}{2}(u_{,y}^2 + v_{,y}^2 + w_{,y}^2) \\ u_{,y} + v_{,x} + (u_{,x}u_{,y} + v_{,x}v_{,y} + w_{,x}w_{,y}) \end{Bmatrix} \tag{4}$$

Substituting Eq. (3) into Eq. (4) and considering the von Karman’s large deflection assumption, the in-plane strain vector can be rewritten as

$$\boldsymbol{\varepsilon} = \boldsymbol{\varepsilon}_m + z\boldsymbol{\varepsilon}_b \tag{5}$$

in which

$$\boldsymbol{\varepsilon}_m = \begin{Bmatrix} u_{0,x} + \frac{1}{2}w_{,x}^2 \\ v_{0,y} + \frac{1}{2}w_{,y}^2 \\ u_{0,y} + v_{0,x} + w_{,x}w_{,y} \end{Bmatrix} = \underbrace{\begin{Bmatrix} u_{0,x} \\ v_{0,y} \\ u_{0,y} + v_{0,x} \end{Bmatrix}}_{\text{linearpart}} + \underbrace{\begin{Bmatrix} \frac{1}{2}w_{,x}^2 \\ \frac{1}{2}w_{,y}^2 \\ w_{,x}w_{,y} \end{Bmatrix}}_{\text{nonlinearpart}} = \boldsymbol{\varepsilon}_m^L + \boldsymbol{\varepsilon}_m^{NL} \tag{6}$$

$$\boldsymbol{\varepsilon}_b = \begin{Bmatrix} \beta_{x,x} \\ \beta_{y,y} \\ \beta_{x,y} + \beta_{y,x} \end{Bmatrix} \tag{7}$$

The transverse shear strain vector is given as

$$\boldsymbol{\gamma} = \begin{Bmatrix} \gamma_{xz} \\ \gamma_{yz} \end{Bmatrix} = \begin{Bmatrix} \beta_x - w_{,x} \\ \beta_y - w_{,y} \end{Bmatrix} \tag{8}$$

The constitutive relationship of the FGM plate can be expressed as

$$\boldsymbol{\sigma}^* = \mathbf{D}^* \boldsymbol{\varepsilon}^* \tag{9}$$

where

$$\boldsymbol{\sigma}^* = \begin{Bmatrix} \mathbf{N} \\ \mathbf{M} \\ \mathbf{T} \end{Bmatrix}, \boldsymbol{\varepsilon}^* = \begin{Bmatrix} \boldsymbol{\varepsilon}_m \\ \boldsymbol{\varepsilon}_b \\ \boldsymbol{\gamma} \end{Bmatrix}, \mathbf{D}^* = \begin{bmatrix} \mathbf{A} & \mathbf{B} & \mathbf{0} \\ \mathbf{B} & \mathbf{D} & \mathbf{0} \\ \mathbf{0} & \mathbf{0} & \mathbf{C} \end{bmatrix} \tag{10}$$

and $\mathbf{N} = [N_x \ N_y \ N_{xy}]$ is the in-plane traction resultant, $\mathbf{T} = [Q_x \ Q_y]$ is the out-of-plane traction resultant and $\mathbf{M} = [M_x \ M_y \ M_{xy}]$ is the out-of-plane moment resultant. \mathbf{A} , \mathbf{B} , \mathbf{D} , and \mathbf{C} are the material constant matrices which are given as follow

$$\begin{aligned} (\mathbf{A}, \mathbf{B}, \mathbf{D}) &= \int_{-h/2}^{h/2} (1, z, z^2) \mathbf{Q}(z) dz \\ \mathbf{C} &= \int_{-h/2}^{h/2} \mathbf{S}(z) dz \end{aligned} \tag{11}$$

with

$$\mathbf{Q}(z) = \frac{E(z)}{1-\nu(z)^2} \begin{bmatrix} 1 & \nu(z) & 0 \\ \nu(z) & 1 & 0 \\ 0 & 0 & (1-\nu(z))/2 \end{bmatrix}; \mathbf{S}(z) = \frac{E(z)}{2(1+\nu(z))} \begin{bmatrix} 1 & 0 \\ 0 & 1 \end{bmatrix} \tag{12}$$

2.2 Strain Smoothing Formulations of MISQ24 Element for Geometric Nonlinear Analysis

As shown in Fig. 2, a quadrilateral element domain Ω_c is further divided into nc smoothing cells. The generalized strain field is smoothed by a weighted average of the original generalized strains using the strain smoothing operation for each smoothing cell as follows.

$$\tilde{\boldsymbol{\varepsilon}}_m^L = \frac{1}{A_c} \int_{\Omega_c} \boldsymbol{\varepsilon}_m^L(\mathbf{x}) d\Omega \tag{13}$$

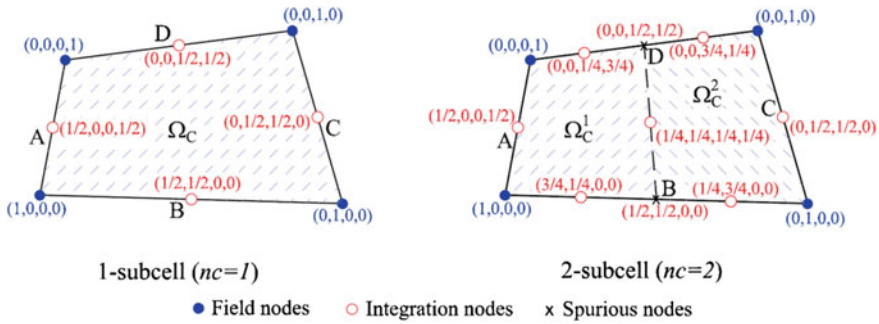


Fig. 2 Subdivision of an element into nc smoothing cells and the values of shape functions at nodes in the format (N1, N2, N3, N4)

$$\tilde{\epsilon}_m^{NL} = \frac{1}{A_c} \int_{\Omega_c} \epsilon_m^{NL}(\mathbf{x}) d\Omega \tag{14}$$

$$\tilde{\epsilon}_b = \frac{1}{A_c} \int_{\Omega_c} \epsilon_b(\mathbf{x}) d\Omega \tag{15}$$

where $\tilde{\epsilon}_m^L$, $\tilde{\epsilon}_m^{NL}$, $\tilde{\epsilon}_b$ are the smoothed strains, and A_c is the area of the smoothing cell Ω_c .

Introducing the approximation of the linear membrane strain by the quadrilateral finite element using Allman-type interpolation functions with drilling degrees of freedom [25] and applying the divergence theorem, the smoothed membrane strain can be obtained as

$$\tilde{\epsilon}_m^L = \frac{1}{A_c} \int_{\Gamma_c} \mathbf{n}(\mathbf{x}) \mathbf{u}(\mathbf{x}) d\Gamma = \frac{1}{A_c} \int_{\Gamma_c} \sum_{i=1}^4 \mathbf{n}(\mathbf{x}) \mathbf{N}_i(\mathbf{x}) \mathbf{q}_i d\Gamma = \sum_{i=1}^4 \tilde{\mathbf{B}}_{mi}^L \mathbf{q}_i \tag{16}$$

where

$$\tilde{\mathbf{B}}_{mi}(\mathbf{x}_C) = \frac{1}{A_c} \int_{\Gamma_c} \begin{pmatrix} N_i n_x & 0 & 0 & 0 & 0 & N_x n_x \\ 0 & N_i n_y & 0 & 0 & 0 & N_y n_y \\ N_i n_y & N_i n_x & 0 & 0 & 0 & N_x n_y + N_y n_x \end{pmatrix} d\Gamma \tag{17}$$

in which $\mathbf{q}_i = [u_i \ v_i \ w_i \ \beta_{xi} \ \beta_{yi} \ \beta_{zi}]$ is the nodal displacement vector; N_x and N_y are Allman's incompatible shape functions defined in [22], and n_x and n_y are the components of the outward unit vector \mathbf{n} normal to the boundary Γ_c .

Applying Gauss integration along with four segments of the boundary Γ_c of the smoothing domain Ω_c , the above equation can be rewritten in algebraic form as

$$\begin{aligned}
 \tilde{\mathbf{B}}_{mi}(\mathbf{x}_C) = & \frac{1}{A_C} \sum_{b=1}^4 \begin{pmatrix} \sum_{n=1}^{nG} w_n N_i(\mathbf{x}_{bn}) n_x & 0 & 0 & 0 & 0 & 0 \\ 0 & \sum_{n=1}^{nG} w_n N_i(\mathbf{x}_{bn}) n_y & 0 & 0 & 0 & 0 \\ \sum_{n=1}^{nG} w_n N_i(\mathbf{x}_{bn}) n_y & \sum_{n=1}^{nG} w_n N_i(\mathbf{x}_{bn}) n_x & 0 & 0 & 0 & 0 \end{pmatrix} \\
 & + \frac{1}{A_C} \sum_{b=1}^4 \begin{pmatrix} 0 & 0 & 0 & 0 & 0 & \sum_{n=1}^{nG} w_n N x_i(\mathbf{x}_{bn}) n_x \\ 0 & 0 & 0 & 0 & 0 & \sum_{n=1}^{nG} w_n N y_i(\mathbf{x}_{bn}) n_y \\ 0 & 0 & 0 & 0 & \sum_{n=1}^{nG} w_n N x_i(\mathbf{x}_{bn}) n_y + \sum_{n=1}^{nG} w_n N y_i(\mathbf{x}_{bn}) n_x & 0 \end{pmatrix}
 \end{aligned} \tag{18}$$

where nG is the number of Gauss integration points, \mathbf{x}_{bn} is the Gauss point and w_n is the corresponding weighting coefficients. The first term in Eq. (18), which relates to the in-plane translations (approximated by bilinear shape functions), is evaluated by one Gauss point ($nG = 1$). The second term, associated with the in-plane rotations (approximated by quadratic shape functions), is computed using two Gauss points ($nG = 2$).

In a similar way, the smoothed nonlinear membrane strain over the element domain Ω_C can be written as

$$\tilde{\boldsymbol{\varepsilon}}_m^{NL} = \sum_{i=1}^4 \tilde{\mathbf{B}}_{mi}^{NL} \mathbf{q}_i \tag{19}$$

where $\tilde{\mathbf{B}}_{mi}^{NL}$ is the smoothed nonlinear gradient matrix in the smoothing cell given as

$$\tilde{\mathbf{B}}_{mi}^{NL} = \tilde{\mathbf{H}} \tilde{\mathbf{G}}_i \tag{20}$$

in which

$$\tilde{\mathbf{G}}_i = \frac{1}{A_C} \sum_{g=1}^4 \begin{pmatrix} 0 & 0 & N_i(\mathbf{x}_g^G) n_x & 0 & 0 & 0 \\ 0 & 0 & N_i(\mathbf{x}_g^G) n_y & 0 & 0 & 0 \end{pmatrix} l_g^c, \tag{21}$$

$$\tilde{\mathbf{H}} = \sum_{i=1}^4 \begin{pmatrix} \frac{1}{A_c} \sum_{j=1}^4 N_i(\mathbf{x}_j^G) n_x l_j^c w_{0i} & 0 \\ 0 & \frac{1}{A_c} \sum_{j=1}^4 N_i(\mathbf{x}_j^G) n_y l_j^c w_{0i} \\ \frac{1}{A_c} \sum_{j=1}^4 N_i(\mathbf{x}_j^G) n_y l_j^c w_{0i} & \frac{1}{A_c} \sum_{j=1}^4 N_i(\mathbf{x}_j^G) n_x l_j^c w_{0i} \end{pmatrix} \quad (22)$$

and w_{0i} is the deflection at the node i of the element.

The smoothed bending strain over the element domain Ω_C is expressed as

$$\tilde{\epsilon}_b = \sum_{i=1}^4 \tilde{\mathbf{B}}_{bi} \mathbf{q}_i \quad (23)$$

where

$$\tilde{\mathbf{B}}_{bi} = \frac{1}{A_c} \sum_{b=1}^4 \begin{pmatrix} 0 & 0 & 0 & N_i(\mathbf{x}_b^G) n_x & 0 & 0 \\ 0 & 0 & 0 & 0 & N_i(\mathbf{x}_b^G) n_y & 0 \\ 0 & 0 & 0 & N_i(\mathbf{x}_b^G) n_y & N_i(\mathbf{x}_b^G) n_x & 0 \end{pmatrix} l_b \quad (24)$$

The shear strain is expressed by independent interpolation fields in the natural coordinate systems as [26]

$$\begin{bmatrix} \gamma_x \\ \gamma_y \end{bmatrix} = \mathbf{J}^{-1} \begin{bmatrix} \frac{1}{2}(1-\xi) & 0 & \frac{1}{2}(1+\xi) & 0 \\ 0 & \frac{1}{2}(1-\eta) & 0 & \frac{1}{2}(1+\eta) \end{bmatrix} \begin{bmatrix} \gamma_\eta^A \\ \gamma_\xi^B \\ \gamma_\eta^C \\ \gamma_\xi^D \end{bmatrix} \quad (25)$$

where \mathbf{J} is the Jacobian matrix and the midside nodes A, B, C, and D are shown in Fig. 2.

Expressing γ_η^A , γ_η^C and γ_ξ^B , γ_ξ^D in terms of the discretized field \mathbf{q} , we obtain the shear gradient matrix

$$\bar{\mathbf{B}}_{si} = \mathbf{J}^{-1} \begin{pmatrix} 0 & 0 & N_{i,\xi} & b_i^{11} N_{i,\xi} & b_i^{12} N_{i,\xi} & 0 \\ 0 & 0 & N_{i,\eta} & b_i^{21} N_{i,\eta} & b_i^{22} N_{i,\eta} & 0 \end{pmatrix}, \quad (26)$$

where

$$b_i^{11} = \xi_i x_{i,\xi}^M, \quad b_i^{12} = \xi_i y_{i,\xi}^M, \quad b_i^{21} = \eta_i x_{i,\eta}^L, \quad b_i^{22} = \eta_i y_{i,\eta}^L \quad (27)$$

in which $\xi_i \in \{-1, 1, 1, -1\}$, $\eta_i \in \{-1, -1, 1, 1\}$, and $(i, M, L) \in \{(1, B, A); (2, B, C); (3, D, C); (4, D, A)\}$

Finally, the element tangent stiffness matrix is modified as

$$\tilde{\mathbf{K}}_T = \tilde{\mathbf{K}}_L + \tilde{\mathbf{K}}_{NL} + \tilde{\mathbf{K}}_g \tag{28}$$

where

$$\tilde{\mathbf{K}}_L = \sum_{i=1}^{nc} \tilde{\mathbf{B}}_{Li}^T \mathbf{D}^* \tilde{\mathbf{B}}_{Li} A_i + \gamma \int_{\Omega} \mathbf{b}^T \mathbf{b} d\Omega \tag{29}$$

$$\tilde{\mathbf{K}}_{NL} = \sum_{i=1}^{nc} \tilde{\mathbf{B}}_{NLi}^T \mathbf{D}^* \tilde{\mathbf{B}}_{NLi} A_i \tag{30}$$

$$\tilde{\mathbf{K}}_g = \sum_{i=1}^{nc} \tilde{\mathbf{G}}_i^T \hat{\mathbf{N}} \tilde{\mathbf{G}}_i A_i \tag{31}$$

$$\tilde{\mathbf{B}}_L = \begin{bmatrix} \tilde{\mathbf{B}}_m^L \\ \tilde{\mathbf{B}}_b \\ \tilde{\mathbf{B}}_s \end{bmatrix}, \tilde{\mathbf{B}}_{NL} = \begin{bmatrix} \tilde{\mathbf{B}}_m^{NL} \\ \mathbf{0} \\ \mathbf{0} \end{bmatrix}, \hat{\mathbf{N}} = \begin{bmatrix} N_x & N_{xy} \\ N_{xy} & N_y \end{bmatrix}, \mathbf{b}_i = \begin{bmatrix} -\frac{1}{2} N_{i,y} \\ -\frac{1}{2} N_{i,x} \\ -\frac{1}{2} (N_{x_{i,y}} + N_{y_{i,x}}) - N_i \end{bmatrix} \tag{32}$$

and the positive penalty parameter $\gamma = G$ and the number of smoothing cells $nc = 2$ are chosen in this study. The penalty matrix, the second term in Eq. (29), is integrated using one point Gauss quadrature to suppress a spurious, zero-energy mode associated with the drilling rotation.

The internal forces at the time t computed from the stress state in the structures are rewritten as

$${}^t \tilde{\mathbf{F}} = \int_{\Omega} (\tilde{\mathbf{B}}_L + \tilde{\mathbf{B}}_{NL})^t \boldsymbol{\sigma}^* d\Omega \tag{33}$$

in which the stress resultant after the i th iteration is

$${}^t \boldsymbol{\sigma}_{i+1}^* = {}^t \boldsymbol{\sigma}_i^* + {}^t \Delta \boldsymbol{\sigma}^* \tag{34}$$

Finally, the nonlinear equations can be rewritten as

$${}^t \tilde{\mathbf{K}}_T \Delta \mathbf{q} = {}^{t+\Delta t} \mathbf{P} - {}^t \tilde{\mathbf{F}} \tag{35}$$

where ${}^{t+\Delta t} \mathbf{P}$ is the element external force at time $t + \Delta t$.

3 Numerical Results and Discussions

In this section, we will test and assess the MISQ24 element through numerical examples. In all examples, the Newton–Raphson method and automatic incremental algorithm are used to solve the nonlinear finite element Eq. (35). The convergence tolerance of displacement is taken to be 0.001. Unless other specified, the shear correction factors are equal to 5/6, and SI units are used. Material properties of the FGM plates used in numerical simulations are: Aluminum (Al) with $E = 70$ GPa; $\nu = 0.3$ and Zirconia (ZrO_2-2) with $E = 151$ GPa; $\nu = 0.3$.

3.1 A Simply Supported Skew FGM Plate

The bending behavior of a skew plate is often considered as a corner stress concentration problem due to a strong singularity in bending moments at the obtuse vertex. It is often avoided for nonlinear analyses of plate bending problems. Therefore, this section deal with the nonlinear bending analysis of clamped skew plates with three skew angles, namely $\alpha = 0^\circ, 30^\circ, 60^\circ$ under a uniform load q . The studied plate have a side length $2a = 2b = 0.2$ m and thickness $h = 0.01$ m. The full plate is modeled using 8×8 elements as shown in Fig. 3. The normalized parameters of the present results are the central deflection $w^* = w/h$ and the load parameter $P = q(2a)^4/(E_A h^4)$.

First, the convergence and accuracy of the present solutions are investigated for a square plate (skew angle $\alpha = 0^\circ$). Table 1 shows the convergence study of the normalized central deflection of the FGM plate with the volume fraction exponent $n = 2.0$. It can be seen that the present method is convergent with mesh refinement only with an 8×8 mesh. The load-deflection curves obtained by the present results with 8×8 elements are also plotted and compared with numerical solutions of Praveen and Reddy [8] using 16×16 isoparametric four-node elements based on the third-order shear deformation theory (TSDT) as shown in Fig. 4a. It is investigated that the present results are in good agreement with those from the

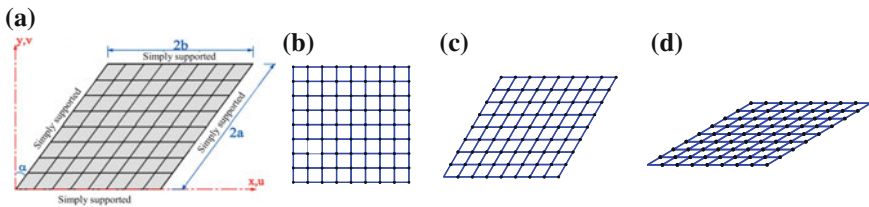


Fig. 3 A simply supported skew plate: **a** geometry, **b** a mesh with $\alpha = 0^\circ$, **c** a mesh with $\alpha = 30^\circ$, **d** a mesh with $\alpha = 60^\circ$

Table 1 Convergence study of an FGM square plate with the volume fraction exponent $n = 2.0$

Load parameter $P = q(2a)^4/(E_A h^4)$	Normalized central deflection $w^* = w/h$			
	Mesh 4×4	Mesh 6×6	Mesh 8×8	Mesh 10×10
1.143	0.035	0.035	0.035	0.035
2.286	0.070	0.070	0.070	0.070
3.428	0.104	0.104	0.104	0.104
4.571	0.138	0.138	0.137	0.137
5.714	0.171	0.170	0.169	0.169
6.857	0.203	0.202	0.201	0.201
8.000	0.234	0.232	0.23	0.23
9.143	0.264	0.261	0.259	0.259
10.286	0.293	0.289	0.286	0.286
11.428	0.321	0.315	0.313	0.312

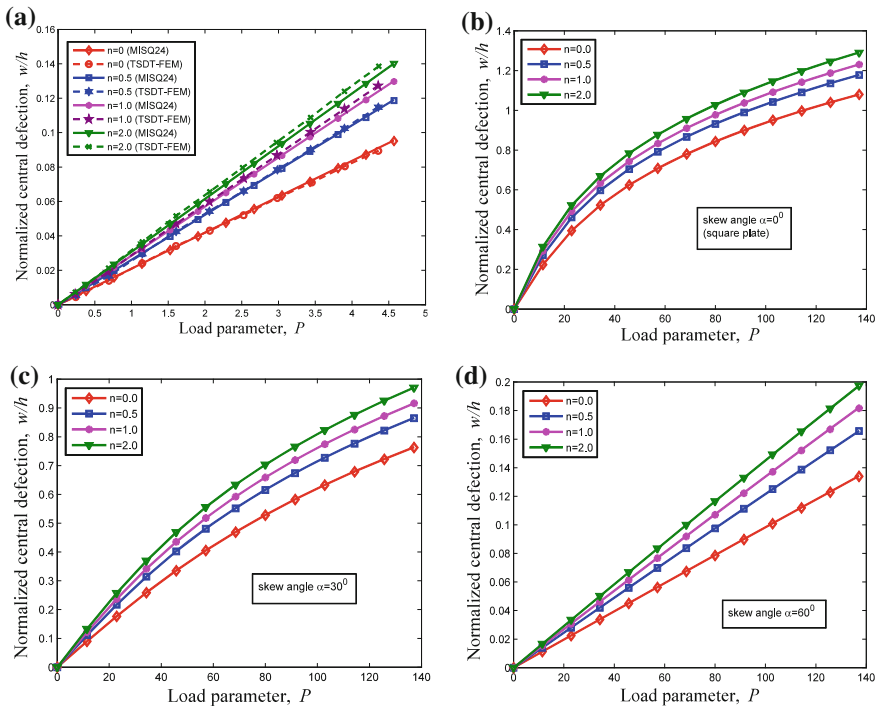


Fig. 4 Load-deflection curves of the skew plate: **a, b** nonlinear behavior with $\alpha = 0^\circ$, **c** nonlinear behavior with $\alpha = 30^\circ$, **d** nonlinear behavior with $\alpha = 60^\circ$

TSDT. This confirms the accuracy of the present MISQ24 element based on FSDT even with a coarse mesh 8×8 elements.

Next, the effect of skew angle α on the normalized central deflection is studied with the load parameter P increasing from 0 to 140. It is followed from Fig. 4b-d that the maximum central deflection decreases as the skew angle of the plate increases with the increase in load for any gradient index. It is also observed that the load-deflection curves for $\alpha = 0^\circ$ and 30° are obviously nonlinear while the curve for $\alpha = 60^\circ$ is almost linear. The normalized central deflections also increase with the increase of the gradient index under the same load. Based on these results, the rigidity of skew plates can be improved by increasing the skew angles or decreasing the gradient index.

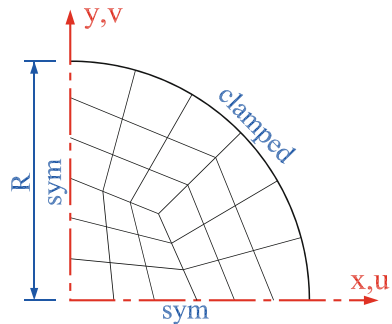
3.2 A Clamped Circular FGM Plate

The large deformation analysis of a clamped circular FGM plate under uniform pressure q is considered in this section. The plate has the radius $R = 1$ m and the thickness $h = 0.1$ m. Owing to symmetry, a quadrant of the plate is modeled with a 27-element mesh as shown in Fig. 5.

The computed normalized central deflection w/h versus the normalized load parameter $P = qR^4/(E_A h^4)$ of the present analysis using MISQ24 element together with the solution by the FSDT-based isogeometric analysis [13] are displayed in Fig. 6. It is interesting to note that the obtained numerical results match very well with those plotted here.

The effect of span-to-thickness (R/h) ratios on the nonlinear bending behavior of the above clamped circular plate is also studied for three values, namely $R/h = 10, 100, 1000$ with the volume fraction exponent $n = 0, 0.5, \text{ and } 2$. Figure 6b illustrates the load-deflection curves for different R/h ratios. From Fig. 6b, it is concluded that the effect of the span-to-thickness (R/h) ratio on the normalized central deflections has no influence for thin circular plates with $R/h > 100$. It is also noted that the shear locking phenomenon is free in this example.

Fig. 5 A mesh of a quadrant of the clamped circular FGM plate



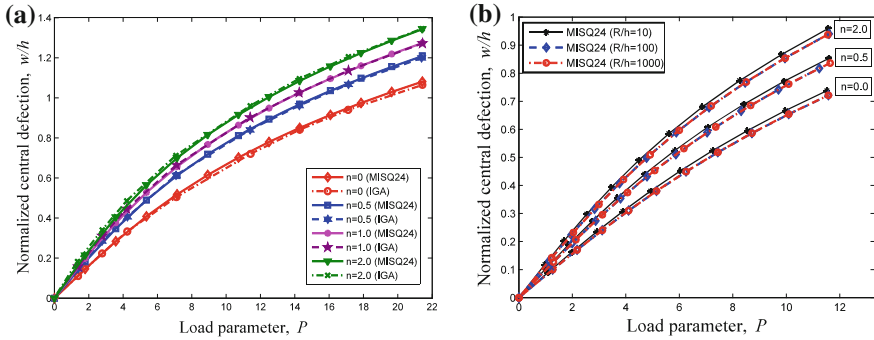


Fig. 6 Load-deflection curves of the circular plate: **a** effect of volume fraction exponent with $R/h = 10$; **b** effect of span-to-thickness (R/h) ratios

4 Conclusion

In this paper, the MISQ24 element is further developed and successfully applied to geometrically nonlinear analysis of functionally graded plate structures in the framework of the FSDT. Numerical examples have been carried out, and the present element is found to yield satisfactory results in comparison with other available numerical results using finite element as well as isogeometric methods. It is observed that the present approach remains accurate for nonlinear analysis of both moderately thin and thick plates even with coarse meshes. In addition, the present element has the advantage of being simple in formulation and ready for use in analysis of both plate and shell structures with a minimal amount of effort to implement. The success of the present flat element provides a further demonstration of efficient flat quadrilateral elements for nonlinear analysis.

References

1. Nguyen-Van H, Mai-Duy N, Karunasena W, Tran-Cong T (2011) Buckling and vibration analysis of laminated composite plate/shell structures via a smoothed quadrilateral flat shell element with in-plane rotations. *Comput Struct* 89(7–8):612–625
2. Nguyen-Van H, Mai-Duy N, Tran-Cong T (2009) An improved quadrilateral flat element with drilling degrees of freedom for shell structural analysis. *Comput Model Eng Sci (CMES)* 49 (2):81–110
3. Udupa G, Rao SS, Gangadharan KV (2014) Functionally graded composite materials: an overview. *Proc Mater Sci* 5:1291–1299
4. Nguyen V-H, Nguyen T-K, Thai H-T, Vo TP (2014) A new inverse trigonometric shear deformation theory for isotropic and functionally graded sandwich plates. *Compos B Eng* 66:233–246
5. Thai HT, Choi DH (2013) A simple first-order shear deformation theory for the bending and free vibration analysis of functionally graded plates. *Compos Struct* 101:332–340

6. Vel SS, Batra RC (2002) Exact solution for thermoelastic deformations of functionally graded thick rectangular plates. *AIAA J* 40:1421–1433
7. Carrera E, Brischetto S, Robaldo A (2008) Variable kinematic model for the analysis of functionally graded material plates. *AIAA J* 46:194–203
8. Praveen GN, Reddy JN (1998) Nonlinear transient thermo elastic analysis of functionally graded ceramic-metal plates. *Int J Solids Struct* 35:4457–4476
9. Gilhooley DF, Batra RC, Xiao JR, McCarthy MA, Gillespie Jr JW (2007) Analysis of thick functionally graded plates by using higher-order shear and normal deformable plate theory and MLPG method with radial basis functions. *Compos Struct* 80:539–552
10. Neves AMA, Ferreira AJM, Carrera E, Cinefra M, Roque CMC, Jorge RMN, Soares CMM (2013) Static, free vibration and buckling analysis of isotropic and sandwich functionally graded plates using a quasi-3D higher-order shear deformation theory and a meshless technique. *Compos B Eng* 44:657–674
11. Thai CH, Zenkour AM, Abdel Wahab M, Nguyen-Xuan H (2016) A simple four-unknown shear and normal deformations theory for functionally graded isotropic and sandwich plates based on isogeometric analysis. *Compos Struct* 139:77–95
12. Zhao X, Liew KM (2009) Geometrically nonlinear of functionally graded plates using the element-free kp-Ritz method. *Comput Methods Appl Mech Eng* 198:1796–2811
13. Yu TT, Yin S, Bui TQ, Hirose S (2015) A simple FSDT-based isogeometric analysis for geometrically nonlinear functionally graded plates. *Finite Elem Anal Des* 96:1–10
14. Jha DK, Kant T, Singh RK (2013) A critical review of recent research on functionally graded plates. *Compos Struct* 96:833–849
15. Liu GR, Dai KY, Nguyen TT, Smoothed TTA (2007) Finite element method for mechanics problems. *Comput Mech* 39:859–877
16. Phung-Van P, Nguyen-Thoi T, Bui-Xuan T, Lieu-Xuan Q (2015) A cell-based smoothed three-node Mindlin plate element (CS-FEM-MIN3) based on the C0-type higher-order shear deformation for geometrically nonlinear analysis of laminated composite plates. *Comput Mater Sci* 96:549–558
17. Tran LV, Nguyen-Thoi T, Thai CH, Nguyen-Xuan H (2015) An edge-based smoothed discrete shear gap method using the C 0-Type higher-order shear deformation theory for analysis of laminated composite plates. *Mech Adv Mater Struct* 22:248–268
18. Nguyen-Van H, Nguyen-Hoai N, Chau-Dinh T, Nguyen-Thoi T (2014) Geometrically nonlinear analysis of composite plates and shells via a quadrilateral element with good coarse-mesh accuracy. *Compos Struct* 112:327–338
19. Nguyen-Xuan H, Tran LV, Nguyen-Thoi T, Vu-Do HC (2011) Analysis of functionally graded plates using an edge-based smoothed finite element method. *Compos Struct* 93:3019–3039
20. Phung-Van P, Nguyen-Thoi T, Luong-Van H, Lieu-Xuan Q (2014) Geometrically nonlinear analysis of functionally graded plates using a cell-based smoothed three-node plate element (CS-MIN3) based on the C0–HSdT. *Comput Methods Appl Mech Eng* 270:15–36
21. Tran LV, Phung-Van P, Lee J, Abdel Wahab M, Nguyen-Xuan H (2016) Isogeometric analysis for nonlinear thermomechanical stability of functionally graded plates. *Compos Struct* 140:655–667
22. Tran LV, Lee J, Nguyen-Van H, Nguyen-Xuan H, Abdel Wahab M (2015) Geometrically nonlinear isogeometric analysis of laminated composite plates based on higher-order shear deformation theory. *Int J Non-Linear Mech* 72:42–52
23. Phung-Van P, Nguyen LB, Tran LV, Dinh TD, Thai CH, Bordas SPA, Abdel-Wahab M, Nguyen-Xuan H (2015) An efficient computational approach for control of nonlinear transient responses of smart piezoelectric composite plates. *Int J Non-Linear Mech* 76:190–202
24. Reddy JN (2004) *Mechanics of laminated composite plates and shells—theory and analysis*. CRC Press

25. Ibrahimbegovic A, Taylor RL, Wilson EL (1990) A robust quadrilateral membrane finite element with drilling degrees of freedom. *Int J Numer Meth Eng* 30:445–457
26. Gruttmann F, Wagner W (2004) A stabilized one-point integrated quadrilateral Reissner-Mindlin plate element. *Int J Numer Meth Eng* 61:2273–2295

A Pull-Out Test to Characterize the Fiber/Matrix Interfaces Aging of Hemp Fiber Reinforced Polypropylene Composites



C. Nguyen-Duy, A. Makke and G. Montay

Abstract The fiber/matrix interface of natural fibers reinforced polymer composites is the weak zone that limits their use in some applications. The existing methods of fiber/matrix interface characterization are usually expensive and complexes. Also, the ‘real’ properties of the interface have not been well taken in the Interfacial Shear Strength (IFSS) calculation. Therefore, a pull-out test has been developed recently in our laboratory to limit these shortcomings. Moreover, the interface aging by environmental factors like relative humidity (RH) is still not clearly characterized. The developed method was then applied to investigate the interface deteriorations of the hemp fibers reinforced polypropylene composites due to moisture accelerated aging. By this way, fifty single fiber micro-composite specimens were tested after one week. The pull-out test was realized using an in situ micro-tensile machine. The IFSS was then determined considering the non-regular geometry and the non-constant of the fiber cross section. The results show that the humidity exposition weakens severely the fiber–matrix adhesion, and then the fibers were pulled out effortlessly from the matrix. Furthermore, qualitative deteriorations of the fiber and the interface were noted by optical observations. The IFSS was also severely reduced to 42.97% after one week. The qualitative deteriorations and the reduction of the mechanical properties of the interface were explicated by the occurrence of several of physicochemical phenomena during the aging.

Keywords Hemp · Polypropylene · Interface characterization · Pull-out test
Moisture aging

C. Nguyen-Duy (✉)

Division of Civil and Industrial Constructions, Faculty of Civil Engineering,
Thuyloi University, Ha Noi, Vietnam
e-mail: cuongnd@tlu.edu.vn

A. Makke

EPF-Ecoles d’Ingenieurs, 10004 Troyes Cedex, France

A. Makke · G. Montay

Laboratory of Mechanical Systems and Concurrent Engineering LASMIS,
University of Technology of Troyes, 10004 Troyes Cedex, France

© Springer Nature Singapore Pte Ltd. 2018

H. Nguyen-Xuan et al. (eds.), *Proceedings of the International Conference on Advances in Computational Mechanics 2017*, Lecture Notes in Mechanical Engineering, https://doi.org/10.1007/978-981-10-7149-2_32

1 Introduction

The natural fibers reinforced polymers composites (agro-composites) have been studied and developed for the purpose of industrial applications thanks to its good mechanical properties and its low environmental impacts due to their vegetal origin [1–4]. However, in such a composite, the weak fiber/matrix interface limits their use in some applications. Though, existing methods of fiber/matrix interface characterization like pull-out test, micro-bond test, fragmentation test, push-out, or micro-indentation test are usually expensive and complexes [5–12]. Also, the ‘real’ geometry of the fiber/matrix interface has not been well taken in the InterFacial Shear Strength (IFSS) calculation. Therefore, to limit these shortcomings, a pull-out test has been recently developed in our laboratory (LASMIS-UTT-France) based on its simplest principle, by the accurate measurement of the displacement and of the force and carried out the limitations of the method [13]. By this method, a tomography inspired method recently developed in our laboratory [14] will be applied in the interfacial shear stress calculations. Indeed, the consideration of the ‘real’ geometry of the fiber and of the interface was better taken.

In other hand, the aging in environmental conditions is another shortcoming of agro-composites. Indeed, many works in the literature have proved that the interface aging can be produced when these materials exposed in environmental conditions. However, few researchers have studied the deteriorations of the interface and the reduction of the IFSS during aging conditions. Furthermore, in the previous works [15–17], the authors usually orientated their studies to the aging of the interface through the water immersion, it is about an extreme condition that does not well described the environment aging in reality. In this case, the simulation of the natural climate is particularly interested to study the aging of interface and of agro-composites. In fact, Jin et al. [18] have studied the influence of the accelerated moisture aging in a climate room simulating the weather of the Paris city in France on the properties of hemp fiber/polypropylene (PP) composites. In this work, the developed pull-out test above will be applied to study the deteriorations of hemp fiber/polypropylene interface after one week of accelerated moisture aging.

2 Materials and Method

Hemp fibers extracted from hemp stalks of nuance E40 (cultivated in Champagne-Ardennes region in France) before being mounted on a carton support. The carton support and its gap dimensions allow the specimens to have 2 mm of the free part length of the fiber. The molding has realized with aid of an oven using a multi-fabrication mold. The molding conditions were 18 min of increasing from initial temperature (about 20 °C) to 173 °C then maintain at this temperature during 42 min. After the cooling and the unmolding at room conditions, the embedded part length

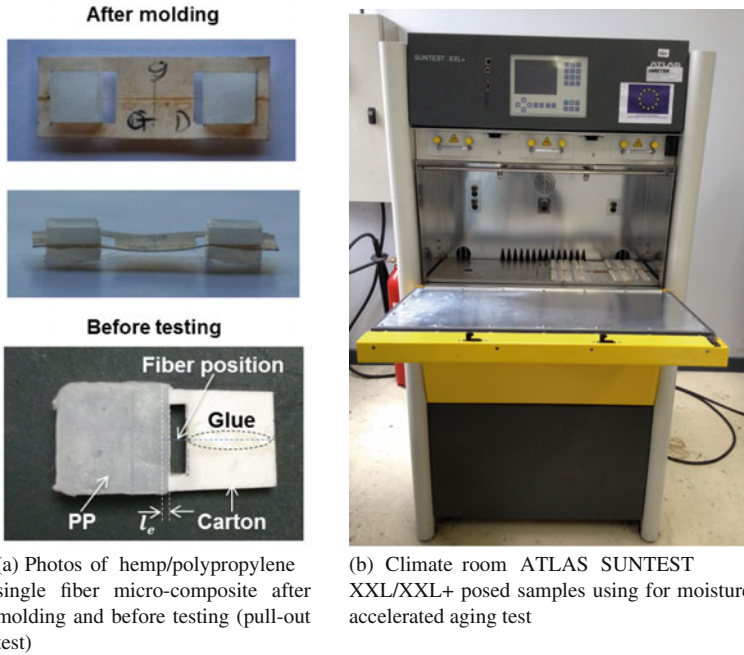


Fig. 1 Sample photos after molding and before testing and climate room using for moisture accelerated aging test

of the fiber was then fixed at 1 mm. All details of the sample preparation steps were described in the previous work of Nguyen et al. [13].

By this way, fifty hemp fiber/polypropylene micro-composite samples were prepared for the purpose of studying the accelerated moisture aging of the interface (Fig. 1a). The specimens were then posed in climate room ATLAS SUNTEST XXL/XXL+ as shown in Fig. 1b. The room conditions were fixed at relative humidity (RH) of 80% and at temperature (T) of 20 °C without lighting. The moisture aging conditions were simulated by cycles of 02 h including 102 min exploring in humidity then 18 min exploring in watering corresponding to the Norm ISO 4892-2 [19]. The duration of this accelerated moisture aging test was one week with 84 aging cycles in total were realized.

After the above time, aged samples were taken off the climate room for drying at room conditions during 24 h before testing. The pull-out tests were then realized thanks an in situ tensile micro-machine. The force cell was 100 N with the precision of 0.001 N and the load speed was 1 μm/s. The pull-out test was monitored through a numerical microscope until the fiber is totally pulled out from the matrix. The force and the displacement of the fiber were acquired by an test control software during the test. The initial free part of the fiber and its final length were also measured on this numerical microscope in order to determine the ‘real’ embedded part length l_e of the

Fig. 2 Typical force–displacement curve of aged samples (N°389, HR aging, T = 1 week)

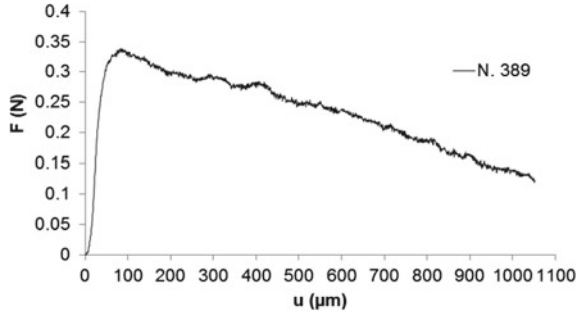


Table 1 Average of fiber diameters d , the surface of contact S_{int} , and the maximum force F_{max} after one week of HR aging and compared to nonaged samples

Aged time	d (μm)	S_{int} (mm^2)	F_{max} (N)
Nonaged	58.26 ± 13.5	$1.93 * 10^{-1} \pm 6.99 * 10^{-2}$	0.62 ± 0.35
1 week	56.63 ± 15.91	$1.90 * 10^{-1} \pm 5.58 * 10^{-2}$	0.35 ± 0.35

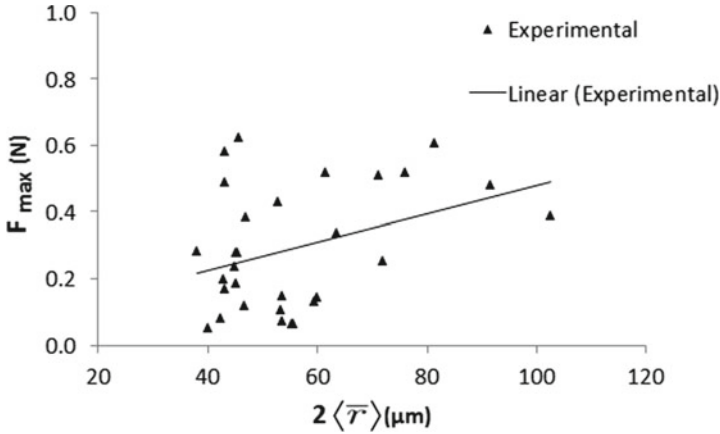
fiber [13]. The fiber diameters d and the contact area between the fiber and the matrix S_{int} were determined at the end of the test with aid of a tomography inspired method [13, 14]. In this work, we used the polygonal approach of the cross section of the hemp fiber which describes better the geometry of the fiber and its interface formed with the polypropylene matrix. In effect, the contact surface at the fiber/matrix interface S_{int} was calculated more accurate by this approach [13]. Finally, the apparent debonding shear stress was then determined to follow the formula:

$$\tau_{app} = \frac{F_{max}}{S_{int}} \tag{1}$$

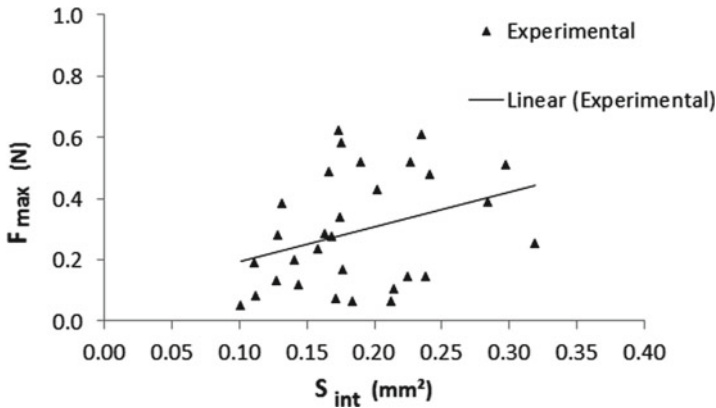
where F_{max} is the maximum measured force corresponding to the total interfacial debonding and S_{int} is the contact area at the fiber/matrix interface. The Interfacial Shear Strength ‘IFSS’ is the average of all calculated τ_{app} .

3 Results and Discussions

After one week of exploring on the accelerated moisture aging, we noted that the humidity and the cycles of watering weaken the interfacial bonding between the hemp fiber and the polypropylene matrix. There were particularly a total debonding of the fiber from the matrix in some cases. Other fibers retaining their bonding with the matrix are used for the pull-out test to determine the maximum shear stress at



(a) Distribution of maximum pull-out force F_{max} in function of fiber diameter d



(b) Distribution of maximum pull-out force F_{max} in function of surface of contact S_{int} of hemp fiber/polypropylene interface

Fig. 3 The pull-out test results of aged specimens through the accelerated moisture aging ($T = 1$ week)

the interface τ_{app} . By consequent, 31 fibers were successfully carried out from the matrix bloc among fifty-aged samples. The force–displacement curve of each test is also traced as shown in Fig. 2. The nomenclature of the maximum pull-out force, F_{max} , of the fiber diameter d and of the surface of contact S_{int} are presented in Table 1.

The Fig. 3 represents the distribution of the maximum pull-out force depending on the contact area S_{int} .

By results, we first noted that the maximum pull-out force F_{max} increased with the fiber diameter (Fig. 3a). The evolution of the maximum pull-out force in function of

Fig. 4 Fiber detachment observed on free part (arrow 1) and on embedded part (arrow 2) of the fiber (N°370, HR aging, T = 1 week)

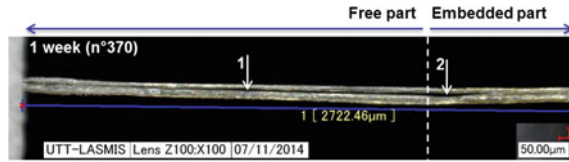


Table 2 IFSS of nonaged samples compared to aged specimens (T = 1 week)

Aged time	IFSS (Mpa)
Nonaged	3.09 ± 1.11
1 week	1.76 ± 1.34

the fiber diameters was also observed with nonaged specimens in the work of Nguyen et al. [13].

Secondly, we observed that the hemp fiber was retired from the polypropylene more easier in the case of aged samples compared than nonaged samples. Indeed, the average of the pull-out force maximum F_{max} was reduced significantly to 0.35 ± 0.35 N compared to 0.62 ± 0.35 N [13] (−43.55%) in the case of nonaged specimens. The InterFacial Shear Strength—‘IFSS’ was then determined equals to 1.76 ± 1.34 MPa. The results have shown that the IFSS was reduced upto 43.04% the initial value tested with nonaged specimens that was 3.09 ± 1.11 MPa [13]. All test results described above are presented in Table 1.

The reduction of the pull-out force maximum F_{max} and of the InterFacial Shear Strength can be the result of several chemico-physical phenomena. In this first study, we suppose that the reduction of interface properties was caused by the plasticization effects due to water absorptions in the fiber and in the fiber/matrix interface [20–22]. Indeed, the absorbed water lead destructions of chemical liaisons at the interface. Furthermore, the cycles of watering can cause the material corrosion at the interface by water fluid during the aging process. The coupling of above reasons results in the deteriorations of hemp fiber/polypropylene interface. By consequent, the quality and also the mechanical properties of the interface were significantly reduced. Figure 4 shows an example of physical degradation of the fiber and of the interface where the fiber detachment was observed (Table 2).

4 Conclusions

A recently developed pull-out test was applied successfully to characterize the moisture (RH) aging of hemp fiber/polypropylene interface. Fifty specimens were fabricated and submitted to the moisture accelerated aging during one week. The behavior of accelerated moisture aged interfaces after one week has been investigated. The results have shown that the both the pull-out forces maximum— F_{max} and the InterFacial Shear Strength—‘IFSS’ have greatly reduced. The decrease of F_{max} and of ‘IFSS’ has explained relating to the plasticization effects due to water absorptions

in the fiber and also in the fiber/matrix interface. These effects will be interesting to investigate during longer aging time (two weeks, three weeks, four weeks). Moreover, from the test results, the interfacial shear modulus and the strain shear rupture of the interface are interesting to study in order to better evaluate the effects of water absorption on the fiber/matrix interface. These studies will be presented in a future paper.

Acknowledgements This work is in the research project CIFIaMa financed by the General Council of Aube. The hemp plants have been provided by the FRD (Fibers Recherche Developpement) society in Aube (France).

References

1. Henrique P, Pereira F, Rosa MDF, Odila M, Cioffi H, Cristina K, Carvalho CD, Milanese AC, Jacobus H, Voorwald C, Mulinari DR (2016) Vegetal fibers in polymeric composites: a review. *Polimeros* 25:9–22
2. Pickering KL, Efendy MGA, Le TM (2016) A review of recent developments in natural fibre composites and their mechanical performance. *Compos Part A* 83:98–112
3. Ku H, Wang H, Pattarachaiyakoo N, Trada M (2011) A review on the tensile properties of natural fiber reinforced polymer composites. *Compos Part B Eng* 42(4):856–873
4. Gurunathan T, Mohanty S, Nayak SK (2015) A review of the recent developments in biocomposites based on natural fibres and their application perspectives. *Compos Part A Appl Sci Manuf* 77:1–25
5. Huber T, Mussig J (2008) Fibre matrix adhesion of natural fibres cotton, flax and hemp in polymeric matrices analyzed with the single fibre fragmentation test. *Compos Interfaces* 15(2–3):335–349
6. Zhou XF, Wagner HD, Nutt SR (2001) Interfacial properties of polymer composites measured by push-out and fragmentation tests. *Compos Part A Appl Sci Manuf* 32(11):1543–1551
7. Stamboulis A, Baillie C, Schulz E (1999) Interfacial characterisation of flax fibre-thermoplastic polymer composites by the pull-out test. *Die Angewandte Makromolekulare Chemie* 272(4759):117–120
8. Yue CY, Looi HC, Quek MY (1995) Assessment of fibre-matrix adhesion and interfacial properties using the pull-out test. *Int J Adhes Adhes* 15(2):73–80
9. Zhandarov S, Pisanova E, Mader E, Nairn JA (2001) Investigation of load transfert between the fiber and the matrix in pull-out tests with fibers having different diameters. *J Adhes Sci Technol* 15(2):205–222
10. Miller B, Muri P, Rebenfeld L (1987) A microbond method for determination of the shear strength of a fiber/resin interface. *Compos Sci Technol* 28(1):17–32
11. Sockalingam S, Nilakantan G (2012) Fiber-Matrix Interface Characterization through the Microbond Test. *Int J Aeronaut Space Sci* 13(3):282–295
12. Chandra N, Ghonem H (2001) Interfacial mechanics of push-out tests: theory and experiments. *Compos Part A Appl Sci Manuf* 32(3–4):575–584
13. Nguyen DC, Makke A, Montay G (2015) A pull-out fiber/matrix interface characterization of vegetal fibers reinforced thermoplastic polymer composites: the influence of the processing temperature. *Int J Chem Mol Nucl Mater Metall Eng* 9:720–724
14. Ilczyszyn F, Cherouat A, Montay G (2012) Effect of the fibre morphology on the mechanical properties of hemp fibres: digital imaging treatments coupled to 3D computational analysis. In: *ECCM15—15th European conference on composite materials*, Jun 2012
15. Liang C, Hutchinson JW (1993) Mechanics of the fiber push-out test. *Mech Mater* 14:207–221

16. Duigou AL, Davies P, Baley C (2003) Exploring durability of interfaces in flax fibre/epoxy micro-composites. *Compos Part A Appl Sci Manuf* 48:121–128
17. Seki Y, Sever K, Sarkanat M, Sen I, Aral A (2011) Jute/polyester composites: the effect of water aging on the interlaminar shear strength. 6th International advanced technologies symposium, Elazg, Turkey, May 2011, pp 368–371
18. Jin S (2013) Etude de vieillissement du comportement m canique des agro- mat riaux base de fibres de Chanvre. PhD thesis (2013), pp 1–174
19. Jin S, Gong XL (2012) Effect of ultraviolet and moisture aging on the mechanical properties of hemp fibers composites. *Appl Mech Mater* 226–228:1739–1742
20. Azwa ZN, Yousif BF, Manalo AC, Karunasena W (2013) A review on the degradability of polymeric composites based on natural fibres. *Mater Des* 47:424–442
21. Rangaraj SV, Smith LV (2000) Effects of moisture on the durability of a wood/thermoplastic composite. *J Thermoplast Compos Mater* 13(2):140–161
22. Dhakal H, Zhang Z, Richardson M (2007) Effect of water absorption on the mechanical properties of hemp fibre reinforced unsaturated polyester composites. *Compos Sci Technol* 67(7–8):1674–1683

A Modified Moving Kriging Interpolation-Based Meshfree Method with Refined Sinusoidal Shear Deformation Theory for Analysis of Functionally Graded Plates



V. Vu-Tan and S. Phan-Van

Abstract This paper presents an efficient approach based on a modified Moving Kriging–interpolation meshfree method integrated with the refined sinusoidal shear deformation plate theory to analyze static bending and free vibration of functionally graded plates. Unlike traditional higher order shear deformation plate theories, this theory presented retains only four governing equations, accounts for a sinusoidal distribution of the transverse shear strains through the thickness of the plate, and satisfies the zero traction boundary conditions on the top and bottom surfaces of the plate without using shear correction factor. A new modified Gaussian correlation function to construct MK interpolation shape functions is presented. We first propose the formulation and then provide comparison studies via numerical examples, which are performed to confirm the accuracy and reliability of the proposed method.

Keywords Functionally graded material • Meshfree methods
Sinusoidal shear deformation theory • Moving Kriging interpolation

1 Introduction

Functionally graded material (FGM) also known as a multi-phase composite material which has a smooth and continuous variation of material properties along the certain directions. Due to own properties that vary gradually with respect to

V. Vu-Tan (✉)

Faculty of Civil Engineering, Ho Chi Minh City University of Architecture,
Ho Chi Minh, Vietnam
e-mail: van.vutan@uah.edu.vn

S. Phan-Van

Faculty of Civil Engineering, Ho Chi Minh City University of Technology,
Ho Chi Minh, Vietnam
e-mail: phansonxdbk@gmail.com

© Springer Nature Singapore Pte Ltd. 2018

H. Nguyen-Xuan et al. (eds.), *Proceedings of the International Conference on Advances in Computational Mechanics 2017*, Lecture Notes in Mechanical Engineering, https://doi.org/10.1007/978-981-10-7149-2_33

485

spatial coordinates, FGM can prevent the interface cracking, debonding and residual stresses and thus maintain structural integrity to a desired degree. At present, FGM structures are primarily used as thermal barrier, wear coating, and corrosion resistant coating in many engineering fields such as biomechanical, automotive, electronic, mechanical, civil, and shipbuilding industries. With such its widely applications, understanding their structure responses under various loading becomes an essential task. It is well recognized that transverse shear deformation effect can be more significant in thick or FGM plates than in isotropic, homogeneous plates. Hence, the shear deformation theories were developed to predict of the responses of FGMs plates. The first plate model was proposed by Kirchhoff and Love [1] and is mostly known as the classical plate theory (CPT). This model is well capable of predicting the behavior of thin plates. However, since the CPT neglects the transverse shear deformation, this leads to an overestimation of vibrational frequencies and underestimation of deflections for the analysis of thick and moderately thick plate structures. The theory of moderately thick plates, known as the first-order shear deformation plate theory (FSDT) was introduced by Reissner [2] and Mindlin [3] was a first attempt to consider the effect of transverse shear deformation. The FSDT assumed that transverse planes remain plane but not necessarily perpendicular to the mid-surface of the plate; hence, it suffers from the unrealistic distribution of shear stresses and strains across the plate thickness and therefore requires shear correction factor to precise determination of transverse shear strain. However, this factor value depends on the geometry of the plate, the variation of Poisson's ratio through the thickness, the applied loading and the boundary conditions of the plate. To overcome this drawback, new mathematical models were developed to better capture static and dynamic responds of plates with considering the distribution of the transverse shear deformation and normal stress in its thickness direction. To address this challenging, several higher order plate theories (HSDTs) have been developed by various researchers. Among them, the plate model proposed by Reddy [4], Soldatos [5] and Shi [6] which considers cosine shear stress distribution, the hyperbolic and third-order shear deformable, respectively, are the most common ones. Although the existing HSDTs do not require the shear correction factor, its equilibrium equations involving in many unknowns, hence are more complicated than those of the FSDT. In order to reduce computational cost, a class of HSDTs which employed higher order distribution of the in-plane displacement field and constant transverse deflection through the plate thickness is developed. These theories are commonly referred to as simple higher order shear deformation theories (SHSDTs) and have the same number of unknowns as the FSDT. The works of Ambartsumian [7] and Karama et al. [8] are among the most notable investigations in this context.

In this paper, a refined sinusoidal shear deformation plate theory (R-SSDT) developed by Touratier [9] is used along with the Moving Kriging interpolation (MKI) meshless method for the first time. A new correlation function used for construction of the MKI shape functions which is depended only on the distance between the source point and the target point is also presented. The developed method is then employed for the investigation of the static deflection and free vibration of thin to thick FGM plates. The results of several examples problems

analyzed in this work are compared to other results found in literature. The rest of the paper is structured as follows. A brief review of the FGM plates is given in Sect. 2, MKI meshfree formulation integrated with the R-SSDT for bending and free vibration analyzes of FGM plates is presented in Sect. 3. Numerical validations and discussions are presented in Sect. 4. Finally, some conclusions drawn from the study are given in Sect. 5.

2 Functionally Graded Plates

Consider a FGM plate made from a mixture of metal and ceramic material with thickness h as shown in Fig. 1. The bottom and top faces of the plate are assumed to be fully metallic and ceramic, respectively [7].

In this study, the Poisson’s ratio ν is assumed to be constant for simplicity, whereas the young’s modulus and the density are assumed to vary continuously through the thickness. The effective material properties are computed by a power law distribution with Voigh’s rule of mixtures. The young’s modulus $E(z)$ and mass density $\rho(z)$ are hence given by

$$E(z) = E_m + (E_c - E_m)V_c \tag{1}$$

$$\rho(z) = \rho_m + (\rho_c - \rho_m)V_c \tag{2}$$

where the subscripts m and c represent the metallic and ceramic constituents, respectively; $V_c = (0.5 + z/h)^n$ is the volume fraction of the ceramic; n is the gradient index, which governs the volume fraction gradation. Figure 2 shows the variation in the ceramic volume V_c with respect to the thickness ratio z/h for different values of the index n [1].

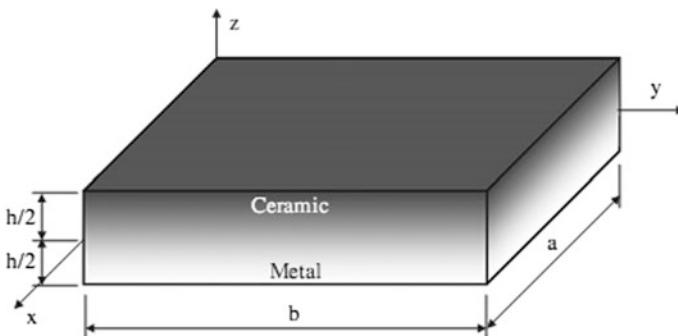


Fig. 1 Geometry notation and coordinates of an FGM plate

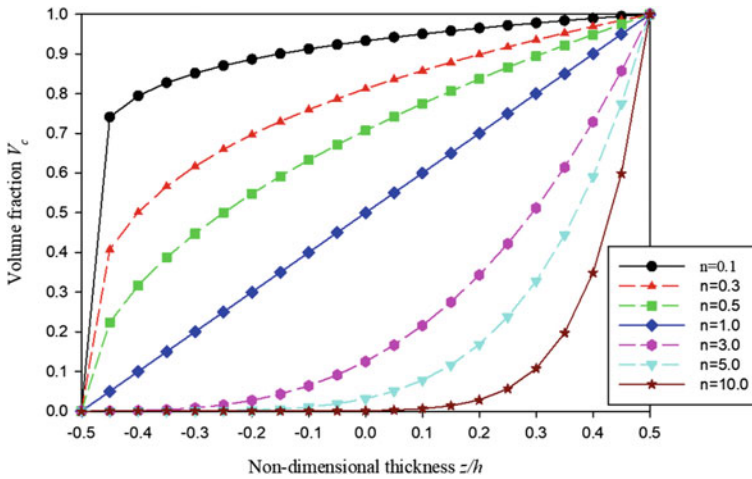


Fig. 2 Variation of ceramic volume fraction V_c with respect to the thickness ratio z/h for different values of the index n

3 Formulation of the Refined Sinusoidal Shear Deformation Theory

Let Ω be the domain in \mathbb{R}^2 occupied by the mid-plane of the plate. The displacements of the plate in the x, y and z directions are denoted as $u(x, y, z), v(x, y, z)$ and $w(x, y, z)$, respectively. According to the refined plate theory [7], the displacement field of the plate can be expressed in terms of four unknown variables as follows,

$$u(x, y, z) = u_0(x, y) - z \frac{\partial w_b(x, y)}{\partial x} + g(z) \frac{\partial w_s(x, y)}{\partial x} \tag{3}$$

$$v(x, y, z) = v_0(x, y) - z \frac{\partial w_b(x, y)}{\partial y} + g(z) \frac{\partial w_s(x, y)}{\partial y} \tag{4}$$

$$w(x, y, z) = w_b(x, y) + w_s(x, y) \tag{5}$$

where $u_0(x, y), v_0(x, y)$ are the displacements on the middle surface ($z=0$) in the x, y directions, respectively; $w_b(x, y)$ and $w_s(x, y)$ are the bending and shear components of the transverse displacement; $g(z)$ represents shape function defining the distribution of the transverse shear strains and stresses along the plate thickness and is chosen as $g(z) = f(z) - z$ such that the tangential value of the effective function $f(z)$ at $z = \pm h/2$ are equal to zeros satisfying the boundary conditions $\gamma_{xz} = \gamma_{yz} = 0$ on the top and bottom surfaces. Some effective functions across the plate thickness have been proposed, see Table 1.

Table 1 Two distribution functions and their derivatives

Model	$f(z)$	$f'(z)$
Ambartsumain (PSDPT) [7]	$zh^2/8 - z^3/6$	$h^2/8 - z^2/2$
Karama (ESDT) [8]	$ze^{-2(z/h)^2}$	$ze^{-2(z/h)^2} [1 - (2z/h)^2]$

In this paper, we employed the distribution function introduced in [9] $f(z) = \frac{h}{\pi} \sin(\frac{\pi z}{h})$. This plate model is variationally consistent, does not require shear correction factor, and accounts for the parabolic distribution of transverse shear strain which is not vanished through the thickness, satisfying shear stress free surface conditions. By using the usual small strain assumptions, the strain–displacement relations can be expressed as follow,

$$\begin{pmatrix} \epsilon_x \\ \epsilon_y \\ \gamma_{xy} \\ \gamma_{xz} \\ \gamma_{yz} \end{pmatrix} = \begin{pmatrix} \frac{\partial u_0(x,y)}{\partial x} - z \frac{\partial^2 w_b(x,y)}{\partial x^2} + g(z) \frac{\partial^2 w_s(x,y)}{\partial x^2} \\ \frac{\partial v_0(x,y)}{\partial x} - z \frac{\partial^2 w_b(x,y)}{\partial y^2} + g(z) \frac{\partial^2 w_s(x,y)}{\partial y^2} \\ \frac{\partial u_0(x,y)}{\partial y} + \frac{\partial v_0(x,y)}{\partial x} - 2z \frac{\partial^2 w_b(x,y)}{\partial x \partial y} + 2g(z) \frac{\partial^2 w_s(x,y)}{\partial x \partial y} \\ f'(z) \frac{\partial w_s(x,y)}{\partial x} \\ f'(z) \frac{\partial w_s(x,y)}{\partial y} \end{pmatrix} \tag{6}$$

or in matrix form

$$\epsilon = \begin{Bmatrix} \epsilon_0 \\ 0 \end{Bmatrix} + \begin{Bmatrix} z\kappa^b + g(z)\kappa^s \\ f'(z)\gamma \end{Bmatrix} \tag{7}$$

with

$$\epsilon_0 = \begin{Bmatrix} \frac{\partial u_0(x,y)}{\partial x} \\ \frac{\partial v_0(x,y)}{\partial y} \\ \frac{\partial u_0(x,y)}{\partial y} + \frac{\partial v_0(x,y)}{\partial x} \end{Bmatrix}, \kappa^b = \begin{Bmatrix} -\frac{\partial^2 w_b(x,y)}{\partial x^2} \\ -\frac{\partial^2 w_b(x,y)}{\partial y^2} \\ -2\frac{\partial^2 w_b(x,y)}{\partial x \partial y} \end{Bmatrix} \tag{8a, b}$$

$$\kappa^s = \begin{Bmatrix} \frac{\partial^2 w_s(x,y)}{\partial x^2} \\ \frac{\partial^2 w_s(x,y)}{\partial y^2} \\ 2\frac{\partial^2 w_s(x,y)}{\partial x \partial y} \end{Bmatrix}, \gamma = \begin{Bmatrix} \frac{\partial w_s(x,y)}{\partial x} \\ \frac{\partial w_s(x,y)}{\partial y} \end{Bmatrix} \tag{9a, b}$$

4 MKI Meshless Formulation for Bending and Free Vibration of FGM Plates

4.1 The Moving Kriging (MK) Shape Function

The shape function of the MKI technique and its derivatives are briefly introduced in this subsection. For completed description of the method and its mathematical properties one can be found at Ref. [10, 11]. Assuming that a distribution function $u(\mathbf{x}_i)$ in a sub-domain Ω_x ($\Omega_x \subseteq \Omega$) with its values can be interpolated based on the nodal values $\mathbf{x}_i (i \in [1, n_{\Omega_x}])$, wherein n_{Ω_x} is the total number of the nodes in Ω_x , the approximated function $u^h(\mathbf{x})$ can be calculated by

$$\mathbf{u}^h(\mathbf{x}) = [\mathbf{p}^T(\mathbf{x})\mathbf{A} + \mathbf{r}^T(\mathbf{x})\mathbf{B}]\mathbf{u}(\mathbf{x}) \quad \text{or} \quad \mathbf{u}^h(\mathbf{x}) = \sum_{I=1}^{n_{\Omega_x}} \phi_I(x)\mathbf{u}_I \quad (10)$$

where $\phi_I(x)$ are the MK shape functions defined by

$$\phi_I(\mathbf{x}) = \sum_{j=1}^{m_{\Omega_x}} p_j(\mathbf{x})A_{jI} + \sum_{k=1}^{n_{\Omega_x}} r_k(\mathbf{x})B_{kI} \quad (11)$$

and matrixes \mathbf{A} and \mathbf{B} are expressed as follows

$$\mathbf{A} = (\mathbf{P}^T\mathbf{R}^{-1}\mathbf{P})^{-1}\mathbf{P}^T\mathbf{R}^{-1}, \quad \mathbf{B} = \mathbf{R}^{-1}(\mathbf{I} - \mathbf{P}\mathbf{A}) \quad (12a, b)$$

where \mathbf{I} is the unit matrix, and the vector $\mathbf{p}(\mathbf{x})$ in Eq. (10) is the polynomial with m_{Ω_x} basis functions can be calculated by

$$\mathbf{p}^T(x) = [p_1(\mathbf{x}), p_2(\mathbf{x}), p_3(\mathbf{x}) \dots, p_{m_{\Omega_x}}(\mathbf{x})] \quad (13)$$

The matrix $\mathbf{P}(n_{\Omega_x} \times m_{\Omega_x})$ is collected values of the polynomial basis functions

$$\mathbf{P} = \begin{bmatrix} p_1(\mathbf{x}_1) & p_2(\mathbf{x}_1) & \dots & p_{m_{\Omega_x}}(\mathbf{x}_1) \\ p_1(\mathbf{x}_2) & p_2(\mathbf{x}_2) & \dots & p_{m_{\Omega_x}}(\mathbf{x}_2) \\ \vdots & \vdots & \ddots & \vdots \\ p_1(\mathbf{x}_{n_{\Omega_x}}) & p_2(\mathbf{x}_{n_{\Omega_x}}) & \dots & p_{m_{\Omega_x}}(\mathbf{x}_{n_{\Omega_x}}) \end{bmatrix} \quad (14)$$

and the term $\mathbf{r}(\mathbf{x})$ in Eq. (10) is given by

$$\mathbf{r}^T(x) = [R(\mathbf{x}_1, \mathbf{x}), R(\mathbf{x}_2, \mathbf{x}), \dots, R(\mathbf{x}_{n_{\Omega_x}}, \mathbf{x})] \quad (15)$$

where $R(\mathbf{x}_i, \mathbf{x}_j)$ is the correlation function between pairs of the nodes \mathbf{x}_i and \mathbf{x}_j , it is the covariance of the value $u(\mathbf{x})$ which expressed as $R(\mathbf{x}_i, \mathbf{x}_j) = \text{cov}[u(\mathbf{x}_i), u(\mathbf{x}_j)]$ and $R(\mathbf{x}_i, \mathbf{x}) = \text{cov}[u(\mathbf{x}_i), u(\mathbf{x})]$. In this paper, we present new modified Gaussian

correlation functions which depend only on the distance between the source and target point as follows:

$$R(\mathbf{x}_i, \mathbf{x}_j) = e^{-0.5(r_{ij}/l_c)^2} \tag{16}$$

where l_c is the internal length factor of the model, which can be taken as the average distance between nodes in the model. It is obvious that the correlation function no longer depends on the correlation parameter θ , which is known that strong effect on the solution [11]. Hence, the quality of the MK interpolation shape function depends only on the scaling factor. We will discuss its effect on the accuracy of solutions by numerical example in Sect. 4.1. The quadratic basic $\mathbf{p}^T(\mathbf{x}) = [1 \ x \ y \ x^2 \ y^2 \ xy]$ is employed for the numerical analysis. The correlation matrix $\mathbf{R}[R(\mathbf{x}_i, \mathbf{x}_j)]_{n_{\Omega_x} \times n_{\Omega_x}}$ is given by

$$\mathbf{R}[R(x_i, x_j)] = \begin{bmatrix} 1 & R(\mathbf{x}_1, \mathbf{x}_2) & \cdots & R(\mathbf{x}_1, \mathbf{x}_{n_{\Omega_x}}) \\ R(\mathbf{x}_2, \mathbf{x}_1) & 1 & \cdots & R(\mathbf{x}_2, \mathbf{x}_{n_{\Omega_x}}) \\ \vdots & \vdots & \ddots & \vdots \\ R(\mathbf{x}_{n_{\Omega_x}}, \mathbf{x}_1) & R(\mathbf{x}_{n_{\Omega_x}}, \mathbf{x}_2) & \cdots & 1 \end{bmatrix} \tag{17}$$

For thin plate problems, not only the first-order derivatives of shape functions are required, but also the second-order derivatives are needed to be computed, these derivatives are obtained by direct differentiation of Eq. (11), as follows:

$$\phi_{I,i}(\mathbf{x}) = \sum_{j=1}^{m_{\Omega_x}} p_{j,i}(\mathbf{x})A_{jI} + \sum_{k=1}^{n_{\Omega_x}} r_{k,i}(\mathbf{x})B_{kI}, \quad \phi_{I,ii}(\mathbf{x}) = \sum_{j=1}^{m_{\Omega_x}} p_{j,ii}(\mathbf{x})A_{jI} + \sum_{k=1}^{n_{\Omega_x}} r_{k,ii}(\mathbf{x})B_{kI} \tag{18a, b}$$

In meshfree approaches [10], the influence domain is usually a circle or sphere, defined by a radius and centered at the point of interest. This domain is used to determine the scattered nodes which are used for interpolation. The size of the support domain can be calculated by

$$d_{m_{\Omega_x}} = \alpha d_c \tag{19}$$

where d_c defines the characteristic length relative to the nodal spacing near the point of interest, and α is a scaling factor. It should be noted that the shape function $\phi_I(\mathbf{x}_j)$ at node \mathbf{x}_j for the interpolation node \mathbf{x}_j possesses the delta function property.

$$\phi_I(x_j) = \delta_{Ij} = \begin{cases} 1 & \text{for } I=j \\ 0 & \text{for } I \neq j \end{cases} \tag{20}$$

4.2 Discrete Governing Equations

In the parametric domain in terms of meshfree method, the generalized displacements in the middle surface of the plate are approximated by Eq. (10), in which

$$\mathbf{u}^h = [u^h \quad v^h \quad w_b^h \quad w_s^h]^T, \quad \mathbf{u}_I = [u_I \quad v_I \quad w_{bI} \quad w_{sI}]^T \tag{21a, b}$$

By substituting Eq. (10) into Eqs. (8a, b), (9a, b), one can obtain:

$$\boldsymbol{\varepsilon}_0 = \sum_{I=1}^{n_{\Omega_x}} \mathbf{B}_I^m \mathbf{u}_I, \quad \boldsymbol{\kappa}^b = \sum_{I=1}^{n_{\Omega_x}} \mathbf{B}_I^{b1} \mathbf{u}_I, \quad \boldsymbol{\kappa}^s = \sum_{I=1}^{n_{\Omega_x}} \mathbf{B}_I^{b2} \mathbf{u}_I, \quad \boldsymbol{\gamma} = \sum_{I=1}^{n_{\Omega_x}} \mathbf{B}_I^s \mathbf{u}_I \tag{22a, b, c}$$

with

$$\mathbf{B}_I^m = \begin{bmatrix} \phi_{I,x} & 0 & 0 & 0 \\ 0 & \phi_{I,y} & 0 & 0 \\ \phi_{I,y} & \phi_{I,x} & 0 & 0 \end{bmatrix}, \mathbf{B}_I^{b1} = \begin{bmatrix} 0 & 0 & -\phi_{I,xx} & 0 \\ 0 & 0 & -\phi_{I,yy} & 0 \\ 0 & 0 & -2\phi_{I,xy} & 0 \end{bmatrix}, \tag{23a, b}$$

$$\mathbf{B}_I^{b2} = \begin{bmatrix} 0 & 0 & 0 & \phi_{I,xx} \\ 0 & 0 & 0 & \phi_{I,yy} \\ 0 & 0 & 0 & 2\phi_{I,xy} \end{bmatrix}, \mathbf{B}_I^s = \begin{bmatrix} 0 & 0 & 0 & \phi_{I,x} \\ 0 & 0 & 0 & \phi_{I,y} \end{bmatrix} \tag{24a, b}$$

For the static problem, the weak form can be expressed as follows:

$$\int_{\Omega} \delta \boldsymbol{\varepsilon}^T \mathbf{D}^e \boldsymbol{\varepsilon} d\Omega + \int_{\Omega} \delta \boldsymbol{\gamma}^T \mathbf{D}^s \boldsymbol{\gamma} d\Omega = \int_{\Omega} \delta (w_b + w_s) q_0 d\Omega \tag{25}$$

where q_0 is the transverse loading per unit area and

$$\boldsymbol{\varepsilon} = \{ \boldsymbol{\varepsilon}_0 \quad \boldsymbol{\kappa}^b \quad \boldsymbol{\kappa}^s \}^T, \quad \mathbf{D}^e = \begin{bmatrix} \mathbf{A} & \mathbf{B} & \mathbf{E} \\ \mathbf{B} & \mathbf{C} & \mathbf{K}^e \\ \mathbf{E} & \mathbf{K}^e & \mathbf{H} \end{bmatrix}, \quad \mathbf{D}^s = \int_{-h/2}^{h/2} \mathbf{D}_s(z) dz \tag{26a, b, c}$$

$$A_{ij}, B_{ij}, C_{ij}, E_{ij}, K_{ij}^e, H_{ij} = \int_{-h/2}^{h/2} [1, z, z^2, g(z), zg(z), g^2(z)] Q_{ij} dz, \tag{27a, b}$$

$$D_{ij}^s = \int_{-h/2}^{h/2} [f'(z)]^2 G_{ij} dz$$

wherein the material matrices are

$$\mathbf{Q} = \frac{E(z)}{1-\nu^2} \begin{bmatrix} 1 & \nu & 0 \\ \nu & 1 & 0 \\ 0 & 0 & (1-\nu)/2 \end{bmatrix}, \quad \mathbf{G} = \frac{E(z)}{2(1+\nu)} \begin{bmatrix} 1 & 0 \\ 0 & 1 \end{bmatrix} \tag{28a, b}$$

For the free vibration, the weak form can be expressed:

$$\int_{\Omega} \delta \boldsymbol{\varepsilon}^T \mathbf{D}^e \boldsymbol{\varepsilon} d\Omega + \int_{\Omega} \delta \boldsymbol{\gamma}^T \mathbf{D}^s \boldsymbol{\gamma} d\Omega = \int_{\Omega} \delta \mathbf{u}^T \mathbf{m} \ddot{\mathbf{u}} d\Omega \tag{29}$$

where

$$\mathbf{m} = \begin{bmatrix} I_0 & I_1 & I_3 \\ I_1 & I_2 & I_4 \\ I_3 & I_4 & I_5 \end{bmatrix}, \quad (I_0, I_1, I_2, I_3, I_4, I_5) = \int_{-h/2}^{h/2} \rho(z) [1, z, z^2, zg(z), zg(z), g^2(z)] dz \tag{30a, b}$$

and $\mathbf{u} = \{ \mathbf{u}_0 \quad \mathbf{u}_b \quad \mathbf{u}_s \}^T$ can be expressed as

$$\begin{aligned} \mathbf{u}_0 &= \begin{Bmatrix} u^h \\ v^h \\ w_b^h + w_s^h \end{Bmatrix} = \sum_{I=1}^n \mathbf{N}_I^1 \mathbf{u}_I, & \mathbf{u}_b &= \begin{Bmatrix} -\partial w_b^h / \partial x \\ -\partial w_b^h / \partial y \\ 0 \end{Bmatrix} = \sum_{I=1}^n \mathbf{N}_I^2 \mathbf{u}_I, \\ \mathbf{u}_s &= \begin{Bmatrix} \partial w_s^h / \partial x \\ \partial w_s^h / \partial y \\ 0 \end{Bmatrix} = \sum_{I=1}^n \mathbf{N}_I^3 \mathbf{u}_I \end{aligned} \tag{31a, b, c}$$

and

$$\begin{aligned} \mathbf{N}_I^1 &= \begin{bmatrix} \phi_I & 0 & 0 & 0 \\ 0 & \phi_I & 0 & 0 \\ 0 & 0 & \phi_I & \phi_I \end{bmatrix}, & \mathbf{N}_I^2 &= \begin{bmatrix} 0 & 0 & -\phi_{I,x} & 0 \\ 0 & 0 & -\phi_{I,y} & 0 \\ 0 & 0 & 0 & 0 \end{bmatrix}, \\ \mathbf{N}_I^3 &= \begin{bmatrix} 0 & 0 & 0 & \phi_{I,x} \\ 0 & 0 & 0 & \phi_{I,y} \\ 0 & 0 & 0 & 0 \end{bmatrix} \end{aligned} \tag{32a, b, c}$$

By substituting Eqs. (22–24) into Eqs. (25) and (29) the formulations of the static, free vibration are rewritten in the following form:

$$\mathbf{K}\mathbf{u} = \mathbf{F}, \quad (\mathbf{K} - \omega^2 \mathbf{M})\mathbf{u} = \mathbf{0} \tag{33a, b}$$

where the global stiffness matrix \mathbf{K} is computed through

$$\mathbf{K} = \int_{\Omega} \begin{Bmatrix} \mathbf{B}^m \\ \mathbf{B}^{b1} \\ \mathbf{B}^{b2} \end{Bmatrix}^T \begin{bmatrix} A & B & E \\ B & C & K^e \\ E & K^e & H \end{bmatrix} \begin{Bmatrix} \mathbf{B}^m \\ \mathbf{B}^{b1} \\ \mathbf{B}^{b2} \end{Bmatrix} d\Omega + \int_{\Omega} (\mathbf{B}^s)^T \mathbf{D}^s \mathbf{B}^s d\Omega \quad (34)$$

The load vector \mathbf{F} is computed as follows:

$$\mathbf{F} = \int_{\Omega} q_0 \mathbf{N}_I d\Omega \quad \text{where} \quad \mathbf{N}_I = [0 \quad 0 \quad \phi_I \quad \phi_I]^T \quad (35)$$

The global mass matrix \mathbf{M} is expressed as

$$\mathbf{M} = \int_{\Omega} \begin{Bmatrix} \mathbf{N}^1 \\ \mathbf{N}^2 \\ \mathbf{N}^3 \end{Bmatrix}^T \begin{bmatrix} I_0 & I_1 & I_3 \\ I_1 & I_2 & I_4 \\ I_3 & I_4 & I_5 \end{bmatrix} \begin{Bmatrix} \mathbf{N}^1 \\ \mathbf{N}^2 \\ \mathbf{N}^3 \end{Bmatrix} d\Omega \quad (36)$$

5 Numerical Validations

In this section, we investigate the accuracy of the present approach in predicting the static bending and free vibration responses of homogeneous and FGM plates with square shape. For convenience, the boundaries of these plates are denoted as follows: completely free (F), simply supported (S), or fully clamped (C) edges. It is worth noting that these boundary conditions can be enforced by employing the simple rotation-free technique addressed in meshfree analysis [12].

5.1 Effect of the Scaling Factor on the Solution Accuracy

Consider a simply supported square plate with the length $a = 1$, the thickness h , the simply supported boundary condition (SSSS), the uniform transverse load $q_0 = 1$. The following parameters are assumed as the length-to-thickness ratio $a/h = 5$, young's modulus $E = 1.0 \times 10^7$, poisson's ratio $\nu = 0.3$. The normalized displacements at the center of the plate are defined as $\bar{w} = \frac{Eh^3 w_c}{q_0 a^4}$. To study the effect of the influence of scaling factor α to solutions, the normalized displacement \bar{w} of the plate is calculated using different sets of 17×17 , 21×21 , 25×25 , 29×29 , 33×33 , and 37×37 . Figure 3 shows the convergence of the dimensionless displacements for various values of the scaling factor parameter varied within a specified wide range from 2.0 to 3.5 using the proposed correlation function. Table 2 shows the results for various values of correlation parameter using the proposed correlation functions.

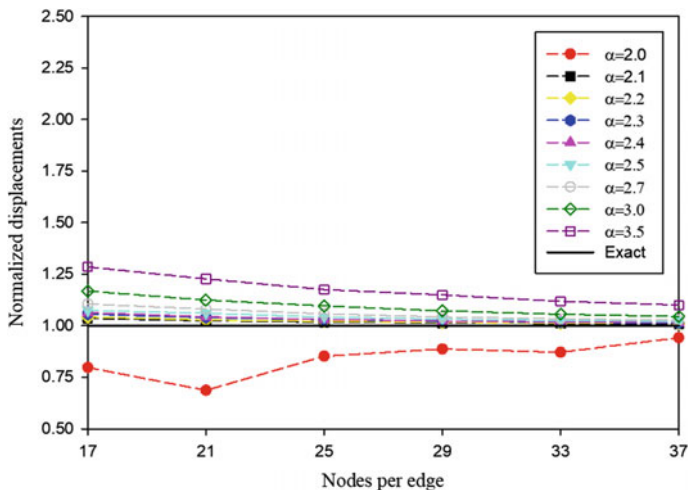


Fig. 3 Convergence of displacements $\bar{w}_{num}/\bar{w}_{exact}$ of the SSSS square plate ($a/h=5$)

It can be concluded that obtained dimensionless displacements from present method which converges to exact solution [13] when increasing the sets of nodes per edge and decreasing the scaling factor parameter as expected. However, the proposed correlation model show convergence for solutions of the normalized displacement as the scaling factors $\alpha > 2.0$. Hence, we decide to use $\alpha = 2.1$ throughout the study if not specified otherwise.

Furthermore, Table 2 shows that good results are obtained with the mesh 25×25 nodes (error 1.69%), and therefore this level mesh of nodes can be used for all next examples.

5.2 Static Bending Analysis

Next example deals with an Al/ZrO_2 square plate subjected to a uniform load $q_0 = 1$. The material property of FGM plates is listed in Table 3. The young's modulus and mass density are evaluated using Voigt's rule of mixtures, see Eqs. (1) and (2).

Different boundary conditions such as SSSS, SFSS, various values of the length-to-thickness ratios $a/h = 5, 100$, and different values of the gradient index $n = 0, 0.5, 1.0$ and 2.0 are examined. The normalized central deflection of the plate $\bar{w} = \frac{100w_c E_m h^3}{12(1-\nu_m^2)q_0 a^4}$ is used to study the accuracy of the obtained results. Table 4 reports the normalized central deflections, where the obtained results are compared

Table 3 Material properties of the FGM plates used for the analysis

Properties	Aluminum (<i>Al</i>)	Ceramic	
		Alumina (Al_2O_3)	Zirconia (ZrO_2)
$E(GPa)$	70	380	200
ν	0.3	0.3	0.3
$\rho(kg/m^3)$	2707	3800	5700

Table 4 Normalized deflection of an *Al/ZrO₂* square plate with different length-to-thickness ratio *a/h*, gradient indices *n*, and boundary conditions

Boundary condition	<i>a/h</i>	Method	<i>n</i> = 0	<i>n</i> = 0.5	<i>n</i> = 1.0	<i>n</i> = 2.0	
SSSS	5	TSDT-MK [12]	0.1712	0.2549	0.2949	0.3326	
		HOSNDPT [12]	0.1671	0.2505	0.2905	0.3280	
		S-FSDT based IGA [14]	0.1717	0.2324	0.2719	0.3115	
		S-FSDT-MK [15]	0.1723	0.2331	0.2723	0.3116	
		ESDT [7] -MK	0.1773	0.2397	0.2810	0.3239	
		PSDPT [8] -MK	0.1775	0.2400	0.2813	0.3241	
		Present	0.1775	0.2399	0.2812	0.3241	
	100	S-FSDT based IGA [14]	0.1423	0.1949	0.2284	0.2597	
		S-FSDT-MK [15]	0.1432	0.1960	0.2292	0.2603	
		ESDT [7] -MK	0.1483	0.2031	0.2379	0.2705	
		PSDPT [8] -MK	0.1483	0.2031	0.2379	0.2705	
		Present	0.1483	0.2031	0.2379	0.2705	
	SFSF	5	TSDT-MK [12]	0.5098	0.7621	0.8793	0.9846
			HOSNDPT [12]	0.5019	0.7543	0.8708	0.9744
S-FSDT based IGA [14]			0.5083	0.6918	0.8099	0.9247	
S-FSDT-MK [15]			0.5053	0.6874	0.8042	0.9177	
ESDT [7] -MK			0.5121	0.6963	0.8160	0.9354	
PSDPT [8] -MK			0.5125	0.6967	0.8165	0.9357	
Present			0.5124	0.6966	0.8164	0.9357	
100		S-FSDT based IGA [14]	0.4584	0.6281	0.7360	0.8367	
		S-FSDT-MK [15]	0.4566	0.6251	0.7319	0.8316	
		ESDT [7] -MK	0.4627	0.6339	0.7427	0.8443	
		PSDPT [8] -MK	0.4627	0.6339	0.7427	0.8443	
		Present	0.4627	0.6339	0.7427	0.8443	

with the third-order (TSDT), higher order shear plate theory (HOSNDPT) [12], S-FSDT-based isogeometric analysis (IGA) [14], and MK [15] method for different values of the gradient indices. It is clear that the results obtained by the present method are accurate when compared with those obtained by the reference methods.

5.3 Free Vibration Analysis

To further investigate the effects of the boundary conditions on the natural frequency, a Al/Al_2O_3 square thin plate with a length-to-thickness ratio of $a/h = 100$ under different boundary conditions and gradient indices is analyzed. The first five modes normalized natural frequencies $\omega^* = \omega\pi^2(a^2/h)\sqrt{\rho_m/E_m}$ obtained with different methods are listed in Table 5.

It can be seen that the results obtained by the present method are in a remarkable agreement with the results obtained by the S-FSDT-based IGA [14], S-FSDT-based MK [15], and analytical solutions [16]. It is clear that, as the boundary conditions change from SCSC to CCCC, the values of the natural frequency gradually

Table 5 The first five mode normalized natural frequencies of an Al/Al_2O_3 thin plate with different boundary conditions and gradient indices

<i>n</i>	Method	Mode 1	Mode 2	Mode 3	Mode 4	Mode 5
<i>(a) SCSC</i>						
1	S-FSDT based IGA [14]	129.6605	245.0927	310.2664	423.1599	457.3585
	S-FSDT-MK [15]	129.9227	246.0544	311.5795	429.6741	456.0445
	Exact [16]	129.6496	245.1310	-	423.6904	-
	ESDT [7] -MK	129.0710	239.6964	306.5713	408.7160	441.1219
	PSDPT [8] -MK	129.0706	239.6954	306.5693	408.7131	441.1188
	Present	129.0707	239.6956	306.5698	408.7138	441.1195
2	S-FSDT based IGA [14]	117.8818	222.8238	282.0750	384.7018	415.7952
	S-FSDT-MK [15]	117.9340	223.2098	279.5867	389.7883	412.6522
	Exact [16]	117.8104	222.8111	-	385.0672	-
	ESDT [7] -MK	117.4276	218.1388	278.9060	372.3346	401.4844
	PSDPT [8] -MK	117.4275	218.1386	278.9057	372.3341	401.4839
	Present	117.4275	218.1384	278.9053	372.3335	401.4833
<i>(b) CCCC</i>						
1	S-FSDT based IGA [14]	161.1242	328.4308	328.4308	483.9866	588.3962
	S-FSDT-MK [15]	161.0227	328.6780	328.6780	488.7393	591.5320
	ESDT [7] -MK	161.3034	325.3422	325.3422	471.7727	574.0112
	PSDPT [8] -MK	161.3027	325.3400	325.3400	471.7684	574.0048
	Present	161.3029	325.3405	325.3405	471.7694	574.0063
2	S-FSDT based IGA [14]	146.4868	298.5884	298.5884	439.9988	534.9293
	S-FSDT-MK [15]	146.9611	297.6900	297.6900	441.7803	531.8659
	ESDT [7] -MK	146.7832	296.1097	296.1097	430.0749	522.4546
	PSDPT [8] -MK	146.7831	296.1094	296.1094	430.0743	522.4536
	Present	146.7829	296.1089	296.1089	430.0734	522.4523

Table 6 The first five mode normalized natural frequencies of an Al/ZrO_2 SSSS thick plate gradient index $n = 1$

Model	Mode 1	Mode 2	Mode 3	Mode 4	Mode 5
S-FSDT-MK [15]	0.0153	0.0378	0.0378	0.0586	0.0721
TSDT-based Meshless [17]	0.0149	0.0378	0.0378	0.0595	0.0749
HSDT-based Meshless [18]	0.0149	0.0377	0.0377	0.0593	0.0747
3D-SSDT-based Meshless [19]	0.0153	0.0377	0.0377	0.0596	0.0739
3D-HSDT-based Meshless [20]	0.0153	0.0377	0.0377	0.0596	0.0739
ESDT [7] -MK	0.0157	0.0384	0.0384	0.0597	0.0747
PSDPT [8] -MK	0.0157	0.0384	0.0384	0.0597	0.0746
Present	0.0157	0.0384	0.0384	0.0597	0.0747

increase. Furthermore, values of the natural frequency increase as the gradient index decreases.

In the last example for natural frequency analysis, a Al/ZrO_2 square thick plate with simply supported boundary condition, the gradient index $n = 1$, and ratio of $a/h = 20$ are considered. In Table 6, the first five modes normalized natural

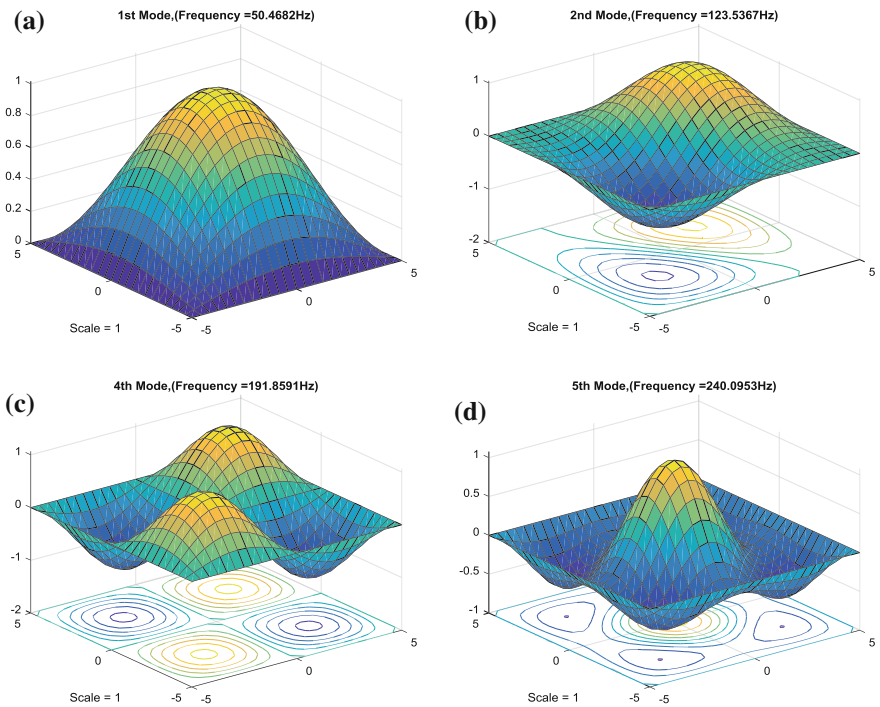


Fig. 4 The first five mode shapes of a simply supported Al/ZrO_2 thick plate with $a/h = 20$ and $n = 1$: **a** mode 1, **b** mode 2–3, **c** mode 4, and **d** mode 5

frequencies $\omega^* = \omega h \sqrt{\rho_m / E_m}$ calculated by the present method are compared with those obtained by the TSDT-based meshless of Ferreira et al. [17], HSDT meshless-based Petrov-Galerkin of Qian et al. [18], and the quasi-3DSSDT-, HSDT-based meshless of Neves et al. [18, 19]. It is observed that the present method provides acceptable results when compared with the reference ones. The first five eigenmodes of the thick plate are visualized in Fig. 4.

6 Conclusions

In the present work, the modified Moving Kriging–interpolation meshfree method based on the existing refined sinusoidal shear deformation theory for the analysis of static deflection and free vibration of FGM plate was developed. This plate model only uses four variables per each node, thus no high computational cost is required while the parabolic variations of the shear stresses are retained. Also, the chosen displacement field also satisfies the vanishing of the shear stresses on the free surfaces of the FGM plate while the shear correction factor is negligible. A remarkable point is that the modified Gaussian exponential correlation function is integrated into the MK interpolation function. As a result, the obtained solutions by proposed method are stable than those obtained by the traditional MK meshfree method. Thorough the numerical validations, it was proved that the proposed meshfree method is capable of accurately predicting the static and dynamic behavior of FGM thin to thick plates with different boundary conditions and the gradient index, length-to-thickness ratios.

References

1. Love AEH (1888) The small free vibrations and deformation of a thin elastic shell. *Philos Trans R Soc Lond A* 179:491–546
2. Reissner E (1945) The effect of transverse shear deformation on the bending of elastic plates. *J Appl Mech* 12:69–77
3. Mindlin RD (1951) Influence of rotary inertia and shear on flexural motions of isotropic, elastic plates. *J Appl Mech* 18:31–38
4. Reddy JN (1984) A simple higher-order theory for laminated composite plates. *J Appl Mech* 51:745–752
5. Soldatos KP (1992) A transverse shear deformation theory for homogeneous monoclinic plates. *Acta Mech* 94:195–220
6. Shi G (2007) A new simple third-order shear deformation theory of plates. *Int J Solids Struct* 44(13):4299–4417
7. El Meiche N, Tounsi A, Ziane N, Mechab I, Adda Bedia EA (2011) A new hyperbolic shear deformation theory for buckling and vibration of functionally graded sandwich plate. *Int J Mech Sci* 53(4):237–247
8. Ferreira AJM, Roque RMN, Jorge RMN (2006) Static and free vibration analysis of composite shells by radial basis functions. *Eng Anal Bound Elem* 30:719–733
9. Touratier M (1991) An efficient standard plate theory. *Int J Eng Sci* 29:901–916

10. Gu L (2003) Moving Kriging interpolation and element free Galerkin method. *Int J Numer Meth Eng* 56:1–11
11. Bui TQ, Nguyen NT, Nguyen-Dang H (2009) A moving Kriging interpolation-based meshless method for numerical simulation of Kirchhoff plate problems. *Int J Numer Meth Eng* 77:1371–1395
12. Thai CH, Nguyen TN, Rabczuk T, Nguyen-Xuan H (2016) An improved moving Kriging meshfree method for plate analysis using a refined plate theory. *Comput Struct* 176:34–49
13. Reddy JN (1984) A refined nonlinear theory of plates with transverse shear deformation. *Int J Solids Struct* 20(9–10):881–896
14. Yin SH, Jack SH, Yu TT, Bui TQ, Boras PAS (2014) Isogeometric locking-free plate element: a simple first order shear deformation theory for functionally graded plates. *Compos Struct* 118:121–138
15. Vu TV, Nguyen NH, Khosravifard A, Hematiyan MR, Tanakad S, Bui TQ (2017) A simple FSDT-based meshfree method for analysis of functionally graded plates. *Eng Anal Bound Elem* 79:1–12
16. Baferani AH, Saidi AR, Jomehzadeh E (2011) An exact solution for free vibration of thin functionally graded rectangular plates. *Proc IMechE Part C J Mech Eng Sci* 225(C3):526–536
17. Ferreira AJM, Batra RC, Roque CMC, Qian LF, Jorge RMN (2006) Natural frequencies of functionally graded plates by a meshless method. *Compos Struct* 75:593–600
18. Qian LF, Batra RC, Chen LM (2004) Static and dynamic deformations of thick functionally graded elastic plate by using higher-order shear and normal deformable plate theory and meshless local Petrov-Galerkin method. *Compos Part B Eng* 35:685–697
19. Neves AMA, Ferreira AJM, Carrera E, Roque CMC, Cinefra M, Jorge RMN (2012) A quasi-3D sinusoidal shear deformation theory for the static and free vibration analysis of functionally graded plates. *Compos Part B Eng* 43:711–725
20. Neves AMA, Ferreira AJM, Carrera E, Cinefra M, Roque CMC, Jorge RMN (2013) Static, free vibration and buckling analysis of isotropic and sandwich functionally graded plates using a quasi-3D higher-order shear deformation theory and a meshless technique. *Compos Part B Eng* 44:657–674

Bending Analysis of Laminated Composite Beams Using Hybrid Shape Functions



Ngoc-Duong Nguyen, Trung-Kien Nguyen, Thien-Nhan Nguyen
and Thuc P. Vo

Abstract Bending behaviours of laminated composite beams are presented in this study. The present theory is based on a higher-order shear deformation beam theory. The governing equations are derived from Lagrange's equations. Ritz method is applied in which new hybrid shape functions are proposed for analysis of laminated composite beams with various boundary conditions. Numerical results are presented and compared with those from earlier works to validate the accuracy of the proposed solutions and to investigate effects of the span-to-height ratio, boundary conditions, fibre orientation and material anisotropy on the displacement and stresses.

Keywords Composite beams • Ritz method • Shape function
Bending

1 Introduction

In the recent years, laminated composite beams have been used commonly in many engineering fields due to their high specific stiffness and strength-to-weight ratios, and the bending behaviours are one of the interest and importance to the performance of beams. A large number of researches have been conducted for flexural behaviours of laminated composite beams. Many theories have been considered such as layer-wise theories (LWT), equivalent single-layer theories (ESLT), zigzag theories (ZZT), Carrera's Unified Formulation (CUF)... in which the ESLT are widely used owing to its simplicity in formulation as well as programming. ESLT

N.-D. Nguyen (✉) · T.-K. Nguyen · T.-N. Nguyen
Faculty of Civil Engineering, Ho Chi Minh City University of Technology and Education,
1 Vo van Ngan Street, Thu Duc District, Ho Chi Minh City, Vietnam
e-mail: duongnn@hcmute.edu.vn

T. P. Vo
Faculty of Engineering and Environment, Northumbria University,
Newcastle upon Tyne NE1 8ST, UK

can be classified as classical beam theory (CBT), first-order beam theory (FOBT) and higher-order beam theory (HOBT). General reviews on analysis of laminated composite beams can be found in [1, 2]. For computational methods, many numerical and analytical approaches have been presented to analyse behaviours of laminated composite beams and only some of them are mentioned here. Finite element method (FEM) has been mostly used for analysis of composite beams in which different finite element models based on various beam theories have been proposed. Han and Hoa [3] developed a three-dimensional multilayer composite finite element for stress analysis of composite beams. Based on FOBT and HOBT, Maiti and Sinha [4] used FEM to predict vibration and static behaviour of laminated composite beams. Subramanian [5] introduced a two-node C^1 -finite element for flexural analysis of symmetric laminated composite beams with simply-supported boundary condition. Murthy et al. [6] studied static and free vibration analysis of un-symmetric composite beams. In this study, HOBT and a two-node beam element was presented. Vidal and Polit [7] proposed a new three-node beam finite element for dynamic and static analysis of composite beams. Lezgy et al. [8] developed a refined higher-order global-local beam theory and used FEM to derive natural frequency, displacement and stress of composite and sandwich beams. A two-node C^1 -finite element with six degree-of-freedom per node is developed by Vo et al. [9] for static analysis of composite beams. Mantari and Canals [10] also used FEM to determine displacement and stress of laminated composite beams. For analytical approaches, Navier's solution known as the simplest one for simply-supported beams has been used by many researchers [11–16]. Ritz method has been also interested and developed for analysing composite beams. Based on this approach with a polynomial shape function, Nguyen et al. [17] presented vibration and buckling analysis of functionally graded sandwich beams by using new higher-order shear deformation theory with various boundary conditions. By using the same shape functions as [17], Nguyen et al. [18] investigated the hygro-thermal effects on vibration and thermal buckling responses of functionally graded beams. Aydogdu introduced a Ritz solution method for vibration [19] and buckling [20] analysis of cross-ply laminated beams in which the orthogonal approximative polynomials for the displacement field have been used. Mantari and Canales [21] studied vibration and buckling behaviours of composite beams by using polynomial series and hybrid polynomial–trigonometric series. Recently, Nguyen et al. [22] proposed a Ritz solution for vibration, buckling and bending analysis of laminated composite beams by using trigonometric shape functions and HOBT. Other analytical methods can be also found in the works of Kant et al. [23], Apetre et al. [24], Khdeir and Reddy [25]. Although the Ritz method is efficient to analyse behaviours of composite beams with various boundary conditions, the available literature shows that the number of researches used the Ritz method for static analysis of laminated composite beams is still limited. Moreover, the accuracy and efficiency of this approach strictly depend on a choice of approximative shape functions for the field variables. Therefore, this problem needs for further studies.

The objective of this paper is to develop new approximative shape functions for bending analysis of laminated composite beams. The HOBt is used to describe the displacement field. The governing equations are derived by using Lagrange’s equations. The convergence and verification studies are carried out to demonstrate the accuracy of the present study. Numerical results are presented to investigate the effects of span-to-height ratio, boundary conditions and material anisotropy on the displacement and stresses of laminated composite and sandwich beams.

2 Strain and Stress Relation

Consider a laminated composite beam with length L and rectangular section ($b \times h$) as shown in Fig. 1. It includes n plies of orthotropic materials in different fibre angles θ with respect to the x -axis.

The elastic strain and stress relation of k th-layer in global coordinate are given by [26]:

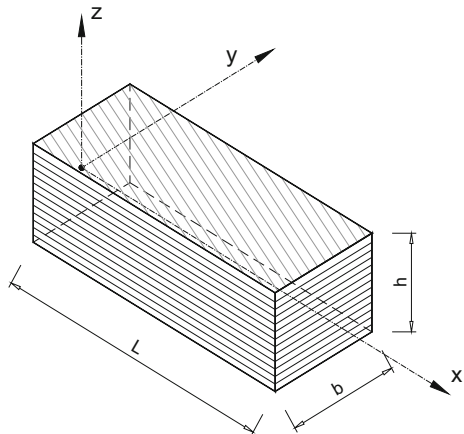
$$\begin{Bmatrix} \sigma_x^{(k)} \\ \sigma_{xz}^{(k)} \end{Bmatrix} = \begin{pmatrix} \bar{Q}_{11}^{(k)} & 0 \\ 0 & \bar{Q}_{55}^{(k)} \end{pmatrix} \begin{Bmatrix} \varepsilon_x^{(k)} \\ \gamma_{xz}^{(k)} \end{Bmatrix} \tag{1}$$

where the $\bar{Q}_{11}^{(k)}$ and $\bar{Q}_{55}^{(k)}$ are reduced stiffness constants of k th-layer in global coordinates and determined as follows [26]:

$$\bar{Q}_{11}^{(k)} = Q_{11}^{(k)} \cos^4 \theta + 2(Q_{12}^{(k)} + 2Q_{66}^{(k)}) \sin^2 \theta \cos^2 \theta + Q_{22}^{(k)} \sin^4 \theta \tag{2a}$$

$$\bar{Q}_{55}^{(k)} = Q_{55}^{(k)} \cos^2 \theta + Q_{44}^{(k)} \sin^2 \theta \tag{2b}$$

Fig. 1 Geometry of a laminated composite beam



$$Q_{11}^{(k)} = \frac{E_1^{(k)}}{1 - \nu_{12}^{(k)} \nu_{21}^{(k)}}, Q_{12}^{(k)} = \frac{\nu_{12}^{(k)} E_2^{(k)}}{1 - \nu_{12}^{(k)} \nu_{21}^{(k)}}, Q_{22}^{(k)} = \frac{E_2^{(k)}}{1 - \nu_{12}^{(k)} \nu_{21}^{(k)}} \quad (2c)$$

$$Q_{44}^{(k)} = G_{23}^{(k)}, Q_{55}^{(k)} = G_{13}^{(k)}, Q_{66}^{(k)} = G_{12}^{(k)} \quad (2d)$$

with $E_1^{(k)}, E_2^{(k)}, G_{12}^{(k)}, G_{13}^{(k)}, G_{23}^{(k)}$ are orthotropic elastic constants; $\nu_{12}^{(k)}, \nu_{21}^{(k)}$ are Poisson's ratios.

3 Variational Formulation

3.1 Displacement Field

The displacement field of laminated composite beams is given by [26, 27]:

$$u_1(x, z) = u(x) - z \frac{\partial w(x)}{\partial x} + \left(\frac{5z}{4} - \frac{5z^3}{3h^2} \right) \psi(x) = u(x) - zw_{,x} + \Omega(z)\psi(x) \quad (3a)$$

$$u_3(x, z) = w(x) \quad (3b)$$

where u and w are the axial and transverse displacements of mid-plan of the beams, respectively; ψ is the rotation of a transverse normal about the y -axis; Ω represents the higher-order variation of axial displacement; the comma indicates partial differentiation with respect to the coordinate subscript that follows.

The strain field of beams is given by:

$$\varepsilon_x = u_{1,x} = u_{,x} - zw_{,xx} + \Omega\psi_{,x} \quad (4a)$$

$$\gamma_{xz} = u_{1,z} + u_{3,x} = \psi\Omega_{,z} \quad (4b)$$

3.2 Variational Formulation

The strain energy U of system is given by:

$$\begin{aligned} U &= \frac{1}{2} \int_V (\sigma_x \varepsilon_x + \sigma_{xz} \gamma_{xz}) dV \\ &= \frac{1}{2} \int_0^L \left[A(u_{,x})^2 - 2Bu_{,x}w_{,xx} + D(w_{,xx})^2 + 2B^s u_{,x}\psi_{,x} - 2D^s w_{,xx}\psi_{,x} + H^s(\psi_{,x})^2 + A^s(\psi)^2 \right] dx \end{aligned} \quad (5)$$

where the stiffness coefficients A, B, D, B^s, D^s, H^s of the beam are determined as follows:

$$(A, B, D, B^s, D^s, H^s) = \sum_{k=1}^n \int_{z_k}^{z_{k+1}} \bar{Q}_{11}^{(k)}(1, z, z^2, \Omega, z\Omega, \Omega^2)bdz \tag{6a}$$

$$A^s = \sum_{k=1}^n \int_{z_k}^{z_{k+1}} \bar{Q}_{55}^{(k)}(\Omega, z)^2bdz \tag{6b}$$

The work done V by transverse load q can be written in the following form:

$$V = - \int_0^L qwb dx \tag{7}$$

The total potential energy of system is expressed by:

$$\begin{aligned} \Pi &= U + V \\ \Pi &= \frac{1}{2} \int_0^L \left[A(u_{,x})^2 - 2Bu_{,x}w_{,xx} + D(w_{,xx})^2 + 2B^su_{,x}\psi_{,x} \right. \\ &\quad \left. - 2D^sw_{,xx}\psi_{,x} + H^s(\psi_{,x})^2 + A^s(\psi)^2 \right] dx - \int_0^L qwb dx \end{aligned} \tag{8}$$

4 Ritz Solutions

Based on Ritz method, the mid-plan displacements in Eq. (8) are approximated in the following forms:

$$\{u(x), w(x), \psi(x)\} = \sum_{j=1}^m \{\varphi_{j,x}(x)a_j, \varphi_j(x)b_j, \varphi_{j,x}(x)c_j\} \tag{9}$$

Table 1 Kinematic boundary conditions of beams

BCs	Position	Value
S-S	$x = 0$	$w = 0$
	$x = L$	$w = 0$
C-F	$x = 0$	$u = 0, w = 0, w_{,x} = 0, \psi = 0$
	$x = L$	–
C-C	$x = 0$	$u = 0, w = 0, w_{,x} = 0, \psi = 0$
	$x = L$	$u = 0, w = 0, w_{,x} = 0, \psi = 0$

where a_j, b_j, c_j are unknown values to be determined; $\varphi_j(x)$ are the approximative shape functions which impact on the accuracy and efficiency of solutions. In the present study, the following hybrid shape functions are proposed for simply-supported (S-S), clamped-free (C-F) and clamped-clamped (C-C) boundary conditions (BCs):

$$\text{S-S: } \varphi_j(x) = x(L - x)e^{x/jL} \tag{10a}$$

$$\text{C-F: } \varphi_j(x) = x^2 e^{x/jL} \tag{10b}$$

$$\text{C-C: } \varphi_j(x) = x^2(L - x)^2 e^{x/jL} \tag{10c}$$

It is known that the accuracy and efficiency of the Ritz method strictly depend on a choice of approximative shape functions for the field variables, and the inappropriate shape functions may cause slow convergence rates and numerical instabilities [19, 20]. For the functions which do not satisfy the boundary conditions, Lagrangian multipliers method can be used to impose the boundary conditions [17, 18]. The proposed hybrid functions in Eqs. (10a–10c) are combinations of exponential and admissible functions which meet properties of approximative shape functions of the Ritz method [26] and satisfy essential boundary conditions given in Table 1.

Substituting Eqs. (10a–10c) into Eq. (9) and using Lagrange’ equations for static analysis, $\Pi_{,q_j} = 0$ with q_j representing the values of (a_j, b_j, c_j), the governing equations are obtained as follows:

$$\begin{bmatrix} \mathbf{K}^{11} & \mathbf{K}^{12} & \mathbf{K}^{13} \\ {}^T\mathbf{K}^{12} & \mathbf{K}^{22} & \mathbf{K}^{23} \\ {}^T\mathbf{K}^{13} & {}^T\mathbf{K}^{23} & \mathbf{K}^{33} \end{bmatrix} \begin{Bmatrix} \mathbf{a} \\ \mathbf{b} \\ \mathbf{c} \end{Bmatrix} = \begin{Bmatrix} \mathbf{0} \\ \mathbf{F} \\ \mathbf{0} \end{Bmatrix} \tag{11}$$

where the components of stiffness matrix \mathbf{K} are given by:

$$\begin{aligned}
 K_{ij}^{11} &= A \int_0^L \varphi_{i,xx} \varphi_{j,xx} dx, & K_{ij}^{12} &= -B \int_0^L \varphi_{i,xx} \varphi_{j,xx} dx, \\
 K_{ij}^{13} &= B^s \int_0^L \varphi_{i,xx} \varphi_{j,xx} dx, & K_{ij}^{22} &= D \int_0^L \varphi_{i,xx} \varphi_{j,xx} dx \\
 K_{ij}^{23} &= -D^s \int_0^L \varphi_{i,xx} \varphi_{j,xx} dx, & K_{ij}^{33} &= H^s \int_0^L \varphi_{i,xx} \varphi_{j,xx} dx + A^s \int_0^L \varphi_{i,x} \varphi_{j,x} dx, \\
 F_i &= \int_0^L q \varphi_i dx
 \end{aligned} \tag{12}$$

5 Numerical Examples

In this section, a number of numerical examples are carried out to demonstrate the accuracy of the present solution and to investigate effects of the span-to-height ratio, boundary conditions, fibre orientation and material anisotropy on the displacement and stresses of laminated composite and sandwich beams. The beam is supposed to be subjected to a uniformly distributed load q . Unless other states, laminates have the same thickness. The material (MAT) properties throughout numerical examples are given as follows:

- MAT I [28]: $E_1/E_2 = 25$, $G_{12} = G_{13} = 0.5E_2$, $G_{23} = 0.2E_2$, $\nu_{12} = 0.25$.
- MAT II [15]: MAT I for faces, and $E_1/E_2 = 1$, $G_{13} = G_{23} = 1.5E_2$, $G_{12} = 0.4E_2$, $\nu_{12} = 0.25$ for core.

For convenience, the following non-dimensional terms are used:

$$\bar{w} = \frac{10^2 w E_2 b h^3}{q L^4}, \quad \bar{\sigma}_x = \frac{b h^2}{q L^2} \sigma_x \left(\frac{L}{2}, \frac{h}{2} \right), \quad \bar{\sigma}_{xz} = \frac{b h}{q L} \sigma_{xz}(0, 0) \tag{13}$$

To study convergence of the proposed solution, $(0^\circ/90^\circ/0^\circ)$ composite beams (MAT I, $L/h = 5$) are considered. The variation of non-dimensional mid-span displacement with respect to the series number m of the beams with different boundary conditions is presented in Table 2. It can be seen that $m = 12$ is the convergence point for all BCs. So, this number of series terms will be used in the examples. In comparison, the convergence obtained from the present solution is faster than that from Nguyen et al. [22].

Table 2 Convergence of non-dimensional mid-span displacements of (0°/90°/0°) composite beams (MAT I, $L/h = 5$)

BCs	m							
	2	4	6	8	10	12	14	16
S-S	2.3507	2.4210	2.4103	2.4127	2.4123	2.4124	2.4124	2.4124
C-F	3.9694	6.7575	6.7829	6.8272	6.8234	6.8240	6.8239	6.8239
C-C	1.5211	1.5084	1.5396	1.5366	1.5370	1.5369	1.5369	1.5369

Table 3 Non-dimensional mid-span displacement of (0°/90°/0°) and (0°/90°) composite beams under uniformly distributed load (MAT I)

BCs	Reference	Symmetric (0°/90°/0°)			Un-symmetric (0°/90°)		
		$L/h = 5$	10	50	$L/h = 5$	10	50
S-S	Present	2.4124	1.0963	0.6645	4.7768	3.6883	3.3363
	Khdeir and Reddy [25]	2.4120	1.0960	0.6650	4.7770	3.6880	3.3360
	Zenkour [15]	2.4141	1.0800	0.6650	4.7879	3.6973	3.3447
	Murthy et al. [6]	2.3980	1.0900	0.6610	4.7500	3.6680	3.3180
	Nguyen et al. [22]	2.4120	1.0960	0.6650	4.7770	3.6880	3.3360
	Vo et al. [9]	2.4141	1.0980	0.6662	4.7845	3.6958	3.3437
C-F	Present	6.8240	3.4554	2.2511	15.2791	12.3435	11.3368
	Khdeir and Reddy [25]	6.8240	3.4550	2.2510	15.2790	12.3430	11.3370
	Murthy et al. [6]	6.8360	3.4660	2.2620	15.3340	12.3980	11.3920
	Nguyen et al. [22]	6.8130	3.4470	2.2500	15.2600	12.3300	11.3350
	Vo et al. [9]	6.8304	3.4607	2.2568	15.3050	12.3690	11.3630
C-C	Present	1.5369	0.5315	0.1468	1.9216	1.0051	0.6786
	Khdeir and Reddy [25]	1.5370	0.5320	0.1470	1.9220	1.0050	0.6790
	Murthy et al. [6]	1.5380	0.5320	0.1470	1.9240	1.0070	0.6810
	Nguyen et al. [22]	1.5360	0.5310	0.1470	1.9200	1.0040	0.6790
	Vo et al. [9]	1.5378	0.5320	0.1473	1.9227	1.0062	0.6796

5.1 Laminated Beams

In order to validate the accuracy of the present solution on displacement responses, symmetric (0°/90°/0°) and un-symmetric (0°/90°) composite beams (MAT I) with different BCs and subjected to uniformly distributed load are considered. The results are calculated with three ratios of span-to-height $L/h = 5, 10, 50$ and reported in Table 3. The non-dimensional transverse displacements are compared with those obtained from Khdeir and Reddy [25], Zenkour [15], Murthy et al. [6], Nguyen et al. [22] and Vo et al. [9], which are based on the HOBTs. It can be seen that the present solutions are in good agreements with those from previous studies, and the non-dimensional mid-span transverse displacements decrease with increase

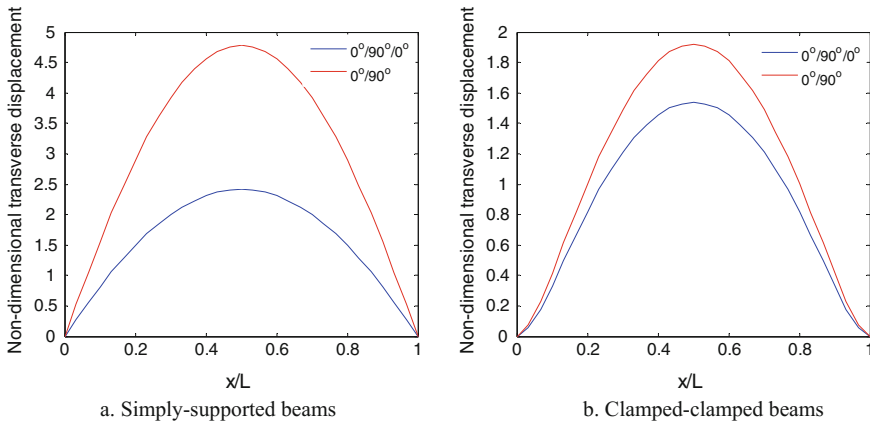


Fig. 2 Non-dimensional transverse displacement (\bar{w}) in x -direction (MAT I, $L/h = 5$)

Table 4 Non-dimensional axial and shear stresses of $(0^\circ/90^\circ/0^\circ)$ and $(0^\circ/90^\circ)$ simply-supported laminated beams under uniformly distributed load (MAT I)

Reference	Symmetric $(0^\circ/90^\circ/0^\circ)$			Un-symmetric $(0^\circ/90^\circ)$		
	$L/h = 5$	10	50	$L/h = 5$	10	50
<i>a. Normal stress ($\bar{\sigma}_x$)</i>						
Present	1.0677	0.8503	0.7806	0.2361	0.2342	0.2336
Zenkour [15]	1.0669	0.8500	0.7805	0.2362	0.2343	0.2336
Nguyen et al. [22]	1.0696	0.8516	–	0.2362	0.2343	–
Vo et al. [9]	1.0670	0.8503	0.7809	0.2361	0.2342	0.2336
<i>b. Shear stress ($\bar{\sigma}_{xz}$)</i>						
Present	0.4056	0.4311	0.4529	0.9204	0.9567	0.9888
Zenkour [15]	0.4057	0.4311	0.4514	0.9211	0.9572	0.9860
Nguyen et al. [22]	0.4050	0.4289	–	0.9174	0.9483	–
Vo et al. [9]	0.4057	0.4311	0.4518	0.9187	0.9484	0.8445

of L/h , the maximum and minimum values are obtained from C-F and C-C boundary conditions, respectively. Figure 2a and b display the variation of non-dimensional transverse displacements in the x -direction of beams with S-S and C-C BCs. Obviously, owing to the symmetry of load and BCs, the displacements are symmetric with respect to the mid-point of the beams. Table 4 presents the non-dimensional axial and transverse shear stresses of $(0^\circ/90^\circ/0^\circ)$ and $(0^\circ/90^\circ)$ simply-supported composite beams (MAT I). The obtained results are compared to those derived from Zenkour [15], Nguyen et al. [22] and Vo et al. [9]. Good agreements between the theories are again found. The variations of non-dimensional axial and transverse shear stresses through the beam thickness of $(0^\circ/90^\circ/0^\circ)$ and $(0^\circ/90^\circ)$ composite beams (MAT I, $L/h = 5$) are also plotted in

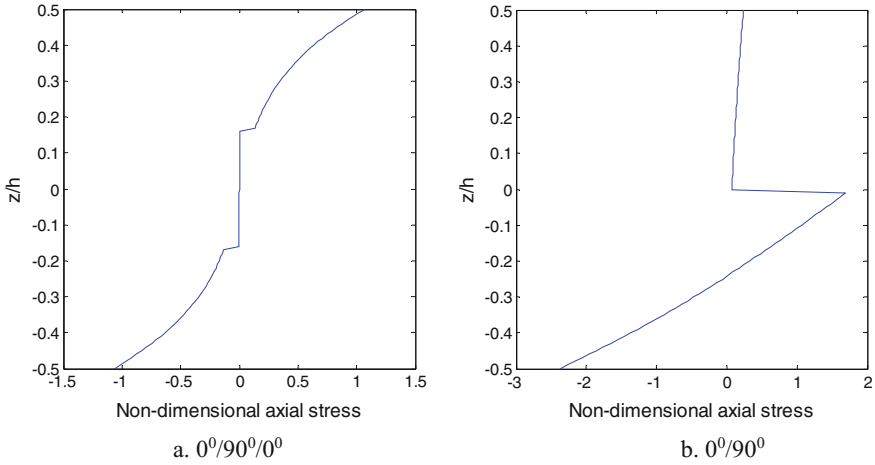


Fig. 3 Distribution of $\bar{\sigma}_{xx}$ through the beam depth of S-S beams (MAT I, $L/h = 5$)

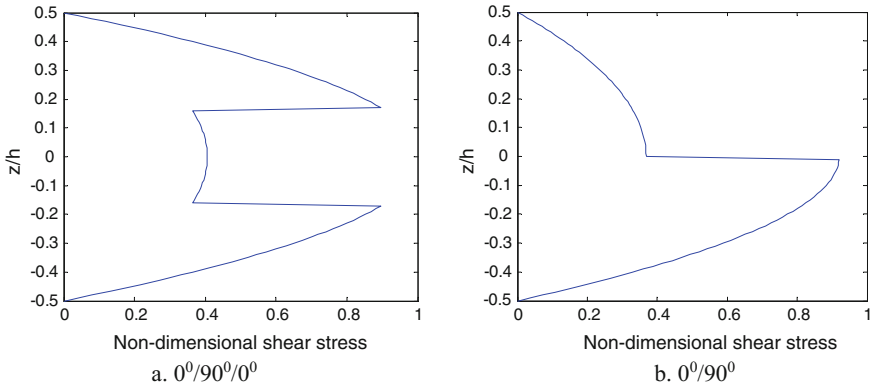


Fig. 4 Distribution of $\bar{\sigma}_{xz}$ through the beam depth of S-S beams (MAT I, $L/h = 5$)

Figs. 3 and 4 in which the nonlinear variations of the stresses and traction-free boundary conditions on the top and bottom surfaces of the beams are observed.

The next example aims to investigate the effects of material anisotropy and fibre orientation on displacements of laminated composite beams. Figure 5 displays variations of the non-dimensional mid-span transverse displacements with respect to E_1/E_2 of $(0^\circ/90^\circ/0^\circ)$ and $(0^\circ/90^\circ)$ composite beams (MAT I, $L/h = 5$) with different boundary conditions. It can be seen that the displacements decrease with the increase of E_1/E_2 , and this effect is the most significant for beams with C-F boundary condition. Moreover, the effect of fibre orientation on the displacement of $(\theta^\circ / -\theta^\circ)_s$ laminated beams (MAT I, $L/h = 5$) is shown in Fig. 6 from which it is

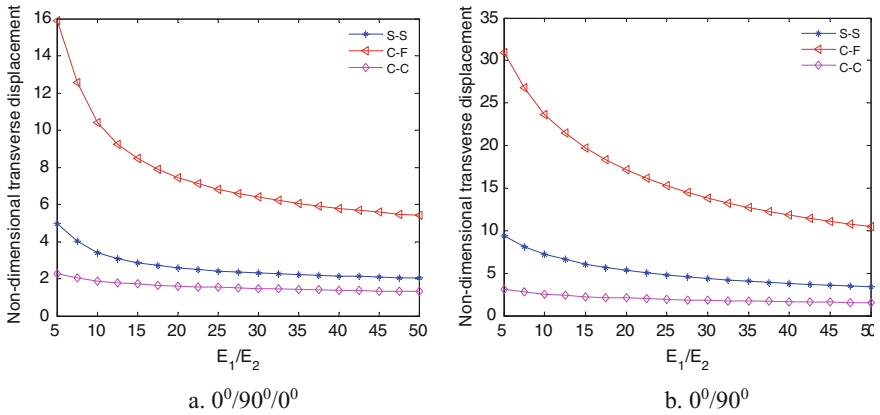
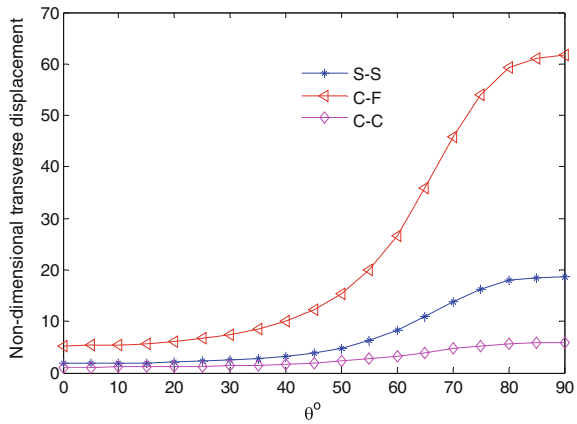


Fig. 5 Effects of material anisotropy on non-dimensional displacement of composite beams (MAT I, $L/h = 5$)

Fig. 6 Effects of fibre orientation on non-dimensional transverse displacement of $(\theta^\circ / -\theta^\circ)_s$ composite beams (MAT I, $L/h = 5$)



observed that the non-dimensional mid-span displacements increase with the increase of θ° for all BCs.

5.2 Sandwich Beams

In this section, symmetric sandwich beams are considered in which the thicknesses of face layers and core layer are h_1 and h_2 , respectively. For comparison purposes, $0^\circ/90^\circ/0^\circ$ sandwich beams (MAT II) with core-to-face thickness ratio $h_2/h_1 = 3$ and 8 are investigated. Tables 5 and 6 present the non-dimensional mid-span displacements and stresses of sandwich beams, which are calculated with different

boundary conditions and span-to-height ratios ($L/h = 5, 10, 50$) and compared with previous works based on the HOBTs of Zenkour [15] and Vo et al. [9]. It can be seen that the present results are in excellent agreements with those from earlier studies. In addition, the effect of thickness ratio of core-to-face h_2/h_1 on the transverse displacement of $0^\circ/90^\circ/0^\circ$ sandwich beams is also plotted in Fig. 7. It is interesting to observe that the displacements vary with respect to L/h , h_2/h_1 and boundary conditions. For S-S beams with $L/h = 50$, the non-dimensional displacement increases monotonically with the increase of h_2/h_1 , whereas for $L/h = 5$ and 10, it decreases to a minimum value and then increases with respect to h_2/h_1 .

Table 5 Non-dimensional mid-span displacement of ($0^\circ/90^\circ/0^\circ$) sandwich beams under uniformly distributed load (MAT II)

BCs	Reference	$h_2/h_1 = 3$			$h_2/h_1 = 8$		
		$L/h = 5$	10	50	$L/h = 5$	10	50
S-S	Present	1.1829	0.8854	0.7900	1.5603	1.3073	1.2263
	Zenkour [15]	1.1853	0.8879	0.7925	1.5661	1.3135	1.2325
	Vo et al. [9]	1.1853	0.8879	0.7925	1.5661	1.3135	1.2325
C-F	Present	3.8069	2.9631	2.6841	5.1412	4.4065	4.1679
	Vo et al. [9]	3.8148	2.9717	2.6927	5.1619	4.4281	4.1892
C-C	Present	0.5250	0.2526	0.1611	0.5667	0.3265	0.2479
	Vo et al. [9]	0.5257	0.2534	0.1616	0.5257	0.2534	0.1616

Table 6 Non-dimensional axial and shear stresses of ($0^\circ/90^\circ/0^\circ$) of simply-supported sandwich beams under uniformly distributed load (MAT II)

Reference	$h_2/h_1 = 3$			$h_2/h_1 = 8$		
	$L/h = 5$	10	50	$L/h = 5$	10	50
<i>a. Normal stress ($\bar{\sigma}_x$)</i>						
Present	0.9978	0.9586	0.9461	1.5010	1.4786	1.4715
Zenkour [15]	0.9980	0.9592	0.9467	1.5044	1.4823	1.4753
Vo et al. [9]	0.9984	0.9596	0.9471	1.5050	1.4830	1.4760
<i>b. Shear stress ($\bar{\sigma}_{xz}$)</i>						
Present	0.7497	0.7657	0.7780	0.6791	0.6879	0.6928
Zenkour [15]	0.7495	0.7641	0.7755	0.6779	0.6852	0.6906
Vo et al. [9]	0.7495	0.7644	0.7771	0.6781	0.6860	0.6922

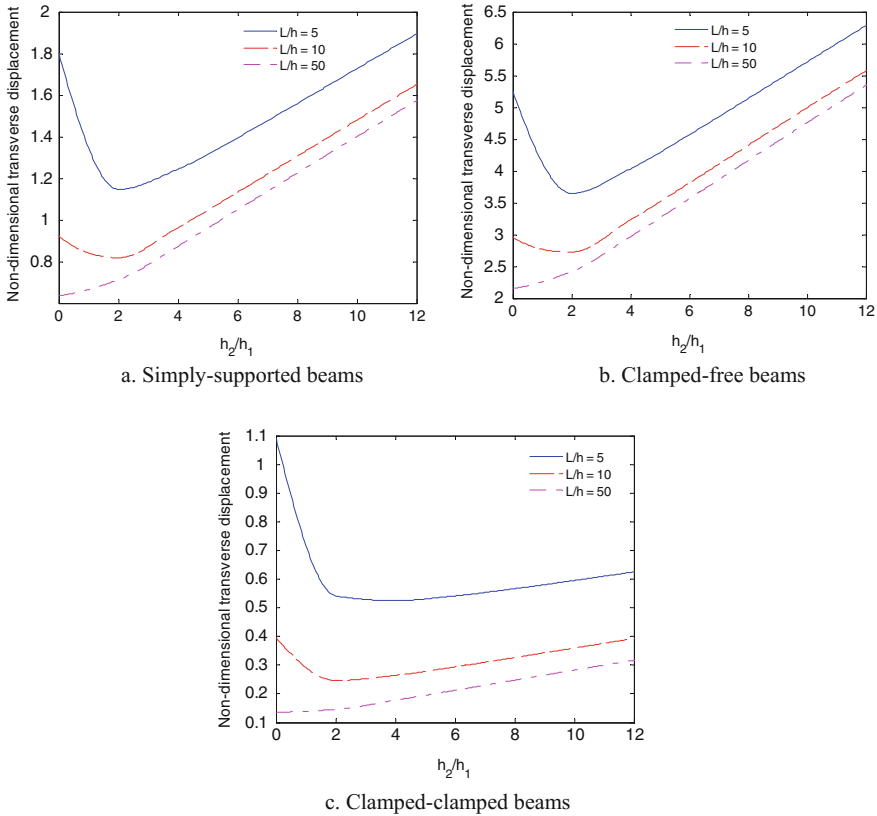


Fig. 7 Effect of h_2/h_1 ratio on non-dimensional mid-span transverse displacement of sandwich beams under uniformly distributed load (MAT II)

6 Conclusion

Static behaviours of laminated composite beams are presented in this paper. The displacement field of present theory is based on the HOBt which accounts for a higher-order variation of axial displacement. Ritz method is applied in which hybrid shape functions are proposed for analysis of composite beams with various boundary conditions. Numerical results are obtained to compare with previous studies and investigate effects of material anisotropy, span-to-height ratio and fibre orientation on the stresses and displacement of laminated composite and sandwich beams. The numerical examples showed that the proposed solution is simple and efficient for static analysis of composite beams.

Acknowledgements This research is funded by Vietnam National Foundation for Science and Technology Development (NAFOSTED) under Grant No. 107.02-2015.07.

References

1. Ghugal YM, Shimpi RP (2001) A review of refined shear deformation theories for isotropic and anisotropic laminated beams. *J Reinf Plast Compos* 20(3):255–272
2. Sayyad AS, Ghugal YM (2017) Bending, buckling and free vibration of laminated composite and sandwich beams: a critical review of literature. *Compos Struct*
3. Han J, Hoa S (1993) A three-dimensional multilayer composite finite element for stress analysis of composite laminates. *Int J Numer Meth Eng* 36(22):3903–3914
4. Maiti DK, Sinha P (1994) Bending and free vibration analysis of shear deformable laminated composite beams by finite element method. *Compos Struct* 29(4):421–431
5. Subramanian P (2001) Flexural analysis of symmetric laminated composite beams using C 1 finite element. *Compos Struct* 54(1):121–126
6. Murthy M, Mahapatra DR, Badarinarayana K, Gopalakrishnan S (2005) A refined higher order finite element for asymmetric composite beams. *Compos Struct* 67(1):27–35
7. Vidal P, Polit O (2008) A family of sinus finite elements for the analysis of rectangular laminated beams. *Compos Struct* 84(1):56–72
8. Lezgy-Nazargah M, Shariyat M, Beheshti-Aval S (2011) A refined high-order global-local theory for finite element bending and vibration analyses of laminated composite beams. *Acta Mech* 217(3–4):219–242
9. Vo TP, Thai H-T, Nguyen T-K, Lanc D, Karamanli A (2017) Flexural analysis of laminated composite and sandwich beams using a four-unknown shear and normal deformation theory. *Compos Struct*
10. Mantari J, Canales F (2016) Finite element formulation of laminated beams with capability to model the thickness expansion. *Compos B Eng* 101:107–115
11. Mantari J, Canales F (2016) A unified quasi-3D HSDT for the bending analysis of laminated beams. *Aerosp Sci Technol* 54:267–275
12. Ghugal ASY (2011) Effect of transverse shear and transverse normal strain on bending analysis of cross-ply laminated beams. *Int J Appl Math Mech* 7(12):85–118
13. Karama M, Afaq K, Mistou S (2003) Mechanical behaviour of laminated composite beam by the new multi-layered laminated composite structures model with transverse shear stress continuity. *Int J Solids Struct* 40(6):1525–1546
14. Matsunaga H (2002) Interlaminar stress analysis of laminated composite beams according to global higher-order deformation theories. *Compos Struct* 55(1):105–114
15. Zenkour AM (1999) Transverse shear and normal deformation theory for bending analysis of laminated and sandwich elastic beams. *Mech Compos Mater Struct* 6(3):267–283
16. Cook GM, Tessler A (1998) A {3, 2}-order bending theory for laminated composite and sandwich beams. *Compos B Eng* 29(5):565–576
17. Nguyen T-K, Truong-Phong Nguyen T, Vo TP, Thai H-T (2015) Vibration and buckling analysis of functionally graded sandwich beams by a new higher-order shear deformation theory. *Compos Part B Eng* 76:273–285
18. Nguyen T-K, Nguyen B-D, Vo TP, Thai H-T (2017) Hygro-thermal effects on vibration and thermal buckling behaviours of functionally graded beams. *Compos Struct* 176:1050–1060
19. Aydogdu M (2005) Vibration analysis of cross-ply laminated beams with general boundary conditions by Ritz method. *Int J Mech Sci* 47(11):1740–1755
20. Aydogdu M (2006) Buckling analysis of cross-ply laminated beams with general boundary conditions by Ritz method. *Compos Sci Technol* 66(10):1248–1255
21. Mantari J, Canales F (2016) Free vibration and buckling of laminated beams via hybrid Ritz solution for various penalized boundary conditions. *Compos Struct* 152:306–315
22. Nguyen T-K, Nguyen N-D, Vo TP, Thai H-T (2017) Trigonometric-series solution for analysis of laminated composite beams. *Compos Struct* 160:142–151
23. Kant T, Pendhari SS, Desai YM (2007) On accurate stress analysis of composite and sandwich narrow beams. *Int J Comput Methods Eng Sci Mech* 8(3):165–177

24. Apetre N, Sankar B, Ambur D (2008) Analytical modeling of sandwich beams with functionally graded core. *J Sandwich Struct Mater* 10(1):53–74
25. Khdeir A, Reddy J (1997) An exact solution for the bending of thin and thick cross-ply laminated beams. *Compos Struct* 37(2):195–203
26. Reddy JN (2004) *Mechanics of laminated composite plates and shells: theory and analysis*. CRC Press
27. Reissner E (1975) On transverse bending of plates, including the effect of transverse shear deformation. *Int J Solids Struct* 11(5):569–573
28. Pagano N (1994) Exact solutions for composite laminates in cylindrical bending. In: *Mechanics of composite materials*. Springer, pp 72–85

Part VI
Numerical Methods and High
Performance Computing

Numerical Analysis of Hybrid Members Using FEM



T. V. Tran

Abstract The paper presents the numerical study dealing with the behavior and the real load-bearing capacity of hybrid members by Abaqus software. Especially identify the behavior of the composite steel-concrete members with several fully encased steel profiles (hybrid members) while the materials were yielded until failure. Structural hybrid members, material constitutive law for steel and concrete, load schematic, element types, numerical solution controls, interactions, steel-concrete bond and mechanical contact, . . . will be described in detail. It is expected that nonlinear FEM analysis can give more details on behavior as well as on shear and bending resistance mechanisms until failure of the hybrid members. The nonlinear FEM analysis will be able to predict specimen strength, maximum displacement, strains and stress distribution, crack pattern, and failure modes. The reliability of this method was evaluated by comparing the analysis results with a part of the experimental results.

Keywords Numerical analysis · Hybrid member · Profile · Connection
Simple bending · Failure

1 Introduction

Nowadays, finite element method (FEM) is widely adopted as a potential numerical method to investigate the behavior of composite steel-concrete structures because of many achieved advances in numerical techniques, material models, and computer performance. Especially, some various concrete models and sophisticated contact elements have been implemented in commercial FEM packages that make modeling and analysis become much easier.

One of the most FEM software used nowadays is ABAQUS software. Abaqus has several built-in models to predict the behavior of materials as well as the provision

T. V. Tran (✉)

Faculty of Construction Engineering, Thuy Loi University, Hanoi City, Vietnam
e-mail: tranvantoan@wru.vn

© Springer Nature Singapore Pte Ltd. 2018

H. Nguyen-Xuan et al. (eds.), *Proceedings of the International Conference on Advances in Computational Mechanics 2017*, Lecture Notes in Mechanical Engineering, https://doi.org/10.1007/978-981-10-7149-2_35

521

to add user-defined models. The program offers a wide range of options regarding element types, material behavior, and numerical solution controls, as well as graphic user interfaces, auto-meshes, sophisticated post-processors, and graphics to speed the analyses [1].

In this paper, this commercial software is employed to develop reliable three-dimensional finite element model for estimating the bearing capacity of the hybrid steel-concrete member specimens. It is expected that nonlinear FEM analysis can give more details on behavior as well as on shear and bending resistance mechanisms until failure of test specimens in our experimental program. The nonlinear FEM analysis will be able to predict specimen strength, maximum displacement, strain and stress distribution, slip distribution, crack pattern, and failure modes.

2 Description of Hybrid Member Specimens

The research program consists of six member specimens which are composite member with three-encased steel profiles (hybrid member). All specimens had the same size, geometry, and longitudinal reinforcing bar arrangements. The primary differences between six specimens were the type of the structural steel-concrete connection and the stirrup spacing. Details evaluated in the test include the contributions of the steel profiles, shear studs, stiffeners, bond and stirrup spacing to the bending, and

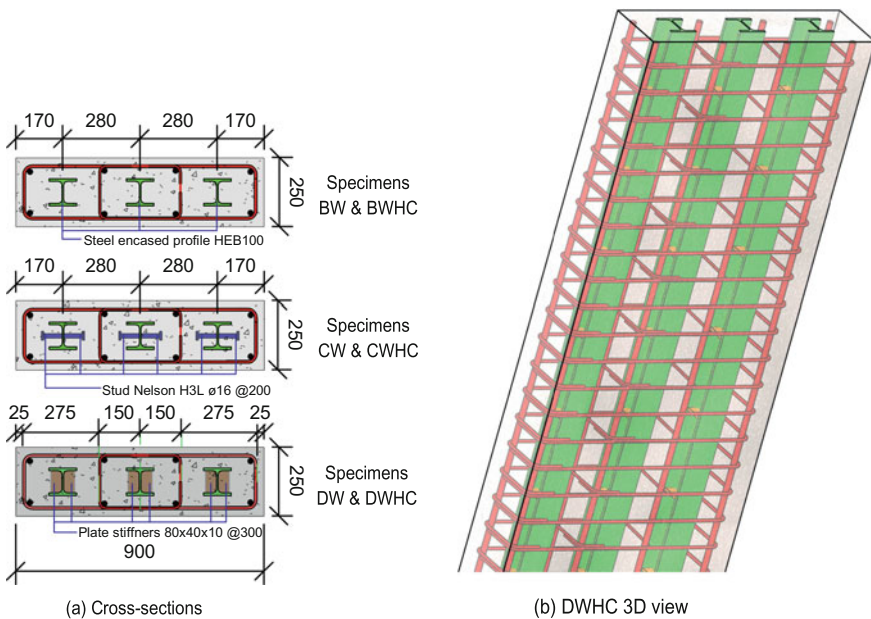


Fig. 1 Details of the hybrid member specimens

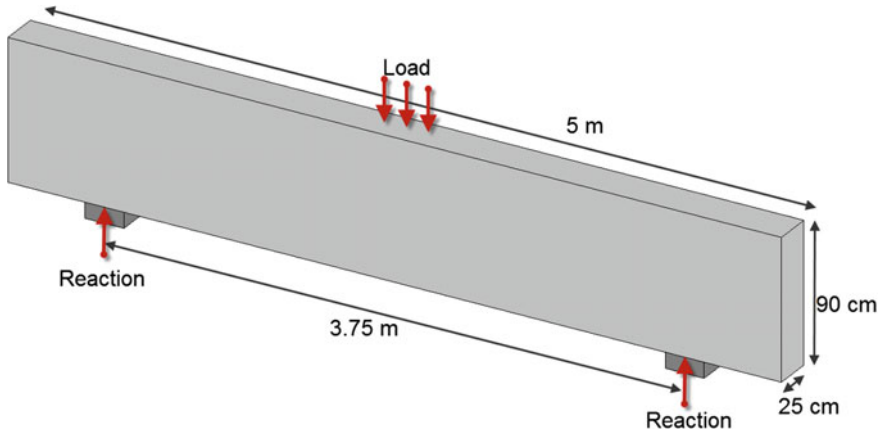


Fig. 2 Typical model for hybrid member specimen bending and shear analysis

shear resistance. Figure 1 shows the design details of all the six specimens of hybrid members. All specimens consisted of RC member that had 5 m length, 25 × 90 cm rectangular cross section and were reinforced with eight 20 mm diameter vertical reinforcing bars (Grade B). The horizontal reinforcement consisting of 14 and 6 mm reinforcing bars was made in form of stirrups. The reinforcing bar arrangement is the same in all specimens except the stirrup spacing which was 200 mm in BW, CW, and DW specimens and 100 mm in BW-HC, CW-HC, and DW-HC specimens. Moreover, they had additional three *HEB* 100 which were totally encased in the concrete with shear stud connectors between the concrete and the steel profiles for the CW and CW-HC specimens (50 × 3 Nelson S3L16 – 75, 200 mm spacing), with stiff connectors between the concrete and the steel profiles for the DW and DW-HC specimens (30 × 3 plate stiffeners, 10 mm thickness, 300 mm spacing) and without connectors for the BW and BW-HC specimens.

In the model, the solution of third-point flexural member specimens configuration was adopted to evaluate the resistance of specimens to combined bending and shear without axial force in Fig. 2. Specimens were loaded at the mid-length by vertical displacement. Pinned boundary conditions at each end of the specimens were simulated by two supports. No restraint was provided against rotation along any axis.

3 Finite Element Model

We have simulated 3D models for 6 hybrid members (namely BW, BW-HC, CW, CW-HC, DW, DW-HC as described above) in the Abaqus software. Due to the symmetry of the specimen geometry and loading, in order to save the calculation time, only half of the specimen was modeled as shown in Fig. 3. Four components of

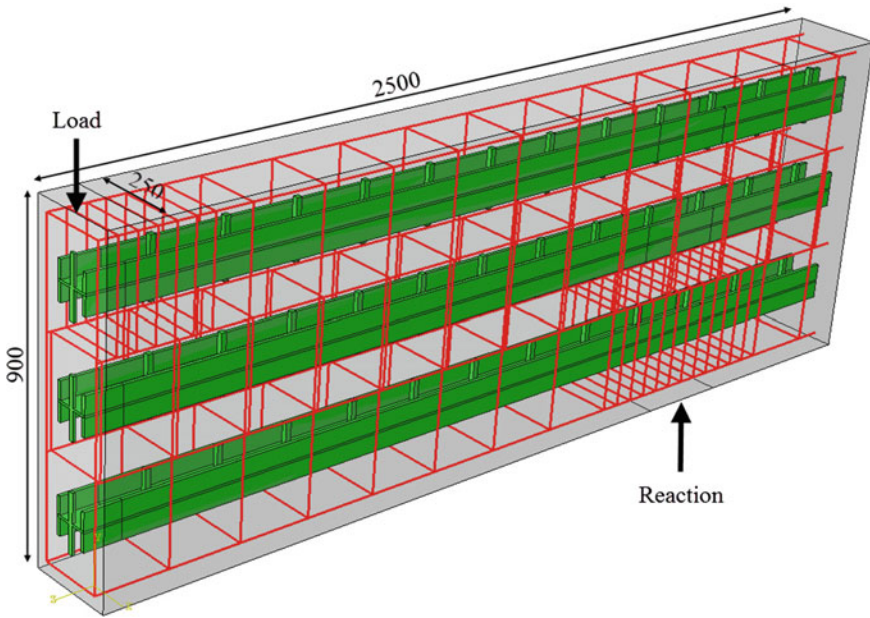


Fig. 3 Model of a half hybrid member specimens

specimen (concrete, rebars, steel profile, and connector) are modeled separately and assembled to make a complete specimen model.

3.1 Type of Finite Elements

The hybrid members proposed for finite element modeling embody situations of material discontinuity, yielding, stress concentration, contact, and composite behavior. These complex 3D phenomena are reproduced by adopting hexahedra solid elements [1], which are used to model majority of the parts of the specimens. Exception is the ordinary reinforcement in the concrete members, where truss elements are used. In ABAQUS, the finite elements C3D8 (8 nodes) and C3D20 (20 nodes) are continuum stress/displacement 3D solid finite elements of first and second order, respectively, either with reduced or full integration. The 8-node element with reduced integration is chosen for the general numerical simulations. A sensitivity analysis is performed with respect to the element type to check the required mesh density for application. For this purpose, the second-order element (C3D20R) with reduced integration is used to obtain the “correct” solution. The truss element (T3D2) used to model the ordinary reinforcement is a 2-node linear 3D truss element that can only transmit axial forces.

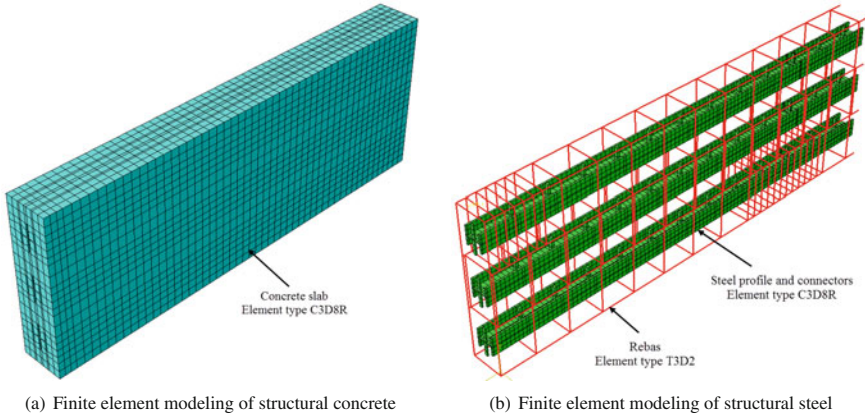


Fig. 4 Finite element type and mesh

3.2 Finite Element Mesh

Figure 4 shows the meshing of the FE model for the concrete member, rebar, steel member, and headed studs. The element size is 0.025 m for the elements of concrete member, steel profiles, reinforcement bars and shanks of the shear connectors, plate stiffeners and 0.005 m for a head of the shear connectors. The head and the stud of the connectors are approximated by a hexagon.

3.3 Constitutive Laws and Mechanical Properties

The constitutive laws used to model the mechanical behavior of the different materials and interactions considered include five types: Concrete Damage Plasticity for the concrete slab and Isotropic Material for the structural steel, the rebars, and connectors. The Concrete Damage Plasticity was chosen because it is simpler to model and more stable for the numeric calculation. The Concrete Damage Plasticity constitutive model is defined by a uni-axial compression and tension response (Fig. 5), where five constitutive parameters are needed to identify the shape of the flow potential surface and the yield surface [2, 3]. In this constitutive model, a nonlinear stress–strain relation is assumed for compression. As the entire stress–strain curve is not available from the test reports and only the usual parameters are reported (compression strength and Young’s modulus), the concrete uni-axial compressive behavior is obtained by applying Eq. (1), as specified in Eurocode 2 [4] for nonlinear analysis.

$$\sigma_c = \frac{k\eta - \eta^2}{1 + (k - 2)\eta} f_{cm} \tag{1}$$

Table 1 Material parameter of concrete damage plasticity model for concrete of $f_{cm} = 30$ MPa

Density		Parameters of concrete damaged plasticity model		
$P(\text{tonne/mm}^3)$	2.4×10^{-9}	Dilation angle	38°	
Elasticity		Eccentricity	0.1	
$E(\text{MPa})$	33346	f_{co}/f_{co}	1.16	
ν	0.2	K	0.67	
		Viscosity parameter	0.0001	
Compressive behavior		Tensile behavior		
Yield stress (MPa)	Inelastic strain	Yield stress (MPa)	Displacement (mm)	Damage
12.80	0	2.870	0	0
19.40	0.00016	2.428	0.0225	0.492
24.37	0.00037	1.706	0.0662	0.802
28.86	0.00066	1.192	0.1084	0.904
30.00	0.00102			
28.41	0.00156			
23.77	0.00219			
16.27	0.00291			

In Eq. 1, σ_c is the concrete stress, f is the mean concrete cylinder compressive strength, k and η are two factors determined according to Eqs. (2) and (3), E_{cm} is the secant modulus of elasticity of concrete, ϵ_c is the concrete strain, ϵ is the compressive strain at the peak stress f_{cm} and ϵ_{cu1} is the ultimate compressive strain in the concrete.

$$\eta = \frac{\epsilon_c}{\epsilon_{c1}} \tag{2}$$

$$k = 1.05 \frac{E_{cm} |\epsilon_{c1}|}{f_{cm}} \tag{3}$$

In tension, the behavior is assumed elastic up to the onset of cracking and then followed by tension softening. In the absence of experimental information to characterize the strain softening response of the concrete in tension, the concept of stress–displacement curve was used in the model. The stress–displacement curve is defined by Lubliner et al. (1989) and by Lee and Fenves (1988) according to David et al. [1]. Finally, for the five constitutive parameters (ψ —dilatation angle; ϵ —flow potential eccentricity; f_{bo}/f_{co} —ratio of initial equibiaxial compressive yield stress to initial compressive yield stress; k —ratio of second stress invariant on the tensile meridian; μ —viscosity parameter) required to complete the definition of the constitutive model, no information was available from the experimental tests and therefore default values [1, 5] were used (see Table 1). Design concrete class is the C30 [4, 6].

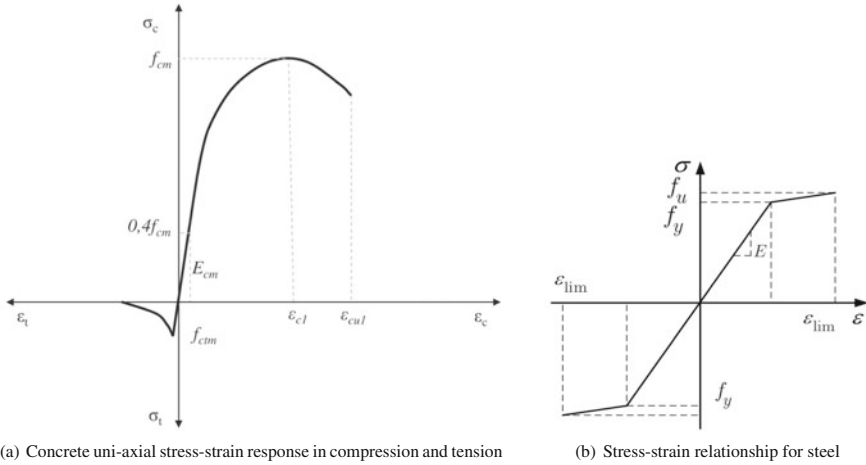


Fig. 5 Stress–strain material laws

3.4 Relation for Steel Profiles and Rebars and Connectors Behavior

To model the behavior of structural steel and reinforcement, the classical isotropic material law that implements the von Mises plasticity model (isotropic yielding) is used. For the generality of the steel parts, an elasto-plastic behavior with hardening is assumed (see Fig. 5). For the steel profiles and rebars, the true stress–strain ($\sigma_{true} - \epsilon_{true}$) material curve available from the experimental tests is considered. The latter properties are calculated as expressed in Eqs. (4) and (5) [5, 7] using the nominal properties (ϵ, σ) obtained in the tests.

$$\sigma_{true} = \sigma(1 + \epsilon) \tag{4}$$

$$\epsilon_{true} = \ln(1 + \epsilon) \tag{5}$$

The steel profile and the steel plate stiffener grade are S460. The steel longitudinal rebar class, the steel stirrups class, and the steel shear stud class are S500B [4, 6, 8, 9]. The material behavior was considered as bilinear stress–strain diagram with hardening until $\epsilon_{lim} = 0.05$. And their detailed values are presented in Table 2.

3.5 Steel Reinforcement-Concrete Interaction

In ABAQUS, the 3D modeling of reinforced concrete may be performed using steel rebars (truss element (2-nodes)), steel profiles, steel shear studs, steel plate stiffeners

Table 2 Structural and reinforcing steel strengths

Item	f_y (MPa)	f_u (MPa)	$\frac{f_u}{f_y}$	E (GPa)	Applying
HEB 100	462.7	583.5	1.26	214.45	Profiles, plate stiffener
$\phi 20$ mm bars	383.91	542.62	1.41	210.74	Longitudinal rebar
$\phi 14$ mm bars	633.26	656.34	1.04	207.46	Stirrups class, shear stud

(solid (continuum) element (8-nodes)), and all ordinary reinforcement embedded or not in the concrete. Due to the importance of the steel profiles and connectors reinforced in the hybrid member, they are modeled with 3D solid elements. For this type of element, bond behavior may be defined to model the interaction between the steel profiles and the concrete, whereby it is modeled by an approximation of the bond-slip response (this model proposed by Eligehausen et al. (1983) [6] and the typical traction-separation response available in ABAQUS [1]. The first technique consists of physically superposing the two parts. It is based on master and slave regions, where the nodes of the embedded region (slave, the steel profiles) displace by the same amount as the closest node of the host region (master, the concrete). Such type of modeling enforces a perfect bond between master and slave. However, it is only valid when stress transfer is medium-low. For highly stressed regions, e.g., near cracks, there are different strains in the concrete and in the reinforcement, as slip occurs due to the loss of bond. Therefore, modeling the interaction with perfect bond leads to excessive stresses in concrete and stiffer response of the reinforcement. Contact with cohesive behavior may be considered to model the bond behavior in the reinforcement-concrete interface. The contact and interface stresses are treated using the “hard” contact model with frictional behavior. In the “hard” contact: (i) pressure is transmitted when nodes of slave surface contact the master surface; (ii) no penetration is allowed; (iii) no limit to the pressure is assumed when the surfaces are in contact. The frictional behavior is guaranteed by the stiffness (penalty) method, and the sliding conditions between bodies are reproduced with the classical isotropic Coulomb friction model. For more detailed information, reference is given to [1, 5].

In order to reduce the modeling time, the “real” bond behavior is only applied in regions around the steel profiles-concrete slab interface with the coefficient of friction between the steel and the concrete is assumed to be 0.45. The test BW and BW-HC specimens were carried out without shear connectors welded to the encased steel profiles allowing, however, achieving the full bending resistance of the element without any apparent problem related to longitudinal shear, like slippage between concrete and steel profile. Particularly in the stage after cracking formation, the bond behavior still is only 0.45 of friction coefficient be applied in regions between the steel profiles with the concrete surround. Therefore, the perfect bond is simulated

for these 2 specimens. Moreover, the perfect bond model is applied in all the other parts of these reinforcement bars and for all ordinary reinforcement.

3.6 Boundary Conditions

For the application of the support conditions, all the nodes at the support location (concrete reaction surface) in the opposite direction of loading are restricted from moving in the Y direction to resist the flexion load. All the nodes of the concrete member, steel profile flanges, and the rebar web that lie on the opposite symmetry surface are restricted due to symmetry from moving in the Z direction and rotating in the Y and Z direction. All the concrete nodes and steel profile flange nodes that lie on the perpendicular to symmetry surface are restricted from moving in the X direction and rotating in the Y and Z direction.

3.7 Application of the Load

A deformation controlled load is applied at the mid-span of the hybrid member, i.e., above the concrete load surface on the symmetrical surface as shown in Fig. 3. Load can be applied using the arc length method. An initial increment of displacement is given on the data line, and the initial load proportionality factor is assigned to this initial increment using the automatic incremental scheme.

4 Results of Numerical Analysis

The analysis results are compared with the experimental results. The load-bearing capacity, stress and strain analysis, and failure modes have been investigated.

4.1 Load-Deflection Response

The load-displacement curves obtained from the FE model for all test specimens are compared to the experimental ones in Fig. 6. It can be observed that the numerical load-deflection behavior resembles the experimental behavior reasonably well. The numerical response is the load up to failure. It can be noticed that the stiffness of the elements obtained in the numerical analysis is higher than the stiffness obtained in the experimental tests. This difference appears firstly due to the different material pattern (homogeneous in case of numerical analysis and in-homogeneous in the

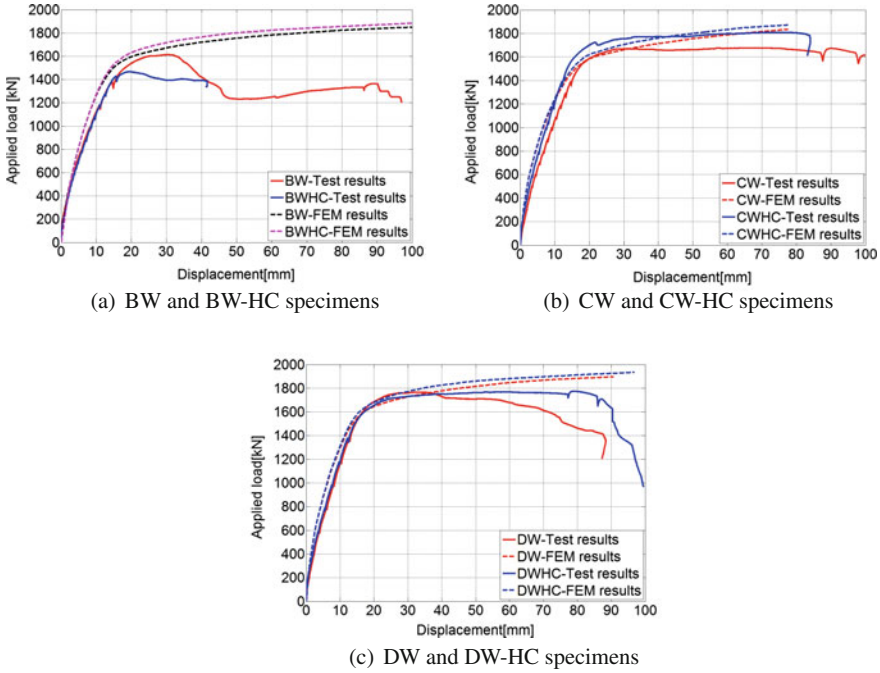


Fig. 6 Numerical–experimental comparison of load-displacement curves

Table 3 Comparative study of the load-bearing capacity

Specimen	Δ_{F_s} (mm)	Experimental F_{max}^{Exp} (kN)	Numerical F_{max}^{Num} (kN)	$\frac{F_s^{Num}}{F_s^{Exp}}$
BW	30.0	1613.4	1730.5	1.07
BW-HC	19.6	1567.5	1690.4	1.08
CW	57.2	1677.9	1780.8	1.06
CW-HC	76.6	1809.2	1870.7	1.03
DW	33.6	1767.6	1747.2	0.99
DW-HC	78.8	1774.2	1910.7	1.08

experimental tests) and secondly due to the different way in simulating the connection between steel profiles and concrete surrounding.

Nevertheless, the values of the load-bearing capacities of the elements obtained in the experimental tests [10] and those obtained in the numerical analysis are very close (1 ÷ 8% difference). Table 3 shows the load-bearing capacities of the test specimens predicted by the FE model in comparison with those from the experiment (The load-bearing capacity is maximum load obtained in the experimental or in the numerical corresponding to the displacement of the experimental).

4.2 Stress Comparison

The stresses of the longitudinal and the steel profile versus applied load from the FE model for six hybrid test specimens are compared to the experimental ones in Figs. 8 and 9. Good agreement between numerical and experimental results can be observed. Again the fact that the reinforcement and the steel profile are embedded in concrete (full interaction) in the FE model leads to higher stresses in reinforcement compared to the experimental ones. This observation highlights indeed the tension stiffening effect which takes place in reinforced concrete elements in tension. As can be seen from the Fig. 8 for all specimens the bottom layer of longitudinal rebars (J1 strain gauges pasted at the middle bottom layer of longitudinal rebars) and the bottom layer of steel profiles were yielded (R1 strain gauge rosettes pasted at the middle bottom layer of steel profiles). As a result, the load-bearing capacities of the specimens did not significantly improve when a double number of stirrup were used. In other words, the specimens were yielded first by flexion (Fig. 7).

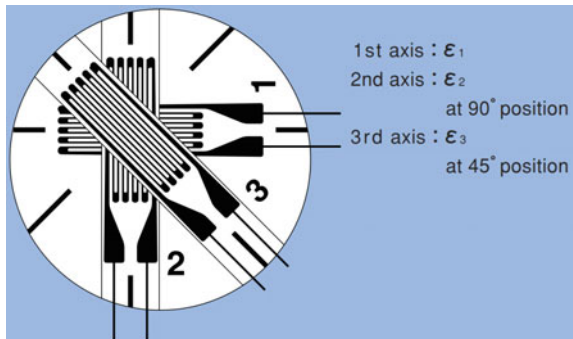
For all specimens, the yielding Von Mises stress in the bottom steel encased profile layer was attained at a load of (1400–1500) kN after the yielding stress in the bottom horizontal reinforcement layer attained at a load of (850–1050) kN. The yielding shear stresses in the bottom steel encased profile layer were attained at total loads from 1350 to 1450 kN for the BW, CW, DW specimens, the yielding shear stress was not reached the bottom steel encased profile of the other specimens.

It should be noted that during the experimental tests, the strains at different point on rebars, on steel profiles, and on concrete were measured using strain gauges and rosettes. From there, stresses at the locations of the strain gauges are calculated as follows:

- Regarding the strain gauges attached on the rebars, the axial stresses are computed by the following expressions:

$$f_{yk} = \begin{cases} \epsilon E_s & \text{if } \epsilon E_s \leq f_y \\ f_y + k(\epsilon - \epsilon_{c1}) & \text{if } \epsilon E_s > f_y \end{cases} \quad \text{with } k = \frac{f_u - f_y}{\epsilon_{cu1} - \epsilon_{c1}} \quad (6)$$

Fig. 7 Rosette description



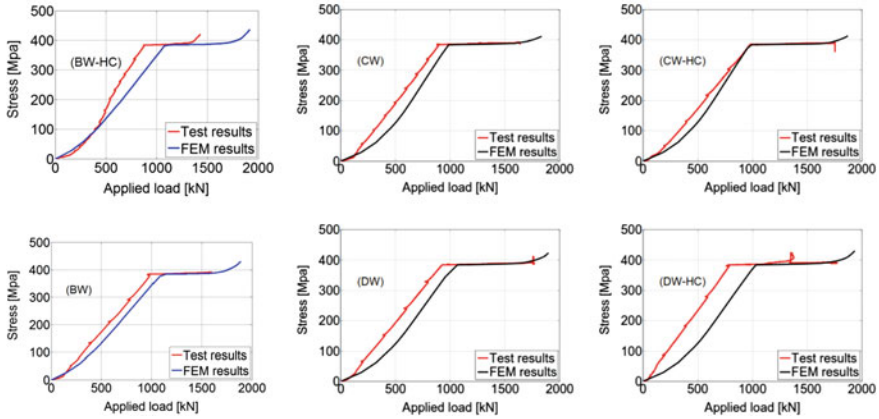


Fig. 8 Numerical—experimental comparison of stress at strain gauge J_1 location versus applied load

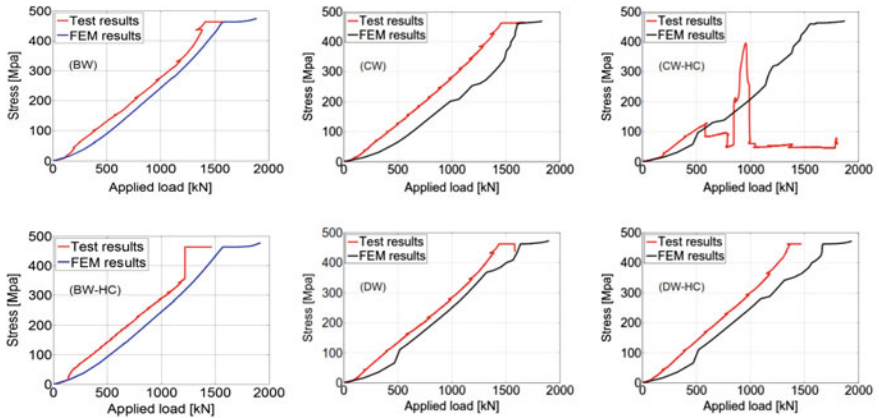


Fig. 9 Numerical—experimental comparison of stress at rosette R_1 location versus applied load (note: Rosette R_1 of specimen CW-HC was failed from 580 kN)

- Regarding the rosettes attached on the steel profiles, the principal strains and stresses are computed by the following expressions:
Maximum principal strain:

$$\epsilon_{\max} = \frac{1}{2} \left[\epsilon_1 + \epsilon_2 + \sqrt{2 \{ (\epsilon_1 - \epsilon_3)^2 + (\epsilon_2 - \epsilon_3)^2 \}} \right] \quad (7)$$

Minimum principal strain:

$$\epsilon_{\min} = \frac{1}{2} \left[\epsilon_1 + \epsilon_2 - \sqrt{2 \{ (\epsilon_1 - \epsilon_3)^2 + (\epsilon_2 - \epsilon_3)^2 \}} \right] \quad (8)$$

Maximum shear strain:

$$\gamma_{\max} = \sqrt{2 \{(\varepsilon_1 - \varepsilon_2)^2 + (\varepsilon_2 - \varepsilon_3)^2\}} \quad (9)$$

Maximum principal stress:

$$\sigma_{\max} = \frac{E}{1 - \nu^2} (\varepsilon_{\max} + \nu \varepsilon_{\min}) \quad (10)$$

Minimum principal stress:

$$\sigma_{\min} = \frac{E}{1 - \nu^2} (\nu \varepsilon_{\max} + \varepsilon_{\min}) \quad (11)$$

Maximum shear stress:

$$\tau_{\max} = \frac{E}{2(1 + \nu)} \gamma_{\max} \quad (12)$$

where: E : Elastic modulus (Young's modulus); ν : Poisson's ratio; $\varepsilon_1, \varepsilon_2, \varepsilon_3$: 1st strain axis, 2nd strain axis, 3rd strain axis (see Fig. 7). So, Von Mises stress criterion:

$$\sigma_v = \sqrt{\sigma_{\max}^2 + \sigma_{\min}^2 - \sigma_1 \sigma_2} = \begin{cases} \sigma_v & \text{if } \sigma_v \leq f_y \\ f_y & \text{if } \sigma_v > f_y \end{cases} \quad (13)$$

- The concrete stresses are computed the strains obtained on the strain gauges attached on surfaces of the concrete specimens by the expressions (1), (2) and (3) with: $E_{cm} = 22 \left(\frac{f_{cm}}{10} \right)^{0.3}$.

The yield stress was not reached in the stirrups of the others specimens. This is due to the fact that a part of the shear force carried by RC wall is transferred to the steel profile after the concrete cracking. It can be observed that the stresses increased due to the development of diagonal cracks in the specimens, which intersect the stirrups. It should be noted that the strain measured in stirrup depends strongly on the crack pattern. Indeed, if there is a shear crack that goes through the strain gauge position, the measured strain in this case is much greater than the case without cracks.

4.3 Crack Pattern

Figure 10 illustrates the tensile damage distribution in the concrete at deflection level 60 mm. Note that the concrete model adopted for FEM is a continuous model, therefore, the cracking cannot be reproduced in the discrete way as can be seen in the experiment. However, by analyzing the distribution of the tensile damage variable one can have an idea about the crack pattern at different load level. It can be observed

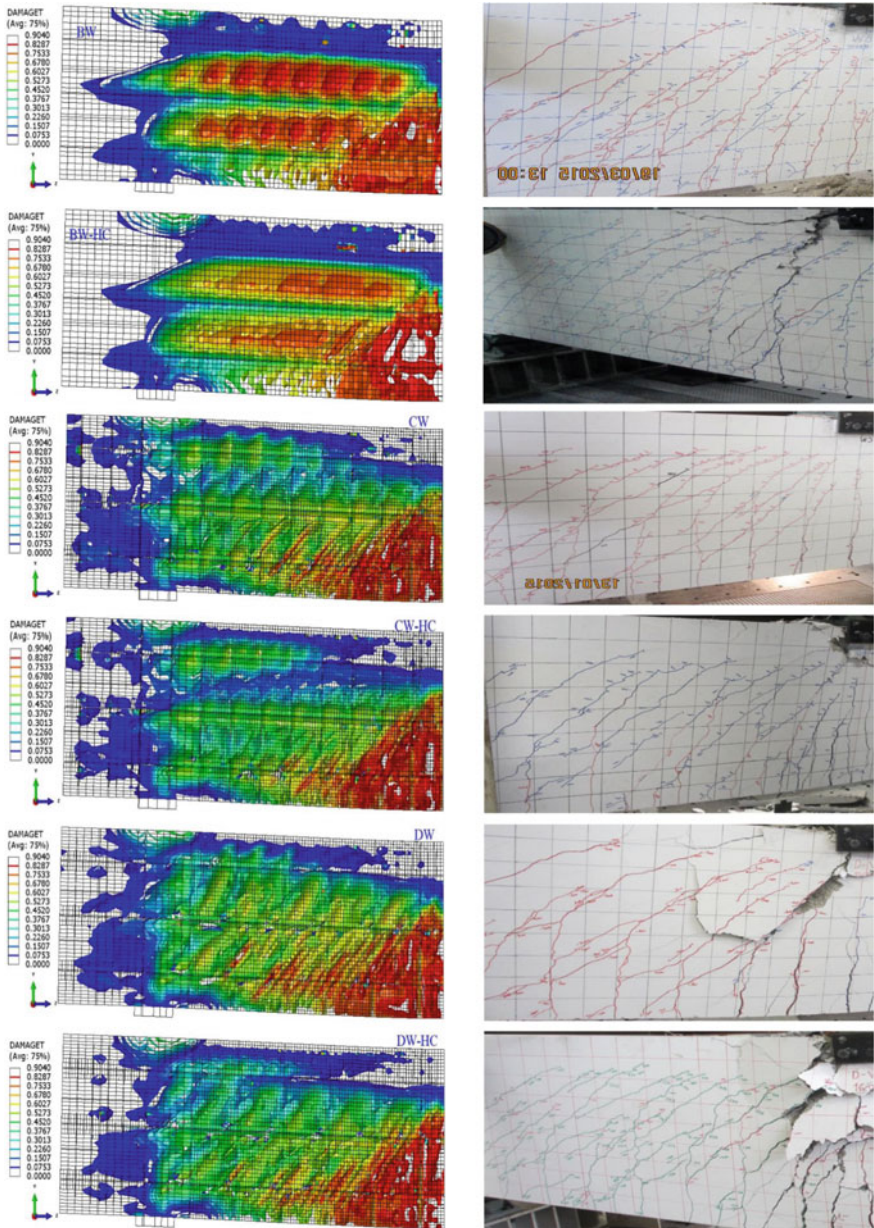


Fig. 10 Comparative of crack pattern in the concrete at deflection level 60 mm

that initially the specimens were principally damaged by flexion effect at mid-span region, after that the concrete “struts” were formed in the regions in between steel profiles. The concrete struts between upper and middle profiles were more pronounced in BW and BW-HC specimens than the other specimens. It should be noted that in the FE model of BW and BW-HC specimens the steel profiles were embedded in concrete. That means that full interaction between steel profile and concrete was assumed. Therefore, the slip is prevented in BW and BW-HC specimens and that explains why the concrete between upper and middle profiles was more mobilized in tension. In other words, by preventing the slip, the concrete struts are totally anchored, therefore, the shear effect is more active. It also explains the fact that in BW and BW-HC specimens the concrete region after the support is not damaged. In contrast, in other specimens the slip is not prevented, therefore, one can see the effect of the longitudinal shear which is locally active at the connector location and that makes the concrete region after the support damaged as can be seen in Fig. 10.

It can be observed in the right part of Fig. 10 and that at 60 mm of deflection the concrete damaged by shear is more pronounced, especially in BW specimen. One can see clearly the concrete struts in the region at the middle between load point and support. By regarding the direction of the tensile damaged zone one can say that the angle of the concrete struts is about 45° . This numerical observation confirms what has been observed in the experiment.

The concrete confinement effect can be noticed by comparing the damage zone of BW specimen with the one of BW-HC specimen. As can be seen, the concrete is indeed less damaged in the specimens where a double number of stirrups were placed to make the concrete confinement.

5 Conclusion

A 3D FE model has been developed in Abaqus Software to investigate the nonlinear behavior of hybrid member. The results of the numerical analysis show that some main behaviors of the studied hybrid member specimens such as load-bearing capacity, relation of load and displacement, strains and stress distribution, crack pattern, and failure modes predicted by FE model are in good agreement with test results.

The numerical analysis using FEM method by Abaqus software identified the behavior of the hybrid members while the materials were yielded until failure.

The developed FE model can be eventually used in the future works to perform a parametric study or to propose a design method on hybrid members.

Acknowledgements The authors gratefully acknowledge financial support by the European Commission (Research Fund for Coal and Steel) through the project SMARTCOCO (SMART COmposite COmponents: concrete structures reinforced by steel profiles) under grant agreement RFSR-CT-2012-00039.

References

1. David H et al (2012) ABAQUS standard user's manual (Version 6.12.1). USA
2. Jankowiak T, Lodygowski T (2005) Identification of parameters of concrete damage plasticity constitutive model. *Found Civil Environ Eng* 6:53–62
3. Eligehausen R, Popov E, Bertero V (1983) Local bond stress-slip relationship of deformed bars under generalized excitation. FReport No. UCB/EERC-83/23, Earthquake Engineering Center, University of California, Berkeley
4. Eurocode 2 (2004) EN 1992-1-1: Design of concrete structures—Part 1: General rules and rules for buildings. European Commission, Brussels
5. José H, Luís S, Isabel B (2013) Numerical modeling of composite beam to reinforced concrete member joints—Part I: Calibration of joint components. *Eng Struct* 52:747–761
6. Eurocode 4 (2005) EN 1994-1-1: Design of composite steel and concrete structures—Part 1.1: General rules and rules for buildings. European Commission, Brussels
7. Girao Coelho A, Simoes da Silva L, Bijlaard F (2006) Numerical evaluation of the behaviour of the T-Stub. *J Struct Eng* 132(6):918–928
8. ACI-318 (2005) Building code requirements for reinforced concrete. American Concrete Institute, USA
9. ACI-2010 (2010) Specification for structural steel buildings. American Concrete Institute, USA
10. Tran VT, Nguyen QH (2016) Experimental study of hybrid members with several fully encased steel sections. In: The 7th international conference of Asian Concrete Federation ACF 2016, Hanoi, Vietnam

Effect of Hyper-Parameters on Deep Learning Networks in Structural Engineering



Seunghye Lee, Mehriniso Zokhirova, Tan Tien Nguyen and Jaehong Lee

Abstract Since the first journal article on structural engineering applications of neural networks (NN) was published, a large number of articles about structural engineering have been published on these fields. However, over the last decade, researchers who attempt to apply the neural network concept to structural analysis problems have reduced significantly because of a fundamental limitation. At the beginning of the new millennium, in a deep learning field, newer methods have been proposed by using new activation functions, loss functions, alleviating overfitting methods with hyper-parameters, and other effective methods. Recent advances in deep learning techniques can provide a more suitable solution to the problem. The aim of our study is to show effects and differences of newer deep learning techniques on neural networks of structural analysis topics. A well-known 10-bar truss example is presented to show condition for neural networks and role of hyper-parameters in the structures.

Keywords Deep learning · Structural analysis · Feedforward neural network
Hyper-parameter

1 Introduction

Deep learning methods are representation-learning methods with multiple processing layers composed of linear and nonlinear transformations [1]. The multiple processing has a neural network with several layers of nodes between input and output. While the neural network is a biologically inspired programming paradigm which enables a computer to learn from observational data, the deep learning is a

S. Lee · M. Zokhirova · T. T. Nguyen · J. Lee (✉)
Department of Architectural Engineering, Deep Learning Architecture Research Center,
Sejong University, Seoul, Korea
e-mail: jhlee@sejong.ac.kr

S. Lee
e-mail: seunghye@sejong.ac.kr

© Springer Nature Singapore Pte Ltd. 2018
H. Nguyen-Xuan et al. (eds.), *Proceedings of the International Conference on Advances in Computational Mechanics 2017*, Lecture Notes in Mechanical Engineering, https://doi.org/10.1007/978-981-10-7149-2_36

powerful set of techniques for learning in the neural networks. An artificial intelligence (AI), machine learning (ML), and the deep learning (DL) are terms that are often used interchangeably. The machine learning is often described as a sub-discipline of the artificial intelligence; the deep learning is a subfield of the machine learning category.

In the first decades of the twenty-first century, some researchers have made some fundamental conceptual breakthroughs called the deep learning technique, namely, a deep belief network (DBN) [2], rectified linear unit (ReLU) [3], and dropout algorithm [4]. Because the deep learning has turned out to be very good at discovering intricate structures in high-dimensional data, it has resisted the best attempts of the artificial intelligence community for many years. However, in spite of the fact that the neural modeling paradigm has been improved to the deep learning by innovative methods, there have been few applications of newer algorithms in the structural analysis since the first journal article on structural engineering applications of neural networks (NN) was published [5, 6].

The purpose of our study was to show effects of hyper-parameters on deep learning networks in structural analysis problems. The state-of-the-art deep learning techniques have been then used to solve a 10-bar planar truss problem. Prior to the analysis, training and test sets are needed for making input and output layers. After fixing the neural network structures using obtained weight function of each layer, we can predict the result of specific test sets. The main contribution of this paper is to serve to lower barriers to apply deep learning techniques in structural engineering topics.

2 Neural Network Architectures

The well-known 10-bar planar truss shown in Fig. 1 is considered to build neural network architectures [7]. This particular truss problem has been used extensively in the literature to evaluate optimization algorithms. The objective of the 10-bar truss problem is to minimize the total weight of the structure while meeting some constraints. Generally, axial stresses of ten elements and maximum displacements of node numbers 1 to 4 are used as the constraints for static analysis. The material density and the modulus of elasticity are 0.1 lb/in^3 (2768.0 kg/m^3) and $10,000 \text{ ksi}$ ($68,950 \text{ MPa}$), respectively.

In this study, the cross-sectional areas are used as input of the neural network architectures and the constraints, namely, axial stresses and nodal displacements are used for the output layer. Their relationship between design variable and numerical results can be clarified by using the neural network architecture. After obtaining their weight functions of the fully connected neural network, we can predict numerical results from specific cross-sectional areas. The training sets generated by a random distribution of cross-sectional area design variables ranging from 0.1 to 35.0 in^2 (from 0.6 to 225.8 cm^2) were used to train the neural network. Note that all of input data are normalized with respect to the maximum cross-sectional area 35.0 for

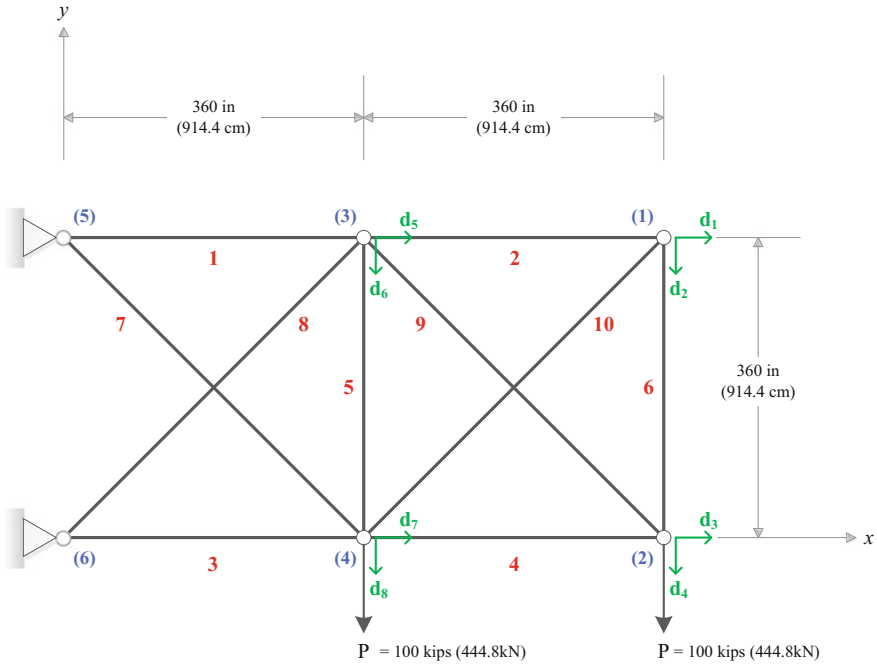


Fig. 1 A 10-bar truss example

regularization. We used 500 training sets randomly; 20% of these sets are used for test sets.

Figure 2 shows the fully connected neural network architectures for the 10-bar truss. The ten cross-sectional areas are used in the input layer units. In this example, only one hidden layer using 20 units is used for two different conditions; one of them is (10-20-2) architecture, and the other is (10-20-18) architecture. While the (10-20-2) architecture used two units in the output layer, namely, maximum vertical displacements of node numbers 1 and 2 (d_2 and d_4), the whole displacement (four horizontal and four vertical displacements (d_1 to d_8)) and stress of each element are used as output units in the (10-20-18) architecture.

3 Deep Learning Techniques

(1) Activation function

In computational networks, activation or transfer functions establish bounds for the output of neurons. Many different activation functions have been presented for better accuracy. Because the activation function can affect the neural networks, choosing an activation function is an important consideration. Table 1 shows the most com-

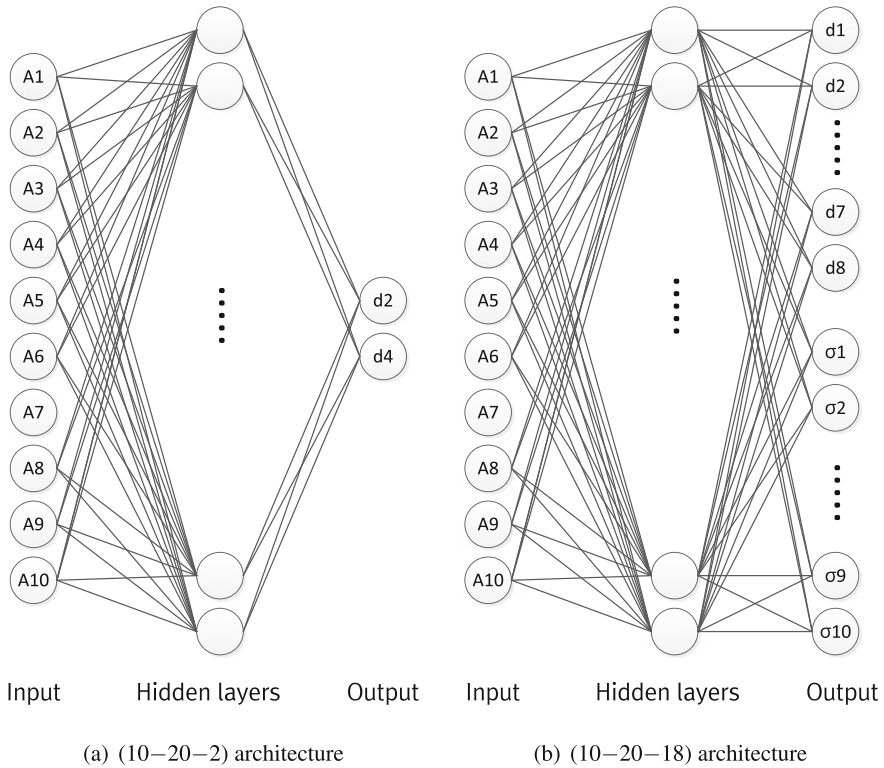


Fig. 2 Neural network architectures for the 10-bar truss problem

Table 1 Various activation functions

Activation function	Equation
Logistic (Sigmoid)	$f(u) = \frac{1}{1 + e^{-u}}$
Hyperbolic tangent (Tanh)	$f(u) = \tanh(u) = \frac{e^u - e^{-u}}{e^u + e^{-u}}$
Softplus	$f(u) = \ln(1 + e^u)$
Rectified linear units (ReLU)	$f(u) = \begin{cases} 0 & \text{for } u < 0 \\ u & \text{for } u \geq 0 \end{cases}$

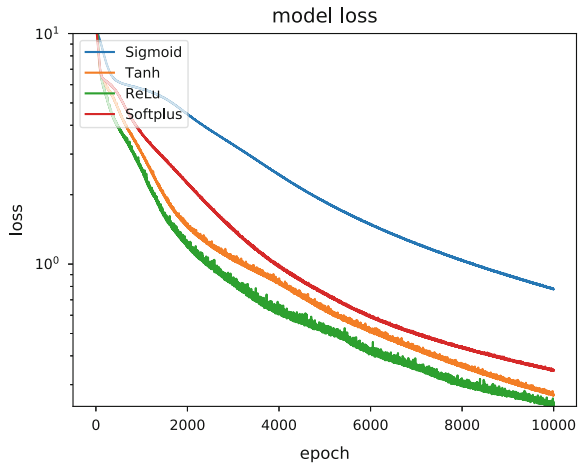
mon activation functions and their equations. More recently, the rectified linear unit (ReLU) [3] or the softplus activation [8] are preferred activation functions.

An appropriate error function should be chosen for each problem type. Table 2 shows the activation and error functions according to the problem types. Because the 10-bar truss is a simple regression problem, the identity mapping type and the norm calculation type are pertinent for the activation and error, respectively. In this study, a mean square error (MSE) function E_{MSE} is used as follows.

Table 2 Activation and error function types according to problem definitions

Problem type	Activation function	Error function
Regression	Identity mapping	Norm
Binary classification	Logistic function	Maximum likelihood
Multiple category classification	Softmax function	Negative log likelihood

Fig. 3 Training mean square error for (10–20–2 architecture): comparisons among various activation functions. The stochastic gradient descent (SGD) ($\epsilon = 0.01$ and $\eta = 0.9$) and 500 input sets are used for the basic neural network structure. Log scale



$$E_{MSE} = \frac{1}{n} \sum_k^n (y_k - t_k)^2 \tag{1}$$

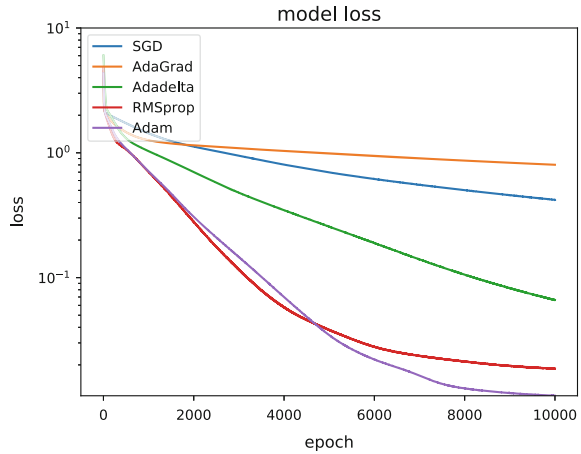
where n contains the number of training elements multiplied by number of output neurons.

Figure 3 indicates graph of training mean square errors for (10–20–2 architecture) during comparisons among various activation functions. We trained the basic model using the logistic sigmoid, hyperbolic tangent (tanh), softplus, and rectified linear unit (ReLU) functions for 10,000 epochs. According to Fig. 2, the ReLU activation function outperforms all other functions and achieves the lowest training mean square loss after 10,000 epochs as shown in Table 1.

(2) Optimizer

Several state-of-the-art algorithms for optimizing deep learning models have been evolved. In machine learning processes, the learning rate value (ϵ) is an important factor; when the learning rate is too small, the learning algorithm converges very slowly, on the contrary, if the value is too large, the network behaves chaotically and fails to converge. An effective way to determine an optimum learning rate is a learning rate decay. By using this method, lower learning rate is calculated as the training progresses.

Fig. 4 Mean square error for training set with (10–20–18) architecture after 10,000 epochs: comparisons among various gradient descent optimization algorithms in combination with the softplus activation function. Log scale



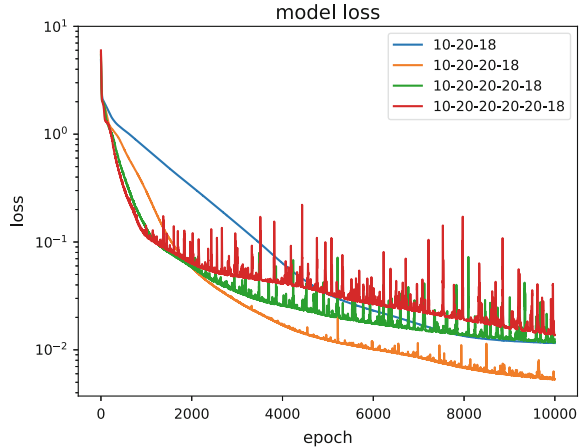
AdaGrad (adaptive gradient algorithm) [9] stems from this paradigm in stochastic optimization; that is a learning-theoretic technique for learning rate adaptation which is given by the square root of sum of squares of the historical, component-wise gradient. Adadelata [10] is an extension of the AdaGrad that can improve upon the continual decay of learning rates throughout training and the need for a manually selected global learning rate. RMSProp [11] is another extension of the AdaGrad in which the learning rate is adapted for each of the parameters. In this method, the learning rate is divided by an exponentially decaying average of squared gradients. Adam (adaptive moment estimation) is a method for efficient stochastic optimization that only requires first-order gradients with less memory requirement [12]. This method is designed to combine the advantages of AdaGrad and RMSProp.

Figure 4 shows mean square error tendencies for training set with (10–20–18) architecture after 10,000 epochs. The softplus activation function is then used. Throughout the comparison of use of various optimizers, the convergence of the case which uses the Adam algorithm based on the softplus activation function shows the minimum loss. After the 4,000th epoch, the combination converges rapidly toward zero. The Adam might be the best overall choice; however, there is no most efficient method among gradient descent optimization algorithms. Because it depends on problems and conditions, various optimizers can be selected to obtain the optimum solution.

4 Multilayer Neural Network

So far, we simulated the numerical example of single-layer network. The size and complexity of a neural network depend on both the total number of neurons and the number of hidden layers. More layers can handle complex decision and multiple

Fig. 5 Mean square error for training set with (10–20–18), (10–20–20–18), and (10–20–20–20–18) architectures after 10,000 epochs: comparisons among various number of hidden layers in combination with the softplus activation function and Adam optimization. Log scale



interactions between parameters. However, because implementations of multilayer neural networks will demand huge resource, it might not converge toward a feasible solution. In Fig. 5, the results of mean square error for training set are presented to compare effects of number of hidden layers. On this occasion, the softplus activation function and Adam optimization were used; other conditions are same as the previous examples. We note that the case of two hidden layers, namely, (10–20–20–18) architecture, achieves the competitive convergence performance.

5 Conclusion

There are many deep learning techniques that are currently in development. However, the innovative methods have not been used to structural analysis research topics. This article introduced some deep learning techniques which can directly help guide structural engineers. We conducted experiments to compare the results of conditions using various activation functions and optimizers for the networks. For the 10-bar truss example, the softplus activation function and Adam optimization are effective in (10-20-18) architecture. Nevertheless, it depends on architectures or complexity of the examples, hence, the information can be extended to find more effective methods or conditions for the structures. After fixing the neural network structures using obtained weight function of each layer, we can predict the result of specific test sets. The main contribution of this paper is to present some methods for automatically leading to structural analysis results without any traditional programs.

Acknowledgements This research was supported by grants (NRF-2015R1C1A2A01055897, NRF-2015R1A2A1A01007535) from NRF (National Research Foundation of Korea) funded by MEST (Ministry of Education and Science Technology) of Korean government.

References

1. LeCun Y, Bengio Y, Hinton G (2015) Deep learning. *Nature* 521(7553):436–444
2. Hinton GE, Osindero S, Teh YW (2006) A fast learning algorithm for deep belief nets. *Neural Comput* 18(7):1527–1554
3. Nair V, Hinton GE (2010) Rectified linear units improve restricted Boltzmann machines. In: *Proceedings of the 27th international conference on machine learning (ICML-10)*. pp 807–814
4. Hinton GE, Srivastava N, Krizhevsky A, Sutskever I, Salakhutdinov RR (2012) Improving neural networks by preventing co-adaptation of feature detectors. [arXiv:1207.0580](https://arxiv.org/abs/1207.0580)
5. Adeli H (2001) Neural networks in civil engineering: 1989/2000. *Comput Aided Civ Infrastruct Eng* 16(2):126–142
6. Gupta T, Sharma RK (2011) Structural analysis and design of buildings using neural network: a review. *Int J Eng Manage Sci* 2(4):216–220
7. Haftka RT, Gürdal Z (1992) *Elements of structural optimization*, vol 3. Springer Science and Business Media
8. Dugas C, Bengio Y, Blisle F, Nadeau C, Garcia R (2001) Incorporating second-order functional knowledge for better option pricing. *Adv Neural Inf Process Syst* 472–478
9. Duchi J, Hazan E, Singer Y (2011) Adaptive subgradient methods for online learning and stochastic optimization. *J Mach Learn Res* 12:2121–2159
10. Zeiler MD (2012) ADADELTA: an adaptive learning rate method. [arXiv:1212.5701](https://arxiv.org/abs/1212.5701)
11. Tieleman T, Hinton G (2012) Lecture 6.5—RMSPprop, COURSERA: neural networks for machine learning. Technical report
12. Kingma D, Ba J (2014) Adam: a method for stochastic optimization. [arXiv:1412.6980](https://arxiv.org/abs/1412.6980)

DOF Condensation of Thick Curved Beam Element Formulated by Isogeometric Approach



Buntara S. Gan, Dinh-Kien Nguyen, Aylie Han
and Sofia W. Alisjahbana

Abstract The study of a thick in-plane curved beam is more complex than that of the straight beam because the structural deformations of the curved beam depend not only on the rotation and transverse displacement but also on the coupled tangential displacement caused by the curvature of the structure. The Isogeometric approach is a computational geometry based on a piecewise ratio function (Non-Uniform Rational B-Spline (NURBS)) used to represent the exact geometry. In the Isogeometric approach, the free curvature geometry of the beam element can be represented exactly. A thick two-node curved beam element can be developed by using the Isogeometric approach based on Timoshenko beam theory, which allows the transverse shear deformation and rotatory inertia effects. The natural shape of the beam curvature and the shape functions formulation of the element can be formulated by using the Isogeometric approach. However, in the Isogeometric approach, the number of equations will increase according to the number of degree of the polynomial and its control points. A novel technique is been proposed to condense the number of equations of the DOFs at control points so that it is equal to the standard two-node six DOFs beam element. This paper highlights the application of the NURBS for a curved Timoshenko beam element in the context of finite element analysis and proposes a new condensation method to eliminate the

B. S. Gan (✉)

Department of Architecture, College of Engineering, Nihon University,
Koriyama, Japan

e-mail: buntara@arch.ce.nihon-u.ac.jp

D.-K. Nguyen

Institute of Mechanics, Vietnam Academy of Science and Technology,
Hanoi, Vietnam

e-mail: ndkien@imech.vast.vn

A. Han

Department of Civil Engineering, Diponegoro University, Semarang, Indonesia

e-mail: hanaylie@hccnet.nl

S. W. Alisjahbana

Faculty of Engineering and Informatics, Bakrie University, Jakarta, Indonesia

e-mail: sofia.alisjahbana@bakrie.ac.id

© Springer Nature Singapore Pte Ltd. 2018

H. Nguyen-Xuan et al. (eds.), *Proceedings of the International Conference on Advances in Computational Mechanics 2017*, Lecture Notes in Mechanical Engineering, https://doi.org/10.1007/978-981-10-7149-2_37

drawbacks raised from the Isogeometric approach. Examples are given to verify the effectiveness of the condensation method in static and free vibration problems.

Keywords Thick curved beam • Isogeometric approach • Condensation
Finite element analysis

1 Introduction

For centuries in history, human being has been using the curved-like beams in sculptures, wheeled vehicles, buildings, bridges, and mechanical tools to obtain both combinations of strength and artistic aspects. Along with the rapid growth of the computing technologies, vast element models for the analyses of the thick curved beam have been proposed by many researchers. Yamada and Ezawa [1] have compiled a comprehensive study of literatures on the computation methods of the thick curved beam element. Ashwell and Sabir [2, 3], Babu and Prathap [4], and Stolarski and Chiang [5] have conducted studies to make a proper choice of element models for the analysis of the thick curved beam problems.

Recent progress in modeling and design is the integration of the CAD-based Isogeometric approach into the finite element method which has been brought up by several authors [6, 7]. The integration of the Isogeometric approach with the finite element method in the broad range of modeling contexts has become a trendy subject of numerous papers and many authors have devoted their works to it. Luu et al. [8] formulated the finite free-form Timoshenko curved beam element. Huynh et al. [9] analyzed the bending, buckling and free vibration of functionally graded curved beams with variable curvatures using Isogeometric approach. This paper implemented the Isogeometric approach in the finite element for solving the thick curved beam problems.

In the Isogeometric approach, the convergence is usually achieved by using some refinement strategies such as adaptive, h-, p-, and k-refinements [10] as the state of the art. We observed that most of the authors who use the Isogeometric approach, do not have many concerns regarding the increasing number of DOFs at the control points due to the refinements strategies adopted. Instead of using refinements strategies, this paper attempted to apply the substructuring method for reducing the DOF at the control points.

In the finite element analysis, substructuring method has been used to carry out condensation of complex model such as a complete airplanes, ships, or vehicles. The traditional static condensation and dynamic condensation is known to be effective in reducing the DOFs of a beam which has more than two nodes. The amounts of DOFs of the mid-nodes are “hidden” so that only the DOFs at both ends of the beam still retained [11–13]. Condensing numerous DOFs to the standard two-node six DOFs beam element has a lot of benefits for real practices. After the condensation, the DOFs can be plugged seamlessly into the existing beam finite element codes.

In this context, we introduce a combination of static and modified dynamic condensation methods which can reduce the DOF of the control points to the standard two-node six DOF thick curved beam element accurately. The validity of this new condensation technique is demonstrated. Various types of thick curved beam elements in static and free vibration problems are solved to show the robustness of the present method.

2 Governing Equations of Thick Beam Element

The horizontal (u_P) and vertical (v_P) displacements of an arbitrary point P at the beam cross section can be expressed as

$$u_P = u - r\theta - vd\varphi, \quad v_P = v - ud\varphi \quad (1)$$

where u , v , r , θ , and φ are the respective point P tangential displacement, radial displacement, radial coordinate, rotation of cross section, and curve angle.

From the theory of elasticity, we can obtain the strain components as

$$\varepsilon_s = \frac{du}{ds} - r \frac{d\theta}{ds} + \frac{v}{R(s)}, \quad \gamma_{sr} = \frac{dv}{ds} - \theta + \frac{u}{R(s)} \quad (2)$$

where s is the tangential coordinate, and $1/R(s)$ is the curvature of the beam element.

The stress components, then take the form

$$\sigma_s = E\varepsilon_s = E \left(\frac{du}{ds} - r \frac{d\theta}{ds} + \frac{v}{R(s)} \right), \quad \tau_{rs} = G\gamma_{rs} = G \left(\frac{dv}{ds} - \theta + \frac{u}{R(s)} \right) \quad (3)$$

where G is the elastic shear modulus of the beam.

The equation of motion is then derived via Hamilton's principle as follow

$$\delta H = \int_{t_1}^{t_2} (\delta S_E - \delta K_E - \delta W_E) dt = 0 \quad (4)$$

where δH , δS_E , δK_E and δW_E are the variation of total energy, strain energy, kinetic energy, and external work of the beam, respectively.

3 NURBS for Thick Beam Element

The geometry of the center line of the thick curved beam elements is constructed by the x and y coordinates on a plane, by using the NURBS curvature functions. The path of the curve is measured as the local coordinate ξ . In the Isogeometric

approach, the coordinate of the geometry of the beam can be represented by using the NURBS curves as follow,

$$x = \sum_{i=0}^n S_{i,p}(\xi)CP_{xi}, \quad y = \sum_{i=0}^n S_{i,p}(\xi)CP_{yi}, \quad -1 \leq \xi \leq 1 \quad (5)$$

where

$$S_{i,p}(\xi) = \frac{N_{i,p}(\xi)w_i}{\sum_{j=0}^n N_{j,p}(\xi)w_j}, \quad w_i > 0$$

where $N_{i,p}(\xi)$, w_i , $S_{i,p}(\xi)$, and $CP_{x/y-i}$ are the i th of the p th-order B-Spline basis functions, weight, the NURBS basis functions, and the associated control points in x and y coordinates, respectively.

The displacements (u , v) and rotation (θ) of any arbitrary point along the beam can be calculated from the general nodal displacements of the beam element by using the NURBS basis functions which are given by

$$u = \sum_{i=0}^{nu} S_{i,pu}(\xi)u_i; \quad v = \sum_{i=0}^{nv} S_{i,pv}(\xi)v_i; \quad \theta = \sum_{i=0}^{n\theta} S_{i,p\theta}(\xi)\theta_i \quad (6)$$

It is worth to be noted that in Isogeometric approach, the nodal displacements and rotations are treated independently by using each NURBS basis functions. Thus, they are not coupled in the formulation.

Depending on the degree of polynomial and knot vector (Ξ) being selected, we need to prepare the corresponding number of control points (CP) required. The increasing of control points being used to construct the NURBS curve will increase the number DOFs of the beam as illustrated in Fig. 1. The figure shows the illustration of a three general degree-of-freedom (horizontal, vertical, and rotation) at each control point between both end nodes of the beam.

The undamped equilibrium equation is obtained by substituting Eq. (6) into the variational equations of Eq. (4), which results in

$$\mathbf{Kd} - \mathbf{M}\ddot{\mathbf{d}} - \mathbf{f} = \mathbf{0} \quad (7)$$

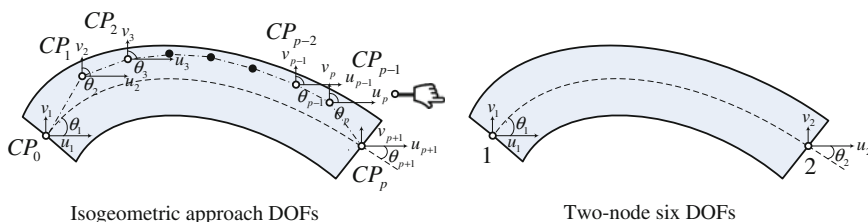


Fig. 1 Schematic illustration of the DOF condensation of thick curved beam element

where \mathbf{K} , \mathbf{M} , \mathbf{f} , \mathbf{d} , and $\ddot{\mathbf{d}}$ are the stiffness matrix, mass matrix, loading vector, general displacement vector, and general acceleration vector, respectively.

The stiffness matrix is given by

$$\mathbf{K} = \begin{bmatrix} \mathbf{k}_{11} & \mathbf{k}_{12} & \mathbf{k}_{13} \\ \mathbf{k}_{21} & \mathbf{k}_{22} & \mathbf{k}_{23} \\ \mathbf{k}_{31} & \mathbf{k}_{32} & \mathbf{k}_{33} \end{bmatrix}, \quad \text{where}$$

$$\mathbf{k}_{11} = \sum_{j=1}^{ng_u} \left[\begin{array}{l} \frac{EA}{J_j^2} \left(\sum_{i=0}^{nu} S_{i,pu}^1(\xi_j) \right)^T \left(\sum_{i=0}^{nu} S_{i,pu}^1(\xi_j) \right) \\ + \frac{\kappa GA}{R(\xi_j)^2} \left(\sum_{i=0}^{nv} S_{i,pv}(\xi_j) \right)^T \left(\sum_{i=0}^{nv} S_{i,pv}(\xi_j) \right) \end{array} \right] Det(J_j)w_j$$

$$\mathbf{k}_{12} = \mathbf{k}_{21} = \sum_{j=1}^{ng_u} \left[\begin{array}{l} \frac{EA}{R(\xi_j) J_j} \left(\sum_{i=0}^{nu} S_{i,pu}^1(\xi_j) \right)^T \left(\sum_{i=0}^{nv} S_{i,pv}(\xi_j) \right) \\ - \frac{\kappa GA}{R(\xi_j) J_j} \left(\sum_{i=0}^{nu} S_{i,pu}(\xi_j) \right)^T \left(\sum_{i=0}^{nv} S_{i,pv}^1(\xi_j) \right) \end{array} \right] Det(J_j)w_j$$

$$\mathbf{k}_{13} = \mathbf{k}_{31} = \sum_{j=1}^{ng_u} \left[\frac{\kappa GA}{R(\xi_j)} \left(\sum_{i=0}^{nu} S_{i,pu}(\xi_j) \right)^T \left(\sum_{i=0}^{n\theta} S_{i,p\theta}(\xi_j) \right) \right] Det(J_j)w_j \quad (8)$$

$$\mathbf{k}_{22} = \sum_{j=1}^{ng_v} \left[\begin{array}{l} \frac{\kappa GA}{J_j^2} \left(\sum_{i=0}^{nv} S_{i,pv}^1(\xi_j) \right)^T \left(\sum_{i=0}^{nv} S_{i,pv}^1(\xi_j) \right) \\ + \frac{EA}{R(\xi_j)^2} \left(\sum_{i=0}^{nv} S_{i,pv}(\xi_j) \right)^T \left(\sum_{i=0}^{nv} S_{i,pv}(\xi_j) \right) \end{array} \right] Det(J_j)w_j$$

$$\mathbf{k}_{23} = \mathbf{k}_{32} = \sum_{j=1}^{ng_v} \left[\frac{\kappa GA}{J_j} \left(\sum_{i=0}^{nv} S_{i,pv}^1(\xi_j) \right)^T \left(\sum_{i=0}^{n\theta} S_{i,p\theta}(\xi_j) \right) \right] Det(J_j)w_j$$

$$\mathbf{k}_{33} = \sum_{j=1}^{ng_\theta} \left[\begin{array}{l} \frac{EI}{J_j^2} \left(\sum_{i=0}^{n\theta} S_{i,p\theta}^1(\xi_j) \right)^T \left(\sum_{i=0}^{n\theta} S_{i,p\theta}^1(\xi_j) \right) \\ + \kappa GA \left(\sum_{i=0}^{n\theta} S_{i,p\theta}(\xi_j) \right)^T \left(\sum_{i=0}^{n\theta} S_{i,p\theta}(\xi_j) \right) \end{array} \right] Det(J_j)w_j$$

where the term $S_{i,pv}^1$ shows the first derivative of the NURBS basis function $S_{i,pv}$ with respect to the ξ coordinate. The parameters $C(\xi_j)$, J_i and $1/R(\xi_j)$ are the respective length of segment, Jacobian operator, and the curvature of the i th NURBS basis functions at the quadrature point j which are given by,

$$C(\xi) = \int_{\xi_t = -1}^{\xi_t = \xi} \sqrt{\left(\frac{dx}{d\xi_t}\right)^2 + \left(\frac{dy}{d\xi_t}\right)^2} d\xi_t$$

$$J = \frac{dC(\xi)}{d\xi} = \sqrt{\left(\frac{dx}{d\xi}\right)^2 + \left(\frac{dy}{d\xi}\right)^2}; \quad R(\xi) = \frac{\left|\frac{dx}{d\xi} \frac{d^2y}{d\xi^2} - \frac{dy}{d\xi} \frac{d^2x}{d\xi^2}\right|}{J^3}$$

The mass matrix is given by

$$\mathbf{M} = \begin{bmatrix} \mathbf{m}_{11} & 0 & 0 \\ 0 & \mathbf{m}_{22} & 0 \\ 0 & 0 & \mathbf{m}_{33} \end{bmatrix}, \text{ where}$$

$$\mathbf{m}_{11} = \sum_{j=1}^{ngu} \left[\rho A \left(\sum_{i=0}^{nu} S_{i,pu}(\xi_j) \right)^T \left(\sum_{i=0}^{nu} S_{i,pu}(\xi_j) \right) \right] Det(J_j) \quad (9)$$

$$\mathbf{m}_{22} = \sum_{j=1}^{ngv} \left[\rho A \left(\sum_{i=0}^{nv} S_{i,pv}(\xi_j) \right)^T \left(\sum_{i=0}^{nv} S_{i,pv}(\xi_j) \right) \right] Det(J_j) w_j$$

$$\mathbf{m}_{33} = \sum_{j=1}^{ng\theta} \left[\rho I \left(\sum_{i=0}^{n\theta} S_{i,p\theta}(\xi_j) \right)^T \left(\sum_{i=0}^{n\theta} S_{i,p\theta}(\xi_j) \right) \right] Det(J_j) w_j$$

The loading vector is given by

$$\mathbf{f} = \begin{Bmatrix} \mathbf{P} \\ \mathbf{Q} \\ \mathbf{M} \end{Bmatrix} + \left\{ \begin{array}{l} \sum_{j=1}^{ngu} \left[\left(\sum_{i=0}^{nu} S_{i,pu}(\xi_j) \right) p \right] Det(J_j) w_j \\ \sum_{j=1}^{ngv} \left[\left(\sum_{i=0}^{nv} S_{i,pv}(\xi_j) \right) q \right] Det(J_j) w_j \\ \sum_{j=1}^{ng\theta} \left[\left(\sum_{i=0}^{n\theta} S_{i,p\theta}(\xi_j) \right) m \right] Det(J_j) w_j \end{array} \right\} \quad (10)$$

4 DOF Condensation

The traditional static condensation and dynamic condensation are known to be effective in reducing the DOFs of a beam which has more than two nodes. The amounts of DOFs of the mid-nodes are “hidden” so that only the DOFs at both ends of the beam still retained [11–13].

Although the importance of condensation is not significant in beam problems because the amounts of DOFs are not vast, condensing DOFs to the standard two-node six DOFs beam element (Fig. 1) will bring benefits in real practices. First,

the introduction of NURBS into the design practice will hinder some design practitioners that are not familiar with the new concept. Second, the condensed NURBS element codes can be integrated seamlessly into the existing beam finite element codes.

In the conventional static and dynamic condensation methods, the beam element matrix is usually partitioned into two sub-matrices consisted of retained and condensed parts. Therefore, there are only two simultaneous equations to solve that is a linear relationship of two unknowns. From where the condensed part will be eliminated from the equations, hence the modified retained part is used to solve the beam problems. This concept is very suitable for the NURBS functions where the DOFs of the mid-nodes are increased when using higher degree of the polynomial.

4.1 Proposed Condensation Method

In present proposed condensation method, the element matrices are breakdown to three sub-matrix simultaneous equations, where the mid-nodes DOFs are subjected to condensation. The conventional dynamic condensation is then extended further by taking the twice derivatives to the free vibration equilibrium equations respected to time t . Then, we can obtain a relationship between the stiffness matrix \mathbf{k} and the acceleration vector $\ddot{\mathbf{d}}$.

4.2 Static Condensation

A static equilibrium of the beam element can be expressed by three simultaneous equations which is represented in the following matrix form,

$$\begin{bmatrix} \mathbf{k}_{11} & \mathbf{k}_{12} & \mathbf{k}_{13} \\ \mathbf{k}_{21} & \mathbf{k}_{22} & \mathbf{k}_{23} \\ \mathbf{k}_{31} & \mathbf{k}_{32} & \mathbf{k}_{33} \end{bmatrix} \begin{Bmatrix} \mathbf{d}_1 \\ \mathbf{d}_2 \\ \mathbf{d}_3 \end{Bmatrix} = \begin{Bmatrix} \mathbf{f}_1 \\ \mathbf{f}_2 \\ \mathbf{f}_3 \end{Bmatrix} \quad (11)$$

From Eq. (11), the second equation is solved for \mathbf{d}_2 as

$$\mathbf{d}_2 = \mathbf{k}_{22}^{-1}(\mathbf{f}_2 - \mathbf{k}_{21}\mathbf{d}_1 - \mathbf{k}_{23}\mathbf{d}_3) \quad (12)$$

Substituting Eq. (12) into the first and third simultaneous equations results in,

$$\begin{bmatrix} \bar{\mathbf{k}}_{11} & \bar{\mathbf{k}}_{13} \\ \bar{\mathbf{k}}_{31} & \bar{\mathbf{k}}_{33} \end{bmatrix} \begin{Bmatrix} \mathbf{d}_1 \\ \mathbf{d}_3 \end{Bmatrix} = \begin{Bmatrix} \bar{\mathbf{f}}_1 \\ \bar{\mathbf{f}}_3 \end{Bmatrix} \quad (13)$$

where

$$\begin{aligned}\bar{\mathbf{k}}_{11} &= \mathbf{k}_{11} - \mathbf{k}_{12}\mathbf{k}_{22}^{-1}\mathbf{k}_{21}; & \bar{\mathbf{k}}_{13} &= \mathbf{k}_{13} - \mathbf{k}_{12}\mathbf{k}_{22}^{-1}\mathbf{k}_{23}; & \bar{\mathbf{f}}_1 &= \mathbf{f}_1 - \mathbf{k}_{12}\mathbf{k}_{22}^{-1}\mathbf{f}_2 \\ \bar{\mathbf{k}}_{31} &= \mathbf{k}_{31} - \mathbf{k}_{32}\mathbf{k}_{22}^{-1}\mathbf{k}_{21}; & \bar{\mathbf{k}}_{33} &= \mathbf{k}_{33} - \mathbf{k}_{32}\mathbf{k}_{22}^{-1}\mathbf{k}_{23}; & \bar{\mathbf{f}}_3 &= \mathbf{f}_3 - \mathbf{k}_{32}\mathbf{k}_{22}^{-1}\mathbf{f}_2.\end{aligned}$$

4.3 Modified Dynamic Condensation

Similarly, an undamped dynamic equilibrium of the beam element can be expressed by three simultaneous equations which is represented in the following matrix form,

$$\begin{bmatrix} \mathbf{k}_{11} & \mathbf{k}_{12} & \mathbf{k}_{13} \\ \mathbf{k}_{21} & \mathbf{k}_{22} & \mathbf{k}_{23} \\ \mathbf{k}_{31} & \mathbf{k}_{32} & \mathbf{k}_{33} \end{bmatrix} \begin{Bmatrix} \mathbf{d}_1 \\ \mathbf{d}_2 \\ \mathbf{d}_3 \end{Bmatrix} + \begin{bmatrix} \mathbf{m}_{11} & \mathbf{m}_{12} & \mathbf{m}_{13} \\ \mathbf{m}_{21} & \mathbf{m}_{22} & \mathbf{m}_{23} \\ \mathbf{m}_{31} & \mathbf{m}_{32} & \mathbf{m}_{33} \end{bmatrix} \begin{Bmatrix} \ddot{\mathbf{d}}_1 \\ \ddot{\mathbf{d}}_2 \\ \ddot{\mathbf{d}}_3 \end{Bmatrix} = \begin{Bmatrix} \mathbf{0} \\ \mathbf{0} \\ \mathbf{0} \end{Bmatrix} \quad (14)$$

To relate the displacement \mathbf{d} and acceleration $\ddot{\mathbf{d}}$, Eq. (14) is derived two times with respect to time t , which results in,

$$\begin{bmatrix} \mathbf{k}_{11} & \mathbf{k}_{12} & \mathbf{k}_{13} \\ \mathbf{k}_{21} & \mathbf{k}_{22} & \mathbf{k}_{23} \\ \mathbf{k}_{31} & \mathbf{k}_{32} & \mathbf{k}_{33} \end{bmatrix} \begin{Bmatrix} \ddot{\mathbf{d}}_1 \\ \ddot{\mathbf{d}}_2 \\ \ddot{\mathbf{d}}_3 \end{Bmatrix} + \begin{bmatrix} \mathbf{m}_{11} & \mathbf{m}_{12} & \mathbf{m}_{13} \\ \mathbf{m}_{21} & \mathbf{m}_{22} & \mathbf{m}_{23} \\ \mathbf{m}_{31} & \mathbf{m}_{32} & \mathbf{m}_{33} \end{bmatrix} \begin{Bmatrix} \ddot{\ddot{\mathbf{d}}}_1 \\ \ddot{\ddot{\mathbf{d}}}_2 \\ \ddot{\ddot{\mathbf{d}}}_3 \end{Bmatrix} = \begin{Bmatrix} \mathbf{0} \\ \mathbf{0} \\ \mathbf{0} \end{Bmatrix} \quad (15)$$

Neglecting the fourth-order derivative terms and solving for $\ddot{\mathbf{d}}$ from the second matrix equation yield to the following relationship,

$$\ddot{\mathbf{d}}_2 = \mathbf{k}_{22}^{-1}(-\mathbf{k}_{21}\ddot{\mathbf{d}}_1 - \mathbf{k}_{23}\ddot{\mathbf{d}}_3) \quad (16)$$

Substituting Eq. (16) into the second equation of Eq. (14) and solving for \mathbf{d}_2 result in

$$\mathbf{d}_2 = -\mathbf{k}_{22}^{-1}\mathbf{k}_{21}\mathbf{d}_1 - \mathbf{k}_{22}^{-1}\mathbf{k}_{23}\mathbf{d}_3 - \mathbf{k}_{22}^{-1}\bar{\mathbf{m}}_{21}\ddot{\mathbf{d}}_1 - \mathbf{k}_{22}^{-1}\bar{\mathbf{m}}_{23}\ddot{\mathbf{d}}_3 \quad (17)$$

Substituting back Eq. (17) into the first and third equations of Eq. (14) yields to the following condensed matrix equation,

$$\begin{bmatrix} \bar{\mathbf{k}}_{11} & \bar{\mathbf{k}}_{13} \\ \bar{\mathbf{k}}_{31} & \bar{\mathbf{k}}_{33} \end{bmatrix} \begin{Bmatrix} \mathbf{d}_1 \\ \mathbf{d}_3 \end{Bmatrix} + \begin{bmatrix} \bar{\mathbf{m}}_{11} & \bar{\mathbf{m}}_{13} \\ \bar{\mathbf{m}}_{31} & \bar{\mathbf{m}}_{33} \end{bmatrix} \begin{Bmatrix} \ddot{\mathbf{d}}_1 \\ \ddot{\mathbf{d}}_3 \end{Bmatrix} = \begin{Bmatrix} \mathbf{0} \\ \mathbf{0} \end{Bmatrix} \quad (18)$$

where,

$$\begin{aligned} \bar{\mathbf{m}}_{11} &= \mathbf{m}_{11} - \mathbf{m}_{12}\mathbf{k}_{22}^{-1}\mathbf{k}_{21} - \mathbf{k}_{12}\mathbf{k}_{22}^{-1}\bar{\mathbf{m}}_{21}; & \bar{\mathbf{m}}_{13} &= \mathbf{m}_{13} - \mathbf{m}_{12}\mathbf{k}_{22}^{-1}\mathbf{k}_{23} - \mathbf{k}_{12}\mathbf{k}_{22}^{-1}\bar{\mathbf{m}}_{23} \\ \bar{\mathbf{m}}_{31} &= \mathbf{m}_{31} - \mathbf{m}_{32}\mathbf{k}_{22}^{-1}\mathbf{k}_{21} - \mathbf{k}_{32}\mathbf{k}_{22}^{-1}\bar{\mathbf{m}}_{21}; & \bar{\mathbf{m}}_{33} &= \mathbf{m}_{33} - \mathbf{m}_{32}\mathbf{k}_{22}^{-1}\mathbf{k}_{23} - \mathbf{k}_{32}\mathbf{k}_{22}^{-1}\bar{\mathbf{m}}_{23} \\ \bar{\mathbf{m}}_{21} &= \mathbf{m}_{21} - \mathbf{m}_{22}\mathbf{k}_{22}^{-1}\mathbf{k}_{21}; & \bar{\mathbf{m}}_{23} &= \mathbf{m}_{23} - \mathbf{m}_{22}\mathbf{k}_{22}^{-1}\mathbf{k}_{23}. \end{aligned}$$

5 Numerical Examples

In this section, illustrative examples are presented to demonstrate the validity and novelty of the proposed condensation method. Comparison of the present numerical results with other works is shown.

5.1 Circular Arch Beam Example

Consider 90° circular thick arch beams with different supports and material properties as shown in Fig. 2. For solving free vibration problems, we need to divide the beam element into sub-elements to get several mode shapes and frequencies (ω) of the vibration.

The degree of polynomial used for the NURBS functions is $p_u = 3$, $p_v = 3$, and $p_\theta = 3$. The constructed twelve DOFs are condensed to the six DOFs beam element. Four Gauss integration points are required to integrate the mass matrix.

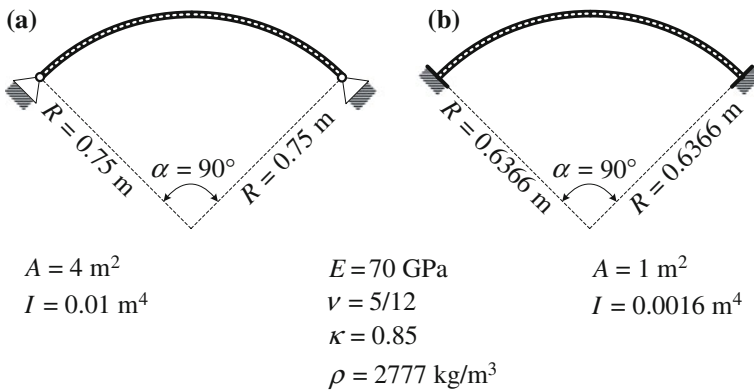


Fig. 2 Circular arch beam examples: a Pinned–pinned; b Clamped–clamped supports

Table 1 Non-dimensional frequencies of a pinned–pinned circular curved beam

Mode <i>i</i>	Non-dimensional frequency $\lambda_i = \omega_i(\alpha R)^2 \sqrt{\frac{\rho A}{EI}}$			
	Eisenberger and Efraim [14]	Veletsos and Austin [15]	Sedaghati and Esmailzadeh [16]	Present
1	29.280	29.61	29.306	29.280
2	33.305	33.01	33.243	33.306
3	67.124	67.24	67.123	67.131
4	79.971	79.60	79.950	79.977
5	107.851	107.7	107.844	107.880
6	143.618	144.5	143.679	143.670
7	156.666	155.2	156.629	156.720
8	190.477	191.3	190.596	190.635
9	225.361	223.7	225.349	225.460
10	234.524	235.3	234.809	234.825

Table 2 Non-dimensional frequencies of a clamped–clamped circular curved beam

Mode <i>i</i>	Non-dimensional frequency $\lambda_i = \omega_i(\alpha R)^2 \sqrt{\frac{\rho A}{EI}}$			
	Eisenberger and Efraim [14]	Veletsos and Austin [15]	Sedaghati and Esmailzadeh [16]	Present
1	36.703	36.81	36.657	36.703
2	42.264	42.44	42.289	42.264
3	82.233	82.50	82.228	82.243
4	84.491	84.30	84.471	84.495
5	122.305	122.5	122.298	122.341
6	154.945	155.1	154.998	154.990
7	168.203	167.7	168.174	168.271
8	204.472	–	204.599	204.642
9	238.992	–	238.973	239.088
10	249.011	249.6	249.320	249.326

In Fig. 2, a pinned–pinned circular arch beam and a clamped–clamped circular arch beam are considered. The results of the first ten non-dimensionalized λ_i are listed in Tables 1 and 2, respectively. We can observe the very close agreements between the present approach by using proposed condensation method and those reported in the references.

5.2 Typical Curved Beam Example

Consider typical parabolic with pinned–pinned supports, elliptic with pinned–clamped and sinusoidal with clamped–clamped curved beams and their material properties as shown in Fig. 3 for free vibration examples.

The non-dimensional equation of the typical curved beams is given as

Parabolic curve $y = h(1 + \xi)(1 - \xi)$, $-1 \leq \xi \leq +1$
 where, $\xi = 2x/L - 1$

Elliptical curve $y = b_2 \sqrt{1 - \left\{ 1 - \frac{[\xi + 1 - b_1 \cos(a)]}{4b_1} \right\}^2} - b_2 \sin(a)$, $-1 \leq \xi \leq +1$
 where, $\xi = (2x/L - 1)$, $b_1 = \varepsilon + 0.5$, $a = \pi - \cos^{-1}(0.5/b_1)$, $b_2 = h/[1 - \sin(a)]$

Sinusoidal curve $y = h - c_1 + c_1 \sin\left(c_2 \left[\frac{\xi + 1}{4}\right] + \varepsilon c_2\right)$, $-1 \leq \xi \leq +1$
 where, $\xi = (2x/L - 1)$, $c_2 = \frac{\pi}{1 + 2\varepsilon}$, $c_1 = \frac{h}{[1 - \sin(\varepsilon c_2)]}$

The beam is divided into twenty sub-elements to get several mode shapes and frequencies (ω) of the vibration. Four Gauss integration points are necessary to integrate the mass matrix. The degree of polynomial used in the NURBS functions is $p_u = 3$, $p_v = 3$, and $p_\theta = 3$. The constructed twelve DOFs are condensed to the six DOFs beam element. The arch rise to the span length ratio is defined by $f = h/L$. The slenderness ratio is defined as $S_R = L/\sqrt{A/I}$.

For the parabolic curved beam free vibration analysis, $f = 0.3$, $S_R = 75$, and $\kappa G/E = 0.3$ are defined. For the elliptic curved beam free vibration analysis, $f = 0.2$, $S_R = 50$, $\varepsilon = 0.5$, and $\kappa G/E = 0.3$ are defined. For the elliptic curved beam

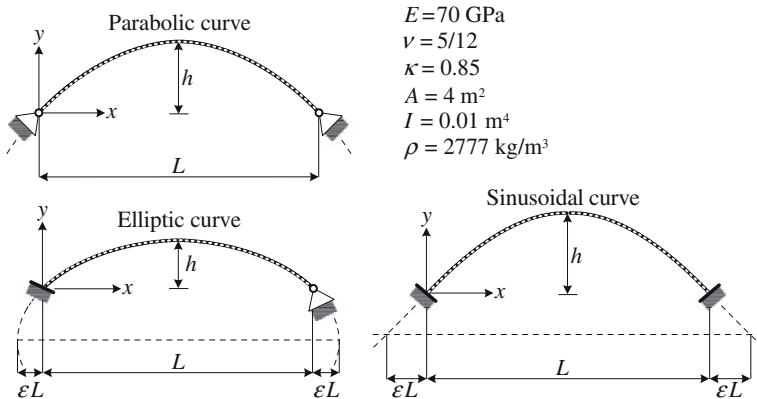


Fig. 3 Typical curved beam examples: parabolic, elliptic, and sinusoid

Table 3 Non-dimensional frequencies of parabolic curved beam

Mode i	λ_i			
	Veletsos and Austin [15]	Yang et al. [16]	Luu et al. [8]	Present
1	21.83	21.759	21.759	21.758
2	56.00	55.493	55.493	55.501
3	102.3	100.701	100.701	100.788
4	113.4	113.302	113.302	113.414
5	–	–	157.168	157.539
6	–	–	208.969	209.360
7	–	–	224.470	225.469
8	–	–	294.916	297.429
9	–	–	375.630	380.817
10	–	–	411.114	413.366

Table 4 Non-dimensional frequencies of elliptic curved beam

Mode i	λ_i			
	Veletsos and Austin [15]	Yang et al. [16]	Luu et al. [8]	Present
1	35.25	34.892	34.900	34.896
2	57.11	56.766	56.778	56.780
3	83.00	81.420	81.513	81.498
4	128.2	124.288	124.898	124.565
5	–	–	155.629	155.720
6	–	–	189.888	187.349
7	–	–	264.924	254.530
8	–	–	291.999	292.712
9	–	–	364.547	328.191
10	–	–	432.310	404.479

free vibration analysis, $f = 0.1$, $S_R = 100$, $\varepsilon = 0.5$, and $\kappa G/E = 0.3$ are defined. The results of the first ten non-dimensionalized λ_i are listed in Tables 3, 4, and 5, respectively. As an overall remark, we can observe very close agreements between the present proposed method and those reported in the references.

5.3 Free Curved Beam Example

Consider a spring-shape curved cantilever beam subjected to horizontal loading $P = 15$ kN at the free end of the structure (Fig. 4). The material properties of the beam are shown in the figure. The static and free vibration analyses were conducted.

Table 5 Non-dimensional frequencies of sinusoidal curved beam

Mode i	λ_i		
	Veletsos and Austin [15]	Yang et al. [16]	Present
1	56.30	56.083	56.088
2	66.14	66.047	66.068
3	114.3	113.406	113.464
4	181.7	179.264	179.490
5	–	–	264.874
6	–	–	311.424
7	–	–	363.879
8	–	–	473.102
9	–	–	595.667
10	–	–	619.024

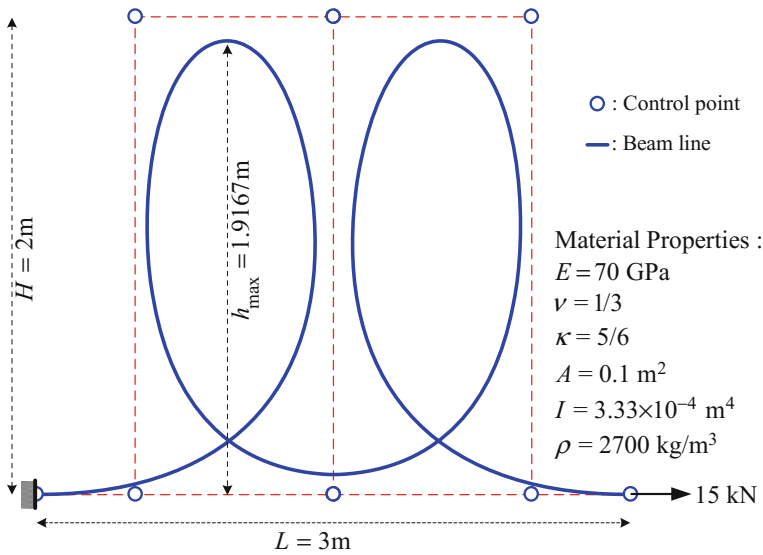


Fig. 4 Spring-shape curved cantilever beam example

Four Gauss integration points are used to integrate the stiffness and mass matrices. The degree of polynomial used in the NURBS functions is $p_u = 3$, $p_v = 3$, and $p_\theta = 3$. The beam is modeled by using only one element. The constructed twelve DOFs are condensed to the six DOFs beam element. The knot vector is given as $\Xi = [-1 \ -1 \ -1 \ -1 \ 1 \ 1 \ 1 \ 1]$.

The control points and their corresponding weight are given in Table 6. The results of computed vertical displacement and the first three natural frequencies are given in Table 7. The present numerical results solutions are provided as a benchmark for future reference solution, since no other reported works available for comparison.

Table 6 Input data for the spring-shape curved cantilever beam

CPx_i	CPy_i	w_i
0.00	0.00	1
1.50	0.00	1
1.50	2.00	1
0.50	2.00	1
0.50	0.00	1
2.50	0.00	1
2.50	2.00	1
1.50	2.00	1
1.50	0.00	1
3.00	0.00	1

Table 7 Result of static and free vibration analyses of a spring-shape curved beam

Static analysis	Horizontal displacement at the free end $u = 1.0554$ mm, Vertical displacement at the free end $v = -0.2877$ mm, Rotational displacement at the free end $\theta = 0.0011$ radians		
Free vibration mode i	1	2	3
ω_i (rad/s)	234.6	1186.9	5438.2
Eigenvector	0.9774	0.2785	-0.0494
	-0.2422	-0.7568	0.1717
	1.0000	1.0000	-1.0000

6 Concluding Remarks

A thick curved beam element condensed DOF formulation is developed by using the Isogeometric approach and used to evaluate the vibration behaviors of various curved beam structures. The efficiency and accuracy of the proposed modified condensation method are verified by numerical examples. From the numerical results, the following concluding remarks can be drawn,

- a. The present proposed condensation method yields to accurate natural frequencies of the thick curved beam elements, accordingly perfect stiffness and mass matrices of a two-node six-DOF beam element. Therefore, the condensed matrices can be used for dynamic problems absolutely.
- b. No refinement strategies in the Isogeometric approach are necessary to be adopted. The conventional sub-division element procedure can be applied, since the beam DOF has been condensed to the two-node six-DOF beam element.
- c. The “hidden” DOF after being condensed can be retrieved back completely by using Eq. (12) for the static problems and Eqs. (16) and (17) for the free vibration and dynamic problems.

- d. This new condensation technique is bridging the curves created by CAD, then solved by the state-of-the-art finite element analysis software, because the condensed Isogeometric DOFs beam element yields to the conventional two-node six-DOF beam element library.

References

1. Yamada Y, Ezawa Y (1977) On curved finite elements for the analysis of curved beams. *Int J Numer Method Eng* 11(11):1635–1651
2. Ashwell DG, Sabir AB (1971) Further studies in the application of curved finite elements to circular arches. *Int J Mech Sci* 13(6):507–517
3. Ashwell DG, Sabir AB (1971) Limitations of certain curved finite elements when applied to arches. *Int J Mech Sci* 13(2):133–139
4. Babu CR, Prathap G (1986) A linear thick curved beam element. *Int J Numer Method Eng* 23(7):1313–1328
5. Stolarski H, Chiang MM (1989) The mode-decomposition, C^0 formulation of curved, two-dimensional structural elements. *Int J Numer Method Eng* 28(1):145–154
6. Hughes TJR, Cottrell JA, Bazilevs Y (2005) Isogeometric analysis: CAD, finite elements, NURBS, exact geometry and mesh refinement. *Comput Methods Appl Mech Eng* 194(39–41):4135–4195
7. Cottrell JA, Bazilevs Y, Hughes TJR (2009) Isogeometric analysis: towards integration of CAD and FEA. Wiley, New York
8. Luu AT, Kim NI, Lee J (2015) Isogeometric vibration analysis of free-form Timoshenko curved beams. *Meccanica* 50(1):169–187
9. Huynh TA, Luu AT, Lee J (2017) Bending, buckling and free vibration analyses of functionally graded curved beams with variable curvatures using isogeometric approach. *Meccanica* 1–20
10. Vuong AV (2012) Adaptive hierarchical isogeometric finite element methods. Springer Spektrum, Germany
11. Bathe KJ (1982) Finite element procedures in engineering analysis. Prentice-Hall, New Jersey
12. Cook RD (1981) Concepts and applications of finite element analysis, 2nd edn. Wiley, New York
13. Hart GC, Wong K (2000) Structural dynamics for structural engineers. Wiley, New York
14. Eisenberger M, Efraim E (2001) In-plane vibrations of shear deformable curved. *Int J Numer Method Eng* 52(11):1221–1234
15. Veletsos W, Austin W (1973) Free vibration of arches flexible in shear. *J Eng Mech Div* 99(4):735–753
16. Yang F, Sedaghati R, Esmailzadeh E (2008) Free in-plane vibration of general curved beams using finite element method. *J Sound Vib* 318(4–5):850–867

Optimal Airplanes' Paths For Minimizing Airline Company's Cost Subjected to Passengers' Demand: Formulation and Verification



V. H. Nguyen, M. Ehsaei, J. Creedon, G. Sanjabi and D. T. Nguyen

Abstract A new formulation which addresses a new/specific/practical problem facing the airline industry, such as “Optimal Airplanes’ Paths For Minimizing Airline Company’s Cost Subjected to Passengers’ Demand”, is presented in this paper. If the flying paths are explicitly used as unknown variables, then one has to deal with a very large number of unknown variables. To avoid such bottlenecks, our proposed approach consists of finding which city-pair flight legs are flown and how many times the optimum flight paths will use these flight legs. With this obtained information, the optimum flight paths can be obtained by a post-processing phase! The mentioned “Optimal Airplanes’ Paths” problem can be formulated as a **nonlinear integer programming (NLIP)** problem. Numerical results are also included in this paper to validate the proposed NLIP formulation.

Keywords Optimal airplanes’ paths • Nonlinear integer programming (NLIP) Formulation • Passengers’ demands • Minimizing airline company’s cost

V. H. Nguyen (✉)

Faculty of Engineering, Vietnamese German University,
Ho Chi Minh City, Vietnam
e-mail: vnguy025@odu.edu

M. Ehsaei · G. Sanjabi · D. T. Nguyen
Department of Civil and Environmental Engineering (CEE),
Old Dominion University, Norfolk, USA
e-mail: mehsa001@odu.edu

G. Sanjabi
e-mail: gbakh001@odu.edu

D. T. Nguyen
e-mail: dnguyen@odu.edu

J. Creedon
Department of Mechanical and Aerospace Engineering (MAE),
Old Dominion University, Norfolk, USA
e-mail: JCreedon@odu.edu

© Springer Nature Singapore Pte Ltd. 2018

H. Nguyen-Xuan et al. (eds.), *Proceedings of the International Conference on Advances in Computational Mechanics 2017*, Lecture Notes in Mechanical Engineering, https://doi.org/10.1007/978-981-10-7149-2_38

1 Introduction

Air transportation plays an essential role in transportation and economic development. Despite the steadily growing in passenger demands, airline companies have been faced with thin profit margins, especially after the United States Airline Deregulation Act in 1978 which allows airlines to select their network, choose which markets (origin and destination pairs) to serve, determine the frequency of service to provide in each market as well as their fare [1]. To be profitable in the extremely competitive environment, airline companies have to efficiently develop their operations planning which includes schedule design, fleet assignment, aircraft routing, and crew scheduling. In schedule design, the target is to generate an efficient schedule which offers the high potential revenue. To do that, the airline company must determine their set of flights, which should be operated, the specific origin and destination cities as well as departure and arrival times. The schedule design is based on the market demand forecasts, available aircraft operating characteristics, available workforce, regulations, and the behavior of competing airlines. Following the schedule design, the fleet assignment is the next step to determine right fleet to support the scheduled flights. Based on fleet capabilities, availabilities, operational costs, and potential revenues, aircraft is assigned to flight segments in a schedule to optimize some objective function and meet various operation constraints [2]. Then, the aircraft routing assigns each individual aircraft within each fleet to flight legs to maximize the revenue or minimizing operating cost while satisfying maintenance requirements. Finally, the crew scheduling problem, like aircraft routing, is normally performed after the fleet assignment process to construct a minimum cost set of crew rotations or pairings [3]. In recognition of the importance of airline operation planning to minimize the operation cost and maximizing profits, many researchers in both air industry and academics have already been seriously working on this problem.

Abara [2] formulated an integer linear programming model to solve the fleet assignment problem. Sherali et al. [4] presented a tutorial on the basic and enhanced models and approaches that have been developed for the fleet assignment problem. Bartholomew-Biggs et al. [5] described a global optimization problem which arises in the calculation of flight paths and discussed the performance of a number of recently proposed solution algorithms when applied to some demonstration examples. Papadakos [6] presented several integrated models for the optimization of airline scheduling and solved them by applying an enhanced Benders decomposition method combined with accelerated column generation. Belanger et al. [7] proposed a nonlinear integer model for the periodic fleet assignment problem with time windows in which departure times are also determined and developed new branch-and-bound strategies which are embedded in their branch-and-price solution strategy.

In this paper, different issues and practical constraints that need to be addressed by airline companies are discussed and formulated as a nonlinear integer programming (NLIP) problem. Section 2 presents a new integrated model for the optimization of airline scheduling. Each airline company has the set of potential markets

(origin-destination pairs of cities) to operate. The target of this section is to assign aircrafts to serve for one or several markets and choose their original departure city as well as optimal route [8, 9]. While determining which aircraft departs in which city and serves which market, the flight path of the aircraft is also optimized to minimize the total operation cost and to satisfy the customer demand and airline constraints (e.g. aircraft need to return to the city that it departed at the end of day to be maintained overnight and to repeat its same operations on the next day). In Sect. 3, definitions of some known (and unknown) variables are given. A mixed NLIP mathematical formulation with the objective and constraint functions is explained in Sect. 4. Due to the complexity of the investigated problem [10, 11, 12], a small-scale example is used in Sect. 5. This example validates our proposed formulation to make sure that the proposed formulation provides the correct optimal solution or at least the near-optimal solution. This can be further verified by “eyes-observation” solution. Conclusion and future works are summarized in Sect. 6.

2 Problem Definition

Specifically, this investigation will address the issues that commonly faced by the commercial aircraft industry, which can be described as following:

“Knowing a particular airline company’s total number of available airplanes and the passengers’ travel demand matrix” from certain *i*th original cities to other certain *j*th destination cities, how can we make decisions on:

- Which aircraft (AC) and what type of AC should be originally parked at which city airport?
- How to compute the optimal (or near-optimal) path for each aircraft for minimizing the airline company’s cost, subject to realistic constraints, such as satisfying passengers’ travel demand matrix, and every AC must return to the same city airport (where it was originally parked) within 24 h, so that the AC operations can be repeated on the next day?

To facilitate the discussion (formulation and solution) for the remaining of this study, the following specific data/example is used (say, for 6 city-airports), as shown in Table 1:

Table 1 Passengers’ demand matrix data

	C1 = ATL	C2 = ORD	C3 = LAX	C4 = DFW	C5 = PHX	C6 = DEN
C1 = ATL	0	600 persons	800	0	700 persons	0
C2 = ORD	600	0	0	1100	0	800
C3 = LAX	800	0	0	0	600	1200
C4 = DFW	0	1100	0	0	900	0
C5 = PHX	700	0	600	900	0	800
C6 = DEN	0	800	1200	0	800	0

Table 2 Distances between six cities (miles) [13]

	C1 = ATL	C2 = ORD	C3 = LAX	C4 = DFW	C5 = PHX	C6 = DEN
C1 = ATL	0	607	1944	731	1586	1198
C2 = ORD		0	1743	803	1439	887
C3 = LAX			0	1234	370	862
C4 = DFW				0	867	642
C5 = PHX					0	602
C6 = DEN						0

Table 3 Aircraft attributes/features

	Number of seats (two classes)	Empty weight (lb)	Maximum take-off weight (lb)	Maximum range of operation (miles)	Fuel can take (gallons)	Fuel cost (US \$)	Fuel consumption per flying hour (kg/hr)	Average Burn rate (\$ per hr)	Cruise velocity (mile/hr) (km/hr)
Boeing 747 (747-400)	524	372,250	870,000	8,350	53,765	59,142	14400	13,380	570 (920)

To simplify the discussion, we assume all cities’ airports have the earliest flight started at 6:00 am (say, Eastern Time). The distances between each city-pair are known, as shown in Table 2.

We assume two types of AC are available: AC type I and AC type II. Each of these AC types has known attributes, such as:

- (a) Number of passenger seats available
- (b) Maximum operational range (the longest distance it can fly without refueling gasoline)
- (c) Cost/hour to operate, AC operation cost \$/hr per AC
- (d) Cost per day to pay off the purchase price
- (e) Cruise velocity (in miles/hours)
- (f) Kg fuel/hour used while in flight
- (g) It is assumed that the turn-around (waiting) time at any airport and for any AC type is 1 h (time between arriving and leaving on a subsequent flight).

For the above-given data, shown in Tables 1 and 2 (including the known attributes for two different AC types), one would like to find the “optimal airline paths for minimizing airline company’s cost subject to passengers’ (and other realistic) constraints”. Although both formulation and numerical examples are discussed/presented in this study, the focus of this research has been placed on the formulation itself.

3 Definitions of Notations and Variables Used in this Study

The following variables and remarks are defined/provided:

- (a) \mathbf{M} is the set of markets—origin–destination pairs of cities which have passenger's demands larger than zero.
- (b) \mathbf{J} is set of flight legs. A flight leg is basically a direct flight from one city to another city.
- (c) Remarks:
 - The # legs are always greater than (or equal to) the # markets.
 - For a 6 city-airports Point-to-Point network example (Table 2) with every city connected to all remaining cities (hence number of legs = 30), we may have only 18 markets (Table 1), and 18 origin–destination pairs of cities have the number of passenger's demand larger than zero.
- (d) N_m is the number of passengers in market m
 - For example: City 1 \rightarrow city 3 is a market, and $N_m = 800$ passengers' demand to travel from city 1 to city 3 [see Table 1].
- (e) $C_{in}(c)$ is the set of flight legs go into city c .
- (f) $C_{out}(c)$ is the set of flight legs go out from city c
 - $c = 1, \dots$, number of cities.
- (g) Ca_i is the capacity of aircraft i .
- (h) **Integer variable** X_{ij} represents AC # i , flies over leg # j . Value for $X_{ij} = 0, 1, 2, 3$, etc.
 - 0 means AC # i does not fly over leg # j
 - 1 means AC # i does fly over leg # j ONCE
 - ...
 - 5 means AC # i does fly over leg # j FIVE TIMES
- (i) R_i is the range of aircraft i .
- (j) L_j is distance of leg j .
- (k) **Integer variable** Pa_{mij} : the number of passengers from market m using the aircraft i on flight leg j , the value of $Pa_{mij} \in [0; N_m]$.
- (l) Y_{ip} is a binary variable, has the value 1 if aircraft i originally parks at city p and 0 otherwise.
- (m) **Integer variable** Z_{ijk} shows the number of passengers using the aircraft i over leg j at time flight number k , the value of $Z_{ijk} \in [0; Ca_i]$. $K \in [0; K]$, K is the maximum number of times AC i flies over leg j .

4 Objective and Constraint Functions

The **objective function** is to minimize the total operation cost, which can be defined as:

$$\text{Total operation cost} = \sum_{i=1}^I [\sum_{j=1}^J \{X_{ij} * (\text{time} = \frac{\text{length of leg } j}{\text{velocity of AC } i}) * (AC_i \text{ operation cost/hour} + \text{fuel consumption cost/hour})\} + \text{waiting cost at each stop} * (\{\sum_{j=1}^J X_{ij}\} - 1)].$$

There are several constraints that need to be properly applied on the proposed formulation, which are defined in the next sections.

4.1 Constraints to Show the Relationship Between Cities and Flight Legs

$$\sum_{j \in C_{in}(c)} X_{ij} = \sum_{j \in C_{out}(c)} X_{ij} \tag{1}$$

Constraint (1) is the balance constraint:

The number of flight legs into city number c equals to the number of flight legs out from city number c.

where

- $i = 1, \dots, I$: AC number
- j is the flight leg j
- c represents the city # (could be any number between 1 – # cities) (Fig. 1).

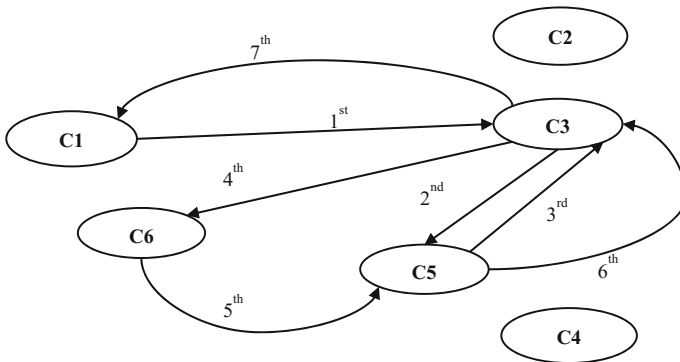


Fig. 1 A possible optimal flight path for AC i , originally parked at airport-city 1

4.2 Constraint for the Total Time Flights

$$\sum_{j=1}^J \left(X_{ij} * \left[\frac{\text{length of leg } j}{\text{velocity of } i} \right] \right) + \left(\left[\sum_{j=1}^J X_{ij} \right] - 1 \right) * \text{waiting_time_at_airport} \leq 24 \text{ hrs} \tag{2}$$

Notes: X_{ij} = # of times AC # i flies over leg # j , and X_{ij} may have any of the following values

$$X_{ij} = 0, 1, 2, 3, 4, 5$$

4.3 Constraint for Customers' Travel Demand

$$Pa_{mij} \leq N_m \quad \forall m \in M; j = 1, \dots, J; i = 1, \dots, I \tag{3}$$

Constraint 3 presents that the number of passengers in market “ m ”, using AC “ i ”, and flies over leg “ j ” must smaller or equal the total number of passenger in market m . In the definition, market m is an origin–destination pair (O-D).

4.4 Constraints on Number of Passengers Flying into (Out from) the Original City

$$\sum_{j \in C_{out}(O)} \sum_{i=1}^I Pa_{mij} = N_m \tag{4}$$

$$\sum_{j \in C_{in}(O)} \sum_{i=1}^I Pa_{mij} = 0 \tag{5}$$

Constraints (4) and (5) state that the total number of customer in an individual market m using the aircrafts that fly on the legs out from O, the original city of market m , must equal the total customer demand of market m . Because the customers in market m want to fly from the city O to the city D, the total number of customers in an individual market m using the aircrafts that fly on the legs into O must be equal 0.

4.5 Constraints on Number of Passengers Flying into (Out from) the Destination City

$$\sum_{j \in C_{in}(D)} \sum_{i=1}^I Pa_{mij} = N_m \tag{6}$$

$$\sum_{j \in C_{out}(D)} \sum_{i=1}^I Pa_{mij} = 0 \tag{7}$$

Constraints (6) and (7) show that the total number of customers in individual market m using the aircrafts that fly on the legs into D , the destination city of market m , must be equal the total customer demand of market m . When the customers in market m reach the destination (D), they do not need to use the services anymore; therefore, the total number of customers in individual market m using the aircrafts that fly on the legs out from D must be equal 0.

Figure 2 is an example to illustrate how to apply Eqs. (4)–(7):

N_m = Passengers in market “ m ” = say, 700 passengers corresponding to O-D pair of cities $c_1 - c_5$

O = city 1; D = city 5; c = any “intermediate” city, EXCEPT city 1 & city

$$\sum_{j \in C_{out}(C1)} \sum_{i=1}^I Pa_{mij} = N_m \Rightarrow Pa_{m11} + Pa_{m32} + Pa_{m24} + Pa_{m55} = 700$$

$$\sum_{j \in C_{in}(C1)} \sum_{i=1}^I Pa_{mij} = 0 \Rightarrow Pa_{m36} = 0$$

$\sum_{j \in C_{in}(C5)} \sum_{i=1}^I Pa_{mij} |_{X_{ij} \neq 0} = N_m =$ say 700 passengers arrive “in” to destination city

$\sum_{j \in C_{out}(C5)} \sum_{i=1}^I Pa_{mij} = 0 \Rightarrow$ no passenger comes “out” after all 700 passengers arrived at their destination city!

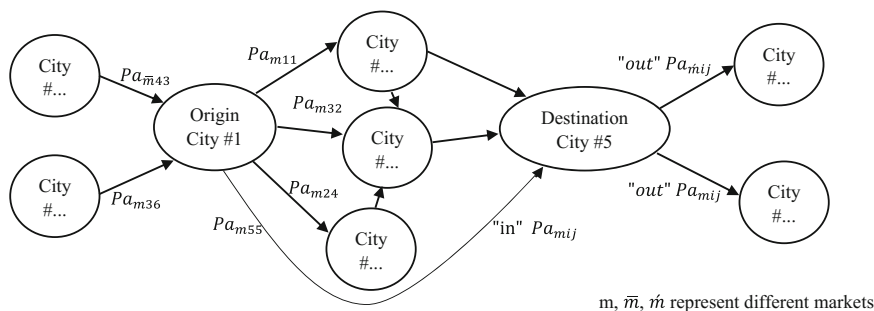


Fig. 2 Number of passengers flying into (out from) the original city

4.6 Constraints on Number of Passengers Flying into (Out from) the "Intermediate" City

$$\sum_{j \in C_{out}(c)} \sum_{i=1}^I Pa_{mij} = \sum_{j \in C_{in}(c)} \sum_{i=1}^I Pa_{mij} \tag{8}$$

$$\sum_{j \in C_{out}(c)} \sum_{i=1}^I Pa_{mij} \leq N_m \tag{9}$$

where c are "intermediate" cities, the cities that are different with origin-destination (O-D) of market m .

Constraint (8) is the customer balance constraint for intermediate cities c : The total of customers in market m using the aircrafts that fly on the legs out from c must be equal the total of customers in market m using the aircrafts that fly on the legs into c .

Constraint (9) states that the total number of passengers in market m using ACs that fly over legs that are out from c must be smaller or equal the total number of passenger demand of market m .

In Fig. 3, we define:

c = any "intermediate" city, EXCEPT the original and destination cities (corresponding to the market m).

Using a 6 city-airports example, assuming a particular market " m " (that has, say 800 passengers who want to fly from city # 1 to city # 3). Thus, in this case, original city = city # 1 and destination city = city # 3. Also assuming a portion of the (optimum) fly path is C1-C5-C4-C3 (where C1-C5 = say, leg # $j = 1$; C5-C4 = say, leg # $j = 7$; C6-C5 = say, leg # $j = 6$; etc.). Thus, $c = C5, C4$. Then, at city " c " = C5, we may have:

$Pa(m, i = 2, j = 7) =$ say, 800 passengers "out" from city # 5, and

$Pa(m, i = 1, j = 1) = 500 + Pa(m, i = 3, j = 6) = 300$ passengers "in" to city # 5.

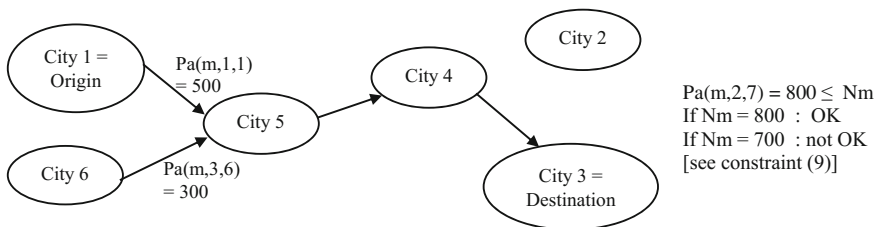


Fig. 3 Number of passengers flying into (out from) an "intermediate" city

4.7 Constraint on Aircraft Capacity

$$\sum_{m=1}^M Pa_{mij} \leq X_{ij} * Ca_i \quad i = 1, \dots, I; j = 1, \dots, J \tag{10}$$

The number of passengers from ALL markets, on AC # *i*, flights over leg # *j* (could be multiple times over leg # *j*) should not exceed (capacity of AC # *i*)*(# times fly over leg # *j*).

As an example, AC # *i*'s capacity = 300 passenger seats, flying over leg # *j* THREE times [hence $X(i, j) = 3$] from all markets M. There were 100, 300, and 250 passengers fly over leg # *j* in the first, second, and third time, respectively. Then, the above (capacity) constraint is (CORRECTLY) satisfied, because: $(100 + 300 + 250 = 650) \leq (3 * 300 = 900)$

However, if there were 100, 350, and 250 passengers fly over leg # *j* in the 1-st, 2-nd, and 3-rd time, respectively. Then, the above (capacity) constraint is (WRONGLY) satisfied, because $(100 + 350 + 250 = 700) \leq (3 * 300 = 900)$, because for the 2-nd time fly over leg # *j*, there were 350 passengers, which is EXCEEDING the AC's seat capacity of 300 passengers. This (potential) problem can be resolved by introducing the new variables Z_{ijk} and the associated constraints # 15-# 17!

4.8 Constraints to Show the Relationship Between Variables X_{ij} and Pa_{mij}

$$(1 - X_{ij}) * Pa_{mij} \leq 0 \tag{11}$$

This constraint indicates that:

If aircraft *i* flies over leg *j* or $X_{ij} \neq 0$, then the number of passengers of market *m* using the aircraft *i* on flight leg *j*, Pa_{mij} , can be 0 or non-zero. In other words, aircraft *i* may or may not carry customers of market *m* when it flies over flight leg *j*.

If $X_{ij} = 0$, then the above constraint becomes $Pa_{mij} \leq 0$; since Pa_{mij} cannot be NEGATIVE, therefore, $Pa_{mij} = 0$ or if aircraft *i* not fly over leg *j*, it obviously cannot carry any customer of market *m* on flight leg *j*.

Say $N_m = 800 = N_1 = N_2$

If $X_{ij} \neq 0 \Leftrightarrow$ AC *i* flies over leg *j* $\Rightarrow (1 - X_{ij}) * Pa_{mij} \leq 0$ will be always satisfied

$(1 - X_{11})(Pa_{211} = 800) \leq 0$ will be satisfied

If $X_{ij} = 0$ and $Pa_{211} = 800 \Rightarrow (1 - X_{ij}) * Pa_{mij} \text{ XXXX } 0 \Rightarrow$ This case makes no sense. Thus, this constraint prevents this nonsense case from happening.

$(1 - 0)(Pa_{211} = 800) \leq 0$ will *not* be satisfied.

4.9 Constraint on Aircraft Operational Range

$$X_{ij} * (L_j - R_i) \leq 0 \tag{12}$$

The above linear constraint indicates that:

- If $X_{ij} = 0$ (the AC # i not flying on leg # j), then the range (R_i) of AC_i can be either larger than or smaller than the distance of leg # j .
- If $X_{ij} \neq 0$ (such as $X_{ij} = 1, 2, 3, 4,$ or 5), then the AC # i flying on leg # j , then the range (R_i) of AC_i must be larger than the distance of leg # j .

4.10 Constraint on Variable Y_{ip}

$$Y_{ip} \left(1 - \sum_{j \in C_{out}(\text{originally parking city})} X_{ij} \right) \leq 0 \tag{13}$$

Constraint (13) shows the relationship between original parking city and its out-going flight legs: The above constraint is always satisfied when $Y_{ip} = 0 = AC\ i$, originally not parked at city # p (see Fig. 4).

If $Y_{ip} = 1$, then the above constraint is only true when:

- $\sum_{j \in C_{out}(\text{originally parking city})} X_{ij} \geq 1$
- $X_{11} + X_{12} + X_{13} \geq 1$
- $(0 \rightarrow 5) + (0 \rightarrow 5) + (0 \rightarrow 5) \geq 1$

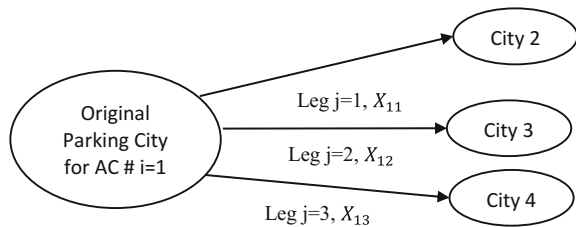
This constraint prevents nonsense case where $X_{11} = X_{12} = X_{13} = 0$

Notes:

- $X_{ij} = \#$ times AC # “ i ” flies over leg “ j ”
- $= 1, 2, 3, 4, 5$; if flying over leg “ j ” once (or more time)
- $= 0$; if not flying over leg “ j ” (Fig. 4).

$$\sum_{p=1}^{\# \text{ of cities}} Y_{ip} = 1 \tag{14}$$

Fig. 4 Relationship between original parking city and its out-going flight legs



Constraint (14) show that each aircraft originally can only park at one city. The above constraint will make sure that the same AC # i cannot originally park in more than one cities!

4.11 Constraints Show the Relationship Between Variables Z and Ca

$$Z_{ijk} \leq Ca_i \quad (15)$$

Constraint (15) makes sure that the total number of passengers using the aircraft i fly over leg j at time flight number k always is smaller than or equal to that capacity of aircraft i .

4.12 Constraints Show the Relationship Between Variables Pa and Z

$$\sum_{m=1}^M Pa_{mij} = \sum_{k=1}^K Z_{ijk} \quad (16)$$

The total number of customers from all markets using aircraft i that fly over leg j always equal the number of passenger that the aircraft i carries over leg j at total time flight number k

For example:

Aircraft i fly over legs j and carries 200 customers of market m , 300 customers of market m' , and 500 customers of market \bar{m} : $Pa_{mij} = 200$, $Pa_{m'ij} = 300$, $Pa_{\bar{m}ij} = 500$

Aircraft i flies over leg j three times ($k = 1, 2, 3$): Z_{ij1} , Z_{ij2} , Z_{ij3}

Then Eq. (16) is written as $Pa_{mij} + Pa_{m'ij} + Pa_{\bar{m}ij} = Z_{ij1} + Z_{ij2} + Z_{ij3}$

4.13 Constraint to Show the Relationship Between Variables Z and X

$$(k - X_{ij}) * Z_{ijk} \leq 0 \quad k = 1, 2, \dots, K \quad (17)$$

If $X_{ij} = 0$, then $Z_{ijk} = 0$, or if aircraft i does not fly over leg j , the number of passenger using the aircraft i over leg j at time flight number k ($k = 1, 2, \dots, K$) obviously must be 0.

If $X_{ij} \neq 0$ & $k \leq X_{ij}$, Z_{ijk} can be 0 or $\neq 0$, and if aircraft i flies over leg j and the time flight number k smaller than the total number time AC i flies over leg j , then the number of passengers using the aircraft i over leg j at time flight number k ($k = 1, 2, \dots, K$) can be larger than or equal to 0.

If $X_{ij} \neq 0$ && $k > X_{ij}$, $Z_{ijk} = 0$ or if aircraft i fly over leg j , at the time flight number k that is bigger than the total number time AC i fly over leg j , the number of passenger using the aircraft i equal to 0.

5 Numerical Verification by Numerical Example

The formulation presented in Sect. 4 can be solved by general purpose NLP (nonlinear programming) algorithm/solver, with INTEGER variables. Since MATLAB built-in functions for handling NLIP problems are not robust/reliable, a differential evolution (DE) optimization code has also been developed based on the presented formulation. It should be noted here that NLIP solvers are not the focus of this study. To verify the correctness of the formulation that has been explained in the previews sections, a small example whose optimal solution can be obtained by “eye-observation” can also be found by the DE code.

Problem statement is presented in Table 4. Even though this example has only three cities and six legs, it contains 63 variables and 193 constraints. Only one aircraft has been considered for this example. To be realistic, Boeing 747 (747–400) data has been used for this example. The related data is shown in Table 3.

It has been estimated that the total cost, which includes fuel cost, operating cost, crew cost, and other expenses, for Boeing 747 (747–400) [14] is 25,500 dollars per hour of operation, which is considered in the following examples. Also, it has been assumed that the waiting cost of the aircraft in each transshipment city is \$30.

5.1 Numerical Example/Solution Obtained by “Eye-Observation”

A *feasible* solution by “eye-observation” is shown in Fig. 5.

Notation: (f) Market m means f-th flight, transport customers of market m

Table 4 Example input data

Origin	Destination	Leg #	Distance (miles)	Market ID	Demand
1	2	1	300	1	300
2	1	2	300	2	150
2	3	3	500	3	300
3	2	4	500	4	400
3	1	5	450	5	200
1	3	6	450	6	300

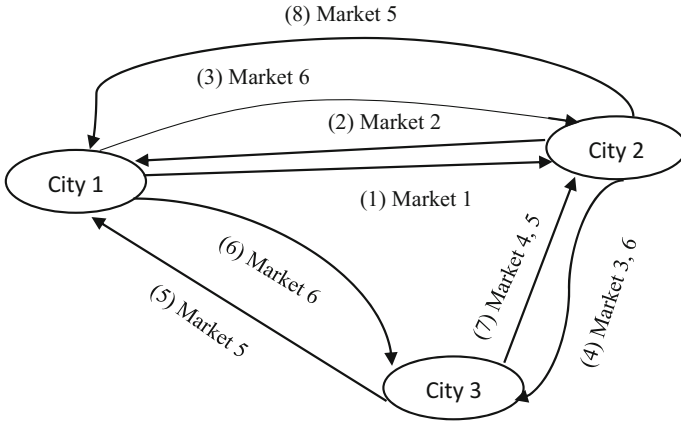


Fig. 5 Feasible solution by eye-observation

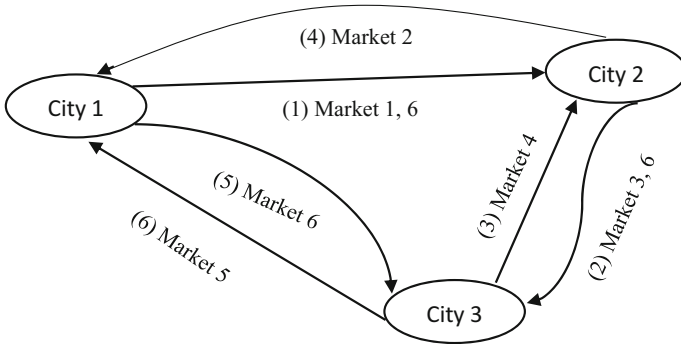


Fig. 6 Optimum solution by eye-observation

$Y_{11} = 1 = \text{Air - Craft 1 originally parked in Airport - City 1}, \quad Y_{12} = 0, \quad Y_{13} = 0$
 $Pa_{111} = 300, \quad Pa_{212} = 150, \quad Pa_{611} = 200, \quad Pa_{313} = 300$
 $Pa_{515} = 100, \quad Pa_{616} = 100, \quad Pa_{414} = 400, \quad Pa_{514} = 100$
 $Pa_{512} = 100, \quad Pa_{613} = 200$
 $X_{11} = 2, \quad X_{12} = 2, \quad X_{13} = 1, \quad X_{14} = 1, \quad X_{15} = 1, \quad X_{16} = 1$

Objective function = Cost = \$138,894.21

An *optimal* feasible solution by “eye-observation” is shown in Fig. 6.

$Y_{11} = 1, \quad Y_{12} = 0, \quad Y_{13} = 0,$
 $Pa_{111} = 300, \quad Pa_{611} = 200, \quad Pa_{613} = 200, \quad Pa_{313} = 300$
 $Pa_{414} = 400, \quad Pa_{212} = 150, \quad Pa_{616} = 100, \quad Pa_{515} = 200$
 $X_{11} = 1, \quad X_{12} = 1, \quad X_{13} = 1, \quad X_{14} = 1, \quad X_{15} = 1, \quad X_{16} = 1$

Optimal Objective function = Cost = \$111,992.11

5.2 Numerical Example/Solution Obtained by the DE Code

The authors have initially attempted to solve the formulated NLIP problem, using MATLAB built-in NLIP solvers. These initial efforts have failed, due to the un-reliable (non-robust) MATLAB NLIP solvers. Using the authors' self-developed DE optimizer, with "randomly" generated the initial populations, **the same optimal objective function (as compared to optimal solution by "eye-observation") can be observed in all four computer runs**, as shown below:

1st Computer Run

Objective function = 1.1199e + 05

$$\begin{aligned} Pa_{111} &= 296, & Pa_{114} &= 4, & Pa_{116} &= 4 \\ Pa_{212} &= 119, & Pa_{213} &= 31, & Pa_{215} &= 31 \\ Pa_{313} &= 300, & Pa_{414} &= 400 \\ Pa_{512} &= 58, & Pa_{514} &= 58, & Pa_{515} &= 142 \\ Pa_{611} &= 3, & Pa_{613} &= 3, & Pa_{616} &= 297, \\ X_{11} &= 1, & X_{12} &= 1, & X_{13} &= 1, & X_{14} &= 1, & X_{15} &= 1, & X_{16} &= 1, \\ Y_{11} &= 1 \\ Z_{111} &= 299, & Z_{121} &= 177, & Z_{131} &= 334, & Z_{141} &= 462, & Z_{151} &= 173, & Z_{161} &= 301 \end{aligned}$$

2nd Computer Run

Objective function = 1.1199e + 05

$$\begin{aligned} Pa_{111} &= 227, & Pa_{114} &= 73, & Pa_{116} &= 73 \\ Pa_{212} &= 120, & Pa_{213} &= 30, & Pa_{215} &= 30, \\ Pa_{312} &= 25, & Pa_{313} &= 275, & Pa_{316} &= 25, \\ Pa_{411} &= 88, & Pa_{414} &= 312, & Pa_{415} &= 88 \\ Pa_{515} &= 200, & Pa_{616} &= 300 \\ X_{11} &= 1, & X_{12} &= 1, & X_{13} &= 1, & X_{14} &= 1, & X_{15} &= 1, & X_{16} &= 1, \\ Y_{11} &= 1 \\ Z_{111} &= 315, & Z_{121} &= 145, & Z_{131} &= 305, & Z_{141} &= 385, & Z_{151} &= 318, & Z_{161} &= 398 \end{aligned}$$

3rd Computer Run

Objective function = 1.1199e + 05

$$\begin{aligned} Pa_{111} &= 300, & Pa_{212} &= 150, & Pa_{313} &= 300 \\ Pa_{414} &= 400, & Pa_{515} &= 200 \\ Pa_{611} &= 200, & Pa_{613} &= 200, & Pa_{616} &= 100 \\ X_{11} &= 1, & X_{12} &= 1, & X_{13} &= 1, & X_{14} &= 1, & X_{15} &= 1, & X_{16} &= 1, \\ Y_{11} &= 1 \\ Z_{111} &= 500, & Z_{121} &= 150, & Z_{131} &= 500, & Z_{141} &= 400, & Z_{151} &= 200, & Z_{161} &= 100 \end{aligned}$$

4th Computer Run

Objective function = 1.1199e + 05

$$\begin{aligned}
Pa_{111} &= 300, Pa_{212} = 150, Pa_{313} = 300, \\
Pa_{414} &= 400, Pa_{515} = 200, Pa_{616} = 300 \\
X_{11} &= 1, X_{12} = 1, X_{13} = 1, X_{14} = 1, X_{15} = 1, X_{16} = 1, \\
Y_{13} &= 1 \\
Z_{111} &= 300, Z_{121} = 150, Z_{131} = 300, Z_{141} = 400, Z_{151} = 200, Z_{161} = 300
\end{aligned}$$

6 Conclusion and Future Works

In this paper, we have investigated and built a new integrated model for the optimization of airline scheduling which includes aircraft assignment and optimal aircraft's path to minimize the total operation cost. The main contribution of this paper is the development of a mathematical formulation for effective modeling of airplane's optimal path/scheduling. A comparison of optimal results obtained by "eyes-observation" and DE programming based on a case study indicates that our mathematical model provides an efficient solution for airline scheduling problem.

Further research work is needed to apply this approach to large-scale airline scheduling applications. It can include the development of algorithms for the efficient solution of difficult mixed integer nonlinear programming (MINLP) model and increasing its application to more challenging airline scheduling problems.

Acknowledgements Partially financial support provided in this work through the ODU-RF project #845700-009 is acknowledged.

References

1. Bae K-H (2010) Integrated airline operations: schedule design, fleet assignment, aircraft routing, and crew scheduling. PhD Dissertation, Virginia Polytechnic Institute and State University
2. Abara J (1989) Applying integer linear programming to the fleet assignment problem. *Interfaces* 19(4):20–28
3. Bazargan M (2011) Airline operations and scheduling, 2nd edn. Ashgate
4. Sherali HD, Bish EK, Zhu X (2006) Airline fleet assignment concepts, models, and algorithms. *Eur J Oper Res* 172(1):1–30
5. Bartholomew-Biggs M, Parkhurst S, Wilson S (2003) Global optimization approaches to an aircraft routing problem. *Eur J Oper Res* 146:417–431
6. Papadakos N (2009) Integrated airlines scheduling. *Comput Oper Res* 36(1):176–195
7. Belanger N, Desaulniers G, Soumis F, Desrosiers J, Lavigne J (2006) Periodic airline fleet assignment with time windows, spacing constraints, and time dependent revenues. *Eur J Oper Res* 175(3):1754–1766
8. Erdmann A, Nolte A, Noltemeier A, Schrader R (2001) Modeling and solving an airline schedule generation problem. *Ann Oper Res* 107:117–142
9. Desaulniers G, Desrosiers J, Dumas Y, Solomon M, Soumis F (1997) Daily aircraft routing and scheduling. *Manag Sci* 43:841–855

10. Gao C (2007) Airline integrated planning and operations. PhD Dissertation, Georgia Institute of Technology, Atlanta, GA
11. Barnhart C, Lu F, Shenoi R (1998) Integrated airline schedule planning. Operations research in the airline industry. Kluwer, Boston, pp 384–403
12. Ioachim I, Desrosiers J, Soumis F, Belanger N (1999) Fleet assignments and routing with schedule synchronization. Eur J Oper Res 119:75–90
13. <http://www.airmilescalculator.com>
14. https://en.wikipedia.org/wiki/Boeing_747-400

A New Beam Theory Considering Horizontal Shear Strain



T. Vu-Thanh

Abstract Methods of setting up and solving problems of flexural members, considering the horizontal shear strain, have been studied since the 1970s but there has not been any complete theory. When considering the influence of horizontal shear strain, with the horizontal shear strain approaching zero (when shear elastic modulus $G \rightarrow \infty$ or the ratio h/l is very small), the presented solutions do not converge to the case of zero horizontal shear strain, due to the *shear locking* phenomenon. Many authors have conducted studies to overcome this problem. Although they have achieved acceptable solutions, theoretical mistakes are unavoidable. In this article, the author will present a new method, in which the displacement and shear force functions are considered as functions that need to be determined to set up a new Beam Theory Considering Horizontal Shear Strain. To develop beam problems based on the Method of Gauss's Principle of Least Constraint, the author uses the calculus of variations and partial integral to establish two differential equations to determine two unknown functions and beams' boundary conditions. The beam theory (not considering the horizontal shear strain) is a separated condition of this theory. Using this theory in calculating beams and frames does not encounter *shear locking* phenomenon. The author will present equations of elastic line; analytic formulas determining deflection, angle of rotation, moment and shear force of beams, with different supports and static loads. When considering horizontal shear strain, changes occur in both the displacement and internal forces of beams and frames. However, while the displacement increases considerably, the redistribution of internal forces is quite insignificant.

Keywords Shear strain • Timoshenko beam • Shear locking
Gauss's principle of least constraint • Variational calculus

T. Vu-Thanh (✉)

Hanoi Architectural University, Hanoi, Vietnam
e-mail: vuthanhthuy.hau@gmail.com

© Springer Nature Singapore Pte Ltd. 2018

H. Nguyen-Xuan et al. (eds.), *Proceedings of the International Conference on Advances in Computational Mechanics 2017*, Lecture Notes in Mechanical Engineering, https://doi.org/10.1007/978-981-10-7149-2_39

579

1 Current Methods Considering Shear Strain

The Euler-Bernoulli Beam Theory is satisfied when the height/span ratio is negligible ($\frac{h}{l} \leq \frac{1}{8} \div \frac{1}{10}$). Recently, with the increasing popularity of structures with high shear deformation such as deep beams and transfer beams in high-rise buildings, foundation beams, short cantilevers, structures with suddenly changed cross-section and concentrated forces, taking horizontal shear strain into account becomes necessary.

Timoshenko is the first to present the idea of considering the horizontal shear strain by considering the shear angle caused by the shear force Q placed at the beam or plate axis. According to Timoshenko, the shear force Q causes shearing at the cross section of the beam or plate, making the cross section no longer perpendicular to the beam axis. This shear angle is calculated as:

$$\gamma = k \frac{Q}{GA} \quad (1)$$

In formula (1):

Q is the shear force at the section being considered;

A is the cross-sectional area of the beam or plate;

G is the elastic shear modulus, $G = \frac{E}{2(1+\mu)}$;

M is Poisson's ratio;

k is the shear stress concentration factor, considering the non-uniform distribution of cross-sectional shear stress with non-negligible shear strain (*Timoshenko shear coefficient*). The factor K is determined based on the principle of energy balance [1, 2]. $k = 1.2$ in beams with solid rectangular cross section, and $k = 1.11$ in beams with solid circular cross section.

Under this condition, the displacement of flexural structures depends on two factors: flexural strain due to moment and shear strain due to shear force:

$$\frac{dy}{dx} = \beta + \gamma \quad (2)$$

In which:

y is displacement function;

β is angle of rotation due to moment.

From expression (2), there are three quantities needed to be determined: y , β , γ . Hence, we need to choose two from these three quantities to be independent variable.

After Timoshenko, many studies started to focus on analyzing flexural structures with considerable shear strain. Today's common theories of analyzing flexural

beams with considerable shear strain are based on Timoshenko’s theory, using the unknowns y and β as variables [1, 3–7]. These studies also assume that the continuity conditions are the conditions of displacement y and rotational angle β .

When considering shear strain, moment and shear force in flexural beams are determined by the following formula (Zienkiewicz and Taylor [7]):

$$\left. \begin{aligned} M_z &= -\frac{Eh^3}{12} \cdot \frac{d\beta}{dx} & (a) \\ Q_y &= k \cdot Gh \left(-\beta + \frac{dy}{dx} \right) & (b) \end{aligned} \right\} \quad (3)$$

Based on the beam theories that consider shear strain, the authors of the Finite Element Methods used two independent elements to describe the flexural structure: one with only displacement and one with only angle of rotation due to moment, to set up and solve the beam problem with considerable horizontal shear strain [1, 3, 5–8].

However, when shear strain approaches zero, the beam theory considering the shear strain using two unknowns y and β did not converge to Euler-Bernoulli beam theory. When not considering the horizontal shear strain or when horizontal shear strain approaches 0, $\gamma = \left(-\beta + \frac{dy}{dx} \right) \rightarrow 0$, Q from Eq. (3b) is 0. Numerical solutions also encounter this phenomenon when horizontal shear strain are infinitesimal, corresponding to the ratio $h/l < 1/100$. This phenomenon is called *shear locking* [6, 8].

Since 1971, there have been many solutions proposed to counter *Shear locking* when analyzing the structures considering shear strain. These solutions usually fall into either of the two categories:

- Using incompatible (inappropriate) low-degree elements; using polynomials of low degree to present interpolation functions. The most common one is Hught element with interpolation functions being linear polynomials [3, 5, 6]. This is achieved by using reduced Gaussian integrals instead of the original [7].
- Adding secondary points and conditions of the shear force Q as well as static shear strain in a specific direction for specific cases. However, these conditions are complicated and lacking in generalization [7, 8] (Fig. 1).

When incompatible elements were introduced in 1971, mathematics *professor Strang* of MIT stated “*Two Wrongs Make a Right.*” The two theoretical crimes were that displacement compatibility was violated and the method was not verified with examples using non-rectangular elements [9].

A new method using horizontal displacement function which is polynomials of high degree and static shear force condition ($Q = const$) on the element length has been adopted by the finite element software SAP 2000 [8].

In recent studies considering shear strain, authors are still applying the aforementioned method to their work [10–14].

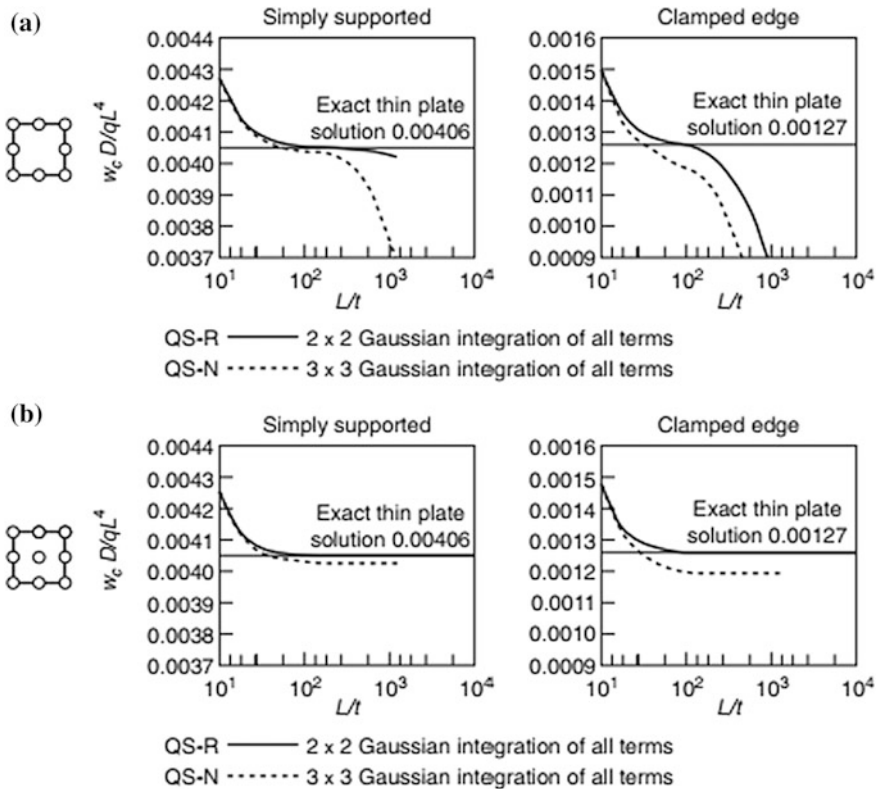


Fig. 1 Performance of **a** quadratic serendipity (QS) and **b** Lagrangian (QL) element with varying span-to-thickness L/t , ratios, uniform load on a square plate with 4×4 normal subdivision in a quarter. R is reduced 2×2 quadrature and N is normal 3×3 quadrature [7]

2 A New Beam Theory Considering Horizontal Shear Strain

2.1 Theoretical Base

According to the author, the fact that beam theories considering shear strain being used today do not converge to Euler-Bernoulli beam theory when shear strain approaches zero. It is due to the incorrect selection of unknowns (displacement y and angle of rotation β) when constructing the problem. Such condition can only

distinguish the two cases: $\gamma = 0$ and $\gamma \neq 0$, but cannot distinguish the case $\begin{cases} \gamma = 0 \\ Q = 0 \end{cases}$ (pure bending) from $\begin{cases} \gamma = 0 \\ Q \neq 0 \end{cases}$ (ordinary bending does not consider shear strain).

Based on the idea of considering shear strain by Timoshenko, the author proposes a new theory with the use of two functions: *displacement y and shear force Q as the independent variables* to develop and solve the problem of flexural beams considering horizontal shear strain.

The remaining quantities, such as the shear angle γ due to shear force, angle of rotation β due to moment, flexural moment M and flexural deformation χ are determined via y and Q :

$$\beta = \frac{dy}{dx} - \frac{kQ}{GA} \tag{4}$$

$$M = EI \left[-\frac{d^2y}{dx^2} + \frac{d}{dx} \left(\frac{kQ}{GA} \right) \right] \tag{5}$$

$$\chi = \frac{M}{EI} = -\frac{d\beta}{dx} = \left[-\frac{d^2y}{dx^2} + \frac{d}{dx} \left(\frac{kQ}{GA} \right) \right] \tag{6}$$

2.2 Construction of the System of Two Differential Equations for the Equilibrium of the Beam

From the equations of balanced force factors:

$$\left. \begin{aligned} \frac{d^2M}{dx^2} + q &= 0 & \text{(a)} \\ -\frac{dM}{dx} + Q &= 0 & \text{(b)} \end{aligned} \right\} \tag{7}$$

By using (4)–(6):

$$\left. \begin{aligned} EI \left[\frac{d^4y}{dx^4} - \frac{d^3}{dx^3} \left(\frac{kQ}{GA} \right) \right] &= q \\ EI \left[-\frac{d^3y}{dx^3} + \frac{d^2}{dx^2} \left(\frac{kQ}{GA} \right) \right] &= Q \end{aligned} \right\} \tag{8}$$

If shear strain (corresponding to the case that shear modulus G approaches infinity and/or the ratio h/l is infinitesimal) is not considered, the above quotations converge to the form of differential equations of Euler-Bernoulli beam:

$$\left. \begin{aligned} EI \frac{d^4 y}{dx^4} &= q \\ -EI \frac{d^3 y}{dx^3} &= Q \end{aligned} \right\} \quad (9)$$

Theoretically, the method considering horizontal shear strain proposed by the author does not encounter the shear locking phenomenon.

2.3 Construction of Boundary Conditions

The boundary conditions are often presented in Strength of Materials documents as apparent factors without being proven.

According to the Gauss's principle of least constraint [15], the equation of the beam problem when the effects of flexural deformation χ due to shearing moment and shear strain γ due to shear force are fully considered can be expressed as:

$$Z = \int_l M[\chi]dx + \int_l Q[\gamma]dx - \int_l q[y]dx \rightarrow \min \quad (10)$$

According to the Gauss's principle of least constraint, the displacements and strains are considered as virtual quantities. Therefore, we need to assume the internal force M to be independent from the strain χ , the shear force Q to be independent from the strain γ , and the load q to be independent from the displacement y . Under these conditions, the extremum condition of function Z is written as follows:

$$\delta Z = \int_l M.\delta[\chi]dx + \int_l Q.\delta[\gamma]dx - \int_l q.\delta[y]dx = 0 \quad (11)$$

Rewriting the above expression to variable y and Q gives us:

$$\delta Z = \int_l M.\delta \left[-\frac{d^2 y}{dx^2} + \frac{d}{dx} \left(\frac{kQ}{GA} \right) \right] dx + \int_l Q.\delta \left[\frac{kQ}{GA} \right] dx - \int_l q.\delta[y]dx = 0 \quad (12)$$

Calculating the partial integral in the first element of expression (12) for the beam with the length limited by boundaries $[0; l]$:

$$\begin{aligned}
 \int_0^l M \cdot \delta \left[-\frac{d^2y}{dx^2} + \frac{d}{dx} \left(\frac{kQ}{GA} \right) \right] \cdot dx &= \int_0^l M \cdot d \left(\delta \left[-\frac{dy}{dx} + \frac{kQ}{GA} \right] \right) \\
 &= M \cdot \delta \left[-\frac{dy}{dx} + \frac{kQ}{GA} \right] \Big|_0^l - \int_0^l \delta \left[-\frac{dy}{dx} + \frac{kQ}{GA} \right] \cdot dM \\
 &= M \cdot \delta \left[-\frac{dy}{dx} + \frac{kQ}{GA} \right] \Big|_0^l + \int_0^l \delta \left[\frac{dy}{dx} \right] \cdot \frac{dM}{dx} \cdot dx - \int_0^l \delta \left[\frac{kQ}{GA} \right] \cdot \frac{dM}{dx} \cdot dx \\
 &= M \cdot \delta \left[-\frac{dy}{dx} + \frac{kQ}{GA} \right] \Big|_0^l + \int_0^l \frac{dM}{dx} \cdot d[\delta y] - \int_0^l \delta \left[\frac{kQ}{GA} \right] \cdot \frac{dM}{dx} \cdot dx \\
 &= M \cdot \delta \left[-\frac{dy}{dx} + \frac{kQ}{GA} \right] \Big|_0^l + \frac{dM}{dx} [\delta y] \Big|_0^l - \int_0^l [\delta y] \cdot \frac{d^2M}{dx^2} \cdot dx - \int_0^l \delta \left[\frac{kQ}{GA} \right] \cdot \frac{dM}{dx} \cdot dx
 \end{aligned}$$

Replacing the above result into expression (12), we have the following equation:

$$-M \cdot \delta[\beta] \Big|_0^l + \frac{dM}{dx} [\delta y] \Big|_0^l - \int_0^l \left[\frac{d^2M}{dx^2} + q \right] [\delta y] \cdot dx - \int_0^l \left[\frac{dM}{dx} - Q \right] \cdot \delta[\gamma] \cdot dx = 0 \quad (13)$$

Because the variation quantities $\delta[y]$, $\delta[\beta]$ and $\delta[\gamma]$ are infinitesimal and random, so formula (13) can be split as followed:

$$\left. \begin{aligned}
 M \cdot \delta[\beta] \Big|_0^l &= 0 & (a) \\
 Q \cdot \delta[\gamma] \Big|_0^l &= 0 & (b) \\
 \frac{d^2M}{dx^2} + q &= 0 & (c) \\
 -\frac{dM}{dx} + Q &= 0 & (d)
 \end{aligned} \right\} \quad (14)$$

in which:

- Expressions (14c) và (14d) are force equilibrium equations, presenting expressions (14c) and (14d) by the variables y và Q , giving us the system of differential Eq. (8).
- The expressions (14a) and (14b) present boundary conditions or continuity condition. Hence, we have the conditions of deformation and displacement at boundaries 0 and 1 as followed:

– Condition of angle of rotation:

$$\beta \neq 0 \rightarrow M = 0 \rightarrow \text{simple support or free end}$$

$$\beta = 0 \rightarrow M \neq 0 \rightarrow \text{clamped connection}$$

– Condition of displacement:

$$y \neq 0 \rightarrow Q = 0 \rightarrow \text{Without support}$$

$$y = 0 \rightarrow Q \neq 0 \rightarrow \text{With clamped or hinge support}$$

The above expressions have shown that boundary conditions or continuous conditions are those of displacement y and angle of rotation β due to moment. Boundary conditions of displacement y and angle of rotation β due to moment are always true in both cases: with and without the effects of shear strain. When the effects of shear strain is not considered, angle of rotation due to moment is: $\beta = \frac{dy}{dx}$, when the shear strain is taken into account, it becomes: $\beta = \left(\frac{dy}{dx} - \frac{KQ}{GA}\right)$.

3 Application

The author applies the new Beam Theory Considering Horizontal Shear Strain with two unknowns y and Q to set up the problem of flexural beams considering shear strain and gives mathematical analytics solutions for beam problem. Tables 1 and 2 only present the displacement results, deformation and internal forces of a beam with rectangular cross section, having one clamped and one hinge support subjected to uniform load and a beam with both clamped supports subjected to a concentrated load at the middle of the beam when considering and not considering shear strain.

Table 1 Displacement and interior forces of the beam with rectangular cross section having clamped-hinge supports subjected to uniform load when considering and not considering shear strain

Displacement and interior forces	Beam not considering shear strain	Beam considering shear strain
Displacement at the middle of the beam	$y = \frac{ql^4}{192EI}$	$y = \frac{ql^4}{192EI} \left(1 + \frac{3}{10} \frac{95 + 48\left(\frac{h}{l}\right)^2(1 + \mu)}{5 + 3\left(\frac{h}{l}\right)^2(1 + \mu)} \left(\frac{h}{l}\right)^2(1 + \mu) \right)$
Angle of rotation at the cross section next to the clamped support	$\frac{dy}{dx} = \beta = 0$	$\frac{dy}{dx} = \frac{ql^3}{40EI} \left(\frac{25 + 12\left(\frac{h}{l}\right)^2(1 + \mu)}{5 + 3\left(\frac{h}{l}\right)^2(1 + \mu)} \right) \left(\frac{h}{l}\right)^2(1 + \mu)$
Moment at the cross section next to the clamped support	$-\frac{ql^2}{8}$	$-\frac{ql^2}{8} \left(1 - \frac{3\left(\frac{h}{l}\right)^2(1 + \mu)}{5 + 3\left(\frac{h}{l}\right)^2(1 + \mu)} \right)$
Moment at the middle of the beam	$\frac{ql^2}{16}$	$\frac{ql^2}{16} \left(1 + \frac{6\left(\frac{h}{l}\right)^2(1 + \mu)}{5 + 3\left(\frac{h}{l}\right)^2(1 + \mu)} \right)$
Shear force at the cross section next to the clamped support	$\frac{5ql}{8}$	$\frac{5ql}{8} \left(1 - \frac{\frac{3}{5}\left(\frac{h}{l}\right)^2(1 + \mu)}{5 + 3\left(\frac{h}{l}\right)^2(1 + \mu)} \right)$
Shear force at cross section next to the hinge support	$-\frac{3ql}{8}$	$-\frac{3ql}{8} \left(1 + \frac{\left(\frac{h}{l}\right)^2(1 + \mu)}{5 + 3\left(\frac{h}{l}\right)^2(1 + \mu)} \right)$

Table 2 Displacement and interior force of the beam with rectangular cross section having both clamped supports subjected to a concentrated load at the middle of the beam when considering and not considering shear strain

Displacement and interior force	Beam not considering shear strain	Beam considering shear strain
Displacement at the middle of the beam	$y_{\max} = \frac{Pl^3}{192EI}$	$y_{\max} = \frac{Pl^3}{192EI} \left(1 + \frac{48}{5EI} \left(\frac{h}{l}\right)^2 (1 + \mu) \right)$
Angle of rotation at the cross section next to the clamped support	$\frac{dy}{dx} = \beta = 0$	$\frac{dy}{dx} = \frac{Pl^2}{10EI} \left(\frac{h}{l}\right)^2 (1 + \mu)$
Jump of angle of rotation at the site of concentrated force	$\Delta \left(\frac{dy}{dx}\right) = 0$	$\Delta \left(\frac{dy}{dx}\right) = \frac{Pl^2}{5EI} \left(\frac{h}{l}\right)^2 (1 + \mu)$
M, Q	No change when considering and not considering shear strain	

The changes of displacement and internal forces of the beam with considering shear strain compared to the beam without considering shear strain in case $K = 1.2$ and $\mu = 0 \rightarrow G = E/2$ are presented in Table 3.

The calculation results of the beam considering shear strain in case $K = 1.2$ and $G = E/2$ are also presented under the form of chart in Figs. 2 and 3.

When considering horizontal shear strain, in many cases, the displacement of beam increases significantly compared to the case of not considering shear strain. When considering shear strain, although the change is not considerable, there is a redistribution of internal forces within the beam. When considering horizontal shear strain, the total angle of rotation at clamped supports has nonzero value. At the position of the concentrated force, there is an interruption of the first-order derivation of elastic line or there is a total angle of chamfer's jump of elastic line's tangent (not in the case of considering the shear strain). As for symmetrical

Table 3 Change of displacement and internal force of beam with shear strain compared to beam without shear strain in case $K = 1.2$ and $G = E/2$

Ratio h/l	Beam with both the clamped supports	Beam with one the clamped and one hinge support		
	Difference of displacement at the middle of the beam (%)	Difference of displacement at the middle of the beam (%)	Difference of moment next to the clamped support (%)	Difference of shear force next to the clamped support (%)
1/1000	0.00096	0.00057	-0.00006	-0.000012
1/100	0.096	0.057	-0.006	-0.0012
1/10	9.60	5.695	-0.596	-0.1193
1/8	15.0	8.893	-0.929	-0.1858
1/5	38.4	22.72	-2.344	-0.4686
1/3	106.67	62.71	-6.25	-1.25

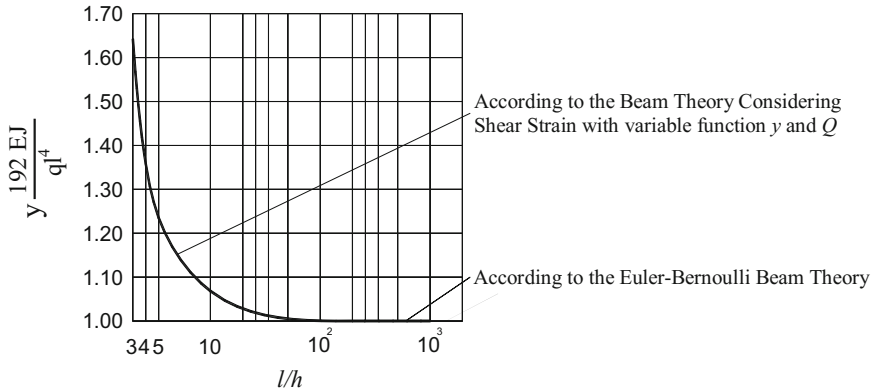


Fig. 2 Chart presents the deflection at the middle of the beam with clamped-hinge supports subjected to a uniform load when l/h varies

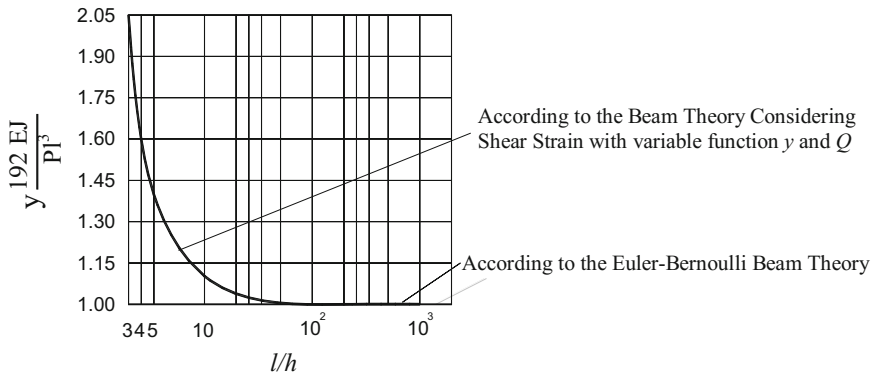


Fig. 3 Chart presents the deflection at the middle of the beam with both clamped supports subjected to a concentrated load at the middle of the beam when l/h varies

structures, considering shear strain only affects the result of displacement and strain; the internal forces remain unchanged compared to the case of not considering shear strain.

When shear strain approaches zero, the results converge to the Bernoulli's beam theory without the effect of shear strain. *Shear locking* phenomenon does not occur when the h/l ratio is infinitesimal ($h/l = 1/100 \div 1/1000$).

4 Conclusion

- The use of unknowns such as displacement y and shear force Q to construct and solve beam problems considering the shear strain has overcome the drawbacks of the current theories in similar area.
- By applying the variational calculus and partial integration, beam's boundary conditions in case of considering and not considering shear strain are also mathematically presented. These expressions conform that: Boundary condition of hinge support is not $\frac{dy}{dx} = 0$, instead, the angle of rotation due to moment equals zero: $\beta = \left(\frac{dy}{dx} - k \frac{Q}{GA}\right) = 0$. Hinge support can only constrain the angle of rotation due to moment, but cannot constrain the shear angle due to shear force.
- The new calculating beam theory with shear strain proposed by the author with differential equations and boundary conditions is a holistic beam theory, in which the case with negligible shear strain is a specific case.

References

1. Bathe KJ (2016) Finite element procedure, 2nd edn. Prentice-Hall International, Inc., Fourth printing
2. Timoshenko S, Woinowsky-Krieger S (1959) Theory of plates and shells. Copyright by the McGraw-Hill Book Company, Inc. Reissued 1987
3. Felippa CA (2017) Introduction to finite element methods (ASEN 5007). Department of Aerospace Engineering Sciences, University of Colorado at Boulder, USA. <http://www.colorado.edu/engineering/CAS/courses.d/IFEM.d/>. Updated 18 May 2017
4. Li F, Sun Z (2007) A finite difference scheme for solving the Timoshenko beam equations with boundary feedback. *J Comput Appl Math* 200:606–627. Elsevier press
5. Kien ND (2007) Free vibration of prestress Timoshenko beams resting on elastic foundation. *Vietnam J Mech VAST* 29(1):1–12
6. Wilson EL, Taylor RL, Doherty WP, Ghaboussi J (1971) Incompatible displacement models. In: Proceedings, ONR symposium on numerical and computer method in structural mechanics, University of Illinois, Urbana. Academic Press
7. Zienkiewicz OC, Taylor RL (2000) The finite element method: solid mechanics, 5th edn, vol 2. Published by Butterworth-Heinemann
8. Wilson EL (2002) Three-dimensional static and dynamic analysis of structures. In: Computers and Structures, 3rd edn. Berkeley Inc., California, USA. Reprint January 2002
9. Strang G (1972) Variational crimes in the finite element method in the mathematical foundations of the finite element method. Academic Press, pp 689–710
10. Dehrouyeh-Semnani AM, Bahrami A (2016) On size-dependent Timoshenko beam element based on modified couple stress theory. *Int J Eng Sci* 107:134–148. ScienceDirect, Elsevier
11. Kahrobaiyan MH, Asghari M, Ahmadian MT (2014) A Timoshenko beam element based on the modified couple stress theory. *Int J Mech Sci* 79:75–83. ScienceDirect, Elsevier
12. Kryskoa AV, Awrejcewicz J, Zhigalove MV, Pavlove SP, Kryskoe VA (2016) Nonlinear behaviour of different flexible size-dependent beams models based on the modified couple stress theory. Part 1: Governing equations and static analysis of flexible beams. *Int J Non-Linear Mech*. Accepted 5 March 2017

13. Ma HM, Gao X-L, Reddy JN (2008) A microstructure-dependent Timoshenko beam model based on a modified couple stress theory. *J Mech Phys Solids* 56:3379–3391. ScienceDirect, Elsevier
14. Romanoff J, Reddy JN, Jelovica J (2016) Using non-local Timoshenko beam theories for prediction of micro- and macro-structural responses. *Composite Struct* 156:410–420. ScienceDirect, Elsevier
15. Ха Зуй Кыонг. Прим-рие экстремального принципа Гаусса к задачам расчета жестких покрытий аэродромов и автомо-ных дорог. Дисс. На соиск. Учен. Степени докт. Техн. наук, МАДИ, Москва (1984)

Analytical Study on In-plane and Out-of-plane Responses of a Curved Floating Bridge



B. K. Lim, J. Dai, K. K. Ang and G. C. Yap

Abstract The in-plane and out-of-plane responses of a curved floating bridge that is vertically supported by pontoons and laterally held by shore abutments at two ends are studied analytically. The in-plane solution is derived based on strain compatibility. An Euler curved beam model is used to develop the solution to the out-of-plane response of the bridge. Trigonometric trial functions are adopted to approximate the vertical displacement and the torsional rotation of the curved beam. Both solutions are verified against FE analysis results and good agreement is found between the results. The studies will focus on the effect of end support stiffness on the in-plane response of the bridge and the out-of-plane response of the bridge subject to tidal variation.

Keywords Floating bridge · Pontoon bridge · Curved bridge
Strain compatibility · Euler beam

1 Introduction

The use of floating bridge has served human civilization for a long time and can be traced back to 4000 years ago where a boat-floating bridge was used by Persian King Xerxes to move his troops to Europe at Hellespont (See Fig. 1) [1]. These days, floating bridges remained as one of the popular methods to cross waterbodies

B. K. Lim · J. Dai · K. K. Ang (✉) · G. C. Yap (✉)

Department of Civil & Environmental Engineering, National University of Singapore,
Kent Ridge 119260, Singapore

e-mail: kk_ang@nus.edu.sg

G. C. Yap

e-mail: ceeygc@nus.edu.sg

B. K. Lim

e-mail: e0130762@u.nus.edu

J. Dai

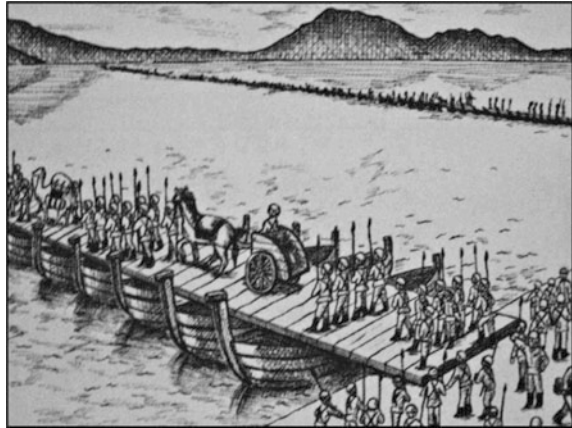
e-mail: ceedj@nus.edu.sg

© Springer Nature Singapore Pte Ltd. 2018

H. Nguyen-Xuan et al. (eds.), *Proceedings of the International Conference on Advances in Computational Mechanics 2017*, Lecture Notes in Mechanical Engineering, https://doi.org/10.1007/978-981-10-7149-2_40

591

Fig. 1 King Xerxes' floating boat bridge across the Hellespont



and connect people from different regions. When the water depth is deep or soil condition is soft, conventional pile-founded bridge faces challenges including expensive pile installation and difficult marine operation. Under the conditions, floating bridge becomes an attractive alternative that is cost effective and easier to construct. Floating bridge, in general, will be vertically supported by floaters through buoyancy in various forms (semi-submersible, pontoon, pontoon girder, etc.). The design of these floaters is usually governed by the bridge's superstructure and independent of the water depth. In addition, the construction of floating bridge can be carried out off-site in segments which can then be towed to the site for assembly. As such, marine operations required for constructing floating bridge is greatly reduced and the construction quality can be better assured.

As shown in Fig. 2, a horizontally curved floating bridge that is vertically supported by pontoons along its length without side moorings and held in position

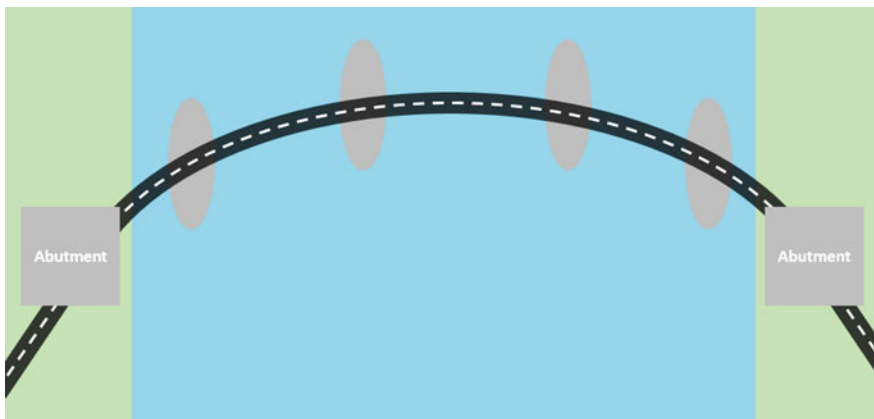


Fig. 2 Plan view of horizontally arch floating bridge

only at the ends by the shore abutment that sits on soft ground is proposed. The arch configuration is adopted to efficiently carry the environmental loads (wave/current and wind) through in-plane membrane actions to achieve economical design. However, such force transfer mechanism requires the end supports to be rigid. Therefore, the effect of end support stiffness on the internal member forces needs to be investigated to ensure the curved bridge remains structurally effective.

The proposed bridge model shall also take into account of daily water surface variation due to the tide. It is crucial to adopt an appropriate bridge structure stiffness that is able to resist the design loads but with sufficient flexibility to account for the vertical tidal motion effects.

This paper presents the analytical solutions to both in-plane and out-of-plane responses of a horizontally arch floating pontoon bridge. The accuracy of results from both solutions is verified against FE analysis results. The solutions will be used to investigate the effect of end support stiffness and tidal motion.

2 Methodology

Figure 3 presents the beam model of the bridge with subtended angle θ , length L , radius R . In the global Y -direction, the beam is discretely supported by pontoons which are represented by linear springs, $k_{y,k}$ and torsional springs, $k_{t,k}$. Additionally, translational and torsional restraints are provided at the ends to prevent the beam from displacing in global Y -direction as well as rotating about its local z' -axis. In global X -direction, linear springs, k_x are added at both ends to represent the effect of soft soil foundation. Similar boundary conditions should also be applied to the beam in global Z -direction. However, the beam is assumed to be simply supported at two ends instead. This is because the reaction forces in Z -direction are always

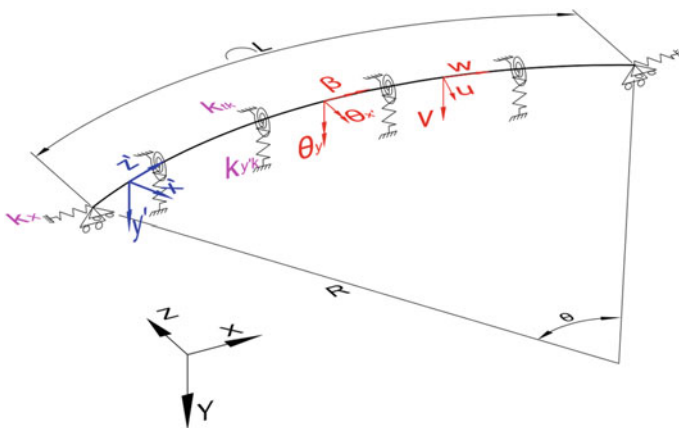


Fig. 3 Coordination and boundary conditions of curved beam

statically determinate and have no effect on the internal forces. Therefore, it is reasonable to adopt this simplification. The movement of the abutment in global Z-direction is a rigid body motion which can be easily computed once the foundation stiffness is known.

It was revealed in [2] that the in-plane response of curved beam is decoupled from its out-of-plane response. Hence, the solutions to the responses can be developed individually.

2.1 In-plane Response

Consider a simplified beam model for the study of the in-plane response. The wave/current force will be acting as concentrated loads and the spring deformations at the ends are denoted as δ_H (see Fig. 4).

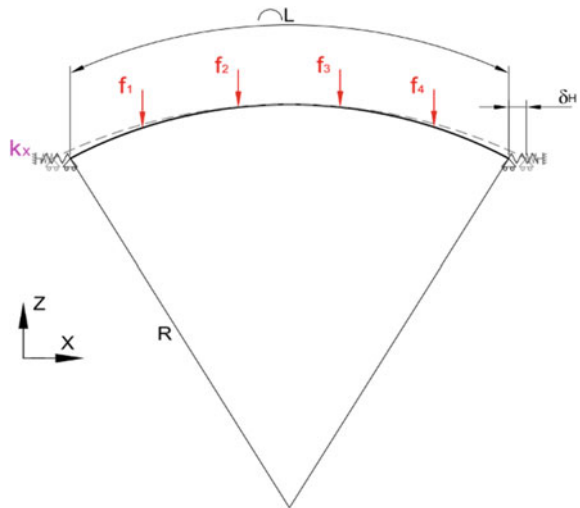
Young and Budynas [3] studied arches of various boundary and loads conditions. Two cases, as shown in Fig. 5, which are the roller-pinned arches subjected to (a) a vertical concentrated along the beam or (b) a horizontal concentrated load acting at roller end, respectively, are used in this study.

The horizontal deformation at beam end for case (a) is given below

$$\delta_{Ha,i} = -\frac{R^3}{EI_{y'}}(LP_{Ha}) \tag{1a}$$

where LP_{Ha} is the loading terms which takes into account of the geometry and properties of the beam, as well as the location and magnitude of applied load, which can be written as

Fig. 4 Curved beam under in-plane actions



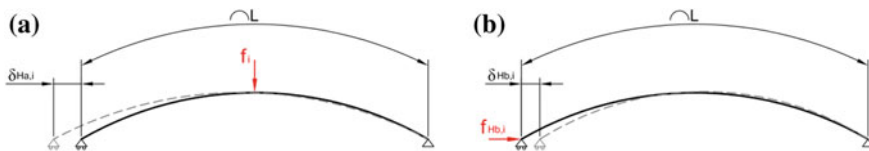


Fig. 5 Pinned-roller arches subjected to **a** vertical and **b** horizontal point load

$$LP_{Ha} = f_i \left[\frac{\theta}{2} \sin \frac{\theta}{2} \cos \frac{\theta}{2} - \phi \sin \phi \cos \frac{\theta}{2} + \frac{k_1}{2} \left(\cos^2 \frac{\theta}{2} - \cos^2 \phi \right) + k_2 \cos \frac{\theta}{2} \left(\cos \frac{\theta}{2} - \cos \phi \right) \right] \tag{1b}$$

where f_i is the load applied. θ and ϕ is the subtended angle of the arch and the angle measured counter clockwise from the midspan of the arch to the position of load, respectively. k_1 and k_2 are the correction factors for shear and hoop stress, respectively.

Similarly, for case (b), the movement of the roller support can be computed from

$$\delta_{Hb,i} = - \frac{R^3}{EI_y} (LP_{Hb}) \tag{2a}$$

where

$$LP_{Hb} = f_{Hb,i} \left[\theta \cos^2 \frac{\theta}{2} + \frac{k_1}{2} (\theta - \sin \theta) - k_2 \sin \theta \right] \tag{2b}$$

It is clear from Eqs. (2a) and (2b) that $f_{Hb,i}$ can be used to represent the reaction force of spring shown in Fig. 3. A strain compatibility relationship can be employed to obtain the actual spring deformation due to the i th concentrated load.

$$\delta_{H,i} = \frac{k_x}{2} (\delta_{Ha,i} + \delta_{Hb,i}) \tag{3a}$$

Hence, the total spring deformation can be calculated from

$$\delta_H = \sum_{i=1}^n \delta_{H,i} \tag{3b}$$

The internal member forces can then be evaluated from equilibrium equations upon obtaining the total spring deformation.

2.2 Out-of-plane Response

A simplified curved beam model, as shown in Fig. 6, is considered. The motion equation for curved beam resting on continuous foundation employed in [2] can be extended to develop the solution for this case.

For static problem, the motion equation for curved beam resting on discrete supports can be simplified as

$$EI_{x'} \left(\frac{\partial^4 v}{\partial z'^4} - \frac{1}{R} \frac{\partial^2 \beta}{\partial z'^2} \right) - \frac{GJ}{R} \left(\frac{1}{R} \frac{\partial^2 v}{\partial z'^2} + \frac{\partial^2 \beta}{\partial z'^2} \right) + \sum_{k=1}^{N_p} k_{y'k} v \delta(z - z_k) = \rho Ag \tag{4a}$$

$$\frac{EI_{x'}}{R} \left(\frac{\beta}{R} - \frac{\partial^2 v}{\partial z'^2} \right) - GJ \left(\frac{\partial^2 \beta}{\partial z'^2} + \frac{1}{R} \frac{\partial^2 v}{\partial z'^2} \right) + \sum_{k=1}^{N_p} k_{tk} \beta \delta(z - z_k) = 0 \tag{4b}$$

where $EI_{x'}$ is the flexural rigidity. v and β are the vertical displacement and torsional deformation, respectively. $k_{y'k}$ and k_{tk} are, respectively, the vertical and torsional hydrostatic stiffness provided by pontoon. N_p refers to the number of pontoons.

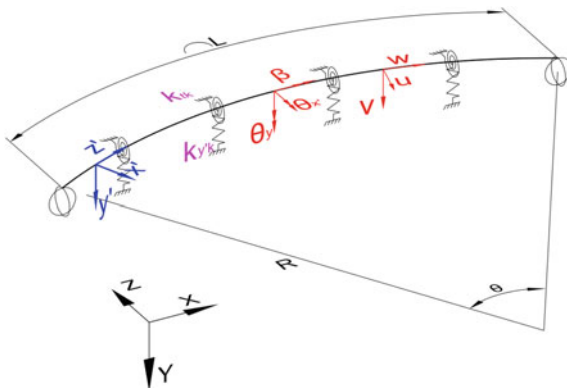
Given that the beam is restrained at both ends in torsion and translation. v and β can then be approximated by a summation of series of sinusoidal functions

$$v = \sum_{i=1}^n q_{vi} \sin \frac{i\pi z}{L} \tag{5a}$$

$$\beta = \sum_{i=1}^n q_{\beta i} \sin \frac{i\pi z}{L} \tag{5b}$$

where q_{vi} and $q_{\beta i}$ denote the generalized coordinates of i th mode. n is the number of modes. The motion equations can be solved by formulating the weighted residual forms using Galerkin's approach, this gives

Fig. 6 Curved beam model for out-of-plane response



$$\sum_{j=1}^n a_{ij}q_{vj} + b_i q_{\beta i} = \frac{2g}{i\pi} (1 - \cos i\pi) \tag{6a}$$

$$\sum_{j=1}^n c_{ij}q_{\beta j} + d_i q_{vi} = 0 \tag{6b}$$

where

$$a_{ij} = \begin{cases} EI_{x'} \left(\frac{i\pi}{L}\right)^4 + \frac{GJ}{R^2} \left(\frac{i\pi}{L}\right)^2 + \sum_{k=1}^{Np} \frac{2k_{y'k}}{L} \sin^2\left(\frac{i\pi z'_k}{L}\right), & \text{if } i=j \\ \sum_{k=1}^{Np} \frac{2k_{y'k}}{L} \sin\left(\frac{i\pi z'_k}{L}\right) \sin\left(\frac{j\pi z'_k}{L}\right), & \text{if } i \neq j \end{cases}, \quad b_i = \frac{1}{R} \left(\frac{i\pi}{L}\right)^2 (EI_{x'} + GJ) \tag{6c}$$

$$c_{ij} = \begin{cases} \frac{EI_{x'}}{R^2} + GJ \left(\frac{i\pi}{L}\right)^2 + \sum_{k=1}^{Np} \frac{2k_{y'l}}{L} \sin^2\left(\frac{i\pi z'_k}{L}\right), & \text{if } i=j \\ \sum_{k=1}^{Np} \frac{2k_{y'l}}{L} \sin\left(\frac{i\pi z'_k}{L}\right) \sin\left(\frac{j\pi z'_k}{L}\right), & \text{if } i \neq j \end{cases}, \quad d_i = \frac{1}{R} \left(\frac{i\pi}{L}\right)^2 (EI_{x'} + GJ) \tag{6d}$$

v and β can be obtained by solving Eqs. (6a)–(6d) in a $2N_m \times 2N_m$ matrix, where N_m refers to the total number of modes considered. Equations (7a) and (7b) shows the general formulation of the matrix.

$$\begin{bmatrix} a_{11} & a_{12} & \dots & a_{1(Nm-1)} & a_{1Nm} & b_1 & 0 & \dots & 0 & 0 \\ a_{21} & a_{22} & \dots & a_{2(Nm-1)} & a_{2Nm} & 0 & b_2 & \dots & 0 & 0 \\ \dots & \dots & \dots & \dots & \dots & \dots & \dots & \dots & \dots & \dots \\ a_{(Nm-1)1} & a_{(Nm-1)2} & \dots & a_{(Nm-1)(Nm-1)} & a_{(Nm-1)Nm} & 0 & 0 & \dots & b_{Nm-1} & 0 \\ a_{Nm1} & a_{Nm2} & \dots & a_{Nm(Nm-1)} & a_{NmNm} & 0 & 0 & \dots & 0 & b_{Nm} \\ d_1 & 0 & \dots & 0 & 0 & c_{11} & c_{12} & \dots & c_{1(Nm-1)} & c_{1Nm} \\ 0 & d_2 & \dots & 0 & 0 & c_{21} & c_{22} & \dots & c_{2(Nm-1)} & c_{2Nm} \\ \dots & \dots & \dots & \dots & \dots & \dots & \dots & \dots & \dots & \dots \\ 0 & 0 & \dots & d_{Nm-1} & 0 & c_{(Nm-1)1} & c_{(Nm-1)2} & \dots & c_{(Nm-1)(Nm-1)} & c_{(Nm-1)Nm} \\ 0 & 0 & \dots & 0 & d_{Nm} & c_{Nm1} & c_{Nm2} & \dots & c_{Nm(Nm-1)} & c_{NmNm} \end{bmatrix} \times \begin{pmatrix} q_{v1} \\ q_{v2} \\ \dots \\ q_{vNm-1} \\ q_{vNm} \\ q_{\beta 1} \\ q_{\beta 2} \\ \dots \\ q_{\beta Nm-1} \\ q_{\beta Nm} \end{pmatrix} = \begin{pmatrix} s_1 \\ s_2 \\ \dots \\ s_{Nm-1} \\ s_{Nm} \\ 0 \\ 0 \\ \dots \\ 0 \\ 0 \end{pmatrix} \tag{7a}$$

where f_i is given as

$$s_i = \begin{cases} \frac{2g}{i\pi} (1 - \cos i\pi), & \text{for } i \leq N_m \\ 0, & N_m < i \leq 2N_m \end{cases} \quad (7b)$$

3 Results Verification

Two models were set up using commercial FE analysis software, ETABS, to verify the accuracy of the proposed solutions.

3.1 In-plane Response

Consider a curved bridge subjected to four concentrated loads applied at a constant interval. Figure 7 shows the FE model. The bridge parameters are given in Table 1.

Figure 8 compares the moment outputs between the proposed solution and the ETABS. Excellent agreement is found between the two results, and hence, the accuracy of proposed solution is verified.

Fig. 7 FE model of curved beam (in-plane response)

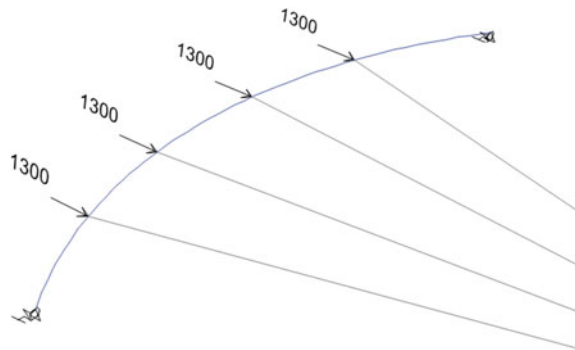


Table 1 Curved bridge properties I

Parameter	Value
L	523.6 m
R	500 m
A	5 m ²
I_y	10 m ⁴
E	2×10^{11} N/m ²
θ	60°
k_x	5×10^6 N/m

Fig. 8 Numerical verification—in-plane moment

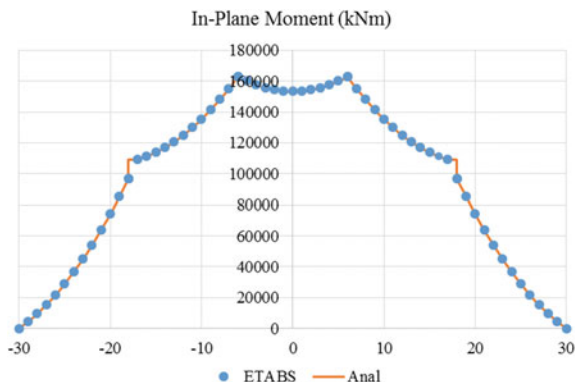


Table 2 Curved bridge properties II

Parameter	Value	Parameter	Value
L	523.6 m	I_x	50 m ⁴
R	500 m	J	130 m ⁴
A	5 m ²	ν	0.3
E	2×10^{11} N/m ²	θ	60°
ρ	11734.2 kg/m ³	$k_{y,k}$	1.04×10^7 N/m

3.2 Out-of-plane Response

A curved bridge supported by four pontoons at a constant interval is analyzed (see Table 2 for the bridge parameters). The buoyancies provided by the pontoons are assumed to be zero initially (when the tide level = 0). Figure 9 shows the vertical displacements reported by the current solution and ETABS when the bridge is subjected to high sea level of +2 m. The analytical result matches the FE output well.

4 Results and Discussion

4.1 Effect of Soft Foundation on In-plane Response

It is observed that the in-plane response of the bridge will only be affected only by the stiffness ratio of the bridge’s flexural rigidity, EI_y/L^3 to the foundation stiffness at bridge ends, k_x .

The investigation is carried out by conducting a series of parametric studies on bridges with different relative stiffness. Table 3 summarizes the bridge properties used in these studies. For ease of comparison, all the parameters including the foundation stiffness will be kept at constant whilst the second moment of inertia

Fig. 9 Numerical verification of vertical displacement

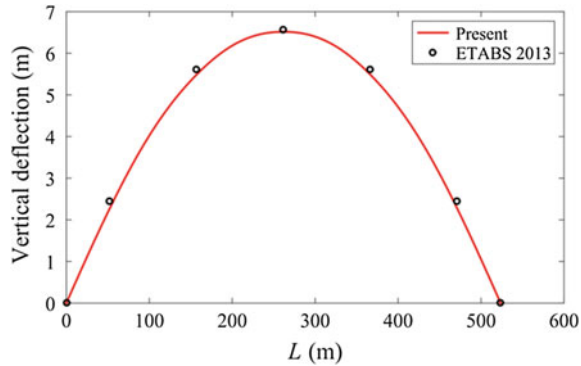


Table 3 Curved bridge properties III

Parameter	Value
L	523.6 m
R	500 m
A	5 m ²
I_y	1–100 m ⁴
E	2×10^{11} N/m ²
θ	60°
k_x	5×10^6 N/m
f_i	2000 kN

varies from 1 to 100 m⁴. The number and distribution of the concentrated loads are identical to those shown in Fig. 7 but the load magnitude of 2000 kN is used instead.

Figure 10 compares the internal forces of a curved bridge subjected to soft soil foundation ($k_x = 5 \times 10^6$ N/m) to a bridge that is rigidly held in place. Both bridges have the same second moment of inertia of 10⁴ m. It can be seen that the softening of the foundation will result in the reduction of membrane forces. Furthermore, more loadings will be carried by bending action which leads to significant increase in shear and moment. For this particular case, a 1/3 reduction in axial force could result in 86% increment in shear and 820% increment in bending moment. It is clear that the membrane arch action becomes ineffective due to the present soft soil foundation.

Figure 11 provides the loss/gain (with respect to rigid arch) in maximum responses of arch with soft boundaries with respect to the stiffness ratio of bridge’s flexural rigidity to its foundation stiffness.

It can be seen that for this particular load arrangement, the reduction in axial force can be up to 70% which amplifies the bending moment by 18 times as the foundation stiffness reduced. Hence, it is crucial to maintaining sufficient rigidity to ensure that the arch can act effectively with high membrane action. For example, a maximum stiffness ratio of 1×10^{-4} is required in order to maintain at least 85% of the axial force accompanied by 467% increment in bending moment.

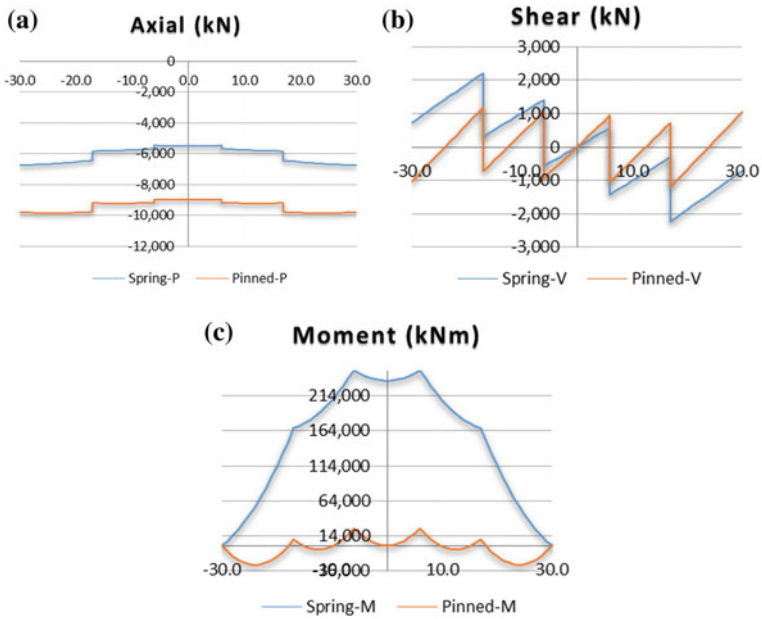


Fig. 10 Comparison of **a** axial, **b** shear and **c** moment of curved bridges ($I_y = 10^4 \text{ m}^4$)

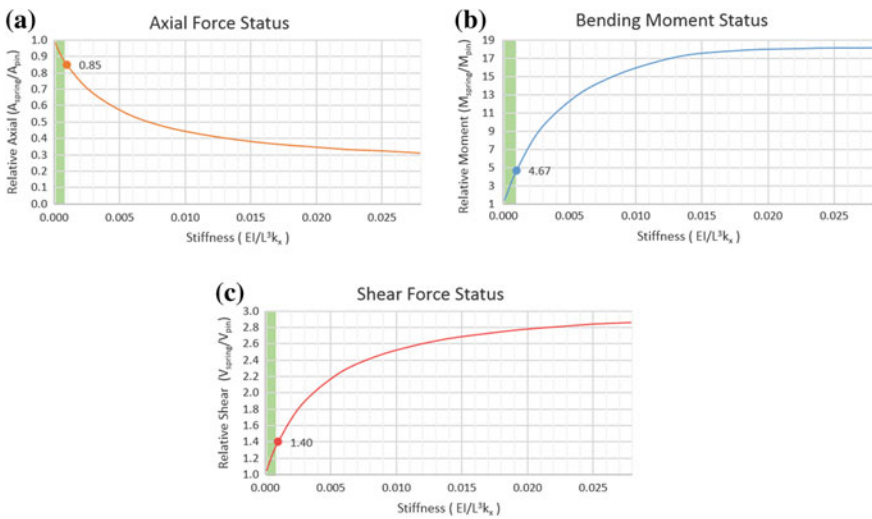


Fig. 11 Summary of in-plane response **a** axial force **b** bending moment and **c** shear force

4.2 Effect of Tidal Variation on Out-of-plane Response

The responses for a set of bridges (design parameters to refer Table 4) of different flexural rigidity are computed. Note that the second moment of inertia, I_x , ranging from 1 to 30 m^4 is selected to investigate the behavior response due to tide.

Vertical displacements (v) and rotation (θ) of the bridges at low tide of -2 m are shown in Fig. 12.

Table 4 Curved bridge properties IV

Parameter	Value	Parameter	Value
L	523.6 m	I_x	1–30 m^4
R	500 m	v	0.3
A	5 m^2	θ	60°
E	2×10^{11} N/m ²	$k_{y/k}$	1.09×10^7 N/m
ρ	11734.2 kg/m ³	k_{tk}	1.94×10^9 Nm/rad

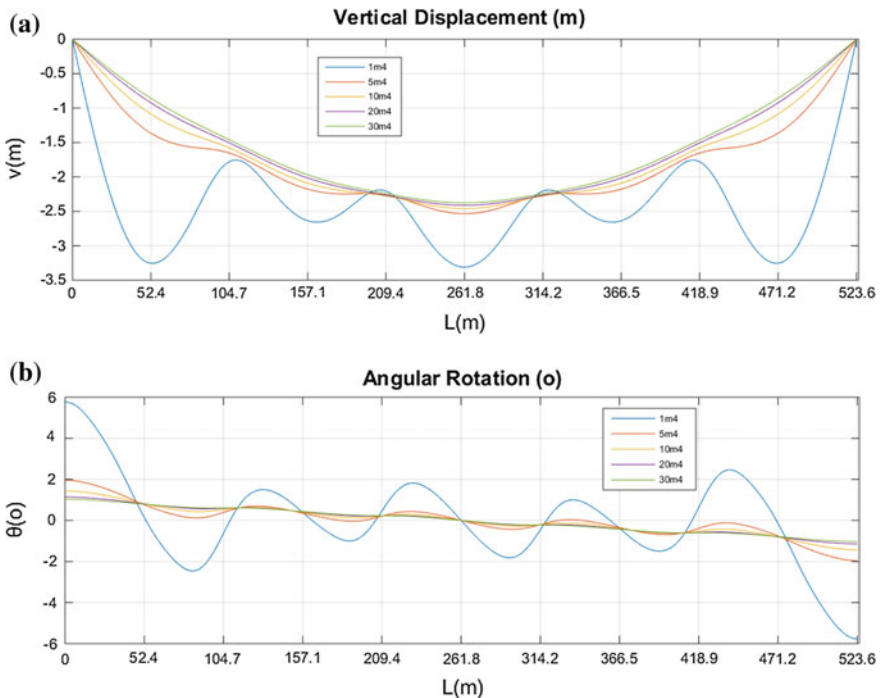


Fig. 12 Curved bridge subjected to tidal variations: **a** vertical deformation and **b** rotation

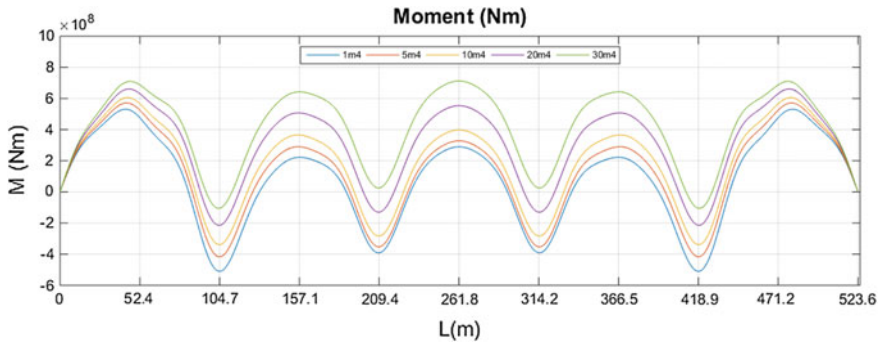


Fig. 13 Tide-induced bending moment

Table 5 Comparison of bending moments and rotation angles of curved bridges

Second moment of inertia (m^4)	Maximum moment (Nm)	Reduction in moment (%)	Maximum rotation ($^\circ$)	Increment in rotation (%)
1	5.31×10^8	25.4	5.77	460.6
5	5.71×10^8	19.8	1.96	90.5
10	6.06×10^8	14.9	1.43	39.2
20	6.61×10^8	7.2	1.14	10.8
30	7.12×10^8		1.03	

It is observed that for bridges with second moment equal to 1 and 5 m^4 , both the vertical deformation and rotation angle are fluctuating, which creates unevenness to the road surfaces. Such unevenness will need to be evaluated further to ensure that the rideability of the road is not compromised.

On the other hand, bridges with second moment of inertia higher than or equal to 10 m^4 are found to have their responses to be similar and start converging. Given that the tide-induced moment (see Fig. 13 and Table 5) is lower for the bridge with smaller flexural rigidity. It is hence reasonable and economical to adopt a bridge with slightly lower flexural rigidity provided that the bridge has fulfilled all other strength and serviceability requirements. For example, in this case, by adopting bridge with second moment of inertia of 10 m^4 , the tide-induced bending moment can be lowered by 14.9% as compared to the bridge of 30 m^4 (see Table 5). Note that even though the maximum rotation angle (maximum slope) in this case is increased from 1.03 $^\circ$ to 1.43 $^\circ$ (39% increment), it is deemed to be acceptable as the deformed bridge profile is still gentle and close to the one with the highest second moment of inertia.

5 Results and Discussion

Presented in this paper are the analytical solutions to both in-plane and out-of-plane curved bridge. Both solutions are validated with the commercial FE analysis software, ETABS and the results match well.

The proposed solutions are used to investigate the effect of soft foundation and tidal variation, on in-plane and out-of-plane response, respectively. For study in the effect of the soft soil foundation on in-plane response, it is found that with lower foundation stiffness, the bridge will tend to carry the loading through beam action, which results in a significant reduction in membrane force. A maximum stiffness ratio of 1×10^{-4} is recommended to ensure the loss in membrane action is kept within 15%.

In the study on the out-of-plane response, the bridges can be divided into two groups according to their second moment of inertia. Those bridges with second moment of inertia less than 5 m^4 , the deformed road profiles are found to be highly uneven. This phenomenon is not favorable as it will affect the rideability of the road and endanger the road users. For the second group, no significant differences are found between the deformed bridge profiles. Hence, with the premise that all other strength and serviceability requirements can be fulfilled, it is recommended to adopt a bridge that has slightly lower flexural rigidity in order to enjoy the advantage of smaller tide-induced bending moment to yield economical design.

Acknowledgements This material is based on research/work supported by the Singapore Ministry of National Development, National Research Foundation and JTC Corporation under L2 NIC Award No. L2NICTDF1-2015-2.

References

1. Watanabe E, Utsunomiya T (2003) Analysis and design of floating bridges. *Progress Struct Mater* 5:144–157
2. Dai J, Ang KK (2015) Steady-state response of a curved beam on a viscously damped foundation subjected to a sequence of moving loads. *Proc Inst Mech Eng F J Rail Rapid Transit* 229:391–442
3. Young WC, Budynas RG (2002) Roark's formulas for stress and strain, 7th edn. McGraw-Hill, USA

Establishment of Artificial Accelerogram for Shaking Table Test



T. Nguyen-Vo, T. Do-Tien and K. Nguyen-Trung

Abstract In order to evaluate behavior of building and other structures under seismic action, one of the methods is testing the specimen on the shaking table. This paper presents the establishment of artificial accelerogram for testing of semi-precast specimen on the shaking table by using similitude theory to convert the artificial accelerogram of the prototype building to artificial accelerogram of the small-scale specimen and compare the test result and analysis result.

Keywords Testing specimen • Artificial accelerogram • Shaking table test

1 Introduction

In the present, shaking table test for small-scale specimen is one of the common methods to study the behavior of the building structures under seismic action. From the shaking table test, it can determine the failure mode, seismic performance, and distribution of seismic force along the height of the specimen, local damage. From the test results, lessons can be withdrawn for seismic design of the building structures.

On the world, countries such as USA, Taiwan, Japan, China [1, 2]... have established artificial accelerogram for their own territory. In Vietnam, up to now, there is no official artificial accelerogram that corresponded to the soil condition and seismic characteristic of Vietnam as well as shaking table available in Vietnam.

This paper presents the theory and method to establish artificial accelerogram for shaking table test of structures in Vietnam and applied for testing a 12-story semi-precast concrete building prototype in Vietnam.

T. Nguyen-Vo (✉) · T. Do-Tien · K. Nguyen-Trung
Vietnam Institute for Building Science and Technology - IBST, Hanoi, Vietnam
e-mail: thongnguyenvo@gmail.com

© Springer Nature Singapore Pte Ltd. 2018
H. Nguyen-Xuan et al. (eds.), *Proceedings of the International Conference on Advances in Computational Mechanics 2017*, Lecture Notes in Mechanical Engineering, https://doi.org/10.1007/978-981-10-7149-2_41

2 Similitude Theory for Seismic Testing of Structures

In order to design specimens for dynamic testing, it can use one type or combination of some type of model such as: strength model, artificial mass model, ignoring gravity model, and strain fuzzy model. For strength model of structure under seismic action, physical parameters of the prototype and model were expressed by the dimension of fundamental parameters [3, 4]: mass [M], length [L], and time [T], as follows:

$$\Pi_1 = \frac{\delta}{L} = idem \rightarrow \left(\frac{\delta}{L}\right)_{(N)} = \left(\frac{\delta}{L}\right)_{(M)} \rightarrow \frac{s_\delta}{s_L^*} = 1 \quad (1)$$

$$\Pi_2 = \frac{\rho g L}{E} = idem \rightarrow \left(\frac{\rho g L}{E}\right)_{(N)} = \left(\frac{\rho g L}{E}\right)_{(M)} \rightarrow \frac{s_\rho s_g s_L}{s_E} = 1 \quad (2)$$

$$\Pi_3 = \varepsilon = idem \rightarrow \varepsilon_{(N)} = \varepsilon_{(M)} \rightarrow s_\varepsilon = 1 \quad (3)$$

$$\Pi_4 = \frac{F}{EL^2} = idem \rightarrow \left(\frac{F}{EL^2}\right)_{(N)} = \left(\frac{F}{EL^2}\right)_{(M)} \rightarrow \frac{s_F}{s_E \cdot s_L^2} = 1 \quad (4)$$

$$\Pi_5 = \frac{\sigma}{E} = idem \rightarrow \left(\frac{\sigma}{E}\right)_{(N)} = \left(\frac{\sigma}{E}\right)_{(M)} \rightarrow \frac{s_\sigma}{s_E} = 1 \quad (5)$$

$$\Pi_6 = \frac{gT^2}{L} = idem \rightarrow \left(\frac{gT^2}{L}\right)_{(N)} = \left(\frac{gT^2}{L}\right)_{(M)} \rightarrow \frac{s_g \cdot s_T^2}{s_L} = 1 \quad (6)$$

$$\Pi_7 = \frac{a}{g} = idem \rightarrow \left(\frac{a}{g}\right)_{(N)} = \left(\frac{a}{g}\right)_{(M)} \rightarrow \frac{s_a}{s_g} = 1 \quad (7)$$

$$\Pi_8 = \frac{vT}{L} = idem \rightarrow \left(\frac{vT}{L}\right)_{(N)} = \left(\frac{vT}{L}\right)_{(M)} \rightarrow \frac{s_v \cdot s_T}{s_L} = 1 \quad (8)$$

$$\Pi_9 = f \cdot T = idem \rightarrow (fT)_{(N)} = (fT)_{(M)} \rightarrow s_f \cdot s_T = 1 \quad (9)$$

$$\Pi_{10} = \frac{(En)}{EL^3} = idem \rightarrow \left(\frac{(En)}{EL^3}\right)_{(N)} = \left(\frac{(En)}{EL^3}\right)_{(M)} \rightarrow \frac{s_{(En)}}{s_E \cdot s_L^3} = 1 \quad (10)$$

where L—length; E—Young modulus; F—force; and T—time.

3 Establishment of Specimen for Shaking Table Test

With the prototype in this study, in order to be suitable with the capacity of the shaking table at the laboratory of Vietnam Institute for Building Science and Technology, the length scale factor s_L was selected as 1/12. Other scale factors were calculated follow s_L and s_E and are shown in Table 1. The testing specimen was designed and constructed as shown in Fig. 1.

4 Establishment of Accelerogram for Shaking Table Test

The prototype building located at Dong Anh, Hanoi, soil type D with shear wave velocity <180 m/s. According to Appendix H of TCVN 9386:2012 [5], for this location, the reference PGA agr is 0, 1 g. Establishment of artificial accelerogram in Vietnam was conducted based on the information provided by the Institute of Geophysics such as: magnitude, location of epicenter, and source of earthquake. Using elastic response spectrum provided in TCVN 9386:2012, the authors created eight artificial accelerograms with PGA value, time steps, and time duration so that suitable with the capacity of the shaking table. The steps for establishing of the accelerograms are shown in Fig. 2. Each accelerogram has the relationship between power spectrum density and frequency. Accelerograms were created by using Seismo Artif and Seismo Signal software.

Table 1 Scale factors of fundamental and dependent dimensions

Dimensions	Name and notation	Similitude equation	Scale factors
Geometry	Length, L	$s_L = s_L^*$	$s_L^* = 12$
	Displacement, δ	$\frac{s_\delta}{s_L} = 1$	$s_L = 12$
Material	Young modulus, E	$s_E = s_E^*$	$s_E^* = 2.4$
	Density, ρ	$s_\rho = s_\rho$	$s_\rho = 1$
	Strain, ϵ	$s_\epsilon = 1$	$s_\epsilon = 1$
Force	Force, F	$\frac{s_F}{s_E \cdot s_L^2} = 1$	$s_F = 345.6$
	Stress, σ	$\frac{s_\sigma}{s_E} = 1$	$s = 2.4$
Other dimensions	Acceleration, a	$\frac{s_a \cdot s_a \cdot s_L^*}{s_E} = 1$	$s_a = 1/5$
	Time, T	$\frac{s_T}{s_L} \left(\frac{s_E^*}{s_\rho} \right)^{\frac{1}{3}} = 1$	$s_T = 7.747$
	Velocity, v	$\frac{s_v \cdot s_T}{s_L} = 1$	$s_v = 1.549$
	Frequency, f	$s_f \cdot s_T = 1$	$s_f = 0.129$
	Energy, En	$\frac{s(En)}{s_E^* \cdot s_L^3} = 1$	$s(En) = 4.147 \times 10^3$



Fig. 1 Testing specimen

Artificial accelerogram was established for shaking table test with return periods of 95 year, 475 year, 2475 year, and the power spectrum density was shown in Figs. 3, 4 and 5.

5 Testing Results

Comparing the recorded displacements, accelerations at floor levels from the testing with analysis results of prototype building for three input motions: El Centro accelerogram, 95 years return period artificial accelerogram, and 475 years return period artificial accelerogram, it can be seen that the recoded and analysis values are very similar as shown in Figs. 6, 7, 8 and Table 2.

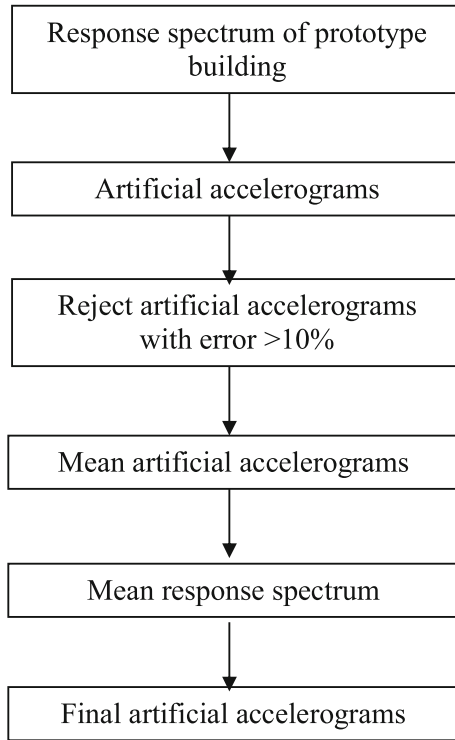


Fig. 2 Block diagram for creating artificial accelerogram

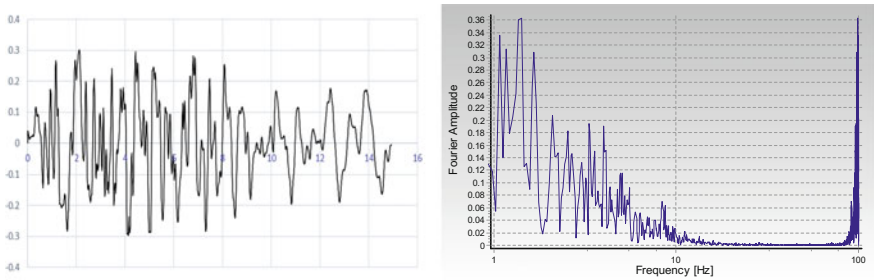


Fig. 3 Accelerogram and power spectrum density, return period 95 year

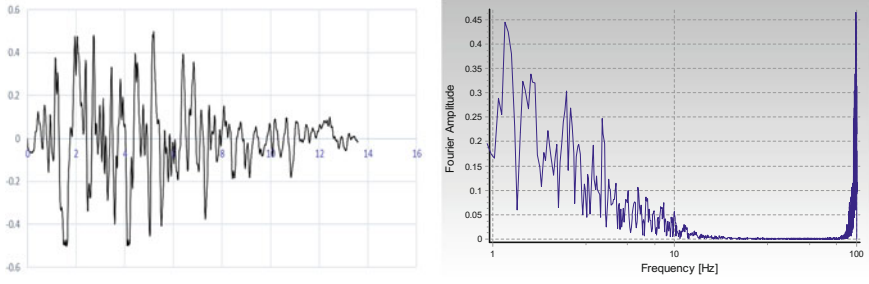


Fig. 4 Accelerogram and power spectrum density, return period 475 year

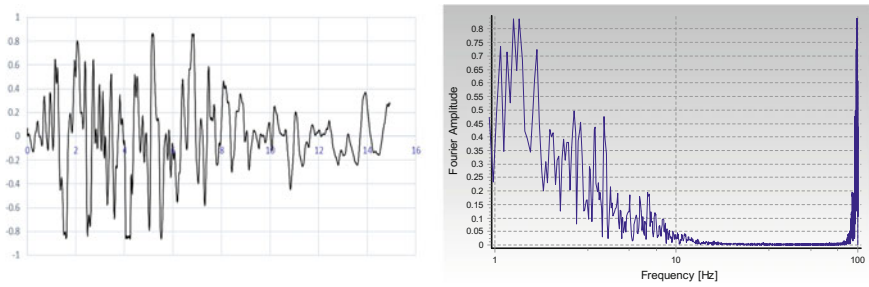


Fig. 5 Accelerogram and power spectrum density, return period 2475 year

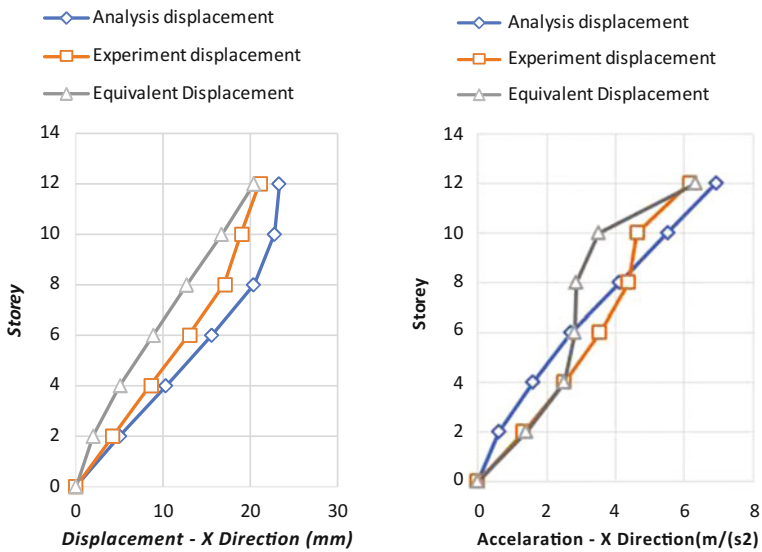


Fig. 6 Compare displacement, acceleration result recorded from testing and analysis results with Elcentro accelerogram

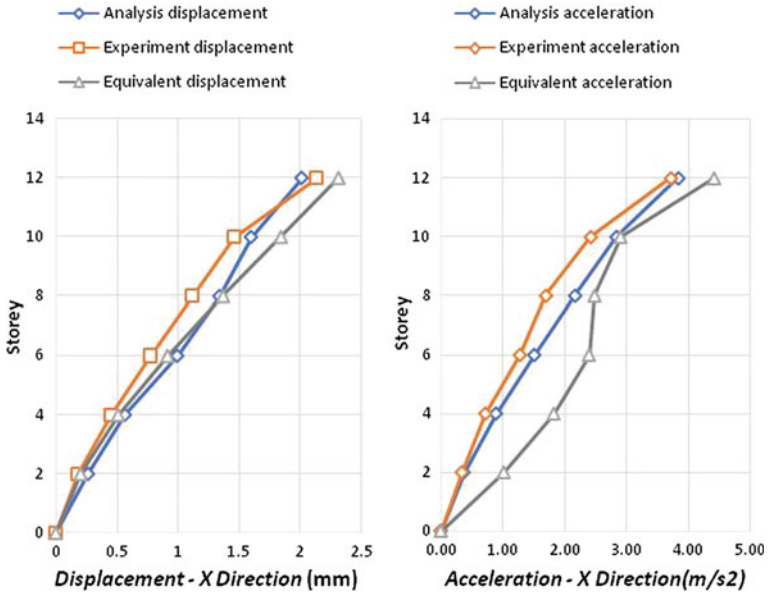


Fig. 7 Compare displacement, acceleration result recorded from testing and analysis results with artificial accelerogram, return period 95 year

Notes:

- Analysis displacement (acceleration): displacement (acceleration) received from analysis by Etabs with small-scale specimen.
- Experimental displacement (acceleration): displacement (acceleration) recorded from shaking table test of the specimen.
- Equivalent displacement (acceleration): displacement (acceleration) of the prototype that was converted from small-scale specimen by using scale factors corresponded with each artificial accelerogram.

The testing results show that the errors between recorded results of the small-scale specimen and analytical results of the prototype building are small (see Table 2).

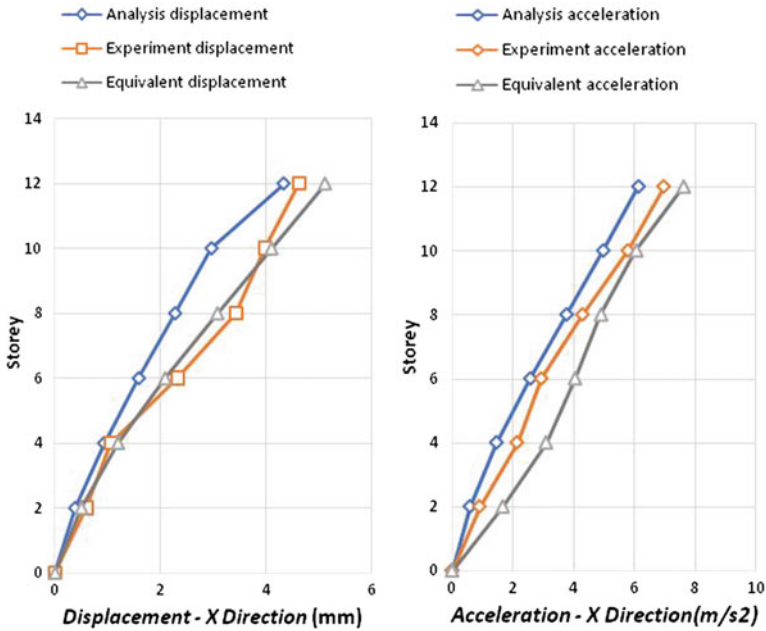


Fig. 8 Compare displacement, acceleration result recorded from testing and analysis results with artificial accelerogram, return period 475 year

Table 2 Error between displacement, acceleration at roof of prototype converted by scale factors (1) with recorded result from shaking table testing (2) and analysis result of small-scale specimen by Etabs software (3)

	Elcentro 1940		Return period 95 year		Return period 475 year	
	$\frac{[(3)-(1)]}{(1)} (\%)$	$\frac{[(2)-(1)]}{(1)} (\%)$	$\frac{[(3)-(1)]}{(1)} (\%)$	$\frac{[(2)-(1)]}{(1)} (\%)$	$\frac{[(3)-(1)]}{(1)} (\%)$	$\frac{[(2)-(1)]}{(1)} (\%)$
Displacement	12.52	9.5	12.82	7.53	15.14	9.66
Acceleration	9.52	2.68	13.24	15.93	19.42	15.09

6 Conclusions

On the basis data of geometry and mechanical properties of the prototype building, soil condition and source of earthquake, and Vietnamese seismic design code TCVN 9386:2012, the authors have established the artificial accelerograms for testing of building structures on shaking table in Vietnam.

The authors have established the procedure for creating the artificial accelerograms that are suitable with Vietnam condition. The authors have established the procedure to create artificial accelerograms that are suitable with Vietnam’s seismic and equipment condition.

The testing results from specimen such as displacement and acceleration were well suitable with the analysis result by ETABS software, on prototype and on small-scale specimen.

References

1. Lu X, Zhou Y, Lu W (2007) Shaking table model test and numerical analysis of a complex high-rise building. In: The structural design of tall and special building
2. Lu X, Zou Y, Lu W, Zhao B (2007) Shaking table model test on Shanghai World Financial Center Tower. Earthq Eng Struct Dyn
3. Harris HG, Sabnis GM (1999) Structural modelling and experimental techniques, CRC Press
4. Vo Van T (1990) Modelling of structures, National University of Civil Engineering
5. TCVN 9386:2012 Design of structures for earthquake resistances, part 1: general rules, seismic actions and rules for buildings

A Naturally Stabilized Nodal Integration Meshfree Formulation for Thermo-Mechanical Analysis of Functionally Graded Material Plates



Chien H. Thai, Dung T. Tran and Hung Nguyen-Xuan

Abstract This chapter presents naturally stabilized nodal integration (NSNI) meshfree formulations for thermo-mechanical analysis of functionally graded material (FGM) plates. The effective material properties of FGM plates are homogenized by a rule of mixture. Gradient strains from the present approach are directly computed at nodes, the same as the direct nodal integration (DNI). The current approach is to alleviate the instability of solutions in the DNI and to significantly decrease computational cost when compared to the high-order Gauss quadrature scheme. The enforcement of essential boundary conditions is completely similar to the finite element method (FEM) due to satisfying the Kronecker delta function property of moving Kriging integration shape functions. Numerical validations are given to show the efficiency of the present approach.

Keywords Naturally stabilized nodal integration • Moving kriging interpolation • Meshfree method • Functionally graded material

C. H. Thai (✉)

Division of Computational Mechanics, Ton Duc Thang University,
Ho Chi Minh City, Vietnam
e-mail: thaihoangchien@tdt.edu.vn

C. H. Thai

Faculty of Civil Engineering, Ton Duc Thang University,
Ho Chi Minh City, Vietnam

D. T. Tran

Faculty of Construction & Electricity, Ho Chi Minh City Open University,
97 Vo Van Tan Street, Ho Chi Minh City, Vietnam

H. Nguyen-Xuan

Center for Interdisciplinary Research, University of Technology (Hutech),
Ho Chi Minh City 700000, Vietnam

© Springer Nature Singapore Pte Ltd. 2018

H. Nguyen-Xuan et al. (eds.), *Proceedings of the International Conference on Advances in Computational Mechanics 2017*, Lecture Notes in Mechanical Engineering, https://doi.org/10.1007/978-981-10-7149-2_42

1 Introduction

Thanks to outstanding properties such as high stiffness and strength-to-weight ratios, long fatigue life, wear resistance, lightweight, and composite materials have attracted considerations in many researches. These materials are not capable to perform well when subjected to high-temperature environments and suffer the delamination phenomena due to the reduction in the inter-laminar stresses [1]. Advanced composite materials, namely functionally graded materials (FGMs), were proposed by materials scientists in the Sendai area of Japan in 1984 [2] to remedy these drawbacks of composite materials. FGMs are usually made from a mixture of ceramic and metal, and they vary continuously across the thickness direction which is to overcome the phenomenon of reduced material strength in high-temperature environments and low toughness of the ceramic in many applications. Thanks to these characteristics, FGMs are appropriate for design in various industrial fields.

Generally, there are two theories used for computations of FGM plate structures: the three-dimensional (3D) elasticity theory and two-dimensional (2D) elasticity theory. The 3D elasticity requires very long computational times due to being considered full 3D solid, and the actual behavior of plates can be predicted. It is suitable for solving problems with simple geometries and boundary conditions. For arbitrary problems, the 2D plate theory is an appropriate choice. This theory includes the classical plate theory (CPT), the first-order shear deformation theory (FSDT), and the higher order shear deformation theory (HSDT). The first one [3] is only suitable for thin plates due to ignoring the effects of transverse shear strains. The second is coincided for both thin and moderately thick plates, but an additionally shear correction factor is needed in the shear term to match the strain energy obtained from the 3D elasticity solution with those from FSDT solution. The HSDT includes the third-order shear deformation theory (TSDT) [4], the fifth-order shear deformation theory (FiSDT) [5], the seventh-order shear deformation theory [6], the trigonometric shear deformation theory [7], the inverse trigonometric shear deformation theory [8, 9], the exponential shear deformation theory (ESDT) [10], and so on. In this chapter, we present the higher order shear deformation theory for thermo-mechanical analysis of FGM plates.

Meshfree methods based on the Galerkin weak form have been applied and developed for analysis of FGM plates. It needs background cells similar to FEM to compute the integration for the Galerkin weak form. To get stable and accurate solutions, the high-order Gauss quadrature scheme is used due to the rational shape functions in meshfree methods, but it takes very long computational times. On the other hand, solutions may not be converged and stabilized [11] when using the lower-order Gauss quadrature. To achieve both, the nodal integration scheme should be chosen. However, the direct nodal integration scheme is usually an instable solution due to rank deficiency in computational formulations. To reduce instable solutions, several nodal integration schemes are introduced as a stabilized conforming nodal integration (SCNI) by Chen et al. [11]; a modified SCNI by Hillman et al. [12], a least-squares method by Beissel and Belytschko [13], a Taylor

series expansion of the displacement fields by Nagashima [14] and Liu et al. [15], a Taylor expansion combined with displacement smoothing by Wu and Koishi [16], the naturally implicit gradient expansion by Hillman and Chen [17], and so on. In this study, the nodal integration scheme proposed by Hillman and Chen [17] is applied for MKI shape functions to investigate thermo-mechanical behavior of FGM plates.

2 Basic Equations

2.1 Problem Description

FGM is made from an isotropic homogeneous material by mixing ceramic and metal, in which ceramic-rich and metal-rich surfaces are distributed at the top and bottom, respectively. Material properties vary continuously across the thickness direction due to their behavior which is similar to isotropic material. In this chapter, effective material properties including Young's modulus and Poisson's ratio are homogenized by the rule of mixture, in which the volume fraction of the ceramic and metal phases are assumed to have continuous variation through thickness by Reddy [4]:

$$V_c(z) = \left(\frac{1}{2} + \frac{z}{h} \right)^n, z \in \left[-\frac{h}{2}, \frac{h}{2} \right]; \quad V_m = 1 - V_c \quad (1)$$

where the metal and ceramic are expressed using the symbols m and c , respectively. The parameter n defines a power index corresponding to the volume fraction variation in the thickness direction. Based on the rule of mixture according to Eq. (1), effective material properties are expressed as follows:

$$E_{eff} = E_c V_c(z) + E_m V_m(z); \quad \nu_{eff} = \nu_c V_c(z) + \nu_m V_m(z) \quad (2)$$

2.2 Kinematics of FGM Plate

Let us consider a plate carrying a domain $\mathbf{V} = \Omega \times (-h/2, h/2)$, where $\Omega \in \mathbb{R}^2$ and h are the middle surface and the thickness of the plate, respectively. The displacement field of any points in the plate according to the generally higher order shear deformation theory is written as follows:

$$\mathbf{u}(x, y, z) = \mathbf{u}^0(x, y) + z\mathbf{u}^1(x, y) + f(z)\mathbf{u}^2(x, y) \quad (3)$$

where

$$\mathbf{u} = \begin{Bmatrix} u \\ v \\ w \end{Bmatrix}; \mathbf{u}^0 = \begin{Bmatrix} u_0 \\ v_0 \\ w_0 \end{Bmatrix}; \mathbf{u}^1 = - \begin{Bmatrix} w_{0,x} \\ w_{0,y} \\ 0 \end{Bmatrix}; \mathbf{u}^2 = \begin{Bmatrix} \theta_x \\ \theta_y \\ 0 \end{Bmatrix} \tag{4}$$

in which $u_0, v_0, w_0, \theta_x,$ and θ_y are the in-plane, transverse displacements and the rotation components in the $y - z$ and $x - z$ planes, respectively; and symbols ‘0, x ’ and ‘0, y ’ denote the derivative of any function following x and y directions, respectively, while $f(z)$ is any function in the z -coordinate direction.

From Eqs. (3) and (4), the slope components are not defined as the approximation variables; thus, it is very difficult to enforce boundary conditions corresponding to them. To alleviate the above mentioned disadvantages, the following additional assumptions are made:

$$w_{0,x} = \beta_x \text{ and } w_{0,y} = \beta_y \tag{5}$$

Substituting Eq. (5) into Eq. (4), yields:

$$\mathbf{u}^0 = \{u_0 \ v_0 \ w_0\}^T; \mathbf{u}^1 = - \{\beta_x \ \beta_y \ 0\}^T; \mathbf{u}^2 = \{\theta_x \ \theta_y \ 0\}^T \tag{6}$$

Hence, the compatible strain fields obtained from Eq. (6) only request C^0 continuity. Bending and shear strains corresponding to C^0 -type higher order shear deformation theory are described as:

$$\boldsymbol{\varepsilon} = \{ \varepsilon_{xx} \ \varepsilon_{yy} \ \gamma_{xy} \}^T = \boldsymbol{\varepsilon}^0 + z\boldsymbol{\varepsilon}^1 + f(z)\boldsymbol{\varepsilon}^2 - \boldsymbol{\varepsilon}^{th} \text{ and } \boldsymbol{\gamma} = \{ \gamma_{xz} \ \gamma_{yz} \}^T = \boldsymbol{\varepsilon}^{s0} + f'(z)\boldsymbol{\varepsilon}^{s1} \tag{7}$$

where

$$\boldsymbol{\varepsilon}^0 = \begin{Bmatrix} u_{0,x} \\ v_{0,y} \\ u_{0,y} + v_{0,x} \end{Bmatrix}; \boldsymbol{\varepsilon}^1 = - \begin{Bmatrix} \beta_{x,x} \\ \beta_{y,y} \\ \beta_{x,y} + \beta_{y,x} \end{Bmatrix}; \boldsymbol{\varepsilon}^2 = \begin{Bmatrix} \theta_{x,x} \\ \theta_{y,y} \\ \theta_{x,y} + \theta_{y,x} \end{Bmatrix}; \boldsymbol{\varepsilon}^{th} = \alpha(z)\Delta T \begin{Bmatrix} 1 \\ 1 \\ 0 \end{Bmatrix}$$

$$\boldsymbol{\varepsilon}^{s0} = \begin{Bmatrix} w_{0,x} - \beta_x \\ w_{0,y} - \beta_y \end{Bmatrix}; \boldsymbol{\varepsilon}^{s1} = \begin{Bmatrix} \theta_x \\ \theta_y \end{Bmatrix}; \tag{8}$$

where $\alpha(z)$ and $f'(z)$ are the coefficient of thermal expansion and the derivation of the function $f(z)$, respectively. In this study, the cubic function $f(z) = z - \frac{4z^3}{3h^2}$ proposed by Reddy [4] is used.

Using Hooke’s law, the linear constitutive relations are written as:

$$\begin{Bmatrix} \sigma_{xx} \\ \sigma_{yy} \\ \tau_{xy} \\ \tau_{xz} \\ \tau_{yz} \end{Bmatrix} = \begin{bmatrix} Q_{11} & Q_{12} & 0 & 0 & 0 \\ Q_{21} & Q_{22} & 0 & 0 & 0 \\ 0 & 0 & Q_{66} & 0 & 0 \\ 0 & 0 & 0 & Q_{55} & 0 \\ 0 & 0 & 0 & 0 & Q_{44} \end{bmatrix} \begin{Bmatrix} \varepsilon_{xx} \\ \varepsilon_{yy} \\ \gamma_{xy} \\ \gamma_{xz} \\ \gamma_{yz} \end{Bmatrix} \tag{9}$$

where

$$Q_{11} = Q_{22} = \frac{E_{eff}}{1 - \nu_{eff}^2}, Q_{12} = \frac{\nu_{eff} E_{eff}}{1 - \nu_{eff}^2}, Q_{66} = Q_{55} = Q_{44} = \frac{E_{eff}}{2(1 + \nu_{eff})} \tag{10}$$

where E_{eff} and ν_{eff} are the effective Young module and Poisson’s ratio according to Eq. (2), respectively.

The discrete Galerkin weak form for essential equations of the FGM plate under all transverse loading q_0 and the thermal effect are described by

$$\int_{\Omega} \delta \begin{Bmatrix} \varepsilon^0 \\ \varepsilon^1 \\ \varepsilon^2 \end{Bmatrix}^T \begin{bmatrix} \mathbf{A}^b & \mathbf{B}^b & \mathbf{E} \\ \mathbf{B}^b & \mathbf{D}^b & \mathbf{F1} \\ \mathbf{E} & \mathbf{F1} & \mathbf{H} \end{bmatrix} \begin{Bmatrix} \varepsilon^0 \\ \varepsilon^1 \\ \varepsilon^2 \end{Bmatrix} d\Omega + \int_{\Omega} \delta \begin{Bmatrix} \varepsilon^{s0} \\ \varepsilon^{s1} \end{Bmatrix}^T \begin{bmatrix} \mathbf{A}^s & \mathbf{B}^s \\ \mathbf{B}^s & \mathbf{D}^s \end{bmatrix} \begin{Bmatrix} \varepsilon^{s0} \\ \varepsilon^{s1} \end{Bmatrix} d\Omega - \int_{\Omega} \delta \begin{Bmatrix} \varepsilon^0 \\ \varepsilon^1 \\ \varepsilon^2 \end{Bmatrix} \begin{Bmatrix} \mathbf{Ith} \\ \mathbf{Jth} \\ \mathbf{Sth} \end{Bmatrix} d\Omega = \int_{\Omega} \delta w_0 q_0 d\Omega \tag{11}$$

where

$$\begin{aligned} \left(A_{ij}^b, B_{ij}^b, D_{ij}^b, E_{ij}, F1_{ij}, H_{ij} \right)^{(k)} &= \int_{-h/2}^{h/2} \left(1, z, z^2, f(z), zf(z), f^2(z) \right) Q_{ij}^k dz \text{ where } (i, j = 1, 2, 6) \\ \left(A_{ij}^s, B_{ij}^s, D_{ij}^s \right)^{(k)} &= \int_{-h/2}^{h/2} \left(1, f'(z), f'^2(z) \right) Q_{ij}^k dz \text{ where } (i, j = 4, 5) \\ \{ \mathbf{Ith} \mathbf{Jth} \mathbf{Sth} \} &= \int_{-h/2}^{h/2} \mathbf{Q} \{ \alpha_x \quad \alpha_y \quad \alpha_{xy} \}^T \{ 1 \quad z \quad f(z) \} \Delta T dz \end{aligned} \tag{12}$$

2.3 Moving Kriging Interpolation Shape Functions

The moving Kriging interpolation shape functions are chosen to interpolate kinematic variables in FGM plates. The domain Ω is discretized by a set of nodes \mathbf{x}_I ($I = 1, \dots, NP$), in which NP is the quantity of the nodes. The moving Kriging interpolation of a variable $u(\mathbf{x})$, defined by $u^h(\mathbf{x})$, can be written as follows:

$$u^h(\mathbf{x}) = \sum_{I=1}^{NP} \phi_I(\mathbf{x})u_I \tag{13}$$

where ϕ_I and u_I are the shape function and the unknown coefficient associated with node I , and

$$\phi_I(\mathbf{x}) = \sum_{j=1}^m p_j(\mathbf{x})A_{jI} + \sum_{k=1}^n r_k(\mathbf{x})B_{kI} \text{ or } \phi_I(\mathbf{x}) = \mathbf{p}^T(\mathbf{x})\mathbf{A} + \mathbf{r}^T(\mathbf{x})\mathbf{B} \tag{14}$$

in which n and m are number of nodes in a support domain $\Omega_x \in \Omega$ (see Fig. 1) and the order of polynomial basis function, respectively. Four terms of \mathbf{A} , \mathbf{B} , $\mathbf{P}(\mathbf{x})$, and $\mathbf{r}(\mathbf{x})$ are defined as follows:

$$\mathbf{A} = (\mathbf{P}^T \mathbf{R}^{-1} \mathbf{P})^{-1} \mathbf{P}^T \mathbf{R}^{-1}, \mathbf{B} = \mathbf{R}^{-1}(\mathbf{I} - \mathbf{P}\mathbf{A}) \tag{15}$$

$$\mathbf{p}(\mathbf{x}) = \{ 1 \quad x \quad y \quad x^2 \quad xy \quad y^2 \quad \dots \}^T \text{ and}$$

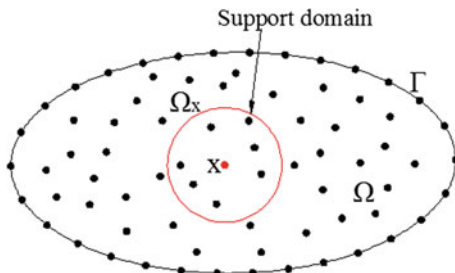
$$\mathbf{r}(\mathbf{x}) = [R(\mathbf{x}_1, \mathbf{x}) \quad R(\mathbf{x}_2, \mathbf{x}) \quad \dots \quad R(\mathbf{x}_n, \mathbf{x})]^T$$

where \mathbf{I} is a unit matrix with the size $n \times n$.

For two-dimensional problem, the polynomial basis function of quadratic form is chosen as:

$$\mathbf{p}(\mathbf{x}) = \{ 1 \quad x \quad y \quad x^2 \quad xy \quad y^2 \quad \dots \}^T (m=6) \tag{16}$$

Fig. 1 Domain representation and support domain of 2D model



In addition, two matrices \mathbf{P} and \mathbf{R} are expressed by:

$$\mathbf{p} = \begin{bmatrix} p_1(\mathbf{x}_1) & \dots & p_m(\mathbf{x}_1) \\ \dots & \dots & \dots \\ p_1(\mathbf{x}_n) & \dots & p_m(\mathbf{x}_n) \end{bmatrix} \text{ and } \mathbf{R} = \begin{bmatrix} R(\mathbf{x}_1, \mathbf{x}_1) & \dots & R(\mathbf{x}_1, \mathbf{x}_n) \\ \dots & \dots & \dots \\ R(\mathbf{x}_n, \mathbf{x}_1) & \dots & R(\mathbf{x}_n, \mathbf{x}_n) \end{bmatrix} \quad (17)$$

where $R(\mathbf{x}_I, \mathbf{x}_J)$ is a correlation function and is defined by:

$$R(\mathbf{x}_I, \mathbf{x}_J) = \frac{1}{2} E \left[(u^h(\mathbf{x}_I) - u^h(\mathbf{x}_J))^2 \right] \quad (18)$$

in which E defines an expected value of a random function.

The correlation function $R(\mathbf{x}_I, \mathbf{x}_J)$, which can be multi-quadrics, thin plate splines, Gaussian, etc., can be chosen to build MKI shape function. In this chapter, we use the Gaussian function described by:

$$R(\mathbf{x}_I, \mathbf{x}_J) = e^{-\left(\frac{\beta r_{IJ}}{a_0}\right)^2} \quad (19)$$

where $r_{IJ} = \|\mathbf{x}_I - \mathbf{x}_J\|$; the correlation parameter β is related to the variance σ^2 of the normal distribution function $\beta^2 = 1/2\sigma^2$, and a_0 is the scale factor used to normalize the distance. The maximum distance between a pair of nodes in the support domain is chosen for this value. In addition, the correlation parameter is fixed to be equal to 1 ($\beta = 1$).

The first-order derivative of the MKI shape functions is written as follows:

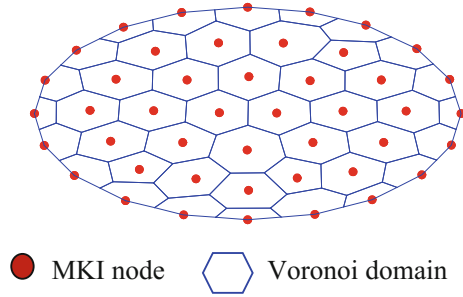
$$\phi_{I,x}(\mathbf{x}) = \sum_{j=1}^m p_{j,x}(\mathbf{x})A_{jI} + \sum_{k=1}^n r_{k,x}(\mathbf{x})B_{kI} \text{ and } \phi_{I,y}(\mathbf{x}) = \sum_{j=1}^m p_{j,y}(\mathbf{x})A_{jI} + \sum_{k=1}^n r_{k,y}(\mathbf{x})B_{kI} \quad (20)$$

Generally speaking, to construct the shape functions for meshfree methods, a support domain (influence domain) of nodes is needed. For this reason, a circular influence domain with a support size is defined as:

$$d_m = \alpha d_c \quad (21)$$

where d_c describes an average distance between nodes, and α stands for a scale factor. In the numerical computation, the radius of influence domain is large enough to support a sufficient number of nodes to construct shape functions. In this study, a circular support domain with a radius fixed at 2.4 times nodal spacing ($\alpha = 2.4$) is used in the numerical computation.

Fig. 2 Geometry of a representative node domain and its Voronoi domain



2.4 Nodal Integration Formulations for FGM Plates Based on the C_0 -Type HSDT

Generally, there are two types of integration for the Galerkin weak form in Eq. (11), including the Gauss quadrature and nodal integration. As presented in the introduction section, the nodal integration has more advantages than the Gauss integration. To apply nodal integration scheme, the problem domain Ω is needed to be divided into a set of non-overlapping sub-domains Ω_I ($I = 1, 2, \dots, NP$), where each of which includes a node ($\Omega = \sum_{I=1}^{NP} \Omega_I$), as shown in Fig. 2. For any distributed nodes according to Fig. 2, a Voronoi diagram can always be generated automatically. Based on this Voronoi geometry, the weak form for thermo-mechanical analysis can be directly computed at the nodes as follows:

$$\sum_{I=1}^{NP} \int_{\Omega_I} \delta \begin{Bmatrix} \varepsilon^0 \\ \varepsilon^1 \\ \varepsilon^2 \end{Bmatrix}^T \begin{bmatrix} \mathbf{A}^b & \mathbf{B}^b & \mathbf{E} \\ \mathbf{B}^b & \mathbf{D}^b & \mathbf{F1} \\ \mathbf{E} & \mathbf{F1} & \mathbf{H} \end{bmatrix} \begin{Bmatrix} \varepsilon^0 \\ \varepsilon^1 \\ \varepsilon^2 \end{Bmatrix} d\Omega_I + \sum_{I=1}^{NP} \int_{\Omega_I} \delta \begin{Bmatrix} \varepsilon^{s0} \\ \varepsilon^{s1} \end{Bmatrix}^T \begin{bmatrix} \mathbf{A}^s & \mathbf{B}^s \\ \mathbf{B}^s & \mathbf{D}^s \end{bmatrix} \begin{Bmatrix} \varepsilon^{s0} \\ \varepsilon^{s1} \end{Bmatrix} d\Omega_I - \sum_{I=1}^{NP} \int_{\Omega_I} \delta \begin{Bmatrix} \varepsilon^0 \\ \varepsilon^1 \\ \varepsilon^2 \end{Bmatrix} \begin{Bmatrix} \mathbf{I}th \\ \mathbf{J}th \\ \mathbf{S}th \end{Bmatrix} d\Omega_I = \sum_{I=1}^{NP} \int_{\Omega_I} \delta w_{0I} q_0 d\Omega_I \tag{22}$$

3 Naturally Stabilized Nodal Integration

The naturally stabilized nodal integration scheme, which is a naturally implicit gradient expansion of the displacements field in Eq. (13), was proposed by Hillman and Chen [17] for the two-dimensional problem. Moreover, it is also extended for the laminated composite plate by Thai et al. [18] as follows:

$$\mathbf{u}^h(\mathbf{x}) \approx \sum_I^{NP} \phi_I(\bar{\mathbf{x}}) \mathbf{q}_I + \sum_I^{NP} \nabla \phi_I(\bar{\mathbf{x}}) (\mathbf{x} - \bar{\mathbf{x}}) \mathbf{q}_I \quad (23)$$

where ‘.’ defines an inner product, and $\nabla \phi_I(\bar{\mathbf{x}})$ is the derivation of shape function $\phi_I(\bar{\mathbf{x}})$. To reduce the order of high-order derivations in the approximation formulation, a new shape function ϕ_I is constructed so that the following condition is satisfied:

$$\sum_I^{NP} \phi_I(\bar{\mathbf{x}}) \mathbf{q}_I + \sum_I^{NP} \nabla \phi_I(\bar{\mathbf{x}}) \mathbf{q}_I = \hat{\mathbf{u}}^h(\mathbf{x}) \quad (24)$$

The condition in Eq. (24) is easily obtained in the MKI as

$$\phi_I(\mathbf{x}) = \sum_{j=1}^m p_{j,x}(\mathbf{x}) A_{jI} + \sum_{k=1}^n r_{k,x}(\mathbf{x}) B_{kI}; \quad \phi_{Iy}(\mathbf{x}) = \sum_{j=1}^m p_{j,y}(\mathbf{x}) A_{jI} + \sum_{k=1}^n r_{k,y}(\mathbf{x}) B_{kI} \quad (25)$$

The implicit gradient expansion in Eq. (23) naturally leads to the stabilized integration scheme while computing the displacements and strains at each node. Inserting Eq. (23) into Eq. (8), the bending and shear strains with nodal integration zones at $\bar{\mathbf{x}} = \mathbf{x}_I$ are described as:

$$\begin{aligned} \boldsymbol{\varepsilon}_I^0(\mathbf{u}^h(\mathbf{x})) &\approx \bar{\boldsymbol{\varepsilon}}_I^0(\bar{\mathbf{u}}^h(\mathbf{x}_I)) + (x - x_I) \boldsymbol{\varepsilon}_{xI}^0(\hat{\mathbf{u}}_x^h(\mathbf{x}_I)) + (y - y_I) \boldsymbol{\varepsilon}_{yI}^0(\hat{\mathbf{u}}_y^h(\mathbf{x}_I)); \\ \boldsymbol{\varepsilon}_I^1(\mathbf{u}^h(\mathbf{x})) &\approx \bar{\boldsymbol{\varepsilon}}_I^1(\bar{\mathbf{u}}^h(\mathbf{x}_I)) + (x - x_I) \boldsymbol{\varepsilon}_{xI}^1(\hat{\mathbf{u}}_x^h(\mathbf{x}_I)) + (y - y_I) \boldsymbol{\varepsilon}_{yI}^1(\hat{\mathbf{u}}_y^h(\mathbf{x}_I)); \\ \boldsymbol{\varepsilon}_I^2(\mathbf{u}^h(\mathbf{x})) &\approx \bar{\boldsymbol{\varepsilon}}_I^2(\bar{\mathbf{u}}^h(\mathbf{x}_I)) + (x - x_I) \boldsymbol{\varepsilon}_{xI}^2(\hat{\mathbf{u}}_x^h(\mathbf{x}_I)) + (y - y_I) \boldsymbol{\varepsilon}_{yI}^2(\hat{\mathbf{u}}_y^h(\mathbf{x}_I)); \\ \boldsymbol{\varepsilon}_I^{s0}(\mathbf{u}^h(\mathbf{x})) &\approx \bar{\boldsymbol{\varepsilon}}_I^{s0}(\bar{\mathbf{u}}^h(\mathbf{x}_I)) + (x - x_I) \boldsymbol{\varepsilon}_{xI}^{s0}(\hat{\mathbf{u}}_x^h(\mathbf{x}_I)) + (y - y_I) \boldsymbol{\varepsilon}_{yI}^{s0}(\hat{\mathbf{u}}_y^h(\mathbf{x}_I)); \\ \boldsymbol{\varepsilon}_I^{s1}(\mathbf{u}^h(\mathbf{x})) &\approx \bar{\boldsymbol{\varepsilon}}_I^{s1}(\bar{\mathbf{u}}^h(\mathbf{x}_I)) + (x - x_I) \boldsymbol{\varepsilon}_{xI}^{s1}(\hat{\mathbf{u}}_x^h(\mathbf{x}_I)) + (y - y_I) \boldsymbol{\varepsilon}_{yI}^{s1}(\hat{\mathbf{u}}_y^h(\mathbf{x}_I)) \end{aligned} \quad (26)$$

where

$$\bar{\mathbf{u}}^h(\mathbf{x}_I) = \sum_I^{NP} \phi_I(\mathbf{x}) \mathbf{q}_I; \quad \hat{\mathbf{u}}_x^h(\mathbf{x}_I) = \sum_I^{NP} \phi_{Ix}(\mathbf{x}_I) \mathbf{q}_I; \quad \hat{\mathbf{u}}_y^h(\mathbf{x}_I) = \sum_I^{NP} \phi_{Iy}(\mathbf{x}_I) \mathbf{q}_I \quad (27)$$

A compact form of the bending and shear strains can be rewritten as:

$$\begin{aligned} \boldsymbol{\varepsilon}_I^0 &\approx \mathbf{B}_I^0 \mathbf{q}_I + (x - x_I) \mathbf{B}_{Ix}^0 \mathbf{q}_I + (y - y_I) \mathbf{B}_{Iy}^0 \mathbf{q}_I; \quad \boldsymbol{\varepsilon}_I^1 \approx \mathbf{B}_I^1 \mathbf{q}_I + (x - x_I) \mathbf{B}_{Ix}^1 \mathbf{q}_I + (y - y_I) \mathbf{B}_{Iy}^1 \mathbf{q}_I; \\ \boldsymbol{\varepsilon}_I^2 &\approx \mathbf{B}_I^2 \mathbf{q}_I + (x - x_I) \mathbf{B}_{Ix}^2 \mathbf{q}_I + (y - y_I) \mathbf{B}_{Iy}^2 \mathbf{q}_I; \quad \boldsymbol{\varepsilon}_I^{s0} \approx \mathbf{B}_I^{s0} \mathbf{q}_I + (x - x_I) \mathbf{B}_{Ix}^{s0} \mathbf{q}_I + (y - y_I) \mathbf{B}_{Iy}^{s0} \mathbf{q}_I; \\ \boldsymbol{\varepsilon}_I^{s1} &\approx \mathbf{B}_I^{s1} \mathbf{q}_I + (x - x_I) \mathbf{B}_{Ix}^{s1} \mathbf{q}_I + (y - y_I) \mathbf{B}_{Iy}^{s1} \mathbf{q}_I \end{aligned} \quad (28)$$

where

$$\mathbf{B}_I^0 = \begin{bmatrix} \phi_{I,x} & 0 & 0 & 0 & 0 & 0 & 0 \\ 0 & \phi_{I,y} & 0 & 0 & 0 & 0 & 0 \\ \phi_{I,y} & \phi_{I,x} & 0 & 0 & 0 & 0 & 0 \end{bmatrix}; \mathbf{B}_{Ix}^0 = \begin{bmatrix} \phi_{Ix,x} & 0 & 0 & 0 & 0 & 0 & 0 \\ 0 & \phi_{I,y} & 0 & 0 & 0 & 0 & 0 \\ \phi_{I,y} & \phi_{I,x} & 0 & 0 & 0 & 0 & 0 \end{bmatrix} \quad (29)$$

$$\begin{aligned} \mathbf{B}_{Iy}^0 &= \begin{bmatrix} \phi_{Ix,x} & 0 & 0 & 0 & 0 & 0 & 0 \\ 0 & \phi_{I,y} & 0 & 0 & 0 & 0 & 0 \\ \phi_{I,y} & \phi_{I,x} & 0 & 0 & 0 & 0 & 0 \end{bmatrix}; \mathbf{B}_I^1 = - \begin{bmatrix} 0 & 0 & 0 & 0 & 0 & \phi_{I,x} & 0 \\ 0 & 0 & 0 & 0 & 0 & 0 & \phi_{I,y} \\ 0 & 0 & 0 & 0 & 0 & \phi_{I,y} & \phi_{I,x} \end{bmatrix}; \\ \mathbf{B}_{Ix}^1 &= - \begin{bmatrix} 0 & 0 & 0 & 0 & 0 & \phi_{Ix,x} & 0 \\ 0 & 0 & 0 & 0 & 0 & 0 & \phi_{Ix,y} \\ 0 & 0 & 0 & 0 & 0 & \phi_{Ix,y} & \phi_{Ix,x} \end{bmatrix}; \mathbf{B}_{Iy}^1 = - \begin{bmatrix} 0 & 0 & 0 & 0 & 0 & \phi_{Iy,x} & 0 \\ 0 & 0 & 0 & 0 & 0 & 0 & \phi_{Iy,y} \\ 0 & 0 & 0 & 0 & 0 & \phi_{Iy,y} & \phi_{Iy,x} \end{bmatrix}; \\ \mathbf{B}_I^2 &= - \begin{bmatrix} 0 & 0 & 0 & \phi_{I,x} & 0 & 0 & 0 \\ 0 & 0 & 0 & 0 & \phi_{I,y} & 0 & 0 \\ 0 & 0 & 0 & \phi_{I,y} & \phi_{I,x} & 0 & 0 \end{bmatrix}; \mathbf{B}_{Ix}^2 = - \begin{bmatrix} 0 & 0 & 0 & \phi_{Ix,x} & 0 & 0 & 0 \\ 0 & 0 & 0 & 0 & \phi_{Ix,y} & 0 & 0 \\ 0 & 0 & 0 & \phi_{Ix,y} & \phi_{Ix,x} & 0 & 0 \end{bmatrix}; \\ \mathbf{B}_{Iy}^2 &= - \begin{bmatrix} 0 & 0 & 0 & \phi_{Iy,x} & 0 & 0 & 0 \\ 0 & 0 & 0 & 0 & \phi_{Iy,y} & 0 & 0 \\ 0 & 0 & 0 & \phi_{Iy,y} & \phi_{Iy,x} & 0 & 0 \end{bmatrix}; \mathbf{B}_I^{s0} = \begin{bmatrix} 0 & 0 & \phi_{I,x} & 0 & 0 & -\phi_I & 0 \\ 0 & 0 & \phi_{I,y} & 0 & 0 & 0 & -\phi_I \end{bmatrix}; \\ \mathbf{B}_{Ix}^{s0} &= \begin{bmatrix} 0 & 0 & \phi_{Ix,x} & 0 & 0 & -\phi_{Ix} & 0 \\ 0 & 0 & \phi_{Ix,y} & 0 & 0 & 0 & -\phi_{Ix} \end{bmatrix}; \mathbf{B}_{Iy}^{s0} = \begin{bmatrix} 0 & 0 & \phi_{Iy,x} & 0 & 0 & -\phi_{Iy} & 0 \\ 0 & 0 & \phi_{Iy,y} & 0 & 0 & 0 & -\phi_{Iy} \end{bmatrix}; \\ \mathbf{B}_I^{s1} &= \begin{bmatrix} 0 & 0 & 0 & \phi_{I,x} & 0 & 0 & 0 \\ 0 & 0 & 0 & 0 & \phi_{I,y} & 0 & 0 \end{bmatrix}; \mathbf{B}_{Ix}^{s1} = \begin{bmatrix} 0 & 0 & 0 & \phi_{Ix,x} & 0 & 0 & 0 \\ 0 & 0 & 0 & 0 & -\phi_{Ix,y} & 0 & 0 \end{bmatrix}; \end{aligned}$$

$$\mathbf{B}_{Iy}^{s1} = \begin{bmatrix} 0 & 0 & 0 & -\phi_{Iy,x} & 0 & 0 & 0 \\ 0 & 0 & 0 & 0 & -\phi_{Iy,y} & 0 & 0 \end{bmatrix};$$

Substituting the expansions in Eq. (28) into Eq. (22) and ignoring the zero terms ($\int_{\Omega_I} (x-x_I)d\Omega_I = \int_{\Omega_I} (y-y_I)d\Omega_I = 0$), the weak form for bending thermo-mechanical analysis with naturally stabilized nodal integration is rewritten in the compact form of equation:

$$\mathbf{Kq} = \mathbf{F} + \mathbf{F}th \quad (30)$$

where \mathbf{K} , \mathbf{F} , and $\mathbf{F}th$ are the global stiffness matrix, force vector, and thermal load vector, respectively, in which:

$$\mathbf{K} = \mathbf{K}_0 + \mathbf{K}_x + \mathbf{K}_y \tag{31}$$

and

$$\begin{aligned} \mathbf{K}_0 &= \sum_{I=1}^{NP} \left(\begin{matrix} \mathbf{B}_I^0 \\ \mathbf{B}_I^1 \\ \mathbf{B}_I^2 \end{matrix} \right)^T \begin{bmatrix} \mathbf{A}^b & \mathbf{B}^b & \mathbf{E} \\ \mathbf{B}^b & \mathbf{D}^b & \mathbf{F1} \\ \mathbf{E} & \mathbf{F1} & \mathbf{H} \end{bmatrix} \begin{matrix} \mathbf{B}_I^0 \\ \mathbf{B}_I^1 \\ \mathbf{B}_I^2 \end{matrix} \Bigg\} + \left\{ \begin{matrix} \mathbf{B}_I^{s0} \\ \mathbf{B}_I^{s1} \end{matrix} \right\}^T \begin{bmatrix} \mathbf{A}^s & \mathbf{B}^s \\ \mathbf{B}^s & \mathbf{D}^s \end{bmatrix} \begin{matrix} \mathbf{B}_I^{s0} \\ \mathbf{B}_I^{s1} \end{matrix} \Bigg\} W_I; \\ \mathbf{K}_x &= \sum_{I=1}^{NP} \left(\begin{matrix} \mathbf{B}_{Ix}^0 \\ \mathbf{B}_{Ix}^1 \\ \mathbf{B}_{Ix}^2 \end{matrix} \right)^T \begin{bmatrix} \mathbf{A}^b & \mathbf{B}^b & \mathbf{E} \\ \mathbf{B}^b & \mathbf{D}^b & \mathbf{F1} \\ \mathbf{E} & \mathbf{F1} & \mathbf{H} \end{bmatrix} \begin{matrix} \mathbf{B}_{Ix}^0 \\ \mathbf{B}_{Ix}^1 \\ \mathbf{B}_{Ix}^2 \end{matrix} \Bigg\} + \left\{ \begin{matrix} \mathbf{B}_{Ix}^{s0} \\ \mathbf{B}_{Ix}^{s1} \end{matrix} \right\}^T \begin{bmatrix} \mathbf{A}^s & \mathbf{B}^s \\ \mathbf{B}^s & \mathbf{D}^s \end{bmatrix} \begin{matrix} \mathbf{B}_{Ix}^{s0} \\ \mathbf{B}_{Ix}^{s1} \end{matrix} \Bigg\} M_{Ix}; \\ \mathbf{K}_y &= \sum_{I=1}^{NP} \left(\begin{matrix} \mathbf{B}_{Iy}^0 \\ \mathbf{B}_{Iy}^1 \\ \mathbf{B}_{Iy}^2 \end{matrix} \right)^T \begin{bmatrix} \mathbf{A}^b & \mathbf{B}^b & \mathbf{E} \\ \mathbf{B}^b & \mathbf{D}^b & \mathbf{F1} \\ \mathbf{E} & \mathbf{F1} & \mathbf{H} \end{bmatrix} \begin{matrix} \mathbf{B}_{Iy}^0 \\ \mathbf{B}_{Iy}^1 \\ \mathbf{B}_{Iy}^2 \end{matrix} \Bigg\} + \left\{ \begin{matrix} \mathbf{B}_{Iy}^{s0} \\ \mathbf{B}_{Iy}^{s1} \end{matrix} \right\}^T \begin{bmatrix} \mathbf{A}^s & \mathbf{B}^s \\ \mathbf{B}^s & \mathbf{D}^s \end{bmatrix} \begin{matrix} \mathbf{B}_{Iy}^{s0} \\ \mathbf{B}_{Iy}^{s1} \end{matrix} \Bigg\} M_{Iy}; \end{aligned} \tag{32}$$

$$\mathbf{F} = \sum_{I=1}^{NP} q_0 \{ 0 \ 0 \ w_{0I} \ 0 \ 0 \ 0 \ 0 \}^T W_I;$$

$$\mathbf{Fth} = \sum_{I=1}^{NP} \left\{ (\mathbf{B}_I^0)^T \mathbf{I}th + (\mathbf{B}_I^1)^T \mathbf{J}th + (\mathbf{B}_I^2)^T \mathbf{S}th \right\} W_I$$

in which $W_I = \int_{\Omega_I} d\Omega_I, M_{Ix} = \int_{\Omega_I} (x - x_I)^2 d\Omega_I$, and $M_{Iy} = \int_{\Omega_I} (y - y_I)^2 d\Omega_I$ in Eq. (32) are the area and the second moments of inertia of each nodal domain, respectively.

4 Numerical Examples and Discussions

4.1 FGM Circular Plate Subjected to the Mechanical Loading

Firstly, an FGM circular plate with a radius R and thickness h under a uniform transverse loading q_0 is studied. We consider two different types of boundary conditions as simply supported and fully clamped. Figure 3 shows the geometry and distributed node (567 nodes) of the circular plate, respectively. The plate is made from Ti/ZrO2-1, as shown in Table 1. The material properties are homogenized following the rule of mixture:

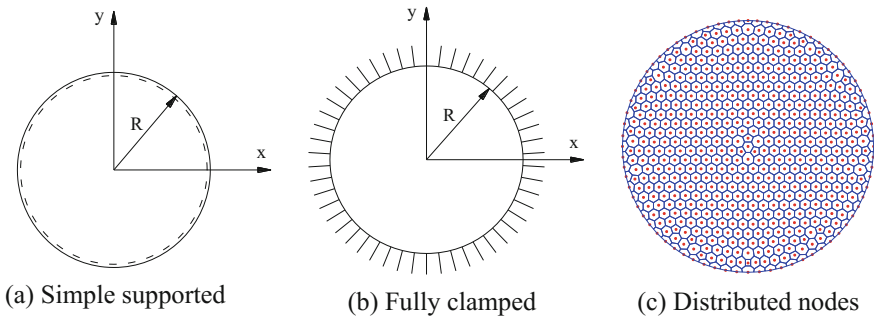


Fig. 3 Circular plates

Table 1 Material properties

	Al	Ti	ZrO ₂ -1	ZrO ₂ -2
E (GPa)	70	278.41	110.25	151
ν	0.3	0.288	0.288	0.3
k (W/mK)	204	–	–	2.09
α (°C)	23×10^{-6}	–	–	10×10^{-6}

$$E_{eff} = E_c V_c(z) + E_m V_m(z); \nu_{eff} = \nu_c V_c(z) + \nu_m V_m(z); V_m(z) = \left(\frac{1}{2} - \frac{z}{h}\right)^n; V_c = 1 - V_m \tag{33}$$

Various radius-to-thickness ratios and power index values are investigated. The central displacement is normalized by $\bar{w} = w \frac{E_c h^3}{12(1-\nu_c^2)} \times \frac{64}{q_0 R^4}$, where E_c and ν_c are Young’s modulus and Poisson’s ratio of the ceramic, respectively. Figure 4 plots the

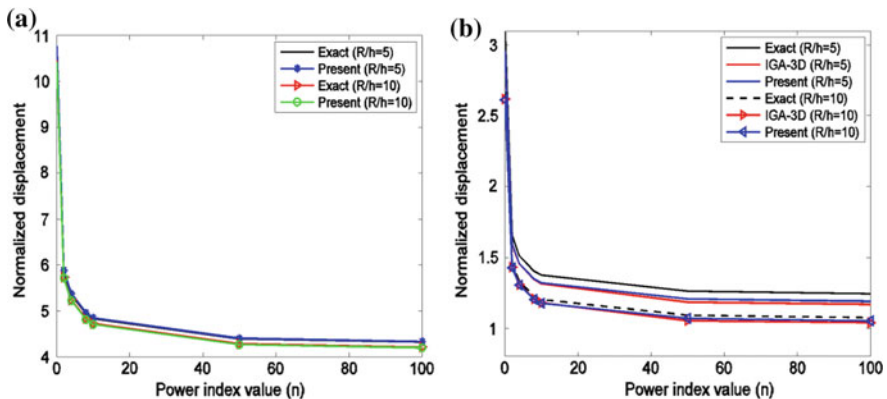


Fig. 4 Normalized central displacement of circular plates: a simply supported; b fully clamped

normalized central displacement of the present solution, an exact solution based on 3D elasticity theory [19] and an isogeometric analysis (IGA) based on 3D elasticity theory [20] corresponding with two boundary conditions. It can be seen that the present solution matches well with the exact solution [19] for the simply supported case, while it is between the exact solution [19] and the IGA solution for fully clamped case. It can be also observed that the normalized central displacement is decreased by increasing the radius-to-thickness ratios and power index values. In addition, the normalized central displacement is decreased when increasing the radius/thickness ratio.

4.2 FGM Square Plate Subjected to Thermo-Mechanical Loading

We consider an Al/ZrO₂-2 FGM simply supported square plate subjected to thermo-mechanical loading. The properties for Al/ZrO₂-2 materials are listed in Table 1 and are homogenized following the rule of mixture by Eq. (1). The length-to-thickness ratio is taken equal to 20. The central displacement and load parameter are normalized as: $\bar{w} = \frac{w}{h}$ and $\bar{P} = \frac{q_0 a^4}{E_m h^4}$, respectively, in which E_m is the Young module of metal.

The FGM square plate subjected to temperature field is firstly studied corresponding to various values of power index n . The temperature at the top (ceramic) surface is changed from 0 to 600 °C, while the bottom (metal) surface is fixed to 20 °C. The normalized central displacements of FGM plate under a thermal loading corresponding with various index values is shown in Fig. 5a. We observe that the maximum displacement is the metal surface (bottom surface), which is very sensitive to temperature. Moreover, the obtained displacement of isotropic plates, e.g.,

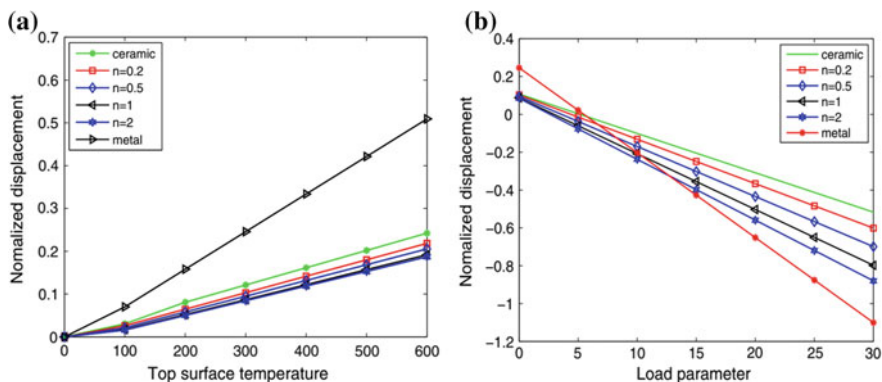


Fig. 5 Normalized central displacement for various values of volume fraction exponent: **a** thermal load; **b** thermo-mechanical load

fully ceramic ($n = 0$) or fully metal ($n = \infty$) plates, are always much higher than those of FGM plates. It is concluded that the FGM plate is capable of performing well under the high-temperature environments.

Next, thermo-mechanical effect is considered for the FGM square plate. The temperature at the bottom (metal) and the top (ceramic) surfaces is fixed at 20 °C and 300 °C, respectively. The uniform load parameter P changes from 0 to 30. Again, the normalized central displacement of FGM square plate with various load parameters is plotted in Fig. 5b. The FGM plate is only subjected to thermal load or the load parameter $P = 0$, and the displacement amplitude is positive, as shown in Fig. 5b. In addition, the displacement amplitude of the plates varies from positive value to negative values corresponding with increasing the mechanical loading, in which the fully ceramic plate has the smallest displacement amplitude. The obtained results from Fig. 5 are similar to those results given in [21] by Aliaga and Reddy.

Acknowledgements This research is funded by Vietnam National Foundation for Science and Technology Development (NAFOSTED) under grant number 107.02-2016.19.

References

1. Brischetto S, Tomabene F, Fantuzzi N, Viola E (2016) 3D exact and 2D generalized differential quadrature models for free vibration analysis of functionally graded plates and cylinders. *Meccanica* 51:2059–2098
2. Swaminathan K, Naveenkumar DT, Zenkour AM, Carrera E (2015) Stress, vibration and buckling analyses of FGM plates-A state-of-the-art review. *Compos Struct* 120:10–31
3. Cheng ZQ, Batra RC (2000) Deflection relationships between the homogeneous Kirchhoff plate theory and different functionally graded plate theories. *Arch Mech* 52:143–158
4. Reddy JN (2000) Analysis of functionally graded plates. *Int J Numer Meth Eng* 684:663–684
5. Nguyen-Xuan H, Thai HC, Nguyen-Thoi T (2013) Isogeometric finite element analysis of composite sandwich plates using a higher order shear deformation theory. *Compos Part B Eng* 55:558–574
6. Nguyen NT, Thai HC, Nguyen-Xuan H (2016) On the general framework of high order shear deformation theories for laminated composite plate structures: a novel unified approach. *Int J Mech Sci* 110:242–255
7. Soldatos KP (1992) A transverse shear deformation theory for homogenous monoclinic plates. *Acta Mech* 94:195–220
8. Thai HC, Ferreira AJM, Rabczuk T, Bordas SPA, Nguyen-Xuan H (2014) Isogeometric analysis of laminated composite and sandwich plates using a new inverse trigonometric shear deformation theory. *Eur J Mech A Solids* 43:89–108
9. Thai HC, Kulasegaram S, Tran VL, Nguyen-Xuan H (2014) Generalized shear deformation theory for functionally graded isotropic and sandwich plates based on isogeometric approach. *Comput Struct* 141:94–112
10. Karama M, Afaq KS, Mistou S (2003) Mechanical behavior of laminated composite beam by new multi-layered laminated composite structures model with transverse shear stress continuity. *Int J Solids Struct* 40:1525–1546
11. Chen JS, Wu CT, Yoon S, You Y (2001) A stabilized conforming nodal integration for Galerkin mesh-free methods. *Int J Numer Meth Eng* 50:435–466

12. Hillman M, Chen JS, Chi SW (2014) Stabilized and variationally consistent nodal integration for meshfree modeling of impact problems. *Comput Part Mech* 1:245–256
13. Beissel S, Belytschko T (1996) Nodal integration of the element-free Galerkin method. *Comput Methods Appl Mech Eng* 139:49–74
14. Nagashima T (1999) Node-by-node meshless approach and its applications to structural analyses. *Int J Numer Meth Eng* 46:341–385
15. Liu GR, Zhang GY, Wang YY, Zhong ZH, Li GY, Han X (2007) A nodal integration technique for meshfree radial point interpolation method (NI-RPIM). *Int J Solids Struct* 44:3840–3890
16. Wu CT, Koishi M, Hu W (2015) A displacement smoothing induced strain gradient stabilization for the meshfree Galerkin nodal integration method. *Comput Mech* 56:19–37
17. Hillman M, Chen JS (2016) An accelerated, convergent, and stable nodal integration in Galerkin meshfree methods for linear and nonlinear mechanics. *Int J Numer Meth Eng* 107:603–630
18. Thai CH, Ferreira AJM, Nguyen-Xuan H (2017) Naturally stabilized nodal integration meshfree formulations for analysis of laminated composite and sandwich plates. *Compos Struct* 178:260–276
19. Li XY, Ding HJ, Chen WQ (2008) Elasticity solutions for a transversely isotropic functionally graded circular plate subject to an axisymmetric transverse load qr^k . *Int J Solids Struct* 45:191–210
20. Nguyen KD, Nguyen-Xuan H (2015) An isogeometric nite element approach for three-dimensional static and dynamic analysis of functionally graded material plate structures. *Compos Struct* 132:423–439
21. Aliaga JW, Reddy JN (2004) Nonlinear thermoelastic analysis of functionally graded plates using the third-order shear deformation theory. *Int J Eng Sci* 5:753–779

Nondestructive Vibrational Tests and Analytical Solutions to Determine the Young's Modulus of Rammed Earth Material



Quoc-Bao Bui

Abstract Rammed earth (RE) is a construction material which is manufactured from the soil. The soil is dynamically compacted at its optimum water content, inside a formwork to build a monolithic wall. The RE wall is composed of several layers, about 10–12 cm thick. In the last decades, RE material has been the focus of numerous scientific researches because of sustainable properties of this material: low embodied energy, positive hygrothermal behavior and a particular esthetic aspect. In several situations, nondestructive methods are needed to assess the mechanical characteristics of RE material, for both old and new RE constructions. This paper presents how in situ vibrational measurements can be used to identify the dynamic behavior of RE walls and to determine the Young's modulus of the RE walls measured. To determine Young's modulus from the dynamic characteristics, an analytical model based on Timoshenko's beam theory is presented, both for flexural and torsional modes. Then, the proposed analytical model is verified with measurements on several walls having different cross-sectional forms: rectangle and L-shape. The walls' natural frequencies were identified from the dynamic measurements by using the Frequency Domain Decomposition method. In parallel, for comparison, the Young's modulus of the RE material studied was also determined by classical static measurements (on the walls, prismatic and cylindrical specimens). The displacements were measured by using the Image Correlation technique. The comparisons showed that the results from the proposed analytical method provided high accuracies and better than that obtained by measurements on the usual specimens (prismatic and cylindrical).

Keywords Rammed earth • Natural frequencies • Young's modulus
Nondestructive testing • Sustainable development

Q.-B. Bui (✉)

Sustainable Developments in Civil Engineering Research Group,
Faculty of Civil Engineering, Ton Duc Thang University, Ho Chi Minh City, Vietnam
e-mail: buiquocbao@tdt.edu.vn

© Springer Nature Singapore Pte Ltd. 2018

H. Nguyen-Xuan et al. (eds.), *Proceedings of the International Conference on Advances in Computational Mechanics 2017*, Lecture Notes in Mechanical Engineering, https://doi.org/10.1007/978-981-10-7149-2_43

631

1 Introduction

Rammed earth (RE) is a construction material which is manufactured from the soil. The materials are sandy-clayey gravel soils that are compacted inside a formwork to build a monolithic wall. The soil composition varies greatly but should not include any organic components. The soil is compacted at its optimum water content, which provides the highest dry density for the given compaction energy [1]. The RE wall is composed of several layers. For each layer, the soil is put about 15 cm thick into a formwork and then rammed with a rammer (manual or pneumatic). After compaction, the thickness of each layer is typically about 10–12 cm. The procedure is repeated until the wall is completed. Figure 1 presents example of a school built with RE in France.

Recent scientific researches have focused on RE for three main reasons. First, the earthen construction is sustainable because it uses a natural and local material [2]. Second, the earth material can act as a natural moisture buffering for indoor environments [3]. Finally, the number of historic RE buildings in Europe and in the world remains high; maintaining this heritage requires scientific knowledge to have appropriate renovations [4].

Several research investigations have recently been conducted to study the properties of RE: durability, mechanical characteristics, and hygrothermal behavior. The in situ mechanical characteristics of RE walls now need to be determined using nondestructive or minor-destructive tests. Lombillo et al. [5] used minor-destructive techniques such as flat jack, hole-drilling, and mini-pressure meter.

In the present paper, the nondestructive technique using vibrational measurements (with accelerometers or velocimeters) to identify the dynamic characteristics (natural frequencies, mode shapes) will be investigated. From these dynamic characteristics, Young's modulus can be determined using a model. This technique has already been investigated for conventional materials [6, 7]. The application of this technique for nonconventional materials is also promising. In a previous study, Bui et al. [1] successfully applied this strategy to RE walls. In that study, the authors used a finite element model, and Young's modulus was determined by searching the best value giving the nearest natural frequencies in comparison with experimental values.

The present paper investigates an analytical method to provide the natural frequencies of RE walls. If this approach is validated, it can considerably reduce



Fig. 1 A school with walls in RE constructed recently in France, Architect: V. Rigassi

computer time and can be widely used, obviating the user’s need for special skills on finite element modeling. Indeed, although the analytical solutions for translational modes have been reported in the literature for conventional materials, to our knowledge, the analytical approach for torsional modes remains to be investigated and validated, most particularly for RE walls where an apparent inhomogeneity can be observed.

2 Analytical Model for Dynamic Behavior

RE wall is composed by different earthen layers, but it was showed that under small deformations, a homogeneous and isotropic model can be acceptable for RE material [1, 8]. During a nondestructive test by vibrational measurements, RE wall is still under small deformation. That is why RE wall is assumed to be homogeneous and isotropic in the analytical model.

Translational modes. Among many possible beam models for translational modes (flexural, shear, and Timoshenko’s beam), it is well known that the most robust model is Timoshenko, which can simultaneously take into account bending and shear behaviors [7]:

- the bending motion characterized by the bending parameter EI , where E and I are Young’s modulus and the flexural inertia moment, respectively.
- the shear motion characterized by the shear parameter GS_c , where G is the shear modulus ($G = E/[2(1 + \nu)]$, with ν representing Poisson’s ratio) and S_c is the shear cross section for Timoshenko’s beam: $S_c = 5/6 S$, with S the beam’s cross section.

It is well known in dynamic of structures that the horizontal translational motion of the section $u(x)$, where x is the position along the beam, is governed by:

$$EI \frac{\partial^4 u}{\partial x^4} + \frac{EI}{GS_c} \lambda \omega^2 \frac{\partial^2 u}{\partial x^2} - \lambda \omega^2 u = 0 \tag{1}$$

where ω is the angular frequency. The usual modal analysis applied to this Timoshenko beam, clamped at the base and free at the top, gives the k th eigen frequency [7]:

$$\omega_k^2 = \frac{\delta_k^4}{\frac{\lambda H^4}{EI} + \frac{\lambda H^2}{GS_c} \delta_k^2} \tag{2}$$

where H is the beam's height, λ is the linear density; δ_k can be determined by solving a system of two equations or can be taken as $\delta_k \approx 2k + 1$.

Torsional modes. The analytical solutions for torsional modes are less well reported in the literature than for translational modes. The demonstration will be detailed here.

Following the Strength of Materials theory:

$$\rho \cdot J \cdot \dot{\theta} = \frac{\partial M_t}{\partial x} \quad (3)$$

where M_t is the moment of torsion, ρ is the beam's density; J is the polar inertia moment of the section,

$$J = \iint_S r^2 dS = \frac{a^3 b}{12} + \frac{b^3 a}{12} \quad (a \text{ and } b: \text{ the edges of the section}) \quad (4)$$

On the other hand, following the theory of a Timoshenko's beam in torsion:

$$\frac{d\theta}{dx} = \frac{M_t}{G \cdot J_P} \Rightarrow M_t = G \cdot J_P \cdot \frac{d\theta}{dx} \quad (5)$$

where J_P is the torsional stiffness of the section:

$$J_P = \beta \cdot b \cdot a^3 \quad (6)$$

with β is the torsional constant depending on the cross-sectional dimensions (a and b).

For example, for a rectangle section: $\beta = \frac{1}{3} (1 - 0.63 \frac{a}{b})$.

θ is the angular rotation, in the harmonic regime:

$$\theta = \phi(x) \cdot e^{i\omega t} \quad (7)$$

From the above equations, the main equation of vibration can be obtained:

$$\phi''(x) + \frac{\rho \cdot J \cdot \omega^2}{G \cdot J_P} \phi(x) = 0 \quad (8)$$

The general solution of this equation: $\phi(x) = e^{i\delta x}$ and by replacing in the above equation, we have:

$$\phi(x) = A \cos \delta x + B \sin \delta x \quad (A \text{ and } B \text{ are constant}) \quad (9)$$

with

$$\delta = \pm \sqrt{\frac{\rho \cdot J}{G \cdot J_p}} \cdot \omega \tag{10}$$

Using the limit conditions for a beam clamped at the base and free at the top:

$$\phi(0) = 0; \quad M_t(H) = 0$$

we can determine constants A and B, so results of the Eigen frequencies can be obtained:

$$\omega = \sqrt{\frac{G \cdot J_p}{\rho \cdot J}} \cdot \frac{\pi}{2H}; \quad \omega_k = (2k - 1)\omega_1 \tag{11}$$

Inputs for the analytical model. From Eq. (2) for translational modes and Eq. (11) for torsional modes, the analytical models need the inputs: Young’s modulus E ; shear modulus G or Poisson’s ratio ν to calculate G from E ; the density ρ ; the wall dimensions: the height H and the cross section to calculate I , J_p , and J .

3 Assessing the Method on Rectangular Cross-Sectional Walls

Walls manufacturing. The earth used was provided by a RE company. The clay content in the soil used was approximately 19%. Water was added to the earth to obtain the optimum manufacturing water content [1], approximately 12% by weight in this case. The mixture was then compacted in layers into a formwork by using a pneumatic rammer. Each wall was built on a 0.25 m × 0.25 m × 1.8 m-long concrete beam (Fig. 2). The wall’s dimensions were (1.5 m high × 1.5 m wide × 0.25 m thick). Two walls (called A and B) were investigated in the present study.

The wall was unmolded from its formwork after the manufacturing and then cured at laboratory ambient conditions (20 °C and 60% relative humidity, RH) for 2 months. This is the time necessary to obtain quasi-dry specimens [1]. The moisture contents of the walls after 2 months were approximately 3% (determined after the tests). When an RE wall has been built, a 0.25 m × 0.25 m × 1.8 m concrete beam was placed on top of the wall (Fig. 2, on the left). This beam enabled the loading system to distribute the vertical loads uniformly from two vertical actuators on the top of the wall. Before installing the concrete beam, a thin lime mortar layer was added on the top surface of the wall to increase the bonding between the wall and the beam.

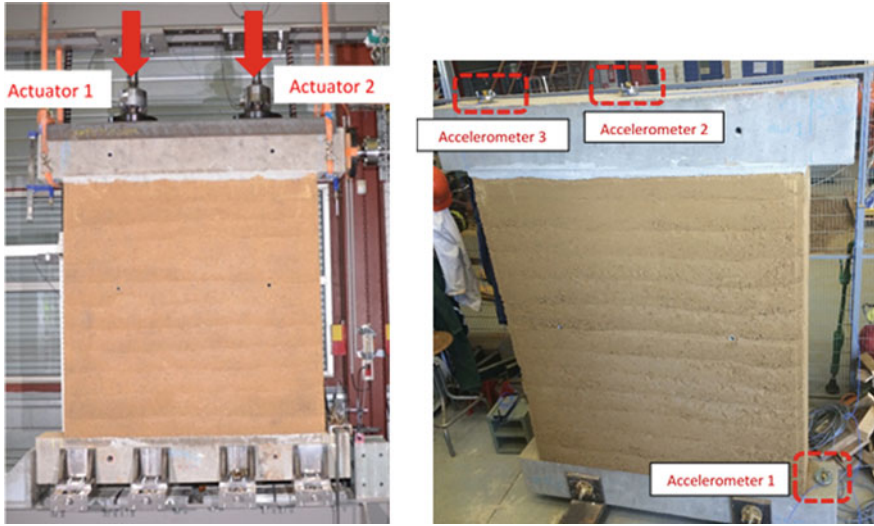


Fig. 2 Left: compression test setup on a RE wall. Right: dynamic test setup with accelerometers

Vibrational measurements. The sensors used were triaxial accelerometers that could measure accelerations in three perpendicular directions at the same time. For a measurement, three accelerometers were used (Fig. 2 on the right): accelerometer 1 was placed at the bottom of the RE wall, on the lower concrete beam; this accelerometer was used as a reference point to measure the movements of the wall's base. Accelerometers 2 and 3 were placed on the upper concrete beam to measure the vibration of the wall. Accelerometer 3, near the end of the beam, could capture torsional movements. The frequency of the data acquisition was 2048 Hz. For each wall, twelve measurements were carried out and for each measurement, the wall vibration was recorded for 10 min.

Dynamic data processing. The FDD method (Frequency Domain Decomposition [9]) was used to determine the natural frequencies and mode shapes from the dynamic measurements. Any displacement vector \mathbf{v} (static or dynamic) of a structure can be developed by superposing suitable amplitudes of the normal modes:

$$\mathbf{v}(t) = \Phi_1 q_1(t) + \Phi_2 q_2(t) + \dots + \Phi_N q_N(t) = \Phi \mathbf{q}(t) \quad (12)$$

In time domain, the covariance matrix of the responses:

$$\mathbf{R}_{\mathbf{v}\mathbf{v}}(\tau) = E\{\mathbf{v}(t+\tau)\mathbf{v}(t)^T\} \quad (13)$$

$$\Rightarrow \mathbf{R}_{\mathbf{v}\mathbf{v}}(\tau) = E\{\Phi \mathbf{q}(t+\tau)\mathbf{q}(t)^H \Phi^H\} = \Phi \mathbf{C}_{\mathbf{q}\mathbf{q}}(\tau) \Phi^H \quad (14)$$

H is the Hermitian transposed operator. The equivalent relation in the frequency domain is obtained by using the Fourier transform:

$$\mathbf{S}_{vv}(\omega) = \Phi \mathbf{S}_{qq}(\tau) \Phi^H \tag{15}$$

If the modal coordinates (q_1, q_2, \dots) are uncorrelated, then the power spectral density (PSD) matrix $\mathbf{S}_{qq}(\omega)$ is diagonal. And if the mode shapes are orthogonal, then the above equation is a singular value decomposition (SVD) of the response matrix $\mathbf{S}_{vv}(\omega)$.

Therefore, FDD is based on taking the SVD of the spectral density matrix:

$$\mathbf{S}_{vv}(\omega) = \mathbf{U}(\omega) [\mathbf{s}_i] \Phi(\omega)^H \tag{16}$$

The matrix $\mathbf{U}(\omega)$ is a matrix of singular vectors, and the matrix $[\mathbf{s}_i]$ is a diagonal matrix of singular values. As it appears from this explanation, plotting the singular values of the spectral density matrix will provide an overlaid plot of the auto spectral densities of the modal coordinates. Note that here the singular matrix $\mathbf{U}(\omega)$ is a function of frequency because of the sorting process that is taking place as a part of the SVD algorithm.

Dynamic experimental results. Table 1, in the second column, presents the experimental natural frequencies obtained from the dynamic measurements on Wall A.

Analytical results. The density of the tested wall was estimated by measuring the density of similar specimens (presented in the next section), which gave a density of 1860 kg/m^3 ; Poisson’s ratio was 0.22 [10]. It was observed that the dynamic behavior of RE walls was dominated by shear modes [11]; so the Poisson’s ratio (relative to bending modes) does not play an important role in this case.

Using equations in the previous section (Eq. (2) for translational modes and Eq. (11) for torsional modes) and by varying Young’s modulus E , the best-adapted value of E was determined. The “best” E was chosen as that the value which gave a minimum difference between first three modes of experiment and analytic. Only the first three modes were considered because they were the most important which were the first modes in each direction: vibrations in the transversal, longitudinal, and torsional directions. That means the minimum of a function g was sought with $g = (f_{1,a} - f_{1,e})^2 + (f_{2,a} - f_{2,e})^2 + (f_{3,a} - f_{3,e})^2$.

Table 1 Results from the dynamic tests and the analytical model, for Wall A

Mode	Experiment, f_e (Hz)	Analytic, with $E = 390 \text{ MPa}$, f_a (Hz)	Mode shape	f_a/f_e
Mode 1	6.0 ± 0.2	5.9	1st transversal	0.99
Mode 2	12.5 ± 0.3	12.7	1st torsion	1.01
Mode 3	30.3 ± 0.6	27.8	1st longitudinal	0.92
Mode 4	35.5 ± 0.9	35.9	2nd transversal	1.01
Mode 5	45.1 ± 2.2	39.2	2nd torsion	1.15

For Wall A, the results showed that the best Young's modulus of the measured wall was of 390 MPa. The corresponding frequencies are presented in the third column of Table 1, which shows a high accuracy for the first four modes (1–8% difference). The fifth mode (corresponding to the second torsional mode) showed a greater difference (15%), which may be influenced by the accuracy during the identification of the higher modes as mentioned above. The mode shapes of the analytical model were also checked, which corresponded to the experimental results.

In the same way, the Young's modulus of the Wall B was determined of 420 MPa.

4 Static Measurements

Devices: The experimental device consists of a steel loading frame having HEB400 cross sections. The bottom concrete beam was attached to the steel frame using four steel brackets that can be mechanically adjusted to provide satisfactory embedment (Fig. 1, left). To determine Young's modulus, the strain of the wall should be measured in the part corresponding to about 20% of the maximum stress [10]. For the tested wall, Young's modulus was calculated with the strains between 0 and 0.3 MPa because the mean compressive strengths obtained on cylindrical and prismatic specimens were about 1.5 MPa (see in the next section). Two electrical actuators were used to apply these vertical loads, at a rate of 1 kN/s, up to a normal stress of 0.3 MPa in the wall. The wall was not tested up to failure, because only Young's modulus was measured.

The DIC technique (digital image correlation) was used to measure the displacements of the walls during the test [12]. Before the test, one face of the wall was speckled to facilitate the DIC data processing after the test. The displacements at every point on this face were recorded during the test using a high-resolution camera (16 Mpixels). The images were recorded every 2 s. The displacement fields were determined by comparing the images taken after and before loading (reference image). The DIC data were processed with the 7D software.

To determine Young's modulus, the strains were calculated from the displacements of the middle part (following the height) of the wall (Fig. 3). The mean strain was the average of 5 values taken in this zone (an example can be found in Fig. 4). The mean Young's moduli obtained for walls A and B were of 391 ± 30 and 435 ± 25 MPa, respectively. It is worth noting that the variation was relatively important (about $\pm 8\%$) in the same zone. This can be explained by a non-homogeneity of the material studied. Table 2 illustrates the Young's moduli determined from the experimental and analytical approaches which shows the relevance of the results obtained by the analytical model. The differences between the analytical solutions and the experiments are less than 4%.

Tests on cylindrical and prismatic specimens. In practice, the mechanical characteristics of a material are usually measured on "standard" specimens:

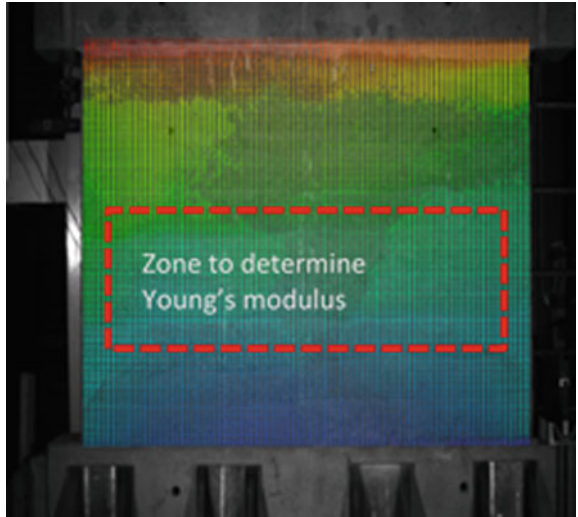


Fig. 3 Displacement vectors of the wall under the static loading

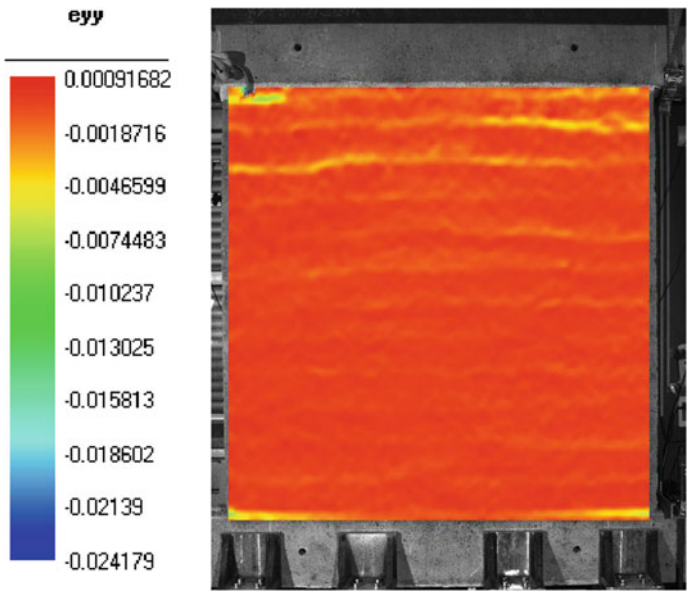


Fig. 4 Vertical strains at the end of the preloading phase of wall A determined from DIC

Table 2 Comparison of Young's moduli determined by two approaches

Wall number	$E_{\text{experimental}}$ (MPa)	$E_{\text{analytical}}$ (MPa)
A	391 ± 30	390
B	435 ± 25	420

representative element volumes (REVs) following the classical theory of Continuum Mechanics. For example, for the concrete in France, the current type is the cylindrical specimens with 16 cm in diameter and 32 cm high. For RE, several studies also used this type of specimen, although their representativeness remains questionable [1]. To assess the relevance of these specimens, small specimens were also manufactured and tested in uniaxial compression. Two types of specimen were studied: cylindrical and prismatic. Three cylindrical specimens (20 cm in diameter and 40 cm high), and three prismatic specimens (measured 25 cm × 25 cm × 50 cm high) were manufactured. The dimensions of these specimens were chosen to be able to reproduce the compaction energy applied to the walls during manufacturing (which has already been discussed in Bui et al. [1]). The specimens were compacted with the same soil, water content, and layer thickness of the walls. For the cylindrical specimens, a circular piston was used for the pneumatic rammer to facilitate the ramming on a circular section. The prismatic and cylindrical specimens were also unmolded after the manufacturing and were cured in laboratory ambient conditions (20 °C and 60% RH) for 2 months.

Prior to the unconfined compression tests, the specimens were surfaced with a lime mortar to obtain a plane surface (Fig. 5). The strains were also measured for the central zone of specimens, as the case of the wall, and the mean values were calculated from three values in the central zone [13]. Results obtained from unconfined compression tests are presented in Table 3.



Fig. 5 Left: prismatic specimens. Right: cylindrical specimen

Table 3 Results of unconfined compression tests

Specimens	Compressive strength (MPa)	Young's modulus (MPa)
Prisms (25 × 25 × 50 cm ³)	1.15 ± 0.10	365 ± 65
Cylinders (20 cm · D × 40 cm · H)	2.00 ± 0.19	763 ± 54

Discussion. Different results were obtained in four different ways: by dynamic and static measurements on the wall, as well as static measurements on the prismatic and cylindrical specimens; the dynamic and static measurements on the wall gave the same Young’s modulus (about 400 MPa). This result confirms the relevancy of the approach proposed, which uses the dynamic tests to determine Young’s modulus, and also confirms the robustness of the analytical method used.

A substantial difference in the results of the cylindrical specimens ($E = 763$ MPa) and prismatic specimens (365 MPa) from that of the walls (about 400 MPa for both walls) can be observed. This difference shows that the current way of using the usual specimens, which works for conventional materials (e.g., concrete) may differ for RE. Indeed, the overestimation of the results obtained on cylindrical specimens has already been noted in previous studies in the literature [1]. The friction during ramming—between the RE and the formwork—was greater in the prismatic specimens and the wall than in the cylindrical specimens, especially in the corners. Consequently, cylindrical specimens were better compacted and had better mechanical characteristics. This is why Young’s moduli were in the order: cylindrical > wall > prismatic.

5 Assessing the Method on in situ Walls with L-Section

In order to verify the robustness of the method proposed on in situ walls and with more complex cross sections, rammed earth walls under construction of an RE house in France were chosen for the present study (Figs. 6 and 7). The rammed earth walls 2.3 m in height were built on 0.3 m of concrete base paved with stones. Dynamic measurements were taken by accelerometers placed on the top and at the base of the walls, similar to the case of rectangular cross-sectional walls mentioned above. The walls were investigated in a previous study [1] for the dynamic measurements and the modeling by using the Finite Element Modeling (FEM). The procedure (dynamic measurements and data processing) was the same as for the



Fig. 6 In situ RE walls

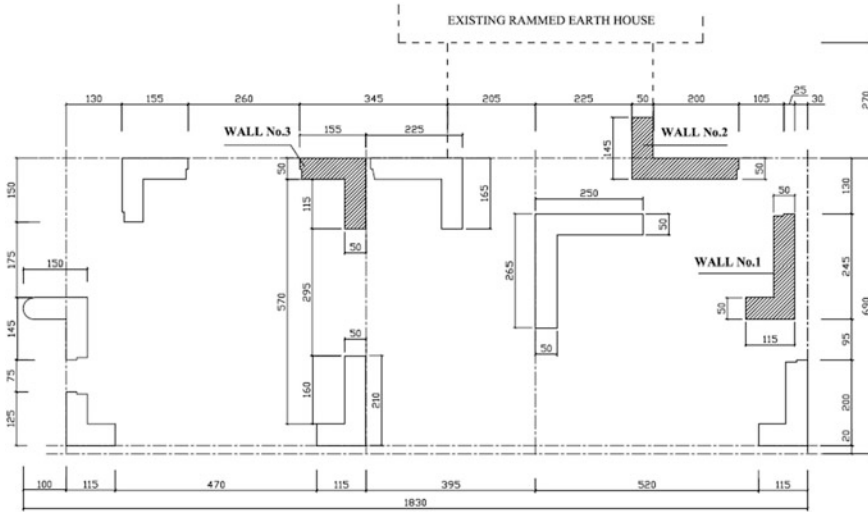


Fig. 7 Plan of the RE house studied (dimensions are in cm)

walls presented in the previous section. The Young’s modulus was determined from FEM by varying the Young’s modulus and search the most adapted value. The results are summarized in Table 4.

The Young’s modulus presented in Table 4 is the values determined by using FEM. The results show that, between the analytical results and that obtained from the experiments, the difference is low for the translational modes ($\leq 6\%$, last column of Table 4); the differences for torsional modes are higher, but still less than 10%. This confirms the robustness of the analytical method.

Table 4 Natural frequencies obtained from three different approaches

Wall	Mode	f_{exp} (Hz)	f_{ana} (Hz)	f_{FEM} (Hz)	Mode shape	f_{ana}/f_{exp}
1 (E = 470 MPa)	1	10.75	11.10	10.77	1st translation	1.03
	2	18.20	16.51	17.45	Torsion	0.91
	3	24.00	23.67	24.01	2nd translation	0.99
2 (E = 470 MPa)	1	11.30	12.02	11.17	1st translation	1.06
	2	17.10	16.01	16.83	Torsion	0.94
	3	23.25	22.39	23.08	2nd translation	0.96
3 (E = 465 MPa)	1	13.87	13.49	13.88	1st translation	0.97
	2	15.10	15.72	15.00	Torsion	1.04
	3	25.25	24.96	24.34	2nd translation	0.99

6 Conclusion and Prospect

In this paper, the strategy using vibrational measurements to assess the mechanical characteristics of the in situ walls was presented. From the vibrations measured, the natural frequencies and the mode shapes of the walls could be determined. These dynamic characteristics are a function of the wall's Young modulus. This paper proposed an inverse method using Timoshenko's theory to rapidly determine the wall's Young modulus from natural frequencies. The formula presented here is particularly useful for nondestructive verification of the elements tested in laboratory and also interesting for the seismic assessment of existing RE buildings [7, 11].

The method proposed was verified firstly by experiments on two RE walls manufactured in laboratory. The results showed that the proposed method was robust by providing satisfying analytical results. The paper also showed that the current testing method using usual specimens (cylindrical and prismatic) was less effective than that of the proposed analytical method.

In the near future, an empirical relationship between Young's modulus and the compressive strength of RE material will be investigated, as the case of concrete material [14]. If this relationship is determined, the compressive strength of the in situ walls can be directly determined by using vibrational measurements. This will be an advantageous nondestructive testing method.

The proposed method was applied in this paper for RE material, but the approach can also be used for other nonconventional materials.

References

1. Bui QB, Morel JC, Hans S, Meunier N (2009) Compression behaviour of nonindustrial materials in civil engineering by three scale experiments: the case of rammed earth. *Mater Struct* 42:1101–1116
2. Morel JC, Mesbah A, Oggero M, Walker P (2001) Building houses with local materials: means to drastically reduce the environmental impact of construction. *Build Environ* 36:1119–1126
3. Soudani L, Fabbri A, Morel JC, Woloszyn M, Chabriac PA, Wong H, Grillet AC (2016) Assessment of the validity of some common assumptions in hygrothermal modelling of earth based materials. *Energy Build* 116:498–511
4. Bui QB, Morel JC, Reddy BVV, Ghayad W (2009) Durability of rammed earth walls exposed for 20 years to natural weathering. *Build Environ* 44:912–919
5. Lombillo I, Villegas L, Fodde E, Thomas C (2014) In situ mechanical investigation of rammed earth: calibration of minor destructive testing. *Constr Build Mater* 51(31):451–460
6. Hans S, Boutin C, Ibraim E, Roussillon P (2005) In-situ experiments and seismic analysis of existing buildings. Part I: experimental investigations. *Earthq Eng Struct Dyn* 34:1513–1529
7. Boutin C, Hans S, Ibraim E, Roussillon P (2005) In-situ experiments and seismic analysis of existing buildings. Part II: seismic integrity threshold. *Earthq Eng Struct Dyn* 34:1531–1546
8. Bui QB, Morel JC (2009) Assessing the anisotropy of rammed earth. *Constr Build Mater* 23:3005–3011

9. Andersen P, Brincker R, Goursat M, Mevel L (2007) Automated modal parameter estimation for operational modal analysis of large systems. In: Proceedings of the 2nd international operational modal analysis conference. Copenhagen, Denmark, pp 299–308
10. Bui QB, Morel JC, Hans S, Walker P (2014) Effect of moisture content on the mechanical characteristics of rammed earth. *Constr Build Mater* 54:163–169
11. Bui QB, Hans S, Morel JC, Do AP (2011) First exploratory study on dynamic characteristics of rammed earth buildings. *Eng Struct* 33:3690–3695
12. Vacher P, Dumoulin S, Morestin F, Mguil-Touchal S (1999) Bidimensional strain measurement using digital images. Proceedings of the institution of mechanical engineers, part C: journal of mechanical engineering science 213:811–817
13. El-Nabouch R, Bui QB, Plé O, Perrotin P (2017) Assessing the in-plane seismic performance of rammed earth walls by using horizontal loading tests. *Eng Struct* 145:153–161
14. NF EN 1992-1-1, Eurocode 2—Calcul des structures en béton—Partie 1-1 : règles générales et règles pour les bâtiments. AFNOR, 2005

Investigation of A5052 Aluminum Alloy to SS400 Steel by MIG Welding Process



Quoc Manh Nguyen, Huong Thao Dang Thi, Van Thinh Nguyen, Minh Hue Pham Thi, Khac Thong Nguyen, Shyh-Chour Huang and Van Nhat Nguyen

Abstract This paper aims to investigate the simulation and experiment of the welding of butt joint 5052 aluminum alloy to SS400 steel by SYSWELD software and metal inert gas (MIG) welding process with AR4043 welding wire. Welding seams were evaluated by mechanical testing and metallurgical analysis, and surface morphology welding seam and other welding defects were investigated. The microstructure of intermetallic layer has been observed using microhardness testing and scanning electron microscopy (SEM). A without intermetallic layer and intermetallic layer joint between welding seam and SS400 steel at fusion area appeared after the welding process. To improve the quality of welds, the best thickness of the intermetallic (IMC) layer was from 3 μm to 7 μm . The fracture tensile inspection results of welding seam achieved at 230 MPa and the fracture

Q. M. Nguyen (✉) · H. T. Dang Thi · V. T. Nguyen
Hung Yen University of Technology and Education, Khoai Chau, Hung Yen, Vietnam
e-mail: nguyenquocmanh@utehy.edu.vn

H. T. Dang Thi
e-mail: dangthihuongthao@utehy.edu.vn

V. T. Nguyen
e-mail: thinhspkt@gmail.com

M. H. P. Thi
Faculty of Mechanical Engineering, Hanoi University of Industry, Hanoi, Vietnam
e-mail: huespkt@gmail.com

K. T. Nguyen
Senior Official Department of Science, Technology and Environment,
Ministry of Education and Training, Hanoi, Vietnam
e-mail: nkthong@moet.edu.vn

S.-C. Huang (✉) · V. N. Nguyen
Faculty of Mechanical Engineering, National Kaohsiung University of Applied Sciences,
Kaohsiung, Taiwan
e-mail: shuang@cc.kuas.edu.tw

V. N. Nguyen
e-mail: nguyenvannhat@utehy.edu.vn

© Springer Nature Singapore Pte Ltd. 2018

H. Nguyen-Xuan et al. (eds.), *Proceedings of the International Conference on Advances in Computational Mechanics 2017*, Lecture Notes in Mechanical Engineering, https://doi.org/10.1007/978-981-10-7149-2_44

occurred at the IMC layer, the average microstructure hardness of IMC layer zone is 346.3 HV and without IMC layer zone is 117.85 HV. The intermetallic layer was at the minimum to improve the quality of welds.

Keywords MIG welding process • Butt joint • IMC layer • A5052 alloys
SS400 steel • SYSWELD software

1 Introduction

Aluminum alloys have been extensively applied in the aerospace, automotive industry, industrial defense, and many other areas with its superior features [1–5]. SS400 steel plate is used in the most manufacturing industries with its superior advantages [6–9]. Joining dissimilar materials is a great technological and engineering challenge, and the need for joining dissimilar materials often arises in industrial applications of complex function. The combination of steel with aluminum alloys is to reduce fuel consumption because it saves the material weight but still ensures the stability and reliability of the operated texture. Welding aluminum to steel is extremely difficult because of the mutual solubility, thermal conductivities, and differences in melting temperatures [9–12]. So many welding methods have been used to achieve optimal results between these materials such as friction stir welding [6], laser welding [4], metal inert gas welding [13], resistance spot welding [14], diffusion bonding [15], magnetic pressure seam welding [16], and ultrasonic welding [17]. The welding seam of these materials will bring many outstanding advantages over their own benefits and reduce the manufacturing cost significantly. The welding seam of the aluminum and steel was only found during the phase transformation at the weld which caused negative effect to the weld. Metal inert gas (MIG) welding is used as welding heat source to weld steels and aluminums, and welding wire is provided semiautomatically throughout the process to fill the weld. The heat source causes highly non-uniform temperature distributions across the welding seam and the base metals. Types of joining such as butt, tee, corner, lap, and edge are employed for various applications in training and industry, e.g., ship building, pressure vessel, structure manufacturing [18–20]. Butt joint research is one of the complex problems of welding process, in heat affected area (HAZ) bearing capacity and reduced quality due to the stress and distortion always exists after welding. FEM has been widely used in researching, designing, and analyzing welding structures. It is one of the most useful and important methods in predicting stress and distortion due to the heat generation when welding at the first phase in the process of product design and the development of welding

process. The aim of the paper is feasible for the simulation and experimental welding for A5052 and SS400 steel with sizes $200 \times 70 \times 5$ mm.

2 Welding Simulation

Materials are set up in a virtual environment with the same experimental materials. The properties of the materials such as thermal and metallurgic properties and mechanical properties in simulation process are taken directly from the database of SYSWELD software.

A schematic illustration of finite element models of butt joint is shown in Fig. 1a. It includes two symmetrical plates: A5052 aluminum alloys and SS400 steel with the same size $200 \times 70 \times 5$ mm. A weld line and reference line are designed in the model. The conditions of the clamping are applied in simulations and experimental welding process as shown in Fig. 1b.

Goldak et al. proposed a double-ellipsoidal heat source model as shown in Fig. 2, which has the capability of analyzing the thermal fields of deep penetration welds. It describes the welding seam and distribution of thermal energy between two different ellipses. The capacity density of the two ellipsoid heat flux $q_{(v,f)}(x, y, z)$ and $q_{(v,r)}(x, y, z)$ describes the distribution of heat flux inside the quadrant of the front and rear heat source and is calculated by the equation [21]:

$$q_{v,f}(x, y, z) = \frac{6\sqrt{3}f_f Q}{abc_f \pi \sqrt{\pi}} e^{-3\frac{x^2}{a^2}} \cdot e^{-3\frac{y^2}{b^2}} \cdot e^{-\frac{3z^2}{c_f^2}} \tag{1}$$

$$q_{v,r}(x, y, z) = \frac{6\sqrt{3}f_r Q}{abc_r \pi \sqrt{\pi}} e^{-3\frac{x^2}{a^2}} \cdot e^{-3\frac{y^2}{b^2}} \cdot e^{-\frac{3z^2}{c_r^2}} \tag{2}$$

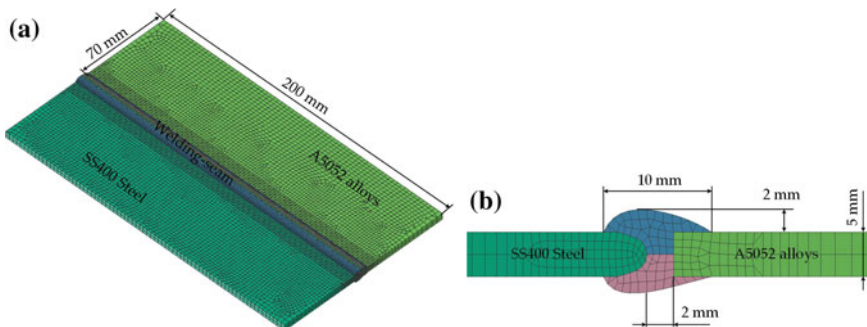


Fig. 1 a Finite element models and b meshing of butt joint models

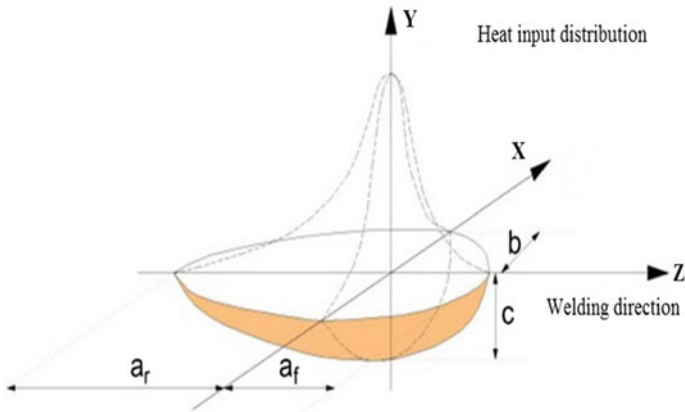


Fig. 2 Double ellipsoidal heat source of Goldak

where f_f and f_r are the fractional factors of the heat deposited in the front and rear quadrant, which can be determined by $f_f + f_r = 2$. Constants, a , b , and c are heat source parameters that define the size and shape of the ellipsoids therefore the heat source distribution and Q are the welding energy input.

Figure 3a–f shows the temperature distribution results during welding simulation process between A5052 alloys and SS400 steel at various time periods. From results could see the temperature field around the MIG heat source increasing from 20 to 600 °C between time periods 0 and 2 s at initial zone. This can understand that at this period the models as subjected three heat transmission includes conductivity, radiation, and convection. Figure 3b–f shows the initial, central, and final zone lengths of butt joint models. This time is part fixed of center zone with the isotherm moving regular and at this stage the heat transmission due conduction will be large than the heat transfer by radiation and convection. Besides that when the MIG sources move from the next points of model to end model with the steady state also as affected by boundary condition and heat radiation. A large difference at the distribution of the isotherm heat in welding simulation aluminum alloy to steel. Although the two materials have same thickness, conductivity distribution of isotherm closes together and tends to focus around the welding area at the steel sheets. But at the aluminum plate, the thermal conductivity is big so the heat dissipation is faster and the isotherm distributes more widely. This shows that coefficient of thermal conductance is importantly special in the convective heat transfer in the surface and the radiation affected the melting and the heat affected the boundaries in the welding process of the different materials. Simulation results are considered as a basis for handling these issues in the course of the most effective way for the experimental welding. The distribution temperature on the model showed the heat distribution is unassymmetric between aluminum alloys and steel also as stainless steel at the different time.

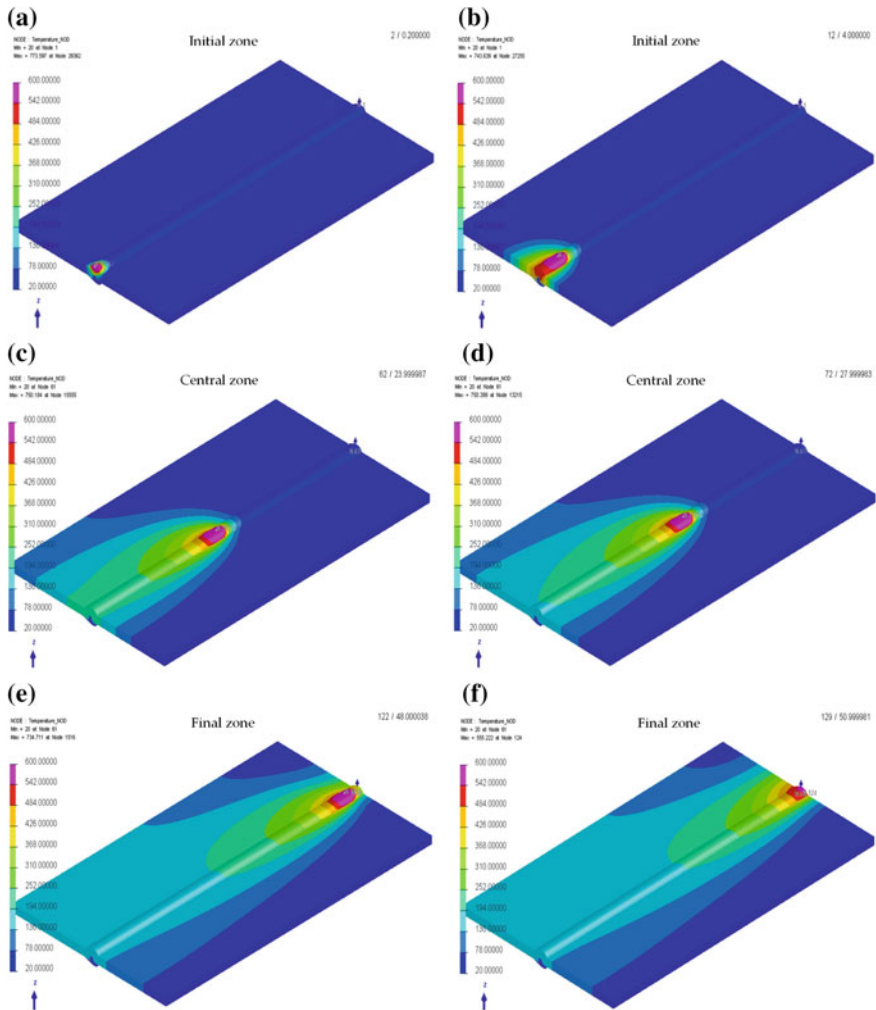


Fig. 3 Temperature distribution during MIG welding at different time periods: **a–b** initial time; **c–d** central time; and **e–f** final time

Figure 4 shows the comparison of simulation results and experimental results at fusion area of dissimilar welding between aluminum alloys and steel. From results, simulation can see normalize dilution of SS400 steel in the fusion zone. This is good indicator for the alloy density in the welding bead during welding process. This is a good sign for the blend of welding metals inside welding area, and it is usually used for estimating the alloy content and also used as the uniformity of welding bead during welding process. The results also showed, the metallurgical calculate during simulation present in Fig. 4a shows that the components formed phase 1 in the welding zone different about from range 19–77% of butt joint.

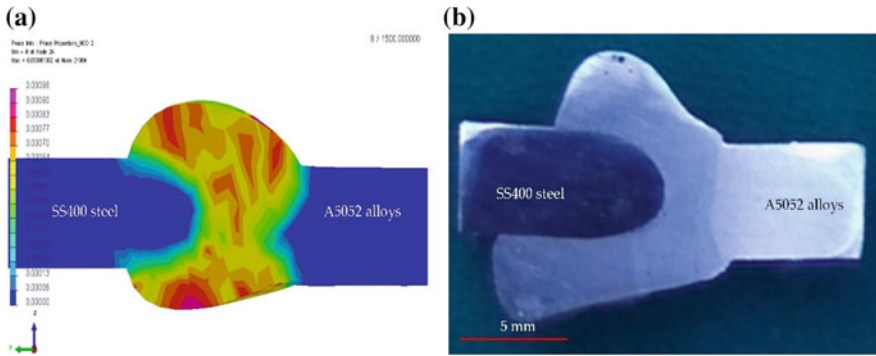


Fig. 4 Comparison of simulation result and experimental result

3 Experimental Procedure

The materials used are aluminum alloy A5052 and steel SS400 sheets with thickness of 5 mm, and the chemical composition materials used are experimentally shown in Tables 1, 2, and 3 [6, 7, 13, 22–25]. The equipment was used to implement all experiments including a MIG/MAG-pulsed welding machine, universal testing machines, Vickers hardness testing machines, and SEM/EDS system.

The welding process used argon, an industrial shield gas, ER4043 welding wire of 0.8 mm was selected, protective gas was 10.5l/min, welding speed was 4.5 mm/s, welding voltage was 17 V, and welding current intensity was 90 A. All experiments were performed on A5052 aluminum alloys and SS400 steel plate with a fixed thickness of 5 mm.

Table 1 Chemical composition of steel SS400 (wt%)

Materials	Fe	C	Si	Mn	Ni	Cu	P	Cr	Al
SS400	Bal	0.13	0.19	0.81	0.049	0.063	0.015	0.021	0.024

Table 2 Chemical composition of steel A5052 alloys (wt%)

Materials	Al	Si	Mn	Cu	Mg	Fe	Cr	Zn	Ti
A5052	Remain	0.08	0.04	0.02	2.51	0.15	0.22	0.01	0.01

Table 3 Chemical composition of steel ER4043 welding wire (wt%)

Materials	Al	Si	Mn	Cu	Mg	Fe	Zn	Ti
A5052	Remain	4.5–6	0.05	0.03	0.05	0.8	0.1	0.2

4 Results and Discussion

Seven specimens were selected to test the tensibility, and Table 4 shows the results of the tensile test. From the results, we can see that the shear strength of the welding seam is achieved at 225.9 MPa. The results of the tensile test of seven weld specimens are presented in Table 4.

Microstructure hardness testing of butt joints was performed on the typical cross section of weld joint samples through load force of 10 g and 10-s downtime by the Vickers testing method. The microhardness results were used as one of the data for researching the microstructure of weld joints and also as the adjacent area of welds. To investigate microstructure of welded, the typical weld joints cross-section of typical weld joints has been grinding and polishing follow metallurgical standards. The hardness of weld joints tended to increase at adjacent area of welds and descend at area far from center of the welds, and the microhardness of weld surface area is higher than that at the two base metals. The results of the microstructural hardness tests in the IMC layer zone are shown in Fig. 5. At the intermetallic layer zone, the maximum testing result is 850 HV was observed at central of IMC layer compound, the minimum value measured was observed at the adjacent between IMC layer and welding seam of 182 HV, the average values hardness measured in the SS400 steel side was 280 HV and average values hardness measured in the A5052 aluminum alloy side was 150.72 HV such as presented in Table 5. The hardness average values at the IMC layer zone in this research were higher than that of the welding wire ER4043 (56–64 HV), as compared to the hardness reported in [14], with the evidence of the low dynamic load capacity and brittleness of the welds. Because the

Table 4 Results of tensile test of 7 specimens of welded A5052 and SS400 butt joints

Materials	T1	T2	T3	T4	T5	T6	T7	Average
Values (MPa)	206.5	203	195.5	220	225.9	215	193.5	208.5

Fig. 5 Microstructure hardness test in IMC layer

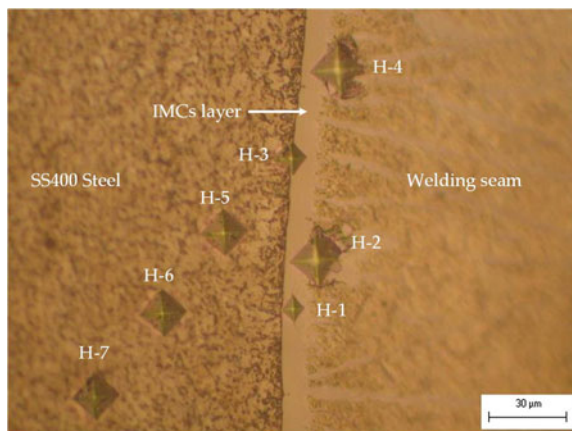


Table 5 Results of microhardness test at IMC layer area

Specimens	H-1	H-2	H-3	H-4	H-5	H-6	H-7	Average
Values (HV)	850	209	468	182	240	237	239	346.43

IMC layer was not good for the dynamic load and the load of the welds, it was necessary to find a way to reduce the thickness of the IMC layer as much as possible in order to increase the load capacity and the strength of the welding joints. The specific values of the tested positions for the hardness of the weld microstructures with the IMC layer and without the IMC layer zone are shown in Table 5.

The OM and SEM were used for observed microstructure of weld joints. All specimens was grinding and polishing following metallographic standard by machine with abrasive paper have been different distribution grain size. The chemical composition of two base metals and the filler metal and also the cooling rate of the welding process are decided for the formation of microstructure of weld joints and phase transformation after welding.

Figure 6a shows the microstructure of the welding seam and the SS400 steel plate, when welding A5052 aluminum alloy and steel, and our study used a welding

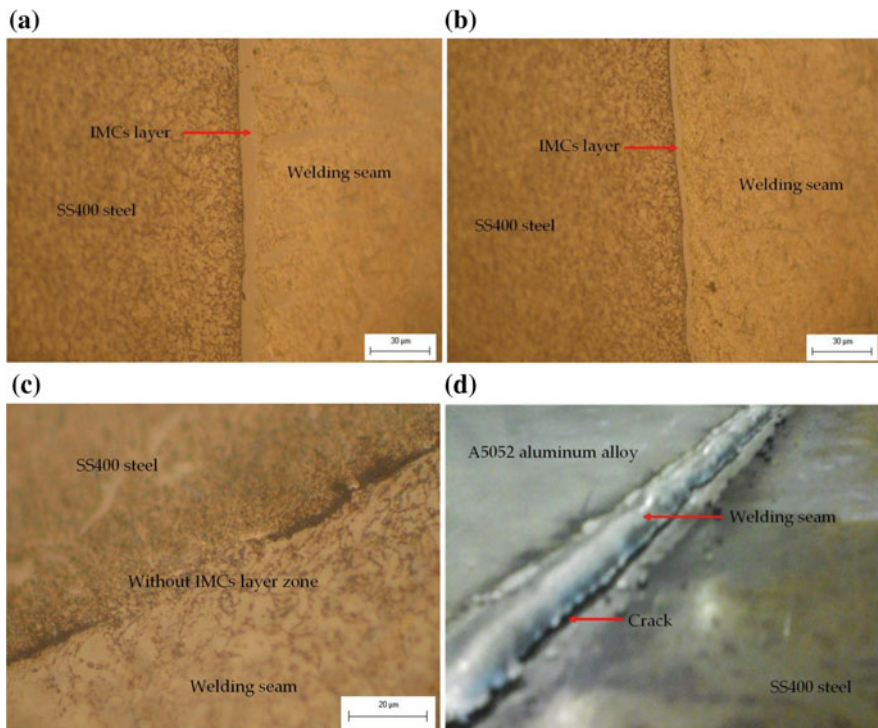


Fig. 6 Microstructure of welded A5052 aluminum alloy/SS400 steel: **a** IMC layer zone on the top side; **b** IMC layer zone on the bottom side; **c** without the IMC layer zone; and **d** cracking after welding

intensity of 95 A and a welding speed from 3.5 to 4 mm/s. Figure 6b shows the results of the welding on the bottom side. A minimum IMC layer about 3 μm in thickness was produced with a suitable intensity and velocity; the welding seam was a seamless crystal lattice, which helped the weld to possess high mechanical properties. Figure 6a shows the welding of the top side; the two metal plates were at room temperature so the IMC layer here was thicker than that on the bottom side. The bottom side was welded after the two metal plates had cooled. When welding the bottom side, because the first background layer was created, the Fe atoms at the solid–liquid interface reach a supersaturated concentration faster because of the current power from the welding process and the background of the top side. Furthermore, the first IMC layers were thin and stable so the flow of the metal liquid on the steel surface was better, as shown in Fig. 6b. Other areas had better mechanical properties, especially near the welding area, some far from the center heat source and many parts without IMCs, as shown in Fig. 6c. As shown in Fig. 6d, an IMC layer appeared or did not appear depending on the welding process used and on the appropriate welding speed and intensity. The temperature of the steel sheets increased when the arc directly affected the surface of the steel plate during the welding process. Furthermore, on a thick IMC layer, cracks appeared between the surface of the SS400 steel sheets and the welding seam when a high welding intensity and low welding speed were used. We could see that choosing a suitable welding intensity has great influence on the fusion of Al base metal as well as on the wettability and spreading ability of the weld metal; it can also lead to the quality change of welds and, as seen, affect the formation of the continuous surface appearance.

The morphology of the brazed interface layer between the welding seam metal and the SS400 steel is shown in Fig. 7. It is shown that two main IMC layers formed along the brazed interface and that a thin layer is connected to the SS400 steel sheet surface; it includes the undulating surface structure in the welding seam metal and the serrated structure and rupture in the welding seam. The welding seam joint was formed between the base aluminum alloy and the welding wire in the welding process, and a thin IMC layer formed mainly along the brazed interface and the adjacent SS400 steel surface. The IMC layer was found to be about 1.95–5 μm thick between the welding seam and the SS400 steel surface after SEM testing. There were no defects at the welding seam, and the area had good mechanical properties, as shown in Fig. 7a. With the 5 wt% of Si additions in the ER4043 welding wire, Si atoms inside the molten pool enrich the interface and often tend to aggregate the interface because it can decrease the enthalpy of formation of the IMC layer [26]. The IMC layer was thick and uneven as the welding was done by hand and the temperature in the area was uneven. Figure 7b shows the microstructure of the IMCs between the welding seam and SS400 steel. A seamless metal structure with no defects has good mechanical properties, as found at the welding seam with length about 3–7 μm . It was clear that Si atoms appeared in the welding seam due to the use of ER4043 welding wire in the welding process. As the welding was done by hand, the temperatures of different areas were uneven, which made the IMC layer thick and uneven. Before welding, the edge of the SS400 steel

plate was chamfered using a hand grinding machine and then cleaned using sandpaper. The cleaning process for the steel plate surface before welding was not good; this affected the welding quality and caused other defects, as shown in Fig. 7c. Figure 7d shows the microstructural cracks on the surface steel sheet because of the high welding intensity and low welding speed, which caused the steel sheet surface to overheat and cracks to appear along the welds.

The energy-dispersive X-ray spectrometer mapping of the elements at the intermetallic layer zone between the SS400 steel and the welding seam at the IMC layer zone and without the IMC layer is shown in Fig. 8a. Some atoms diffused during the welding process. Figure 8b shows the elements with their corresponding amounts which appeared at the welding seam area: Al (47.4%), Fe (27.8%), C (2.31%), and Si (1.7%). Figure 8c shows the results of the scanning of the weld without the intermetallic layer. At the investigated position, the four elements and its corresponding amounts were Al (45.9%), Fe (30.2%), C (2.18%), and Si (2.1%), as shown in Fig. 8d.

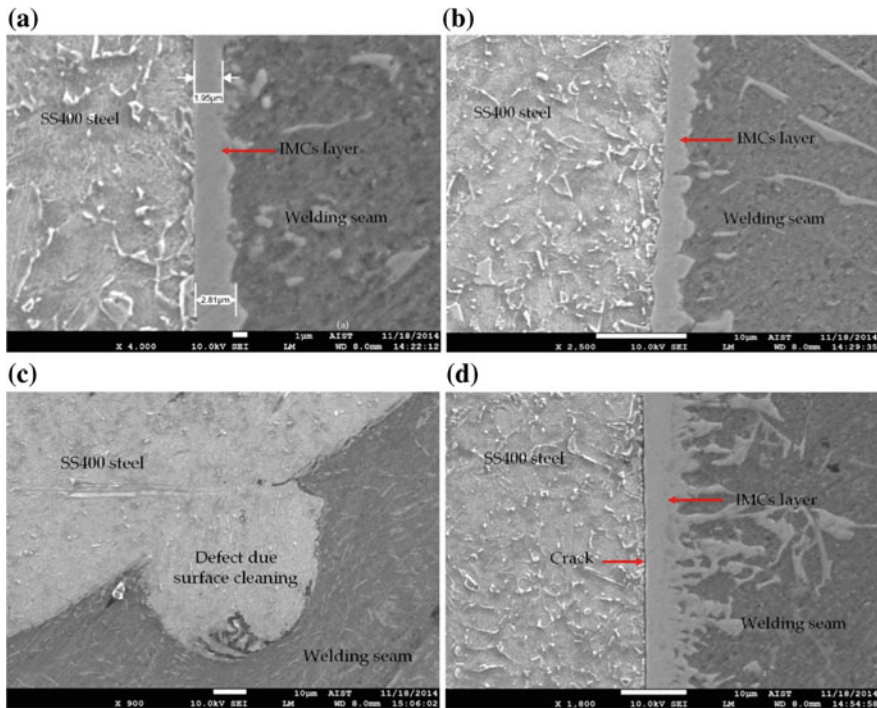


Fig. 7 SEM microstructure at area between the welding seam and SS400 steel sheet: **a** IMC layer area; **b** without IMC layer area; **c** defects due to surface cleaning; and **d** microstructural crack on the surface of the steel sheets

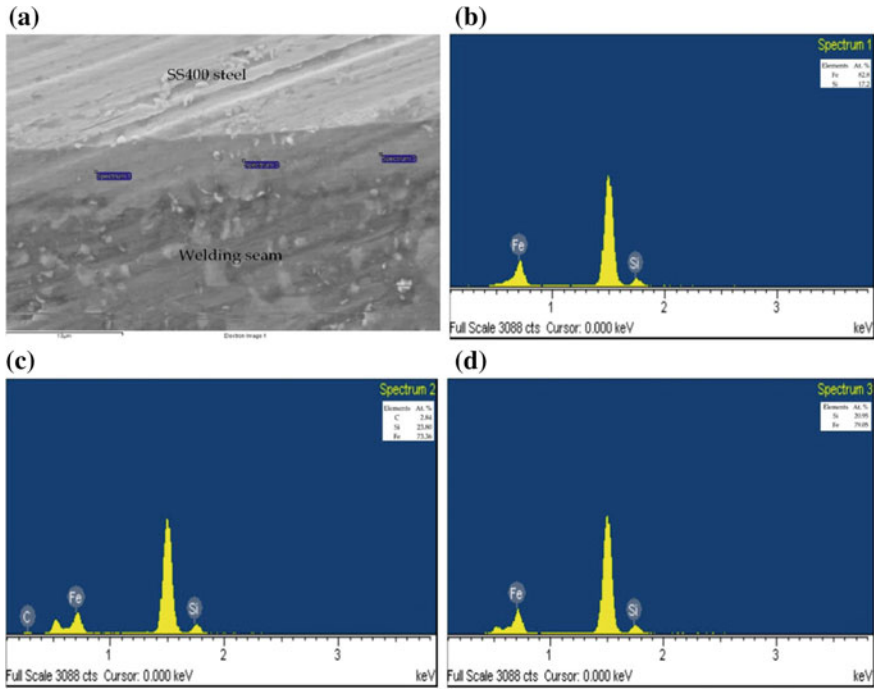


Fig. 8 SEM microstructure at area between the welding seam and SS400 steel sheet: **a** IMC layer area; **b** without IMC layer area; **c** defects due to surface cleaning; and **d** microstructural crack on the surface of the steel sheets

5 Conclusions

The dissimilar joint of A5052 aluminum alloys and SS400 steel was made by MIG welding process with ER 4043 welding wire. The tensile strength, the microstructure hardness, and the microstructure characteristics were investigated. The major conclusions of this paper could be summarized as follows:

To make the welding process successful, we had to choose the appropriate welding materials to welded materials, the groove of the welding edge, careful clean, suitable welding conditions, and good welding gaps. In addition, cleaning metal sheet surfaces before welding is very important, especially the oxide layer on every plate after welding the opposite side.

This research used appropriate gas shield to protect the welding pool well in the welding process. On the other hand, not only must the welders be very skillful but also the steels' microstructure surfaces were smooth and rounded beveled before fitting, assembling, and implementing the welding process to make the intermetallic layer thin and even throughout the length of the weld.

The interaction of the solid steel and the liquid aluminum in the welding process had been controlled by the diffusion of the IMC layer areas. Furthermore, Si atoms

which were found in the welding seam were involved actively in forming the IMC layers. The IMC layer found with thickness of about 3–7 μm .

The average microstructure hardness achieved is 346.43 HV, average tensile strength achieved is 225.9 MPa, and a fracture occurred at the surface layer of welding seam and SS400 steel plate. The cracks, which derived from using high power in the welding process, have been found between the welding seam and SS400 chamfered steel when the thickness of IMC layer was high.

References

1. Tu JF, Paleocrassas AG (2011) *J Mater Process Technol* 211:95–102
2. Xua W, Liu J, Luan G, Dong C (2009) *Mater Des* 30:1886–1893
3. Sierra G, Peyre P, Beaume FD, Stuart D, Fras G (2007) *Mater Sci Eng, A* 447:197–208
4. Torkamany MJ, Tahamtan S, Sabbaghzadeh J (2010) *Mater Des* 31:458–465
5. Elrefaey A, Gouda M, Takahashi M, Ikeuchi K (2005) *J Mater Eng Perform* 14:10–17
6. Kimapong K, Watanabe T (2005) *Mater Trans* 46:835–841
7. Ito K, Okuda T, Ueji R, Fujii H, Shiga C (2014) *Mater Des* 61:275–280
8. Shih JS, Tzeng YF, Lin YF, Yang JB (2012) *Adv Mech Design Syst Manuf* 6:222–235
9. Hangai Y, Saito M (2013) *Mater Trans* 54:1012–1017
10. Taban E, Gould JE, Lippold JC (2010) *Mater Des* 31:2305–2311
11. Kobayashi S, Yakou T (2002) *Mater Sci Eng, A* 338:44–53
12. Qiu R, Iwamoto C, Satonaka S (2009) *J Mater Process Technol* 209:4186–4193
13. Zhang H, Liu J (2011) *Mater Sci Eng, A* 528:6179–6185
14. Qiu R, Shia H, Zhanga K, Tua Y, Iwamotoc C, Satonaka S (2010) *Mater Charact* 61:684–688
15. Travessa D, Ferrante M, Ouden G (2002) *Mater Sci Eng, A* 296:287–337
16. Lee KJ, Kumai S, Arai T, Aizawa T (2007) *Mater Sci Eng, A* 471:95–101
17. Watanabe T, Sakuyama H, Yanagisawa A (2009) *J Mater Process Technol* 209:5475–5480
18. Weman K, Lindén, G (2006) *MIG Weld Guider* 3–10
19. Groover MP (2007) *Fundam Modern Manuf Mater Process Syst* 3:689–701
20. Degarmo EP, Black JT, Kohser RA (2007) *Mater Process Manuf* 10:829–856
21. Long H, Gery D, Carlier A, Maropoulos PG (2009) *Mater Des* 30:4126–4135
22. Yong Y, Tong ZD, Cheng Q, Wen Z (2010) *Trans Nonferrous Met Soc China* 20:619–623
23. Lee CY, Lee WB, Kim JW, Choi DH, Yeon YM, Jung SB (2008) *J Mater Sci* 43:3296–3304
24. Zhang DQ, Li J, Joo HG, Lee KY (2009) *Corros Sci* 51:1399–1404
25. Specification for bare aluminum and aluminum alloy welding electrodes and rods, AWS A5.10/A5.10 M:1999 (R2007)
26. Nguyen QM, Huang S-C (2015) An investigation of the microstructure of an intermetallic layer in welding aluminum alloys to steel by MIG process. *Materials* 8(12):8246–8254

Behaviour of Two Chamber Aluminium Profiles Under Axial Crushing: An Experimental and Numerical Study



Nguyen-Hieu Hoang, Magnus Langseth, Gaute Gruben
and Terence Coudert

Abstract The present study investigated experimentally and numerically the structural behaviour of two chamber extruded profiles in AA6060-T7 alloy subjected to axial crushing under quasi-static loading conditions. Experimental tests were performed (including uniaxial tests, in-plane shear test and plane strain tension tests) to characterize the elastic–plastic, anisotropy and fracture behaviour of the investigated material. The material under investigation exhibited anisotropic properties and isotropic yield models such as von-Mises were not able to predict correctly the shear and plane strain test behaviour. It depicted that the advanced material model with anisotropic Yld2004-18p yield function and ECL criterion was necessary to predict the material tests results (UT, ISS and PST) both in terms of force–displacement curves and ductile fracture. Axial crushing tests were also conducted to investigate the energy absorption capacity of two chamber profiles made of this alloy. A solid element-based numerical model of these component tests was established in the commercial finite element code LS-DYNA, and simulations were run with the calibrated material models and fracture criterion. The predicted force–displacement curves, the energy absorption and fracture were in a good agreement with the experimental results. These results demonstrate that numerical models can be used as a reliable design tool for optimizing aluminium profiles for automotive applications.

Keywords Simulations · Testing · Two chamber profiles · Aluminium Fracture

N.-H. Hoang (✉) · G. Gruben · T. Coudert
SINTEF Materials and Chemistry, 7465 Trondheim, Norway
e-mail: Hieu.Nguyen.Hoang@sintef.no

M. Langseth
Structural Impact Laboratory (SIMLab), Department of Structural Engineering,
Centre for Research–Based Innovation, Norwegian University of Science
and Technology, 7491 Trondheim, Norway

© Springer Nature Singapore Pte Ltd. 2018
H. Nguyen-Xuan et al. (eds.), *Proceedings of the International Conference
on Advances in Computational Mechanics 2017*, Lecture Notes in Mechanical
Engineering, https://doi.org/10.1007/978-981-10-7149-2_45

1 Introduction

The AA6xxx aluminium alloys are used extensively for crash-relevant components in automotive vehicles due to its light weight and high energy absorption capacity. To protect to car passengers during car crash events, the crash component should be designed to optimize the energy absorption capacity and buckling modes, i.e. the crash component should fold in a controlled manner without the formations of significant cracks and does not tend to fragmentation during fracture [1]. However, design and selection of light but crashworthy structural components in aluminium for the automotive industry are challenging and time-consuming tasks. In order to reduce the time and cost needed to develop a new component product, it is necessary to use finite element analysis as an effective design tool. The capacity to predict the energy absorption and fracture of the components is thus crucial for a robust and reliable design.

Different geometries for thin-walled structures have been adopted in recent years by a number of researchers to investigate their energy efficiencies and capacities for car crash components [2–10]. Investigations show that aluminium tubes have proved to give an excellent crashing behaviour and energy absorbing characteristics, and numerical simulations have shown to be a veritable tool. However, prior studies have also shown that the aluminium alloys used in automotive applications have complex mechanical properties with anisotropic strength and ductility. It may, therefore, be necessary to use relatively complicated constitutive models to obtain the required accuracy in the numerical analysis [10–17].

In the present study, work was carried out to investigate experimentally and numerically the structural behaviour of two chamber extruded profiles in AA6060-T7 alloy subjected to axial crushing under quasi-static loading conditions. Material tests were performed (including uniaxial tests, in-plane shear test and plane strain tension tests) to characterize the elastic–plastic, anisotropy and fracture behaviour of the investigated material. The material test data were then used to calibrate user-defined material constitutive and fracture models, as required for non-finite elements methods. Axial crushing tests were conducted to investigate the energy absorption capacity of two chamber profiles made of this alloy. A solid element-based numerical model of the component tests was established in the commercial finite element code LS-DYNA, and simulations were run with the calibrated material models and fracture criterion. The performance of the established model was then verified and demonstrated by comparing the experimental results with the tests results, in terms of energy absorption capacity and fracture.

2 Material and Experimental Programme

The investigated aluminium alloy is AA6060 in overaged temper T7, received as extruded profiles. The cross-sectional geometry is given in Fig. 1a. The nominal thickness of the outer wall is 3.5 mm and while the nominal thickness of the inner wall is 2 mm.

A material test programme was carried out to investigate the materials constitutive and fracture behaviour. The material test programme included uniaxial tension tests (UT) plane-strain tension tests (PST) and in-plane simple shear tests (ISS). Uniaxial tensile specimens were cut out 0°, 45° and 90° to the extrusion direction, plane-strain tension specimens were cut out 0° and 90° to the extrusion direction, and in-plane simple shear specimens were cut out in the extrusion direction. For each test type and extrusion direction, three parallel tests were carried out. In the following, the tests are denoted as *Test- α -x*, in which *Test* designates the type of test (UT, ISS and PST), α corresponds to the angle with respect to the extrusion direction, and *x* refers to the test repetition. All the tests specimens were machined out from the outer wall (WO), and their geometries are shown in Fig. 2. The material test matrix is summarized in Table 1. In all the tests, extensometers were used to monitor the displacement on the test specimens.

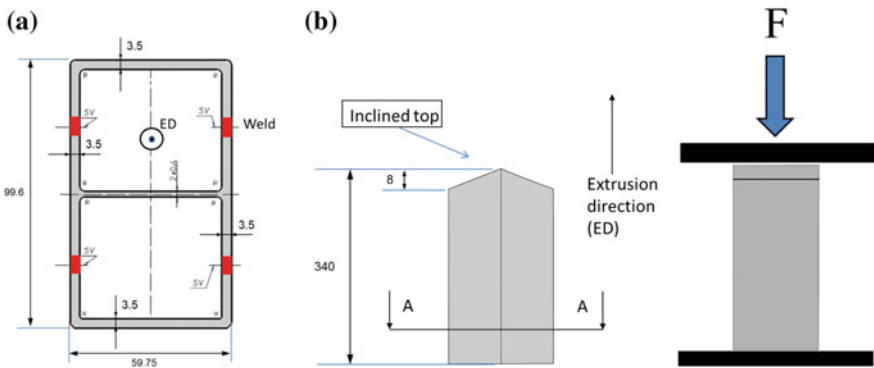


Fig. 1 a Geometry of as received profile (cross section A-A) and b axial crushing test setup

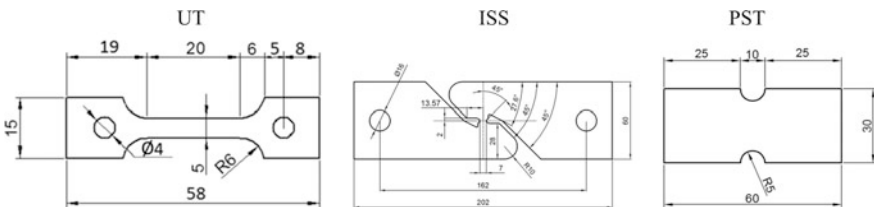


Fig. 2 Material test specimens

Table 1 Material test matrix

Section	Test	Number of test in ED	Number of test in 45° w.r.t ED	Number of test in 90° w.r.t ED
WO	UT	3	3	3
WO	PST	3	0	3
WO	ISS	3	0	0

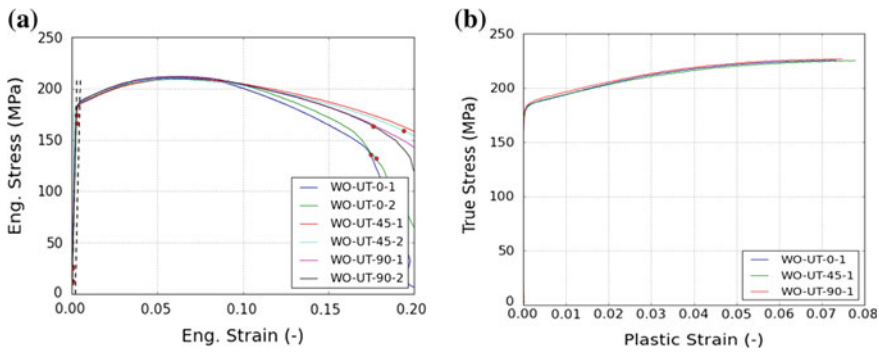


Fig. 3 Tensile test results. **a** Engineering stress–strain curves and **b** true stress–strain curves up to onset of diffuse necking

To study the energy absorption capability of the two chamber extruded profile, axial crushing tests were performed at room temperature at a quasi-static cross-head velocity. The component test geometry is shown in Fig. 1b. An inclined shape was introduced at the top of the specimen to trigger a repeatable folding pattern. Prior to testing, the wall thickness of the profiles was measured. Three repetitions were carried out for each test and during testing the axial force versus cross-head displacement histories were recorded.

3 Test Results

3.1 Material Test Results

The tensile test results are reported in Fig. 3 in terms of engineering and true stress–strain curves in the three different orientations α with respect to the extrusion direction (i.e. $\alpha = 0^\circ, 45^\circ$ and 90°). It is noted that only one representative true stress–strain curve for each orientation is shown in Fig. 3b, and the curves are plotted up to onset of diffuse necking. The tests clearly show that the investigated material exhibits minor anisotropy in strength. This minor anisotropy in strength of the material is also shown in Fig. 4a, plotting the stress ratio r_α which is defined as ratio between the flow stress in α direction and extrusion direction ED at equal

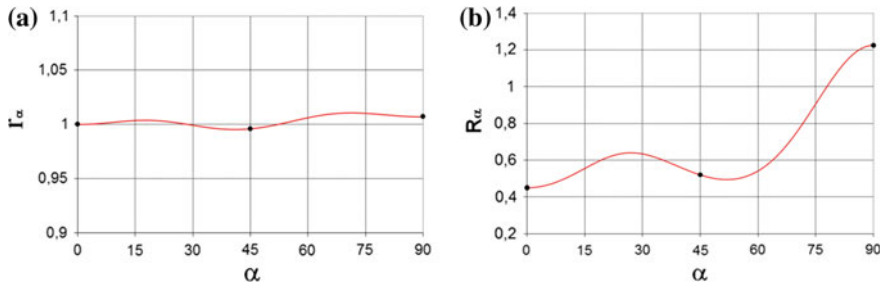


Fig. 4 **a** Stress ratio r_α and **b** strain Lankford ratio R_α of AA6060-T7. The back dots represent the experimental data, while the red curves are numerical results predicted by the calibrated anisotropic model Yld2004 with $m = 8$

amounts of specific plastic work. Here, the extrusion direction is used a reference direction. However, the material under investigation exhibits an anisotropy in terms of flow properties with respect to different directions, as shown by the Lankford ratios in Fig. 4b. The Lankford ratio is defined as the ratio between the plastic strain in the width direction, ϵ_w^p , and in the thickness direction, ϵ_t^p , of the tested specimens

$$R_\alpha = \epsilon_w^p / \epsilon_t^p \tag{1}$$

The stress and strain ratios will be used later on for calibrating an anisotropic yield criterion.

The results from the in-plane simple shear tests and the plane-strain tension tests in terms of force versus the displacement monitored by extensometer are shown in Fig. 5. As in the uniaxial tensile tests, only a small scatter was observed in these tests. Thus, only one representative experimental curve was plotted for clarity reason. As seen from the PST test results in ED (PST-0) and in 90° direction (PST-90), the present material exhibits a stronger anisotropy in strength in-plane-strain tension than in uniaxial tension.

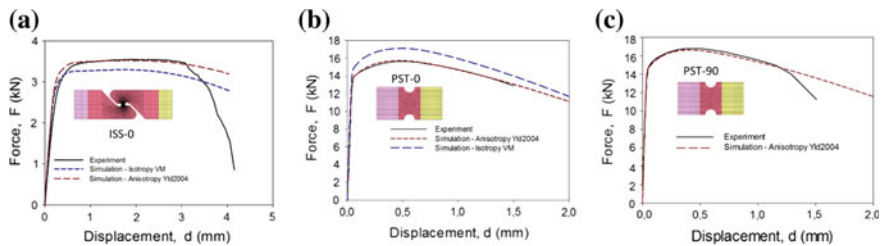


Fig. 5 Experimental and numerical results of **a** in-plane simple shear tests and **b, c** plane strain tension tests

3.2 Axial Crushing Test Results

The axial crushing tests results are shown in Fig. 6 in terms of the force–displacement curves, the mean force–displacement curves and the buckling modes. If E_a is the energy absorption of the profile at a displacement d , then the mean force is defined by $F_m = E_a/d$. The material exhibits high ductility and only small cracks were observed in the profile corner and in the T-junction between the inner and outer walls for all the profiles; see Fig. 7. Due to insignificant fracture and the geometrical trigger, no variation in the folding mode was found. All the tests exhibited a progressive and regular ‘step case’ buckling mode.

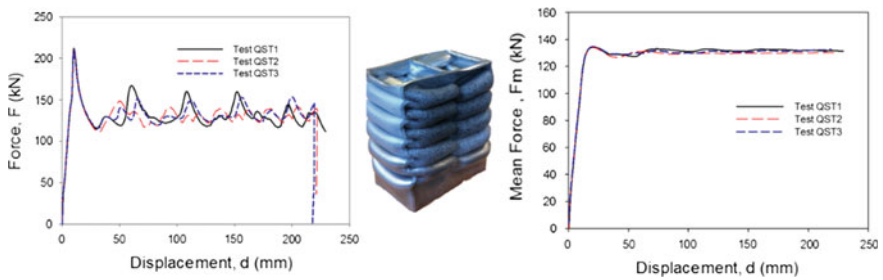


Fig. 6 Axial crushing test results (Axial crushing force, buckling mode and mean force)

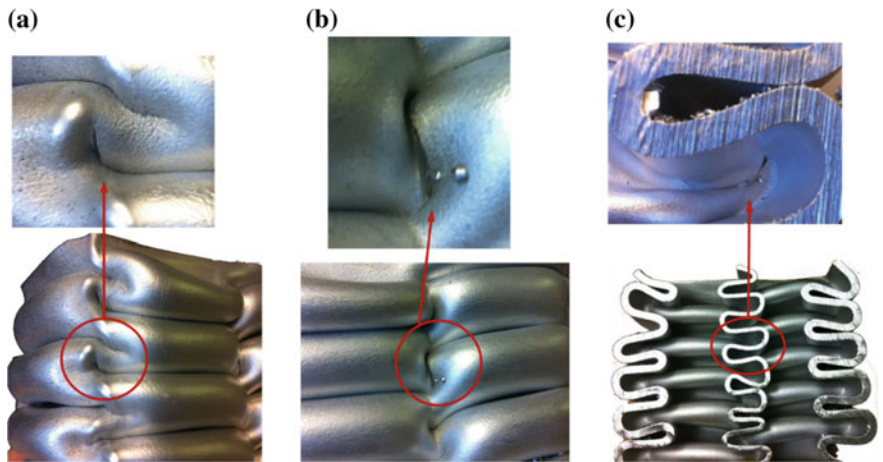


Fig. 7 Fracture in tested profiles. **a** Fracture in corner, **b** and **c** fracture at T-junction of the inner wall and the outer wall (outer surface and inner surface)

4 Constitutive Models

4.1 Material Modelling

The test results have shown that the investigated alloy 6060-T7 exhibits minor difference in strength in different axes with respect to the extrusion direction. However, the material possesses an anisotropic property in terms of plastic flow ratio, which defines the following direction at a given stress state on the yield surface. In order to account for this anisotropy, an appropriate material model in combination with an anisotropic yield criterion is necessary. The main ingredients of the material model used in the present work, are isotropic elasticity, anisotropic yielding, associated plastic flow rule and isotropic strain hardening. Here, the anisotropic yield criterion YLD2004-18p proposed by Barlat et al. [18] was adopted, and the equivalent stress is written:

$$\sigma_{eq} = \left(\frac{1}{4} \phi \right)^{1/m} \tag{2}$$

where

$$\phi = [s'_1 - s'_1]{}^m + [s'_1 - s'_2]{}^m + [s'_1 - s'_3]{}^m + [s'_2 - s'_1]{}^m + [s'_2 - s'_2]{}^m + [s'_2 - s'_3]{}^m + [s'_3 - s'_1]{}^m + [s'_3 - s'_2]{}^m + [s'_3 - s'_3]{}^m \tag{3}$$

In this equation, m is a yield surface shape parameter, and $\tilde{s}'_i, \tilde{s}''_i$ are principal values of the stress tensors \tilde{s}' and \tilde{s}'' , defined by linear transformations of the deviator of the co-rotational Cauchy stress

$$\tilde{s}' = C' : \hat{s} = C' : T : \hat{\sigma} \text{ and } \tilde{s}'' = C'' : \hat{s} = C'' : T : \hat{\sigma} \tag{4}$$

where the fourth-order tensor T transforms the co-rotational Cauchy stress $\hat{\sigma}$ into its deviatoric part \hat{s} . For orthotropic symmetries, only 9 of these constants are non-trivial so that the tensors C', C'' and T in Voigt notation read

$$C' = \begin{bmatrix} 0 & -c'_{12} & -c'_{13} & 0 & 0 & 0 \\ -c'_{21} & 0 & -c'_{23} & 0 & 0 & 0 \\ -c'_{31} & -c'_{32} & 0 & 0 & 0 & 0 \\ 0 & 0 & 0 & c'_{44} & 0 & 0 \\ 0 & 0 & 0 & 0 & c'_{55} & 0 \\ 0 & 0 & 0 & 0 & 0 & c'_{66} \end{bmatrix}, C'' = \begin{bmatrix} 0 & -c''_{12} & -c''_{13} & 0 & 0 & 0 \\ -c''_{21} & 0 & -c''_{23} & 0 & 0 & 0 \\ -c''_{31} & -c''_{32} & 0 & 0 & 0 & 0 \\ 0 & 0 & 0 & c''_{44} & 0 & 0 \\ 0 & 0 & 0 & 0 & c''_{55} & 0 \\ 0 & 0 & 0 & 0 & 0 & c''_{66} \end{bmatrix}$$

And

$$\mathbf{T} = \frac{1}{3} \begin{bmatrix} 2 & -1 & -1 & 0 & 0 & 0 \\ -1 & 2 & -1 & 0 & 0 & 0 \\ -1 & -1 & 2 & 0 & 0 & 0 \\ 0 & 0 & 0 & 3 & 0 & 0 \\ 0 & 0 & 0 & 0 & 3 & 0 \\ 0 & 0 & 0 & 0 & 0 & 3 \end{bmatrix}$$

The coefficients in the tensors C' , C'' are material parameters characterizing the anisotropy of the yield function. It is to note that the isotropic yield function of this material model can be obtained by setting all the coefficients of C' and C'' to unity. For more details on Yld2004-18p, the reader is referred to Barlat et al. [18].

The evolution of the flow stress is defined assuming isotropic hardening, using a Voce hardening rule written as follows:

$$\bar{\sigma} = \sigma_0 + \sum_{i=1}^3 Q_i (1 - \exp(-C_i \bar{\epsilon}_p)) \quad (5)$$

In which

Here $\bar{\epsilon}_p$ is the equivalent plastic strain; σ_0 , Q_i and C_i are the material parameters, respectively, defining the yield stress, and strain hardening

The yield function is assumed convex and is, thus, written as

$$f = \sigma_{eq} - \bar{\sigma} = 0 \quad (6)$$

4.2 Fracture Criterion

To model the ductile fracture of the present aluminium alloy, the extended Cockcroft–Latham criterion (ECL) presented by Gruben et al. [19] was adopted. The ECL criterion explicitly accounts for the influence on the materials ductility from both the hydrostatic and the deviatoric stress state and can be expressed as an accumulative damage variable as

$$D = \frac{1}{W_c} \int_0^{\bar{\epsilon}_p} \left\langle \phi \frac{\sigma_I}{\bar{\sigma}} + (1 - \phi) \left(\frac{\sigma_I - \sigma_{III}}{\bar{\sigma}} \right)^\gamma \right\rangle \bar{\sigma} d\bar{\epsilon}_p \quad (7)$$

where $\langle \cdot \rangle$ is the Macaulay brackets and $W_c \geq 0$, $\gamma \geq 0$ and $0 \ll \phi \ll 1$ are the fracture parameters. In addition σ_I , σ_{II} and σ_{III} are, respectively, the first, second and third principal values of the co-rotational Cauchy stress tensor. In this uncoupled damage model, the fracture is assumed to initiate when $D = 1$. The readers are referred to Gruben et al. [19] for more detailed description of the model.

5 Calibration

5.1 Strain Hardening

The yield stress and the Voce work-hardening parameters of the investigated material were first calibrated by fitting with the experimental true stress–plastic strain curves of the tensile tests in ED upto the diffuse necking point. However, in order to describe the strain hardening behaviour of the material beyond the necking point to the final fracture with a reasonable accuracy, the Voce parameters were finally refined by inverse modelling of the tensile tests in ED.

A 3-D solid element-based model was established in the commercial non-linear finite elements code LS-DYNA for this numerical test. A reasonably fine mesh size of 0.25 mm × 0.25 mm and eight-node solid elements with one integration point were used for the numerical model. As seen in Fig. 8a, the numerical force–displacement curve is in a good agreement with the tests up to the final fracture.

5.2 Anisotropic Yield Model

Since the material investigated in the present study is aluminium alloy, the m parameter of the yield function described in section was set equal to 8. Hosford [20] and Hill [21] showed that this value is suitable to isotropic f.c.c. crystal structures. The anisotropy of the material is accounted for through the anisotropic coefficients C' , C'' , which are calibrated using the experimental results obtained in Sect. 2.

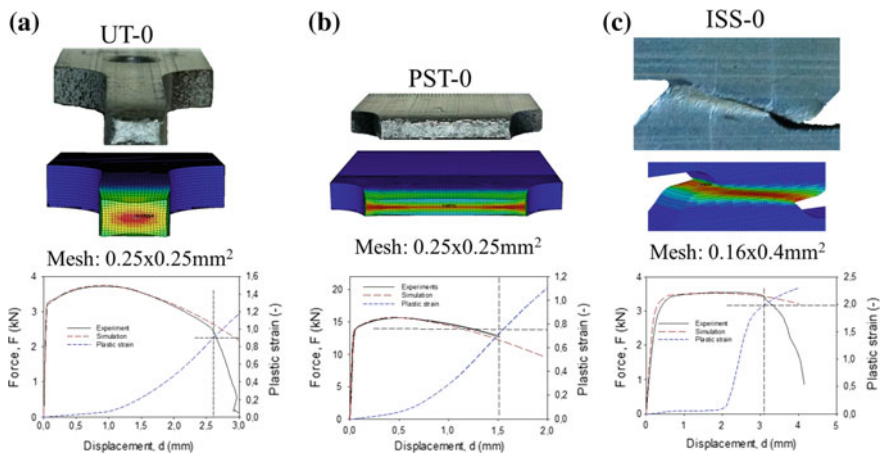


Fig. 8 Comparison of numerical and experimental test results in extrusion direction: **a** Tensile test UT-0, **b** in-plane shear test ISS-0 and **c** plane strain tensile test PST-0

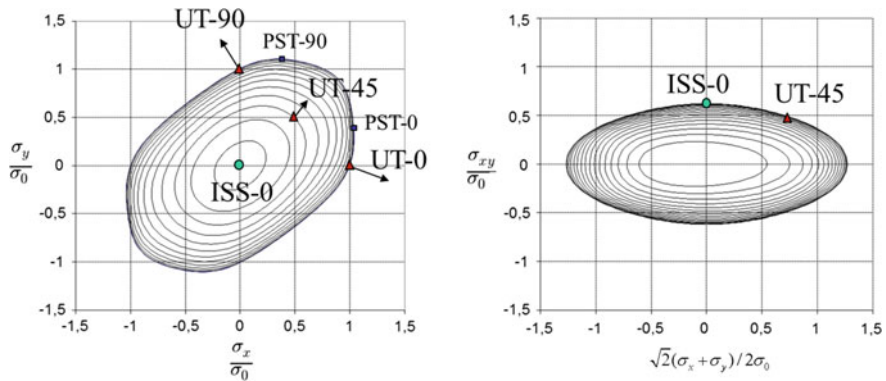


Fig. 9 Yield surface Yld2004-18p for AA6060-T7

The initial set of anisotropic parameters was determined using the experimental results in Sect. 3.1. The anisotropic coefficients are finally refined by running numerical simulations of the ISS and PST tests, using the initial set of C' , C'' parameters and the strain hardening properties determined in Sect. 5.1.

The constitutive relations described in Sect. 4 were implemented as a user-defined material subroutine in the nonlinear finite element code LS-DYNA. The numerical models of the ISS and PST tests were established using 8-node solid elements with one integration point and stiffness-based hourglass control. The element size of the numerical models is shown in Fig. 8.

Figure 9 shows representative contour plots of the final yield surfaces obtained by Yld2004-18p for the alloy 6060-T7 under investigation. As can be seen in Fig. 4, the obtained yield model captured with a good accuracy the experimental flow stress ratios (a) and strain ratios (b). A more detailed information about the calibration process can be found in the work by Barlat et al. [18].

Figure 5 shows the numerical force–displacement curves obtained both with an isotropic and calibrated anisotropic yield function, plotted along with the experimental ones for the test ISS and PST tests. It can be seen that numerical models with anisotropic yield function together with the strain hardening properties calibrated in Sect. 5.1 were able to predict very well the global behaviour (force–displacement curve) of the shear test and plane–strain test. The numerical models with an isotropic von-Mises yield model underestimated the force in the shear tests and overshoot the force–displacement curves of the plane strain tests PST-0.

5.3 Fracture Criterion

As discussed in Sect. 4.2, the used fracture model ECL has three parameters, i.e. W_c , γ and ϕ , as expressed by Eq. (7). Since the model has three parameters, three tests are thus necessary for a full calibration. Here, the model was calibrated in the extrusion direction, by using three tests namely UT-0, ISS-0 and PST-0.

Numerical simulations of these tests were run with anisotropic yield model Yld2004-18p, and the results were shown in Fig. 8. Since the extrusion direction was used as a reference direction for anisotropic yield model, the force–displacement curve of UT-0 test was not influenced by the yield function shape. However, the plastic deformation is dependent on the yield function, which describes the plastic follow through the associate plastic follow rule. To evaluate the fracture strain, the plastic strain in the critical element was collected from the simulation result of each test and plotted together with the force–displacement curves as shown in Fig. 8. The strain at fracture was assumed when the global fracture occurred, as displayed in the force–displacement curves. As seen, the significantly large plastic strain at fracture in these tests confirmed an important ductility of the investigated material.

The stress state (σ_I , σ_{II} , σ_{III}) were then collected from the same elements to determine the stress state trajectories towards the fracture strain from each test. By integrating the obtained stress–strain paths from three tests in Eq. (7), the ECL fracture criterion was fully calibrated. Figure 10 shows the numerical results of the three tests with the calibrated ECL fracture model. It can be observed that the used fracture model can predict with a reasonable accuracy the fracture initiation of the investigated tests.

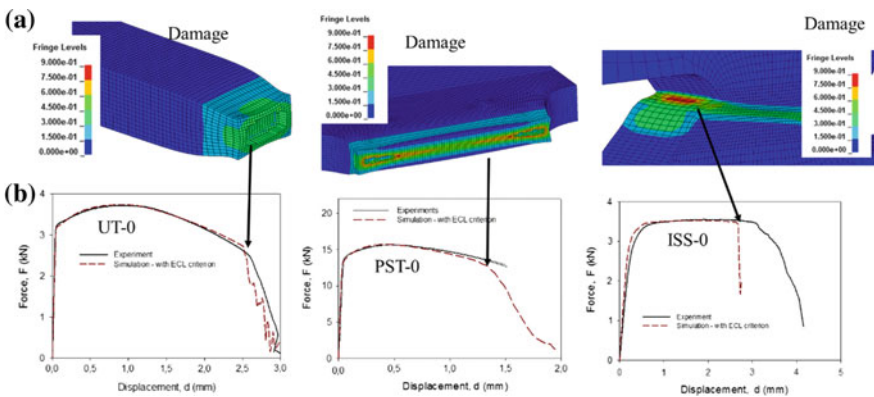


Fig. 10 Numerical simulation results with fracture criterion: **a** Damage contour plot and **b** force–displacement curves

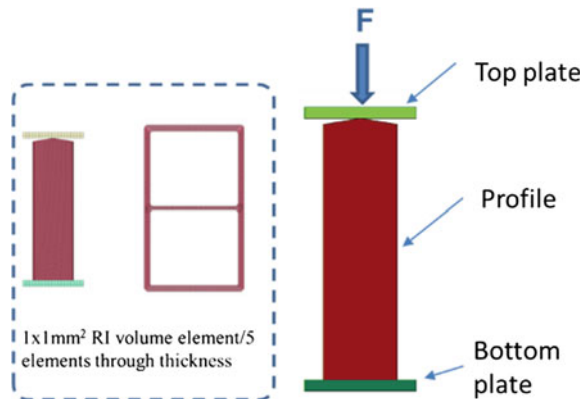
6 Numerical Analyses of Axial Crushing Tests

6.1 Numerical Model

A full solid-based model was generated in the FEM code LS-DYNA to simulate the axial crushing tests of the two chamber extruded profiles made of AA6060-T7. The model consisted of three parts: profile, bottom plate and top plate, as illustrated in Fig. 11. Reduced integrated eight-node solid elements a characteristic element size of 1 mm and 5 elements through the wall thickness were used to describe the whole model. Hourglass control was employed to inhibit zero-energy deformation modes. The node-to-surface contact algorithm was used to model the contact between the plates and profile, while the single-surface contact type was used for the self-contact within the profile.

Both the top and bottom plates were modelled as rigid bodies, while the profile was modelled as an elastic–plastic material, using the anisotropic material model as described in Sect. 4.1. The calibrated ECL criterion together with element erosion was used to model the fracture of the profiles during the test. The explicit solver of LS-DYNA was used for the axial crushing problem and the loading was applied by velocity control. While all degrees of freedom were constrained in the bottom plate, a downward velocity was prescribed for the top plate. The velocity was carefully chosen to keep the kinetic energy at a low level compared with the internal energy and thus ensure quasi-static loading. Coulomb friction (with a friction coefficient of 0.3) was specified in the contact between the plates and the profile and in the self-contact of the profile walls.

Fig. 11 Finite element model of axial crushing test



6.2 Numerical Results and Discussions

The simulation of the axial crushing was run using the calibrated ECL criterion, and the global numerical results are shown in Fig. 12 together with experimental ones, both in terms of force–displacement curves and in mean force–displacement curves. It can be observed that the global numerical results were in good agreement with the tests. Moreover, the numerical model was able to predict the complex buckling mode of the two chamber extruded profiles under axial crush loading.

The numerical model was also able to capture the fracture in the corners (location 1) and the T-junction between inner and outer wall (location 2) as observed in experimental tests; see Fig. 13a. Only few elements at these positions were eroded due to the fracture criterion in the profiles, as shown in Fig. 13b. This is consistent with the experimental results where only small cracks were observed due to the high ductility of the investigated material. This insignificant fracture has not

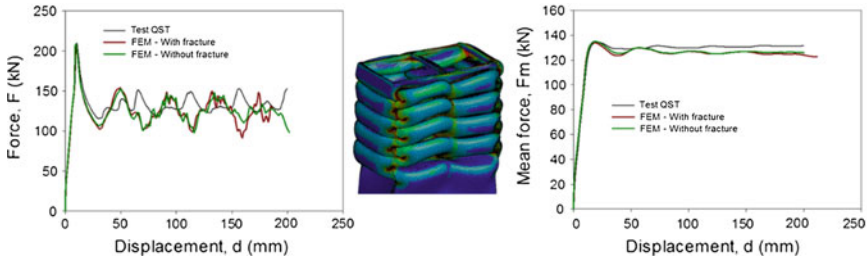


Fig. 12 Comparison between numerical and experimental results of axial crushing tests (axial crushing force, buckling mode and mean force)

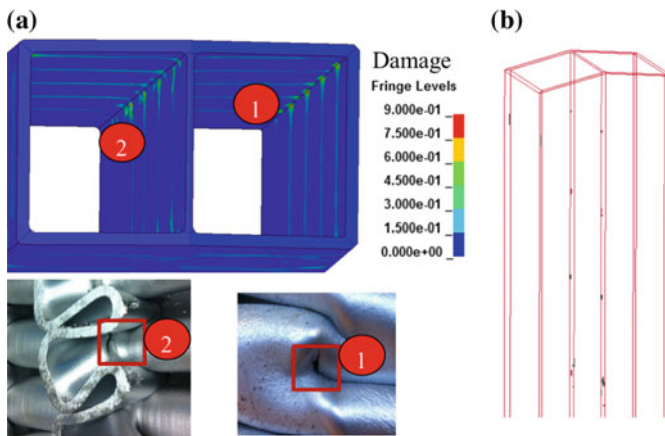


Fig. 13 a Fracture in the profiles predicted by numerical models in comparison with the test results, and b elements eroded by ECL fracture criterion in numerical simulations

influenced the global buckling mode or the energy absorption capacity of the two chamber profiles at hand, as depicted in Fig. 12 where numerical results of the simulation without considering any fracture criterion (i.e. assuming that no crack is initiated in the aluminium profile during testing) also have been plotted. As seen, the mean force–displacement curves obtained with these two simulations were almost identical.

7 Concluding Remarks

The present paper investigated experimentally and numerically the structural behaviour of two chamber extruded profiles in AA6060-T7 alloy subjected to axial crushing under quasi-static loading conditions. The main findings are summarized as follows:

- Several material tests were carried out to characterize the behaviour of the alloy AA6060-T7. The present alloy exhibits a strong ductility. The tests results also showed that the anisotropy in strength is minor in tension, but somewhat higher in-plane strain tension condition. In addition, the anisotropic properties in plastic follow were also observed.
- Due to the present anisotropic properties, isotropic yield models such as von-Mises was not able to predict correctly the shear and plane strain test behaviour. An anisotropic yield function was necessary to describe the observed anisotropic properties.
- In the present study, a material model with anisotropic yield model Yld2004-18p was used in combination with Extended Cockcroft–Latham (ECL) fracture criterion to model the material constitutive and fracture behaviour. The material model was implemented as a user-defined material subroutine in the nonlinear finite element code LS-DYNA. Material test results were used to calibrate the material model. It depicted that the advanced material model with Yld2004-18p yield function and ECL criterion can predict very good the material test results (UT, ISS and PST) both in terms of force–displacement curves and ductile fracture.
- Axial crushing test was conducted to investigate the energy absorption capacity of two chamber profiles made of this alloy. All test results revealed a progressive and regular “*step case*” buckling mode, with a small fracture observed in the profiles corner and at the T-junction between inner wall and outer wall.

A solid element-based numerical model of the axial crushing test was established in the commercial finite element code LS-DYNA, and simulations were run with the calibrated material models and fracture criterion. The predicted force–displacement curves, the energy absorption and fracture were in a good agreement with the experimental results. These results demonstrate that it is now possible to use numerical models as a design tool for optimizing aluminium profiles for automotive applications.

Acknowledgements The authors would like to thank the Structural Impact Laboratory (SIMLab), Centre for Research-based Innovation (CRI) at the Norwegian University of Science and Technology (NTNU), for their financial support

References

1. ©European Aluminium Association (2015) The aluminium automotive manual. Book, Version 2015
2. Ma J, You Z (2014) Energy absorption of thin-walled square tubes with a prefolded origami pattern—Part I: geometry and numerical simulation. *J Appl Mech Trans ASME* 81(2014): 1–11
3. Mirzaei M, Shakeri M, Sadighi M, Akbarshahi H (2012) Experimental and analytical assessment of axial crushing of circular hybrid tubes under quasi-static load. *Compos Struct* 94(6)(2012):1959–1966
4. Isaac CW, Oluwole O (2015) Finite element comparative analysis of the crushing behaviour of square steel tubes. *Int J Sci Eng Res* 6(7):1650–1655
5. Borvik T, Hopperstad OS, Reyes A, Langseth M, Solomos G, Dyngeland T (2003) Empty and foam filled circular aluminum tubes subjected to axial and oblique quasi static loading. *Int J Crashworth* 8(2003):481–494
6. Seitzberger M, Rammerstorfer FG, Gradinger R, Degischer HP, Blaimachein M, Walch C (2000) Experimental studies on the quasi static axial crushing of steel columns filled with aluminum foam. *Int J Solids Struct* 37(30):4125–4147
7. Fyllingen O, Hopperstad OS, Hanssen AG, Langseth M (2010) Modelling of tubes subjected to axial crushing. *Thin Walled Struct* 48(2010):134–142
8. Reddy TY, Wall RJ (1988) Axial compression of foam filled thin walled circular tubes. *Int J Impact Eng* 7(2):151–166
9. Hoang Nguyen-Hieu, Hopperstad Odd Sture, Myhr Ole Runar, Marioara Calin, Langseth Magnus (2015) An improved nano-scale material model applied in axial-crushing analyses of square hollow section aluminium profiles. *Thin-Walled Struct* 92(2015):93–103
10. Barlat F (1987) Crystallographic texture, anisotropic yield surfaces and forming limits of sheet metals. *Mater Sci Eng* 91(1987):55–72
11. Barlat F, Lian J (1989) Plastic behaviour and stretchability of sheet metals. Part I: a yield function for orthotropic sheets under plane stress conditions. *Int J Plast* 5(1989):51–66
12. Barlat F, Maeda Y, Chung K, Yanagawa M, Brem JC, Hayashida Y et al (1997) Yield function development for aluminum alloy sheets. *J Mech Phys Solids* 45(1997):1727–1763
13. Lademo O-G (1999) Engineering models of elastoplasticity and fracture for aluminium alloys. PhD thesis 1999:39, Department of Structural Engineering, Norwegian University of Science and Technology, Trondheim, Norway
14. Lademo O-G, Hopperstad OS, Langseth M (1999) An evaluation of yield criteria and flow rules for extruded aluminium alloys. *Int J Plast* 15(1999):191–208
15. Lademo O-G, Hopperstad OS, Malo KA, Pedersen KO (2002) Modelling of plastic anisotropy in heat-treated aluminium extrusions. *J Mater Process Technol* 125–126(2002): 84–88
16. Lademo O-G, Berstad T, Eriksson M, Tryland T, Furu T, Hopperstad OS, Langseth M (2008) A model for process-based crash simulation. *Int J Impact Eng* 35(5):376–388
17. Pickett AK, Pyttel T, Payen F, Lauro F, Petrinic N, Werner H et al (2004) Failure prediction for advanced crashworthiness of transportation vehicles. *Int J Imp Eng* 30(2004):853–872
18. Barlat F, Aretz H, Yoon JW, Karabin ME, Brem JC, Dick RE (2005). Linear transformation-based anisotropic yield functions. *Int J Plast* 21(5):1009–1039

19. Gruben G, Hopperstad OS, Børvik T (2012) Evaluation of uncoupled ductile fracture criteria for the dual-phase steel Docol 600DL. *Int J Mech Sci* 62(1):133–146
20. Hosford WF (1972) A generalized isotropic yield criterion. *J Appl Mech* 39(1972):607–609
21. Hill R (1979) Theoretical plasticity of textured aggregates. *Math Proc Camb Philos Soc* b85:179–191

Part VII
Flow Problems

Evaluating the Saltwater Intrusion to Aquifer Upper-Middle Pleistocene (qp₂₋₃) in Coastal Area of Tra Vinh Province Due to Groundwater Exploitation



Huynh Van Hiep, Nguyen The Hung and Pham Van Long

Abstract Today, one of the most serious problems in Tra Vinh as other coastal provinces in Mekong Delta is the exploitation of groundwater for different purposes. In many cases, the aquifers are pumped or withdrawn with greater discharge to its natural ability, thus making seawater draw into the system [1]. This paper aims at evaluating the saltwater intrusion into aquifer upper-middle Pleistocene in Tra Vinh province area due to groundwater extraction. The calculated area includes 2,176 nodes, 2,079 elements, and grid steps $\Delta x = \Delta y = 1,000$ m. The program is set up to determine the interface between freshwater and saltwater which moves from the sea into the mainland of upper-middle Pleistocene aquifer. The calculating results show that at the initial point when pumping with outflow $Q = 29,987 \text{ m}^3/\text{day}$, the toe interface in position is of 2,019 m from the sea, then with the time of exploitation $t = 150,000$ days, the interface moving into in the mainland is approximately 21,000–24,000 m. The calculation results enable managers and abstraction units to know the process of salt line by time in order to launch sound plan for exploitation.

Keywords Saltwater intrusion • Upper-middle pleistocene aquifer
Interface depth • Coastal • Tra Vinh

H. Van Hiep (✉) • N. T. Hung

University of Science and Technology, The University of Da Nang, Da Nang, Vietnam
e-mail: hvhiepv1@gmail.com

N. T. Hung

e-mail: profhungthenguyen@gmail.com

P. Van Long

Vina Mekong Engineering Consultants Joint Stock Company, Ho Chi Minh City, Vietnam
e-mail: longvinamekong@gmail.com

© Springer Nature Singapore Pte Ltd. 2018

H. Nguyen-Xuan et al. (eds.), *Proceedings of the International Conference on Advances in Computational Mechanics 2017*, Lecture Notes in Mechanical Engineering, https://doi.org/10.1007/978-981-10-7149-2_46

675

1 Introduction

Water is a precious natural resource for human life since it is very important for socioeconomic development and contributes to environmental sustainability. Groundwater extraction in coastal areas is a matter of concern and careful management; otherwise, the water quality will be degraded due to seawater intrusion [2]. The population increase and water demand for livelihood and economy have strained water resources in the world seriously. Due to pollution and degradation of surface water, groundwater aquifers are more and more exploited. However, if the groundwater reserve is over-extracted, this will cause adverse impacts, more specifically, the groundwater level drops down causing ground subsidence and the salinity intrudes into the mainland deeply [3]. Coastal aquifers are connected by freshwater in the field and saltwater in the sea. Those are important sources of groundwater which is often over-exploited due to high population density. Coastal aquifers are prone to salinity intrusion due to other factors such as sea level rise by climate change [4]. To cope with these situations, intrusive salinity management models need to be developed to design optimal and sustainable groundwater extraction strategies [1]. Tra Vinh province is located in the east of the Mekong Delta. It shares borders with Ben Tre province in the north by Co Chien river (a tributary of the Tien river), by Soc Trang province in the southwest and Can Tho city across Hau river, by Vinh Long province in the west, and the East Sea in the east (length of 65 km) (Fig. 1).

In Tra Vinh province, water supply for daily lives, industrial zones, and factories are all extracted from groundwater. Consequently, the assessment of salinity intrusion into the upper-middle Pleistocene aquifer is an urgent issue today. This is very useful for managers in distributing and licensing of groundwater exploitation reasonably and efficiently.

2 Materials and Methods

In Tra Vinh province where the groundwater in the natural state does not move or lightly move and its one side contacts the river or the coast, this will form the interface between saltwater and freshwater. If the freshwater is over-extracted, it will be lowered. This causes pressure drop and the interface will gradually move to the pump position all triggering the freshwater reserve to be minimized and the ground to be subsided [5]. Therefore, the location of the interface over time by freshwater pumping can be performed by mathematical model [6–8].



Fig. 1 Location of cadastral boundaries of Tra Vinh province

2.1 The General Basic Differential Equations for Describing the Interface

The governing equations for describing the interface between saltwater and freshwater of groundwater in coastline, two horizontal dimensions 2DH (x,y) with confined aquifer [6–8] (Fig. 1) are formulated as follows:

$$-\nabla \cdot (\alpha T \nabla f) + \nabla \cdot (\alpha T_a \nabla h) = I_f + I_s + q'_f + q'_s \tag{1}$$

$$S \partial h / \partial t - \nabla \cdot (\alpha T_a) \nabla h + \nabla \cdot (\alpha T_a \nabla f) = -I_s - q'_s \tag{2}$$

with $f = \phi_f / \alpha$; $T = K(H_1 - H_2)$; $T_a = T(H_1 - h) / (H_1 - H_2)$

where T is transmissivity coefficient of aquifer, with aquifer anisotropic $T = (T_x, T_y)$, where T_x and T_y are the coefficients of transmissivity in x, y directions. Eqs. (1) and (2) have set up separate formula of intrusion flows with two confined horizontal dimensions; the 2DH equation is rewritten in the general form as follows:

$$\left[\frac{\partial}{\partial x} \left(\alpha T_x \frac{\partial f}{\partial x} \right) + \frac{\partial}{\partial x} \left(\alpha T_y \frac{\partial f}{\partial y} \right) \right] + \left[\frac{\partial}{\partial x} \left(\alpha T_{ax} \frac{\partial h}{\partial x} \right) + \frac{\partial}{\partial y} \left(\alpha T_{ay} \frac{\partial h}{\partial y} \right) \right] \quad (3)$$

$$= I_f + I_s + q'_f + q'_s$$

$$S_0 \frac{\partial h}{\partial t} - \left\{ \frac{\partial}{\partial x} \left(\alpha T_{ax} \frac{\partial h}{\partial x} \right) + \frac{\partial}{\partial y} \left(\alpha T_{ay} \frac{\partial h}{\partial y} \right) \right\} + \left\{ \frac{\partial}{\partial x} \left(\alpha T_{ax} \frac{\partial f}{\partial x} \right) + \frac{\partial}{\partial y} \left(\alpha T_{ay} \frac{\partial f}{\partial y} \right) \right\}$$

$$= -I_s - q'_s \quad (4)$$

with $f = \frac{(1-\beta)h_f + \beta\phi_f}{\alpha}$; $\alpha = \frac{\rho_s - \rho_f}{\rho_f}$

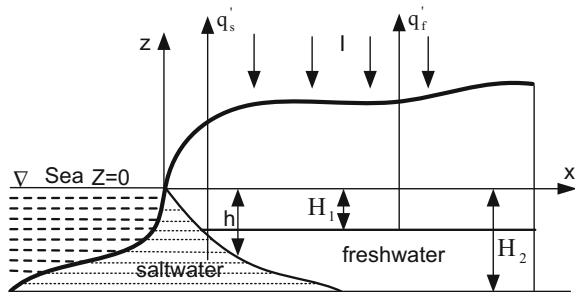
$$T_x = K_x [H_1 + (1 - \beta)h_f - \beta H_2]; \quad T_y = K_y [H_1 + (1 - \beta)h_f - \beta H_2]$$

$$T_{ax} = T_x \times \frac{(H_1 - h)}{[H_1 + (1 - \beta)h_f - \beta H_2]}; \quad T_{ay} = T_y \times \frac{(H_1 - h)}{[H_1 + (1 - \beta)h_f - \beta H_2]}$$

and with $\beta = 1$ if the aquifer is confined; $\beta = 0$ if the aquifer unconfined, and where ρ_f denotes density of freshwater; ρ_s denotes density of saltwater; S_0 denotes the storativity; t denotes the time; h_f denotes the freshwater head above sea level; ϕ_f denotes the piezometric head for freshwater; q'_f, q'_s denote the freshwater and saltwater sink; I_f, I_s denote the freshwater and saltwater recharge in aquifer; K_x, K_y denote the hydraulic conductivity in the x, y directions (Fig. 2).

Eqs. (3) and (4) are nonlinear partial differential equations, and their accurate solution cannot be performed by analytical method but by numerical method.

Fig. 2 Confined aquifer (represented by the A-A section and lies in the oxz plane at perpendicular to the oxy plane given in Fig. 1)



2.2 Numerical Method

The above equations are approximated by using the Galerkin finite element method (FEM) with the triangle element, and assuming that the values of the permeability coefficients pass or permeability coefficients at each element under the xz or xy directions remain unchanged, then the equation for any element is set up as follows:

$$\int_{A^{(e)}} N_i^{(e)} L(M)_m dA = 0 \tag{5}$$

where $N_i^{(e)}$ with $i = 1, 2, 3$ is the triangle element function (first degree chosen); $L(M)_m$ with $m = 1, 2$ is the differential Eqs. (3) or (4) to be set for any element; $A^{(e)}$ is the area of element. The value h is approximated by the formula:

$$h^{(e)} = \sum_{i=1}^n N_i^{(e)} \times h_i \tag{6}$$

where $h^{(e)}$ is the approximate value of the interface depth at a point in the element; n is nodes of element; h_i is the interface depth at the nodes of element. After performing mathematical transformations, we get the following linear system of equations:

$$\begin{aligned}
 & [K_a] \begin{Bmatrix} f_1 \\ \cdot \\ \cdot \\ f_n \end{Bmatrix} - [K_b] \begin{Bmatrix} h_1 \\ \cdot \\ \cdot \\ h_n \end{Bmatrix} \\
 & = \begin{Bmatrix} (I_{f1}^{(e)} + I_{s1}^{(e)}) \frac{A_1}{3} \\ \cdot \\ \cdot \\ (I_{fn}^{(e)} + I_{sn}^{(e)}) \frac{A_n}{3} \end{Bmatrix} + \begin{Bmatrix} q_{f1} + q_{s1} \\ \cdot \\ \cdot \\ q_{fn} + q_{sn} \end{Bmatrix} + \frac{[(1 - \beta)h_f - \beta H_2 + h]}{[H_1 + (1 - \beta)h_f - \beta H_2]} \begin{Bmatrix} R_1 \\ \cdot \\ \cdot \\ R_n \end{Bmatrix} \tag{7}
 \end{aligned}$$

$$\begin{aligned}
 & - [K_b] \begin{Bmatrix} f_1 \\ \cdot \\ \cdot \\ f_n \end{Bmatrix} + \left[[K_b] + \frac{[C]}{\Delta t} \right] \begin{Bmatrix} h_1 \\ \cdot \\ \cdot \\ h_n \end{Bmatrix}_{t+\Delta t} = - \begin{Bmatrix} \frac{I_{s1}^{(e)} \times A_1}{3} \\ \cdot \\ \cdot \\ \frac{I_{sn}^{(e)} \times A_n}{3} \end{Bmatrix} - \begin{Bmatrix} q_{s1} \\ \cdot \\ \cdot \\ q_{sn} \end{Bmatrix} + \frac{[C]}{\Delta t} \begin{Bmatrix} h_1 \\ \cdot \\ \cdot \\ h_n \end{Bmatrix} \tag{8}
 \end{aligned}$$

with

$$\begin{aligned}
 [K_a] &= \sum_{e=1}^m [K_a^{(e)}]; [K_b] = \sum_{e=1}^m [K_b^{(e)}]; [C] = \sum_{e=1}^m [C^{(e)}] \\
 [q_{fi} + q_{si}] &= \sum_{e=1}^m [q_{fi}^{(e)} + q_{si}^{(e)}]; [q_{si}] = \sum_{e=1}^m [q_{si}^{(e)}]; [R_i] = \sum_{e=1}^m [R_i^{(e)}] \quad (i = 1, n) \\
 [K_a^{(e)}] &= \frac{\alpha T_x^{(e)}}{4A} \begin{bmatrix} b_1^2 & b_1 b_j & b_1 b_k \\ b_j b_i & b_j^2 & b_j b_k \\ b_k b_i & b_k b_j & b_k^2 \end{bmatrix} + \frac{\alpha T_y^{(e)}}{4A} \begin{bmatrix} c_i^2 & c_i c_j & c_i c_k \\ c_j c_i & c_j^2 & c_j c_k \\ c_k c_i & c_k c_j & c_k^2 \end{bmatrix} \\
 [K_b^{(e)}] &= \frac{\alpha T_{ax}^{(e)}}{4A} \begin{bmatrix} b_1^2 & b_1 b_j & b_1 b_k \\ b_j b_i & b_j^2 & b_j b_k \\ b_k b_i & b_k b_j & b_k^2 \end{bmatrix} + \frac{\alpha T_{ay}^{(e)}}{4A} \begin{bmatrix} c_i^2 & c_i c_j & c_i c_k \\ c_j c_i & c_j^2 & c_j c_k \\ c_k c_i & c_k c_j & c_k^2 \end{bmatrix} \\
 [C^{(e)}] &= S_0^{(e)} \times \frac{A}{3} \begin{bmatrix} 1 & 0 & 0 \\ 0 & 1 & 0 \\ 0 & 0 & 1 \end{bmatrix}
 \end{aligned}$$

where $S_0^{(e)}$ denotes the specific storativity of the triangle element; a_i, b_i, c_i are coefficients of the function N_i [6–8].

2.3 Diagram Calculation for Checking the Program

Selected calculation area a horizontal rectangle (1,500 m × 600 m), the axis ox (1,500 m), the coastline oy edge (600 m) [7, 8].

The calculated domain is divided into 90 quadrilateral elements (applied in the manner of [6] each quadrilateral elements consists of four triangular elements), 112 nodes, grid step $\Delta x = \Delta y = 100$ m with boundaries as shown in Fig. 3 and the coordinate $Z = 0$ coincides with sea level. Average permeability coefficients $K_{tb} = 8.5$ m/day, average saturation thickness of aquifer $B = 30$ m, storativity $S = 0.6$.

2.4 Boundary and Initial Conditions

At the initial time $t = 0$, the height of the groundwater table and the depth (h) of the interface at the node points along the axis were preliminarily determined according to the approximate analytical formula Ghyben–Herzberg, we have (Table 1).

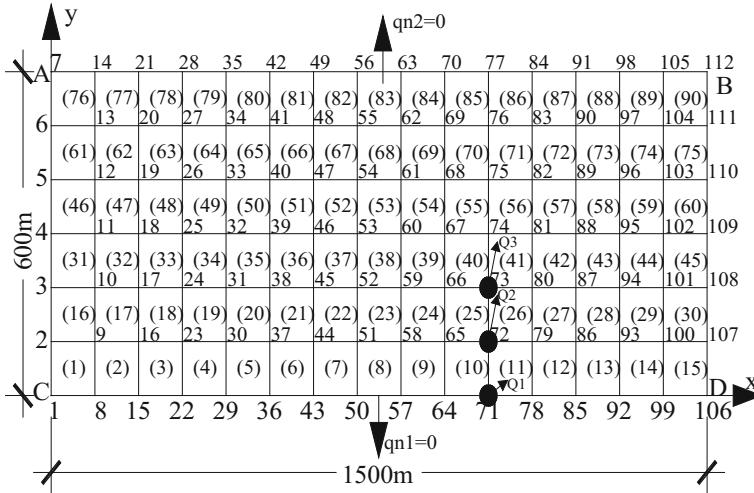


Fig. 3 Domain calculated with quadrilateral elements spacing 100 m nodes

Table 1 Head of freshwater value and initial interface depth (m)

X	0	100	200	300	400	500	600	700	800
(ϕ_f)	0	0.59	0.84	1.03	1.19	1.32	1.45	1.57	1.68
$h_{initial}$	0	-33.76	-40.0	-40.0	-40.0	-40.0	-40.0	-40.0	-40.0
X	900	1,000	1,100	1,200	1,300	1,400	1,500		
(ϕ_f)	1.78	1.88	1.97	2.06	2.14	2.22	2.3		
$h_{initial}$	-40.0	-40.0	-40.0	-40.0	-40.0	-40.0	-40.0		

Boundary conditions: flow across AB boundaries: $q_{n1} = 0$ and symmetric CD boundaries: $q_{n2} = 0$; sea water level AC: $h = -10$ m; with the BD boundary, the function f does not change in the axial direction oy , meaning $BD: \partial f / \partial y = 0$.

2.5 Calculation Results

The calculating program determined the value of the depth of the interface at nodes over time. In straight vertical planes with shoreline passing through the wells Q1, Q2, the values are shown in Figs. 4 and 5.

The above figures show that at the initial time ($t = 0$), saltwater toe is located 160 m away from the coastline, 840 m from the exploitation well, after a extract time $t = 10,000$ days ≈ 27.39 years, saltwater toe will move to the position of 525 m from the coastline and 475 m from the well.

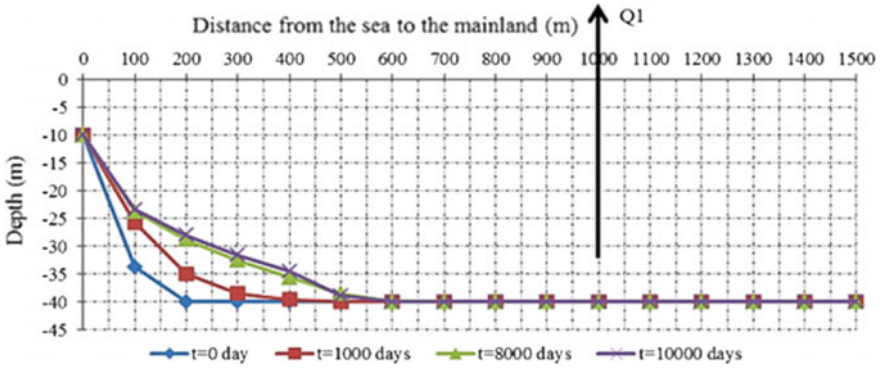


Fig. 4 Position and depth of the interface by time at the section through the well Q1

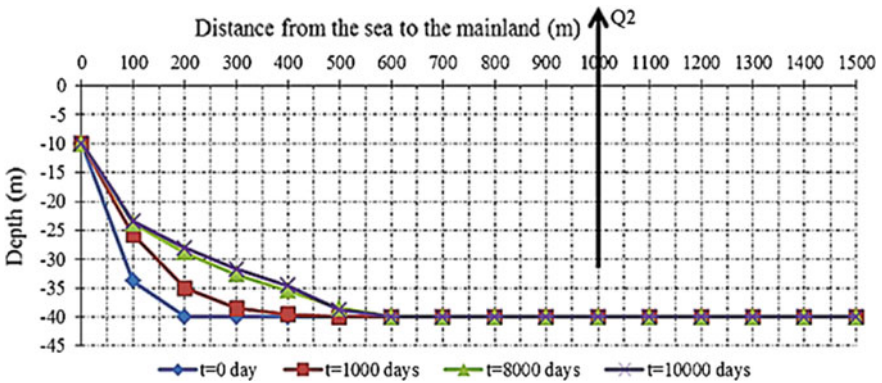


Fig. 5 Position and depth of the interface by time at the section through the well Q2

2.6 Checking and Discussing the Calculation Results

By using the finite element method (FEM), the results of calculation are compared with the most common formulas such as the Thesis and the superposition formula. The position of saltwater toe by each method is shown in Table 2.

The differences between the three methods from the above results were negligible. The above data show that at the initial time ($t = 0$), saline wedge is located

Table 2 Position of saltwater toe according to methods

X	Thesis formula	FEM method	Superposition formula
The distance from the coast to the saltwater toe position farthest (m)	516.3	525.0	534.4

160 m away from the shore, 840 m from the exploitation well. After a mining time $t = 10,000$ days ≈ 27.39 years, saline season will move to the position 525 m from the shore, 475 m from the well in the case of FEM method. In the case of the Thesis formula, at the beginning of the salinity boundary at $x_0 = 159.4$ m, after the extraction time of 10,000 days ≈ 27.39 years the salinity boundary will advance to the mainland by about 356.9 m, 516.3 m from the shore, 483.7 m from the well. As for the piling formula, the simultaneous exploitation of the three wells and saltwater wells is 534.4 m far from the coastline, 465.4 m away from the pavement. The difference in finite element method compared with the Thesis formula was 0.087 and 0.094% as compared to the superposition formula. Especially, the results from the FEM method have average value higher than the Thesis formula but lower than the superposition formula. These results are fairly reasonable. On the other hand, the FEM solution demonstrates the shape and position of the interface at each computing time with any geological structure which corresponds to the different freshwater exploitation flows, the complex boundary shape, and many anisotropic pumping and infiltration positions. The problem can be complex at any time that is convenient for use. From the discussed results and remarks, we find that the used model is well suited to the reality. This is considered as a steady basis for using this model to evaluate the salinity intrusion into the groundwater aquifer in the coastal area.

3 Calculating the Salinity Intrusion into the Upper-Middle Pleistocene Aquifer in Tra Vinh Province

3.1 Hydrogeology Characteristic

In Tra Vinh province, there are seven aquifers: Holocene, the upper Pleistocene, the upper-middle Pleistocene, the lower Pleistocene, the middle Pliocene, the lower Pliocene, and the upper Miocene. Alternating between these porous aquifers are poorly formed aquifers with, respectively, geologic ages: Holocene, upper Pleistocene, upper-middle Pleistocene, lower Pleistocene, middle Pliocene, lower Pliocene, upper Miocene. Figures 6, 7, and 8 illustrate the above-mentioned aquifers.

The upper-middle Pleistocene layer has depth to top varies from 69.0 to 140.0 m, average 106.60 m; depth to base varies from 118.0 to 201.5 m, average 154.9 m; minimum thickness is 10.30 m, maximum thickness is 73.50 m, average 44.41 m. Average permeability coefficient is 35.85 m/day. The average specific yield coefficient (μ) is 0.19, and the average specific storage coefficient (μ^*) is 0.0032. The composition of this layer is mostly granular sand, sand, and gravel.

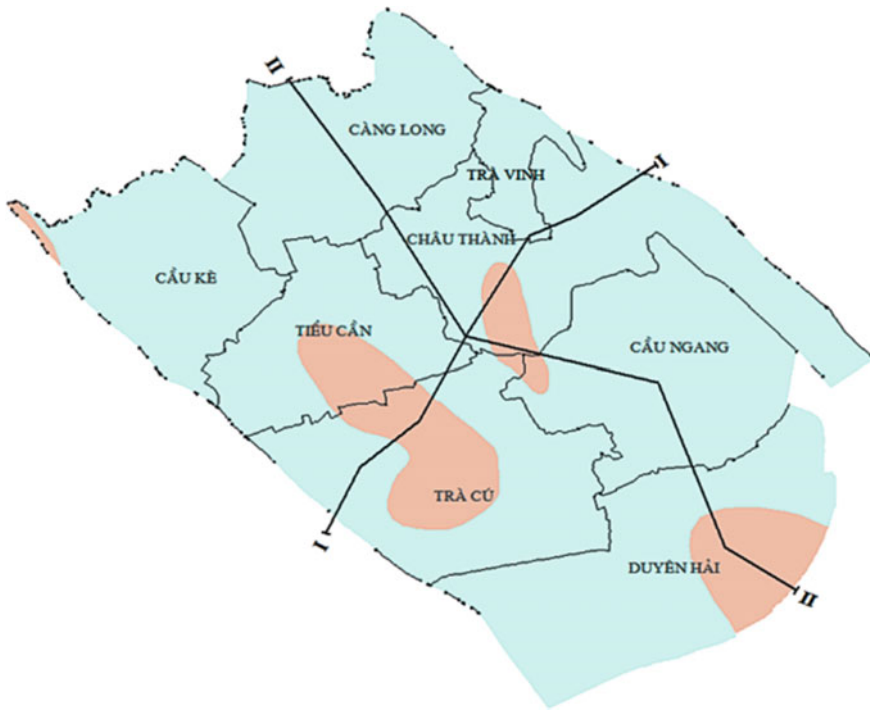


Fig. 6 Map of hydrogeology in Tra Vinh province [9]

3.2 Chart of Calculation

The mathematical domain is modeled as a horizontal quadrilateral which has the width of 33,000 m (OY) overlapping the shoreline, the length of 63,000 m (OY) along Hau river and perpendicularly to the shoreline. Based on the coast length and the location of the pump wells, the computing domain is divided into quadrilateral elements and the coordinate angle $z = 0$ coincides with the mean sea level. The calculation chart is divided into 2,176 nodes, 2,079 quadrilateral elements, and a grid step $\Delta x = \Delta y = 1,000$ m (Fig. 9). The study area is arranged with 89 wells with a total exploitation volume of 29,987 m³/day, and the exploitation layer is mainly concentrated in the upper-middle Pleistocene aquifer (qp₂₋₃).

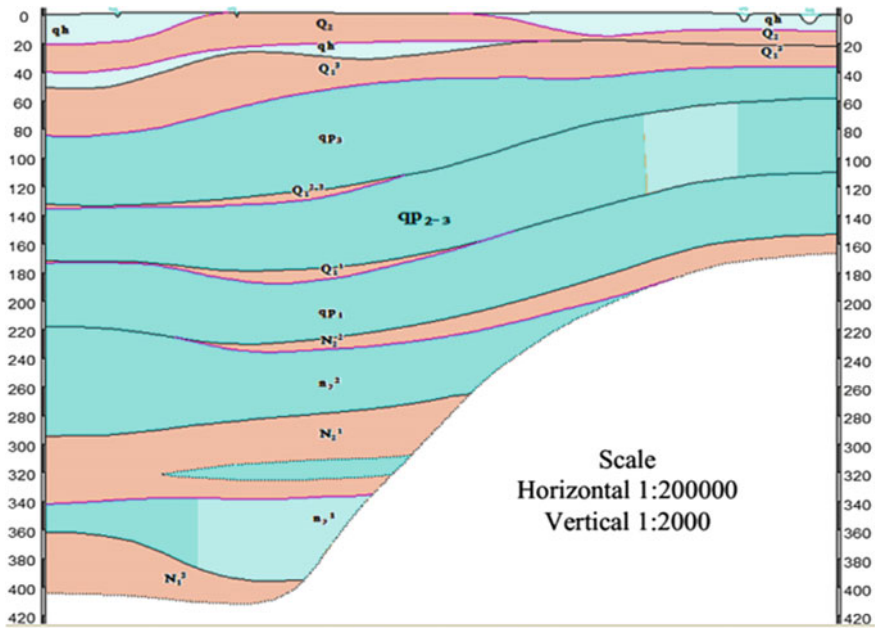


Fig. 7 Cross section of hydrogeology I-I [9]

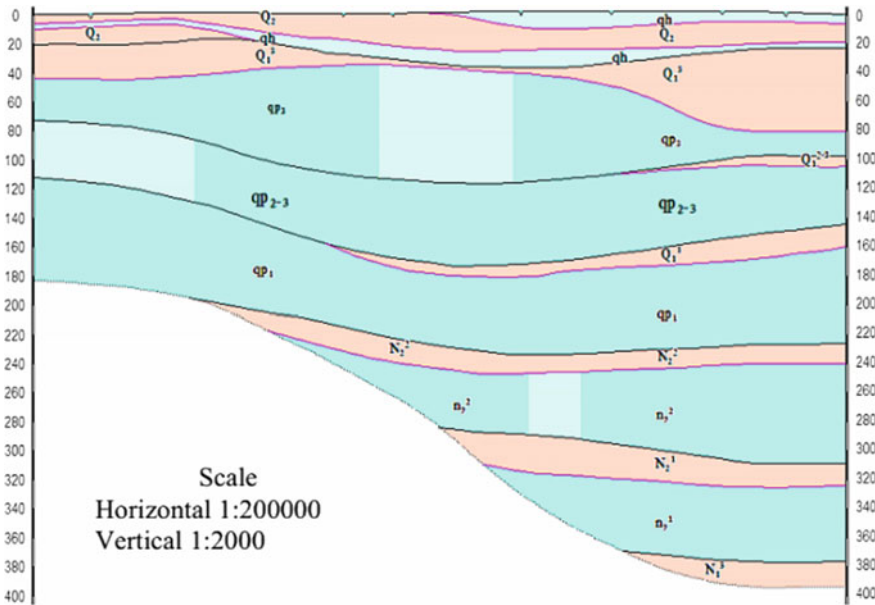


Fig. 8 Cross section of hydrogeology II-II [9]

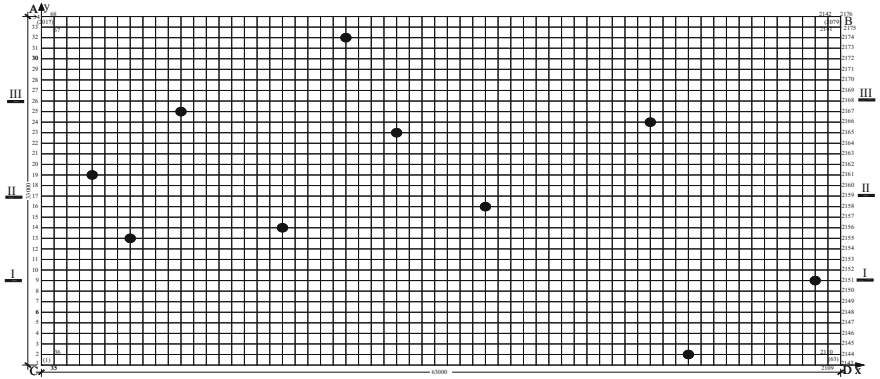


Fig. 9 Chart of calculation and layout of pumping wells in the study area

3.3 Boundary and Initial Conditions

- Boundary condition: boundary AB: $q_{n1} = 0$; boundary CD $q_{n2} = 0$; boundary AC: $h = -107$ m; boundary BD: $\partial f / \partial y = 0$
- Initial condition: The initial condition for the interface between saltwater and freshwater was assumed when freshwater has not been exploited yet; given the height of piezometric head (ϕ_f) and the depth (h) of the interface to the upper-middle Pleistocene (qp₂₋₃) porous aquifer at the nodes in the vertical section (Fig. 9, cross sections II–II and III–III).

3.4 Results and Discussion

Algorithm and modeling program were established by FEM method in weak Galerkin formulation in order to predict the position, the interface shape over time between fresh and salt water of upper-middle Pleistocene aquifer. The change of the interface position at the wells of the aquifer is shown in Figs. 10, 11, 12, 13, and 14.

Commenting calculation results: From the above results, we find that depending on the location and time, the displacement value of saltwater toe varies despite the same pumping flow (Figs. 10, 11, 12, 13, and 14). For example, saltwater toe at the beginning is located at a distance of 2,019 m from the sea, but after $t = 10,000$ days of exploitation, saltwater toe moved into the mainland with a distance of 14,000 m in the section along Hau river, 8,000 m in section I–I, 10,000 m in section II–II, 7,000 m in section III–III and 12,000 m in the section along Co Chien river. But then, at $t = 50,000$ days, the salinity displaced 18,000 m from the sea into mainland for the sections, except for I–I section when it moved 15,000 m only. Especially, at the time of $t = 50,000$ days (≈ 410.9 years) with the specific outflow,

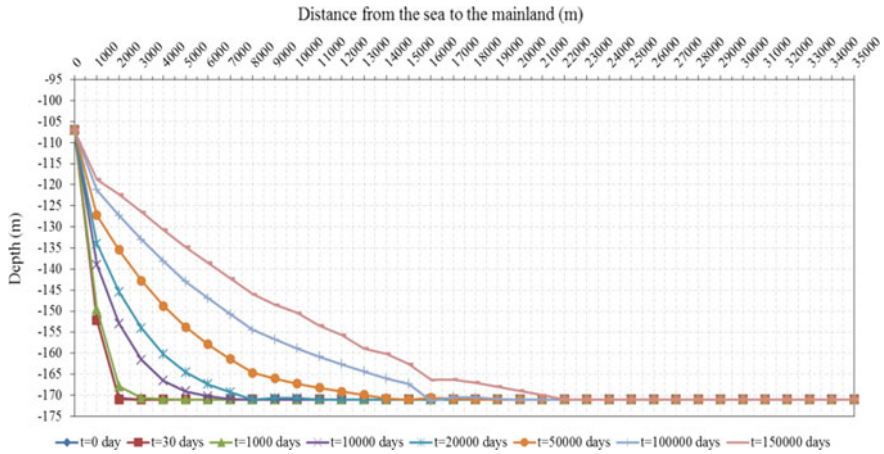


Fig. 10 Position and depth of the interface along Hau River by time

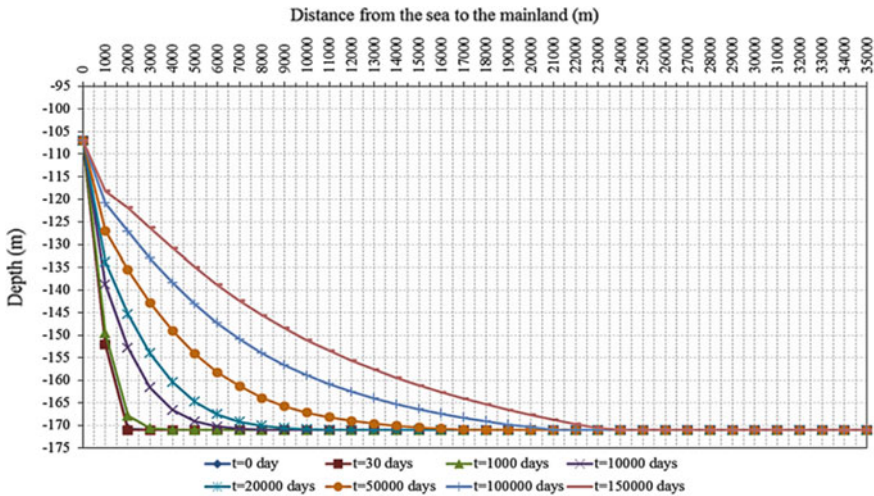


Fig. 11 Position and depth of the interface at the cross section I-I by time

the displacement of salinity at sections II-II and III-III was 24,000 m, the largest value as compared to other sites. More specifically, it was 2,000 m larger than that at the site of section II, 3,000 m larger than at the section along Hau River, and 1,000 m larger than at the cross section along Co Chien River. The calculation results also indicated that in the initial time, the saltwater moved very fast from 7,000 to 14,000 m at $t = 10,000$ days, then from 4,000 to 11,000 m at time $t = 50,000$ days and only about 3,000–7,000 m at $t = 150,000$ days (Table 3). This is appropriate to the fact that the deeper the displacement of salinity into the

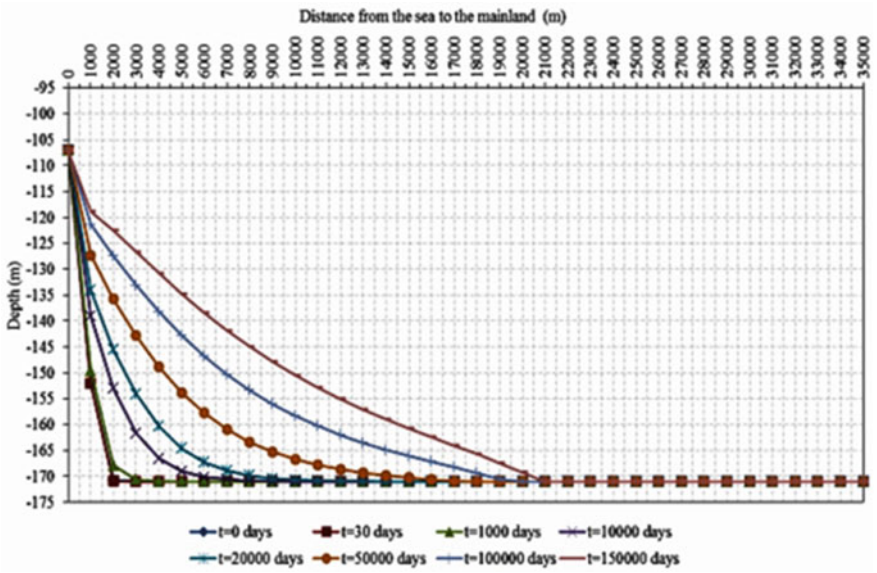


Fig. 12 Position and depth of the interface at the cross section II-II by time

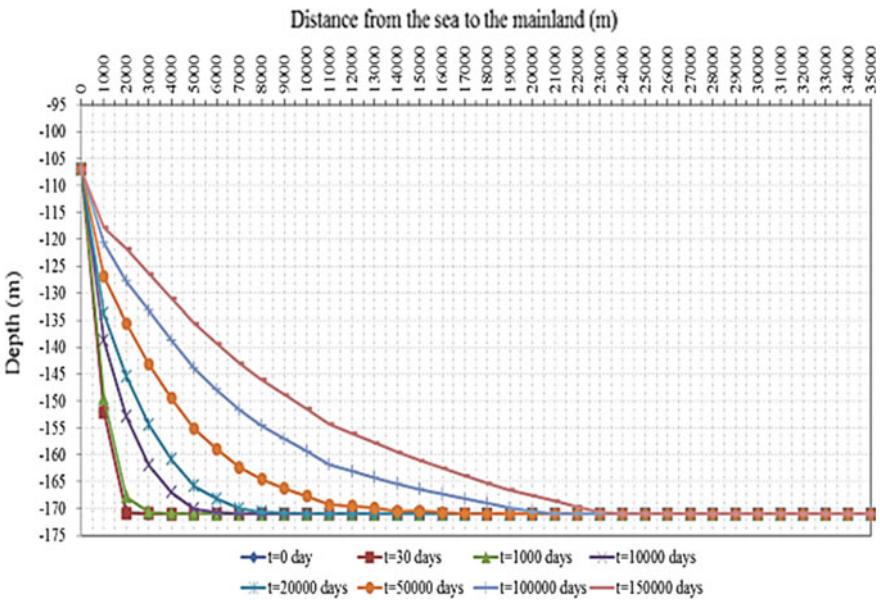


Fig. 13 Position and depth of the interface at the cross section III-III by time

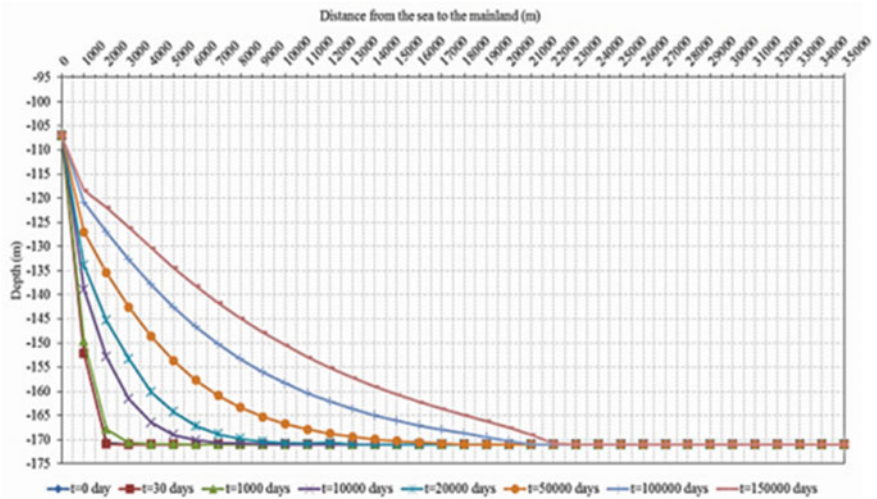


Fig. 14 Position and depth of the interface along Co Chien River by time

Table 3 Displacement value of salinity compared to the position of saltwater toe over time

Cross section	Distance from the coast to the farthest saltwater toe position (m)			
	t = 0 day	t = 10,000 days	t = 50,000 days	t = 150,000 days
Along Hau River	2,019	14,000	18,000	21,000
I-I	2,019	8,000	15,000	22,000
II-II	2,019	10,000	18,000	24,000
III-III	2,019	7,000	18,000	24,000
Along Co Chien River	2,019	12,000	18,000	23,000

mainland is the less it is near the sea. The calculation results also show that when the groundwater is pumped (freshwater), the surface value of the interface moves in the horizontal direction (from the sea to the mainland) corresponding to the pump flow and time.

4 Conclusions

The mathematical model of salinity intrusion into the aquifer was set up to calculate for the coastal area algorithm and calculation program calculated for confined aquifer in Tra Vinh province. The calculation results are identified as follows:

- Determining the depth and shape of boundaries that salinity moves into the mainland from the sea over time, depending on the location of the cross section

considered differently in the calculation area. For example, at the II–II section at the beginning of salt wedge at 2,019 m from the sea, but after pumping time $t = 150,000$ days ≈ 410.9 years, the salt wedge shifted to 24 km.

- Evaluating the level of salinity intrusion into the upper-middle Pleistocene aquifer (qp₂₋₃) over time corresponding to the specific exploitation flows. Based on this, the model can predict the salinity intrusion into the aquifer over time corresponding to the different exploitation flows.
- Algorithms and calculation programs can be calculated for all confined and unconfined aquifers, corresponding to different areas in the coastal zone.
- The results of this calculation are significant for planning, laying out wells, and forecasting salinity intrusion so that the managers can devise feasible plans for exploiting groundwater in order to meet the need of the socioeconomic development needs, and also to ensure the sustainable development of Tra Vinh province as well as other coastal areas in the country and in the world.

References

1. Qahman K, Larabi A, Ouazar D, Naji A, Cheng AH-D (2009) Optimal extraction of groundwater in Gaza coastal aquifer. *J Water Resour Protect* 4:249–259
2. Qahman K, Rabi A (2005) Evaluation and numerical modeling of seawater intrusion in the Gaza aquifer (Palestine). *Hydrogeo J*
3. Ndambuki JM (2011) A novel approach to solving multi-objective groundwater problems with uncertain parameters. *Open Hydrol J* 5:19–25
4. Janardhanan S (2012) Integrated multi-objective management of saltwater intrusion in coastal aquifers using couple simulation-optimisation and monitoring feedback information. Thesis of Doctor of Philosophy, James Cook University, Australia
5. Hung NT, Van Minh T (2008) On the finite element technique for the shallow-water equations. In: *Proceeding of the 8th national conference of mechanics, Vietnam*, pp 271–279
6. Bear J, Cheng AHD, Sorek S, Ouazar D, Herrera I (1999) *Seawater intrusion in coastal aquifers-concepts, methods, and practices*. Kluwer Academic Publishers, Dordrecht
7. Van Minh T, Hung NT (2005) Saltwater intrusion to groundwater in coastal regions of Hoa Khanh when exploits fresh water by pumping. In: *National scientific conference of fluid mechanics, Vietnam*, pp 398–415
8. Van Minh T, Hung NT (2006) A General mathematical model of two dimensional horizontal flow of seawater intrusion. In: *Proceeding of conference on applying modern technologies in transport infrastructure construction, Vietnam*, pp 271–280
9. Vuong BT, Chan ND, Nam LH (2013) Report on assessing the impact of climate change on groundwater resources in the Mekong Delta and proposing the respond measures. Report number: 22. Division for Water Resources Planning and Investigation for the South of Vietnam (DWRPIS)

Study the Hull Form and Propeller-Rudder System of the Fishing Vessel for Vietnam



Victor G. Bugaev, Dam Van Tung and Yana R. Domashevskaya

Abstract Currently, the construction of steel fishing vessels in Vietnam is extremely important. For the traditional fishing vessels were built in Vietnam, the characteristic form of the contours corresponding to low-speed running and block coefficient is increased. The transition to a new level of construction and operation of fishing vessels requires a thorough and detailed analysis of the hull form and the characteristics of propeller-rudder system, as well as their interaction in the process of fishing operations. In this paper we discuss the characteristics of the hull form and propeller-rudder system (propeller inside the nozzle) of the fishing vessel (project 70133), intended for the manufacture and operation in Vietnam by using Computational Fluid Dynamics.

Keywords Fishing vessel • Propeller-rudder system • Resistance of ship

1 Introduction

Today, computational fluid dynamics (CFD—Computational Fluid Dynamics) is widely used both in its traditional fields: shipbuilding, aviation, design vehicles, and at the creation of home appliances, printing equipment, etc. Modern software products of hydrodynamic simulation combine high level of functionality, accuracy, and ease of use.

V. G. Bugaev · D. Van Tung (✉) · Y. R. Domashevskaya
Far Eastern Federal University, Vladivostok, Russia
e-mail: damvantung@mail.ru

V. G. Bugaev
e-mail: v_bugaev@mail.ru

Y. R. Domashevskaya
e-mail: 100-70-100dom@mail.ru

Features of designing and operation of fishing vessels are [1, 2]:

Search of fishing objects and fishing practices by various fishing gear;
Storage and transportation of whole cooled fish and seafood in refrigerated tanks with water from 6 to -1 °C;
Changing load during fishing and during the voyage;
Long-term stay in the sea under various meteorological conditions;
Conducting fishing in conditions of the agitated sea and in various modes of movement.

The organization of fishing is autonomous, in which the fishing vessel will deliver the catch or the cooled products ashore, receiving from the shore bases all types of supplies.

Errors in the selection of fishing speed, maneuverability, and seaworthiness can lead to a significant decrease in the efficiency of the vessel.

Currently, the construction of steel fishing vessels in Vietnam is extremely important. For the traditional fishing vessels had been built in Vietnam, the characteristic form of the contours corresponding to low-speed running and block coefficient is increased. The transition to a new level of construction and operation of fishing vessels requires a thorough and detailed analysis of the hull form and the characteristics of propeller-rudder system, as well as their interaction in the process of fishing operations.

The purpose of research is studying the characteristics of the hull form and propeller-rudder system (propeller in the nozzle) of the fishing vessel project 70133, intended for the manufacture and operation in Vietnam.

In this study, the following problems have been solved:

1. Created 3D models: of the hull vessel surface and propeller-rudder system, which allows carrying out parametric study and optimization.
2. Determined dependence of the resistance water from the vessel's speed and hull form.
3. Determined the hydrodynamic characteristics of the propeller-rudder system in the free water.
4. Determined the features of interaction of the propeller-rudder system with the vessel's hull.
5. Developed recommendations for improving the hull form and propeller-rudder system.

The vessel project 70133 is intended for seafood catching in the coastal areas of the exclusive economic zone of Vietnam and their transportation in the cooled condition (Fig. 1).

The vessel has been designed taking into account the requirements of the rules of the Russian Maritime Register of Shipping for compliance with foreign rules and regulations. The vessel has a diesel engine, single-screw, with transom stern, continuous upper deck and with two-tier forward deckhouse. The speed is 11.0 knots.

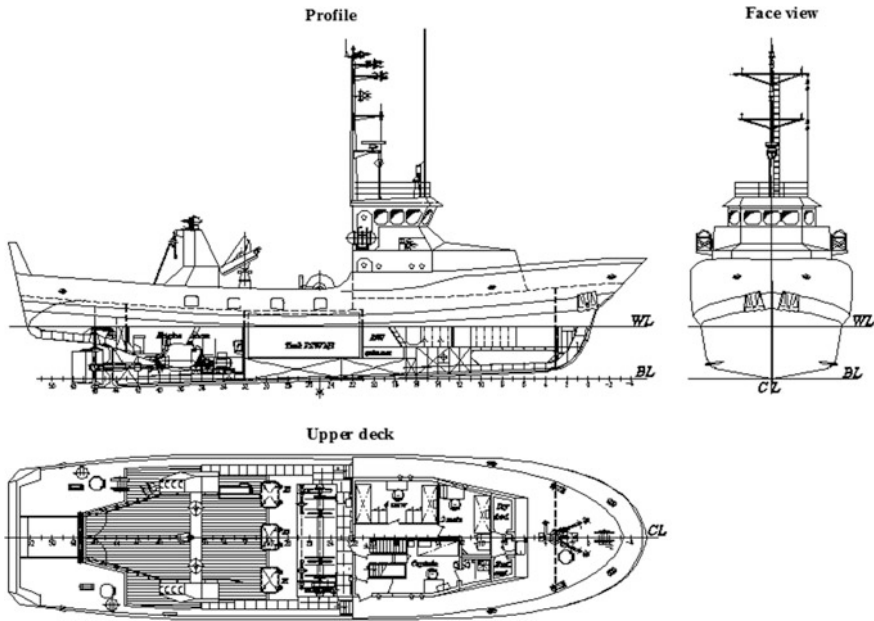


Fig. 1 General arrangement of ship

Table 1 Main characteristics of fishing vessel project 70133

Characteristics	Value
Lpp-length between perpendiculars, m	27.31
B-breadth by construction waterline, m	7.08
T-draft by load line, m	2.4
H-depth molded, m	3.42
β -mid-ship area coefficient	0.823
δ -block coefficient	0.534
φ -vertical prismatic coefficient	0.662

On modern fishing vessels, operating in various driving modes (on crossing, trawling, etc.), the use of controllable pitch propeller in the guide nozzle [3] is typical. Experience in the design and operation of these vessels has shown that they have large values of the coefficient of thrust and efficiency at low speeds as compared with vessels having a conventional propeller-rudder system.

The vessel has a controllable pitch propeller, with a diameter of 1.5 m and four blades of Ni-AL-BZ in the rotating guide nozzle (Table 1) [4].

The 3D model of the hull surface. The ship’s surface has been made of ruled surfaces, interconnected by knuckles. The only exceptions are the bilge lines with rounded radius of 500 mm and part of the extreme end in the forepeak region. All knuckles are located higher the construction waterline. Thus, an increase in the process ability of the hull construction is achieved without a significant increase in

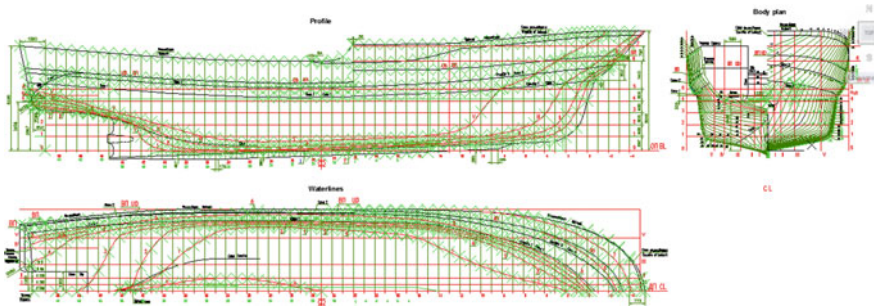


Fig. 2 Lines plan of ship

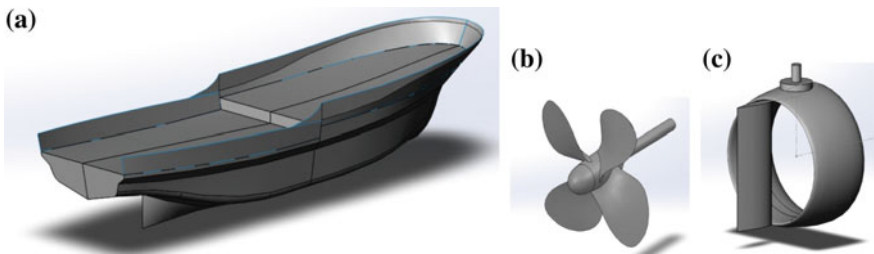


Fig. 3 3D models: a ship's surface; b propeller; and c nozzle with rudder

water resistance [5]. The line drawing is shown in Fig. 2, and a 3D model of the surface of the hull without a lito-welded stern frame, propeller, and nozzle with rudder in Fig. 3a

To study the hydrodynamic characteristics of the propeller-rudder system, a parametric model of four-blade propeller was created, which allows modeling the work of the vessel in various modes of field operations and transitions. The base screw has been chosen with a diameter of 1.5 m, with constructive pitch 1.24 m, pitch ratio 0.653, and the disk-area ratio 0.63 (Fig. 3b).

The model of the basic version of the nozzle is shown in Fig. 3c.

1.1 Simulation and Results

Dependence of water resistance on ship's speed and the hull shape

Simulation of the vessel's motion is carried out in a mode of transition (without regard to agitation) with Froude numbers, which allow calculating the water resistance of the vessel by traditional methods and comparing it with the results of the present studies. The focus is on the movement of the vessel at speeds of 4.06 m/s. The flow is laminar and turbulent. The surface roughness of the hull is assumed to

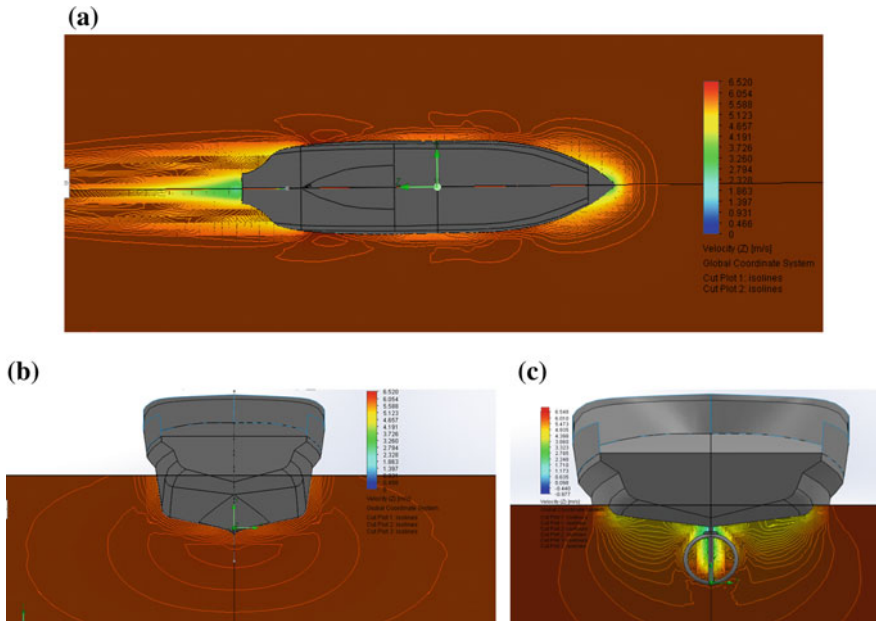


Fig. 4 Diagrams (field) of velocities: **a** in the plane of CWL; **b** in the plane of the mid-ship frame; and **c** in the plane of the disk propeller(in the system the hull—nozzle), the rear view

be 100 μm (micrometer). The dimensions of the computational domain have been chosen in such a way as to exclude the influence of the boundary conditions on the results of flow past the surface of the hull. As indicators determining the quality of the hull form, the following are accepted: complete resistance, pressure resistance, and frictional resistance, as well as flow velocities in the boundary layer and surface pressure [6]. In Fig. 4 is shown the diagrams of velocity distribution in various planes of the ship’s hull, and in Fig. 6 curves of the resistance of the vessel, obtained in this study (R2) and calculated using the method Eroshin V.A. (R1).

Conclusion (Fig. 4):

In the area of the stern extremity, a significant decrease in pressure (flow velocity) is observed, which causes the formation of vortices and the separation of the flow in places of the sharp increase in pressure.

The velocity field in the plane of the propeller disk has a significant circumferential irregularity, which is associated with the V-shaped shape of the contours in the aft extremity.

Installing the wheel with the rudder (without screw) leads, on the one hand, to some leveling of the flow and, on the other, to increasing of the joint and frictional resistance, respectively, by 3 and 2%.

The thickness of the boundary layer in the middle part of the ship is changed significantly around the perimeter of the frame, and the greatest value is in the bilge area, which is explained by the presence of bilge vortices in this region.

A significant perturbation of the boundary layer is observed in the region of 06fr. and 40fr., which makes us pay attention to the shape of the surface of the hull in these areas.

The curvature of the flow lines in the boundary layer leads to the appearance of vortices and flow separation in the form of discrete vortices, which affects the resistance and associated flow.

The character of the distribution of velocities and flow lines in the location of the propeller in many (but not only) depends on the shape of the aft extremity and protruding parts.

Hydrodynamic characteristics of propeller-rudder systems in free water

In the simulation, the following initial conditions are assumed:

The propeller rotational speed is 350, 400, 450 rpm;

Speed motion 8 m/s with lead 2 m/s;

The dimensions of the computational domain exclude the influence of the walls on the hydrodynamic characteristics of the propeller in addition to the previous ones, and the following quality indicators have been introduced: K_t —coefficient of thrust; K_q —coefficient of moment; CE—Coefficient of efficiency sizes of mesh allow to obtain results with sufficient accuracy.

Fig. 5 shows the calculation results: (a) Diagram of velocity in the DP; (b) Line flow through the nozzle and rudder, and in Fig. 6—curves of the action of the propeller K_t , K_q , and CE.

The results of the calculations are in good agreement with the values obtained from the diagrams of the propeller in the guide nozzles, given in the references (so the difference in the coefficients of thrust is 5–10%) [7]. The calculated value of the efficiency of the propeller installed on the ship is slightly smaller (by 5%) than for the B-series propeller. However, the advantage of the controllable pitch propeller in the nozzle is its versatility and possibility of thrust control.

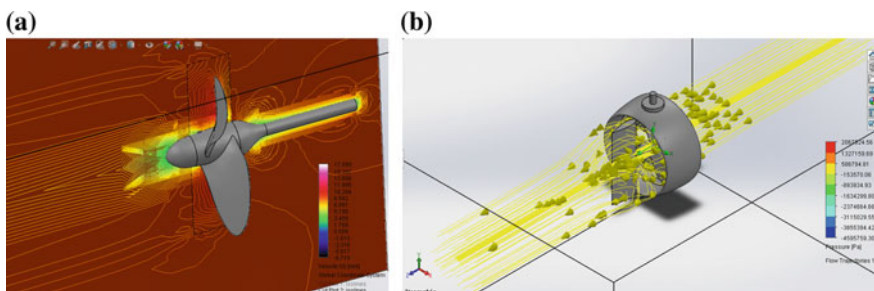


Fig. 5 Visualization of calculation results: **a** diagram of velocity in the DP; **b** line flow through the nozzle and rudder

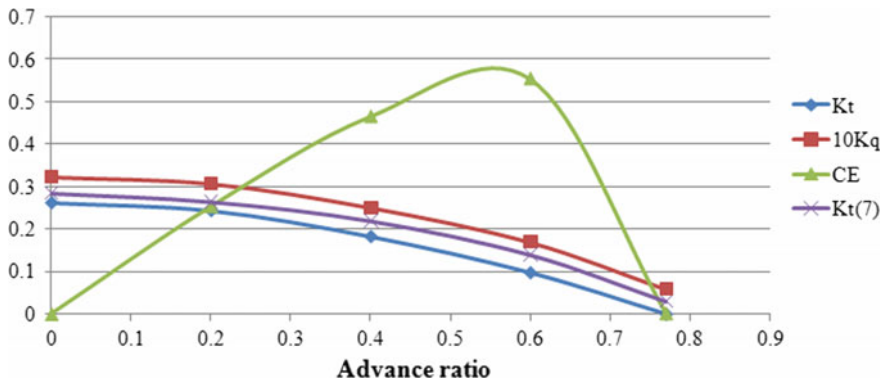


Fig. 6 Curves of the action of the propeller K_t , K_q , and CE

A drawback of some propellers in the nozzle is the screw twisting of the water flows inside the nozzle which, under the action of the centrifugal force, move radially and create an increased pressure between the end of the blade and the nozzle, which leads to the appearance of an additional component of the torque and a decrease in the efficiency.

The dimensions and shape of the nozzle with the rudder and propeller have been chosen in such a way as to exclude the phenomenon described above.

Features of interaction of the propeller-rudder systems with the hull

After creating the assembly surface of the body—the screw in the nozzle, a new study has been made in order to determine the influence of the elements on the entire system

Figure 7 shows: (a) the assembly model; (b) the diagram of the speeds of assembling the vessel’s ship’s surface with propeller-rudder systems in the plane of the mid-ship frame and (c) in the plane DP.

In Fig. 8 along with the ship’s resistance curves obtained in this study (R2) and calculated using the method Eroshin V.A. (R1), the dependence of the resistance of the vessel with the nozzle and the propeller (R3) is shown.

At the end of the study, passport diagram is constructed to analyze the interaction of the hydrodynamic complex and the propelling engine (Fig. 9).

On the profile of the nozzle installed behind the hull of the vessel, circulation of the velocity is created, so the speed of water flow through the propeller disk increases, which contributes to an additional increase in its efficiency, in comparison with the value in free water (see Fig. 6). As a result, the use of the power of the main engine in various modes is improved due to the fact that the speed of the flow in the propeller disk varies more slowly than the speed of the vessel. When the propeller rotation speed of 450 per/min, obtaining at power of propelling engine $N_g = 350$ kW, the ship has a top speed of 11.2 knots (see Fig. 9) which corresponds sufficiently to the speed of the project vessel 70133 in free water.

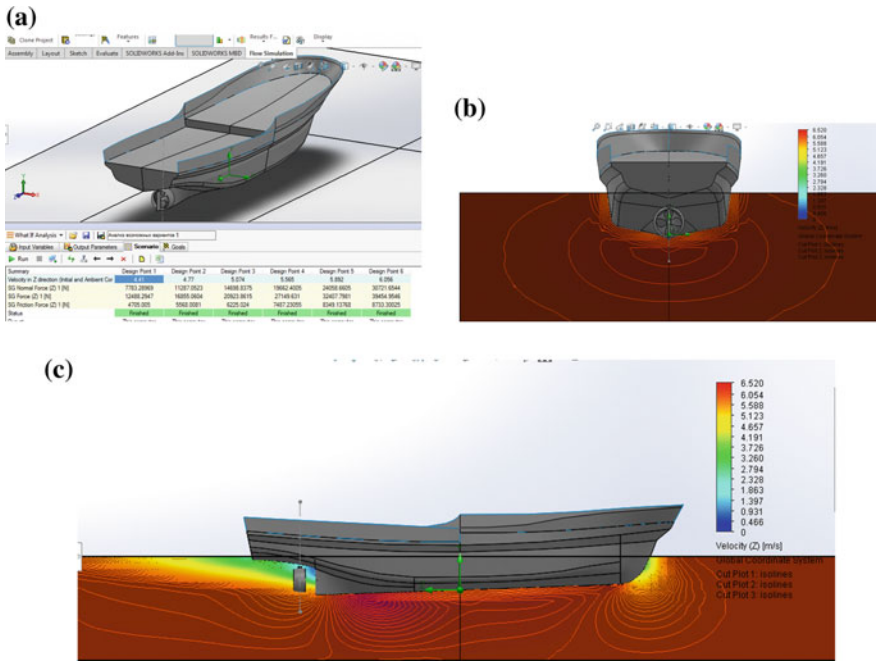


Fig. 7 Interaction of the propeller-rudder system with the hull: **a** assembly model; **b** diagram of velocity in the plane of the mid-ship frame; and **c** in the DP

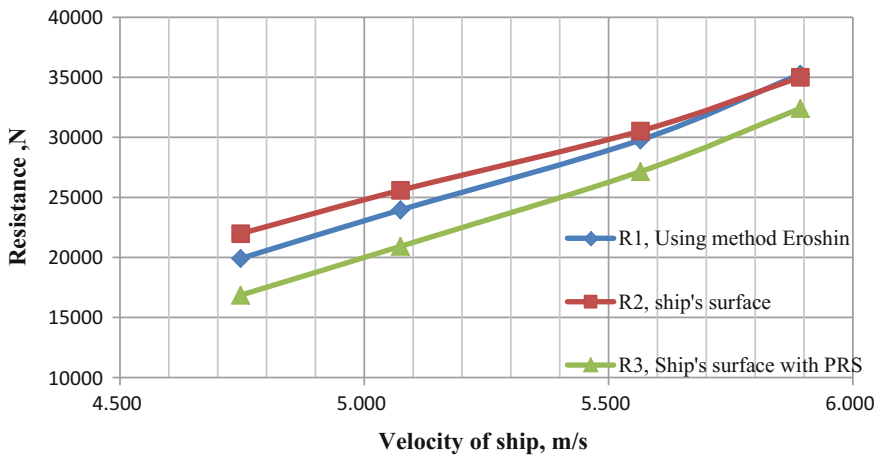


Fig. 8 Dependence of ship's resistance on speed

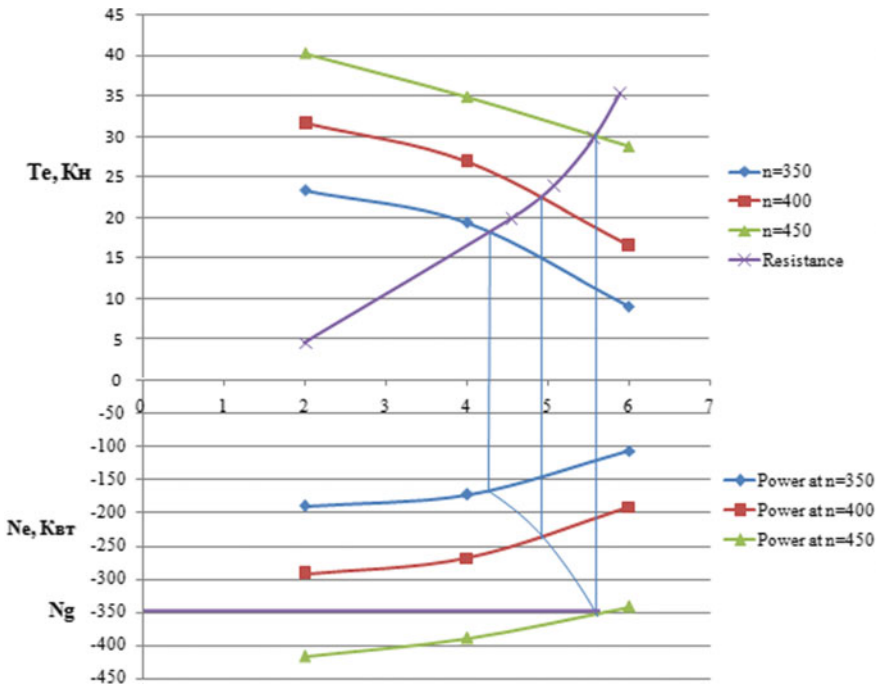


Fig. 9 Passport diagram

2 Conclusion

- (1) In the area of the stern extremity, a significant decrease in pressure (flow velocity) is observed, which causes the formation of vortices and the separation of the flow in places of the sharp increase in pressure.
- (2) The velocity field in the plane of the propeller disk has a significant circumferential irregularity and the installation of a nozzle with rudder somewhat smooth out this irregularity.
- (3) The results of calculations of the resistance to movement of the vessel (R_2) are in good agreement with calculations using the method Eroshin V.A. (R_1), at a speed of 4.75 m/s the difference is 10%, and at a speed of 5.9 m/s decreases to a value of 0.6%.
- (4) Estimation the nozzle with rudder behind the ship's hull leads to decrease of joint resistance (ship surface and propeller-rudder system) (R_3) of the system, 20% (at medium speeds) and 8% (at high speeds) respectively. The positive effect of the propeller-rudder system has an impact on formation of streams of flow around the elements of the whole system.

- (5) The picture of fishing vessel simulation and also numerical values of the parameters (speed and resistance) shows the suitability of SolidWorks Flow Simulation for using it at the stage of design and engineering analysis before carrying out experimental research.

References

1. Rakov AI (1966) Features of design of fishing vessels. Shipbuilding, 144 pp
2. Rakov AI (1978) Optimization of the main characteristics and elements of fishing vessels. Shipbuilding, 232 pp
3. Russian Maritime Register of Shipping (2015) Register of ships. St. Petersburg, p 926
4. Specification for fishing boat 31m, project 70133, drawing 70133-020-002, Poseidon-Zvezda Co., Ltd, Vladivostok
5. Turban VK, Shpakov VS, Stumpf VM (1983) Design contours and propulsion marine vessels. Shipbuilding, 304 pp
6. Antonenko SV, Kitaev MV, Novikov VV (2012) Methodical instructions “Calculation of water resistance vessel motion”. Publishing House FEFU, Vladivostok, p 48
7. OST 5.4129-75 (1975) Complex propeller—guide nozzle. Calculation technique and design rules. Pub. Standards, Moscow, 202 pp

Research the Strength of the Decking Overlap of the Fishing Vessel for Vietnam



Victor G. Bugaev, Dam Van Tung and Yana R. Domashevskaya

Abstract SolidWorks Simulation allows to analyze the local strength of hull construction and to determine the strength characteristics of structural elements and equipment. It is possible to assess the strength of a structure or assembly as a whole, to determine which structural elements or parts of the assembly will reduce the product's operational reliability, and make changes to obtain an equivalent construction or assembly. The purpose of the study is to research the strength of the decking overlap of the fishing vessel by using SolidWorks Simulation.

Keywords Fishing vessel · Strength · Decking overlap

1 Introduction

Vietnam is a country with a long coastline, with rich and diverse marine resources, including fishes. The efficient development of fishery resources leads to the rapid growth of both fishery and shipbuilding industry, as well as Vietnam's marine economy as a whole. The Vietnamese fishing fleet is low-tonnage fleet, made mostly (90%) of wood. Steel fishing vessels exist in limited numbers that are designed and built in foreign shipyards, including Russia. Therefore, the development of the shipbuilding industry of Vietnam is a promising direction, and the construction of modern fishing vessels at shipyards in Vietnam is extremely important.

V. G. Bugaev · D. Van Tung (✉) · Y. R. Domashevskaya
Far Eastern Federal University, Vladivostok, Russia
e-mail: damvantung@mail.ru

V. G. Bugaev
e-mail: v_bugaev@mail.ru

Y. R. Domashevskaya
e-mail: 100-70-100dom@mail.ru

The vessel of project 70133 is intended for catching seafood in the coastal areas of the exclusive economic zone of Vietnam and their transportation in the cooled condition.

The vessel is designed, taking into account the requirements of the rules of the Russian Maritime Register of Shipping for compliance with foreign rules and regulations. The model is diesel powered vessel, single-screw, with transom counter, upper continuous deck and twolevel forward deckhouse. Its speed is 11.0 knots.

The structure of the hull is made of shipbuilding steel of normal strength category A with the guaranteed yield strength of at least 235 mPa (24 kg/mm²) in accordance with GOST 5521-86.

1.1 Theoretical Propositions

At the stage of creating constructions and making final decision construction elements are subjected to thorough engineering analysis in order to provide strength, fabricability and other properties as a result of mechanical and thermal effects, according to criteria that are related to the product quality indicators [1]. Engineering analysis is carried out using the CAE-applications SolidWorks Simulation, which allows analyzing the local strength of hull structures, to determine the strength characteristics of structural elements.

SolidWorks Simulation allows to analyze the local strength of hull construction and to determine the strength characteristics of structural elements and equipment. It is possible to assess the strength of a structure or assembly as a whole to determine which structural elements or parts of the assembly will reduce the operational reliability of the product and make changes to obtain an equivalent construction or assembly.

The SolidWorks Simulation module provides the ability to assess the strength of structures using various strength criteria for ductile materials:

- the equivalent maximum stress for Misses;
- normal stresses by x, y, z;
- main stresses σ_1 , σ_2 , σ_3 , and other.

Permissible stresses for structures are taken in accordance with the theory of Misses, taking into account the joint influence of bending and shear. The essence of Misses theory (the maximum energy forming) consists in the assertion that the ductile material begins to collapse in places where von Misses stresses are limiting stress. The maximum (maximum permissible) stress may be the yield strength, ultimate strength, or other criterion, in our study the yield strength σ_y . Factor of safety $k_{\text{vonMisses}} = \sigma_{\text{предел}}/\sigma_{\text{vonMisses}}$.

The maximum values of normal and tangential stresses are assumed equal

$$\sigma_{\text{предел}} = \sigma_y = 235 \text{ мПа};$$

$$\tau_{\text{предел}} = 0,9\tau_y = 122,7 \text{ мПа, где } \tau_y = 0,58\sigma_y.$$

1.2 3D Model Description

The hull of the vessel is a complex technical system consisting of separate inter-connected overlap and structures that provide the ship with sufficient strength, reliability, and economic efficiency in the course of its operation. In order to analyze the strength of structures under the influence of local loads, overlapping is separated from the general system and considered autonomously, and the influence of adjacent structures is taken into account by modeling fixity of the overlap along the perimeter. Strictly speaking, isolating overlaps from the system is a forced measure, and it would be more correct to consider a closed loop as a whole, but such a calculation is very laborious and costly.

The overlap supporting contour forms the sides of the vessel and transverse bulkheads. The longitudinal bulkheads and deck plates are considered rigidly fixed on transverse bulkheads, and the beams on the sides are resiliently fixed with a certain elastic compliance factor.

The vessel is built by transverse system framing with frame spacing 540 mm. The frames and beams are made of bulb flat. Longitudinal and transverse bulkheads are welded and flat, reinforced with vertical bulb stiffeners. Three cargo hatches measuring 800 × 1200 mm in size are installed on the upper deck for access to RSW tanks. The cuts are supported by stiffeners of longitudinal and transverse directions. The corners of the cuts are rounded in order to prevent the creation of stress concentration [2, 3]. Between the hatches, there are two longitudinal bulkheads, dividing the hold into three compartments. On the deck, there is a trawl winch with a drum (3 tons × 60 m/min); Net drum (8 tons × 40 m/min); and Extraction winch (2 tons × 40 m/min) (Fig. 1).

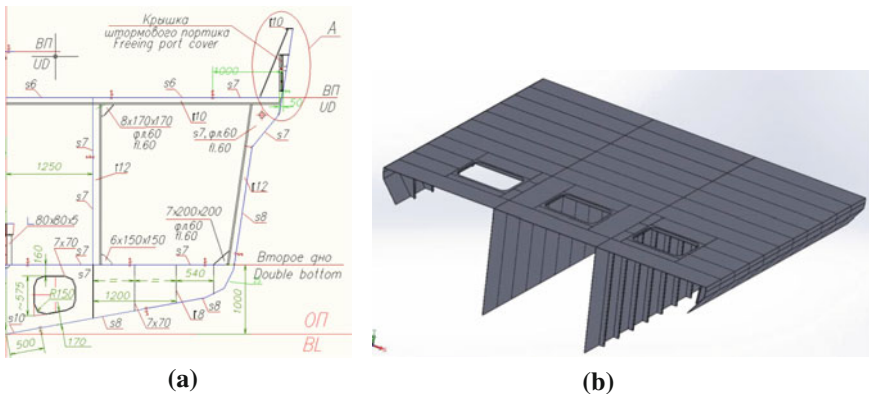


Fig. 1 Hull construction of: a frame spacing (mm) 25; b 3D model of overlap

1.3 Creating of the Project

Mounting. Overlap lean on the ship's side and transverse bulkheads. The overlap beams are located parallel to the sides of the supporting contour. The overlap is rigidly fixed on transverse bulkheads, and it is leaned on the sides and longitudinal bulkheads, which in turn are rigidly fixed at the bottom (Fig. 2a).

Load. The strength of the overlap bonds is checked for the effect of a transversely uniformly distributed load of the weight of the cargo (catch) on the deck and the weight of the water falling on the deck during the storm, but not less than 20 kPa of vessels (Fig. 2a) [4].

Grid. An important step in the analysis of structures is the creation of a grid. The quality and time of research depend on its parameters. In this study, it is customary to automatically create a grid based on the geometric dimensions of the structures using grid controls in the nodes that are subject to more detailed analysis. At the initial stages of the analysis of structures, a grid with linear tetrahedral solid-state elements is used, in the final stages—with parabolic elements (Fig. 2b).

To connect the coincident nodes along the boundary of the bodies, a binding contact is established, which gives a compatible grid.

The grid characteristics: type—on a solid body; The size of the element is 173.147 mm; Tolerance: 8.65735 mm; Quality is high; Total number of nodes is 100524; and Total number of elements is 51681.

1.4 Calculation Results

The diagrams of equivalent Misses stresses arising in the overlap (Fig. 3), displacements (Fig. 4), deformations (Fig. 5), and graphs of their distribution along the beams of the transverse framing from side to side are given below.

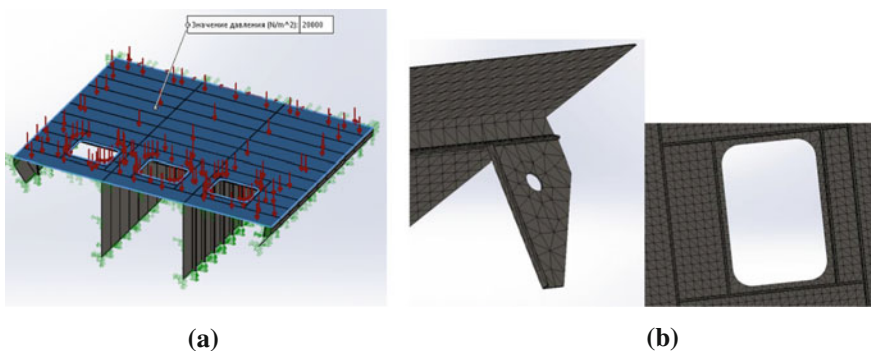


Fig. 2 Project creation: **a** scheme of fixing the overlap and application of the load; **b** the grid in the problem nodes of the structure

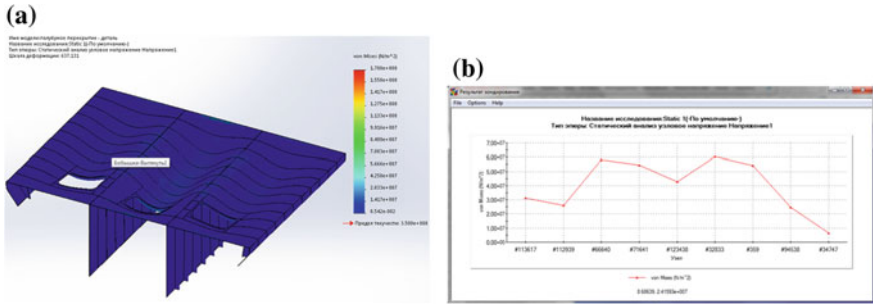


Fig. 3 Stresses according to Misses: a the distribution diagram; b the probing results

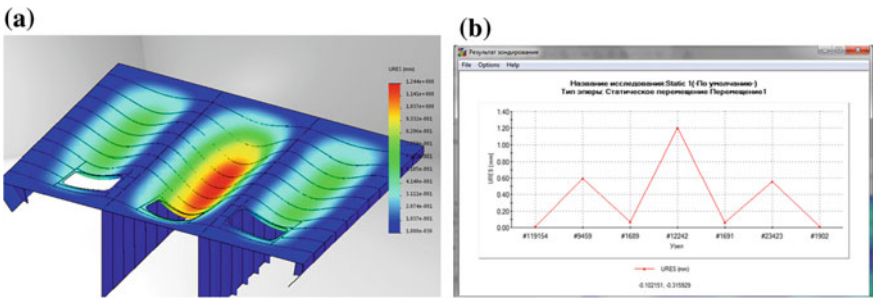


Fig. 4 Displacement: a the distribution diagram; b the probing results

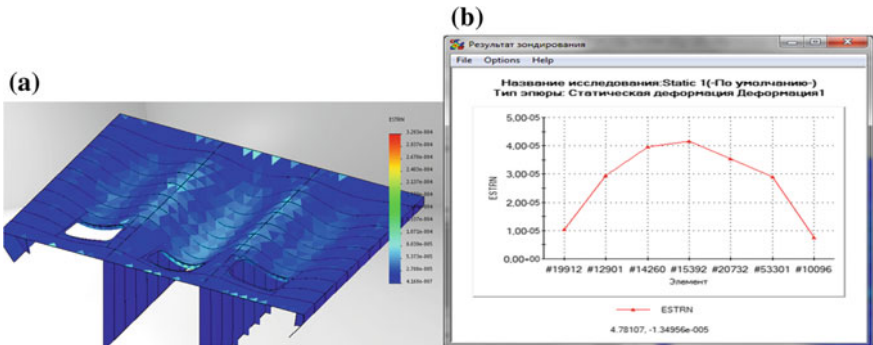


Fig. 5 Deformations: a the distribution diagram; b the probing results

Conclusions:

1. The maximum stresses in the deck overlap reach 170 MPa, which does not exceed the yield strength of steel. The node must be found and represented in the graphics. The safety factor is 1.38.

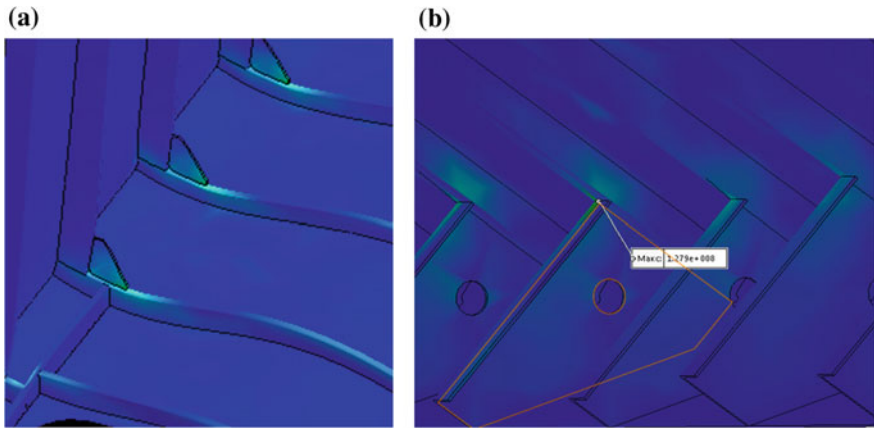


Fig. 6 Most problem places of structures: **a** joints of beams with vertical stiffeners of longitudinal bulkheads; **b** with frames

The most stressed places are the fastening place of the beams to the side bracket and the area where the trawl winch base is fixed to the deck floor.

2. The maximum displacement is 1.2 mm in the center of the plates in the area of the fr.26–27.
3. The maximum deformations reach values of $4.15e-005$ and are also observed in the region of the fr.26–27.

The most problem places of constructions are knots connection beams with vertical stiffeners of longitudinal bulkheads and with frames with the help of brackets (Fig. 6).

In the places of maximum stresses and displacements, it is recommended to perform the following structural changes:

- In the area of connection of beams with vertical stiffeners of longitudinal bulkheads, the knee with straight free edge is welded butt-joint, which significantly increases the stresses in this area (Fig. 6a). Using knee somewhat larger with a rounded free edge will significantly reduce the stress in the rounded edge of brackets and beams. Simultaneously with this, the value of stress concentration in the beams will decrease.
- It is advisable to modify the knots at the nodes of connection of the beam and frame, giving them curvilinear shape in order to reduce the value of the stress concentration (Fig. 6b).
- The accepted thickness of decking plate provides sufficient safety factor for structures. In this case, the maximum displacements in the center of the plates in the area of the fr.26–27 reach values of 1.2 mm (Fig. 4). The presence of additional compressive forces can lead to large displacements and increase in stress concentration in the node of connection of the structures. In this case, it is

recommended to increase the thickness of the decking plate by 0.5–1.0 mm, which will lead to an increase in the mass of structures and will require additional research.

2 Conclusions

1. The results analysis of the study shows that the strength of the deck overlap is provided under the influence of loads, regulated by the rules and norms of strength and operating conditions: the maximum stresses on Misses do not exceed the yield strength of the material; Tangential stresses do not exceed permissible limits.
2. Taking into account the deck overlap of real (not excluded) side structures in the investigation significantly changes pictures of the operation of overlap and leads to the stresses redistribution and deformations along the length of the beams, which indicates the sensitivity of the software to types of fixed end and obtaining more accurate results.
3. The picture of the load perception by overlap as well as the numerical values of the parameters (stresses, displacements, and deformations) indicates the suitability of SolidWorks Simulation at the design and engineering analysis stage.

References

1. Bugaev VG (2008) CAD/CAM/CAE-system. Computer-aided design of ships/Tutorial. Publishing House FESTU, Vladivostok, 276 pp
2. (2015) Rules for the classification and construction of ships. Russian Maritime Register of Shipping. In: 5 volumes. Volume 1. St. Petersburg, 505 pp
3. Bugaev VG, Kirichek PI, Marinchenko DG, Radchenko AB (2009) Technology and organization of computer-aided design and maintenance of ships. Part 1 Ship surface design drawings: teaching manual. Publishing House FESTU, Vladivostok, 172 pp
4. Novikov VV (2012) Architecture ships: (design and strength): monograph. In: Novikov VV, Turmov GP (eds). Publishing House FEFU, Vladivostok, 276 pp

Analysis and Evaluation of the Ground Wave Propagation Due to Blasting Activities of the Road Construction by Numerical Models and Experiments



Lan Nguyen, Huy Hung Pham and Phuong Hoa Hoang

Abstract Blasting activities of the road construction could damage to the neighboring buildings because of the ground wave propagation. This paper focused on analyzing the numerical models of blasting in tunnel construction by using FEM software—MIDAS GTS NX and comparing to empirical measurements. From the results of analysis, we can identify the relationship of the wave propagation speed in the ground and the radius from the considering point to the source of vibration. Based on the results of this analysis assess the potential damage to neighboring buildings as well as designs the way to limit the impact of the wave propagation to neighboring buildings for similar projects.

Keywords The finite element method (FEM) • The ground wave propagation Peak particle velocity (PPV) • Vibration sources • Radius • Vibration limit velocity

1 Introduction

Currently, the process of tunnel construction method NATM (New Austrian Tunneling Method), blasting activities have caused the propagation seismic wave that can could damage to the neighboring buildings. Cause of vibration makes the floors, beams, pillars, walls structure to be cracked and broken, especially, the building structure was solidly built or appeared cracks for a long time in form III under TCVN 7378-2004.

This is not conducive to the investors when the risk occurs, the cost of compensation for influence will make the total cost of construction increased, especially, the public projects (use the capital budgets, the state's capital, etc.) go against the spirit of saving and cut down spending under Resolution 11/2011/ND-CP issued by the Government of the solutions to curb inflation and macroeconomic stability.

L. Nguyen (✉) · H. H. Pham · P. H. Hoang
The University of Da Nang, University of Science and Technology, Da Nang, Vietnam
e-mail: nguyentanstic@gmail.com

Therefore, the research, analysis and evaluation of the impact of the seismic waves propagation will exactly predict the influences of blasting activities, reduce to the smallest consequences for people and property, decrease compensative expenses so that the savings for the budget and the investors.

2 The Theoretical Basis

2.1 Peak Particle Velocity

When blasting activities in tunnel construction takes place, the explosive charge is detonated in a blast hole the rock is immediately fractured and splitted apart, pressure is high enough, they will make waveforms spread in rock, include: Shear waves (S), compression waves (P) and Rayleigh waves (R). Essentially, they can be divided into two waves: Body waves—propagating below ground, and Surface waves—propagating on the face of the ground.

The waveform moves at different speeds. The P wave is the fastest moving wave through the ground, the particles in the wave move in the same direction as the propagation of the 50–60% of the velocity of the P wave and the particles within the wave move at right angles to the direction of motion of the wave. The Rayleigh wave is the latest and the particles within the wave move in elliptic orbits, it makes scrambling on the face that influences works of the ground under results research in former times.

All of these waveforms have the same in damping attenuation of energy, because of energy dispersion and force of friction when it moves in an infinite elastic medium and an infinite elastic plane, which leads to dependence of displacement (x), velocity (v), and acceleration (a) on vibration energy sources, propagation medium condition of wave, and distance that they moved.

According to the experience of the researchers, peak particle velocity correlates with damage more closely than peak of displacement or acceleration. Therefore, peak particle velocity, which influence on experimental mensuration of seismic wave, are used in assessing ground vibration (Fig. 1).

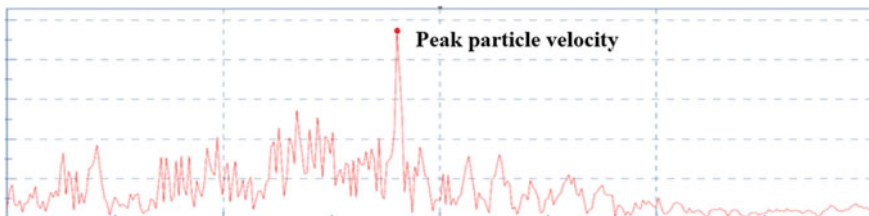


Fig. 1 Peak particle velocity of vibration velocity spectrum

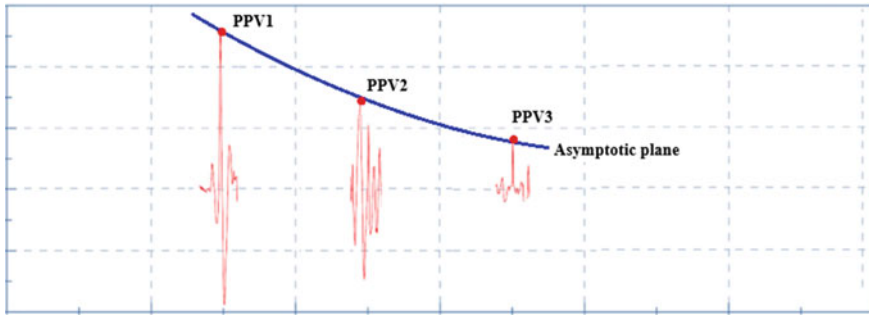


Fig. 2 Attenuation of peak particle velocity

Table 1 List of the existing equations for estimation of peak particle velocity

Ambraseys–Hendron [1] (1968)	$ppv = K \left(\frac{R}{\sqrt[3]{Q}} \right)^{-\beta}$
Nicholls, Johnson–Duvall [2] (1971)	$ppv = K \left(\frac{R}{\sqrt{Q}} \right)^{-\beta}$
Langefours–Kihlstrom [1] (1973)	$ppv = K \left(\sqrt{\frac{R^{2/3}}{Q}} \right)^{-\beta}$
United States Bureau of Mines [3] (USBM-1959)	$ppv = K \left(\frac{R}{\sqrt{Q}} \right)^{-\beta}$
Indian Standard [4] (IS 6922-1973)	$ppv = K \left(\frac{R^{2/3}}{Q} \right)^{\beta}$
Australia Standard [5] (AS 2187.2-2006)	$ppv = K \left(\frac{R}{\sqrt{Q}} \right)^{-\beta}$

Where:

ppv peak particle velocity (mm/s)

R distance from charge (m)

Q Instantaneous charge (kg)

K; β Site constant and site exponent

Proceed to build logarithm curve that it is asymptotic plane of point of peak particle velocity so evaluation of the ground wave propagation (Fig. 2; Table 1).

2.2 Proposed Predictor for Blasting Vibration

Based on data of experimental measuring and calculations analyzed, the proposed predictor equation of peak particle velocity (*ppv*) is under the Australia Standard [5] (AS 2187.2–2006) of explosives, storage, and use.

$$ppv = K \left(\frac{R}{\sqrt{Q}} \right)^{-\beta} \tag{1}$$

where:

ppv peak particle velocity (mm/s).

R distance from charge (m).

Q Instantaneous charge (kg).

K is site and rock factor constant. Free face—hard or highly structured rock = 500; Free face average rock = 1140; Heavily confined = 5000

β is constant related to the rock and site (usually -1.6)

- Rhyodacite/Rhyolite: 2.2–2.5
- Granite: 2.1–2.4
- Limestone: 2.1
- Ordovician sediments: 2.8
- Coal mine overburden: 1.5–1.8
- Basalt (clay floor): 1.5–1.6
- Basalt (massive): 1.9–3.0.

2.3 Calculation Results

According to terrain conditions of site measurement in Sect. 3, free face average rock $K = 1140$, weathering rock $\beta = 1.6$. We have equation of peak particle velocity (Table 2):

$$ppv = 1140 \left(\frac{R}{\sqrt{Q}} \right)^{-1.6} \tag{2}$$

where:

ppv peak particle velocity (mm/s).

R distance from charge (m).

Q Instantaneous charge (kg).

Table 2 Theoretical calculation results

STT	R (m)	ppv (mm/s)
1	227	7.84
2	257	6.43
3	287	5.38
4	517	2.10

3 Experimental Measurement in Site

3.1 Experimental Site

The experiment was performed on November 26, 2015. The experimental field included a section near the source of vibrating, belong to the center line of a tunnel the approach to left tunnel in the South tunnel construction works through the Eo mountain in the 4th package—highway construction project in Da Nang–Quang Ngai, from Km21 + 500 to Km32 + 600, Duy Son Commune, Duy Xuyen District, Quang Nam Province [6] (Figs. 3 and 4; Table 3).

Layout of the probe on the ground is described in Fig. 5, each of the vibrant sensor location on the ground has an iron bar attached to the ground. On the iron bar, attached two vibrant probes, one is vertical vibration (denoted V) and one is the vibration according to diameter (denoted R). The vibrant probe is connected to the receiving and signal processing parts. The distance of the probe to vibrant source is 227, 257, 287, and 517 m (Fig. 6).

3.2 Vibratory Measuring Equipment

Vibratory measuring system includes vibratory sensors (transducers), signal systems (datalogger), and a software to receive and process signals (software). The requirements on the equipment according to the TCVN 7378 are as follows: Frequency range is 1–100 Hz, the non-linear is 10%, and velocity range is 0.01–500 mm/s (Fig. 7).

A geophone is automatically calibrated to follow a service characteristic of manufacturer. Before laboratory activities, this geophone is checked by standard impulses equipment.



Fig. 3 Experimental site



Fig. 4 Checking 102 kg of explosive type P113

Table 3 Explosive parameters of P113

Specification	Unit	Parameters
Potential work	cm ³	320–330
Blasting velocity	m/s	≥ 4200
Conducting explosion	cm	≥ 6
Explosive density	g/cm ³	1.10–1.25
Being able to leave water	h	≥ 12

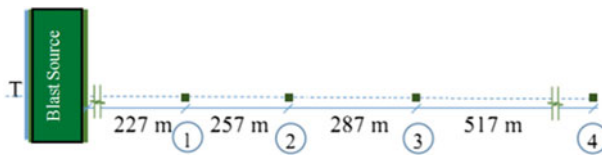


Fig. 5 Layout of the probe on the ground at the field

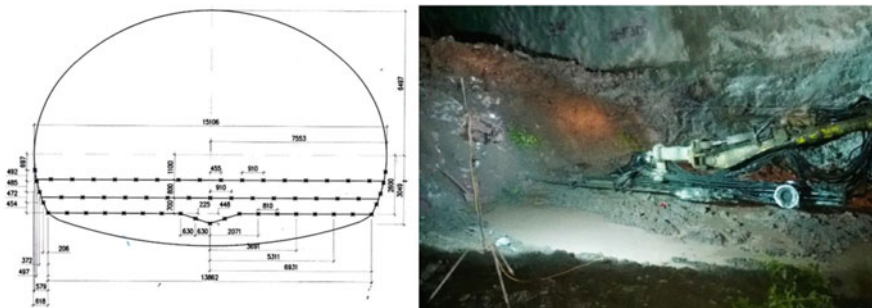


Fig. 6 102 kg of explosive type P113 installed as designed at the source of vibration

The data were stored in the computer at field and analyzed by use the dedicated software Vibration Monitoring.



Fig. 7 Block diagram for vibration measurement system

3.3 The Works Needed to Protect

The works need to protect is the homes level 4 built solidly. Figure 8 describes the surrounding works. According to TCVN 7378:2004, with the kind of works is on type III and measured frequency are in the very wide range from 39 to 184 Hz [6], take the most adverse 39 Hz is near the upper of the selected range from 10 to 50 Hz, the safe values of vibratory velocity allow to selected is 6.63 mm/s for the works has not been damaged before construction. With uncertainty works that were damaged before the construction of the road, the values of vibratory velocity for the selected license are 3 mm/s in order to protect the works from being more crack.

3.4 Vibration Measurement Results

The measuring results and analysis of vibrations at the measuring point include vertical vibrant velocity and velocity according to diameters during the experiment. From this measuring results [6], conduct sum data of direction, detailed analysis of significant instant at the right time peak particle.

- Peak particle velocity of vertical, max V_z (mm/s);
- Peak particle velocity of horizontal, max V_r (mm/s);
- Peak particle velocity of sum, ppv (mm/s) (Fig. 9; Table 4).



Fig. 8 Works needed to protect

Based on the results from the experiment, we proposed the gradually decrease rules the peak velocity value according to the distance under formula:

$$ppv = 4500 \left(\frac{R^2}{Q} \right)^{-1} \tag{3}$$

where:

ppv peak particle velocity (mm/s).
R distance from charge (m).

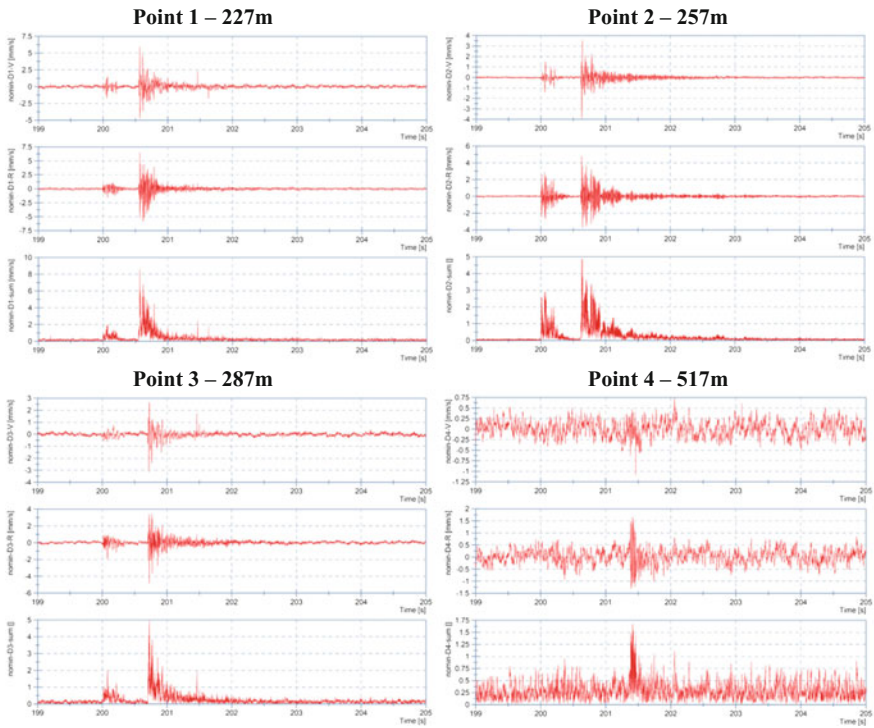


Fig. 9 Wave spectrum of experiment

Table 4 Experimental measurement results (unit: mm/s)

STT	R (m)	V _z	V _r	ppv
1	227	5.93	6.47	8.78
2	257	3.95	4.81	6.22
3	287	3.21	3.80	4.98
4	517	1.08	1.65	1.97

Q Instantaneous charge (kg).
 4500; -1 Site constant and site exponent.

The propagating rules of seismic wave depend on distance from charge in formula (3) to be true of experimental data in site. Showing that it is reliable.

4 Simulation on Midas GTS NX

GTS NX is a comprehensive finite element analysis software package that is equipped to handle the entire range of geotechnical design applications including deep foundations, excavations, complex tunnel systems, seepage analysis, consolidation analysis, embankment design, and dynamic and slope stability analysis. GTS NX also has an advanced user-friendly modeling platform that enables unmatched levels of precision and efficiency (Figs. 10, 11, 12 and 13).

- Peak particle velocity of vertical, max V_z (mm/s);
- Peak particle velocity of horizontal, max V_r (mm/s);
- Peak particle velocity of sum, ppv (mm/s) (Table 5).

Based on simulation results of Midas GTS NX, damping rules of peak particle velocity direct ratio distance from charge with amount of explosives 102 kg, approximate formula:

$$ppv = 570429 \times R^{-2.035} \tag{4}$$

where:

ppv peak particle velocity (mm/s).
 R distance from charge (m).
 570429; -2.035 constant of simulation.

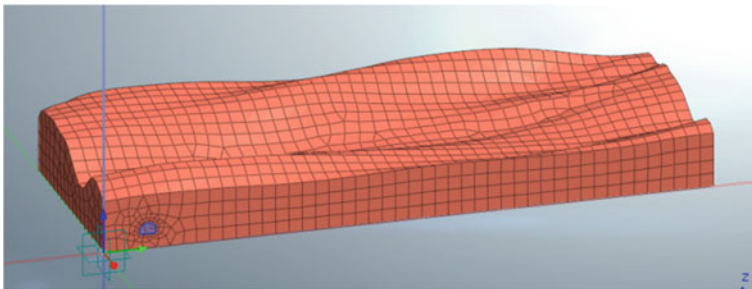


Fig. 10 Simulated model

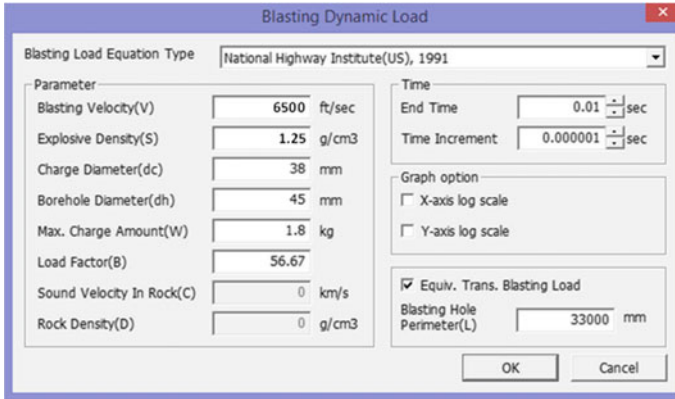


Fig. 11 Blasting dynamic load definition

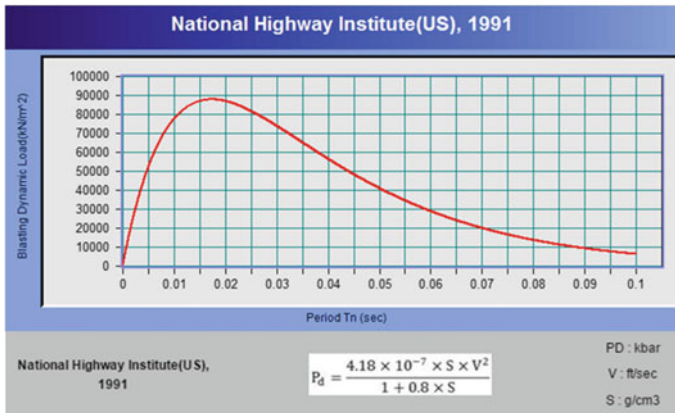


Fig. 12 Graph and formula of blasting pressure

5 Comparison Results and Evaluation

To conduct vibration impact assessments, we compare the results between experiment, model, and theory for a more accurate and complete view.

With this results in Tables 6, 7, 8, and Fig. 14, the calculated values from experiment, Midas GTS, and theory have points of similarity. With regard to the software, maximum relative error is 13.5%, and calculated theory is 10.7%. Showing that it is predictable basis of safety distance based on simulation on Midas GTS and to calculating of theory.

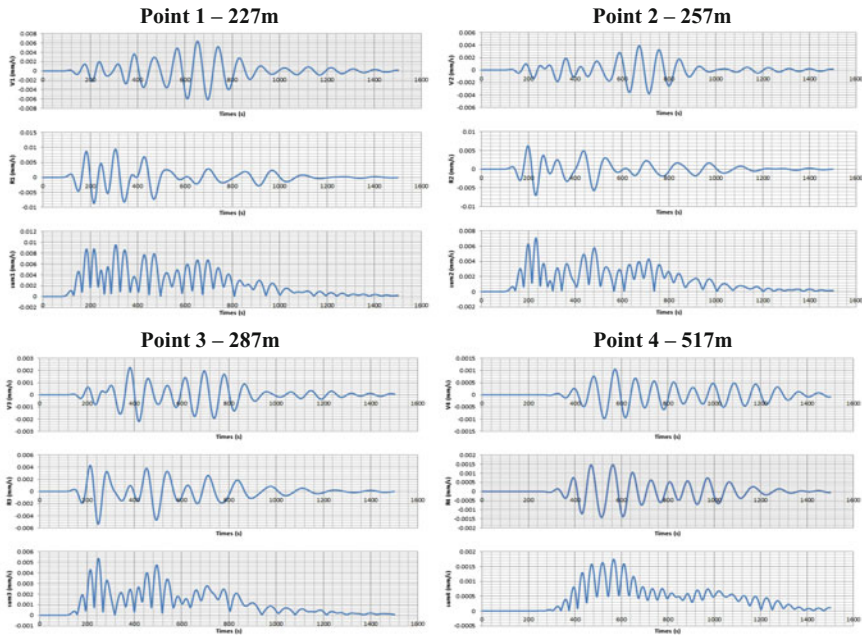


Fig. 13 Wave spectrum of Midas

Table 5 Simulation results of Midas GTS NX (unit: mm/s)

STT	R (m)	V_z	V_r	ppv
1	227	6.39	9.50	9.55
2	257	3.90	6.25	7.06
3	287	2.26	4.29	5.37
4	517	1.06	1.47	1.74

Table 6 To comparing results of velocity damping of experiment, Midas GTS and theory

R (m)	Peak particle velocity (mm/s)		
	Experiment	Midas GTS	Theory
227	8.78	9.55	7.84
257	6.22	7.06	6.43
287	4.98	5.37	5.38
517	1.97	1.74	2.10

We proceed to build logarithm curve that it is asymptotic plane of point of peak particle velocity from data Table 6.

Based on results, the group of researchers proposed safety distance for the works in Sect. 3.3 (Table 9).

Table 7 Relative errors between experiment and Midas GTS software

R (m)	Peak particle velocity (mm/s)		Relative errors (%)
	Experiment	Midas GTS	
227	8.78	9.55	8.77
257	6.22	7.06	13.50
287	4.98	5.37	7.83
517	1.97	1.74	11.67

Table 8 Relative errors between experiment and theory

R (m)	Peak particle velocity (mm/s)		Relative errors (%)
	Experiment	Theory	
227	8.78	7.84	10.7
257	6.22	6.43	3.38
287	4.98	5.38	8.03
517	1.97	2.10	6.60

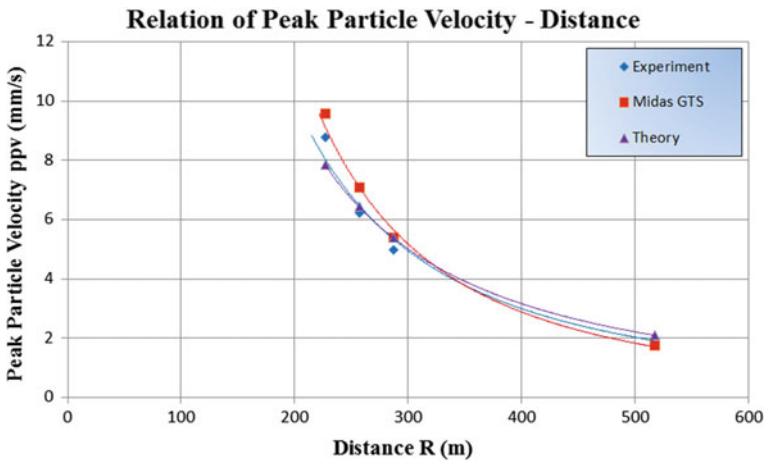


Fig. 14 To comparing rules of velocity damping of experiment, Midas GTS and theory

Table 9 Determined safety distance for the works in form III under TCVN 7378-2004 with amount of explosives 102 kg

Limit velocity (mm/s)	Experiment (m)	Midas GTS (m)	Theory (m)
6.63	263	266	252
3	391	393	414

6 Conclusion and Recommendation

- From the empirical data, we can construct the relation of PPV and R. Using this relationship defines the radius of influence if we know the allowable vibration threshold.
- The law of PPV decline from empirical R and numerical analysis by MIDAS GTS software is quite appropriate. It is possible to use MIDAS GTS to calculate the rough forecast of wave propagation due to blasting.
- To determine the ground wave propagation law that is more reliable for each project, it is necessary to experimentally determine filed factor K and exponent factor β .

References

1. Rai R, Singh TN (2004) A new predictor for ground vibration prediction and its comparison with other predictors, India
2. Richards AB, Moore AJ. Blast vibration course measurement, assessment and control, Australia
3. Giraudi A, Cardu M, Kecojevic V (2009) An assessment of blasting vibrations: a case study on quarry operation, USA
4. Indian Standard, IS 6922.1973. Criteria for safety and design of structures subject to underground blasts (second reprint August 1997)
5. Australian Standard, AS 2187.2-2006. Explosives, storage and use
6. Lan N, Chau Ngoc Bao E (2015) Reported explosion caused by blasting tunnel construction, Da Nang
7. Ministry of Natural Resources and Environment (2010) QCVN 27/2010/BTNMT—National technical regulation on vibration
8. Ministry of Science and Technology (2004) Vibrations and vibrations—vibrations for buildings vibration—limits and methods of evaluation
9. Barkan DD (1957) Dynamics of bases and foundations, Russia
10. Das BM, Ramana GV. Principles of soil dynamics, USA
11. Lan N, Hoa HP, An TH (2016) Rung chan do hoat dong thi cong xay dung, ket qua thuc nghiem do rung chan xac dinh ban kinh anh huong den cong trinh lan can, Da Nang. <http://www.tapchigiaothong.vn/rung-chan-do-hoat-dong-thi-cong-xay-dung-ket-qua-thuc-nghiem-do-rung-chan-xac-dinh-ban-kinh-anh-huong-den-cong-trinh-lan-can-d33558.html>
12. Kumar R, Choudhury D, Bhargava K (2016) Determination of blast-induced ground vibration equations for rocks using mechanical and geological properties, China. <http://www.sciencedirect.com/science/article/pii/S167477551600024X>
13. Akande JM, Aladejare AE, Lawal AI (2014) Evaluation of the environmental impacts of blasting in Okorusu Fluorspar Mine, Namibia
14. Gorgulu K, Arpaz E, Uysal O, Duruturk YS, Demirci A, Dilmac MK, Kocaslan A (2000) Comparison of blast-induced ground vibration predictors in case of Tulu-plain open pit colemanite mine of Eti Mine, Turkey

15. Snodgrass JJ, Siskind DE (1974) Report of investigation 7937—vibrations from underground blasting, USA
16. Bich DH (2000) Ly thuyet dan hoi. Dai hoc Quoc Gia
17. Verruijt A (2008) Soil dynamics. Delft University of Technology
18. Ngoc TD. Mot bien phap giam anh huong chan dong dong coc den cong trinh lan can. Science and Technology Institute of Construction

Fluid–Structure Interaction Analysis of Revetment Structures—An Overview



T. Vu-Huu, C. Le-Thanh, Phuc Phung-Van, Hung Nguyen-Xuan and M. Abdel-Wahab

Abstract The strong development of numerical models, especially, *computational fluid dynamic* (CFD, i.e., the using of computational software to visualize how liquid affects objects as it flows past) and *fluid–structure interaction* (FSI, i.e., the coupling applications of fluid and structural mechanics disciplines) brought engineers more good measures to investigate the interaction problems. Meanwhile, the understanding gap of interaction between fluid and revetment structure (RS, i.e., a special structure lean on the slope of dikes to keep the safe of slope and core from erosion due to current and wave) is one of the biggest interests. Hence, the priority aim of this study is to develop computer simulations, which will be used as the tools during the construction of RS that will better protect the coasts from flood and erosion.

Keywords Revetment • Fluid–structure interaction (FSI) • Monolithic approach
Partitioned approach • Conforming mesh • Non-conforming mesh

T. Vu-Huu (✉) · C. Le-Thanh · P. Phung-Van · M. Abdel-Wahab (✉)
Laboratory Soete, Faculty of Engineering and Architecture,
Ghent University, Ghent, Belgium
e-mail: huutruong.vu@ugent.be

M. Abdel-Wahab
e-mail: magd.abdelwahab@ugent.be

C. Le-Thanh
e-mail: le.thanhcuong@ugent.be

P. Phung-Van
e-mail: phuc.phungvan@ugent.be

H. Nguyen-Xuan
Center for Interdisciplinary Research in Technology, HUTECH University,
Ho Chi Minh City, Vietnam
e-mail: ngx.hung@hutech.edu.vn

1 Introduction

Due to the flow and wave attack, the beach or riverbank will be eroded, as indicated in Fig. 1. The consequence is the disappearance of living sides. The fact is that thousands of square meter of coastal zone in Vietnam as well as in the world have been vanishing, annually.

In order to avoid such damages, the revetments, bulkheads, seawalls, emerged or submerged breakwaters, groins, jetties, dikes, levees, etc., could be used to saving the landsides, as shown in Fig. 2.

In the above protection structures, revetment is one of the most common structural solutions to protect the landsides because of its effectiveness [2]. The revetment structure (RS) can be riprap rock (granular), concrete blocks, or various mattresses, i.e., asphalt, vegetation, etc., as shown in Fig. 3. Furthermore, concrete block revetment is the coastal engineer’s current trend owing to its better capability in absorbing wave energy.

In fact, most of the design tools for each type of revetment structures still have a lot of limitations. This is the reason why the design methodology for revetments has recently been extended in applicability by means of a number of desk-studies for other revetments [2]. The existence of many guided criterions for the designing of revetment structures is a proof, such as PIANC (the World Association for Waterborne Transport Infrastructure) guidelines, design of revetments [2], design of

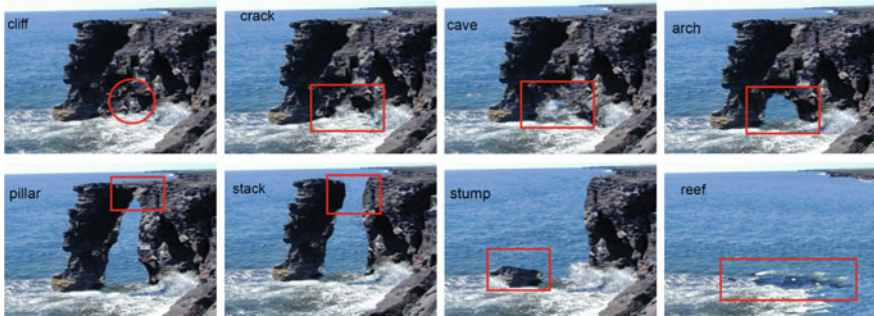


Fig. 1 Coastal retreat under wave attack [1]



Fig. 2 Coastal structures [1]

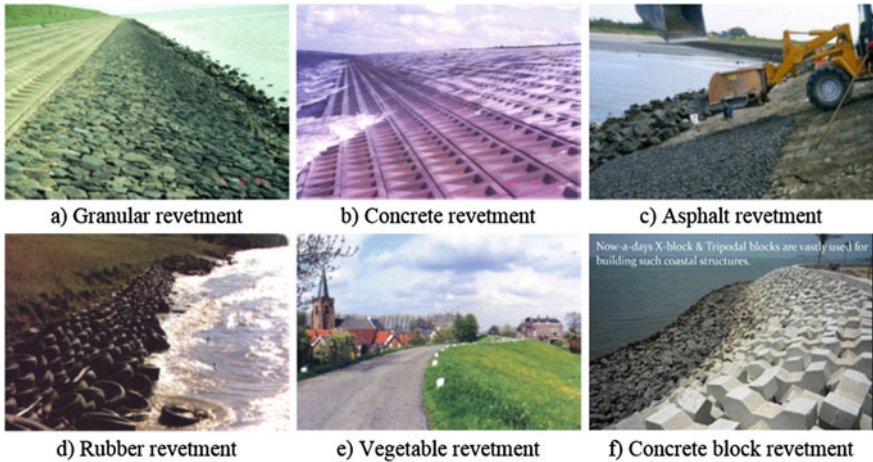


Fig. 3 Types of revetment structures [3]

riprap revetment [4], revetment structure [5], design of coastal revetments, seawalls, and bulkheads [6], recommendations for updating EM 1110-2-1614, design of coastal revetments, seawalls, and bulkheads [7], river and channel revetments: a design manual [8], the rock manual [9]. In addition, such designing tools are almost based on the particular real revetment’s data or the physical experiments in the modern laboratory. It absolutely is a big disadvantage for the developing countries, especially in Vietnam where the limitations of financial condition, as well as, modern laboratory equipment are common. Furthermore, the demand of the better concrete revetment is increasingly urgent in Vietnam, and the country of “vulnerable” Southeast Asia is facing on the threats from sea-level rise, global warming, because of the less effectiveness of the current coastal protection structures under the raise of severe storms and floods. The analytical approach, moreover, is almost impossible as in Jo’s [10] confirmation owing to the too complex fluid–structure interaction problem even with the simple governing equations.

As a result, the numerical approach, which can overcome all drawbacks of finance, equipment will be good alternative solution. This is realistic because of the present great development of numerical methods. That is the reason why this research is to develop the specialized computational simulations for the construction of RS that will better protect coasts from erosion. This paper, therefore, aims to make a review on the fluid–structure interaction analysis of the revetment structure.

2 Fluid–Structure Interaction (FSI) Concept

Firstly, a simple definition for fluid–structure interaction, presented in Ref. [10], firmed that a flexible solid structure contacting on a flowing fluid is subjected to a fluid-induced pressure, which may cause structural deformation and displacement that return to alter the fluid field. The altered fluid field then exerts another pressure on the structure. That process is called fluid–structure interaction (FSI). It allows you to model scenarios showing where fluid deforms a structure, how the structure responses to its deformation, and how such deformations influence the fluid flow. For example, the fluid flows through pipe connections, flow meters, valves, airplane wings, turbine blades, and other structures [11], as shown in Fig. 4.

Secondly, for numerical approach of FSI problem, we consider a fluid–solid interaction problem domain as in Fig. 5; with a total area domain, $\Omega = \Omega_f \cap \Omega_s$, consists of a fluid domain, Ω_f , and a solid domain, Ω_s . The contacting boundary between the fluid and the solid domain is denoted, Γ_{sf} , the remaining of fluid boundary, Γ_f , the remaining solid boundary, Γ_s .

Thirdly, the equations of motion for the fluid and structure are expressed in the same index form, as a result of the D’Alembert’s principle [13]:

$$\rho \dot{v}_i - \sigma_{ij,j} + f_i = 0 \tag{1}$$

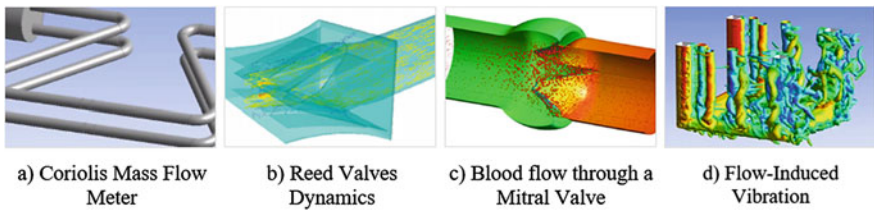
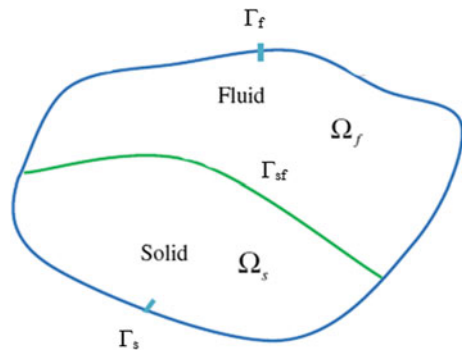


Fig. 4 Some examples for the fluid–structure interaction [11]

Fig. 5 A domain of the fluid–solid interaction problems [12]



where

- f_i is the body force, such as gravity
- v_i is the velocity; the time derivative of the displacement u_i
- $\sigma_{ij,j}$ is the internal stresses

In the structural domain, the equation is rewritten as follows:

$$\rho^s \dot{v}_i^s - \sigma_{ij,j}^s + f_i^s = 0 \quad \text{in } \Omega_s \tag{2}$$

where

- s denotes the quantity associated with the structure
- $\sigma_{ij,j}^s$ denotes the structural stress and is a function of the strains ϵ_{ij}

$$\sigma_{ij,j}^s = \lambda \cdot \delta_{ij} \epsilon_{ij} + 2G \epsilon_{ij} \tag{3}$$

- λ, G are Lamé constants
- ϵ_{ij} is the structural strains

$$G = \frac{E}{2(1 + \vartheta)} \tag{4}$$

$$\lambda = \frac{E\nu}{(1 + \vartheta)(1 - 2\vartheta)}$$

$$\epsilon_{ij} = \frac{1}{2} (u_{i,j} + u_{j,i}) \tag{5}$$

E, ϑ are the Young’s modulus and the Poisson’s ratio, respectively (4).

The fluid domain is usually represented by the Eulerian description as the subsequent equations:

$$\rho^f \dot{v}_i^f - \sigma_{ij,j}^f + f_i^f = 0 \quad \text{in } \Omega_f \tag{6}$$

where

- f denotes the quantity associated with the flow–fluid.
- And the gradient of current velocity is defined as follows:

$$\dot{v}_i^f = \frac{du_i^f}{dt} = \frac{\partial v_i^f}{\partial t} + v_j^f v_{i,j}^f \tag{7}$$

In order to consider the incompressible flow, Newtonian fluid theory will be used to compute the stress as:

$$\sigma_{ij}^f = -p\delta_{ij} + \tau_{ij} \quad (8)$$

where

p is the static pressure;

$$\begin{aligned} \tau_{ij} &= 2\mu(e_{ij} - \delta_{ij}e_{kk}/3) \\ e_{ij} &= \left(v_{j,i}^f + v_{i,j}^f\right) \end{aligned} \quad (9)$$

Finally, on the fluid–structure interface boundary Γ_{sf} with no-slip conditions, the Dirichlet and Neumann conditions can be defined as follows:

$$v_i^s = v_i^f \quad \text{on } \Gamma_{sf} \quad (10)$$

$$\sigma_{ij}^s n_i = \sigma_{ij}^f n_i \quad \text{on } \Gamma_{sf} \quad (11)$$

In other words, the displacement of both fluid and structure on the interface boundary is the same, i.e.:

$$x_{ij}^s = x_{ij}^f \quad \text{on } \Gamma_{sf} \quad (12)$$

It means that the Eq. (12) can replace (10) in the computational boundary conditions. And Eqs. (11) and (12) represent the coupling condition in the FSI problem.

3 Computational Procedure Approaches for FSI

To start with, the need for a wide range of scientific and engineering disciplines has been leading to a marvelous number of numerical techniques development for FSI [13]. The fact is that it still continually growing and contributing more enormous efforts to scientists and engineers. In this section, a review on the fluid–structure interaction approaches is presented.

In addition, we can easily find many books and reviews of FSI problems, recently. Morand and Ohayon [14] presented a number of numerical methods in modeling the linear vibrations of elastic structures coupled with internal fluids, with applications focused on sloshing, hydro elasticity, and structural acoustics. Dowell and Hall provided an in-depth discussion of non-linear dynamical modeling of FSI problems, largely drawn from applications in aerospace engineering, with an emphasis on the construction of reduced-order models (ROM) based on rigorous fluid dynamical theory [15]. Chakrabarti represented a collection of several numerical works in modeling FSI problems in the context of ocean engineering [16]. Mittal and Iaccarino extensively reviewed FSI computational techniques

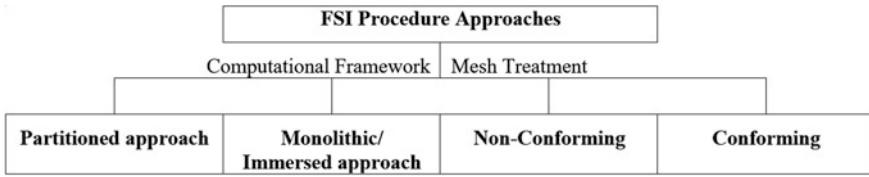


Fig. 6 Procedure approaches of FSI problem

based on the immersed boundary formulation [17], originally proposed by Peskin [18]. Shyy et al. [19] described a variety of computational methods for general moving boundary problems in fluid dynamics, which also cover FSI applications, etc.

Based on such documents, the numerical procedures to solve the FSI problems may be broadly classified into four main approaches, as indicated in Fig. 6.

The first approach, named the monolithic/immersed approach, is a method creating only one system of equations for the entire problem by simultaneously solving both fluid and structure dynamics in an unified mathematical framework. Its interfacial conditions are implicit in the solution procedure. This approach can achieve better accuracy for a multidisciplinary problem, but it may require substantially more resources and expertise to develop and maintain such a specialized code.

In the second method, the partitioned approach, two computational frameworks of fluid and structure are created and separately solved with their respective mesh and numerical algorithm. Another difference between monolithic and the partitioned approach is about the interfacial conditions. The interfacial data will be explicitly exchanged between the fluid and structure problems. Furthermore, the partitioned approach reduces the code development time by using the validated existing codes or numerical algorithms that are used for solving many complicated fluid or structural problems.

The above two approaches are classified by computational framework and shown as in Fig. 7.

The next classification is based on the treatment of mesh. The conforming mesh approach treats the fluid, structural field, and mesh in a sequential process. This process, to begin with, solves the fluid field at a given time and an assumed interface location. The resulting fluid fields (pressure and stress) then are applied to the structure field as external forces. The computation in structural field finishes with the update of deformations and coordinates of the structure. New fluid mesh, at the end of each computational time step, is created to adjust the new interface location [13].

The non-conforming mesh approach means that there is no any re-meshing after each computational time step. In this method, a term called force-equivalent term is added into fluid equations. That term is the representation for the interaction between fluid and structures and will be used to compute the fluid velocity. Such result and the no-slip condition then are applied to find the structural velocity. As a

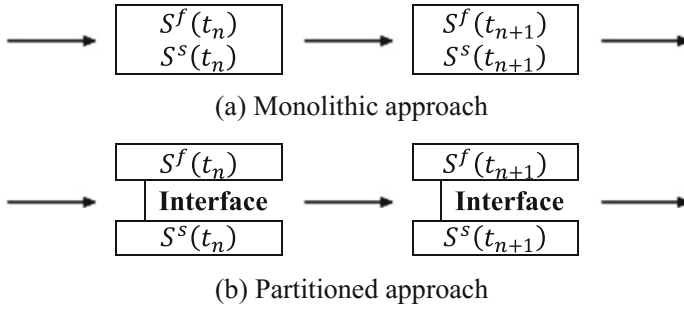


Fig. 7 **a** Monolithic approach and **b** the partitioned approach for fluid–structure interaction, in which S_f and S_s are solution for fluid and structure, respectively [13]

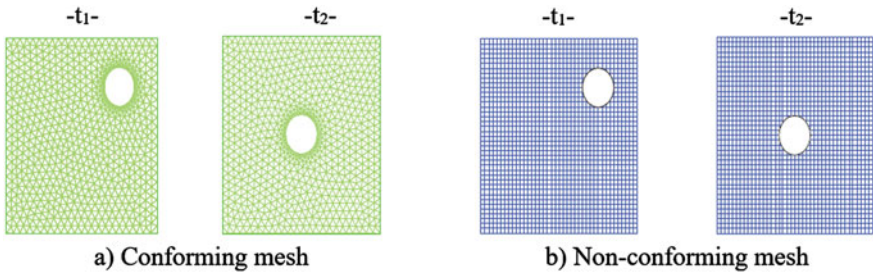


Fig. 8 **a** Conforming mesh and **b** the non-conforming mesh [13]

result, the need for mesh update is completely eliminated. Peskin [18] and Mittal and Iaccarino [17] showed the analysis, as well as, applications for this method.

The major difference between two above approaches is figured in Fig. 8. In the conforming mesh, it is clear that the new mesh for fluid is formed at time step t_2 . In contrast, the mesh of non-conforming approach has no change after time step t_1 .

It is obvious that each computational procedure approach of FSI problems has its own advantages and disadvantages. The choice completely depends on the researchers’ desire. In this paper, the detail computational process, as well as, formulations, equations, etc., of each approach is not illustrated.

4 Conclusions

Some basic definitions as well as classifications of FSI problems were revealed so that the new researchers can have a better approach in FSI field. Furthermore, as the driving task of this project is to investigate the interaction between currents, waves, and revetment structure, meanwhile, the understanding for this problem is

inadequate. Hence, this article hopefully provides the general revetment definitions and the rules in coastal protection so that in the next stages, the best approach is chosen.

Acknowledgements The authors acknowledge the financial support of VLIR-OUS TEAM Project, VLIRUOS2017-2021-75900, funded by the Flemish Government.



References

1. Rahaman AZ. Coastal structures
2. Pilarczyk KW (2003) Design of revetments. Rijkswaterstaat, DWW
3. Dorst K (2012) Rijkswaterstaat-Ministry of Infrastructure and the Environment. <https://www.rijkswaterstaat.nl/english/index.aspx>
4. Brown S, Clyde ES (1989) Design of rip rap revetment, HEC-11. US Army Corps of Engineers
5. Alan AS (1975) Revetment structure. Google patents
6. Manual E (1995) Design of coastal revetments, seawalls, and bulkheads
7. Ahrens J (1989) Recommendations for updating EM 1110-2-1614, design of coastal revetments, seawalls, and bulkheads. Draft report, US Army Waterways Experiment Station, Vicksburg, MS
8. Escarameia M (1998) Design manual: river and channel revetments. Thomas Telford
9. Ciria C (2007) The rock manual: the use of rock in hydraulic engineering, pp 487–756
10. Jo JC (2004) Fluid-structure interactions. Korea Institute of Nuclear Safety, Republic of Korea
11. ANSYS web page. www.ansys.com
12. Nguyen-Thoi T, Phung-Van P, Nguyen-Hoang S, Lieu-Xuan Q (2014) A smoothed coupled NS/nES-FEM for dynamic analysis of 2D fluid–solid interaction problems. *Appl Math Comput* 232:324–346
13. Hou G, Wang J, Layton A (2012) Numerical methods for fluid-structure interaction-a review. *Commun Comput Phys* 12(02):337–377
14. Morand HJ-P, Ohayon R (1995) Fluid structure interaction. Wiley
15. Dowell EH, Hall KC (2001) Modeling of fluid-structure interaction. *Annu Rev Fluid Mech* 33 (1):445–490
16. Chakrabarti SK (2005) Numerical models in fluid-structure interaction. WIT
17. Mittal R, Iaccarino G (2005) Immersed boundary methods. *Annu Rev Fluid Mech* 37:239–261
18. Peskin CS (1977) Numerical analysis of blood flow in the heart. *J Comput Phys* 25(3):220–252
19. Shyy W, Udaykumar H, Rao MM, Smith RW (2012) Computational fluid dynamics with moving boundaries. Courier Corporation

Building the Empirical Formula Defining Parameters of Blast Wave in Coral Environment



L. Vu-Dinh and T. Nguyen-Huu

Abstract The article presents the empirical method to determine the characteristics of coral material and coral foundation serving for computation and design of defense security works on islands. The authors built the empirical formula to define the parameters of blast wave in coral medium and compared the computation results using AUTODYN software and then drew the conclusion as the basis for application in reality.

Keywords Blast loading • Blast wave propagation • Soil

1 Raising the Problem

At present, there are not many scientific works which declare the study results about blast wave propagation in coral medium [1–5]. Thus, the empirical study defining blast wave parameters in coral medium is an urgent demand with practical value. In this article, the authors will focus on solving some following detailed issues.

An explosive charge is put in coral medium. Deformation medium can be constitutive of one layer or multi-layers. Loading on coral medium is the pressure of blast wave caused by focused explosive charge. So, it is necessary to define the parameters of blast wave at different locations in the medium (Figs. 1 and 2).

The medium is assumed to be constitutive of one layer or multi-layers with various physico-mechanical properties. But each medium layer is homogeneous and isotropic.

The authors measure blast wave parameters at positions with different explosive charges by using AUTODYN software to simulate the explosion process in coral. The detailed process is shown by the computing graph in Fig. 3. The parameters from this test are compared with experimental results to draw the conclusion.

L. Vu-Dinh • T. Nguyen-Huu (✉)

Le Quy Don Technical University (LeTech), 236 Hoang Quoc Viet St, Hanoi, Vietnam
e-mail: nguyenthe_p7@yahoo.com.vn; thepp@mta.edu.vn

© Springer Nature Singapore Pte Ltd. 2018

H. Nguyen-Xuan et al. (eds.), *Proceedings of the International Conference on Advances in Computational Mechanics 2017*, Lecture Notes in Mechanical Engineering, https://doi.org/10.1007/978-981-10-7149-2_51

733

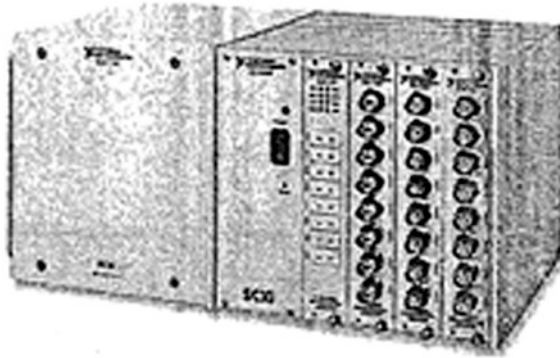


Fig. 1 Vibrometer NI SCXI-1000DC

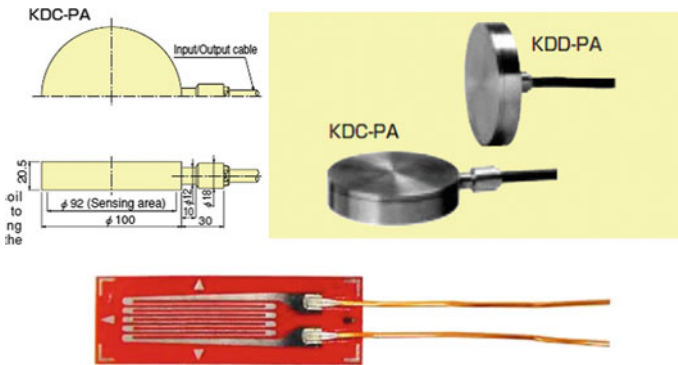


Fig. 2 Experimental instruments

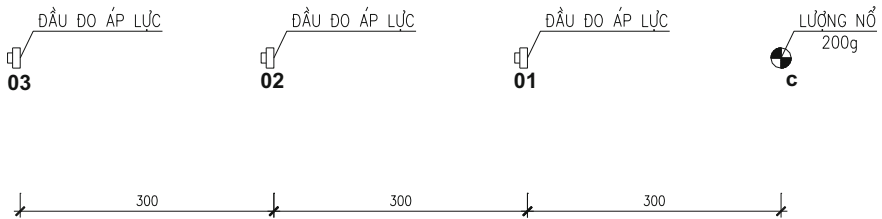


Fig. 3 Layout of explosive charges and the locations of pressure gauges

2 Empirical Method Defining the Parameters of Blast Wave in Coral Foundation

2.1 Experimental Equipment

Multi-channel vibrometer NI SCXI-1000DC is a modern device of multi-channel fluctuation measurement made by National Instrument Firm—USA, which is an intelligent measurement system with elastic configuration by integrating various measuring cards depending on the users' experimental purposes. The device has the direct current source with the attached battery which can be continuously used at field within 10 h without charging.

Sampling speed of this device can reach 333 kS/s with very low interference level. There are four slots on the device for inserting different types of measuring cards. NI company supplies a wide range of types of measuring cards SCXI suitable with the line SCXI-1000DC. These types of measuring cards can be used for different measurement such as acceleration, deformation, displacement, and voltage.

Vibrometer NI SCXI-1000DC is totally controlled by computer through USB connector. Driving software LABVIEW is a well-known software of analysis measurement in the world, which allows to design the programs of measurement and direct data analysis during measurement and cold-handles after measurement with the channel quantity up to thousands each measurement.

Soil pressure gauge KDC-1MPA (produced by TML, Japan).

Pressure gauge KDC-PA is made of stainless steel and can be corrosion-resistant in seawater. This gauge is used to measure pressure of blast wave in soil medium and the blast wave pressure on work structure. The maximum pressure of gauge type KDC-1MPA is about 1 MPa.

In this study, the gauge is used to measure the blast wave pressure on structure model and compressive wave propagation in coral medium.

Strain gauge PLA-5 (produced by TML, Japan)

Strain gauge PLA-5 is a deformation measurement device for steel structure. This gauge is used to measure the deformation of steel structure under the effect of static load and dynamic load.

2.2 Experiment Description and the Measurement Results

(Figs. 4, 5, 6, 7 and 8), (Table 1).

Fig. 4 Graph of gauge pressure 01

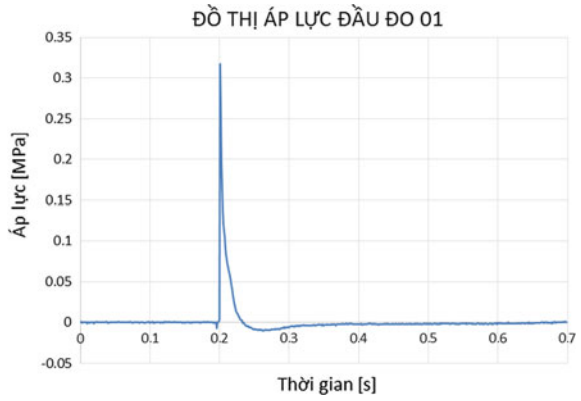


Fig. 5 Graph of gauge pressure 02

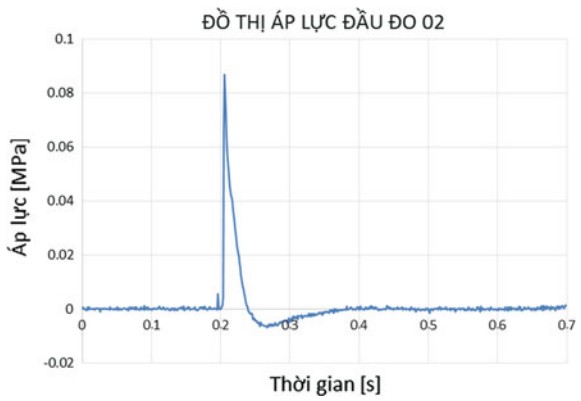
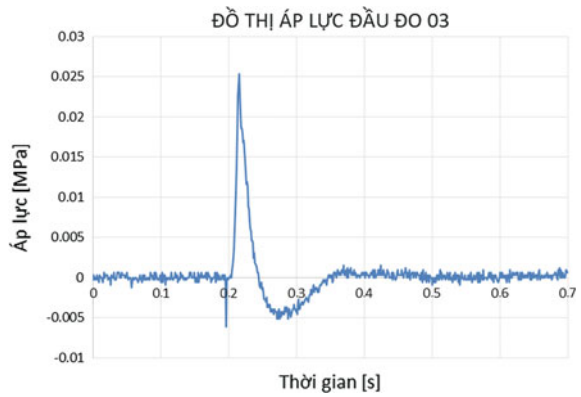


Fig. 6 Graph of gauge pressure 03



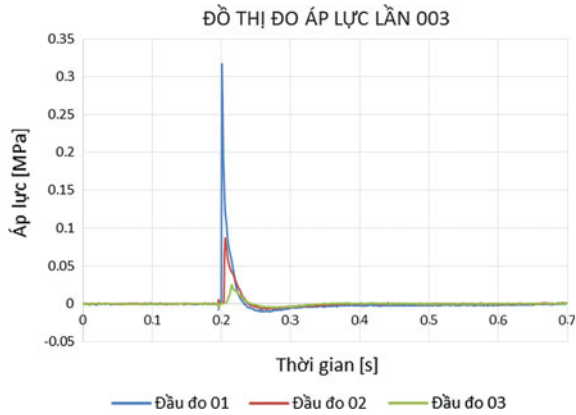


Fig. 7 Graph of three measurement combination

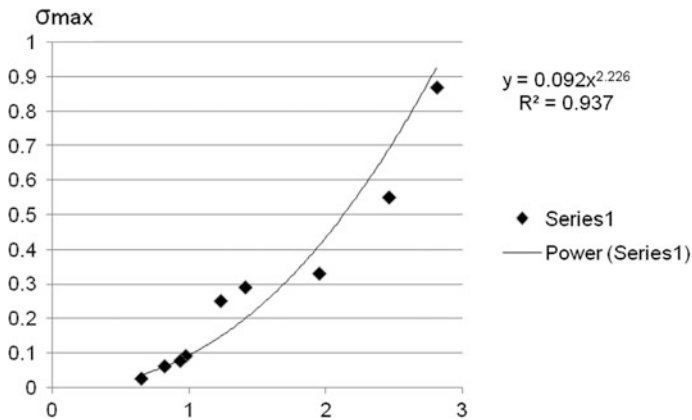


Fig. 8 Graph of processed experimental data

Table 1 Summary of detonation results in coral medium

Parameters	Summary of detonation results in coral medium					
$\frac{\sqrt{C}}{R}$	2.46	1.95	1.23	0.975	0.82	0.65
ΔP_{max} (MPa)	0.55	0.33	0.25	0.09	0.06	0.024

2.3 Empirical Formula

We build the empirical formula to define the maximum load in compressive wave.

(a) General formula of compressive wave pressure:

$$\Delta P_{max} = A \left(\frac{\sqrt[3]{C}}{R} \right)^m \tag{1}$$

(b) The formula built from the detonation experiment in coral at Truong Sa island:

$$\Delta P_{max} = 0.092 \left(\frac{\sqrt[3]{C}}{R} \right)^{2.226} \tag{2}$$

The formula determining blast loading in Truong Sa region for designing works of defense has not been built yet, so on-site testing and building empirical formula to define blast load are totally suitable. Empirical formula is applied for shallow placement of explosive charge with hopper and affected by the surface.

3 Comparing the Result from Experimental Studies and Numerical Stimulation Using AUTODYN Software

3.1 Material Model

3.1.1 Coral

Table 2

3.1.2 Explosive TNT

Equation of state (EOS) shows the relationship among pressure p , density ρ , and specific energy e . In calculation of mine explosion mechanism, the empirical equation of state for explosive Jones–Wilkins–Lee (JWL) is used widely. The equation of state (EOS) JWL [6–8] can be written in aspect of initial energy per each bulk unit, as:

$$P = A \left(1 - \frac{\omega}{R_1 V} \right) e^{-R V_1} + B \left(1 - \frac{\omega}{R_2 V} \right) e^{-R_2 V} + \frac{\omega E}{V} \tag{3}$$

Table 2 Coral material

Elastic module	Density	Poisson ratio	Cohesive force	Internal friction angle
$E = 2.19 \times 10^4$	$\rho = 2.2 \text{ g/cm}^3$	$\nu = 0.3$	$C = 0$	$\varphi = 31.65$

Table 3 Parameters of explosive TNT used in the equation JWL [6]

C_d	A	B	R_1	R_2	ω	ρ_0	E_{mo}
6930 m/s	373.8 GPa	3.747 GPa	4.15	0.9	0.35	1630 kg/m ³	3.63 Jun/kg

where, P—pressure; E—specific internal energy; V—relative volume; A, B, R_1 , R_2 and ω are empirical coefficients for each type of explosive, respectively. The parameters of explosive TNT are listed in Table 3.

3.2 Boundary Condition

In the survey model, the author solves above problems by supplementing the spring and dashpot system at the boundary positions without deformation and wave reflection so that the wave reflection from the boundaries is small enough to not affect the process of pressure and velocity value survey at the positions in the environment. Empirical data measured in tests are shown in Table 4.

Based on experimental data by least squares method, we have the following formula to determine the load duration in compressive wave.

- Load duration:

$$\theta = 0.0105R + 0.0282\sqrt[3]{C} \tag{4}$$

- Load increase time:

$$\theta_1 = 0.0079R - 0.002\sqrt[3]{C} \tag{5}$$

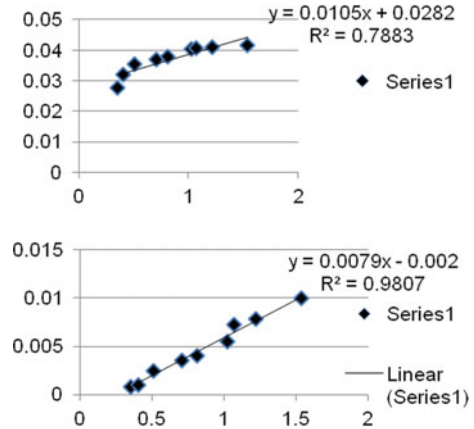
- Dimensionality of variables in empirical formula is as follows:

$$[\theta, \theta_1] = \text{second}; [R] = \text{m}, [C] = \text{kg (Fig. 9)}$$

Table 4 Empirical data measured

$R/(C^{1/3})$	0.3558	0.4065	0.5128	0.7092	0.813	1.0256	1.0706	1.2195	1.5384
$\sigma_{max}(\text{Mpa})$	0.87	0.55	0.33	0.29	0.25	0.09	0.076	0.06	0.024
$\theta/(C^{1/3})$	0.0277	0.032	0.0355	0.037	0.038	0.0405	0.0408	0.041	0.0415
$\theta_1/(C^{1/3})$	0.00081	0.001	0.0025	0.0035	0.004	0.0055	0.0073	0.0078	0.01

Fig. 9 Graph of experimental data processing to determine θ , θ_1



4 Conclusion

Empirical formula determining the parameters of blast wave built on the basis of field experiment at Son Ca island of Truong Sa archipelago can be used to compute the impact load on military works constructed on coral islands.

References

1. Nguyễn Hoa Thịnh (2000), *Báo cáo tổng kết đề tài KHCN.06.09*, Trung tâm thông tin Khoa học kỹ thuật Quốc gia
2. Hoàng Xuân Lượng (2004), *Báo cáo tổng kết đề tài KC.09.08*, Cục thông tin Khoa học và Công nghệ Quốc gia, Hà Nội
3. Henrych J (1979) The dynamics of explosion and its use, chapter 5. Elsevier, New York
4. Saleeb AF (1981) Constitutive models for soils in landslides. PhD thesis, Purdue University
5. TM5-855-1 (1984) Fundamental of protective design for conventional weapons. US Army Engineer Waterways Experiment Station, Vicksburg
6. AUTODYN Theory Manual, revision 3.0 (1997), Century Dynamics, San Ramon, California
7. Shamsheer P (1981) Soil dynamics, chapter 4. McGraw-Hill, New York
8. Pande GN, Zienkiewicz OC (1982) Soil mechanics, transient and cyclic loads, chapter 2. Wiley, Chichester

A CFD Modeling of Subcooled Pool Boiling



T. T. Nguyen, H. N. Duong, V. T. Tran and H. Kikura

Abstract Subcooled pool boiling is of immense importance in many industrial and engineering systems because of its great heat transfer coefficient in comparison with other heat transfer mechanisms. However it is one of the most complicated two-phase phenomena due to, for example, the simultaneous liquid/vapor motion at the same time with heat and mass transfer across the phase interfaces, distorted and deformable phase interface geometry with complicated bubble breakup/coalescence mechanisms etc. As the accuracy of the CFD simulation of two-phase flows has much improved, numerical study of subcooled pool boiling two-phase flow by using the CFD approach is desirable. To incorporate experimental and numerical studies of subcooled boiling, the objective of this study is to setup a numerical modeling of the subcooled pool boiling in a vertical pipe by using the CFD approach. The numerical setup is based on the physical experimental model developed in our previous study. For the numerical simulation of subcooled pool boiling and wall boiling, the extended RPI boiling model is exploited in the framework of the two-fluid CFD approach. Test simulations by using the numerical setup have been carried out for three cases: a single air bubble rising in still water, a vapor Taylor bubble rising in saturated still water, and a vapor bubble rising and condensing in subcooled still water. Evaluation of the model setup has been clarified. An initial simulation of subcooled pool boiling has also been demonstrated.

Keywords Subcooled boiling · Two-phase flow · Bubbly flow
CFD simulation · Two-fluid approach · Wall boiling · Heat mass transfer

T. T. Nguyen (✉)

Institute of Mechanics, Vietnam Academy of Science and Technology,
264—Doi Can, Ba Dinh, Hanoi, Vietnam
e-mail: ntthang@imech.vast.vn; ntthang_imech@yahoo.com

T. T. Nguyen · H. N. Duong

Graduate University of Science and Technology, Vietnam Academy
of Science and Technology, 18—Hoang Quoc Viet, Cau Giay, Hanoi, Vietnam

V. T. Tran · H. Kikura

Tokyo Institute of Technology, 2-12-1-N1-7 Ookayama, Meguro-Ku,
Tokyo 152-8550, Japan

© Springer Nature Singapore Pte Ltd. 2018

H. Nguyen-Xuan et al. (eds.), *Proceedings of the International Conference on Advances in Computational Mechanics 2017*, Lecture Notes in Mechanical Engineering, https://doi.org/10.1007/978-981-10-7149-2_52

1 Introduction

Subcooled boiling is one of the most efficient heat transfer modes because of the tremendous latent heat of vaporization. Thus, it is widely exploited in various important industrial and engineering processes such as in the cooling system (i.e. the thermal hydraulic system) of nuclear reactors, heat exchangers, electronic cooling devices etc. (e.g. see [1, 2]). Therefore, it not only implies the economic significance but also has great industrial safety importance. However, subcooled boiling is inherently one of the most complicated flow phenomena that makes high-accuracy calculation, prediction and hence control of the flow behaviors difficult (e.g. see [3, 4]).

For the study of subcooled boiling, both physical experiments and numerical calculations have been applied (e.g. see [1–4]). On the physical experimental side, measured data are lack and scattered since the experimental conditions are critically industrially aggressive. Thus, most of the measured data were obtained for particular conditions (e.g. high pressure, temperature etc.) which are most relevant to nuclear safety (e.g. see [5, 6]). In our previous study, a physical experimental subcooled pool boiling apparatus has been setup to measure the condensation phenomena (specifically, the condensation rate of vapor bubbles) in subcooled boiling at ambient pressure. A novel method for condensation-rate measurement has been devised [7]. In order to incorporate the measured data of these physical experimental measurements into CFD simulation, a numerical experimental model setup is desirable.

In the CFD simulation of two-phase flows, there exist a number of theoretical formulation approaches that include the single-fluid and multi/two-fluid ones (e.g. see [8, 9]). The single-fluid approach is based on the solution of single continuity and momentum equations of a multiphase mixture. Regarding the simulation of boiling and condensation by using this approach, a number of phase interface treatment techniques such as VOF (Volume of Fluid), level set, phase field, front-tracking has been extensively used. These techniques have provided a number of detailed physical aspects of the boiling and condensation phenomena (e.g. see [8–10]). However, several assumptions must be satisfied for the application of the single-fluid approach. For example, the phases should be strongly coupled. In some practical situations, such assumptions may not be adequately fulfilled, e.g. in the counter-current two-phase flow which is widely accounted for in nuclear engineering. Moreover, the accuracy of the interface treatment techniques depends on the computational mesh resolution. Therefore, the computational cost would be extremely expensive in order to resolve accurately a large range of the size of the dispersed phase in, for example, bubbly flow.

The two-fluid approach is based on the Eulerian framework, in association with mechanistic component/closure models of the phase interactions. It is the most detailed and accurate formulation of the thermal and hydrodynamic behaviors of the two-phase boiling systems (e.g. see [1, 3–5, 11]). This approach is based on the solution of the continuity and momentum equations written for each phase

separately [12–14]. It is most appropriate for the highly complicated flow phenomenon under investigation here. Hence it would be most suitable for this study.

In the CFD simulation of boiling and condensation with wall boiling, the RPI model is most widely/successfully used to account for the generation, development and detachment of vapor bubbles from the heated walls. The combination of the RPI model with the two-fluid approach has been implemented in a number of previous studies for specific problems, typically for flow boiling over heated surfaces (e.g. see [5, 11, 15–17]). Nevertheless, CFD simulations of boiling and condensation in wall bounded flows, with conjugate heat transfer through solid walls, were less accounted for in the published literature.

The objective of this study is to setup a numerical modeling of subcooled pool boiling in a vertical pipe by using the CFD approach. The prototype of the model is based on the physical experimental model [7]. For the numerical simulation, the extended RPI boiling model (i.e. the non-equilibrium boiling model) (e.g. see [9]) is exploited in the two-fluid CFD approach. Test simulations by using the numerical setup have been carried out for three cases: a single air bubble rising in still water, a vapor Taylor bubble rising in saturated still water, and a vapor bubble rising and condensing in subcooled still water. Evaluation of the setup has been clarified. An initial simulation of subcooled pool boiling has also been demonstrated.

2 Theoretical Formulation and Numerical Method

Governing Equations for Multiphase Flow Modeling of Unsteady Subcooled Pool Boiling

Phase Mass Conservation Equations

The equations shown below are used in the calculation of the phase volume fractions [9]:

$$\frac{\partial}{\partial t} (\alpha_q \rho_q) + \nabla \cdot (\alpha_q \rho_q \vec{v}_q) = \sum_{p=1}^n (\dot{m}_{pq} - \dot{m}_{qp}) + S_q \quad (1)$$

where p and q denote the two-phases (water and vapor). The equation for the p phase has exactly the same form. α_q, ρ_q and \vec{v}_q are the volume fraction, density and velocity of the phase q , respectively; \dot{m}_{pq} represents the mass exchange from the phase p to the phase q (by definition $\dot{m}_{pq} \geq 0$); \dot{m}_{qp} denotes the mass transfer from the phase q to the phase p (similarly $\dot{m}_{qp} \geq 0$); S_q is the source term which is 0 by default [9].

Phase Momentum Conservation Equations

$$\frac{\partial}{\partial t} (\alpha_q \rho_q \vec{v}_q) + \nabla \cdot (\alpha_q \rho_q \vec{v}_q \vec{v}_q) = -\alpha_q \nabla p + \nabla \cdot \bar{\tau}_q + \alpha_q \rho_q \vec{g} + \sum_{p=1}^n (R_{pq} + \dot{m}_{pq} \vec{v}_{pq} - \dot{m}_{qp} \vec{v}_{qp}) + (\vec{F}_q + \vec{F}_{lift,q} + \vec{F}_{wl,q} + \vec{F}_{vm,q} + \vec{F}_{td,q}) \quad (2)$$

where p stands for the pressure shared by all phases; $\bar{\tau}_q = \alpha_q \mu_q (\nabla \vec{v}_q + \nabla \vec{v}_q^T) + \alpha_q (\lambda_q - 2/3\mu_q) \nabla \cdot \vec{v}_q \bar{I}$ represents the stress-strain tensor of the phase q ; \bar{I} means the unit tensor; μ_q and λ_q are the shear and bulk viscosity of the phase q ; \vec{g} is the acceleration due to gravitational force; $R_{pq} = K_{pq} (\vec{v}_p - \vec{v}_q)$ denotes an interaction force between the two phases where $K_{pq} = (K_{qp})$ is the interphase momentum exchange coefficient. Here R_{pq} represents the mean interphase momentum exchange and does not include any contribution due to turbulence. The turbulent interphase momentum exchange is modeled with the turbulent dispersion source term $\vec{F}_{td,q} \cdot \vec{v}_{pq}$ is the interphase velocity which is defined as follows. If $\dot{m}_{pq} > 0$ (that is, phase p mass is being transferred to phase q), $\vec{v}_{pq} = \vec{v}_q$. Likewise, if $\dot{m}_{qp} > 0$ then $\vec{v}_{qp} = \vec{v}_p$. \vec{F}_q is an external body force; $\vec{F}_{lift,q}$ is a lift force; $\vec{F}_{wl,q}$ is a wall lubrication force; $\vec{F}_{vm,q}$ is a virtual mass force; $\vec{F}_{td,q}$ is a turbulent dispersion force. These forces are all referred to phase q [9].

Phase Enthalpy Conservation Equations

Equation of the fluid zones

$$\frac{\partial}{\partial t} (\alpha_q \rho_q h_q) + \nabla \cdot (\alpha_q \rho_q \vec{v}_q h_q) = \alpha_q \frac{dp}{dt} + \bar{\tau}_q \cdot \nabla \vec{v}_q - \nabla \cdot \vec{q}_q + S_q + \sum_{p=1}^n (Q_{pq} + \dot{m}_{pq} h_{pq} - \dot{m}_{qp} h_{qp}) \quad (3)$$

where h_q is the specific enthalpy of the phase q which relates to the fluid temperature T by $h_q = \int_{T_{ref,q}}^T c_{p,q} dT + h_q^0(T_{ref,q}) + \frac{p}{\rho_q}$ where $T_{ref,q}$ is the reference temperature which is usually taken to be 298.15 K; $c_{p,q}$ is the heat capacity of the phase q at the temperature T ; $h_q^0(T_{ref,q})$ is the phase q 's formation enthalpy at the reference temperature $T_{ref,q}$; \vec{q}_q is the heat flux to the phase q ; S_q is a source term that includes sources of enthalpy; Q_{pq} is the intensity of the heat exchange between the phase p and the phase q , which must comply with the local balance condition $Q_{pq} = -Q_{qp}$ and $Q_{qq} = 0$; h_{pq} is the interphase enthalpy [9].

Equation of the solids zones in the conjugate heat transfer problems

$$\partial(\rho h) / \partial t + \nabla \cdot (\vec{v} \rho h) = \nabla \cdot (k \nabla T) + S_h \quad (4)$$

where h denotes the sensible enthalpy defined by $h = \int_{T_{ref}}^T c_p dT$; \vec{v} is the (bulk) velocity of the solid regions; k is the thermal conductivity of the solid material; S_h is the volumetric heat source [9].

Equation for the Calculation of the Shared Pressure Field

$$\sum_{k=p,q} \frac{\partial}{\partial t} (\alpha_k \rho_k) + \nabla \cdot \alpha_k \rho_k \vec{v}'_k + \nabla \cdot \alpha_k \rho_k \vec{v}^*_k - \left(\sum_{l=p,q} (\dot{m}_{lk} - \dot{m}_{kl}) \right) = 0 \quad (5)$$

where \vec{v}'_k is the velocity correction for the k th phase, and \vec{v}^*_k is the value of \vec{v}_k at the current iteration.

Turbulence Consideration

The per-phase turbulence model is used as shown below [9]:

$$\begin{aligned} \frac{\partial}{\partial t} (\alpha_q \rho_q k_q) + \nabla \cdot (\alpha_q \rho_q \vec{v}_q k_q) = & \nabla \cdot \left(\alpha_q \left(\mu_q + \frac{\mu_{t,q}}{\sigma_k} \right) \nabla k_q \right) + (\alpha_q G_{k,q} - \alpha_q \rho_q \varepsilon_q) \\ & + \sum_{l=p,q} K_{lq} (C_{lq} k_l - C_{ql} k_q) \\ & - \sum_{l=p,q} K_{lq} (\vec{v}_l - \vec{v}_q) \cdot \frac{\mu_{t,l}}{\alpha_l \sigma_l} \nabla \alpha_l \\ & + \sum_{l=p,q} K_{lq} (\vec{v}_l - \vec{v}_q) \cdot \frac{\mu_{t,q}}{\alpha_q \sigma_q} \nabla \alpha_q + \Pi_{k_q} \end{aligned} \quad (6)$$

where $\mu_{t,q} = \rho_q C_\mu k_q^2 / \varepsilon_q$; $C_\mu = 0.09$; k_q and ε_q are the turbulence kinetic energy and the turbulence dissipation rate of the phase q , respectively; $\sigma_k = 1.0$ is the turbulence Prandtl number for k_q in phase q ; $G_{k,q}$ is the turbulence production of the phase q $G_{k,q} = \mu_{t,q} \left(\nabla \vec{v}_q + (\nabla \vec{v}_q)^T \right) : \nabla \vec{v}_q$; K_{lq} is the interface momentum exchange coefficient; C_{lq} and C_{ql} are the model coefficients that are described as $C_{lq} = 1$, $C_{ql} = 2(\eta_{lq}/1 + \eta_{lq})$ where η_{lq} is the ratio between the eddy particle interaction time to the characteristic particle relaxation time; σ_l and σ_q coefficients are set to 0.75 by default; Π_{k_q} is the source term included to model the turbulent interaction between the dispersed phases and the continuous phase [9].

$$\begin{aligned} \frac{\partial}{\partial t} (\alpha_q \rho_q \varepsilon_q) + \nabla \cdot (\alpha_q \rho_q \vec{v}_q \varepsilon_q) = & \nabla \cdot \left(\alpha_q \left(\mu_q + \frac{\mu_{t,q}}{\sigma_\varepsilon} \right) \nabla \varepsilon_q \right) \\ & + \frac{\varepsilon_q}{k_q} \left[C_{1\varepsilon} \alpha_q G_{k,q} - C_{2\varepsilon} \alpha_q \rho_q \varepsilon_q + C_{3\varepsilon} \left(\sum_{l=p,q} K_{lq} (C_{lq} k_l - C_{ql} k_q) \right. \right. \\ & \left. \left. - \sum_{l=p,q} K_{lq} (\vec{v}_l - \vec{v}_q) \cdot \frac{\mu_{t,l}}{\alpha_l \sigma_l} \nabla \alpha_l + \sum_{l=p,q} K_{lq} (\vec{v}_l - \vec{v}_q) \cdot \frac{\mu_{t,q}}{\alpha_q \sigma_q} \nabla \alpha_q \right) \right] + \Pi_{\varepsilon_q} \end{aligned} \quad (7)$$

where $\sigma_\varepsilon = 1.3$ is the turbulence Prandtl number for ε in the phase q ; the constant coefficients are $C_{1\varepsilon} = 1.44$, $C_{2\varepsilon} = 1.92$; Π_{ε_q} is the source term included to model the turbulence interaction between the two phases [9].

Non-equilibrium Wall Boiling Model

Generalized Non-equilibrium Model of Wall Heat Flux Partitioning

The total heat flux from the heated wall to the liquid phase (included in the source term in Eq. (3)) can be partitioned into three basic components including the convective heat flux (\dot{q}_C), the quenching heat flux (\dot{q}_Q), the evaporative heat flux (\dot{q}_E). In addition, two components \dot{q}_V and \dot{q}_G are used to consider vapor and gas temperature [9, 15–17].

$$\dot{q}_W = (\dot{q}_C + \dot{q}_Q + \dot{q}_E)f(\alpha_l) + (1 - f(\alpha_l))\dot{q}_V + \dot{q}_G \quad (8)$$

The heated wall surface is subdivided into an area A_b covered by nucleating bubbles, and a portion $(1 - A_b)$ covered by the liquid phase.

Convective Heat Flux

$$\dot{q}_C = h_C(T_w - T_l)(1 - A_b) \quad (9)$$

where h_C is the single phase heat transfer coefficient of the liquid; T_w and T_l are the wall and liquid temperatures, respectively.

Quenching Heat Flux

$$\dot{q}_Q = (T_w - T_l)2k_l/\sqrt{\pi\lambda_l T} \quad (10)$$

where k_l is the thermal conductivity of the liquid phase; T is the periodic time of bubble departure; and $\lambda_l = k_l/\rho_l C_{pl}$ is the thermal diffusivity of the liquid phase [9, 15–17].

Evaporative Heat Flux

$$\dot{q}_E = V_d N_w \rho_v h_{fv} f \quad (11)$$

where V_d is the volume of the bubble calculated based on the bubble departure diameter; N_w is the active nucleate site density; ρ_v is the vapor density; h_{fv} is the latent heat of evaporation; and f is the bubble departure frequency [9].

Convective Heat Flux to the Vapor Phase

$$\dot{q}_V = h_V(T_w - T_V) \quad (12)$$

where h_V is the single phase heat transfer coefficient of vapor; T_V is the vapor temperature.

In Eq. (8), the function $f(\alpha_l)$ depends on the local liquid volume fraction with similar limiting values as the liquid volume fraction. In this study, the expression shown below is used:

$$f(\alpha_l) = \begin{cases} 1 - 0.5e^{-20(\alpha_l - \alpha_{l,crit})} \\ 0.5(\alpha_l/\alpha_{l,crit})^{20\alpha_{l,crit}} \end{cases} \quad (13)$$

where $\alpha_{l,crit} = 0.2$ is exploited [9].

Area of Influence

$$A_b = \min(1, KN_w\pi D_w^2/4) \quad (14)$$

where $K = 4.8e^{(-Ja_{sub}/80)}$ with $Ja_{sub} = \rho_l C_{pl} \Delta T_{sub} / \rho_v h_{fv}$ is the subcooled Jacob number; $\Delta T_{sub} = T_{sat} - T_l$.

Bubble Departure Frequency

$$f = 1/T = \sqrt{4g(\rho_l - \rho_v)/3\rho_l D_w} \quad (15)$$

Nucleation Site Density

$$N_w = C^n (T_w - T_{sat})^n \quad (16)$$

where $n = 1.805$ and $C = 210$.

Bubble Departure Diameter

$$D_w = \min(0.0014, 0.0006e^{-\Delta T_w/45}) \quad (17)$$

Interfacial Transfer Modeling

Momentum Transfer

Bubble diameter

$$D_b = \begin{cases} 0.0015 & \Delta T_{sub} < 0 \\ 0.0015 - 0.0001\Delta T_{sub} & 0 \leq \Delta T_{sub} \leq 13.5K \\ 0.00015 & \Delta T_{sub} > 13.5K \end{cases} \quad (18)$$

with $\Delta T_{sub} = T_{sat} - T_l$.

Interfacial drag force

The drag force included in the interaction force R_{pq} shown in Eq. (2) is written as follows:

$$\vec{F}_{drag} = (\vec{v}_q - \vec{v}_p) / \tau_r \quad (19)$$

where $\tau_r = \frac{\rho_p D_b^2}{18\mu_q C_d Re}$ denotes the droplet or particle relaxation time; ρ_p is the density of the phase p (the dispersed phase); C_d is the drag coefficient; $Re = \rho_q D_b |\vec{v}_q - \vec{v}_p| / \mu_q$ is the relative Reynolds number of the dispersed phase; Ishii's model of the drag force includes: $C_d = \min(C_D^{vis}, C_D^{dis})$ where $C_D^{vis} = (1 + 0.15Re^{0.75})24/Re$ is the drag

coefficient of the viscous regime, $C_D^{dis} = D_b 2/3 / \sqrt{\sigma/g|\rho_q - \rho_p|}$ is the drag coefficient of the distorted regime and σ is the surface tension.

Interfacial lift force

$$\vec{F}_{if} = -C_l \rho_q \alpha_p (\vec{v}_q - \vec{v}_p) \times (\nabla \times \vec{v}_q) \quad (20)$$

where C_l is the lift coefficient calculated by using the Moraga's correlation (referred to in [9]).

$$C_l = \begin{cases} 0.0767 & \varphi \leq 6000 \\ -\left(0.12 - 0.2e^{-10^{-5}\varphi/3.6}\right)e^{10^{-7}\varphi/3} & 6000 < \varphi < 5 \times 10^7 \\ -0.6353 & \varphi \geq 5 \times 10^7 \end{cases} \quad (21)$$

where $\varphi = \text{Re} \times \text{Re}_\omega$ with the vorticity Reynolds number $\text{Re}_\omega = \rho_q D_b^2 |\nabla \times \vec{v}_q| / \mu_q$.

Wall lubrication force

$$\vec{F}_{wl} = -C_{wl} \rho_q \alpha_p \left| (\vec{v}_q - \vec{v}_p)_{\parallel} \right|^2 \vec{n}_w \quad (22)$$

where C_{wl} is the wall lubrication coefficient; $\left| (\vec{v}_q - \vec{v}_p)_{\parallel} \right|$ is the phase relative velocity component tangential to the wall surface; \vec{n}_w is the unit normal pointing away from the wall; $C_{wl} = \max(0, C_{w1}/d_b + C_{w2}/y_w)$, $C_{w1} = -0.01$ and $C_{w2} = 0.05$; y_w is the distance to the nearest wall [9].

Turbulent dispersion force

$$\vec{F}_{td,q} = -\vec{F}_{td,p} = C_{TD} \rho_q k_q \nabla \alpha_p \quad (23)$$

where $C_{TD} = 1$ by default [9].

Turbulence interaction model

The Troshko Hassan per-phase turbulence interaction model is used. The model of the source terms are shown bellows.

$$\Pi_{k_q} = C_{ke} \alpha_q \sum_{p=1}^M K_{pq} |\vec{v}_p - \vec{v}_q|^2; \quad \Pi_{\varepsilon_q} = C_{id} \frac{1}{\tau_p} \Pi_{k_q} \quad (24)$$

where $C_{ke} = 0.75$; $C_{id} = 0.45$; $\tau_p = 2C_{VM} D_b / 3C_D |\vec{v}_p - \vec{v}_q|$ is the characteristic time of the induced turbulence [9].

Virtual mass force

$$\vec{F}_{vm} = C_{vm} \alpha_p \rho_q (d_q \vec{v}_q / dt - d_p \vec{v}_p / dt) \quad (25)$$

where $C_{vm} = 0.5$ is the virtual mass coefficient; $d_q(\phi)/dt = \partial(\phi)/\partial t + (\vec{v}_q \cdot \nabla)\phi$ with ϕ is any scalar variable [9].

Surface tension

The Brackbill's continuum surface force (CSF) method (referred to in [9]) is exploited to model the surface tension force:

$$F_{vol} = \sigma_{ij}\rho\kappa_i\nabla\alpha_i/1/2(\rho_i + \rho_j) \quad (26)$$

where $\sigma_{ij} = 0.057$ is the surface tension coefficient (in the case of subcooled boiling vapor-water two-phase flow); $\rho = \sum \alpha_q\rho_q$ is the volume-averaged density; κ_i is the curvature defined by $\kappa_i = \nabla \cdot \hat{n}_i$; $\hat{n}_i = n_i/|n_i|$ and $n_i = \nabla\alpha_i$; $(i,j) = (p,q)$ [9].

Interfacial area concentration

An algebraic formulation (the symmetric model) is used in accordance with the Sauter mean diameter used as shown previously in Eq. (18) [9]:

$$A_i = 6\alpha_p/D_b \quad (27)$$

Heat Transfer

Interface to liquid heat transfer

$$Q_{pq} = \dot{q}_{lt} = h_{sl}(T_{sat} - T_l) \quad (28)$$

where T_{sat} is the vapor saturation temperature; T_l is the liquid bulk temperature; h_{sl} is the surface to liquid heat transfer coefficient [9].

Interface to vapor heat transfer

$$Q_{qp} = \dot{q}_{vt} = (T_{sat} - T_v)\alpha_v\rho_v C_{p,v}/\delta t \quad (29)$$

where $\delta t = 0.05$ is the time scale; T_v is the vapor temperature; $C_{p,v}$ is the isobaric heat capacity of the vapor phase [9].

Mass Transfer

Mass transfer from the heated wall to vapor

$$\dot{m}_E = \dot{q}_E / (h_{fv} + C_{p,t}\Delta T_{sub}) \quad (30)$$

Interfacial mass transfer

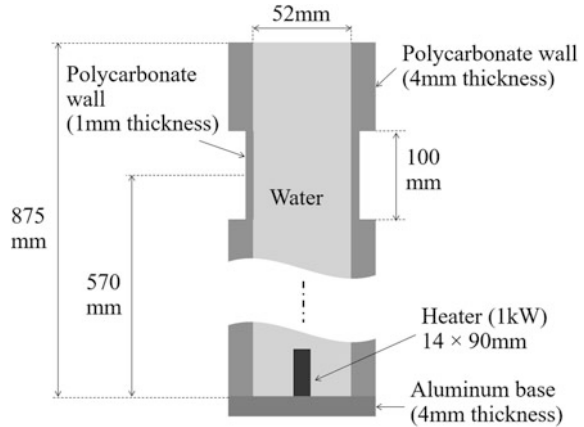
$$\dot{m} = \dot{m}_{lt} + \dot{m}_{vt} = (\dot{q}_{lt} + \dot{q}_{vt})/h_{fv} \quad (31)$$

Computational Domain, Boundary and Setting Conditions

Computational Domain

The computational domain and its dimensions are shown in Fig. 1. It consists of a round tube made of polycarbonate, an aluminum base, an electric heater and water/vapor phases inside the pipe. All these components are modeled by using the

Fig. 1 Computational domain



CFD approach. Convective heat transfer with the surrounding air is allowed between the pipe walls, base walls and the ambient.

In the solid regions of the polycarbonate walls, aluminum base and heater, the temperature field is calculated by using the energy Eq. (4). Heat transfer is calculated at the boundaries between fluids (water and vapor) and solids.

Boundary and Setting Conditions

At the free surface of the fluid mixture inside the pipe, a pressure outlet boundary condition is used. In addition, single-phase flow of only water through this boundary is allowed. This means that the volume fraction of the vapor phase at this boundary is zero. The temperature of the liquid through this boundary is set to 372 K.

At the fluid-solid interface, the non-slip boundary condition is used for flow simulation of both phases. The coupled boundary condition is used for heat transfer calculation.

A near-wall modeling approach that allows a consistent mesh refinement (modification) without any deterioration of the results, especially in the near wall regions, is exploited for the calculation of the variables at the cells adjacent to the wall.

As for the thermal boundary condition at the heater surface, the heat flux to the computational domain is set to 72 kW/m^2 based on the heater surface area and heater power.

Convective heat transfer boundaries are used along the outer boundaries of the pipe walls and of the base wall.

Other setting conditions are as follows. The two fluids used include liquid water and vapor. The saturation temperature of water is 373.15 K. The operating pressure is set to ambient pressure (i.e. atmospheric pressure). The properties of the fluids are set temperature dependence.

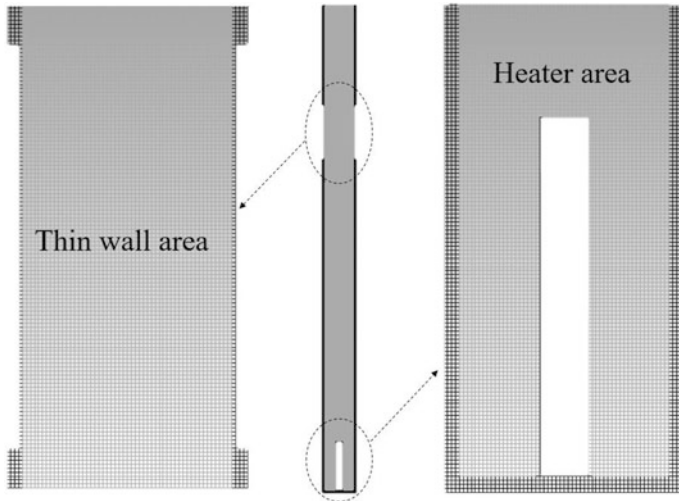


Fig. 2 Computational mesh with two enlarged regions

Computational Mesh and Numerical Discretization of the Governing Equations

Computational Mesh

The computational mesh is shown in Fig. 2. Meshing has been carried out for both fluid and solid regions. The computational domain is divided into 54180 2D quadrilateral cells. For ease of visualization, the meshing in two areas (thin wall area and heater area, Fig. 2) is shown in the enlarged pictures.

Numerical Discretization of the Governing Equations

The Finite Volume Method (FVM) is used for discretizing and for the approximate transient solution of the governing Eqs. (1)–(5), with the closure relationships/mechanistic models shown in Eqs. (6)–(31). The solution strategy is known as the pressure-based multiphase solution method. Details can be referred to [9].

In this study, the following specific selections are implemented in the solution algorithm:

- For the pressure-velocity coupling, the coupled scheme is used. The momentum and pressure-based continuity equations are solved altogether. Moreover, the continuity equation of both liquid and vapor phases are solved (i.e. Solve N-Phase Volume Fraction Equations).
- For the spatial discretization, the following techniques are exploited:
 - The Green-Gauss Node Based approach is used for the calculation of the gradient terms.
 - The Second Order Upwind and Modified HRIC (High Resolution Interface Capturing) schemes are applied to the discretization of the momentum, continuity, turbulence transport and energy equations.

- For the transient formulation (discretization of the time dependent term), the Bounded Second Order Implicit technique is applied.

3 Tests of the Numerical Model Setup

Computational Grid Refinement Investigation

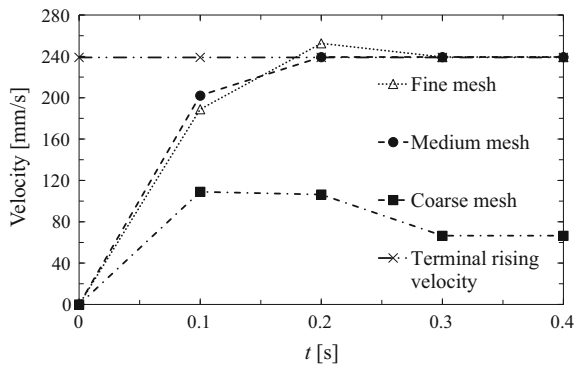
In order to evaluate the effects of the computational mesh refinement, three mesh resolutions have been investigated. The coarse mesh (cell size 2×2 mm) has 10000 elements approximately. The medium mesh (cell size 1×1 mm) has about 51000 elements. And the fine mesh (cell size 0.5×0.5 mm) has about 170000 elements.

Simulations of a single air bubble rising in still water at 20°C in the pipe are used for mesh resolution study. Initially, the bubble has a spherical shape, a diameter of 8 mm. It is placed at the pipe center, at a distance of 150 mm from the bottom of the pipe. When released, the bubble rises freely under the effects of buoyancy, drag forces and so on [18]. Three computational meshes mentioned above are used to evaluate the mesh resolution dependency. Figure 3 illustrates the initial rising velocity and terminal rising velocity of the bubble. As shown in the figure, the difference between the calculated results derived by using the fine mesh and the medium one could be negligible. Moreover, both results are in good agreement with the experimental data and theoretically predicted data of the terminal rising velocity of 8 mm—diameter air bubble in pure still water [3, 18–20]. On the contrary, the calculated result obtained by using the coarse mesh is clearly inaccurate. As the result, in this study, the use of the medium mesh for further investigations shown later on would be reasonable.

Test Cases

The CFD model is initially tested by three test cases:

Fig. 3 Instantaneous bubble rising velocity calculated by using different mesh resolutions



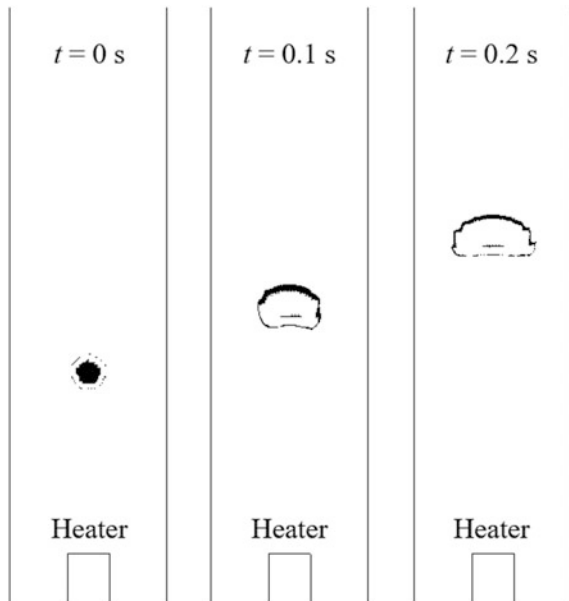
1. An initially spherical air bubble (initial diameter of 10 mm) rising in the water column in the pipe (at ambient temperature, still-water condition): adiabatic, non-condensable case without heat/mass exchange;
2. A Taylor bubble rising in the water column at saturated water temperature (still-water condition). The bubble (or slug) has an initially cylindrical body (40 mm diameter, 60 mm in length) with a spherical nose (i.e. the leading head). The nose diameter is 40 mm: adiabatic, 0 condensation case with 0 heat/mass exchange;
3. An initially spherical vapor bubble (initial diameter of 12 mm) rising and condensing in subcooled liquid (the subcooling degree is 1.15 K, still-water condition): heat/mass transfer without wall boiling.

Case 1: Rising Air Bubble

A fundamental element of the simulation of bubbly flows in a vertical pipe would be the simulation of a single rising bubble. For brevity, the distribution of the volume fraction of air is shown in Fig. 4, for three time instances: $t = 0, 0.1$ and 0.2 s.

As shown in the figure, the numerical experimental setup would be able to generate and reproduce the development of an air bubble rising in viscous liquid (i.e. water in this study). The initially spherical bubble becomes a generally observed shell-shape under the effects of the inertial force, viscosity, surface tension etc. [3]. As shown in Fig. 5a, the rising velocity of the bubble reaches the terminal rising velocity after approximately 0.2 s. In order to evaluate quantitatively the calculated result of the bubble terminal rising velocity, the CFD result of the

Fig. 4 The development of the 10 mm—diameter air bubble rising in still water in the water column



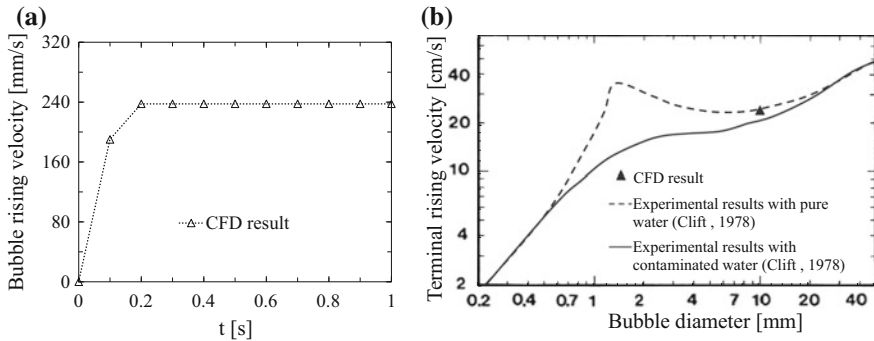


Fig. 5 Rising velocity of the 10 mm—diameter air bubble in still water: **a** time data; **b** terminal rising velocity (CFD result)

terminal rising velocity is plotted against a large number of experimental data presented in Clift 1978 (Fig. 5b). The figure shows that the result of this study agrees fairly well with the experimentally measured data reported in the published literature.

Consequently, a conclusion can be obtained that, once detached vapor bubbles enter liquid water, their development would be modeled by using the CFD model setup in this study. Moreover, based on the simulation result, the dynamics of rising air/vapor bubbles in viscous liquids can be further investigated in details. In the next step, the numerical model will be evaluated in the simulation of a liquid-vapor two-phase system.

Case 2: Taylor Vapor Bubble Rising in Saturated Water

In bubbly flows, big cap bubbles (i.e. Taylor or slug bubbles) can exist in the flows. Hence, in the next stage, correctly modelling of the development of Taylor bubbles is of importance. For brevity, only the distribution of the volume fraction of the vapor phase is shown in Fig. 6, for three time instances: $t = 0, 0.1$ and 0.2 s.

As shown in Fig. 6, the numerical experimental setup would be capable of generating and reproducing the development of a Taylor vapor bubble rising in saturated water. A self-rearrangement of the bubble from the originally initialized shape is captured. The shedding of smaller bubbles from the bubble trailing end is reasonably observed [3].

Moreover, as illustrated in Fig. 7, quantitatively, the rising velocity of the Taylor vapor bubble in saturated still water is obtained. In addition, in Fig. 7, the terminal rising velocities are also shown for two slug bubbles that have Froude numbers 0.27 and 0.33, respectively. The range of the Froude number from 0.33 to 0.37 is widely suggested for the terminal rising velocity of slug bubbles when the viscosity and surface tension forces would be negligible [19, 21–23]. Nonetheless, the Froude value of 0.27 (or even smaller) has been also mentioned elsewhere for specific cases [22, 23]. The calculated result of the terminal rising velocity shown in Fig. 7 would be corresponding to a Froude number of 0.27 approximately.

Fig. 6 Development of a Taylor vapor bubble rising in saturated water

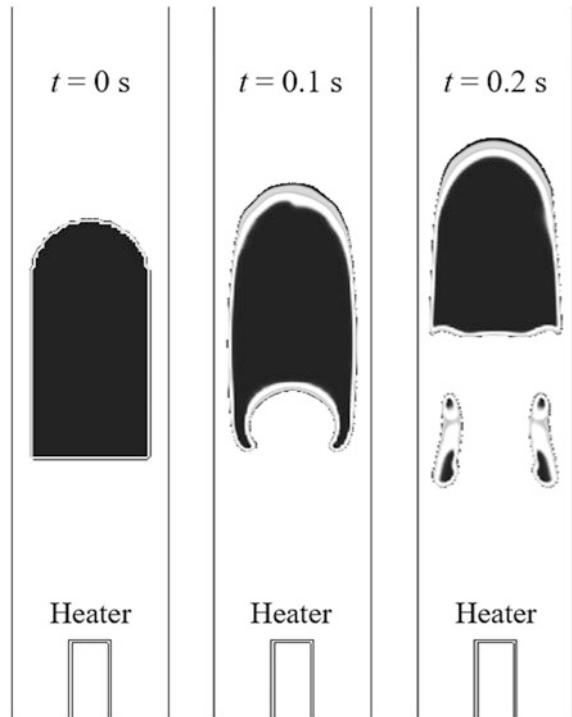
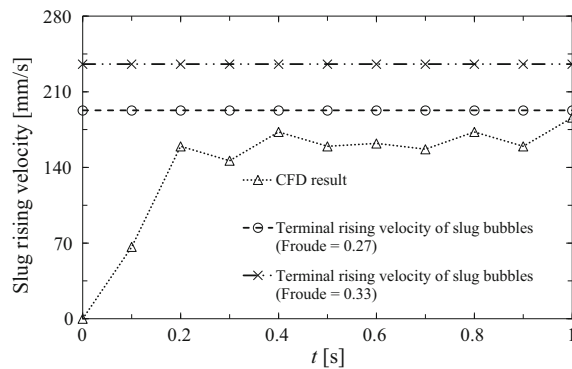


Fig. 7 Rising velocity of the vapor slug in saturated water (CFD result); published correlations shown for the slug-bubble Froude numbers 0.27 and 0.33



Case 3: Rising and Condensing Vapor Bubble

Approaching to the full problem of subcooled boiling, a simulation of a rising and condensing vapor bubble in subcooled liquid is executed. Similar to the previous cases, for brevity, the distribution of the volume fraction of the vapor phase is shown in Fig. 8, for three time instances: $t = 0, 0.1$ and 0.2 s.

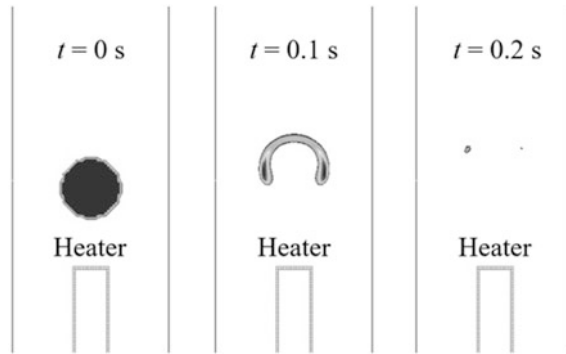


Fig. 8 Development of a vapor bubble rising and condensing in subcooled water (1.15 K degree of subcooling)

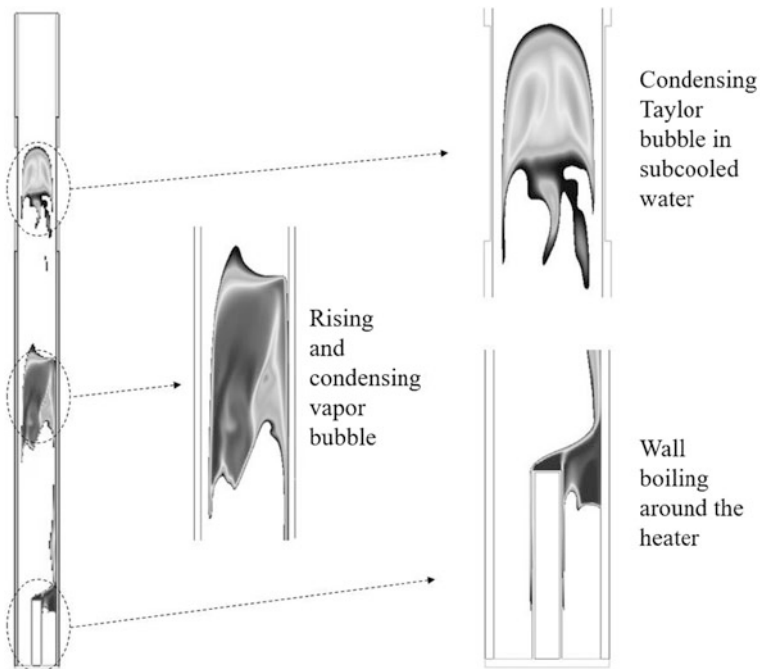


Fig. 9 An instantaneous CFD calculated result of the volume fraction of the vapor phase in the pipe

As shown in the figure, the numerical model would enable to generate and capture the development/condensation of a rising/condensing vapor bubble in subcooled water [3]. In the next stage, the wall boiling model is activated for the execution of the full problem.

4 Initial Application to Pool Boiling

The numerical model, which is tested by the three test cases shown above, is initially applied to the simulation of subcooled boiling in the pipe. In this case, the full model, which includes wall boiling model, is executed. Initial results are shown in Fig. 9 below for a time instance during the transient development of the flow in the pipe.

As shown in the figure, qualitatively, a conclusion would be derived that the numerical experimental setup would generate and capture the formation and development of the observed flow regime of subcooled pool boiling [3, 4]. The obtained results can be used for further studies to incorporate physical experimental measurements with numerical modelling of boiling flow.

5 Concluding Remarks

In order to setup a CFD model for the simulation of subcooled boiling, relevant theoretical background has been summarized and presented. Analogous to the development of a physical experimental model, suitable component models have been considered and included in the CFD model. Computational mesh refinement study has been performed. Evaluations of the model setup have been carried out. Test simulation of subcooled pool boiling has been demonstrated.

Based on the obtained results, the following concluding remarks have been derived:

- A CFD model of subcooled pool boiling has been setup.
- The model has been tested using three test cases. Fairly good results have been obtained.
- The simulation result of one flow regime of subcooled pool boiling has been demonstrated.
- In next studies, quantitative assessments of the simulation results of wall boiling and bubble condensation are required. Comparisons with experimentally measured data are necessary to further validate the model.
- As accurate modeling of the interfacial area concentration (IAC) plays a crucially important role in two-fluid model, IAC modeling is necessarily applied in next studies.
- Since boiling is one of the most complicated flow phenomena, most of the boiling correlations are empirical and valid only for a specific range of parameters, much research effort (both physical experiments and numerical simulations) is required in this field, e.g. to develop specifically required correlations, universal correlations of boiling phenomena etc.

Acknowledgements Financial support from the following scientific research project of Vietnam Academy of Science and Technology (VAST) to carry out this study is gratefully acknowledged: VAST01.04/17-18 project.

References

1. Ishii M, Hibiki T (2010) Thermo-fluid dynamics of two-phase flow. Springer Science & Business Media
2. Ghiaasiaan SM (2007) Two-phase flow, boiling, and condensation: in conventional and miniature systems. Cambridge University Press
3. Yeoh GH, Tu J (2009) Computational techniques for multiphase flows basics and applications. Elsevier
4. Yeoh GH, Tu J (2009) Modelling subcooled boiling flows. Nova Science Publishers, Inc
5. Krepper E, Končar B, Egorov Y (2007) CFD modelling of subcooled boiling—concept, validation and application to fuel assembly design. *Nucl Eng Des* 237(7):716–731
6. Warriar GR, Basu N, Dhir VK (2002) Interfacial heat transfer during subcooled flow boiling. *Int J Heat Mass Transf* 45(19):3947–3959
7. Nguyen TT, Tsuzuki N, Murakawa H, Duong NH, Kikura H (2016) Measurement of the condensation rate of vapor bubbles rising upward in subcooled water by using two ultrasonic frequencies. *Int J Heat Mass Transf* 99:159–169
8. Dykas S, Wróblewski W (2011) Single- and two-fluid models for steam condensing flow modeling. *Int J Multiph Flow* 37(9):1245–1253
9. Končar B, Krepper E, Egorov Y (2005) CFD modeling of subcooled flow boiling for nuclear engineering applications. In: International conference on nuclear energy for new Europe, pp 140.1–140.14
10. Kharangate CR, Mudawar I (2017) Review of computational studies on boiling and condensation. *Int J Heat Mass Transf* 108:1164–1196
11. Tu JY, Yeoh GH (2002) On numerical modelling of low-pressure subcooled boiling flows. *Int J Heat Mass Transf* 45(6):1197–1209
12. Kataoka I (2010) Development of research on interfacial area transport. *J Nucl Sci Technol* 47(1):1–19
13. Brooks CS, Ozar B, Hibiki T, Ishii M (2012) Two-group relative velocity in boiling two-phase flow. In: 20th International conference on nuclear engineering and the ASME 2012 power conference. American Society of Mechanical Engineers, pp 235–242
14. Kataoka I, Yoshida K, Naitoh M, Okada H, Morii T (2012) Transport of interfacial area concentration in two-phase flow. *Nuclear Reactors*. InTech
15. Talebi S, Abbasi F, Davilu H (2009) A 2D numerical simulation of sub-cooled flow boiling at low-pressure and low-flow rates. *Nucl Eng Des* 239(1):140–146
16. Li H, Vasquez SA, Punekar H, Muralikrishnan R (2011) Prediction of boiling and critical heat flux using an Eulerian multiphase boiling model. In: ASME 2011 International mechanical engineering congress and exposition. American Society of Mechanical Engineers, pp 463–476
17. Punekar H, Das S (2013) Numerical simulation of subcooled nucleate boiling in cooling jacket of IC engine (No. 2013-01-1651). SAE Technical Paper
18. Talaia MA (2007) Terminal velocity of a bubble rise in a liquid column. *World Acad Sci Eng Technol* 28:264–268
19. Clift R, Grace JR, Weber ME (1978) Bubbles, drops, and particles. Courier Corporation
20. Tomiyama A, Nakahara Y, Adachi Y, Hosokawa S (2003) Shapes and rising velocities of single bubbles rising through an inner subchannel. *J Nucl Sci Technol* 40(3):136–142
21. Bui DT (2001) Taylor bubble velocity measurements in two-phase air/water vertical flow. *Vietnam J Mech* 23(3):183–192
22. Lu X, Prosperetti A (2008) A numerical study of Taylor bubbles. *Ind Eng Chem Res* 48(1):242–252
23. Ambrose S (2015) The rise of Taylor bubbles in vertical pipes. PhD thesis, University of Nottingham

Optimization of Precision Die Design on High-Pressure Die Casting of AlSi_9Cu_3



T. A. Do and V. T. Tran

Abstract Precision high-pressure die casting for nonferrous casting applications is increasingly used in the foundries. This paper focuses on the following issues: filling simulation, defect analysis by computer-aided simulation, experiment with Taguchi analysis to select optimal parameters when design die for high-pressure die casting aluminum AlSi_9Cu_3 . After analysis, the optimal parameters are as follows: cross section area of gate 40 mm^2 , location of gate at type 2, gate velocity 50 m/s , and liquid alloy temperature $640 \text{ }^\circ\text{C}$. Based on the results of calculation parameters, we conducted design die by computer aided with the main objective is to optimize the die design parameters. The use of this integrated solution can shorten the cycle of die design and manufacture, and result in the production of high-quality die castings in the shortest time with the biggest profit.

Keywords Die design · Taguchi method · Die casting · Shrinkage porosity AlSi_9Cu_3 aluminum

1 Introduction

High-pressure die casting (HPDC) process is significantly used in the industry for its high productivity and less post-machining requirement. Due to light weight and good forming-ability, aluminum die casting plays an important role in the production of transportation and vehicle components. It has a much faster production rate in comparison with other methods and it is an economical and efficient method for producing components with low surface roughness and high dimensional accuracy. All major aluminum automotive components can be processed with this technology. The development of industrial die casting and requirements for higher

T. A. Do (✉) · V. T. Tran

Faculty of Mechanical Engineering, Hung Yen University of Technology and Education, Hung Yen, Vietnam

e-mail: giaotuan79@gmail.com

© Springer Nature Singapore Pte Ltd. 2018

H. Nguyen-Xuan et al. (eds.), *Proceedings of the International Conference on Advances in Computational Mechanics 2017*, Lecture Notes in Mechanical Engineering, https://doi.org/10.1007/978-981-10-7149-2_53

759

quality product, shorter development times and more complex geometry, the use of computer-aided simulation has become essential in industry.

The HPDC castings production process has many defects, such as: shrinkage porosity, misrun, cold-shut, blister, scab, hot-tear. Techniques such as cause-effect diagrams, design of experiments, casting simulation, fuzzy logic controller, genetic algorithms, and artificial neural networks are used by various researchers for analysis of casting defects. Dargusch et al. [1] used pressure sensor in the cavity to make a confident statement of aluminum that molten metal velocity increases and porosity development with high-pressure die casting. Verran et al. [2] used the design of experiments (DOE) to find out the best parameters in production and notice that: porosity low indices are related with low speeds from slow and fast shots and high upset pressures. Mousavi Anijdan et al. [3] used genetic algorithm (GA) methods to determine the optimum conditions leading to minimum porosity in aluminum alloy die casting. Tsoukalas [4, 5] used the design of experiments (DOE) and genetic algorithm (GA) methods to determine the optimum conditions leading to minimum porosity in aluminum alloy die castings. Syrcos [6] used Taguchi method to determine the optimum conditions leading to casting density in aluminum alloy die castings. Yue et al. [7] used CAD/CAE/CAM simulation and analysis with the purpose the quality of the die castings improved greatly in a shorter time. Yarlalagadda and Chiang [8] used the artificial neural network (ANN) methods to determine the optimum conditions in aluminum alloy die castings. Seo [9] used CAD/CAE simulation and analysis with purpose minimizing the porosities and hot spots for applying in die casting. However, most researchers were used to predict solidification and optimize aluminum alloy casting process parameters in the condition of production foundry factory. Little was published die design in die casting, gating, and die casting parameters. Approximately 90% of defects in die casting components are due to die design errors (Shehata [10]). Die design is a very difficult work, and the company often does not published because of economic competition. In order to obtain good die design, it requires extensive knowledge in mechanical engineering and experience in die castings foundry factory.

In this paper, the ProCAST[®] Software commercial is used for analysis casting defects and die filling simulation to enhance the quality and efficiency of die casting. The Taguchi method control with design of experiments will be developed to improve aluminum die casting quality and productivity in the cold chamber die casting method. After conducting a series of initial experiments in a controlled environment, significant factors for die casting processes are selected to find the optimal parameters to increase the aluminum die casting quality and efficiency. Based on the results from analysis by considering the influence of defects on quality castings, we conducted die design for die casting with optimal parameters. It is suggested to reduce casting defects, reduce time and money, increasing with better casting product quality and die design die casting efficiency.

2 Materials and Methods

2.1 Basic Design

Die casting of this study with the 3D solid model of automobile start motor casing part is shown in Fig. 1.

The 3D drawings of objects cast to represent the color with different meanings. Accordingly, the white light is the portion need to be machined or cut later. Depending on the material molding, casting method and mechanical processing methods after casting product finished that the designer will select the size, tolerances, and metal machining appropriate for requirements. This study using cast material is the aluminum alloy $AlSi_9Cu_3$ with chemical composition of the aluminum shown in Table 1.

Some of the very important properties of the material $AlSi_9Cu_3$ used in the experiments as fraction solid are shown in Fig. 2 and conductivity in Fig. 3.

The die with a specific gating system will perform differently on different die casting machines. Only by considering both the die and machine characteristics could optimal flow conditions be achieved. Therefore, $P-Q^2$ technique is employed to predict the best gate area, flow rate, filling time, and gate velocity. This will avoid excessive calculation and ensure that the gating system is designed properly. With the computer-aided design software, we design the simply filling system with die casting gate and runner. We design three location of gates with the basic shapes as Fig. 4.

Analysis software is used as ProCAST[®] commercial with finite element method (FEM) analysis for a casting process. The designer based on FEM simulation to visualize the metal flow in the die cavity, the temperature variation, the solidification progress, and the evolution of defects such as shrinkage porosity, cold-shut, hot-tear.

Fig. 1 Model 3D of object



Table 1 Composition of alloy $AlSi_9Cu_3$

Elements	Al	Si	Mg	Mn	Zn	Cu	Ni	Ti
%	Balance	9.0	0.3	0.6	1.2	3.0	0.5	0.2

Fig. 2 Fraction solid of $AlSi_9Cu_3$ material

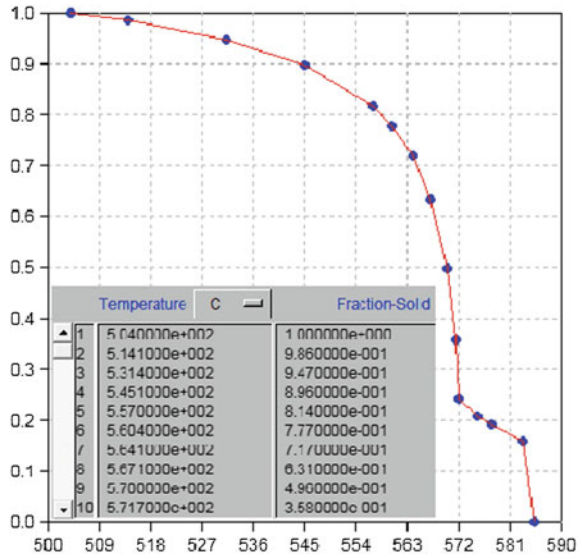
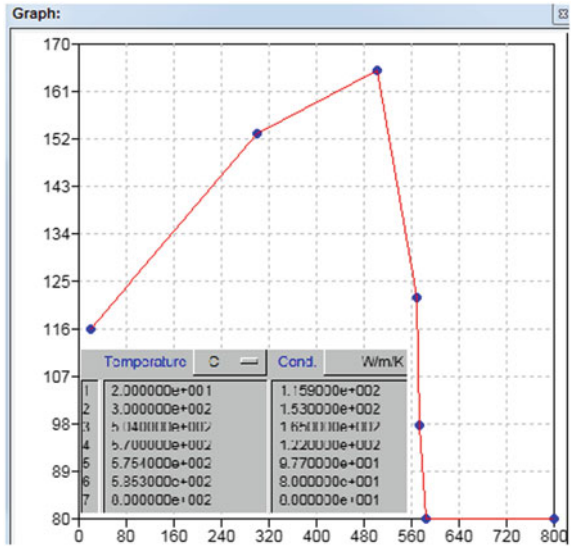


Fig. 3 Conductivity of $AlSi_9Cu_3$ material



2.2 Experiment and Analysis

The shrinkage porosity formation in pressure die casting is the result of a so much number of parameters. Figure 5 shows a cause and effect diagram that was constructed to identify the casting process parameters that may affect die casting porosity. In this case, liquid alloy temperature (holding furnace temperature),

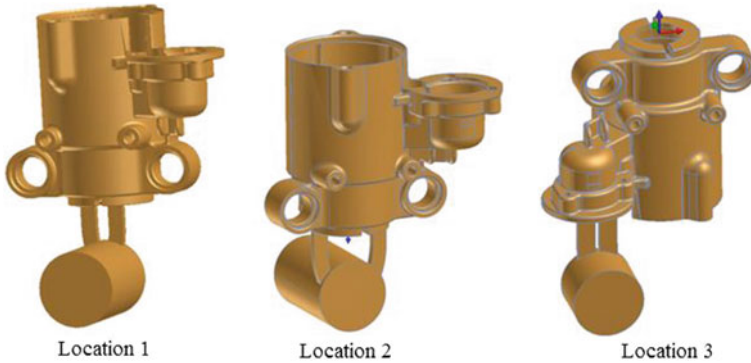


Fig. 4 Location of gates

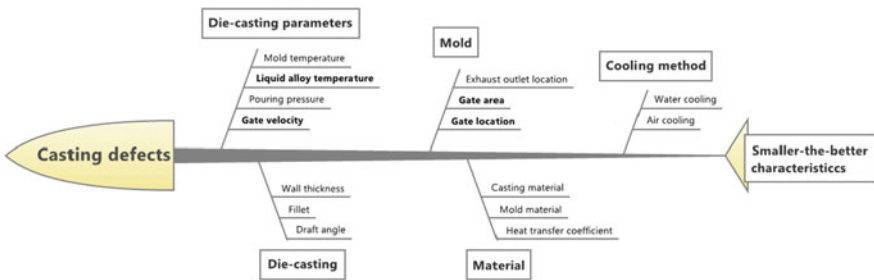


Fig. 5 Fish-bone diagram

speed of molten alloys of the gate (Gate velocity), cross section of the gate (Gate area), and location of the gate (Gate location) were selected as the most critical in the experimental design. The other parameters were kept constant in the entire experimentation. Gate velocity has an influence on mechanical properties of the casting and on the properties in the casting surface quality. High gate velocity produces higher mechanical properties and less porosity than lower gate velocity. New high-pressure casting machine capable of velocity generated at the gate up to 100 m/s. The die erosion started to increase already around 60 m/s, so that reason the higher gate velocity range from 60 m/s to 100 m/s rarely used in normal conditions (Shehata [10], Weishan et al. [11]). Based on technical parameters of high-pressure die casting machine SD-500CF from LIKW Enterprise Corp-Taiwan, we select the velocity of the liquid alloy in range: 30–50 m/s. This paper used cast material $AlSi_9Cu_3$ with the super-heated range (640–720)°C. The selected casting process parameters are given in Table 2.

Fishbone diagram [2, 4–7] of the configuration shown in Fig. 5, in which with the aim is minimum shrinkage porosity die casting defect, so that objective “smaller-is the-better” is selected.

Table 2 Factor levels

Factors		Levels					
A	Gate area (total cross section area) (mm ²)	1	70	2	55	3	40
B	Gate location	1	Position 1	2	Position 2	3	Position 3
C	Gate velocity (m/s)	1	50	2	40	3	30
D	Liquid alloy temperature (°C)	1	720	2	680	3	640

Table 3 Parameters of nine experiments were performed

Trials	Gate area (mm ²)	Gate location (position)	Gate velocity (m/s)	Liquid alloy temperature (°C)
	A	B	C	D
1	70	p1	50	720
2	70	p2	40	680
3	70	p3	30	640
4	55	p1	40	640
5	55	p2	30	720
6	55	p3	50	680
7	40	p1	30	680
8	40	p2	50	640
9	40	p3	40	720

Table 4 Experimental data

	Shrinkage Porosity (%)					MSD	S/N
	1	2	3	4	5		
1	1.604	1.677	1.597	1.589	1.588	2.596444	-4.143789
2	1.646	1.645	1.591	1.590	1.534	2.565576	-4.091848
3	1.685	1.599	1.599	1.591	1.584	2.598633	-4.147449
4	1.616	1.588	1.573	1.570	1.566	2.504957	-3.988003
5	1.580	1.559	1.558	1.566	1.545	2.438725	-3.871629
6	1.567	1.563	1.560	1.553	1.556	2.433001	-3.861422
7	1.675	1.661	1.645	1.641	1.592	2.699583	-4.312967
8	1.437	1.467	1.468	1.457	1.459	2.124722	-3.273022
9	1.590	1.567	1.564	1.566	1.566	2.466379	-3.921479
						Average	-3.956845

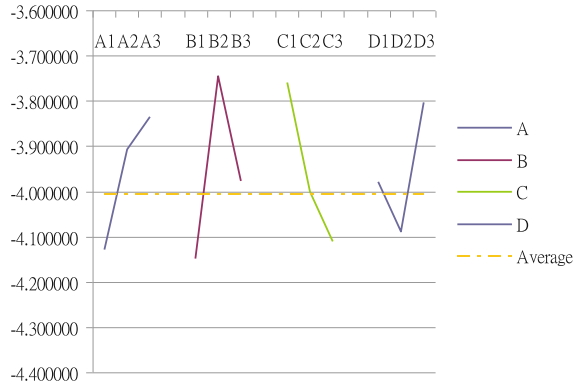
According to cause and effect diagram, we have factor level table shown in Table 2, so that nine experiments parameters are shown in Table 3.

The results of the nine shrinkage porosity experiments were analyzed and the results shown in Table 4.

Table 5 S/N response

	A	B	C	D
1	-4.127696	-4.148253	-3.759411	-3.978966
2	-3.907018	-3.745500	-4.000443	-4.088746
3	-3.835823	-3.976784	-4.110682	-3.802825

Fig. 6 S/N response graphs



Measure of interactions between these factors with regard to robustness is signal-to-noise (S/N) ratio. S/N characteristics formulated for three different categories are as follows: the bigger the better, the smaller the better, and the nominal the best. This paper focused on studying the effects of four input parameters (A, B, C, and D) to defect shrinkage porosity in the process of casting, so the criteria “the smaller the better” is selected.

The smaller the better:

$$S/N = -10 \log \left(\frac{1}{n} \sum_{i=1}^n y_i^2 \right) \tag{1}$$

where:

- n: number of measurement.
- y_i: value of shrinkage porosity.

The measurement results calculated by formula (1) after sorting out the S/N response as Table 5 and S/N response graphs in Fig. 6. We found the best combination in this study for aluminum die casting shrinkage porosity defects are A₃B₂C₁D₃ corresponding to the gate area of 40 mm², group 2 of the gate location, the speed of the liquid metal at the gate is 50 m/s, the temperature of molten aluminum 640 °C.

The contribution rate of each factor results is shown in Table 6.

Table 6 The ANOVA table

Factors	S	F (Degrees of freedom)	V (Variation)	S'	Contribution rate (%)	Contribution
A	0.277270	2	0.138635	0.277268	37.285	2
B	0.372506	2	0.186253	0.372504	50.091	1
C	0.034864	2	0.017432	0.034862	4.688	4
D	0.059011	2	0.029505	0.059009	7.935	3
e (Error)	0.000001	1	0.000001		0.00108	5
Total		9			100%	

2.3 Computer-Aided Die Design

High-pressure die casting (HPDC) with the gating system consists of a biscuit or a sprue, runners system, a gate, overflows, and vents. There are two basic gate types: tangential and fan-gate (Gating manual, NADCA, USA. 2006. p. 56 [12], Wu et al. [13], Hu et al. [14]). Both gates are usually designed with converging cross-sectional area. The selection between the gate types depends on the part requirements. Fan-gate is the simplest in structure and easier to machine. Tangential gates are more difficult to design and machine, but the design is flexible and easy to adapt to different technical requirements. The designer should ensure that the gate and runner system to maintain smooth, continuous flow profiles and by designing the casting so that no backflow occurs or two lines overlap. Based on the technical side-core and molding direction, we design two types of gate systems with components of a biscuit (diameter: 70 mm), a runner, a gate, and overflows. Two types runner is designed as Figs. 7 and 8 with a cross section of gate: 40 mm².

The results of the optimum parameters will be installed in ProCAST software with two cases (full inlet and half inlet):

- gate area of 40 mm²
- gate location: group 2
- velocity of the molten metal at the gate: 50 m/s
- the temperature of molten metal: 640 °C
- the die temperature: 180 °C

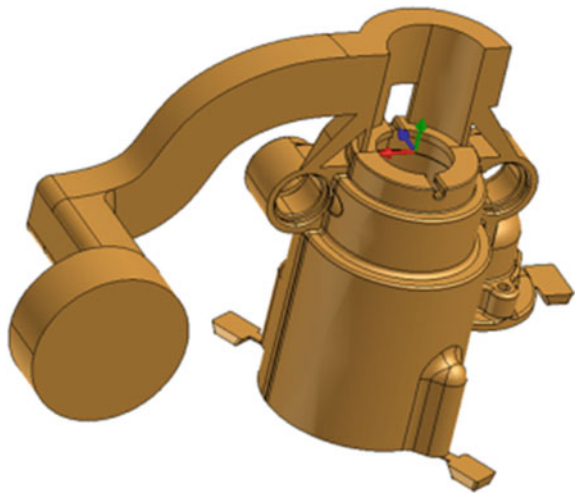
With full inlet filling of the liquid metal flow in the die cavity is good. In case of half inlet, not fill in all the volume of die cavity, high pressure increased. The shortage metal occurs as Fig. 9 mean that having a disability and the option half inlet design cannot be used for further study.

Shrinkage porosity analysis as in Fig. 10 with full inlet case shows that need additional overflows in some locations important to reduce this phenomenon shrinkage porosity. Figure 11 shows solid 3D of dies with full gating system.

Fig. 7 Die casting with full inlet



Fig. 8 Die casting with half inlet



The simulation results with the parameters setting on the ProCAST are calculated in the previous steps. The result of test is the liquid metal fill in full of die cavity. Figure 12 shows that the casting no defects and shrinkage porosity acceptable.

Fig. 9 Shortage of the casting with half inlet

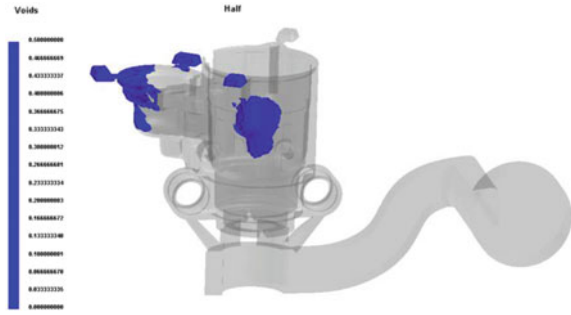


Fig. 10 Shrinkage porosity of the casting with full inlet

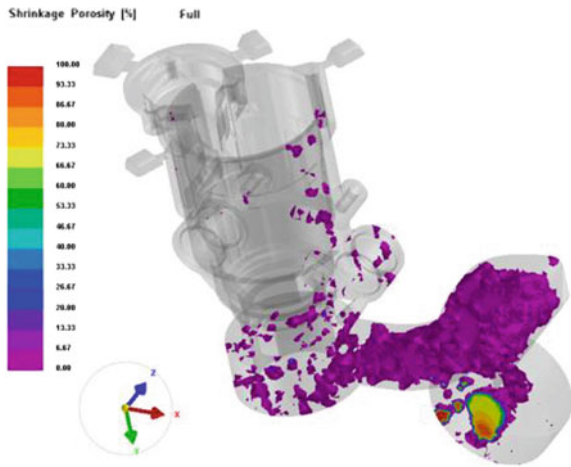


Fig. 11 3D solid model of die casting dies

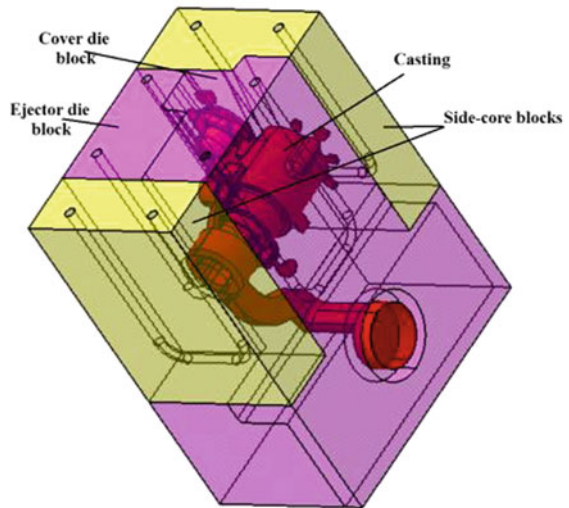


Fig. 12 Shrinkage porosity of castings

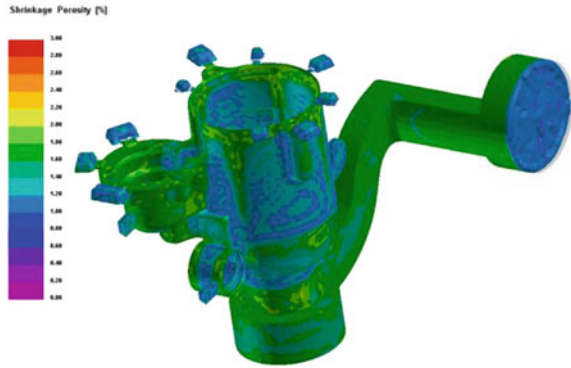


Fig. 13 Casting in SD-500CF die casting machine



3 Results and Discussion

The die for this study is the result of collaboration between the LIKW Enterprise Corp, Taiwan and Department of Mechanical Engineering—Hung Yen University of Technology and Education.

The entire die will be installed on the SD-500 CF casting machine as Fig. 13 with the parameters setting on the machine are calculated in the previous steps.

The product after casting to the naked eye without disabilities is shown in Fig. 14. X-ray inspection with ERESKO 160 MF4-R for castings with parameters: 2% sensitivity, 30 s time exposure in the critical sections of castings. Results showed no defects shrinkage porosity and no cracks inside, good quality castings, as shown in Fig. 15.

The results of simulation and experiment indicate that the liquid metal in the die filling full, no cracks inside, and shrinkage porosity acceptable. That means the die is designed and manufactured optimization in accordance with the conditions of the foundry factory production.

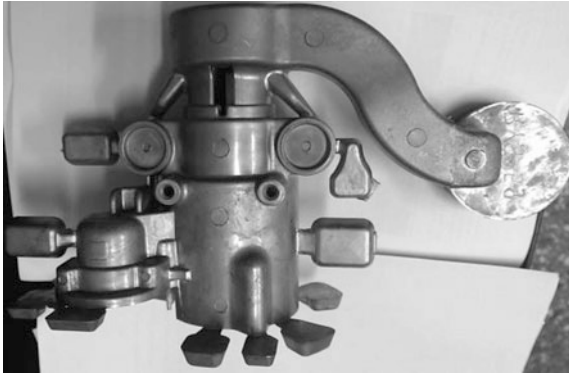


Fig. 14 Product after casting

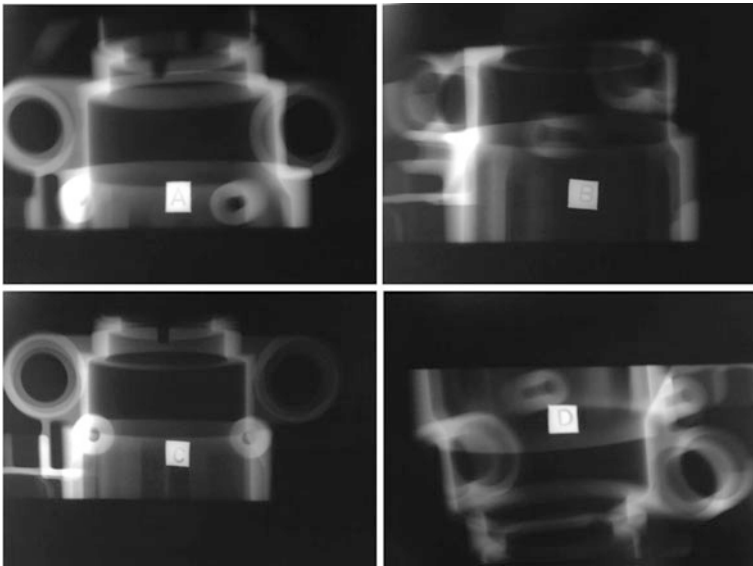


Fig. 15 X-ray film testing of samples casting

4 Conclusions

The design experiments by Taguchi method and computer-aided casting simulation technique for analysis of the optimal condition is a good combination in die design. The results of the optimum parameters for design die are as follows: the cross section of gate 40 mm^2 , the gate location at group two, the velocity of the molten metal at the gate at 50 m/s , the temperature of liquid aluminum at $640 \text{ }^\circ\text{C}$. For analysis of defect such as shrinkage porosity, computer-aided casting simulation

technique is the most efficient and accurate method. The quality of the casting product can be efficiently improved by computer-assisted casting simulation technique in the shortest possible time and without the conventional trial and error on foundry factory. This in turn implies that the resources (materials, saving time, and money) required for the experiments are also minimized.

References

1. Dargusch MS, Dour G, Schauer N, Dinnis CM, Savage G (2006) The influence of pressure during solidification of high pressure die cast aluminum telecommunications components. *J Mater Process Technol* 180, 37–43
2. Verran GO, Mendes RPK, Dalla Valentina LVO (2008) DOE applied to optimization of aluminum alloy die castings. *J Mater Process Technol* 200, 120–125
3. Mousavi Anijdan SH, Bahrami A, Madaah Hoseini HR, Shafyei A (2006) Using genetic algorithm and artificial neural network analyses to design an Al–Si casting alloy of minimum porosity. *Mater Des* 27, 605–609
4. Tsoukalas VD (2004) A study of porosity formation in pressure die casting using the Taguchi approach. *J Eng Manuf* 218, 77–86
5. Tsoukalas VD (2008) Optimization of porosity formation in AlSi₉Cu₃ pressure die castings using genetic algorithm analysis. *Mater Des* 29, 2027–2033
6. Syrcos GP (2003) Die casting process optimization using Taguchi methods. *J Mater Process Technol* 135, 68–74
7. Yue S, Wang G, Yin F, Wang Y, Yang J (2003) Application of an integrated CAD/CAE/CAM system for die casting dies. *J Mater Process Technol* 139, 465–468
8. Yarlagadda PKDV, Chiang ECW (1999) A neural network system for the prediction of process parameters in pressure die casting. *J Mater Process Technol* 89–90, 583–590
9. Seo PK, Kim HC, Kang CG (2007) Numerical integration design process to development of suspension parts by semi-solid die casting process. *J Mater Process Technol* 183, 18–32
10. Shehata F, Abd-Elhamid M (2003) Computer aided foundry die-design. *Mater Des* 24, 577–583
11. Weishan Z, Shoumei X, Baicheng LIU (1997) Study on a CAD/CAE system of die casting. *J Mater Process Technol* 63, 707–711
12. Gating Manual (2006) NADCA, USA, p. 56
13. Wu SH, Fuh JYH, Lee KS (2007) Semi-automated parametric design of gating systems for die casting die. *Comput Ind Eng* 53, 222–232
14. Hu BH, Tong KK, Niu XP, Pinwill I (2000) Design and optimization of runner and gating systems for the die casting of thin-walled magnesium telecommunication parts through numerical simulation. *J Mater Process Technol* 105, 128–113

Flow and Performance Analysis of a Valveless Micropump



P. K. Das and A. B. M. T. Hasan

Abstract The flow behaviour and performance parameters of a diffuser-nozzle element of a valveless micropump have been investigated for different geometric and flow properties. When a fluctuating pressure is imposed on the inlet boundary of a diffuser-nozzle element, there is a net flow in diffuser direction due to the dynamic effect. The variation of this net flow along with rectification capacity, and diffuser efficiency has been investigated for different inlet-outlet length combination and frequencies of driving pressure. Flow behaviour and recirculation region have been studied. Pressure and velocity have been analyzed for quantitative analysis and for validation with results found in literature. 2-D geometry has been used in the present study. 3-D geometry has been modeled to justify the results obtained from 2-D analysis. Different inlet-outlet length combinations ranging from 0.2 to 1.0 mm has been investigated. Five different pressure frequencies in the range from 5 to 50 kHz have been considered to identify their effects on the performance of diffuser-nozzle element. The net flow and performance of the nozzle-diffuser element are found to be less dependent on outlet length while more dependency was found on inlet length. Further, the performance becomes weaker with the increase of frequency of inlet driving pressure pulsation.

Keywords Diffuser-nozzle element • Micropump • Pressure frequency
Dynamic effect • Recirculation

1 Introduction

According to the convention for microelectromechanical systems (MEMS), micropump is a specialized pump having a length scale in the order of 100 μm or smaller which meets the demand of both small scale flow (usually less than 15 $\mu\text{L}/\text{min}$)

P. K. Das • A. B. M. T. Hasan (✉)

Department of Mechanical Engineering, Bangladesh University of Engineering and Technology, Dhaka, Bangladesh
e-mail: toufiquehasan@me.buet.ac.bd

© Springer Nature Singapore Pte Ltd. 2018

H. Nguyen-Xuan et al. (eds.), *Proceedings of the International Conference on Advances in Computational Mechanics 2017*, Lecture Notes in Mechanical Engineering, https://doi.org/10.1007/978-981-10-7149-2_54

773

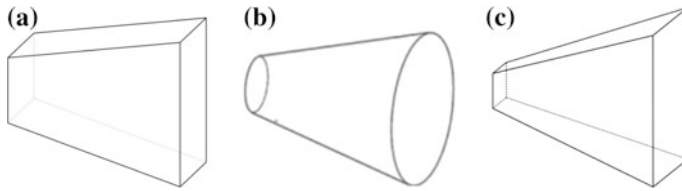


Fig. 1 Diffuser-nozzle element **a** planer, **b** conical, **c** pyramidal

and high pressure fluid transport. In mechanical displacement micropumps, a moving boundary forces the fluid along by volume changes. Some of the examples are piezoelectric, thermo-pneumatic, electromagnetic, and so on. In the recent past, different types of micropumps are described [1–5]. Micropumps having nozzle-diffuser elements as flow rectification devices are commonly known as valveless micropumps. The name “valveless” is due to the absence of conventional dynamic valves with moving parts. The general types of nozzle-diffuser elements are shown in Fig. 1. If a diffuser-nozzle element is subjected to a pulsatile pressure, there will be a net flow in the diffuser direction after each pressure cycle although the time dependent pressure differences through the element remain the same at each half cycle. This phenomenon is known as the dynamic effect. Because of the lower flow resistance through the diffuser direction than that in the nozzle direction, larger flow occurs in the diffuser direction in one half cycle. In the inlet portion of the micropump, the minimum cross-sectional area of the diffuser nozzle element is mounted with the inlet chamber while the maximum cross-sectional area is mounted with the pump chamber. In the outlet portion another element is mounted in opposite way. Thus a net flow can be achieved from inlet to outlet.

The absence of moving parts and the simplicity in geometric construction of a valveless micropump make them suitable for electronic cooling, bioMEMS and other small scale technical applications. Effects of geometry of diffuser and inlet/outlet port, actuation frequency and amplitude of actuation pressure on the performance of conical diffuser-nozzle element were investigated by Wang et al. [6]. Results showed the best rectification performance can be obtained with diffuser diverging angle of 10° , and a slenderness ratio of 7.5. Further, it was noted that small pump chamber and inlet/outlet port deteriorate the pump performance. Nabavi and Mongeau [7] studied the effects of various geometric and flow parameters on the performance of diffuser-nozzle element. The performance of the pump was found to be strongly dependent on diffuser half angle, pressure amplitude and frequency. Several other researches [8, 9] showed the suitability of the diffuser-nozzle element for flow rectification instead of dynamic valves (check valves, flap valves, etc.). Flow separation was also observed at different frequencies. However, performance of the diffuser-nozzle element at very high frequencies

and effects of different inlet-outlet length combinations are not clearly understood till now. In the present study, an attempt is taken to address these fluid mechanical and geometric issues through computational approach.

2 Performance Parameters of Diffuser-Nozzle Element

The performance parameters of a diffuser-nozzle element, which determine the suitability of the element in flow rectification purpose, are: net velocity, net volume flow rate, rectification capability and diffuser efficiency. Net velocity is the time-averaged net velocity measured at inlet of the diffuser section of the element during the positive and negative pressure cycle. Accordingly, net flow rate can be calculated.

Rectification capability is the measure of the capability of a nozzle-diffuser element to direct the flow through the element in a definite direction. It is defined as the net volume of the fluid transported from the inlet to outlet divided by the swept volume and is expressed as,

$$\xi = \frac{\Phi^+ - \Phi^-}{\Phi^+ + \Phi^-} \quad (1)$$

where Φ^+ and Φ^- are the total volume flow in the diffuser and nozzle directions, respectively. To produce an effective flow rectification, ξ must be positive. Generally, it is less than 100%. High rectification capability indicates higher amount of flow towards diffuser direction than the nozzle direction. Diffuser efficiency (η) is the most important performance parameter indicating the net flow rate through diffuser-nozzle element which can be defined as,

$$\eta = \frac{\varepsilon_n}{\varepsilon_d} \quad (2)$$

where ε_n and ε_d are the measure of the flow resistance or pressure loss coefficients of the nozzle and diffuser directions, respectively. These parameters are defined as,

$$\varepsilon_n = \frac{2\Delta p_n}{\rho u_n^2} \quad (3)$$

$$\text{and } \varepsilon_d = \frac{2\Delta p_d}{\rho u_d^2} \quad (4)$$

where Δp_n and Δp_d are time averaged total pressure drops in the narrowest zone downstream of the inlet and the broadest zone upstream of the outlet of the element

during negative and positive pressure cycle, respectively. u_n and u_d are the corresponding time averaged velocities. To produce a net flow, η should be greater than one.

3 Numerical Procedure

A CFD package ANSYS FLUENT [10] is used for present computation which discretizes the governing equations using finite volume method. Pressure based solver has been used. Fluid material is considered as water with density, $\rho = 998.2 \text{ kg/m}^3$ and viscosity, $\mu = 0.001003 \text{ kg/m-s}$. The flow is assumed as laminar and incompressible. At the inlet, pressure is imposed which is varied as sinusoidal profile in the form of $P_0 \sin(2\pi ft)$, where P_0 is the peak pressure amplitude and f is the frequency of pulsation. At the outlet, 0 Pa gauge pressure is assigned. Walls are considered as no-slip and midplane symmetry is assumed in the present problem as in Fig. 2. The governing fluid mechanical equations for the present problem are:

$$\frac{\partial u}{\partial x} + \frac{\partial v}{\partial y} = 0 \tag{5}$$

$$\frac{\partial u}{\partial t} + u \frac{\partial u}{\partial x} + v \frac{\partial u}{\partial y} + \frac{1}{\rho} \frac{\partial p}{\partial x} = \nu \left(\frac{\partial^2 u}{\partial x^2} + \frac{\partial^2 u}{\partial y^2} \right) \tag{6}$$

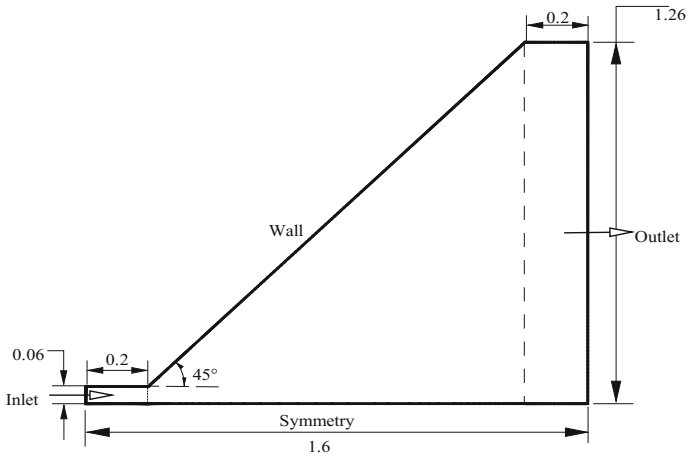


Fig. 2 2-D geometry of the nozzle-diffuser element (dimensions are in mm)

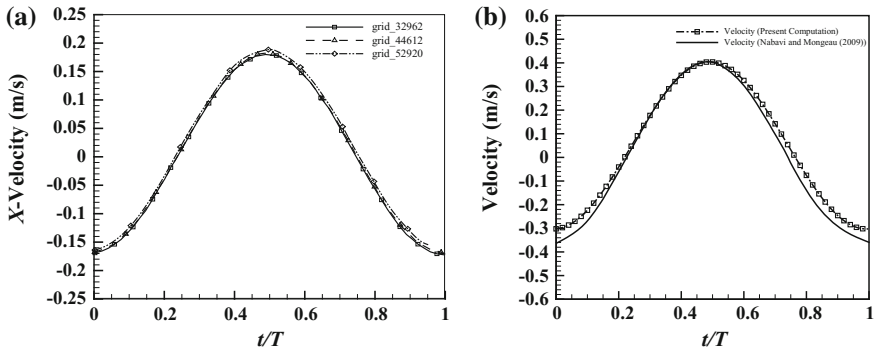


Fig. 3 **a** X-velocity over one period of oscillation for different grid numbers; **b** Comparison of inlet velocity with reference data

$$\frac{\partial v}{\partial t} + u \frac{\partial v}{\partial x} + v \frac{\partial v}{\partial y} + \frac{1}{\rho} \frac{\partial p}{\partial y} = \nu \left(\frac{\partial^2 v}{\partial x^2} + \frac{\partial^2 v}{\partial y^2} \right) \tag{7}$$

where (u, v) are the velocity components and ν is the kinematic viscosity of the fluid. A pressure-implicit with splitting of operators (PISO) has been used as the pressure-velocity coupling scheme. Pressure has been discretized with a pressure-based segregated solver only (PRESTO!) scheme. Second order upwind momentum discretization and second order implicit transient formulation has been considered.

Inlet velocity is evaluated for different grid sizes to determine the grid independent solution. It is found that the transient behaviour of velocities are almost the same for 30,000–50,000 number of grids as shown in Fig. 3a. In the present study, computational validation is done by comparing inlet velocity for 10 kPa peak pressure at 10 kHz frequency, 0.2 mm inlet and 0.2 mm outlet length with the reference data [6]. The results have been found in good agreement with the reference results as shown in Fig. 3b. From the inlet y-velocity (Fig. 4a), it is found that the values of y-component of velocity are in the range of 10^{-3} m/s meaning that it has almost no contribution to the resultant velocity for the calculation of performance parameters. Further, the use of two-dimensional approach has been justified based on another 3-D computation. Figure 4b shows that the inlet x-velocity is remained the same both in 2-D and 3-D computation. Further, z-velocity is found to be very small as shown in Fig. 4c. Above findings confirmed the accuracy of the 2-D approach which is adopted in the present study.

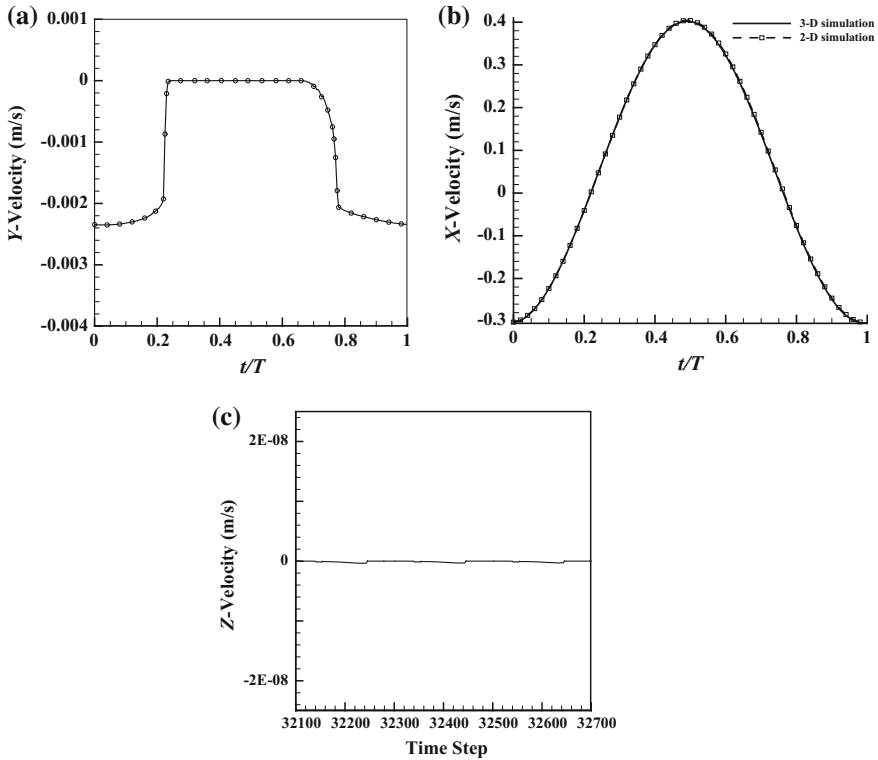


Fig. 4 **a** Inlet Y-velocity over one period of oscillation; **b** Comparison of inlet velocity for 3-D and 2-D simulation; **c** Inlet Z-velocity over time steps for 3-D simulation

4 Results and Discussion

4.1 Stream Function Contour

Stream function contours for different pressure phase angles (α) at 10 kPa peak pressure with 10 kHz frequency are shown in Fig. 5. Flow separation appears near the peak pressure in both positive and negative cycle. This flow separation is the result of using large diffuser half angle and the dynamic effect of a nozzle-diffuser element. Due to this flow separation and associated recirculation zone, there is a significant energy loss in the peak pressure (change in velocity direction) region. During all other phases of pressure, continuous contours are found. From the stream function contours for positive and negative pressure cycle, it is found that, flow separation and the associated recirculation last for a longer period ($\alpha = 260^\circ$ – 295°) in peak pressure region of negative pressure cycle when velocity initiates in

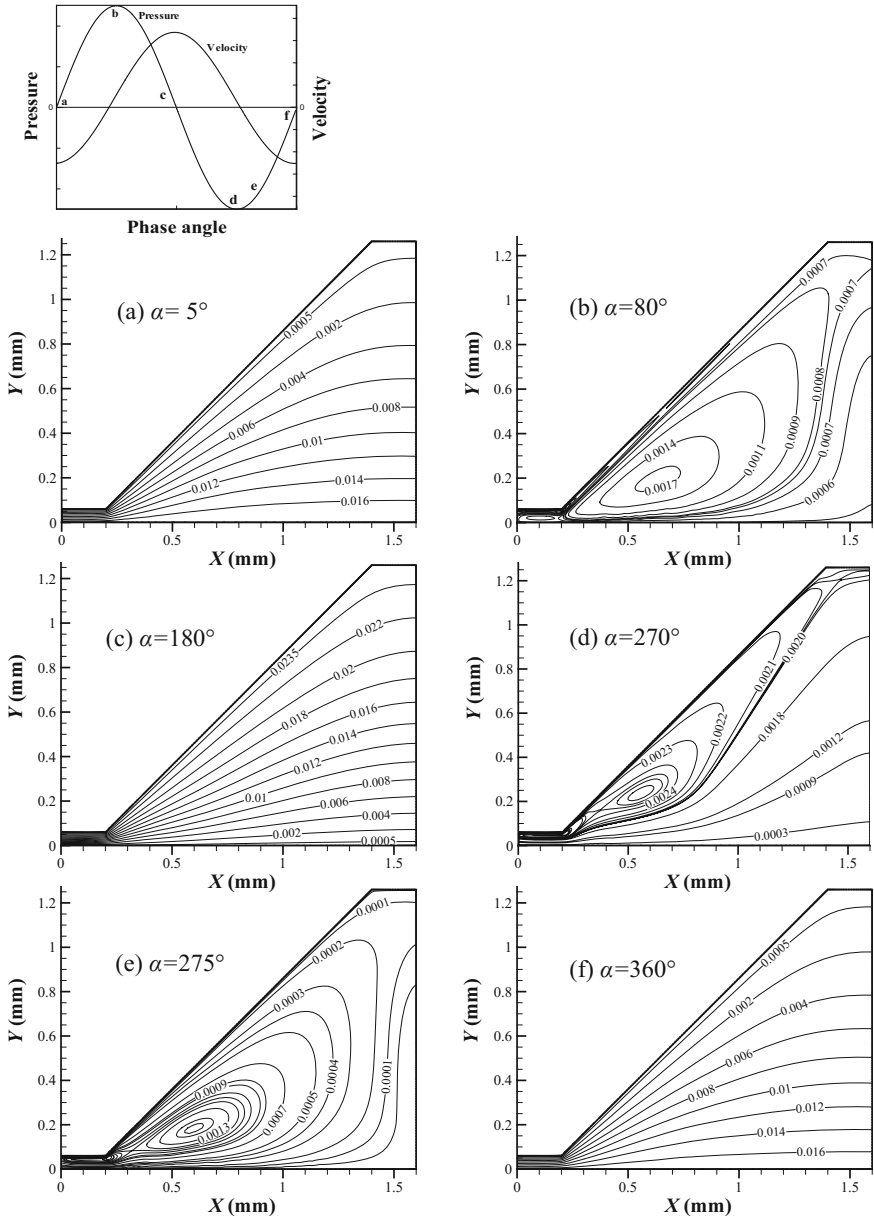


Fig. 5 Stream function (kg/s) contour for pressure phase angle, α ; **a** $\alpha = 5^\circ$, **b** $\alpha = 80^\circ$, **c** $\alpha = 180^\circ$, **d** $\alpha = 270^\circ$, **e** $\alpha = 275^\circ$, **f** $\alpha = 360^\circ$

negative nozzle direction than in peak pressure region of positive pressure cycle ($\alpha = 68^\circ\text{--}90^\circ$) when velocity initiates in positive diffuser direction. There is a stronger retardation to increase the velocity in negative direction than in positive direction. This influences to rectify the flow more in positive diffuser direction than in nozzle direction.

4.2 Effects of Inlet and Outlet Length on Performance Parameters

For a constant peak pressure value of 10 kPa and frequency of 10 kHz, three different inlet lengths of 0.2, 0.3 and 0.6 mm and three different outlet lengths of 0.2, 0.3, and 1.0 mm are used in case of planar geometry. From Table 1, it is observed that, net velocity, net volume flow, rectification capability, and diffuser efficiency are more dependent on inlet length than outlet length. Maximum performance is found for 0.2–0.3 mm inlet-outlet length combination. In case of axisymmetric geometry, net velocity is found almost the same as in case of planar geometry for the same 0.2–0.2 mm inlet-outlet length combination. Rectification capability and diffuser efficiency are reduced in axisymmetric model indicating more backflow towards nozzle direction.

4.3 Effects of Pressure Frequency on Performance Parameters

Effects of pressure frequency is observed in case of planer geometry. For a peak pressure, $P_0 = 10$ kPa, it is found that, diffuser-nozzle element becomes ineffective in rectifying flow towards diffuser direction at high frequencies (Table 2). All the

Table 1 Comparison of performance parameters for different inlet-outlet length combination

Inlet and outlet length	Planar					Axisymmetric
	0.6 and 1.0 mm	0.3 and 0.3 mm	0.3 and 0.2 mm	0.2 and 0.3 mm	0.2 and 0.2 mm	0.2 and 0.2 mm
Net velocity (mm/min)	477	1760	1848	3165	3156	3252
Net volume flow rate (mL/min)	0.0572	0.2112	0.2208	0.3798	0.3786	0.0368
Rectification capability, $\xi = \frac{\Phi^+ - \Phi^-}{\Phi^+ + \Phi^-}$	6.33%	15.4%	16%	22.7%	22.34%	15.3%
Diffuser efficiency, $\eta = \frac{\epsilon_n}{\epsilon_d}$	1.144	1.462	1.437	1.753	1.726	1.6

Table 2 Comparison of performance parameters for different pressure frequency

Driving frequency (kHz)	5	10	20	30	50
Net velocity (mm/min)	8922	3156	1336	423	252
Net volume flow rate (mL/min)	1.07065	0.3786	0.1603	0.05076	0.03024
Rectification capability, $\xi = \frac{\phi^+ - \phi^-}{\phi^+ + \phi^-}$	32.01%	22.34%	19.33%	10.02%	9.2%
Diffuser efficiency, $\eta = \frac{\epsilon_n}{\epsilon_d}$	2.149	1.726	1.62	1.2731	1.279

performance parameters including net velocity, net volume flow, rectification capability, and diffuser efficiency are observed to decrease with increasing frequency. Higher the frequency, higher is the backflow towards the nozzle direction lowering the flow rectification objective of diffuser-nozzle element. At a very high pressure frequency range (greater than 50 kHz), the performance of diffuser-nozzle element becomes insensitive to frequency.

5 Conclusions

In the present study, a numerical computation is performed to investigate the performance of a diffuser-nozzle element of a valveless micropump. Pressure pulsation has been imposed at the inlet of the element. Following conclusions can be drawn:

- In the flow field of the diffuser-nozzle element, flow separation appears near the peak pressure phase both in positive and negative pressure cycle. Flow separation and the associated recirculation exist for a longer period in negative pressure cycle than in positive pressure cycle. This indicates stronger retardation to increase the velocity in negative direction than in positive direction. Accordingly, a net flow is achieved in the positive diffuser direction.
- For planar geometry, net velocity, net volume flow, rectification capability, and diffuser efficiency are strongly dependent on inlet length than outlet length. Maximum performance is found for 0.2–0.3 mm inlet-outlet length combination for the cases studied in the present investigation. In case of axisymmetric geometry, there was no effect of geometric size on the net velocity. However, rectification capability and diffuser efficiency are reduced in axisymmetric model.
- All the performance parameters are observed to decrease with frequency. The planar diffuser-nozzle element becomes inefficient in rectifying the flow towards the diffuser direction at high frequencies.

Acknowledgements The present work has been carried out with computational resource support from Higher Education Quality Enhancement Project (HEQEP), AIF (2nd Round)-Sub-Project CP 2099, UGC, MoE, Government of Bangladesh (Contract no. 28/2012).

References

1. Nisar A, Afzulpurkar N, Mahaisavariya B, Tuantranont A (2008) MEMS-based micropumps in drug delivery and biomedical applications. *Sens Actuator B: Chem* 130:917–942
2. Woias P (2005) Micropumps—past, progress and future prospects. *Sens Actuators B: Chem* 105(1):28–38
3. Amirouche F, Zhou Y, Johnson T (2009) Current micropump technologies and their biomedical applications. *Microsyst Technol* 15(5):647–666
4. Au AK, Lai H, Utela BR, Folch A (2011) Microvalves and micropumps for BioMEMS. *Micromachines* 2(4):179–220
5. Yokota S (2014) A review on micropumps from the viewpoint of volumetric power density. *Mech Eng Rev* 1(2):DSM0014–DSM0014
6. Wang Y, Lin S, Jang D (2010) Unsteady analysis of the flow rectification performance of conical microdiffuser valves for valveless micropump application. *J Mech* 26(3)
7. Nabavi M, Mongeau L (2009) Numerical analysis of high frequency pulsating flows through a diffuser-nozzle element in valveless acoustic micropumps. *Microfluid Nanofluid* 7(5):669–681
8. Lee J, Jang DJ, Sung HJ (2012) Direct numerical simulations of turbulent flow in a conical diffuser. *J Turbul* 13(30)
9. Wang SS, Huang XY, Yang C (2009) Valveless micropump with acoustically featured pumping chamber. *Microfluid Nanofluid* 8(4):549–555
10. ANSYS FLUENT INC (2014) Fluent 14.5. www.ansys.com

Aeroelastic Analysis on Wing Structure Using Immersed Boundary Method



D. T. K. Hoang, S. V. Pham, K. N. Tran, C. D. Nguyen
and K. P. Nguyen

Abstract Flutter of airplane's wing is a critical issue determining reliability of aircraft. Flutter phenomenon is the result of fluid–structure interaction and is usually involved with complicated phenomena such as shock wave–boundary layer interaction, flow separation, and nonlinear limited cycle oscillation. Accurate prediction of flutter is very challenging due to perplexing physical phenomena and requires large amount of computation. In this paper, a developed code based on immersed boundary method (IBM) was realized to predict aeroelastic response and characteristic parameters of the wing structure. There were two rectangular and two trapezoid 3D-shapes of wing; each 3D-shape of wing had NACA65A004 and supercritical airfoil, respectively. Results from IBM method were first analyzed to carry out behaviors of flow on and around airplane wings and then were compared with experimental results at low speed.

Keywords Aeroelasticity · Flutter · FSI · IBM

1 Introduction

Aeroelasticity is a science to study the interaction between aerodynamic force, elastic force, and inertial force. Flutter which is one of the most dangerous aeroelastic phenomena is defined as the dynamic instability of an elastic body in an airstream. Reason is unsteady aerodynamic forces generated from elastic deformations of the structure. It can lead to a disastrous structural failure. Therefore, flutter problem should be calculated in the early phase of the air-vehicle structural design.

D. T. K. Hoang (✉) · S. V. Pham · K. N. Tran · K. P. Nguyen
Hanoi University of Science and Technology, Hanoi, Vietnam
e-mail: dung.hoangthikim@hust.edu.vn; dunghtk.dase@gmail.com

C. D. Nguyen
Vietnam Aerospace Association, Hanoi, Vietnam
e-mail: cuongnd45@gmail.com

Actually, these aeroelastic solution procedures solved two-way fluid–structure interaction (FSI) that used strongly coupled algorithms between Computational Fluid Dynamics and Computational Structural Dynamics [1–4].

Immersed boundary method carried out fluid–structure interaction by solving Navier–Stokes equations for flow momentum in couple with Newton equation for structure movement under the effect of friction force exerting on structure surface. Due to change of structure position in time, computational mesh needed to be re-calculation in each time step. To overcome this obstacle, Pham et al. [5] invoked both immersed boundary and finite volume methods in solving the interaction between fluid flow and moving structure.

The aim of this paper was to estimate numerical and experimental results on wing structure at low speed. Numerical results were performed by a developed code based on immersed boundary method (IBM) [5], while experimental results were carried out by using subsonic wind tunnel which was located at Hanoi University of Science and Technology (HUST) [6]. Both experimental research and numerical research were effectuated at air velocity 20 m/s and attack angle 5°. Four different wing models were carried out in order to analyze the effect of wing structure. There were two rectangular and two trapezoid 3D-shapes of wing, each 3D-shape of wing had symmetric (NACA65A004) and asymmetric (supercritical) airfoil, respectively.

2 Methodology

2.1 IBM method

Having assumption that structure was linear elastic, fluid flow and deformation of structure were governed by below equations [5]:

$$\frac{\partial u}{\partial t} = \frac{1}{\text{Re}} \nabla^2 u - u \nabla u - \nabla p + f \quad (1)$$

$$\nabla u = 0 \quad (2)$$

$$\frac{d(m_p U_c)}{dt} = F + g \quad (3)$$

$$\frac{dx_c}{dt} = U_c \quad (4)$$

$$\frac{d(I_p \cdot \omega_p)}{dt} = T \quad (5)$$

$$\frac{d\theta_p}{dt} = \omega_p \quad (6)$$

where u was fluid velocity vector; p was fluid pressure; f was force that affected on wing; Re was Reynolds number; U_c , ω_p , x_c , and θ_p were displacement velocity, angular velocity, center of gravity, and rotation of wing, respectively; m_p and I_p were mass and inertial moment of wing; and F and T were force and moment that created by fluid go pass through the wing.

To solve out Eqs. (1–6), this research used IBM method. The most important of this method was that the interaction force (f) between wing and fluid was calculated so that boundary condition of fluid was satisfied on the surface of wing: velocity of the fluid at fluid–solid interface was equal velocity of wing. The Cartesian grid and immersed boundary were illustrated in Fig. 1, in which moving surface of wing was described by Lagrangian points (rounded points), and fixed points in fluid were called Eulerian points. To distinguish, parameters of Lagrangian points were noted as capitalization.

Discrete partial derivative of velocity over time of Eq. (1) with intermediate velocity, \hat{U}^k , was velocity at zero force of Lagrangian point, F of Lagrangian points was estimated as follows

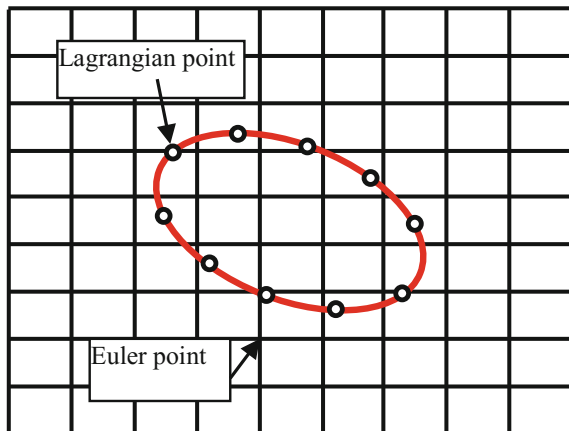
$$F = \frac{U^{k+1} - \hat{U}^k}{\Delta t} - \left(\frac{1}{Re} \nabla^2 U - U \nabla U - \nabla P \right) \tag{7}$$

where k was time step; U^{k+1} was identified from moving of wing, so this velocity was known as $U^{(b)}$.

To calculate force, which created from displacement, affected on fluid element, following interpolation formula was applied:

$$f = \sum_{l=1}^N F(x_l) \delta_h(x - x_l) \Delta V_l \tag{8}$$

Fig. 1 Cartesian grid and immersed boundary



where x was coordinate of Eulerian point; N was set of Lagrangian points around Eulerian point l ; x_l was coordinate of Lagrangian point; ΔU_l was volume of effect corresponded to Lagrangian point l ; and δ_h was 3D delta function was identified as follows:

$$\delta_h(x - x_l) = \delta_h^{1D}(x - x_l)\delta_h^{1D}(y - y_l)\delta_h^{1D}(z - z_l) \tag{9a}$$

$$\delta_h^{1D}(r) = \frac{1}{h}\varphi(r) \quad r = \frac{x - x_l}{h} \tag{9b}$$

$$\varphi(r) = \begin{cases} \frac{1}{6} \left(5 - 3|r| - \sqrt{1 - 3(1 - |r|)^2} \right) & \frac{1}{2} \leq |r| \leq \frac{3}{2} \\ \frac{1}{3} \sqrt{1 - 3|r|^2} & |r| \leq \frac{1}{2} \\ 0 & |r| \geq \frac{3}{2} \end{cases} \tag{9c}$$

To incorporate this method to solve Navier–Stokes equations and Newton equations, three-step Runge–Kutta method was applied:

- *Step 1:* Identify instantaneous velocity at Eulerian points with assumption that there was no immersed boundary surface, i.e., $f = 0$

$$\tilde{u} = u^{k+1} + \Delta t \left(2\alpha_k v \nabla^2 u^{k-1} - 2\alpha_k \nabla p^{k-1} - \gamma_k ((u \cdot \nabla)u)^{k-1} - \zeta_k ((u \cdot \nabla)u)^{k-2} \right) \tag{10}$$

where k was step calculation of Runge–Kutta method ($k = 1, 2, 3$); α_k , γ_k , and ζ_k were the coefficient of k th step calculation; and v was kinematic viscosity.

Apply this instantaneous velocity to calculate Lagrangian velocity on surface of wing:

$$\tilde{U}_{x_l} = \sum_{k=1}^N \tilde{u}_x \delta_h(x - x_k) h^3 \tag{11}$$

This velocity was combined with wing velocity, $U_{x_l}^{(b)}$, which was calculated from the dynamic equation of wing, to calculate forces of Lagrangian points (F) following Eq. (7). Then, these forces are applied to Eq. (8) to calculate forces of Eulerian points (f).

- *Step 2:* Solve Navier–Stokes Eq. (1) to bring the effect of flutter of wing into velocity field around wing:

$$\nabla^2 u^* - \frac{u^*}{\alpha_k \nu \Delta t} = -\frac{1}{\nu \alpha_k} \left(\frac{\tilde{u}}{\Delta t} + f_x \right) + \nabla^2 u^{k-1} \quad (12)$$

To satisfy continuity equation, a temporary pressure was described:

$$\nabla^2 \Phi^k = \frac{\nabla \cdot u^*}{2\alpha_k \Delta t} \quad (13)$$

- *Step 3*: Solve Eq. (11) and calculate velocity and pressure at kth step of Runge–Kutta method:

$$u^k = u^* - 2\alpha_k \Delta t \nabla \Phi^k \quad (14a)$$

$$p^k = p^{k-1} + \Phi^k - \alpha_k \Delta t \nabla^2 \Phi^k \quad (14b)$$

From estimated forces at Lagrangian points, translational and angular movements of wing were carried out by solving Eqs. (3) and (5):

$$U_c^k = U_c^{k-1} + 2\alpha_k \frac{\Delta t}{M} (F + G) \quad (15a)$$

$$\omega_p^k = \omega_p^{k-1} + 2\alpha_k \frac{\Delta t}{I_c} T \quad (15b)$$

After calculating the velocity of the center of gravity (U_c^k) and angular velocity of wing (ω_p^k), coordinates of Lagrange points were estimated by same expressions.

2.2 Aircraft wings

Rectangular and trapezoidal wings were studied in this research (Fig. 2). Rectangular wing had chord length 7.5 cm, semi-span-wise length 30 cm. While, trapezoidal wing had no sweep angle at leading edge line with tip chord length 5 cm, root chord length 10 cm, semi-span-wise length 30 cm. There were two cross sections of wing in this research. One was NACA 65A004 airfoil in stream-wise direction, which was a symmetric airfoil with a maximum thickness of 4% of local chord (Fig. 2a, b), and other was supercritical airfoil (Fig. 2c, d). NACA65A004 airfoil was thin and symmetric airfoil that its sections were particularly adaptable to airplanes having high-level flight speeds. Supercritical airfoil was asymmetric and was characterized by its flattened upper surface, highly cambered (curved) aft

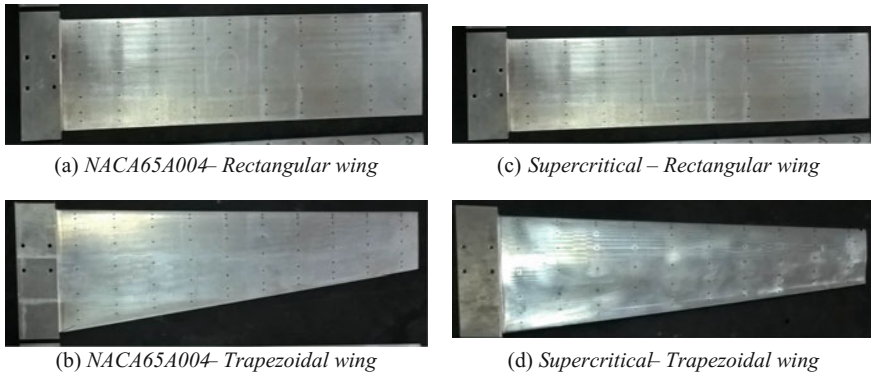


Fig. 2 Wing models for experiment

section, and larger leading edge radius compared with NACA 6-series laminar airfoil shapes. The wing was constructed by aluminum.

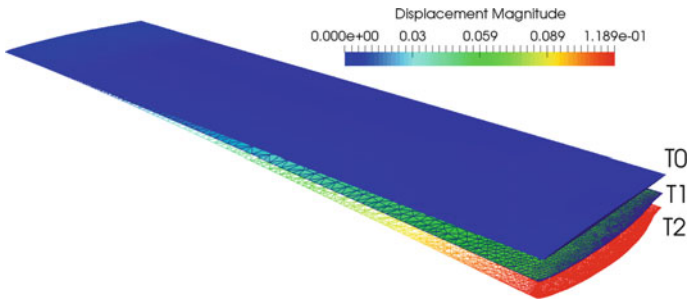
Experiments were conducted at the low-speed blowdown wind tunnel, which belongs to Department of Aeronautic and Space Engineering at Hanoi University of Science and Technology (HUST), Vietnam. Maximum free-stream velocity in empty test section was 30 m/s corresponding to Reynolds number 10^6 , and turbulence level was slightly less than 1%. Wind tunnel was operated continuously, and a centrifugal blower was driven by an 8 kW electric motor. Free-stream velocity was kept constant within $\pm 2\%$. Total pressure of free-stream and dynamic pressures was measured by Pitot tube within $\pm 2\%$. Air temperature was measured within $\pm 1\%$. Both experimental research and numerical research were effectuated at air velocity 20 m/s and attack angle 5° .

For experimental study, wing model had 160 pressure taps (Fig. 2). These pressure taps were connected to an external digital manometer via stainless and silicon tubes. Each pressure tap was measured, using Keyence pressure measurement, one time with waiting time of 5 s (average of about 1000 instant values). The standard deviation of measurement errors was within ± 0.001 Pa. Moreover, flutter of wing was captured with help of high-performance camera.

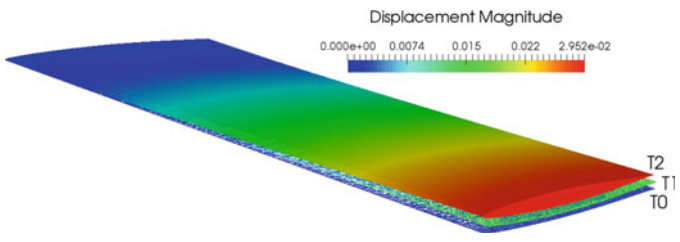
3 Results

The results of deformation and stress of wings were analyzed at three different instants (Fig. 3):

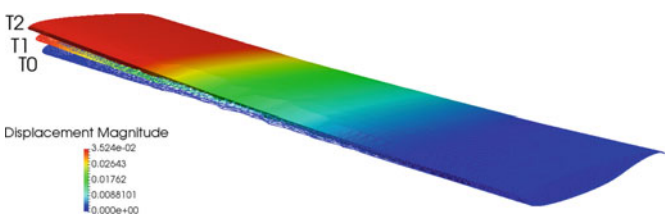
- Time T0: Initial time when distortion did not occur.
- Time T1: Time between maximum deformation and non-deformation.
- Time T2: Time of maximum distortion.



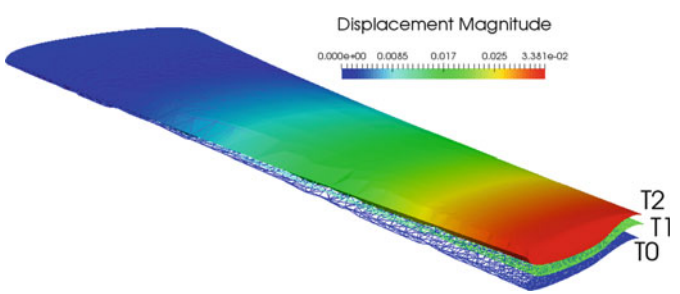
(a) *NACA65A004 – Rectangular wing*



(b) *NACA65A004 – Trapezoidal wing*



(c) *Supercritical – Rectangular wing*



(d) *Supercritical – Trapezoidal wing*

Fig. 3 Instant displacement of wings

Table 1 Maximum deformation of wing tip

Wing	IBM method (mm)	Experiment method (mm)	Relative error (%)
NACA65A004-Rectangular	0.119	0.131	9.7
NACA65A004-Trapezoidal	0.030	0.033	8.6
Supercritical Rectangular	0.035	0.039	9.9
Supercritical Trapezoidal	0.034	0.037	9.2

The maximum deformation was found at the tip of wing and raised down gradually into the root of wing over time. This remark was also observed by experimental results within a relative error less than 10% (Table 1).

Comparing the maximum distortion between two 3D-shapes of the wing with same airfoil, rectangular wing has more distortion than trapezoidal wing. Thus, 3D-shape of wing contributed significantly to deformation of wing when aeroelastic phenomenon occurred (Table 1).

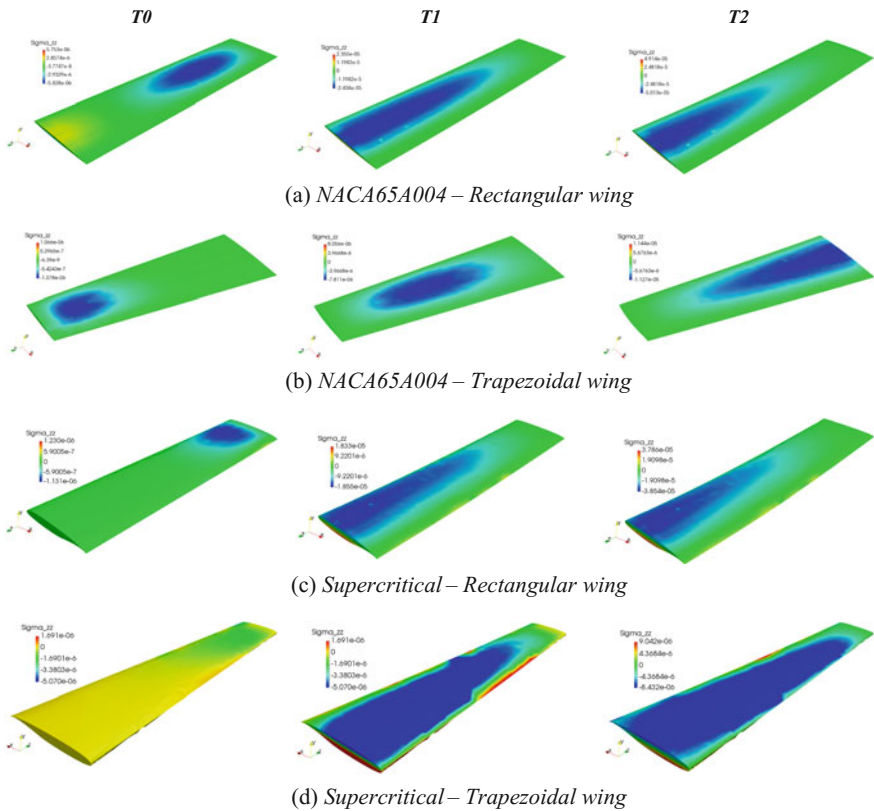


Fig. 4 Instant normal stress

In comparison with the same 3D-shape of wing but different airfoils, NACA65A004 rectangular wing was deformed more than supercritical rectangle wing. Meanwhile, NACA65A004 trapezoidal wing was deformed less than the supercritical trapezoidal wing. It could be concluded that the 3D-shape or airfoil of wing played an important role in creating the durability of the structure (Table 1).

Normal stress was remarked that has an opposite tendency in comparison with deformation. Wing root must support maximum stress while wing tip supports minimum stress (Fig. 4). This observation could be explained by the fixed support of wing root at fuselage, while at wing tip, it was a free support [1].

At non-distortion instant (T_0), normal stress had important value near wing tip. During flutter behaviors of wing, important normal stress propagated from wing tip to wing root. Maximum value of normal stress was found out at wing root and at T_2 instant.

With same airfoil, maximum normal stress at wing root of rectangular wing was higher than that of trapezoidal wing. At the same 3D-shape of wing, maximum normal stress of NACA65A004 rectangular wing was higher than that of supercritical rectangle wing. Meanwhile, this value of NACA65A004 trapezoidal wing was less than supercritical trapezoidal wing.

4 Conclusion

Numerical method based on IBM and experimental methods was carried out to predict the flutter of aircraft wing. The main results could be summarized as follows:

- During flutter phenomenon, deformation of wing tip was maximum and minimum at wing root. In contrast with deformation, normal stress was minimum at wing tip, but maximum at wing root.
- Experimental results were in good agreement with numerical results within a relative error less than 10%.
- Geometry of wing (3D-shape, airfoil) contributed significantly to the deformation of wing when aeroelastic phenomenon occurred.

In the future work, the aeroelastic experimental research at low speed and high speed will be realized for AGARD 445.6 wing. The numerical research will be also performed in order to compare with experimental results and with other results.

Acknowledgements This work was supported by bilateral Project 10/2014/HĐ-NĐT of Ministry of Science and Technology Vietnam and CRI Project 06/CRI 2014-2016 of AUNSEED/Net JICA—Japan.

References

1. Yates EC (1985) AGARD standard aeroelastic configuration for dynamic response I—Wing 445.6. AGARP Report No. 765
2. Liu F, Cai J, Zhu Y, Tsai HM, Wong ASF (2001) Calculation of wing flutter by a coupled fluid-structure method. *J Aircr* 38(2):334–342
3. Lee-Rausch EM, Batina JT (1993) Calculation of AGARD wing 445.6 flutter using Navier-Stokes aerodynamic. AIAA Paper No. 93–3476
4. Nguyen PK, Mori K, Hoang TKD, Nguyen VH, Nguyen HA (2015) Research on simulation and experiment of dynamic aeroelastic analysis on wing structure. *Appl Mech Mater* 798:541–545
5. Pham VS, Luu HQ, Nguyen PK, Hoang TKD (2015) Immersed boundary method for simulating fluid structure interaction. In: *Proceeding of national fluid mechanics conference*, pp 568–576
6. Nguyen PK, Mori K, Hoang TKD (2015) Experiment study of aeroelasticity phenomenon. In: *Proceeding of national fluid mechanics conference*, pp 424–430

Development of a 3-DOF Haptic Tele-manipulator System Using Magnetorheological Brakes



Nguyen Ngoc Diep, Hung Nguyen-Xuan, Nguyen Ngoc Tuyen
and Nguyen Quoc Hung

Abstract In this work, a tele-manipulator system with force feedback (Haptic tele-manipulator) is designed and manufactured. The haptic tele-manipulator system in this study consists of two main parts: slave and master manipulator. The slave manipulator is a three 3-rotary degrees of freedom (DOF) manipulator and driven by AC servo motors. At the end effector of the slave manipulator a 3D force sensor are mounted to measure impact force from the environment. The master manipulator is used to control the slave manipulator; it has a structure and shape similar to the slave manipulator. At the joints of the master manipulator, magneto-rheological brakes (MRBs) are installed. They are means to create the variable braking torque in order to generate a required resultant force acting to the master operator. The value of required resultant force is obtained from sensors mounted on the slave manipulator. In this way, the operator of the master manipulator can feel the force at the end effector of the slave during its operation.

Keywords Magneto-rheological brake • Optimal design • Haptic system
Haptic tele-manipulator

N. N. Diep · N. N. Tuyen
Department of Mechanical Engineering, Industrial University
of Hochiminh City (IUH), Ho Chi Minh City, Vietnam
e-mail: nguyennngocdiep@iuh.edu.vn

N. N. Tuyen
e-mail: tuyen.vinalpg@gmail.com

H. Nguyen-Xuan
Hochiminh University of Technology (HuTech), Ho Chi Minh City, Vietnam
e-mail: ngx.hung@hutech.edu.vn

N. Q. Hung (✉)
Computational Engineering, Vietnamese-German University (VGU),
Ho Chi Minh City, Vietnam
e-mail: hung.nq@vgu.edu.vn

© Springer Nature Singapore Pte Ltd. 2018

H. Nguyen-Xuan et al. (eds.), *Proceedings of the International Conference on Advances in Computational Mechanics 2017*, Lecture Notes in Mechanical Engineering, https://doi.org/10.1007/978-981-10-7149-2_56

1 Introduction

Recently, position feedback and force feedback techniques have been in use to increase the effectiveness of human-machine interfaces. The applications range from medicine, space technologies, military application to computer games and virtual reality devices such as virtual rehabilitation. In robotics, the well-known concept of “tele-presence” is based on the force feedback techniques. The tele-presence is defined as the ideal of sensing sufficient information about the tele-operator and task environment, and communicating this to the human operator in a sufficient natural way, that the operator feels physically present at the remote site [1]. Such a system is often referred to as a haptic master-slave system. This allows the operator to perform tasks in hazardous or distant environments by knowledgeably guiding the robot slave from a safe distant location. For such operations to be successful it is necessary to virtually immerse the human operator in the remote environment through haptic feedback, otherwise the manipulation requires too much effort and becomes slow and imprecise.

Many tele-manipulator systems have been proposed such as five-fingered haptic interface system [2], the Polish cardio-robot RobIn Heart (RIH) system [3], MR Brake for haptic wrist application [4] and Control of haptic master-slave robot system for minimally invasive surgery [5]. Although there have been several researches on haptic tele-manipulator systems, no research effort on haptic system for industrial robot are conducted so far.

The main objective of this research is to focus on the development of a haptic system for industrial robots with 3 degrees of freedom. Haptic robots with force feedback devices featuring magneto-rheological fluid (MRF), these devices are called magneto-rheological brakes (MRB). In this study, we propose a new configuration of MRB modified from previous one [6–8] by using a thin-wall for separation between the coils and MRF duct, which is referred as thin-wall MRB. With this configuration, the MRB can be manufactured more accurately and easily, especially at the MRF ducts. The MRBs located at the joints of the master manipulator are used to feedback the torque/force from slave manipulator to the master manipulator. In addition, the slave manipulator is driven by AC servo motors and its trajectory is the same as that of the master manipulator. This paper is organized as following: Introduction is presented in Sect. 1; The thin-wall MRB is introduced in Sect. 2; Haptic tele-manipulator system is displayed in Sect. 3; Tele-operation control and experiment results are shown in Sect. 4, and finally some conclusions are shown in Sect. 5.

2 Description of Thin-Wall MRB

A new configuration of a disc-type MRB with two coils placed on each side of the brake housing is introduced and its braking torque is analyzed based on Bingham-plastic model of MRF. Figure 1a shows the previously developed MRB in which the two coil on each side of the housing directly contact with MRF [6], while Fig. 1b shows the configuration of the proposed MRB in which the coils are separated with MRF by a thin wall.

As shown in the Fig. 1, a disc (rotor) made of magnetic steel is fastened to the flange of the MRB shaft made of nonmagnetic steel. The disc is embedded inside a stationary envelop (housing) made of magnetic steel. In Fig. 1a, two wire-coils are directly placed on each side of the housing and directly contact with the MRF (In this study, this is referred as contact side-coil MRB). In Fig. 1b, there are not any slots on the inner face of the side housing, the side housing is composed of two parts and the coils are placed on the inner part of the housing from outside. In this case, the coils do not contact with the MRF (In this study, this is referred as non-contact side-coil MRB). The space between the rotary disc and the housing is filled with MRF. In order to prevent the leaking of MRF, radial lip seals are employed. It is noted that, for the non contact MRB, the wall should be manufactured as thin as possible to prevent magnetic flow going through it.

With the new configuration of MRB (Fig. 1b), the coils are separated with the MRF by thin walls of the side housing, the inner face of the side housing can be manufactured continually. This allows the MR fluid duct to be manufactured more easily and accurately, and avoid the contamination of the coils with MRF. The MR

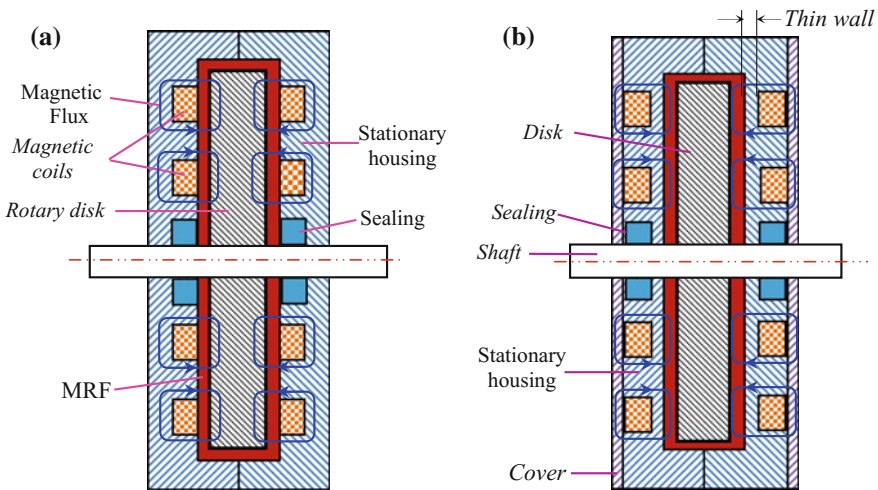


Fig. 1 Configuration of the conventional **a** and the proposed disc-type MR brake **b**

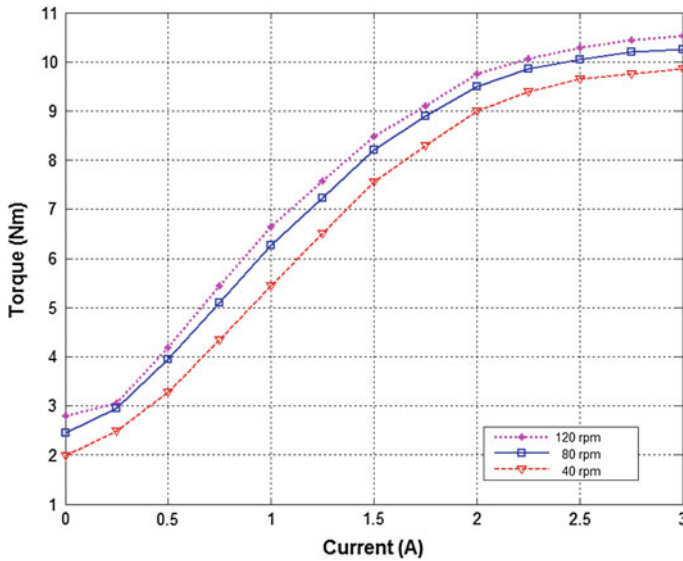


Fig. 2 Braking torque versus current at different speeds of the rotary disk

fluid using in this study is Lord Corporation's MRF – 132DG that has plastic viscosity of 0.09 Pa s.

When an electrical current is applied on the coil of MRB, due to the generated magnetic fields, the MR fluid in the gap becomes solid-like instantaneously. The shear friction between the rotating disk and the solidified MR fluid provides the required braking torque on the shaft. As such, depending on the current supplied to the MRB, the corresponding torque is obtained. The change in braking torque by change in the applied current is shown in the Fig. 2 [7, 8]. It can be seen that at the start when current is not applied only viscous torque acts on the fluid, but when the current is applied the braking torque increases.

3 Haptic Tele-manipulator System

3.1 The Master Manipulator

The configuration of the master manipulator is shown in Fig. 3. It is noted that this master manipulator is designed and manufactured by our research group to control the commercial manipulator shown in Fig. 4. Three MRBs are installed at the three corresponding rotary joints for force feedback. The manipulator is made of aluminum alloy material (5052-H38). At the joints there are encoders installed to determine the rotational angle of the joint. Besides, the torque sensors are installed to measure the torque at the joints. In this system we used three encoders type:

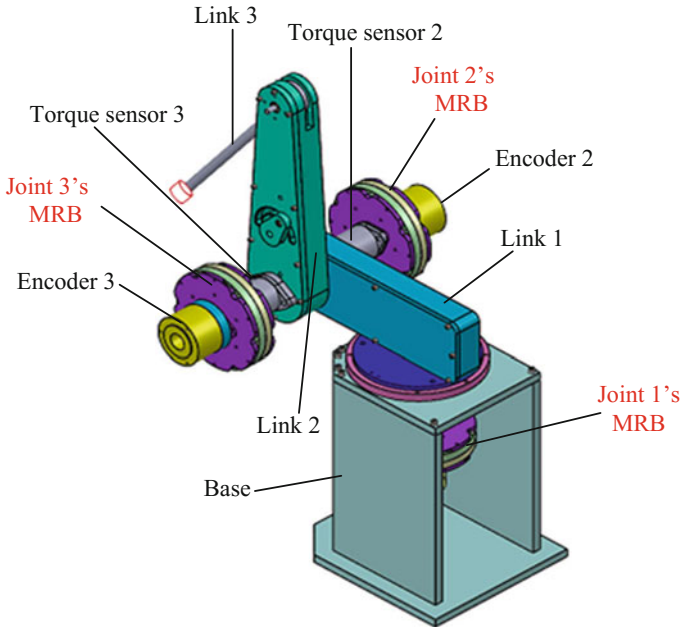


Fig. 3 Configuration of the master manipulator

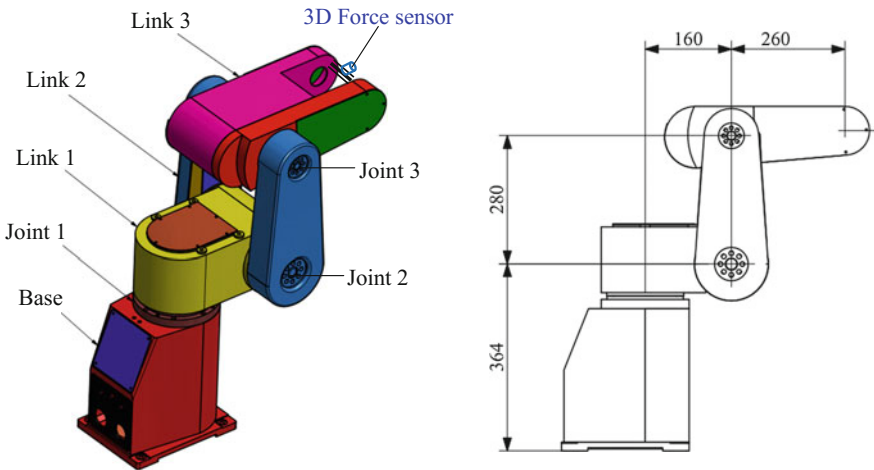


Fig. 4 Configuration of the slave manipulator

LBJ-096-2000, power 5VDC, resolution 2000 pulse/rotation (Sumtak) and three torque sensors type: AZM 350, measure range 0–20 Nm, power ± 15 V DC (Giken). At the end of the master manipulator a 3D force sensor is mounted to measure the

forces that verify the results of the force feedback control problem. The length of the links are: $L_1 = 160$ mm, $L_2 = 280$ mm, $L_3 = 260$ mm.

In this study, dynamics of the manipulators are neglected and equation of momentum at the joints of the master manipulator can be derived as following [9, 10, 11]:

$$M(q)_i = [D_{ij}] (F_{xyz}) - [G_{ij}] (m_i); i = 1, .3 \quad (1)$$

where $M(q)_i$ is the equilibrium momentum at the joints when the armature operates, $G(q)$ is the inertia matrix, and F is the control input torque. The mentioned matrix of the 3 DOF articulated manipulator can be computed by:

$$D(1, 1) = L_1 + L_2 \cos \theta_2 + L_3 \cos(\theta_2 + \theta_3); D(1, 2) = 0; D(1, 3) = 0 \quad (2)$$

$$D(2, 1) = 0; D(2, 2) = 0; D(2, 3) = L_3 + L_2 \cos \theta_3 + L_2 \sin \theta_3 \quad (3)$$

$$D(3, 1) = 0; D(3, 2) = L_3; D(3, 3) = 0 \quad (4)$$

$$G(1, 1) = 0; G(1, 2) = 0; G(1, 3) = 0 \quad (5)$$

$$G(2, 1) = 0; G(2, 2) = -g \frac{L_2}{2} \cos \theta_2; G(2, 3) = -g \left(L_2 \cos \theta_2 + \frac{L_3}{2} \cos(\theta_2 + \theta_3) \right) \quad (6)$$

$$G(3, 1) = 0; G(3, 2) = 0; G(3, 3) = g \frac{L_3}{2} \cos(\theta_2 + \theta_3) \quad (7)$$

$$[F_{xyz}] = \begin{bmatrix} F_x \\ F_y \\ F_z \end{bmatrix} \quad (8)$$

$$[m_i] = \begin{bmatrix} m_1 \\ m_2 \\ m_3 \end{bmatrix} \quad (9)$$

where F_x, F_y, F_z are forces acting on the slave arm at the end-effector. L_1, L_2, L_3 are length of the three links, m_1, m_2, m_3 are weight of the links, $\theta_1, \theta_2, \theta_3$ are rotation angles of the joints and m_1, m_2, m_3 are weigh of the links, respectively.

3.2 The Slave Manipulator

The slave manipulator is shown in Fig. 4. This is a 6-DOF commercial manipulator which is modified by our research group to make it suitable for this research. It is observed that the joints of the machine arm are driven by AC servo motors. At the

end-effector, a 3D force sensor are mounted to measure impact force from the environment. These forces will be calculated by the controller and converted into current signals; these signals are supplied to the MRBs on the master arm to produce feedback forces to the operator. The slave manipulator is controlled by the master manipulator and it must travel in the same trajectory as the master manipulator.

The slave manipulator with maximum payload is 1.5 kg; max. reach is 700 mm; max. operation speed is 0.5 m/s; robot weight is 19 kg.

Using forward and inverse kinematics of robot, the rotation angle of each slave robot arm is derived as follows:

$$\theta_1 = \text{actan2}(d_y, d_x) \quad (10)$$

$$\theta_2 = \text{actan2}(r, d_z) - \text{actan2}(L_2 + L_3 \cos \theta_3, L_3 \sin \theta_3) \quad (11)$$

$$\theta_3 = \text{acos} \left(\frac{d_z^2 + d_x^2 + d_y^2 - L_2^2 - L_3^2}{2L_2L_3} \right) \quad (12)$$

where

$$\begin{aligned} d_x &= (L_1 + L_2 \cos \theta_2 + L_3 \cos(\theta_2 + \theta_3)) \cos \theta_1; & d_y &= (L_1 + L_2 \cos \theta_2 + L_3 \cos(\theta_2 + \theta_3)) \sin \theta_1; \\ d_z &= L_2 \sin \theta_2 + L_3 \sin(\theta_2 + \theta_3); & r &= L_1 + L_2 \cos \theta_2 + L_3 \cos(\theta_2 + \theta_3). \end{aligned}$$

4 Tele-operation Control

Figure 5a shows the photograph of the manufactured haptic master combined with the MRBs, encoders, torque sensors installed in the joints. Figure 5b shows the photograph of the manufactured slave manipulator. The control system diagram of the tele-manipulator system showed in Fig. 6, this system is controlled by a NI card 6289 (National Instruments) and PID controllers are used. When operator moves the master arm, position information such as rotational angles is obtained from encoders, and transferred to controller to control the servomotors of slave arm, so this arm must move according to the movement path of the master arm. At the same time, the forces acting on the slave arm are also transfer to the controller, and then converted into the control signals to supply to the MRBs on the master arm, which is to be reflected to the user. The forces acting on the slave arm are measured by a 3 axes force sensor at the end-effector. The generated force/torque at the joints of haptic master is measured by three torque sensors installed at the joints.

Rotational angle (in degrees) of the corresponding joints on the master (θ_{master}) and slave (θ_{slave}) manipulator is determined:



a) *Manufactured haptic master* b) *Manufactured slave manipulator*

Fig. 5 The photograph of the manufactured tele-manipulator system

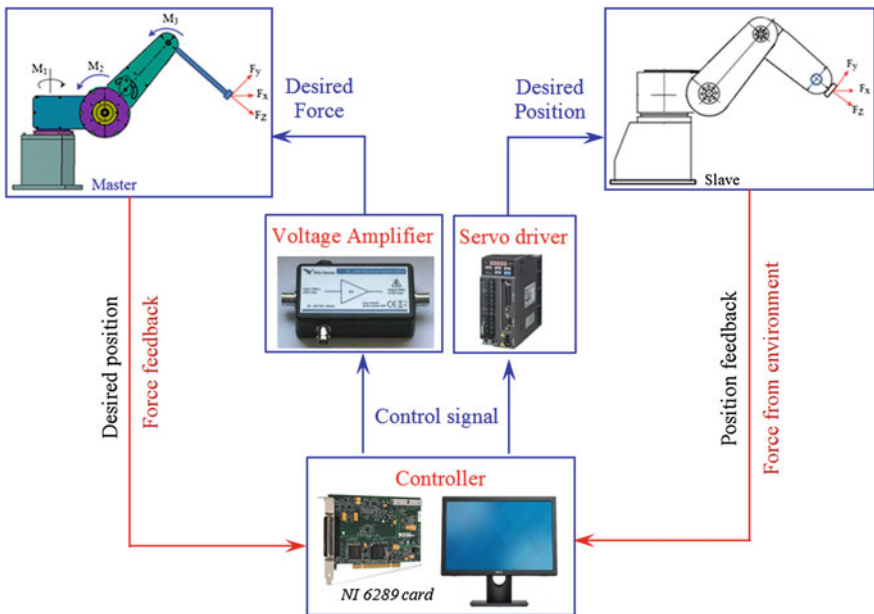


Fig. 6 Experimental apparatus of master and slave manipulator system

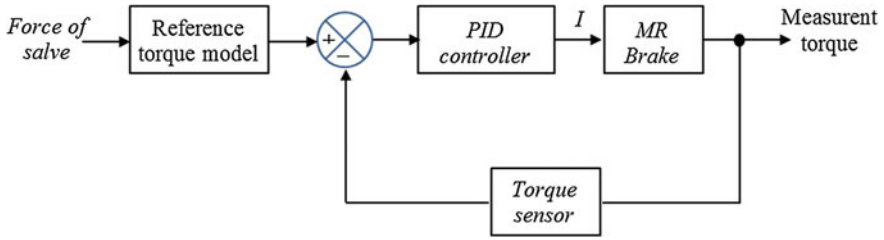


Fig. 7 Block diagram of the force feedback control systems

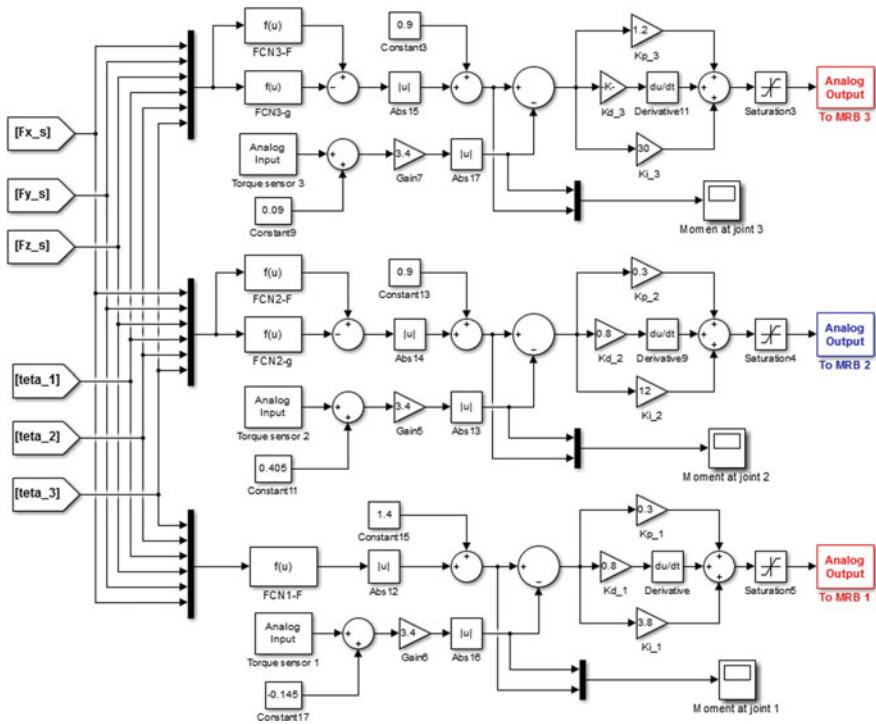
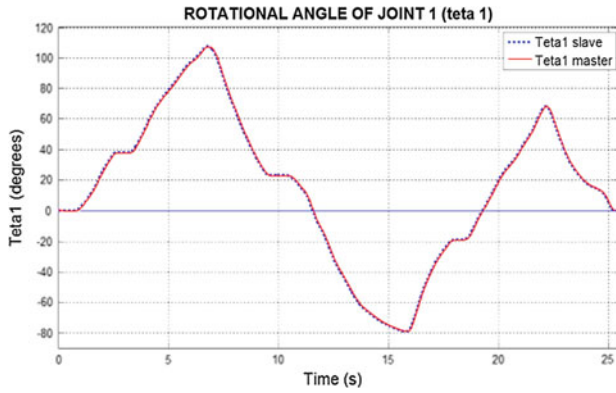


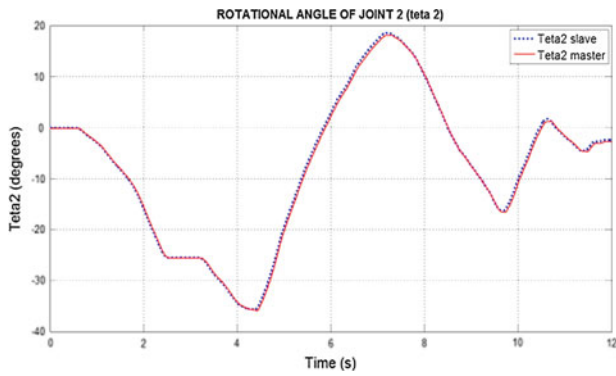
Fig. 8 Force feedback control program in Matlab Simulink

$$\theta_{i_slave} = i \frac{n}{2000} 360 \theta_{i_master}; \quad i = 1, .3 \quad (13)$$

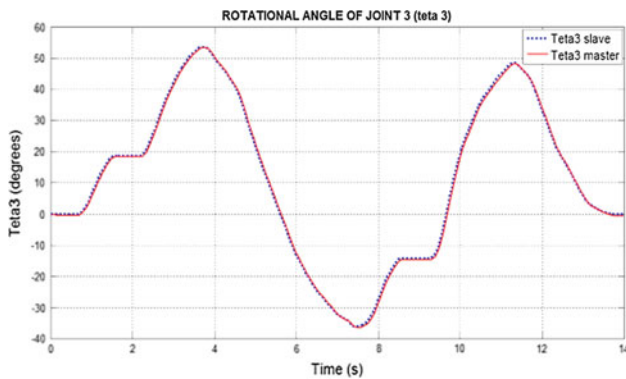
where n is the number of pulses counted of the encoder at the joint of master manipulator; i is the transmission ratio of the harmonic box; θ_{i_slave} , θ_{i_master} are rotational angles of the joints of the slave and master manipulator, respectively.



a) θ_1 angle

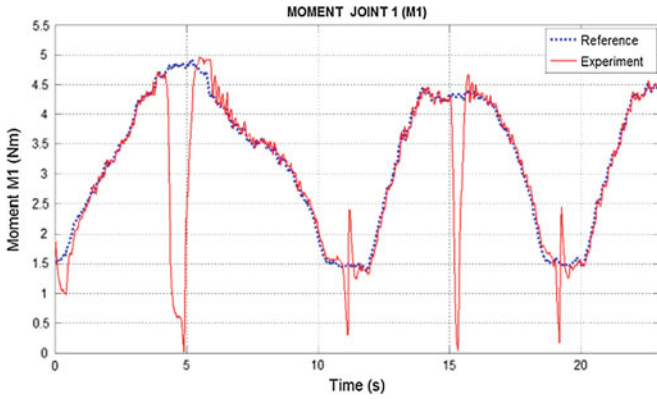


b) θ_2 angle

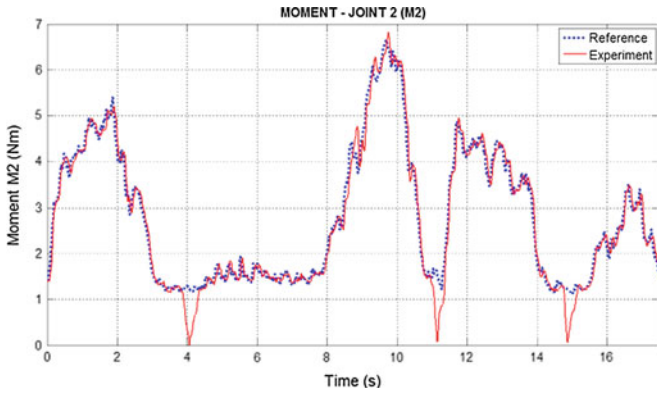


c) θ_3 angle

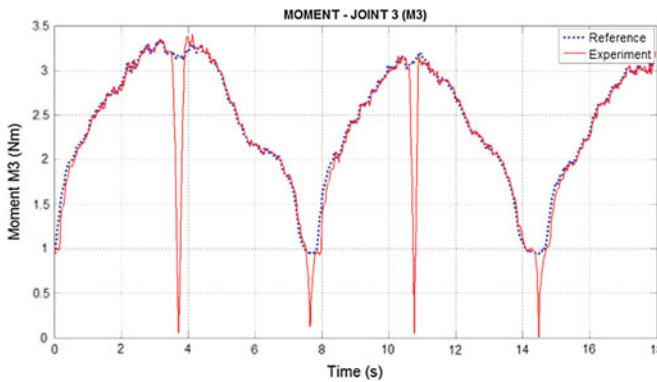
Fig. 9 Comparison of rotational angles of the joints of the master and slave arms



a) Moment at joint 1



b) Moment at joint 2



c) Moment at joint 3

Fig. 10 Reflected torques at the joints of the master arm

Besides, the block diagram of PID controller for the force feedback of the master and slaver system has been brought in Fig. 7, and the control program in Matlab Simulink showed in Fig. 8. In this control program the F_{x_s} , F_{y_s} , F_{z_s} are the acting forces at the end-effector of the slave manipulator.

Figure 9 presents rotational angles results of the corresponding joints on the master and slave manipulator. Accordingly, deviation of the rotational angle of two corresponding joints on the master and slave manipulator is about 0.5° . At the same time, the torque tracking control responses of rotation motion at the joints of master manipulator showed in Fig. 10. From the result, it is clearly seen that the torques at the joints of the mater track the desired signal except at the times that the direction of manipulator is inverted, errors between be desired torque from measuring torque of the master manipulator is about 0.1 Nm. Also from these results, the proposed haptic master system was successfully operated and communicated with the slave without time delay problem.

5 Conclusion

In this study, a novel configuration of a disc-type MRB with two coils placed on each side of the brake housing is introduced and its braking torque is analyzed based on Bingham-plastic model of MRF. A haptic master manipulator using new MRBs for forces feedback was proposed and integrated with the slave manipulator, the master manipulator is used to control the slave manipulator; it has a structure and shape similar to the slave manipulator. Kinematic analysis of the slave and master arm was studied. The interface communication between master and slave system has been analyzed. Accordingly, the haptic master-slave system has been established by incorporating the slave manipulator with the master manipulator in which the repulsive force/torque and desired position are transferred to each other. In order to obtain the desired torque trajectories, a PID controller was used, the system control program has been built and the experiments have been done. It has been demonstrated that the desired effective torque tracking and position control performances are well achieved.

Acknowledgements This work was supported by the Vietnam National Foundation for Science and Technology Development (NAFOSTED) under grant no. 107.01-2015.32.

References

1. Stone RJ (2000) Haptic feedback: a brief history from telepresent to virtual reality. In: Proceedings of the 1st international workshop on haptic human-computer interaction LNCS 2085, pp 1–16
2. Kawasaki H, Mouri T (2007) Design and control of five-fingered haptic interface opposite to human hand. *IEEE Trans Robot* 23(5) October 2007

3. Nawrat Z, Kostka P (2006) Polish cardio-robot 'Robin heart'. System description and technical evaluation. *Int J Med Robot Comp* 2(1):36–44
4. Nguyen QH, Nguyen PB, Choi SB (2011) Optimal design of a hybrid MR brake for haptic wrist application. In: *Proceedings of SPIE 7977, active and passive smart structures and integrated systems 2011*, pp 797718 (April 27, 2011). <https://doi.org/10.1117/12.880396>
5. Oh JS, Shin WK, Uhm CH, Lee SR, Han YM, Choi SB (2013) Control of haptic master–slave robot system for minimally invasive surgery. *J Phys Conf Ser* 412(012041). <https://doi.org/10.1088/1742-6596/412/1/012041>
6. Nguyen QH, Nguyen ND, Choi SB (2015) Design and evaluation of a novel magnetorheological brake with coils placed on the side housings. *Smart Mater Struct* 24(4):047001
7. Diep NN, Hung NX, Hiep LD, Hung NQ (2016) Design and evaluation of a new magnetorheological brake with two coils placed on each side of the brake housing considering manufacturing benefits. *Vietnam Mech Eng J*. ISSN 0866-7056
8. Nguyen QH, Nguyen ND, Choi SB (2014) Optimal design of a novel configuration of MR brake with coils placed on the side housings of the brake. In: *Proceedings of SPIE 9059, industrial and commercial applications of smart structures technologies 2014*, pp 90590I (March 10, 2014)
9. Baghli FZ, Bakkali LEI, Lakhali Y, Nasri A, Gasbaoui B (2014) Arm manipulator position control based on multi-input multi-output PID strategy. *J Aut Mob Robot Intell Syst*, vol 8, no 2
10. Lafmejani HS, Zarabadipour H (2014) Modeling, simulation and position control of 3DOF articulated manipulator. *Indonesian J Electr Eng Inf* 2(3), September 2014
11. Zhang Z, Zhao D (2009) Master-slave control strategy of tele-manipulator. In: *International conference on robotics and biomimetics*, December 19–23, 2009, Guilin, China

Studying Convective Flow in a Vertical Solar Chimney at Low Rayleigh Number by Lattice Boltzmann Method: A Simple Method to Suppress the Reverse Flow at Outlet



Y. Q. Nguyen

Abstract Solar chimneys absorb solar radiation heat and induce natural convective airflow for natural ventilation of buildings. In this study, we simulate induced airflow in a two-dimensional vertical solar chimney by Lattice Boltzmann Method (LBM) and focus on laminar flow region at low Rayleigh (Ra) number. Standard D2Q9 and D2Q4 models with single relaxation time are used for flow and temperature fields, respectively. Airflow and air temperature distributions inside the chimney are investigated under effects of main parameters of solar chimneys: heat flux, chimney height H , and chimney width b . Typical characteristics of a solar chimney were well reproduced in our simulations. Particularly, we analyze flow reversal region near the outlet of the chimney. The flow separation regions were observed at low ratio of H/b at a given Ra number or at high Ra number at a given H/b ratio and significantly reduced the induced flowrate. To suppress the flow reversal, we propose a simple method of rearranging the heat transfer surface on the opposite side in the upper and lower halves of the chimney. The results show that this method can eliminate the separation region and increases the induced flowrate at low ratio of H/b at a given Ra number.

Keywords Lattice Boltzmann Method • Solar chimney • Convective flow
Natural ventilation • Reverse flow

Y. Q. Nguyen (✉)
Department of Civil Engineering, Ho Chi Minh City University,
Ho Chi Minh City, Vietnam
e-mail: nguyenquocy@hcmut.edu.vn

© Springer Nature Singapore Pte Ltd. 2018
H. Nguyen-Xuan et al. (eds.), *Proceedings of the International Conference on Advances in Computational Mechanics 2017*, Lecture Notes in Mechanical Engineering, https://doi.org/10.1007/978-981-10-7149-2_57

1 Introduction

Solar chimney has been studied by many researchers as an effective method for natural ventilation of buildings [1–3]. An example of using solar chimneys for natural ventilation is the zero-energy building (ZEB) in Singapore [4].

A solar chimney absorbs solar radiation heat to induce thermal effect, or stack effect, inside the air channel. A typical configuration of a solar chimney consists of a glass plate, or a glazing plate, an air channel, and an absorber surface opposite to the glazing surface. Solar radiation heat is transmitted through the glazing and then received by the absorber surface. Heat transfer between the air inside the channel and the absorber surface, which is mainly in convection mode, creates thermal effect to induce airflow through the chimney. The airflow can be used for ventilating buildings naturally [1, 2].

There are two main types of solar chimneys: vertical ones and inclined ones. Induced flowrate through a solar chimney is affected by many parameters, such as inclined angle, dimensions of the air channel, and materials of the absorber surface [1–3]. For the vertical solar chimneys, dimensions of the air channel significantly affect the structure of the airflow and the ventilation performance accordingly [1, 2]. Chen et al. [1] conducted experiments with a vertical solar chimney of 1.5 m height and reported that there was a flow separation zone at the outlet of the chimney as the width of the chimney was greater than 0.3 m. Khanal and Lei [2], with their experimental and numerical studies, focused on effects of the separation zone at the outlet of a vertical solar chimney on the induced flowrate. Their results showed that the reverse flow at the outlet significantly reduced the induced flowrate through the chimney. They then proposed a simple method to suppress the separation zone by using an inclined glazing surface.

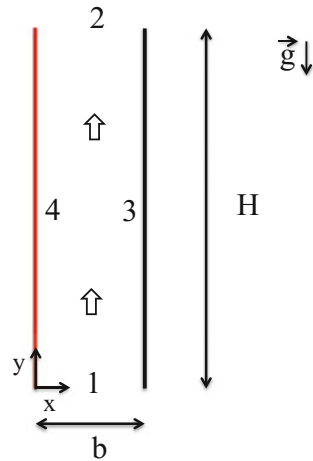
Khanal and Lei [2] reported that the height of the separation zone increased with the heat flux, or the Rayleigh number, Ra , which is defined in Eqs. (10) and (11) below. The value of Ra at which the separation zone existed in their chimney was from 10^9 to 10^{11} . Chen et al. [1] reported that transition to turbulent flow happened in a vertical solar chimney at around 10^{13} . Therefore, the airflow in Khanal and Lei's experiment [2] was in the upper laminar regime.

In this study, natural convection flow at lower laminar regime is investigated numerically. Lattice Boltzmann Method is used to model flow and temperature fields inside a vertical solar chimney to examine effects of flow separation zone at the outlet. A simple method is then proposed to suppress the reverse flow to enhance the induced flowrate through the chimney.

2 Numerical Method

Main characteristics of a solar chimney can be studied numerically by a two-dimensional model [1–3] as depicted in Fig. 1.

Fig. 1 Two-dimensional model of a vertical solar chimney, where H and b are the height and the width of the chimney, respectively; 1 is the inlet; 2 is the outlet; 4 is the absorber plate; and 3 is the glazing surface



In real solar chimneys, transmission and absorption of solar radiation take place at the glazing place and the absorber surface, respectively. Major portion of the absorbed heat is transferred to the air in the channel in convection mode. In simulation, to focus on thermal effect, only the convection mode is modeled, while the others are ignored, such as radiation heat loss through the glazing plate or conduction heat loss through the absorber plate. The convection heat transfer on the absorber surface can be described by an applied heat flux or a specific surface temperature which is higher than the ambient temperature [2]. In this simulation, both methods are applied to validate the model (with an applied temperature) with experimental results [5] and to examine flow structure (with an applied heat flux).

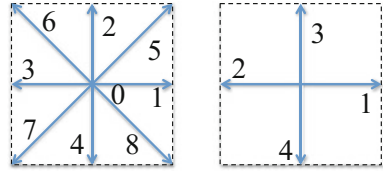
In the numerical model, coupled field of airflow and temperature is described with Lattice Boltzmann Method (LBM). The following assumptions are used:

- The airflow and temperature fields are two-dimensional and steady. The airflow is incompressible.
- Heat and airflow coupling follows the Boussinesq approximation.
- The airflow is laminar. Particularly, the considered Ra number is from 10^4 to 10^7 .

LBM has some advantages over traditional computational fluid dynamics methods, such as readiness for parallelization or treatment of complex solid geometries [6]. Details of LBM can be found in a number of previous studies [6–9]. Only fundamental equations of LBM employed in this study are presented here.

In LBM, motions of a group of fluid particles at a point as well as temperature distribution are described by directional distribution functions. For this two-dimensional problem, the airflow is described by the D2Q9 model with nine distribution functions f_i , where i is from 0 to 8, while the temperature field is modeled by the D2Q4 scheme with four distribution functions g_k , where k is from 1

Fig. 2 Directions of nine distribution functions f_i for airflow (left) and four distribution functions g_k for the temperature field (right)



to 4, as shown in Fig. 2. Mohamad and Kuzmin [8] reported that this combination is suitable for the natural convection problems.

2.1 D2Q9 Model for the Airflow

The D2Q9 model with BGK approximation [6–8] is described by Eq. (1).

$$f_i(\mathbf{x} + \mathbf{c}_i \Delta t, t + \Delta t) - f_i(\mathbf{x}, t) = - \frac{f_i(\mathbf{x}, t) - f_i^{eq}(\mathbf{x}, t)}{\tau} + \Delta t F_i \tag{1}$$

In Eq. (1), \mathbf{x} is the spatial vector; t and Δt are the time and time step, respectively; \mathbf{c}_i is the velocity in i direction, $i = 0, \dots, 8$ as in Fig. 2; $\tau = 1/\omega_m$ is the relaxation time; and F_i is the body force in i direction, which is the buoyancy force in this problem.

The equilibrium distribution function f_i^{eq} is calculated by Eq. (2).

$$f_i^{eq} = w_i \rho \left[1 + 3 \frac{c_i u}{c^2} + \frac{9}{2} \frac{(c_i \cdot u)^2}{c^4} - \frac{3}{2} \frac{(u \cdot u)^2}{c^2} \right] \tag{2}$$

where w_i is the weighting factor in the direction i :

$$w_i = \begin{cases} 4/9, & i = 0 \\ 1/9, & i = 1, 2, 3, 4 \\ 1/36, & i = 5, 6, 7, 8 \end{cases}$$

\mathbf{u} is the velocity vector; ρ is the air density; and c is the lattice speed, $c = \Delta x / \Delta t$ where Δx is the lattice spacing.

The directional vector \mathbf{c}_i has the following values in each direction: $\mathbf{c}_0 = (0, 0)$, $\mathbf{c}_1 = c(1, 0)$, $\mathbf{c}_2 = c(0, 1)$, $\mathbf{c}_3 = c(-1, 0)$, $\mathbf{c}_4 = c(0, -1)$, $\mathbf{c}_5 = c(1, 1)$, $\mathbf{c}_6 = c(-1, 1)$, $\mathbf{c}_7 = c(-1, -1)$, $\mathbf{c}_8 = c(1, -1)$.

The body force F_i is calculated by the Boussinesq approximation:

$$F_i = w_i F \cdot c_i / c_s^2 \tag{3}$$

where $\mathbf{F} = \rho \mathbf{g} \beta \Delta T$. \mathbf{g} is the gravitational acceleration. β is the thermal expansion coefficient of air. $\Delta T = T - T_a$ is the temperature difference between air temperature T and the ambient temperature T_a .

The relationship of density and velocity is described by Eq. (4).

$$\rho(\mathbf{x}, t) = \sum_i f_i(\mathbf{x}, t), \rho \mathbf{u}(\mathbf{x}, t) = \sum_i \mathbf{c}_i f_i(\mathbf{x}, t) \tag{4}$$

Air macroscopic viscosity ν is determined from the time relaxation τ and the lattice sound speed $c_s = c/\sqrt{3}$.

$$\nu = \left(\tau - \frac{1}{2} \right) c_s^2 \Delta t \tag{5}$$

or

$$\omega_m = \frac{1}{3\nu + 0.5} \tag{5'}$$

2.2 D2Q4 Model for the Temperature

For the temperature field T , the distribution function g_k can be written as [6, 8, 9]:

$$g_k(\mathbf{x} + \mathbf{c}_k \Delta t, t + \Delta t) = g_k(\mathbf{x}, t) [1 - \omega_s] + \omega_s g_k^{eq}(\mathbf{x}, t) \tag{6}$$

where $k = 1, 2, 3, 4$ as shown in Fig. 2.

The distribution function g_k^{eq} has a form of:

$$g_k^{eq} = w_k \theta(\mathbf{x}, t) \left[1 + \frac{\mathbf{c}_k \cdot \mathbf{u}}{c_s^2} \right] \tag{7}$$

The weighting factors w_k have the values of:

$$w_1 = w_2 = w_3 = w_4 = 1/4$$

The constant ω_s relates to the thermal diffusivity as:

$$\omega_s = \frac{1}{3\alpha + 0.5} \tag{8}$$

Temperature T is determined from the distribution functions g_k :

$$T(\mathbf{x}, t) = \sum_k g_k(\mathbf{x}, t) \tag{9}$$

In LBM, the variables in Eqs. (1) and (6) and ρ , \mathbf{u} , and T in Eqs. (4) and (9) are nondimensional. Details can be found in the Ref. [6].

2.3 Rayleigh Number

Natural convection flows in a solar chimney can be modeled from a specific temperature T_s of the absorber surface or a given heat flux q_s from the surface [2]. In both cases, the most important nondimensional parameter is the Rayleigh number [1, 2, 6]:

$$Ra = \frac{g\beta\Delta T_s H^3}{\alpha\nu} = \frac{g\beta(T_s - T_a)H^3}{\alpha\nu} \quad (10)$$

for the case of given surface temperature T_s , or

$$Ra = \frac{g\beta q_s H^4}{\alpha\nu k} \quad (11)$$

for the case of given heat flux q_s , where k is the heat conductivity of air.

2.4 Boundary Conditions

For the airflow, the following boundary conditions are applied, as shown in Fig. 1:

- At the inlet 1: Zhou and He [7] pressure boundary conditions.
- At the outlet: outflow condition with zero velocity gradient in y direction.
- On wall surfaces 3 and 4: no-slip boundary condition with bounce back scheme in LBM [6, 7].

For the temperature:

- At the inlet 1: The air temperature is equal to the ambient one.
- At the outlet 2: Outflow condition with zero temperature gradient in y direction is applied.
- On the surface 4: Either a uniform heat flux q_s or uniform surface temperature T_s is used.
- On the surface 3: A uniform wall temperature, a uniform heat flux, or adiabatic condition is applied.

Equations (1) and (6) are solved by the standard collision–streaming scheme [6–9]. At first, in the collision step, the right-hand sides of Eqs. (1) and (6) are evaluated at each lattice point. Uniform lattice size is used in both x and y directions in this study. Secondly, in the streaming step, the left-hand sides of the two

equations are calculated at the next time step by streaming the distribution functions f_i and g_k in according directions. The boundary conditions are applied after the streaming step. The process is repeated until a steady solution is achieved.

3 Results and Discussion

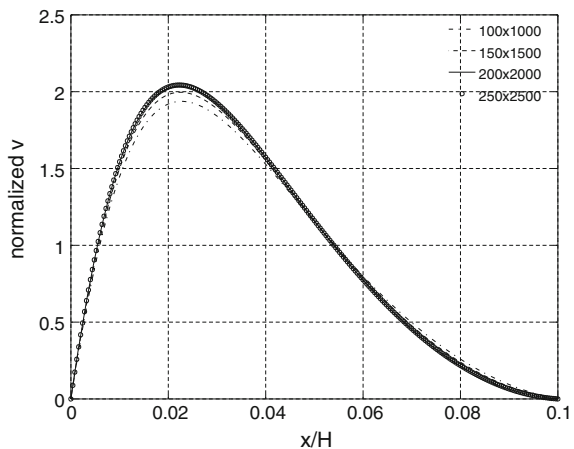
3.1 Grid Convergence

To check grid convergence, a solar chimney with a ratio of $H/b = 10$ and a Rayleigh number of $Ra = 10^7$ was tested with four different grid resolutions, 100×1000 , 150×1500 , 200×2000 , and 250×2500 , in the horizontal and vertical directions, respectively. The distribution of velocity, which is normalized by the average velocity, at the outlet is presented in Fig. 3. It shows that the velocity distribution converged at the two highest grid resolutions. For tests at other Ra numbers, similar grid convergence tests were also conducted to find the appropriate grid resolution.

3.2 Validation of the Numerical Model

Numerical results with the present model were compared with the experimental and numerical results by Aung et al. [5]. The tested solar chimney has the ratio of $H/b = 10$ and $Ra = 1.24 \times 10^5$. Distribution of velocity in the vertical direction and temperature distribution across the air channel are presented in Fig. 4. In this test, temperature of the left surface (at $x/b = 0.0$) was $T = 0.5$, while that of the right

Fig. 3 Velocity at the outlet of a solar chimney with $H/b = 10$ and $Ra = 10^7$ at different grid resolutions



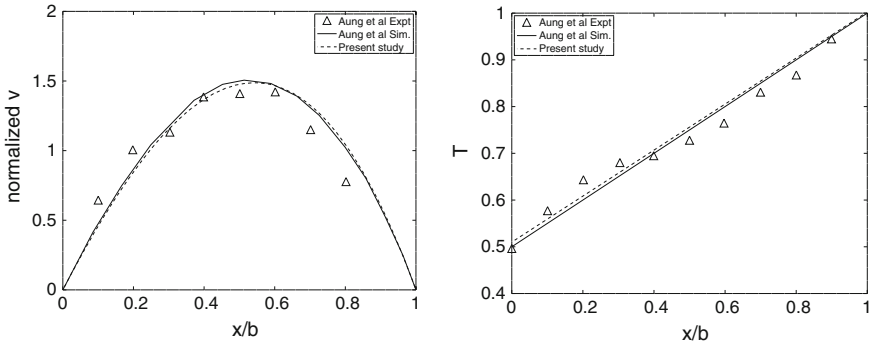


Fig. 4 Comparison of the numerical results of the present model and the results of Aung et al. [5]

surface (at $x/b = 1.0$) was $T = 1.0$. Distributions of velocity and temperature obtained from our model are seen to match well with Aung et al. [5] results.

3.3 Effects of the Ratio of H/B and Rayleigh Number on the Temperature and Velocity Distributions

The numerical model is now used to investigate flow structure and temperature field in solar chimneys. As suggested in the literature [1–3, 5], dimensions of the air channel and heat flux from the absorber surface are the main factors determining the performance of a solar chimney. Our previous study [3] showed that combination of the height H and the width b of a channel can be described by the ratio of H/b and is the suitable parameter for representing the dimensions. The heat flux is in term of the Rayleigh number, Ra , in Eq. (11).

To test effects of H/b and Ra , firstly, the Rayleigh number was kept constant, while the ratio of H/b varied. As shown in Fig. 1, the heat flux was distributed uniformly on the left side (wall 4) of the air channel. This distribution is similar to real configuration of a solar chimney where the absorber surface (wall 4) receives solar radiation transmitted through the glazing plate (wall 3). Velocity and temperature fields for a test case with $Ra = 1.10^6$ and $H/b = 3, 4, 6, 8$ are presented in Fig. 5. Velocity and temperature are higher near the heated surface. As the channel length is short, for $H/b = 3$, the thermal and induced airflow layers only occupy near the left half of the air channel. The right half of the air channel has lower temperature, which is approximately around the ambient one, and hence is less induced by the buoyancy effect. As a result, a reverse flow exists at the outlet of the chimney. As the length of the chimney, or the ratio H/b , increases, the thermal and the accordingly induced air layers expand and gradually suppress the reverse flow, at $H/b = 6$ and 8.

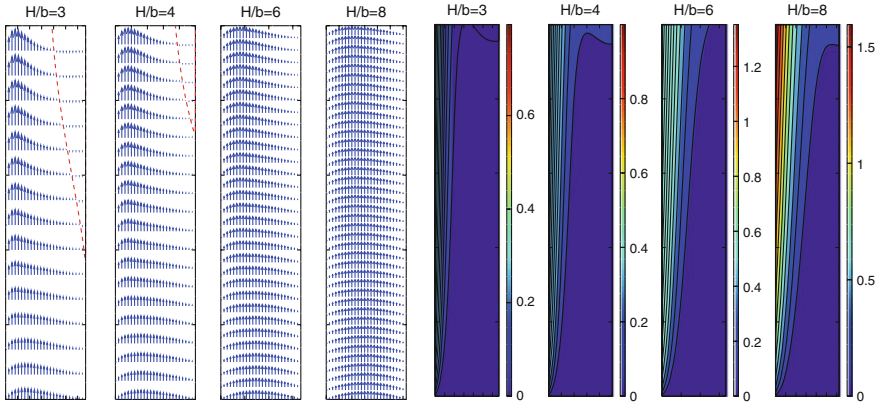


Fig. 5 Velocity and temperature fields for the test case of different H/b 's at $Ra = 1.10^6$. Red line indicates the separation zone

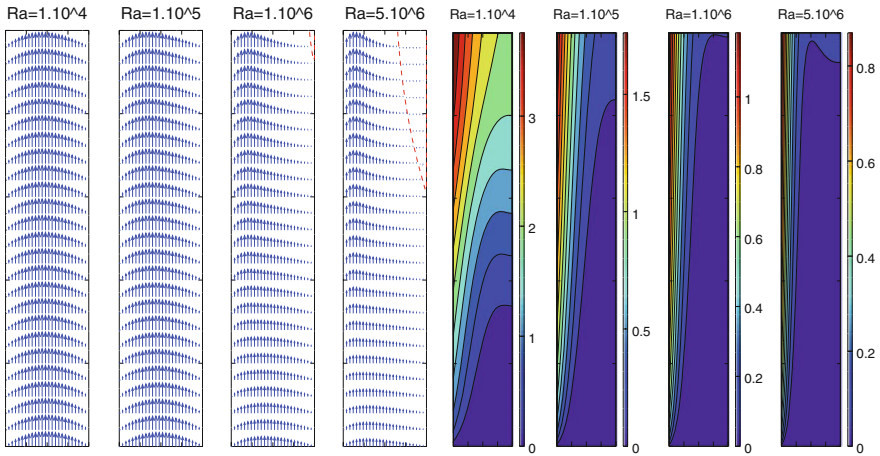


Fig. 6 Velocity and temperature fields for the test case of different Ra 's at $H/b = 5$. Red line indicates the separation zone

Secondly, the ratio of H/b was fixed, while the Rayleigh number changed. Figure 6 shows the results for the test case of $H/b = 5$ and $Ra = 10^4, 10^5, 10^6$, and 5.10^6 . The thermal layer becomes thinner as Ra increases. At $Ra = 5.10^6$, the induced airflow occupies the left half of the upper part of the channel, while a reverse flow exists on the right half. At low $Ra (10^4)$, heat transfer under thermal diffusion mode dominates [10]. As Ra increases, the convection mode affects more and yields thinner thermal layers as shown in Fig. 6. Similar to the case of $H/b = 3$ in Fig. 5, a reverse flow is clear for the case of $Ra = 5.10^6$ in Fig. 6.

The above characteristics of the thermal and induced airflow layers, as well as the appearance of the reverse flow, are similar to the results in the literature [1, 2]. Chen et al. [1] reported that a reverse flow appeared in their chimney of 1.5 m height as the width was larger than 0.3 m. As the width of the channel further increased, the separation zone enhanced and penetrated further into the channel [1, 2]. The penetration depth also increased with Ra [2].

3.4 Suppressing the Reverse Flow by Redistributing Heat Source on Both Sides of the Channel

As reported in the literature [1, 2], from our previous study [3], and as shown in the Figs. 8 and 9, the induced air flowrate through a solar chimney increases with the height and the heat flux. However, beyond the value of H/b or Ra from which the reverse flow happens, the increase rate of the induced flowrate decreases significantly. A relationship between H/b and Ra where the reverse flow initiates at the outlet of a vertical solar chimney was proposed in our previous study [3]:

$$H/b = 0.224 Ra^{0.2415} \quad (12)$$

To enhance the performance (induced flowrate) of a solar chimney, it is necessary to suppress the separation zone at the outlet. A simple method is to redistribute the heat source on the surfaces inside the air channel so that the thermal layer can expand to the space of the separation zone. In this study, it is proposed that the heat source is distributed both on lower half of one wall and on the upper half of the opposite wall of the air channel. This distribution does not change the total heat transfer rate inside the air channel since the total surface area for heat transfer is unchanged.

Figure 7 shows velocity and temperature distributions inside the channel in Fig. 6 ($H/b = 5$ and $Ra = 10^4, 10^5, 10^6$, and $5 \cdot 10^6$) with uniform heat flux applied on lower half of the left wall and upper half of the right wall. The separation zones at the outlet of the chimney of the case $Ra = 10^6$ and $Ra = 5 \cdot 10^6$ did not exist. Comparison of the temperature distribution in Figs. 6 and 7 shows that the thermal layer in Fig. 6 on the left wall continues to expand on the upper half, where there is no heat source, although the temperature value is lower. The thermal layer on the upper half of the right wall combines with the one on the left wall at the outlet to induce nonnegative velocity in the y direction. The velocity distribution for the case of lowest Ra (10^4) is similar as the one in Fig. 6. As the Ra increases, toward the upper half of the channel, with weaker thermal layer near the left wall and new thermal layer on the right wall, the velocity distribution is shifted to the right wall.

To suppress the flow reversal at the outlet, Khanal and Lei [2] proposed that the glazing plate is inclined toward the top of the absorber surface. By that way, the

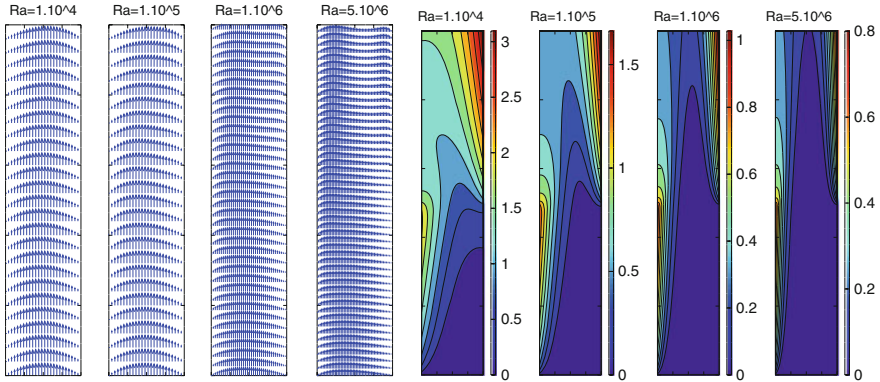
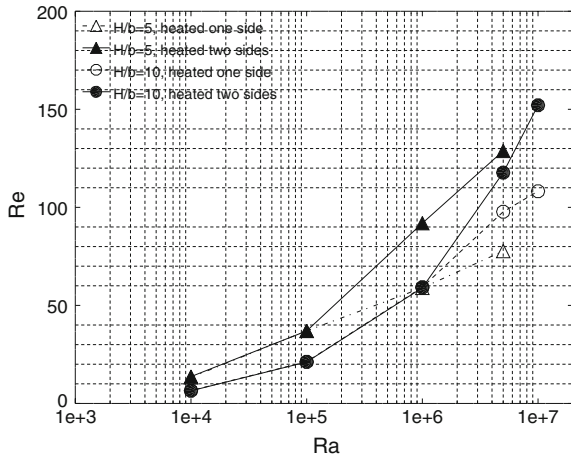


Fig. 7 Velocity and temperature distributions for the chimney in Fig. 6 with heat source distributed on both lower half of the left wall and upper half of the right wall

Fig. 8 Induced flowrate in term of the Reynolds number at different Ra's for $H/b = 5$ and 10

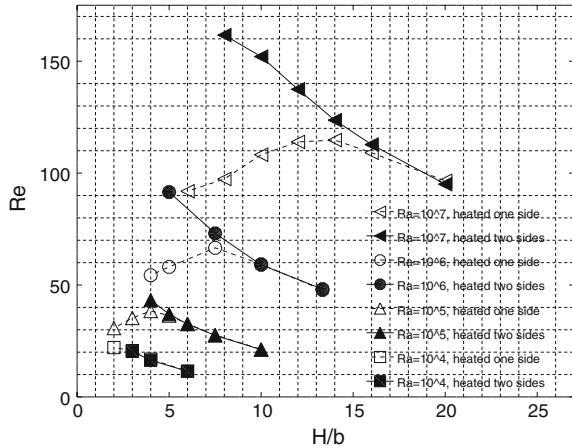


region of weakly heated air near the outlet was eliminated in their chimneys at Ra from 10^9 to 10^{11} .

3.5 Induced Air Flowrate

Induced air flowrate for the chimneys in Figs. 6 and 7 is presented in Fig. 8 together with another test case with $H/b = 10$. The flowrate is expressed in term of the Reynolds number which is based on the mean velocity in the channel and the width of the channel. For both cases of H/b , at low Ra, the induced flowrate is indistinguishable from each other as the heat source is on one side or two sides.

Fig. 9 Induced flowrate at different channel heights (H/b) and heat fluxes (Ra)

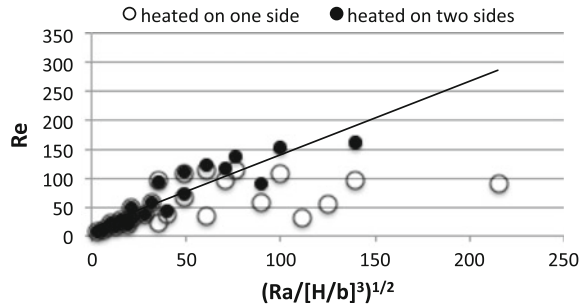


However, as the Ra increases and reverse flow exists at the outlet, the induced flowrate when the heat source is distributed on both sides is significantly higher. Khanal and Lei [2] also reported that eliminating the reverse flow enhanced the induced flowrate.

It is also noted in Fig. 8 that induced flowrate of the case $H/b = 10$ is below that of the case $H/b = 5$. This trend seems to be opposite to the findings in the literature at higher Rayleigh numbers [1, 2]. To further investigate this point, numerical simulations were conducted with more values of H/b and Ra . The results for the induced flowrate are plotted in Fig. 9, for $Ra = 10^4, 10^5, 10^6,$ and 10^7 , while H/b is from 2 to 20. When the heat source is on one side, the induced flowrate is seen to increase with the ratio of H/b up to a particular ratio and then decreases as H/b increases further. The value of the critical H/b at which the induced flowrate peaks is seen to be higher for higher Ra value. Below the critical H/b , the induced flowrate through the chimney heated on one side is always below that of the chimney heated on both sides.

However, the induced flowrate for the chimney heated on both sides drops steadily with the increase of H/b at all values of Ra . This can be explained as the dominance of viscous effect at low Rayleigh number [11]. Khanal and Lei [11] showed a linear relationship between the induced flowrate and a scaling factor of $(Ra/[H/b]^3)^{1/2}$ as a result of the viscous effect. To check this effect in our results, the data in Fig. 9 are replotted in Fig. 10 using their proposed scaling factor. It is seen that the induced flowrate for the cases of the heat source on both sides and the heat source on one side of the channel without a reverse flow fits this scaling, while the data points for the cases with flow separation at the outlet do not follow. The difference can be explained as effects of the reverse flow.

Fig. 10 Induced flowrate in Fig. 9 as a function of the scaling factor $(Ra/[H/b]^3)^{1/2}$



4 Conclusions

In this paper, a Lattice Boltzmann Method model was used to investigate flow structure and temperature field inside a vertical solar chimney under effects of the dimensions of the chimney and heat flux. The results showed that flow structure, and hence the induced flowrate, was influenced by both thermal and viscous effects. Particularly, reverse flow existed at the outlet of the chimney at low ratio of the chimney height and width or high Rayleigh number. The separation zone reduced the increase rate of the induced flowrate with the Raleigh number. A simple method to suppress the reverse flow by distributing the heat source on both sides of the air channel was proposed and showed to enhance the induced flowrate significantly.

References

1. Chen ZD, Bandopadhyay P, Halldorsson J, Byrjalen C, Heiselberg P, Li Y (2003) An experimental investigation of a solar chimney model with uniform wall heat flux. *Build Environ* 38:893–906
2. Khanal R, Lei C (2012) Flow reversal effects on buoyancy induced air flow in a solar chimney. *Sol Energy* 86:2783–2794
3. Nguyen Quoc Y (2016) Numerical simulations of characteristics of the induced air flowrate through inclined solar chimneys. *J Sci Technol—DaNang University* 102(5):137–141
4. <https://www.bca.gov.sg/zeb/daylightsystems.html>
5. Aung W, Fletcher LS, Sernas V (1972) Developing laminar free convection between vertical flat plates with asymmetric heating. *Int J Heat Transf* 15:2293–2308
6. Mohamad AA (2011) *Lattice Boltzmann method: fundamentals and engineering applications with computer codes*. Springer
7. Zou Q, He X (1997) On pressure and velocity boundary conditions for the lattice Boltzmann BGK model. *Phys Fluids* 9:1591–1598
8. Mohamad AA, Kuzmin A (2010) A critical evaluation of force term in lattice Boltzmann method, natural convection problem. *Int J Heat Mass Transf* 53:990–996
9. Mohamad AA, El-Ganaoui M, Bennacer R (2009) Lattice Boltzmann Simulation of natural convection in an open ended cavity. *Int J Therm Sci* 48:1870–1875

10. Bergman TL, Lavine AS, Dewitt DP (2011) Introduction to heat transfer, 6th edn. Wiley
11. Khanal R, Lei C (2014) A scaling investigation of the laminar convective flow in a solar chimney for natural ventilation. *Int J Heat Fluid Flow* 45:98–108

A Dual Approach to Modeling Solute Transport



H. Nguyen-The

Abstract The classic average method is usually applied to describe the solute transport equation of one-dimensional horizontal flow or two-dimensional horizontal flow. The solute transport equation is totally integrated one time from the bed to the water surface; the average values received by classic average method do not generalize by means of dual approach. So, in this paper, a dual approach is applied to solve the solute transport equation of two-dimensional horizontal flow. The equation describing the depth average concentration is obtained by two times integration: The first time integral is from the bed to the intermediate surface lays between bed and water surface, and the second time integral is from the bed to the water surface. With the dual approach, the received depth average concentration is better, particularly, in the case of stratification, mixed solute, and so on. The received governing equation based on the dual approach describes more accurately the physical characteristic of the transport phenomena in nature. Moreover, it provides flexible parameter adjustment based on the experimental data. A case study of salinity transport in Huong river is illustrated.

Keywords Dual approach • Solute transport equation • Depth average concentration

1 Introduction

To obtain the solute transport of one-dimensional (1D) or two-dimensional (2D) horizontal flow equations, one often integrated the three-dimensional (3D) flow equation from the bed to the water surface [1]; the average values received in the 1D or 2D equations are called the global average value (GAV). According to [2], the global-local average values (GLAVs) obtained using the dual approach are more general than the GAV. Thus, in this paper, the author establishes the 2D solute

H. Nguyen-The (✉)

Faculty of Water Resources Engineering, The University of Danang, Danang, Vietnam
e-mail: hungnt@ud.edu.vn; profhungthenguyen@gmail.com

© Springer Nature Singapore Pte Ltd. 2018

H. Nguyen-Xuan et al. (eds.), *Proceedings of the International Conference on Advances in Computational Mechanics 2017*, Lecture Notes in Mechanical Engineering, https://doi.org/10.1007/978-981-10-7149-2_58

821

transport equation based on the dual approach [2, 3], the 3D solute transport integrated twice: The first time integral is from the bed to the intermediate surface layers between bed and the water surface, and the second time integral is from the bed to the water surface. The obtained average solute transport equation can describe complex physical phenomena such as the stratification solute transport average equation, mixed solute, and so on.

2 Building 2D Solute Transport Equation Based on the Dual Approach

The three-dimensional transport equation in the form of conservation [1]:

$$\underbrace{\frac{\partial c}{\partial t}}_{(I)} + \underbrace{\frac{\partial(uc)}{\partial x}}_{(J)} + \underbrace{\frac{\partial(vc)}{\partial y}}_{(K)} + \underbrace{\frac{\partial(wc)}{\partial z}}_{(L)} \tag{1}$$

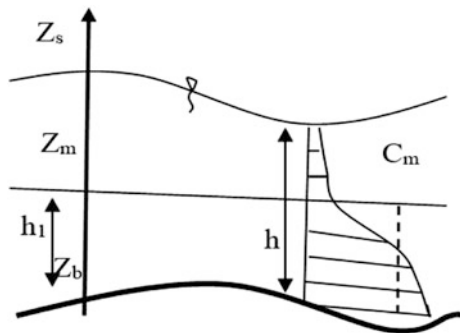
$$= \underbrace{\frac{\partial}{\partial x} \left\{ (D + \varepsilon_x) \frac{\partial c}{\partial x} \right\}}_{(M)} + \underbrace{\frac{\partial}{\partial y} \left\{ (D + \varepsilon_y) \frac{\partial c}{\partial y} \right\}}_{(N)} + \underbrace{\frac{\partial}{\partial z} \left\{ (D + \varepsilon_z) \frac{\partial c}{\partial z} \right\}}_{(P)}$$

First, integrating the term (I) from the bed to the intermediate surface Z_m layers between the bed and the water surface (see Fig. 1).

In Fig. 1, h is water depth; h_1 is the depth at which the concentration C_m is nearly equal to zero; Z_b , Z_m , and Z_s are corresponding bed, h_1 , and water surface elevation.

$$TI = \int_{Z_b}^{Z_m} \frac{\partial c}{\partial t} dz = \frac{\partial}{\partial t} \int_{Z_b}^{Z_m} c dz - \int_{Z_b}^{Z_m} c \frac{\partial(dz)}{\partial t} = \frac{\partial}{\partial t} (\bar{C}h_1) - \bar{C}_1 \cdot \frac{\partial h_1}{\partial t} \tag{2}$$

Fig. 1 Sketch of dual approach the solute transport equations



where \bar{C} and \bar{C}_1 are the average concentrations of the depth h and h_1 , respectively, given by:

$$\bar{C} = \frac{1}{h} \int_{Z_b}^{Z_s} c dz = \frac{1}{h} \left(\int_{Z_b}^{Z_m} c dz + \int_{Z_m}^{Z_s} c dz \right) = \frac{1}{h} \int_{Z_b}^{Z_m} c dz \tag{3a}$$

(because, from Z_m to Z_s , $C = 0$).

Posing \bar{C}_1 is average concentration, such that:

$$\int_{Z_b}^{Z_m} c \cdot \frac{\partial(dz)}{\partial t} = \bar{C}_1 \int_{Z_b}^{Z_m} \frac{\partial(dz)}{\partial t} = \bar{C}_1 \frac{\partial h_1}{\partial t} \tag{3b}$$

$$\bar{C}_1 = \frac{1}{\frac{\partial h_1}{\partial t}} \int_{Z_b}^{Z_m} c \cdot \frac{\partial(dz)}{\partial t}$$

$$\bar{C}_1 = \alpha_1 \cdot \bar{C} \tag{3c}$$

where

$$\alpha_1 = \frac{\bar{C}_1}{\bar{C}} = \frac{1}{\bar{C} \frac{\partial h_1}{\partial t}} \int_{Z_b}^{Z_m} c \cdot \frac{\partial(dz)}{\partial t} \tag{3d}$$

Then, integrating the term (I) in Eq. (1), the second time, from the bed to the water surface:

$$T^2 I = \int_{Z_b}^{Z_s} \left\{ \frac{\partial}{\partial t} (\bar{C} \cdot h_1) - \bar{C}_1 \cdot \frac{\partial h_1}{\partial t} \right\} dh_1 = \underbrace{\int_{Z_b}^{Z_s} \left\{ \frac{\partial}{\partial t} (\bar{C} h_1) \right\} dh_1}_{I_1} - \underbrace{\int_{Z_b}^{Z_s} \bar{C}_1 \cdot \frac{\partial h_1}{\partial t} dh_1}_{I_2} \tag{4.a}$$

$$T^2 I_1 = \int_{Z_b}^{Z_s} \left\{ \frac{\partial}{\partial t} (\bar{C} h_1) \right\} dh_1 = \underbrace{\frac{\partial}{\partial t} \int_{Z_b}^{Z_s} \bar{C} h_1 \cdot dh_1}_{I_{11}} - \underbrace{\int_{Z_b}^{Z_s} \bar{C} h_1 \cdot \frac{\partial}{\partial t} (dh_1)}_{I_{12}} \tag{4.b}$$

where

$$I_{11} = \frac{1}{2} \cdot \frac{\partial}{\partial t} \{ \bar{C}(Z_s^2 - Z_b^2) \} \tag{4.c}$$

$$I_{12} = \underbrace{\int_{Z_b}^{Z_s} \bar{C} h_1 \cdot \frac{\partial}{\partial t} (dh_1)}_{I_{12}} \cong I_2 = \underbrace{\int_{Z_b}^{Z_s} \bar{C}_1 \cdot \frac{\partial h_1}{\partial t} dh_1}_{I_2} = \frac{1}{2} \cdot \bar{C}_{12} \left\{ \frac{\partial}{\partial t} (Z_s^2 - Z_b^2) \right\} \tag{4.d}$$

Let

$$\bar{C}_{12} = \alpha_{12} \cdot \bar{C} \tag{4.e}$$

where

$$\alpha_{12} = \frac{2}{\bar{C} \frac{\partial}{\partial t} (Z_s^2 - Z_b^2)} \cdot \int_{Z_b}^{Z_s} \bar{C}_1 \cdot \frac{\partial}{\partial t} (z dz) = \frac{2}{\bar{C} \frac{\partial}{\partial t} (Z_s^2 - Z_b^2)} \cdot \int_{Z_b}^{Z_s} \left\{ \frac{1}{\frac{\partial h}{\partial t}} \int_{Z_b}^{Z_m} c \cdot \frac{\partial (dz)}{\partial t} \right\} \cdot \frac{\partial}{\partial t} (z dz) \tag{4.f}$$

With

$$T^2 I = I_1 - I_2 = (I_{11} - I_{12}) - I_2 = I_{11} - 2I_{12} \tag{4.g}$$

$$T^2 I = \frac{1}{2} \cdot \frac{\partial}{\partial t} \{ \bar{C}(Z_s^2 - Z_b^2) \} - \alpha_{12} \bar{C} \left\{ \frac{\partial}{\partial t} (Z_s^2 - Z_b^2) \right\} \tag{5.a}$$

In the non-conservative form,

$$T^2 I \cong \frac{1}{2} (Z_s^2 - Z_b^2) \cdot \frac{\partial}{\partial t} (\bar{C}) - \frac{1}{2} \alpha_{12} \bar{C} \cdot \frac{\partial}{\partial t} (Z_s^2 - Z_b^2) \tag{5.b}$$

Similarly, integrating the second term (J), the first time, from the bed to the intermediate surface Z_m layers between the bed and the water surface (see Fig. 1):

$$TJ = \int_{Z_b}^{Z_m} \frac{\partial uc}{\partial x} \cdot dz = \frac{\partial}{\partial x} \int_{Z_b}^{Z_m} ucdz - \int_{Z_b}^{Z_s} uc \frac{\partial}{\partial x} (dz) = \frac{\partial}{\partial x} (h_1 \cdot \bar{UC}) - \beta_1 \cdot \bar{UC} \cdot \frac{\partial}{\partial x} (h_1) \tag{6.a}$$

where

$$\overline{UC} = \frac{1}{h_1} \int_{Z_b}^{Z_m} (uc) \cdot dz \tag{6.b}$$

$$\beta_1 = \frac{1}{\overline{UC} \frac{\partial h}{\partial x}} \cdot \int_{Z_b}^{Z_m} uc \frac{\partial}{\partial x} (dz) \tag{6.c}$$

Integrating the term (J) or Eq. (6.a), the second time, from the bed to the water surface:

$$T^2 J = \underbrace{\int_{Z_b}^{Z_s} \frac{\partial}{\partial x} (h_1 \cdot \overline{UC}) dz}_{J_1} - \underbrace{\int_{Z_b}^{Z_s} \beta_1 \cdot \overline{UC} \cdot \frac{\partial}{\partial x} (h_1) dz}_{J_2} \tag{7.a}$$

where

$$J_1 = \int_{Z_b}^{Z_s} \frac{\partial}{\partial x} (h_1 \cdot \overline{UC}) dz = \underbrace{\frac{\partial}{\partial x} \int_{Z_b}^{Z_s} h_1 \cdot \overline{UC} dz}_{J_{11}} - \underbrace{\int_{Z_b}^{Z_s} \beta_1 h_1 \overline{UC} \frac{\partial}{\partial x} (dz)}_{J_{12}} \tag{7.b}$$

$$J_1 = \underbrace{\frac{\partial}{\partial x} \left\{ \beta_2 \overline{UC} \frac{1}{2} (Z_s^2 - Z_b^2) \right\}}_{J_{11}} - \underbrace{\beta_1 \beta_3 \overline{UC} \frac{1}{2} \frac{\partial}{\partial x} (Z_s^2 - Z_b^2)}_{J_{12}}$$

Noticed

$$J_2 = J_{12} \tag{7.c}$$

So,

$$T_{2J} = J_1 - J_2 = (J_{11} - J_{12}) - J_2 = J_{11} - 2J_{12} \tag{8.a}$$

$$J_1 = \frac{1}{2} \beta_2 \frac{\partial}{\partial x} \{ \overline{UC} \cdot (Z_s^2 - Z_b^2) \} - \beta_1 \beta_3 \overline{UC} \frac{\partial}{\partial x} (Z_s^2 - Z_b^2) \tag{8.b}$$

where

$$\beta_2 = \frac{1}{\overline{UC} \frac{h^2}{2}} \int_{Z_b}^{Z_s} \overline{UC} h_1 dz \tag{8.c}$$

$$\beta_3 = \frac{1}{\overline{UC} \frac{\partial}{\partial x} (Z_s^2 - Z_b^2)} \int_{Z_b}^{Z_s} \overline{UC} \frac{\partial}{\partial x} (z dz) \tag{8.d}$$

Again, integrating, the first time, the third term (K) on the left-hand side of the Eq. (1) from bed to the water surface, we have:

$$TK = \int_{Z_b}^{Z_m} \frac{\partial}{\partial y} (vc) dz = \underbrace{\frac{\partial}{\partial y} \int_{Z_b}^{Z_m} (vc) dz}_{K_1} - \underbrace{\int_{Z_b}^{Z_m} (vc) \frac{\partial}{\partial y} (dz)}_{K_2} \tag{9.a}$$

where

$$K_1 = \frac{\partial}{\partial y} \int_{Z_b}^{Z_m} (vc) dz = \frac{\partial}{\partial y} (\overline{VC} \cdot h_1) \tag{9.b}$$

$$K_2 = \int_{Z_b}^{Z_m} (vc) \frac{\partial}{\partial y} (dz) = \delta_1 \cdot (\overline{VC}) \cdot \frac{\partial}{\partial y} (Z_m - Z_b) = \delta_1 \cdot (\overline{VC}) \cdot \frac{\partial}{\partial y} (h_1) \tag{9.c}$$

Thus,

$$TK = \frac{\partial}{\partial y} (\overline{VC} \cdot h_1) + \delta_1 \cdot (\overline{VC}) \cdot \frac{\partial}{\partial y} (h_1) \tag{9.d}$$

where

$$\overline{VC} = \frac{1}{h_1} \int_{Z_b}^{Z_m} (vc) dz \tag{10.a}$$

$$\delta_1 = \frac{1}{(\overline{VC}) \cdot \frac{\partial}{\partial y} (h_1)} \int_{Z_b}^{Z_m} (\overline{VC}) \frac{\partial}{\partial y} (dz) \tag{10.b}$$

Similarly, integrating the term (K) in the Eq. (9.d), the second time, we receive:

$$T^2 K = \underbrace{\int_{Z_b}^{Z_s} \frac{\partial}{\partial y} (\overline{VC} \cdot h_1) dz}_{K_{11}} + \underbrace{\int_{Z_b}^{Z_s} \delta_1 \cdot (\overline{VC}) \cdot \frac{\partial}{\partial y} (h_1) dz}_{K_{22}} \tag{11.a}$$

$$K_{11} = \int_{Z_b}^{Z_s} \frac{\partial}{\partial y} (\overline{VC} \cdot h_1) dz = \underbrace{\frac{\partial}{\partial y} \int_{Z_b}^{Z_s} \overline{VC} \cdot h_1 \cdot dz}_{K_{111}} - \underbrace{\int_{Z_b}^{Z_s} (\overline{VC}) \cdot h_1 \frac{\partial}{\partial y} (dz)}_{K_{112}} \tag{11.b}$$

$$K_{11} = \underbrace{\frac{\partial}{\partial y} \left\{ \delta_2 \cdot \overline{VC} \cdot \frac{1}{2} (Z_s^2 - Z_b^2) \right\}}_{K_{111}} - \underbrace{\delta_3 \cdot \overline{VC} \frac{1}{2} \frac{\partial}{\partial y} (Z_s^2 - Z_b^2)}_{K_{112}}$$

We have:

$$K_{22} \approx K_{112}$$

Therefore,

$$T_{2k} = K_{11} - K_{22} = (K_{111} - K_{112}) - K_{22} = K_{111} - 2K_{112} \tag{11.c}$$

The correction coefficients δ_2 and δ_3 are calculated as follows:

$$\delta_2 = \frac{2}{(\overline{VC}) \cdot (Z_s^2 - Z_b^2)} \int_{Z_b}^{Z_m} \left(\frac{1}{h_1} \int_{Z_b}^{Z_m} (vc) dz \right) h(dz) \tag{11.d}$$

$$\delta_3 = \frac{2}{(\overline{VC}) \cdot \frac{\partial}{\partial y} (Z_s^2 - Z_b^2)} \int_{Z_b}^{Z_m} \left(\frac{1}{h_1} \int_{Z_b}^{Z_m} (vc) dz \right) \frac{\partial}{\partial y} (z dz) \tag{11.e}$$

Integrating the fourth term (L) on the left-hand side of Eq. (1) the first time, we obtain:

$$TL = \int_{Z_b}^{Z_m} \frac{\partial(\omega c)}{\partial z} dz = 0 \quad (\omega \approx 0) \tag{12}$$

Integrating the first term (M) on the right-hand side of Eq. (1), the first time, we have:

$$TM = \int_{Z_b}^{Z_m} \frac{\partial}{\partial x} \left\{ (D + \varepsilon_x) \cdot \frac{\partial c}{\partial x} \right\} dz = \gamma_1 \frac{\partial}{\partial x} \left\{ (D + \varepsilon_x) \cdot \frac{\partial \bar{C}}{\partial x} \right\} \cdot (Z_m - Z_b) \quad (13.a)$$

where

$$\gamma_1 = \frac{1}{\frac{\partial}{\partial x} \left\{ (D + \varepsilon_x) \cdot \frac{\partial \bar{C}}{\partial x} \right\} \cdot (Z_m - Z_b)} \cdot \int_{Z_b}^{Z_m} \frac{\partial}{\partial x} \left\{ (D + \varepsilon_x) \cdot \frac{\partial c}{\partial x} \right\} dz \quad (13.b)$$

Integrating the term (M) of Eq. (13.a), the second time, we receive:

$$T^2M = \int_{Z_b}^{Z_s} \gamma_1 \frac{\partial}{\partial x} \left\{ (D + \varepsilon_x) \cdot \frac{\partial \bar{C}}{\partial x} \right\} \cdot h_1 dz = \frac{1}{2} \cdot \gamma_1 \cdot \gamma_2 \frac{\partial}{\partial x} \left\{ (D + \varepsilon_x) \cdot \frac{\partial \bar{C}}{\partial x} \right\} \cdot (Z_s^2 - Z_b^2) \quad (14.a)$$

The coefficient γ_2 is calculated by:

$$\gamma_2 = \frac{2}{\frac{\partial}{\partial x} \left\{ (D + \varepsilon_x) \cdot \frac{\partial \bar{C}}{\partial x} \right\} \cdot (Z_s^2 - Z_b^2)} \cdot \int_{Z_b}^{Z_s} \frac{\partial}{\partial x} \left\{ (D + \varepsilon_x) \cdot \frac{\partial \bar{C}}{\partial x} \right\} \cdot h_1 dz \quad (14.b)$$

Thus,

$$T^2M = \frac{1}{2} \cdot \gamma_1 \cdot \gamma_2 \frac{\partial}{\partial x} \left\{ (D + \varepsilon_x) \cdot \frac{\partial \bar{C}}{\partial x} \right\} \cdot (Z_s^2 - Z_b^2) \quad (14.c)$$

Similarly, integrating the second term (N) on the right-hand side of Eq. (1), the first time, we have:

$$TN = \int_{Z_b}^{Z_m} \frac{\partial}{\partial y} \left\{ (D + \varepsilon_y) \cdot \frac{\partial c}{\partial y} \right\} dz = \theta_1 \frac{\partial}{\partial y} \left\{ (D + \varepsilon_y) \cdot \frac{\partial \bar{C}}{\partial x} \right\} \cdot (Z_m - Z_b) \quad (15.a)$$

where

$$\theta_1 = \frac{1}{\frac{\partial}{\partial y} \left\{ (D + \varepsilon_y) \cdot \frac{\partial \bar{C}}{\partial y} \right\} \cdot (Z_m - Z_b)} \cdot \int_{Z_b}^{Z_m} \frac{\partial}{\partial y} \left\{ (D + \varepsilon_y) \cdot \frac{\partial c}{\partial y} \right\} dz \quad (15.b)$$

Integrating the term (N) of Eq. (15.a), the second time, we obtain:

$$T^2N = \int_{Z_b}^{Z_s} \theta_1 \frac{\partial}{\partial y} \left\{ (D + \varepsilon_y) \cdot \frac{\partial \bar{C}}{\partial y} \right\} \cdot h_1 dz = \frac{1}{2} \cdot \theta_1 \cdot \theta_2 \frac{\partial}{\partial y} \left\{ (D + \varepsilon_y) \cdot \frac{\partial \bar{C}}{\partial y} \right\} \cdot (Z_s^2 - Z_b^2) \tag{15.c}$$

The coefficient θ_2 is calculated by:

$$\theta_2 = \frac{2}{\frac{\partial}{\partial y} \left\{ (D + \varepsilon_y) \cdot \frac{\partial \bar{C}}{\partial y} \right\} \cdot (Z_s^2 - Z_b^2)} \cdot \int_{Z_b}^{Z_s} \frac{\partial}{\partial y} \left\{ (D + \varepsilon_y) \cdot \frac{\partial \bar{C}}{\partial y} \right\} \cdot h_1 dz \tag{15.d}$$

Therefore,

$$T^2N = \frac{1}{2} \cdot \theta_1 \cdot \theta_2 \frac{\partial}{\partial y} \left\{ (D + \varepsilon_y) \cdot \frac{\partial \bar{C}}{\partial y} \right\} \cdot (Z_s^2 - Z_b^2) \tag{15.e}$$

Integrating the thirist term (P) on the right-hand side of Eq. (1), the first time, we have:

$$TP = \int_{Z_b}^{Z_m} \frac{\partial}{\partial z} \left\{ (D + \varepsilon_z) \cdot \frac{\partial c}{\partial z} \right\} dz = (D + \varepsilon_z) \cdot \frac{\partial c}{\partial z} \Big|_m - (D + \varepsilon_z) \cdot \frac{\partial c}{\partial z} \Big|_b \tag{16.a}$$

Integrating the term (P) the second time, we obtain:

$$T^2P = \int_{Z_b}^{Z_s} (D + \varepsilon_z) \cdot \frac{\partial c}{\partial z} \Big|_m dz - \int_{Z_b}^{Z_s} (D + \varepsilon_z) \cdot \frac{\partial c}{\partial z} \Big|_b dz \tag{16.b}$$

$$T^2P = (D + \varepsilon_z) \cdot \frac{\partial c}{\partial z} \Big|_m \cdot h - (D + \varepsilon_z) \cdot \frac{\partial c}{\partial z} \Big|_b \cdot h = (D + \varepsilon_z) \cdot h \cdot \left\{ \frac{\partial c}{\partial z} \Big|_m - \frac{\partial c}{\partial z} \Big|_b \right\} \tag{16.c}$$

In case,

$$\frac{\partial c}{\partial z} \Big|_{Z_m} = \frac{\partial c}{\partial z} \Big|_{Z_b}, \text{ then the term } T^2P = 0$$

Therefore, the 2D solute transport equation based on the dual approach can be presented as:

$$T^2I + T^2J + T^2K + TL = T^2M + T^2N + T^2P$$

$$\begin{aligned}
& \frac{1}{2} \cdot \frac{\partial}{\partial t} \{ \bar{C}(Z_s^2 - Z_b^2) \} - \alpha_{12} \bar{C} \left\{ \frac{\partial}{\partial t} (Z_s^2 - Z_b^2) \right\} + \frac{1}{2} \beta_2 \frac{\partial}{\partial x} \{ \overline{UC} \cdot (Z_s^2 - Z_b^2) \} - \beta_1 \beta_3 \overline{UC} \frac{\partial}{\partial x} (Z_s^2 - Z_b^2) \\
& + \frac{1}{2} \delta_2 \cdot \frac{\partial}{\partial y} \{ \overline{VC} \cdot (Z_s^2 - Z_b^2) \} - \delta_1 \delta_3 \cdot \overline{VC} \frac{\partial}{\partial y} (Z_s^2 - Z_b^2) = \frac{1}{2} \cdot \gamma_1 \cdot \gamma_2 \frac{\partial}{\partial x} \left\{ (D + \varepsilon_x) \cdot \frac{\partial \bar{C}}{\partial x} \right\} \cdot (Z_s^2 - Z_b^2) \\
& + \frac{1}{2} \cdot \theta_1 \cdot \theta_2 \frac{\partial}{\partial y} \left\{ (D + \varepsilon_y) \cdot \frac{\partial \bar{C}}{\partial y} \right\} \cdot (Z_s^2 - Z_b^2) + (D + \varepsilon_z) \cdot h \cdot \left\{ \frac{\partial c}{\partial z} \Big|_m - \frac{\partial c}{\partial z} \Big|_b \right\}
\end{aligned} \tag{17}$$

From Eq. (17), we receive the 1D solute transport equation as follows:

$$\begin{aligned}
& \frac{1}{2} \cdot \frac{\partial}{\partial t} \{ \bar{C}(Z_s^2 - Z_b^2) \} - \alpha_{12} \bar{C} \left\{ \frac{\partial}{\partial t} (Z_s^2 - Z_b^2) \right\} + \frac{1}{2} \beta_2 \frac{\partial}{\partial x} \{ \overline{UC} \cdot (Z_s^2 - Z_b^2) \} - \beta_1 \beta_3 \overline{UC} \frac{\partial}{\partial x} (Z_s^2 - Z_b^2) \\
& = \frac{1}{2} \cdot \gamma_1 \cdot \gamma_2 \frac{\partial}{\partial x} \left\{ (D + \varepsilon_x) \cdot \frac{\partial \bar{C}}{\partial x} \right\} \cdot (Z_s^2 - Z_b^2) + (D + \varepsilon_z) \cdot h \cdot \left\{ \frac{\partial c}{\partial z} \Big|_m - \frac{\partial c}{\partial z} \Big|_b \right\}
\end{aligned} \tag{18}$$

3 Comments

It is easy to see that the 2D transport equation averaged by the classical method is a special case of the general form Eq. (17). In fact, if $Z_s - Z_b = h \approx \text{Const}$, so: $\frac{\partial}{\partial t} (Z_s^2 - Z_b^2) \approx 0$, $\frac{\partial}{\partial x} (Z_s^2 - Z_b^2) \approx 0$, $\frac{\partial}{\partial y} (Z_s^2 - Z_b^2) \approx 0$ (the water level changes insignificantly over time and space) and the coefficients $(\alpha_i, \beta_i, \delta_i, \gamma_i, \theta_i) = 1$, $\frac{\partial c}{\partial z} \Big|_m \cong \frac{\partial c}{\partial z} \Big|_b$ then Eq. (17) arrive at the 2D transport equation averaged by the classical method [Eq. (19)]:

$$\begin{aligned}
\frac{\partial}{\partial t} \{ \bar{C}(Z_s^2 - Z_b^2) \} + \frac{\partial}{\partial x} \{ \overline{UC} \cdot (Z_s^2 - Z_b^2) \} + \frac{\partial}{\partial y} \{ \overline{VC} \cdot (Z_s^2 - Z_b^2) \} &= \frac{\partial}{\partial x} \left\{ (D + \varepsilon_x) \cdot \frac{\partial \bar{C}}{\partial x} \right\} \cdot (Z_s^2 - Z_b^2) \\
&+ \frac{\partial}{\partial y} \left\{ (D + \varepsilon_y) \cdot \frac{\partial \bar{C}}{\partial y} \right\} \cdot (Z_s^2 - Z_b^2)
\end{aligned} \tag{19}$$

From Eq. (19), we receive the 1D classical equation as follows:

$$\frac{\partial}{\partial t} \{ \bar{C}(Z_s^2 - Z_b^2) \} + \frac{\partial}{\partial x} \{ \overline{UC} \cdot (Z_s^2 - Z_b^2) \} = \frac{\partial}{\partial x} \left\{ (D + \varepsilon_x) \cdot \frac{\partial \bar{C}}{\partial x} \right\} \cdot (Z_s^2 - Z_b^2) \tag{20}$$

Simplifying Eq. (20), we achieve:

$$\frac{\partial}{\partial t} \{ \bar{C} \} + \frac{\partial}{\partial x} \{ \overline{UC} \} = \frac{\partial}{\partial x} \left\{ (D + \varepsilon_x) \cdot \frac{\partial \bar{C}}{\partial x} \right\} \tag{21}$$

Equation (21) is the familiar classical 1D solute transport equation.

4 Results and Discussions

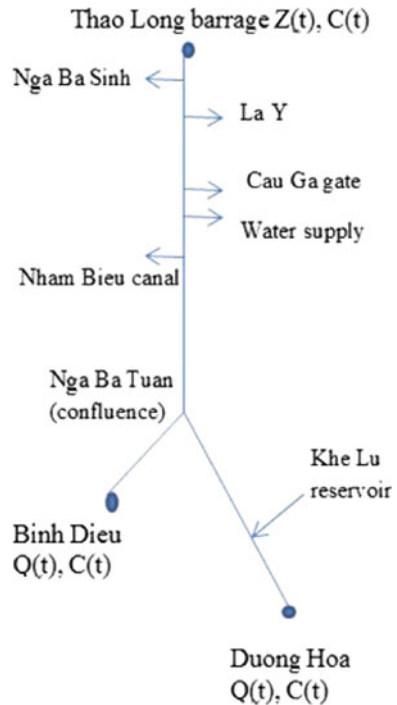
To illustrate the generality of the Eqs. (17) and (18), a case study of the salinity intrusion of Huong river in the dry season is presented [4]. The Huong river system is simply simulated by two branches: Ta Trach and Huu Trach. The confluence is at Nga Ba Tuan, and then it flows along the mainstream of Huong river to the Thao Long barrage [4], see Fig. 2.

The upstream discharge boundary condition is implied at the junction Nga Ba Tuan $Q = Q_{\text{BinhDieu}} + Q_{\text{DuongHoa}} + Q_{\text{KL}} = (0.98 + Q_{\text{KL}}) \text{ m}^3/\text{s}$. The downstream boundary condition is tidal water level with frequency $P = 25\%$ and is implied at Thao Long barrage, Fig. 3.

To determine the size of Khe Lu reservoir, all step discharge from Khe Lu reservoir is assumed in the document [4].

Applying the finite difference method and using the Preissmann scheme with the weight $\theta = 0.66$ for solving the 1D Saint-Venant equations system [1, 4–7], after that solving the solute transport Eqs. (20) and (21). Equations (20) and (21) are solved by fraction steps: transport equation and diffusion equation. The transport equation is solved by the characteristic method, while the diffusion equation is solved by the weighted finite difference scheme [4, 5].

Fig. 2 Huong river system simplified scheme



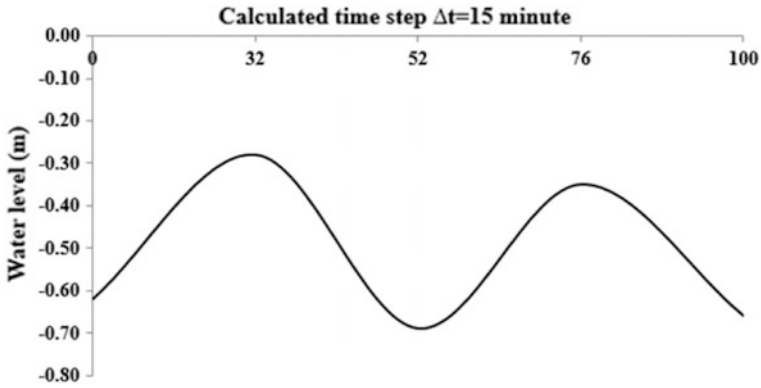


Fig. 3 Downstream water level boundary condition corresponding

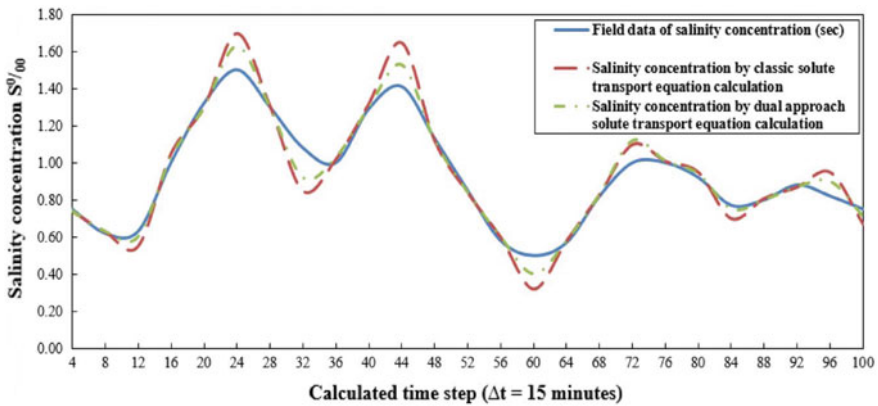


Fig. 4 Changing of salinity at La-Y in a tidal period

The calculated results from Eqs. (20) and (21), the salinity at La-Y corresponding the Khe Lu discharge $Q_{KL} = 10.00 \text{ m}^3/\text{s}$, are plotted in Fig. 4.

5 Comments

Figure 4 shows that results based on the dual approach {Eq. (20)} are more accurate than the classical method {Eq. (21)}. In addition, better results could be potentially achieved by changing the coefficients α_i , β_i , δ_i , γ_i , and θ_i in the general Eq. (18). Though the simulation results based on the dual approach are better than

the classical method, it still cannot capture all the observed data. This is because of the variation of cross-sectional shape and roughness at different water depths and at different locations along the Huong river.

6 Conclusions

The solute transport equations derived from the dual approach, Eqs. (17) and (18), are more general than those received from the classic approach with the appearance of new terms: 2nd, 4th, 6th on the left-hand side of the Eq. (18). As a result, it could be used to describe the solute transport phenomena better compared to the classical method. The correlation coefficients α_i , β_i , δ_i , γ_i , and θ_i increase the adjustable ability of calculated results.

References

1. Weiming W (2008) Computational river dynamics. Taylor & Francis Group, UK
2. Cunge JA et al (1980) Practical aspects of computational river hydraulics. Pitman Publishing INC
3. Anh ND (2012) Dual approach to averaged values of functions. Vietnam J Mech VAST 34 (3):211–214
4. Nguyen The H (1992) Salinity intrusion in Huong river network and the measure of hydraulic construction. J Sci Technol (Five University of Technology) (2):17–21
5. Anh ND (2012) Dual approach to averaged values of functions: advanced formulas. Vietnam J Mech Vast 34(4):321–325
6. Dac NT (1987) One-dimensional mathematical model of salinity intrusion in rivers network. Physical mathematical dissertation, Hanoi
7. Preissmann A (1961) Propagation des intumescences dans les canaux et Les Rivieres. Congres de l'Association Francaise de Calcule, Grenoble, France

A Nonlocal Formulation for Weakly Compressible Fluid



Huilong Ren and Xiaoying Zhuang

Abstract In this paper, we propose a nonlocal formulation for both solid and weakly compressible fluid. The nonlocal fluid formulation is based on the nonlocal interaction of each material point with its neighbors, which is analogous to the peridynamic theory, a nonlocal formulation for solid. By considering the direction of the interaction, the horizon and dual-horizon are defined, and the dual property between horizon and dual-horizon is proved. The nonlocal divergence is introduced, which enables to derive the nonlocal interaction with the local formulation. The formulations allow the varying horizon size and satisfy the conservation of linear momentum, angular momentum, and energy at the same time. Two numerical examples are tested to verify the accuracy of the current method.

Keywords Dual-horizon · Nonlocal formulation · Weakly compressible fluid

1 Introduction

Nonlocality is a general property of material that exists in certain scales including the spatial scale and temporal scale. The nonlocality in spatial scale means that the state of one material point depends on the collective states of its neighbors as well as its own state. The nonlocality in temporal scale often manifests itself as the memory-dependent or history-dependent effect of the material [1]. The nonlocality can be considered as a generalization of local theory, where the interaction and state are defined in the infinitesimal. The theories based on nonlocality are formulated in

H. Ren

Institute of Structural Mechanics, Bauhaus Universität Weimar, Marienstrasse 15,
99423 Weimar, Germany
e-mail: huilong.ren@uni-weimar.de

X. Zhuang (✉)

Institute of Continuum Mechanics, Leibniz University Hannover,
30167 Hannover, Germany
e-mail: zhuang@ikm.uni-hannover.de

© Springer Nature Singapore Pte Ltd. 2018

H. Nguyen-Xuan et al. (eds.), *Proceedings of the International Conference on Advances in Computational Mechanics 2017*, Lecture Notes in Mechanical Engineering, https://doi.org/10.1007/978-981-10-7149-2_59

835

integral form, circumventing the difficulty such as the nonexistence of differential operator for local models and thus showing some advantages in solving problems with strong discontinuities such as cracks.

There have been numerous research on the nonlocal models: for examples, the nonlocal damage model [2], the nonlocal plasticity theory [3], the nonlocal continuum mechanics [1, 4], peridynamics [5], and the nonlocal image processing [6], to name a few. For the conventional nonlocal continuum solid, the controlling equations are obtained by replacing the local material constitution with the nonlocal differential constitutive relations of Eringen that relates the stress tensor to the strain tensor field [1]. One outstanding application among these nonlocal models is the peridynamics theory, which has been successfully used to solve problems involving fractures, strong discontinuities. Peridynamics proposed by Silling [7] contains two main categories: bond-based peridynamics [7] and state-based peridynamics [5]. Peridynamics has clear physical meaning for the nonlocal interaction and thus allows the modeling of fractures with ease. The horizon of one point in peridynamics represents the nonlocal domain, the neighbors of that point. Peridynamics allows for variable horizons [8] and the conventional various material constitutions. However, most of them concentrate on the solid mechanics; there is very few formulation on the nonlocal fluid. In this paper, we propose a simple formulation for nonlocal fluid, to model the weakly compressible fluid dynamics.

The content of the chapter is organized as follows. In sect. 2 some concepts on the horizon and dual-horizon based on Newton's third law are presented. sect. 3 derives the nonlocal forms of equation of motion and energy equation, and calculates the various bond forces based on the nonlocal divergence theory. sect. 4 discusses the numerical implementation of the nonlocal formulation. In sect. 5, two numerical examples including thermal conduction and dam break on the dry bed are presented to validate the method.

2 Basic Concepts

Consider the domain in the initial and current configuration as shown in Fig. 1a, for any material point i ; let \mathbf{R}_i be the material coordinate in the initial configuration Ω_0 , $\mathbf{r}_i := \mathbf{r}(\mathbf{R}_i, t)$ the spatial coordinates of i in the current configuration Ω_t . Let $\rho_i := \rho(\mathbf{R}_i, t)$, $\mathbf{u}_i := \mathbf{u}(\mathbf{R}_i, t)$ and $\mathbf{v}_i := \mathbf{v}(\mathbf{R}_i, t)$ be point i 's density, displacement, and the velocity, respectively. Let ij denote the bond from i to j ; $\mathbf{R}_{ij} := \mathbf{R}_j - \mathbf{R}_i$ is initial bond vector, the relative distance vector for bond ij ; $\mathbf{v}_{ij} := \mathbf{v}_j - \mathbf{v}_i$ is the relative velocity vector for bond ij ; $\mathbf{r}_{ij} := \mathbf{r}_j - \mathbf{r}_i = \mathbf{R}_{ij} + \mathbf{u}_{ij}$ is the current bond vector for bond ij . For point i , the domain H_i with radius of h_i is called as the horizon of i , where any point j falling inside forms a bond ij , as shown in Fig. 1b. More discussion of horizon H_i will be presented subsequently. Bond is the basis where interaction happens. The interaction usually includes the force and heat flux. The nonlocal force interaction acting on particle i due to bond ij is defined as

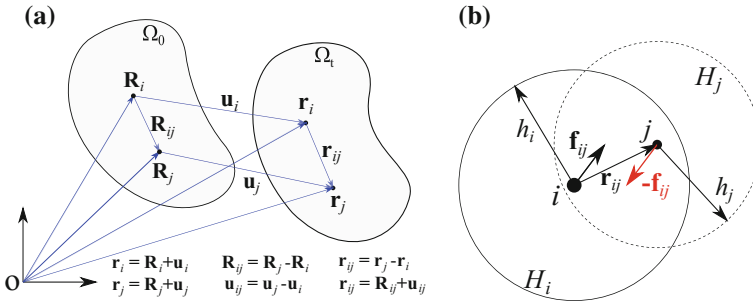


Fig. 1 **a** The x velocity at different time; **b** The bond forces in H_i , as $j \in H_i$, bond ij exerts direct force \mathbf{f}_{ij} on i , based on Newton’s third law, j receives reaction force $-\mathbf{f}_{ij}$

$$\mathbf{f}_{ij} := \mathbf{f}_{ij}(\rho_i, \mathbf{R}_{ij}, \mathbf{r}_{ij}, \mathbf{u}_{ij}, \mathbf{v}_{ij}, \dots). \tag{1}$$

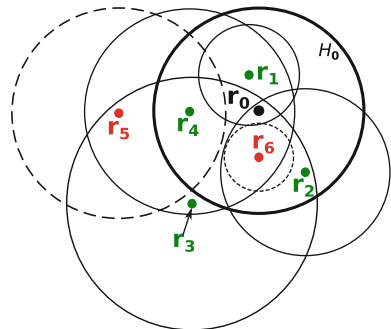
\mathbf{f}_{ij} is also called the force vector density in peridynamics. \mathbf{f}_{ij} is the direct force on i due to bond ij , meanwhile there is a reaction force $-\mathbf{f}_{ij}$ acting on j , as shown in Fig. 1b. The horizon H_i is the domain where any material point j falling inside forms bond ij . From the force point of view, bond ij will exerts direct force on i and reaction force on j . Hence, i will undertake all the direct forces from bonds in H_i .

Dual-horizon of particle i is defined as a union of the points whose horizons include i , denoted by

$$H'_i = \{j | i \in H_j\}. \tag{2}$$

The bond in dual-horizon is in terms of dual-bond; for example, $i \in H_j$ forms bond ji ; bond ji is called the dual-bond of H'_i since $j \in H'_i$. Therefore, the symbol ji has two meanings: One is the dual-bond of material point i , and the other is the bond of material point j . As dual-bond ji exerts reaction force on i , the dual-horizon of i can be viewed as reaction force horizon. One example to show the horizon and dual-horizon is Fig. 2, where $H_0 = \{r_1, r_2, r_4, r_6\}$, $H'_0 = \{r_1, r_2, r_3, r_4\}$.

Fig. 2 Schematic diagram for horizon and dual-horizon, all circles above are horizons



The dual property of dual-horizon

Let $\mathcal{F}(i, j)$ be any expression depend on two points i, j . The dual property of dual-horizon is that the double integration of the term $\mathcal{F}(i, j)$ from dual-horizon can be converted to the double integration of the term $\mathcal{F}(j, i)$ from horizon, as shown in Eq. (3). The key idea lies in that the term $\mathcal{F}(i, j)$ can be both interpreted in H_i and H'_j . For the detailed proof, please see Ref. [8].

$$\int_{i \in \Omega} \int_{H'_i} \mathcal{F}(i, j) dV_j dV_i = \int_{i \in \Omega} \int_{H_i} \mathcal{F}(j, i) dV_j dV_i. \tag{3}$$

3 The Nonlocal Formulation for Fluid

The continuum media can be described by a set of equations as

$$\frac{d\rho}{dt} + \rho \nabla \cdot \mathbf{v} = 0 \tag{4}$$

continuity equation

$$\rho \frac{d\mathbf{v}}{dt} = \nabla \cdot \boldsymbol{\sigma} + \rho \mathbf{b} \tag{5}$$

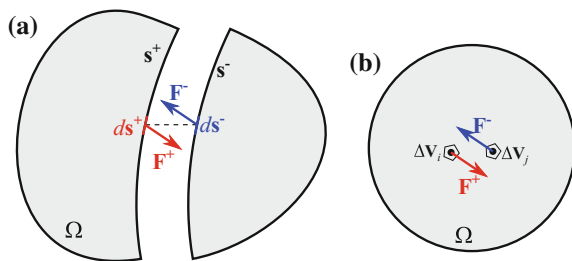
equation of motion

$$\rho \frac{de}{dt} = \boldsymbol{\sigma} : \nabla \mathbf{v} - \nabla \cdot \mathbf{q} + \rho s \tag{6}$$

energy equatoin,

where $\frac{d}{dt}$ is the material derivative, ρ is the density, \mathbf{v} the velocity, $\boldsymbol{\sigma}$ the Cauchy stress tensor, e the specific energy density, and s the energy source per unit mass. The above set of equations cannot be solved directly since they are based on local formulation, where the ‘local’ can be understood as the equations are based on differential form. In local theory, the interaction happens between two material points where their distance is infinitesimal. For example, as shown in Fig. 3a, cutting Ω with virtual surface s creates two surfaces s^+ and s^- , where the internal surface forces \mathbf{F}^+ and \mathbf{F}^- are exposed. In the nonlocal theory, the local surface is not required since the interaction can be transmitted a over finite distance. As shown in Fig. 3b, two points i and j with finite distance are associated with volume ΔV_i and ΔV_j , respectively;

Fig. 3 a Local interaction b Nonlocal interaction



there exists a pair of forces \mathbf{F}^+ , \mathbf{F}^- satisfying $\mathbf{F}^+ = -\mathbf{F}^-$. Therefore, the local surface interaction is not required in the nonlocal theory. The difference in interaction indicates that the derivation of the governing equations can be obtained in a different way.

3.1 Nonlocal Equation of Motion

Consider material point i with volume ΔV_i , averaged density ρ_i , material coordinate \mathbf{R}_i , current coordinate \mathbf{r}_i , velocity \mathbf{v}_i , temperature T_i , internal energy density ϵ_i , stress state σ_i , horizon H_i , and dual-horizon H'_i . The internal forces exerted at i from any other material point include two parts, namely the direct forces from the horizon and the reaction forces from the dual-horizon. The other forces applied to a particle include the body force $\rho_i \Delta V_i \cdot \mathbf{b}$ and the inertia force $\rho_i \Delta V_i \cdot \ddot{\mathbf{u}}_i$, where \mathbf{b} is the body force density, e.g., the gravity.

At any time t , for j in the dual-horizon of i , the force vector of dual-bond ji is defined as $\mathbf{f}_{ji} \Delta V_i \Delta V_j$, where \mathbf{f}_{ji} is the force density due to bond ji in H_j (or dual-bond ji in H'_i) with unit of force per volume squared. The forces from the dual-horizon are reaction forces. The total force applied to i from its dual-horizon, H'_i , can be computed by

$$-\sum_{H'_i} \mathbf{f}_{ji} \Delta V_i \Delta V_j. \tag{7}$$

For any j inside the horizon of i , the force acting on i due to bond ij is defined as $\mathbf{f}_{ij} \Delta V_j \Delta V_i$. The total force i undertaken from horizon H_i is

$$\sum_{H_i} \mathbf{f}_{ij} \Delta V_i \Delta V_j. \tag{8}$$

By summing over all forces on particle i , including inertia force, body force, and reaction forces in Eq. (7) and direct forces in Eq. (8), we obtain the equation of motion

$$\rho_i \Delta V_i \ddot{\mathbf{u}}_i = \sum_{H_i} \mathbf{f}_{ij} \Delta V_j \Delta V_i - \sum_{H'_i} \mathbf{f}_{ji} \Delta V_j \Delta V_i + \mathbf{b} \rho_i \Delta V_i. \tag{9}$$

Dividing ΔV_i yielding the governing equation based on i :

$$\rho_i \ddot{\mathbf{u}}_i = \sum_{H_i} \mathbf{f}_{ij} \Delta V_j - \sum_{H'_i} \mathbf{f}_{ji} \Delta V_j + \rho_i \mathbf{b}. \tag{10}$$

When the discretisation is sufficiently fine, the summation is approximating the integration of the force on the dual-horizon and horizon. Thus, the integral form of the

equation of motion is given as

$$\rho_i \ddot{\mathbf{u}}_i = \int_{H_i} \mathbf{f}_{ij} dV_j - \int_{H'_i} \mathbf{f}_{ji} dV_j + \rho_i \mathbf{b}. \quad (11)$$

Note that here we do not specify whether the domain is solid or fluid as long as the domain is in Lagrangian description. When the computational region is solid and \mathbf{f}_{ji} depends mainly on \mathbf{R}_{ji} and \mathbf{u}_{ji} , i.e., $\mathbf{f}_{ji} = \mathbf{f}_{ji}(\mathbf{R}_{ji}, \mathbf{u}_{ji})$, we have

$$\rho_i \ddot{\mathbf{u}}_i = \int_{H_i} \mathbf{f}_{ij}(\mathbf{R}_{ij}, \mathbf{u}_{ij}) dV_j - \int_{H'_i} \mathbf{f}_{ji}(\mathbf{R}_{ji}, \mathbf{u}_{ji}) dV_j + \rho_i \mathbf{b}, \quad (12)$$

the dual-horizon peridynamics; for more details, please refer to [9]. Note that for solid, the horizon and dual-horizon are defined on the initial configuration (the Lagrangian type). When the computational region is fluid and \mathbf{f}_{ji} depends mainly on ρ_j , \mathbf{r}_{ji} , and \mathbf{v}_{ji} , i.e., $\mathbf{f}_{ji} = \mathbf{f}_{ji}(\rho_j, \mathbf{r}_{ji}, \mathbf{v}_{ji})$, we have the nonlocal form of fluid,

$$\rho_i \ddot{\mathbf{u}}_i = \int_{H_i} \mathbf{f}_{ij}(\rho_i, \mathbf{r}_{ij}, \mathbf{v}_{ij}) dV_j - \int_{H'_i} \mathbf{f}_{ji}(\rho_j, \mathbf{r}_{ji}, \mathbf{v}_{ji}) dV_j + \rho_i \mathbf{b}. \quad (13)$$

Since the deformation of configuration in fluid is large and the history effect is insignificant, the horizon and dual-horizon in fluid are defined on the current configuration, and we may call this horizon the Eulerian type horizon. In some cases with complicated material properties, both Lagrangian type horizon and Eulerian type horizon can be introduced to describe the nonlocal interaction forces. For simplicity, we only discuss the application in fluid.

3.2 Nonlocal Energy Equation

Let e_i denote the specific energy density (energy per unit mass) for material point i . The specific energy density contains kinematic energy density (denoted by $\frac{1}{2}v_i^2$), internal energy density (denoted by ϵ_i), and other possible forms. Here, we restrict that e_i comprises only two forms of energy, that is, $e_i = \frac{1}{2}v_i^2 + \epsilon_i$. The variation of the energy results from internal force interaction, external force (body force), heat conduction, and so on. For the internal force interaction, the variation of the energy density for i is comprised with two parts: (a) the work from bond ij in H_i and (b) the work from dual-bond ji in H'_i .

Let point i be the reference point, $j \in H_i$, reaction bond force $-\mathbf{f}_{ij}$ does work to j along j 's velocity \mathbf{v}_j in the period of time Δt . When Δt is sufficiently small, \mathbf{f}_{ij} can be considered as constant; the energy changed on i due to bond ij can be expressed as

$$-(\mathbf{f}_{ij}\Delta V_i\Delta V_j) \cdot \mathbf{v}_j\Delta t = \mathbf{f}_{ij} \cdot \mathbf{v}_j\Delta V_i\Delta V_j\Delta t, \quad (14)$$

where the first negative represents the energy subtracted from i . The total energy changed in H_i is

$$\sum_{H_i} \mathbf{f}_{ij} \cdot \mathbf{v}_j\Delta V_i\Delta V_j\Delta t. \quad (15)$$

For any point $j \in H'_i$, let point j be the reference point, reaction bond force $-\mathbf{f}_{ji}$ does work to i along i 's velocity \mathbf{v}_i in the period of time Δt , i gains energy

$$(-\mathbf{f}_{ji}\Delta V_i\Delta V_j) \cdot \mathbf{v}_i\Delta t. \quad (16)$$

The total energy variation in H'_i is

$$\sum_{H'_i} (-\mathbf{f}_{ji}\Delta V_i\Delta V_j) \cdot \mathbf{v}_i\Delta t = - \sum_{H'_i} \mathbf{f}_{ji} \cdot \mathbf{v}_i\Delta V_j\Delta V_i\Delta t. \quad (17)$$

When considering the heat conduction, let \mathbf{q}_{ji} denote the heat flux density j gained due to bond ji , the lost internal energy for i is $-\mathbf{q}_{ji}\Delta V_i\Delta V_j\Delta t$. The energy changed due to heat flux for particle i in H'_i is

$$- \sum_{H'_i} \mathbf{q}_{ji}\Delta V_i\Delta V_j\Delta t. \quad (18)$$

The gained internal energy for particle i due to bond ij is $\mathbf{q}_{ij}\Delta V_i\Delta V_j\Delta t$. The energy changed due to heat flux for particle i in H_i is

$$\sum_{H_i} \mathbf{q}_{ij}\Delta V_i\Delta V_j\Delta t. \quad (19)$$

The total energy variation in interval Δt

$$\begin{aligned} \rho_i\Delta V_i\Delta e_i = & \sum_{H_i} \mathbf{f}_{ij} \cdot \mathbf{v}_j\Delta V_j\Delta V_i\Delta t - \sum_{H'_i} \mathbf{f}_{ji} \cdot \mathbf{v}_i\Delta V_j\Delta V_i\Delta t \\ & + \sum_{H_i} \mathbf{q}_{ij}\Delta V_i\Delta V_j\Delta t - \sum_{H'_i} \mathbf{q}_{ji}\Delta V_i\Delta V_j\Delta t + \rho_i\mathbf{b}\Delta V_j \cdot \mathbf{v}_i\Delta t, \end{aligned} \quad (20)$$

where $\rho_i\mathbf{b}\Delta V_j \cdot \mathbf{v}_i\Delta t$ is the work due to body force. Dividing by $\Delta V_i\Delta t$ and applying $\Delta t \rightarrow 0$, $\Delta V_j \rightarrow 0$ in Eq. (20), we have the continuous nonlocal energy equation:

$$\rho_i \frac{de_i}{dt} = \int_{H_i} \mathbf{f}_{ij} \cdot \mathbf{v}_j dV_j - \int_{H'_i} \mathbf{f}_{ji} \cdot \mathbf{v}_i dV_j + \int_{H_i} \mathbf{q}_{ij} dV_j - \int_{H'_i} \mathbf{q}_{ji} dV_j + \rho_i \mathbf{b} \cdot \mathbf{v}_i. \quad (21)$$

Note that during the derivation of nonlocal energy equation, we don't specify whether the domain is fluid or solid. Since $\rho_i \frac{de_i}{dt} = \rho_i \mathbf{v}_i \frac{dv_i}{dt} + \rho_i \frac{d\epsilon_i}{dt}$, Eq. (21)– $\mathbf{v}_i \cdot$ Eq. (13) leads to the internal energy equation

$$\rho_i \frac{d\epsilon_i}{dt} = \int_{H_i} \mathbf{f}_{ij} \cdot \mathbf{v}_{ij} dV_j + \int_{H_i} \mathbf{q}_{ij} dV_j - \int_{H'_i} \mathbf{q}_{ji} dV_j. \tag{22}$$

With the momentum equation and energy equation available, the remaining work is how to determine the bond force density \mathbf{f}_{ij} for bond ij and dual-bond force density \mathbf{f}_{ji} for dual-bond ji . The dual-bond force density \mathbf{f}_{ji} in H'_i can be determined when calculating the force in H_j for j since dual-bond ji for i is the bond ji for j . In this sense, it is not necessary to know the dual-horizon geometry to calculate the bond force in dual-horizon; we only need to determine the force \mathbf{f}_{ij} for bond ij . In the context of peridynamics, the bond force is determined by the equivalence of strain energy density in local formulation and nonlocal formulation; for more details, please refer to as [5, 9]. However, such strain energy principle is not easy to be established in the field of fluid. As this chapter focuses on the nonlocal formulation of fluid, we will present an approach called nonlocal divergence method to determine the bond force density \mathbf{f}_{ij} and nonlocal heat flux \mathbf{q}_{ij} in fluid.

3.3 Nonlocal Divergence

The divergence of a tensor field $\boldsymbol{\sigma}$ at a point p is defined as the limit of the net flow of $\boldsymbol{\sigma}$ across the smooth boundary of a three-dimensional region V divided by the volume of V as V shrinks to p . Formally,

$$\nabla \cdot \boldsymbol{\sigma}(p) = \lim_{V \rightarrow \{p\}} \oint_{S(V)} \frac{\boldsymbol{\sigma} \cdot \mathbf{n}}{|V|} dS \tag{23}$$

where $|V|$ is the volume of V , $S(V)$ is the boundary of V , and the integral is a surface integral with \mathbf{n} being the outward unit normal to that surface; $\boldsymbol{\sigma} \cdot \mathbf{n}$, the projection of $\boldsymbol{\sigma}$ on direction \mathbf{n} , is the flux across the surface dS , as shown in Fig. 4a. Note that here, the out-flux is assumed to be positive, which is the same with the direction in Fig. 1b.

Following the same procedure, we can define the nonlocal divergence. Consider spherical domain H_i , $w(\mathbf{r}_{ij})$ is the scalar-valued influence function. The divergence on point i is the summation of out-flux and influx. When $j \in H_i$, the out-flux for i due to bond ij is assumed as

$$\alpha w(\mathbf{r}_{ij}) \boldsymbol{\sigma}_i \cdot \mathbf{r}_{ij}, \tag{24}$$

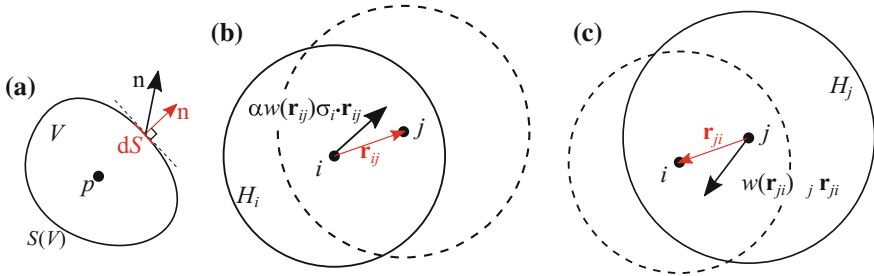


Fig. 4 The out-flux in divergence $\mathbf{a} \cdot \mathbf{n}$ is the out-flux density in local divergence; **b** $\alpha w(\mathbf{r}_{ij})\boldsymbol{\sigma}_i \cdot \mathbf{r}_{ij}$ is the out-flux for bond ij in H_i ; and **c** $\alpha w(\mathbf{r}_{ji})\boldsymbol{\sigma}_j \cdot \mathbf{r}_{ji}$ is the out-flux density for bond ji in H_j

where α is a coefficient to be determined, and \mathbf{r}_{ij} denotes the direction of out-flux, as shown in Fig. 4b. Reversely, when $i \in H_j$ ($j \in H'_i$), the out-flux for j is $\alpha w(\mathbf{r}_{ji})\boldsymbol{\sigma}_j \cdot \mathbf{r}_{ji}$, as shown in Fig. 4c; in the sense of flux conservation, the out-flux for j is the influx for i . Compared with Fig. 1b, we have $\mathbf{f}_{ij} = \alpha w(\mathbf{r}_{ij})\boldsymbol{\sigma}_i \cdot \mathbf{r}_{ij}$ and $\mathbf{f}_{ji} = \alpha w(\mathbf{r}_{ji})\boldsymbol{\sigma}_j \cdot \mathbf{r}_{ji}$.

Summing all flux for i leads to

$$- \int_{H'_i} \alpha w(\mathbf{r}_{ji})\boldsymbol{\sigma}_j \cdot \mathbf{r}_{ji}dV_j + \int_{H_i} \alpha w(\mathbf{r}_{ij})\boldsymbol{\sigma}_i \cdot \mathbf{r}_{ij}dV_j. \tag{25}$$

Assuming any point's horizon radius being constant, and using Taylor expansion $\boldsymbol{\sigma}_j = \boldsymbol{\sigma}_i + \nabla \otimes \boldsymbol{\sigma}_i \cdot \mathbf{r}_{ij} + O(r_{ij}^2)$, the coefficient α can be expressed as

$$\alpha = \frac{n_d}{\text{trace}(\mathbf{K}_i)} = \frac{n_d}{v_i^h}, \mathbf{K}_i = \int_{H_i} w(\mathbf{r}_{ij})\mathbf{r}_{ij} \otimes \mathbf{r}_{ij}dV_j, v_i^h = \int_{H_i} w(\mathbf{r}_{ij})\mathbf{r}_{ij} \cdot \mathbf{r}_{ij}dV_j, \tag{26}$$

where $n_d \in \{1, 2, 3\}$ is the dimensional number. When $h_i \rightarrow 0$, it is easy to prove that Eq. (25) converges to the local divergence operator $\nabla \cdot \boldsymbol{\sigma}_i$. If $w(\mathbf{r}_{ij}) = r_{ij}^{-2}$, v_i^h is the volume of horizon H_i . In this chapter, $w(\mathbf{r}_{ij}) = r_{ij}^{-2}$ is used. Therefore, for constant horizon, the nonlocal divergence corresponding to the local divergence is

$$\nabla \cdot \boldsymbol{\sigma}_i \rightarrow \int_{H_i} \frac{n_d}{v_j^h} w(\mathbf{r}_{ij})\boldsymbol{\sigma}_j \cdot \mathbf{r}_{ij}dV_j + \int_{H_i} \frac{n_d}{v_i^h} w(\mathbf{r}_{ij})\boldsymbol{\sigma}_i \cdot \mathbf{r}_{ij}dV_j. \tag{27}$$

For variable horizon, Eq. (27) can be rewritten as

$$\nabla \cdot \boldsymbol{\sigma}_i \rightarrow - \int_{H'_i} \frac{n_d}{v_j^h} w(\mathbf{r}_{ji})\boldsymbol{\sigma}_j \cdot \mathbf{r}_{ji}dV_j + \int_{H_i} \frac{n_d}{v_i^h} w(\mathbf{r}_{ij})\boldsymbol{\sigma}_i \cdot \mathbf{r}_{ij}dV_j. \tag{28}$$

When the nonlocal divergence is expressed as bond flux f_{ij}, f_{ji} , we have

$$\nabla \cdot \sigma_i \rightarrow - \int_{H'_i} f_{ji} dV_j + \int_{H_i} f_{ij} dV_j, \tag{29}$$

where

$$f_{ji} = \frac{n_d}{v_j^h} w(\mathbf{r}_{ji}) \sigma_j \cdot \mathbf{r}_{ji}, \quad f_{ij} = \frac{n_d}{v_i^h} w(\mathbf{r}_{ij}) \sigma_i \cdot \mathbf{r}_{ij}. \tag{30}$$

3.4 Application of Nonlocal Divergence

Two simple material constitutives for fluid are

$$\begin{aligned} \sigma &= -p\mathbf{I} && \text{ideal gas} \\ \sigma &= -p\mathbf{I} + \frac{\mu}{2}(\nabla\mathbf{v} + \mathbf{v}\nabla) && \text{Newtonian fluid.} \end{aligned} \tag{31}$$

Once the stress state is known, based on Eq. (29), the bond force density can be obtained with ease. We will discuss some special cases for pressure, physical viscosity, and heat flux subsequently.

When σ represents the pressure only, i.e., $\sigma = -p\mathbf{I}$, the bond force in term of pressure is

$$f_{ji}^{pr} = -\frac{n_d}{v_j^h} w(\mathbf{r}_{ji}) p_j \mathbf{r}_{ji}, \quad f_{ij}^{pr} = -\frac{n_d}{v_i^h} w(\mathbf{r}_{ij}) p_i \mathbf{r}_{ij}. \tag{32}$$

Similarly, second-order nonlocal operators can be obtained

$$\nabla \cdot (\mu \nabla \mathbf{v})_i \rightarrow - \int_{H'_i} \frac{n_d}{v_j^h} w(\mathbf{r}_{ji}) (\mu \nabla \mathbf{v})_{ji} \cdot \mathbf{r}_{ji} dV_j + \int_{H_i} \frac{n_d}{v_i^h} w(\mathbf{r}_{ij}) (\mu \nabla \mathbf{v})_{ij} \cdot \mathbf{r}_{ij} dV_j. \tag{33}$$

In order to avoid the nested integral, we use the finite difference to approximate $(\nabla \mathbf{v})_{ij}$, i.e., $(\nabla \mathbf{v})_{ij} \rightarrow \frac{\mathbf{v}_{ij} \otimes \mathbf{r}_{ij}}{r_{ij}^2}$. Hence,

$$\nabla \cdot (\mu \nabla \mathbf{v})_i \rightarrow - \int_{H'_i} \frac{n_d}{v_j^h} w(\mathbf{r}_{ji}) \mu_j \frac{\mathbf{v}_{ji} \otimes \mathbf{r}_{ji}}{r_{ji}^2} \cdot \mathbf{r}_{ji} dV_j + \int_{H_i} \frac{n_d}{v_i^h} w(\mathbf{r}_{ij}) \mu_i \frac{\mathbf{v}_{ij} \otimes \mathbf{r}_{ij}}{r_{ij}^2} \cdot \mathbf{r}_{ij} dV_j \tag{34}$$

$$\rightarrow - \int_{H'_i} \frac{n_d}{v_j^h} w(\mathbf{r}_{ji}) \mu_j \mathbf{v}_{ji} dV_j + \int_{H_i} \frac{n_d}{v_i^h} w(\mathbf{r}_{ij}) \mu_i \mathbf{v}_{ij} dV_j. \tag{35}$$

In fact, Eq. (35) expresses the bond force in terms of physical viscosity of fluid. The bond force for physical viscosity is

$$\mathbf{f}_{ij}^{pv} = \frac{n_d}{v_i^h} w(\mathbf{r}_{ij}) \mu_i \mathbf{v}_{ij}, \quad \mathbf{f}_{ji}^{pv} = \frac{n_d}{v_j^h} w(\mathbf{r}_{ji}) \mu_j \mathbf{v}_{ji}, \tag{36}$$

where μ is the dynamic viscosity.

Similarly, the expression for nonlocal heat flux is

$$\nabla \cdot (-\kappa \nabla T)_i \rightarrow - \int_{H'_i} \mathbf{q}_{ji} dV_j + \int_{H_i} \mathbf{q}_{ij} dV_j, \quad \mathbf{q}_{ji} = - \frac{n_d}{v_j^h} w(\mathbf{r}_{ji}) \kappa_j T_{ji},$$

$$\mathbf{q}_{ij} = - \frac{n_d}{v_i^h} w(\mathbf{r}_{ij}) \kappa_i T_{ij}, \tag{37}$$

where κ is the thermal conductivity. Therefore, the nonlocal flux \mathbf{f}_{ij} and \mathbf{q}_{ij} in Eqs. (12) and (21) are obtained.

3.5 Artificial Viscosity

In order to capture the shock wave or eliminate the unphysical oscillations in the numerical results around the shocked region, we use the von Neumann-Richtmyer artificial viscosity together with linear artificial viscosity term [10]

$$\Pi = \begin{cases} \alpha \rho c \Delta x \nabla \cdot \mathbf{v} + \beta \rho \Delta x^2 (\nabla \cdot \mathbf{v})^2, & \nabla \cdot \mathbf{v} < 0 \\ 0, & \nabla \cdot \mathbf{v} \geq 0 \end{cases} \tag{38}$$

where α and β are adjustable non-dimensional constants, c is the speed of sound, and Δx represent the characteristic length scale used in the computation, e.g., the grid spacing in finite difference method, finite volume method, etc.

In nonlocal fluid, the characteristic length scale is horizon size h_i ; we use the finite difference to represent $\Delta x \nabla \cdot \mathbf{v}$

$$\mu_{ij} := (\Delta x \nabla \cdot \mathbf{v})_{ij} \rightarrow h_i \frac{\mathbf{v}_{ij} \cdot \mathbf{r}_{ij}}{r_{ij}^2}. \tag{39}$$

The artificial viscosity bond force is

$$\mathbf{f}_{ij}^{av} = \frac{n_d}{v_i^h} \omega(\mathbf{r}_{ij}) \mathbf{r}_{ij} \cdot \begin{cases} \alpha \rho_i c_i \mu_{ij} + \beta \rho_i \mu_{ij}^2, & \mathbf{v}_{ij} \cdot \mathbf{r}_{ij} < 0 \\ 0, & \mathbf{v}_{ij} \cdot \mathbf{r}_{ij} \geq 0. \end{cases} \tag{40}$$

3.6 Nonlocal Continuity Equation

The domain is based on Lagrangian description; thus, the conservation of mass is satisfied naturally. However, the pressure in fluid depends heavily on the density state. Based on Eq. (29), the nonlocal form of Eq. (4) can be obtained as

$$\frac{d\rho_i}{dt} = -\rho_i \int_{H_i} \frac{n_d}{v_i^h} w(\mathbf{r}_{ij}) \mathbf{v}_{ij} \cdot \mathbf{r}_{ij} dV_j. \tag{41}$$

3.7 The Conservation of Basic Laws

Based on the dual property of dual-horizon, it would be easy to prove that the Eqs. (13) and (21) satisfy the conservation of momentum, angular momentum, and energy. Due to the length restriction of this chapter, we omit these derivations.

4 Numerical Implementation

We replace $\Delta V_i, \Delta V_j$ with $\frac{m_i}{\rho_i}, \frac{m_j}{\rho_j}$, respectively; then, Eq. (9) and Eq. (22) are converted into

$$m_i \ddot{\mathbf{u}}_i = \sum_{H_i} \mathbf{f}_{ij} \frac{m_i m_j}{\rho_i \rho_j} - \sum_{H'_i} \mathbf{f}_{ji} \frac{m_i m_j}{\rho_i \rho_j} + m_i \mathbf{b}. \tag{42}$$

$$m_i \frac{d\epsilon_i}{dt} = \sum_{H_i} \mathbf{f}_{ij} \cdot \mathbf{v}_{ij} \frac{m_i m_j}{\rho_i \rho_j} - \sum_{H'_i} \mathbf{q}_{ji} \frac{m_i m_j}{\rho_i \rho_j} + \sum_{H_i} \mathbf{q}_{ij} \frac{m_i m_j}{\rho_i \rho_j}, \tag{43}$$

where \mathbf{f}_{ij} may contain pressure bond force \mathbf{f}_{ij}^{pr} in Eq. (32), the physical viscous bond force \mathbf{f}_{ij}^{pv} in Eq. (36), the artificial viscous bond force \mathbf{f}_{ij}^{av} in Eq. (40), and \mathbf{q}_{ij} is the nonlocal heat flux in Eq. (37). The two-step predictor-corrector integral scheme [11] is used to integrate the independent variables. For weakly compressible fluid model, the pressure of water is obtained with the following equation of state

$$p = p_0 \left(\left(\frac{\rho}{\rho_0} \right)^\gamma - 1 \right), \tag{44}$$

where γ is a constant, and $\gamma = 7$ is used, ρ_0 is the reference density, p_0 is the bulk modulus of fluid [12].

The time increment for numerical stability is limited by several criteria [13]. The three main conditions are CFL-condition based on the artificial sound speed c_{max} and the maximum flow speed $|\mathbf{v}_{max}|$, the viscous condition, and the body force condition,

i.e.,

$$\Delta t \leq \min \left(0.25 \frac{h}{c_{max} + |\mathbf{v}_{max}|}, 0.125 \frac{h^2}{\mu}, 0.25 \left(\frac{h}{|\mathbf{g}|} \right)^{1/2} \right). \quad (45)$$

The solid wall is modeled by the reflective boundary conditions:

$$\mathbf{v}' = \mathbf{v} - 2(\mathbf{v} \cdot \mathbf{n})\mathbf{n} \text{ if } \mathbf{v} \cdot \mathbf{n} < 0 \quad (46)$$

where \mathbf{v} denotes the velocity and \mathbf{n} is the inward normal direction of the wall at that point.

5 Numerical Examples

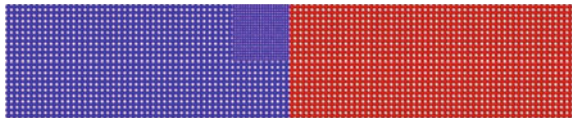
5.1 2D Heat Conduction

Consider a 2d plate of with length $L = 50$ cm and width $W = 10$ cm. The plate is discretized with particles with a particle spacing of $\Delta x = 0.5$ cm or $\Delta x = 0.25$ cm; the heat diffusion coefficient is $\alpha = 1.0 \times 10^{-4} m^2 s^{-1}$. The left half is assigned an internal energy of $e_l^0 = 1 J/m^2$, the right half $e_r^0 = 2 J/m^2$, as shown in Fig. 5. Particularly, the small patch discretized with $\Delta x = 0.25$ cm is designed to test the influence of the variation of the horizon size. During the simulation, the horizon size is set as two times of the particle size, i.e., $h_i = 2\Delta x_i$; therefore, there is a sharp transition of horizon size in the interface of two different particle sizes. The energy conservation can be monitored by tracking the total internal energy. The energy profile is compared to an analytic solution after 4.5 s, as shown in Fig. 6a. The analytical solution is

$$e(x, y, t) = \frac{e_r^0 + e_l^0}{2} + \frac{e_r^0 - e_l^0}{2} \operatorname{erf} \left(\frac{x - x_c}{\sqrt{4\alpha t}} \right). \quad (47)$$

The numerical results agree well with the theoretical solution given by Eq. (47); The maximal error is -2.07% which happened at the interface of two different horizon sizes due to the nonlocal effect of the current formulation. The total energy variation is shown in Fig. 6b.

Fig. 5 Initial configuration of the plate, $e_l^0 = 1 J/m^2$ in blue domain and $e_r^0 = 2 J/m^2$ in red domain



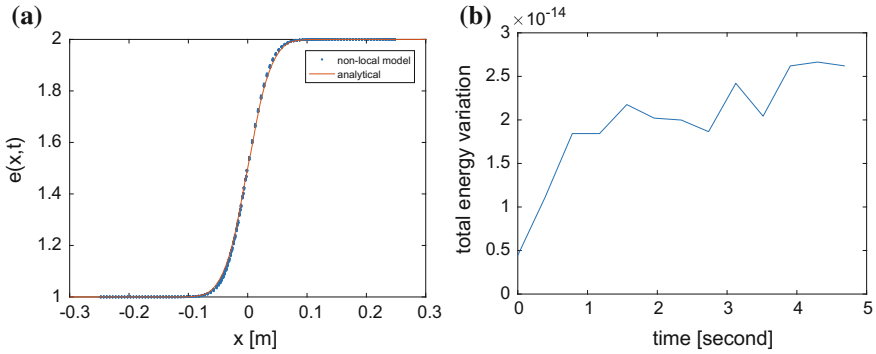


Fig. 6 a The comparison of analytical result with numerical results at $t = 4.5$ s b The total energy variation $var = \int_{\Omega} e(x, y, t) d\Omega / (\int_{\Omega_0} e(x, y, 0) d\Omega) - 1$

5.2 2D Dam Break on Dry Bed

The Dam break experiment, which was described in reference [14], is a benchmark problem in SPH field [15]. The tank is shown in Fig. 7a. The system was solved with a leapfrog predictor-corrector scheme with a specular reflection boundary condition by Eq. (46), artificial viscosity, $\alpha = 0.5$, and $\beta = 0.5$. Fluid particles were initially placed on a staggered grid with zero initial velocity. Two particle sizes are adopted, e.g., $\Delta x = 1.25 \times 10^{-2}$ m in Ω_0 , $\Delta x = 8 \times 10^{-3}$ m in Ω_1 (17,350 particles) in order to test the dual-horizon in the formulation. In order to employ a large time increment, the initial sound speed is set as 100 m/s, which is 10 times larger than the maximum flowing speed. Note that the specular reflection boundary only changes the direction of the particle’s velocity when the particle is approaching the boundary; thus, the kinetic energy is not effected. This enables us to track the global energy during the simulation. The energy equation Eq. (22) is considered in order to track the internal energy.

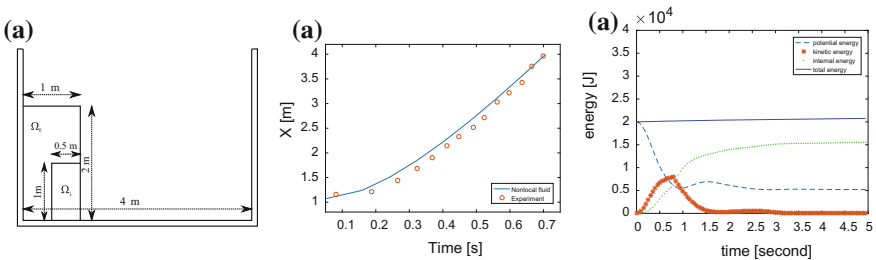


Fig. 7 a Initial configuration b Lines represent the X position of the dam toe c Total energy evolution

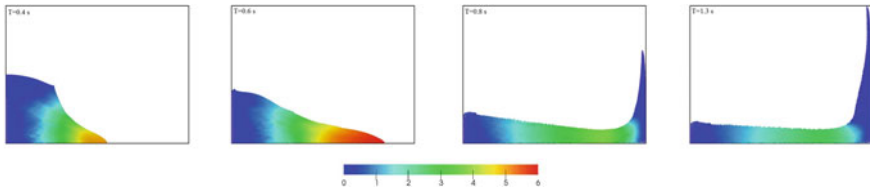


Fig. 8 The x velocity at different time

The toe velocity evolution agreed well with experimental data in Fig. 7b. The motions of the water at different times are shown in Fig. 8. During the simulation, the density variation is always less than 1%. The evolution of kinetic energy, internal energy, and total energy is shown in Fig. 7c. It is safe to conclude that the total energy is well conserved for the nonlocal fluid formulation. The small variation (<5%) of total energy comes from the numerical integration. of the tank, and some particles' density may exceed 1020 kg/m^3 . However, the variation of density for other part of the fluid is small.

6 Conclusions

In this chapter, we developed a simple nonlocal formulation to model the weakly compressible fluid. The nonlocal equation of motion and energy equation are derived. Different bond forces in the aspects of pressure, physical viscosity, artificial viscosity, and the nonlocal heat flux are determined by the nonlocal divergence method. Two numerical examples are presented to show the accuracy of this method.

References

1. Cemal Eringen A (2002) Nonlocal continuum field theories. Springer Science and Business Media, New York
2. Bazant ZP (1994) Nonlocal damage theory based on micromechanics of crack interactions. *J Eng Mech* 120(3):593–617
3. Strömberg L, Ristinmaa M (1996) Fe-formulation of a nonlocal plasticity theory. *Comput Methods Appl Mech Eng* 136(1):127–144
4. Polizzotto C (2003) Unified thermodynamic framework for nonlocal/gradient continuum theories. *Eur J Mech-A/Solids* 22(5):651–668
5. Silling SA, Epton M, Weckner O, Xu J, Askari E (2007) Peridynamic states and constitutive modeling. *J Elast* 88(2):151–184
6. Gilboa G, Osher S (2008) Nonlocal operators with applications to image processing. *Multiscale Model Simul* 7(3):1005–1028
7. Silling SA (2000) Reformulation of elasticity theory for discontinuities and long-range forces. *J Mech Phys Solids* 48(1):175–209

8. Ren H, Zhuang X, Rabczuk T (2017) Dual-horizon peridynamics: a stable solution to varying horizons. *Comput Methods Appl Mech Eng* 318:762–782
9. Ren H, Zhuang X, Cai Y, Rabczuk T et al (2016) Dual-horizon peridynamics. *Int J Numer Methods Eng* 108(12):1451–1476
10. Monaghan JJ, Gingold RA (1983) Shock simulation by the particle method SPH. *J Comput Phys* 52(2):374–389
11. Ren J, Ouyang J, Jiang T, Li Q (2012) Simulation of complex filling process based on the generalized newtonian fluid model using a corrected SPH scheme. *Comput Mech* 49(5):643–665
12. Morris JP, Fox PJ, Zhu Y (1997) Modeling low reynolds number incompressible flows using SPH. *J Comput Phys* 136(1):214–226
13. Monaghan JJ (1992) Smoothed particle hydrodynamics. *Annu Rev Astron Astrophys* 30:543–574
14. Koshizuka S, Oka Y (1996) Moving-particle semi-implicit method for fragmentation of incompressible fluid. *Nucl Sci Eng* 123(3):421–434
15. Crespo AJC, Gesteira MG, Dalrymple RA (2007) Boundary conditions generated by dynamic particles in SPH methods. *CMC-Tech Science Press* 5(3):173–184

CFD Simulations of the Natural Cavitating Flow Around High-Speed Submerged Bodies



T. T. Nguyen, H. N. Duong, T. Q. Nguyen and H. Kikura

Abstract Cavitating flow is of considerable importance in underwater high-speed applications because of the desirable drag-reduction effect that concerns the presence of a cavity around moving objects. In many operating regimes, a proper design of high-speed underwater bodies, e.g., the slender ones, should produce not only a stable motion with a straight trajectory but also maximize the travel distance of the bodies. To this end, both physical experiment and CFD simulation can be exploited to investigate the behaviors of a body. Regarding this issue, a number of previous studies have been carried out. However, little specific data of the body design have been documented in the published literature so far. This study investigates numerically a number of varied designs of high-speed underwater slender bodies. The designs are different in some of the bodies' typical parameters which include the cavitator shape and body length. Steady state simulations of the single/two-phase partial- and super-cavitating flows around the bodies have been carried out by using the CFD approach. A two-phase mixture formulation, turbulence $k-\varepsilon$ model (for the solution of the flow field) and Zwart-Geber-Belamri (ZGB) cavitation modeling (for mass transfer modeling) are exploited. For the model validation, comparisons with the published experimental and numerical data have been performed. The behaviors of the natural cavitating flow around the different bodies investigated are obtained. The modified drag coefficient for these specific bodies and operating conditions are proposed.

T. T. Nguyen (✉) · T. Q. Nguyen
Institute of Mechanics, Vietnam Academy of Science and Technology,
264 – Doi Can, Ba Dinh, Hanoi, Vietnam
e-mail: ntthang@imech.vast.vn; ntthang_imech@yahoo.com

T. T. Nguyen · H. N. Duong
Graduate University of Science and Technology, Vietnam Academy
of Science and Technology, 18 – Hoang Quoc Viet, Cau Giay, Hanoi, Vietnam

H. Kikura
Tokyo Institute of Technology, 2-12-1-N1-7 Ookayama, Meguro-Ku,
Tokyo 152-8550, Japan

Keywords Computational fluid dynamics—CFD • Cavitation
Two-phase flow • Underwater • High-speed

1 Introduction

When a solid body moves at high enough speed underwater, the pressure of the flow around the body can drop below the saturated vapor pressure. A gas pocket can be formed around the body. The gas pocket is filled by water vapor due to the high pressure drop, i.e., water boiling naturally at reduced pressure. The flow is known as the natural cavitating flow. If the vapor pocket completely covers the body, it is called a super-cavity. If not, it is considered as a partial-cavity when the vapor pocket encloses part of the body (e.g., see [1, 2]). The cavitating flow imposes critical effects on the dynamics, control, and guidance of the high-speed underwater bodies.

In the practical operation of high-speed submerged bodies, both the partial- and super-cavitating flow regimes play important roles. In the partial-cavitating flow, the skin friction remarkably reduces because the body comes less in contact with the liquid phase. This regime crucially effects the flow dynamics during flight transients or maneuvering. Furthermore, in the super-cavitating flow, the vapor pocket is long enough to enclose the whole body. Accordingly, super-cavitation enables to minimize the skin friction. High-speed (or even supersonic) underwater motion can be attained in the super-cavitating flow regime [1–4]. Optimal operation of a high-speed submerged body can only be obtained if the dynamics and effects of the cavitating flow regimes are fully addressed and taken into account. Careful considerations must be performed from the initial stage, i.e., body design.

A proper design of high-speed underwater bodies, e.g., high-speed cavitating slender objects, should produce not only a stable motion with a straight trajectory, but also maximize the travel distance of the body. To this end, physical experiments (e.g., see [1]), analytical approximations (e.g., see [5]) and CFD simulations (e.g., see [6–8]) can be exploited to investigate the behaviors of the cavitating flow around the body. A number of previous studies have been carried out (e.g., see [1–8]). However, little specific data of the body design have been documented in the published literature so far. On the experimental side, physical experiments are usually highly difficult. That is typically due to the fact that high velocity and two-phase cavitating flow are involved. Methods for detailed measurements of such demanding flow conditions are not available currently. Presently, optical visualization is extensively used [9–12]. Analytical approximations are computationally efficient, but there are difficulties in obtaining the details of the flow behaviors [5, 13, 14]. Consequently, in this study, the CFD approach is exploited.

The CFD approach to the cavitating flow simulation can be based on several theoretical formulations such as single-fluid, volume of fluid (VOF), two-fluid (e.g., see [15]). For the cavitating flow simulation, the two-phase mixture formulation which is based on the single-fluid approach is most computationally efficient, and

capable of providing sufficiently accurate results. It has been well exploited previously for cavitating flow study (e.g., see [16–18]). Hence, the two-phase mixture approach is applied in this study to the investigation of the cavitating flow dynamics and effects of different body designs.

On the numerical simulation of the cavitating flow by using the CFD approach and analytical approximations, the flow dynamics and cavity behaviors have been well clarified for the flow around some specific body configurations (e.g., see [5, 7, 8]). Both the natural cavitating flow and ventilated one have been investigated (e.g., see [7, 8]). A comparison between the partial- and super-cavitating flow regimes have been carried out for blunt cavitator. The partial-cavitating flow has been investigated with changing the body diameter [5]. In order to clarify the effects of different cavitator shapes (e.g., hemispherical, conical) and/or the body length on the flow dynamics, cavity size, and so on, further investigations are necessarily required.

In this study of high-speed submerged bodies, numerical simulations by using the CFD approach have been performed for a number of varied cavitator designs. The designs are different in some of the body's typical parameters which include the cavitator shape and body length. Steady state simulations of the single/two-phase cavitating flows around the bodies have been conducted. The well-known two-phase mixture formulation with the Realizable $k-\varepsilon$ turbulence model and the ZGB cavitation modeling [19] is exploited to investigate the partial- and super-cavitating flow regimes around the high-speed underwater bodies. For the model validation, comparisons with the published experimental data [20] and numerical data [7, 8] have been carried out. Effects of the computational grid refinement have been investigated. The validated CFD model is then applied to the study of the dynamics of the cavitating flow around the bodies. The effects of cavitator shapes and body lengths are quantified. A modified drag coefficient for the bodies considered is proposed.

2 Theoretical Formulation and Numerical Method

For the CFD simulation of the cavitating flow, the mixture model which uses the single-fluid approach can be exploited (e.g., see [16–18, 21, 22]). In this approach, the two phases (liquid and vapor) are treated mathematically as interpenetrating continua. The mixture model is developed for two (or more) phases (e.g., see [15]). This model solves a set of the governing equations that are written for the two-phase mixture variables (e.g., mixture density, velocity). Additional volume fraction equations for the secondary phases and algebraic representations for the relative velocities between the two phases can be included. This approach considerably reduces the computational expenses. In details, for the CFD simulation of the natural cavitating flow, the following equations are solved numerically.

2.1 Governing Equations for the Natural Cavitating Flow

In the natural cavitating flow, the vapor phase is rapidly generated in the single-phase fluid regions where the static pressure drops below the saturated vapor pressure. Consequently, the variation in the temperature field is small and can be negligible. Hence, a constant ambient temperature is maintained which implies the omission of the energy equation in the governing equations of the natural cavitating flow.

Mixture continuity equation

The mixture continuity equation shown in Eq. (1) is exploited for the calculation of the phase volume fractions [15]. In addition, it is also exploited in the solution method to calculate the mixture pressure distribution as shown later on.

$$\frac{\partial}{\partial t}(\rho_m) + \nabla \cdot (\rho_m \vec{v}_m) = 0 \quad (1)$$

where \vec{v}_m and ρ_m are the mass-averaged velocity and mixture density, respectively. They are written, respectively, as $\vec{v}_m = (\sum_{k=1}^n \alpha_k \rho_k \vec{v}_k) / \rho_m$ and $\rho_m = \sum_{k=1}^n \alpha_k \rho_k$ where α_k , ρ_k and n are the volume fraction, density of the phase k , and the number of phases, respectively.

Mixture momentum equation

For the calculation of the mixture velocity distribution, the mixture momentum equation shown in Eq. (2) is used [15].

$$\frac{\partial}{\partial t}(\rho_m \vec{v}_m) + \nabla \cdot (\rho_m \vec{v}_m \vec{v}_m) = -\nabla p + \nabla \cdot [\mu_m (\nabla \vec{v}_m + \nabla \vec{v}_m^T)] + \rho_m \vec{g} + \vec{F} - \nabla \cdot \left(\sum_{k=1}^n \alpha_k \rho_k \vec{v}_{dr,k} \vec{v}_{dr,k} \right) \quad (2)$$

where, p is the mixture pressure; μ_m is the viscosity of the mixture ($\mu_m = \sum_{k=1}^n \alpha_k \mu_k$ where μ_k is the molecular dynamic viscosity of the phase k); \vec{g} is the gravitational acceleration; \vec{F} is the body force; $\vec{v}_{dr,k}$ is the drift velocity for the secondary (i.e., k th) phase, by definition, $\vec{v}_{dr,k} = \vec{v}_k - \vec{v}_m$ which is the difference between the phase velocity and the mathematically defined velocity of the multiphase mixture.

Mixture pressure-correction equation

In this study, the distribution of the mixture pressure field which appears on the right hand side of Eq. (2) is iteratively calculated by using the pressure-correction equation (i.e., the pressure-based continuity equation) shown in Eq. (3). This is one of the multiphase solution methods of CFD pressure-based solvers [15].

$$\sum_{k=1}^n \left\{ \frac{\partial}{\partial t} \alpha_k + \nabla \cdot \alpha_k \vec{v}'_k + \nabla \cdot \alpha_k \vec{v}^*_k - \frac{1}{\rho_k} \sum_{l=1}^n \dot{m}_{lk} \right\} = 0 \quad (3)$$

where \vec{v}_k , \vec{v}'_k and \vec{v}^*_k are the velocity of the k th phase's velocity, velocity correction and the value of \vec{v}_k at the current iteration, respectively. \dot{m}_{lk} denotes the mass

transfer from the l th to k th phase. With the approach used here, the pressure and velocities are corrected so as to satisfy the continuity constraint [15].

Equation of drift velocity

In Eq. (2), an additional equation for the specification of the drift velocity $\vec{v}_{dr,k}$ is required. It can be obtained by using Eq. (4) that connects $\vec{v}_{dr,k}$ and the relative velocity between the two phases (\vec{v}_{lk}) [15].

$$\vec{v}_{dr,k} = \vec{v}_{kl} - \sum_{i=q}^n c_i \vec{v}_{li} \quad (4)$$

where c_i is the mass fraction of the i th phase, which is defined by $c_i = \alpha_i \rho_i / \rho_m$. In order to close Eq. (4), an algebraic slip formulation can be used to calculate the relative (slip) velocity in the form $\vec{v}_{lk} = (\tau_l / f_{drag}) ((\rho_l - \rho_m) / \rho_l) \vec{a}$ where τ_l and \vec{a} are the relaxation time and acceleration whose specific models can be found in [15].

Phase volume fraction equation

In the last term on the right hand side of Eq. (2), one more additional equation must be required for the phase volume fraction α_k . From the continuity equation for the secondary phase k , the phase volume fraction equation can be derived as shown in Eq. (5) [15].

$$\frac{\partial}{\partial t} (\alpha_k \rho_k) + \nabla \cdot (\alpha_k \rho_k \vec{v}_m) = - \nabla \cdot (\alpha_k \rho_k \vec{v}_{dr,k}) + \sum_{q=1}^n (\dot{m}_{kq} - \dot{m}_{qk}) \quad (5)$$

In order to close this equation, a mechanistic model for the mass transfer terms is required. For the cavitating flow, a cavitation model shown later on in the cavitation modeling is described for that purpose.

Turbulence effects

The natural cavitating flow is typically turbulent one where there exists high flow velocity. For the application of the multiphase mixture model in the CFD simulation of the turbulent natural cavitating flow, the numerical solution of the Reynolds-Averaged Navier-Stokes (RANS) equations derived from Eq. (2) is sought. The multiphase mixture k - ε turbulence model (an extension of the single-phase k - ε model) shown in Eqs. (6) and (7) for the turbulence kinetic energy k and turbulence energy dissipation rate ε , respectively, can be used to close the RANS equations accompanied with the Boussinesq hypothesis [15].

$$\frac{\partial}{\partial t} (\rho_m k) + \nabla \cdot (\rho_m \vec{v}_m k) = \nabla \cdot \left(\left(\mu_m + \frac{\mu_{t,m}}{\sigma_k} \right) \nabla k \right) + G_{k,m} - \rho_m \varepsilon + \Pi_{k_m} \quad (6)$$

$$\frac{\partial}{\partial t} (\rho_m \varepsilon) + \nabla \cdot (\rho_m \vec{v}_m \varepsilon) = \nabla \cdot \left(\left(\mu_m + \frac{\mu_{t,m}}{\sigma_\varepsilon} \right) \nabla \varepsilon \right) + \frac{\varepsilon}{k} (C_{1\varepsilon} G_{k,m} - C_{2\varepsilon} \rho_m \varepsilon) + \Pi_{\varepsilon_m} \quad (7)$$

where, $C_\mu = 0.009$; $\sigma_k = 1.0$ is the turbulent Prandtl number for k and $\sigma_\varepsilon = 1.3$ is that for ε in the mixture; $G_{k,m}$ is the turbulence production (i.e., the production of the turbulent kinetic energy of the mixture): $G_{k,m} = \mu_{t,m} (\nabla \vec{v}_m + (\nabla \vec{v}_m)^T) : \nabla \vec{v}_m$; $C_{1\varepsilon} = 1.44$; $C_{2\varepsilon} = 1.92$; $\Pi_{k,m}$, and $\Pi_{\varepsilon,m}$ are the source terms that can be used to model the turbulent interaction between the phases. Importantly, based on the solution of Eqs. (6) and (7), the turbulent viscosity for the mixture $\mu_{t,m} = \rho_m C_\mu k^2 / \varepsilon$ is obtained.

2.2 Cavitation Modeling

Natural cavitation means liquid boiling and vapor generation, at ambient temperature, in the liquid regions where the static pressure falls below the saturated vapor pressure. In such a case, very large and steep density variations occur in the low-pressure/cavitating regions. In order to correctly model the cavitating process by using the CFD approach, several cavitation models such as Singhal, ZGB, Schnerr and Sauer models have been developed. Based on previous investigations (e.g., see [23, 24]), ZGB model which is robust and more flexibly controllable over the other models is exploited in this study. The details of ZGB model are shown below.

Vapor volume fraction equation (vapor transport equation)

In natural cavitation, the multiphase mixture can be regarded to be composed of liquid and vapor phases. The liquid–vapor mass transfer (i.e., evaporation and condensation) is governed by the vapor transport equation which is a specifically rewritten form of Eq. (5) as shown below.

$$\frac{\partial}{\partial t} (\alpha_k \rho_k) + \nabla \cdot (\alpha_k \rho_k \vec{v}_m) = -\nabla \cdot (\alpha_k \rho_k \vec{v}_{dr,k}) + \dot{m}_{kl} - \dot{m}_{lk} \tag{8}$$

where k and l denote vapor and liquid phases of the two-phase mixture, respectively. The mass transfer terms \dot{m}_{kl} (condensation) and \dot{m}_{lk} (evaporation) are modeled based on the Rayleigh-Plesset equation (shown below) which describes the growth/collapse of a single vapor bubble in a viscous liquid [15].

Effects of bubble dynamics

To account for the bubble growth and collapse, the bubble dynamics equation obtained from the generalized Rayleigh-Plesset equation can be used as shown in Eq. (9). Here, a flowing liquid with zero velocity slip between the fluid and bubbles is assumed.

$$R_b d^2 R_b / dt^2 + 1.5 (dR_b / dt)^2 = (p_b - p) / \rho_l - 4 \nu_l \dot{R}_b / R_b - 2 \sigma / (\rho_l R_b) \tag{9}$$

where R_b , σ , ρ_l , ν_l , p_b , and p are the bubble radius, liquid surface tension coefficient, liquid density, liquid kinematic viscosity, bubble surface pressure, and local far-field pressure, respectively [15].

In the cavitation phenomena, the pressure drop is a dominant force. Hence, the surface tension force can be negligible. In addition, in Eq. (9), by eliminating the second-order terms and noting that the contribution of the second term on the right hand side of Eq. (9) would be negligible since $\dot{R}_b \ll R_b$ and $v_l \ll 1$, the following simplified equation for the bubble dynamics is obtained.

$$dR_b/dt = \sqrt{(2/3)(p_b - p) / \rho_l} \quad (10)$$

ZGB cavitation model

This model calculates the total interface mass transfer rate per unit volume by using the bubble density number n (which is later replaced by the vapor volume fraction α_v since n and α_v are related to each other) and the mass change rate of a single bubble. Moreover, in order to account for the following effects: evaporation, condensation, and cavitation bubble interaction, the final form of ZGB cavitation model is written as shown in Eq. (11) for evaporation (i.e., $p \leq p_v$), and Eq. (12) for condensation (i.e., $p \geq p_v$).

$$\dot{m}_{ik} = F_{vap} 3\alpha_{nuc}(1 - \alpha_v)\rho_v / R_b \sqrt{(2/3)(p_v - p) / \rho_l} \quad (11)$$

$$\dot{m}_{kl} = F_{cond} 3\alpha_v \rho_v / R_b \sqrt{(2/3)(p - p_v) / \rho_l} \quad (12)$$

Suggested values of the coefficients and variables in Eq. (11) and (12) are $R_b = 10^{-6}$ m; $\alpha_{nuc} = 5 \times 10^{-4}$ (nucleation site volume fraction); $F_{vap} = 50$ (evaporation coefficient); $F_{cond} = 0.01$ (condensation coefficient) [15].

2.3 Body Shapes, Computational Domain, Boundary and Setting Conditions

Body shapes and lengths

This study investigates four right circular cylindrical bodies with different cavitator shapes: blunt, 45°-conical, hemispherical, and 1-caliber-ogive, respectively, as shown in Fig. 1 for 2D case. The same body diameter $d_{body} = 6.6$ mm and cavitator diameter $d_c = 6.6$ mm are used for all bodies. Regarding the body length L_{body} , three values which are 50, 100, and 150 mm are investigated.

Computational domain

An example of the computational domain for 100-mm-long bodies is shown in Fig. 2. In the high-speed natural cavitating flow, the inertial force effects are



Fig. 1 Bodies with different cavitator shapes

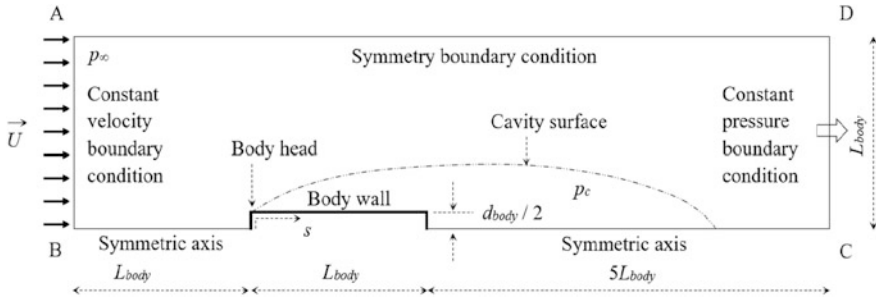


Fig. 2 2D computational domain with blunt cavitator body, 100-mm body length

dominant over the gravitational effects; hence the gravitational acceleration can be ignored. Consequently, the symmetry of the flow field around the body can be suitably assumed. Hence, as shown in Fig. 2, half of the flow field is modeled. The axis of symmetry is the body's symmetric axis. The 2D computational domain is composed of the rectangular ABCD and half of the body wall as shown in Fig. 2 (e.g., of blunt cavitator). For other cavitator types, just the body's fore region is modified accordingly. AB and DC are the upstream and downstream boundaries of the flow field. BC is taken coincidentally with the body's symmetric axis. The body's symmetric axis is aligned parallel with the upstream flow direction. AD is the far-field (free-flow) boundary. The domain size is shown in the figure as well.

The selection of the computational domain size must be carefully considered since the flow field at the upstream and downstream boundaries (AB and CD) where boundary conditions are specified in advance can be strongly affected by the flow inside the computational domain. Moreover, the selection of the computational domain at the rear of the body must be adequate for adequately capturing the wake. Also, the distance between the boundaries AD and BC must be reasonable so that, for the sake of simplicity, available types of the free-flow boundary condition in the CFD approach can be applied with minimal effects on the flow field inside the computational domain.

From the literature review (e.g., see [22, 25]), the selection of the size of the computational domain around the body (as shown in Fig. 2) would be reasonable. The proper selection of the computational domain size is further quantitatively confirmed in the model validation shown later on.

Boundary and setting conditions

For the upstream boundary condition along AB, a constant-velocity boundary condition is selected. The velocity magnitude is taken to be the body's speed underwater. The flow direction is set normal to AB. In order to simulate the natural cavitating flow around high-speed submerged bodies in quiescent water, the turbulence intensity along AB is set to 4% [15].

For the downstream boundary condition along DC, the constant static pressure (i.e., hydrostatic pressure) is applied. The gauge pressure is set to zero. The turbulence intensity along DC is set to 4% as well. Test calculations for varied values

of the turbulence intensity along DC revealed that the effects of the boundary condition for turbulence along DC would be negligible [15].

Along the symmetric axis, the axis boundary type is used. For this type of boundary condition, there is no calculation along the axis boundary. The appropriate physical value of a particular flow variable at any point along this axis is taken to be the cell value in the adjacent cell [15].

Along the free-flow boundary AD, the symmetry boundary condition is selected. This implies that along AD, a zero-shear stress condition (i.e., slip wall) is assumed. Hence, the normal velocity and gradient of all variables are zero across this boundary [15].

Along the body wall, no slip boundary condition is prescribed. In addition, to model turbulent flow, a near-wall modeling approach that allows a consistent mesh refinement (modification) without any deterioration of the results, especially in the near-wall region, is exploited for the calculation of the flow variables at the cells adjacent to the wall [15].

Other setting conditions are as follows. The two-phase mixture composes of liquid water and vapor only. The operating pressure is set to ambient pressure (i.e., atmospheric pressure). Simulations are carried out for adiabatic condition with the operating temperature set to 25 °C. The depth of the submerged bodies is set to 1 m. As a result, the saturated vapor pressure is approximately 2338 Pa with hydrostatic pressure taken into account.

2.4 Computational Grid and Numerical Discretization of the Governing Equations

Computational grid

The computational domain is discretized into structured quadrilateral meshes (cells or elements also). The meshing strategy here is to generate body aligned mesh which, to some extent, also implies flow aligned mesh. Hence, some sources of errors caused by the domain discretization would be minimized. High quality of the computational mesh is prioritized in the regions close to the body wall as shown in Fig. 3. The figure is an example of the computational mesh around the spherical-cavitator, 100-mm-long body. The total number of cell elements is around 41000 for the computational mesh of all 100-mm-long bodies (blunt, 45°-conical, spherical, and 1-caliber-ogive cavitator types). For all 150-mm-long bodies, the number is approximately 56000. For all 50-mm-long bodies, it is about 30000.

Since a near-wall modeling approach is exploited for the calculation in the near-wall regions, and test calculations have shown that the grid resolution in the cavitating and wake regions would be reasonable; these computational meshes will be used for the validation calculations. Once the validation results are acceptable, the meshes will be used in further investigations of the cavitating flow around the bodies.

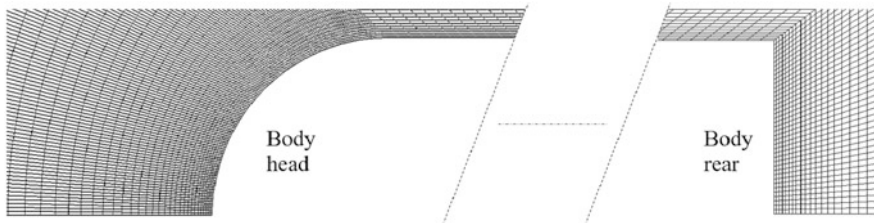


Fig. 3 2D partial-computational mesh around the spherical-cavitator body

Numerical discretization of the governing equations

The governing equations were solved numerically by using the finite volume method (FVM). The pressure-based coupled algorithm was chosen. The algorithm solves a coupled system of equations consisting of the momentum Eq. (2) and the pressured-based continuity Eq. (3). This algorithm significantly improves the convergence of the calculations. The volume fraction equation is solved in a segregated manner in order to reduce the memory requirement [15].

The body force weighted scheme was selected for the calculation of the cell-face pressure. The second-order upwind scheme was used for the momentum and turbulence transport equations. The Quadratic Upstream Interpolation for Convective Kinematics (QUICK) scheme was employed for the volume fraction equation (i.e., the vapor transport equation). The Realizable k - ϵ turbulence model with enhanced wall treatment (i.e., near-wall modeling) for the cells adjacent to the walls was exploited [15].

For the optional calculation of the drift velocity, the Schiller Naumann model of the drag force, Manninen-et al model of the slip velocity would be used. These selections were adopted in all calculations in this study. In addition, corresponding to the flow conditions investigated in this study, a constant surface tension coefficient of 0.072 N/m was used to account for the effects of the surface tension force along the cavity surface.

2.5 Numerical Model Validation for Blunt, 45°-Conical, Spherical, and 1-Caliber-Ogive Cavitator Bodies

Experimental and numerical data for the model validation

The numerical models of the steady state natural cavitating flow around 100-mm-long bodies (for four cavitator shapes) have been setup by using the CFD approach. For the model validation, the data extracted from [7, 8] are used. The published data have been obtained for four bodies with the same body configuration as those of this study [7, 8]. They include the experimental and numerical data of a non-dimensionalized parameter that is the pressure coefficient $C_p = (p_{local} - p_{\infty}) / (0.5\rho_1 U^2)$ against the non-dimensionalized arc length along the body surface s/d_c

(Fig. 2). Here, p_{local} is the local static pressure along the body surface; p is the far-field static pressure; ρ_l is the density of the liquid phase; U is the upstream velocity; s is the arc length; d_c is the cavitator diameter (for the cavitator types of the four bodies used in this study, $d_c = d_{body}$) as shown in Fig. 2. The data of C_p are obtained for different cavitation number $\sigma = (p_\infty - p_c) / (0.5\rho_l U^2)$, which is shown in Table 1 for the partial-cavitating flow (i.e., cavity closes on the body), whose σ is relatively high (i.e., $\sigma > 0.1$). In addition, a comparison for the case of the single-phase flow is also performed. Here p_c is the cavity pressure which means the saturated vapor pressure in the natural cavitating flow in this study (Fig. 2).

The model validation by using C_p is useful and widely used (e.g., see [16]) since the correct calculation of C_p would imply two important factors: the accuracy of the calculation of the flow dynamics would be adequate, and the simulation of the cavity behaviors would also be reliable. Moreover, the calculations involve not only two-phase flows but also single-phase flow (i.e., single-phase non-cavitating flow, and single-phase flow in the non-cavitating, and wake regions in the partial-cavitating flow), therefore, the model setup would be properly acceptable. Consequently, depending on the available data for comparison, the model validation would be conducted by using C_p alone, though the use of additional flow parameters for the model validation would also be highly important.

Computational grid refinement investigation

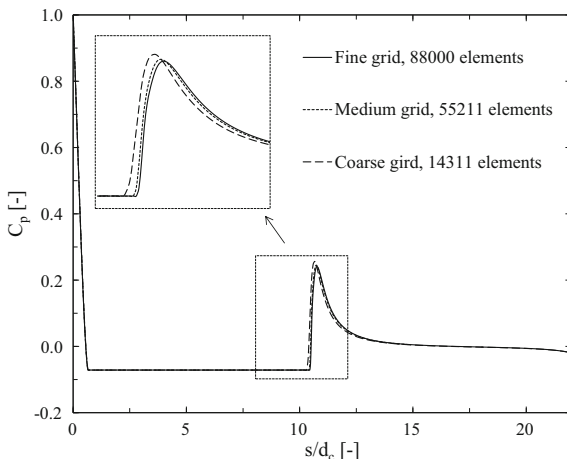
In order to evaluate the effects of the computational grid refinement, three grid resolutions are investigated for all bodies. They are corresponding to coarse, medium, and fine ones. Approximately, the coarse grids have about 15000 computational elements for all cavitator shapes and body lengths. The medium ones have about 56000 elements for all cases. And the fine ones have about 90000 elements. For brevity, the calculation results of the distribution of the pressure coefficient C_p along the body's axis (extended into the cavity wake region) are shown in Fig. 4 for the case of 1-caliber-ogive cavitator, 150-mm body length. For other cases, the behaviors of the obtained results are almost identical to that shown in Fig. 4. Calculations are executed for the same cavitation number $\sigma = 0.0713$ (i.e., $U = 55$ m/s) which corresponds to the partial-natural cavitating flow around 150-mm body length.

As illustrated in Fig. 4, the difference among the results obtained by using three different grids can be negligible except in the wake region of the cavity. Closely investigate the wake region as shown in the enlarged part in Fig. 4, the difference between the result of the medium grid and that of the fine one can also negligible.

Table 1 Cavitation number and upstream velocity for the partial-cavitating and single-phase flow simulations [7, 8]

σ [-]	0.20	0.24	0.30	0.32	0.40	0.46	0.50	Single-phase
U [m/s]	32.81	29.95	26.79	25.94	23.20	21.64	20.75	5.00

Fig. 4 Evaluation of the refinement of the computational grids (s/d_c : non-dimensionalization of the arc length s shown in Fig. 2)



Consequently, the medium grid resolution should be adequate. Hence, it is selected for further investigations later on in this study.

Comparison results

As shown in Fig. 5, for all four bodies, the results of this study would agree fairly well with the experimental data of both the single-phase and two-phase cavitating flow regimes. Moreover, in most cases, the numerical results of this study would be somewhat closer to the experimental data, in comparison with the published numerical results obtained by using another CFD solver and cavitation model.

Consequently, the results of the model validation would suggest that the CFD model setup in this study would be adequate for further investigations of the cavitating flow around the bodies. In more details, the use of the discretization schemes, ZGB cavitation model, the computational mesh quality, boundary and setting conditions would be reasonable and accurate.

3 Simulation Results

3.1 Simulation Conditions

Body shapes and lengths

In order to investigate the effects of the typical cavitator shapes on the partial- and super-cavitating flow regimes, four types of cavitator shape shown in Fig. 1 have been used.

The partial- and super-cavitating flow regimes are dependent relatively on the body length. With a specified body length, a super-cavitating flow will become a partial-one if the body length increases to a value that is larger than the current

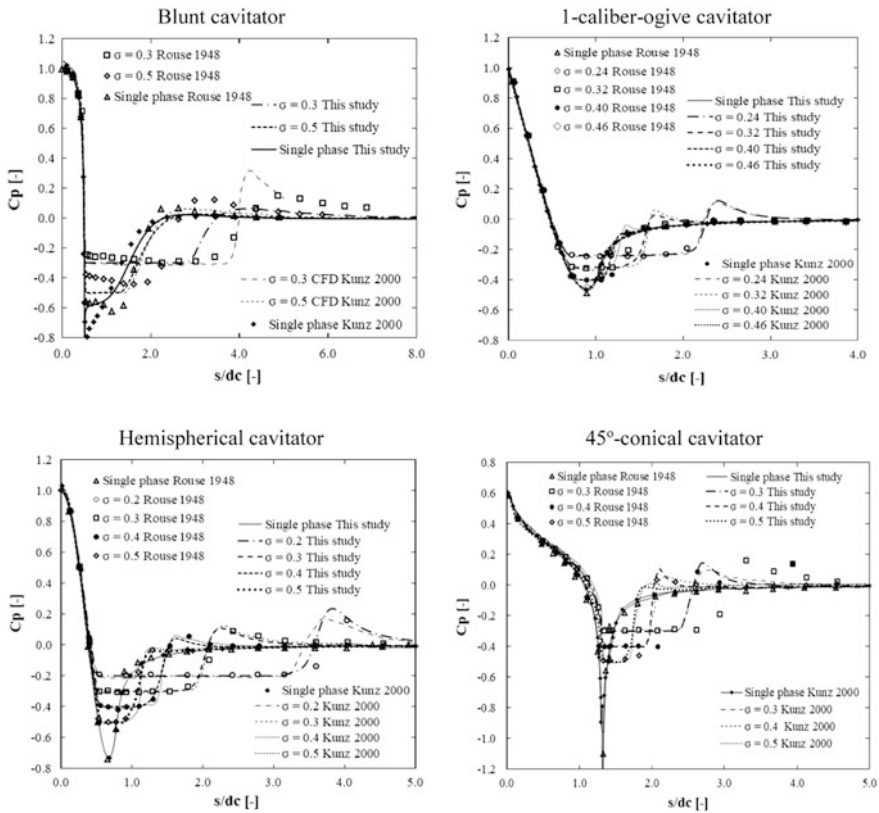


Fig. 5 Comparison of the pressure coefficient C_p for the four bodies (s/d_c : non-dimensionalization of the arc length s shown in Fig. 2)

super-cavity length. Hence, in order to investigate the effects of the body length, for each cavitator shape, simulations have been carried out for three body lengths, i.e., 50, 100, and 150 mm. For each body length, a range of cavitation number that centers on the transitional one (i.e., the value of σ that corresponds to the transition from partial-cavitation to super-one) is investigated.

Flow conditions

For all body shapes and lengths, the operating conditions and settings are remained identical. Only is the upstream velocity U varied, which corresponds to the variation of the cavitation number. The ranges of the upstream velocity U and cavitation number for different cavitator types and body lengths are shown in Tables 2, 3, 4 and 5.

Table 2 Cavitation number and upstream velocity for the case of blunt cavitator with three different body lengths

σ [-], 50 mm long	0.086	0.094	0.102	0.111	0.117	0.122	0.128	0.135	0.142	0.149	0.158	0.166	0.187	0.211	0.240
U [m/s], 50 mm long	50	48	46	44	43	42	41	40	39	38	37	36	34	32	30
σ [-], 100 mm long	0.060	0.064	0.069	0.074	0.077	0.080	0.083	0.086	0.090	0.094	0.098	0.102	0.111	0.122	0.135
U [m/s], 100 mm long	60	58	56	54	53	52	51	50	49	48	47	46	44	42	40
σ [-], 150 mm long	0.050	0.053	0.056	0.060	0.062	0.064	0.066	0.069	0.071	0.074	0.077	0.080	0.086	0.094	0.102
U [m/s], 150 mm long	66	64	62	60	59	58	57	56	55	54	53	52	50	48	46

(the shaded cells corresponding to the partial-cavitating flow condition, the others corresponding to the super-cavitating one)

Table 3 Cavitation number and upstream velocity for the case of hemispherical cavitator with three different body lengths

σ [-], 50 mm long	0.071	0.077	0.083	0.086	0.094	0.098	0.102	0.107	0.111	0.117	0.122	0.128	0.142	0.158	0.176
U [m/s], 50 mm long	55	53	51	50	48	47	46	45	44	43	42	41	39	37	35
σ [-], 100 mm long	0.047	0.05	0.053	0.056	0.058	0.060	0.062	0.064	0.066	0.069	0.071	0.074	0.08	0.086	0.094
U [m/s], 100 mm long	68	66	64	62	61	60	59	58	57	56	55	54	52	50	48
σ [-], 150 mm long	0.037	0.039	0.042	0.044	0.047	0.048	0.050	0.051	0.053	0.054	0.056	0.058	0.06	0.064	0.069
U [m/s], 150 mm long	76	74	72	70	68	67	66	65	64	63	62	61	60	58	56

(the shaded cells corresponding to the partial-cavitating flow condition, the others corresponding to the super-cavitating one)

Table 4 Cavitation number and upstream velocity for the case of 45° -conical cavitator with three different body lengths

σ [-], 50 mm long	0.074	0.08	0.086	0.094	0.098	0.102	0.107	0.111	0.117	0.122	0.128	0.135	0.149	0.166	0.187
U [m/s], 50 mm long	54	52	50	48	47	46	45	44	43	42	41	40	38	36	34
σ [-], 100 mm long	0.045	0.048	0.051	0.054	0.056	0.058	0.060	0.062	0.064	0.066	0.069	0.071	0.077	0.083	0.090
U [m/s], 100 mm long	69	67	65	63	62	61	60	59	58	57	56	55	53	51	49
σ [-], 150 mm long	0.035	0.037	0.039	0.042	0.044	0.045	0.047	0.048	0.050	0.051	0.053	0.056	0.06	0.064	0.069
U [m/s], 150 mm long	78	76	74	72	70	69	68	67	66	65	64	62	60	58	56

(the shaded cells corresponding to the partial-cavitating flow condition, the others corresponding to the super-cavitating one)

Table 5 Cavitation number and upstream velocity for the case of 1-caliber-ogive cavitator with three different body lengths

σ [-], 50 mm long	0.066	0.071	0.077	0.083	0.086	0.090	0.094	0.098	0.102	0.107	0.111	0.117	0.128	0.142	0.158
U [m/s], 50 mm long	57	55	53	51	50	49	48	47	46	45	44	43	41	39	37
σ [-], 100 mm long	0.043	0.045	0.048	0.051	0.053	0.054	0.056	0.058	0.060	0.062	0.064	0.066	0.071	0.077	0.083
U [m/s], 100 mm long	71	69	67	65	64	63	62	61	60	59	58	57	55	53	51
σ [-], 150 mm long	0.032	0.034	0.035	0.037	0.038	0.039	0.040	0.042	0.043	0.044	0.045	0.047	0.050	0.053	0.056
U [m/s], 150 mm long	82	80	78	76	75	74	73	72	71	70	69	68	66	64	62

(the shaded cells corresponding to the partial-cavitating flow condition, the others corresponding to the super-cavitating one)

3.2 Results and Discussions

Calculations with the flow conditions shown in Tables 2, 3, 4 and 5 have been conducted. Convergence of the calculations was satisfied. After each calculation, the cavity region which is bounded by the void fraction contour of 0.5 is specified. The void fraction criteria of 0.5 is selected based on the same value used in the previous study done by Kunz et al. (1999) [7]. The cavity length (L_{cav}) and diameter (D_{cav}) are then determined by following almost the same procedure used in Kunz et al. (1999) [7]. In this study, L_{cav} and D_{cav} are the major and minor axes of an ellipse which is determined as follows. The ellipse shares the same symmetric axis with the body (i.e., the symmetric axis of the body). It contains the flow separation point and the first point (with reference to the flow separation point) on the void fraction contour that is furthest from the body surface. An illustration is depicted in Fig. 6.

The received data of L_{cav} and D_{cav} (non-dimensionalized by d_c) are then plotted against cavitation number in Figs. 7, 8, 9, and 10. Figures 7, 8, 9 and 10 are corresponding to the flow conditions shown in Tables 2, 3, 4 and 5, respectively. In the figures, the data of both the partial- and super-cavitating flow regimes are plotted altogether for all three body lengths. In addition, in the figures, the data calculated by using Garabedian 1956's theoretical correlation [26] for the cavity length and diameter shown in Eqs. (13) and (14) are also plotted.

$$L_{cav} = (d_c/\sigma)\sqrt{C_D \ln(1/\sigma)} \tag{13}$$

$$D_{cav} = d_c\sqrt{C_D/\sigma} \tag{14}$$

where $C_D = C_{D0} \times (1 + \sigma)$ is the drag coefficient; C_{D0} is the drag coefficient corresponding to $\sigma = 0$. For these plots, the following values of the drag coefficient C_{D0} are used as shown in Table 6.

As seen in Figs. 7, 8, 9 and 10, the calculated results of the non-dimensionalized cavity length and diameter against cavitation number are highly in accord with the formulation derived theoretically by Garabedian (1956) [26]. The calculated cavity dimension obtained by using the CFD approach which is validated earlier would be reasonably reliable, for the flow conditions and bodies investigated. This would

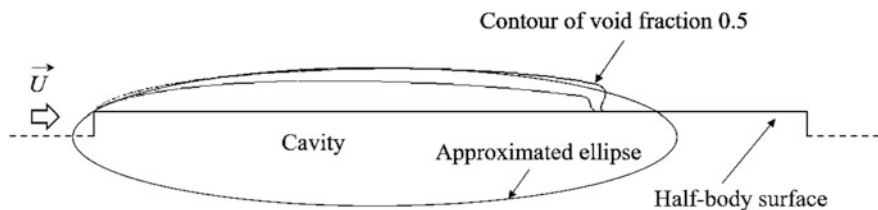


Fig. 6 Reconstruction of the cavity (blunt cavitator, 100-mm-long body; $\sigma = 0.111$; $U = 44$ m/s)

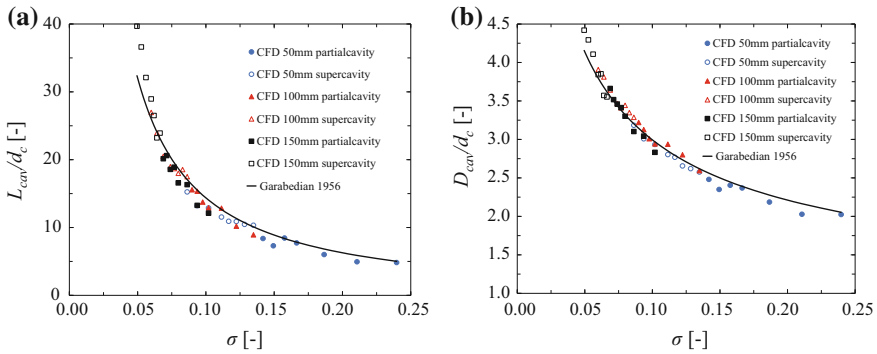


Fig. 7 Non-dimensionalized cavity length (L_{cav}/d_c) (a) and cavity diameter (D_{cav}/d_c) (b) against cavitation number: Blunt cavitator

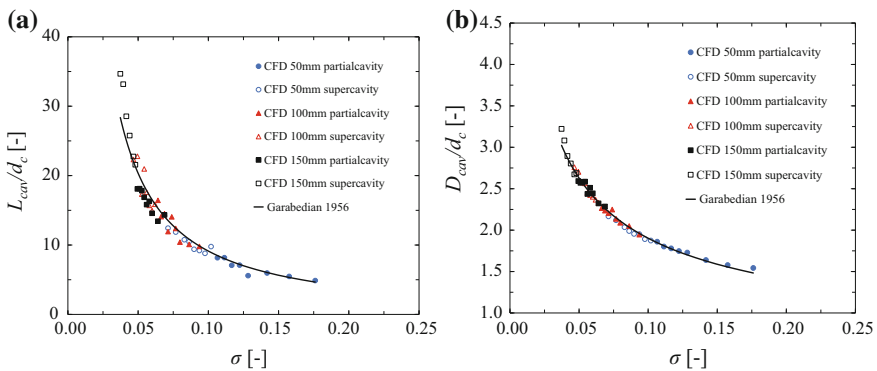


Fig. 8 Non-dimensionalized cavity length (L_{cav}/d_c) (a) and cavity diameter (D_{cav}/d_c) (b) against cavitation number: Hemispherical cavitator

confirm that the calculated results show the correct behaviors of the natural cavitating flow around the bodies with different cavitator shapes and body lengths under investigation.

For each cavitator shape, calculations were carried out for both the partial- and super-cavitating flow regimes and three body lengths. It is worth noting that, the super-cavitating flow around a body with a specific length becomes the partial-one if the body length increases. The flow conditions shown in Table 1 are an example. For the velocity range from 40 to 48 m/s, the flow is super-cavitating for 50 mm long, blunt cavitator body. However, in the same velocity range, the flow is partial-cavitating for 100-mm-long body. Physically there exists difference of the flow field at the cavity closure region (between the partial- and super-cavitating flow regimes); the calculated results show that the partial-cavities appear to be somewhat smaller than the super-ones. From the calculated results in this study for natural cavitation, this behavior seems to be less noticeable in comparison with the

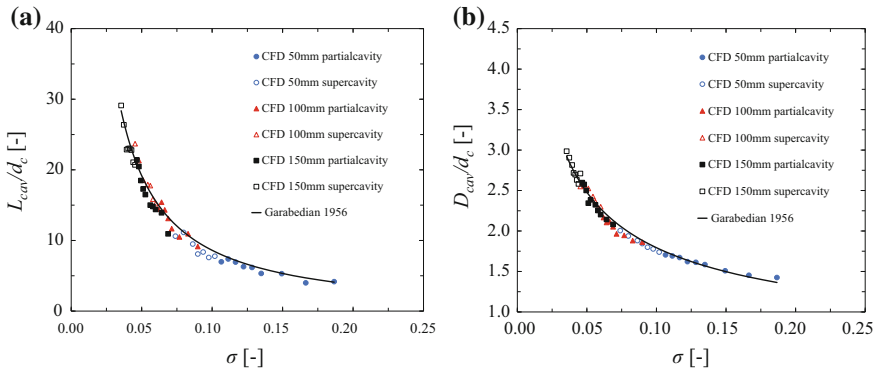


Fig. 9 Non-dimensionalized cavity length (L_{cav}/d_c) (a) and cavity diameter (D_{cav}/d_c) (b) against cavitation number: 45°-conical cavitator

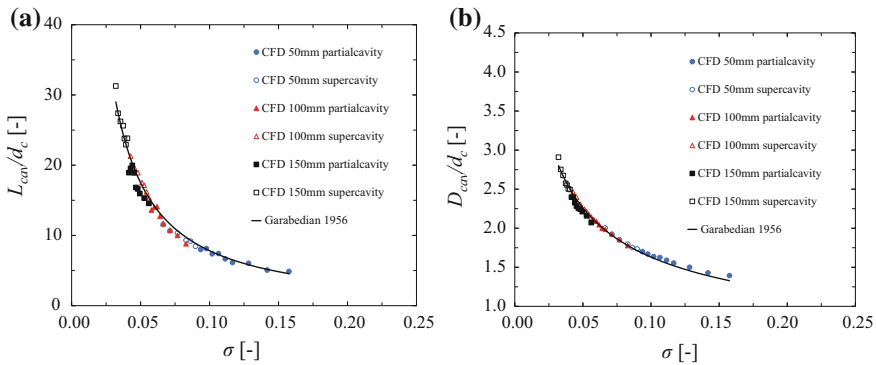


Fig. 10 Non-dimensionalized cavity length (L_{cav}/d_c) (a) and cavity diameter (D_{cav}/d_c) (b) against cavitation number: 1-caliber-ogive cavitator

Table 6 Drag coefficient C_{D0} for each type of cavitator shapes

	Blunt	Hemispherical	45°-conical	1-caliber-ogive
C_{D0} [-]	0.815	0.329	0.293	0.245

case of the water entry cavitating flow [10, 11]. Nevertheless, in general, the calculated results of both flow regimes (i.e., the partial- and super-cavitating flow regimes) align well with the trend predicted by using Garabedian 1956’s formulation.

The results shown in Figs. 7, 8, 9 and 10 also show a well-known fact that the blunt cavitator bodies generate largest cavity. As seen in Garabedian 1956’s formula (Eqs. (13) and (14)), the difference of the cavity size at the same cavitation number (with different cavitator shapes, same body length) depends on the drag

coefficient C_D which in turn depends on C_{D0} . The values of C_{D0} for each cavitator shape are shown in Table 6. The blunt cavitator shape has the largest drag coefficient. The other three cavitator shapes have much smaller drag coefficient C_{D0} . It is also worth noting here that, for the blunt cavitator shape, the value of C_{D0} which is 0.815 is almost the same as what suggested previously (e.g., see [1, 13, 26]). For the other three cavitator shapes, using the value of C_{D0} shown in Table 6 systematically matches all numerically calculated data with the results of Garabedian 1956's theoretical formulation. However, these three values are a little modified in comparison with the values used in the published literature. Approximately, the previously suggested C_{D0} are 0.259, 0.243, and 0.2 for hemispherical, 45°-conical, and 1-caliber-ogive cavitator shapes, respectively. Consequently, the values of C_{D0} proposed in Table 6 would be a suitable modification of the drag coefficient for the bodies and cavitating flow conditions investigated in this study.

4 Concluding Remarks

The natural cavitating flow around high-speed submerged bodies of varied designs has been investigated numerically in this study. The bodies all have a right circular cylindrical shape of 6.6 mm diameter. Different cavitator shapes have been studied. The cavitator shapes include blunt, hemispherical, 45°-conical, and 1-caliber-ogive cavitators. For each cavitator shape, three different body lengths which are 50, 100, and 150 mm have been investigated. The flow regimes studied are the partial- and super-cavitating flow regimes.

Steady state simulations of the single/two-phase cavitating flow around the bodies have been carried out by using the CFD approach. The well-known two-phase mixture formulation and the Realizable $k-\epsilon$ turbulence model are exploited for the solution of the flow field. ZGB cavitation model has been selected for the mass transfer modeling. For the model validation, the pressure coefficient C_p computed in this study has been compared with the experimental and numerical data extracted from the published literature. Fairly good agreements have been obtained that confirm the high accuracy of the calculated results of this study. In addition, the effects of the computational grid refinement have been considered. The reasonable grid resolution has been addressed and selected.

The CFD model has then been applied to the simulations of the partial- and super-cavitating flow around the bodies. The calculated results have been obtained and processed. Based on the received results, the following concluding remarks and new findings have been established:

- For all types of cavitator shape, the calculated cavity size for both the partial- and super-cavitating flow well aligns with the trend predicted by using Garabedian 1956's theoretical formulation.
- For each type of the cavitator shapes, the effects of the body length on the flow behaviors, e.g., the cavity size, have been investigated. At the same cavitation

number, the partial-cavity generated by a longer body appears to be smaller than the super-cavity generated by a shorter body. This behavior seems to be less noticeable in comparison with the cavitating flow after horizontal water entry.

- A set of modified drag coefficient C_{D0} has been proposed for the types of cavitator shapes and flow conditions investigated. This can be useful for the accurate calculation of the drag on high-speed submerged bodies.

Acknowledgements Financial support from the following scientific research projects of Vietnam Academy of Science and Technology (VAST) and Institute of Mechanics (IMECH) to carry out this study is gratefully acknowledged:

- VAST01.04/17-18 and VAST.HTQT.NGA.01/17-18 project of VAST
- Annual Research Fund of 2017 of IMECH (to Eng. Nguyen Quang Thai, the third author of this paper). (Additionally, financial support for the conference attendance and paper publication is from the scientific research VAST01.01/16-17 of VAST.)

References

1. May A (1975) Water entry and the cavity-running behavior of missiles. SEAHAC Technical Report No. 75-2 Naval Surface Weapons Center, White Oak Laboratory, Silver Spring, MD
2. Franc JP, Michel JM (2006) Fundamentals of cavitation. Springer
3. Truscott TT, Brenden PE (2014) Jesse Belden. Water entry of projectiles. *Annu Rev Fluid Mech* 46:355–378
4. Vanek B (2008) Control methods for high-speed supercavitating vehicles. PhD thesis, University of Minnesota
5. Varghese AN, Uhlman JS, Kirschner IN (2005) Numerical analysis of high-speed bodies in partially cavitating axisymmetric flow. *J Fluids Eng* 127(1):41–54
6. Shih TH, Liou WW, Shabbir A, Yang Z, Zhu J (1995) A new eddy-viscosity model for high Reynolds number turbulent flows—model development and validation. *Comput Fluids* 24(3):227–238
7. Kunz RF, Boger DA, Stinebring DR, Chyczewski TS, Lindau JW, Gibeling HJ, Sankaran V, Govindan TR (2000) A preconditioned Navier–Stokes method for two-phase flows with application to cavitation prediction. *Comput Fluids* 29(8):849–875
8. Kunz RF, Lindau JW, Billet ML, Stinebring DR (2001) Multiphase CFD Modeling of developed and supercavitating flows. Pennsylvania State University, University Park Applied Research Lab
9. Karn A, Arndt RE, Hong J (2015) An experimental investigation into the physics of supercavity closure. *J Fluid Mech* 789:259–284
10. Duong NH, Nguyen TT, Truong TP, Nguyen QT (2016) Some results of the experimental measurements of the cavitating flow after horizontal water entry. In: Proceedings of the 8th Asia Pacific workshop on marine hydrodynamics - APHydro 2016, September 20-23, Hanoi, Vietnam, pp 341–353
11. Nguyen TT, Duong NH, Nguyen QT, Truong TP (2017) Experimental measurements of the cavitating flow after horizontal water entry. *Fluid Dyn Res*. <https://doi.org/10.1088/1873-7005/aa885d>
12. Liu T, Huang B, Wang G, Zhang M, Gao D (2017) Experimental investigation of the flow pattern for ventilated partial cavitating flows with effect of Froude number and gas entrainment. *Ocean Eng* 129:343–351

13. Choi JK, Ahn BK, Kim HT (2015) A numerical and experimental study on the drag of a cavitating underwater vehicle in cavitation tunnel. *Int J Naval Architect Ocean Eng* 7 (5):888–905
14. Nouroozi M, Pasandidehfarid M, Djavareshkian MH (2016) Simulation of partial and supercavitating flows around axisymmetric and quasi-3D bodies by boundary element method using simple and reentrant jet models at the closure zone of cavity. *Math Probl Eng*. article ID 1593849
15. Manninen M, Taivassalo V, Kallio S (1996) On the mixture model for multiphase flow. Technical Research Centre of Finland (VTT)
16. Kim DH, Park WG, Jung CM (2012) Numerical simulation of cavitating flow past axisymmetric body. *Int J Naval Architect Ocean Eng* 4(3):256–266
17. Paik KJ, Park HG, Seo J (2013) RANS simulation of cavitation and hull pressure fluctuation for marine propeller operating behind-hull condition. *Int J Naval Architect Ocean Eng* 5 (4):502–512
18. Yang D, Xiong YL, Guo XF (2017) Drag reduction of a rapid vehicle in supercavitating flow. *Int J Naval Architect Ocean Eng* 9(1):35–44
19. Zwart PJ, Gerber AG, Belamri T (2004) A two-phase flow model for predicting cavitation dynamics. In: Proceedings of the fifth international conference on multiphase flow, Yokohama, Japan
20. Rouse H, McNown JS (1948) Cavitation and pressure distribution, head forms at zero angle of yaw. *Stud Eng Bull* 32, State University of Iowa
21. Sarkar T, Sayer PG, Fraser SM (1997) Flow simulation past axisymmetric bodies using four different turbulence models. *Appl Math Model* 21(12):783–792
22. Asnaghi A, Jahanbakhsh E, Seif MS (2010) Unsteady multiphase modeling of cavitation around NACA 0015. *J Mar Sci Technol* 18(5):689–696
23. Saha K, Li X (2013) Assessment of different cavitation models in mixture and Eulerian framework for two-phase flow in diesel injectors. In: Proceedings of the ASME 2013 Internal Combustion Engine Division Fall Technical Conference, pp V002T02A011–V002T02A011. American Society of Mechanical Engineers
24. Liu HL, Wang J, Wang Y, Zhang H, Huang H (2014) Influence of the empirical coefficients of cavitation model on predicting cavitating flow in the centrifugal pump. *Int J Naval Architect Ocean Eng* 6(1):119–131
25. Shereena SG, Vengadesan S, Idichandy VG, Bhattacharyya SK (2013) CFD study of drag reduction in axisymmetric underwater vehicles using air jets. *Eng Appl Comput Fluid Mech* 7 (2):193–209
26. Garabedian PR (1956) Calculation of axially symmetric cavities and jets. *Pac J Math* 6 (4):611–684

Effect of Low-Frequency Flow on Cable Dry-State Galloping



H. Vo-Duy, L. Hoang-Trong, M. Nguyen-Van and V. Nguyen-Hoang

Abstract Cable-stayed bridge has widely been applied for medium-to-very long span. Thanks to advanced construction technology and structural materials, its span length is being broken time by time. Due to the increase of main span, cable length becomes longer and more vulnerable to wind excitation. Common large amplitude vibration types of stay cables are rain-wind-induced vibration (RWIV) and dry-state galloping (DG). Therefore, countermeasure for DG and RWIV is one of the key design factors of cable-stayed bridges. Many studies on its mechanism and countermeasures have been conducted in which its causes and mechanism were explained to some extent. It is typically explained that an axial flow behind the cable and flow fields around the cable at the critical Reynolds number regime suppress Karman vortex shedding, and then low-frequency vortices related to latent Strouhal frequencies become stronger, which causes dry galloping at high reduced wind speeds (U/fD) [1–3], although the complete explanation for the mechanism has not been given. In this study, using a spiral protuberance cable, which was developed as an aerodynamic countermeasure stay cable [4], and a circular cable, wake flow behind the cable as well as wind-induced dynamic response were captured by wind tunnel test. Comparing power spectral densities and coherence along the cable axis of the wake flow between spiral cables and circular cables at different wind speeds, the role of low-frequency vortices/flow on dry galloping and the suppression mechanism of the spiral protuberance were clarified.

Keywords Dry-state galloping · Spiral protuberances · Wake flow
Low-frequency flow · Excitation mode

H. Vo-Duy (✉) · L. Hoang-Trong · M. Nguyen-Van · V. Nguyen-Hoang
Faculty of Bridge and Road Engineering, Bridge Engineering Division,
Danang University of Science and Technology, The University of Danang,
Da Nang, Vietnam
e-mail: vdhung@dut.udn.vn

© Springer Nature Singapore Pte Ltd. 2018
H. Nguyen-Xuan et al. (eds.), *Proceedings of the International Conference on Advances in Computational Mechanics 2017*, Lecture Notes in Mechanical Engineering, https://doi.org/10.1007/978-981-10-7149-2_61

1 Wind-Induced Vibration of Circular and Spiral Protuberance Cable

Cable-stayed bridge has widely been applied for medium-to-very long span. Thanks to advanced construction technology and structural materials, its span length is being broken time by time. At the completion, Tatara Bridge in Japan span with a main span of 890 m used to be known as the longest stay cable bridge in the world. Nevertheless, it was rapidly passed over by Sutong Bridge (2008), Stonecutters Bridge (2009), E'dong Yangtze River Bridge (2010) and Russky Island Bridge (2012). With 1104 m of the main span, Russky Island Bridge is the current first position in the main span-length rank. Due to the increase of main span, cable length becomes longer and more vulnerable to wind excitation. In this scenario, it has been pointed out that a stay cable could gallop under wind actions. Common vibration types are rain-wind-induced vibration (RWIV), dry galloping (DG), vortex-induced vibration and wake galloping. After RWIV phenomenon was reported for the first time by Hikami and Shiraishi [5], cable manufacturers have proposed some types of surface modification on cable sheathing in order to prevent forming water rivulet along the cable which is main cause of RWIV. The proposed control methods are based on researches carried out mainly in Japan and Europe, for instance, a high-density polyethylene tube (HDPE) with indented surfaces, a HDPE tube with twelve parallel protuberances and a HDPE with single spiral protuberances. It has been found to promote the stabilization of these kinds of surface modification under rain–wind interaction. However, Katsuchi and Yamada [6] reported that DG occurred in case of indented cable with a low Scruton number condition. It was also found that the presence of the spiral protuberance significantly reduced the shedding correlation length. Larose and Smitt [7] conducted wind tunnel tests (WTT) with a single spiral protuberance for controlling RWIV. Consequently, their experiments showed a strong reduction of RWIV through the disruption of upper rivulet formation in a rain condition. Nevertheless, it should be paid attention to that recent full-scale monitoring at Øresund Bridge by Acampora and Georgakis [8] revealed that single spiral protuberance was not effective as initially expected.

Recently, Yagi et al. [9] tried to optimize the drag force for a parallel protuberance cable by giving spiral configuration. Finally, a cable with twelve spiral protuberances wound with 27° was proposed to reduce the drag force and wind-induced response. However, a WTT to observe cable response in a rain condition has not been carried out yet. In this study, wind-induced response of a circular cable and a spiral protuberance cable model was first measured at various angles against the wind in not only a no-rain condition but also a rain condition. The generation mechanism of dry galloping and its suppression by multiple spiral protuberances will be explained in detail.

1.1 Wind Tunnel Test

A cable model was fabricated by HDPT. Dimensions of the spiral protuberance are 5 mm high and 7.5 mm wide. Twelve protuberances were formed on the surface with 27° winding angle as shown in Fig. 1. Diameter and length of the cable model are 158 mm and 1500 mm, respectively. The cable model was supported by single degree of freedom (1DOF) spring system in vertical direction. Cable attitude is defined by the vertical angle α and horizontal flow angle β as shown in Fig. 2. The test was conducted with three vertical angles; $\alpha = 9^\circ, 25^\circ$ and 40° and five horizontal angles; $\beta = 0^\circ, 15^\circ, 30^\circ, 45^\circ$ and 60° .

A rain condition was simulated by water nozzles at wind tunnel ceiling, as shown in Fig. 3. Rain volume at the cable model position was 40–50 mm/h in the wind speed range (around 8–15 m/s), which was adjusted to create the critical RWIV amplitude. Other test conditions such as mass, damping, frequency are shown in Table 1.

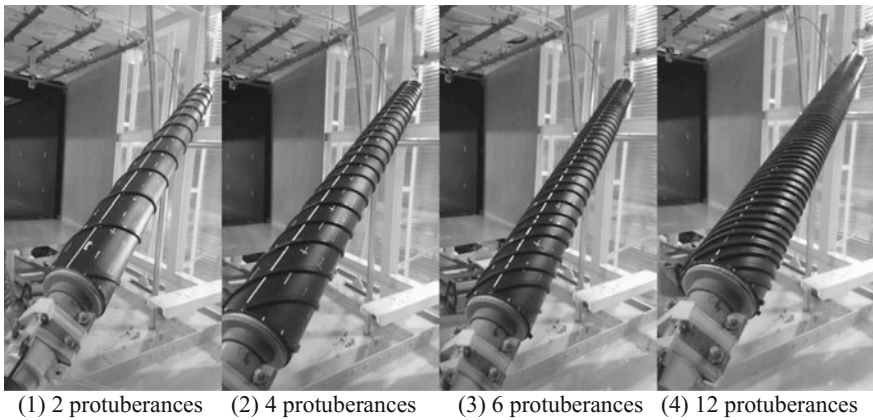


Fig. 1 Spiral protuberance cable model

Fig. 2 Definition of cable attitude

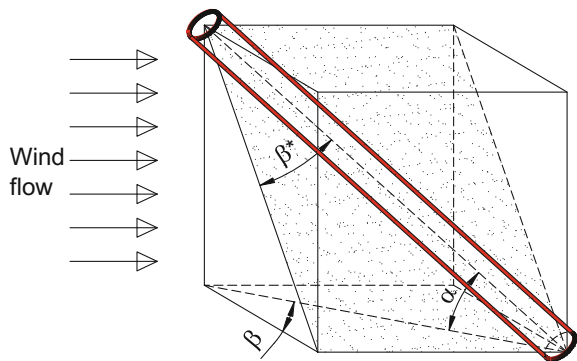


Fig. 3 Cable model orientation



Table 1 Wind tunnel test conditions

Wind condition	Smooth
Diameter: D (mm)	158
Effective length: L (mm)	1,500
Inclination angle: α ($^\circ$)	9, 25, 40
Flow angle: β ($^\circ$)	0, 15, 30, 45, 60
Mass: m (kg/m)	9.9 (circular), 10.8 (spiral)
Natural frequency (Hz)	0.78–1.02
Logarithm decrement: δ	0.005–0.016
Scruton number ($2m/\rho D^2$)	3.3–11.5
Reynolds number	$0-2.1 \times 10^5$

1.2 Wind-Induced Response

Figure 4 shows wind-induced response of a circular cable model in no-rain and rain conditions. The response in a rain condition agrees with former studies [5, 10, 11] where rain-wind-induced vibration (RWIV) only occurred in specific ranges of wind speed and relative angles to wind. Large amplitude vibration with non-dimensional amplitude of more than 1D (D : cable diameter) occurred in cases of the inclined angle 25° and flow angles $15^\circ-45^\circ$. When RWIV occurs, cable can gallop rapidly and divergently. Due to the constraint of the supporting spring system, maximum amplitude can be recorded in this study is around 2D. Diverging characteristic at a constant wind speed is shown by arrows in Fig. 4. In parallel, wind tunnel test was also carried out in a no-rain condition. Results are summarized in Fig. 4. Generally, divergent galloping took place in some specific cases such as the inclined angle (α) 40° with the flow angles (β) 15° , 30° and 45° , and (α) 25° with (β) 30° in the subcritical Reynolds number region ($6 \times 10^4-1.2 \times 10^5$). This

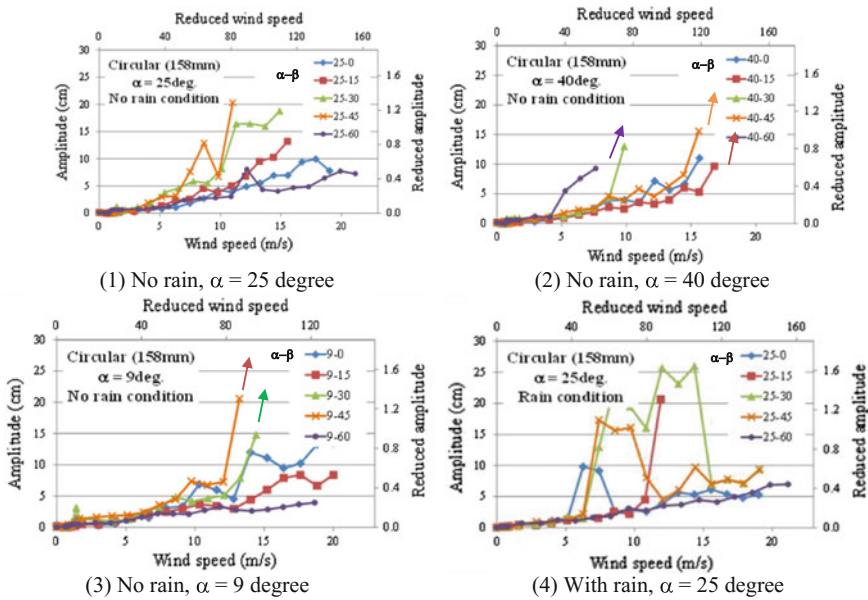


Fig. 4 Wind-induced response of circular cable

experimental result is consistent with previous studies [5, 11] where DG can occur at some specific wind attack angles and wind speed range.

In the other aspect, spiral protuberance or helical fillet-type cable is often applied for aerodynamic countermeasure. Field measurement showed that installing a spiral wire can mitigate wind-induced vibration of stay cables to some extent. It is pointed out that stay cables with small diameter helical fillets still exhibited large amplitude vibration [12]. Besides that, Gu and Du [10] concluded that only proper spiral pitch could mitigate RWIV of cables. Recently, Yagi et al. [9] used twelve spiral protuberances with the winding angle of 27° to control RWIV with lower drag force compared to the parallel protuberances type. In this study, 12 spiral protuberance cables were tested as shown in Fig. 5. Not only RWIV but also DG is almost suppressed, and only small amplitude random vibration is observed. Furthermore, the detail of wake flow characteristics will also be clarified.

2 Excitation Force from Latent Low Frequency

To understand the dry-state galloping mechanism, the fluctuating of wind velocity in the wake of the inclined cable model will be investigated along the model. The circular cylinder was mounted in the wind tunnel with flow angle $\beta = 30^\circ$ and inclined angle $\alpha = 25^\circ$. The hot-wire anemometer was set at $2D$ (D : cable diameter) from the cable wake and $0.5D$ from cable axis as shown in Fig. 6, and its position along the cable direction was varied from the upstream side to the downstream side

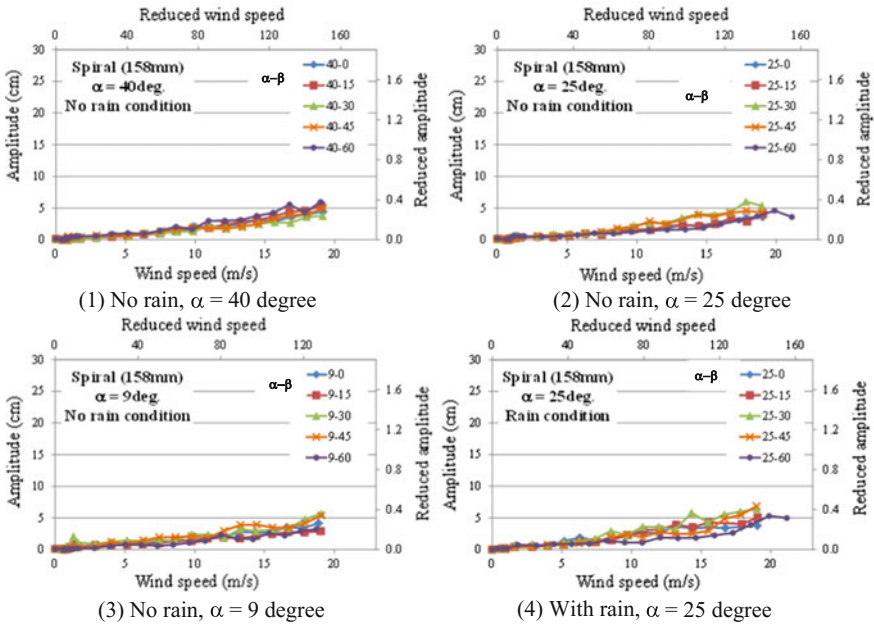
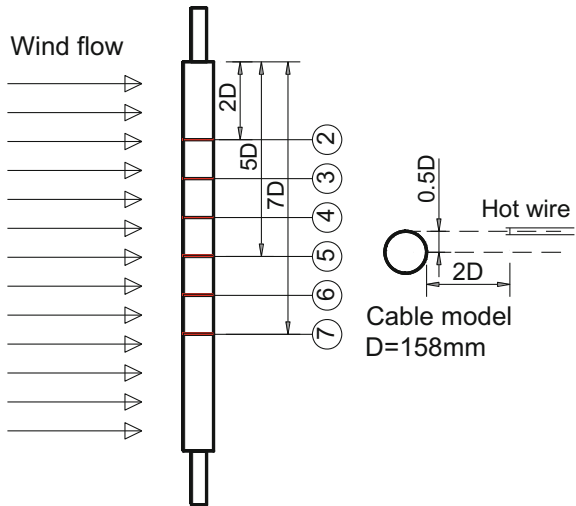


Fig. 5 Wind-induced response of spiral protuberance cable

Fig. 6 Arrangement for measurement wake flow fluctuation



at the distances from 2D to 7D. From this set-up, fluctuation of wind speed in spatial and time will be measured at different wind speeds.

The power spectrum density (PSD) diagrams of fluctuating wind velocity in vertical direction near the wake along the cable direction are shown in Figs. 7 and 8a.

The mean wind velocities in the wind tunnel are fixed as 5/s, 10 m/s, 15 m/s and 20 m/s, respectively. When wind speed at around 5 m/s, Karman vortex frequency with Strouhal number (St) around 0.2 seems to be dominant. However, as wind speed increases to $U = 10$ m/s, the low-frequency components are observed through span-wise direction. Especially at the downstream side corresponding to 6D and 7D locations, these low-frequency components are extremely dominant. These frequency components correspond to reduced wind velocity around $U/f_v D = 110$, where f_v is the dominating frequency of fluctuating velocity. This kind of pattern also detected more clearly at wind speed $U = 15$ m/s. Further, there are two dominant frequency components: one corresponds to $U/f_v D = 110$ which probably driven force of dry galloping phenomenon and the other is $U/f_v D = 60$ where supposed for vortex-induced vibration at high reduced wind speed [10]. Obviously, these vibrations (dry galloping and vortex-induced vibration at high reduced wind speed) apparently differ from the conventional Karman vortex-excited vibration because they appear at much higher reduced wind speed. Furthermore, this kind of trend also appeared in case of flow angle $\beta = 45^\circ$ and inclined angle $\alpha = 25^\circ$ or $\beta = 0^\circ$ and inclined angle $\alpha = 25^\circ$ as shown in Figs. 8b and 9. In this figure, the wind speed is 20 m/s and the low dominant frequency component around $U/f_v D = 110$. Moreover, the dominant frequency is around 0.6–2 Hz, which is close to fundamental frequency of cable, so the vibration can easily occur. This finding is consistent with the DG occurrence range in previous section. In detail, the dominant frequency appeared coincided with wind speed where DG took place.

In addition, the wavelet analysis was carried out to observe the variation of the velocity against time as well as the excitation mode, in which Morlet wavelet is mother function. The results of location = 6D and 7D, $U = 15$ m/s, $\beta = 30^\circ$ and $\alpha = 25^\circ$ are plotted in Fig. 10. Two peaks for first mode and second mode keep their shapes and magnitude almost unchanged along the time. In addition, the low peak frequency can be observed clearly. Similar trends were found at 2D, 3D, 4D and 5D in Figs. 11, 12, 13 and 14. In addition, there are some frequency peaks with

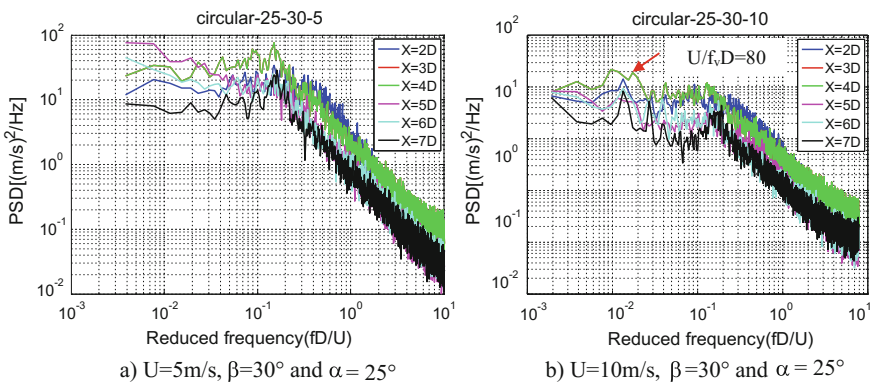


Fig. 7 PSD of fluctuating U in the wake of stationary inclined cable, $U = 5$ and $U = 10$ m/s

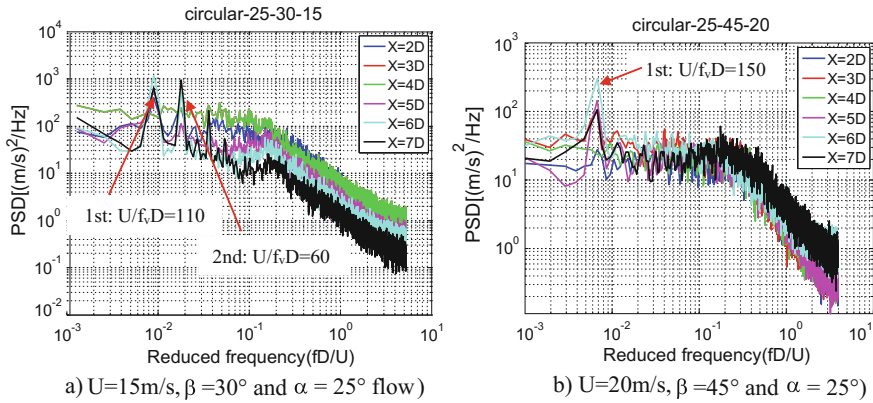


Fig. 8 PSD of fluctuating U in the wake of stationary inclined cable, $U = 15$ and $U = 20$ m/s

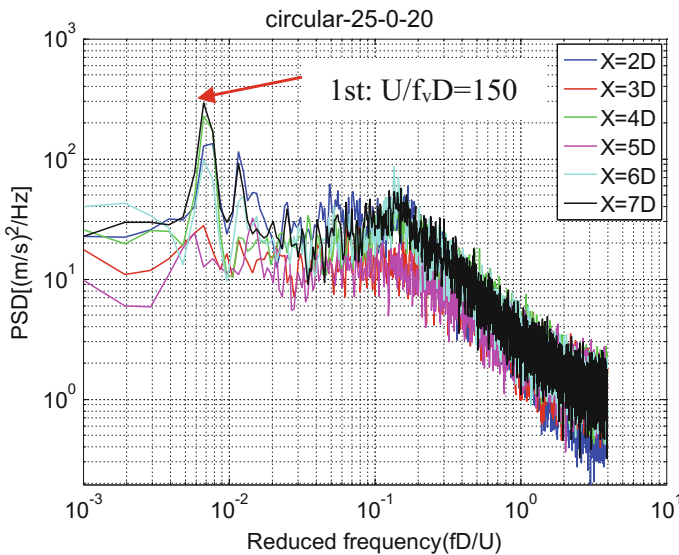


Fig. 9 PSD of fluctuating wind velocity in cable wake ($U = 20$ m/s, $\beta = 0^\circ$ and $\alpha = 25^\circ$)

much shorter period region. Since the reduced velocity for these peak is calculated around $U/f_v D = 5-8$, it can be the conventional Karman vortex-induced vibration. In short, the wake flow fluctuation with very low frequencies and its regular shedding along the cable axis play very important in dry galloping's mechanism. It is obviously that there are many latent low frequencies at high wind speed, and they will only appear at high range of wind velocity with high energy.

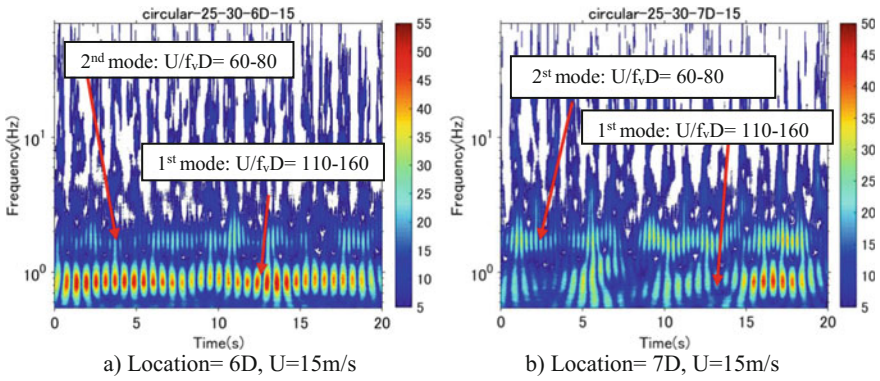


Fig. 10 WA of fluctuating U in the wake of stationary inclined cable, $\beta = 30^\circ$ and $\alpha = 25^\circ$

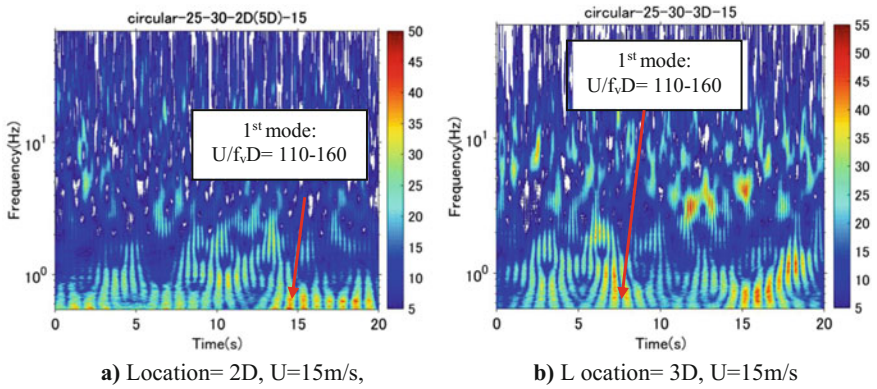


Fig. 11 WA of fluctuating U in the wake of stationary cylinder, $\beta = 30^\circ$ and $\alpha = 25^\circ$

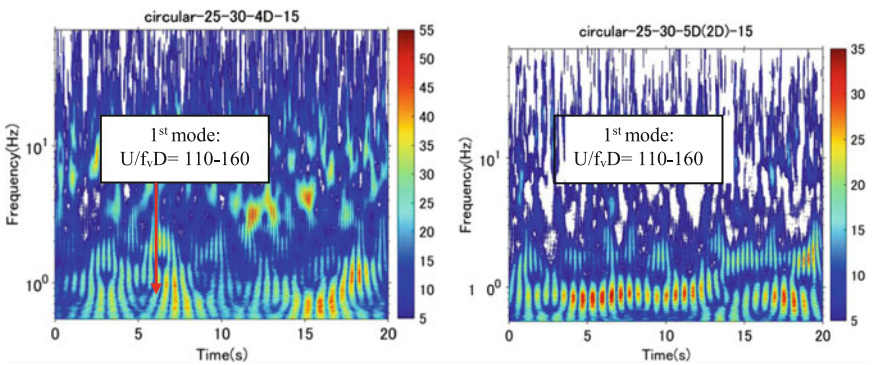


Fig. 12 WA of fluctuating U of inclined circular cylinder

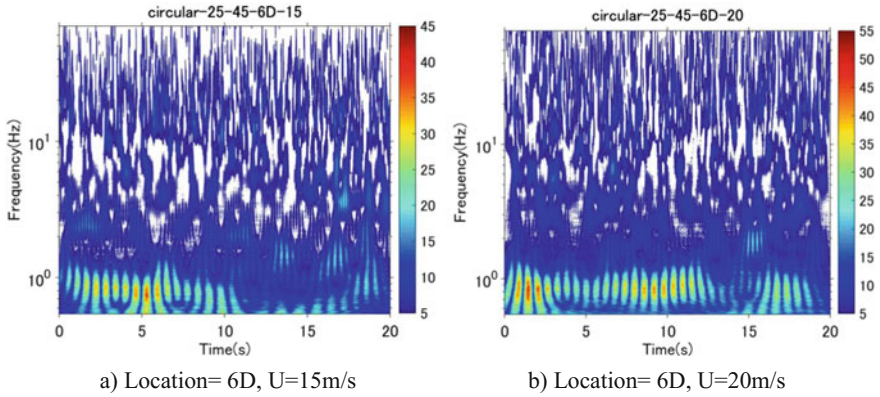


Fig. 13 Wavelet analysis of fluctuating U in the wake of inclined cable, $\beta = 45^\circ$ and $\alpha = 25^\circ$

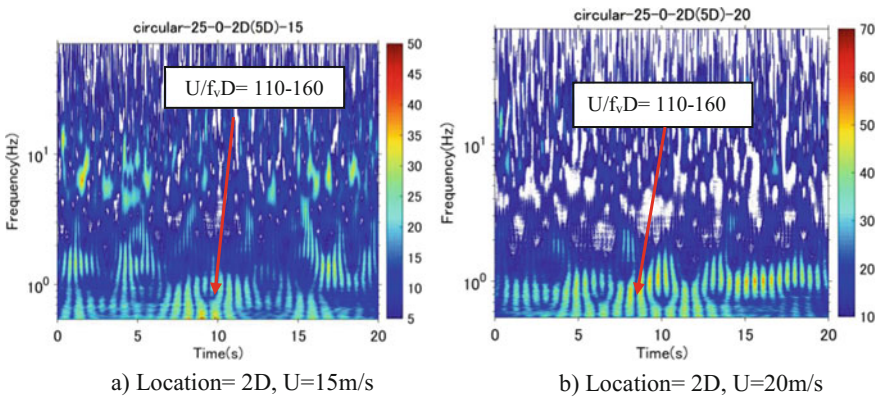


Fig. 14 Wavelet analysis of fluctuating U in the wake of inclined cable, $\beta = 0^\circ$ and $\alpha = 25^\circ$

3 Stabilization Characteristic of Spiral Protuberance Cable

3.1 The Elimination of Low-Frequency Band

To understand the reasons why spiral cable can mitigate the cable dry-state galloping, wake flow velocity of inclined spiral protuberance cable model was recorded along the model. The cable with twelve spiral protuberances was mounted in the wind tunnel with flow angle $\beta = 30^\circ$ and inclined angle $\alpha = 25^\circ$. The experimental set-up was same to measurement of circular cable in Chap. 4. The PSD diagrams of fluctuating wind velocity in the wake along the spiral protuberance in comparison with circular cable can be seen at Figs. 15 and 16.

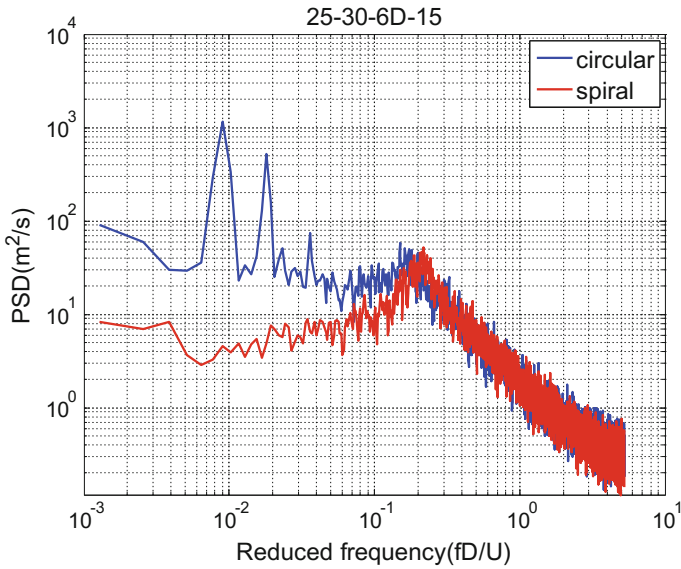


Fig. 15 PSD of fluctuating wind velocity: circular cable versus spiral protuberance cable (smooth flow, location 6D, U = 15 m/s, $\beta = 30^\circ$ and $\alpha = 25^\circ$)

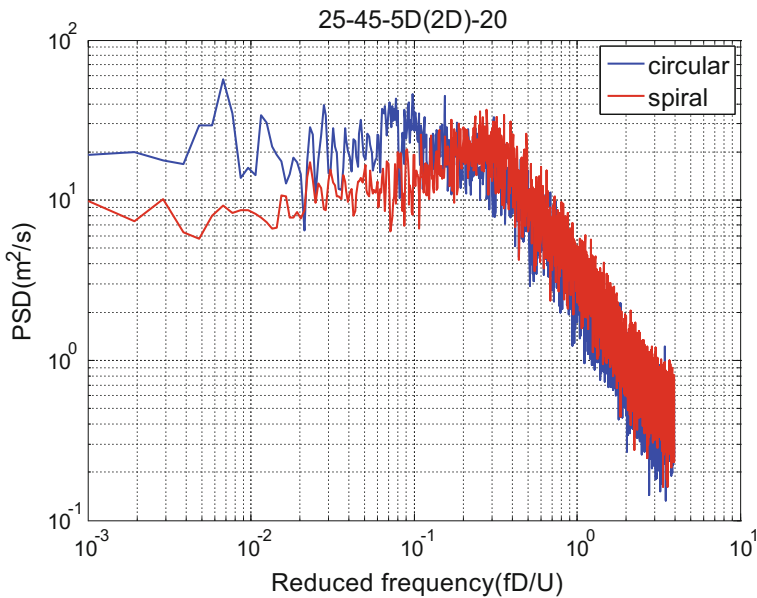


Fig. 16 PSD of fluctuating wind velocity: circular cable versus spiral protuberance cable (smooth flow, location 5D, U = 20 m/s, $\beta = 45^\circ$ and $\alpha = 25^\circ$)

Significantly, the low-frequency flows/vortices were vanished through span-wise direction. In comparison with circular cable, spiral one has much lower power in low-frequency component band. In the other expression, the spiral protuberances mitigated the wake flow fluctuation considerably and made its shedding's energy becomes weaker. In presence of spiral protuberance, Karman vortex ($St = 0.15-0.2$) is most dominant flow, which contained higher energy. Moreover, The Karman vortex flow also decreased as wind speed increased, and it is nearly suppressed at high wind speed, say 15 or 20 m/s. In this case, there were some low-frequency peaks, but the excitation energy is negligible. Furthermore, there was no large amplitude vibration occurred in these cases. It means that the interruption of Karman vortex is only necessary condition, not the sufficient condition for dry galloping. The sufficient conditions for generating dry galloping are both interruption of Karman vortex and formation of low-frequency flow/vortices.

Besides that, according to the wavelet analysis in Fig. 17, there was a shift of frequency from low range in case of circular cable to high-frequency components in presence of spiral protuberances. In particular, the total energy of wake flow reduced considerably. Frequency component from 1–10 Hz seems to be suppressed, and the power of other component was also reduced. In another expression, spiral protuberance changed the wake flow pattern from unstable pattern to the stable one. In addition, the low-frequency peak vortices with reduced wind speed ($U/f_v D = 110-160$) which was also found in circular cable were vanished. Currently, there are high non-stationary frequency peaks correspond to reduced wind velocity around $U/f_v D = 4-6$. This range of reduced wind speed is equivalent to Strouhal number around 0.15–0.25, which is conventional Karman vortex. According to previous publications [13], when Karman vortex shed, amplitude becomes small. Because the Karman vortex would come from the communication of two separation flows, this communication makes the pressure difference of upper and lower sides of cable become zero. As a result, it can reduce galloping.

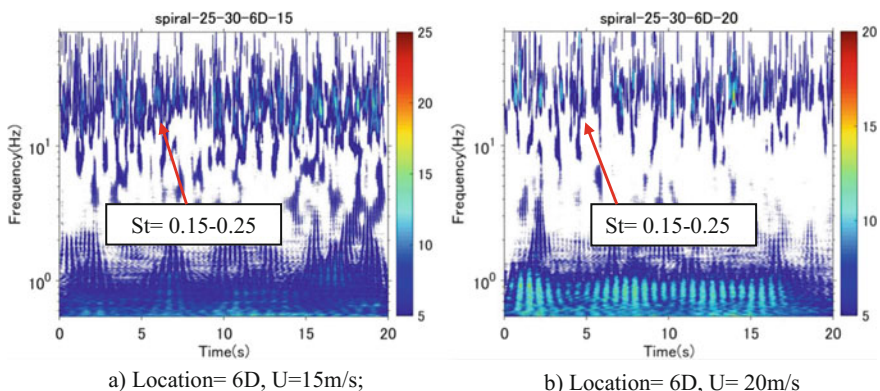


Fig. 17 Wavelet analysis of fluctuating wind velocity in the wake of stationary spiral protuberance cable (Smooth flow $\beta = 30^\circ$ and $\alpha = 25^\circ$)

Furthermore, the Karman vortex-induced oscillation for stay cables is not so dangerous, and it is easy to suppress by increase structural damping. Above findings proved that spiral protuberances destroyed the low-frequency component, which may cause cable vibration at high wind speed. In short, the presence of spiral protuberances suppressed the low-frequency component as well as reduced the energy of wake flow.

3.2 Interruption of Shedding Correlation

In case of circular cylinder, it was found that the low frequency has a high correlation with high energy; therefore, it can create strong excitation force. Currently, coherence also used for assessing the correlation of wake flow in span-wise direction of spiral protuberance cable. The correlation of wake flow of flow angel 30° and inclination 25° can be seen at Fig. 18. Under comparison with circular cable, it is found that spiral cable has higher correlation at Strouhal number (fD/U) around ~ 0.2 which corresponding to Karman vortex component. In the other expression, owing to spiral protuberance, shedding correlation of low-frequency flow was mitigated while the Karman vortex shedding correlation increased again. According to previous studies, when KV shed, amplitude becomes small [13–15]. At low-frequency flow band, spiral protuberance exhibited very low correlation compared to circular surface. In conclusion, the suppression mechanism procedure is as following: in presence of spiral, flow separation point is fixed, the regularity of flow shedding will be maintained even though the Karman Vortex is suppressed in this case. Then, the vortex continues shedding regularly. Consequently, low-frequency vortices do not appear, and spatial shedding correlation also

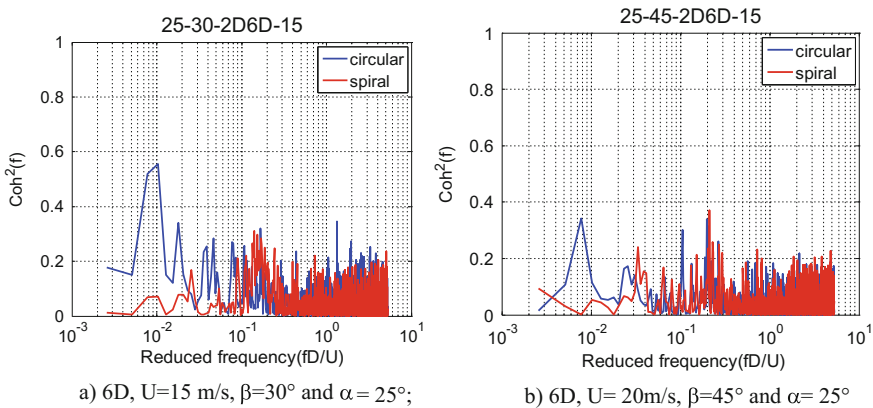


Fig. 18 Coherence of fluctuating wind velocity in the wake (smooth flow)

disrupted. It leads to no excitation force created. Consequently, the dry galloping will be mitigated.

4 Conclusion

In this study, wind-induced response and wake flow structures of circular and spiral protuberance cables were measured in the wind tunnel test. Then, a role of low-frequency vortices on dry galloping and the suppression mechanism of the spiral protuberance cable were clarified. Results obtained are as follows:

In the case of a circular cable, large amplitude dry-state galloping occurs when suppression of Karman vortices collapses the regularity of vortex shedding and increases randomness of vortex shedding along the cable axis, and as a result, it increases PSD in the low-frequency range.

In the case of a spiral protuberance cable, protuberance fixes the location of vortex shedding even under suppression of Karman vortices and collapse of the regularity of vortex shedding. As a result, it does not increase largely the randomness of vortex shedding along the cable axis, peaks of PSD in the low-frequency range do not appear, DG does not occur, either.

Acknowledgements This research is funded by Funds for Science and Technology Development of the University of Danang under project number B2017-ĐN02-25.

References

1. Matsumoto M, Kitazawa M, Kanaji H (1989) Wind tunnel test for stay cables of Higashi Kobe Ohashi Bridge (part 2). In: Proceedings of 44th annual conference of JSCE, pp 802–803. (in Japanese)
2. Tanaka T, Matsumoto M, Ishizaki H, Kibe H (2016) Dry galloping characteristic and vibration control of inclined stay cable. In: Proceedings of first international symposium on flutter and its application, Tokyo, pp 639–648
3. Katsuchi H, Yamada H (2011) Dry galloping characteristics of indented stay cables in turbulent flow. In: Proceedings of 9th international symposium on cable dynamics (CD-ROM), Shanghai, China
4. Flamand O (1994) Rain/wind-induced vibration of cables. In: Proceedings of international conference on cable-stayed and suspension bridges (AFPC), Deauville, France, pp 523–531
5. Hikami Y, Shiraishi N (1988) Rain–wind induced vibrations of cables in cable-stayed bridges. *J Wind Eng Ind Aerodyn* 29:409–418
6. Katsuchi H, Yamada H (2009) Wind-tunnel study on dry-galloping of indented-surface stay cable. In: Proceedings of 11th Americas conference on wind engineering, Puerto Rico, pp 22–26
7. Larose G, Smitt LW (1999) Rain/wind induced vibrations of parallel stay cables. In: Proceedings of the IABSE conference, cable-stayed bridges—past, present and future, Malmo, Sweden

8. Acampora A, Georgakis CT (2011) Recent monitoring of the Oresund Bridge: rain-wind induced cable vibrations. In: Proceedings of the 13th international wind engineering conference, Amsterdam
9. Yagi T, Okamoto K, Sakaki I, Koroyasu H, Liang Z, Narita S, Shirato H (2011) Modification of surface configurations of stay cables for drag force reduction and aerodynamic stabilization. In: Proceedings of the 13th international conference on wind engineering, Amsterdam
10. Gu M, Du X (2005) Experimental investigation of rain-wind- induced vibration of cables in cable-stayed bridges and its mitigation. *J Wind Eng Ind Aerodyn* 93:79–95
11. Jakobsen JB, Andersen TL, Macdonald JHG, Nikitas N, Larose GL, Savage G, McAuliffe BR (2012) Wind-induced response and excitation, characteristic of an inclined cable model in the critical Reynolds number range. *J Wind Eng Ind Aerodyn* 110:100–112
12. Vo HD, Katsuchi H, Yamada H, Nishio M (2014) Experimental study on dry-state galloping with various wind relative angles and its countermeasures. *J Struct Eng JSCE* 60A:428–436
13. Matsumoto M et al (2001) Vortex-induced cable vibration of cable-stayed bridges at high reduced wind velocity. *J Wind Eng Ind Aerodyn* 89:633–647
14. Nakamura Y, Hirata K, Urabe T (1991) Galloping of rectangular cylinders in the presence of a splitter plate. *J Fluids Struct* 5:521–549
15. Matsumoto M et al (2010) Dry-galloping characteristics and its mechanism of inclined/yawed cables. *J Wind Eng Ind Aerodyn* 98:317–327

Investigation on Turbulence Effects on Flutter Derivatives of Suspended Truss Bridge Section



L. Hoang-Trong, V. Nguyen-Hoang and H. Vo-Duy

Abstract This paper presents the flutter derivatives extracted from a stochastic state-space system identification method under difference turbulent flows. The aim of the study is to clarify the effects of oncoming turbulence on the flutter of suspended long-span bridges by using section model wind tunnel test. Several wind tunnel tests on a trussed deck section have been carried out with different oncoming turbulent properties involving turbulence intensities and turbulent scales. The analysis includes the transient response data from wind tunnel test which have been analyzed by the system identification technique in extracting flutter derivatives (FDs) and the difficulties involved in this method. The time-domain analysis stochastic system identification is proposed to extract simultaneously all FDs from two degree of freedom systems. Finally, the results under different condition were discussed and concluded.

Keywords Flutter derivative · Stochastic system identification
Wind turbulence · Flutter critical velocity

1 Introduction

The wind in the atmospheric boundary layer is always turbulent. Therefore, any research of wind-induced vibration problems must consider this issue. Not many researches have focused clearly on the effects of turbulence on aeroelastic forces. Scanlan (1978) [1] is the pioneer who used a trussed deck section model and then concluded that flutter derivatives had an insignificant difference from smooth and turbulent flows. However, Huston (1986) conducted a test on a model of the Golden Gate Bridge deck section, and the results showed a significant discrepancy in flutter derivatives between smooth and turbulence flows [2]. Sarkar et al. (1994) [3]

L. Hoang-Trong (✉) · V. Nguyen-Hoang · H. Vo-Duy
Bridge Engineering Division, Faculty of Bridge and Road Engineering, Danang University
of Science and Technology, The University of Danang, Da Nang, Vietnam
e-mail: hoanglam289@gmail.com

© Springer Nature Singapore Pte Ltd. 2018
H. Nguyen-Xuan et al. (eds.), *Proceedings of the International Conference
on Advances in Computational Mechanics 2017*, Lecture Notes in Mechanical
Engineering, https://doi.org/10.1007/978-981-10-7149-2_62

conducted a streamlined steel box girder section model test under both smooth and turbulence flows and applied robust system identification method, Modified Ibrahim Time Domain (MITD) [4]. Their study showed two valuable conclusions: (1) The turbulence flow does not appreciably affect self-excited forces via the FDs, and (2) the MITD method is based on the assumption that there is no external excitation of the system. For a section model immersed in turbulent flow, the buffeting forces and these responses are considered external forces, and hence free vibration condition is conflicted theoretically. The MITD method treats the resulting forced response as though additional noise is presented in the signals. This made the identification flutter derivatives more difficult and most likely reduced the accuracy.

For a study on FDs, the free vibration technique of sectional model is used, and system identifications (SID) technique to extract FDs is widely applied [3–5]. Various SID techniques were developed by many authors: the Extended Kalman Filter Algorithm, Modified Ibrahim Time-Domain method, Unifying Least-squares method, and Iterative Least-Squares method. In these systems, the buffeting force and their response are considered as external noise, so this causes more difficulties at high wind velocity such as noise increase due to turbulence.

Kirkegaard and Andersen [6] compared three state-space systems: stochastic subspace identification (SSI), stochastic realization estimator matrix block Hankel (MBH), and prediction error method (PEM). The results showed that the SSI gave good results in terms of estimated modal parameters and mode shapes. The MBH was found to give poor estimates of the damping ratios and the mode shapes compared with the other two techniques. In addition, the SSI was approximately ten times faster than the PEM.

This study is to clarify the effects of oncoming turbulence on self-excited force of a suspended long-span bridge deck. The more challenging is the application of a stochastic system identification method to identify flutter derivatives from free decay response for the section model which is obtained by an experimental wind tunnel test for a truss deck section. The output only time-domain analysis stochastic system identification, also known as data driven stochastic system (SSI-data) methods is proposed to extract simultaneously all flutter derivatives (FDs) from two degrees of freedom system (DOF).

2 Wind Tunnel Test

A wind tunnel test was conducted in a closed-circuit wind tunnel of Yokohama National University. The investigated profile is trussed deck section (Fig. 1). Since the truss deck with closed open grating exhibits torsional flutter at a relatively low wind speed, FDs (particularly A_2^*) identified can be validated by a flutter onset wind speed. The width and depth of the section model are 363 mm and 162.5 mm, respectively. The unit mass is 8.095 kg/m, and moment of inertia is 0.2281 kg m²/m. The vertical frequency and damping ratio are 1.869 Hz and 0.0051, respectively.

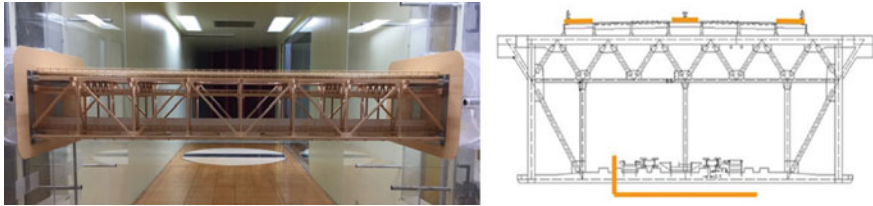


Fig. 1 Truss deck section model

Table 1 Turbulence intensity and scale

	I_u (%)	I_w (%)	L_u (cm)	L_w (cm)
Case 1	6.2	4.6	11.3	9.1
Case 2	9.1	6.9	9.0	8.7
Case 3	15.6	13.2	6.8	6.4

I turbulence intensity, L turbulence integral length scales with horizontal u and vertical direction w

The torsional frequency and damping ratio are 3.296 Hz and 0.00419, respectively. The tests have been carried out in both smooth and different turbulent flows. The turbulent flows used in this study are generated with biplane wooden grids. The turbulent properties are controlled by changing the distances to the model. The flow conditions and turbulence properties are shown in Table 1.

3 Identification of Flutter Derivatives

3.1 Stochastic Discrete-Time State-Space System

Considering a 2 DOF section model of bridge deck in turbulent flow, equation of motion is written by

$$\begin{aligned}
 m[\ddot{h} + 2\xi_h\omega_h\dot{h} + \omega_h^2h] &= L_{se} + L_b \\
 I[\ddot{\alpha} + 2\xi_\alpha\omega_\alpha\dot{\alpha} + \omega_\alpha^2\alpha] &= M_{se} + M_b
 \end{aligned}
 \tag{1}$$

where h and α are the vertical and torsional displacement; m and I are mass and mass moment of inertia per unit length, respectively; $\omega_h = 2\pi f_h$ and $\omega_\alpha = 2\pi f_\alpha$ are circular frequencies of heaving and pitching mode; ξ_h and ξ_α are damping ratio to critical; L_{se} and M_{se} are the aerodynamic self-excited lift and moment, respectively, given by Simiu and Scanlan [7]

$$\begin{aligned}
 L_{se} &= \frac{1}{2} \rho U^2 B \left[K_h H_1^*(K_h) \frac{\dot{h}}{U} + K_\alpha H_2^*(K_\alpha) \frac{B\dot{\alpha}}{U} + K_\alpha^2 H_3^*(K_\alpha) \alpha + K_h^2 H_4^*(K_h) \frac{h}{B} \right] \\
 M_{se} &= \frac{1}{2} \rho U^2 B^2 \left[K_h A_1^*(K_h) \frac{\dot{h}}{U} + K_\alpha A_2^*(K_\alpha) \frac{B\dot{\alpha}}{U} + K_\alpha^2 A_3^*(K_\alpha) \alpha + K_h^2 A_4^*(K_h) \frac{h}{B} \right]
 \end{aligned}
 \tag{2}$$

where ρ is the air density; U is the mean wind velocity; B is the width of bridge deck; $K_i = \omega_i B/U$ the reduced frequency ($i = h, \alpha$); H_i^* and A_i^* ($i = 1, 2, 3, 4$) are the flutter derivatives. L_b and M_b (factorized into matrix B_2 and input vector $u(t)$) are the buffeting forces in the vertical and torsional directions, respectively. By substituting L_{se} , M_{se} , L_b , and M_b into Eq. (1) and moving the aerodynamic damping and stiffness terms to the left-hand side, Eq. (1) can be transformed into a first-order state equation by Eq. (3) [8]

$$\dot{x}(t) = \begin{bmatrix} 0 & I \\ -[M]^{-1}[K^e] & -[M]^{-1}[C^e] \end{bmatrix}_{4 \times 4} x(t) + \begin{bmatrix} 0 \\ [M]^{-1}B_2 \end{bmatrix} u(t) \tag{3}$$

where $x(t)$ is state vector; $[M]$ is mass matrix; $[C^e]$ is gross damping matrix including the structural damping and aerodynamic damping; $[K^e]$ is gross stiffness matrix including the structural stiffness and aerodynamic stiffness.

In the modal analysis, sometimes the input is unknown and measurements are mostly sampled at discrete-time. On the other hand, it is impossible to measure all DOFs, and measurements always have disturbance effects. For all these reasons, the continuous deterministic system will be converted to suitable form, discrete-time stochastic state-space model, as follows:

$$\begin{aligned}
 x_{k+1} &= Ax_k + w_k \\
 y_k &= Cx_k + v_k
 \end{aligned}
 \tag{4}$$

where $x_k = x(k\Delta t)$ is the discrete-time state vector containing the discrete sample displacement and velocity; w_k is the process noise; v_k is the measurement noise due to sensor inaccuracy. Assuming w_k and v_k are zero mean and $\{x_k\}$, $\{w_k\}$, and $\{v_k\}$ are mutually independent, the output covariance $R = E[y_{k+i} y_k^T]$ for any arbitrary time lags $i\Delta t$ can be considered as impulse response (Eq. (5)) of the deterministic linear time-invariance system A , C , and G , where $G = E[x_{k+1} y_k^T]$ is the next state-output covariance matrix.

$$R_i = CA^{i-1}G \tag{5}$$

3.2 Stochastic System Identification (SSI)

Data-driven stochastic subspace identification (SSI-data) method [9] is used in this study. It works directly with time series of experimental data without the need to convert output data to correlation, covariance, or spectra. The main step of SSI-data is a projection of the row space of the future outputs into the row of past outputs. The orthogonal projection P_i is defined as follows:

$$P_i = Y_f / Y_p = Y_f Y_p (Y_p Y_p^T)^{-1} Y_p \tag{6}$$

where the matrix Y_f and Y_p are the under half part and upper part half of a block Hankel matrix H as below.

$$H = \begin{bmatrix} y_0 & y_1 & \dots & y_{j-1} \\ y_1 & y_2 & \dots & y_j \\ \dots & \dots & \dots & \dots \\ y_{i-1} & y_i & \dots & y_{i+j-2} \\ y_i & y_{i+1} & \dots & y_{i+j-1} \\ y_{i+1} & y_{i+2} & \dots & y_{i+j} \\ \dots & \dots & \dots & \dots \\ y_{2i-1} & y_{2i} & \dots & y_{2i+j-2} \end{bmatrix}_{2i \times j} = \begin{bmatrix} Y_{0|i-1} \\ Y_{i|2i-1} \end{bmatrix} = \begin{bmatrix} Y_p \\ Y_f \end{bmatrix} \begin{matrix} \Downarrow li \\ \Downarrow li \end{matrix} \tag{7}$$

where $y = (y_0, y_1, y_2, y_2 \dots y_n) \in R^{lxn}$ is the output measurement data obtained from l sensors (in this study $l = 2$ for heaving and torsion modes), $2i$ is the number of block rows, and j is the number of columns.

The main theorem of stochastic subspace identification states that the projection P_i can be factorized as the product of observability matrix O_i and the Kalman filter state sequence \hat{X}_i . The observability matrix O_i and the Kalman filter sequence \hat{X}_i are obtained by applying SVD to the projection matrix P_i . The Kalman state sequences \hat{X}_i, \hat{X}_{i+1} are calculated using only output data. The system matrices can now be recovered from overdetermined set of linear equations and obtained by extending Eq. (4)

$$\begin{pmatrix} \hat{X}_{i+1} \\ Y_{i|i} \end{pmatrix} = \begin{pmatrix} A \\ C \end{pmatrix} \begin{pmatrix} \hat{X}_i \end{pmatrix} + \begin{pmatrix} \rho_w \\ \rho_v \end{pmatrix} \tag{8}$$

where $Y_{i|i}$ is a Hankel matrix with only one block row. Since the Kalman state sequence and the outputs are known and the residuals $(\rho_w^T \ \rho_v^T)^T$ are uncorrelated with \hat{X}_i , the set of equation can be solved for A and C in the least-squares, where $(.)^u$ is pseudo-invert of a matrix

$$\begin{pmatrix} A \\ C \end{pmatrix} = \begin{pmatrix} \hat{X}_{i+1} \\ Y_{i|i} \end{pmatrix} (\hat{X}_i)^\dagger \quad (9)$$

3.3 Identification of Flutter Derivatives

The modal parameters of system can be obtained by solving the eigenvalue problem state matrix A as

$$A = \Psi \Lambda \Psi^{-1}, \quad \Phi = C\Psi \quad (10)$$

where Ψ is the complex eigenvector; Λ the complex eigenvalue is the diagonal matrix; Φ the mode shape matrix. When the complex modal parameters are known, the gross damping C^e and gross stiffness K^e in Eq. (3) are determined by following:

$$[K^e \quad C^e] = -M \begin{bmatrix} \Phi \Lambda^2 & \Phi^* (\Lambda^*)^2 \end{bmatrix} \begin{bmatrix} \Phi & \Phi^* \\ \Phi \Lambda & \Phi^* \Lambda^* \end{bmatrix}^{-1} \text{ and } \begin{cases} \bar{C}^e = M^{-1} C^e; & \bar{K}^e = M^{-1} K^e \\ \bar{C} = M^{-1} C^0; & \bar{K} = M^{-1} K^0 \end{cases} \quad (11)$$

where C^0 and K^0 are the mechanical damping and stiffness matrix of the system under no-wind condition.

Thus, the flutter derivatives of 2 DOF can be defined as follows:

$$\begin{aligned} H_1^*(K_h) &= -\frac{2m}{\rho B^2 \omega_h} (\bar{C}_{11}^e - \bar{C}_{11}), & H_2^*(K_\alpha) &= -\frac{2m}{\rho B^3 \omega_\alpha} (\bar{C}_{12}^e - \bar{C}_{12}) \\ H_3^*(K_\alpha) &= -\frac{2m}{\rho B^3 \omega_\alpha^2} (\bar{K}_{12}^e - \bar{K}_{12}), & H_4^*(K_h) &= -\frac{2m}{\rho B^3 \omega_h^2} (\bar{K}_{11}^e - \bar{K}_{11}) \\ A_1^*(K_h) &= -\frac{2I}{\rho B^3 \omega_h} (\bar{C}_{21}^e - \bar{C}_{21}), & A_2^*(K_\alpha) &= -\frac{2I}{\rho B^4 \omega_\alpha} (\bar{C}_{22}^e - \bar{C}_{22}) \\ A_3^*(K_\alpha) &= -\frac{2I}{\rho B^4 \omega_\alpha^2} (\bar{K}_{22}^e - \bar{K}_{22}), & A_4^*(K_h) &= -\frac{2I}{\rho B^4 \omega_h^2} (\bar{K}_{21}^e - \bar{K}_{21}) \end{aligned} \quad (12)$$

4 Flutter Derivatives

The decay responses are acquired at a sampling frequency 100 Hz, and these samples are set to zero before operating with MATLAB (Fig. 2).

The actual implementation of SSI-data consists of projecting (P_i) the row space of the under part outputs (Y_f) into the row space of the upper part outputs (Y_p) by applying robust numerical techniques QR factorization Eq. (6) and shifted projecting matrix P_{i-1} , computing SVD of P_i , truncating the SVD into the model order.

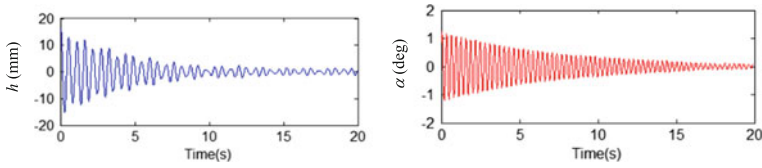


Fig. 2 Free decay response ($V = 2.91$ m/s) of the bridge deck section model (h -vertical; α -torsional)

The Kalman filter state sequence \hat{X}_i is calculated by P_i then the SVD is found out. Continuously, the state matrix A and C is obtained by least-square solution Eq. (9). The system order n can be determined from the number nonzero singular values of projecting matrix. In practice, affect by noise thus singular values that are all different from zero. Therefore, it is suggested to look at the “gap” between two successive singular values. The order will be selected by a maximum number of singular values at “gap” occur. Finally, the flutter derivatives will be obtained by comparing the gross damping and gross stiffness with mechanical damping and mechanical stiffness Eq. (12).

4.1 The Effects of Turbulence on Flutter Derivatives

In order to clarify the effects of oncoming flow turbulence on FDs, the SSI-data method is applied to extract FDs from free decay response with different turbulence intensity. Figure 3 shows the damping ratio of heaving and torsional mode versus reduced wind speed (V_r). Compared with smooth flow, the damping ratio of heaving mode increases more slowly, at certain reduced velocity; torsional damping ratio decreases when turbulence intensity increases.

Figures 4 and 5 show the FDs under smooth and turbulent flows with the different turbulence intensity versus reduced wind speed. H_1^* , H_4^* , A_1^* , A_4^* associated with vertical oscillation are identified using the vertical frequency, and

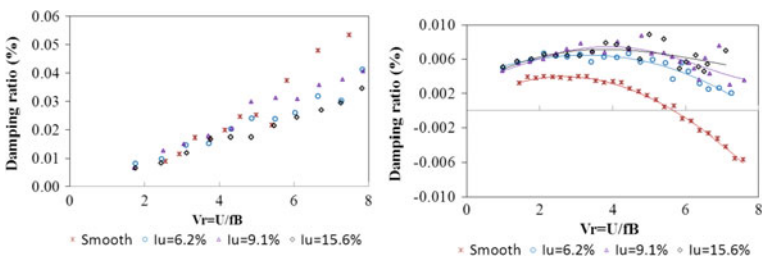


Fig. 3 Damping ratio of heaving (left) and torsional (right) mode of the bridge section model under smooth and turbulence flows (solid curves are fitted polynomial)

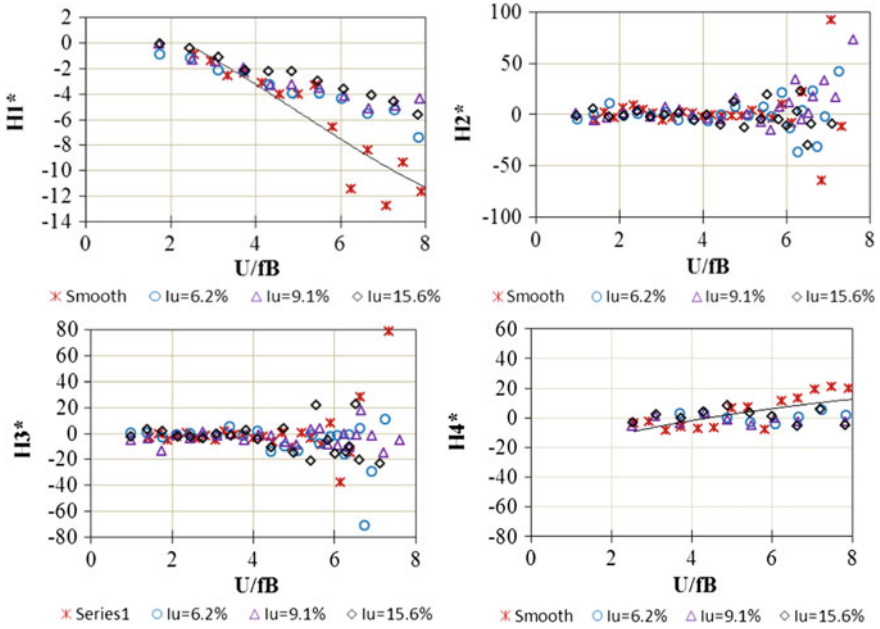


Fig. 4 FDs (H_i) of the bridge section model under smooth and turbulent flows by free decay response (solid curves are fitted polynomial of smooth case)

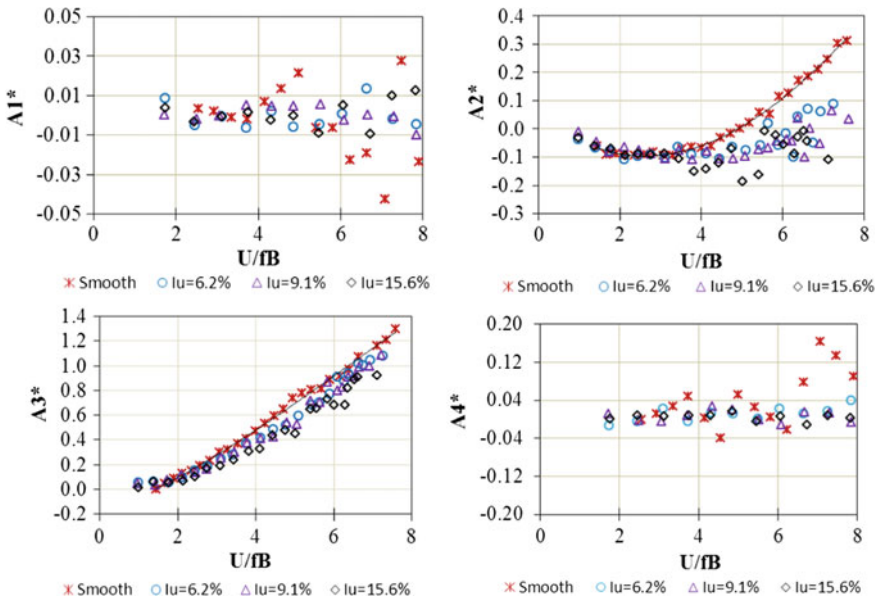


Fig. 5 FDs (A_i) of the bridge section model under smooth and turbulent flows by free decay response (solid curve is fitted polynomial of smooth case)

$H_2^*, H_3^*, A_2^*, A_3^*$ associated with torsional oscillation are calculated using torsional frequency. The torsional damping term A_2^* plays an important role in torsional flutter instability since its positive/negative value corresponds to the aerodynamic instability/stability of torsional flutter. On the other hand, the coupled term H_3^* and A_1^* together with the aerodynamically uncoupled term A_2^* has significant role on heaving-torsional 2 DOF-coupled flutter instability.

From Figs. 4 and 5, it can be found that in smooth flow, the FD H_1^* increases faster than that extracted from turbulent flows. This means that damping ratio of heaving mode under smooth flow is higher compared with that from turbulent flow. Turbulence has a very small effect on vertical and torsional frequency terms H_4^* and A_3^* .

In this experiment, the onset flutter is defined zero cross of reduced velocity axis with the A_2^* . Under smooth flow, the positive value A_2^* at reduced wind speed ($V_r = 5.2$) coincides with the negative total torsional damping. The significant effects of turbulence flows on flutter derivatives are also illustrated particularly for aerodynamic torsional damping term A_2^* , the positive value correspond to the V_r around 6.5 to 7.8 under $I_u = 6.2\%$ and $I_u = 9.1\%$, respectively, whereas in case of $I_u = 15.6\%$, flutter does not occur up to $V_r = 8$. On the other hand, the effects of different turbulent intensities on FDs are fairly modest. Slight difference can be seen that A_2^* tends to be lower in a high reduced velocity range as turbulence intensity increases. The influence of turbulence on FDs will depend on the section. Sarkar (1994) [4] found small effect for a streamlined section, while tests on a truss section showed appreciable effect which is shown clearly by torsional damping term A_2^* .

The off-diagonal terms H_2^*, H_3^*, A_1^* , and A_4^* are fluctuated around zero value, which means that in this experiment, the coupled vibration does not appear at small wind velocity.

4.2 Flutter Critical Velocity

In order to confirm results of identified FDs under free decay responses, the flutter critical velocity will be obtained from an equation of motion of a 2DOF system [10]

$$[M]\{\ddot{u}\} + [C]\{\dot{u}\} + [K]\{u\} = [F]\{\ddot{u}\} \tag{13}$$

where

$$[M] = \begin{bmatrix} m & 0 \\ 0 & I \end{bmatrix} \quad [C] = \begin{bmatrix} 2m\xi_h\omega_h & 0 \\ 0 & 2I\xi_\alpha\omega_\alpha \end{bmatrix} \quad [K] = \begin{bmatrix} m\omega_h^2 & 0 \\ 0 & I\omega_\alpha^2 \end{bmatrix}$$

$$[F] = \begin{bmatrix} L_h & L_\alpha \\ M_h & M_\alpha \end{bmatrix} \quad \{u\} = \begin{Bmatrix} h \\ \alpha \end{Bmatrix}$$

For stability check, self-excited force is only considered, and L_z , L_θ , M_z , and M_θ are self-excited force components defined by

$$\begin{aligned} L_h &= -\pi\rho B^2(L_{hR} + iL_{hl}), \quad L_\alpha = -\pi\rho B^2(L_{\alpha R} + iL_{\alpha I}) \\ M_h &= -\pi\rho B^4(M_{hR} + iM_{hl}), \quad M_\alpha = -\pi\rho B^4(M_{\alpha R} + iM_{\alpha I}) \end{aligned} \tag{14}$$

where L_{hR} , L_{hl} , $L_{\alpha R}$, $L_{\alpha I}$, M_{hR} , M_{hl} , $M_{\alpha R}$, and $M_{\alpha I}$ are self-excited force coefficients (flutter derivatives) those can be compared with those by Scanlan’s format as follows:

$$\begin{aligned} L_{hR} &= H_4^*/2\pi, \quad L_{hl} = H_1^*/2\pi, \quad L_{\alpha R} = H_3^*/2\pi, \quad L_{\alpha I} = H_2^*/2\pi \\ M_{hR} &= A_4^*/2\pi, \quad M_{hl} = A_1^*/2\pi, \quad M_{\alpha R} = A_3^*/2\pi, \quad M_{\alpha I} = A_2^*/2\pi \end{aligned} \tag{15}$$

Flutter derivatives of truss bridge deck section given in this study are approximated polynomials of the results from Figs. 4 and 5.

Assuming sinusoidal motion $\{u\} = \{u_0\} \exp(i\omega t)$ and since structural damping of a long-span bridge can be negligibly small, the damping matrix in Eq. (13) can be dropped. Then, the aerodynamically influenced equation of motion can be written by

$$[K]^{-1}([M] - [F])\{\ddot{u}\} = \frac{1}{\omega^2} \{\ddot{u}\} \tag{16}$$

Solving Eq. (16) as an eigenvalue (λ) problem gives the modal frequency and modal damping ratio as Eq. (17).

$$\begin{aligned} \omega_i &= \sqrt{\text{Re}(\lambda_i)^2 + \text{Im}(\lambda_i)^2} \\ \zeta_i &= \text{Re}(\lambda_i) / \sqrt{\text{Re}(\lambda_i)^2 + \text{Im}(\lambda_i)^2} \end{aligned} \tag{17}$$

where λ is an eigenvalue, $\text{Re}(\lambda)$ and $\text{Im}(\lambda)$ are real and image parts of eigenvalue, respectively.

The stability condition of the system is estimated based on modal damping ratio (or logarithmic decrement). Figure 6 shows the change of aerodynamic damping of torsional mode. The flutter critical wind speed (U_{cr}) is defined by the cross point of torsional aerodynamic logarithmic decrement and equivalent torsional structural logarithmic decrement ($\delta = -0.0263$). The flutter critical velocity increases with increase of turbulence intensity (Fig. 6). In the case of smooth flow the $U_{cr} = 5.7$. And $U_{cr} = 7.2$, $U_{cr} = 7.7$ and $U_{cr} = 8.2$ correspond to $I_u = 6.2\%$, $I_u = 9.1\%$ and $I_u = 15.6\%$, respectively.

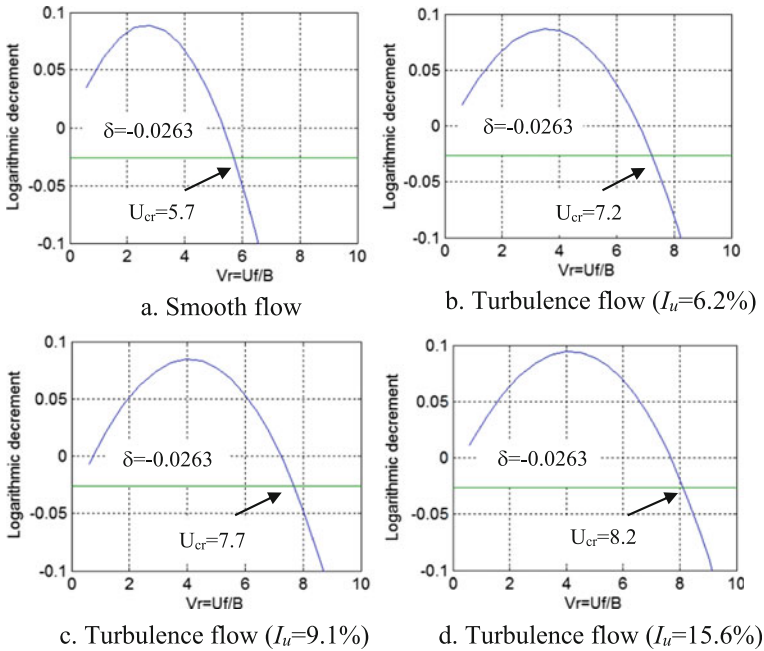


Fig. 6 Change of total logarithms decrement and flutter critical velocity

5 Conclusions

This study has investigated the effects of turbulence on flutter derivatives of the truss bridge deck section by using wind tunnel test and output only state-space stochastic system identification technique. Conclusions from this study are summarized as follows:

- SSI-data shows good results because of an advantage of the method considered buffeting force and its response as inputs instead of noise
- Turbulent flow significantly affects self-excited force via FDs of the truss bridge deck section. A_2^* became positive at $V_r = 5.2$ in the smooth flow and delayed to $V_r = 6.5-7.8$ in the turbulent flows of $I_u = 6.2\%$ and 9.1% , respectively; and in case of $I_u = 15.6\%$, positive value did not appear.
- Turbulence induces buffeting response but increases flutter critical velocity.

References

1. Scanlan RH, Lin WH (1978) Effects of turbulence on bridge flutter derivatives. J Eng Mech Div 104:719-733
2. Haan FL (2000) The effects of turbulence on the aerodynamics of long-span bridges. PhD dissertation; University of Notre Dame, US

3. Sarkar PP, Jones NP, Scanlan RH (1994) Identification of aeroelastic parameters of flexible bridges. *J Eng Mech ASCE* 120:1718–1742
4. Sarkar PP, Jones NP, Scanlan RH (1992) System identification for estimation of flutter derivatives. *J Wind Eng Ind Aerodyn* 42:1243–1254
5. Yamada H, Miyata T, Ichikawa H (1992) Measurement of aerodynamic coefficients by system identification method. *J Wind Eng Ind Aerodyn* 42:1255–1263
6. Kirkegaard PH, Andersen P (1997) State space identification of civil engineering structures from output measurement. In: *Proceedings of the 15th international modal analysis conference*, Orlando, Florida, USA
7. Simiu, E., Scanlan RH (1996) *Wind effects on structures*, 3rd edn. Wiley, New York
8. Lam HT, Katsuchi H, Yamada H (2017) Stochastic identification of flutter derivatives of long span bridge deck by gust response. *J Struct Eng-Jpn* 63A:421–429
9. Peeters B, Roeck GD (1999) Reference based stochastic subspace identification for output-only modal analysis. *Mech Syst Signal Process* 13(6):855–878
10. Fujino Y, Kimura K, Tanaka H (2012) *Wind resistant design of bridge in Japan*. Springer

Numerical Modelling of the Aeroelastic Response of Irregular Slender Structures



Cung H. Nguyen

Abstract This paper presents a general framework for the evaluation of the aeroelastic response of a complex slender structure with generic cross sections. First, the Rayleigh–Ritz approach and the Lagrange equation are employed to describe the vibrations of a continuous coupled structure through a system of ordinary differential equations in common forms which are familiar to structural analysts. Then, the general framework for instability analysis will be presented. Finally, the theory is then applied to a real telecommunication pole with an irregular shape. The numerical results show different aspects from traditional findings, emphasizing the structural irregularity.

Keywords Numerical modelling • Aeroelasticity • Wind–structure interaction
Irregular structure • Eccentricity

1 Introduction

Nowadays, the speedy development of advanced technology and research has provided powerful tools for engineers to design and build structures lighter, longer, higher and more complex. In general, irregular structures can appear with eccentricity between mass centre and stiffness centre. For example, buildings with asymmetry shapes, or a telecommunication mast attached with antenna and parabolae.

Such irregular slender structures are tremendously susceptible to wind actions. Their aerodynamic behaviour becomes sophisticated and sensitive to potential aeroelastic instabilities such as galloping, leading to collapses or serious damages unable to be repaired [1–3]. The eccentricity gives rise to the three-dimensional (3D) modes, shapes and structural responses, resulting in the coupling among

C. H. Nguyen (✉)

Department of Civil Engineering, Industrial University of Ho Chi Minh City,
Ho Chi Minh City, Vietnam
e-mail: nguyenhucung@iuh.edu.vn

© Springer Nature Singapore Pte Ltd. 2018

H. Nguyen-Xuan et al. (eds.), *Proceedings of the International Conference on Advances in Computational Mechanics 2017*, Lecture Notes in Mechanical Engineering, https://doi.org/10.1007/978-981-10-7149-2_63

903

responses and generalized force components. Then, the traditional analysis may not be suitable to evaluate the behaviour of structures under wind actions since the eccentricity is often ignored. With the presence of eccentricity, previous studies have mainly focused on buildings; moreover, the aeroelastic forces have not been considered [4]. These limitations prevent the full understanding the aeroelastic behaviour of structures.

Aeroelasticity is the study of the interaction between aerodynamic forces and structural motion. Phenomenon which is characterized by a rapid increase of the structural response due to the aeroelastic forces is referred to as aeroelastic instability phenomenon.

Aeroelastic stability has been analyzed since over 80 years ago but not all aeroelastic phenomena are entirely understood. The first study of the aeroelastic galloping instability, along with the quasi-steady theory, was introduced by Den Hartog with a criterion for the critical condition for one degree of freedom (1-DOF) transversal galloping [5]. According to that, the galloping occurs in the crosswind direction when the aerodynamic damping is negative. This criterion is referred to as Den Hartog's criterion, which has become a crucial method in engineering application. Starting from this investigation, a number of models have been proposed to understand deeper such a topic.

In 1992, Jones introduced a 2-DOF model for the translational coupled galloping [6]. The result can be archived only when the first two natural frequencies are the same. This hypothesis is not appropriate in reality for structures having asymmetrical sections; therefore, only a class of particular problems can be dealt with. To overcome this limitation, Luongo and Piccardo applied the perturbation technique to formulate analytically the critical condition for translational coupled galloping, taking into account the different values of natural frequencies [7]. The perturbation method was also employed to study the 3-DOF coupled instability of the transmission lines [8].

It is worth noting that all researches mentioned above have not considered the eccentricity between mass and stiffness centres. In addition, most of the analyses have been carried out for simple structures with a hypothesis that the aerodynamic coefficients, mean wind velocity, mass per unit length and size of cross sections are constant along the structure. This assumption is actually not correct since those parameters, in reality, usually vary along the structure.

This paper aims to present a general framework for the evaluation of the aeroelastic response of a complex slender structure with generic cross sections. First, the Rayleigh–Ritz approach and the Lagrange equation are employed to describe the vibrations of a continuous coupled structure through a system of ordinary differential equations (Sect. 2). Based on that, Sect. 3 presents the modal analysis to derive the natural frequencies and mode shapes. In Sect. 4, the general framework for instability analysis will be presented. The coupling among modes, the general direction of the wind with respect to structures, the variation of mean wind, aerodynamic coefficients and mass per unit length along the structure are taken into account. Besides, essentially particular cases in which the analytical solutions can be derived are discussed. The theory is then applied to a real

telecommunication pole with irregular shape (Sect. 5). The numerical results show different aspects from traditional findings, emphasizing the structural irregularity. Finally, critical remarks will be discussed.

2 Numerical Derivation of Equation of Motion

Let us now consider a slender structure whose length \mathcal{L} with a generic cross section subjected to the wind with mean velocity U (Fig. 1). Let x, y, z be a Cartesian reference system with origin in O coincided the stiffness centre; x and y are horizontal axes, z coincides with the structural axis. The coordinate of the eccentricity between the mass centre M and O is e_x and e_y .

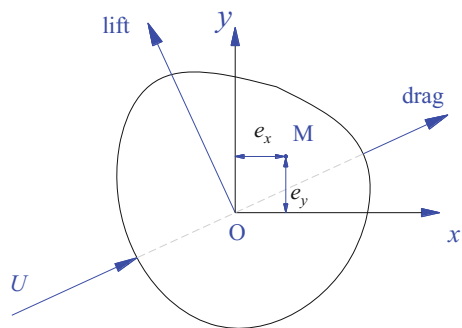
The structural response vector to external load is denoted as

$$\mathbf{r}(z, t) = \begin{Bmatrix} r_x(z, t) \\ r_y(z, t) \\ r_z(z, t) \end{Bmatrix} \tag{1}$$

where r_x and r_y are translational displacement responses in x and y directions; r_z is rotation response around z -axis; t denotes time.

In determination of the structural response, analytical solutions can be found for simple structures with simple shapes, e.g. a cantilever beam with square section. For a general case, a numerical procedure is applied. In numerical approaches, the Rayleigh–Ritz technique is an efficient tool to offer an approximation to the exact response of a structure. This method has been presented in many text books, e.g. [9, 10], and used widely in engineering, particularly in structural dynamics. It is worth pointing out that most of the applications of this approach are for uncoupled structures, i.e. no eccentricity between mass and stiffness centres. This section, for that reason, extends such a technique for the coupled structures where the eccentricity is present.

Fig. 1 A cross section with eccentricity between mass and stiffness centres



Using the Rayleigh–Ritz method, each displacement response component can be approximated as a linear combination of a series of N trial functions:

$$r_\alpha(z, t) = \sum_{k=1}^N \phi_k^\alpha(z) q_k^\alpha(t) \tag{2}$$

where $q_k^\alpha(t)$ are unknown generalized responses and $\phi_k^\alpha(z)$ are the trial functions.

Substituting Eq. (2) into Eq. (1), the response can be also rewritten in a matrix form as follows:

$$\mathbf{r}(z, t) = \mathbf{\Phi}(z)\mathbf{Q}(t) \tag{3}$$

where

$$\mathbf{\Phi}(z) = \begin{bmatrix} \Phi_x(z) & \emptyset & \emptyset \\ \emptyset & \Phi_y(z) & \emptyset \\ \emptyset & \emptyset & \Phi_z(z) \end{bmatrix}, \Phi_\alpha(z) = [\phi_1^\alpha(z) \quad \phi_2^\alpha(z) \quad \dots \quad \phi_N^\alpha(z)] \tag{4}$$

$$\mathbf{Q}(t) = \begin{Bmatrix} \mathbf{Q}_x(t) \\ \mathbf{Q}_y(t) \\ \mathbf{Q}_z(t) \end{Bmatrix}, \mathbf{Q}_\alpha(t) = \begin{Bmatrix} q_1^\alpha(t) \\ q_2^\alpha(t) \\ \dots \\ q_N^\alpha(t) \end{Bmatrix} \tag{5}$$

From Eq. (2), it is apparent that the trial functions $\phi_k^\alpha(z)$ decide the goodness of the approximation. The choice of these functions will be discussed later. Meanwhile, the generalized responses $q_i^\alpha(t)$ will be determined through equations of motion, which will be formulated later, starting from the Lagrange’s equation.

Assuming the rotation is small, then the translational displacements of the mass centre M are given by:

$$\begin{aligned} r_{Mx}(z, t) &= r_x(z, t) - e_y(z)r_z(z, t) \\ r_{My}(z, t) &= r_y(z, t) + e_x(z)r_z(z, t) \end{aligned} \tag{6}$$

The Lagrange’s equations are written as:

$$\frac{d}{dt} \left[\frac{\partial T(t)}{\partial \dot{q}_k^\alpha(t)} \right] - \frac{\partial T(t)}{\partial q_k^\alpha(t)} + \frac{\partial V(t)}{\partial q_k^\alpha(t)} = F_k^\alpha(t), k = \overline{1, N}, \quad \alpha = x, y, z \tag{7}$$

where T , V and F_k^α are referred to as the kinetic energy, potential energy and generalized load, respectively. These terms can be determined as below.

$$T(t) = \sum_{\alpha=x,y,z} T_{M\alpha}(t) \tag{8}$$

$$T_{M\alpha}(t) = \frac{1}{2} \int_{(\mathcal{L})} [m_\alpha(z) \dot{r}_{M\alpha}^2(z, t)] dz \tag{9}$$

$$V(t) = \sum_{\alpha=x,y,z} V_\alpha(t) \tag{10}$$

$$V_\alpha(t) = \frac{1}{2} \int_{(\mathcal{L})} J_\alpha \left[\frac{\partial^2 r_\alpha(z, t)}{\partial z^2} \right]^2 dz \tag{11}$$

$$F_k^\alpha(t) = \int_{(\mathcal{L})} f_\alpha(z, t) \phi_k^\alpha(z) dz \tag{12}$$

in which $m_x(z) = m_y(z) = m(z)$, which is the mass per unit length; $m_z(z) = I_M(z)$ is the moment of inertia at the centre of mass M ; $J_x = EI_y(z)$ and $J_y = EI_x(z)$ are the modulus of bending stiffness, and $J_z = GI_z(z)$ is the modulus of torsional stiffness.

Substituting Eqs. (8), (10) and (12) in Eq. (7) with the use of Eqs. (2), (6), (9) and (11), after some mathematical manipulations, the Lagrange's equation can be rewritten as:

$$\mathbf{M}\mathbf{Q}(t) + \mathbf{K}\mathbf{Q}(t) = \mathbf{F}(t) \tag{13}$$

where

$$\mathbf{M} = \begin{bmatrix} \mathbf{M}_x & \emptyset & -\mathbf{M}_{xz} \\ \emptyset & \mathbf{M}_y & \mathbf{M}_{yz} \\ -\mathbf{M}_{xz} & \mathbf{M}_{yz} & \mathbf{M}_z \end{bmatrix}, \mathbf{K} = \begin{bmatrix} \mathbf{K}_x & \emptyset & \emptyset \\ \emptyset & \mathbf{K}_y & \emptyset \\ \emptyset & \emptyset & \mathbf{K}_z \end{bmatrix} \tag{14}$$

$$\mathbf{F}(t) = \begin{Bmatrix} \mathbf{F}_x(t) \\ \mathbf{F}_y(t) \\ \mathbf{F}_z(t) \end{Bmatrix}, \mathbf{F}_\alpha(t) = [F_1^\alpha(t) \quad F_2^\alpha(t) \quad \dots \quad F_N^\alpha(t)]^T \tag{15}$$

The element (i, j) of matrices $\mathbf{M}_\alpha, \mathbf{M}_{\alpha\theta}, \mathbf{K}_\alpha$ in Eq. (14) are given by:

$$(\mathbf{M}_\alpha)_{ij} = m_{ij}^\alpha, (\mathbf{M}_{\alpha z})_{ij} = m_{ij}^{\alpha z}, (\mathbf{K}_\alpha)_{ij} = k_{ij}^\alpha \tag{16}$$

where

$$m_{ij}^\alpha = \int_{(\mathcal{L})} m_\alpha(z) \phi_i^\alpha(z) \phi_j^\alpha(z) dz \tag{17}$$

$$m_{ij}^{xz} = \int_{(\mathcal{L})} m(z)e_y(z)\phi_i^x(z)\phi_j^z(z)dz \quad (18)$$

$$m_{ij}^{yz} = \int_{(\mathcal{L})} m(z)e_x(z)\phi_i^y(z)\phi_j^z(z)dz \quad (19)$$

$$k_{ij}^\alpha = \int_{(\mathcal{L})} J_\alpha(z) \frac{d^2\phi_i^\alpha(z)}{dz^2} \frac{d^2\phi_j^\alpha(z)}{dz^2} dz \quad (20)$$

Finally, involving the damping matrix \mathbf{C} , the full 3D coupled motion equations can be expressed as follows:

$$\mathbf{M}\ddot{\mathbf{Q}}(t) + \mathbf{C}\dot{\mathbf{Q}}(t) + \mathbf{K}\mathbf{Q}(t) = \mathbf{F}(t) \quad (21)$$

It can be realized that thanks to the Rayleigh–Ritz approximation and the Lagrange’s equations, the motion of a continuous structure is governed by a system of ODEs, as shown in Eq. (21), instead of PDEs. This looks like that such a system with infinite degrees of freedom is reduced to the discretized one with $(3N \times 3N)$ degrees of freedom. As shown in the next section, however, the properties of a distributed structure are still remained, such as the continuity of mode shapes or displacements, which are not appeared in multi-degrees of freedom. This highlights the advantage of the proposed technique since working with a discrete system governed by ODEs in Eq. (21) is basically more familiar to structural analysts than PDEs corresponding to a continuous structure.

3 Modal Analysis

The natural frequencies and mode shapes of the structure can be determined through the modal analysis. This can be done by solving the eigenvalue problem below, which is formulated from the equation for undamped free vibration, resulting from neglecting damping and external load from Eq. (21), i.e. $\mathbf{C} = \mathbf{0}$ and $\mathbf{F}(t) = \mathbf{0}$:

$$(-\omega^2\mathbf{M} + \mathbf{K})\mathbf{q} = \mathbf{0} \quad (22)$$

In Eq. (22), ω and \mathbf{q} are referred to as eigenvalue (or natural circular frequency) and Ritz eigenvector. The eigenvalues are the solutions of the following equation:

$$\det(-\omega^2\mathbf{M} + \mathbf{K}) = \mathbf{0} \tag{23}$$

It can be realized that, for given trial functions, matrices \mathbf{M} and \mathbf{K} are determined and real symmetric matrices. Then Eq. (23) results in $3N$ real roots ω_i , $i = \overline{1, 3N}$. For each value ω_i , there is a corresponding Ritz eigenvector \mathbf{q}_i . As a result, the i th mode shapes $\Psi_i(z)$ and their modal matrix $\Psi(z)$ can be determined as:

$$\Psi(z) = [\Psi_1(z) \quad \Psi_2(z) \dots \Psi_{3N}(z)] = \Phi(z)\boldsymbol{\varphi} \tag{24}$$

$$\Psi_i(z) = [\Psi_i^x(z) \quad \Psi_i^y(z) \quad \Psi_i^z(z)]^T = \Phi(z)\mathbf{q}_i \tag{25}$$

$$\boldsymbol{\varphi} = [\mathbf{q}_1 \mathbf{q}_2 \dots \mathbf{q}_{3N}] \tag{26}$$

As mentioned before, the choice of the trial functions $\phi_i^\alpha(z)$ decides the goodness of the approximated natural frequencies and mode shapes and consequently the structural response. These functions are chosen such that the boundary conditions of the structure are satisfied. This requirement is evident if the all trial functions are selected from a set of comparison functions, which are differentiable as many times as the order of the system and satisfy all the boundary conditions. Unfortunately, it is difficult for all the trial functions to agree with all the boundaries in practice. For instance, it is impossible for a comparison function which is continuous to satisfy the shear discontinuity, which is associated with the third-order derivative of such a function, of a beam having a concentrated mass. This condition is usually ignored in this case. In addition, a higher derivative of mode shape, such as moment or shear, is more susceptible to a specific trial function than a lower one, such as displacement or its slope. As a consequence, the trial functions may be chosen from the class of admissible functions, which are differentiable half as many times as the order of the system and satisfy only the geometric boundary conditions which are related to the deformation of the structure, i.e. the deflection and its slope [10].

An efficient way to choose the trial functions is that these functions selected from the mode shapes of a similar structure with uniform properties in which the analytical solutions may be found. Increasing the number of trial functions improves the accuracy of the approximation. When an approximated function is closer to the exact mode shape, the boundary conditions tend to be satisfied with higher order derivatives.

Finally, it is remembered that Eq. (21) is a system of $3N$ coupled equation. To solve this equation, it is useful to decouple it into $3N$ uncouple equations. This can be done by substituting the linear transformation $\mathbf{Q}(t) = \boldsymbol{\varphi}P(t)$ into Eq. (21) that results in

$$\tilde{M}\ddot{\mathbf{P}}(t) + \tilde{C}\dot{\mathbf{P}}(t) + \tilde{K}\mathbf{P}(t) = \tilde{\mathbf{F}}(t) \tag{27}$$

where

$$\tilde{\mathbf{M}} = \boldsymbol{\varphi}^T \mathbf{M} \boldsymbol{\varphi} \tag{28}$$

$$\tilde{\mathbf{K}} = \boldsymbol{\varphi}^T \mathbf{K} \boldsymbol{\varphi} \tag{29}$$

$$\tilde{\mathbf{C}} = \boldsymbol{\varphi}^T \mathbf{C} \boldsymbol{\varphi} \tag{30}$$

$$\tilde{\mathbf{F}}(t) = \boldsymbol{\varphi}^T \mathbf{F}(t) \tag{31}$$

4 Galloping Instability Analysis

To evaluate the aeroelastic stability of the structure, it is necessary to introduce the aeroelastic wind load to the Eq. (27). The load is expressed as [11]:

$$\tilde{\mathbf{F}}(t) = -\tilde{\mathbf{C}}_a \dot{\mathbf{P}}(t) - \tilde{\mathbf{K}}_a \mathbf{P}(t) \tag{32}$$

where $\tilde{\mathbf{C}}_{a0}$ and $\tilde{\mathbf{K}}_{a0}$ are the generalized aerodynamic damping and stiffness matrices, respectively, given by:

$$\tilde{\mathbf{C}}_a = \int_{(\mathcal{L})} \boldsymbol{\Psi}^T(z) \mathbf{c}_a(z) \boldsymbol{\Psi}(z) dz \tag{33}$$

$$\tilde{\mathbf{K}}_a = \int_{(\mathcal{L})} \boldsymbol{\Psi}^T(z) \mathbf{k}_a(z) \boldsymbol{\Psi}(z) dz \tag{34}$$

$$\mathbf{k}_a(z) = \frac{1}{2} \rho U^2(z) b(z) \begin{bmatrix} 0 & 0 & c'_d(z) \\ 0 & 0 & c'_l(z) \\ 0 & 0 & b(z) c'_m(z) \end{bmatrix} \tag{35}$$

$$\mathbf{c}_a(z) = \frac{1}{2} \rho U(z) b(z) \begin{bmatrix} 2c_d(z) & c'_d(z) - c_l(z) & 0 \\ 2c_l(z) & c_d(z) + c'_l(z) & 0 \\ 2b(z)c_m(z) & b(z)c'_m(z) & 0 \end{bmatrix} \tag{36}$$

in which U, ρ and b are the mean wind velocity, air density and characteristic size of cross section, respectively; c_d, c_l, c_m are, respectively, the drag, lift and moment coefficients, which are dependent on the angle of attack and determined through wind tunnel tests; d are the derivatives of corresponding coefficients with respect to the angle of attack.

Inserting the Eq. (32) with the use of Eqs. (33)–(36) and then arranging it in state-space form, it yields:

$$\dot{\mathbf{X}}(t) = \tilde{\mathbf{A}}\tilde{\mathbf{X}}(t) \quad (37)$$

where

$$\mathbf{X}(t) = \begin{bmatrix} \mathbf{P}(t) \\ \dot{\mathbf{P}}(t) \end{bmatrix} \quad (38)$$

$$\tilde{\mathbf{A}} = \begin{bmatrix} \emptyset & \mathbf{I} \\ -\tilde{\mathbf{M}}^{-1}(\tilde{\mathbf{K}} + \tilde{\mathbf{K}}_a) & -\tilde{\mathbf{M}}^{-1}(\tilde{\mathbf{C}} + \tilde{\mathbf{C}}_a) \end{bmatrix} \quad (39)$$

The Eq. (37) represents a 3D problem for aeroelastic stability. The criteria for stability conditions are based on the sign of the real values of the eigenvalues λ_j of the state-space matrix $\tilde{\mathbf{A}}$ [10]. The structure is unstable if there is at least a positive value of $\text{Re}(\lambda_j)$. Corresponding to this value, there is critical wind velocity U_{cr} for the instability occurrence.

In general, the eigenvalues λ_j and critical wind velocity U_{cr} can be estimated through a numerical procedure. For a commonly interesting case in practical engineering along with 2-DOF model where two consecutive modes (mode $2k-1$ and mode $2k$) associated with two translational directions (x and y) are equal, analytical solution for galloping instability can be found [12]. Then, the necessary condition for the instability occurrence is given by:

$$\text{tr}\tilde{\mathbf{C}}_{a,xy,2k} < 0 \text{ or } \text{tr}\tilde{\mathbf{C}}_{a,xy,2k} \geq 0 > \det\tilde{\mathbf{C}}_{a,xy,2k} \quad (40)$$

in which $\text{tr}(\cdot)$ and $\det(\cdot)$ stand for the trace and determinant of a matrix, respectively.

The critical wind velocity at the reference height z_r is then given by:

$$U_{cr,xy,2k}(z_r) = -\frac{8\omega_{2k}\xi_{2k}\tilde{m}_{2k,eq}}{\rho b(z_r)c_{a,xy,2k}} \quad (41)$$

$$c_{a,xy,2k} = \text{Re} \left[\text{tr}\tilde{\mathbf{C}}_{a,xy,2k} - \sqrt{\text{tr}^2\tilde{\mathbf{C}}_{a,xy,2k} - 4 \det\tilde{\mathbf{C}}_{a,xy,2k}} \right] \quad (42)$$

$$\tilde{m}_{2k,eq} = \int_{(\mathcal{L})} m(z) \|\Psi_{2k}(z)\|^2 dz / \int_{(\mathcal{L})} \|\Psi_{2k}(z)\|^2 dz \quad (43)$$

5 Numerical Application

The theoretical framework described above is derived for the general case and can be applied for any slender structures. It is herein applied to investigate the aeroelastic stability a particular real structure, which is an antenna pole. The pole has

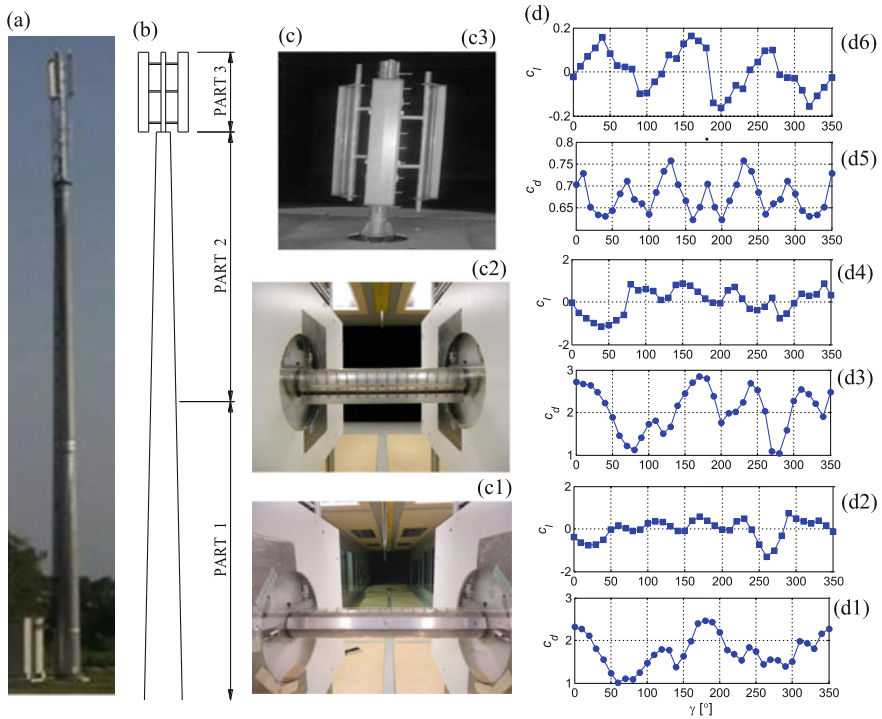


Fig. 2 a Pole in study; b pole sketch to define its 3 parts; c wind tunnel testing models for the 3 parts; d. drag and lift coefficients of the 3 models

height $H = 30$ m and is composed by two shafts (Fig. 2a). The first shaft is 24 m long; the outer diameter of its section, whose thickness is constant and equal to 5 mm, varies from 950 mm at the bottom to 350 mm at the top. There are cables attached to this shaft with a distributed mass per unit length 5 kg/m. The second shaft, put above the first one, is 6 m long and with 6 antennas attached. Its section has constant outer diameter 193.7 mm and constant thickness 7.1 mm; the total mass of the shaft is 540 kg. The whole pole is also attached with a stair from the bottom to the top. Its mass per unit length 7 kg/m. The additional stair, cables and antennas create a distributed mass eccentricity. It is reasonable to assume that they are ineffective to the structural stiffness. The pole is located in a terrain characterized by a roughness length 0.3 m and a basic reference wind velocity 25 m/s.

The static aerodynamic coefficients have been determined by wind tunnel tests, reported in [13] and described herein. Since the outer diameter of the main shaft varies significantly along the pole, the measurements have been carried out by dividing this shaft into two uniform parts (part 1 and part 2, Fig. 2b) and antenna part (part 3, Fig. 2b). The tests on the main shaft have been conducted in the wind tunnel of the Faculty of Engineering of the University of Genoa, Italy (Fig. 2c1–c2). The corresponding drag and lift coefficients are shown in Fig. 2d1–d4. The wind

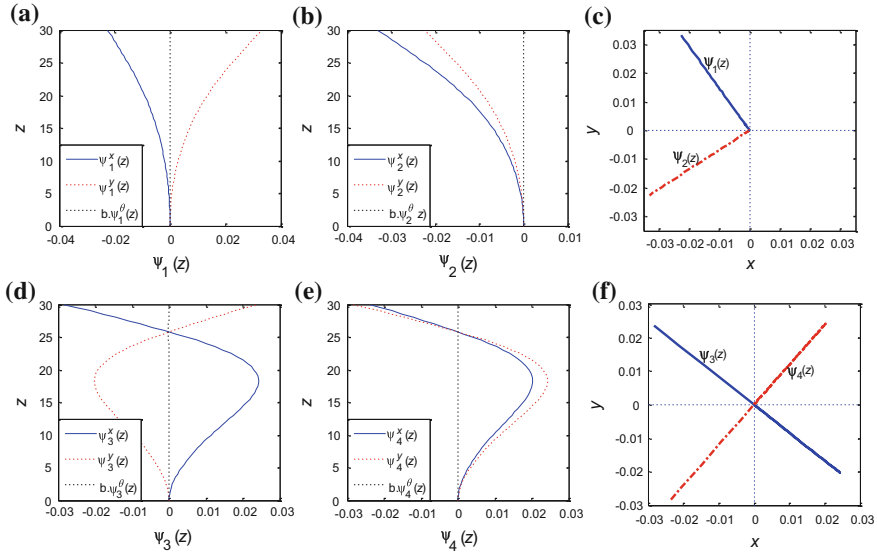


Fig. 3 First four mode shapes **a** and **b** first and second modes in front view; **c** first and second modes in top view; **d** and **e**: third and fourth modes in front view; **f** third and fourth modes in top view

tunnel test for the antenna part of the pole (Fig. 2c3) has been carried out at Milan Polytechnic University. The corresponding drag and lift coefficients are shown in Fig. 2d5–d6. As for the structural type, the rotation is small and can be neglected [2]. So, the moment coefficients are not shown here and any rotational terms in the stability analysis are neglected.

As mentioned above, the presence of the stairs and cable bundles creates the eccentricity distributed along the pole. The natural frequencies and mode shapes are derived by employing the method presented in Sects. 2 and 3, in which the trial functions are chosen as the mode shapes of the cantilever prismatic beam.

Figure 3 shows the first four modes' shapes of the pole, considering the eccentricities. It can be seen that each coupled mode shape has three components that is different from the case without eccentricity where each mode shape has only one dimension restricted to the principle axes. Also, it is confirmed that the torsional component is almost irrelevant.

Based on the obtained aerodynamic coefficients and mode shapes, it is checked that the trace of the aerodynamic damping matrix $\text{tr}\hat{\mathbf{C}}_{a,xy,2k}$ is always positive. So, the second condition given in Eq. (40) is used for checking if the structure is potentially unstable. Figure 4 shows the condition for galloping instability occurrence (Fig. 4a) and critical wind velocity, in comparison with 1-DOF and 2-DOF cases (Fig. 4b).

It can be seen that, on the one hand, the instability can occur not only for the first two modes but also for higher modes. Moreover, at angle 230°, the structure is

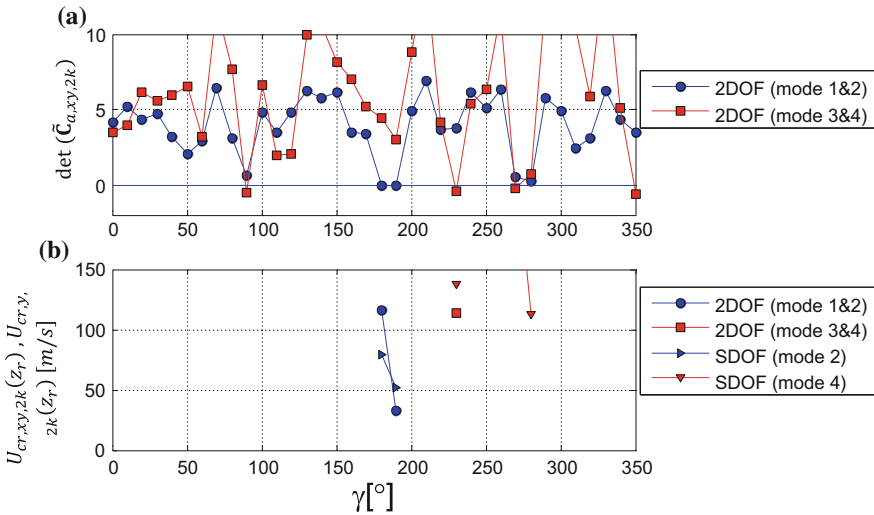


Fig. 4 a Condition for galloping occurrence; b critical velocity

unstable for higher mode instead of first two modes. This prediction is not given in traditional analysis. On the other hand, at angle 190° and 230° , the critical velocities for the 2-DOF case are lower than those for the 1-DOF case. All of these mean that using the conventional analysis will provide an incorrect prediction for instability occurrence that is unsafe for the structure.

6 Conclusions

This paper presents an efficient numerical procedure for evaluating the aeroelastic stability condition of irregular slender structures with the presence of eccentricity between mass and stiffness centre. Using the Rayleigh–Ritz technique, dynamic characteristics of the structures can be obtained through modal analysis.

Literature usually deals with lighting poles and antenna masts as slender vertical structures endowed with polar symmetry. This approach is conflicting with the frequent presence of several devices along the main shaft of the structure. Several damages and even collapses of this structural type not fully understood or explained may give rise to the idea that the above devices play a significant role also from the structural engineering standpoint.

The proposed method is applied to a real telecommunication antenna mast. Although the selected test case represents only one of the infinite possible arrangements in which this structural type may be realized, it clearly points out the importance of the mechanical and aerodynamic eccentricities, of the upper modes of vibration, of the coupling between the crosswind and alongwind components of

the motion and of the aerodynamic damping. In its whole, this paper shows that traditional calculations based on neglecting eccentricities lead to relevant errors that may make classical engineering approaches seriously unsafe.

For the aeroelastic stability aspect, it is pointed out the importance of the aerodynamic eccentricities, of the upper modes, and of the coupling between the crosswind and alongwind motion. A comparison between the results provided herein and the classical engineering approaches emphasizes that relevant errors may occur, especially for particular sets of parameters and specific configurations. In such conditions, the structure may exhibit very low critical galloping velocity able to produce unexpected damages and collapses. This might explain a lot of damages and collapses of slender poles that this structural type has often suffered without clear and suitable explanations.

All the analyses carried out in this paper are based on a quasi-steady theory supported by wind tunnel experiments involving static sectional model tests. This choice is justified by the wish of opening a new research line, not considered in the traditional literature, inspecting the potential occurrence of critical situations unpredictable by means of classic engineering models. Provided that the preliminary results illustrated in this paper confirm the existence of such critical situations, it is now necessary to improve the above evaluations in order to quantify their reliability by means of refined analyses. For this reason, aeroelastic wind tunnel tests are currently carried out with the aim of confirming, correcting, generalizing or revising the results illustrated in the present paper.

References

1. Robertson AP, Hoxey RP, Short JL, Burges LR, Smith BW, Ko RHY (2001) Wind-induced fatigue loading of tubular steel lighting columns. *Wind Struct* 4:163–176
2. Caracoglia L, Jones NP (2007) Numerical and experimental study of vibration mitigation for highway light poles. *Eng Struct* 29:821–831
3. Phares BM, Sarkar PP, Wipf TJ, Chang B (2007) Development of fatigue procedure for slender, tapered support structures for highway sign, luminaires and traffic signals subjected to wind induced excitation from vortex shedding and buffeting. A final report from Midwest Transportation Consortium, US Department of Transportation, MTC project, 2007
4. Chen X, Kareem A (2005) Probabilistic wind-induced response of buildings with 3-D coupled Modes. In: *Proceedings of 9th international conference on structural safety and reliability*, Millpress, Rotterdam
5. Hartog JPD (1932) Transmission-line vibration due to sleet. *Inst Electr Eng* 51:1074–1086
6. Jones KF (1992) Coupled vertical and horizontal galloping. *J Eng Mech ASCE*, 118(1):92–107
7. Luongo A, Piccardo G (2005) Linear instability mechanisms for coupled translational galloping. *J Sound Vib* 4–5:1027–1047
8. Yu P, Desai YM, Shah AH, Popplewell N (1993) Three degree-of-freedom model for galloping. Part I: formulation. *J Eng Mech ASCE*, 119(12):2404–2425
9. Hurty WC, Rubinstein MF (1964) *Dynamics of structures*. Prentice Hall
10. Meirovitch L (1986) *Elements of vibration analysis*. In: 2nd edition. McGraw-Hill

11. Solari G (1994) Gust-excited vibrations. In: Sockel H (ed) Wind-excited vibrations of structures, Springer, Vienna, Austria
12. Nguyen CH, Macdonald JHG Galloping analysis of a stay cable with attached viscous damper considering complex modes. J Eng Mech ASCE (In press)
13. Nguyen CH (2013) Aerodynamic and Aeroelastic analysis of complex structures. PhD thesis, University of Genoa

Analysis of Fluid–Structures Interaction Problem of Revetment Slope Thin-Walled Structure Using Abaqus



**P. Truong-Thi, L. Dang-Bao, M. Abdel Wahab, H. Duong-Ngoc,
T. Hoang-Duc and Hung Nguyen-Xuan**

Abstract This paper aims to analyze fluid–structure interaction (FSI) problems of revetment slope thin-walled structures using ABAQUS software. The method is based on a combination of computational fluid dynamics (CFD) for fluids and finite element method (FEM) for structures. During the simulation process, the required data are exchanged by the subsystems. Based on the co-simulation FSI, behaviors of solid structures under impact of flow are examined. The purpose of the co-simulation is to reduce costs and time consumed in manufacturing revetment slope (RS) structures. The expected results help improve geometry of blocks.

P. Truong-Thi (✉) · L. Dang-Bao · H. Nguyen-Xuan
Center for Interdisciplinary Research, HUTECH University, Ho Chi Minh City, Vietnam
e-mail: tphuong89@imech.vast.vn

L. Dang-Bao
e-mail: dangbaoloi@muce.edu.vn

H. Nguyen-Xuan
e-mail: ngx.hung@hutech.edu.vn

M. Abdel Wahab
Laboratory Soete, Faculty of Engineering and Architecture, Ghent University, Ghent, Belgium
e-mail: Magd.AbdelWahab@UGent.be

H. Duong-Ngoc
Vietnam Academy of Science and Technology (VAST), Graduate University of Science and Technology (GUST), 18 – Hoang Quoc Viet, Cau Giay, Hanoi, Vietnam
e-mail: dnhai@vast.vn

P. Truong-Thi
Institute of Mechanics, VAST, Hanoi, Vietnam

L. Dang-Bao
Mien Trung University of Civil Engineering, Tuy Hoa City, Vietnam

T. Hoang-Duc
Ba Ria Vung Tau Urban Sewerage and Development One Member Limited Company (BUSADCO), Vung Tau, Vietnam

© Springer Nature Singapore Pte Ltd. 2018

H. Nguyen-Xuan et al. (eds.), *Proceedings of the International Conference on Advances in Computational Mechanics 2017*, Lecture Notes in Mechanical Engineering, https://doi.org/10.1007/978-981-10-7149-2_64

Geometry dimensions of blocks of revetment slope thin-walled structure are supported by Busadco Company (Ba Ria Vung Tau Urban Sewerage and Development One Member Limited Company). In this article, an overview of computational aspect of FSI is presented. We expect to provide application of simulation technology to deal with such RS structures.

Keywords Co-simulation • Fluid–Structure Interaction (FSI) • ABAQUS software • Revetment slope structure • Thin-walled structure

1 Introduction

A strong RS structure can protect riverbanks, coastlines, and dikes under impact of floods, sea waves, and erosion. The designing of a RS that suits each flexible ground needs to take into consideration fluid–structure interaction analysis. Most FSI problems are very complicated, and closed-form solutions are hard to obtain, while laboratory experiments are limited in scope. In other words, numerical simulation is proven to be an effective method to handle this kind of problem. Due to their strong non-linearity and multi-disciplinary nature, these problems remain a challenge [1]. Nowadays, numerical methods are developed quickly, and FSI problems are solved through separate analysis and couple analysis. Several researchers have studied fluid–structure interaction problems through various softwares, such as ABAQUS and FlowVision [2], ABAQUS and Fluent to investigate fluid flow [3].

The co-simulation technique is a multi-physics capability that serves several functions, available within ABAQUS or as separate add-on analysis capabilities, for run-time coupling of ABAQUS and other analysis programs. We can perform complex FSI problems by coupling ABAQUS/Standard or ABAQUS/Explicit to predict damages of structures and ABAQUS/CFD to solve for fluids using ABAQUS software [4, 5]. In previous studies, modeling of RS has not yet been considered.

In this study, we apply co-simulation method in ABAQUS software for simulation of RS structures, which are formed by interlocking thin-walled blocks, and put on a flexible ground (see Fig. 1) provided by Busadco <http://busadco.com.vn/en/>. This work proposes redesign solution of such structures at low costs. The innovation of RS contributes to protecting countries adjacent to the sea, e.g., Vietnamese coastline, against floods and erosion caused by global climate change. Some thin-walled concrete block shapes have been put into use and have not been simulated yet.



Fig. 1 Several blocks shape have been built to protect coast and riverbank
 (Source <http://busadco.com.vn/en/>)

2 Computational Aspects

2.1 Governing Equations

The dynamic equilibrium (for the discrete model in finite element system) is defined in terms of the external applied forces (**P**), the internal element forces (**I**), and the nodal accelerations:

$$M \frac{d^2 \mathbf{u}}{dt^2} = \mathbf{P} - \mathbf{I} \tag{1}$$

where **M** is the mass matrix, **u** is the displacement vector, and **P** is the sum of forces that act on the structure including forces from the fluid.

This fluid flow is described by the incompressible Navier–Stokes equations for the velocity field:

$$\frac{\partial \mathbf{V}}{\partial t} + \nabla(\mathbf{V} \otimes \mathbf{V}) = - \frac{\nabla p}{\rho} + \frac{1}{\rho} \nabla(\mu \nabla \mathbf{V}) + \mathbf{F} \tag{2}$$

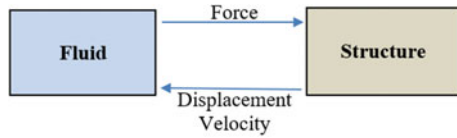
$$\nabla \mathbf{V} = 0$$

where **V** is the velocity, *p* is pressure, μ is effective viscosity, ρ is density, and **F** is volume force affecting the fluid [2].

2.2 Boundary Conditions

Except ordinary boundary conditions for simulating structure deformations, boundary conditions of the fluid–structure interface are specified in terms of pressure loading from the fluid, calculated for each element face that is in contact

Fig. 2 Boundary conditions between the fluid and the structure on FSI interface



with the fluid (Fig. 2) [6, 7]. Fluid domain is specified for the inlet, outlet characteristics. Boundary conditions of structure are clamped at the bottom. The aims of this is to evaluate the bearing capacity of concrete component and simplify the model as well. In addition, special boundary condition of interface between fluid and structure are specified following formula:

$$\mathbf{V}_{ij} = \sum_{n=1,N} w_{nij} \frac{d\mathbf{u}_{nij}}{dt} \tag{3}$$

where N is the number of nodes for element face, \mathbf{F}_{ij} and \mathbf{w}_{nij} are weight coefficients for calculating face velocity depending on the face geometry.

The displacements and velocities that are being imported into ABAQUS/CFD from ABAQUS/Standard or ABAQUS/Explicit serve as the necessary boundary conditions at the FSI interface [2].

2.3 Numerical Scheme

Co-simulation controls are used to control the time increment process and the frequency of exchange between the two ABAQUS analyses. These controls are specified automatically in ABAQUS/CAE. The coupling step size is the period between two consecutive co-simulation data exchanges. To determine the coupling step size, each analysis suggests a coupling step size, which is the next increment suggested by its automatic increment scheme. ABAQUS/CFD always uses a time increment size that is the same as the coupling step size (no sub-cycling), while ABAQUS/Standard and ABAQUS/Explicit are allowed to sub-cycle.

2.3.1 Coupling Scheme

FSI analysis attributes are Gauss–Seidel (serial) coupling scheme. One solver waits while the other solver proceeds. ABAQUS/Standard or Explicit leads the simulation and ABAQUS/CFD lags. Coupling step size is determined automatically (Fig. 3). There are two methods to determine the coupling step size:

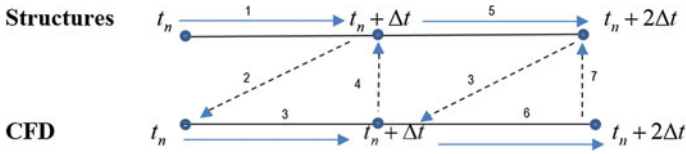


Fig. 3 Gauss–Seidel (serial) coupling scheme

Min/Max

- Minimum coupling step size is based on the suggested coupling step size of structural and CFD models

Import/Export

- Structural model imports the time step size from CFD model

Apply semi-implicit projection method

$$\text{Momentum solve (2): } \rho \frac{\bar{\mathbf{V}}^{n+1} - \mathbf{V}^n}{\Delta t} + \rho \frac{\mathbf{V}^{n+1} - \bar{\mathbf{V}}^{n+1}}{\Delta t} + \nabla P^{n+1} = \mathbf{f} \quad (4)$$

$$\Delta \bar{\mathbf{V}}^{n+1} \neq 0$$

$$\text{Pressure Solve } \rho \frac{\mathbf{V}^{n+1} - \bar{\mathbf{V}}^{n+1}}{\Delta t} = -\nabla P^{n+1} - P^n \quad (5)$$

$$\nabla^2 P^{n+1} - P^n = \frac{\rho}{\Delta t} \nabla \cdot \bar{\mathbf{V}}^{n+1}$$

$$\text{Obtain velocity } \mathbf{V}^{n+1} = \bar{\mathbf{V}}^{n+1} - \frac{\Delta t}{\rho} \nabla P^{n+1} - P^n \quad (6)$$

These equations ignore pressure gradient at time $n + 1$. The intermediate velocity $\bar{\mathbf{V}}^{n+1}$ is not divergence free, and \mathbf{f} is a function of velocity and $\Delta \mathbf{V}^{n+1} = 0$ [5].

$$\text{ABAQUS/Standard solves(1): } \frac{d^2 \mathbf{u}}{dt^2} \Big| ^n = \mathbf{M}^{-1}(\mathbf{P} - \mathbf{I}) \Big| ^n \quad (7)$$

$$\frac{d\mathbf{u}}{dt} \Big| ^{n+1/2} = \frac{d\mathbf{u}}{dt} \Big| ^{n-1/2} + \frac{(\Delta t^{n+1} + \Delta t^n)}{2} \frac{d^2 \mathbf{u}}{dt^2} \Big| ^n \quad (8)$$

$$\mathbf{u}^{n+1} = \mathbf{u}^{n-1} + \Delta t^{n+1} \left. \frac{d\mathbf{u}}{dt} \right|^{n+1/2} \tag{9}$$

ABAQUS/CFD solves the numerical solution for system (4–6), and ABAQUS/Standard or ABAQUS/explicit solves the system (7–9).

3 SetUp Model in Abaqus

3.1 Setting Up FSI Analyses in ABAQUS

For solving every FSI problem in ABAQUS, the following tasks will be performed (Fig. 4).

This method is especially about boundary conditions, and the names of the interaction of the structure model and the fluid model have to be identical between. In addition, the surfaces of both models must be matched. The sets of data exchange with each other in the same step and the same increment time. The first step ABAQUS/CFD solves fluid domain, and then the sets of data are imported through interaction surfaces by Eq. (3), and ABAQUS/standard or ABAQUS/explicit solves the structure domain.

As a simple example, an FSI analysis of seawater impact on RS feature is carried out by employing co-simulation. Two models are created: one for fluid domain and the other for structure domain. In this example, fluid is seawater, so the density is

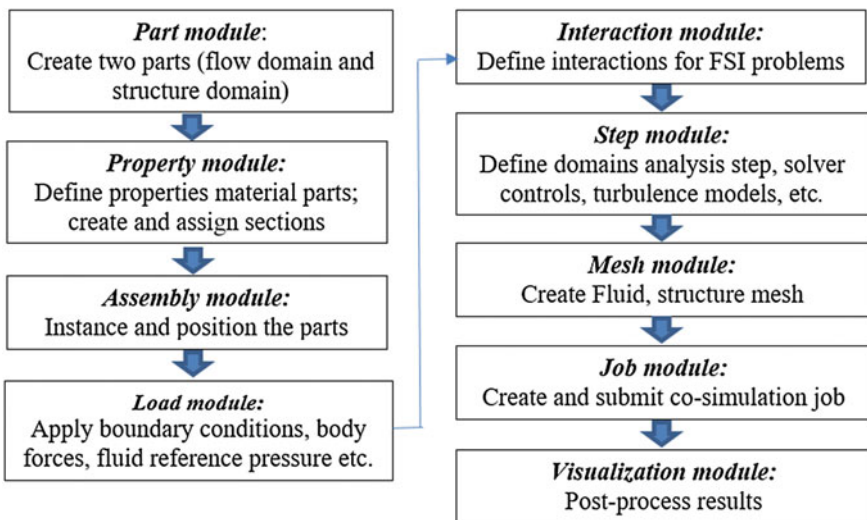


Fig. 4 Setup steps for an FSI problem in ABAQUS

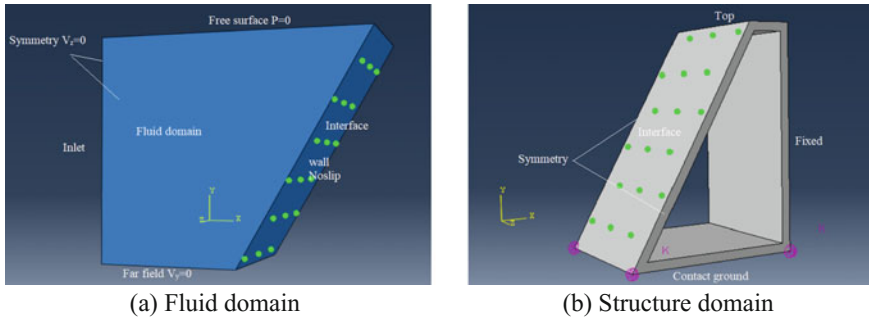


Fig. 5 Models are created in ABAQUS and boundary conditions

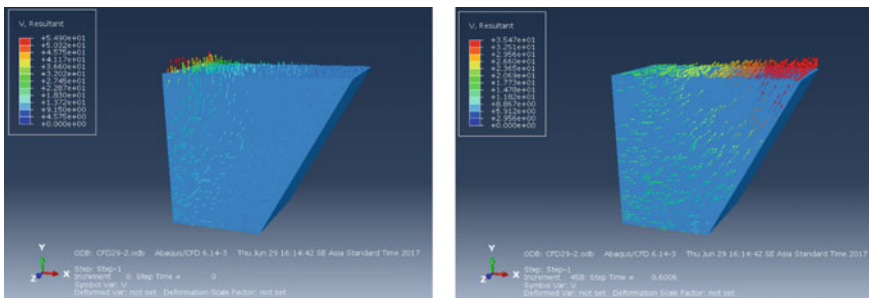


Fig. 6 Velocity field in fluid domain

1020 kg/m³ and viscosity is 0.001 Pa s [8]. Material of the structure domain is concrete, with a density of 2500 kg/m³, a modulus of elasticity $E = 2.5 \times 10^{10}$ N/m² and Poisson’s ratio $\nu = 0.2$. Boundary conditions of fluid domain are showed in Fig. 5, velocity inlet $V = 20.83$ m/s corresponding to hurricane 9 level. The problem was solved using ABAQUS/explicit solver for structure domain. A turbulent flow is applied with the standard $k - \epsilon$ model. Partially contact to the ground is defined by a spring with linear stiffness $k = 1$ N/m. The nodes at the interface between the two models match.

4 Numerical Results

Velocity and pressure fields are obtained as shown in Figs. 6 and 7 when ABAQUS/CFD solves fluid domain. Max velocity is 54.9 m/s, and max pressure is 6.379×10^5 Pa. At this stage of the research, we have not yet analyzed and validated the results. This will be done in the next stage of the project and is considered as future work of the current paper.

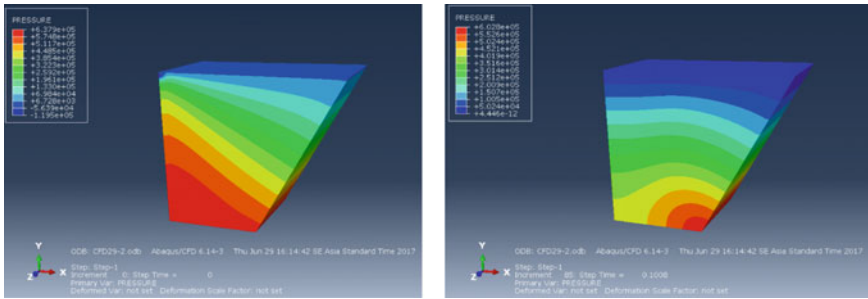


Fig. 7 Pressure contours in fluid domain

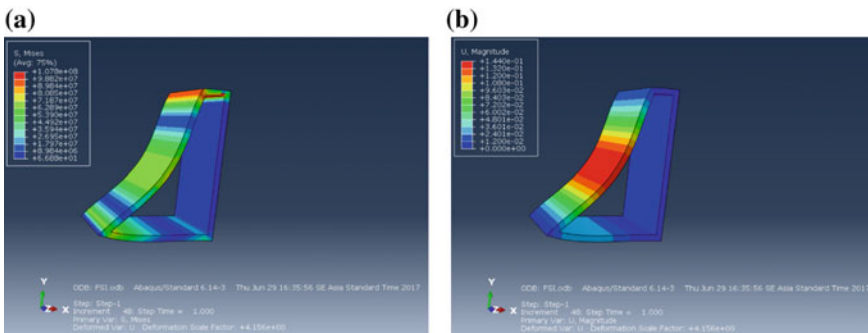


Fig. 8 a Von-Mises' stress distribution, b displacements

The results of the stress and displacement of structure concrete are shown in Fig. 8 when exposed to storm waves of level 9.

The results show that the behavior of structure RS thin-walled has quite small displacements with the largest displacement of 0.144 m with max stress magnitude 1.078×10^8 Pa. The obtained results need to be compared with experiment.

5 Conclusion

An overview of the computational aspect of FSI problems was presented in this article. Such problems require researchers with high education and modeling skills. Moreover, many factors of the simulation process need to be investigated carefully to ensure the accuracy. The paper has presented the co-simulation method to predict behavior of RS thin-walled structure under impact of flow. Using ABAQUS/CFD and ABAQUS/standard in ABAQUS software, fluid–structure interaction is simulated. The behavior of a simple RS structure is considered. Next, this method is

applied to simulate a complex RS structure. Further analysis and validation of the interlocking blocks are also required and will be done as future work.

Acknowledgements The authors gratefully acknowledge the financial support of VLIR-OUS TEAM Project, VLIRUOS2017-2021-75900, funded by the Flemish Government.



 The supports of the Busadco company (Ba Ria Vung Tau Urban Sewerage and Development One Member Limited Company) for practical data are highly appreciated.

References

1. Chakrabarti SK (2005) Numerical models in fluid structure interaction. In: Advances in fluid mechanics, vol 42. WIT Press
2. Aksenov A, Dyadkin A, Luniewski T, Pokhilko V (2004) Fluid structure interaction analysis using ABAQUS and FlowVision. In: ABAQUS users' conference
3. Prasad S, Lu YY, Harwood S, Mukundakrishnan K, Rocha MS (2011) Co-simulation and multiphysics technologies for coupled fluid-structure interaction problems
4. ABAQUS version 6.14 Analysis User's Manual (2011) Dassault Systemes Simulia Corp
5. Introduction to ABAQUS/CFD (2010)
6. Degroote J, Bruggeman P, Haelterman R, Vierendeels J (2008) Stability of a coupling technique for partitioned solvers in FSI applications. Comput Struct 86:2224–2234
7. Idelsohn SR, Marti J, Limache A, Onate E (2008) Unified Lagrangian formulation for elastic solids and incompressible fluids: application to fluid-structure interaction problems via the PFEM. Comput Methods Appl Mech Eng 197:1762–1776
8. <https://vi.wikipedia.org/wiki>

Influence of Swelling Pressure on Pore Water in Embankment Core with Swelling Clay Soil



Tuong Nguyen Ke, Hung Nguyen Pham Khanh, Hung Nguyen Minh, Hung Nguyen Viet and Thi Nguyen Minh

Abstract Swelling clay soil used to fill at core of and used to waterproof for soil dam will swell and increase volume when soaked. This expansion status created the expansion pressure inside dam, increased volume of dam, and harmed the construction. It needs a cover soil to balance and keep the volume of core from expansion due to swell, make soil swelled in cover pressure condition, unchange soil volume, and reduce pore inside soil and permeability coefficient. Swelling pressure reduced pore water pressure and saturated water curve. When swelling finished, permeability coefficient reduced and saturated water curve inside dam raised up, it made pressure to the stability of dam. Changes in swelling pressure depended on type of soil, soil conditions, and density of soil. When swelling finished, friction angle and stickiness of soil increased and the stability of construction did not decrease. Recommendation applies result of this research to constructing earth dam and construction over swelling clay.

Keywords Swelling clay soil · Pore water pressure · Swelling pressure Earth dam

T. N. Ke (✉)

Faculty of Civil Engineering, Ton Duc Thang University,
Ho Chi Minh City, Vietnam
e-mail: nguyenketuong@tdt.edu.vn

H. N. P. Khanh

Van Thanh Hung Ltd, Co, Ho Chi Minh City, Vietnam
e-mail: khanhhung1310@gmail.com

H. N. Minh · H. N. Viet · T. N. Minh

Faculty of Civil Engineering, Thu Dau Mot University,
Binh Duong Province, Vietnam
e-mail: hungnm@tdmu.edu.vn

H. N. Viet

e-mail: hungnv@tdmu.edu.vn

T. N. Minh

e-mail: thinm@tdmu.edu.vn

© Springer Nature Singapore Pte Ltd. 2018

H. Nguyen-Xuan et al. (eds.), *Proceedings of the International Conference on Advances in Computational Mechanics 2017*, Lecture Notes in Mechanical Engineering, https://doi.org/10.1007/978-981-10-7149-2_65

1 Introduction

Pore water pressure in soil will be changed when impact pressure changed. Soaked swelling soil used for core of earth dam or ground will swell, and if it was pressed and obstructed the swelling by cover layer, soil pore would be decreased. And pore water pressure would be changed when swelling pressure inside soil appeared as a force reducing volume of pore. When pore reduced, permeability coefficient also reduced and pore water pressure increased, while permeability pressure caused by water in lake did not change. Saturated water curve increased inside construction effected to the stability of construction. Some earth dam worked many years damaged caused of excluding this incident.

Other authors have also studied swollen soil in the world, such as [2–18]:

- Amer Ali Al-Rawas & Matheus F.A. Goosen (2006) study of expansive soil properties [2];
- B. Xu, Z.-Z. Yin, and S.-L. Liu, “Experimental study of factors influencing expansive soil strength” [3];
- The Effect of Interlayer cations on the Expansion of the Mica [4];
- J.-P. Yuan, Z.-Z. Yin, and C.-G. Bao, “Quantitative description method & index for fissures in expansive soils [10];
- J.-J. Zhang, B.-W. Gong, B. Hu, X.-W. Zhou, and J. Wang. “Study of evolution law of fissures of expansive clay under wetting and drying cycles” [11];
- S.-H. Zheng, J.-L. Jin, H.-L. Yao, X.-R. Ge, “Analysis of initial cracking behavior of expansive soil due to evaporation” [13];
- H.-B. Lü, Z.-T. Zeng, Y.-L. Zhao, and H. Lu, “Experimental studies of strength of expansive soil in drying and wetting cycle” [14].

The authors study the issue that the authors previously did not mention, as follows: “Influence of swelling pressure on pore water pressure in embankment core with swelling clay soil”. This paper presents the principle of changing pore water pressure by time when swelling pressure appeared in the swelling clay. This paper analyzed effecting of swelling inside ground and dam to pore water pressure and stability of construction.

2 Study Content

1. Theoretical basis

Stress inside earth dam, and effected stress and effected pore water pressure in saturated soil are related as follows [1, 2, 4, 6, 7, 8, 9, 15, 16]:

$$\sigma = \sigma' + u \quad (1)$$

where

- σ : acted stress;
- σ' : effected stress, transferred thought interface soil particles;
- u : pore water pressure, transferred to water in pore.

From formula (1) and swelling process [2, 5, 6, 8, 13]:

$$\begin{cases} u = \sigma - \sigma' \\ u = (\sigma - \sigma')^N + P^N \end{cases} \tag{2}$$

With swelling clay soil, during absorbed clay swelled volume due to soil structure, swelling pressure P^N reduced effecting of effected stress (σ'), formula (2) may be wrote [2–18]:

$$\begin{cases} u = (\sigma - \sigma')^N + P^N \\ u = u^N + P^N \end{cases} \tag{3}$$

At a moment, effected stress (σ') unchanged, according to formula (3) [2–18], we found that increasing swelling pressure P^N made pore water pressure (u) reduced.

Swelling pressure $P^N \rightarrow 0$ [2, 5, 6, 8, 13] when swelling process finished; $\rightarrow u = u^N$, pore water pressure (u) will change as in non-swelling soil [4].

According to testing result and calculating swelling pressure in Table 6, theoretical basic of formula (2), (3) consisted with testing result in Table 6.

2. Selected swelling soil to study

This research used strongly swelling clay soil to study the change in pore water pressure due to swelling pressure with outside pressure.

The authors used swelling clay soils which are used to make some dam in South Center of Vietnam. Testing to determine swelling property, selecting strongly swelling soil to study changing of pore water pressure due to changing of swelling pressure (Table 1).

Table 1 Physical properties of soil for testing [1, 3, 10, 11, 17]

	Grading (%)				Plastic limit (%)			Gravity Δ	Proctor compacting	
	Grit	Sand	Dust	Clay	W_L	W_P	I_P		$\gamma_{emax}, T/m^3$	$W_{op} (%)$
Thuan Ninh	10.5	57	14	18.5	48.89	22.19	26.7	2.61	1.75	19
Thuan Ninh core	8.98	58.2	18.37	17.2	30.26	17.17	13.08	2.62	1.88	13
Am Chua	14.3	36.9	16.5	32.2	38.9	21.07	17.83	2.64	1.68	18
Suoi Dau	8.7	40.3	21.8	34.7	58.32	32.66	25.66	2.62	1.57	24
Cam Tan	9.3	37.7	25.4	33.5	59.13	32.84	26.28	2.63	1.67	22
Vinh Son	0	18.41	24.52	57.1	48.9	33.92	14.98	2.90	1.72	19.5

Table 2 Physical properties of testing samples [1, 3, 10, 11, 17]

Testing samples soil	Saturation testing G (%)	Specific gravity of the experimental soil γ_{cb} , T/m ³
Thuan Ninh	100	1.66
Thuan Ninh core	100	1.79
Am Chua	100	1.60
Suoi Dau	100	1.49
Cam Tan	100	1.59
Vinh Son	100	1.63

Table 3 Value of swelling testing R^N of above soils by time T (h) [1, 3, 10, 11, 17]

Testing time	Thuan Ninh dam soil mine	Thuan Ninh dam core	Am Chua dam soil mine	Suoi Dau dam soil mine	Cam Tan dam soil mine	Vinh Son dam soil mine
T (h)	R^N (%)	R^N (%)	R^N (%)	R^N (%)	R^N (%)	R^N (%)
0	0	0	0	0	0	0
0.02	0.22	0.3	0.26	0.1	0.12	0
0.04	0.3	0.5	0.34	0.2	0.22	0
0.06	0.9	1.1	1.02	0.3	0.4	0
0.08	1.6	1.8	1.71	0.3	0.7	0
0.1	3.4	3.8	3.47	0.3	1.2	0
0.15	6	7.1	6.89	0.3	2.1	0
0.3	8	9.2	8.9	0.3	2.5	0
0.5	10	11.5	10.9	0.3	2.5	0
1	10.9	12.3	11.2	0.3	2.5	0
2	11.4	12.8	11.9	0.3	2.5	0
4	11.8	13.4	12.5	0.3	2.5	0
8	12	13.9	12.9	0.3	2.5	0

Swelling testing did with samples $\gamma_c = 0, 95\gamma_{cmax}$ and humidity $W_{cb} = W_{op}$ at left side of Proctor compacting curve followed each soil (Tables 2 and 3).

According to testing result shown in Table 3 and Fig. 1 and classification standard CHII 2-05-08-85, the authors selected strongly swelling soils to study changing of swelling pressure affected to pore water pressure.

Selected soils were:

- Soil mine used to make Thuan Ninh Lake, Binh Dinh;
- Soil mine used to make Am Chua Lake, Nha Trang, Khanh Hoa;
- Soil form core of Thuan Ninh Lake’s dam, Binh Dinh.

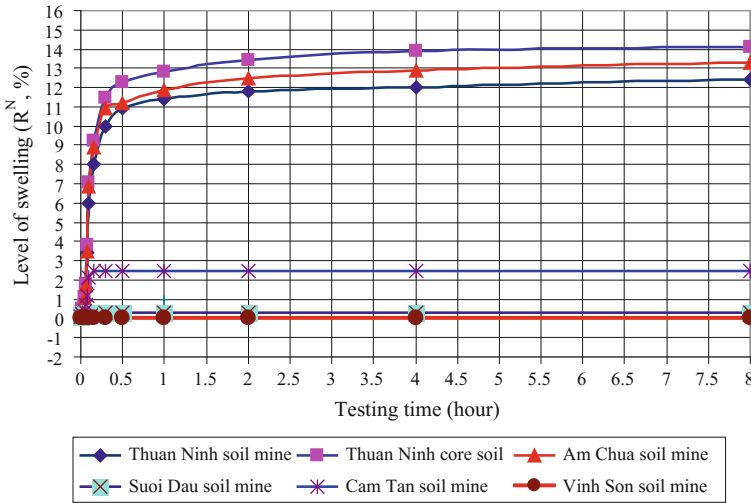


Fig. 1 Level of free swelling (R^N) by the time of studying soils (soil samples prepared with compacting $K = 0.95$) [1, 3, 10, 11, 17]

3. Studying effecting of swelling pressure (P^N) to pore water pressure (u) in pressed condition

3a. Testing condition

According to free swelling testing of samples presented at Fig. 1 showed that: soil samples soaked after time less than (4–8) h, reached nearly maximum of swelling level R^N , then swelling negligible. Testing carried out is given in the following cases with each soil:

Case 1 [1–18]:

The testing sample covered with rubber film is assembled in the pressure chamber of the triaxial compressor. Pressure chamber was filled by water. The backpressure method is used to make soil completely saturate, while soil absorbing and swelling measure pore water pressure by time (t) under different pressure levels $\sigma_3 = 100, 200, 300$ and 400 kPa and time less than 4 h, and the testing is finished.

Case 2 [1–18]:

Soil sample assembled as case 1, but after saturated by backpressure method and absorbed, swelled by time more than 4 h, when sample finished swelling measured pore water pressure in sample by time under different pressure levels $\sigma_3 = 100, 200, 300$ and 400 kPa.

3b. Testing result

Soil mine used to make Thuan Ninh Lake, Binh Dinh.

Reviewed:

Result in Table 4 and Figs. 2, 3, 4, and 5 showed that pore water pressure was affected by swelling pressure.

Table 4 Value of pore water pressure u under each pressure level according to time of soaking and swelling [1–18]

Compacting test time with compress level of pressure chamber (s)	Soaking time less than 4 h; swelling and compress level of pressure chamber				Soaking time more than 4 h; swelling and compress level of pressure chamber			
	100 kPa	200 kPa	300 kPa	400 kPa	100 kPa	200 kPa	300 kPa	400 kPa
0	-4	-2	0	0	-4	0	0	0
1	12	15	22	45	12	34	64	83
2	13	16	25	65	23	43	86	125
4	15	17	37	89	30	65	116	145
6	15	22	44	124	41	89	130	176
8	15	23	45	157	46	92	141	212
10	16	24	46	187	51	94	167	254
15	17	25	53	192	65	95	177	276
30	18	26	66	212	82	96	183	295
60	19	27	77	218	89	130	205	344
120	20	27	90	228	92	150	245	365
180	20	29	99	235	94	167	266	378
240	21	33	108	240	95	177	275	382
300	21	34	117	243	96	183	280	387
360	21	37	123	245	96	185	291	388
420	22	39	129	247	96	190	293	393
480	22	40	132	248	96	194	294	394
600	22	40	136	250	96	194	294	394
900	22	41	141	251	96	194	295	394
1200	22	41	148	253	96	194	295	394

When clay soil started soak, swelling pressure started swell and swelling pressure reduced pore water pressure, Fig. 4; pore water pressure’s value was small at swelling phase.

When clay soil saturated, swelling pressure stopped and go to 0; pore water pressure increased as shown in Fig. 4. Pore water pressure’s value was strong when swelling finished.

Soil mine used to make Vinh Son Lake, Binh Dinh [1–18].

It was Bazan soil, non-swelling soil, tested to determine pore water pressure under pressure levels to compare with swelling soil: $P^N + u^N = u; u^N = (\sigma - \sigma') - P^N \rightarrow (u^N + P^N) = u = (\sigma - \sigma')$ (Fig. 6; Table 5)

Reviewed:

Bazan was non-swelling soil, pore water pressure was not affected, and pore water pressure followed formula $P^N + u^N = u; u^N = (\sigma - \sigma') - P^N \rightarrow (u^N + P^N) = u = (\sigma - \sigma')$

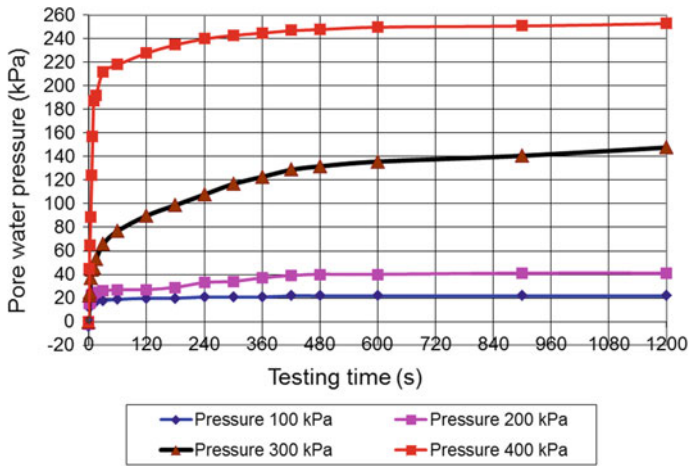


Fig. 2 Pore water pressure (u) by time of soil mine made Thuan Ninh Lake, Binh Dinh; samples prepared with compacting coefficient $K = 0.95$; specific gravity of the experimental soil $\gamma_c = 1,66T/m^3$; humidity $w = 12\%$ with saturation and swelling time t less than 4 h. Soil started swell with outside pressure corresponded to the chamber pressure levels $\sigma_3 = 100, 200, 300$ and 400 kPa [1–18]

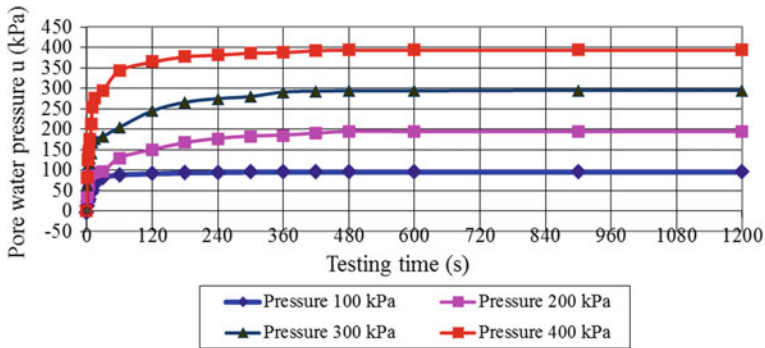


Fig. 3 Pore water pressure (u) by the time of soil mine made Thuan Ninh Lake, Binh Dinh; samples prepared with compacting coefficient $K = 0.95$; specific gravity of the experimental soil $\gamma_c = 1.66T/m^3$; humidity $w = 12\%$ with saturation and swelling time t more than 4 h. Soil started swell with outside pressure corresponded to the chamber pressure levels $\sigma_3 = 100, 200, 300$ and 400 kPa [1–18]

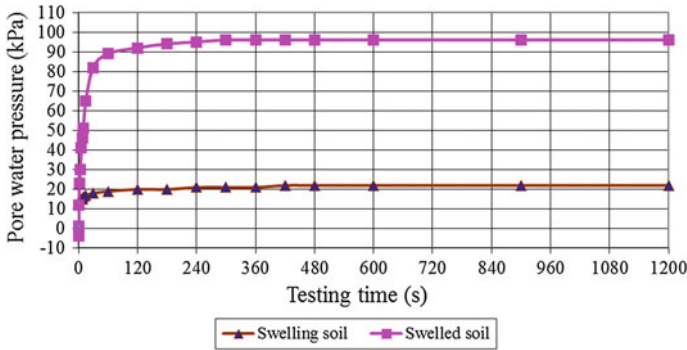
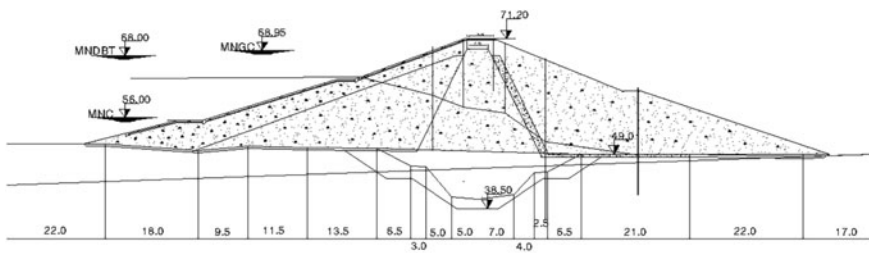
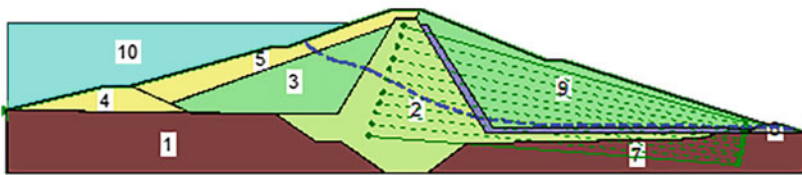


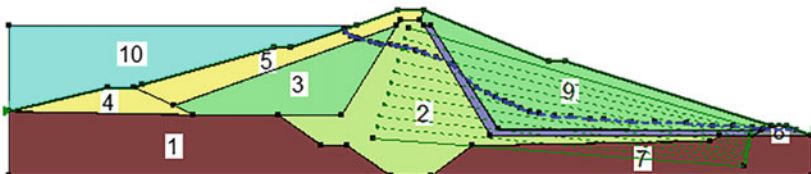
Fig. 4 Pore water pressure (u) by time of soil mine made Thuan Ninh Lake, Binh Dinh; samples prepared with compacting coefficient $K = 0.95$; specific gravity of the experimental soil $\gamma_C = 1.66T/m^3$; humidity $w = 12\%$ with saturation and swelling time t less than 4 h and more than 4 h. Soil started swell with outside pressure corresponded to the chamber pressure levels $\sigma_3 = 100\text{ kPa}$ [1–18]



a, Cross section of Thuan Ninh dam's body



b, Low saturated water curve cause of started accumulating water, swelling phase



c, Stability saturated water curve cause of accumulated water many years, finished swelling phase

Fig. 5 Cross section showed saturated water curve inside Thuan Ninh dam's body according to reality monitory data to calculate slope stability [1–18]

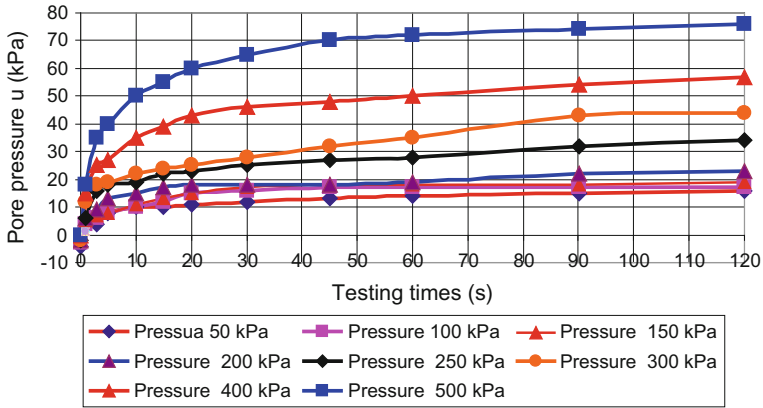


Fig. 6 Pore water pressure (u) by time of soil mine made Vinh Son lake, Binh Dinh; samples prepared with compacting coefficient $K = 0.95$; specific gravity of the experimental soil $\gamma_c = 1.66T/m^3$; humidity $w = 12\%$ with saturation, Bazan, non-swelling soil

Table 5 Pore water pressure under pressure levels of Bazan soil, Vinh Son soil mine [1–18]

Testing time (s)	Chamber pressure (kPa)							
	50	100	150	200	250	300	400	500
	Pore water pressure value (u)							
0	-4	-3	-2	-2	-2	-2	0	0
1	3	4	5	6	6	12	15	18
3	4	6	7	9	16	18	25	35
5	8	8	8	13	18	19	27	40
10	10	10	11	15	19	22	35	50
15	10	12	13	17	22	24	39	55
20	11	15	15	18	23	25	43	60
30	12	16	17	18	25	28	46	65
45	13	17	18	18	27	32	48	70
60	14	17	18	19	28	35	50	72
90	15	17	18	22	32	43	54	74
120	16	17	19	23	34	44	57	76

Table 6 Analyzing result swelling pressure effected to pore water pressure of swelling clay soil and non-swelling Bazan

Testing soil	Specific gravity of the experimental soil (T/m^3)	Compressing pressure levels 3 (kPa)	Saturation time < 4 h, swelling			Saturation time > 4 h, end expands		
			Pore water pressure u (kPa)		Swelling pressure (kPa)	Pore water pressure u (kPa)		Swelling pressure (kPa)
			Min	Max		Min	Max	
(1)	(2)	(3)	(4)	(5)	(6)	(7)	(8)	(9)
Thuan Ninh soil mine	1.66	100	-4	22	78	-4	96	4
		200	-2	41	159	0	194	6
		300	0	148	152	0	295	5
		400	0	283	117	0	394	6
Vinh Son soil mine	1.63	100	-4			17		
		200	-4			23		
		300	-2			44		
		400	0			57		

3 Conclusion

With swelling clay soil, swelling under cover pressure [1–18] :

1. During swelling phase, swelling pressure (P^N) reduced pore water pressure (u);
2. Finished swelling, swelling pressure $P^N \rightarrow 0$, pore water pressure increased, changed as non-swelling soil;
3. Testing’s result is compared with theoretical basis;
4. This research served for construction on swelling clay soil, the solution reduced damage cause by swelling soil made soil saturate and swell with pressure when constructed. Swelling pressure was determined by testing to choose the appropriate pressure.

References

1. ASTM (1951) Triaxial testing of soils and bituminous mixtures, ASTM, Philadelphia
2. Rawas Amer Ali Al-, Goosen Matheus FA (2006) Expansive Soils. Taylor & Francis Group, UK
3. Xu B, Yin Z-Z, Liu S-L (2001) Experimental study of factors influencing expansive soil strength. Rock Soil Mech 32(1):44–50
4. Barshadj The effect of interlayer cations on the expansion of the mica

5. Bei-xiao S, Sheng-shui C, Hua-qiang H, Cheng-feng Z (2014) Expansive soil crack depth under cumulative damage. Hindawi Publishing Corporation The Science World Journal, vol. 2014, 498437, 9 papers; <http://dx.doi.org/10.1155/2014/498437>
6. Bishop, Alan W. The measurement of soil properties in the triaxial test
7. Braja M Das (2000) Fundamentals of geotechnical engineering
8. David Muir W (1994) Soil behavior and critical states soil mechanics
9. Fredlund DG, Rahardjo H (2000) Soils mechanics for unsaturated soils
10. Yuan J-P, Yin Z-Z, Bao C-G (2003) Quantitative description method & index for fissures in expansive soils. J Yangtze River Sci Res Inst 20(6):27-30
11. Zhang J-J, Gong B-W, Hu B, Zhou X-W, Wang J (2011) Study of evolution law of fissures of expansive clay under wetting and drying cycles. Rock Soil Mech 32, 2729-2734
12. John A (1994) The Mechanics of soil and foundations
13. Zheng S-H, Jin J-L, Yao H-L, Ge X-R (2006) Analysis of initial cracking behavior of expansive soil due to evaporation. Rock Soil Mech 27(12): 2229-2233
14. Li H-B, Zeng Z-T, Zhao Y-L, Lu H (2009) Experimental studies of strength of expansive soil in drying and wetting cycle. Rock Soil Mech 30(12):3797-3802
15. Karl T, Ralph BP (1970) Soil mechanics in engineering practice, tenth printing
16. Muni B (2007) Soil mechanics and foundations, second edition
17. Norrish K The swelling of Montmorillonite, Discussion Faraday
18. Ralph EG (1968) Clay mineralogy McGraw-Hill, Inc

Part VIII
Catastrophic Destruction Mechanics
and Numerical Modelling

Concrete Mesoscopic Model and Numerical Simulation Based on Quadtree Mesh Refinement Technology



Guojian Shao and Shengyong Ding

Abstract In the concrete mesoscopic model established by using the traditional background mesh method, a mesh refinement technology based on balanced quadtree is proposed to refine the elements of interfacial transition zone (ITZ). Considering the control standards of the minimum size requirement and the balancing condition, the implementation program of mesh refinement is studied. The polygonal FEM is applied to ensure the consistency of the mesh after quadtree refinement. Then, the modified concrete mesoscopic model is given, which is more reasonable for reflecting the constitutive behavior of ITZ. In the proposed concrete mesoscopic model, the correlative material parameters can directly assign to the elements of ITZ. The sawtooth defect of meshes around the aggregates in the background mesh method is also enhanced to a certain degree. Accordingly, the geometrical morphology and material property of ITZ are simulated better and more realistic. In the end, the numerical simulation is presented to preliminarily compare the differences between the background mesh method and the proposed method.

Keywords Concrete • Mesoscopic model • Quadtree structure
Mesh refinement • Numerical simulation

1 Introduction

At the mesoscopic level, concrete is usually regarded as the three-phase composite composed of aggregate, mortar matrix, and interfacial transition zone (ITZ). In previous studies, the background mesh method [1] is a common method for the finite

G. Shao (✉) · S. Ding
College of Mechanics and Materials, Hohai University, Nanjing, China
e-mail: gjshao@hhu.edu.cn

S. Ding
e-mail: dingshengyong6@163.com

S. Ding
China Design Group Co., Ltd., Nanjing, China

© Springer Nature Singapore Pte Ltd. 2018
H. Nguyen-Xuan et al. (eds.), *Proceedings of the International Conference on Advances in Computational Mechanics 2017*, Lecture Notes in Mechanical Engineering, https://doi.org/10.1007/978-981-10-7149-2_66

element discretization of concrete mesoscopic model. In this method, a uniform square mesh as the background mesh is pre-generated, and then the aggregates are randomly placed inside the region of background mesh. The material types of elements in background mesh can be identified by the relationship between aggregate and element: aggregate element located inside the aggregate, mortar element located outside the aggregate, and ITZ element partly located inside the aggregate.

Many studies [2, 3] reveal that the cracks of concrete first appear in the ITZ along the boundary of aggregate, and thus the macro-performance of concrete depends largely on the geometric and physical properties of the ITZ. Thus, how to reasonably reflect the ITZ as the weak part is the important aspect in the mesoscopic simulating of concrete. Because the element size is single in the background mesh method, if the coarse meshes are chosen, the selected elements of ITZ are too large compared with its actual thickness (20–100 μm). The increased percentage of ITZ weakens the whole mechanical property of concrete. Conversely, the reasonable proportion of ITZ can be obtained by using the refined meshes, but the huge scale of mesh has caused a sharp increase in computing time. At present, there are several methods to treat the above-mentioned problem. One potential solution [3] is to appropriately improve the elasticity modulus and material strength of ITZ, but the improved ratio is not stable between the element sizes. In the second method [4, 5], the elements of ITZ are considered as the composite element composed of aggregate, mortar, and ITZ. Using the Voigt-Reuss averaging scheme, the influence of ITZ is smeared into the composite element. The difficulty of this method is to determine the percentages of various materials in the composite element. The third method [2] employs the interface element with no thickness to simulate the ITZ. Because the crack path grows along the edge of element, this method has the mesh dependence problem.

In this paper, the alternative mesoscopic model of concrete with lower computing cost is developed for reflecting the percentage and material property of ITZ accurately. Based on the background mesh method, the coarse elements of ITZ are refined to decrease the size of elements by using the quadtree refinement technology, which is more suited to the refinement of uniform square mesh. The rest of this paper is organized as follows: A brief review about quadtree mesh is described in Sect. 2. In Sect. 3, the quadtree refinement strategy for the background mesh is proposed by adhering to the minimum size requirement and the balancing condition. In Sect. 4, a brief overview of the polygonal FEM is given. In Sect. 5, the study to compare the concrete mesoscopic models with uniform mesh and quadtree refined mesh is performed. Our concluding remarks are given in Sect. 6.

2 Quadtree Data Structure

Quadtree is a kind of hierarchical data structure, and it is often used in computer graphics and digital image processing. The origin, application, and related algorithms of quadtree structure are described in detail in [6]. The work of Yerry and

Shephard [7] shows the first use of quadtree in finite element mesh generation. Subsequently, the mesh generation methods coupling quadtree for h-adaptivity has been actively used and proved to be a simple, fast, and efficient method [8–11].

The establishment of quadtree is a process of recursive decomposition, and this process can be described as that the target geometry is first placed inside a square element. This square element is then subdivided into four new homogeneous square sub-elements. Next, each new sub-element is tested to confirm that if it reaches the stopping criterion such as errors or sizes of elements, and the sub-elements unreached the stopping criterion are subdivided into four new square sub-elements again. The process continues until meeting the stopping criterion in all sub-elements, and the target geometry is covered by the varied dimensions of non-overlapping square sub-elements.

Some terminology is introduced for the quadtree structure as shown in Fig. 1. The original square element A is called the root element of quadtree. Four children elements B_1, B_2, B_3, B_4 are created, all of which have the same element A as their father element. An element is called the leaf element if this element is not to be decomposed, e.g., the leaf elements B_1, B_3, B_4 . In addition, some extra lists are built up once by performing a search over the base structure. Two elements are neighbors if they share the same edge, e.g., the elements B_1 and C_1 as shown in Fig. 1b. The level of an element is the number of subdivisions from the root element. Finally, the elements, the basic parts of quadtree structure, are characterized by network and layer and can easily communicate with each other through pointers.

The direct application of quadtree for the finite element mesh generation may occur inappropriately; e.g., some elements may undergo more subdivision than its neighbors. The balanced quadtree [6, 12] is employed to improve the defect of the standard quadtree. In the balanced quadtree, the variation gradient of size between adjacent elements has been controlled by adding the balancing condition, which allows that only a one-level difference exists between any neighboring elements. This method is easy to ensure the size of element with uniform change and obtain the guaranteed-quality transition elements in quadtree mesh.

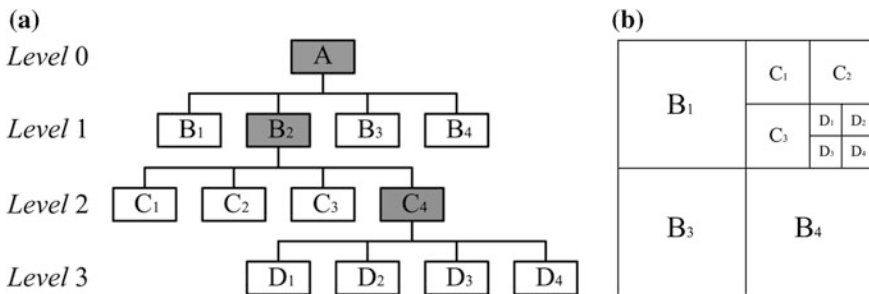


Fig. 1 Quadtree data structure: a tree structure, b Quadtree mesh

3 Modified Concrete Mesoscopic Model with Quadtree Refinement

In the present study, the quadtree refinement is adopted for modifying concrete mesoscopic model. The performance of quadtree refinement adopted in this study is driven by the minimum size requirement and the balancing condition.

3.1 The Control Criterion of Quadtree Refinement

(1) The minimum size requirement

Take the composite with the single circular inclusion, for example, as shown in Fig. 2, the whole material domain Ω is divided into two parts of Ω^+ and Ω^- by the interface Γ . We define the following function

$$\phi(x) = \|x - x_c\| - r_c \tag{1}$$

where \mathbf{x} is the coordinates of node, \mathbf{x}_c is the coordinates of center of circular inclusion, and r_c is the radius of circular inclusion. The sign of Eq. (1) is positive/negative if the node (\mathbf{x}) is outside/inside of the circular inclusion.

Beginning with the uniform square mesh, all nodes are classified into interior nodes and exterior nodes by the *IN/OUT* test of Eq. (1). For an element including *NP* nodes, it regards *NIN* as the number of the interior nodes and *NOU* as the number of the exterior nodes. Table 1 synthesizes the statistical information of nodes about the different element patterns as shown in Fig. 3. In Table 1, d_i denotes the size of the element and can be computed by

$$d_i = (1/2)^i d_0 \tag{2}$$

where i is the level of the current element, and d_0 is the size of its root element. The array *Epre* allows the user to control the minimum size of element in various material regions. The quadtree refinement is performed if the size of element does not reach the minimum size requirement. When the refinement process is

Fig. 2 Domain with discontinuous circular interfaces

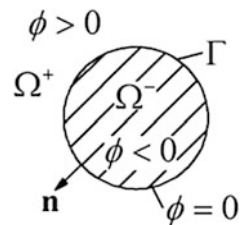


Table 1 Determination of element patterns and its decomposition condition

Element patterns	Material property	NIN	NOU _T	Decomposition condition
Type 1	Aggregate	NP	0	$d_i > Epre(1)$
Type 2	ITZ	a	b	$d_i > Epre(2)$
Type 3	Mortar	0	NP	$d_i > Epre(3)$

Note: $a + b = NP, NP \geq 4$

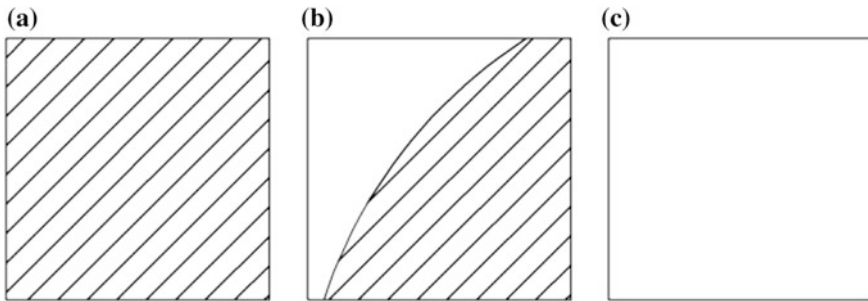
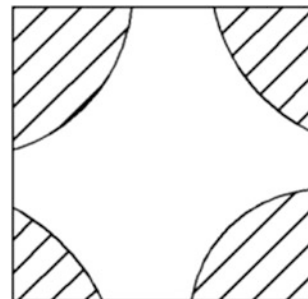


Fig. 3 Element patterns in the single inclusion problem: **a** Type 1, **b** Type 2, **c** Type 3

completed, the elements of Type 1–3 correspond to the inclusion, the ITZ, and the mortar, respectively.

To the composite with the multiple circular inclusions, the element patterns are more complicated than the element patterns with single inclusion. Programs will return wrong results if it continues to use the standard of Table 1 directly. For example, the pattern in Fig. 4, as the element of Type 2, holds the same values of NIN and NOU_T as the element of Type 1. Here the solution is to save the element type only with the patterns with single inclusion and set the priorities of element types: first Type 1, second Type 2, and third Type 3. In every step with single inclusion, the current type of each element is compared with the previous type, and the higher priority element type can replace the lower one. Otherwise no previous element type is modified. After the cycle for all inclusions is completed, the types of

Fig. 4 Element pattern in the multiple inclusions problem



elements are determined and then the corresponding elements are divided according to the decomposition condition in Table 1.

(2) The balancing condition

In order to obtain uniform variation of mesh with density, the balancing condition is enforced in the refinement process. This treatment may cause some elements to be decomposed although the parts of them have met the minimum size requirement. Therefore, when an element is marked to be decomposed, its neighbor elements will be determined whether they should be further decomposed. Since the quadtree structure has always maintained a balance in the refinement process, Fig. 5 makes simple classification of the situations between two neighbors. In the example of Fig. 5, the element *A* and its left element *B* are neighbors, and let *Level (A)* be the level of the element *A*. If the element *A* is marked to be decomposed, its neighbor *B* also needs to be marked when $Level(A) - Level(B) = 1$ is true, and thus the decomposition of the element *B* is triggered only in the situations of Case 3 and Case 4. Similarly, the other neighbors of the element *A* can be treated equally. According to the level information of element and the geometric property of neighboring elements sharing the common edge, the balancing process for all elements is complete with the tree traversal.

3.2 The Implementation Program of Modified Model

With all the methods mentioned above, the specific procedure for generating the modified model is as follow:

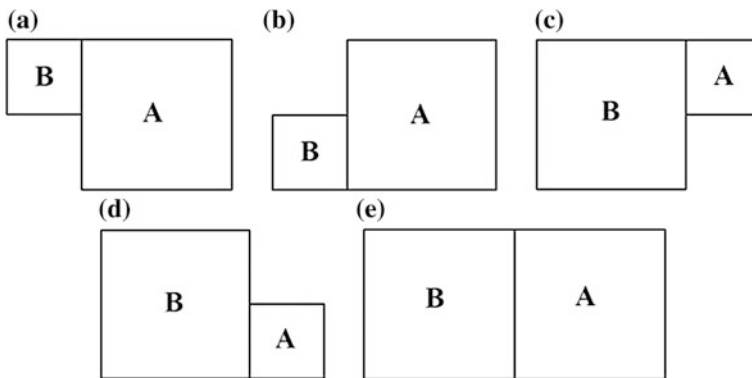


Fig. 5 Geometric relationships between element *A* and its neighborhood element *B*: **a** Case 1, **b** Case 2, **c** Case 3, **d** Case 4, **e** Case 5

- (a) Input the information of random aggregate particles and the minimum size requirements in various material regions, and generate an initial uniform square mesh, in which each of these elements is considered as the root of a different tree.
- (b) Traverse the leaf elements and mark the elements which do not reach the minimum size requirement.
- (c) Traverse the marked elements and their neighbors and mark those neighbors which should be further decomposed to achieve the balancing condition.
- (d) Repeat step (c) until the number of the elements marked in step (c) is constant.
- (e) Decompose the elements marked and save the information of new nodes and elements.
- (f) Repeat step (b) to step (e) until the number of the elements marked in step (b) is constant.
- (g) Output the information of nodes and leaf elements.

4 The Polygonal Finite Element Method

To the above-mentioned mesh after quadtree refinement, hanging nodes may be present along the common edges between adjacent elements that differ in size, thereby leading to an incompatibility problem in traditional finite element method (FEM). In this paper, the polygonal FEM based on the Wachspress interpolation [13] is employed to obtain C^0 admissible approximations along edge that includes hanging nodes. A brief overview of the polygonal FEM based on the Wachspress interpolation is given in this section, and further detailed discussion can be referred in the literature [14, 15] and the references therein.

At first, considering with a convex polygonal element $\Omega \subset R^2$ in Fig. 6, P_1, P_2, \dots, P_n are vertex points in Ω and arranged counterclockwise. Any point P with coordinates $x \equiv (x, y) \in \Omega$, has a set of associated shape functions $N_i(x)$. An interpolation scheme for a function $u(x): \Omega \rightarrow R^2$ can be expressed as

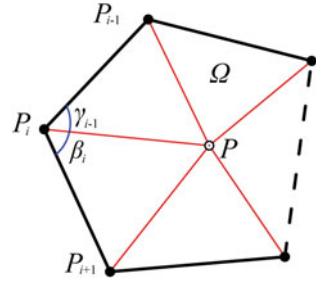
$$u^h(x) = \sum_i^n N_i(x) u_i \quad (3)$$

where u_i is the unknown at P_i , and the polygonal shape function $N_i(x)$ is represented in the general form

$$N_i(x) = \omega_i(x) / \sum_{j=1}^n \omega_j(x) \quad (4)$$

where $\omega_i(x)$ is the weight function as following [13]

Fig. 6 Polygonal element with the Wachspress interpolation



$$\omega_i(x) = \frac{\cot \gamma_{i-1} + \cot \beta_i}{\|P - P_i\|^2} \tag{5}$$

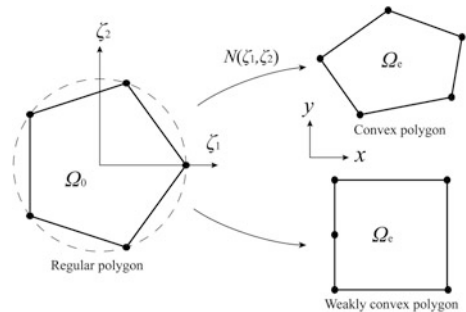
in which the angles γ_{i-1} and β_i are given in Fig. 6. Equation (4) satisfies the following properties: nonnegative and bounded; interpolation; constant and linear precision; and C^0 function along the edges. Thus, the polygonal element is easily incorporated into traditional FE codes.

In fact, the Wachspress interpolation can only describe the convex polygons. In order to expand the scope of the Wachspress interpolation to the elements with hanging nodes, an isoparametric transformation technique proposed by Sukumar and Tabarraei [14] is introduced here, in which the affine mapping from the regular polygon to any convex polygon is constructed, as shown in Fig. 7. The isoparametric mapping is expressed as

$$x = \sum_{i=1}^n N_i(\zeta_1, \zeta_2)x_i \tag{6}$$

In Fig. 8, for the purpose of numerical integration, the regular polygon is decomposed into sub-triangles [15], and this process is performed to integrate by the following transformations

Fig. 7 Isoparametric mapping from the regular polygon to any convex polygon



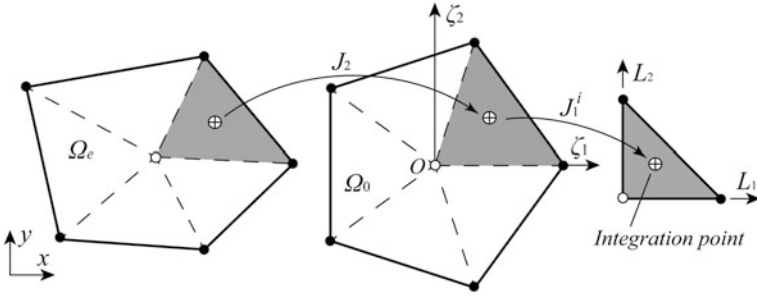


Fig. 8 Numerical integration schemes for polygonal element

$$\int_{\Omega_e} f d\Omega = \int_{\Omega_0} f |J_2| d\Omega = \sum_{j=1}^n \int_0^1 \int_0^{1-L_2} f |J_1^j| |J_2| dL_1 dL_2 \tag{7}$$

where n is the number of sub-triangles, $|J_1^j|$ and $|J_2|$ are the Jacobi determinant of the transform matrix. Finally, Gauss integration rule is used in each triangle.

5 Numerical Simulation

In this section, the application of the quadtree refinement scheme to mesoscopic model of concrete is investigated. The concrete model consisting of aggregates, mortar matrix, and ITZ is considered. The side length of the square specimen is 100 mm. The area fraction of the aggregates is 60% with nominal diameters between 2 and 20 mm. Aggregate particles of various sizes in mesoscopic model are generated by the aggregate area fraction and the aggregate gradation curve given in literature [16]. The two models with uniform mesh and quadtree refinement mesh are summarized in Fig. 9. The element size of uniform mesh in Fig. 9a is 1.25 mm, and the minimum size requirement of ITZ of quadtree refinement mesh in Fig. 9b is 0.1 mm.

In general, the elastic modulus of element is randomly assigned in accord with certain probability distribution to simulate the property change in the same material [1]. Because the concrete is a kind of highly inhomogeneous and discontinuous composites, in this paper, the random parametric model following Weibull distribution is assumed for describing the random characteristics of mechanical properties of concrete mecro-components, as listed in Table 2. Considering the change of Poisson’s ratio is small, its randomness can be ignored, and thus the Poisson’s ratios of aggregate, ITZ, and mortar are chosen as 0.18, 0.25, and 0.2, respectively.

As quasi-brittle materials, the nonlinear stress–strain relationship of concrete is boiled down to the cracks growth, propagation, penetration, and failure of concrete

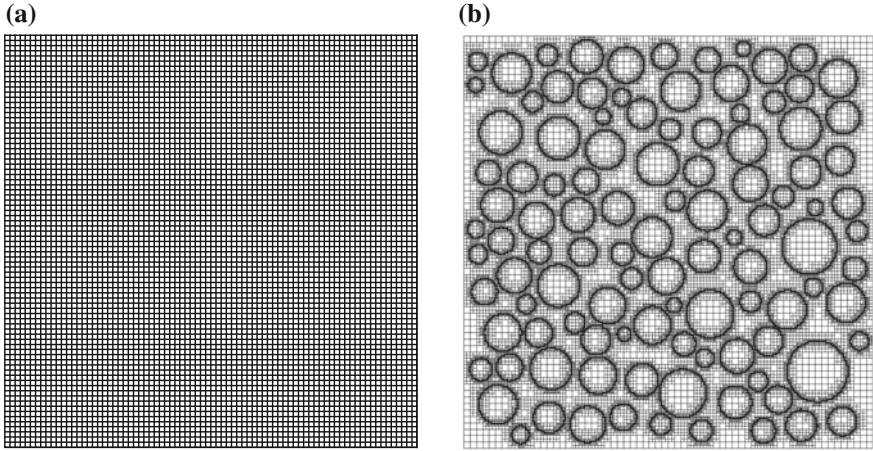


Fig. 9 Concrete mesoscopic model with **a** uniform mesh and **b** quadtree refinement mesh

Table 2 Material parameters of the concrete specimen-based Weibull distribution

Material property	Elastic modulus/ GPa	Strength (pressure/tension)/ MPa	Homogeneity
Aggregate	80.0	500/50	6
ITZ	15.0	150/15	1.5
Mortar	28.6	175/17.5	3

material. In numerical simulation, this change process can be expressed by the local degradation of the global stiff matrix. Here, the sample elastic-brittle damage constitutive law is adopted to describe the mechanical behavior of mecro-components of concrete. Supposing the material in the state of uniaxial load, the damage constitutive law of mecro elements is illustrated in Fig. 10, where D is the damage factor, E_0 is the initial elasticity modulus, and f_{tr}/f_{cr} is the residual tensile/compressive strength. When the state of the element strain achieves the strain value $(\epsilon_{tr}/\epsilon_{cr})$ corresponding to the elastic limit, the element begins to be damaged. In the damage model, the maximum tensile strain criterion is regarded as the first damage criterion, and the Mohr–Coulomb criterion is regarded as the second damage criterion. In the other words, if the strain state of the element achieved first damage criterion, the second damage criterion does not need to be tested. When the state of the element strain exceeds the stain limit $(\epsilon_{tr}/\epsilon_{cu})$, the element fails. Under the complicated stress state, the strain value ϵ in Fig. 10 can be replaced by using the equivalent strain $\bar{\epsilon}$ as follows

$$\bar{\epsilon} = \sqrt{\langle \epsilon_1 \rangle^2 + \langle \epsilon_2 \rangle^2 + \langle \epsilon_3 \rangle^2} \tag{8}$$

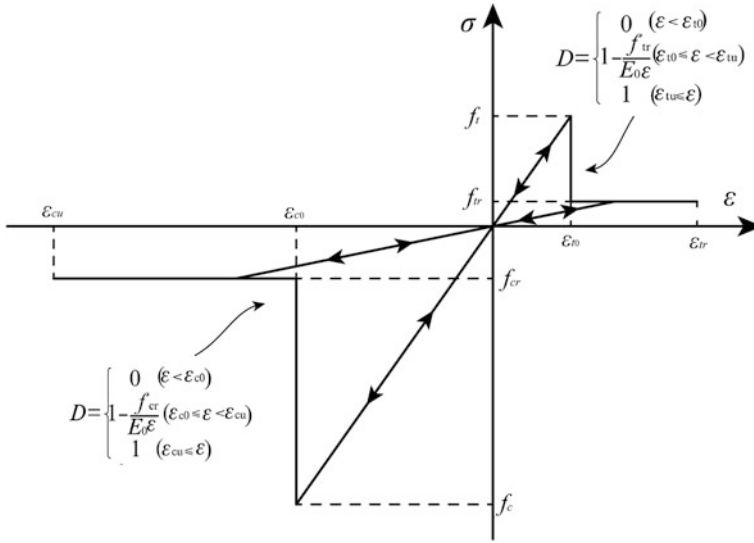


Fig. 10 Elastic-brittle damage constitutive law of material in the state of uniaxial load [1]

where $\varepsilon_1, \varepsilon_2,$ and ε_3 are three principal strains, and the symbolic function $\langle x \rangle$ is the function defined by

$$\langle x \rangle = \begin{cases} x & x \geq 0 \\ 0 & x < 0 \end{cases} \tag{9}$$

Both uniaxial tension and uniaxial compression tests are carried out for two models with uniform mesh (Sample 1) and quadtree refinement mesh (Sample 2). The specimen is fixed at the bottom, and a uniform vertical load is applied at the top. The whole load process applies the displacement control mode, in which the displacement step length is 0.5 $\mu\text{m}/5.0 \mu\text{m}$ under uniaxial tension/compression.

Figure 11 shows the comparison of the final damage distribution observed for concrete mesoscopic models with two kinds of meshes. One main crack grows perpendicular to the loading direction under uniaxial tension. In the uniaxial compression test, the specimen cracks along the loading direction and shows several intersecting cracks. As can be seen, the sawtooth defect of meshes around the aggregates gets well improved, and the geometric shapes of mecro-components of concrete are more accurate and vivid after refining the elements of ITZ. It can be concluded that the cracks form in the ITZ and propagate along an aggregate concentrated path. Finally, the cracks interconnect with each other in the mortar, resulting in the macroscopic failure of concrete.

Figure 12 shows the relationship between the average stress and the average strain over the region of concrete. In both simulations, the curves with the same

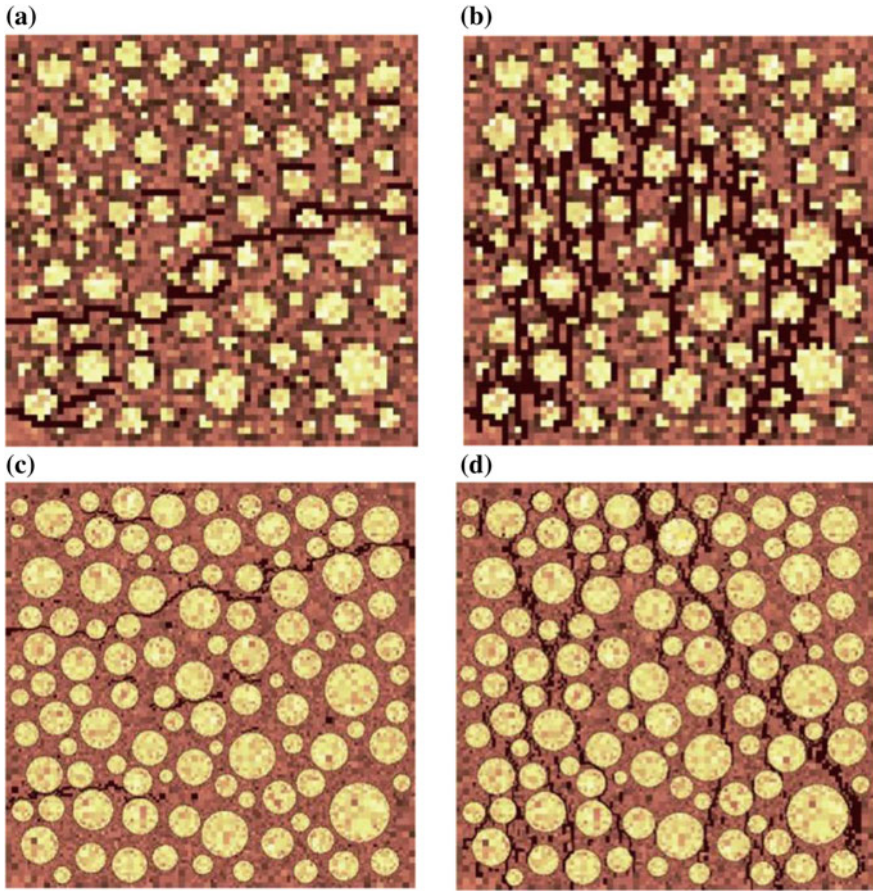


Fig. 11 Comparison of the final damage distribution observed for concrete mesoscopic models with different meshes: **a** Sample 1—uniaxial tension, **b** Sample 1—uniaxial compression, **c** Sample 2—uniaxial tension, **d** Sample 2—uniaxial compression

changing tendency are obtained. The peak stresses of the curves corresponding to Sample 2 are slightly larger than Sample 1. The differences result between Sample 1 and Sample 2 can probably be ascribed to the lower percentage of ITZ in the refined mesh. Furthermore, the results of curves with the refined ITZ element [1] are also given. As depicted in Fig. 12, the curve results of Sample 2 and reference show good agreement, so that it can be found that the proposed concrete mesoscopic model is competent.

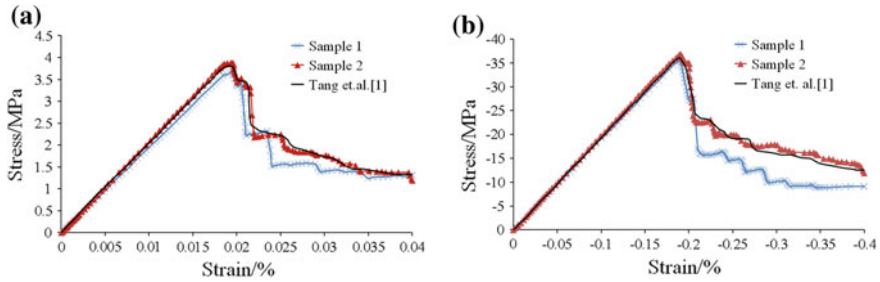


Fig. 12 Relationship between the average stress and the average strain over the region of concrete: **a** uniaxial tension, **b** uniaxial compression

6 Conclusions

The ITZ, as the weak part of concrete, has significant influence on the macro-performance of concrete. In this paper, the quadtree refinement scheme using control standards of the minimum size requirement and the balancing condition are proposed to refine the meshes of ITZ, where the elements may be coarse in the background mesh method. The percentage of ITZ in concrete is more accurate after the performance of refinement, and thus the correlative material parameters can be assigned to the elements of ITZ without other additional measures. Furthermore, the sawtooth defect of meshes around the aggregates is improved by using the finer description of ITZ in the modified model, in which the change of stress and strain near the region of ITZ is more reasonable. It is simple and easy for the proposed method to extend to three-dimensional problems when the octree is used. Further verification studies for the influence of ITZ with different element sizes are currently under investigation.

Acknowledgements The work described in this paper was supported by the National Natural Science Foundation of China (No. 51278169).

References

1. Tang C, Zhu W (2003) Damage and fracture of concrete-numerical test. Science Publishing House, Beijing (in Chinese)
2. Unger JF, Eckardt S (2011) Multiscale modeling of concrete. Arch Comput Methods Eng 18 (3):341
3. Caballero A, Carol I, López CM (2006) A meso-level approach to the 3D numerical analysis of cracking and fracture of concrete materials. Fatigue Fract Eng Mater Struct 29(12):979–991
4. Liu Z (2012) Research on fracture simulation and dynamic behavior of concrete. Dalian University of Technology, Dalian (in Chinese)
5. Lilliu G, van Mier JG (2003) 3D lattice type fracture model for concrete. Eng Fract Mech 70 (7):927–941

6. Samet H (1984) The quadtree and related hierarchical data structures. *ACM Comput Surveys (CSUR)* 16(2):187–260
7. Yerry M, Shephard MS (1983) Modified quadtree approach to finite element mesh generation. *IEEE Comp Graph Appl* 3(1):39–46
8. Man H, Song C, Natarajan S, Ooi ET, Birk C (2014) Towards automatic stress analysis using scaled boundary finite element method with quadtree mesh of high-order elements. [arXiv:1402.5186](https://arxiv.org/abs/1402.5186)
9. Tabarraei A, Sukumar N (2007) Adaptive computations using material forces and residual-based error estimators on quadtree meshes. *Comput Meth Appl Mech Eng* 196(25):2657–2680
10. Krysl P, Grinspun E, Schröder P (2003) Natural hierarchical refinement for finite element methods. *Int J Numer Meth Eng* 56(8):1109–1124
11. Kagan P, Fischer A, Bar Yoseph PZ (2003) Mechanically based models: Adaptive refinement for B-spline finite element. *Int J Numer Meth Eng* 57(8):1145–1175
12. Tabarraei A, Sukumar N (2005) Adaptive computations on conforming quadtree meshes. *Finite Elem Anal Des* 41(7):686–702
13. Malsch EA, Dasgupta G (2004) Interpolations for temperature distributions: a method for all non-concave polygons. *Int J Solids Struct* 41(8):2165–2188
14. Sukumar N, Tabarraei A (2004) Conforming polygonal finite elements. *Int J Numer Meth Eng* 61(12):2045–2066
15. Sukumar N, Malsch EA (2006) Recent advances in the construction of polygonal finite element interpolants. *Arch Comput Meth Eng* 13(1):129–163
16. Walraven JC, Reinhardt HW (1981) Concrete mechanics. Part A: theory and experiments on the mechanical behavior of cracks in plain and reinforced concrete subjected to shear loading. *Heron* 26(1):26–33

A Coupling of Three-Dimensional Finite Element Method and Discontinuous Deformation Analysis Based on Complementary Theory



C. Su, Z. M. Ren, V. H. Dao and Y. J. Dong

Abstract The continuous and discontinuous deformation analysis is essential for the stability analysis of the anchor bar-surrounding rock masses system. To eliminate the open-close iteration and the penalty factor of the 3D-DDA, the CDDA is proposed to extend into the three-dimensional block system. Then a novel simulation approach, the coupling method of 3D CDDA-FEM, is demonstrated, which combines the specific benefits of two numerical methods: the contacts between blocks are described by 3D-CDDA, while the displacement field inside block is described by FEM. Two numerical examples verify that the new coupling method is feasible and the displacement solution is more accurate. Taking different initial stress conditions of anchor bars into account, the stability analysis of anchor bar-surrounding rock masses system demonstrates that the appropriate installation and the optimal initial stress of anchor bar efficiently improve the stability of surrounding rock masses system of underground chamber.

Keywords Complementary discontinuous deformation analysis (CDDA) · Finite element method (FEM) · Stability analysis · Prestressed anchor bar · Surrounding rock masses system

1 Introduction

In a large underground chamber group excavation, the crack and fracture of complicated earth media may cause a large displacement and deformation of surrounding rock. To improve the stability, the anchor bar is commonly installed into the surrounding rock. The classifications of on the economic efficiency and

C. Su · Z. M. Ren (✉) · Y. J. Dong
College of Water Conservancy and Hydropower Engineering, Hohai University,
Nanjing, China
e-mail: renzhiming1101@outlook.com

V. H. Dao
Thuyloi University, Hanoi, Vietnam

© Springer Nature Singapore Pte Ltd. 2018
H. Nguyen-Xuan et al. (eds.), *Proceedings of the International Conference on Advances in Computational Mechanics 2017*, Lecture Notes in Mechanical Engineering, https://doi.org/10.1007/978-981-10-7149-2_67

operational technology, the end-point anchorage bar is suitable to reinforce the surrounding rock with many discontinuous interfaces inside the involved domain. So the mechanical analysis of anchor bar-surrounding rock is essential content of the numerical simulation in the rock and soil mechanics. In experimental model, many have conducted the anchor bar experimental models and field test [1–5]. In numerical simulation, many have presented various numerical models of the anchor bar-blocks system [6–10].

The discontinuous deformation analysis (DDA) method is suitable for simulating and analyzing the anchor bar-surrounding rock masses system. In the DDA, the numerical model of anchor bar analyzed the axial force acting on the blocks [11–13], in which the anchor bar was replaced by an equivalent line spring. The anchorage effect of anchor bar in the tangential direction was proposed [14]. The DDA was applied to simulate the tangential anchoring effect of anchor bar by installing the springs between blocks along the crack direction [15–17]. To overcome the shortcomings of the DDA, the discontinuous deformation analysis based on the complementary theory was presented and rewrote the corresponding numerical model of anchor bar [18].

In the analysis of blocks system, the coupling method of 3D DDA-FEM [19] was proposed to the large displacement and large deformation between blocks and to solve the stress field and the displacement field inside block. The corresponding form of contact matrix was expressed [20]. To eliminate the open-close iteration and the penalty factor of 3D-DDA, the complementary discontinuous deformation analysis (CDDA) is extended to analyze the three-dimensional blocks system. Then the coupling method of 3D CDDA-FEM is proposed to analyze the continuous and discontinuous deformation problem of anchor bar-surrounding rock masses system. To demonstrate the feasibility and to investigate the effectiveness of the new coupling method, two simple numerical examples and a practical surrounding rock masses system of underground powerhouse group are presented and the results are compared with the corresponding results of the original method.

2 Three-Dimensional CDDA

To solve and obtain the complete displacement solutions, it is necessary to extend the CDDA method into three-dimensional block system.

2.1 Mixed Complementary Problem

Let G and H be the two continuous vector-valued functions, $G: R^{n_1} \times R^{n_2} \rightarrow R^{n_1}$ and $H: R^{n_1} \times R^{n_2} \rightarrow R^{n_2}$, with n_1 and n_2 being two positive integers. A mixed complementary problem is to find a pair of vectors, $\mathbf{w} \in R^{n_1}$, $\mathbf{v} \in R^{n_2}$, such that:

$$\begin{cases} G(\mathbf{w}, \mathbf{v}) = 0 \\ \mathbf{v} \geq 0, H(\mathbf{w}, \mathbf{v}) \geq 0 \\ \mathbf{v}^T H(\mathbf{w}, \mathbf{v}) = 0 \end{cases} \quad (1)$$

Furthermore, the vector \mathbf{v} is replaced by a continuous vector-valued function $F: R^{n_1} \times R^{n_2} \rightarrow R^{n_2}$, we can obtain a generalized mixed complementary problem:

$$\begin{cases} G(\mathbf{w}, \mathbf{v}) = 0 \\ F(\mathbf{w}, \mathbf{v}) \geq 0, H(\mathbf{w}, \mathbf{v}) \geq 0 \\ F(\mathbf{w}, \mathbf{v})^T H(\mathbf{w}, \mathbf{v}) = 0 \end{cases} \quad (2)$$

The first equation will represent the discrete momentum conservation equations. The second inequality will stand for the constraints on the contact-pairs. The third equation will indicate the complementary conditions on the contact forces and the relative displacements of the contact-pairs. We can rewrite (2) as a system of equations of the form:

$$\begin{cases} G(\mathbf{w}, \mathbf{v}) = 0 \\ \min(F(\mathbf{w}, \mathbf{v}), H(\mathbf{w}, \mathbf{v})) = 0 \end{cases} \quad (3)$$

2.2 Stiffness Equation of a Block

The loads of a block include known point load \mathbf{f} , line load \mathbf{p}_1 , surface load \mathbf{p}_2 , unknown volume load $(\mathbf{b} - \rho\ddot{\mathbf{u}})$, and contact force $\bar{\mathbf{p}}$. Based on the principle of momentum conservation, the variational equation of block Ω_i is written as:

$$\begin{aligned} \int_{\Omega_i} (\delta\boldsymbol{\varepsilon})^T \boldsymbol{\sigma} d\Omega &= \int_{\Omega_i} (\delta\mathbf{u})^T (\mathbf{b} - \rho\ddot{\mathbf{u}}) d\Omega + \int_{S_{p1}} (\delta\mathbf{u})^T \mathbf{p}_1 dS_{p1} \\ &+ \int_{S_{p2}} (\delta\mathbf{u})^T \mathbf{p}_2 dS_{p2} + \sum (\delta\mathbf{u})^T \mathbf{f} + \sum (\delta\mathbf{u})^T \bar{\mathbf{p}} \end{aligned} \quad (4)$$

where $\boldsymbol{\sigma}$ and \mathbf{u} , respectively, represent the stress vector and the displacement vector of a point inside block, $\delta\mathbf{u}$ and $\delta\boldsymbol{\varepsilon}$, respectively, denote the virtual displacement and the virtual strain.

The stress and the strain are described by the displacement function.

$$\boldsymbol{\sigma} = [\mathbf{D}]\boldsymbol{\varepsilon} + \boldsymbol{\sigma}_0 = [\mathbf{D}][\mathbf{L}]\mathbf{u} + \boldsymbol{\sigma}_0 = [\mathbf{D}][\mathbf{B}]\hat{\mathbf{d}} + \boldsymbol{\sigma}_0 \quad (5)$$

where \mathbf{D} is the elastic matrix and $\boldsymbol{\sigma}_0$ is the initial stress. The virtual work of stress is written as:

$$\begin{aligned} \int_{\Omega_i} (\delta \boldsymbol{\epsilon})^T \boldsymbol{\sigma} d\Omega &= \int_{\Omega_i} ([\mathbf{B}]\delta \hat{\mathbf{d}})^T [\mathbf{D}][\mathbf{B}]\hat{\mathbf{d}} d\Omega + \int_{\Omega_i} ([\mathbf{B}]\delta \hat{\mathbf{d}})^T \boldsymbol{\sigma}_0 d\Omega \\ &= (\delta \hat{\mathbf{d}})^T \left[\int_{\Omega_i} [\mathbf{B}]^T [\mathbf{D}][\mathbf{B}] d\Omega \right] \hat{\mathbf{d}} + (\delta \hat{\mathbf{d}})^T \left[\int_{\Omega_i} [\mathbf{B}]^T \boldsymbol{\sigma}_0 d\Omega \right] \end{aligned} \quad (6)$$

The contact force is decomposed as:

$$\bar{\mathbf{p}} = (\tau_1 \quad \tau_2 \quad n)(\bar{p}^{\tau_1} \quad \bar{p}^{\tau_2} \quad \bar{p}^n)^T \quad (7)$$

where $(\tau_1 \quad \tau_2 \quad n)$ is the coordinate of slave block. The virtual work of unknown contact force is:

$$\begin{aligned} \sum (\delta \mathbf{u})^T \bar{\mathbf{p}} &= (\delta \hat{\mathbf{d}})^T \begin{bmatrix} \mathbf{N}_{c_1}^T \mathbf{L}_{c_1} & \cdots & \mathbf{N}_{c_n}^T \mathbf{L}_{c_n} \\ \mathbf{L}_{c_i} = (\tau_{1c_i} \tau_{2c_i} n_{c_i}) & & i = 1, \dots, n \end{bmatrix} \bar{\mathbf{p}} = (\delta \hat{\mathbf{d}})^T [\mathbf{C}]\bar{\mathbf{p}} \end{aligned} \quad (8)$$

where \mathbf{L}_{c_i} and \mathbf{N}_{c_i} , respectively, represent the local coordinate and the shape function matrix of the slave block in the c_n -th contact-pair. The $3c_n \times 1$ unknown contact force vector in Eq. (4) is expressed as:

$$\bar{\mathbf{p}}^T = \left(\bar{p}_{c_1}^{\tau_1}, \bar{p}_{c_1}^{\tau_2}, \bar{p}_{c_1}^n, \dots, \bar{p}_{c_n}^{\tau_1}, \bar{p}_{c_n}^{\tau_2}, \bar{p}_{c_n}^n \right) \quad (9)$$

Since the virtual displacement $\delta \hat{\mathbf{d}}$ is arbitrary, the stiffness equation of a block is simplified as:

$$[\mathbf{M}]_i \ddot{\hat{\mathbf{d}}}_i + [\mathbf{K}]_i \hat{\mathbf{d}}_i - [\mathbf{C}]_i \bar{\mathbf{p}}_i = \mathbf{f}_i \quad (10)$$

where \mathbf{M}_i is the 12×12 mass matrix, \mathbf{K}_i is the 12×12 stiffness matrix, and \mathbf{C}_i is the $12 \times 3c_n$ contact matrix determined from the position and local frame corresponding to all contact forces acting on block. The 24th order generalized force vector is written as:

$$\mathbf{f}_i = - \int_{\Omega_i} [\mathbf{B}]^T \boldsymbol{\sigma}_0 d\Omega + \int_{\Omega_i} \mathbf{N}_i^T \mathbf{b} d\Omega + \int_{S_{p_1}} \mathbf{N}_1^T \mathbf{p}_1 dS_{p_1} + \int_{S_{p_2}} \mathbf{N}_2^T \mathbf{p}_2 dS_{p_2} + \sum \mathbf{N}_i^T \mathbf{f} \quad (11)$$

where \mathbf{N}_i is the shape function matrix. Taking the consistent measure of the original DDA to obtain the equivalent form of $\hat{\mathbf{d}}_i$, the simplified form of the stiffness Eq. (10) of a block is:

$$[\bar{\mathbf{K}}]_i \mathbf{d}_i - [\mathbf{C}]_i \bar{\mathbf{p}}_i = \bar{\mathbf{f}}_i \quad (12)$$

2.3 Global Stiffness Equation of Blocks System

Suppose that the blocks system has n_1 blocks and n_2 contact-pairs within the time step, the Eq. (12) of all blocks is collected as a system of $12n_1$ equations in $12n_1 + 3n_2$ unknowns $(\mathbf{d}, \bar{\mathbf{p}})$. As the contact forces are the variables shared by blocks in contact, the global stiffness equations system of the block system is expressed as:

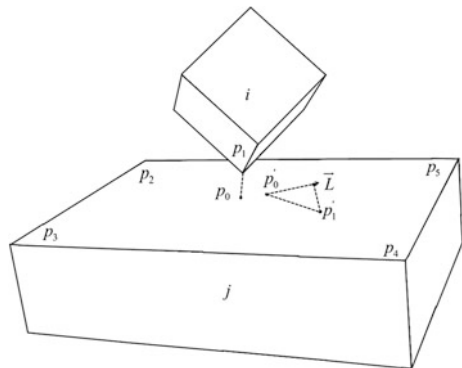
$$\begin{bmatrix} \bar{\mathbf{K}}_1 & \mathbf{0} & \cdots & \mathbf{0} \\ \mathbf{0} & \bar{\mathbf{K}}_2 & \cdots & \mathbf{0} \\ \vdots & \vdots & \ddots & \vdots \\ \mathbf{0} & \mathbf{0} & \cdots & \bar{\mathbf{K}}_{n_1} \end{bmatrix} \begin{bmatrix} \hat{\mathbf{d}}_1 \\ \hat{\mathbf{d}}_2 \\ \vdots \\ \hat{\mathbf{d}}_{n_1} \end{bmatrix} - \begin{bmatrix} \mathbf{C}_1^T \\ \mathbf{C}_2^T \\ \vdots \\ \mathbf{C}_{n_1}^T \end{bmatrix} [\bar{\mathbf{p}}] = \begin{bmatrix} \bar{\mathbf{f}}_1 \\ \bar{\mathbf{f}}_2 \\ \vdots \\ \bar{\mathbf{f}}_{n_1} \end{bmatrix} \tag{13}$$

where \mathbf{C}_i is a $12 \times 3n_2$ submatrix corresponding to global contact matrix. The simple equation of Eq. (13) is written as $[\mathbf{K}]\hat{\mathbf{d}} - [\mathbf{C}]\bar{\mathbf{p}} = \mathbf{f}$.

2.4 Contact Equation

The contact force $\bar{\mathbf{p}}$ is decomposed into $(\bar{p}^{\tau 1}, \bar{p}^{\tau 2}, \bar{p}^n)$, and the contact force $\bar{p}^{\tau 1}$ is zero. To obtain the displacement solutions, $2n_c$ contact equations are associated with the global stiffness equations of block system. The common plane algorithm is used to judge the contact type between blocks in this paper. The unit \mathbf{n} in local coordinate matrix is the inner normal vector of the contact surface $p_0p_2p_3p_4p_5$ shown in Fig. 1. The point p_0 in the contact surface is the predetermined contact point of the vertex p_1 . Since the point p_0 is moving to p'_0 and the point p_1 is moving to p'_1 in this time step, the unit τ_2 in local coordinate matrix is the projection \vec{L} of the line $\vec{p'_0p'_1}$ in contact surface.

Fig. 1 Vertex-to-face contact model of blocks



In the normal \mathbf{n} direction, since the two blocks corresponding to the contact-pair of interest cannot be penetrated into each other, the relative distance should be non-negative:

$$g^n = \mathbf{n}^T (x_i - x_j) = \mathbf{n}^T (\bar{x}_i - \bar{x}_j + \mathbf{N}_i \hat{\mathbf{d}}_i - \mathbf{N}_j \hat{\mathbf{d}}_j) \tag{14}$$

where i and j represent, respectively, the mash and the slave block. \bar{x}_i and \bar{x}_j represent the positions of the two nearest points of the contact-pair at the start of this step. So the complementary equations of normal contact conditions are equivalently expressed as:

$$\min(\bar{p}^n \quad E g^n) = 0 \tag{15}$$

where E is a constant elastic modulus used to transform \bar{p}^n and g^n to the same order.

In the tangential $\boldsymbol{\tau}_2$ direction, a contact-pair may be in one of two contact states: the sticky state and the sliding state. The velocity of movement of the master relative is approximated by the Euler-Backward difference:

$$\dot{g}^{\tau_2} = \frac{1}{\Delta} \boldsymbol{\tau}_2^T (\mathbf{N}_j \hat{\mathbf{d}}_j - \mathbf{N}_i \hat{\mathbf{d}}_i) \tag{16}$$

The friction force is $|p^{\tau_2}| = C + \mu p^n$.

where μ is the friction factor, C is the inner cohesion, and p^{τ_2} is the friction. So the complementary equations of tangential contact conditions are equivalently expressed:

$$\min(G \dot{g}^{\tau_2} \bar{p}^{\tau_2} \quad \mu \bar{p}^n + C - |\bar{p}^{\tau_2}|) = 0 \tag{17}$$

where G is a constant elastic modulus used to transform $\dot{g}^{\tau_2} \bar{p}^{\tau_2}$ and $\mu \bar{p}^n + C - |\bar{p}^{\tau_2}|$ to the same order.

Collecting global stiffness equation system (13) and the contact Eqs. (15) and (17) of the n_2 contact pairs, the equations system of three-dimensional discontinuous deformation analysis based on complementary theory (3D-CDDA) with unknown $(\mathbf{d}, \bar{\mathbf{p}})$ is expressed as:

$$H(\mathbf{d}, \bar{\mathbf{p}}) = \left(\begin{array}{c} [\mathbf{K}]\mathbf{d} - [\mathbf{C}]\bar{\mathbf{p}} - \mathbf{f} \\ \min(\bar{p}^n \quad E g^n) \\ \min(G \dot{g}^{\tau_2} \bar{p}^{\tau_2} \quad \mu \bar{p}^n + C - |\bar{p}^{\tau_2}|) \end{array} \right)_{i=1}^{i=n_2} = 0 \tag{18}$$

3 Coupling Method of 3D CDDA-FEM

The 3D-CDDA chooses the complete first-order polynomial as displacement function for a block in the blocks system. So the 3D-CDDA describes the contact between blocks but restricts the stress and displacement field inside block. The FEM is applied to solve the displacement field by proper internal discretization of deformable blocks. The coupling method of 3D CDDA-FEM implements the continuous and discontinuous deformation analysis of block system.

3.1 Displacement Function of a Finite Element

Taking three-dimensional eight-node hexahedral finite element as example, the displacement field of a finite element is described as:

$$(u \ v \ w)^T = [\mathbf{N}]_{ei} \cdot \mathbf{d}_{ei} = \begin{bmatrix} N_1 & 0 & 0 & \cdots & N_8 & 0 & 0 \\ 0 & N_1 & 0 & \cdots & 0 & N_8 & 0 \\ 0 & 0 & N_1 & \cdots & 0 & 0 & N_8 \end{bmatrix} (u_1 \ v_1 \ w_1 \ \cdots \ u_8 \ v_8 \ w_8)^T \quad (19)$$

where \mathbf{N}_{ei} is the shape matrix and \mathbf{d}_{ei} is the node displacement. The shape function N_{ei} is agreement with the shape function of finite element method.

3.2 Review of Coupling Method of 3D DDA-FEM

The potential energy of a finite element inside a block is:

$$\Pi_b = \sum_{i=1}^{m_b} \frac{1}{2} \mathbf{d}_i^T [\mathbf{k}]_i \mathbf{d}_i - \sum_{i=1}^{m_b} \mathbf{d}_i^T \mathbf{p}_i \quad (20)$$

where $[\mathbf{k}]_i$ is the stiffness matrix and $[\mathbf{p}]_i$ is the equivalent nodal load matrix.

In the discretization model of block system, the discontinuous deformation of contact surface between blocks was controlled by the principles of Mohr–Coulomb and non-tensile stress, and the displacement was solved by the penalty function method in the DDA. In other words, the normal and tangential springs are installed to the contact point and the open-close iteration is the installation-elimination of the equivalent spring. Suppose the blocks system contained n blocks and k contact-pairs, the total potential energy of blocks system is written as:

$$\Pi_p = \sum_{b=1}^n \sum_{i=1}^{m_b} \frac{1}{2} \mathbf{d}_i^T [\mathbf{k}]_i \mathbf{d}_i - \sum_{ij=1}^k \frac{1}{2} \mathbf{d}_{ij}^T [\mathbf{k}]_{ij}^c \mathbf{d}_{ij} - \sum_{b=1}^n \sum_{i=1}^{m_b} \mathbf{d}_i^T \mathbf{p}_i \tag{21}$$

where $[\mathbf{k}]_{ij}^c$ is the contact spring matrix.

According to the variation principle, $\partial \Pi_p = 0$, the global balance equation of block system is expressed as:

$$[\mathbf{K}] \mathbf{d} = \mathbf{P} \tag{22}$$

where \mathbf{K} is the global stiffness matrix and \mathbf{P} is the global load matrix.

3.3 Coupling Method of 3D CDDA-FEM

According to the loads acting on a finite element, the variational equation of momentum conservation of the e ith mesh element is written as:

$$\begin{aligned} \int_{\Omega_{ei}} (\delta \boldsymbol{\varepsilon})^T \boldsymbol{\sigma} d\Omega &= \int_{\Omega_{ei}} (\delta \mathbf{u})^T (\mathbf{b} - \rho \ddot{\mathbf{u}}) d\Omega + \int_{S_{ep1}} (\delta \mathbf{u})^T \mathbf{p}_1 dS_{ep1} \\ &+ \int_{S_{ep2}} (\delta \mathbf{u})^T \mathbf{p}_2 dS_{ep2} + \sum (\delta \mathbf{u})^T \mathbf{f} + \sum (\delta \mathbf{u})^T \bar{\mathbf{p}} \end{aligned} \tag{23}$$

The stress and the strain are described by the displacement function of finite element:

$$\boldsymbol{\sigma}_{ei} = [\mathbf{E}]_i \boldsymbol{\varepsilon}_{ei} = [\mathbf{E}]_i [\mathbf{B}]_{ei} \mathbf{d}_{ei} \tag{24}$$

where \mathbf{B}_{ei} is the geometry matrix and \mathbf{E}_i is the elastic matrix. The virtual work of stress is:

$$\begin{aligned} \int_{\Omega_{ei}} (\delta \boldsymbol{\varepsilon})^T \boldsymbol{\sigma} d\Omega &= \int_{\Omega_{ei}} ([\mathbf{B}] \delta \mathbf{d})^T [\mathbf{E}] ([\mathbf{B}] \mathbf{d}) d\Omega + \int_{\Omega_{ei}} ([\mathbf{B}] \delta \mathbf{d})^T \boldsymbol{\sigma}_0 d\Omega \\ &= (\delta \mathbf{d})^T \left[\int_{\Omega_{ei}} [\mathbf{B}]^T [\mathbf{E}] [\mathbf{B}] d\Omega \right] \mathbf{d} + (\delta \mathbf{d})^T \left[\int_{\Omega_{ei}} [\mathbf{B}]^T \boldsymbol{\sigma}_0 d\Omega \right] \end{aligned} \tag{25}$$

Since the virtual displacement $\delta \mathbf{d}$ is arbitrary, the equation of momentum conservation of a finite element inside block is simplified as:

$$[\bar{\mathbf{K}}]_{ei} \mathbf{d}_{ei} - [\mathbf{C}]_{ei} \bar{\mathbf{p}}_{ei} = \bar{\mathbf{f}}_{ei} \tag{26}$$

where $\bar{\mathbf{K}}_{ei}$ is the 24×24 generalized stiffness matrix and \mathbf{C}_{ei} is the $24 \times 3c_n$ contact matrix (the values of element in the contact matrix are zero except the node effected by contact force).

Suppose that a block has n_1 nodes in the finite element mesh and n_2 contact forces, the stiffness equation system of a block with $3n_1$ and $3n_1 + 3n_2$ unknown $(\mathbf{d}, \bar{\mathbf{p}})$ is established by collecting all the simplified equation of finite elements inside block.

$$[\bar{\mathbf{K}}]_e \mathbf{d}_e - [\mathbf{C}]_e \bar{\mathbf{p}}_e = \bar{\mathbf{f}}_e \tag{27}$$

where $\bar{\mathbf{K}}_e$ is the $3n_1 \times 3n_1$ generalized stiffness matrix and \mathbf{C}_e is the $3n_1 \times 3n_2$ contact matrix.

Suppose that the block system has n_p nodes and n_c contact-pairs in the element mesh of block system, the stiffness equation system of the block system with $3n_p$ and $3n_p + 3n_c$ unknown $(\mathbf{d}, \bar{\mathbf{p}})$ is established by collecting all the stiffness equations of blocks.

$$[\mathbf{K}]\mathbf{d} - [\mathbf{C}]\bar{\mathbf{p}} = \mathbf{f} \tag{28}$$

where \mathbf{K} is the $3n_p \times 3n_p$ generalized stiffness matrix and \mathbf{C} is the $3n_p \times 3n_c$ contact matrix.

Since the finite element mesh is generated in the blocks system, the contact-pairs are transformed to the vertex-to-face contact between finite elements. The relative distance and velocity between finite elements are expressed as:

$$g_e^n = n^T (\mathbf{x}_{ei} - \mathbf{x}_{ej}) = n^T (\bar{\mathbf{x}}_{ei} - \bar{\mathbf{x}}_{ej} + [\mathbf{N}]_i \mathbf{d}_{ei} - [\mathbf{N}]_j \mathbf{d}_{ej}) \tag{29}$$

$$\dot{g}_e^{\tau_2} = \frac{1}{\Delta} \boldsymbol{\tau}_2^T ([\mathbf{N}]_j \mathbf{d}_{ej} - [\mathbf{N}]_i \mathbf{d}_{ei}) \tag{30}$$

Collecting the global stiffness equation system (28) and all the complementary Eqs. (29) and (30) of the n_c contact-pairs, the equations system of the coupling method of 3D CDDA-FEM is expressed as:

$$H(\mathbf{d}, \bar{\mathbf{p}}) = \left(\left(\begin{array}{c} [\mathbf{K}]\mathbf{d} - [\mathbf{C}]\bar{\mathbf{p}} - \mathbf{f} \\ \min(p^n \quad E g_e^n) \\ \min(G \dot{g}_e^{\tau_2} p^{\tau_2} \quad \mu p^n + C - |p^{\tau_2}|) \end{array} \right)_{i=1}^{i=n_c} \right) = 0 \tag{31}$$

4 Numerical Model of Anchor Bar

The rock blot is the main supporting component and plays an important role in the surrounding rock masses system. The coupling method of 3D CDDA-FEM is applied to simulate the anchor bar-surrounding rock masses system, and the corresponding model of anchor bar is expressed in the following section.

The axial force of anchor bar is:

$$s = \begin{cases} 0 & s < 0 \\ \bar{E}A \frac{\Delta l}{l} & 0 < s < T \\ T & s > T \end{cases} \tag{32}$$

where \bar{E} is the elastic modulus, A is the cross-sectional area, T is the yield strength, l , and Δl are, respectively, the length and elongation of anchor bar. The point $M_1(x_1, y_1, z_1)$ in the i th mesh element is connected to the point $M_2(x_2, y_2, z_2)$ in the j th mesh element by anchor bar. The end-points displacements of anchor bar are, respectively, expressed as:

$$\begin{aligned} dx_1 = u_1 = u(x_1, y_1, z_1) & \quad dy_1 = v_1 = v(x_1, y_1, z_1) & \quad dz_1 = w_1 = w(x_1, y_1, z_1) \\ dx_2 = u_2 = u(x_2, y_2, z_2) & \quad dy_2 = v_2 = v(x_2, y_2, z_2) & \quad dz_2 = w_2 = w(x_2, y_2, z_2) \end{aligned} \tag{33}$$

The length of rock blot is $l = \sqrt{(x_2 - x_1)^2 + (y_2 - y_1)^2 + (z_2 - z_1)^2}$

$$\begin{aligned} dl &= \frac{1}{l} [(x_1 - x_2)(u_1 - u_2) + (y_1 - y_2)(v_1 - v_2) + (z_1 - z_2)(w_1 - w_2)] \\ &= \left[(u_1 \quad v_1 \quad w_1) (l_x \quad l_y \quad l_z)^T - (u_2 \quad v_2 \quad w_2) (l_x \quad l_y \quad l_z)^T \right] \\ &= \left[d_i^T N_i^T (l_x \quad l_y \quad l_z)^T - d_j^T N_j^T (l_x \quad l_y \quad l_z)^T \right] \end{aligned} \tag{34}$$

where $l_x = \frac{x_1 - x_2}{l}$, $l_y = \frac{y_1 - y_2}{l}$, $l_z = \frac{z_1 - z_2}{l}$ represent the direction cosines of anchor bar.

When the i th mesh element is reinforced by anchor bar, the directional cosines of the anchor bar are $(-l_x \ -l_y \ -l_z)^T$ and the virtual work of axial forces is:

$$\begin{aligned} (\delta \mathbf{u}_i)^T \tilde{\mathbf{f}}_i &= (\delta \mathbf{d}_i)^T [\mathbf{N}]_i^T \left(-\frac{\bar{E}A}{l} \mathbf{d}_i^T [\mathbf{N}]_i^T \begin{pmatrix} l_x \\ l_y \\ l_z \end{pmatrix} + \frac{\bar{E}A}{l} \mathbf{d}_j^T [\mathbf{N}]_j^T \begin{pmatrix} l_x \\ l_y \\ l_z \end{pmatrix} \right) \begin{pmatrix} l_x \\ l_y \\ l_z \end{pmatrix} \\ &= -\frac{\bar{E}A}{l} (\delta \mathbf{d}_i)^T [\mathbf{G}]_i [\mathbf{G}]_i^T \mathbf{d}_i + \frac{\bar{E}A}{l} (\delta \mathbf{d}_i)^T [\mathbf{G}]_i [\mathbf{G}]_j^T \mathbf{d}_j \end{aligned} \tag{35}$$

When the j th mesh element is reinforced by anchor bar, the directional cosines of rock bolt are $(l_x \ l_y \ l_z)^T$ and the virtual work of axial forces is:

$$\begin{aligned}
 (\delta \mathbf{u}_j)^T \tilde{\mathbf{f}}_j &= (\delta \mathbf{d}_j)^T [\mathbf{N}]_j^T \left(\frac{\bar{E}A}{l} \mathbf{d}_i^T [\mathbf{N}]_i^T \begin{pmatrix} l_x \\ l_y \\ l_z \end{pmatrix} - \frac{\bar{E}A}{l} \mathbf{d}_j^T [\mathbf{N}]_j^T \begin{pmatrix} l_x \\ l_y \\ l_z \end{pmatrix} \right) \begin{pmatrix} l_x \\ l_y \\ l_z \end{pmatrix} \\
 &= \frac{\bar{E}A}{l} (\delta \mathbf{d}_j)^T [\mathbf{G}]_j [\mathbf{G}]_i^T \mathbf{d}_i - \frac{\bar{E}A}{l} (\delta \mathbf{d}_j)^T [\mathbf{G}]_j [\mathbf{G}]_j^T \mathbf{d}_j
 \end{aligned} \tag{36}$$

The node submatrix in coefficient matrix $[\mathbf{G}]_i [\mathbf{G}]_i^T$, $-[\mathbf{G}]_i [\mathbf{G}]_j^T$, $-[\mathbf{G}]_j [\mathbf{G}]_i^T$, and $[\mathbf{G}]_j [\mathbf{G}]_j^T$ is, respectively, added into the corresponding submatrix of the generalized stiffness matrix \mathbf{K}_e of block system.

$$\begin{aligned}
 \frac{\bar{E}A}{l} [\mathbf{G}]_i [\mathbf{G}]_i^T &\rightarrow [\mathbf{K}]_{eii} & - \frac{\bar{E}A}{l} [\mathbf{G}]_i [\mathbf{G}]_j^T &\rightarrow [\mathbf{K}]_{eij} \\
 - \frac{\bar{E}A}{l} [\mathbf{G}]_j [\mathbf{G}]_i^T &\rightarrow [\mathbf{K}]_{eji} & \frac{\bar{E}A}{l} [\mathbf{G}]_j [\mathbf{G}]_j^T &\rightarrow [\mathbf{K}]_{eij}
 \end{aligned} \tag{37}$$

If the axial force $\tilde{\mathbf{f}}$ exceeds the yield strength T of anchor bar, the axial force is equivalent to the yield strength T . The node submatrix in coefficient matrices $-[\mathbf{G}]_i T$ and $-[\mathbf{G}]_j T$ is, respectively, added into the corresponding submatrix of the generalized force vector \mathbf{f} of the block system.

$$-[\mathbf{G}]_i T \rightarrow \mathbf{f}_i \quad -[\mathbf{G}]_j T \rightarrow \mathbf{f}_j \tag{38}$$

5 Numerical Example

The feasibility of the 3D-CDDA and the coupling method of CDDA-FEM in the deformation analysis of blocks system are investigated by solving two typical anchor bar-block systems. The displacement solutions solved by the new method are compared with the displacement of the original methods.

5.1 Rectangle Tunnel

The surrounding rock of rectangle tunnel with fractures along the horizontal and vertical directions is shown in Fig. 2. The boundary conditions contain the fixed surfaces of $X = 0.20$, $Y = 0.25$ and the free surfaces of $Z = 0.4$. The blocks material constants are: the unit weight $\gamma = 2.0 \text{ kN/m}^3$, Young's modulus $E = 2 \text{ MPa}$, and Poisson's ratio $\nu = 0.24$. The friction between blocks is zero. Through the mechanical analysis of blocks system without anchor bar, five rock masses in the top of the surrounding rock of rectangle tunnel are unstable and the other rock masses are stable.

Fig. 2 Model of rectangle tunnel excavated

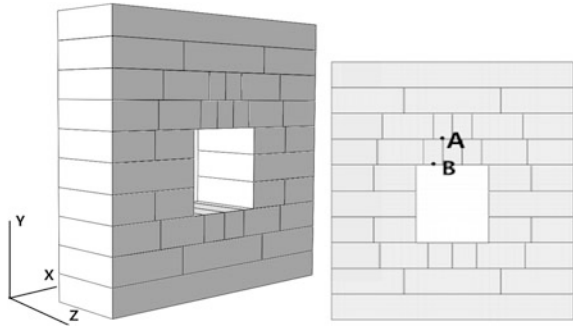


Table 1 Displacement solutions of unstable blocks in surrounding rock of rectangle tunnel

Solving method	3D DDA		3D CDDA		Analytical solution	
	A	B	A	B	A	B
Case a	-1.1334	-1.1333	-1.1841	-1.1844	-1.2500	-1.2500
Case b	-0.4815	-1.1332	-0.2447	-1.1842	—	—
Case c	-0.7146	-0.9259	-0.4786	-0.7512	—	—

The anchor bars are installed into the surrounding rock masses system in the following distributions: (a) the unstable rock masses aren't reinforced, (b) two unstable rock masses on the upper layer of unstable rock masses are reinforced, (c) five unstable rock masses are reinforced by anchor bars. The three cases are, respectively, solved by the three-dimensional DDA and the DDA based on the complementary theory (CDDA). The displacement solutions in the Y negative direction at time $t = 0.5$ s shown in Table 1 indicate that the displacement solved by the 3D-CDDA are bigger and closer to the analytical solutions than the displacement solved by the 3D-DDA.

5.2 Underground Chamber

The surrounding rock of underground chamber is shown in Fig. 3, and two element hexahedron finite elements are generated in all blocks. The boundary conditions contain the fixed faces $X = 0.50$, $Y = 0.50$ and the free faces $Z = 0.60$. The blocks material constants are: the unit weight $\gamma = 2.0$ kN/m³, Young's modulus $E = 2$ MPa, and Poisson's ratio $\nu = 0.24$. The friction between blocks is zero. Through the mechanical analysis of blocks system without anchor bar, eight blocks in the top and the sides of surrounding rock of underground chamber are unstable and the other blocks are stable.

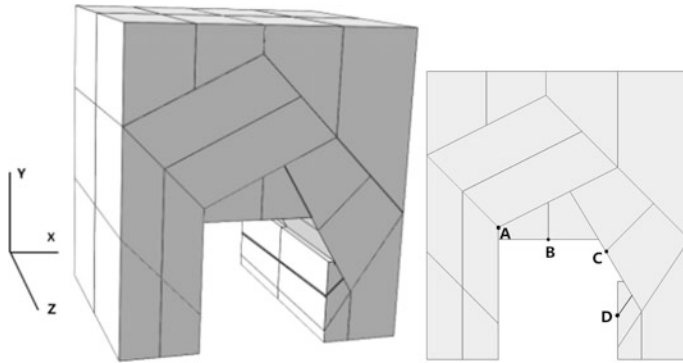


Fig. 3 Model of underground chamber excavated

Table 2 Displacement solutions of unstable blocks in surrounding rock of underground chamber

Solving method	Coupling method of 3D DDA-FEM				Coupling method of 3D CDDA-FEM			
	A	B	C	D	A	B	C	D
Monitoring point								
Case a	-0.7399	-1.1874	-0.7723	-0.8892	-0.8215	-1.2017	-0.9123	-1.0245
Case b	-0.1953	-0.4699	-0.0282	-0.7179	-0.2741	-0.5854	-0.1024	-0.8241
Case c	-0.0926	-1.1332	-0.0379	-0.0199	-0.2138	-1.1634	-0.1687	-0.1344
Case d	-0.1968	-0.4709	-0.0316	-0.0185	-0.3146	-0.5942	-0.1516	-0.1124

The anchor bars are installed into the surrounding rock masses system in the following distributions: (a) the unstable rock masses aren't reinforced, (b) six rock masses in the top of the unstable block system are reinforced, (c) six rock masses in the sides of the unstable block system are reinforced, (d) eight unstable rock masses are reinforced by anchor bars. The four cases are, respectively, solved by the coupling methods of 3D DDA-FEM and CDDA-FEM. The displacement solutions in the Y negative direction at time $t = 0.5$ s shown in Table 2 indicate that the displacement solutions of the coupling method of 3D CDDA-FEM are bigger than the displacement solutions of the coupling method of 3D DDA-FEM.

Since the coupling method of 3D CDDA-FEM eliminates the penalty factor and the open-close iteration, the proposed method accurately solves the large displacement and deformation between blocks and describes the stress field and the displacement field inside block. The anchor bar prevents the large displacement and deformation between blocks.

6 Practical Application

The characters of surrounding rock, such as the fault, shear zone, and anisotropic deformation, may result in the large deformation and large deformation in the surrounding rock masses system. The stability analysis of surrounding rock masses system is important content in the complex deformation of the large underground excavating engineering.

6.1 General Description of Underground Powerhouse

The underground water diversion and power generation system is roughly divided into diversion system, power plant system, and tailrace system. The detailed components contain nine diversion tunnels, main power plant, nine busbar tunnels, main transformer chamber, three surge chambers, and nine tailrace tunnels. The sizes of main powerhouse are $388.5 \times 31.3 \times 74.5$ m (length \times width \times height). The wall thickness between main power plant and transformer chambers is 43 m. The sizes of transformer chamber are $405.5 \times 19.5 \times 33.5$ m. The wall thickness between transformer and surge chambers is 27 m. The surge chambers are arranged in a straight line and the sizes of surge chambers are, respectively, $67.0 \times 21.5 \times 89.5$, $74.5 \times 21.5 \times 89.5$, and $95.5 \times 21.5 \times 89.5$ m.

The rock stratum is monoclinical structure, and stratigraphic occurrence is $345^\circ\text{--}355^\circ/\text{NE}<57^\circ\text{--}60^\circ$ in the surrounding rock. In the model of surrounding rock block system, four major faults are F1, F5, F12, and F18, in which F5, F12, and F18 are arranged in parallel and F1 intersects with the other faults. The finite element mesh of surrounding rock block system is shown in Fig. 4, and the finite element mesh of the intersection of the major faults and the underground water diversion and power generation system is shown in Fig. 5.

6.2 Stability Analysis of Surrounding Rock

The surrounding rock block system is composed of eight rock blocks divided by the major faults. The constrain functions contain that the displacement of the surfaces $x = -176, 176$ are zero in the x direction, the displacement of the surfaces $z = 0, -554$ are zero in the z direction and the displacement of the surfaces $y = -246$ are zero in the x, y, z directions. The material constants of isotropic block are: the unit weight $\gamma = 26000$ kN/m³, Young's modulus $E = 20$ GPa, Poisson's ratio $\nu = 0.24$, the inner cohesion $C = 0$, and internal friction angle $\varphi = 0.15^\circ$. The length and cross-sectional area of linear elastic deformation rock blot are, respectively, 30 m and 0.1 m², and the Young's modulus is $E = 20$ GPa.

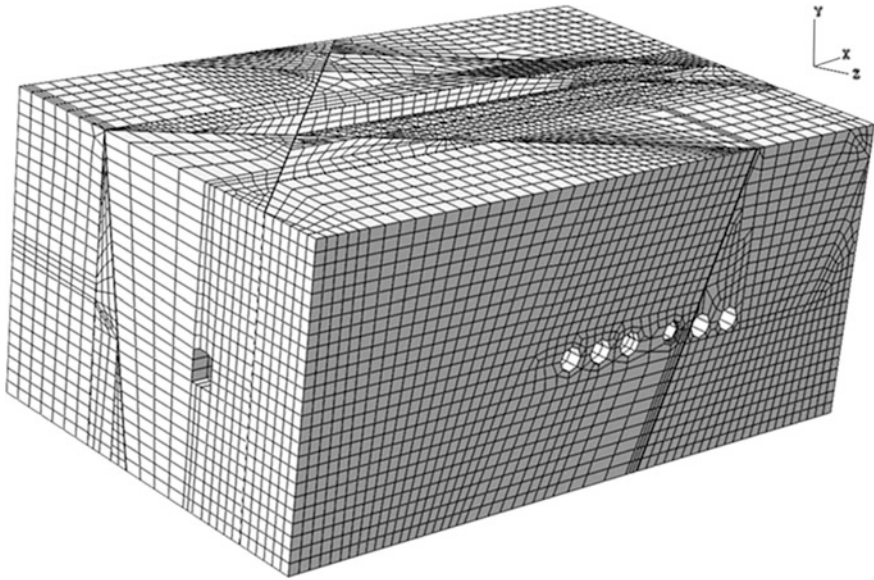


Fig. 4 Surrounding rock with element mesh

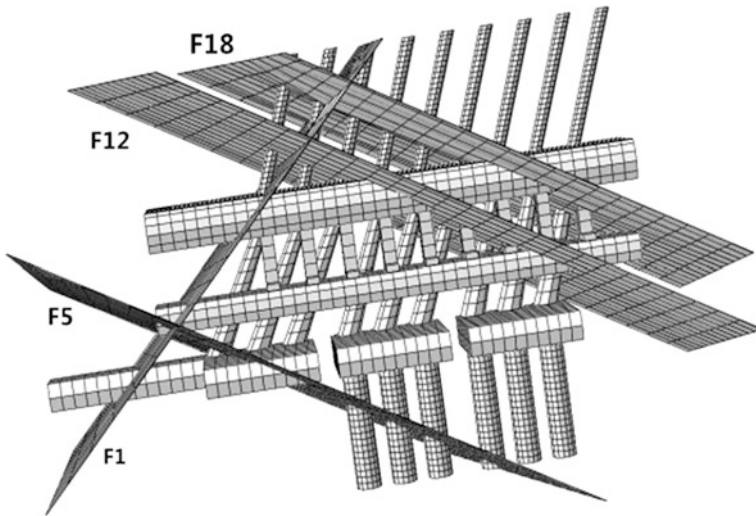


Fig. 5 Underground excavation and faults with element mesh

Since the faults have a great influence on the stability of the surrounding rock block system of underground water diversion and power generation system, the faults of surrounding rock at the across section of $z = -390$ m is shown in Fig. 6 and the distribution of anchor bar in specific section is shown in Fig. 7.

Fig. 6 Model of specific across section in surrounding rock masses system

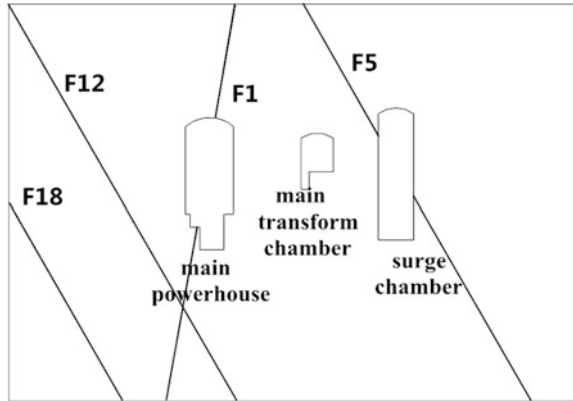
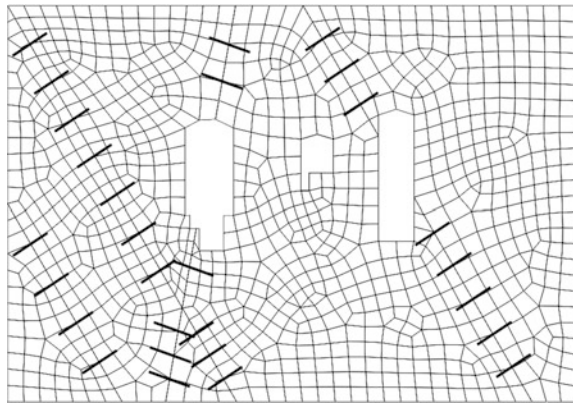


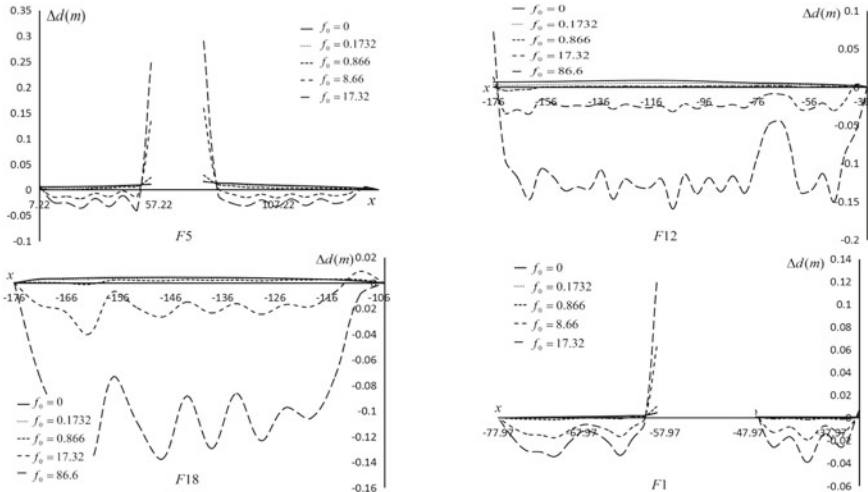
Fig. 7 Distribution of anchor bars in the across section



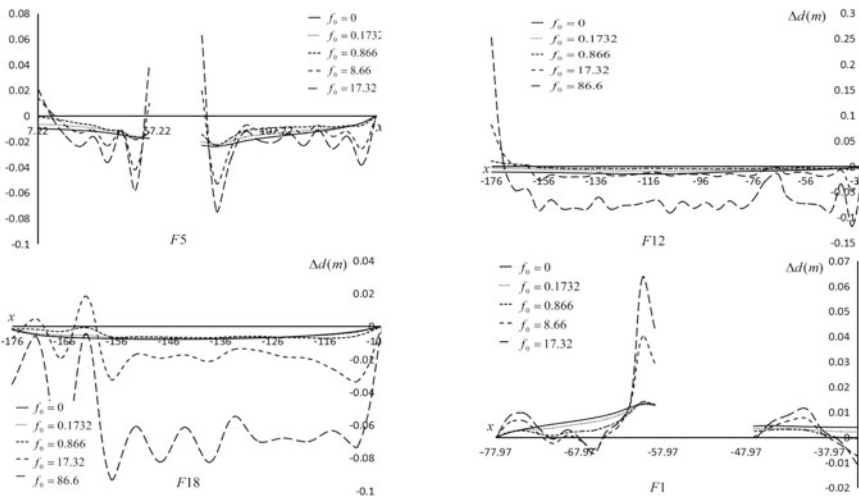
The prestressed anchor bar becomes the main anchorage measure and prevents the displacement of surrounding rock masses system. Suppose the finite element i in block Ω_1 and the finite element j in block Ω_2 is connected by anchor bar, the node submatrices in coefficient matrices $-[\mathbf{G}]_i \mathbf{f}_0$ and $-[\mathbf{G}]_j \mathbf{f}_0$ are added into the corresponding submatrices of the block system generalized force vector f .

$$\begin{aligned}
 -[\mathbf{G}]_i \mathbf{f}_0 &\rightarrow -[\mathbf{N}]_i^T (l_x \ l_y \ l_z)^T \mathbf{f}_0 \rightarrow \mathbf{f}_i \\
 -[\mathbf{G}]_j \mathbf{f}_0 &\rightarrow -[\mathbf{N}]_j^T (l_x \ l_y \ l_z)^T \mathbf{f}_0 \rightarrow \mathbf{f}_j
 \end{aligned}
 \tag{39}$$

When the anchor bar in different initial stress conditions is applied to reinforce the surrounding rock masses system, the relative displacements of contact surfaces between rock masses in the X, Y, Z axis directions are, respectively, shown in Fig. 8a–c. The results indicate that the increasing initial stress condition of anchor bar reduces the relative displacements, but the over-large initial stress condition of rock masses increases the relative displacement of contact surfaces between rock



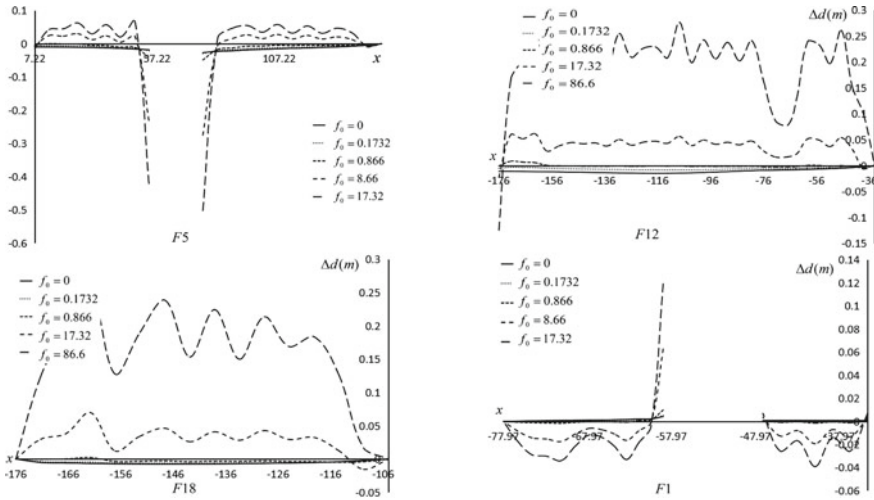
(a) Relative displacements of four major faults in the X axis direction



(b) Relative displacements of major faults in the Y axis direction

Fig. 8 Relative displacements of contact surfaces between rock masses in specific cross section

masses. When the installation of anchor bar is shown in Fig. 8 and the initial stress condition of anchor bar is 0.866 GPa, the relative displacements of contact surfaces between rock masses are minimum. The minimum relative displacement is the most stable surrounding rock of underground water diversion and power generation system.



(c) Relative displacements of major faults in the Z axis direction

Fig. 8 (continued)

7 Conclusion

According to the complementary discontinuous deformation analysis, the study proposes to extend the CDDA to solve three-dimensional block system and presents the coupling method of 3D CDDA and FEM. The novel coupling method enhances the ability of the displacement field and the stress field inside block and describes the large displacement and large deformation between rock masses. The coupling method of 3D CDDA-FEM eliminates the penalty factor and the open-close iteration of the block system. The corresponding numerical model of anchor bar is established to analyze the stability of anchor bar-surrounding rock masses system.

The simple numerical examples demonstrate that the 3D-CDDA can solve the accurate displacement solutions of block system, and the coupling method of 3D CDDA-FEM is feasible to precisely simulate the anchor bar-surrounding rock masses system. The surrounding rock of underground water diversion and power generation system demonstrates that the prestressed anchor bars prevent the large displacement and large deformation of the surrounding rock masses system. So the coupling method of 3D CDDA-FEM is available for the stability analysis of the anchor bar-surrounding rock masses system, and the prestressed anchor bar improves the stability of surrounding rock masses system.

Acknowledgements The authors would like to thank Dr. Liu Jun and Jiang Wei Maura of China for providing the references about the theory and application of novel coupling of 3D CDDA and FEM. The research is supported by the National Nature Science Foundation of China No. 51279053 and Fundamental Research Funds for the Central Universities No. 2014B00481.

References

1. Aydan O (1989) The stabilisation of rock engineering structures by rockbolts. Ph.D. Thesis, Nagoya University, Japan
2. Peng SS, Tang DHY (1984) Roof bolting in underground mining: a state of the art review. *Int J Min Eng* 2:1–42
3. A Anders (2005) Laboratory testing of a new type of energy absorbing rock bolt. *Tunn Undergr Space Technol* 20:291–300
4. Carranza -T (2009) Analytical and numerical study of the mechanics of rockbolt reinforcement around tunnels in rock masses. *Rock Mech. Rock Eng* 42:175–228
5. Bobet A, Einstein HH (2011) Tunnel reinforcement with rockbolts. *Tunn Undergr Space Technol* 26:100–123
6. Chen Yu (2015) Charlie Chunlin Li Performance of fully encapsulated rebar bolts and D-Bolts under combined pull-and-shear loading. *Tunn Undergr Space Technol* 45:99–106
7. Kılıc A, Yasar E, Celik AG (2002) Effect of grout properties on the pull-out load capacity of fully grouted rock bolt. *Tunn Undergr Space Technol* 17:355–362
8. Li B, Qi T, Zhengzheng W, Yang L (2012) Back analysis of grouted rock bolt pullout strength parameters from field tests. *Tunn Undergr Space Technol* 28:345–349
9. Cai Y, Esaki T, Yu JJ (2004) An analytical model to predict axial load in grouted rock bolt for soft rock tunnelling. *Tunn Undergr Space Technol* 19:607–618
10. Kim YI, Amadei B, Pan E (1999) Modeling the effect of water, excavation sequence and rock reinforcement with discontinuous deformation analysis. *Int J Rock Mech Min Sci* 36:949–970
11. Jiang Q-H, Zhou C-B (2007) Some issues in discontinuous deformation analysis for geotechnical engineering. *Chinese J Rock Mech Eng* 26(10):2014–2026
12. Liu J, Kong X-J (2007) Numerical simulation of behavior of jointed rock masses during tunneling and lining of tunnels. *Rock Soil Mech* 28(2):321–326
13. Moosavi M, Grayeli R (2006) A model for cable bolt-rock mass interaction: Integration with discontinuous deformation analysis (DDA) algorithm. *Int J Rock Mech Min Sci* 43:661–670
14. Jiang Q-H (2000) Research on three dimensional discontinuous deformation analysis method. Thesis, Wuhan Institute of Rock & Soil Mechanics, Chinese Academy of Sciences, Wuhan, P. R. China
15. Ke TC (1997) Improved modeling of rockbolting in DDA. In: *Proceedings of 9th International on Computer Methods and Advances in Geomechanics*, Wuhan, China, pp 483–488
16. Zheng C (2010) Study on hydro-mechanical coupling of fractured rock mass based on DDA. Ph.D Thesis, Shandong University, Jinan, P.R. China
17. Yimin WU (2003) Research on three dimensional discontinuous deformation analysis method for jointed rock mass and its application. Ph.D Thesis, Wuhan University, Wuhan, P.R. China
18. Jiang W (2009) Discontinuous deformation analysis method based on complementary theory. Wuhan Institute of Rock and Soil Mechanics of the Chinese Academy of Sciences, P.R. China
19. Liu J (2001) Three dimensional discontinuous deformation analysis coupled with finite element method. Ph. D. Thesis, Dalian University of Technology, Dalian, P.R. China
20. Jun Liu, Xianjing Kong (2002) Three dimensional continuous and discontinuous deformation analysis. *Acta Mech Sin* 34(6):941–948
21. Qinghui J, Chuang-binge Z, Xian-qi L, Hong Z (2006) Coupling method of three-dimensional DDA-FEM and its application. *Chinese J Geotech Eng* 28(8):998–1001

Part IX
Computational Mechatronics

Analysis and Summarization of a Mechanism Featuring Variable Stiffness



Do Xuan Phu, Nguyen Quoc Hung and Ta Duc Huy

Abstract This study presents the analysis of a novel mechanism based on the summarization of conventional models and gyroscope. The theoretical mechanism employs a nonlinear spring and a cantilever beam. This system has only one fixed support for the spring, and one non-contacted support to prevent the impact of friction in operation for cantilever beam. Exciting forces apply to the structure, including vertical and horizontal forces, and a moment. The cantilever beam is symbolized as an Euler–Bernoulli beam which has nonlinear property. After formulating, detections along the 2D coordinate are pointed out by using a nonlinear approximate method as Adomian decomposition method. The results of this method are compared with the numerical method. It is shown that the values of analysis and the numerical simulation are consistent with small errors. In addition, vibrations of the tip mass which is attached at the end of the beam are derived and simulated. The results of the tip mass vibrations are harmonic responses which prove that vibrations of any system always remain under harmonic conditions. This finding and the mentioned results are the base for the development of the new mechanism for both sensors and energy-harvesting devices.

Keywords Adomian decomposition method • Euler–Bernoulli beam
Tip mass vibrations • Flexible beam • Energy-harvesting device

D. X. Phu (✉) • T. D. Huy

Department of Mechatronics and Sensor System Technology, Vietnamese-German
University, Binh Duong Province, Vietnam
e-mail: phu.dx@vgu.edu.vn

T. D. Huy
e-mail: msst2016_huy.td@student.vgu.edu.vn

N. Q. Hung
Department of Computational Engineering, Vietnamese-German University,
Binh Duong Province, Vietnam
e-mail: hung.nq@vgu.edu.vn

© Springer Nature Singapore Pte Ltd. 2018

H. Nguyen-Xuan et al. (eds.), *Proceedings of the International Conference
on Advances in Computational Mechanics 2017*, Lecture Notes in Mechanical
Engineering, https://doi.org/10.1007/978-981-10-7149-2_68

977

1 Introduction

Energy-harvesting devices have been rapidly developing following miniature structure as small as possible. Symbolic developments for this trend are listed in MEMS and NEMS sensors. To serve the structures in energy harvesting, new compliant mechanisms must be invented which inherit advanced properties of conventional models and expand new characteristics pursuing the requirements of the design. There are numerous researches of design and analysis concerning compliant mechanisms. Firstly, a relevant review of bistable system is given. What is the bistable system? Why the bistable structure is applied? To answer these two main questions, it is useful to give a revision on some background knowledge. Normally, there always exists one stable point in a system which can be calculated with mathematical tools. However, this position restricts the ability of the energy-harvesting device in finding vibration frequencies that lie outside the range of equilibrium. Hence, an added stable position aids the expansion of the capacity of the system. This idea has been examined and applied in many studies. In the design of the bistable structure, the characteristic of the spring component is important. Hooke's law is conventionally used to derive the governing equation, but it is not recommended for use to find the equation for the bistable system. The spring must be derived as nonlinear equation where its exponent follows a three-order [1]. The governing equation is also called as Duffing equation. Hence, the structure using Duffing equation is also named as Duffing oscillator. However, a dis-advanced problem of bistable system is that it is difficult to view bistable points. A solution to this problem is applying smart material such as piezoelectric for the control of vibration and two permanent magnets to hold the positions of the system [2]. This solution needs an energy supply for the control of vibration, and energy from the permanent magnetic to the remaining two stable points. It is not difficult if it is a large-scaled system, but the big problem arises if this is applied to the micro-scale system. A general review of bistable system is also transparently given [3]. It can be noticed that the transition of a bistable system could cause large amplitude in motion and could dramatically increase the generated power. This advanced property and the capacity of measurement across a broad-frequency bandwidth make the bistable structure superior. Hence, the application of bistable characteristic to the proposed design is necessary and encouraging. Beside the bistable structure, conventional models which have only one stable point have always been intensively researched. As aforementioned, the bistable mechanism can expand the bandwidth of measurement. But it is not always applied because of commercial aspects, its arrangements, and control. Especially in narrow bandwidth range, the bistable mechanism is not suitable thus we can only resort to the use of conventional structures. There are numerous studies of these structures and the derivation of their characteristic with mathematical tools. In most cases, the Euler–Bernoulli beam and its equation are used for modeling in the study of energy-harvesting systems. It was used in [4] which applied in large deflection of the beam. To solve this equation, the authors used the Cartesian method. It can be noted that the complexity of solving the

equation is decreased by using two exciting forces including vertical force and moment. Similarly, the model of Euler–Bernoulli beam is also used [5]. This study focuses on large deflection with three exciting forces, including vertical force, axial force, and moment. The study was as a synthesis research of methods for finding the result of nonlinear equation such as shooting method, Adomian decomposition method. It is emphasized that the structure in [5] is conventional model which is commonly studied in energy harvesting. Another approach for Euler–Bernoulli equation is the integral method which applied large deflection in [6]. The model [6] is also conventional, and only the vertical force is applied. The Euler–Bernoulli equation can be used for a curved beam with an axial load which is used in [7]. Comprehensive elliptic integral solution for large deflection was thoroughly studied [8]. A planar beam flexure with a tip mass was studied [9] under large deflections. In [9], Hamilton’s principle used to derive the governing equations, and there were solved by using multiple time scales perturbation technique. The Timoshenko beam theory was also used to derive the governing equation in [10]. The elliptic integral method was comprehensively studied [11]. The Euler–Bernoulli beam theory has been surveyed, and the elliptic method has been applied to analyze the cycles of three equations such as angular, vertical, and axial deflections. Application of piezoelectric material to the cantilever beam with the tip mass has been presented [12]. This structure has been studied for its stiffness tunable energy harvester. A full study of parametric response for the cantilever beam with a tip mass-based Timoshenko beam theory has been studied [13]. It has been shown that an increase in the tip mass would reduce the stable periodic region with a known excitation. A simple method based on analysis of angular deflection of the cantilever beam has been suggested [14]. This method is a predicted method and cannot be used in complicated systems. Another mechanism should be noted in the design as a gyroscope. This mechanism is designed using conventional model and can be improved by applying the bistable system. It should be noted that the vibration relating mass is also one of the most important to find for the understanding of the gyroscope and then to use these properties to design another measurement. From the above analysis, the conventional model with cantilever beam/or elastic element is always a main structure for the design of energy harvest. The energy-harvesting devices are concentrated in three groups such as the bistable system, the conventional system, and the gyroscopes. To symbolize these models, the Euler–Bernoulli equation is used and its boundary conditions vary following the required system. Its dynamic parameters are found through many approaches such as Cartesian method [4], elliptic integral method [7, 8, 11], predictive method [14], and approximate method [5, 6, 9]. These tools are nonlinear approach hence they can find the exact values of the system. Hence, the application of nonlinear tools to find the solutions for the proposed model is useful to evaluate the operation before manufacturing. In this study, the models of three groups of energy-harvesting are reassessed to derive a new breakthrough model. This model also inherits the properties of the conventional model and can be expanded to develop high-level models such as a gyroscope. These characteristics are essential for new design of sensors and open new doors for the exploitation of the potential of simple mechanisms.

2 Configuration of the Proposed System

The configuration of the proposed system is depicted in Fig. 4. This configuration includes a nonlinear spring and a cantilever beam with a tip mass. The weight of the tip mass can be designed larger than the cantilever beam in this proposed system. The support of the system is of non-contacted type which has objective to eliminate friction. Hence, some solutions can be chosen for this support such as magnetic devices, electric magnet coil, pointed bearing mount. To analyze the dynamical responses, there are three exciting forces applied to the system, including vertical force, horizontal or axial force, and a moment. Hence, the system is analyzed according to the three forces to show a full-view of vibration of the system, which differentiates itself from the previous studies in choosing one/or two exciting forces for evaluation. A brief summary of operation of the system is given. When the forces are applied, the cantilever beam is vibrated in two dimensions due to vertical and horizontal/or axial vibrations. These vibrations are related and affect the stability of the system. It is noted that the proposed structure does not study the angular velocity of the cantilever beam. Because of the vibrations, the tip mass connected to the cantilever beam is also detected. In these vibrations, it is assumed that the system is symmetric and there is no torsional phenomenon in the section of the beam. In the next sections, the proposed system is derived into two cases: the fixed and the flexible tip mass to find the equations.

3 Non-linear Analysis for the Fixed Tip Mass

In this section, the proposed model is derived based on nonlinear equation. The proposed system is shown in Fig. 1, and its governing equation is obtained based on Euler–Bernoulli equation. Firstly, the moment acting at any point (x, y) on the proposed system is defined by:

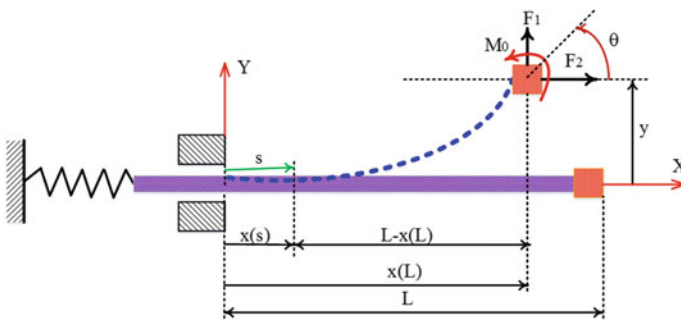


Fig. 1 Configuration of the proposed system

$$M(x, y) = F_y(x(L) - x) - F_x(y(L) - y) + M_0 \tag{1}$$

where L is the length of the cantilever (m), F_x is the axial force (N), F_y is the vertical force (N), L_y^{\max} is the maximal deflection following vertical direction, M_0 is the exciting moment (N.m), δ_x is the axial deflection (m), x and y are the coordinates of the beam. In this analysis, the angular deflection $d\theta$ of the cantilever is determined with respect to the curvature ds of the beam. Using the Euler–Bernoulli moment–curvature relationship, Eq. (1) following small curvature ds can be calculated as:

$$EI \frac{d\theta}{ds} = F_y(x(L) - x) - F_x(y(L) - y) + M_0 \tag{2}$$

where θ is the angular deflection (rad), E is the elastic modulus of cantilever material N/m^2 , I is the inertial moment of cross section of the cantilever beam m^4 , y is the vertical deflection (m), s is the position as a function of the curved deflection of the beam. It is noted that $x(L)$ is the axial position at the end of the cantilever. Taking differentiation of (2), the Euler–Bernoulli moment–curvature relationship can be written as:

$$EI \frac{d^2\theta}{ds^2} = F_x \frac{dy}{ds} - F_y \frac{dx}{ds} \tag{3}$$

From Eq. (3), equations for vibration following the vertical and axial directions are expressed as nonlinear equations:

$$\frac{dx}{ds} = \cos(\theta), \frac{dy}{ds} = \sin(\theta) \tag{4}$$

Substituting (4) into (3), the Euler–Bernoulli moment–curvature relationship can be rewritten as:

$$\frac{d^2\theta}{ds^2} = \frac{1}{EI} (F_x \sin(\theta) - F_y \cos(\theta)) \tag{5}$$

Equation (5) can be written as:

$$\theta \frac{d\theta}{ds} = \frac{1}{EI} (F_x \sin(\theta) - F_y \cos(\theta)) \tag{6}$$

Integrating the left-hand side of (6) from $\theta(s)$ to $\theta_L = \frac{d\theta}{ds}(L) = \frac{M_0}{EI}$ and the right-hand side of (6) from $\theta(s)$ to $\theta_L = \theta(L)$, the relation between angular deflection and the curvature can be found as follows:

$$\int_{\theta}^{\theta_L} \theta d\theta = \int_{\theta}^{\theta_L} \frac{1}{EI} (F_x \sin(\theta) - F_y \cos(\theta)) d\theta \tag{7}$$

$$\frac{1}{2} \left(\frac{d\theta}{ds} \right)^2 = \frac{1}{EI} (-F_y \sin(\theta) - F_x \cos(\theta)) + F_y \sin(\theta_L) + F_x \cos(\theta_L) + \frac{M_0^2}{2E^2I^2} \tag{8}$$

Equation (8) can now be written as:

$$\left(\frac{d\theta}{ds} \right)^2 = \frac{2}{EI} (\beta - F_y \sin(\theta) - F_x \cos(\theta)) \tag{9}$$

where $\beta = F_y \sin(\theta_L) + F_x \cos(\theta_L) + \frac{M_0^2}{2E^2I^2}$. Hence, Eq. (8) can be rewritten as:

$$\frac{d\theta}{ds} = \pm \sqrt{\frac{2}{EI} \sqrt{\beta - F_y \sin(\theta) - F_x \cos(\theta)}} \tag{10}$$

It can be derived from Eq. (10) as follows:

$$s = \int_0^s ds = \sqrt{\frac{EI}{2}} \int_{\theta(0)}^{\theta(s)} \frac{d\theta}{\sqrt{\beta - F_y \sin(\theta) - F_x \cos(\theta)}} \tag{11}$$

Using Eq. (11) at $s = L$, it obtains:

$$\sqrt{\frac{2L^2}{EI}} = \int_{\theta(0)}^{\theta_L} \frac{d\theta}{\sqrt{\beta - F_y \sin(\theta) - F_x \cos(\theta)}} \tag{12}$$

Using non-dimensionless definitions, Eq. (12) is determined as:

$$\sqrt{2} = \int_{\theta(0)}^{\theta_L} \frac{d\theta}{\sqrt{\beta_1 - \alpha_y \sin(\theta) - \alpha_x \cos(\theta)}} \tag{13}$$

where $\alpha_x = \frac{F_x L^2}{EI}$, $\alpha_y = \frac{F_y L^2}{EI}$, $\beta_1 = \alpha_y \sin \theta_L - \alpha_x \cos \theta_L + \frac{1}{2} m^2$, $m = \frac{M_0 L}{EI}$. To find governed equation of vibration $x(s)$, Eq. (10) is modified as:

$$\frac{d\theta}{ds} = \frac{d\theta}{dx} \frac{dx}{ds} = \sqrt{\frac{2}{EI} \sqrt{\beta - F_y \sin(\theta) - F_x \cos(\theta)}} \tag{14}$$

Using (4), Eq. (14) is expressed as:

$$\frac{x(s)}{L} = \frac{1}{\sqrt{2}} \int_{\theta(0)}^{\theta(s)} \frac{\cos \theta d\theta}{\sqrt{\beta - \alpha_y \sin \theta - \alpha_x \cos \theta}} \tag{15}$$

Once again, the Eq. (10) is used for deriving the vibration $y(s)$, and it is modified as follows:

$$\frac{d\theta}{ds} = \frac{d\theta}{dy} \frac{dy}{ds} = \sqrt{\frac{2}{EI}} \sqrt{\beta - F_y \sin \theta - F_x \cos \theta} \tag{16}$$

Using (4), Eq. (16) is written as:

$$\frac{y}{L} = \frac{1}{\sqrt{2}} \int_{\theta(0)}^{\theta(s)} \frac{\sin \theta d\theta}{\sqrt{\beta - \alpha_y \sin \theta - \alpha_x \cos \theta}} \tag{17}$$

Finally, using Eqs. (1), (13), (15), and (17), values such as F_x , F_y , and $M(x, y)$ are found. Their summarization is expressed as follows:

$$\begin{aligned} \sqrt{2} &= \int_{\theta(0)}^{\theta_L} \frac{d\theta}{\sqrt{\beta_1 - \alpha_y \sin(\theta) - \alpha_x \cos(\theta)}}, \quad \frac{x(s)}{L} = \frac{1}{\sqrt{2}} \int_{\theta(0)}^{\theta(s)} \frac{\cos \theta d\theta}{\sqrt{\beta - \alpha_y \sin \theta - \alpha_x \cos \theta}}, \\ \frac{y}{L} &= \frac{1}{\sqrt{2}} \int_{\theta(0)}^{\theta(s)} \frac{\sin \theta d\theta}{\sqrt{\beta - \alpha_y \sin \theta - \alpha_x \cos \theta}} \end{aligned} \tag{18}$$

Equation (18) is the governing equation of the system. To solve this equation, there are numerous methods. In this study, the Adomian decomposition method (ADM) is used to find the approximate solutions. The equation group (18) is nonlinear and can be solved by applying approximate method. To simplify, Eq. (5) is used. Integrating (5) twice with respect to s :

$$\theta(s) = \theta(0) + \theta(L)s + \int_0^s \int_t^L N(z) dz dt \tag{19}$$

where $N(\theta) = -\frac{1}{EI} (F_x \sin \theta - F_y \cos \theta)$. Eq. (19) can be summarized as follows:

$$\theta(s) = \theta(0) + \gamma s + \ell^{-1} \left(\sum_{n=0}^{\infty} A_n \right) \tag{20}$$

where A_n are Adomian polynomials, $\gamma = \frac{M_0}{EI}$. Set $\theta(s) = \sum_{n=0}^{\infty} \theta_n(s)$. Hence, the components $\theta_n(s)$ can be computed by applying the recursive relation:

$$\begin{aligned} \theta_0 &= \theta(0) + \gamma s \\ \theta_n &= \mathcal{L}^{-1}(A_{n-1}) \end{aligned} \tag{21}$$

where Adomian polynomials for $f(\theta) = -\frac{1}{EI}(F_x \sin(\theta) - F_y \cos(\theta)) = -\frac{1}{L^2}(\alpha_x \sin(\theta) - \alpha_y \cos(\theta))$ are given by:

$$\begin{aligned} A_0 &= f(\theta_0) = -\frac{1}{L^2}(\alpha_x \sin \theta_0 - \alpha_y \cos \theta_0) \\ A_1 &= \theta_1 \frac{d}{d\theta_0} [f(\theta_0)] \\ A_2 &= \theta_2 \frac{df(\theta_0)}{d\theta_0} + \frac{\theta_1^2}{2!} \frac{d^2 f(\theta_0)}{d\theta_0^2} \\ A_3 &= \theta_3 \frac{df(\theta_0)}{d\theta_0} + \theta_1 \theta_2 \frac{d^2 f(\theta_0)}{d\theta_0^2} + \frac{\theta_1^3}{3!} \frac{d^3 f(\theta_0)}{d\theta_0^3} \end{aligned} \tag{22}$$

Substituting (22) into (20), the results of (20) are found as follows:

$$\begin{aligned} \theta_0(s) &= \gamma s \\ \theta_1(s) &= -\frac{1}{2L^2} [s(-2L + s)(\alpha_y \cos(\gamma s) - \alpha_x \sin(\gamma s))] \\ \theta_2(s) &= -\frac{1}{4L^2} \left[s^2(-2L + s)^2 (\alpha_y \cos(\gamma s) - \alpha_x \sin(\gamma s)) (\alpha_y \sin(\gamma s) + \alpha_x \cos(\gamma s)) \right] \\ \theta_3(s) &= -\frac{1}{32L^6} [-\alpha_y \cos(\gamma s) + \alpha_x \sin(\gamma s)] [\alpha_x^2 + \alpha_y^2 + 3(\alpha_x^2 - \alpha_y^2) \cos(2\gamma s) + 6\alpha_x \alpha_y \sin(2\gamma s)] \end{aligned} \tag{23}$$

Therefore, the approximate result of $\theta(s)$ is expressed as:

$$\theta(s) = \theta_0(s) + \theta_1(s) + \theta_2(s) + \theta_3(s) \tag{24}$$

Using (4) and (22), the positions of $x(s)$ and $y(s)$ are calculated as follows:

$$x(s) = s - \frac{(\alpha_y + m)^2 s^3}{6L^2} + \frac{(\alpha_y + m)(\alpha_y + 2\alpha_x \alpha_y + 2m\alpha_x) s^4}{8L^3} \tag{25}$$

$$y(s) = \frac{1}{2L} (\alpha_y + m) s^2 - \frac{(\alpha_y + 2\alpha_x \alpha_y + 2m\alpha_x) s^3}{6L^2} \tag{26}$$

To find the values of forces following vertical and horizontal vibrations, the relations of α_x and α_y in (25) and (26) must be found. Equations (23) and (24) at the end of cantilever beam $s = L$ are determined as:

$$\Delta\theta(L) = \frac{1}{2}\alpha_y + m - \alpha_x(\alpha_y + m) \quad (27)$$

$$\Delta x(L) = L - \frac{1}{6}L(\alpha_y + m)^2 + \frac{1}{8}L(\alpha_y + m)(\alpha_y + 2\alpha_x\alpha_y + 2\alpha_x m) \quad (28)$$

$$\Delta y(L) = \frac{1}{2}L(\alpha_y + m) - \frac{1}{6}L(\alpha_y + 2\alpha_x\alpha_y + 2\alpha_x m) \quad (29)$$

4 Nonlinear Analysis of the Rotating Tip Mass

In this section, the vibration of the tip mass is analyzed based on the results of the former section. Using (27), two Eqs. (28) and (29) can be written as follows:

$$\Delta\theta(L) = -\frac{1}{2}\alpha_y + \gamma_m L - \frac{1}{2}\alpha_x^m \gamma_m L \quad (30)$$

$$\Delta x(L) = L - \frac{1}{6}L(\alpha_y^m - \gamma_m L)^2 \quad (31)$$

$$\Delta y(L) = \frac{1}{24} \left[\alpha_y^m \left(-8 + (\alpha_y^m)^2 + \left(12 - 5\alpha_x^m - 3(\alpha_y^m)^2 \right) \gamma_m L + 3\alpha_y^m \gamma_m^2 L - \gamma_m^3 L^3 \right) \right] \quad (32)$$

Solving three Eqs. (30), (31), and (32), the relations of external forces γ_m , α_x^m , and α_y^m applying to the tip mass with internal parameters of the system are expressed as:

$$\gamma_m = \frac{1}{2L^6} \left[-48\Delta y L^4 + 20\Delta\theta L^5 \pm 3\sqrt{6}(5\Delta x + 3L)L^4 \right] \quad (33)$$

$$\alpha_x^m = \mp \frac{2}{27L^5} \left[\pm 9\Delta x L^4 + L^4 \sqrt{6}(-6\Delta y + \Delta\theta L) \right] \quad (34)$$

$$\alpha_y^m = \mp \frac{1}{L^5} \left[\mp 24\Delta y L^4 \pm 10\Delta\theta L^5 + 4L^4 \sqrt{6}(2\Delta x + L) \right] \quad (35)$$

It is noted that values of γ_m , α_x^m , and α_y^m are expanded by using Maclaurin series following $\Delta\theta$, Δx , and Δy . From these values, values of the moment M_m , the vertical force F_x^m , and the horizontal force F_y^m are found. For the simplicity of finding vibrations of the tip mass, conventional method such as Castigliano's method is used [14]. This method [14] is applied to the system based on the cantilever beam with an external exciting force/or moment. Hence, maximal values of moment, the vertical force, and the axial force of the tip mass are found as:

$$M_m = \frac{2EI}{L^2} \Delta y, F_x^m = -\frac{AE}{L} \Delta x, F_y^m = -\frac{EI}{L^3} \Delta y \tag{36}$$

The variations of positions of the rotating tip mass are determined as:

$$\dot{\theta} = \frac{2M_0}{m_D R^2}, \ddot{X} = \frac{F_x}{m_D}, \ddot{Y} = \frac{F_y}{m_D} \tag{37}$$

where m_D is the mass of the tip mass (kg), R is the radius of the tip mass.

5 Simulation Results and Discussion

5.1 Simulation Results for the Fixed Tip Mass System

After formulating, the proposed system is simulated through two methods: numerical method and Adomian method as shown in the above analysis. The simulations are carried out with two cases: change of axial load F_x and vertical load F_y . The results of the first simulation with varied values of F_x are depicted in Fig. 2. In this simulation, small values of F_x , F_y , and M_0 are used. It is noted that it is useful to evaluate responses of this system in small exciting force F_x in three cases: (1) $F_x = 10^{-4}$ N, $F_y = 10^{-3}$ N, $M_0 = 10^{-1}$ Nm, (2) $F_x = 10^{-2}$ N, $F_y = 10^{-3}$ N,

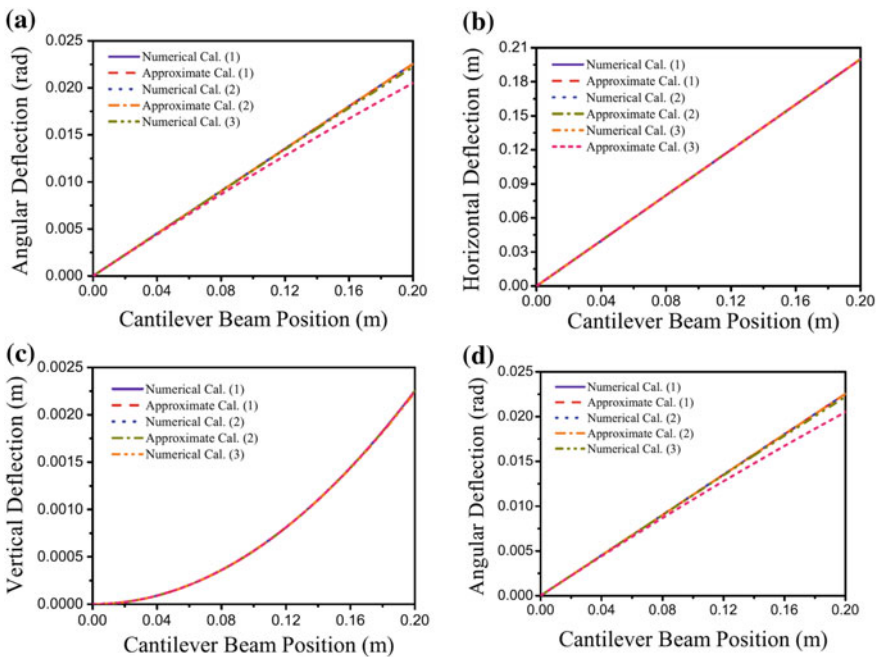


Fig. 2 Simulation results with variation of F_x

$M_0 = 10^{-1}$ Nm, (3) $F_x = 1$ N, $F_y = 10^{-3}$ N, $M_0 = 10^{-1}$ Nm. It is noted that the cantilever beam position follows the arc length in vibration, and values of two vibrations as vertical force F_y and moment M_0 are fixed. The angular deflection of three cases is shown in Fig. 2a. It is shown that the force F_x increases at maximal values are 2.26×10^{-2} (numerical method)/ 2.26×10^{-2} rad (approximate method), 2.26×10^{-2} rad/ 2.25×10^{-2} rad, 2.22×10^{-2} rad/ 2.05×10^{-2} rad for case (1), case (2), and case (3), respectively. Besides, the approximate method is also not stable compared with the numerical method. Responses of horizontal and vertical deflections are shown in Fig. 2c–d. In Fig. 2b and c, the approximate method shows its outstanding calculation compared with the numerical method. Horizontal deflection of three cases is similar, and there are no changes after varying the magnitude of axial force. Variation of horizontal deflection is linear with the position of the cantilever beam. The maximal values for horizontal deflection are 0.1998 m/0.2 m for three cases. The maximal values for vertical deflection are 2.26×10^{-3} m/ 2.25×10^{-3} m, 2.26×10^{-3} m/ 2.25×10^{-3} m, 2.24×10^{-3} m/ 2.25×10^{-3} m for case (1), case (2), and case (3), respectively. Summarization of two deflections is vertical and horizontal deflections depicted in Fig. 2d. In second simulation, it is performed following various vertical force F_y . Figure 3 shows results of variation of vertical exciting force F_y in three cases: (1) $F_x = 10^{-4}$ N, $F_y = 10^{-3}$ N, $M_0 = 10^{-1}$ Nm, (2) $F_x = 10^{-4}$ N, $F_y = 10^{-1}$ N,

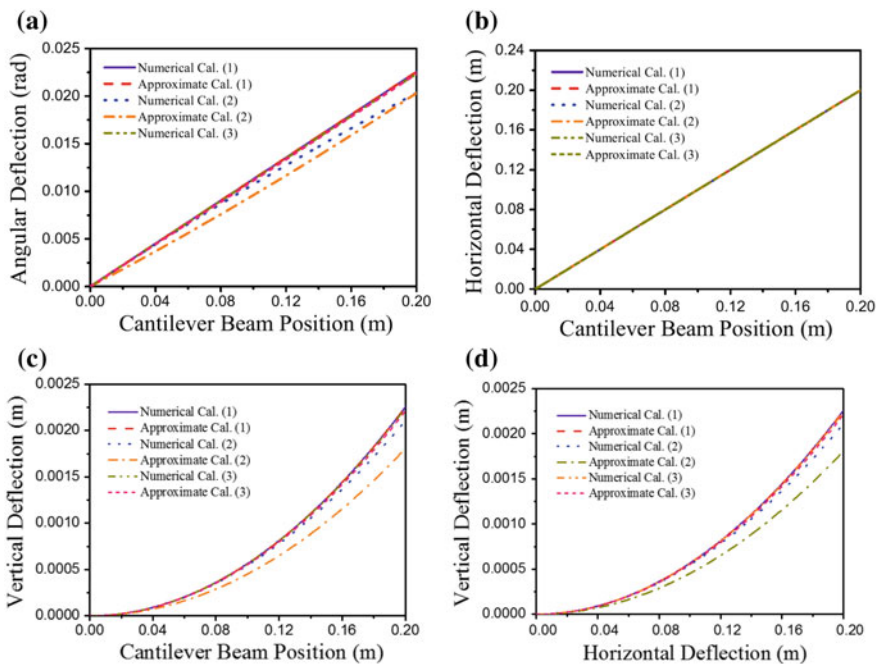


Fig. 3 Simulation results with variation of F_y

$M_0 = 10^{-1}$ Nm, (3) $F_x = 10^{-4}$ N, $F_y = 10^{-2}$ N, $M_0 = 10^{-1}$ Nm. The angular deflection of three cases is shown in Fig. 3a. It is shown that if the force F_y increases, the angular deflection is also increases. In addition, the angular deflection is also not stable compared with the numerical method. Values of these results at maximal values are 2.2552×10^{-2} rad (numerical method)/ 2.2552×10^{-2} rad (approximate method), 2.0319×10^{-2} rad/ $2.0317 \cdot 10^{-2}$ rad, 2.2349×10^{-2} rad/ 2.2349×10^{-2} rad for case (1), case (2), and case (3), respectively. Responses of horizontal and vertical deflection are shown in Fig. 3c–d. In Fig. 3b, the approximate method shows its outstanding calculation compared with numerical method. It is shown that the vertical force is not affected by the horizontal deflection, and variation of horizontal deflection is linear with the position of the cantilever beam. The maximal values for horizontal deflection are 0.19983 m/0.19983 m, 0.19985 m/0.19987 m, 0.19983 m/0.19983 m for case (1), case (2), and case (3), respectively. In Fig. 3c, vertical deflection of three cases is depicted. The affection of vertical force to its responses is not stable. As the vertical force increases, the calculation performance of approximate method decreases. The maximal values for vertical deflection are $2.26 \cdot 10^{-3}$ m/ 2.25×10^{-3} m, 2.11×10^{-3} m/ 1.81×10^{-3} m, 2.24×10^{-3} m/ 2.21×10^{-3} m for case (1), case (2), and case (3), respectively. Summarization of two deflections of vertical and horizontal deflection is depicted in Fig. 3d. The above results show that responses are found through approximate method having small errors compared with the numerical method. Besides, the vibrations of the proposed system are stable, the values of deflection increase with respect to the cantilever position. These vibrations also show that there are similarly shaped as shown in the conventional method. This point proves that the proposed system has equivalent properties, and then can be applied in the design of energy-harvesting devices. It is noted that the breakthrough idea of the new mechanism guarantees flexible and efficient operation, erases the support of fixed end in vibration control.

5.2 Simulation Results for the Rotating Tip Mass System

The proposed system is continually simulated for the tip mass at the end of the cantilever. In this case, it is provided that the connection between the tip mass and the cantilever is flexible. Then the vibrations of the tip mass are separated from the beam. From the governing equations of the tip mass, simulation results are shown in Fig. 4.

The parameters for this simulation are similar to the first case of F_x . It is shown that all responses of the tip mass are harmonic vibrations. Because of vibration of the cantilever, the angular deflection of the tip mass is also harmonic. The axial deflection of the tip mass depicts clearly the extract and stretch at the end of the cantilever. This is different from the responses of horizontal deflection as shown in Figs. 2 and 3. Besides, the vertical vibration is also harmonic. These results show

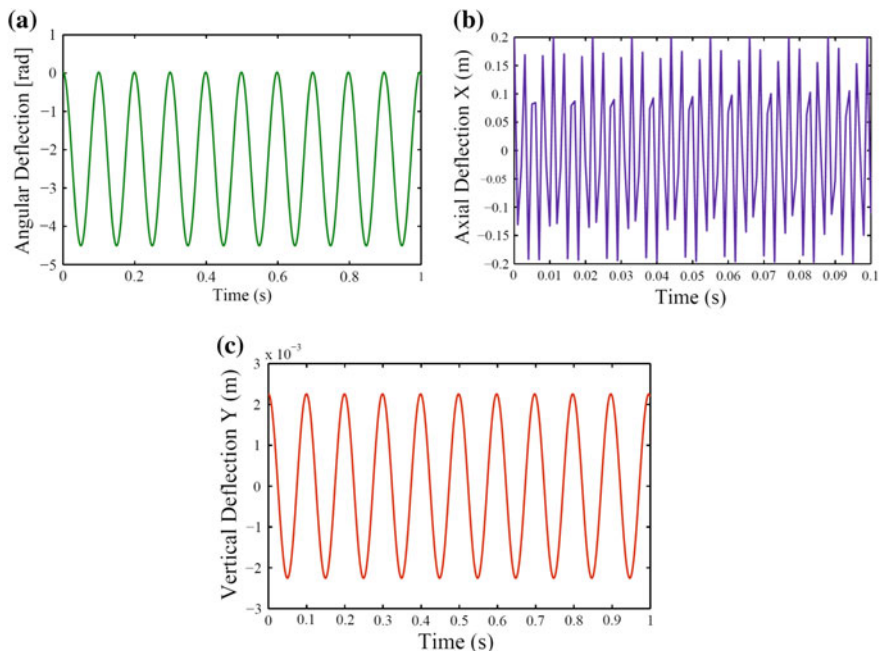


Fig. 4 Simulation results with variation of F_x

that the vibrations of the tip mass are always different from the cantilever. These vibrations also suggest a new solution for controlling the system. Instead of controlling the cantilever, the system can be controlled by adjusting the vibrations of the tip mass. This method is a purely mechanical model, and there is no involvement of external energy. Hence, this solution can save energy, retain its vibration based on the exciting vibrations.

6 Conclusion

The study has presented a new design of compliant mechanism with a nonlinear spring and a cantilever beam. The proposed model is analyzed based on Euler–Bernoulli equation with three external forces such as vertical, horizontal forces and moment. After formulating, forces and moment of the rotating tip mass system are continuing to be derived based on the former Euler–Bernoulli equation. In these analyses, the nonlinear equations are solved by applying the nonlinear approaches such as Adomian decomposition method.

The results of the analysis are simulated with the numerical method. It is shown that the results are good and its performances can satisfy the requirements of the proposed system. The results show that the proposed system has the properties of

the conventional model which is the base for the development of the structure of bistable system energy-harvesting devices, compliant of robotics, MEMS devices. In addition, this study also finds a new method which can control the system through mechanical mechanism without external energy. This exploitation is important in the mechanism where saving energy is crucially necessary. In the future, this model could be manufactured and could estimate its operation in a specific system.

Acknowledgements This research is funded by Vietnam National Foundation for Science and Technology Development (NAFOSTED) under grant number 107.01-2017.28.

References

1. DeMartini Barry E, Rhoads Jeffrey F, Turner Kimberly L, Shaw Steven W, Moehlis Jeff (2007) Linear and nonlinear tuning of parametrically excited MEMS oscillators. *J Microelectromech Syst* 16(2):310–318
2. Erturk A, Inman DJ (2011) Broadband piezoelectric power generation on high-energy orbits of the bistable Duffing oscillator with electromechanical coupling. *J Sound Vib* 330:2339–2353
3. Hame RL, Wang KW (2013) A review of the recent research on vibration energy harvesting via bistable systems. *Smart Mater Struct* 22:023001
4. Hafez T, Kinzel GL, Mendelsohn DA (2015) Cartesian and piece wise parametric large deflection solutions of tip point loaded Euler–Bernoulli cantilever beams. *Int J Mech Sci* 100: 216–225
5. Banerjee A, Bhattacharya B, Mallik AK (2008) Large deflection of cantilever beams with geometric non-linearity: analytical and numerical approaches. *Int J Non-Lin Mech* 43:366–376
6. Chen Li (2010) An integral approach for large deflection cantilever beams. *Int J Non-Lin Mech* 45:301–305
7. Carlos G, Javier L (2005) Stiffness of a curved beam subjected to axial load and large displacements. *Int J Solids Struct* 42: 1537–1545
8. Zhang A, Chen G (2013) A comprehensive elliptic integral solution to the large deflection problems of thin beams in compliant mechanisms. *J Mech Robot* 5:02100601–02100610
9. Moeenfard H, Awtar S (2014) Modeling geometric nonlinearities in the free vibration of a planar beam flexure with a tip mass. *J Mech Des* 136:04450201–04450208
10. Chen G, Ma F (2015) Kinetostatic modeling of fully compliant bistable mechanisms using timoshenko beam constraint model. *J Mech Des* 137:02230101–02230110
11. Dongxu Su, Nakano K, Zheng R, Cartmell Matthew P (2014) Investigations of a stiffness tunable nonlinear vibrational energy harvester. *Int J Struct Stab Dyn* 14(8):1440023
12. Esmailzadeh E, Jalili N (1998) Parametric response of cantilever timoshenko beams with tip mass under harmonic support motion. *Int. J. Non-Lin Mech* 33(5):765–781
13. Saxena A, Kramer SN (1998) A simple and accurate method for determining large deflections in compliant mechanisms subjected to end forces and moments. *Trans ASME* 120:392–400
14. Larry L (2001) Howell. Wiley, Compliant Mechanisms

Dynamic Analysis of Hydraulic–Mechanical System Using Proportional Valve



D. T. Luan, L. Q. Ngoc and P. H. Hoang

Abstract Power hydraulic systems are used very often in industry. Usually, the stroke of piston—a hydraulic actuator is controlled in on–off manner using traditional valves and start/stop switches on the moving way. Another characteristic of traditional hydraulic system is suitable with static load. For applying dynamic load, the behavior of system is not properly good. Nowadays, hydraulic systems with proportional valve are used commonly. Proportional valve allows controlling for a variable stroke of piston. It also allows the system work with variable load. This paper presents the dynamic analysis of a hydraulic–mechanical system using proportional directional valve. The system dynamics is evaluated when the load changes in linear manner. A mathematical model is established to serve for determining dynamic characteristics of the system. PID control is also used in the simulation to enhance the integrity of the system.

Keywords Dynamics • Hydraulic system • Proportional valve

1 Introduction

Hydraulic systems are widely in industry. Providing powerful force and having small size are the advantages of hydraulic system in comparative with electric systems. Proportional valves are significantly improved in frequency response,

D. T. Luan (✉) · P. H. Hoang

Faculty of Mechanical Engineering, Ho Chi Minh City University of Technology,
National University of Ho Chi Minh City, Ho Chi Minh City, Vietnam
e-mail: thanhluanbk@hcmut.edu.vn

P. H. Hoang

e-mail: phhoang@hcmut.edu.vn

L. Q. Ngoc

Industrial Maintenance Training Center, Ho Chi Minh City University of Technology,
National University of Ho Chi Minh City, Ho Chi Minh City, Vietnam
e-mail: lqngoc@hcmut.edu.vn

© Springer Nature Singapore Pte Ltd. 2018

H. Nguyen-Xuan et al. (eds.), *Proceedings of the International Conference on Advances in Computational Mechanics 2017*, Lecture Notes in Mechanical Engineering, https://doi.org/10.1007/978-981-10-7149-2_69

991

accuracy, feedback system, and dead band. Those improvements reduce the distinction between servo valves and proportional valves. Proportional valves can control actuators with more flexibility and lower cost than servo valves. Therefore, proportional valves are suitable to industrial applications. The only difficulty is the control of hydraulic systems with instability.

A lot of studies on proportional valves focus on the dead point of valves [1], dynamic analysis of coil of proportional valves [2], dynamic response of valve [3], dynamic analysis of fluid flow via valves [4]. Those studies just concentrate on the characteristics of proportional valves without any interaction with actuators, hydraulic–mechanical systems.

There are also some studies on hydraulic systems using proportional valves such as the theoretical and experimental analyses of symmetric-two-cylinder systems using proportional valves [5], study on the dynamical properties of hydraulic power systems [6, 7]. In these studies, the mathematical models are simplified with assumption of linearization of the hydraulic system. Actually, hydraulic systems work with nonlinear characteristics; therefore, the linearization is only accepted within a certain range, and this assumption reduces the authenticity of systems.

The control algorithms of hydraulic systems using proportional valves are recently studied. Sliding mode control is applied to a lifting arm with one cylinder [8]. Adaptive control is used for control fluid flow rate in a proportional valve [9]. Mino fuzzy is applied to force and position control of hydraulic cylinder [10]. PID control is also used to improve the control quality of hydraulic cylinder using proportional valve [11]. Generally, recent studies are performed with constant loads rather than variable load as in real systems. The studies also ignored the leakage, elasticity of fluid, and damping of system.

This paper presents a study of a hydraulic–mechanical system using a proportional valve and adhering to the real characteristics of the system in order to accurately describe the system response. Firstly, the differential equations of the dynamic hydraulic system with variable load are established. The equations represent the relationship between flow rate and pressure, the interaction of the valve with the hydraulic cylinder, the variable load causing system instability. The mathematical model is simulated using the MATLAB– Simulink to compare the position response of the cylinder according to the working time and the displacement of the cylinder, with a PID controller. The experiment is performed to validate the control. Research has clarified the dynamics characteristics of hydraulic–mechanical systems with linear change loads.

This study is the first step in studies of vibrator power using proportional valve with the accuracy ± 0.2 mm to test vehicle damping systems or vibration isolation systems. It is necessary to reduce cost of systems.

2 Experimental System

Figure 1 shows the schema of hydraulic–mechanical systems using proportional valve. The mechanical system includes a linear spring and a slider, which causes varied load. Hydraulic system is a linear cylinder actuated by a proportional directional control valve and controlled by a displacement transducer and a PID controller. The maximum flow rate of pump is set at 32 l/min at rotating speed of 1500 rpm. The pump pressure is set at 350 bar. The proportional valve (PONAR—made by the Netherlands) is a directional control valve with four ways and three positive overlaps. Table 1 describes technical characteristics of the valve. The areas of piston head and piston rod side correspondingly are 0.001963 m² và 0.001563 m². Maximum stroke of cylinder is 0.25 m. The variable resistor displacement transducer has resolution 0.01 kΩ/mm and accuracy ±0.05%.

3 Modeling of Dynamic System

The differential equations of the dynamic hydraulic system without considering friction are:

$$M\ddot{x}_p + B_{lx}\dot{x}_p + k_{lx}x_p = P_1A_1 - P_2A_2 \tag{1}$$

where

- M total mass of piston and load,
- x_p piston displacement,
- B_{lx} damping coefficient,

Fig. 1 Schema of the hydraulic–mechanical system

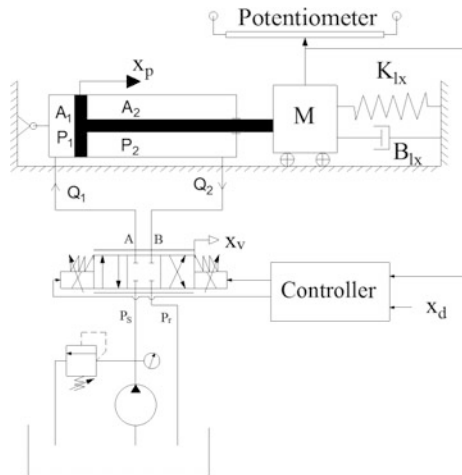


Table 1 Specification of the proportional directional valve

Rated pressure	315 bar
Rated flow	32 lpm
Rated voltage	24 V
Rated current	1.5 A
Resistance of max hot solenoid coil	8.1 Ω

k_{lx} spring stiffness,
 A_1, A_2 areas of the two chambers of the cylinder,
 P_1, P_2 pressures inside two chambers of the cylinder.

Differentiating Eq. 1, we have:

$$M\ddot{x}_p + B_{lx}\ddot{x}_p + k_{lx}\dot{x}_v = \dot{P}_1A_1 - \dot{P}_2A_2 \tag{2}$$

where

$$\begin{aligned} \dot{P}_1 &= \frac{\beta_e}{V_1} \left(Q_1 - A_1 \frac{dx_p}{dt} \right) \\ \dot{P}_2 &= \frac{\beta_e}{V_2} \left(A_2 \frac{dx_p}{dt} - Q_2 \right) \end{aligned} \tag{3}$$

and

$V_1 = V_0 + A_1x_p$ total volume of the first chamber,
 $V_2 = V_0 + A_2(L_0 - x_p)$ total volume of the second chamber,
 V_0 and L_0 dead volume and maximum stroke,
 β_e effective bulk modulus,
 Q_1 and Q_2 fluid flows at head side and rod side.

Flow rate of the valve can be considered as

$$\begin{aligned} Q_1 &= C_d\omega(|x_v| - \varepsilon)\sqrt{2\frac{\Delta P}{\rho}} \quad \Delta P = \begin{cases} P_s - P_1, & x_v \geq 0 \\ P_1 - P_r, & x_v < 0 \end{cases} \\ Q_2 &= C_d\omega(|x_v| - \varepsilon)\sqrt{2\frac{\Delta P}{\rho}} \quad \Delta P = \begin{cases} P_2 - P_r, & x_v \geq 0 \\ P_s - P_2, & x_v < 0 \end{cases} \end{aligned} \tag{4}$$

where

C_d discharge coefficient,
 ω width of the valve port, $\omega = \pi D$, with D —diameter of the valve port,
 x_v spool displacement,
 ε overlapping length,
 P_s supply pressure from the hydraulic pump,

P_r tank returned pressure

Assume that the displacement of spool x_v is proportional to the controlling current i in the coil of proportional valve

$$x_v = k_i i \tag{5}$$

When $x_v > \varepsilon \geq 0$, from Eqs. 4 and 5, we have

$$Q_1 = C_d \omega (k_i i - \varepsilon) \sqrt{2 \frac{P_s - P_1}{\rho}}$$

$$Q_2 = C_d \omega (k_i i - \varepsilon) \sqrt{2 \frac{P_2 - P_r}{\rho}}$$
(6)

Substituting Eqs. 6 and 3 into Eq. 2, we have

$$M \ddot{x}_p = -B_{lx} \ddot{x}_p - k_{lx} \dot{x}_p - \frac{\beta_e}{V_1} A_1^2 \dot{x}_p - \frac{\beta_e}{V_2} A_2^2 \dot{x}_p + C_d \omega (k_i i - \varepsilon) \left(\frac{\beta_e A_1 \sqrt{2(P_s - P_1)}}{V_1 \sqrt{\rho}} + \frac{\beta_e A_2 \sqrt{2(P_2 - P_r)}}{V_2 \sqrt{\rho}} \right)$$
(7)

Change:

$$y_1 = x_p$$

$$y_2 = \dot{x}_p$$

$$y_3 = \ddot{x}_p$$
(8)

We have:

$$\begin{cases} \dot{y}_1 = y_2 \\ \dot{y}_2 = y_3 \\ \dot{y}_3 = \ddot{x}_p = -\frac{B_{lx}}{M} y_3 - \left(\frac{k_{lx}}{M} + \frac{\beta_e}{M V_1} A_1^2 + \frac{\beta_e}{M V_2} A_2^2 \right) y_2 + \frac{C_d \omega}{M} \left(\frac{\beta_e A_1 \sqrt{2(P_s - P_1)}}{V_1 \sqrt{\rho}} + \frac{\beta_e A_2 \sqrt{2(P_2 - P_r)}}{V_2 \sqrt{\rho}} \right) (k_i i - \varepsilon) \end{cases}$$
(9)

The state-space equation of the system is

$$\dot{y} = Ay + Bu$$

where $y = \begin{bmatrix} \dot{y}_1 \\ \dot{y}_2 \\ \dot{y}_3 \end{bmatrix}$
and

$$A = \begin{bmatrix} 0 & 1 & 0 \\ 0 & 0 & 1 \\ 0 & -\left(\frac{K_{lx}}{M} + \frac{\beta_e}{MV_1}A_1^2 + \frac{\beta_e}{MV_2}A_2^2\right) & -\frac{B_v}{M} \end{bmatrix}; B = \begin{bmatrix} 0 \\ 0 \\ \frac{C_d \omega \beta_e}{M} \left(\frac{A_1 \sqrt{2(P_s - P_r)}}{V_1 \sqrt{\rho}} + \frac{A_2 \sqrt{2(P_2 - P_r)}}{V_2 \sqrt{\rho}} \right) \end{bmatrix};$$

$$u = (k_i i - \varepsilon)$$

Therefore, we have

$$\begin{bmatrix} \dot{y}_1 \\ \dot{y}_2 \\ \dot{y}_3 \end{bmatrix} = \begin{bmatrix} 0 & 1 & 0 \\ 0 & 0 & 1 \\ 0 & -\left(\frac{K_{lx}}{M} + \frac{\beta_e}{MV_1}A_1^2 + \frac{\beta_e}{MV_2}A_2^2\right) & -\frac{B_v}{M} \end{bmatrix} \begin{bmatrix} y_1 \\ y_2 \\ y_3 \end{bmatrix} + \begin{bmatrix} 0 \\ 0 \\ \frac{C_d \omega}{M} \left(\frac{\beta_e A_1 \sqrt{2(P_s - P_r)}}{V_1 \sqrt{\rho}} + \frac{\beta_e A_2 \sqrt{2(P_2 - P_r)}}{V_2 \sqrt{\rho}} \right) \end{bmatrix} (k_i i - \varepsilon)$$

(10)

The schema of PID control system is:

See Fig. 2 and Table 2

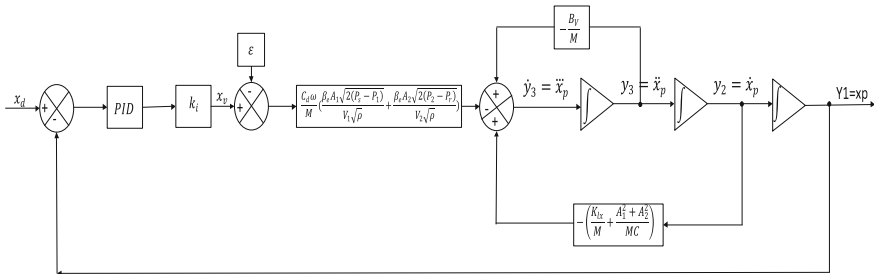


Fig. 2 Schema of position control system with PID controller

Table 2 System parameters

N.O	Name	Symbol	Measure	Value
1	Head side area of cylinder	A_1	m^2	0.0019625
2	Rod side area of cylinder	A_2	m^2	0.0015826
3	Dead volume of cylinder	V_0	m^3	2×10^{-4}
4	Supply pressure	P_s	N/m^2	15×10^6
5	Tank returned pressure	P_r	N/m^2	0
6	Total load	M	kg	10.88
7	Gain of proportional valve	K_i	m/mA	0.55
8	Spring stiffness	K_{lx}	N/m	8640
9	Effective bulk modulus	β_e	N/m^5	10^8
10	Stroke of cylinder	L_0	m	0.25
11	Damping coefficient of spring	B_{lx}	N.s/m	3500
12	Overlapping length	ε	m	1×10^{-3}
13	Diameter of the valve port	D	m	7.26×10^{-3}
14	Discharge coefficient	C_d		0.63

4 Result and Discussion

A. Simulation

The mathematical model is simulated using MATLAB–Simulink R2014a Fig. 2.

The solution method is Ode45 (Dormand–Prince). The parameters used in the system are given in Table 2. The parameters K_p , K_i , K_d are chosen based on the trial and error method.

In Figs. 3 and 4, the system responds the displacement from 50 to 150 mm with settling time about 8 s. In Fig. 5, the system responds from position of 5 to 250 mm with a settling time more than 9 s and oscillation at 250 mm. Input signal of Figs. 4 and 5 is a step signal. The simulation results show that the system has a short transient response time, however, with a long settling time and an error less than ± 0.2 mm.

In Fig. 6, pulse input has amplitude 200 mm, period 8 s and pulse width 50% of period. This figure shows that error of retract stroke is larger than extend stroke. Figure 7 illustrates response with sine signal which has frequency 0.628 rad/s and amplitude 80 mm, it is clear to see that simulated signal is later than designed signal.

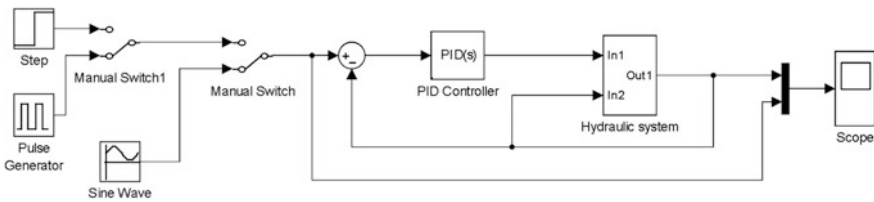


Fig. 3 System with PID controller

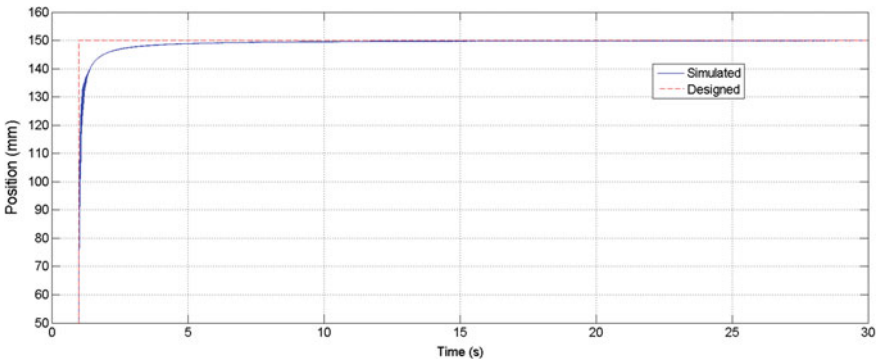


Fig. 4 Response of the system with $k_p = 0.96$, $k_i = 0.005$, $k_d = 0.01$

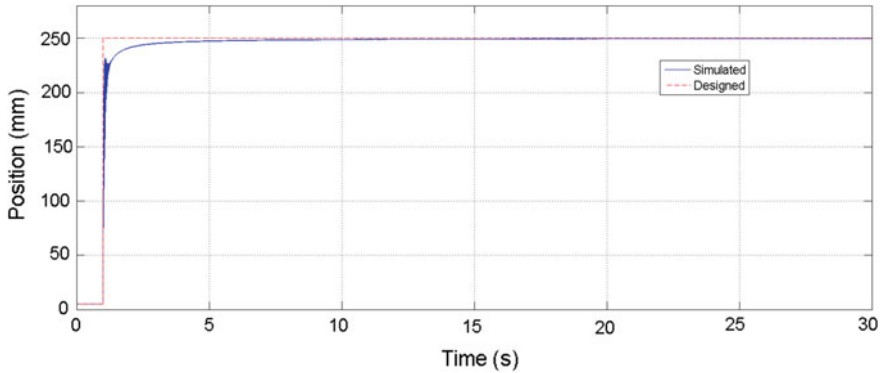


Fig. 5 Response of the system with $k_p = 0.95$, $k_i = 0.0009$, $k_d = 0.01$

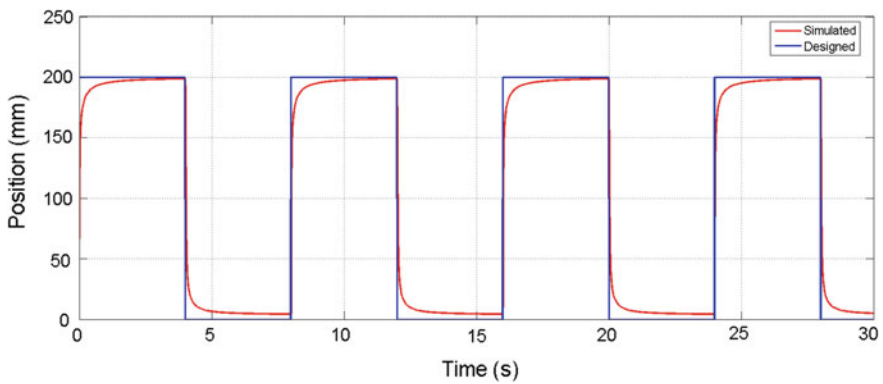


Fig. 6 Response of the system with $k_p = 0.95$, $k_i = 0.0009$, $k_d = 0.01$

B. Experiment

Experiments are conducted to validate the analytical results obtained in the simulation. The displacement and controller parameters used in experiments are the same with the ones used in simulation. The experiment uses the PCI card Ni-6221 and computer to control the proportional valve. Figure 7 is the setup of the experiment. Experimental results show that the settling time of 2 s (Fig. 8) and 4 s in Fig. 9. Through Figs. 8, 9, and 10, transient response is faster than in simulation (settling time is shorter). In Fig. 11, the output signal of experimental system is the same phase with the input signal. However, the system fluctuation is higher than simulation system about ± 0.5 mm Fig. 12.

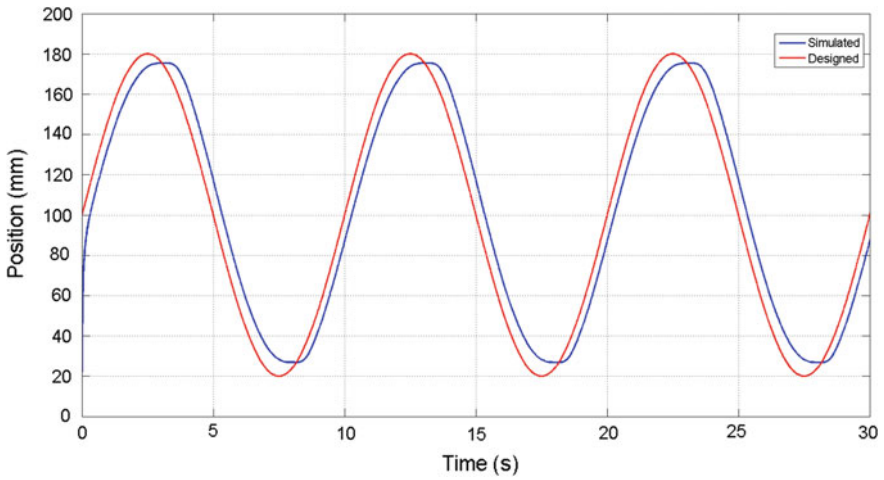


Fig. 7 Response of the system with $k_p = 0.95$, $k_i = 0.0009$, $k_d = 0.01$

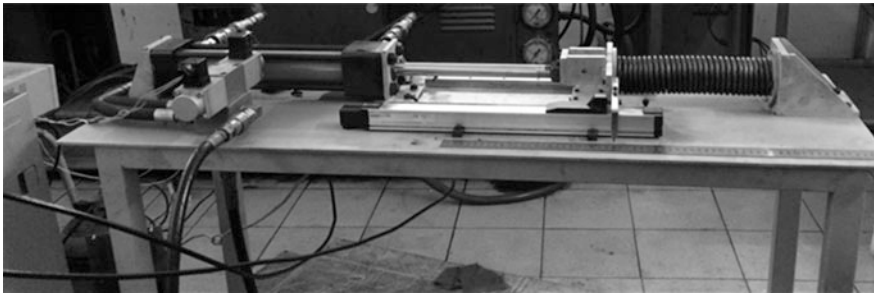


Fig. 8 Experimental system

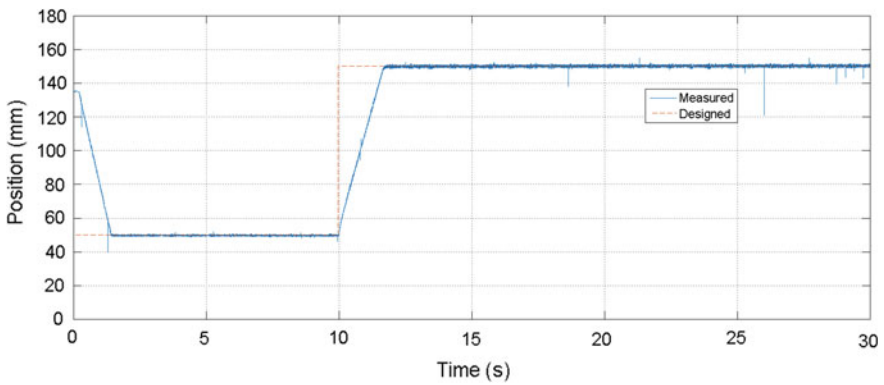


Fig. 9 Response of the system with $k_p = 0.96$, $k_i = 0.0005$, $k_d = 0.01$

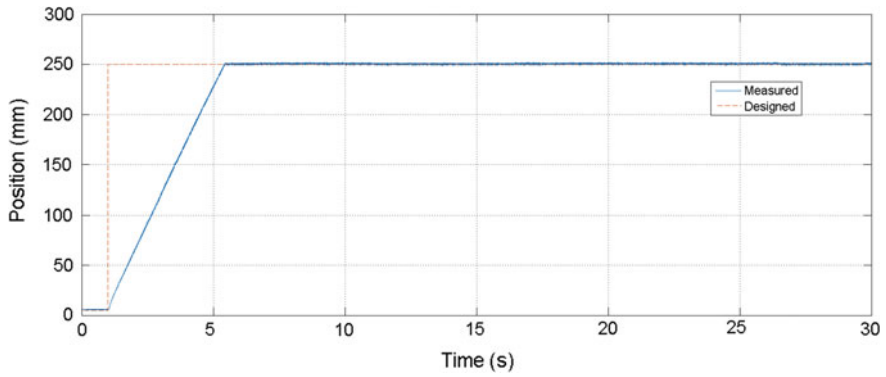


Fig. 10 Response of the system with $k_p = 0.95$, $k_i = 0.0009$, $k_d = 0.01$

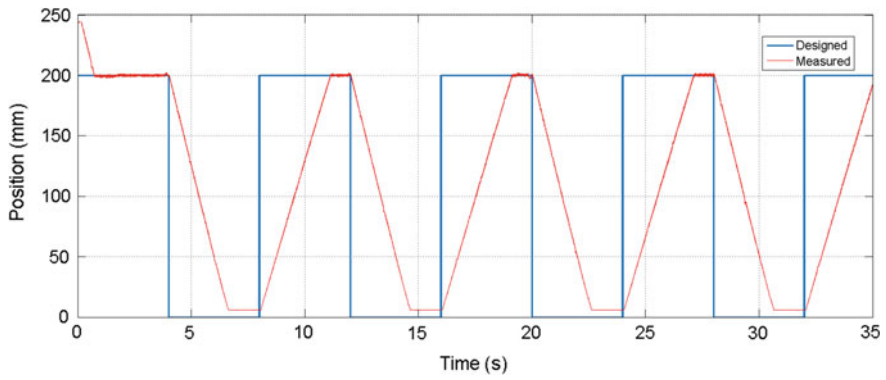


Fig. 11 Response of the system with $k_p = 0.95$, $k_i = 0.0009$, $k_d = 0.01$

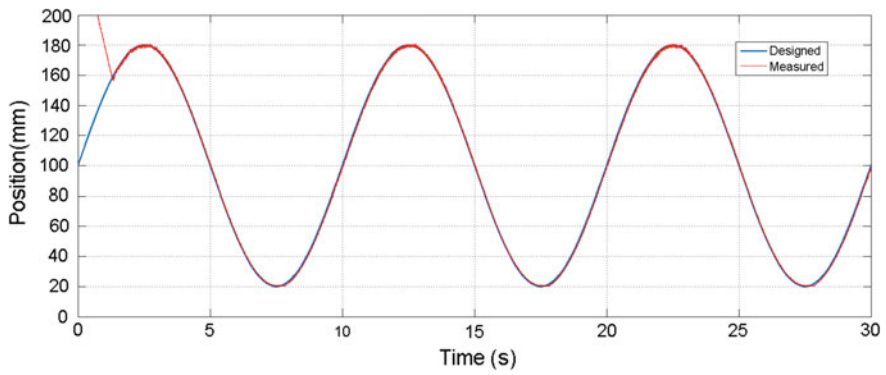


Fig. 12 Response of the system with $k_p = 0.95$, $k_i = 0.0009$, $k_d = 0.01$

5 Conclusions

In this study, the mathematical model of hydraulic–mechanical systems using proportional valve with linear variable load is simulated on a Matlab—Simulink. The system’s displacement is controlled using a PID controller. The mathematical model and its simulation are performed without considering the friction. PID parameters obtained from experiments. The experiment of the system shows that the established mathematical model together with its simulation can describe the dynamic characteristics and responses of the systems. For further studies and for application, the speed and force controls are also need to be studied for a total research in this matter.

Acknowledgements This paper is the result of the project named “Dynamic Analysis of Electro-Hydraulic System using Proportional Valve for Position Control”—project code: **T-BDCN-2016-100**. The project is financially sponsored by Ho Chi Minh City University of Technology.

References

1. Antonio CV, Raul G, Victor Juliano De Negri (2006) New methodology for identification of the dead zone in proportional directional hydraulic valves. *ABC Symposium Series Mechatronics*, vol. 2, pp 377–384
2. Liu YF, Dai ZK, Xu XY, Tian L (2011) Multi-domain modeling and simulation of proportional solenoid valve. *J Cent South Univ Technol*
3. Radu, Iulian R (2012) Theoretical and experimental investigations regarding the dynamic performances of the servo-solenoid directional valve. *UPB Sci Bull Series D*, 74(2)
4. Amirante R, Moscatelli PG, Catalano LA (2007) Evaluation of the flow forces on a direct (single stage) proportional valve by means of a computational fluid dynamic analysis. *Energy Conver Manag* 48
5. Amirante R, Lippolis A, Tamburrano P (2013) Theoretical and experimental analysis of a coupled system proportional control valve and hydraulic cylinder. *Univer J Eng Sci* 1(2):45–56
6. Tamer MM, Mohamed AM, Ahmed HL (2009) Investigation of dynamic performance of an electro-hydraulic proportional system. In: 13th International Conference on Aerospace Sciences & Aviation Technology, ASAT- 13, May 26–28
7. Adam Bure_ek1, Lumír H, Martin V (2016) Simulation of dynamics of hydraulic system with proportional control valve. *EPJ Web of Conferences* 114
8. Bo TX, Indrawanto, Yanada H (2011) Sliding mode control of single-hydraulically actuated manipulator. *Int J Mech Mechatron Eng IJMME-IJENS* 11:05
9. Mohga Abd A, Muawia MA (2013) Design of a tuned PID controller for a hydraulic system. *Int J Sci Res (IJSR)*
10. Pornjit P, Aphaiwong J (2013) Force and position control in the electro-hydraulic system by using a mimo fuzzy controller. In: *IEEE 8th Conference on Industrial Electronics and Applications (ICIEA)*
11. Md Rozali S, Rahmat MF, Abdul Wahab N, Ghazali R, Zulfatman (2010) PID controller design for an industrial hydraulic actuator with servo system. In: *Proceedings of 2010 IEEE Student Conference on Research and Development (SCORED)*

A Tooth Profile Design for Roots Rotors of Vacuum Pump



V. Tran-The and T. Do-Anh

Abstract In traditional tooth designs of the vacuum pump, the circular, cycloidal curves and their combination are usually used for generating the tooth profiles of roots rotor. However, to increase efficiency and to reduce vibration and noise for the pump, a novel tooth profile for the roots rotor of a vacuum pump is proposed, which are comprised of five different segments that are generated by the curves in order: circular arc, extended epicycloid, involute, extended hypocycloidal, and conjugated circular arc. A numeral example is presented to evaluate and compare the performance (volumetric efficiency and seal line length) for the proposed tooth profile and a traditional tooth design of the vacuum pump (cycloidal-cycloidal tooth profile) with considering to the number of rotor lobes. It reveals that the proposed tooth profile provides a much advantage than the traditional tooth profile.

Keywords Tooth profile • Volumetric efficiency • Seal line length
Roots rotor • Vacuum pump

1 Introduction

In the operating process of a pump, the tooth profile of roots rotor (lobe pump) is an important factor for improving the performance of the vacuum pump. It permits the roots rotors to remain meshing with each other. Number of rotor lobes of a pump usually is two, three, or four lobes, and they are used for carrying the fluid. Roots pumps are used in wide range of the life and industrial applications such as the food, medicine, and biotechnology. In addition, they can be able to work with various materials, including low viscosity fluids such as water, very high viscosity fluids such as oil, and even solids. In this paper, a new tooth profile design method is proposed based on the combination of the different traditional curves such as

V. Tran-The (✉) • T. Do-Anh
Faculty of Mechanical Engineering, Hung Yen University of Technology and Education,
Hung Yên, Vietnam
e-mail: vanct4.hut@gmail.com

© Springer Nature Singapore Pte Ltd. 2018
H. Nguyen-Xuan et al. (eds.), *Proceedings of the International Conference
on Advances in Computational Mechanics 2017*, Lecture Notes in Mechanical
Engineering, https://doi.org/10.1007/978-981-10-7149-2_70

1003

circular arc, extended epicycloid, and involute curve. In particular, higher area efficiencies are obtained compared to the traditional cycloidal curve design.

The tooth profile design for roots rotor of vacuum pump has received much attention by many researchers. Firstly, Litvin and Fuentes [1] and Tsay [2] proposed a geometric design for tooth profile of a rotor with two lobes using a single circular arc. Meanwhile, a new tooth profile for rotor is developed by combining circular arcs and a conjugated epicycloidal curve [3]. Fang [4] patented an addendum and a dedendum portions for the tooth profiles of rotor by comprising four circular arcs that can improve area efficiency of a vacuum pump. Subsequently, the tooth profile of the rotor is developed with the combination of five circular arcs by Wang et al. [5]. Previously, Niimura et al. [6] patented an addendum tooth profile consisted a circular arc and an involute to increase pump efficiency. More lately, an extended cycloid curve with a variable trochoid ratio is applied to improve pump performance by Hwang and Hsieh [7, 8]. Kang et al. [9]; Kang [10] developed a new lobe pump rotor profile used circular and epicycloidal curves that can significantly improve pump performance. Besides, a dynamic mesh method is proposed to provide factors affecting on the performance of lobe pumps. A lobe profile design of rotor consisting of a hypocycloid and epicycloid and a manufacturing method are presented by Chiu [11]. More recently, Shujun et al. [12] presented a tooth profile design of rotor by modifying the traditional involute profile and obtains a new involute profile for improving the efficiency of vacuum pump.

This paper proposes a novel tooth profile for the roots rotor of a vacuum pump that is composed of five curves in order circular arc, extended epicycloid, involute, extended hypocycloidal, and conjugated circular arc (CEIEC tooth profile). Mathematical models for conventional and proposed tooth profiles of the roots rotor are also established. A numeral example is presented to illustrate and verify the merits of the proposed roots rotor. The analytical results reveal that the performance produced by proposed roots rotor is higher than that of traditional roots rotor.

2 Mathematical Model for Tooth Profiles of Roots Rotor

2.1 *Mathematical Model for Tooth Profile of the Conventional Roots Rotor*

The generation schematic for generating the cycloid curve is shown in Fig. 1. The tooth profile of roots rotor is comprised of two cycloid curves: addendum portion $\delta_1^{(1)}$ and dedendum portion $\delta_2^{(1)}$, as shown in Fig. 2. According to Fig. 1, the position vector and unit normal vector for the addendum profile of roots rotor $\delta_1^{(1)}$ are represented in coordinate system $S_c(x_c, y_c, z_c)$ as follows

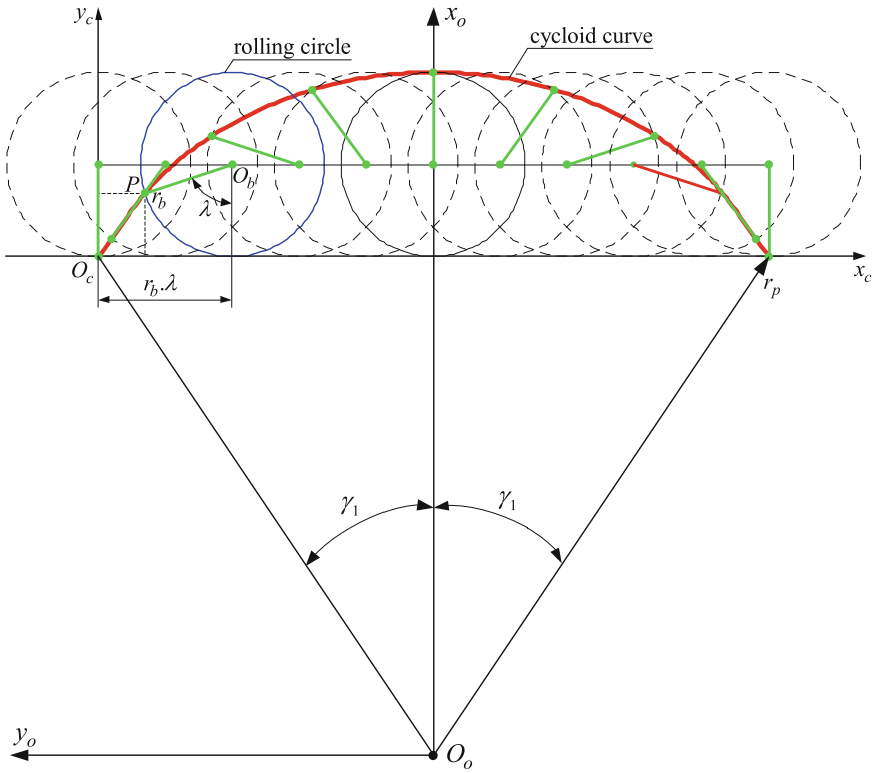


Fig. 1 Generation schematic for generating the cycloid curve

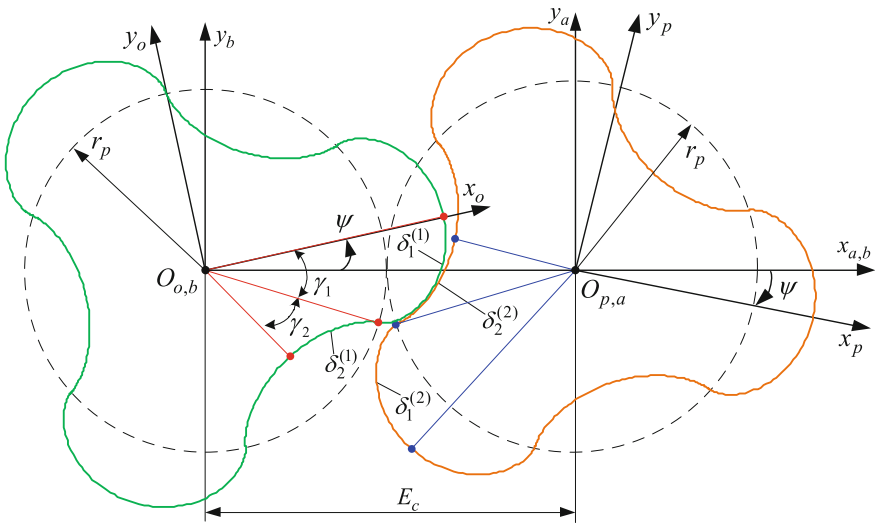


Fig. 2 Conjugated coordinate systems of the CC roots rotors

$$\mathbf{r}_c^{(1)}(\lambda) = [x_c^{(1)}(\lambda), y_c^{(1)}(\lambda), 1]^T = [r_b(\lambda - \sin \lambda), r_b(1 - \cos \lambda), 1]^T, \tag{1}$$

$$\mathbf{n}_c^{(1)} = \frac{\mathbf{N}_c^{(1)}}{\sqrt{\mathbf{N}_c^{(1)} \cdot \mathbf{N}_c^{(1)}}}, \quad \mathbf{N}_c^{(1)} = \frac{\partial \mathbf{r}_c^{(1)}}{\partial \lambda} \times \mathbf{k} = [\sin \lambda, r_b(1 - \cos \lambda), 1]^T \tag{2}$$

where r_b is the radius of the rolling circle and λ is the angular parameter of the rolling circle.

The position vector and unit normal vector of the addendum portion can be presented in coordinate system $S_o(x_o, y_o, z_o)$ as follows:

$$\mathbf{r}_o^{(1)}(\lambda) = \mathbf{M}_{oc} \cdot \mathbf{r}_c^{(1)}(\lambda), \tag{3}$$

$$\mathbf{n}_o^{(1)}(\lambda) = \mathbf{M}_{oc} \cdot \mathbf{n}_c^{(1)}(\lambda). \tag{4}$$

The dedendum portion, $\delta_2^{(2)}$, is conjugate to the meshing addendum curve, $\delta_1^{(1)}$, as shown in Fig. 2. By applying the homogeneous coordinate transformation matrix equation from $S_o(x_o, y_o, z_o)$ to $S_p(x_p, y_p, z_p)$, the position vector and unit normal vector of the addendum curves can be represented in coordinate system S_p as follows:

$$\mathbf{r}_p^{(2)}(\lambda, \psi) = \mathbf{M}_{po}(\psi) \cdot \mathbf{r}_o^{(1)}(\lambda), \tag{5}$$

$$\mathbf{n}_p^{(2)}(\lambda, \psi) = \mathbf{M}_{po}(\psi) \cdot \mathbf{n}_o^{(1)}(\lambda), \tag{6}$$

where ψ is the rotational angle of two rotors and $E_c = 2.r_p$ is the center distance between two rotors, as shown in Fig. 2.

The equation of meshing between the addendum curves and conjugated dedendum curves can be obtained as

$$f_1 = \mathbf{n}_p^{(2)} \frac{\partial \mathbf{r}_p^{(2)}(\lambda, \psi)}{\partial \psi} = \mathbf{n}_p^{(2)} \frac{\partial [x_p^{(2)}(\lambda, \psi), y_p^{(2)}(\lambda, \psi), z_p^{(2)}(\lambda, \psi)]}{\partial \psi} = 0, \tag{7}$$

2.2 Mathematical Model for Tooth Profile of the Proposed Roots Rotor

The tooth profile of roots rotor is comprised of five different curves, as shown in Fig. 3. Wherein tooth profile is the axially symmetrical curves. Therefore, only one-half of the tooth profile requires definition. The tip of the roots rotor AB is the circular arc curve and its center coinciding with the rotation center of rotor, BC is

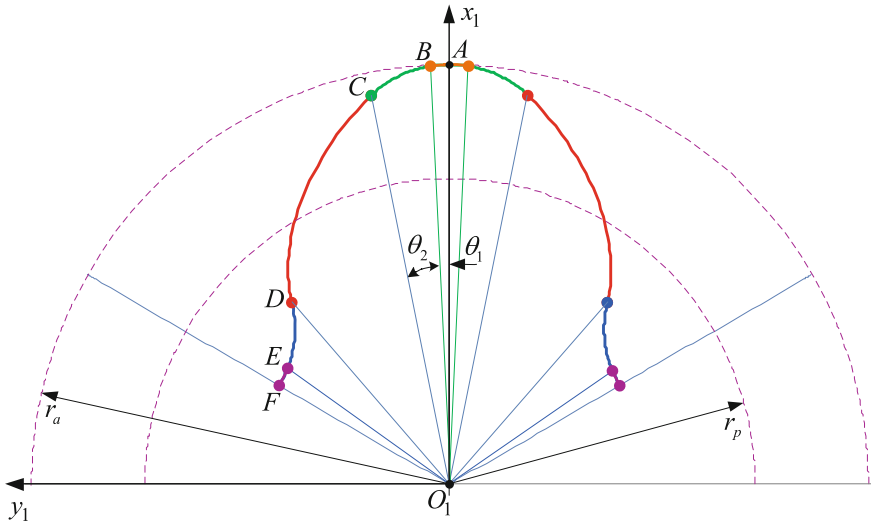


Fig. 3 Tooth profile of the proposed roots rotors

the extended epicycloid curve, CD is the involute curve, DE is the extended hypocycloidal curve, and EF is the circular arc curve. The position vector and unit normal vector of the tooth profile of roots rotor are represented in coordinate system S_1 as follows:

The top land of the proposed rotor profile is a circular arc with its center coinciding with the center of rotation. Therefore, the gap between the top land of the rotor and the wall of the chamber turns into a long and narrow path, which provides better gas sealing and wider inlet opening. The position vector and unit normal vector of the tooth profile for circular arc curve AB as:

$$\mathbf{r}_1^{(AB)} = [x_1^{(AB)}, y_1^{(AB)}, 1]^T = [a_1 + r_1 \sin \theta, b_1 + r_1 \cos \theta, 1]^T, \tag{8}$$

$$\mathbf{n}_1^{(AB)} = [n_{x_1}^{(AB)}, n_{y_1}^{(AB)}, 1]^T = [\cos \theta, -\sin \theta, 1]^T, \tag{9}$$

where r_1 is the radius of the circular arc, $r_1 = r_a$, r_a is the outer radius of roots rotors, (a_1, b_1) are the center of the circular arc AB represented in coordinate system S_1 and coinciding with the rotation center of rotor, $(a_1, b_1) = (0, 0)$. So the curvature difference between the tip of the rotor and the wall of the chamber can be eliminated. And θ is the angular parameter of the circular arc, $0 \leq \theta \leq \theta_1$.

The generation schematic for generating the extended epicycloid curve is shown in Fig. 4. The position vector and unit normal vector of the extended epicycloid curve BC can be presented in coordinate system $S_d(x_d, y_d, z_d)$ as follows:

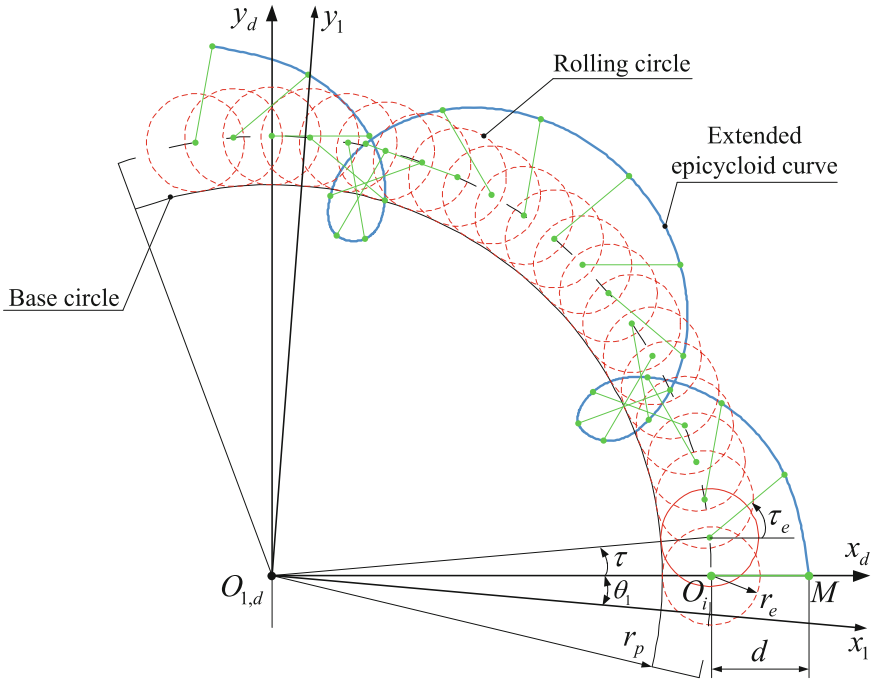


Fig. 4 Generation schematic for generating the extended epicycloid curve

$$\begin{aligned} \mathbf{r}_d^{(BC)} &= [x_d^{(BC)}, y_d^{(BC)}, 1]^T \\ &= [(r_p + r_e) \cos \tau + d \cos(\tau + \tau_e), (r_p + r_e) \sin \tau + d \sin(\tau + \tau_e), 1]^T, \end{aligned} \tag{10}$$

$$\mathbf{n}_d^{(BC)} = [n_{x_d}^{(BC)}, n_{y_d}^{(BC)}, 1]^T = \frac{\mathbf{N}_d^{(BC)}}{\sqrt{\mathbf{N}_d^{(BC)} \cdot \mathbf{N}_d^{(BC)}}}, \quad \mathbf{N}_d^{(BC)} = \frac{\partial \mathbf{r}_d^{(BC)}}{\partial \tau} \times \mathbf{k}, \tag{11}$$

where r_p is the radius of the basic circle, r_e is the radius of the rolling circle, τ is the angular parameter of the basic circle, $\tau_1 \leq \tau \leq \tau_2$ and τ_e is the angular parameter of the rolling circle, $\tau_e = \frac{r_p}{r_e} \tau$, and d is the distance between point M on the rolling circle radius and the center of the rolling circle O_i (called eccentric throw). The eccentric throw, d , can be determined by equation as follows

$$d = r_e + (r_a - r_p - 2r_e + g_a)\kappa. \tag{12}$$

where r_a is the outer radius of the roots rotor, g_a is the normal gap between the rotor and chamber, and κ is the function of the trochoid ratio that is defined as a second order polynomial of the angular parameter of the basic circle τ , $\kappa = 1 - \mu \cdot \tau^2$, with μ is an extended cycloid coefficient.

The position vector and unit normal vector of the extended epicycloid curve BC are represented in coordinate system $S_1(x_1, y_1, z_1)$ as follows:

$$\mathbf{r}_1^{(BC)} = [x_1^{(BC)}, y_1^{(BC)}, 1] = \mathbf{M}_{1d} \cdot \mathbf{r}_d^{(BC)}, \tag{13}$$

$$\mathbf{n}_1^{(BC)} = [n_{x_1}^{(BC)}, n_{y_1}^{(BC)}, 1]^T = \mathbf{M}_{1d} \cdot \mathbf{n}_d^{(BC)}. \tag{14}$$

The generation schematic of the involute curve is shown in Fig. 5. The position vector and unit normal vector of the involute curve CD can be presented in coordinate system $S_e(x_e, y_e, z_e)$ as follows:

$$\mathbf{r}_e^{(CD)} = [x_e^{(CD)}, y_e^{(CD)}, 1]^T = \begin{bmatrix} r_p \cos \varphi + u \cos(\alpha_{on} + \varphi) + (\frac{\pi m}{4} + r_p \varphi) \sin \varphi \\ (\frac{\pi m}{4} + r_p \varphi) \cos \varphi - r_p \sin \varphi - u \sin(\alpha_{on} + \varphi) \\ 1 \end{bmatrix}, \tag{15}$$

$$\mathbf{n}_e^{(CD)} = [n_{x_e}^{(CD)}, n_{y_e}^{(CD)}, 1]^T = [-\sin(\alpha_{on} + \varphi), -\cos(\alpha_{on} + \varphi), 1]^T, \tag{16}$$

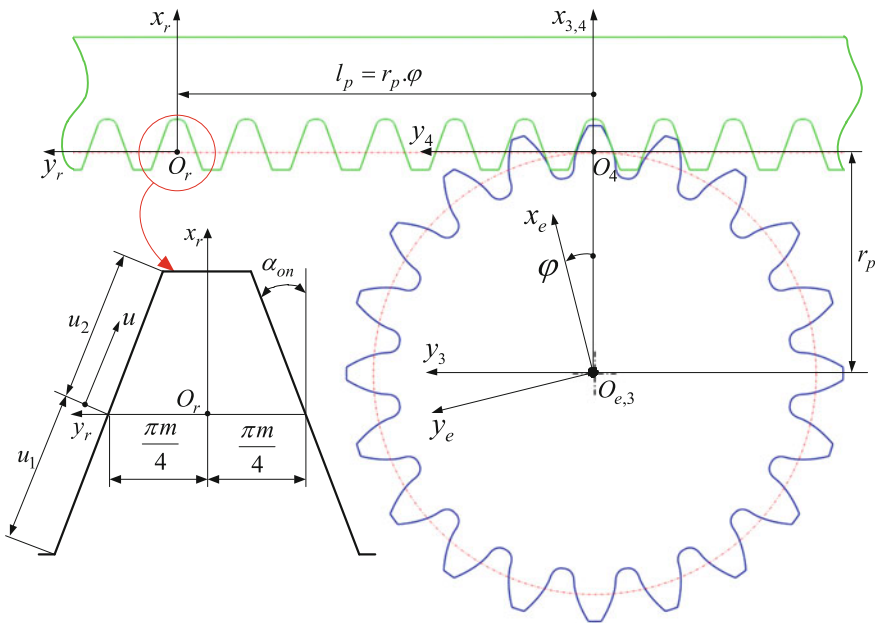


Fig. 5 Generation schematic for generating involute curve

where u is the rack cutter surface parameter, $u_1 \leq u \leq u_2$, α_{on} is the pressure angle of the rack cutter, r_p is the radius of the pitch circle, φ is the angular parameter of the involute curve, and $l_p = r_p\varphi$ the distance of rack cutter translate without rotation.

The position vector and unit normal vector of the involute curve CD are represented in coordinate system $S_1(x_1, y_1, z_1)$ as follows:

$$\mathbf{r}_1^{(CD)} = [x_1^{(CD)}, y_1^{(CD)}, 1]^T = \mathbf{M}_{1e} \cdot \mathbf{r}_e^{(CD)}, \tag{17}$$

$$\mathbf{n}_1^{(CD)} = [n_{x_1}^{(CD)}, n_{y_1}^{(CD)}, 1]^T = \mathbf{M}_{1e} \cdot \mathbf{n}_e^{(CD)}. \tag{18}$$

According to the theory of gearing, the equation of meshing between the rack cutter surface and gear surface can be derived as follows:

$$f_2(u, \varphi) = \mathbf{n}_e^{(CD)} \cdot \frac{\partial [x_e^{(CD)}(u, \varphi), y_e^{(CD)}(u, \varphi), z_e^{(CD)}(u, \varphi)]}{\partial \varphi} = 0 \tag{19}$$

The meshing coordinate system for two roots rotor is shown in Fig. 6, where the coordinate systems $S_1(x_1, y_1)$, $S_2(x_2, y_2)$, and $S_f(x_f, y_f)$ are rigidly connected to the driving rotor, driven rotor, and frame, respectively. By applying the homogeneous coordinate transformation matrix equation from $S_1(x_1, y_1, z_1)$ to $S_2(x_2, y_2, z_2)$, the extended hypocycloidal curve D_1E_1 is conjugate to the extended epicycloid curve

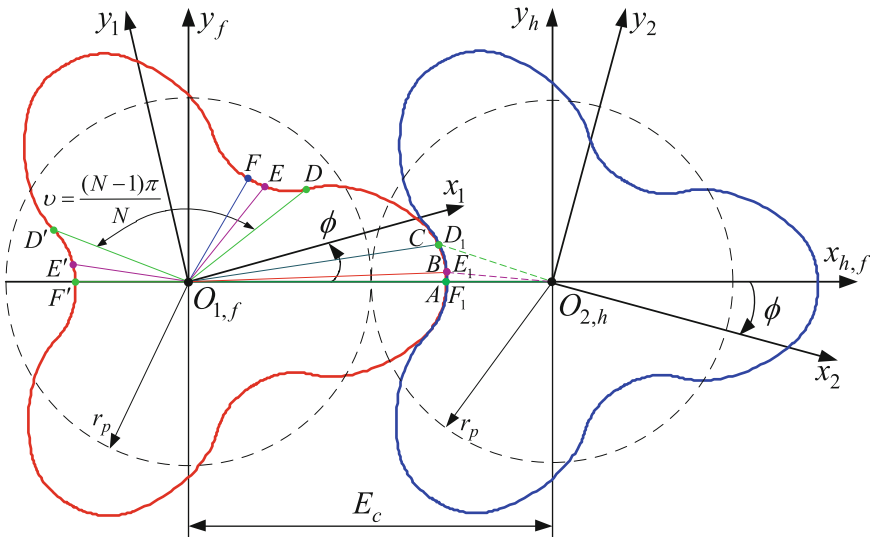


Fig. 6 Conjugated coordinate systems of the roots rotors

BC , as shown in Fig. 6. The position vector and unit normal vector of the curve D_1E_1 can be represented in coordinate system $S_2(x_2, y_2, z_2)$ as follows:

$$\mathbf{r}_2^{(D_1E_1)} = \mathbf{M}_{21}(\phi) \cdot \mathbf{r}_1^{(BC)}, \quad (20)$$

$$\mathbf{n}_2^{(D_1E_1)} = \mathbf{L}_{21}(\phi) \cdot \mathbf{n}_1^{(BC)}, \quad (21)$$

where $\mathbf{L}_{21}(\phi)$ is the upper-left (2×2) sub-matrix of the (3×3) homogeneous coordinate transformation matrix $\mathbf{M}_{21}(\phi)$.

Similarly, the circular arc curve E_1F_1 is conjugate to the circular arc curve AB , as shown in Fig. 6. The position vector and unit normal vector of the curve E_1F_1 are determined in coordinate system $S_2(x_2, y_2, z_2)$ as follows:

$$\mathbf{r}_2^{(E_1F_1)} = \mathbf{M}_{21}(\phi) \cdot \mathbf{r}_1^{(AB)}, \quad (22)$$

$$\mathbf{n}_2^{(E_1F_1)} = \mathbf{L}_{21}(\phi) \cdot \mathbf{n}_1^{(AB)}, \quad (23)$$

where ϕ is the rotational angle of two roots rotors and E_c is the center distance between two rotors, as shown in Fig. 6.

According to the theory of gearing, the equation of meshing between the driving rotor and driven rotor surface can be obtained by:

$$\begin{aligned} f_3 &= \mathbf{n}_2(\phi) \cdot \frac{\mathbf{r}_2^{(D_1E_1, E_1F_1)}(\phi)}{\partial \phi} \\ &= \mathbf{n}_2(\phi) \cdot \frac{\partial [x_2^{(D_1E_1, E_1F_1)}(\phi), y_2^{(D_1E_1, E_1F_1)}(\phi), z_2^{(D_1E_1, E_1F_1)}(\phi)]}{\partial \phi} = 0, \end{aligned} \quad (24)$$

The position vector, $\mathbf{r}_2^{(D_1E_1)}$, $\mathbf{r}_2^{(E_1F_1)}$ of the respective dedendum curves, D_1E_1 , E_1F_1 of the driven rotor are identical to the position vector, $\mathbf{r}_1^{(D'E')}$, $\mathbf{r}_1^{(E'F')}$ of the respective dedendum curves, $D'E'$, $E'F'$ of the driving rotor, as shown in Fig. 6. So, the position vector, $\mathbf{r}_1^{(DE)}$, $\mathbf{r}_1^{(EF)}$ of the respective dedendum curves, DE , EF of the driving rotor, can be derived by rotating the position vector, $\mathbf{r}_1^{(D'E')}$, $\mathbf{r}_1^{(E'F')}$ with an angle of $\vartheta = \frac{(N-1)\pi}{N}$ counter-clockwise about z -axis.

3 Vacuum Pump Performance

3.1 Volumetric Efficiency

The volumetric efficiency of a pump is defined as the ratio of discharged volume to the volume of the chamber that embodies the mating rotors. In two-dimensional

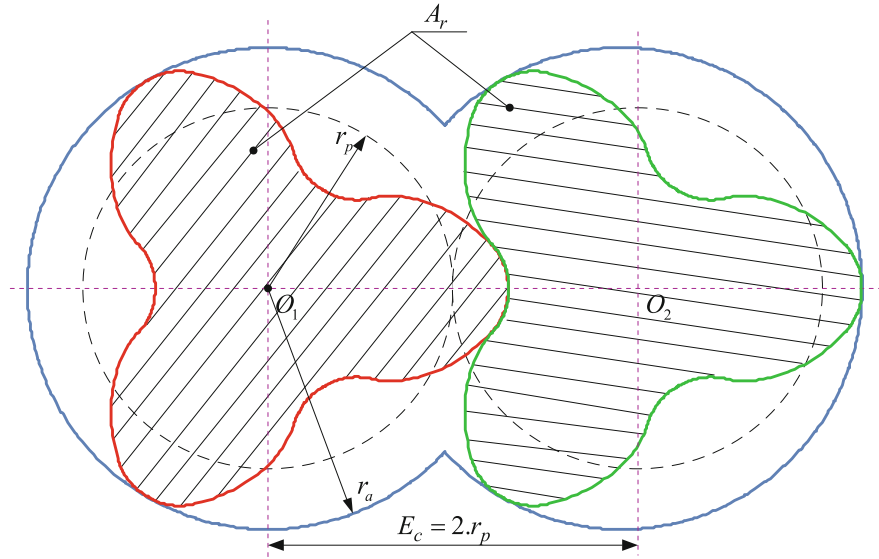


Fig. 7 Cross-sectional area for volumetric efficiency calculation

calculation, the volumetric efficiency can be simplified as area efficiency. Figure 7 illustrates a simple cross-section of a roots pump. The white area is the working domain of the pump, while the shaded areas represent by rotors. The area efficiency can be defined as follows:

$$\eta = \frac{\pi r_a^2 - A_r}{\pi r_a^2} \tag{25}$$

where r_p is the radius of pitch circle of roots rotor, r_a is the outer radius of the rotor, and A_r is the cross-sectional area of roots rotor.

3.2 Seal Line Length Efficiency

The length of seal line at a rotational angle of rotor is shown as in Fig. 8. The average length of seal line at a rotational angle ψ_i of roots rotor can be defined as follows:

$$L_s = \sum_{i=1}^k \frac{L_i}{k}, \text{ in the constraint, } 0 \leq g_{ai} \leq g_{amax} \tag{26}$$

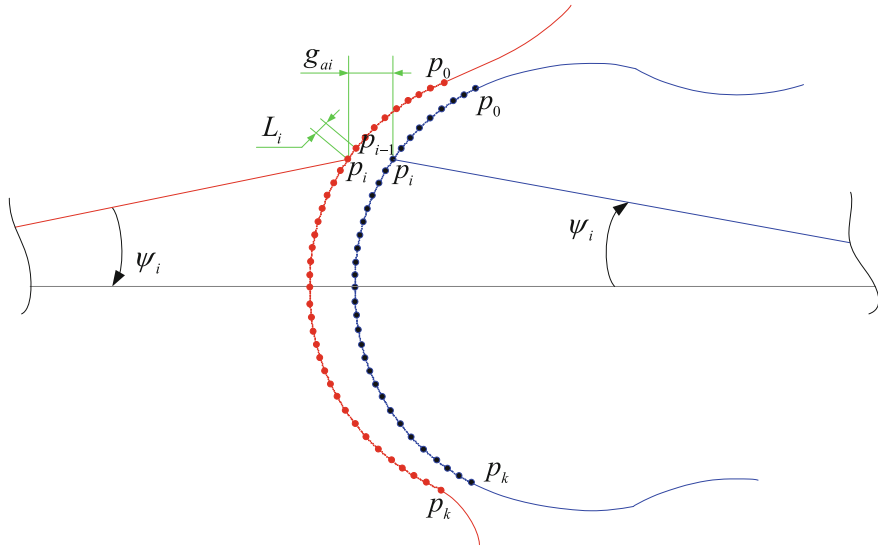


Fig. 8 Model for calculating the length of seal line

Table 1 Basic data of the root rotor

Roots rotor	
Number of rotor lobes (N)	3
Normal module (m)	22
Pitch radius (r_p)	33.0 mm
Outer radius (r_a)	44.88 mm
Normal gap (g_a)	40 μm
Normal pressure angle (α_n)	29.87°
Top tooth arc angle (θ_1)	3°
Extended cycloid coefficient (μ)	0.5×10^3
Center distance (E_c)	66 mm

where L_i is the seal line length between two points p_{i-1} and p_i , g_{ai} is the normal gap at the same point p_i on the driving and driven rotors, and g_{amax} is the maximum normal gap, it is chosen equal to 0.2 mm.

4 Numeral Examples

To validate the proposed tooth profile of the roots rotor, the volumetric efficiency of roots rotor is calculated and compared for two kinds of tooth profiles: One is comprised of two cycloidal curves (addendum $\delta_1^{(1)}$ and dedendum $\delta_2^{(1)}$ (Fig. 2)) and

other one is comprised of five different curves (circular arc curve *AB*, extended epicycloid curve *BC*, involute curve *CD*, extended hypocycloidal curve *DE*, circular arc curve *EF* (Fig. 3)). The basic data of the roots rotor are given in Table 1. The volumetric efficiency of the roots rotor, comprised of two cycloid curves and five different curves, is calculated for three different number of rotor lobes ($N=2, 3, 4$), as shown in Table 2 and Fig. 9. The analytical results reveal that the volumetric efficiency produced by a cycloid profile is smaller than that of a proposed profile. The new rotor profile produces a volumetric efficiency of 7.6% higher than the traditional profiles when the number of rotor lobes equals 3. And it also reveals that for one rotor profile, a higher lobe number will provide lower volumetric efficiency, as shown in Table 2.

In addition, the internal leakage (a small liquid re-circulating around the rotor) is directly affected to the performance efficiency of the roots pump. The length of seal line for three different number of the rotor lobes ($N=2, 3, 4$) is shown in Table 3 and Fig. 10. According to Fig. 10, the average length of seal line of the proposed rotor is much higher than that of the traditional profiles specially for high number of the rotor lobes. Besides, the length of seal line has no change in nearly almost rotational cycle of roots rotor. So, it can reduce noise and vibration for the vacuum pump in its operating process. It is verified that the proposed tooth profile of the roots rotor is more advantages than traditional profile.

Table 2 Volumetric efficiency

	Number of rotor lobes (N)		
	$N = 2$	$N = 3$	$N = 4$
Cycloid roots rotors	0.502	0.409	0.344
Proposed roots rotors	0.558	0.485	0.410

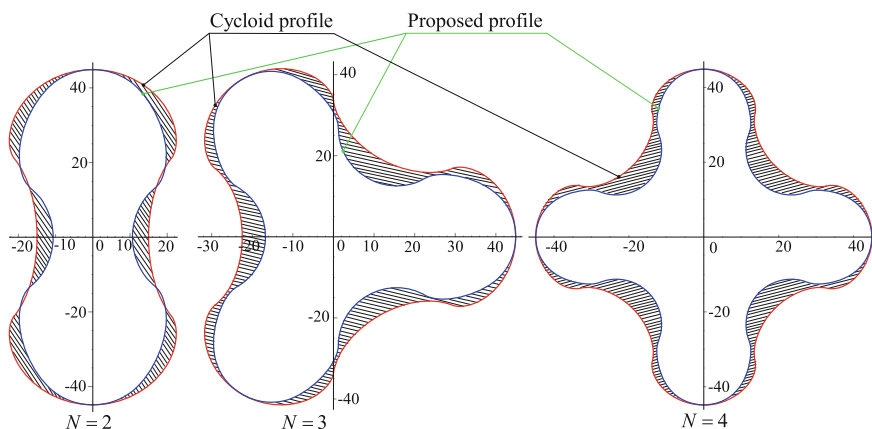


Fig. 9 Comparing volumetric efficiency between cycloid rotor and proposed rotor

Table 3 The average length of seal line of cycloid rotor and proposed rotor

	Number of rotor lobes (N)		
	$N = 2$	$N = 3$	$N = 4$
Cycloid roots rotors	5.685	6.169	6.392
Proposed roots rotors	6.021	7.154	7.267

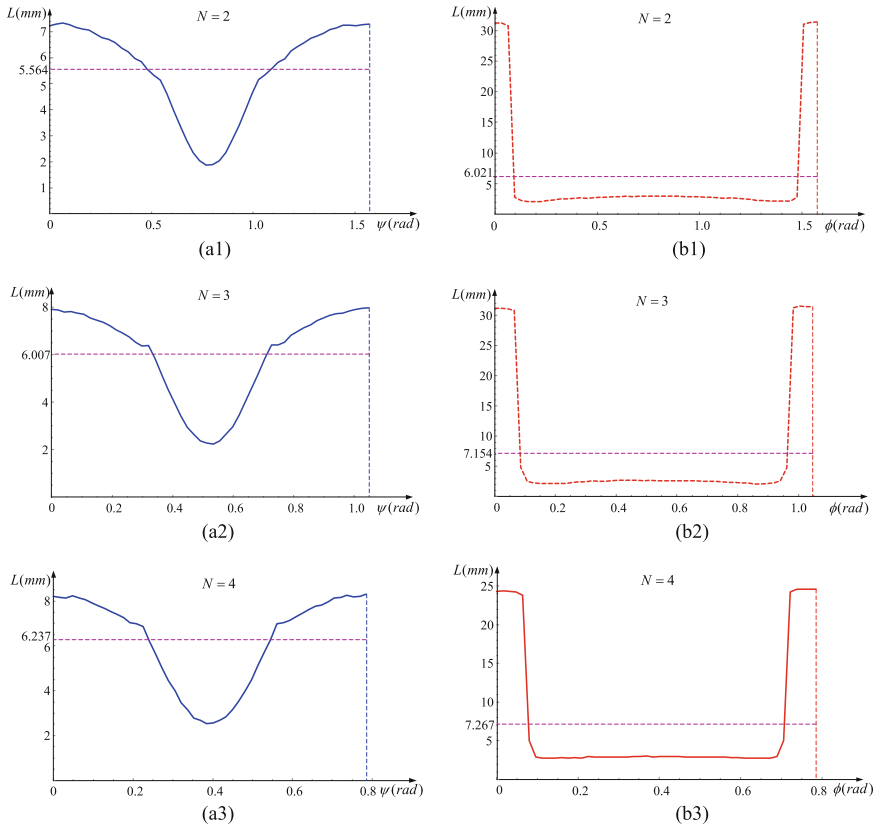


Fig. 10 Length of the seal line of cycloid rotor and proposed rotor: **a1–a3** CC tooth profile; **b1–b3** CEIEC tooth profile

5 Conclusions

In this paper, two mathematical models for CEIEC and CC tooth profiles of roots rotor of the vacuum pump have constructed. A computer program is built for simulating and comparing the volumetric efficiency and length of seal line of roots rotor applying CEIEC tooth profile and CC tooth profile. According to the simulated results of a numeral example, it leads to the following conclusions:

- The volumetric efficiency is calculated and presented for three different number of rotor lobes. It reveals that the volumetric efficiency of roots rotor applying CEIEC tooth profile is higher than that of roots rotor applying CC tooth profile.
- The length of seal line for the roots rotor applying CEIEC tooth profile is also much higher than that of roots rotor applying CC tooth profile especially for high number of the rotor lobes.

References

1. Litvin FL, Fuentes A (2004) Gear geometry and applied theory, Second ed. Cambridge University Press
2. Tsay CB (1987) Solving the conjugated curves of Roots blower lobe profile by analytic method. *J Mach* 13(1):129–133
3. Vecchiato D, Demenego A, Argyris J, Litvin FL (2001) Geometry of cycloidal pump. *Comput Meth Appl Mech Eng* 190:2309–2330
4. Fang HS (1992) Rotor profile for a roots vacuum pump. US Patent 5,152,684
5. Wang PY, Fong ZH, Fang HS (2002) Design constraints of five-arc Roots vacuum pumps. *J Mech Eng Sci Part C* 216(2):225–234
6. Niimura Y, Kikuta R, Usui K (1990) Two-Shaft type rotary machine having a tip circle diameter to shaft diameter within a certain range. US Patent No. 4943214 A
7. Hwang YW, Hsieh CF (2006) Study on high volumetric efficiency of the Roots rotor profile with variable trochoid ratio. *Proc Inst Mech Eng Part C J Mech Eng Sci* 220(C9):1375–1384
8. Hsieh CF, Hwang YW (2008) Tooth profile of a Roots rotor with a variable trochoid ratio. *Math Comput Model* 48:19–33
9. Kang YH, Vu HH, Hsu CH (2012) Factors impacting on performance of lobe pumps: a numerical evaluation. *J Mech* 28(2):229–238
10. Kang YH, Vu HH (2014) A newly developed rotor profile for lobe pumps: generation and numerical performance assessment. *J Mech Sci Technol* 28(3):915–926
11. Chiu HC (1994) The mathematical model and computer aided manufacturing of Roots blower gerotor profile. *J Technol* 9(1):13–19
12. Shujun W, Haiyang L, Yugang Z, Liu H, Wei L (May, 2011) The improvement study of involutes profile type rotor profile in Roots vacuum pump. *IEEE International Conference on New Technology of Agricultural Engineering*, Zibo, China pp 251–253

Cascade Training Multilayer Fuzzy Model for Identifying Nonlinear MIMO System



Cao Van Kien and Ho Pham Huy Anh

Abstract In this paper, a new cascade training Multilayer Fuzzy logic is proposed for identifying the forward model of double-coupled tank system based on experiment. The Multilayer Fuzzy model consists of multiple MISO models; for each MISO model, it consists of multiple single Fuzzy T-S models. The cascade training optimized with DE algorithm sequentially trained Multilayer Fuzzy model one by one. All parameters of the model are optimally trained with differential evolution (DE) algorithm. The experimental results show that proposed method gives better performance than the normal training. This proposed method can be used for optimal Multilayer Fuzzy logic that efficiently applied for identifying nonlinear MISO and MIMO systems. The experimental cascade training tests are presented. It proves more accuracy and takes less time to compute than the normal training method and demonstrates promisingly scalable and simple method as to successfully identify nonlinear uncertain MIMO system.

Keywords Identification of nonlinear MIMO mechanical system
Cascade training Multilayer Fuzzy model · Multiple single Fuzzy T-S model
Differential evolution (DE) optimization algorithm · Double-coupled tank system

1 Introduction

Since Zadeh introduced the concept of Fuzzy set in 1965 [1], there have been lots of studies in this domain. Then, there were also many applications using Fuzzy logic in medicine, engineering, management, and finance [2]. In the intelligent control area, Fuzzy logic has been successfully applied in control, identification, clustering, and classification.

C. Van Kien · H. P. H. Anh (✉)
FEEE, Ho Chi Minh University of Technology, VNU-HCM, Ho Chi Minh City, Vietnam
e-mail: hphanh@hcmut.edu.vn

C. Van Kien
e-mail: kiencv@hcmut.edu.vn

Authors [3] used MGA-based training intelligent model to identify pneumatic artificial muscle manipulators model.

Currently, there are many studies about identification with its approaches from classic to intelligent models, such as neural networks [2, 3] or Fuzzy logic [4, 5]. One main branch of modern control concerns the nonlinear MIMO systems, which are more interested by scientists because of its complexity and uncertainty.

The nonlinear MIMO system is very difficult to identify based on the mathematical model. To overcome this disadvantage, meta-heuristic tools, such as GA and PSO, were increasingly applied for optimizing intelligent models, such as neural networks or Fuzzy logic. Unfortunately, PSO algorithm seems often difficult to get rid of the local minimum solution. Meanwhile, GA algorithm produced good results, but it takes more time to calculate. Recently, DE algorithm [6] rises as a promising optimization technique. It possesses global search ability and takes less time to compute than GA. Hence, in this paper, DE technique is applied for optimizing the novel proposed adaptive Fuzzy model.

Recently, Takagi and Sugeno [4] Fuzzy system in 1985 has been widely applied for many identification and control problems. Authors in [5] proposed a new method for offline training Fuzzy T-S model with hierarchical genetic algorithm (HGA). Authors in [6] used GA for learning Fuzzy system applied for some typical nonlinear model in Simulink.

Fuzzy logic for the identification of nonlinear SISO and MIMO systems has been widely used, but only for simple structure. With a complex system, it required more time for training and a lot of membership functions with eventual complex Fuzzy rule tables. Anh and Ahn [3] used MGA algorithm for training the NARX Fuzzy model with which to identify the pneumatic artificial muscle (PAM) manipulators.

The Hierarchical Fuzzy model was first introduced in 1991 by Raju et al. [7]. With the Hierarchical Fuzzy model, multiple Fuzzy T-S logic was combined into a net with input, hidden, and output layers; the output of the front is the input of behind layer until the last one is output layer. In recent years, there are many researches in this. Sun and Huo [8] used Hierarchical Fuzzy model for control spacecraft. Rodríguez et al. [9] used Hierarchical Fuzzy CMAC control, a nonlinear system in the simulation. But when another input is added into the model, at least one or more Fuzzy T-S was added too, and the hidden layer cannot be extended freely. The hidden and output layers in hierarchical depend on the number of inputs.

Authors in [10] introduced a new Multilayer Fuzzy scheme as a part of the Fuzzy-neural system. Unlike a traditional Fuzzy set, Multilayer Fuzzy model can't be built with the experience of the designer; it is only available to be trained with soft computing optimal algorithm. Then, it can be applied for complex MIMO system and easy to scale for both of large or simple system. The authors [10] used Multilayer Fuzzy for control a cart-pole system in the simulation.

This paper aims to initiatively introduce a new Multilayer Fuzzy cascade training that can be used with better performance and more precision for identifying non-linear MIMO system, such as the investigated coupled tanks system. The Multilayer Fuzzy model can easily scale for the complex or large system. Furthermore, proposed Fuzzy system parameters will be optimally minimized with DE algorithms.

The rest of this paper is organized as follows. Section 2 describes the coupled tanks system modeling. Section 3 proposes the novel Multilayer Fuzzy model for identification. Section 4 introduces DE algorithm used for learning the new proposed Multilayer Fuzzy model with cascade training. In Sect. 5, the experimental setup and results were shown. Finally, the conclusion is drawn in Sect. 6.

2 Quadrature Tanks System

Coupled tanks system is a MIMO nonlinear system that has two inputs (pump 1 and pump 2) and two water-level outputs (x_2 and x_4) (Fig. 1). In this system, pump 1 directly controls the water level of tank 1, tank 2 is affected by the outlet of tank 1, pump 2 directly controls the water level of tank 3, and tank 4 is affected by the outlet of tank 3. There is mutual interaction between u_1 and x_4 and u_2 and x_3 . This coupling effect makes the system difficult to control.

The nonlinear plant equations of the coupled tanks can be obtained by mass balance equation and Bernoulli's law as follows Eq. (1):

Fig. 1 Double-coupled tanks system

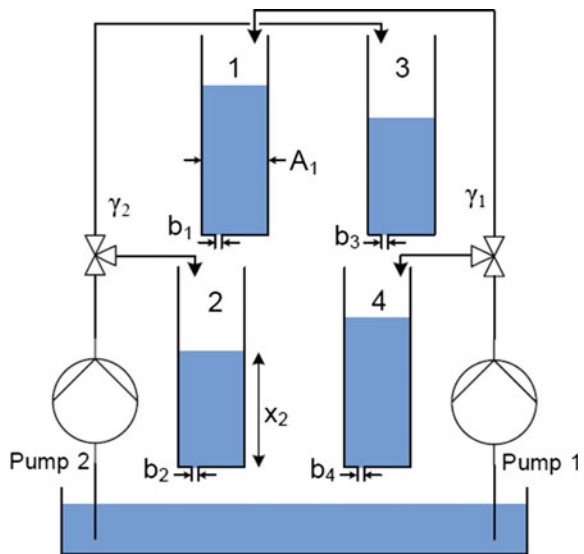


Table 1 Physical meaning and numerical value used in the experiment

Notation	Physical meaning	Value (unit)
A_1	Tank 1 inside diameter	16.619 (cm ²)
A_2	Tank 2 inside diameter	16.619 (cm ²)
A_3	Tank 3 inside diameter	16.619 (cm ²)
A_4	Tank 4 inside diameter	16.619 (cm ²)
b_1	Outflow orifice diameter of Tank 1	0.5027 (cm ²)
b_2	Outflow orifice diameter of Tank 2	0.3318 (cm ²)
b_3	Outflow orifice diameter of Tank 3	0.5027 (cm ²)
b_4	Outflow orifice diameter of Tank 4	0.3318 (cm ²)
C	The discharge coefficient of the outlet	0.8
g	Gravity	981 (cm/s ²)
K	Pump flow constant	6.94 (cm ³ /(s.V))
γ_1	Ratio of flow in tank 1 to flow in tank 4	70 (%)
γ_2	Ratio of flow in tank 2 to flow in tank 3	65 (%)

$$\begin{cases} \frac{dx_1}{dt} = \frac{K\gamma_1 u_1(t)}{A_1} - \frac{b_1 C \sqrt{2gx_1}}{A_1} \\ \frac{dx_2}{dt} = \frac{K(1-\gamma_2)u_2(t)}{A_2} + \frac{b_1 C \sqrt{2gx_1}}{A_2} - \frac{b_2 C \sqrt{2gx_2}}{A_2} \\ \frac{dx_3}{dt} = \frac{K\gamma_2 u_2(t)}{A_3} - \frac{b_3 C \sqrt{2gx_3}}{A_3} \\ \frac{dx_4}{dt} = \frac{K(1-\gamma_1)u_1(t)}{A_4} + \frac{b_3 C \sqrt{2gx_3}}{A_4} - \frac{b_4 C \sqrt{2gx_4}}{A_4} \end{cases} \quad (1)$$

where u_1 and u_2 are voltage control of pump motors 1 and 2. $x_1, x_2, x_3,$ and x_4 are water levels at tanks 1, 2, 3, and 4. Value and physical meaning were shown in Table 1. These values were collected from the experimental system.

3 Multilayer Fuzzy Logic

Multilayer Fuzzy logic was developed from Hierarchical Fuzzy [7], but the output uses sum function instead of a Fuzzy model.

The input of hidden layer can obtain directly from the input or the output of the input layer.

Fuzzy logic has been used for identifying the system, but it is only applied for simple system. For a large-scale system, the structure of Fuzzy model needs a different way to build [4]. In traditional, Fuzzy logic for identification is shown in Fig. 2.

A typical rule in a Sugeno Fuzzy model has the form:

If Input₁ = x and Input₂ = y, then Output is z = ax + by + c.

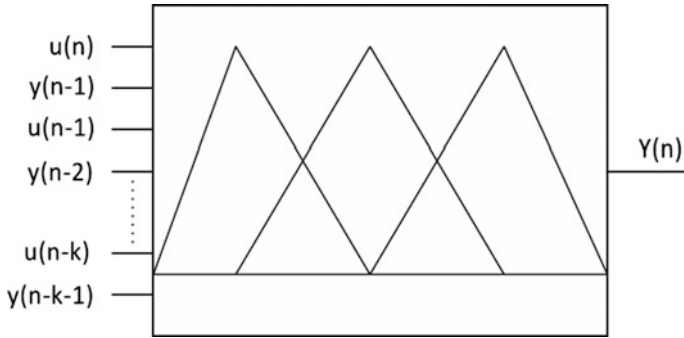


Fig. 2 Fuzzy logic in identification MISO system

For a zero-order Sugeno model, the output level z is a constant ($a = b = 0$). This was used in this paper. Each rule weights its output level z_i , by the firing strength of the rule w_i .

$$w_i = \text{AndMethod}(F_1(x), F_2(y)) \tag{2}$$

where F_1 and F_2 are the membership functions for inputs 1 and 2.

The final output of the system is the weighted average of all rule outputs, computed as:

$$y = \frac{\sum_{i=1}^N w_i z_i}{\sum_{i=1}^N w_i} \tag{3}$$

where N is the number of rules.

In that system, there is only one Fuzzy model for MISO system. The more inputs become, the more Fuzzy rule variables are to be computed. In the MIMO system, there are many inputs then the structure of this system is very complex. This is a disadvantage of Fuzzy in identification [4]. So, for overcoming this problem, we propose a Multilayer Fuzzy logic structure applied to identify the investigated MIMO system.

In this paper, Multilayer Fuzzy logic was proposed for identifying coupled tank system. Multilayer Fuzzy model to identify includes multiple MISO Multilayer Fuzzy models; MISO Multilayer Fuzzy model number is equal output number of systems. For each MISO Multilayer Fuzzy model, it consists of multiple Fuzzy logic models.

Depends on a complex system, the structure of MIMO model can be scalable with more or less single Fuzzy model in the MISO system with the fixed number of inputs.

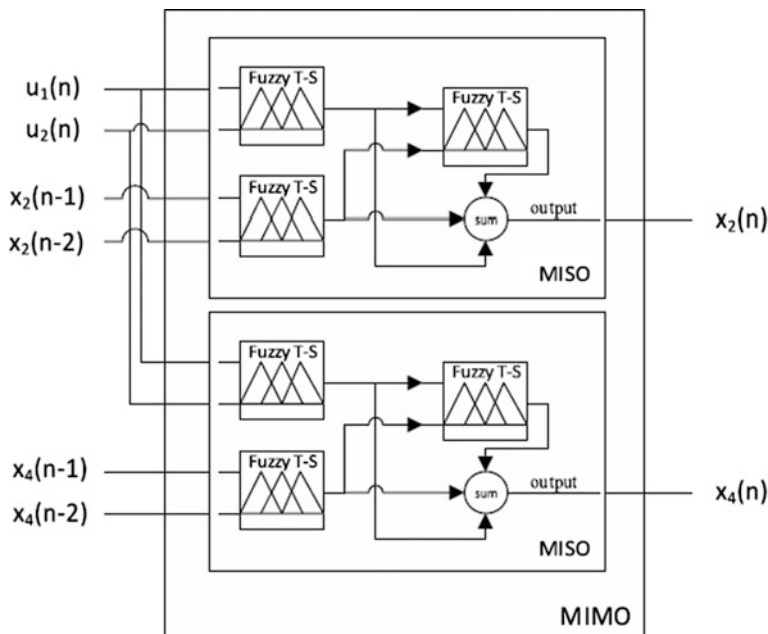


Fig. 3 Multilayer Fuzzy model structure

Multilayer Fuzzy structure using for the Quad-tank system is shown in Fig. 3. In this paper, the structure of Multilayer Fuzzy is chosen as two-Fuzzy model for the first layer and one-Fuzzy model for the second layer. The output is sum of the three-Fuzzy model output.

The final output of each MISO system as:

$$y = \sum_{j=1}^M \frac{\sum_{i=1}^N w_{ji}z_{ji}}{\sum_{i=1}^N w_{ji}} \tag{4}$$

where M is the number of Fuzzy T-S model in MISO Multilayer Fuzzy logic.

Each Fuzzy T-S system consists of two input with three membership Gaussian functions. That means each Fuzzy system has nine rules, 12 variables for membership structure, and 21 variables for the total. One MISO system that has four Fuzzy T-S models has total 84 variables. MIMO system has total 168 variables.

Input variables of Fuzzy Fig. 4 structure as follows: Input range is constant from -1 to 1 . Each input of input layer has a gain with constant value for sure the inputs are inside range.

Each input contains three membership Gaussian functions.

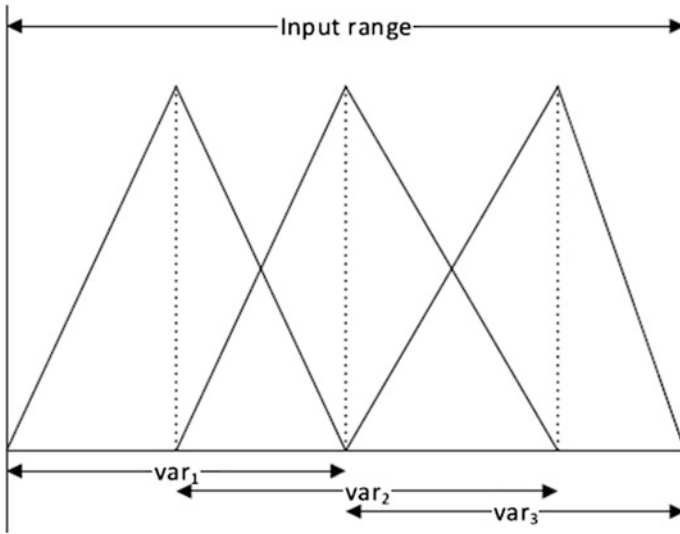


Fig. 4 Input of single Fuzzy T-S

4 Cascade Training Using Deoptimisation Algorithm

4.1 Differential Evolution Training Algorithm

Nowadays, differential evolution (DE) algorithm [11] becomes a popular optimization algorithm. In this paper, it is used for learning Multilayer Fuzzy membership structures and rules. By minimizing the cost function that is the error between actual output and Multilayer Fuzzy predicted output.

Cost function follows mean squared error (MSE) standard:

$$J = \frac{1}{N} \sum e^2$$

In which

$$e = y - \hat{y}$$

N is number of samples

\hat{y} is the output of Fuzzy models and y is the output of real data collected from the experiment.

The DE algorithm as follows:

Initialization

The initial vector was chosen NP D-Dimension randomly and should cover the entire parameter space.

$$X_{i,G} = [x_{1,i,G}, x_{1,i,G}, \dots, x_{D,i,G}]$$

where, G is the number of generations. $G = 0, 1, \dots, G_{\max}$ and $i = 1, 2, \dots, NP$

Mutation

DE generates new parameter vectors by adding the weighted difference between two population vectors to a third vector. This operation is called mutation. For each target vector $x_{i,G}$, a mutant vector is generated according to:

$$v_{i,G+1} = x_{r_1,G} + F(x_{r_2,G} - x_{r_3,G})$$

with random indexes $r_1, r_2, r_3 \in 1, 2, \dots, NP$.

The randomly chosen r_1, r_2, r_3 are also chosen to be different from the running index i . F is the real and constant coefficient $F \in [0, 2]$.

Crossover

After generating the vector through mutation, the crossover step is carried out to enhance the diversity of the population pool. The donor vector exchanges its components with the target vector $\vec{X}_{i,G}$ to form the trial vector $\vec{U}_{i,G} = [u_{1,i,g}, u_{2,i,g}, \dots, u_{D,i,g}]$. The DE algorithm often uses the binomial crossover method. The binomial crossover scheme may be outlined as:

$$u_{j,i,G} = \begin{cases} v_{j,i,G} & \text{If } (\text{rand}_{j,i}[0, 1] < C) \\ v_{j,i,G} & \text{otherwise} \end{cases}$$

Selection

To decide whether or not, it should become a member of Generation $G + 1$. The target vector $\vec{X}_{i,G}$ is compared to the trial vector $\vec{U}_{i,G}$, and the one with a lower function value is survived to the next generation. The selection operation is described as:

$$\vec{X}_{i,G+1} = \begin{cases} \vec{U}_{i,G} & \text{If } f(\vec{U}_{i,G}) < f(\vec{X}_{i,G}) \\ \vec{X}_{i,G} & \text{otherwise} \end{cases}$$

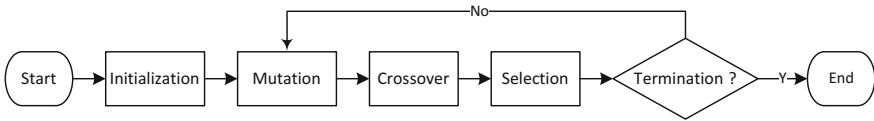


Fig. 5 Flow chart of DE algorithm for training

Termination

This is a condition to stop the loop of DE algorithm. The algorithm terminates when one of the following conditions are satisfied:

- When maximum generations are reached.
- When the best fitness is lower than desired fitness.
- When the best fitness cannot increase for a long time (see Fig. 5).

4.2 Cascade Training Multilayer Fuzzy Logic

In this paper, we proposed a cascade training Multilayer Fuzzy model for identifying the forward model of double-coupled tanks system.

The figure of cascade training is shown in Fig. 6. The core of model was trained for the first time. From the second, new single Fuzzy T-S model was trained and combined with the core model. Only new Fuzzy T-S model was trained while the previous model was remained unchanged. The new Fuzzy T-S model was integrated into hidden layer and can be extended for large-scale system. The process goes on until the cost function achieves its objectives.

Cascade training made the model more accurate, and the time for training reduced in comparison with other models possessed the same parameters.

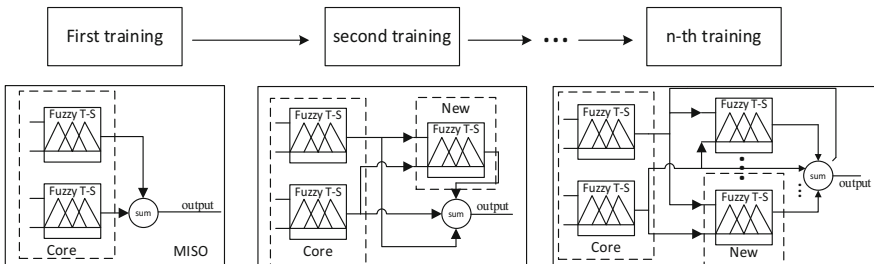


Fig. 6 Cascade training process

5 Experimental Results

5.1 Experimental Setup

In this paper, we are using quadrature tanks model for testing algorithm. Quadrature tanks consist of four tanks. In this experimental, tanks were made from acrylic with the parameter is exactly from Table 1. Figure. 7 is the real experimental setup.

Arduino Due is the microcontroller used to control pump motor and to read sensor. Real-time data exchange with the computer by Real-time Windows Target of Matlab 2014b via RS232-USB cable. The program is running on Arduino Due, and only data are transferred to the PC.

Pressure sensor uses MPX 10 from Freescale Semiconductor. It has a pressure range from 0 to 10 kPa. In the experimental system, when the water level is 30 cm, the pressure at the bottom of the tanks is 2.942 kPa. The pressure sensor has 3.5 mV/kPa. When the water level is maximal, the output goes up to 20 mV and 10.297 kPa, respectively. It is too small for the microcontroller to read. Thus, in this paper, we apply instrumentation amplifier with a gain of 67. It pushes the voltage from 1.34 to 2.029 V corresponding to the 0–30 cm height of the water level in the tanks.

Two 24 V pump motors with 10 L per minutes at 24 V are controlled to change the water flow into the tanks.

In this paper, each MISO system includes 84 variables. It composes of 36 output variables and 48 membership structure variables.

The CPU core i5-3210 m is used for running DE optimal algorithm.

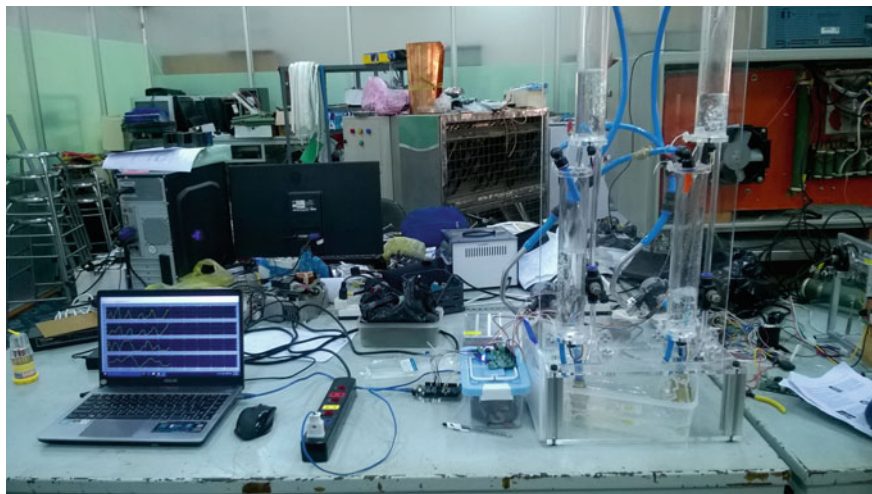


Fig. 7 Quadrature tanks system

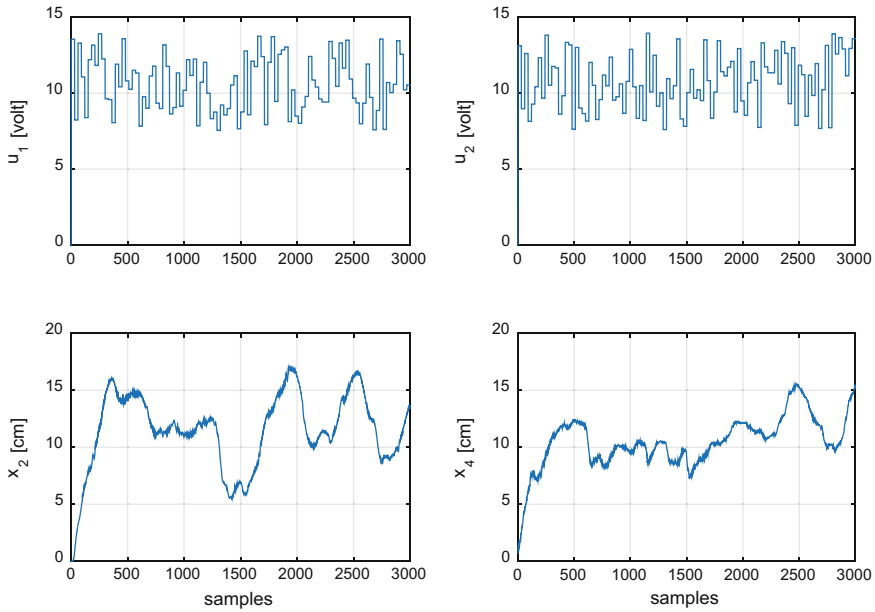


Fig. 8 Data for training purpose

5.2 Getting Data

Data was collected by step time of 0.1 s. Data for training are shown in Fig. 8. Input data are random values from 7.5 to 15 V, and data are changing the value every 10 s interval. Data are the voltage supply for *pump motor 1* (u_1) and *pump motor 2* (u_2) and the water level of *tank 2* (x_2) and *tank 4* (x_4).

Data for validating are shown in Fig. 9. It is different from training data, and its random values are from 7.5 to 15 V within 10 s interval.

5.3 Training Multilayer Fuzzy Model

After getting in/out data, DE algorithm was used for training Multilayer Fuzzy model. The proposed Multilayer Fuzzy model was presented in Sect. 3. In which, each single output of the system described as a MISO model. In the quadrature tank system in Sect. 2, we consider only output (water level) of tank 2 and tank 4. Therefore, the Multilayer Fuzzy model consists of two MISO Multilayer Fuzzy models. For each MISO model, there are three Fuzzy T-S models with two in input layer, one in the middle layer; input layer describes an impact of input to output. Middle layer describes a cross talk between the inputs. The output of MISO model is the summary of 3 T-S Fuzzy model.

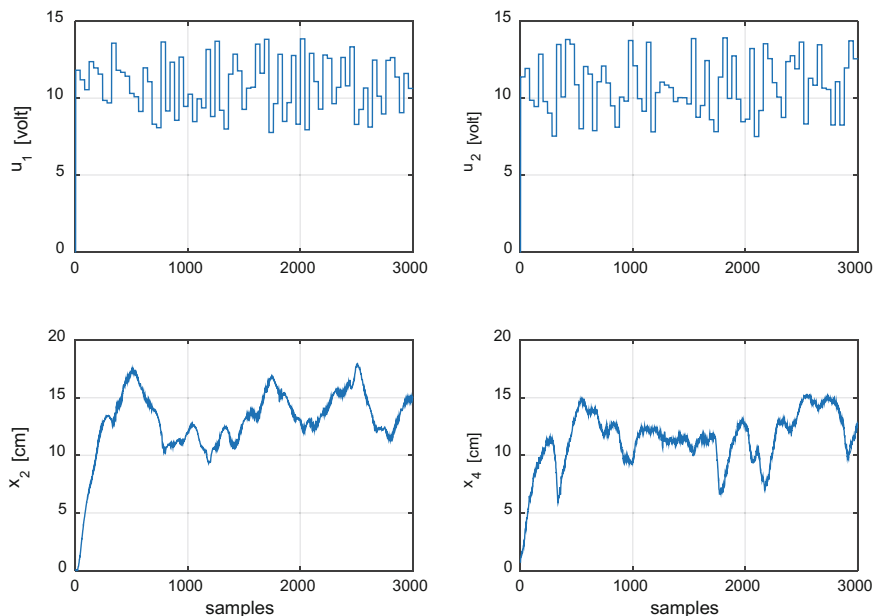


Fig. 9 Data for validating purpose

Apply DE algorithm for each MISO model. The first MISO model has four inputs ($u_1[n]$, $u_2[n]$, $x_2[n - 1]$, $x_2[n - 2]$) and one output ($x_2[n]$). The second also has four inputs ($u_1[n]$, $u_2[n]$, $x_4[n - 1]$, $x_4[n - 2]$) and one output ($x_4[n]$). After training, the model was validated with another dataset.

5.4 Identification Results

The results are compared between normal training and the cascade training.

Cascade training three times with DE algorithm, each training test includes 300 generations.

The normal training includes 900 generations.

All identification results are performed via core i5-3210 m CPU.

A proposed cascade training Multilayer Fuzzy logic using DE was compared with the normal training Multilayer Fuzzy logic using the same DE algorithm. All parameters of DE algorithm are the same. The total generation of cascade training is 900 and equally divided into three-time attempt. The total generation of normal training is 900.

Figure 10 shows the result of training and validation of cascade training for the first time. In the first time, only core model was created. It consists of two Fuzzy T-S models with 42 variables.

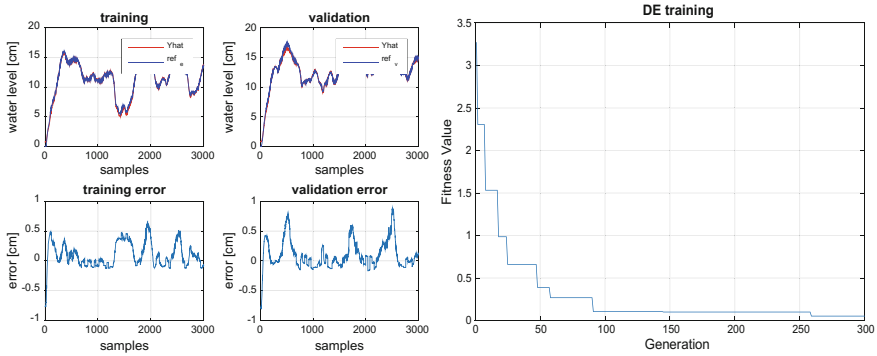


Fig. 10 Cascade training for the first time

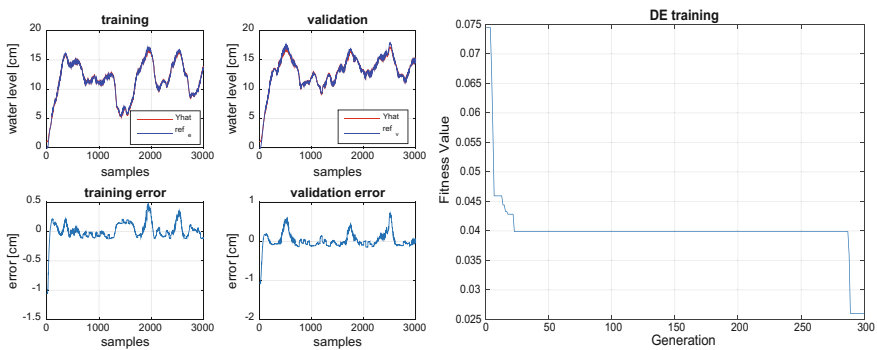


Fig. 11 Cascade training the second time

Figure 11 shows the result of training and validation of the second training. In the second training, a core model was remained, and the new Fuzzy T-S was added and to be trained.

Figure 12 shows the final cascade training. New Fuzzy T-S was added. The more Fuzzy T-S was added, the more accuracy and the less error.

Figure 13 shows the results of normal training Multilayer Fuzzy logic. With the same generation as cascade training, the normal training takes more time, and the fitness function can't reach to the cascade training.

Table 2 shows the summary of the performance comparison of cascade training and normal training, we can see, the cascade training gives a quite better performance than the normal training.

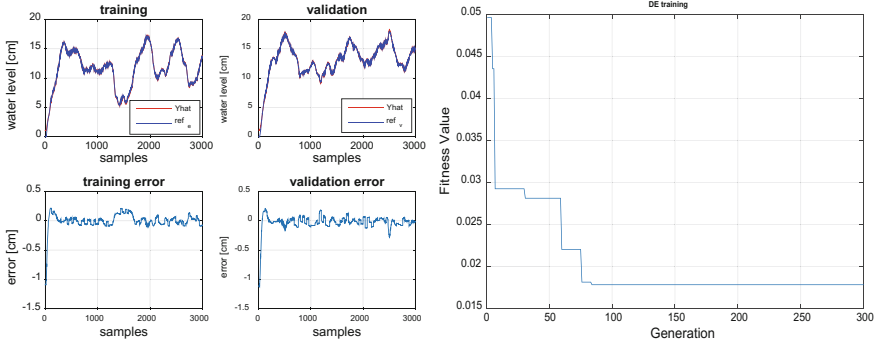


Fig. 12 Cascade training the third time

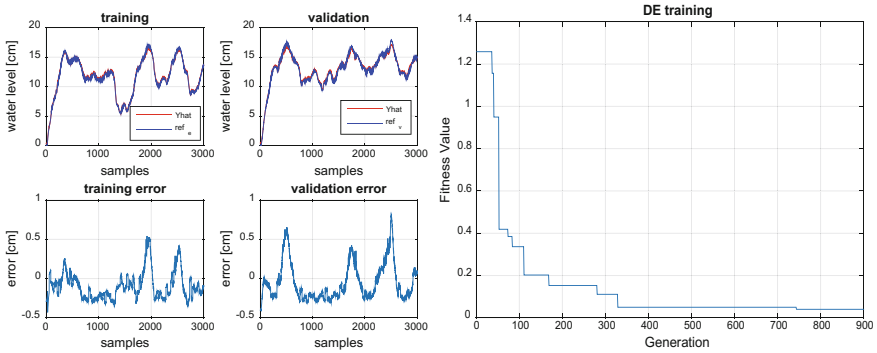


Fig. 13 Normal DE training Multilayer Fuzzy model

Table 2 The performance comparison of cascade training and normal training

	Cascade 1	Cascade 2	Cascade 3	Normal
Number of parameter	42	21	21	84
Start fitness	3.2784	0.666	0.0496	1.2584
End fitness	0.0518	0.026	0.0178	0.0403
Generations	300	300	300	900
Time [total] (s)	84.46	85.29 [169.75]	104.59 [274.34]	655.29

6 Conclusions

In this paper, a novel cascade training Multilayer Fuzzy logic for identifying double-coupled tanks system is proposed based on experiment platform. The Multilayer Fuzzy logic is created from the multiple Fuzzy T-S models. The cascade training optimized with DE algorithm sequentially trained Multilayer Fuzzy model

one by one. The experimental results show that proposed method gives better performance than the normal training method. This proposed method can be applied to the optimal Multilayer Fuzzy logic that efficiently applied for identifying MISO and MIMO system. The results prove that the proposed cascade training give a better performance and more robust than the original normal training. Hence, it is quite available for applying a scalable Multilayer Fuzzy model to a more complex nonlinear uncertain MIMO system. Furthermore, the results also confirm that proposed forward cascade training Multilayer Fuzzy model can be used for model-based control in future studies.

Acknowledgments This paper is funded by Vietnam National Foundation for Science and Technology Development (NAFOSTED) under grant number 107.01-2015.23 and by Vietnam National University Ho Chi Minh City (VNU-HCM) under grant number B2016-20-03.

References

1. Zadeh LA (1965) Fuzzy sets. *Inf Control* 8(8):338–3365
2. Espinosa J, Vandewalle J, Wertz V (2005) Fuzzy logic, identification and predictive control
3. Anh HPH, Ahn KK (2009) Identification of pneumatic artificial muscle manipulators by a MGA-based nonlinear NARX fuzzy model. *Mechatronics* 19(1):106–133
4. Takagi T, Sugeno M (1985) Fuzzy identification of systems and its applications to modeling and control. *IEEE Trans Syst Man Cybern SMC-15*(1):116–132
5. Mendes J, Araújo R, Souza F (2013) Adaptive fuzzy identification and predictive control for industrial processes. *Expert Syst Appl* 40(17):6964–6975
6. Rutkowski L, Korytkowski M, Scherer R, Tadeusiewicz R, Zadeh LA, Zurada JM (2016) New method for fuzzy nonlinear modelling based on genetic programming. In: *Lecture notes in computer science] artificial intelligence and soft computing*, vol 9692, no 38, pp 432–449
7. Raju G, Zhou J, Kisner R (1991) Hierarchical fuzzy control. *Int J Control* 54(5):1201–1216
8. Sun L, Huo W (2015) Adaptive fuzzy control of spacecraft proximity operations using hierarchical fuzzy systems. *IEEE/ASME Trans Mechatron* 4435(c):1–1
9. Rodríguez FO, de Jesús Rubio J, Gaspar CRM, Tovar JC, Armendáriz MAM (2013) Hierarchical fuzzy CMAC control for nonlinear systems. *Neural Comput Appl* 23(S1):323–331
10. Tu KY, Lee TT, Wang WJ (2000) Design of a multi-layer fuzzy logic controller for multi-input multi-output systems. *Fuzzy Sets Syst* 111(2):199–214
11. Storn R, Price K (1997) Differential evolution—a simple and efficient heuristic for global optimization over continuous spaces. *J Global Optim* 11(4):341–359

Enhanced Adaptive Fuzzy Sliding Mode Control for Nonlinear Uncertain Serial Pneumatic Artificial Muscle (PAM) Robot System



Cao Van Kien and Ho Pham Huy Anh

Abstract This chapter proposes a new enhanced adaptive fuzzy sliding mode controller (EAFSMC) with its perfect suitability for use in the control of a highly nonlinear and uncertain serial pneumatic artificial muscle (PAM) robot. The critical proof of the stability and the convergence of the overall system is presented using Lyapunov stability principle. Simulation results of the proposed EAFSMC control, applied to a two-degree-of-freedom nonlinear serial PAM robot, are implemented, and we have evaluated their efficacy in maintaining Lyapunov stability and their good performance.

Keywords Enhanced adaptive fuzzy sliding mode control (EAFSMC) · Adaptive Takagi–Sugeno (T-S) fuzzy rules · Pneumatic artificial muscle (PAM) 2-DOF serial PAM robot · Lyapunov stability principle

1 Introduction

Nowadays, sliding mode control (SMC) is well known with its robustness to system uncertainties and external noises. A SMC algorithm through its switching laws guarantees asymptotic stability of the uncertain nonlinear system. Thus, up to now, SMC control has been increasingly used in versatile industrial engineering [1–3]. Regrettably, the inherent disadvantage of SMC linked to its switching control which makes bad chattering issue. As to deleting chattering effect, researchers often use a saturated function [4] combining the sliding surface. The drawback is that this saturated function term can fail system stability of the closed-loop plant. Thus, conventional SMC approach meets great difficulty in controlling unstructured uncertain systems. Some recently proposed methods try to overcome this difficulty by hybridized a SMC controller and fuzzy set. Then, some of adaptive fuzzy SMC

C. Van Kien · H. P. H. Anh (✉)
FEEE, DCSELAB, Ho Chi Minh City University of Technology,
VNU-HCM, Ho Chi Minh City, Vietnam
e-mail: hphanh@hcmut.edu.vn

methods [5, 6] have been implemented. The adaptive laws in these approaches are designed based on the Lyapunov stability principle. Consequently, some hybrid fuzzy SMC methods have been proposed in which the asymptotic stability of the investigated closed-loop fuzzy SMC system is successfully proved [7–11]. The benefit of this combined fuzzy SMC system is that the fuzzy laws can principally approximately identify arbitrary continuous functions. Nevertheless, in order to approximately model a time-varied nonlinear MIMO system, a fuzzy set often requires a huge number of fuzzy *if-then* laws. Then, a big number of fuzzy *if-then* laws will need a high time-consuming calculation. Hence, nowadays, the requirement of a newly efficient adaptive rule initiatively proposed to a fuzzy SMC method as to online adaptively update the coefficients of the fuzzy rules, is strongly necessary, which will guarantee a reduced computation load.

Improving above-mentioned results, this chapter proposes a novel-enhanced adaptive fuzzy sliding mode EAFSMC method which will be applied on the highly nonlinear uncertain serial PAM robot system. The new proposed EAFSMC method contribution is to efficiently implement adaptation rules of fuzzy sliding mode algorithm which is tested on a nonlinear uncertain serial PAM robot system, and furthermore to introduce the Lyapunov function and then mathematically successfully demonstrate the asymptotic convergence for the closed-loop serial PAM robot and eventually to comparatively evaluate both of classic fuzzy SMC and the novel-enhanced EAFSMC method.

This chapter is organized as follows. Section 2 introduces the investigated nonlinear uncertain serial PAM robot. Section 3 introduces the conventional fuzzy SMC control and its application to an uncertain nonlinear serial PAM robot. Section 4 presents the newly proposed enhanced EAFSMC method with its stability proof based on Lyapunov principle which is well applied to the serial PAM robot application. Section 5 presents the simulation results of the EAFSMC algorithm applied to a nonlinear uncertain serial PAM robot system. Eventually, Sect. 6 is the conclusion.

2 The Nonlinear Serial Pam Robot Setup

A general configuration and working setup of the investigated serial PAM robot are presented in Figs. 1 and 2, respectively.

The configuration setup (see Fig. 2) composes of a PC (2.7 GHz) which provides the voltage values $u_1(t)$ and $u_2(t)$ to the two proportional valves (FESTO, MPYE-5-1/8HF-710B), via a D/A converter (ADVANTECH, PCI 1720) which turns digital values from PC to analog voltage $u_1(t)$ and $u_2(t)$, respectively.

The rotation torque is produced by the pneumatic pressure difference, generated from air compressor, from the antagonistic PAM muscles. Consequently, both joints of the 2-dof serial PAM robot will rotate to track the required joint-angle references ($Y_{REF1}(k)$ and $Y_{REF2}(k)$), respectively. The rotating angles, θ_1 [deg] and θ_2 [deg], are measured with two rotary encoders (METRONIX, H40-8-3600ZO)

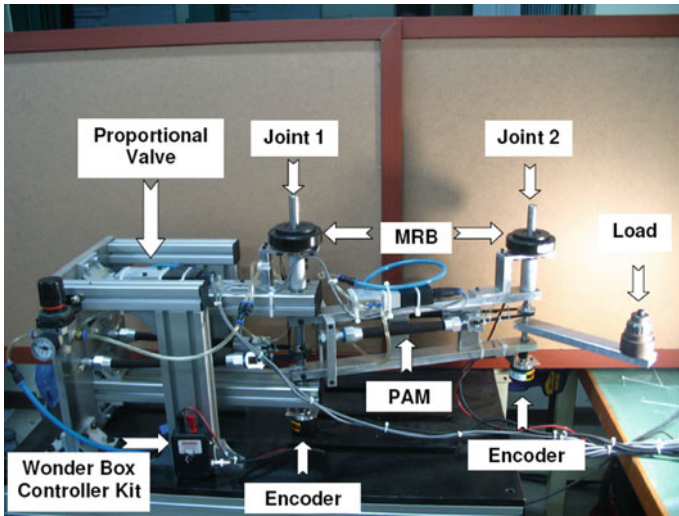


Fig. 1 General configuration of the investigated serial PAM robot

and supplied back to the PC via a 32-bit counter card (COMPUTING MEASUREMENT, PCI QUAD-4) which turns pulse signals to analog angular values $y_1(t)$ and $y_2(t)$. The pneumatic line is supplied with the pressure of 4 bar, and the control algorithm of the closed-loop serial PAM robot system is coded in C-mex code run in Real-Time Windows Target of SIMULINK environment. Table 1 presents the hardware setup installed from Fig. 2. A photograph of the experiment serial PAM robot system is illustrated in Fig. 1.

3 Classic Sliding Mode (SMC) Control of Serial Pam Robot

The serial PAM robot is applied as the simulated robot arm presented in Fig. 3.

The dynamic equation of investigated serial PAM robot is presented as:

$$M(q)\ddot{q} + C_1(q, \dot{q}) = \tau \tag{1}$$

with

$$M = \begin{bmatrix} m_1 l^2 + 2m_2 l^2 + 2m_2 l^2 \cos q_2 & m_2 l^2 + m_2 l^2 \cos q_2 \\ m_2 l^2 + m_2 l^2 \cos q_2 & m_2 l^2 \end{bmatrix}$$

$$C_1(q, \dot{q}) = \begin{bmatrix} -2m_2 l^2 \dot{q}_1 \dot{q}_2 \sin q_2 - m_2 l^2 \dot{q}_2^2 \sin q_2 \\ m_2 l^2 \dot{q}_1^2 \sin q_2 \end{bmatrix}$$

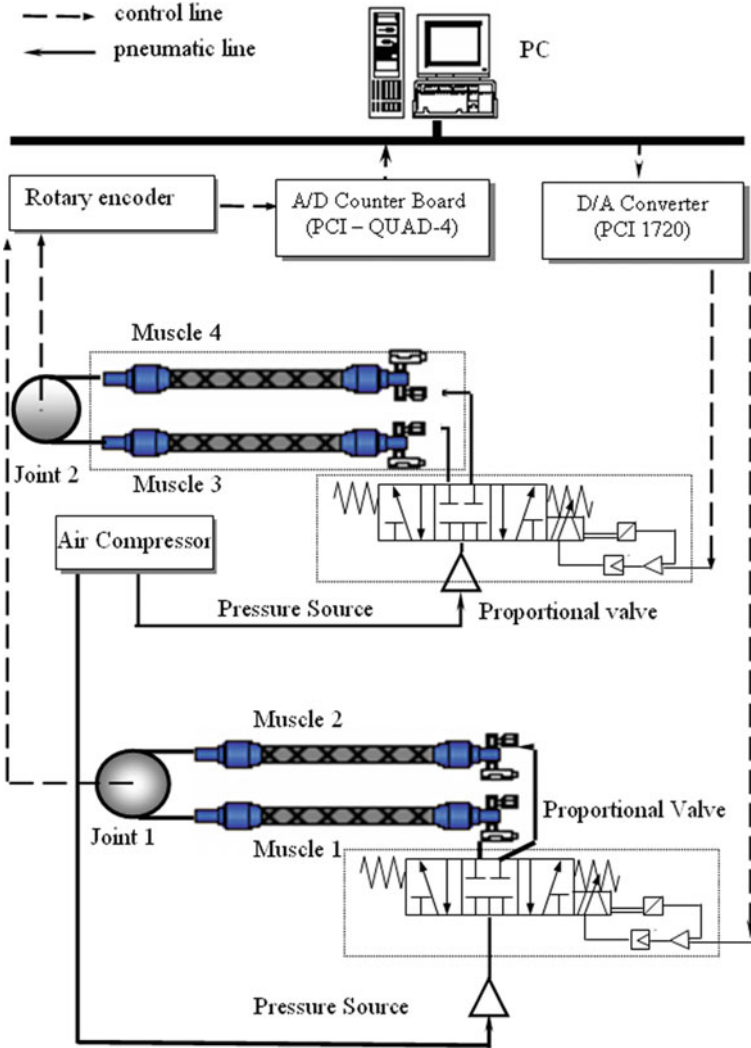


Fig. 2 Working setup of the investigated serial PAM robot system

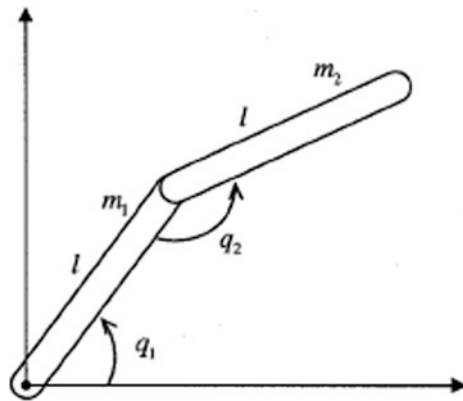
The purpose is to precisely track the required trajectory q_d of the serial PAM robot (1) using SMC controller. The value of \dot{q} is calculated from $C_1(q, \dot{q})$ of (1), and it is described as:

$$\tau = M(q)\ddot{q} + C_1(q, \dot{q})\dot{q} \tag{2}$$

Table 1 Lists of the experimental hardware setup

No.	Name	Model name	Company
1	Proportional valve (2)	MPYE-5-1/8HF-710 B	FESTO
2	Pneumatic artificial muscle (4)	MAS-10-N-220-AA-MCFK	FESTO
3	D/A board	PCI 1720	ADVANTECH
4	Counter board	PCI QUAD-4	COMPUTING MEASUREMENT
5	Rotary encoder (2)	H40-8-3600ZO	METRONIX

Fig. 3 Compact structure of the 2-dof serial PAM robot



Then, the tracking error is considered as:

$$e = q - q_d \tag{3}$$

In which $q = [q_1, q_2]^T$, $q_d = [q_{1d}, q_{2d}]^T$

The sliding surface is defined as:

$$s = \dot{e} + \lambda e \tag{4}$$

with $\lambda = \text{diag}[\lambda_1, \lambda_2]$, λ_1 and λ_2 represent the control bandwidth of the serial PAM robot.

Furthermore, it also needs to choose τ as to ensure the requirement (1). First, the reference state is considered as:

$$\dot{q}_r = \dot{q} - s = \dot{q}_d - \lambda e \tag{5}$$

Then, the control input τ is selected as:

$$\tau = \hat{M}\dot{q}_r + \hat{C}_1\dot{q}_r - As - K\text{sgn}(s) \tag{6}$$

with \hat{M} and \hat{C}_1 represent the estimated values of $M(q)$ and $\hat{C}_1(q, \dot{q})$; $A = \text{diag}[a_1, a_2]$ and $K = \text{diag}[K_1, K_2]$ represent diagonal positive definite vectors. Combining (2) and (6), it leads,

$$Ms + (C_1 + A)s = \Delta f - K\text{sgn}(s) \tag{7}$$

with $\Delta f = \Delta\hat{M}\ddot{q}_r + \Delta\hat{C}_1\dot{q}_r$, $\Delta M = \hat{M} - M$ and $\Delta C_1 = \hat{C}_1 - C_1$. Suppose that the bounded value $|\Delta f_i|_{\text{bound}}$ of Δf_i ($i = 1, 2$) is known, then value K is selected as:

$$K_i \geq |\Delta f_i|_{\text{bound}} \tag{8}$$

The Lyapunov function is selected as:

$$V = \frac{1}{2}s^T Ms \tag{9}$$

Since M represents positive symmetric definite, it leads $V > 0$ with $s \neq 0$. The derivative of M with respect to time in (1) is determined as:

$$\dot{M} = \begin{bmatrix} -2m_2l^2\dot{q}_2 \sin q_2 & -m_2l^2\dot{q}_2 \sin q_2 \\ -m_2l^2\dot{q}_2 \sin q_2 & 0 \end{bmatrix} \tag{10}$$

Combining (7) and (10), it gets,

$$\dot{M} - 2C_1 = \begin{bmatrix} 0 & 2m_2l^2\dot{q}_1 \sin q_2 + m_2l^2\dot{q}_2 \sin q_2 \\ -2m_2l^2\dot{q}_1 \sin q_2 - m_2l^2\dot{q}_2 \sin q_2 & 0 \end{bmatrix} \tag{11}$$

It is easy to see that (11) is a skew-symmetric matrix; then, we have:

$$s^T(\dot{M} - 2C_1)s = 0 \tag{12}$$

The derivative of V is then determined as:

$$\begin{aligned} \dot{V} &= s^T Ms + \frac{1}{2}s^T \dot{M}s \\ &= s^T (Ms + C_1s) \\ &= s^T [-As + \Delta f - K \text{sgn}(s)] \\ &= \sum_{i=1}^2 (s_i[\Delta f_i - K_i \text{sgn}(s_i)] - s^T As) \end{aligned} \tag{13}$$

Choose $K_i \geq |\Delta f_i|$; it always gets $s_i[\Delta f_i - K_i \text{sgn}(s_i)] \leq 0$. Then, \dot{V} can be presented as:

$$\dot{V} = \sum_{i=1}^2 (s_i[\Delta f_i - K_i \text{sgn}(s_i)]) - s^T A s \leq -s^T A s < 0 (s \neq 0) \tag{14}$$

As to delete the chattering issue, a saturation function is used in the control law instead of the sign function as introduced in (6). The control law now has the form as:

$$\tau = \hat{M}\ddot{q}_r + \hat{C}_1\dot{q}_r - A s - K \text{sat}(s/\Phi) \tag{15}$$

In this traditional SMC control approach, the precise model of the serial PAM robot is mostly unknown. We hardly know the real exact values of $m_1 l^2$ and $m_2 l^2$ in M and C_1 components. Let's define $p_1 = m_1 l^2$ and $p_2 = m_2 l^2$. Then, it continues to define \hat{p}_1 and \hat{p}_2 represent estimated values of p_1 and p_2 . In case \hat{p}_1 and \hat{p}_2 , values are far from the real values; it must increase the control gain K to avoid the tracking error in (3) getting bigger. Using (15), the chattering issue may be removed. Unfortunately, there is still now no theoretical Lyapunov stability proof for the control rule in (15).

Simulate this classic sliding mode control method for the 2-joint serial PAM robot in (1). Select $p_1 = 1$ and $p_2 = 2$. Because serial PAM robot cannot follow a step sequence instantaneously, the required trajectory will be the output of the filtered sequential values of unit steps. The transfer function of pre-filter for each joint of the serial PAM robot is defined as [9]:

$$W_m(s) = \frac{2}{s^2 + 4s + 4} \tag{16}$$

The starting values of the serial PAM robot' angular positions are set to 0.5 radians. The estimated dynamic features of the serial PAM robot are $\hat{p}_1 = 1.5$, $\hat{p}_2 = 3$. It selects λ in (4) with the same bandwidth as in (16). For simplicity, choose $A = \text{diag}[1, 1]$ in (6). Then to determine K in (6), it needs to determine the real Δf in (14).

It initially selects $K = [20, 10]^T$. Then, run simulation and plot Δf . It gets $|\Delta f_1| \leq 45$ and $|\Delta f_2| \leq 21$. These results will fail the criterion in (12). As to respond this criterion, it increases $K = [45, 21]^T$ and simulates once more. Eventually, Figs. 4 and 6 present that the tracking precision is obtained with rather significant error. The drawback is that the chattering issue still exists as illustrated in Figs. 5 and 7.

As to overcome this disadvantage, in the next section, the proposed enhanced adaptive fuzzy sliding mode EAFSMC control algorithm is used to successfully estimate and robustly control the investigated serial PAM robot system.

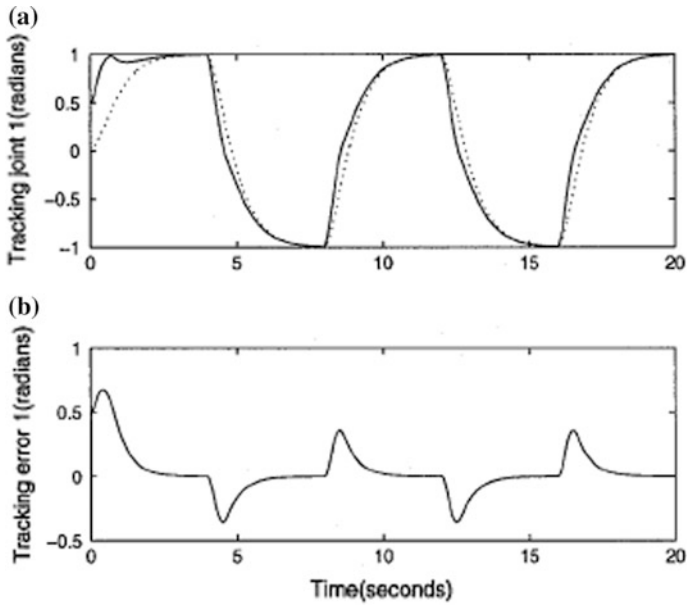


Fig. 4 a Tracking and b tracking errors of joint 1 in classic SMC control. Dash line: desired trajectory; solid line: actual trajectory

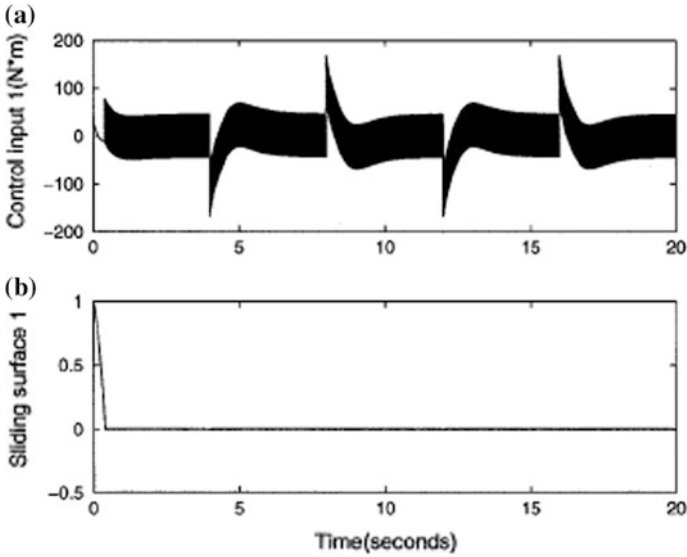


Fig. 5 a Control input value and b SMC surface of 1st joint in classical SMC

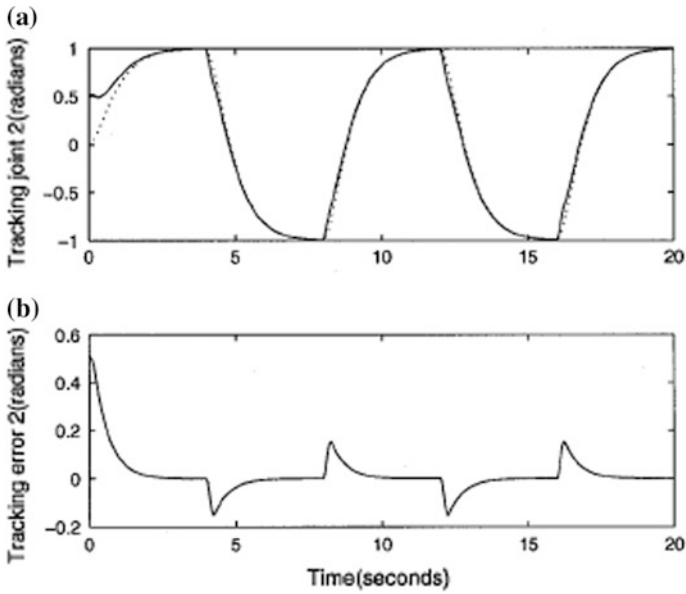


Fig. 6 a Tracking and b tracking errors of joint 2 in classic SMC control. Dash line: desired trajectory; solid line: actual trajectory

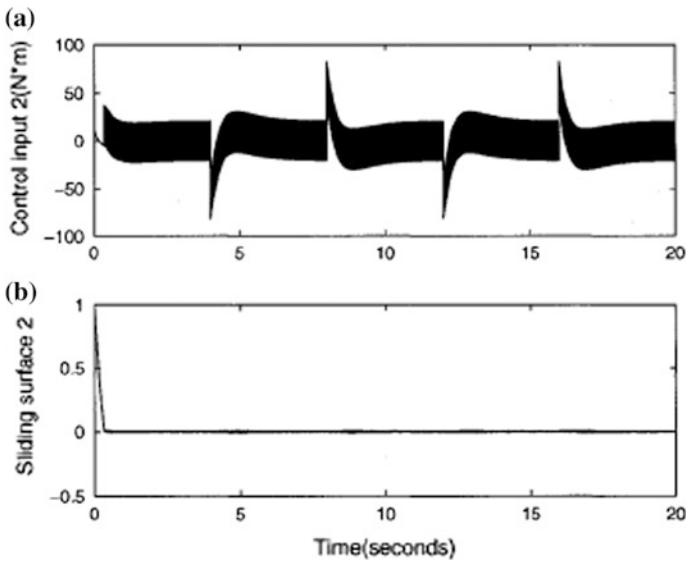


Fig. 7 a Control input value and b SMC surface of 2nd joint in classic SMC control

4 Proposed Enhanced Adaptive Fuzzy Sliding Mode Control (EAFSMC)

4.1 Implementation of proposed Enhanced Adaptive Fuzzy EAFSMC Algorithm

The enhanced adaptive fuzzy sliding mode EAFSMC control algorithm proposes a new method to reduce the MIMO fuzzy model structure presented in previous section to a single fuzzy structure which ensures to approximately identify the residual coupled features of the serial PAM robot and then successfully remove the chattering phenomenon issued from classic SMC control. The dynamic equation of investigated serial PAM robot is defined as:

$$\tau = \mathbf{M}(\mathbf{q})\ddot{\mathbf{q}} + \mathbf{C}_1(\mathbf{q}, \dot{\mathbf{q}})\dot{\mathbf{q}} + \mathbf{G}(\mathbf{q}) \quad (17)$$

The joint-angle error and the sliding SMC surface are defined as follows:

$$\mathbf{e} = \mathbf{q} - \mathbf{q}_d \quad (18)$$

$$\mathbf{s} = \dot{\mathbf{e}} + \lambda \mathbf{e} \quad (19)$$

The state variables are introduced as

$$\dot{\mathbf{q}}_r = \dot{\mathbf{q}} - \mathbf{s} = \dot{\mathbf{q}}_d - \lambda \mathbf{e} \quad (20)$$

$$\ddot{\mathbf{q}}_r = \ddot{\mathbf{q}} - \dot{\mathbf{s}} = \ddot{\mathbf{q}}_d - \lambda \dot{\mathbf{e}} \quad (21)$$

Then, the necessary torque input value is estimated by

$$\tau = \hat{\mathbf{M}}\ddot{\mathbf{q}}_r + \hat{\mathbf{C}}_1\dot{\mathbf{q}}_r + \hat{\mathbf{G}} - \mathbf{A}\mathbf{s} - \mathbf{K} \quad (22)$$

in which $\mathbf{A} = \text{diag}[a_1, \dots, a_m]$ with a_1, \dots, a_m denote positive constant values; $\mathbf{K} = [K_1, \dots, K_m]^T$ with K_j represent the fuzzy gain evaluated from the fuzzy model.

Then, the fuzzy *if-then* rules applied to the j th joint of the serial PAM robot are implemented as

$$R^{(l)} : \text{If } s_j \text{ is } A_j^l \text{ then } y \text{ is } B_j^l. \quad (23)$$

with $j = 1, \dots, m; l = 1, \dots, M$.

The K_j value is determined as:

$$K_j = \frac{\sum_{l=1}^M \theta_j^l \left[\mu_{A_j^l}(s_j) \right]}{\sum_{l=1}^M \left[\mu_{A_j^l}(s_j) \right]} = \theta_j^T \xi_j(s_j) \quad (24)$$

with

$$\xi_j(s_j) = \left[\xi_j^1(s_j), \xi_j^2(s_j), \dots, \xi_j^M(s_j) \right]^T \tag{25}$$

and

$$\xi_j^l(s_j) = \frac{\mu_{A_j^l}(s_j)}{\sum_{l=1}^M \mu_{A_j^l}(s_j)} \tag{26}$$

The membership function $\mu_{A_j^l}(s_j)$ represents a Gaussian one which is defined as follows:

$$\mu_{A_j^l}(s_j) = \exp \left[- \left(\frac{s_j - \alpha_j^l}{\sigma_j^l} \right)^2 \right], \quad (j = 1, \dots, m) \tag{27}$$

The adaptation rule is expressed by

$$\dot{\theta}_j = \gamma_{sj} s_j \xi_j(s_j) \tag{28}$$

in which the γ_{sj} value is constantly positive.

4.2 Stability Proof of Proposed Enhanced Adaptive Fuzzy EAFSMC Control Algorithm

The Lyapunov function is defined as follows:

$$V = \frac{1}{2} s^T M s + \frac{1}{2} \sum_{j=1}^m \frac{1}{\gamma_{sj}} \phi_j^T \phi_j \tag{29}$$

with $\phi_j = \theta_j^* - \theta_j$. The derivation of V gives

$$\dot{V} = s^T \dot{M} s + \frac{1}{2} s^T \dot{M} s + \sum_{j=1}^m \frac{1}{\gamma_{sj}} \phi_j^T \dot{\phi}_j \tag{30}$$

Since $(\dot{M} - 2C_1)$ represents a skew-symmetric matrix, it leads to $s^T \dot{M} s + \frac{1}{2} s^T \dot{M} s = s^T (\dot{M} s + C_1 s)$. From (17) and (22), we have

$$\mathbf{M}(\mathbf{q})\ddot{\mathbf{q}} + \mathbf{C}_1(\mathbf{q}, \dot{\mathbf{q}})\dot{\mathbf{q}} + \mathbf{G}(\mathbf{q}) = \hat{\mathbf{M}}\ddot{\mathbf{q}}_r + \hat{\mathbf{C}}_1\dot{\mathbf{q}}_r + \hat{\mathbf{G}} - \mathbf{A}s - \mathbf{K} \tag{31}$$

Because $\dot{\mathbf{q}}_r = \dot{\mathbf{q}} - s$ and $\ddot{\mathbf{q}}_r = \ddot{\mathbf{q}} - \dot{s}$ in (20) and (21), we get

$$\mathbf{M}\dot{s} + (\mathbf{C}_1 + \mathbf{A})s = \Delta\mathbf{f} - \mathbf{K} \tag{32}$$

with $\Delta\mathbf{f} = \Delta\mathbf{M} \ddot{\mathbf{q}}_r + \Delta\mathbf{C}_1 \dot{\mathbf{q}}_r + \Delta\mathbf{G}$, $\Delta\mathbf{M} = \hat{\mathbf{M}} - \mathbf{M}$, $\Delta\mathbf{C}_1 = \hat{\mathbf{C}}_1 - \mathbf{C}_1$ and $\Delta\mathbf{G} = \hat{\mathbf{G}} - \mathbf{G}$. Then, \dot{V} becomes

$$\begin{aligned} \dot{V} &= s^T(\mathbf{M}\dot{s} + \mathbf{C}_1s) + \sum_{j=1}^m \frac{1}{\gamma_{sj}} \phi_j^T \dot{\phi}_j \\ &= s^T(-\mathbf{A}s + \Delta\mathbf{f} - \mathbf{K}) + \sum_{j=1}^m \frac{1}{\gamma_{sj}} \phi_j^T \dot{\phi}_j \\ &= \sum_{j=1}^m [s_j(\Delta f_j - K_j)] - s^T \mathbf{A}s + \sum_{j=1}^m \frac{1}{\gamma_{sj}} \phi_j^T \dot{\phi}_j \\ &= \sum_{j=1}^m \left[s_j \left(\Delta f_j - \theta_j^T \xi_j(s_j) \right) \right] - s^T \mathbf{A}s + \sum_{j=1}^m \frac{1}{\gamma_{sj}} \phi_j^T \dot{\phi}_j \\ &= \sum_{j=1}^m \left[s_j \left(\Delta f_j - (\theta_j^*)^T \xi_j(s_j) + \phi_j^T \xi_j(s_j) \right) \right] - s^T \mathbf{A}s + \sum_{j=1}^m \frac{1}{\gamma_{sj}} \phi_j^T \dot{\phi}_j \\ &= \sum_{j=1}^m \left[s_j \left(\Delta f_j - (\theta_j^*)^T \xi_j(s_j) \right) \right] - s^T \mathbf{A}s + \sum_{j=1}^m \left(\frac{1}{\gamma_{sj}} \phi_j^T \left[\gamma_{sj} s_j \xi_j(s_j) + \dot{\phi}_j \right] \right) \end{aligned} \tag{33}$$

The adaptation law $\dot{\theta}_j = \gamma_{sj} s_j \xi_j(s_j)$ is chosen. Because $\dot{\phi}_j = -\dot{\theta}_j = -\gamma_{sj} s_j \xi_j(s_j)$, \dot{V} obtains the result:

$$\dot{V} = \sum_{j=1}^m \left(s_j \left[\Delta f_j - (\theta_j^*)^T \xi_j(s_j) \right] \right) - s^T \mathbf{A}s \tag{34}$$

Then, the minimal approximating error is calculated as:

$$\omega_j = \Delta f_j - (\theta_j^*)^T \xi_j(s_j) \tag{35}$$

Then, \dot{V} changes to

$$\begin{aligned} \dot{V} &= \sum_{j=1}^m (s_j \omega_j) - s^T \mathbf{A}s \leq \sum_{j=1}^m |s_j| |\omega_j| - s^T \mathbf{A}s \\ &= \sum_{j=1}^m \left(|s_j| |\omega_j| - a_j s_j^2 \right) = \sum_{j=1}^m (|s_j| (|\omega_j| - a_j |s_j|)) \end{aligned} \tag{36}$$

Equation shows that the minimal approximating error ω_j seems as small as possible. It is possible to select a_j as to ensure $a_j|s_j| > |\omega_j|$ ($s_j \neq 0$). Finally, it proves $\dot{V} < 0$ for $s \neq 0$.

5 Simulation Results

The dynamic equation for the 2-joint serial PAM robot is described as:

$$\tau = M(q)\ddot{q} + C_1(q, \dot{q})\dot{q} \quad (37)$$

with

$$\begin{aligned} M(q) &= \begin{bmatrix} m_1l^2 + 2m_2l^2 + 2m_2l^2 \cos q_2 & m_2l^2 + m_2l^2 \cos q_2 \\ m_2l^2 + m_2l^2 \cos q_2 & m_2l^2 \end{bmatrix} \\ &= \begin{bmatrix} P_1 + 2P_2 + 2P_2 \cos q_2 & P_1 + P_2 \cos q_2 \\ P_1 + P_2 \cos q_2 & P_2 \end{bmatrix} \end{aligned} \quad (38)$$

$$C_1(q, \dot{q}) = \begin{bmatrix} -P_2\dot{q}_2 \sin q_2 & -P_2\dot{q}_1 \sin q_2 - P_2\dot{q}_2 \sin q_2 \\ P_2\dot{q}_1 \sin q_2 & 0 \end{bmatrix} \quad (39)$$

where m_1 and m_2 represent the mass of joint1 and joint2, respectively; l denotes the length of joint1 and joint2; q_1 and q_2 represent joint-angle positions of the joint1 and joint2, respectively. The values of the parameters are chosen as $P_1 = m_1l^2 = 1$ and $P_2 = m_2l^2 = 2$. The serial PAM robot model's transfer function of pre-filter for each link is described as:

$$W_m(s) = \frac{4}{s^2 + 4s + 4} \quad (40)$$

The required trajectory is the output of filtered sequential unique steps. The starting values of the serial PAM robot' joint-angle positions are given to 0.5 radians. For all five algorithms, we choose the parameter λ_j in the sliding surface as same as the bandwidth of our desired model. The predefined adaptation gains in adaptation laws are selected as a *trial and error values*. The number and the type of membership functions for each input variable are selected to be consistent with the proposed fuzzy EAAFSMC algorithm.

The proposed enhanced adaptive fuzzy EAFSMC algorithm has reduced the MIMO fuzzy model to a single SISO fuzzy one in order to not only precisely identify the torque-coupled effect presented in (1), but also attenuate the chattering issue. The estimated values of \hat{M} and \hat{C}_1 are calculated as in previous section. In addition, A is chosen as $A = \text{diag}[250, 100]$ which is described in (22), $\gamma_{s1} = 10^4$, $\gamma_{s2} = 5 \times 10^3$ which are chosen based on (28) by trial and error. As a benefit of proposed

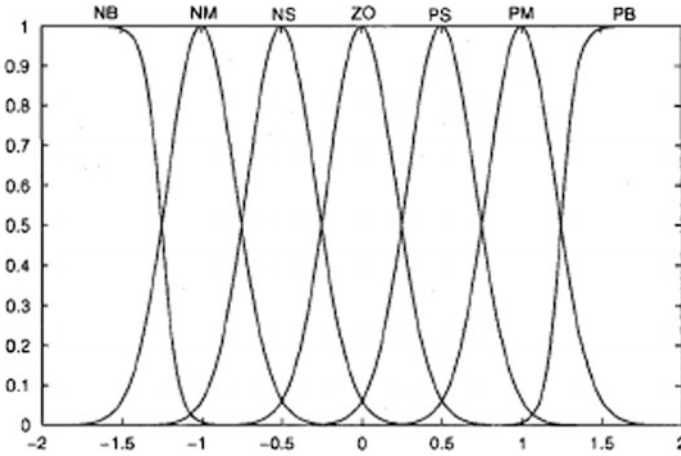


Fig. 8 Membership functions of s_j

EAFSMC, the total number of fuzzy rules is reduced from $3 \times k_1^{2m}$ in classic fuzzy SMC algorithm to k_2 in proposed fuzzy EAFSMC method. Therefore, it is reasonable to choose the value of k_2 larger than the value of k_1 . Since we have chosen $k_1 = 5$ in design process, it is simple to define $k_2 = 7$ fuzzy MPs (membership functions) for each input value: NB NM NS ZO PS PM PB. The parameters of the fuzzy MPs (membership functions) for s_j are selected using the simulation results of the sliding surface s_j . The membership functions for the variable s_j ($j = 1, 2$) in Fig. 8 are expressed as:

$$\begin{aligned}
 \mu_{s_j}NB &= \frac{1}{1 + [\exp((s_j + 1.25)/0.1)]^2} \\
 \mu_{s_j}NM &= \exp\left(-((s_j + 1)/0.3)^2\right) \\
 \mu_{s_j}NS &= \exp\left(-((s_j + 0.5)/0.3)^2\right) \\
 \mu_{s_j}ZO &= \exp\left(-((s_j)/0.3)^2\right) \\
 \mu_{s_j}PS &= \exp\left(-((s_j - 0.5)/0.3)^2\right) \\
 \mu_{s_j}PM &= \exp\left(-((s_j - 1)/0.3)^2\right) \\
 \mu_{s_j}PB &= \exp\frac{1}{1 + [\exp(-(s_j - 1.25)/0.1)]^2}
 \end{aligned} \tag{41}$$

Figures 9 and 11 show that the joint-angle tracking errors are surely bounded in the limit $[-0.005, 0.005]$ radians, which is a bit better than of classic fuzzy SMC

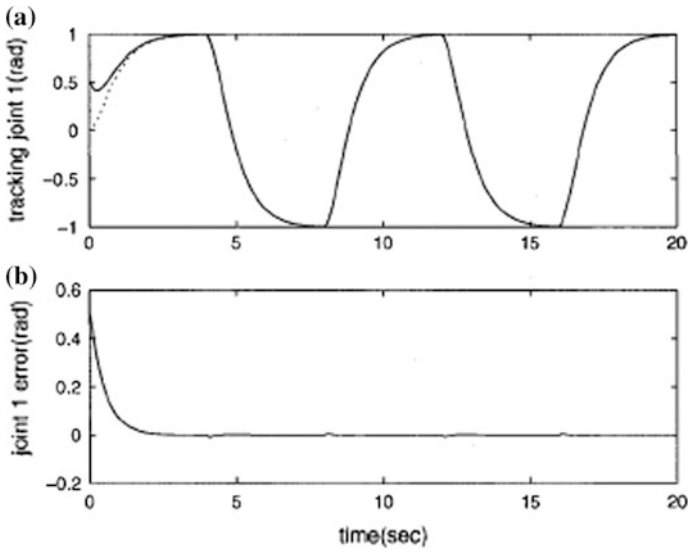


Fig. 9 a Tracking precision and b tracking errors of joint-angle 1 in proposed fuzzy EAFSMC algorithm. Dash line: required trajectory; solid line: real trajectory

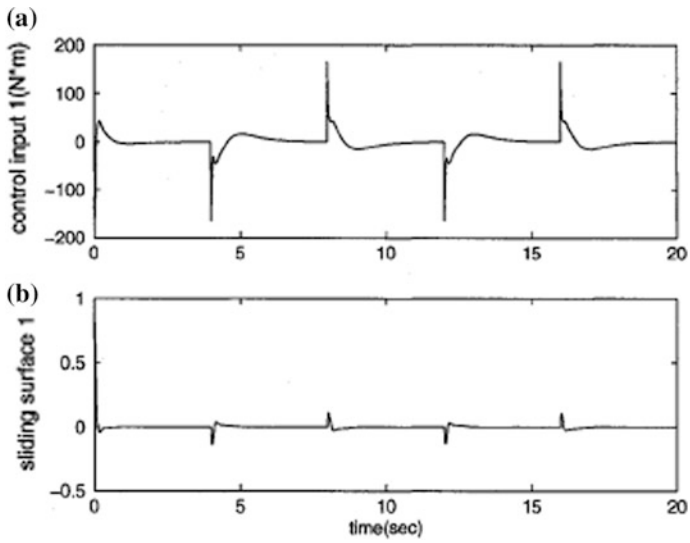


Fig. 10 a Control signal and b SMC surface of joint-angle 1 in proposed enhanced adaptive fuzzy EAFSMC algorithm

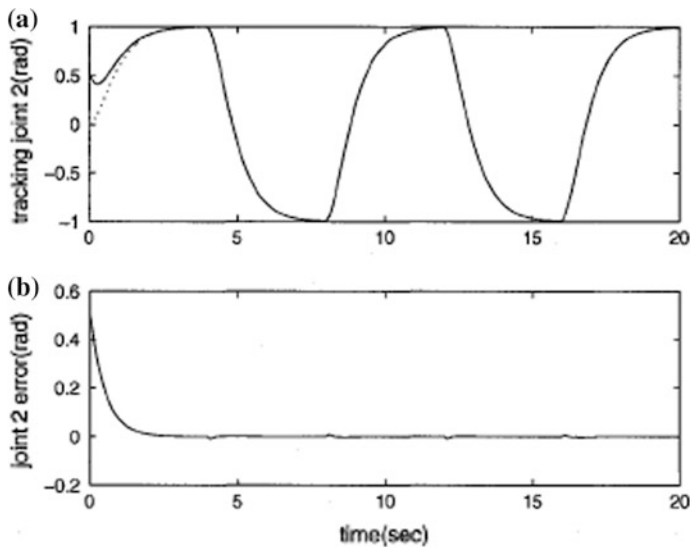


Fig. 11 a Tracking precision and b tracking errors of joint-angle 2 in proposed fuzzy EAFSMC control algorithm. Dash line: required trajectory; solid line: real trajectory

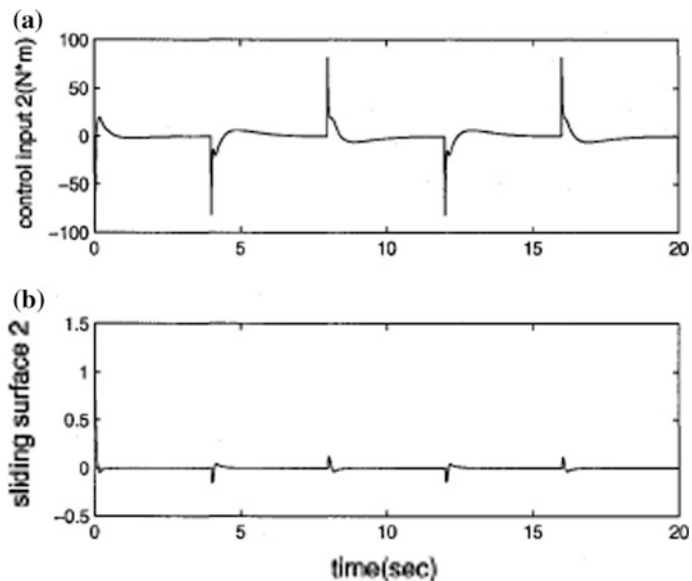


Fig. 12 a Control signal and b SMC surface of joint-angle 2 in proposed enhanced adaptive fuzzy EAFSMC control algorithm

control algorithm. However, unlike classic fuzzy SMC algorithm, Figs. 10 and 12 demonstrate that the chattering phenomenon has been strongly alleviated.

In summary, the proposed EAFSMC algorithm downgrades the initial MIMO fuzzy one to a single fuzzy model that, in addition to helping to identify the parameter, estimates the residual cross-coupled error. Thus, the proposed fuzzy AAFSMC algorithm helps to reduce both high computational load and chattering problems encountered in classic FSMC method. First, with k_2 MF (membership functions) for every input, the amount of fuzzy if-then laws installed for each joint of the serial PAM robot is k_2 which is evidently and spectacularly decreased. Second, by substituting the switching control term in classic fuzzy SMC method for the fuzzy compensator in (22), the chattering issue has been adequately alleviated.

6 Conclusions

In this chapter, a novel-proposed adaptive fuzzy EAFSMC algorithm efficiently alleviates the chattering issue by using an adaptive fuzzy compensator instead of the classical switching control term. Furthermore, the amount of fuzzy if-then laws is also significantly decreased by replacing the previous MIMO fuzzy model with an adaptive SISO fuzzy model instead. The convergence and the stability of the new proposed EAFSMC algorithm for the 2-link serial PAM robot is demonstrated theoretically based on Lyapunov stability concept.

Acknowledgements This research is funded by Vietnam National Foundation for Science and Technology Development (NAFOSTED), by DCSELAB and by Vietnam National University Ho Chi Minh City (VNU-HCM).

References

1. Song Q, Jia C (2016) Robust speed controller design for permanent magnet synchronous motor drives based on sliding mode control. *Energy Proc* 88:867–873
2. Esmaili N, Alfi A, Khosravi H (2017) Balancing and trajectory tracking of two-wheeled mobile robot using backstepping sliding mode control: design and experiments. *J Intell Robot Syst* 1–13
3. Shiri R, Nekoo SR (2017) A general approach to dynamic gain adaptation of sliding mode control for robotic arms with parameter uncertainty. *Majlesi J Mechatron Syst* 5(4)
4. Guo Y, Woo PY (2003) An adaptive fuzzy sliding mode controller for robotic manipulators. *IEEE Trans Syst Man Cybern Part A* 33(2):149–160
5. Lin CM, Hsu CF (2004) Adaptive fuzzy sliding-mode control for induction servomotor systems. *IEEE Trans Energy Convers* 19(2)
6. Medhaffar H, Derbel N, Damak T (2006) A decoupled fuzzy indirect adaptive sliding mode controller with application to robot manipulator. *Int J Model Ident Control* 1(1):23–29
7. Soltanpour MR, Khooban MH, Khalghani MR (2016) An optimal and intelligent control strategy for a class of nonlinear systems: adaptive fuzzy sliding mode. *J Vib Control* 22(1):159–175

8. Anand R, Mary PM (2016) Improved dynamic response of DC to DC converter using hybrid PSO tuned fuzzy sliding mode controller. *Circ Syst* 7(06):946
9. Ullah N, Shaoping W, Khattak MI, Shafi M (2015) Fractional order adaptive fuzzy sliding mode controller for a position servo system subjected to aerodynamic loading and nonlinearities. *Aerosp Sci Technol* 43:381–387
10. Oveisi A, Nestorović T (2016) Robust observer-based adaptive fuzzy sliding mode controller. *Mech Syst Signal Process* 76:58–71
11. Moussaoui S, Boukroune A (2017) Stable adaptive fuzzy sliding-mode controller for a class of underactuated dynamic systems. In: *Recent advances in electrical engineering and control applications*. Springer, pp 114–124

Performance Evaluation of a 2D-Haptic Joystick Featuring Bidirectional Magneto-Rheological Actuators



Tri Bao Diep, Hiep Dai Le, Cuong Van Vo and Hung Quoc Nguyen

Abstract In this research, a new 2D-haptic joystick featuring a 2D-gimbal mechanism and two bidirectional magneto-rheological actuators (BMRAs) is designed, manufactured, and experimentally tested. Firstly, a new configuration of proposed 2D-haptic joystick is introduced; then, the BMRAs for force feedback of the haptic joystick are proposed, optimally designed, and experimentally evaluated. The BMRA has two disks rotating in opposite directions at the same speed. The two disks are placed inside a housing which is connected to the gimbal mechanism. The BMRA has two coils placed directly on each side of the housing. A prototype of the whole haptic joystick is then manufactured, and a controller is designed to feedback a required force to the operator. Force feedback performance of the haptic joystick is then experimentally investigated and compared with simulated one.

Keywords MR fluid · Bidirectional magneto-rheological actuator Joystick · Haptic

T. B. Diep · C. Van Vo · H. Q. Nguyen (✉)
Mechanical Engineering, Ho Chi Minh University of Industry,
Ho Chi Minh City, Vietnam
e-mail: hung.nq@vgu.edu.vn

T. B. Diep
e-mail: 1500103@student.hcmute.edu.vn; diepbaotri@iuh.edu.vn

C. Van Vo
e-mail: hoacuonghpm@gmail.com

H. D. Le
Faculty of Engineering, Vietnamese-German University,
Binh Duong New City, Vietnam
e-mail: ledaihiep1993@gmail.com

1 Introduction

In modern Industry, the application of telemanipulator is very necessary, especially for robots working in hazardous environment (polluted, radioactive) or extreme environment (adventure robots). Basically, a telemanipulator system consists of a slave manipulator and a master operator. An important issue to deal with in a telemanipulator system is the lack of information on forces and torques at the end-effector of the slave manipulator to the master operator. The lack of this information reduces the accuracy and flexibility of the system. Therefore, a telemanipulator system with a force feedback system to the operator (haptic telemanipulator system) is very significant.

In recent years, with the fast development in research and application of smart materials, especially magneto-rheological fluid (MRF), several researches on haptic system featuring MRF have been performed. Kim et al. [1] have designed and manufactured a 5-DOF haptic hand featuring five linear MR brakes. The results showed that the haptic hand can fair reflect required forces to the fingers of human operator (8 N). However, the off-state force is quite high, around 2 N. This is a big challenge for the system to reflect a true force to the operator. Winter and Bouzit [2] have designed and manufactured a 5-DOF haptic glove featuring five linear MR brakes. The maximum force can reach up to 6 N. However, the off-state force is still high in this case (1.5 N), and the brake general size is somewhat large: $50 \times 12 \times 12$ mm. Conrad [3] have designed and manufactured a 3-DOF haptic glove featuring three rotary MR brakes in order to feedback the force to the thumb, the point (index), and the middle finger. The general dimensions of the MR brakes are: $D = 25$ mm and $L = 15$ mm, and the maximum force at the fingertips can reach up to 17 N. Li et al. [4] have researched on a 2-DOF haptic joystick featuring two rotary MR brakes. The general dimensions of the MR brakes are: $D = 156$ mm and $L = 21$ mm. The moment of the brake can be changed from 0.5 to 6 Nm. Nguyen Q. H. et al. have performed several researches on force feedback system using MRF [5, 6].

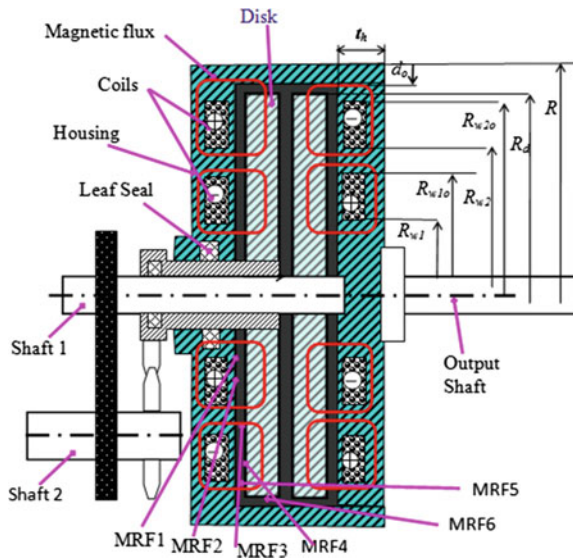
Although there have been several researches on MRF-based haptic system, however, in previous researches MR brakes are used, and off-state friction force (uncontrollable force), which significantly affects performance of the haptic system, is inevitable. In addition, traditional configurations of MR brakes were used in which the coils are placed on the cylindrical housing. This results in “bottleneck” problem of magnetic circuit and manufacturing difficulties. The main technical contribution of this work is to develop and investigate a new configuration of bidirectional MRF actuator (BMRA) for haptic application with two coils placed directly on each side of the housing. With this configuration, the off-state friction force can be eliminated, the “bottleneck” problem of magnetic circuit can be alleviated, and manufacture difficulties can be improved. In addition, by using bidirectional actuators, the inaccuracy use to off-state friction force can be eliminated.

2 The Proposed Bidirectional MRF Actuator

In this study, a configuration of the BMRA is introduced, and its actuating torque is analyzed based on Bingham plastic model of MRF. Figure 1 shows the configuration of the proposed BMRA. As shown in the figure, the BMRA has two disks rotating in opposite directions at the same speed. The two disks are placed inside a housing which is connected to the haptic devices. The space between the rotary disks and the housing is filled with MRF. The BMRA has two coils placed directly on each side of the housing. The coils are separated with the magneto-rheological fluid (MRF) by a thin wall of the housing. With this configuration, the inner face of the side housing, which is interfaced with the MRF, is continuous. This allows the MRF duct being manufactured more easily and accurately. In order to prevent the leaking of MRF, radial lip seals are employed. As an electric current is applied to the coil 1, a magnetic field in the housing and disk 1 is generated, and the MRF in the gap between the disk 1 and the housing becomes solid-like instantaneously. This results in a controllable torque transmitted from disk 1 to the housing connected with the output shaft. On the other hand, as an electric current is applied to the coil 2, a magnetic field in the housing and disk 2 is generated, and the MRF in the gap between the disk 2 and the housing becomes solid-like instantaneously. This results in a controllable torque transmitted from disk 2 to the housing. By controlling the applied currents to the coils, an expected bidirectional torque can be obtained at the output shaft.

By assuming that the MRF rheologically behaves as Bingham plastic fluids and by the assumption of a linear velocity profile in the MRF ducts, the induced transmitting torque of the MRA can be, respectively, determined as follows [7, 8]

Fig. 1 Configuration of the proposed bidirectional MR actuator



$$T = T_1 - T_2 + T_{sf} \tag{1}$$

$$\begin{aligned}
 T_1 = & \frac{\pi\mu_{d11}R_{w1}^4}{2d} \left[1 - \left(\frac{R_i}{R_{w1}}\right)^4\right]\Omega + \frac{2\pi\tau_{yd11}}{3} (R_{w1}^3 - R_i^3) + \frac{\pi\mu_{d12}R_{w1o}^4}{2d} \left[1 - \left(\frac{R_{w1}}{R_{w1o}}\right)^4\right]\Omega \\
 & + \frac{2\pi\tau_{yd12}}{3} (R_{w1o}^3 - R_i^3) + \frac{\pi\mu_{d13}R_{w2}^4}{2d} \left[1 - \left(\frac{R_{w1o}}{R_{w2}}\right)^4\right]\Omega + \frac{2\pi\tau_{yd13}}{3} (R_{w2}^3 - R_{w1o}^3) \\
 & + \frac{\pi\mu_{d14}R_{w2o}^4}{2d} \left[1 - \left(\frac{R_{w2}}{R_{w2o}}\right)^4\right]\Omega + \frac{2\pi\tau_{yd14}}{3} (R_{w2o}^3 - R_{w2}^3) + \frac{\pi\mu_{d15}R_d^4}{2d} \left[1 - \left(\frac{R_{w2o}}{R_d}\right)^4\right]\Omega \\
 & + \frac{2\pi\tau_{yd15}}{3} (R_d^3 - R_{w2o}^3) + 2\pi R_d^2 t_d (\tau_{yd16} + \mu_{d16} \frac{\Omega R_d}{d_o})
 \end{aligned} \tag{2}$$

$$\begin{aligned}
 T_2 = & \frac{\pi\mu_{d21}R_{w1}^4}{2d} \left[1 - \left(\frac{R_i}{R_{w1}}\right)^4\right]\Omega + \frac{2\pi\tau_{yd21}}{3} (R_{w1}^3 - R_i^3) + \frac{\pi\mu_{d22}R_{w1o}^4}{2d} \left[1 - \left(\frac{R_{w1}}{R_{w1o}}\right)^4\right]\Omega \\
 & + \frac{2\pi\tau_{yd22}}{3} (R_{w1o}^3 - R_i^3) + \frac{\pi\mu_{d23}R_{w2}^4}{2d} \left[1 - \left(\frac{R_{w1o}}{R_{w2}}\right)^4\right]\Omega + \frac{2\pi\tau_{yd23}}{3} (R_{w2}^3 - R_{w1o}^3) \\
 & + \frac{\pi\mu_{d24}R_{w2o}^4}{2d} \left[1 - \left(\frac{R_{w2}}{R_{w2o}}\right)^4\right]\Omega + \frac{2\pi\tau_{yd24}}{3} (R_{w2o}^3 - R_{w2}^3) + \frac{\pi\mu_{d25}R_d^4}{2d} \left[1 - \left(\frac{R_{w2o}}{R_d}\right)^4\right]\Omega \\
 & + \frac{2\pi\tau_{yd25}}{3} (R_d^3 - R_{w2o}^3) + 2\pi R_d^2 t_d (\tau_{yd26} + \mu_{d26} \frac{\Omega R_d}{d_o})
 \end{aligned} \tag{3}$$

$$T_{sf} = 0.65(2R_s)^2\Omega^{1/3} \tag{4}$$

In the above, T is the output torque, T_1 and T_2 , are, respectively, the transmitting torque from disk 1 and disk 2 to the housing, and T_{sf} is the friction torque between the housing and the seals at shaft 1. R_d is the outer radius of the disks, R_i is the inner radius of the active MRF volume which is almost equal to the radius of the shaft flange, R_s is the shaft diameter at the sealing, d is the gap size of the MRF ducts between the disks and the housing, d_o is the gap size of the annular MRF duct at the outer cylindrical face of the disks, t_d is the thickness of the disks, Ω is the angular velocity of the rotor, R_{w1} and R_{w1o} are the inner and outer radius of the first coils, and R_{w2} and R_{w2o} are the inner and outer radius of the second coils. $\mu_{d11}, \mu_{d12}, \mu_{d13}, \mu_{d14}, \mu_{d15}, \mu_{d16}$ are, respectively, the average post-yield viscosity of MRF denoted by MRF1, MRF2, MRF3, MRF4, MRF5, and MRF6 relating to disk 1, and $\tau_{yd11}, \tau_{yd12}, \tau_{yd13}, \tau_{yd14}, \tau_{yd15}, \tau_{yd16}$ are the corresponding yield stress, $\mu_{d21}, \mu_{d22}, \mu_{d23}, \mu_{d24}, \mu_{d25}, \mu_{d26}$ are the average post-yield viscosity relating to disk 2, and $\tau_{yd21}, \tau_{yd22}, \tau_{yd23}, \tau_{yd24}, \tau_{yd25}, \tau_{yd26}$ are the corresponding yield stress.

3 Optimal Design of the BMRA

In the design of actuator for haptic application, besides the transmitting torque, another issue that should be taken into account is their mass. It is obvious that the mass of the BMRA should be as small as possible to reduce the BMRA’s size and cost. In addition, smaller mass of the MRA can reduce the effect of inertia in the haptic systems. Therefore, the optimization problem in this study is to find optimal value of significant geometric dimensions of the BMRA that can produce a certain required transmitting torque while the BMRA’s mass is minimized. The BMRA’s mass can be approximately calculated by

$$m_b = V_{d1}\rho_d + V_{d2}\rho_d + V_h\rho_h + V_{s1}\rho_s + V_{s2}\rho_s + V_{MR}\rho_{MR} + V_c\rho_c \tag{5}$$

where V_{d1} , V_{d2} , V_h , V_{s1} , V_{s2} , V_{MR} and V_c are, respectively, the geometric volume of the disk 1, disk 2, the housing, the shaft 1, the shaft 2, the MRF, and the coils of the BMRA. These parameters are functions of geometric dimensions of the BMRA’s structures, which vary during the optimization process. ρ_d , ρ_h , ρ_s , ρ_{MR} , and ρ_c are densities of the disks, the housing, the shafts, the MRF, and the coil material, respectively. The method to solve optimization problem of MR brakes and actuators is mentioned in detail in [7–9]. In this study, the finite element model to analyze magnetic circuit of the BMRA is shown in Fig. 2.

In this research, C45 steel is used for magnetic components of the BMRA such as the housing and the disks, the coil wires are sized as 28-gage (diameter = 0.321 mm), and the MRF is the commercial one made by Lord Corporation, MRF132-DG. Figure 3 and Table 1 show the first optimal solution of the BMRA when the transmitting torque in disk 2 rotational direction is constrained to be greater than 5 Nm with 2% of accuracy, the convergence rate is set by 0.1%. In this case, no current is applied to coil 1 while a current of 1.5 A is applied to coil 2. The shaft radius is set by $R_s = 6$ mm considering the strength of the shaft. As shown in the results, at the optimum, transmitting torque can reach up to 5 Nm as constrained, and the mass of the optimized BMRA is 2.0744 kg. Figure 4 and Table 2 show the second optimal solution of the BMRA when the number of coil turns are rounded and fixed during optimization process.

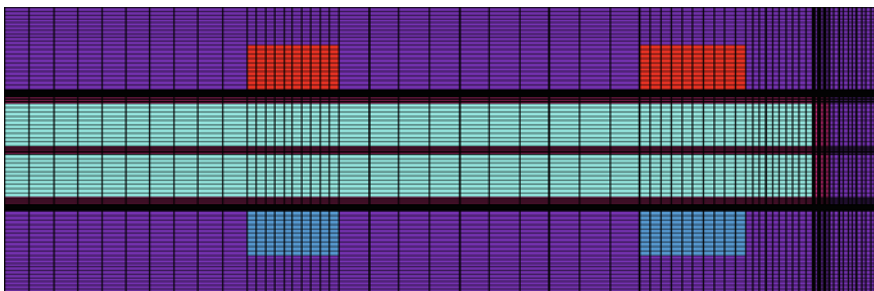


Fig. 2 Finite element model to analyze magnetic circuit of BMRA

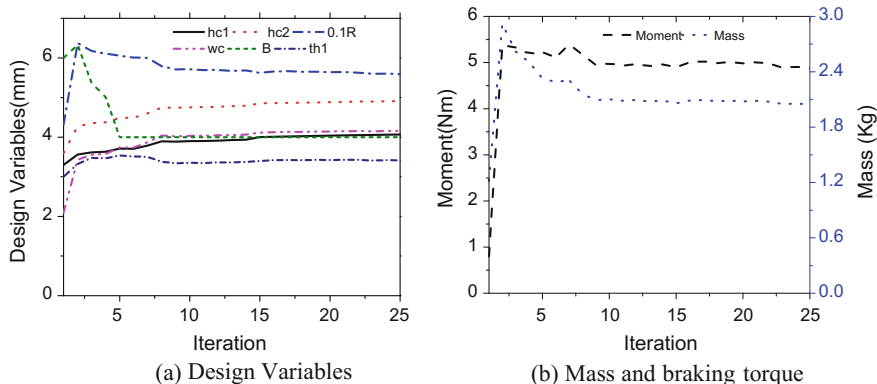


Fig. 3 First optimal solution

Table 1 First optimal solution of the BMRA

Parameter design (mm)	Performance
Coils: $w_c = 4.155$ ($n_{wc} = 13.850$), $h_{c1} = 4.05$ ($n_{hc1} = 13.521$), $h_{c2} = 4.89$ mm ($n_{hc2} = 16.333$)	Moment: 5Nm Mass: 2.0744 kg
Housing: $R = 56,306$, $t_{h1} = 3.4277$, $L = 26.565$	Power: 78.982 W
Disks: $R_i = 16,5$, $R_d = 47.3$, $b = 4$, $R_d = 54.306$	Resistor: $R_{C1} = 5.9082 \Omega$ Resistor: $R_{C2} = 11.643 \Omega$

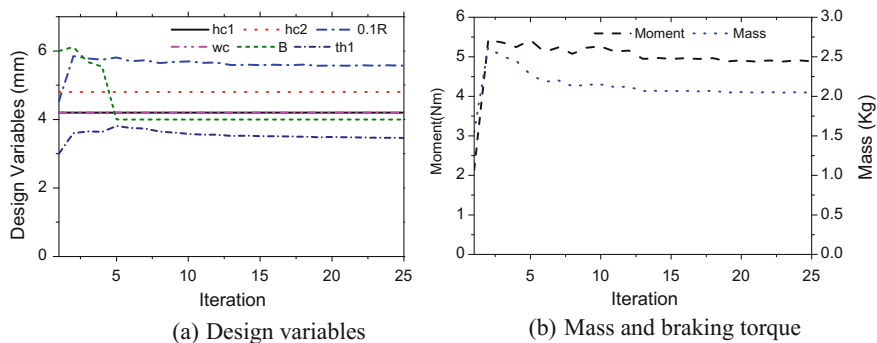


Fig. 4 Second optimal solution when the coil turns are rounded and fixed

Table 2 Second optimal solution of the BMRA

Parameter design (mm)	Performance
Coils: $w_c = 4.2$ mm ($n_{wc} = 14$), $h_{c1} = 4.2$ mm ($n_{hc1} = 14$), $h_{c2} = 5.1$ mm ($n_{hc2} = 17$)	Moment: 5Nm
Housing: $R = 55.956$, $th1 = 3.5084$ $L = 2.6817$	Mass: 2.0700 kg
Disks: $R_i = 16.5$, $R_d = 53.880$, $b = 4$	Power: 79.270 W
	Resistor RC1 = 6.1490Ω
	Resistor RC2 = 11.467Ω

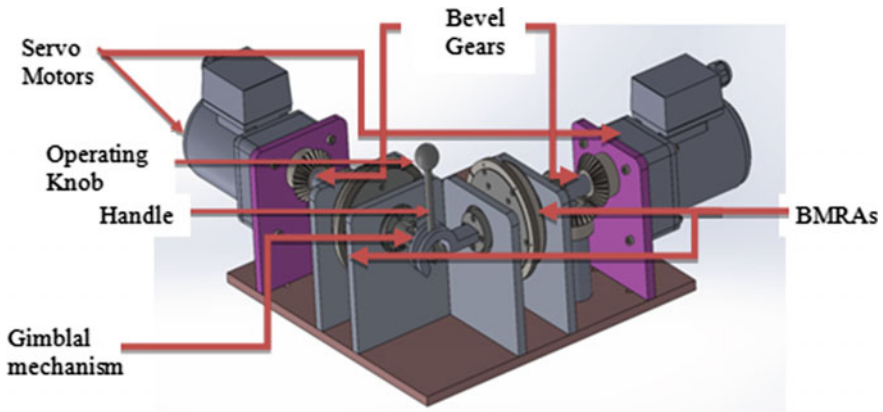


Fig. 5 CAD model of the proposed 2D-haptic joystick

4 Experimental Results

Figure 5 shows the CAD model of the proposed 2D-haptic joystick featuring a gimbal mechanism and two BMRAs. As shown in the figure, the two BMRAs driven by two DC servo motors are connected to the two shafts of the gimbal mechanism. The motion from the motor is transferred to the two shafts of the BMRA through a bevel gear system. The gimbal mechanism is operated through a handle of 150 mm length. By controlling the output torque of the two BMRAs, a desired feedback force can be archived at the operating knob.

Figure 6 shows the experimental setup to test performance of the 2D force feedback system featuring two BMRAs. In the figure, the servo DC motors with gearbox controlled by the computer at a constant angular speed of 0.2π rad/s. The feedback forces of the haptic joystick are measured by a 3D force sensor attached to the end of the handle. Once the experiment process is started, the analog output from the force sensor is sent to the controller (PC) through the NI card. The controller, which is a PID controller in this study, then sends a control signal through the NI card and an amplifier to the coils of BMRAs to control the output torque of the BMRAs. The controlled torques from the two BMRAs reflect the feedback force to the operator through the handle.

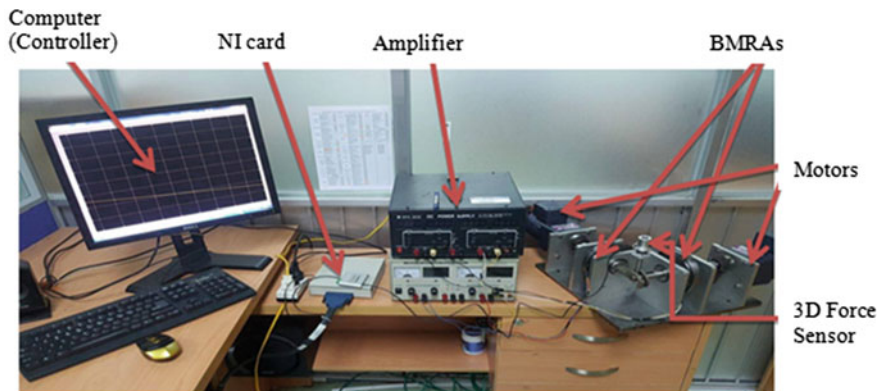


Fig. 6 Experimental setup to test performance of the 2D force feedback

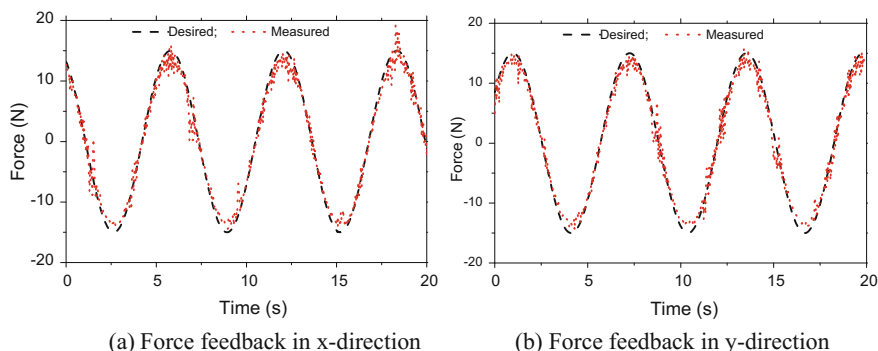


Fig. 7 Experimental results of 2D force feedback system

Figure 7 shows the tracking response of the haptic joystick when the desired input force is a sinusoidal function. The results show a quite good agreement between the actual and the desired values for both x and y directions.

5 Conclusion

In this study, a new 2D-haptic joystick featuring a 2D-gimbal mechanism and two bidirectional magneto-rheological actuators (BMRA) is designed, manufactured, and experimentally tested. Firstly, a new configuration of BMRAs for force feedback of the haptic joystick was proposed, optimally designed, and experimentally evaluated. Then, a 2D-haptic joystick featuring two BMRAs were proposed. The prototype haptic joystick was then manufactured, and a PID controller was

employed to achieve 2D force feedback to the operator. Experimental results showed that the proposed 2D-haptic joystick can quite well achieve a desired sinusoidal feedback force in both x and y directions. As second phase of this study, a new controller will be employed to improve force feedback response to arbitrary required input force, and a 3D-haptic joystick will be considered.

Acknowledgements This work was supported by the Vietnam National Foundation for Science and Technology Development (NAFOSTED) under grant no. 107.01-2015.32

References

1. Kim KH et al (2009) Smart mouse: 5-DOF haptic hand master using magneto-rheological fluid actuators. In: 11th conference on electrorheological fluids and magnetorheological suspensions
2. Winter S, Bouzit S (2007) *IEEE Trans Neural Syst Rehabil Eng* 15(1):2–8
3. Conrad B (2009) *Presence* 18(6):421–433
4. Li WH et al (2007) *Sens Actuators* 137:308–320
5. Nguyen QH, Nguyen PB, Choi SB (2011) Optimal design of a hybrid MR brake for haptic wrist application. *Proc SPIE* 6928
6. Nguyen QH, Choi SB, Lee YS, Han MS (2013) Optimal design of a new 3D haptic gripper for telemanipulation, featuring magnetorheological fluid brakes. *Smart Mater Struct* 22(1)
7. Nguyen QH, Nguyen ND, Choi SB (2015) *Smart Mater Struct* 24(1)
8. Nguyen QH, Nguyen ND, Choi SB (2015) Development of magneto-rheological brake with two coils placed on each side of the brake housing. *Vietnam J Mech* 37(4)
9. Nguyen QH, Han YM, Choi SB, Wereley NM (2007) Geometry optimization of MR valves constrained in a specific volume using the finite element method. *Smart Mater Struct* 16(6):2242–2252

Design and Evaluation of a Shear-Mode MR Damper for Suspension System of Front-Loading Washing Machines



D. Q. Bui, V. L. Hoang, H. D. Le and H. Q. Nguyen

Abstract In this research, a low damping force shear-mode magneto-rheological (MR) damper that can replace conventional passive damper of a front-loading washing machine is designed and experimentally evaluated. In the design of the MR damper, required damping force, off-state friction force, size, and low cost of the MR damper are taken into account. Firstly, a suppression system for washing machines featuring MR dampers is proposed considering required damping force, available space, and cost of the system. Optimization of the proposed MR suspension system is then performed considering required damping force, off-state friction force, size, power consumption, and low cost of the MR damper. From the optimal results, simulated performance of the optimized MR damper is obtained and presented with discussions. A detailed design of the MR damper is then conducted, and a prototype MR damper is manufactured. In addition, experimental results on the prototype MR damper are obtained and compared with simulated ones. Finally, discussions on performance and application of the MR suspension system for front-loading washing machines are given.

Keywords Front-loading washing machine · MR damper
Suspension system · Optimal design

D. Q. Bui · V. L. Hoang

Faculty of Mechanical Engineering, Industrial University of Ho Chi Minh City,
Ho Chi Minh City, Vietnam

e-mail: 1500102@student.hcmute.edu.vn; buiquocduy@iuh.edu.vn

V. L. Hoang

e-mail: hoanglongvuong@iuh.edu.vn

D. Q. Bui

Faculty of Civil Engineering and Applied Mechanics, Ho Chi Minh City University
of Technology and Education, Ho Chi Minh City, Vietnam

H. D. Le · H. Q. Nguyen (✉)

Faculty of Engineering, Vietnamese-German University, Ho Chi Minh City, Vietnam
e-mail: hung.nq@vgu.edu.vn

H. D. Le

e-mail: ledaihiep1993@gmail.com

© Springer Nature Singapore Pte Ltd. 2018

H. Nguyen-Xuan et al. (eds.), *Proceedings of the International Conference
on Advances in Computational Mechanics 2017*, Lecture Notes in Mechanical
Engineering, https://doi.org/10.1007/978-981-10-7149-2_74

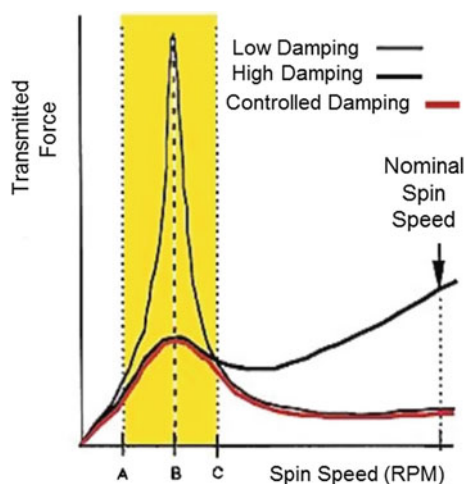
1061

1 Introduction

It is well known that a washing machine is one of helpful equipment in human life as it releases people from hard washing works for more free time. Recently, in order to satisfy the high demands of customers, the laundry capacity and the spin speed are increased, while the machine weight and cost are reduced. With these, the vibration of washing machine becomes a more challenging issue that should be under consideration. The vibration of washing machine is transferred from the washing drum to the frame and then to the floor causing acoustic noises, uncomfortable feeling for human and gradual decrease of the machine life span.

The vibration of washing machine is mostly due to the unbalanced mass of laundry disposed in the drum. Particularly, in a front-loading washing machine, the impact of gravity makes the unbalance more serious. Various suspension systems have been developed to control the vibration of washing machine. In this study, the vibration of front-loading washing machine is suppressed based on the damping control of suspension system. It is found that during the spinning process, the first resonance (rigid body mode) usually appears at quite low speed, around 100–250 rpm while another one occurs at high speed, usually above 1000 rpm. In a conventional suspension system, since passive dampers (constant damping coefficient) are applied, there is a tradeoff between the probability of vibration suppression at low frequency and its increased transmissibility at high frequency. Consequently, in order to effectively attenuate, the vibration of washing machine at low resonance frequency whereas the one at high excitation frequency is well isolated, a semi-active suspension system with controllable damping coefficient should be employed, as shown in Fig. 1. For that, in this paper, a shear-mode magneto-rheological (MR) damper is designed.

Fig. 1 Control of washing machine vibration featuring semi-active suspension system



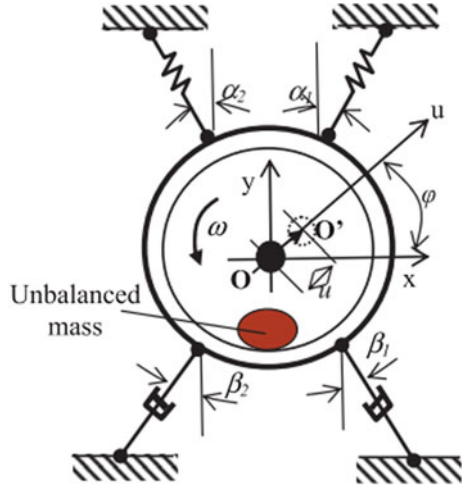
MR fluid is a type of smart material whose solidification depends on external magnetic field. Applications of MR fluid can be found in various industrial fields such as brake, clutch, valve, damper... due to its possibilities of rapid response, easy control and reverse. There are some research works on semi-active suspension system for front-loading washing machines featuring MR fluid. Michael and Carlson [1] have developed a low-cost MR fluid sponge damper for washing machines. Although the sponge MR damper can well eliminate the vibration of washing machine at low frequency [2], wearing and durability of the sponge are still significant challenges. Aydar et al. [3] have researched on design and application of a flow-mode MR damper to control vibration of washing machine. However, the optimal design of the MR damper has not been considered, and the zero-field friction force (the damping force when no current is applied to the coils of the damper), also called the off-state force, is still very high, which may cause a grave vibration of washing machine at high frequency. Furthermore, because a large amount of MR fluid is required for flow-mode, the cost of the damper is also high. Recently, Nguyen et al. [4] have developed an optimal shear-mode MR damper for front-loading washing machines. It is potential that the MR damper can provide a damping force up to 120 N while the zero-field friction force can be considerably small. Yet, this MR damper has not been verified on a front-loading washing machine, where sealing and assembly of the damper are significant problems that should be completely taken into consideration.

The main contribution of this research is to present an optimal design of the shear-mode MR damper for semi-active suspension system which can be applied to vibration control of front-loading washing machines. Firstly, a suppression system for washing machines featuring MR dampers is proposed considering required damping force, available space, and cost of the system. Optimization of the proposed MR suspension system is then performed considering required damping force, off-state friction force, size, power consumption, and low cost of the MR damper. From the optimal results, simulated performance of the optimized MR damper is obtained and presented with discussions. A detailed design of the MR damper is then conducted, and a prototype MR damper is manufactured. In addition, experimental results on the prototype MR damper are obtained and compared with simulated ones. Finally, discussions on performance and application of the MR suspension system for front-loading washing machines are given.

2 Dynamic Modeling of Washing Machine

In this work, the commercial front-loading washing machine, Samsung WF8690NGW, was considered as a prototype. A 2-D simplified schematic of the washing machine is shown in Fig. 2. According to [4], the governing equation of the washing machine can be expressed:

Fig. 2 Two-dimensional simplified schematic of the prototype washing machine



$$m\ddot{u} + c\dot{u}[\sin^2(\varphi + \beta_2) + \sin^2(\varphi - \beta_1)] + ku[\sin^2(\varphi + \alpha_1) + \sin^2(\varphi - \alpha_2)] = F_u(t) \tag{1}$$

where m is the mass of the suspended tub assembly including the drum, laundry, shaft, counterweight, rotor, and stator; c is the damping coefficient of each damper; k is the stiffness of each spring; φ is the angle of an arbitrary direction, u , in which the vibration is considered; u is the displacement of the tube center in the u -direction; and F_u is the excitation force due to an unbalanced mass in the u -direction, defined by $F_u = F_0 \cos(\omega t) = m_u \omega^2 R_u \cos(\omega t)$, where m_u and R_u are the mass and radius from the rotation axis of the unbalanced mass, respectively.

Since the resonance frequencies in all directions of vibration should be controllable, it is easy to realize that, by choosing $\alpha_1 = \alpha_2 = \beta_1 = \beta_2 = 45^\circ$ considering manufacturing and available space, Eq. (1) can be simplified as follows:

$$m\ddot{u} + c\dot{u} + ku = F_u(t) \tag{2}$$

3 Configuration of MR Damper

Generally, there are three operational modes of MR dampers: shear-mode, flow-mode and their combination, mixed-mode. The last two modes result in complicated design and high zero-field friction force as well as high cost due to large amount of MR fluid required. Therefore, the shear-mode MR damper is proposed for this paper.

Figure 3 shows the configuration of proposed shear-mode MR damper. In this configuration, two coils are wound directly on the coil grooves of the housing.

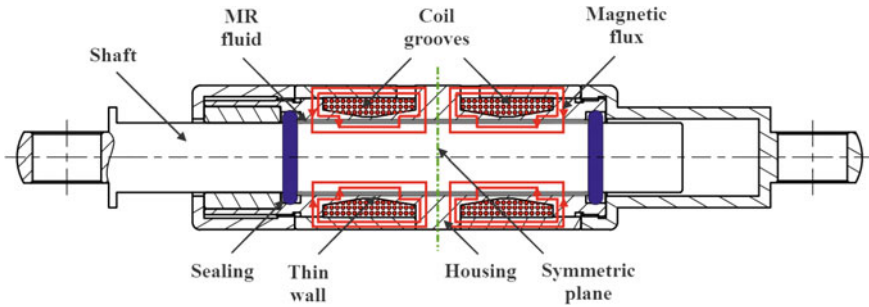


Fig. 3 Schematic configuration of proposed shear-mode MR damper

The section of the thin wall between the coil grooves and the MR gap is designed to have a small area so that the magnetic flux going through it promptly reaches to saturation and hence is forced to go across the MR gap. In response to the magnetic field, the MR fluid solidifies and resists the relative movement between the shaft and the housing producing the damping force. In the literature, a configuration with more than two coils can be used in order to increase the magnetic flux density across the MR gap. However, this induces the difficulties in achieving the accuracy of manufacturing and assembly. On the other hand, more coils mean more applied powers required, which results in high cost of operation and the rising of heat emission. Taking all above issues into account, the configuration with two coils is recommended for our design.

4 Optimal Design of MR Damper

In this work, optimal design of the proposed shear-mode MR damper is performed based on the quasi-static model of the MR damper and the dynamic equation of the washing machine presented in Sect. 2. From Fig. 2, by assuming a linear profile of velocity of the MR fluid in the duct between the shaft and the housing, the damping force F_{sd} and the zero-field friction force F_{s0} can be, respectively, determined by

$$F_{sd} = 2\pi R_s L_e \left(\tau_y + \eta \frac{v}{d} \right) + 2F_{or} \tag{3}$$

$$F_{s0} = 2\pi R_s L_d \left(\tau_{y0} + \eta_0 \frac{v}{d} \right) + 2F_{or} \tag{4}$$

where R_s is the shaft radius, d is the gap size of the MR fluid duct, v is the relative velocity between the shaft and the housing, η and τ_y are, respectively, the field-dependent post-yield viscosity and yield stress of the active MR fluid in the duct, L_d is the length of the MRF duct, and L_e is the effective length of the active MRF in the duct. For the proposed MR damper, L_e can be approximated by $L_e \cong L_d$.

F_{or} is the coulomb friction force between the shaft and the o-ring which can be approximately calculated by [5]

$$F_{or} = f_c L_r + f_h A_r \tag{5}$$

in which L_r is the length of seal rubbing surface, f_c is friction per unit length due to o-ring compression, A_r is the projected area of seal, and f_h is friction force due to fluid pressure on a unit projected area of seal. It is noteworthy that for the shear-mode MR damper, the pressure on the o-rings is very small and thus can be neglected, $f_h \cong 0$. Moreover, the compression of o-rings should be set at a moderate ratio so that the off-state force is not too high while the sealing of the MR damper is well ensured during the operation of washing machine. Therefore, in this paper, 70-durometer rubber o-rings are used and the compression of o-rings is set by 10%. With these, it can be found that $f_c = 116.75$ N/m.

The MR fluid 132-DG made by Lord Corporation is employed for our proposed MR damper. Based on Bingham model, the rheological properties of MR fluid depend on applied magnetic field and can be estimated by the following equation [6]:

$$Y = Y_\infty + (Y_0 - Y_\infty)(2e^{-B\alpha_{SY}} - e^{-2B\alpha_{SY}}) \tag{6}$$

where Y represents one of the rheological parameters of MR fluid such as yield stress and post-yield viscosity. The value of parameter Y tends from the zero applied field value Y_0 to the saturation value Y_∞ . α_{SY} is the saturation moment index of the Y parameter. B is the applied magnetic density. The values of Y_0 , Y_∞ , α_{SY} are determined from experimental results using curve-fitting method, and the results are presented in Table 1.

The objective damping force for the MR damper F_d is defined as follows [4]:

$$|F_d| = \frac{k\pi\zeta m_u r^3 R_u}{2m} \sqrt{\frac{1}{(1-r^2)^2 + (2\zeta r)^2}} \tag{7}$$

in which it is assumed that the spring stiffness, k , is 10 kN/m; the mass of the suspended tub assembly, m , is 40 kg; the equivalent unbalanced mass m_u is 7 kg located at the radius R_u 0.125 m. With the required damping ratio $\zeta = 0.7$ at the resonance frequency ratio $r = \sqrt{1 - \zeta^2}$, the required value of damping force is obtained from Eq. (6), which is around 78.7 N. Accordingly, in this work, the objective damping force for the proposed MR damper is set by 80 N.

Table 1 Rheological properties of MR fluid 132-DG

Bingham model parameters		
$\mu_0 = 0.1 \text{ pa} \cdot \text{s}$	$\tau_{y0} = 15 \text{ pa}$	$\alpha_{s\mu} = 4.5 \text{ T}^{-1}$
$\mu_\infty = 3.8 \text{ pa} \cdot \text{s}$	$\tau_{y\infty} = 40,000 \text{ pa}$	$\alpha_{s\tau} = 2.9 \text{ T}^{-1}$

Another problem should be considered in the MR damper design is the available space of the washing machine. From assembly aspects, with the required maximum stroke of the damper set by 40 mm, the available length of the MR duct is approximately calculated by 80 mm. Despite no strict constraint on the outer radius of the MR damper, it should be as small as possible in order to reduce its cost and weight. Since the outer radius of conventional damper is around 20 mm, the one of the MR dampers is restricted to be smaller than this value. Besides, for the possibility of machining the bushing cylinder without warping, the height of coil grooves should not be so small. In this case, it is set to be larger than 4.6 mm. In summary, the optimization of the MR damper design for the washing machine can be expressed as follows: Find optimal values of significant geometric dimensions of the proposed MR damper that minimize the off-state force F_{s0} , subjected to the maximum damping force F_{sd} is greater than 80 N, the length of MR duct L_d is smaller than 80 mm, the outer radius of the damper R is smaller than 20 mm, and the height of coil grooves h_c is greater than 4.6 mm.

In order to obtain the optimal solution, a FEA code integrated with an optimization tool is employed. In this study, the first-order method with golden section algorithm of ANSYS optimization tool is used. The detailed procedure to obtain the optimal solution of MR fluid devices based on FEA has been mentioned in several researches [7, 8].

5 Results and Discussions

In this section, the optimal results of the MR damper are obtained and the optimized MR damper is then manufactured and tested. From commercial aspects, the C45 steel and the copper wire gauge 24 (0.511 mm-diameter) are employed for magnetic components of the MR damper. The MR fluid gap size is set from 0.5 to 1 mm based on the consideration of manufacturing, amount of MR fluid, and size of o-rings. Furthermore, the applied current is limited by 1.5 A in order to reduce the consumption power and the heating of the coils. The optimal solutions of the proposed MR damper are summarized in Tables 2, and the magnetic flux distribution of the optimized damper is shown in Fig. 4. It is observed from the figure that the magnetic flux density in the shaft and the housing reach to saturation and so does the damping force as the applied current is above 1.5 A.

In order to verify the above optimal results and test performance of the optimized MR damper, a prototype of the optimized MR damper is manufactured and experimental results are obtained and presented. Figure 5 shows the experimental setup to test performance of the prototype MR damper. As shown in the figure, a crank–slider mechanism is used to convert the rotary motion of the motor to the reciprocal motion of the damper shaft. The motor with a gearbox is employed to rotate the crankshaft at a constant angular speed of 10π rad/s. The damping force of the MR damper is measured by a force sensor. The output signal from the force sensor is then sent to the computer via the A/D converter for assessment. During the

Table 2 Optimal parameters of the proposed shear-mode MR damper

Parameters			
Off-state force F_{s0} (N)	13.52	Coil width w_{c0} (mm)	3.53
Max damping force F_{sd} (N)	80	Axial chamfer ch_1 (mm)	10.32
MR duct length L_d (mm)	71.87	Shaft radius R_s (mm)	9
Outer radius R (mm)	18.74	MR duct gap t_g (mm)	0.8
Coil groove height h_c (mm)	4.98	Thin wall t_i (mm)	0.8
Coil height h_{c0} (mm)	3.2	Sliding housing t_0 (mm)	3.17
Radial chamfer ch (mm)	1.78	Coil to centerline t_{fi} (mm)	5.88

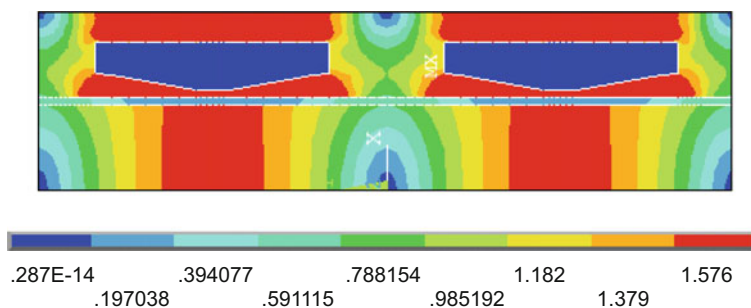


Fig. 4 Magnetic flux density of the proposed optimized MR damper

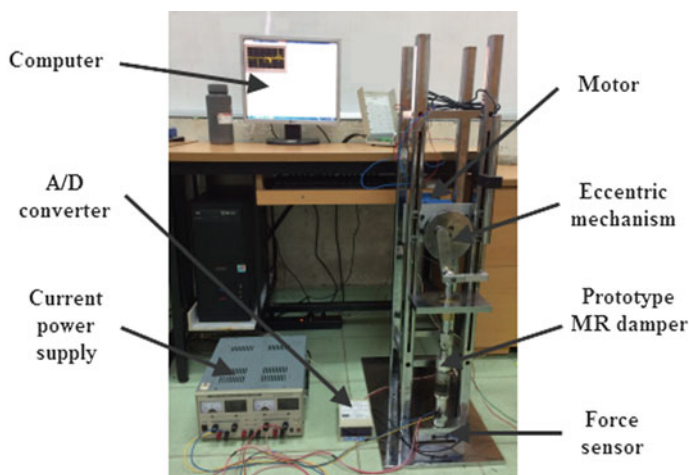


Fig. 5 Experimental setup to test performance of the optimized MR damper

experiment, a constant current is applied to the coils of the MR damper via a current power supply. The crank radius (the distance from the center of the eccentric cam to the pin of the transmission rod) is set by 20 mm so that the mechanism could provide the required maximum stroke of the MR damper, 40 mm.

Figure 6a and b shows the damping force of the prototype MR damper as a function of the damper shaft velocity in the applied currents of 1.5 A and 0 A (off-state), respectively. It is observed from Fig. 6a that the damping force obtained from experiment is a little smaller than that obtained from the static modeling based on finite element analysis. This mainly comes from the loss of magnetic field to the ambient and at the contact between the magnetic parts of the MR damper. The average value of the damping forces at the steady positions (at positions relatively far from the stroke ends) is 76.24 N, which is around 95.3% of the modeling value (80 N). Therefore, a good correlation between experimental results and static modeling based on finite element analysis is achieved. From the results, it is also observed that the damper exhibits nonlinear hysteresis, especially at the stroke ends. From Fig. 6b, it is seen that the off-state force obtained from experiment is a little higher than that obtained from the modeling results. The average value of the off-state forces at the steady positions is 14.03 N, which is around 103.77% of the modeling value (13.52 N). It is believed that the difference mainly comes from the inaccurate estimation of the friction force of the o-rings.

In order to validate the efficiency in operation, the prototype MR dampers are applied to a front-loading washing machine. Figure 7 shows the application of the MR dampers to a washing machine. The laundry mass of 7 kg is put into the washing drum, and an accelerometer is mounted to the frame for the acceleration measurement. The spinning process of the washing machine is operated, and the data is collected in 3 min since the spinning speed of the drum reaches to 100 rpm. The current is applied to the MR dampers at the first resonance (from the second 18–60) while the off-state of the MR dampers is established when the drum speed is

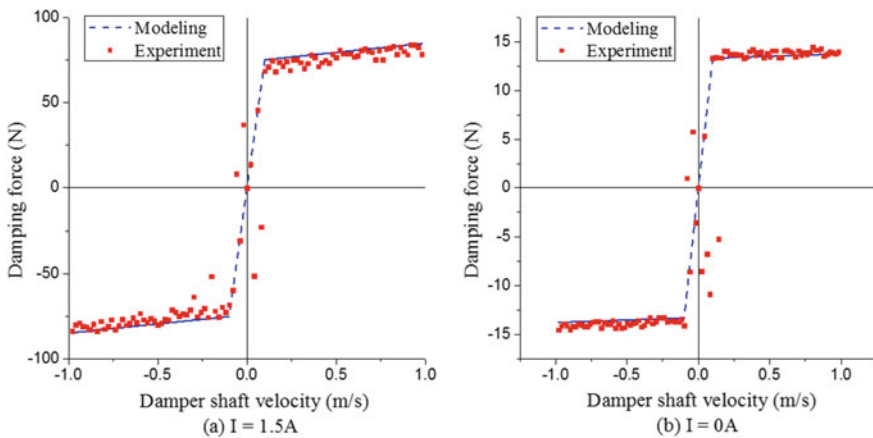


Fig. 6 Experimental results of the prototype MR damper

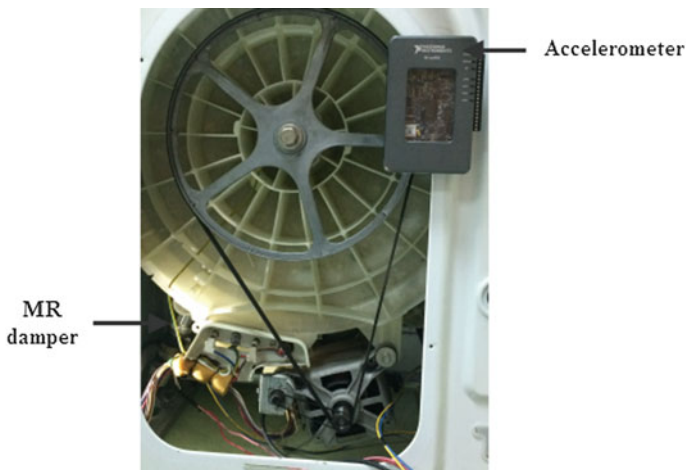
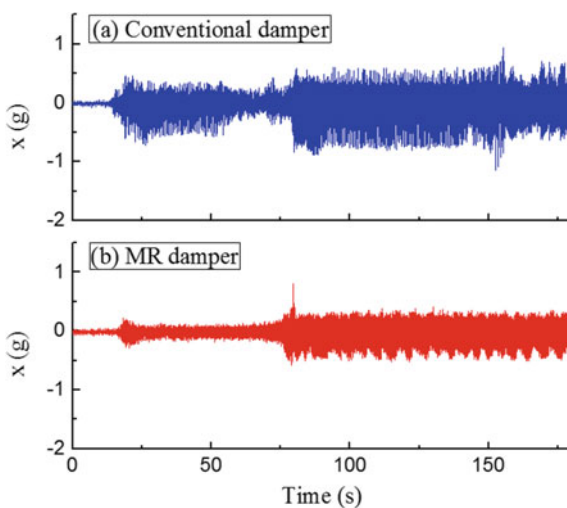


Fig. 7 Application of the proposed MR damper to a front-loading washing machine

Fig. 8 Vibration indices in x-direction of the washing machine



above 900 rpm (at the second 77). The acceleration indices in x-, y-, and z-directions of the MR dampers are obtained and presented in Figs. 8, 9, and 10, respectively. From the figures, it is observed that in the first resonance, the vibration of the washing machine employing MR dampers (Figures b) is well suppressed compared with that using conventional dampers (Figures a). This mainly comes from the greater of damping force of the MR damper in comparison with the one of conventional damper. When the drum speed is above 900 rpm, the vibration in x- and y-directions of the washing machine featuring MR dampers is still well attenuated against those using conventional dampers, but the result in z-direction is

Fig. 9 Vibration indices in y-direction of the washing machine

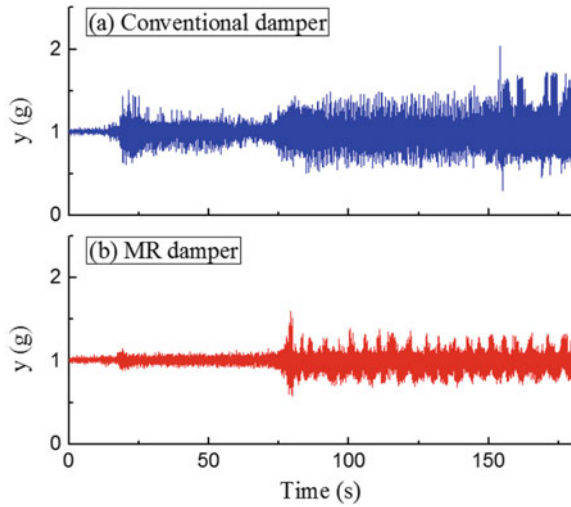
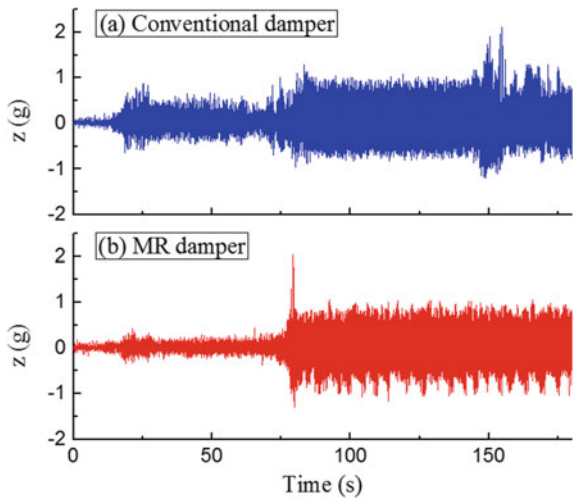


Fig. 10 Vibration indices in z-direction of the washing machine



not much attenuated. The main reason comes from in-plane positioning (x-y plane) of the MR dampers.

6 Conclusions

This paper focused on the design and evaluation of a shear-mode MR damper for suspension system of front-loading washing machines to eliminate vibration due to an unbalanced laundry mass occurring in the washing drum. Firstly, a suppression

system for washing machines featuring MR dampers was proposed considering required damping force, available space, and cost of the system. Optimization of the proposed MR damper was then performed considering required damping force, off-state friction force, size, manufacturing, and low cost. From the optimal results, simulated performance of the optimized MR damper was obtained and presented with discussions. A detailed design of the MR damper was then conducted, and a prototype MR damper was manufactured. In addition, experimental results on the prototype MR damper were obtained and compared with simulated ones. From the results, it was shown that there was a good correlation between experimental results and static modeling based on finite element analysis. The prototype MR dampers were then applied to the suspension system of the prototype front-loading washing machines for evaluation. It was observed that the vibration in all directions of the washing machine featuring MR dampers is well suppressed in comparison with those using conventional dampers, except the vibration in z-direction at the drum speed of above 900 rpm. It is finally remarked that as the second phase of this research, the MR dampers will be employed in appropriate positions to attenuate vibration in z-direction and an appropriate controller is applied for the dampers.

Acknowledgements This work was supported by the Vietnam National Foundation for Science and Technology Development (NAFOSTED) under grant no. 107.01-2015.32 and partially funded by Industrial University of Ho Chi Minh City.

References

1. Michael JC, Carlson JD (2001) MR fluid sponge devices and their use in vibration control of washing machines. In: Proceedings of SPIE 4331, Newport Beach, CA, USA
2. Cristiano S, Fabio P, Sergio MS et al (2009) Control of magnetorheological dampers for vibration reduction in a washing machine. *Mechatronics* 19:410–421
3. Aydar G, Evrensel CA, Gordaninejad F et al (2007) A low force magneto-rheological (MR) fluid damper: design, fabrication and characterization. *J Intel Mater Syst Struct* 18:1155–1160
4. Nguyen QH, Choi SB, Woo JK (2014) Optimal design of magnetorheological fluid-based dampers for front-loading washing machines. *Proc Inst Mech Eng Part C J Mech Eng Sci* 228:294
5. Brian ES (2005) Research for dynamic seal friction modeling in linear motion hydraulic piston applications. Dissertation, University of Texas at Arlington, USA
6. Zubietta M, Eceolaza S, Elejabarrieta MJ et al (2009) Magnetorheological fluids: characterization and modeling of magnetization. *Smart Mater Struct* 18(9):1–6, article no 095019
7. Nguyen QH, Han YM, Choi SB et al (2007) Geometry optimization of MR valves constrained in a specific volume using the finite element method. *Smart Mater Struct* 16:2242–2252
8. Nguyen QH, Choi SB, Wereley NM (2008) Optimal design of magneto-rheological valves via a finite element method considering control energy and a time constant. *Smart Mater Struct* 17(2):1–12, article no 025024

Part X
Computational Dynamics

Transient Analysis of Laminated Composite Shells Using an Edge-Based Smoothed Finite Element Method



D. Pham-Tien, H. Pham-Quoc, V. Tran-The, T. Vu-Khac
and N. Nguyen-Van

Abstract An edge-based smoothed finite element method (ES-FEM) was recently proposed to significantly improve the accuracy and convergence rate of traditional finite element method for static and force vibration analyses of plates and shells. In this paper, the ES-FEM is further extended and incorporated with mixed interpolation of tensorial components for triangular element (MITC3) [1], called ES-MITC3, for transient analysis of laminated composite shells based on the first-order shear deformation theory (FSDT). Numerical results for static analysis of isotropic and transient response of laminated composite shell with various different loadings and boundary conditions are provided. The accuracy and reliability of proposed method are verified by comparing its numerical solutions with those of other available numerical results.

Keywords An edge-based smoothed mixed interpolation of tensorial components (ES-MITC) · Laminated composite shells
The first-order shear deformation theory

D. Pham-Tien · H. Pham-Quoc (✉)
Faculty of Engineering, Le Qui Don University, Hanoi, Vietnam
e-mail: quochoavhp@gmail.com

V. Tran-The
Faculty of Basic Technical, Tran Dai Nghia University, Ho Chi Minh City, Vietnam

T. Vu-Khac
R&D Department, 751 One Member Limited Liability Company,
Ho Chi Minh City, Vietnam

N. Nguyen-Van
Faculty of Mechanical Technology, Industrial University of Ho Chi Minh City,
Ho Chi Minh City, Vietnam

1 Introduction

Nowadays, laminated composite shell structures are widely used in civil, aerospace, naval, automotive, defense industries, and other areas because of their superior properties such as high strength, lightweight, stiffness-to-weight ratios, and excellent fatigue strength. Therefore, there exists a need for full understanding of the transient response of laminated composite shells. Recently, various theories have been successfully applied in order to analyze transient response of the laminated composite shells. Khdeir [2] has proposed a higher-order shear deformation theory (HSDT), based on Sander's shell theory and the state-space technique for exact solution, to investigate transient response of laminated circular cylindrical shells. Based on combining the Rayleigh–Ritz and the normal mode superposition method, Chun and Lam [3] analyzed the dynamic response of laminated panels under step, triangular, and blast loadings. Turkmen [4] studied the displacement time histories of cylindrically curved laminated composite shells subjected to blast loading. In this study, the Runge–Kutta method is employed to solve the governing equation of the cylindrical shells. In addition, Sahan [5] analyzed the dynamic response of laminated spherical shells based on a combination of Laplace transform and Navier method.

In the front of the development of numerical methods, Liu et al. [6] integrated the strain smoothing technique into the traditional FEM to create a series of smoothed FEM such as a cell-based smoothed FEM (CS-FEM) [7], a node-based smoothed FEM (NS-FEM) [8], an edge-based smoothed FEM (ES-FEM) [9], and a face-based smoothed FEM (FS-FEM) [10]. Each of these smoothed FEM has been delivered different desired properties for a wide class of benchmark and practical mechanics' problems. Among these S-FEM models, ES-FEM [9] demonstrated good performances for two-dimensional problem. In the ES-FEM, the stiffness matrix is computed using strains smoothed over the smoothing domains associated with the edges of the elements. Besides, polygonal FEM for plate analysis also provided some good properties [11]. In addition, in recent years, computational approach based on isogeometric analysis (IGA) is very promising for analyzing plate/shell problems [12–15].

Recently, Chau-Dinh et al. [16] developed further the ES-FEM for plate structures by combining the ES-FEM with the MITC3 [1], which can remove the shear-locking phenomenon. The numerical results showed that ES-MITC3 achieves the high accuracy compared to the exact solutions and other existing elements in the literature.

This paper aims to extend further the ES-MITC3 to analyze static of isotropic shell and the transient response of laminated composite spherical shell subjected to different type of dynamic loadings including step, sine, triangular, and blast loadings. In this study, the first-order shear deformation theory (FSDT) is applied in the formulation due to the simplicity and computational efficiency. The equations of motion for the laminated composite shell are solved by Newmark method for time integration. Several numerical examples are provided to illustrate the accuracy and

reliability of the present method in comparison with those of other available numerical results.

2 Theoretical Formulation

2.1 Weak Form of Laminated Composite Shells

Consider a flat shell element deformed by in-plane forces and bending moments, as shown in Fig. 1a, in which the global coordinate is $Oxyz$ and the local coordinate is $\hat{O}\hat{x}\hat{y}\hat{z}$. The middle surface of the shell element is chosen as the reference plane that occupies the domain $\Omega \subset \mathbb{R}^3$. According to the FSDT, the displacements field at any point of shell in the local coordinate can be expressed as follows

$$\begin{cases} \hat{u}(x, y, z) = \hat{u}_0(x, y) + z\hat{\beta}_x(x, y), \\ \hat{v}(x, y, z) = \hat{v}_0(x, y) + z\hat{\beta}_y(x, y), \\ \hat{w}(x, y, z) = \hat{w}_0(x, y), \end{cases} \quad (1)$$

where \hat{u}_0, \hat{v}_0 and \hat{w}_0 are the displacements of the middle plane in the \hat{x}, \hat{y} and \hat{z} directions, respectively; $\hat{\beta}_x, \hat{\beta}_y$ denote the rotations of the middle surface of the shell around the \hat{y} axis and \hat{x} axis, respectively, as indicated in Fig. 1a.

The strain vector can be written as

$$\{\hat{\epsilon}_{xx}, \hat{\epsilon}_{yy}, \hat{\gamma}_{xy}, \hat{\gamma}_{xz}, \hat{\gamma}_{yz}\}^T = \begin{Bmatrix} \hat{\epsilon} \\ 0 \end{Bmatrix} + z \begin{Bmatrix} \hat{\kappa} \\ 0 \end{Bmatrix} + \begin{Bmatrix} 0 \\ \hat{\gamma} \end{Bmatrix}, \quad (2)$$

where the membrane $\hat{\epsilon}$, bending $\hat{\kappa}$, and shear strains $\hat{\gamma}$ in local coordinate can be defined by

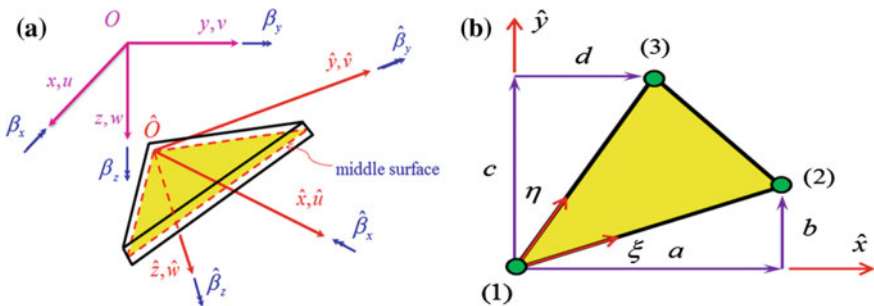


Fig. 1 A shell element with local coordinate system $\hat{O}\hat{x}\hat{y}\hat{z}$ in global coordinate system $Oxyz$ (a) and three-node triangular element and local coordinate (b)

$$\begin{aligned} \hat{\mathbf{e}} &= \{ \hat{u}_{0,x}, \hat{v}_{0,y}, \hat{u}_{0,y} + \hat{v}_{0,x} \}; \hat{\mathbf{k}} = \{ \hat{\beta}_{x,x}, \hat{\beta}_{y,y}, \hat{\beta}_{x,y} + \hat{\beta}_{y,x} \}; \hat{\boldsymbol{\gamma}} \\ &= \{ \hat{w}_{0,x} + \hat{\beta}_x, \hat{w}_{0,y} + \hat{\beta}_y \}. \end{aligned} \tag{3}$$

The linear stress–strain relations are expressed as

$$\begin{Bmatrix} \hat{\sigma}_{xx} \\ \hat{\sigma}_{yy} \\ \hat{\sigma}_{xy} \end{Bmatrix} = \begin{bmatrix} Q_{11} & Q_{12} & 0 \\ Q_{21} & Q_{22} & 0 \\ 0 & 0 & Q_{66} \end{bmatrix} \begin{Bmatrix} \hat{\epsilon}_{xx} \\ \hat{\epsilon}_{yy} \\ \hat{\gamma}_{xy} \end{Bmatrix}; \begin{Bmatrix} \hat{\sigma}_{xz} \\ \hat{\sigma}_{yz} \end{Bmatrix} = \begin{bmatrix} Q_{55} & 0 \\ 0 & Q_{44} \end{bmatrix} \begin{Bmatrix} \hat{\gamma}_{xz} \\ \hat{\gamma}_{yz} \end{Bmatrix}, \tag{4}$$

in which $Q_{11}(z) = Q_{22}(z) = \frac{E(z)}{1-\nu(z)^2}$; $Q_{12}(z) = \nu(z)Q_{11}(z)$; $Q_{44}(z) = Q_{55}(z) = Q_{66}(z) = \frac{E(z)}{2(1+\nu(z))}$.

For forced vibration analysis of the laminated composite shell, a weak form can be derived from the following undamped dynamic equilibrium equation as

$$\int_{\Omega} \delta \begin{Bmatrix} \hat{\mathbf{e}} \\ \hat{\mathbf{k}} \\ \hat{\boldsymbol{\gamma}} \end{Bmatrix}^T \begin{bmatrix} \mathbf{A} & \mathbf{B} & \mathbf{0} \\ \mathbf{B} & \mathbf{D} & \mathbf{0} \\ \mathbf{0} & \mathbf{0} & \mathbf{D}^s \end{bmatrix} \begin{Bmatrix} \hat{\mathbf{e}} \\ \hat{\mathbf{k}} \\ \hat{\boldsymbol{\gamma}} \end{Bmatrix} d\Omega + \int_{\Omega} \delta \mathbf{u}^T \mathbf{m} \ddot{\mathbf{u}} d\Omega = \int_{\Omega} \delta \mathbf{u}^T \mathbf{p} d\Omega, \tag{5}$$

where $\mathbf{p} = \{0, 0, p(x, y, z, t), 0, 0, 0\}^T$ is a distributed load that applied on the shell, in which $p(x, y, z, t)$ is a function depending on time and space; the material constant matrices $\mathbf{A}, \mathbf{B}, \mathbf{D}$ and \mathbf{D}^s can be expressed by

$$\begin{aligned} (A_{ij}, B_{ij}, D_{ij}) &= \int_{-h/2}^{h/2} (1, z, z^2) \bar{Q}_{ij} dz, \quad (i, j = 1, 2, 6); D_{ij}^s = \int_{-h/2}^{h/2} k \bar{Q}_{ij} dz, \quad (i, j \\ &= 4, 5). \end{aligned} \tag{6}$$

where $k = 5/6$ denotes the transverse shear correction coefficient; \bar{Q}_{ij} is the transformed material constants of the k th orthotropic layer [17]. The mass matrix \mathbf{m} is given as

$$\mathbf{m} = \begin{bmatrix} I_0 & 0 & 0 & I_1 & 0 & 0 \\ & I_0 & 0 & 0 & I_1 & 0 \\ & & I_0 & 0 & 0 & 0 \\ & & & I_2 & 0 & 0 \\ & & & & I_2 & 0 \\ \text{sym.} & & & & & 0 \end{bmatrix}, \tag{7}$$

in which $(I_0, I_1, I_2) = \int_{-h/2}^{h/2} \rho(1, z, z^2) dz$ where ρ is the mass density.

2.2 Formulation of Finite Element Method for Triangular Flat Shell Elements

In FEM, the problem domain Ω is discretized using a mesh of n^e three-node finite elements such that $\Omega = \bigcup_{e=1}^{n^e} \Omega^e$ and $\Omega^i \cap \Omega^j = \emptyset$ with $i \neq j$. The finite element approximation $\hat{\mathbf{u}}_h^e$ for laminated composite shell elements can be expressed as

$$\hat{\mathbf{u}}_h^e = \sum_{I=1}^{N_n} N_I(\mathbf{x}) \mathbf{I}_6 \hat{\mathbf{d}}_I = \sum_{I=1}^{N_n} \mathbf{N}_I \hat{\mathbf{d}}_I \tag{8}$$

where \mathbf{I}_6 is the unit matrix of 6-*th* rank; N_n is the total number of nodes of problem domain discretized; $N_I(\mathbf{x})$ is the shape function at the *I*-*th* node; $\hat{\mathbf{d}}_I^e = [\hat{u}_I^e, \hat{v}_I^e, \hat{w}_I^e, \hat{\beta}_{xI}^e, \hat{\beta}_{yI}^e, \hat{\beta}_{zI}^e]^T$ is the displacement vector of the nodal degrees of freedom of $\hat{\mathbf{u}}_h^e$ associated to the *I*-*th* node.

According to Eq. (3), the approximation of the membrane, bending, and shear strains in the triangular element can then be expressed in matrix forms as

$$\begin{aligned} \hat{\boldsymbol{\varepsilon}}^e &= [\mathbf{R}_1^e, \mathbf{R}_2^e, \mathbf{R}_3^e] \hat{\mathbf{d}}^e = \mathbf{R}^e \hat{\mathbf{d}}^e; \hat{\boldsymbol{\kappa}}^e = [\mathbf{B}_1^e, \mathbf{B}_2^e, \mathbf{B}_3^e] \hat{\mathbf{d}}^e = \mathbf{B}^e \hat{\mathbf{d}}^e; \hat{\boldsymbol{\gamma}}^e = [\mathbf{S}_1^e, \mathbf{S}_2^e, \mathbf{S}_3^e] \hat{\mathbf{d}}^e \\ &= \mathbf{S}^e \hat{\mathbf{d}}^e, \end{aligned} \tag{9}$$

where

$$\begin{aligned} \mathbf{R}_i^e &= \begin{bmatrix} N_{i,x} & 0 & 0000 \\ 0 & N_{i,y} & 0000 \\ N_{i,y} & N_{i,x} & 0000 \end{bmatrix}; \mathbf{B}_i^e = \begin{bmatrix} 000 & N_{i,x} & 0 & 0 \\ 000 & 0 & N_{i,y} & 0 \\ 000 & N_{i,y} & N_{i,x} & 0 \end{bmatrix}; \mathbf{S}_i^e \\ &= \begin{bmatrix} 00 & N_{i,x} & N_i & 0 & 0 \\ 00 & N_{i,y} & 0 & N_i & 0 \end{bmatrix}. \end{aligned} \tag{10}$$

Substituting Eq. (9) into Eq. (5), a discretized equation undamped for transient analysis laminated composite shell elements can be rewritten in compact forms as

$$\hat{\mathbf{M}} \hat{\mathbf{a}}_t + \hat{\mathbf{K}} \hat{\mathbf{a}}_t = \hat{\mathbf{F}}_t \tag{11}$$

where

$$\hat{\mathbf{K}} = \sum_{e=1}^{n^e} \hat{\mathbf{K}}^e = \sum_{e=1}^{n^e} \int_{\Omega^e} \left\{ \begin{matrix} \mathbf{R}^e \\ \mathbf{B}^e \\ \mathbf{S}^e \end{matrix} \right\}^T \begin{bmatrix} \mathbf{A} & \mathbf{B} & \mathbf{0} \\ \mathbf{B} & \mathbf{D} & \mathbf{0} \\ \mathbf{0} & \mathbf{0} & \mathbf{D}^s \end{bmatrix} \left\{ \begin{matrix} \mathbf{R}^e \\ \mathbf{B}^e \\ \mathbf{S}^e \end{matrix} \right\} d\Omega; \tag{12}$$

$$\hat{\mathbf{F}} = \sum_{e=1}^{n^e} \hat{\mathbf{F}}^e = \sum_{e=1}^{n^e} \int_{\Omega^e} \mathbf{N}^T \mathbf{b} d\Omega. \tag{13}$$

$$\hat{\mathbf{M}} = \sum_{e=1}^{n^e} \hat{\mathbf{M}}^e = \sum_{e=1}^{n^e} \int_{\Omega^e} \mathbf{N}^T \mathbf{m} \mathbf{N} d\Omega. \tag{14}$$

It should be noted that the above formulas are constructed in the local coordinate system of each shell element. Therefore, the transformation between global coordinates and local coordinates is required before conducting the assembling process of element stiffness matrices. Finally, the dynamic analysis equations of laminated composite shell in the global coordinates can be written as

$$\mathbf{M}\ddot{\mathbf{d}}_t + \mathbf{K}\mathbf{d}_t = \mathbf{F}_t \tag{15}$$

in which

$$\mathbf{K} = \sum_{e=1}^{n^e} \underbrace{\mathbf{T}^T \hat{\mathbf{K}}^e \mathbf{T}}_{\mathbf{K}^e} = \sum_{e=1}^{n^e} \mathbf{K}^e; \mathbf{M} = \sum_{e=1}^{n^e} \underbrace{\mathbf{T}^T \hat{\mathbf{M}}^e \mathbf{T}}_{\mathbf{M}^e} = \sum_{e=1}^{n^e} \mathbf{M}^e; \mathbf{F} = \sum_{e=1}^{n^e} \underbrace{\mathbf{T}^T \hat{\mathbf{F}}^e}_{\mathbf{F}^e} = \sum_{e=1}^{n^e} \mathbf{F}^e. \tag{16}$$

where \mathbf{T} is the transformation matrix of coordinate from global coordinate to the local coordinate system [18]. In order to solve Eq. (15), several methods have been proposed such as Wilson, Newmark, Houbolt, and Crank–Nicholson. In this study, the displacements \mathbf{d}_t and the accelerations $\ddot{\mathbf{d}}_t$ in Eq. (15) are solved by using Newmark method [19].

2.3 Formulation of ES-MITC3 for Laminated Composite Shells

2.3.1 Brief on the MITC3 Formulation

It is well known that shear-locking phenomenon can appear when the shell structures become progressively thinner. In literature, many approaches have been proposed such as the reduced integration method [20], assumed natural strains (ANS) [21, 22], linked interpolation methods [23], family of various elements based on the Timoshenko’s beam formulas [24], and smoothed finite elements [25, 26]. In this study, the MITC3 technique [1, 16] is applied to avoid the shear-locking phenomenon. Accordingly, the covariant transverse shear strains of the MITC3 element are separately interpolated from values of the covariant transverse shear strains evaluated at tying points, as indicated in Fig. 2a. Using the natural coordinates (η, ζ) , the assumed covariant transverse shear strain fields can be rewritten

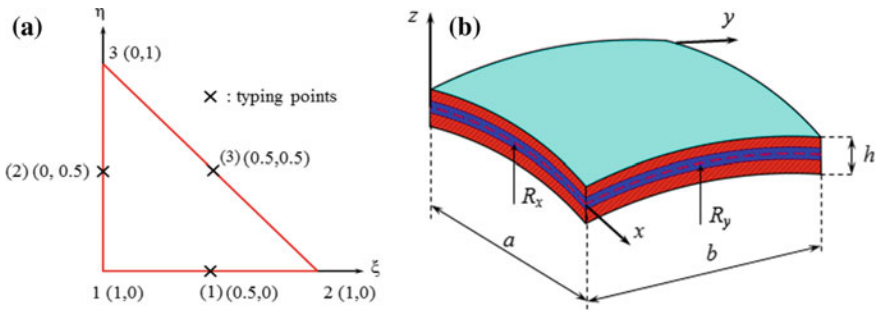


Fig. 2 Typing points (a) and the laminated composite spherical shell (b)

$$\varepsilon_{\zeta\zeta} = \varepsilon_{\zeta\zeta}^{(1)} + c_1\eta; \varepsilon_{\eta\zeta} = \varepsilon_{\eta\zeta}^{(2)} - c_1\zeta \tag{17}$$

with $c_1 = \varepsilon_{\eta\zeta}^{(2)} - \varepsilon_{\zeta\zeta}^{(1)} - \varepsilon_{\eta\zeta}^{(3)} + \varepsilon_{\zeta\zeta}^{(3)}$. Then, explicitly transverse shear strain fields are obtained

$$\hat{\mathbf{Y}}_{MITC3}^e = \underbrace{\left[\mathbf{S}_{MITC3-1}^e \quad \mathbf{S}_{MITC3-2}^e \quad \mathbf{S}_{MITC3-3}^e \right]}_{\hat{\mathbf{S}}_{MITC3}^e} \hat{\mathbf{d}}^e = \hat{\mathbf{S}}_{MITC3}^e \hat{\mathbf{d}}^e, \tag{18}$$

where

$$\begin{aligned} \mathbf{S}_{MITC3-1}^e &= J^{-1} \begin{bmatrix} 00 & -1 & \frac{a}{3} + \frac{d}{6} & \frac{b}{3} + \frac{c}{6} & 0 \\ 00 & -1 & \frac{d}{3} + \frac{a}{6} & \frac{c}{3} + \frac{b}{6} & 0 \end{bmatrix}; \quad \mathbf{S}_{MITC3-2}^e = J^{-1} \begin{bmatrix} 00 & 1 & \frac{a}{2} - \frac{d}{6} & \frac{b}{2} - \frac{c}{6} & 0 \\ 00 & 0 & \frac{d}{6} & \frac{c}{6} & 0 \end{bmatrix}; \\ \mathbf{S}_{MITC3-3}^e &= J^{-1} \begin{bmatrix} 00 & 0 & \frac{a}{6} & \frac{b}{6} & 0 \\ 00 & 1 & \frac{d}{2} - \frac{a}{6} & \frac{c}{2} - \frac{b}{6} & 0 \end{bmatrix}; \quad J^{-1} = \frac{1}{2A_e} \begin{bmatrix} c & -b \\ -d & a \end{bmatrix}. \end{aligned} \tag{19}$$

where $a = x_2 - x_1, b = y_2 - y_1, c = y_3 - y_1, d = x_3 - x_1$, as indicated in Fig. 1b and A_e is the area of the triangular element.

2.3.2 Formulation of ES-MITC3 for Triangular Flat Shell Element

In the ES-FEM, the domain Ω is divided into n_k smoothing domains $\Omega^{(k)}$ based on edges of elements, such as $\Omega = \cup_{k=1}^{n_k} \Omega^{(k)}$ and $\Omega^{(i)} \cap \Omega^{(j)} = \emptyset$ for $i \neq j$. The smoothing domain $\Omega^{(k)}$ associated with each edge is established by connecting two end-nodes of edge k to centroids of the triangles containing the edges, as shown in Fig. 3a. The smoothing domain of an inner edge is formed by combining two sub-domains of two adjacent triangles while the smoothing domain of the edges on the boundary is a single domain. In order to compute the strain smoothing, which

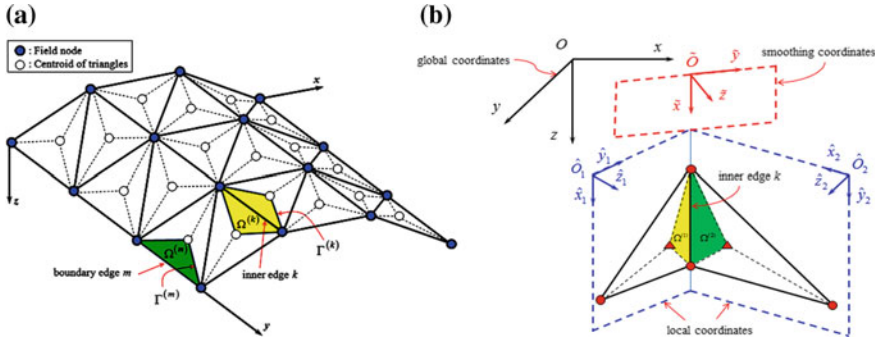


Fig. 3 A mesh of triangular elements and the smoothing domains (a) and the local, global, and smoothing coordinates of flat shell element (b)

defined on sub-domains of adjacent elements sharing an edge, the smoothing coordinate $\tilde{O}\tilde{x}\tilde{y}\tilde{z}$ is introduced. Accordingly, these two adjacent elements are defined by two local coordinate systems $\hat{O}_1\hat{x}_1\hat{y}_1\hat{z}_1$ and $\hat{O}_2\hat{x}_2\hat{y}_2\hat{z}_2$, as shown in Fig. 3b. The smooth coordinate $\tilde{O}\tilde{x}\tilde{y}\tilde{z}$ is defined by the \tilde{x} axis coinciding with the sharing edge k ; the \tilde{z} axis is average direction between the \hat{z}_1 and \hat{z}_2 axis. The \tilde{y} axis is defined by the cross product of the \tilde{x} and \tilde{z} axis.

Using transformation law for each triangular element, the membrane strain $\bar{\epsilon}$, the bending strain $\bar{\kappa}$, and the shear strain $\bar{\gamma}$ of each element in the global coordinate $Oxyz$ are given by

$$\bar{\epsilon} = \Lambda_{m1}\Lambda_{m2}\hat{\epsilon}^e; \bar{\kappa} = \Lambda_{b1}\Lambda_{b2}\hat{\kappa}^e; \bar{\gamma} = \Lambda_{s1}\Lambda_{s2}\hat{\gamma}^e \tag{20}$$

where $\hat{\epsilon}^e$, $\hat{\kappa}^e$, and $\hat{\gamma}^e$ are strains in the local coordinate of each sub-domain attached to edge k , respectively. In Eq. (20), the strain transformation matrices Λ_{m1} , Λ_{m2} , Λ_{b1} , Λ_{b2} , Λ_{s1} , and Λ_{s2} can be seen [18].

Substituting Eqs. (9) and (17) into Eq. (20), the strains in the global coordinate $Oxyz$ can be rewritten by

$$\bar{\epsilon} = \Lambda_{m1}\Lambda_{m2}\hat{\mathbf{R}}\hat{\mathbf{a}}; \bar{\kappa} = \Lambda_{m1}\Lambda_{m2}\hat{\mathbf{B}}\hat{\mathbf{a}}; \bar{\gamma} = \Lambda_{s1}\Lambda_{s2}\hat{\mathbf{S}}\hat{\mathbf{a}}. \tag{21}$$

in which $\hat{\mathbf{R}}$, $\hat{\mathbf{B}}$, and $\hat{\mathbf{S}}$ are the membrane, the bending, and the shear matrices in the local coordinate. A smoothed membrane strain $\bar{\epsilon}^{(k)}$, a smoothed bending strain $\bar{\kappa}^{(k)}$, and a smoothed shear strain $\bar{\gamma}^{(k)}$ in the global coordinate $Oxyz$ can be derived as

$$\bar{\epsilon}^{(k)} = \int_{\Omega^{(k)}} \bar{\epsilon}\Phi^{(k)}d\Omega; \bar{\kappa}^{(k)} = \int_{\Omega^{(k)}} \bar{\kappa}\Phi^{(k)}d\Omega; \bar{\gamma}^{(k)} = \int_{\Omega^{(k)}} \bar{\gamma}\Phi^{(k)}d\Omega, \tag{22}$$

in which $\Phi^{(k)}(\mathbf{x})$ is a given smoothing function that satisfies $\int_{\Omega^{(k)}} \Phi^{(k)}(\mathbf{x})d\Omega = 1$. The smoothing function can be defined by

$$\Phi^{(k)}(\mathbf{x}) = \begin{cases} \frac{1}{A^{(k)}} & \mathbf{x} \in \Omega^{(k)}, \\ 0 & \mathbf{x} \notin \Omega^{(k)}, \end{cases} \tag{23}$$

where $A^{(k)}$ is the area of the smoothing domain $\Omega^{(k)}$ and is computed by

$$A^{(k)} = \int_{\Omega^{(k)}} d\Omega = \frac{1}{3} \sum_{i=1}^{n^{ek}} A^i. \tag{24}$$

in which n^{ek} is the number of the adjacent triangular elements in the smoothing domain $\Omega^{(k)}$, and A^i is the area of the i -th sub-domain in a triangular element.

Substituting Eqs. (21) and (24) into Eq. (22), the smoothed strains on the smoothing domain $\Omega^{(k)}$ in $Oxyz$ can be expressed as

$$\bar{\boldsymbol{\varepsilon}}^{(k)} = \sum_{j=1}^{n^{nk}} \bar{\mathbf{R}}_j^{(k)} \mathbf{d}_j^{(k)}; \bar{\boldsymbol{\kappa}}^{(k)} = \sum_{j=1}^{n^{nk}} \bar{\mathbf{B}}_j^{(k)} \mathbf{d}_j^{(k)}; \bar{\boldsymbol{\gamma}}^{(k)} = \sum_{j=1}^{n^{nk}} \bar{\mathbf{S}}_j^{(k)} \mathbf{d}_j^{(k)}. \tag{25}$$

where n^{nk} is the number of the neighboring nodes of edge k ; $\mathbf{d}_j^{(k)}$ is the nodal degrees of freedom at the j -th node of the smoothing domain $\Omega^{(k)}$ in $Oxyz$; $\bar{\mathbf{R}}_j^{(k)}$, $\bar{\mathbf{B}}_j^{(k)}$, and $\bar{\mathbf{S}}_j^{(k)}$ are the membrane, the bending, and the shear smoothed gradient matrices at the j -th node of the smoothing domain $\Omega^{(k)}$ in $Oxyz$, respectively, and can be computed by

$$\begin{aligned} \bar{\mathbf{R}}_j^{(k)} &= \frac{1}{A^{(k)}} \sum_{i=1}^{n^{ek}} \frac{1}{3} A^i \boldsymbol{\Lambda}_{m1}^{(k)} \boldsymbol{\Lambda}_{m2}^i \mathbf{R}_j^i; \bar{\mathbf{B}}_j^{(k)} = \frac{1}{A^{(k)}} \sum_{i=1}^{n^{ek}} \frac{1}{3} A^i \boldsymbol{\Lambda}_{b1}^{(k)} \boldsymbol{\Lambda}_{b2}^i \mathbf{B}_j^i; \bar{\mathbf{S}}_j^{(k)} \\ &= \frac{1}{A^{(k)}} \sum_{i=1}^{n^{ek}} \frac{1}{3} A^i \boldsymbol{\Lambda}_{s1}^{(k)} \boldsymbol{\Lambda}_{s2}^i \mathbf{S}_j^i. \end{aligned} \tag{26}$$

The global stiffness matrix of the laminated composite shell in Eq. (16) can be rewritten by global stiffness matrix of ES-MITC3 as

$$\mathbf{K}_{ES-MITC3} = \sum_{k=1}^{n^k} \mathbf{K}_{ES-MITC3}^{(k)}. \tag{27}$$

in which $\mathbf{K}_{ES-MITC3}^{(k)}$ are the smoothed stiffness matrices defined by

$$\mathbf{K}_{ES-MITC3}^{(k)} = \mathbf{T}^T \left(\int_{\Omega^{(k)}} \begin{Bmatrix} \bar{\mathbf{R}}^{(k)} \\ \bar{\mathbf{B}}^{(k)} \\ \bar{\mathbf{S}}^{(k)} \end{Bmatrix}^T \begin{bmatrix} \mathbf{A} & \mathbf{B} & \mathbf{0} \\ \mathbf{B} & \mathbf{D} & \mathbf{0} \\ \mathbf{0} & \mathbf{0} & \mathbf{D}^s \end{bmatrix} \begin{Bmatrix} \bar{\mathbf{R}}^{(k)} \\ \bar{\mathbf{B}}^{(k)} \\ \bar{\mathbf{S}}^{(k)} \end{Bmatrix} d\Omega \right) \mathbf{T}. \quad (28)$$

From Eq. (28), it can be seen that the values of element stiffness matrix at the drilling degree of freedom β_z equal zero. To deal with this problem, the null values of the stiffness corresponding to the drilling degree of freedom are then replaced by approximate values. This approximate value is taken to be equal to 10^{-3} times the maximum diagonal value in the element stiffness matrix [27].

3 Numerical Results

In this section, several examples for static analysis of isotropic shell and transient response of laminated composite shell are investigated. The results obtained are compared with other published ones.

3.1 Static Analysis of Isotropic Shell Problem

We consider a pinched cylindrical shell supported by rigid diaphragms and subjected to a point load $P = 1$ at the center of the cylindrical surface as shown in Fig. 4a. The material properties are given by Poisson’s ratio $\nu = 0.3$ and Young’s modulus $E = 3 \times 10^6$. The geometric dimensions of the pinched cylinder are the length $L = 600$, the radius $R = 300$, and the thickness $t = 3$, respectively. Due to its symmetry, only one-eighth of the cylinder is modeled, shown in Fig. 4a. The

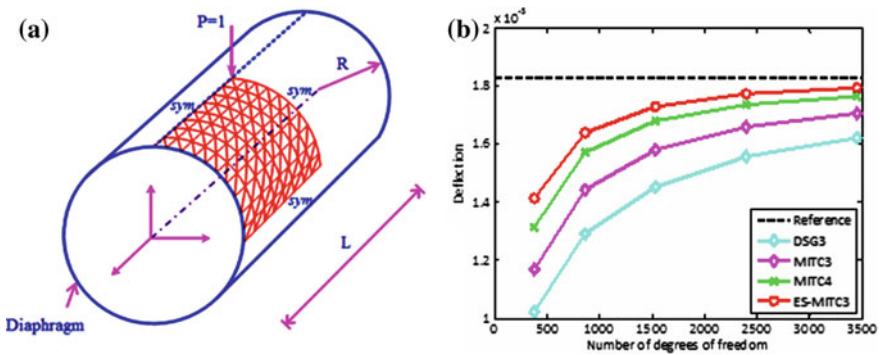


Fig. 4 a Pinched cylinder under central point load; b convergence of the vertical displacement at loaded point

pinched cylinder shell is discretized into uniform triangular and quadrilateral meshes with 8, 12, 16, and 20. The convergence of the displacement at the center point is plotted in Fig. 4b. In comparison with the reference results of Fluge [28], the results of the proposed method are the best accurate compared with those of the triangular shell elements DSG3, MITC3, and the quadrilateral shell element MITC4 in fine meshes.

3.2 Transient Analysis of Laminated Composite Shell Problem

In all the numerical examples, all layers are assumed to be the same thickness, mass density, and made of the same linearly elastic composite material but the fiber orientations may be different among the layers. The spherical shell is uniformly discretized by 8×8 triangular elements. The numerical results for non-dimensional center deflection \bar{w} and stress $\bar{\sigma}_x, \bar{\sigma}_y$ are normalized by $\bar{w} = 100w \times E_2 h^3 / q_0 a^4; \bar{\sigma}_x = \sigma_x / q_0; \bar{\sigma}_y = \sigma_y / q_0$.

Firstly, the dynamic response of simply supported laminated sphere shell subjected to step load is considered. The geometrical parameters are: $a/b = 1; R_x = R_y = 10 \text{ m}; h = 0.1 \text{ m}$, shown in Fig. 2b. The material properties are given as follows: $E_1 = 25 \times 10^9 \text{ Pa}; E_2 = 1 \times 10^9 \text{ Pa}; G_{12} = G_{13} = 0.5 \times 10^9 \text{ Pa}; G_{23} = 0.2 \times 10^9 \text{ Pa}; \nu_{23} = 0.25; \rho = 2000 \text{ kg/m}^3$. The step load can be expressed as Table 1, in which $p_0 = 1000 \text{ N/m}^2$ and $t_1 = 0.04 \text{ s}$.

Figures 5 and 6 show dynamic response of central non-dimensional deflection \bar{w} and normal stress $\bar{\sigma}_y, \bar{\sigma}_x$ of the laminated composite spherical shells $[0^\circ/90^\circ]$ and $[0^\circ/90^\circ/0^\circ]$, respectively. It is seen that the results of proposed method are in good agreement with those from Sahan [5] and overtake those by MITC3. In fact, the edge-based gradient smoothing technique of ES-MITC3 helps soften the over-stiffness of the MITC3 as presented in Ref. [1].

In the next example, the dynamic response of simply supported laminated sphere shell $[0^\circ/90^\circ/0^\circ]$ subjected to such as step, sine, triangular, and blast load is considered. The geometrical parameters are: $a/b = 1; R_x = R_y = \infty; \text{ and } h = 0.1 \text{ m}$. The material properties are given as follows: $E_1 = 172.369 \times 10^9 \text{ Pa}; E_2 = 6.895 \times 10^9 \text{ Pa}; G_{12} = G_{13} = 3.448 \times 10^9 \text{ Pa}; G_{23} = 1.379 \times 10^9 \text{ Pa}; \nu_{23} = 0.25; \text{ and } \rho = 1603.03 \text{ kg/m}^3$. The different loads can be expressed in Table 1, in which $p = 68.895 \times 10^6 \text{ N/m}^2$ and $t_1 = 0.06 \text{ s}$.

The transient solution for non-dimensional deflection \bar{w} and normal stress $\bar{\sigma}_x$ at center of laminated spherical shell for various loadings are presented in Fig. 7 and Fig. 8, respectively. Obtained results from the present method are compared with those of Khdeir [29]. It is observed that the obtained results are in very good agreement with the exact solution for all non-dimensional deflection and normal stress as a function of time.

Table 1 Different loading functions

Loading	Step	Sine	Triangular	Explosive blast
$p(t)$	$\begin{cases} p_0, & t \leq t_1 \\ 0, & t > t_1 \end{cases}$	$\begin{cases} p_0 \sin(\pi t/t_1), & t \leq t_1 \\ 0, & t > t_1 \end{cases}$	$\begin{cases} p_0(1 - t/t_1), & t \leq t_1 \\ 0, & t > t_1 \end{cases}$	$p(t) = p_0(1 - t/t_1)e^{-\alpha(t/t_1)}$

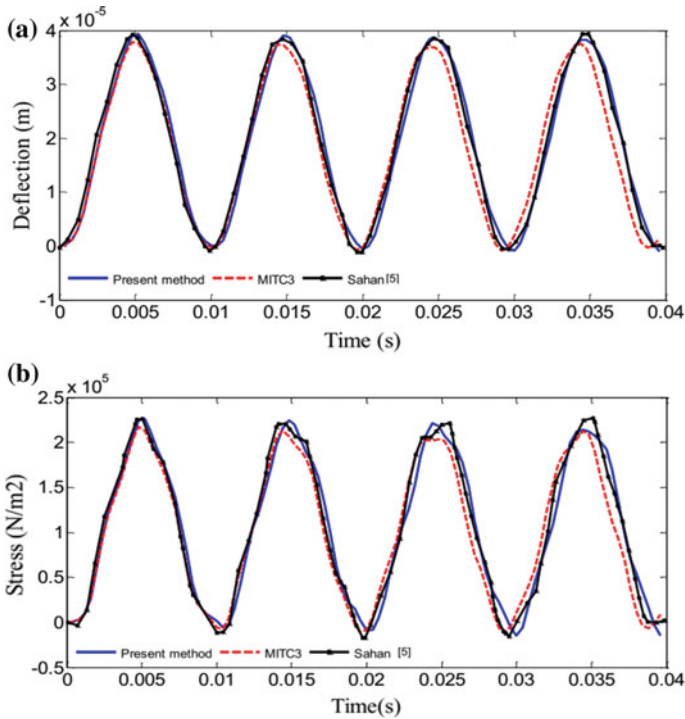


Fig. 5 Central displacement (a); central stress $\bar{\sigma}_y$ (b) versus time for $[0^\circ/90^\circ]$ laminates

Finally, the transient analysis of simply supported laminated composite spherical shell with various boundary conditions subjected to blast loading is investigated. The geometrical parameters are: $a/b = 1$; $R_x = R_y = 10$ m; $h = 0.1$ m. The material properties of shell are the same as the first example. However, the blast load with sinusoidal distributed load, which are expressed by the parameters listed in Table 1, where $p = p_0 \sin(\pi x/a) \sin(\pi x/b)$ with $p_0 = 1000$ N/m²; $t_1 = 0.004$ s; $\alpha = 1.98$ is considered.

Figures 9 and 10 present dynamic response of non-dimensional central deflection (\bar{w}) and normal stress $\bar{\sigma}_y, \bar{\sigma}_x$ of the laminated composite spherical shell $[0^\circ/90^\circ]$; $[0^\circ/90^\circ/0^\circ]$, respectively, with various boundary conditions such as four edges are simply supported (SSSS), four edges are clamped (CCCC) and (SCSC) that mean two edges are simply supported and two edges are clamped, respectively. The plots in these figures reveal that the effects of the boundary conditions are significant to displacement and stress of laminated composite shell subject to blast loading.

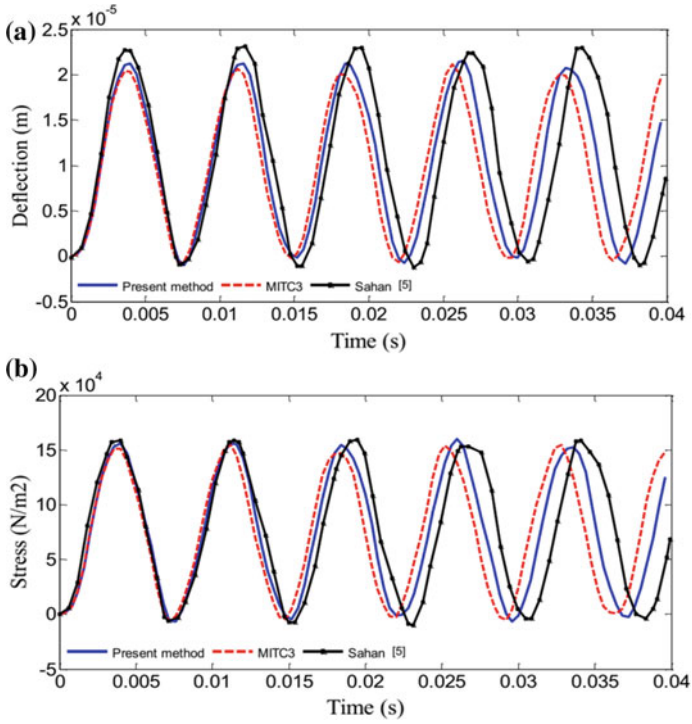


Fig. 6 Central displacement (a); central stress $\bar{\sigma}_x$ (b) versus time for $[0^\circ/90^\circ/0^\circ]$ laminates

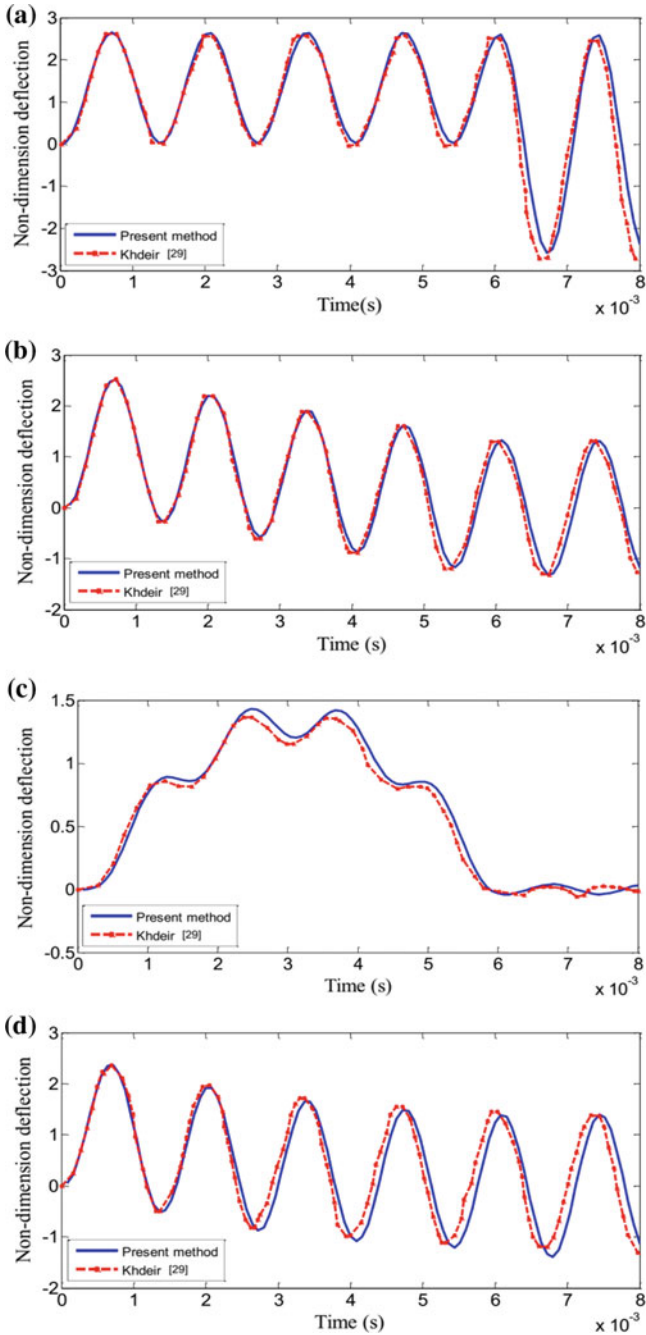


Fig. 7 Variation of the center non-dimensional deflection as a function of time for different loading: **a** step; **b** sine; **c** triangle; and **d** explosion

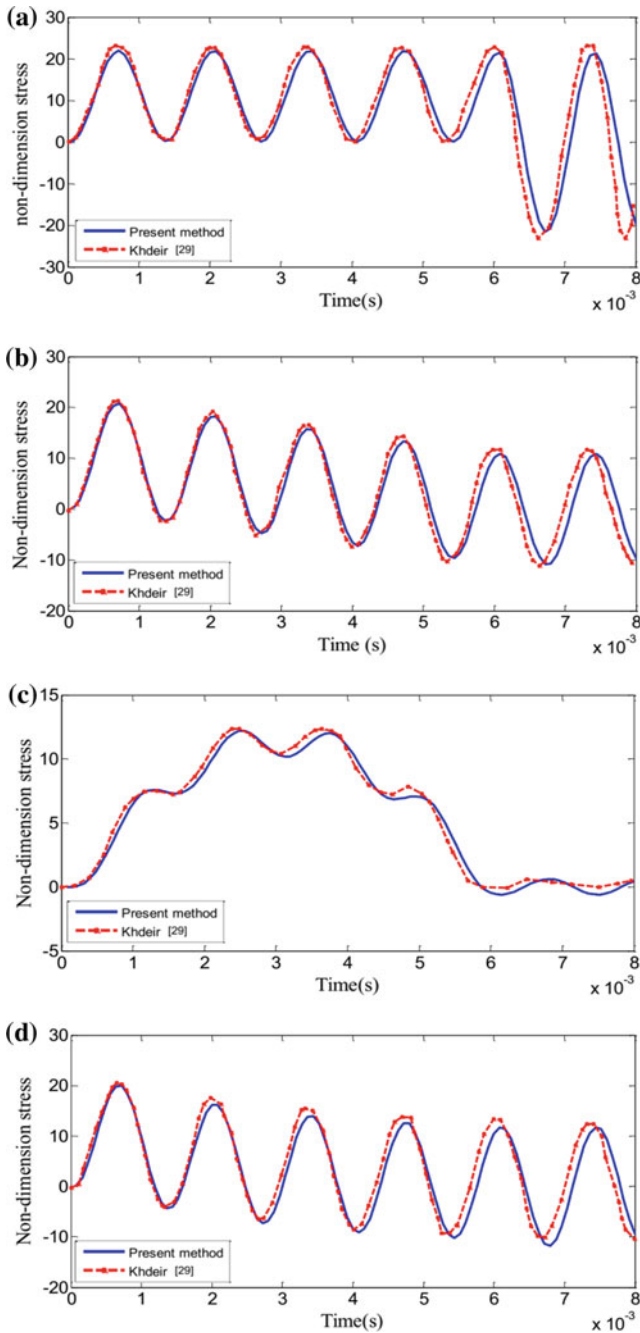


Fig. 8 Variation of the center normal stress as a function of time for different loading: **a** step; **b** sine; **c** triangle; and **d** explosion

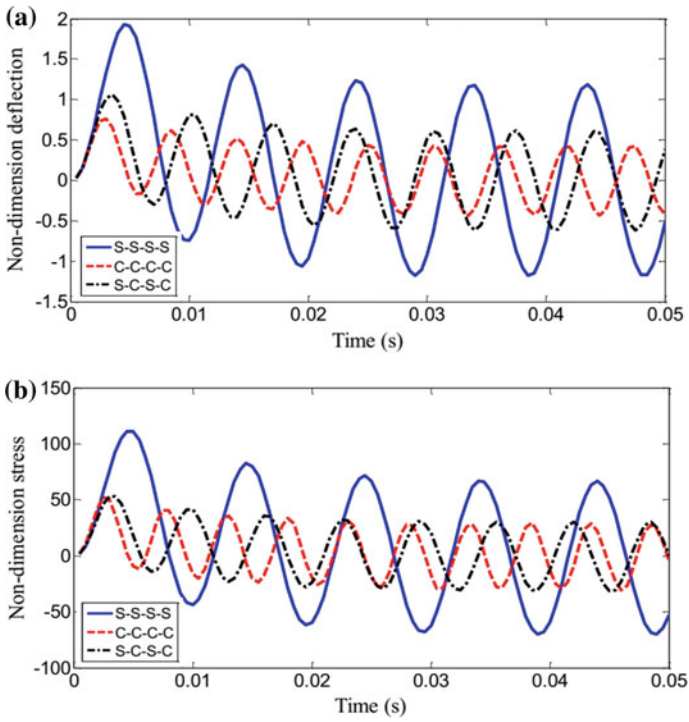


Fig. 9 Central displacement (a); central stress $\bar{\sigma}_y$ (b) versus time for $[0^\circ/90^\circ]$ laminated composite spherical shell subjected to blast loading

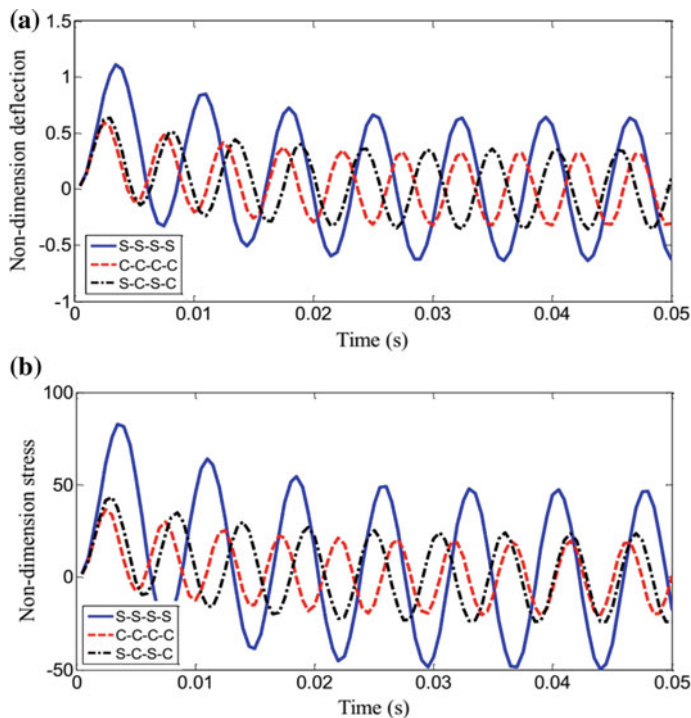


Fig. 10 Central displacement (a); central stress $\bar{\sigma}_x$ (b) versus time for $[0^\circ/90^\circ/0^\circ]$ laminated composite spherical shell subjected to blast loading

4 Conclusions

In this study, the ES-MITC3 is used to investigate for static analysis of isotropic shell problem and transient analysis of laminated composite spherical shells subjected to various loadings based on FSDT. Through the present formulation and numerical results, we can draw some of the following points:

- (i) The proposed ES-MITC3 only uses three-node triangular elements that are much easily generated automatically for complicated geometry domains.
- (ii) Because of using the gradient smoothing technique, which can help soften the over-stiff behavior in the MITC3, the proposed ES-MITC3 improves significantly the accuracy of the numerical results.
- (iii) The accuracy and reliability of the proposed ES-MITC3 are verified by comparing its numerical solutions with those of other available numerical results.
- (iv) Analyses of the effects of various boundary conditions of the laminated composite shells subjected to the blast loading by the ES-MITC3 give the expected results.

References

1. Lee P-S, Bathe K-J (2004) Development of MITC isotropic triangular shell finite elements. *Comput Struct* 82:945–962
2. Khdeir A, Reddy J, Frederick D (1990) On the transient response of cross-ply laminated circular cylindrical shells. *Int J Impact Eng* 9:475–484
3. Chun L, Lam K (1995) Dynamic analysis of clamped laminated curved panels. *Compos Struct* 30:389–398
4. Türkmen H (1999) Structural response of cylindrically curved laminated composite shells subjected to blast loading. *ARI Int J Phys Eng Sci* 51:175–180
5. Şahan MF (2016) Dynamic analysis of linear viscoelastic cross-ply laminated shallow spherical shells. *Compos Struct* 149:261–270
6. Liu G-R, Nguyen TT (2010) Smoothed finite element methods, vol 1. CRC Press Boca Raton
7. Liu G, Dai K, Nguyen T (2007) A smoothed finite element method for mechanics problems. *Comput Mech* 39:859–877
8. Liu G, Nguyen-Thoi T, Nguyen-Xuan H, Lam K (2009) A node-based smoothed finite element method (NS-FEM) for upper bound solutions to solid mechanics problems. *Comput Struct* 87:14–26
9. Liu GR, Nguyen-Thoi T, Lam KY (2009) An edge-based smoothed finite element method (ES-FEM) for static, free and forced vibration analyses of solids. *J Sound Vib* 320:1100–1130
10. Nguyen-Thoi T, Liu GR, Lam KY, Zhang GY (2009) A face-based smoothed finite element method (FS-FEM) for 3D linear and geometrically non-linear solid mechanics problems using 4-node tetrahedral elements. *Int J Numer Methods Eng* 78:324–353
11. Nguyen-Xuan H (2017) A polygonal finite element method for plate analysis. *Comput Struct* 188:45–62
12. Nguyen TN, Thai CH, Nguyen-Xuan H (2016) On the general framework of high order shear deformation theories for laminated composite plate structures: a novel unified approach. *Int J Mech Sci* 110:242–255
13. Nguyen HX, Nguyen TN, Abdel-Wahab M, Bordas S, Nguyen-Xuan H, Vo TP (2017) A refined quasi-3D isogeometric analysis for functionally graded microplates based on the modified couple stress theory. *Comput Methods Appl Mech Eng* 313:904–940
14. Nguyen N-T, Hui D, Lee J, Nguyen-Xuan H (2015) An efficient computational approach for size-dependent analysis of functionally graded nanoplates. *Comput Meth Appl Mech Eng* 297:191–218
15. Thai CH, Kulasegaram S, Tran LV, Nguyen-Xuan H (2014) Generalized shear deformation theory for functionally graded isotropic and sandwich plates based on isogeometric approach. *Comput Struct* 141:94–112
16. Chau-Dinh T, Nguyen-Duy Q, Nguyen-Xuan H (2017) Improvement on MITC3 plate finite element using edge-based strain smoothing enhancement for plate analysis. *Acta Mech* 1–23
17. Reddy JN (2004) *Mechanics of laminated composite plates and shells: theory and analysis*. CRC Press
18. Cui X, Liu G-R, Li G-Y, Zhang G, Zheng G (2010) Analysis of plates and shells using an edge-based smoothed finite element method. *Comput Mech* 45:141–156
19. Newmark NM (1959) A method of computation for structural dynamics. *J Eng Mech Div* 85:67–94
20. Zienkiewicz O, Taylor R, Too J (1971) Reduced integration technique in general analysis of plates and shells. *Int J Numer Methods Eng* 3:275–290
21. Tessler A, Hughes TJ (1985) A three-node Mindlin plate element with improved transverse shear. *Comput Methods Appl Mech Eng* 50:71–101
22. Bathe KJ, Dvorkin EN (1985) A four-node plate bending element based on Mindlin/Reissner plate theory and a mixed interpolation. *Int J Numer Methods Eng* 21:367–383

23. Zienkiewicz OC, Xu Z, Zeng LF, Samuelsson A, Wiberg NE (1993) Linked interpolation for Reissner-Mindlin plate elements: Part I—A simple quadrilateral. *Int J Numer Meth Eng* 36:3043–3056
24. Bletzinger K-U, Bischoff M, Ramm E (2000) A unified approach for shear-locking-free triangular and rectangular shell finite elements. *Comput Struct* 75:321–334
25. Nguyen-Xuan H, Rabczuk T, Bordas S, Debongnie J-F (2008) A smoothed finite element method for plate analysis. *Comput Methods Appl Mech Eng* 197:1184–1203
26. Nguyen-Thanh N, Rabczuk T, Nguyen-Xuan H, Bordas SP (2008) A smoothed finite element method for shell analysis. *Comput Methods Appl Mech Eng* 198:165–177
27. Nguyen-Thoi T, Phung-Van P, Thai-Hoang C, Nguyen-Xuan H (2013) A cell-based smoothed discrete shear gap method (CS-DSG3) using triangular elements for static and free vibration analyses of shell structures. *Int J Mech Sci* 74:32–45
28. Fluge W (1960) *Stress in shells*. Springer
29. Khdeir A, Reddy J (1989) Exact solutions for the transient response of symmetric cross-ply laminates using a higher-order plate theory. *Compos Sci Technol* 34:205–224

Estimating Modal Parameters of Structures Using Arduino Platform



Tuan Ta Duc, Tuan Le Anh and Huong Vu Dinh

Abstract This paper presents the identification of the modal parameters as frequencies, damping coefficients, and mode shapes based on using Arduino platform to measure oscillation signals of structure in time domain. The use of Arduino platform aims to reduce costs in the experimental field. Experiments are carried out on a cantilever beam; the measurement process collects input/output or only output signal. MATLAB software is also used for the computing and data processing; these signals are transformed from time domain to frequency domain by fast Fourier transform (FFT). Modal parameters are estimated in the frequency domain. Comparing obtained modal parameters from experimental method with those from analysis method. Results are found to be in agreement with the theory.

Keywords Modal parameters · Frequencies · Damps · Mode shapes
Arduino · Sensors

1 Introduction

Carrying out an experiment on building structures is a difficult task, demanding the complexity of instruments and high costs. Thanks to the development of science and technologies, electronic devices and methods were applied in practice [1, 2]. In order to reduce costly experiments, the previous studies used the Arduino platform and achieved some results [3, 4]. This paper presents how to design a measurement system based on Arduino platform. The Arduino is a data acquisition system of the

T. Ta Duc (✉) · T. Le Anh · H. Vu Dinh
Institute of Techniques for Special Engineering,
Le Quy Don Technical University, Hanoi, Vietnam
e-mail: tuantaduc@mta.edu.vn

T. Le Anh
e-mail: tuanleanh@mta.edu.vn

H. Vu Dinh
e-mail: dinhvu259@gmail.com

sensors. Experimental data collected are used for signal processing to obtain modal parameters. Input–output methods [5] are used to determine the dynamic characteristics of small- and medium-sized structures. Output-only methods [6] are used on large structure; these methods do not require any controlled excitation. Since the forcing function is unknown, frequency response function between input force and output response signal cannot be calculated. Instead, the analysis relies on correlation function and spectral density function estimated from the operational response.

2 A Measurement System Based on Arduino Platform

a. Hardware

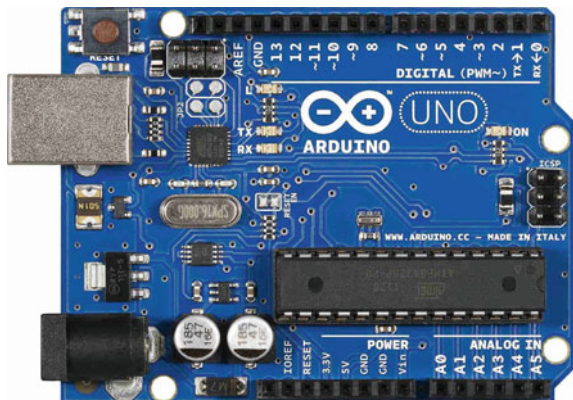
Arduino

Arduino was born at the Ivrea Interaction Design Institute as an easy tool for fast prototyping. Arduino is a completely open-source electronics platform based on an easy-to-use hardware and software that has been the “brain” of thousands of projects, from everyday objects to complex scientific instruments.

This measurement system was built with the board Arduino Uno (Fig. 1). This is a microcontroller board based on the ATmega328P. It has 14 digital input/output pins (of which 6 can be used as PWM outputs), 6 analog inputs, a USB connection, a 16 MHz quartz crystal, a power jack, a reset button [7].

In the IDE, there is a built-in serial monitor that can be used to send and receive information. When connected over USB to a computer, the Arduino shows up as a virtual COM-port and any software capable of serial communication can be used.

Fig. 1 Arduino Uno board



Accelerometer

An accelerometer is a device that measures proper acceleration. It can detect magnitude and direction of the proper acceleration. In this system, we used the ADXL345 accelerometer (Fig. 2).

The ADXL345 is a small, thin, ultralow power, 3-axis accelerometer with many measurement ranges at ± 2 , ± 4 , ± 8 , ± 16 g [8]. Digital output data is 16-bit twos complement and is accessible through a SPI or I2C digital interface. The ADXL345 is well suited for most experimental works. It measures the static acceleration of gravity, as well as dynamic acceleration resulting from the effects of impacts on the structure. It has high resolution which enables to measure of slight changes of acceleration.

Force-Sensitive Resistor

Force-sensing resistors (FSR) are a polymer thick film (PTF) device which exhibits a decrease in resistance with an increase in the force applied to the active surface. They are simple to use and low cost.

This is a photograph of an FSR (Fig. 3)—the Interlink 402 model. It is basically a resistor that changes its resistive value (in ohms Ω) depending on how much it is pressed [9].

Fig. 2 Accelerometer ADXL345

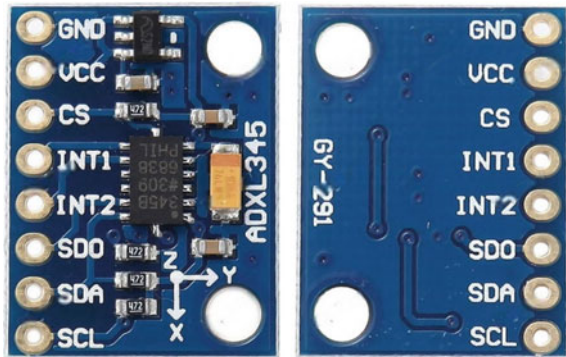
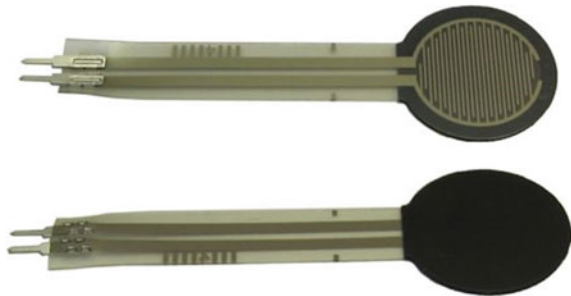


Fig. 3 Force-sensitive resistor



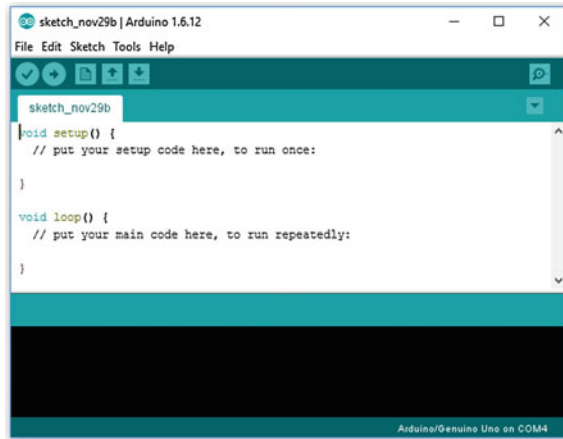


Fig. 4 Arduino software

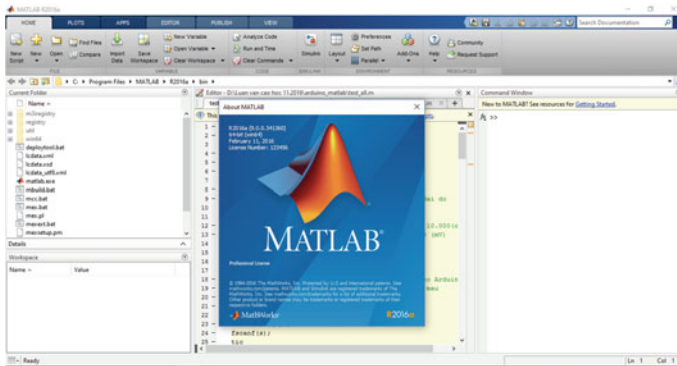


Fig. 5 MATLAB software

b. Software

Arduino software

Arduino Software (Fig. 4) allows to write code and upload it to the board. It can run on many operating systems such as Windows, Mac OS X, and Linux [10].

MATLAB software

MATLAB is a high-level language and an interactive environment. It enables to implement numerical computation, visualization, and programming [11]. It includes built-in mathematical functions fundamental to solve engineering and scientific problems and an interactive environment ideal for iterative exploration, design, and problem solving. In this paper, a serial port communication is initialized between Arduino and computer and programming on MATLAB software (Fig. 5) to process data from the port.

3 Experimental Setup

a. Circuit diagram

On the basis of the techniques, methods and testing procedures to measure structural oscillation and circuit diagram of the experimental program are set out as shown in Fig. 6.

This diagram enables to measure the both acceleration and force or only acceleration with different methods in vibration research.

b. Experimental structure

The experimental structure is a cantilever beam. The physical properties of the beams are described in Table 1.

c. Measuring vibration of structure using two measurement systems

The purpose of this test is to evaluate the accuracy of an Arduino system compared to a specialized measurement equipment at the same rate. Experimental model is set up as shown in Fig. 7.

Experimental equipment

The first measurement system is based on the Arduino platform: Arduino, acceleration sensor ADXL345, and force-sensitive resistor (Figs. 1, 2, and 3).

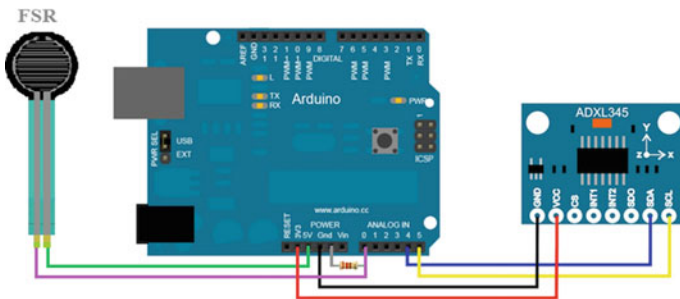
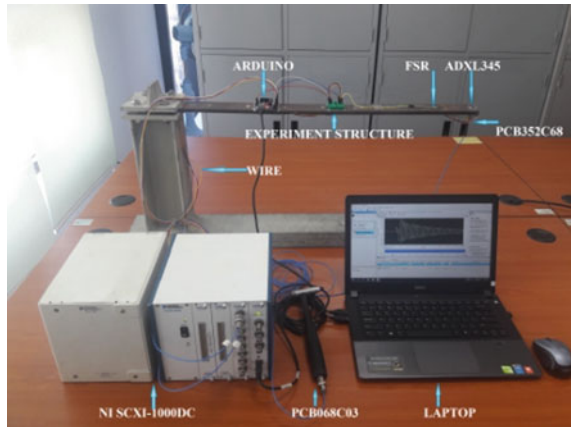


Fig. 6 Circuit diagram

Table 1 Physical properties of the beam

Property	Value	Unit
Material type	Steel	
Length	710	mm
Mass per unit volume	7850	kg/m ³
Modulus of elastic	2.03E5	MPa
Width—cross section	8	mm
Height—cross section	60	mm

Fig. 7 Experimental model

The second measurement system is based on the specialized measurement equipment and software from National Instruments Corporation NI SCXI-1000DC, acceleration sensor PCB352C68, and hammer PCB086C03 (Fig. 7). Detailed information about these devices can be found in [12–15].

Experimental model

Experimental method

The experiment was performed according to the method of measuring structural oscillations by simultaneous two measurement systems.

Testing and evaluating this measurement system involve mounting two accelerometers at one location. Using hammer PCB086C03 to strike the structure and measuring response of the structure by accelerometers.

As a result of the experiments (Fig. 8), we can confirm that this measurement system is suitable for measuring oscillation of structures.

d. Estimating modal parameters from collected data

With the employment of the measurement system based on the Arduino platform, measurement data obtained from responses of the structure are used to estimate the parameters of the model.

Experimental method

The experimental structure is small, and thus, input–output methods are used to determine the dynamic characteristics.

The structure is divided into the points corresponding to the degree of freedom to be measured. Force is applied to the structure to induce vibrations and compute frequency response functions (FRFs) $H_{ij}(\omega)$.

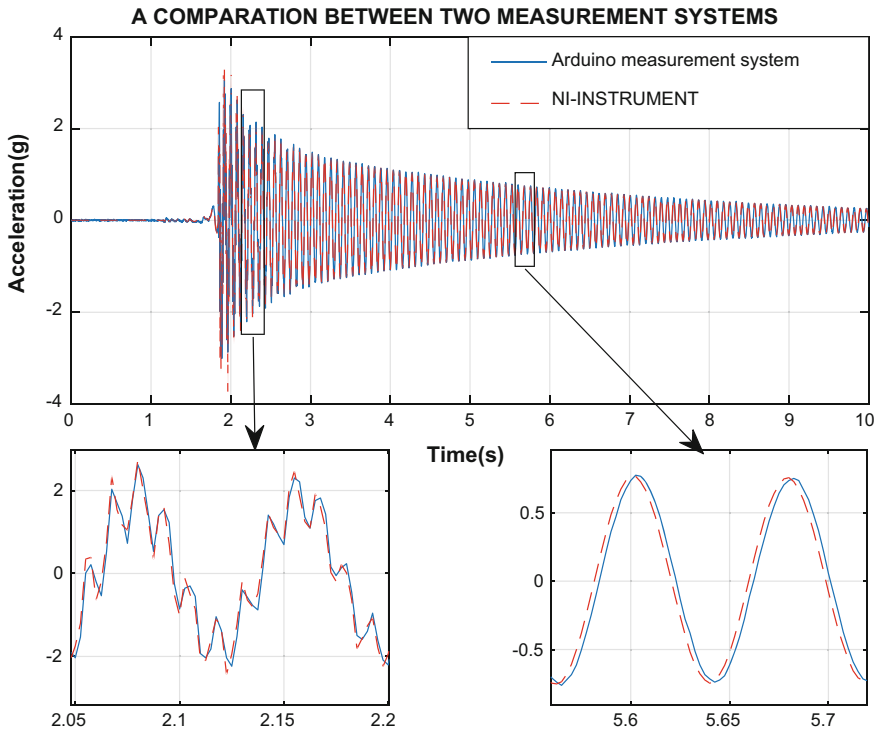


Fig. 8 Results of the comparison between Arduino and NI-INSTRUMENT

Input excitation in force and response outputs in acceleration are used to compute an experimental FRF. The FRF is used to identify the resonant frequencies, damping, and mode shapes of the physical structure.

The modal parameters are extracted from a set of FRF measurements between the reference position and a number of measurement positions required in the model.

Spectra are generated and then averaged in order to produce an average spectrum. This average spectrum represents true vibration behavior, and the averaging process minimizes the effect of random variations or noise, as shown in Fig. 9.

Comparison between the results for obtaining the modal parameters through the experimental and analytical methods is presented in Table 2 and Fig. 10.

b. Result

Estimating natural frequencies and damping

Analysis of signal input/output procedures is performed with the help of MATLAB software. Using the Window function, cross-spectrum and least squares procedures to filter the signal noise are calculated [16].

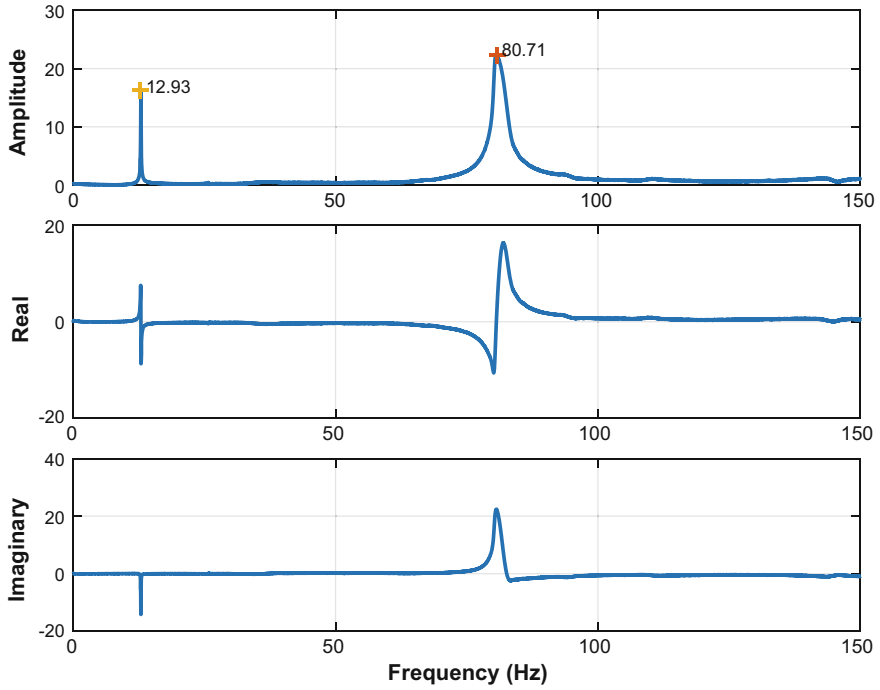


Fig. 9 Experimental frequency response function and obtained natural frequencies

Table 2 Comparison of first natural frequencies

Mode	Analytical method f (Hz)	Experimental method f (Hz)	Error (%)
1	12.90	12.93	0.23
2	80.88	80.71	0.21

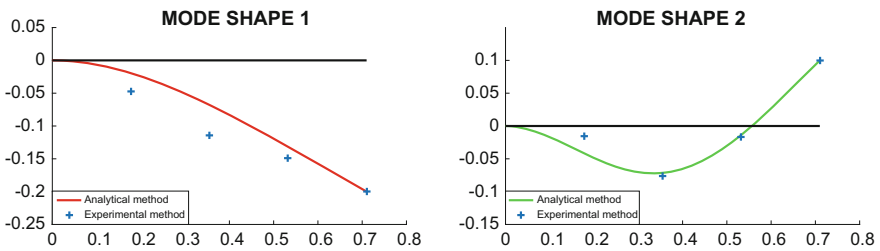


Fig. 10 Comparing mode shapes of vibration of beam

Table 3 Damping ratio ξ

Mode	ξ
1	0.00298
2	0.013850

The Uniform Window can be used for data processing. This window is applied to data where the entire signal is captured in one sample or record of data or when the data are guaranteed to satisfy the periodicity requirement of the FFT process.

Frequency response function $H(\omega)$ of averaging measurements is shown in Fig. 8.

Comparison between obtained natural frequencies through experimental method and analytical method can be seen in Table 2. The experimental results are very close to the values obtained from analytical method [17].

The damping ratio ξ through spectral characteristics of FRF function is shown in Table 3.

Estimating mode shape

The FRFs acquired to a reference FRF on a structure are used to determine the mode shape. The results of comparison estimating the mode shapes through analytical method and experimental method are shown in Fig. 10.

4 Conclusions

The results of this system are satisfied when comparing with National Instruments equipment while the price is very low.

The measurement system based on Arduino platform is suitable for using a signal acquisition. It is easy to be installed and able to give accurate results.

The results of paper suggested that this measurement system can be used in structural health monitoring with low cost.

References

1. Morris AS, Langari R (2012) Measurement and instrumentation, theory and application. Butterworth-Heinemann, Oxford
2. Rao SS (2011) Mechanical vibrations. University of Miami, New Jersey
3. Hjør A, Holmberg M (2015) Measuring mechanical vibrations using arduino as a slave I/O to an EPICS control system. Uppsala University, Uppsala
4. Marcus V, Silva AL, Brunetto PHA Gregolin RF (2015) Instrumentation for mechanical vibrations analysis in the time domain and frequency domain using the Arduino platform
5. Brincker R, Zhang L, Andersen P (2000) Modal identification from ambient responses using frequency domain decomposition. In: Proceedings of IMAC 18, the international modal analysis conference, San Antonio, TX, USA, Feb 2000, pp 625–630

6. Ewins DJ (2000) Modal testing: theory, practice, and application, 2nd edn. Research studies, New York
7. Arduino LLC (2017) Arduino Uno. <http://www.arduino.cc/en/Main/ArduinoBoardUno>
8. Analog Devices Inc. (2017) ADXL345. <http://www.analog.com/en/products/mems/accelerometers/adxl345.html>
9. Interlink electronics, FSR 402 data sheet
10. Arduino LLC (2017) Language reference. <http://www.arduino.cc/en/Reference/HomePage>
11. MathWorks Inc. (2017) MATLAB overview. <https://www.mathworks.com/products/matlab.html>
12. PCB Group, Model 352C68, Installation and operating manual
13. National instruments (2017) Instruments. <http://sine.ni.com/nips/cds/view/p/lang/en/nid/10675>
14. I2C Info, I2C Info – I2C Bus (2017) Interface and protocol. <http://i2c.info/i2c-bus-specification>
15. PCB Group, Model 086C03, ICP® Impact hammer installation and operating manual
16. Harris FJ (1978) On the use of windows for harmonic analysis with the discrete Fourier transform
17. Stokey WF (2002) Vibration of systems having distributed mass and elasticity. In: Harris CM (ed) Harris' shock and vibration handbook, 5th edn, Chapter 7. McGraw-Hill, New York

Analysis of Dynamic Impact Factors of Bridge Due to Moving Vehicles Using Finite Element Method



T. Nguyen-Xuan, Y. Kuriyama and T. Nguyen-Duy

Abstract This article presents analysis of dynamic impact factors for displacement, bending moment, and shear force of bridge under moving vehicles by finite element method. Vehicle is a dumper truck with three axles. Each axle of vehicle is idealized as two mass dynamic systems, in which a mass is supported by a spring and a dashpot. The structural bridges are simulated as bending girder elements. The finite element method is applied to establish the overall model of vehicle–bridge interaction. Galerkin method and Green theory are used to discrete the motion equation of vehicle–bridge system in space domain. Solutions of the motion equations are solved by Runge–Kutta–Merson method (RKM) in time domain. The numerical results are in good agreement with full-scale dynamic testing under controlled traffic condition of the super T concrete girder at NguyenTriPhuong Bridge in Danang city, Vietnam. Numerical results figure out that there are significant differences between dynamic factors for displacement, bending moment, and shear force. Therefore, the common use of only one dynamic impact factor for displacements, bending moment, and shear forces of bridge structure in each limited state should add more consideration. Furthermore, current results are references for bridge engineers to have more information for safety design requirements and suitability in bridge operation.

Keywords Dynamic impact factor for displacement • Dynamic impact factor for bending moment • Dynamic impact factor for shear force • Moving vehicle Finite element method • Vehicle–bridge interaction

T. Nguyen-Xuan · T. Nguyen-Duy (✉)
Faculty of Road and Bridge Engineering, University of Danang,
University of Science and Technology, Da Nang, Vietnam
e-mail: ngduythao1978@yahoo.com

T. Nguyen-Xuan
e-mail: nguyexuantoan2007@gmail.com

Y. Kuriyama
Research into Artifacts, Center for Engineering, The University of Tokyo, Tokyo, Japan
e-mail: kuriyama@race.u-tokyo.ac.jp

1 Introduction

Dynamic impact of moving vehicles on bridges is an important and long-standing issue in the design and evaluation of bridges and has received much attention from researchers and engineers. The use of the dynamic impact factor (IM) to account for the impact effect of vehicles has been widely accepted in bridge engineering, which is described by the dynamic impact factor (IM) or the dynamic amplification factor (DAF) or dynamic load allowance (DLA) that reflects how many times the constant load must be multiplied to cover additional dynamic effects, Fryba [1]. To account for such an effect, a dynamic impact factor (IM) is typically proposed in design practice, and the total live-load (LL) effect is usually calculated as follows:

$$LL = (1 + IM) \times R_{sta} \rightarrow (1 + IM) = \frac{LL}{R_{sta}} = \frac{R_{dyn}}{R_{sta}} \quad (1)$$

where R_{sta} is static load effect; R_{dyn} is dynamic load effect; and $(1 + IM)$ represents the dynamic amplification for the static load effect. The dynamic IM plays a vital role in the practice of bridge design and condition assessment. Accurate evaluations of IMs lead to safe and economical designs for new bridges and provide valuable information for condition assessment and management of existing bridges.

The earliest analytical study of moving loads can be found in Willis (1847) [2], who investigated the case with a point mass moving on a simply supported massless beam at a constant speed. Many of these early developments were summarized by Fryba [1] and Paultre et al. [3]. Currently, with the advances in computer technologies; the finite element method has been widely applied to obtain results that are in good agreement with those measured from field tests (e.g., Huang et al. [4]; Wang et al. [5]; Kwasniewski et al. [6], Shi [7]; and Ashebo et al. [8]). Au et al. [9] presented a numerical study of the effects of surface road unevenness and long-term deflection on the dynamic impact factor of prestressed concrete girder and cable-stayed bridges due to moving vehicles. The results showed that the effects of random road unevenness and the long-term deflection of concrete deck on bridge vary a lot at the sections closed to the bridge tower, with significant effects on the short cables. Lombaert and Conte [10] proposed the random vibration analysis of dynamic vehicle–bridge interaction due to road unevenness by an original frequency domain method. The road unevenness was modeled by the random non-stationary process. Due to the complexity of the problem, the authors presented only the results of simple supported beam model subjected to a moving concentrated load. Nguyen et al. [11–13] analyzed the dynamic three-axle vehicle–bridge interaction considering the change of vehicle velocity through braking force by finite element method. The numerical results showed that the influence of braking force has significant effects on bridge dynamic impact factor. However, most of the previous researches studied dynamic impact factor for displacement or bending moment. Nevertheless, few of the studies have focused on analysis dynamic impact factor for displacement, bending moment, and shear force. Additionally, the

full-scale dynamic field testing under controlled traffic condition of the bridge is needed in order to obtain a clearer understanding of the relationship between dynamic interaction for bridges and vehicle models. Moreover, in the practice of bridge design works, a lot of engineers still consider the dynamic impact factor to be the same for displacement, bending moment, and shear force in each limited state. However, from the authors' study results, there is a significant difference of dynamic impact factor for displacement, bending moment, and shear force.

This paper analyzes the dynamic impact factor for displacement, bending moment, and shear force in the super T concrete girder subjected to three-axle dumper truck by the finite element method. The numerical results are validated with full-scale testing model at NguyenTriPhuong Bridge in Danang city, Vietnam.

2 Vehicle and Bridge Model

Consider a three-span super T concrete girder with link slab subjected to a three-axle dumper truck vehicle as in Fig. 1. Assume that the body weight of vehicle and goods on the vehicle distributes to three axles m_{11} , m_{12} , and m_{13} , respectively. The mass of three axles is m_{21} , m_{22} , and m_{23} , respectively. The dynamic interaction model between a three-axle vehicle and a girder element is described as in Fig. 2.

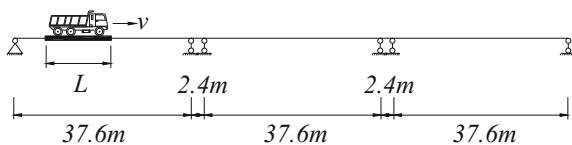
Where $w_i(x_i, t)$ is the vertical displacement of girder element at position x_i ; x_i is the coordinate of the i th axle of the vehicle at time t ($i = 1, 2, 3$); z_{1i} is the vertical displacement of chassis at i th axle of vehicle; z_{2i} is the vertical displacement of i th axle of vehicle; y_{1i} is the relative displacement between the chassis and i th axle; y_{2i} is the relative displacement between i th axle and girder element; k_{1i} and d_{1i} are the spring and dashpot of suspension at i th axle, respectively; k_{2i} and d_{2i} are the spring and dashpot of tire at i th axle, respectively.

According to Clough and Penzien [14], the governing equation for the flexure vibration of damped girder due to uniform loading $p(x, z, t)$ can be written as follow:

$$EJ \cdot \left(\frac{\partial^4 \omega}{\partial x^4} + \theta \frac{\partial^5 \omega}{\partial x^5 \cdot \partial t} \right) + \rho_m \cdot \frac{\partial^2 \omega}{\partial t^2} + \beta \cdot \frac{\partial \omega}{\partial t} = p(x, z, t) \tag{2}$$

$$p(x, z, t) = \sum_{i=1}^n \xi_i(t) \cdot [-(m_{1i} + m_{2i}) \cdot g - m_{1i} \cdot \ddot{z}_{1i} - m_{2i} \cdot \ddot{z}_{2i}] \cdot \delta(x - x_i) \tag{3}$$

Fig. 1 Schematic of vehicle moving on bridge



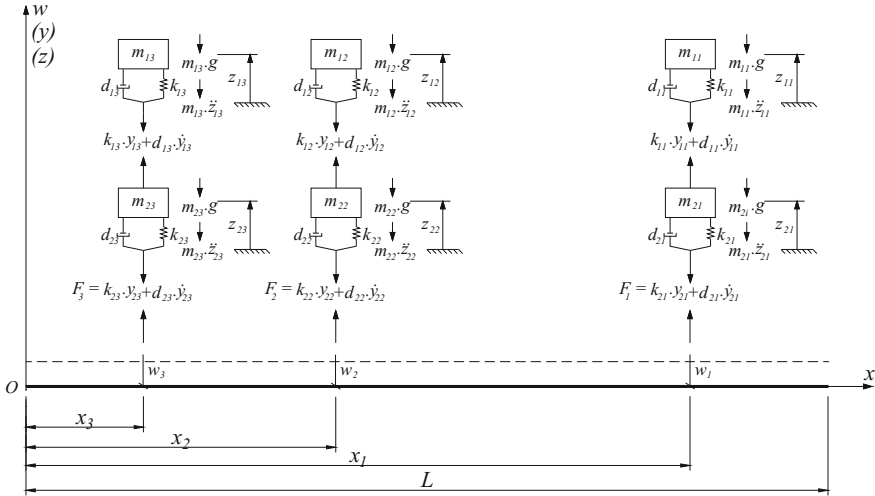


Fig. 2 Model of vehicle–bridge interaction

where EJ is the bending stiffness of girder element; θ and β are the coefficient of internal friction and external friction of girder element; ρ_m is the mass of girder per unit length; n is the number of axle ($n = 3$); $\delta(x - x_i)$ is the Dirac delta function; $\zeta_i(t)$ is the logic control function; it is used to determine the position of vehicle on the bridge and is described as follows:

$$\zeta_i(t) = \begin{cases} 1 & \text{if } t_i \leq t \leq t_i + T_i \text{ ; } T_i = \frac{L}{v} \\ 0 & \text{if } t < t_i \text{ and } t > t_i + T_i \end{cases} \quad (4)$$

Using the finite element method, Eqs. (2) and (3) can be written in a matrix form as following:

$$[M_e] \cdot \{\ddot{q}\} + [C_e] \cdot \{\dot{q}\} + [K_e] \cdot \{q\} = \{f_e\} \quad (5)$$

where $\{\ddot{q}\}$, $\{\dot{q}\}$, $\{q\}$, and $\{f_e\}$ are the complex acceleration vector, complex velocity vector, complex displacement vector, and complex forces vector of the system (girder element and vehicle), respectively.

$$\{\ddot{q}\} = \begin{Bmatrix} \ddot{w} \\ \ddot{z}_1 \\ \ddot{z}_2 \end{Bmatrix} ; \{\dot{q}\} = \begin{Bmatrix} \dot{w} \\ \dot{z}_1 \\ \dot{z}_2 \end{Bmatrix} ; \{q\} = \begin{Bmatrix} w \\ z_1 \\ z_2 \end{Bmatrix} ; \{f_e\} = \begin{Bmatrix} F_w \\ F_{z1} \\ F_{z2} \end{Bmatrix} ; \{w\} = \begin{Bmatrix} w_{y1} \\ \varphi_1 \\ w_{y2} \\ \varphi_2 \end{Bmatrix} \quad (6)$$

where w_{y1} and φ_1 are the vertical displacement and rotation angle of the left end of girder element, respectively;

w_{y2} and φ_2 are the vertical displacement and rotation angle of the right end of element, respectively;

$[M_e]$, $[C_e]$, and $[K_e]$ are the mass matrix, damping matrix, and stiffness matrix of the system (girder element and vehicle), respectively.

$$\begin{aligned}
 [M_e] &= \begin{bmatrix} M_{ww} & M_{wz1} & M_{wz2} \\ 0 & M_{z1z1} & 0 \\ 0 & 0 & M_{z2z2} \end{bmatrix} \\
 &= \begin{bmatrix} K_{ww} & 0 & 0 \\ 0 & K_{z1z1} & K_{z1z2} \\ K_{z2w} & K_{z2z1} & K_{z2z2} \end{bmatrix} \\
 [C_e] &= \begin{bmatrix} C_{ww} & 0 & 0 \\ 0 & C_{z1z1} & C_{z1z2} \\ C_{z2w} & C_{z2z1} & C_{z2z2} \end{bmatrix} [K_e]
 \end{aligned} \tag{7}$$

where $[M_{ww}]$, $[C_{ww}]$, and $[K_{ww}]$ are mass matrix, damping matrix, and stiffness matrix of the girder elements, respectively. They can be found in Zienkiewicz et al. [15]

$$\begin{aligned}
 M_{z1z1} &= \begin{bmatrix} m_{11} & & & & 0 \\ & m_{12} & & & \\ & & \dots & & \\ & & & m_{1i} & \\ & 0 & & & \dots \\ & & & & & m_{1n} \end{bmatrix} \\
 &= \begin{bmatrix} m_{21} & & & & 0 \\ & m_{22} & & & \\ & & \dots & & \\ & & & m_{2i} & \\ & 0 & & & \dots \\ & & & & & m_{2n} \end{bmatrix}
 \end{aligned} \tag{8}$$

$$\begin{aligned}
 M_{wz1} &= P \cdot M_{z1z1}; M_{wz2} = P \cdot M_{z2z2}; P \\
 &= \begin{bmatrix} P_{11} & P_{12} & \dots & P_{1i} & \dots & P_{1n} \\ P_{21} & P_{22} & \dots & P_{2i} & \dots & P_{2n} \\ P_{31} & P_{32} & \dots & P_{3i} & \dots & P_{3n} \\ P_{41} & P_{42} & \dots & P_{4i} & \dots & P_{4n} \end{bmatrix}
 \end{aligned} \tag{9}$$

$$P_i = \begin{Bmatrix} P_{1i} \\ P_{2i} \\ P_{3i} \\ P_{4i} \end{Bmatrix} = \frac{\xi_i(t)}{L^3} \begin{Bmatrix} (L + 2x_i) \cdot (L - x_i)^2 \\ L \cdot x_i \cdot (L - x_i)^2 \\ x_i^2 \cdot (3L - 2x_i) \\ L \cdot x_i^2 \cdot (x_i - L) \end{Bmatrix} \tag{10}$$

$$\begin{aligned}
 C_{z_1z_1} &= \begin{bmatrix} d_{11} & & & & \\ & d_{12} & & & 0 \\ & & \dots & & \\ & & & d_{1i} & \\ & 0 & & & \dots \\ & & & & & d_{1n} \end{bmatrix}_{(n \times n)} \\
 C_{z_2} &= \begin{bmatrix} d_{21} & & & & \\ & d_{22} & & & 0 \\ & & \dots & & \\ & & & d_{2i} & \\ & 0 & & & \dots \\ & & & & & d_{2n} \end{bmatrix}_{(n \times n)}
 \end{aligned} \tag{11}$$

$$C_{z_1z_2} = C_{z_2z_1} = -C_{z_1z_1}; \quad C_{z_2z_2} = C_{z_1z_1} + C_{z_2}; \quad C_{z_2w} = (-N_i \cdot C_{z_2})^T \tag{12}$$

$$N_i = \left\{ \begin{array}{l} \begin{bmatrix} N_{11} & N_{12} & \dots & N_{1i} & \dots & N_{1n} \\ N_{21} & N_{22} & \dots & N_{2i} & \dots & N_{2n} \\ N_{31} & N_{32} & \dots & N_{3i} & \dots & N_{3n} \\ N_{41} & N_{42} & \dots & N_{4i} & \dots & N_{4n} \end{bmatrix}_{(n \times n)} \\ ; \quad \begin{array}{l} N_{1i} = \frac{1}{L^3} \cdot (L^3 - 3Lx_i^2 + 2x_i^3) \\ N_{2i} = \frac{1}{L^2} \cdot (L^2x_i - 2Lx_i^2 + x_i^3) \\ N_{3i} = \frac{1}{L^3} \cdot (3Lx_i^2 - 2x_i^3) \\ N_{4i} = \frac{1}{L^2} \cdot (x_i^3 - Lx_i^2) \end{array} \end{array} \right\} \tag{13}$$

$$\begin{aligned}
 K_{z_1z_1} &= \begin{bmatrix} k_{11} & & & & \\ & k_{12} & & & 0 \\ & & \dots & & \\ & & & k_{1i} & \\ & 0 & & & \dots \\ & & & & & k_{1n} \end{bmatrix}_{(n \times n)} \\
 K_{z_2} &= \begin{bmatrix} k_{21} & & & & \\ & k_{22} & & & 0 \\ & & \dots & & \\ & & & k_{2i} & \\ & 0 & & & \dots \\ & & & & & k_{2n} \end{bmatrix}_{(n \times n)}
 \end{aligned} \tag{14}$$

$$\begin{aligned}
 K_{z_1z_2} = K_{z_2z_1} &= -K_{z_1z_1}; \quad K_{z_2z_2} = K_{z_1z_1} + K_{z_2}; \\
 K_{z_2w} &= -(N_i \cdot K_{z_2})^T - (\dot{N}_i \cdot C_{z_2})^T
 \end{aligned} \tag{15}$$

$$F_w = \sum_{i=1}^n [-(m_{1i} + m_{2i})g] \cdot P_i \tag{16}$$

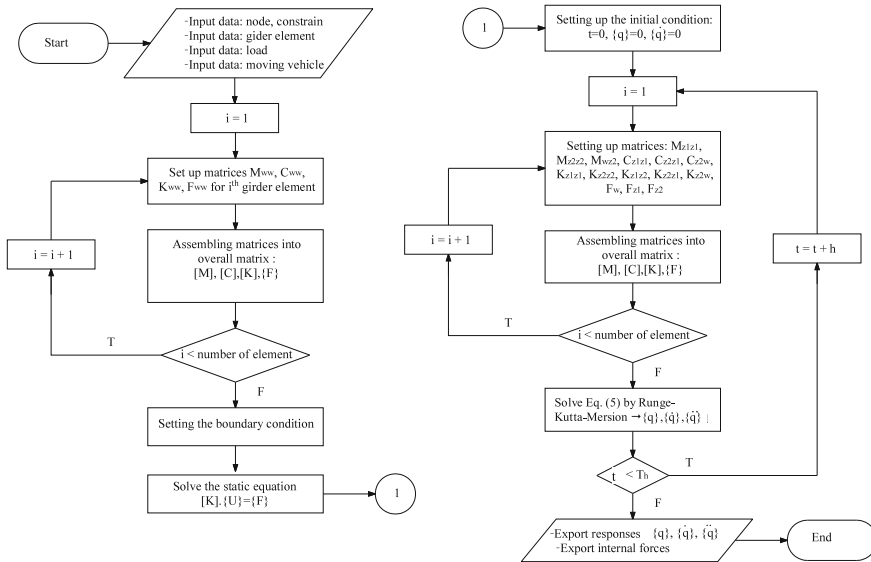


Fig. 3 Algorithm procedure in dynamic analysis vehicle-bridge interaction

$$F_{z1} = \begin{Bmatrix} -m_{11} \cdot g \\ \vdots \\ -m_{1i} \cdot g \\ \vdots \\ -m_{1n} \cdot g \end{Bmatrix}; \quad F_{z2} = \begin{Bmatrix} -m_{21} \cdot g \\ -m_{22} \cdot g \\ \dots \\ -m_{2i} \cdot g \\ -m_{2n} \cdot g \end{Bmatrix}_{n \times 1} \quad (17)$$

After assembling mass matrices, damping matrices, stiffness matrices, and forces vectors, the solution of Eq. (5) can be solved by using direct integration method, Runge-Kutta-Merson method (RKM) in time domain to obtain displacements, bending moment, and shear force of the bridge structure. The algorithm procedure in dynamic analysis vehicle-bridge interaction is described in Fig. 3.

3 Analysis Vibration of NguyenTriPhuong Bridge

3.1 Properties of Structural Bridge and Vehicle

NguyenTriPhuong Bridge is located in Danang city, Vietnam. The approaching spans of NguyenTriPhuong Bridge include three spans of super T concrete girder; the deck of girder is connected in the flexible joints between two span with 2.4 m length, shown in Fig. 1.

The cross section of the concrete girder and position of dumper truck is shown in Fig. 4. The three-axle vehicle used in the numerical simulation and full-scale field testing is FOTON dumper truck as shown in Fig. 5. The properties of super T concrete girder are collected from design documents of the bridge management unit; the properties of three-axle dumper truck FOTON are given by the manufactory company and checked on site. The parameters of super T concrete girder and dumper truck are listed in Table 1.

The cross section of the concrete girder and position of dumper truck is shown in Fig. 4. The three-axle vehicle used in the numerical simulation and full-scale field testing is FOTON dumper truck as shown in Fig. 5. The properties of super T concrete girder are collected from design documents of the bridge management unit; the properties of three-axle dumper truck FOTON are given by the manufactory company and checked on site. The parameters of super T concrete girder and dumper truck are listed in Table 1.

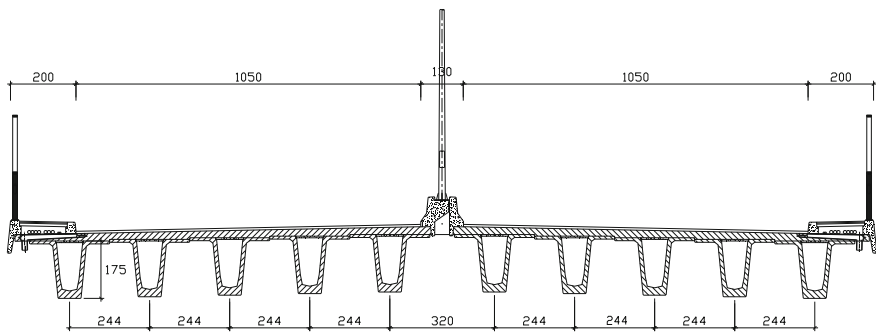


Fig. 4 Cross section of super T concrete girder

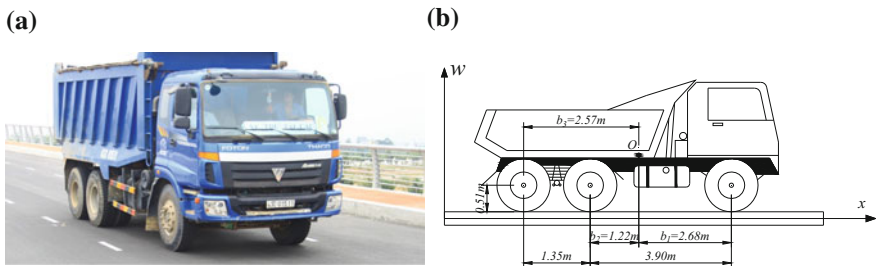


Fig. 5 The FOTON dumper truck: a picture of vehicle; b vehicle dimensional parameters

Table 1 Properties of super T concrete girder and dumper truck FOTON

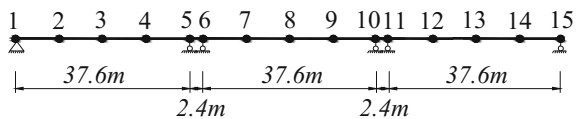
Item	Notation	Unit	Value
<i>Super T concrete girder</i>			
Length	L	m	37.6
Young's modulus	E	GPa	30
Density	ρ	kg/m ³	2500
Coefficient of internal friction	θ	–	0.027
Coefficient of external friction	β	–	0.01
Cross sectional area	A	m ²	1.21
Second moment of area	I	m ⁴	0.537
<i>Link slab (deck)</i>			
Height	h	m	0.2
Cross sectional area	A	m ²	0.488
Second moment of area	I	m ⁴	1.63×10^{-3}
<i>Dumper truck vehicle</i>			
Mass m_{11}	m_{11}	kg	5000
Mass m_{21}	m_{21}	kg	260
Mass m_{12}, m_{13}	m_{12}, m_{13}	kg	9000
Mass m_{22}, m_{23}	m_{22}, m_{23}	kg	870
Suspensions spring $k_{11}; k_{12}; k_{13}$	k_{1i}	N/m	2.6×10^6
Tires spring $k_{21}; k_{22}; k_{23}$	k_{2i}	N/m	3.8×10^6
Suspensions dashpot $d_{11}; d_{12}; d_{13}$	d_{1i}	Ns/m	4000
Tires dashpot $d_{21}; d_{22}; d_{23}$	d_{2i}	Ns/m	8000

3.2 Numerical Results

Using the finite element method, the bridge structure was discrete as Fig. 6. Setting vehicle velocity moving on the bridge is 10 (m/s) (36 km/h). Equation (10) is solved by the Runge–Kutta–Mersion method to obtain the static and dynamic responses of super T concrete girder, shown in Fig. 7.

From the time history of 1st span in Fig. 7, it can be seen that responses of 1st span decreased quickly when the dumper truck went over the 1st span. The cause for that issue is that bending stiffness of concrete link slab in the flexible joints is very smaller than bending stiffness of super T concrete girder.

Fig. 6 Schematic of discrete bridge structure



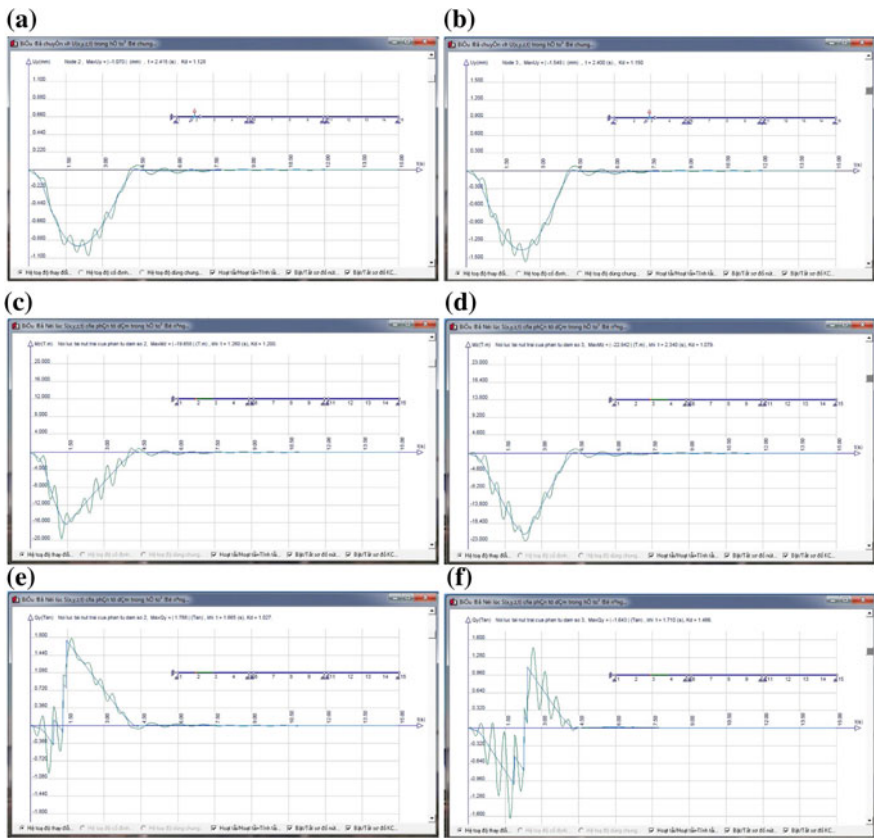


Fig. 7 Static and dynamic responses of 1st span: **a** displacement at $1/4$ of 1st span; **b** displacement at $1/2$ of 1st span; **c** bending moment at $1/4$ of 1st span; **d** bending moment at $1/2$ of 1st span; **e** shear force at $1/4$ of 1st span; **f** shear force at $1/2$ of 1st span

3.3 Field Measurement Results

In order to validate the numerical results, the full-scale field measurement of dynamic response of super T concrete girder was conducted at NguyenTriPhuong Bridge in Danang city, Vietnam. This section presents a measurement system and results obtained so far.

Since large vibration of super T concrete girder had been observed, displacement sensors (LVDT) were placed on $1/2$ of 1st span as Fig. 8.

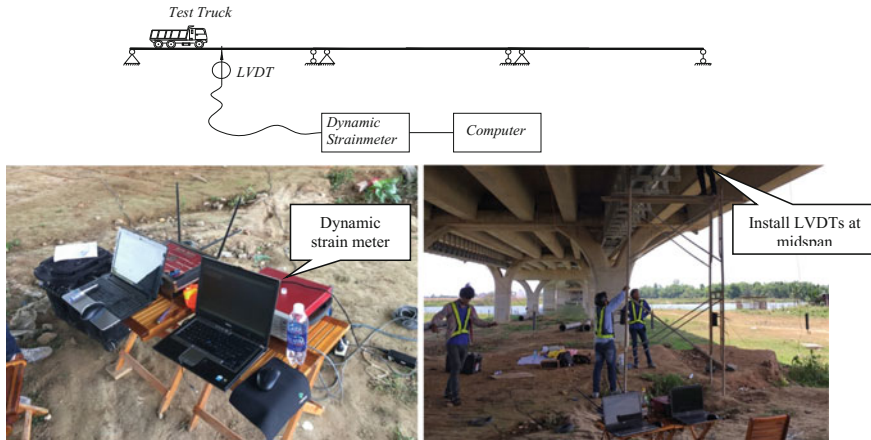


Fig. 8 Measurement system in NguyenTriPhuong bridge

Super T concrete girder vibration was measured after the girder was excited by a dumper truck with various velocities. Properties of super T concrete girder and dumper truck FOTON are listed in Table 1. Since traffic velocity has been limited by the bridge management company, the testing velocity of dumper truck was suggested 2.8, 5.6, 8.3, and 11.1 (m/s). For each velocity level of testing vehicle, dynamic displacement of super T concrete girder was recorded and compared with the numerical results, shown in Fig. 9.

From the time history of 1st midspan displacement in Fig. 9, it can be seen that the numerical results (FEM results) show quite good agreement with the full-scale experiment results on site. The maximum differences of dynamic displacement between FEM results and experiment results are 3.83, 4.77, 5.24, and 6.12%, in accordance with vehicle velocity 2.8, 5.6, 8.3, and 11.1 (m/s). Therefore, the algorithm and numerical model mentioned above are quite reliable. This numerical model is continuously used to investigate the influence of vehicle velocity on dynamic impact factor for displacement, bending moment, and shear force of super T concrete girder in the next section.

3.4 Numerical Investigation

Based on the validated numerical model with experimental results above, it carried out to investigate dynamic vehicle–bridge interaction for this numerical model with various vehicle velocities. Assume that vehicle velocity (FOTON dumper truck) changed in the range [1 ÷ 45] m/s. The other parameters of structural bridge and

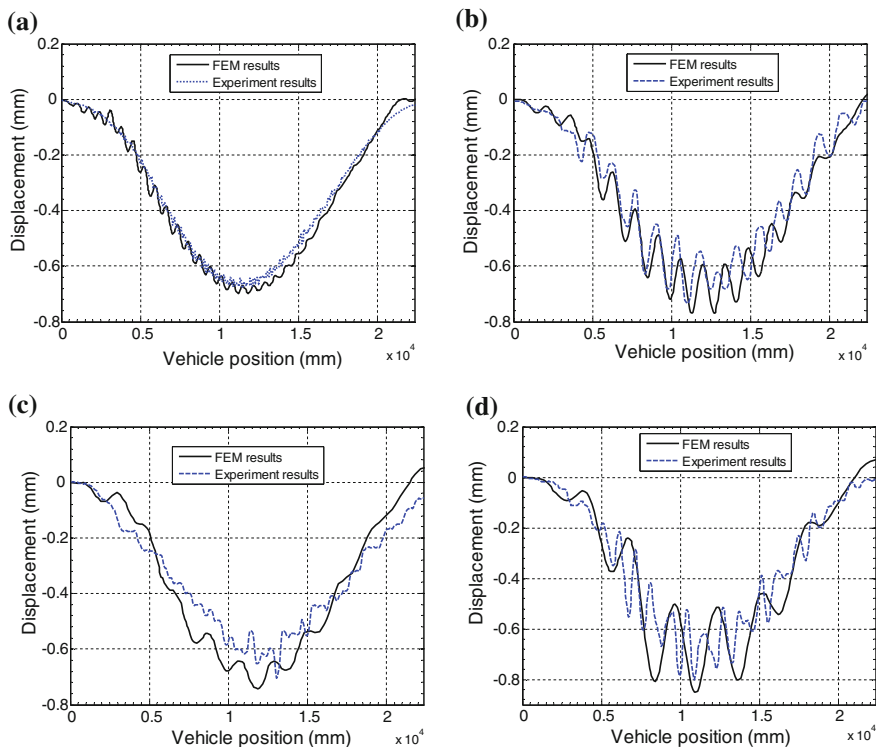


Fig. 9 Time history of displacement at 1st midspan: **a** $v = 2.8$ (m/s); **b** $v = 5.6$ (m/s); **c** $v = 8.3$ (m/s); **d** $v = 11.1$ (m/s)

dumper truck vehicle were given as Table 1. For each vehicle velocity level, the governing equation of vehicle–bridge interaction is solved by Runge–Kutta–Merson to obtain static and dynamic displacements, bending moment, and shear force output of super T concrete girder. From static and dynamic displacement, bending moment, and shear force, it can determine dynamic impact factor for displacement, bending moment, and shear force of super T concrete girder as in Eq. (1). The numerical results are shown in Fig. 10.

In the investigative range of vehicle velocity $v = [1 \div 45]$ m/s, the comparison of the average dynamic impact factors for displacement, bending moment, and shear force is described as in Fig. 11.

From the Fig. 11, it can be seen that the difference between $(1 + IM)$ for displacement and $(1 + IM)$ for bending moment has been 12.08%. Especially, the difference between $(1 + IM)$ for displacement and $(1 + IM)$ for shear force has reached 18.56%. These differences are significantly and should be considered in the practice of bridge design works [16, 17].

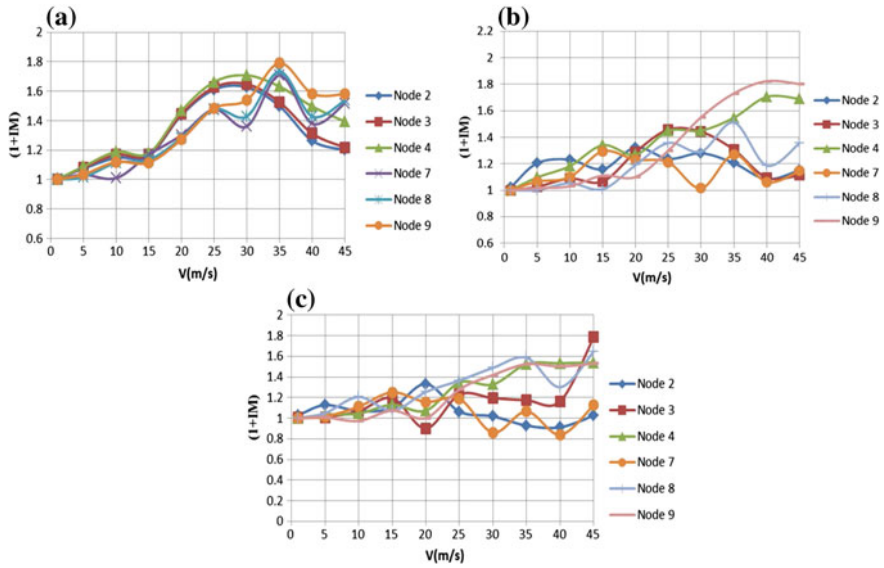


Fig. 10 Dynamic impact factors $(1 + IM)$ versus vehicle velocity due to dumper truck: **a** $(1 + IM)$ for displacement; **b** $(1 + IM)$ for bending moment; **c** $(1 + IM)$ for shear force

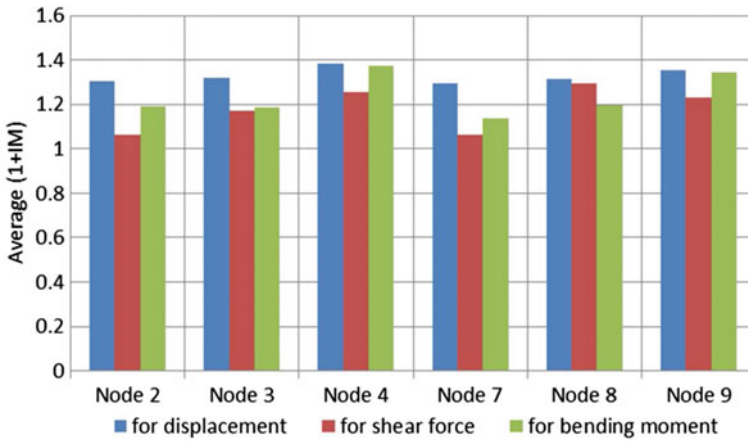


Fig. 11 Average dynamic impact factors for displacement, bending moment, and shear force

4 Conclusion

In this paper, the analysis of dynamic impact factors for displacement, bending moment, and shear force of a three-span super T concrete girder with link slab under a three-axle dumper truck vehicle is investigated by finite element method. In comparison with field measurement results, the FEM was verified. The numerical results showed that there are significant differences between IM for displacement, bending moment, and shear force. Especially, the difference between $(1 + IM)$ for displacement and $(1 + IM)$ for shear force has reached 18.56%. Therefore, the common use of only one of dynamic impact factor for both displacement and internal forces of structures in the bridge design code [16, 17] should be further consideration. In addition, the current outcomes can be good references for bridge engineers to have more information for safety design requirements and suitability with the actual operation of bridges.

References

1. Frýba L (1996) Dynamics of railway bridges. Thomas Telford, London
2. Willis R (1847) The effect produced by causing weights due to travel over elastic bars. Report of commissioners appointed to inquire into application of iron to railway structures, Appendix, H.M. Stationery Office, London
3. Paultre P, Chaallai O, Proulx J (1992) Bridge dynamics and dynamic amplification factors—a review of analytical and experimental findings. *Can J Civ Eng* 19:260–278
4. Huang D, Wang T-L, Shahawy M (1993) Impact studies of multigirder concrete bridges. *J Struct Eng* 119(8):2387–2402. [https://doi.org/10.1061/\(ASCE\)0733-9445](https://doi.org/10.1061/(ASCE)0733-9445)
5. Wang T-L, Huang D, Shahawy M (1994) Dynamic behavior of slant-legged rigid-frame highway bridge. *J Struct Eng* 120(3):885–902. [https://doi.org/10.1061/\(ASCE\)0733-9445](https://doi.org/10.1061/(ASCE)0733-9445)
6. Kwasniewski L, Li H, Wekezer J, Malachowski J (2006) Finite element analysis of vehicle-bridge interaction. *Finite Elem Anal Des* 42(11):950–959
7. Shi X (2006) Structural performance of approach slab and its effect on vehicle induced bridge dynamic response. Ph.D. Thesis, Department of Civil and Environmental Engineering, Louisiana State University, Baton Rouge, LA
8. Ashebo DB, Chan THT, Yu L (2007) Evaluation of dynamic loads on a skewbox girder continuous bridge part I: field test and modal analysis. *Eng Struct* 29(6):1052–1063
9. Au FTK, Cheng YS, Cheung YK (2001) Effects of random road surface roughness and long-term deflection of prestressed concrete girder and cable-stayed bridges on impact due to moving vehicles. *Comput Struct* 79(2001):853–872
10. Lombaert G, Conte JP (2012) Random vibration analysis of dynamic vehicle-bridge interaction due to road unevenness. *J Eng Mech* 2012(138):816–825
11. Nguyen XT, Tran VD (2014) A finite element model of vehicle—cable stayed bridge interaction considering braking and acceleration. In: The 2014 world congress on advances in civil, environmental, and materials research. Busan, Korea, p 109 (20p)
12. Nguyen XT (2014) Dynamic interaction between the two axle vehicle and continuous girder bridge with considering vehicle braking forces. *Vietnam J Mech* 36:49–60
13. Nguyen XT, Tran VD, Hoang ND (2017) A study on the dynamic interaction between three-axle vehicle and continuous girder bridge with consideration of braking effects. *J Constr Eng* 2017, Article ID 9293239, 12 p

14. Clough R, Penzien J (1995) Dynamics of structures, 3rd edn. Computers & Structures, Inc., Berkeley, CA94704, USA
15. Zienkiewicz OC, Taylor RL, Zhu JZ (2013) The finite element method: its basis and fundamentals, 7th edn. Butterworth-Heinemann
16. American Association of State Highway and Transportation Officials (AASHTO) (2012) LRFD Bridge design specifications. Washington (DC), USA
17. Vietnamese Specification for Bridge Design (2005) 22TCN 272-05

Stationary Random Vibration Analysis of Dynamic Vehicle-Bridge Interaction Due to Road Unevenness



T. Nguyen-Xuan, Y. Kuriyama and T. Nguyen-Duy

Abstract This article presents stationary random vibration analysis of dynamic vehicle-bridge interaction due to road unevenness based on the Finite element method and Monte-Carlo simulation method. The road unevenness are described by a zero-mean stationary Gaussian random process. The vehicle is a dumper truck with three axles. Each axle of vehicle is idealised as two mass dynamic system, in which a mass is supported by a spring and a dashpot. The structural bridges are simulated as bending beam elements. The finite element method is applied to established the overall model of vehicle-bridge interaction. Galerkin method and Green theory are used to discrete the motion equation of vehicle-bridge system in space domain. Solutions of the motion equations are solved by Runge-Kutta-Mersion method (RKM) in time domain. The numerical results are in good agreement field test results of the prestressed beam-slab at Nguyen-Tri-Phuong bridge, Danang city, Vietnam. Also, the effects of road surface condition on dynamic impact factor of bridge are investigated detail. The numerical results show that dynamic impact factor of bridge has increased significantly when road unevenness have changed from Grade A-road to Grade E-road according to ISO 8608:1995 [1] “Mechanical vibration—Road surface profiles—Reporting of measured data”.

Keywords Monte-Carlo simulation method · Finite element method
Road unevenness · Moving vehicles · Vehicle-bridge interaction

T. Nguyen-Xuan · T. Nguyen-Duy (✉)
Faculty of Road and Bridge Engineering,
University of Danang, University of Science and Technology, Da Nang, Vietnam
e-mail: ngduythao1978@yahoo.com

T. Nguyen-Xuan
e-mail: nguyensexuantoan2007@gmail.com

Y. Kuriyama
Research into Artifacts, Center for Engineering, The University of Tokyo, Tokyo, Japan
e-mail: kuriyama@race.u-tokyo.ac.jp

1 Introduction

Vehicle-bridge interaction has been a subject of significant research for a long time. The aim of these studies is to investigate the structural behaviour of bridge under moving vehicles, as well as the ride comfort of vehicles travelling a bridge. Dynamic vehicle-bridge interaction results in a increase or decrease of the bridge deformation, which is described by the dynamic impact factor (IM) or the dynamic amplification factor (DAF) or dynamic load allowance (DLA) that reflects how many times the constant load must be multiplied to cover additional dynamic effects, Frýba [2]. The dynamic IM plays a vital role in the practice of bridge design and condition assessment. Accurate evaluation of IMs will lead to safe and economical designs for new bridges and provide valuable information for condition assessment and management of existing bridges.

Honda et al. [3] derived the power spectral density (PSD) of road surface roughness on 56 highway bridges, measured using a surveyor's level. For each bridge, 84 lines at 10–20 cm intervals and 0.5 and 2.0 m from the centerline of the road were measured. The authors observed that the PSD of roadway roughness can be approximated by an exponential function, and proposed different functions for certain bridge structural systems. Palamas et al. [4], Coussy et al. [5] presented a theoretical study of the effects of surface road unevenness on the dynamic response of bridges under suspended moving loads. A single-degree-of-freedom system was used for the vehicle and a Rayleigh-Ritz method was used for the dynamic analysis. This study showed that in some cases, the DAF could be two to three times that recommended by current international design codes, suggesting that road unevenness could no longer be neglected. Inbanathan and Wieland [6] presented an analytical investigation on the dynamic response of a simply supported box girder bridge due to a moving vehicle. In particular, they considered the profile of the roadway using a response spectrum and 10 artificially generated time history loads for speeds of 19 and 38 km/h. The study of the response of a bridge due to a generated dynamic force was justified in view of the random nature of the problem. Some of the findings reported were the following: 1-The effect of vehicle mass on the bridge response is more significant for high speeds; 2-The maximum response is not affected by damping; 3-The stresses developed by a heavy vehicle moving over a rough surface at high speeds exceed those recommended by current bridge design codes. Hwang and Nowak [7] presented a procedure to calculate statistical parameters for dynamic loading of bridges, to be used in design codes. These parameters, based on surveys and tests, included vehicle mass, suspension system and tires, and roadway roughness, which was simulated by stochastic processes. This procedure was applied to steel and prestressed concrete girder bridges, for single and side-by-side vehicle configurations. Values of the DAF were computed using prismatic beam models for the bridges and step-by-step integrations. It was found that: 1-the DAF decreases with an increase in vehicle weight; 2- the DAF for two side-by-side vehicles is lower than that for a single vehicle; and 3- the dynamic load is generally uncorrelated with the static live load. But the vehicle model of

Hwang and Nowak didn't consider the dashpot of suspension system and tires. Au et al. [8] presented a numerical study of the effects of surface road unevenness and long-term deflection on the dynamic impact factor of prestressed concrete girder and cable-stayed bridges due to moving vehicles. The results showed that the effects of random road unevenness and the long-term deflection of concrete deck on bridge vary a lot at the sections closed to the bridge tower, with significant effects on the short cables. Lombaert and Conte [9] proposed the random vibration analysis of dynamic vehicle-bridge interaction due to road unevenness by an original frequency domain method. The road unevenness was modeled by the random nonstationary process. Due to the complexity of the problem, the authors presented only the results of simple supported beam model subjected to a moving concentrated load. Xuan-Toan Nguyen et al. [10, 11] and [12] analyzed the dynamic three-axle vehicle-bridge interaction considering the change of vehicle velocity through braking force by finite element method. The numerical results showed that the influence of braking force has effects significantly on dynamic impact factor of bridge. However, most of the previous research on dynamic interaction between the vehicle and simply supported bridge, very few studies have focused on the multi-span prestressed beam-slab bridge with link deck considering the random road unevenness effects. Additionally, the field test is needed in order to obtain a clearer understanding of the relationship between dynamic interaction for bridge types and vehicle models.

This study develops the FEM to analyze the stationary random dynamic interaction between three-axle dumper truck vehicle and two-span prestressed beam-slab bridge with link deck due to road unevenness. In addition, this research evaluates the effects of the road surface condition on dynamic impact factor of the prestressed beam-slab bridge. The road unevenness is simulated by a zero-mean stationary Gaussian random process. The bridge is modelled by finite element method. The dumper-truck has three axles. Each axle is idealised by two mass, in which a mass is supported by a spring and dashpot. The governing equation of random dynamic vehicle-bridge interaction is derived by means of dynamic balance principle. Galerkin method and Green theory are employed to discrete the governing equation in space domain. The solutions of equation are solved by Runge-Kutta-Mersion method. Monte-Carlo simulation is applied to generate the random road unevenness input. The numerical results are in good agreement field test results of two-span prestressed beam-slab at Nguyen-Tri-Phuong bridge in Danang city, Vietnam.

2 Vehicle and Bridge Model

Consider an Euler-Bernoulli beam subjected to a three-axle dumper truck vehicle. Assume that the body weight of vehicle and goods on the vehicle distribute to three axle m_{11} , m_{12} and m_{13} , respectively. The mass of three axles are m_{21} , m_{22} and m_{23} respectively. The dynamic interaction model between a three-axle vehicle and a girder element considering random road unevenness effects is described as in Fig. 1.

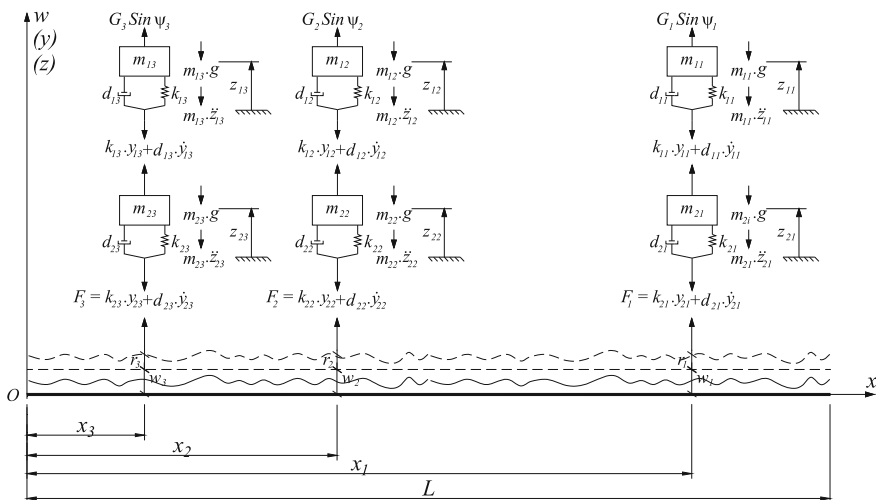


Fig. 1 Model of dynamic three-axle dumper truck vehicle—bridge interaction

where $w_i(x_i, t)$ is the vertical displacement of girder element at i th axle of vehicle; r_i is road unevenness at i th axle of vehicle; z_{1i} is the vertical displacement of chassis at i th axle of vehicle; z_{2i} is the vertical displacement of i th axle of vehicle; y_{1i} is the relative displacement between the chassis and i th axle; y_{2i} is the relative displacement between i th axle and girder element; $G_i \cdot \sin \psi_i$ is the engine excitation force at i th axle; k_{1i} and d_{1i} are the spring and dashpot of suspension at i th axle respectively; k_{2i} and d_{2i} are the spring and dashpot of tire at i th axle respectively; x_i is the coordinate of the i th axle of the vehicle at time t ($i = 1, 2, 3$).

Based on the model of dynamic vehicle-bridge interaction in Fig. 1 and using d’Alembert’s principle, the dynamic equilibrium of each mass m_{1i} , m_{2i} on the vertical axis can be written as follows:

$$m_{1i} \cdot \ddot{z}_{1i} + d_{1i} \cdot \dot{z}_{1i} - d_{1i} \cdot \dot{z}_{2i} + k_{1i} \cdot z_{1i} - k_{1i} \cdot z_{2i} = G_i \cdot \sin \psi_i - m_{1i} \cdot g \quad (1)$$

$$\begin{aligned} m_{2i} \cdot \ddot{z}_{2i} - d_{1i} \cdot \dot{z}_{1i} + (d_{1i} + d_{2i}) \cdot \dot{z}_{2i} - k_{1i} \cdot z_{1i} + (k_{1i} + k_{2i}) \cdot z_{2i} \\ = k_{2i}(w_i + r_i) + d_{2i} \cdot (\dot{w}_i + \dot{r}_i) - m_{2i} \cdot g \end{aligned} \quad (2)$$

where \dot{r}_i is the first derivation of road unevenness at i th axle of vehicle. Adding on the logic control function, Eqs. (1) and (2) can be rewritten as follows:

$$\begin{aligned} \xi_i(t) \cdot [m_{1i} \cdot \ddot{z}_{1i} + d_{1i} \cdot \dot{z}_{1i} - d_{1i} \cdot \dot{z}_{2i} + k_{1i} \cdot z_{1i} - k_{1i} \cdot z_{2i}] \\ = \xi_i(t) \cdot [G_i \cdot \sin \psi_i - m_{1i} \cdot g] \end{aligned} \quad (3)$$

$$\begin{aligned} \xi_i(t) \cdot [m_{2i} \cdot \ddot{z}_{2i} - d_{1i} \cdot \dot{z}_{1i} + (d_{1i} + d_{2i}) \cdot \dot{z}_{2i} - k_{1i} \cdot z_{1i} + (k_{1i} + k_{2i}) \cdot z_{2i}] \\ = \xi_i(t) \cdot [k_{2i}(w_i + r_i) + d_{2i} \cdot (\dot{w}_i + \dot{r}_i) - m_{2i} \cdot g] \end{aligned} \quad (4)$$

$$\xi_i(t) = \begin{cases} 1 & \text{if } t_i \leq t \leq t_i + T_i; \quad T_i = \frac{L}{v} \\ 0 & \text{if } t < t_i \quad \text{and} \quad t > t_i + T_i \end{cases} \quad (5)$$

From Fig. 1, the contact force between the i th axle and girder element is described by:

$$F_i = k_{2i} \cdot y_{2i} + d_{2i} \cdot \dot{y}_{2i} \quad (6)$$

The combined Eqs. (3)–(6), the contact force between the i th axle and girder element can be rewritten as follows:

$$p_i(x, z, t) = \xi_i(t) \cdot [G_i \cdot \sin \psi_i - (m_{1i} + m_{2i}) \cdot g - m_{1i} \cdot \ddot{z}_{1i} - m_{2i} \cdot \ddot{z}_{2i}] \cdot \delta(x - x_i) \quad (7)$$

where $\delta(x - x_i)$ is the Dirac delta function.

According to Ray [13], the governing equation for the flexure vibration of damped girder due to uniform loading $p(x, z, t)$ can be written as follow:

$$EJ \cdot \left(\frac{\partial^4 \omega}{\partial x^4} + \theta \frac{\partial^5 \omega}{\partial x^5 \cdot \partial t} \right) + \rho_m \cdot \frac{\partial^2 \omega}{\partial t^2} + \beta \cdot \frac{\partial \omega}{\partial t} = p(x, z, t) \quad (8)$$

$$p(x, z, t) = \sum_{i=1}^n \xi_i(t) \cdot [G_i \cdot \sin \psi_i - (m_{1i} + m_{2i}) \cdot g - m_{1i} \cdot \ddot{z}_{1i} - m_{2i} \cdot \ddot{z}_{2i}] \cdot \delta(x - x_i) \quad (9)$$

where EJ is the bending stiffness of girder element; θ and β are the coefficient of internal friction and external friction of girder element; ρ_m is the mass of girder per unit length; n is the number of axle ($n = 3$).

The Galerkin method and Green theory are applied to Eqs. (3), (4) and (8) transform into matrix form, and the differential equations of girder element can be written in a matrix form as follow:

$$[M_e] \cdot \{\ddot{q}\} + [C_e] \cdot \{\dot{q}\} + [K_e] \cdot \{q\} = \{f_e\} \quad (10)$$

where $\{q\}$, $\{\dot{q}\}$, $\{\ddot{q}\}$, $\{f_e\}$ are the complex acceleration vector, complex velocity vector, complex displacement vector, complex forces vector, respectively.

$$\{\ddot{q}\} = \begin{Bmatrix} \ddot{w} \\ \ddot{z}_1 \\ \ddot{z}_2 \end{Bmatrix}; \{\dot{q}\} = \begin{Bmatrix} \dot{w} \\ \dot{z}_1 \\ \dot{z}_2 \end{Bmatrix}; \{q\} = \begin{Bmatrix} w \\ z_1 \\ z_2 \end{Bmatrix}; \{f_e\} = \begin{Bmatrix} F_w \\ F_{z1} \\ F_{z2} \end{Bmatrix}; \{w\} = \begin{Bmatrix} w_{y1} \\ \varphi_1 \\ w_{y2} \\ \varphi_2 \end{Bmatrix} \quad (11)$$

In which w_{y1} , φ_1 are the vertical displacement and rotation angle of the left end of girder element, respectively; w_{y2} , φ_2 are the vertical displacement and rotation angle of the right end of element, respectively;

$[M_e]$, $[C_e]$ and $[K_e]$ are the mass matrix, damping matrix and stiffness matrix, respectively

$$\begin{aligned}
 [M_e] &= \begin{bmatrix} M_{ww} & M_{wz1} & M_{wz2} \\ 0 & M_{z1z1} & 0 \\ 0 & 0 & M_{z2z2} \end{bmatrix} [C_e] = \begin{bmatrix} C_{ww} & 0 & 0 \\ 0 & C_{z1z1} & C_{z1z2} \\ C_{z2w} & C_{z2z1} & C_{z2z2} \end{bmatrix} [K_e] \\
 &= \begin{bmatrix} K_{ww} & 0 & 0 \\ 0 & K_{z1z1} & K_{z1z2} \\ K_{z2w} & K_{z2z1} & K_{z2z2} \end{bmatrix} \tag{12}
 \end{aligned}$$

where $[M_{ww}]$, $[C_{ww}]$ and $[K_{ww}]$ are mass, damping and stiffness matrices of the girder elements, respectively. They can be found in Zienkiewicz [14]

$$\begin{aligned}
 M_{z1z1} &= \begin{bmatrix} m_{11} & & & & & \\ & m_{12} & & 0 & & \\ & & \dots & & & \\ & 0 & & m_{1i} & & \\ & & & & m_{1n} & \\ & & & & & \dots \end{bmatrix}_{(n \times n)} M_{z2z2} \\
 &= \begin{bmatrix} m_{21} & & & & & \\ & m_{22} & & 0 & & \\ & & \dots & & & \\ & 0 & & m_{2i} & & \\ & & & & \dots & \\ & & & & & m_{2n} \end{bmatrix}_{(n \times n)} \tag{13}
 \end{aligned}$$

$$M_{wz1} = P.M_{z1z1}; M_{wz2} = P.M_{z2z2}; P = \begin{bmatrix} P_{11} & P_{12} & \dots & P_{1i} & \dots & P_{1n} \\ P_{21} & P_{22} & \dots & P_{2i} & \dots & P_{2n} \\ P_{31} & P_{32} & \dots & P_{3i} & \dots & P_{3n} \\ P_{41} & P_{42} & \dots & P_{4i} & \dots & P_{4n} \end{bmatrix}_{(n \times n)} \tag{14}$$

$$P_i = \begin{Bmatrix} P_{1i} \\ P_{2i} \\ P_{3i} \\ P_{4i} \end{Bmatrix} = \frac{\xi_i(t)}{L^3} \begin{Bmatrix} (L + 2x_i) \cdot (L - x_i)^2 \\ L \cdot x_i \cdot (L - x_i)^2 \\ x_i^2 \cdot (3L - 2x_i) \\ L \cdot x_i^2 \cdot (x_i - L) \end{Bmatrix} \tag{15}$$

$$\begin{aligned}
 C_{z_1z_1} &= \begin{bmatrix} d_{11} & & & & & \\ & d_{12} & & 0 & & \\ & & \cdots & & & \\ & & & d_{1i} & & \\ & 0 & & & \cdots & \\ & & & & & d_{1n} \end{bmatrix}_{(n \times n)} C_{z_2} \\
 &= \begin{bmatrix} d_{21} & & & & & \\ & d_{22} & & 0 & & \\ & & \cdots & & & \\ & & & d_{2i} & & \\ & 0 & & & \cdots & \\ & & & & & d_{2n} \end{bmatrix}_{(n \times n)} \quad (16)
 \end{aligned}$$

$$C_{z_1z_2} = C_{z_2z_1} = -C_{z_1z_1}; C_{z_2z_2} = C_{z_1z_1} + C_{z_2}; C_{z_2w} = (-N_i \cdot C_{z_2})^T \quad (17)$$

$$N_i = \left[\begin{array}{cccccc} N_{11} & N_{12} & \cdots & N_{1i} & \cdots & N_{1n} \\ N_{21} & N_{22} & \cdots & N_{2i} & \cdots & N_{2n} \\ N_{31} & N_{32} & \cdots & N_{3i} & \cdots & N_{3n} \\ N_{41} & N_{42} & \cdots & N_{4i} & \cdots & N_{4n} \end{array} \right]_{(n \times n)} ; \left. \begin{array}{l} N_{1i} = \frac{1}{L^3} \cdot (L^3 - 3Lx_i^2 + 2x_i^3) \\ N_{2i} = \frac{1}{L^2} \cdot (L^2x_i - 2Lx_i^2 + x_i^3) \\ N_{3i} = \frac{1}{L^3} \cdot (3Lx_i^2 - 2x_i^3) \\ N_{4i} = \frac{1}{L^2} \cdot (x_i^3 - Lx_i^2) \end{array} \right\} \quad (18)$$

$$\begin{aligned}
 K_{z_1z_1} &= \begin{bmatrix} k_{11} & & & & & \\ & k_{12} & & 0 & & \\ & & \cdots & & & \\ & & & k_{1i} & & \\ & 0 & & & \cdots & \\ & & & & & k_{1n} \end{bmatrix}_{(n \times n)} K_{z_2} \\
 &= \begin{bmatrix} k_{21} & & & & & \\ & k_{22} & & 0 & & \\ & & \cdots & & & \\ & & & k_{2i} & & \\ & 0 & & & \cdots & \\ & & & & & k_{2n} \end{bmatrix}_{(n \times n)} \quad (19)
 \end{aligned}$$

$$K_{z_1z_2} = K_{z_2z_1} = -K_{z_1z_1}; K_{z_2z_2} = K_{z_1z_1} + K_{z_2}; K_{z_2w} = -(N_i \cdot K_{z_2})^T - (\dot{N}_i \cdot C_{z_2})^T \quad (20)$$

$$F_w = \sum_{i=1}^n [G_i \cdot \sin \psi_i - (m_{1i} + m_{2i})g] \cdot P_i \quad (21)$$

$$F_{z1} = \begin{Bmatrix} G_1 \cdot \sin \Psi_1 - m_{11} \cdot g \\ \vdots \\ G_i \cdot \sin \Psi_i - m_{1i} \cdot g \\ \vdots \\ G_N \cdot \sin \Psi_N - m_{1n} \cdot g \end{Bmatrix}; F_{z2} = \begin{Bmatrix} -m_{21} \cdot g + k_{21} \cdot r_1 + d_{21} \cdot \dot{r}_1 \\ -m_{22} \cdot g + k_{22} \cdot r_2 + d_{22} \cdot \dot{r}_2 \\ \dots \\ -m_{2i} \cdot g + k_{2i} \cdot r_i + d_{2i} \cdot \dot{r}_i \\ -m_{2n} \cdot g + k_{2n} \cdot r_n + d_{2n} \cdot \dot{r}_n \end{Bmatrix}_{n \times 1} \quad (22)$$

3 Simulation of Stationary Random of Road Unevenness

Assume that the PSD (Power spectral density) roughness represented by the angular frequency of a pavement section is known as $S_r(\omega)$. According to Shinozuka [15], Honda [3] and Sun [16] the temporal random excitation formed by a road unevenness can be expressed by means of:

$$r(t) = \sum_{k=1}^M A_k \cos(\omega_k t + \Phi_k) \quad (23)$$

where M is a positive integer and Φ_k is an independent random variable with uniform distribution at range $[0, 2\pi]$. Also, the discrete frequency ω_k is given by:

$$\omega_k = \omega_1 + \left(k - \frac{1}{2}\right) \Delta\omega \quad (24)$$

In which frequency interval $\Delta\omega = (\omega_m - \omega_l)/M$ and $[\omega_l, \omega_m]$ is the range of frequency where $S_r(\omega)$ has significant values. The amplitude A_k in Eq. (23) is represented by:

$$A_k = \sqrt{2S_r(\omega_k)\Delta\omega} = \sqrt{2S_r(\Omega_k)\Delta\Omega} \quad (25)$$

In which $S_r(\Omega_k) = v \cdot S_r(\omega)$ is the PSD roughness in terms of wave number, Ω , which represents spatial frequency; v is vehicle velocity. From ISO 8608:1995 [1], the PSD roughness in terms of wave number Ω are described by:

$$S_r(\Omega) = S_r(\Omega_0) \left(\frac{\Omega}{\Omega_0}\right)^{-\gamma} \quad (26)$$

where the fix-datum wave number Ω_0 is set as $1/2\pi$ cycle/m. The measurement shows that various values exist for exponential γ and the so-called roughness coefficient $S_r(\Omega_0)$, ranging from 1.5 to 3.0 for γ and from $2 \times 10^{-6} \text{ m}^3/\text{cycle}$ to $8192 \times 10^{-6} \text{ m}^3/\text{cycle}$ for $S_r(\Omega_0)$. The values of roughness coefficient $S_r(\Omega_0)$ are classified by ISO

Table 1 Road roughness values classified by ISO 8608:1995

Road class	Roughness coefficient		
	$S_r(\Omega_o)$ [$10^{-6} \text{ m}^2/(\text{cycle/m})$]		
	Lower limit	Geometric mean	Upper limit
A (very good)	–	16	32
B (good)	32	64	128
C (average)	128	256	512
D (poor)	512	1024	2048
E (very poor)	2048	4096	8192

8608:1995 in Table 1. These different values reflect the components of wavelength in elevation fluctuation and surface condition. Equation (26) is used as PSD road unevenness later on to generate random road profile.

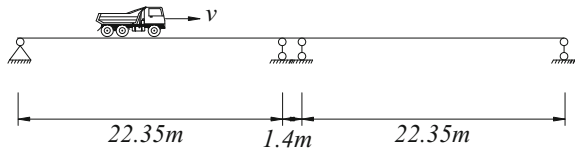
4 Analysis Random Vibration of Slab-Beam at Nguyentriphuong Bridge

4.1 Properties of Structural Bridge and Vehicle

Nguyen-Tri-Phuong bridge located in Danang city, Vietnam. The approach bridge of Nguyen-Tri-Phuong Bridge, which is a two-span slab beam prestressed concrete. The deck of slab beam is connected in the flexible joint between two spans, shown in Fig. 2. The cross section of the prestressed concrete slab beam and position of vehicle is shown in Fig. 3. The three-axle vehicle used in the numerical simulation and the field test is FOTON dumper truck as shown in Fig. 4.

The properties of slab beam are collected from design documents of the bridge management unit; the properties of three-axle dumper truck FOTON are given by the manufactory company and checked on site. The parameters of slab beam and dumper truck are listed in Table 2.

Fig. 2 Model of two-span slab beam and three-axle dumper truck vehicle



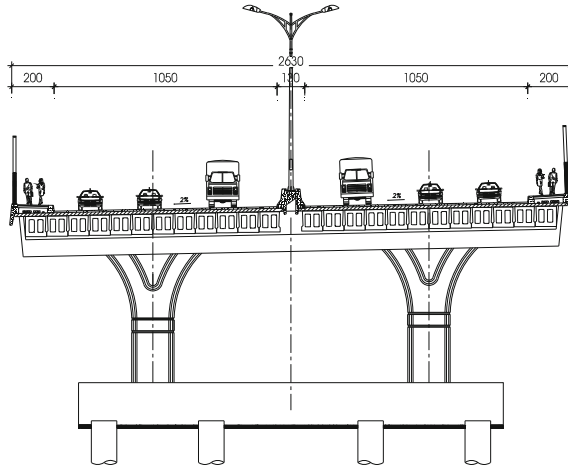


Fig. 3 Cross section of slab beam

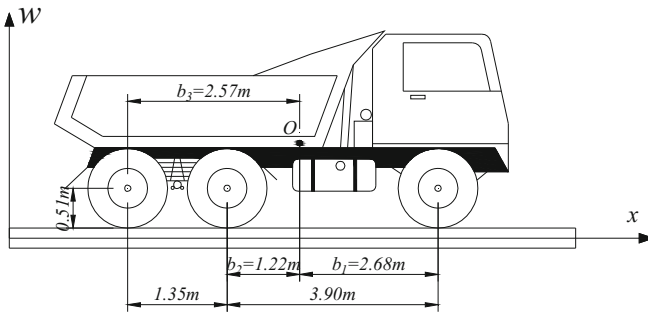


Fig. 4 The FOTON dumper truck

Table 2 Properties of slab beam and dumper truck FOTON

Item	Notation	Unit	Value
<i>Slab beam prestressed concrete</i>			
Lenght	L	m	22.35
Young's modulus	E	Gpa	36
Density	ρ	kg/m ³	2500
Coefficient of internal friction	θ	–	0.027
Coefficient of external friction	β	–	0.01
Cross sectional área	A	m ²	0.723
Second moment of area	I	m ⁴	0.097
<i>Link slab (deck)</i>			
Height	h	m	0.15
Cross sectional area	A	m ²	0.15
Second moment of area	I	m ⁴	0.28×10^{-3}
<i>Dumper truck vehicle</i>			
Mass m_{11}	m_{11}	kg	5200
Mass m_{21}	m_{21}	kg	260
Mass m_{12}, m_{13}	m_{12}, m_{13}	kg	8900
Mass m_{22}, m_{23}	m_{22}, m_{23}	kg	870
Suspensions spring $k_{11}; k_{12}; k_{13}$	k_{1i}	N/m	2.6×10^6
Tires spring $k_{21}; k_{22}; k_{23}$	k_{2i}	N/m	3.8×10^6
Suspensions dashpot $d_{11}; d_{12}; d_{13}$	d_{1i}	Ns/m	4000
Tires dashpot $d_{21}; d_{22}; d_{23}$	d_{2i}	Ns/m	8000

4.2 Numerical Results

Base on the survey at site, assume that the road surface condition of Nguyen-Tri-Phuong bridge is Grade C-road (ISO 8608:1995): roughness coefficient $S_r(\Omega_0) = 256 \times 10^{-6} \text{ m}^3/\text{cycle}$; exponential $\gamma = 2$; $M = 1000$; the range of spatial frequency (wave number) $\Omega_k = [0.011 \div 2.83] \text{ cycle/m}$. Monte-Carlo simulation method is applied to generate road unevenness profiles. Some of random road unevenness profiles are described as follows: (Fig. 5).

Using the finite element method, the bridge structure was discrete as Fig. 6. The deck of slab beam prestressed concrete are connected in the flexible joint with 1.4 m of length. Setting vehicle velocity moving on the bridge is 10 m/s. For each road unevenness input, Eq. 10 is solved by the Runge-Kutta-Merison method to obtain the static and dynamic displacements of slab beam, shown in Fig. 7.

From the time history of 1st span displacements in Fig. 7. It can be seen that displacements of 1st span decreased quickly when the dumper truck went over the 1st span. The cause for that issue is that bending stiffness of concrete link slab in the flexible joint is very smaller than bending stiffness of slab beam prestressed concrete.

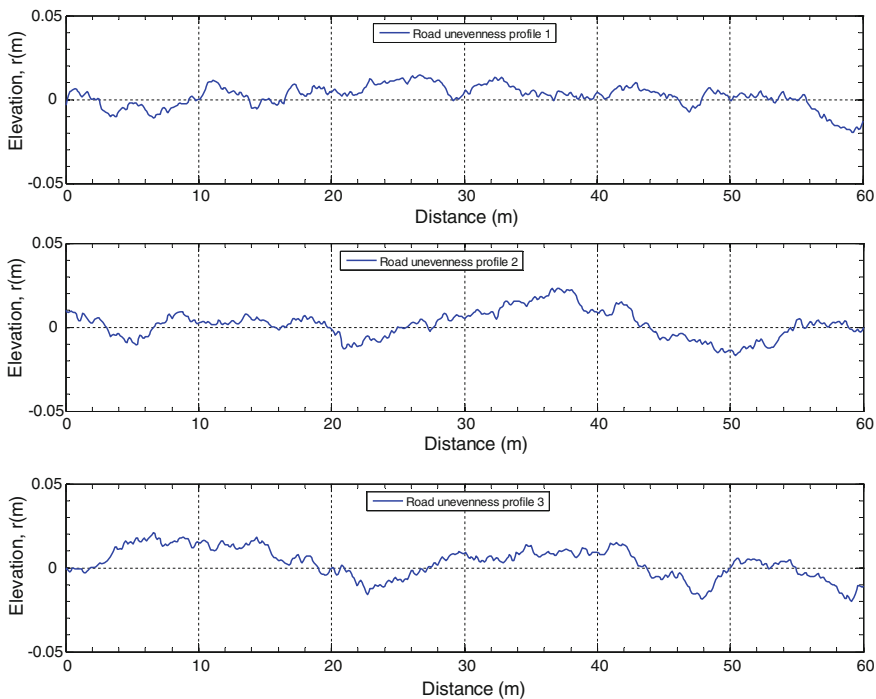


Fig. 5 Typical random road unevenness profiles

Fig. 6 Schematic of discrete bridge structure

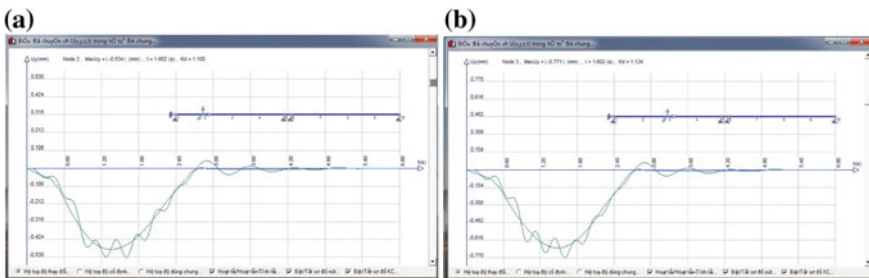
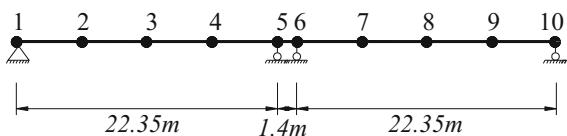


Fig. 7 Static and dynamic displacement of 1st span: **a** $\frac{1}{4}$ of 1st span; **b** $\frac{1}{2}$ of 1st span

4.3 Field Measurement Results

In order to validate the numerical results, field measurement of dynamic response of slab beam prestressed concrete was conducted at Nguyen-Tri-Phuong bridge in Danang city, Vietnam. This section presents a measurement system and results obtained so far.

Since large vibration of slab beam prestressed concrete had been observed, displacement sensors (LVDT) were placed on $\frac{1}{2}$ of 1st span as Fig. 8.

Slab beam vibration was measured after the slab beam was excited by a dumper truck with various velocity. Properties of slab beam prestressed concrete and dumper truck FOTON are listed in Table 2. Since traffic velocity have been limited by the bridge management company, the testing velocity of dumper truck was suggested 10, 20, 30 and 40 km/h. For each velocity level of testing vehicle, dynamic displacement of slab beam prestressed concrete was recorded and compared with the numerical results, shown in Fig. 9.

From the time history of 1st midspan displacement in Fig. 9, it can be seen that the numerical results (FEM results) show quite good agreement with the experiment results at the field. The difference of maximum dynamic displacement between them are 3.83%; 4.77%, 5.24% and 6.12%, respectively with the moving vehicle velocity 10 km/h, 20 km/h, 30 km/h and 40 km/h. Therefore, the algorithm and numerical model mentioned above are quite reliable. Therefore this numerical model are used continuously to investigate the influence of the road surface condition on dynamic impact factor of slab beam prestressed concrete in the next section.

4.4 Numerical Investigation

Base on the validated numerical model with experiment results above, it carried out to investigate dynamic vehicle-bridge interaction for this numerical model with

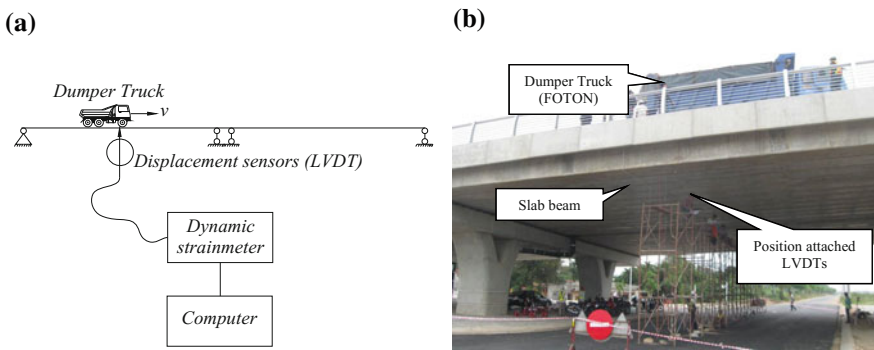


Fig. 8 Measurement system in Nguyen-Tri-Phuong bridge. **a** diagram of installing system; **b** measurement system at site

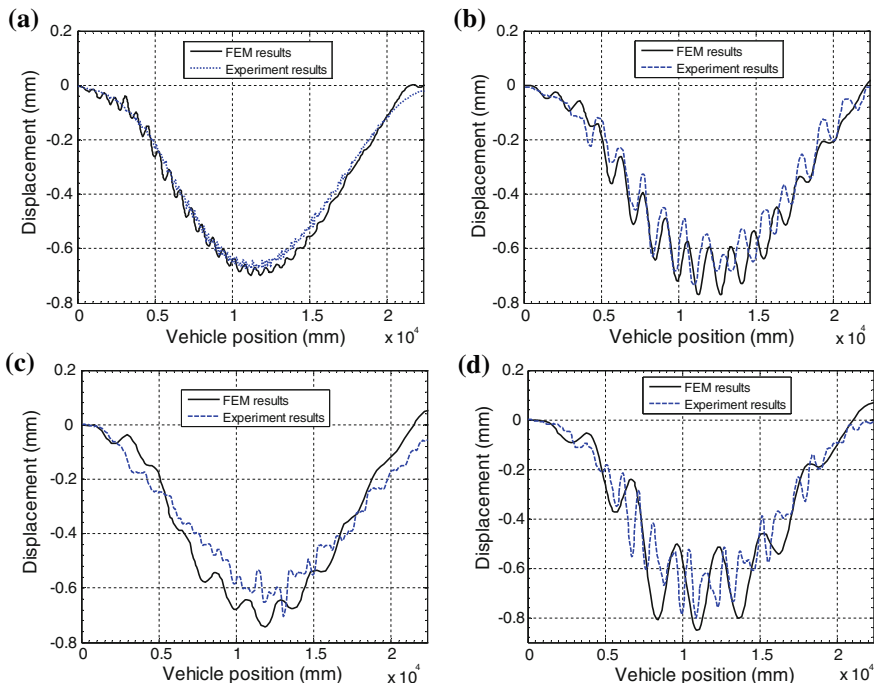


Fig. 9 Time history of displacement at 1st midspan: **a** $v = 10$ km/h; **b** $v = 20$ km/h; **c** $v = 30$ km/h; **d** $v = 40$ km/h

various road surface condition. Assume that the roughness coefficient changed in the range, $S_r(\Omega_0) = [0, 32, 128, 512, 2048, 8192] \times 10^{-6} \text{ m}^3/\text{cycle}$, corresponding to the road surface condition: ideal smooth, Grade A, B, C, D and E (ISO 8608:1995). The velocity of dumper truck was 10 m/s. The other parameters of structural bridge and dumper truck vehicle was given as Table 2. For each the road surface condition, Monte-Carlo simulation method is applied to generate 100 road unevenness profiles. With each road profile input, the governing equation of vehicle-bridge interaction is solved to obtain static and dynamic displacements output of slab beam prestressed concrete. From static and dynamic displacement, it can determine dynamic impact factor of slab beam prestressed concrete as shown in Eq. (27):

$$(1 + IM)_x^j = \frac{R_D^j(x)}{R_s^j(x)} \tag{27}$$

where $R_D^j(x)$ is the dynamic displacement of slab beam prestressed concrete at position x due to dumper truck moving on j th road unevenness profile; $R_s^j(x)$ is the static displacement of slab beam prestressed concrete at position x due to dumper truck moving on j th road unevenness profile.

After analyzing with a series of road profiles input, it can obtain a series of dynamic impact factor output which are also random process as shown in Fig. 10. The statistical characteristics of the dynamic impact factor (IM) at 1st midspan are described in Table 3.

Base on statistical characteristics of IM in Table 3, the relationship between the mean value of IM and the road unevenness condition can be established in Fig. 11.

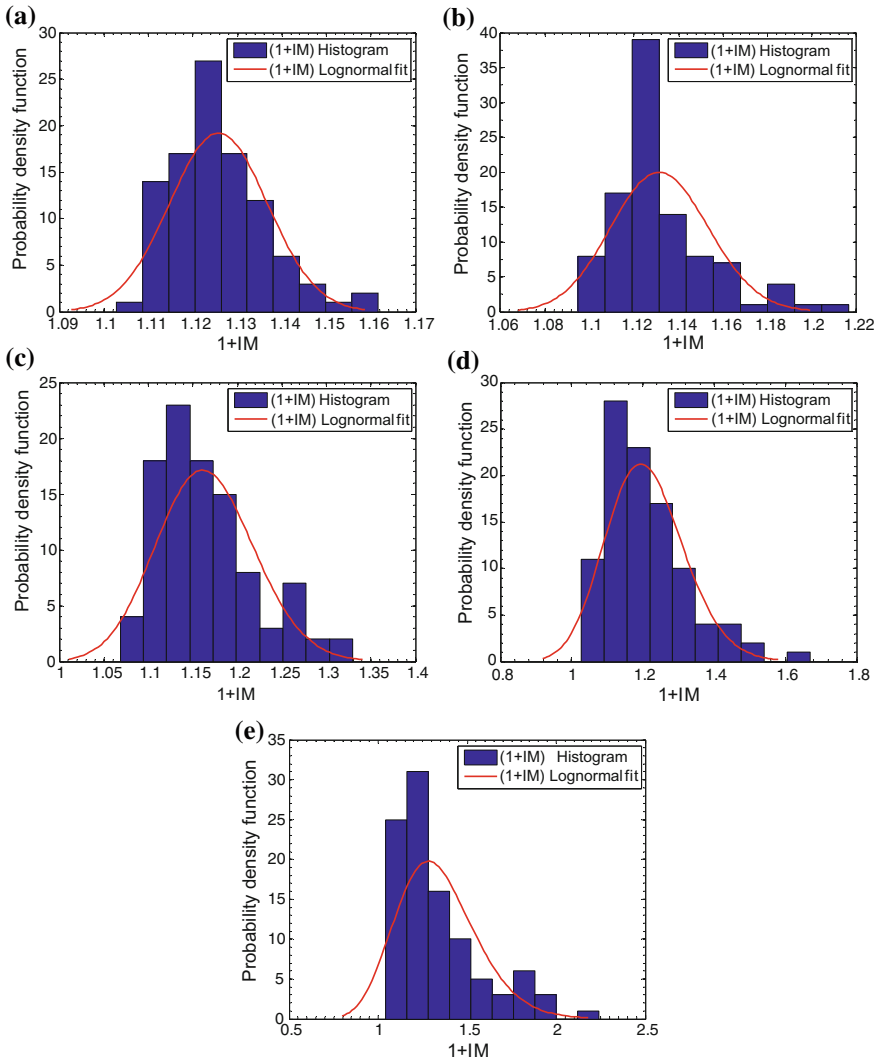


Fig. 10 Dynamic impact factor at 1st midspan due to dumper truck: **a** grade A-road; **b** grade B-road; **c** grade C-road; **d** grade D-road; **e** grade E-road

Table 3 Statistical characteristics of dynamic impact factor at 1st midspan

Items	Dynamic impact factor (1 + IM) $S_r(\Omega_0) \times 10^{-6} \text{ m}^3/\text{cycle}$					
	0	32	128	512	2048	8192
Mean	1.120	1.126	1.134	1.175	1.249	1.488
Max	–	1.159	1.199	1.340	1.579	2.180
Min	–	1.093	1.068	1.011	0.918	0.796
Standard deviation	–	0.019	0.038	0.096	0.194	0.405

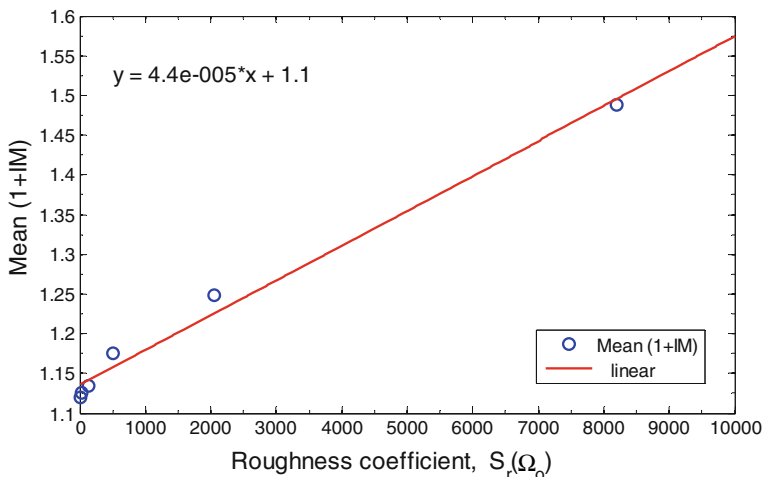


Fig. 11 Mean value of IM versus the roughness coefficient

In the Fig. 11, the correlation equation between the mean value of IM and road surface condition are also found out, in which x is the roughness coefficient.

From the investigation results in Fig. 11, it can be seen that when the road surface condition changes to be grade A-road, grade B-road, grade C-road the mean value of IM increases 0.54%, 1.25% and 4.91%, respectively. Specially, the mean value of IM reaches 11.52% and 32.85%, respectively, while the road surface condition changes to be grade D-road and grade E-road. This increase in dynamic impact factors are quite large and exceed those recommended by current bridge design codes as AASHTO [17] and Vietnamese Specification for Bridge Design [18]. Therefore, it is necessary to consider the influence of road surface condition on analyzing dynamic response of structural bridge, especially bridges have passed long time in operation and the pavement have been damaged as well as seriously downgraded.

5 Conclusion

In this paper, the analysis of stationary random dynamic interaction between three-axle dumper truck vehicle and two-span slab beam prestressed concrete with link slab due to road unevenness is investigated by means of finite element method and Monte-Carlo simulation method. The road unevenness are described by a zero-mean stationary Gaussian random process. The bridge is modeled by finite element method. The dumper-truck has three axles. Each axle is idealised by two mass, in which a mass is supported by a spring and dashpot. The governing equation of random dynamic vehicle-bridge interaction is derived by means of dynamic balance principle. Galerkin method and Green theory are employed to discretize the governing equation in space domain. The solutions of governing equation are solved by Runge-Kutta-Merson method in time domain. Monte-Carlo simulation is applied to generate the random road unevenness input. The numerical results are in good agreement test results at Nguyen-Tri-Phuong bridge in Danang city, Vietnam. In addition, this research evaluates the effects of the road surface condition on dynamic impact factor of slab beam prestressed concrete. The numerical results showed that the road surface condition has significantly effects on dynamic impact factor of slab beam prestressed concrete. Specially, the mean value of IM reaches 32.85%, respectively, while the road surface condition changes to be grade E-road. This value of dynamic impact factors are quite large and exceed those recommended by current bridge design codes. Therefore, it is necessary to consider the influence of road surface condition on analyzing dynamic response of structural bridge subjected to moving vehicles, especially bridges have passed long time in operation and the pavement have been damaged as well as seriously downgraded.

References

1. ISO 8608:(1995) Mechanical vibration—Road surface profiles—Reporting of measured data issued by the International Organization for Standardization (ISO)
2. Frýba L (1996) Dynamics of railway bridges. Thomas Telford, London
3. Honda H, Kajikawa Y, Kobori T (1982) Spectral of road surface roughness on bridges. ASCE Struct Div 108(9):1956–1966
4. Palamas J, Coussy O, Bamberger Y (1985) Effects of surface irregularities upon the dynamic response of bridges under suspended moving loads. J Sound Vib 99(2):235–245
5. Coussy O, Said M, Van Hoore JP (1989) The influence of random surface irregularities on the dynamic response of bridges under suspended moving loads. J Sound Vib 130(2):313–320
6. Inbanathan MJ, Wieland M (1987) Bridge vibrations due to vehicle moving over rough surface. ASCE J Struct Eng 113(9):1994–2008
7. Hwang ES, Nowak AS (1991) Simulation of dynamic load for bridges. ASCE J Struct Eng 117(5):1413–1434
8. Au FTK, Cheng YS, Cheung YK (2001) Effects of random road surface roughness and long-term deflection of prestressed concrete girder and cable-stayed bridges on impact due to moving vehicles. Comput Struct 79(2001):853–872

9. Lombaert Geert, Conte Joel P (2012) Random vibration analysis of dynamic vehicle-bridge interaction due to road unevenness. *J Eng Mech* 2012(138):816–825
10. Toan XN, Duc VT (2014) A finite element model of vehicle—cable stayed bridge interaction considering braking and acceleration. In: *Proceedings the 2014 world congress on advances in civil, environmental, and materials research, Busan, Korea*, p 109 (20p)
11. Toan XN (2014) Dynamic interaction between the two axle vehicle and continuous girder bridge with considering vehicle braking forces. *Vietnam J Mech* 36:49–60
12. Nguyen XT, Tran VD, Hoang ND (2017) A study on the dynamic interaction between three-axle vehicle and continuous girder bridge with consideration of braking effects. *J Constr Eng* 2017:12, Article ID 9293239
13. Ray WC, Joseph P (1995) *Dynamics of structures*, 3rd edn. Computers & Structures, Berkeley, California
14. Zienkiewicz OC, Taylor RL, Zhu JZ (2013) *The finite element method: its basis and fundamentals*, 7th edn. Butterworth-Heinemann
15. Shinozuka M (1972) Digital simulation of random processes and its applications. *J Sound Vib* 25:111–128
16. Sun L (2003) Simulation of pavement roughness and IRI based on power spectral density. *Math Comput Simul* 61:77–88
17. AASHTO LRFD (2012) *Bridge design specifications*, AASHTO, Washington, DC, USA
18. Vietnamese specification for bridge design (2005) 22TCN 272-05

Dynamic Analysis of Beams on Two-Parameter Viscoelastic Pasternak Foundation Subjected to the Moving Load and Considering Effects of Beam Roughness



T. Tran-Quoc, H. Nguyen-Trong and T. Khong-Trong

Abstract In this paper, improved moving element method (IMEM) is intended to analyze the dynamic response of the beam resting on the two-parameter viscoelastic Pasternak foundation subjected to the moving load and considering effects of beam roughness. Beams are modeled by moving elements, while the load is fixed. The differential equation of motion of the structural system is established based on the principle of virtual public balance and solved by means of numerical integration based on the Newmark algorithm. The characteristic parameters of the foundation and the loads are investigated in order to analyze the dynamic response of the beam such as the second parameter of foundation, the roughness of beam, the velocity and acceleration of moving load.

Keywords Moving element method · Beam · Foundation · Dynamic Roughness amplitude · Roughness wavelength · Moving load

1 Introduction

Beam and plate structures are applied widely in the construction field nowadays. The topic of the structural beam on the soil–foundation interaction is much attracted and interested by many foreign and Vietnamese scientists. Majority of constructions for building and traffic infrastructures are built up on the soil–foundation interaction, so the scope of this application is wide. The moving load on structure is also

T. Tran-Quoc · H. Nguyen-Trong (✉) · T. Khong-Trong (✉)
Faculty of Civil Engineering, HUTECH University, Ho Chi Minh, Vietnam
e-mail: tronghieu221287@gmail.com

T. Khong-Trong
e-mail: kt.toan@hutech.edu.vn

T. Tran-Quoc
e-mail: quachtinhxd3012@gmail.com

represented by many researchers by different variety of types such as moving force, moving mass, various moving forces, moving vehicles. The foundation alone when analyzing the behavior of the structure which is described very complicated the same as the one-parameter foundation model such as Winkler [1] or multiparameter foundation models of Filonenko-Borodich [2], Hentényi [3], Pasternak [4], Reissner [5]. The typical characteristics of these models are that the elastic layer (the first parameter) that is illustrated based on the elastic Winkler foundation, with the stiffness of elastic foundation layer which is represented by the non-mass elastic springs; in respect to the multiparameter models, the second parameter is presented by the stress layer elements, beams or bending plates or shear layers without the mass of connection with the surface of springs on Winkler foundation model in order to describe the continuous interaction of foundation. Therefore, a more realistic model is needed for soil foundation under the loads of moving mass. Because of its wide and realistic application, this issue is concerned deeply by many researchers such as Chang-Yong and Yang [6], and they have analyzed the infinite Euler–Bernoulli beam resting on Pasternak foundation subjected to moving load which has constant velocity obtained by Fourier transformation technique to solve the problem. Kumari et al. [7] have investigated an infinite Euler–Bernoulli beam on Pasternak foundation; the beam is put placed on a concentrated mass which is equal to the constant motion, and the velocity is equal to beam's parameters.

Recently, many models of structures resting on viscoelastic and Pasternak foundation have been developed. Luong-Van et al. [8] and Phung-Van et al. [9] analyzed dynamics response of composite plates resting on viscoelastic foundation. Phung-Van et al. [10] analyzed dynamics response of Mindlin plates on viscoelastic foundation subjected to a moving sprung vehicle. Nguyen-Thoi et al. [11] analyzed the dynamics response of composite plates on the Pasternak foundation subjected to moving mass.

Lou and Au [12] have studied the response of Euler–Bernoulli beam under moving mass vehicles by employing a finite element method (FEM). FEM has been used widely to solve many complicated problems, but encountered issues when the mass moves to the margin of the elements and also from one element to another, while vector of moving mass must be updated at every time step. So as to make good those shortcomings, Koh et al. [13] have proposed to put a moving coordinate to solve the proposed moving mass of railway track. This method is called moving element method (MEM). In this method, the railway is considered as an infinite Euler–Bernoulli resting on beam on Winkler foundation and the train is simplified by a “mass-spring-dashpot” system. Tran et al. [14] have employed MEM to study the dynamic response of express railway under inconstant speed of moving mass. Ang et al. [15] have studied a calculation to employ MEM to examine the dynamic response of the rail on viscoelastic foundation with moving mass. Ang and Dai [16] analyzed the reaction of the high-speed railway on foundation which has inconstant stiffness, and the author employed the moving element method to have analytical solutions for the response of the train. Ang et al. [17] have used MEM to research the dynamic response of the railway system. The railway model as a mass spring system which includes train body, cross section and wheels. Recently, Tran et al. [18] also

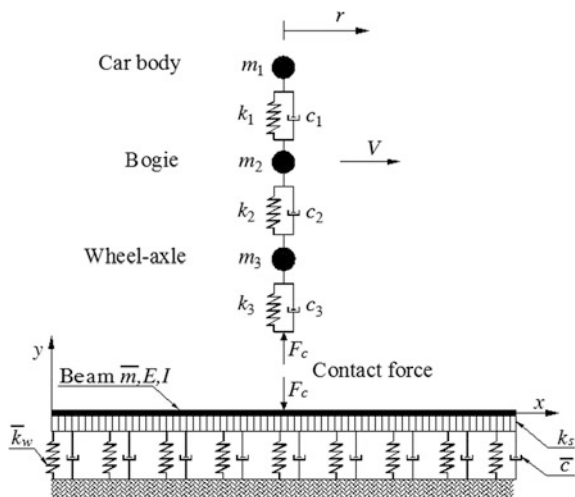
utilized the moving element method to analyze the dynamics of the express railway. In which the railway track is modeled as based on Euler–Bernoulli beam on the elastic two-parameter, the impacts of reducing velocity process and the roughness levels of railway track are also investigated. MEM has a lot of advantages such as the load would never approach the margin because the limited elements system always moves, and the moving load would not have to move from this element to another, so it avoids updating the mass vector. This method enables the limited elements with different lengths, and each interaction distance can be divided more effective. However, the weak point of MEM is that must be re-updated the stiffness matrix and dashpot matrix at every time step. It resulted in increasing the volume of calculation, prolonging the time of analysis, and wasting the resources.

Therefore, this paper introduces one new method, that is, improved moving element (IMEM) to analyze the dynamic response of the beam resting on viscoelastic two-parameter Pasternak foundation which is under moving mass and with the consideration of beam surface. The mass matrices, the stiffness matrices, and dashpot matrices of the moving elements are also represented in details later on. All results obtained will be the helpful documents for studying and designing the structural beams placed on moving loads in reality.

2 Theoretical Basis

Investigating an infinite Euler–Bernoulli beam with elastic module E , moment of inertia I , and mass per unit length of the rail beam \bar{m} , beam is on a viscoelastic foundation comprising of dashpots \bar{c} , vertical springs \bar{k}_w , cross section k_s . Figure 1 shows the beam model, foundation, and load that are applied in this research.

Fig. 1 Train–track model



According to the coordinates in Fig. 1, the general equation of the car model Do and Luong [19] can be expressed mathematically as follows

$$m_1\ddot{u}_1 + c_1(\dot{u}_1 - \dot{u}_2) + k_1(u_1 - u_2) = -m_1g \tag{1}$$

$$m_2\ddot{u}_2 + c_2(\dot{u}_2 - \dot{u}_3) - c_1(\dot{u}_1 - \dot{u}_2) + k_2(u_2 - u_3) - k_1(u_1 - u_2) = -m_2g \tag{2}$$

$$m_3\ddot{u}_3 - k_2(u_2 - u_3) - c_2(\dot{u}_2 - \dot{u}_3) = -m_3g + F_c \tag{3}$$

in which:

$m_1, m_2, m_3; c_1, c_2, c_3; k_1, k_2, k_3$ in turn are mass, dashpots of the car, vertical springs, and wheels;
 $u_1, \dot{u}_1, \ddot{u}_1; u_2, \dot{u}_2, \ddot{u}_2; u_3, \dot{u}_3, \ddot{u}_3$ in turn vertical displacements, velocity, car body acceleration, and wheel and axle;
 g gravitational acceleration;
 F_c the contact force between wheels and beam, produced by the non-flat of the beam or the roughness of the beam.

The contact force F_c (with the roughness at the contact point between the moving load and the beam) is defined according to Koh et al. [13] as follows:

$$F_c = c_3(\dot{u}_d - \dot{u}_3) + k_3(u_d - u_3) + F_t \tag{4}$$

where:

$F_t = c_3\dot{y}_t + k_3y_t$ the track force, produced by the roughness of the beam;
 u_d denotes the vertical displacement at the contact point of the beam;
 u_3 denotes the vertical displacement of the wheel and axle;
 y_t denotes the magnitude of the track irregularity at the contact point, and according to Koh et al. [13], the track irregularity profile can be written in terms of a sinusoidal function as follows:

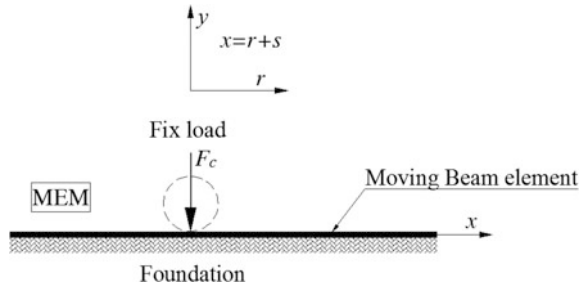
$$y_t = a_t \sin \frac{2\pi S}{\lambda_t} \tag{5}$$

where:

a_t, λ_t denotes the amplitude and wavelength of the track irregularity, respectively;
 S denotes the displacement of the object.

In the moving element method, Koh et al. [13] use x - y coordinates where x -axis is the beam course. The moving r - y coordinates whose origin is attached to the contact force as in Fig. 2. Therefore, this coordinates move along with the velocity V as a moving load.

Fig. 2 Coordinates of MEM



The relationship between two axes of coordinates is demonstrated as follows:

$$\begin{cases} x = r + s \\ y = y \end{cases} \tag{6}$$

where: x = fixed axis; r = movable axis; s = displacement; $V(a,t)$ = velocity function; t = moving time; a = acceleration.

The connection between the derivative operators of the coordinates when the load moves with various velocities is as follows:

$$\frac{\partial^4 w(x, t)}{\partial x^4} = \frac{\partial^4 w^*(r, t)}{\partial r^4} \tag{7}$$

$$\frac{\partial^2 w(x, t)}{\partial x^2} = \frac{\partial^2 w^*(r, t)}{\partial r^2} \tag{8}$$

$$\frac{\partial w(x, t)}{\partial t} = \frac{\partial w^*(r, t)}{\partial t} \frac{\partial t}{\partial t} + \frac{\partial w^*(r, t)}{\partial r} \frac{\partial r}{\partial t} = \frac{\partial w^*(r, t)}{\partial t} - V \frac{\partial w^*(r, t)}{\partial r} \tag{9}$$

$$\frac{\partial^2 w(x, t)}{\partial t^2} = \frac{\partial^2 w^*(r, t)}{\partial t^2} - a \frac{\partial w^*(r, t)}{\partial r} \frac{\partial r}{\partial t} + V^2 \frac{\partial^2 w^*(r, t)}{\partial r^2} - 2V \frac{\partial^2 w^*(r, t)}{\partial r \partial t} \tag{10}$$

where $w(x, t)$ = transverse deflection of the beam in the x - y axial coordinates; $w^*(r, t)$ = deflection of the beam in r - y coordinates.

By applying principle of virtual work and using displacement functions N , we can write \mathbf{M}^e , \mathbf{C}^e , \mathbf{K}^e as generalized mass, damping and stiffness matrices of the beam as follows:

$$\mathbf{M}^e = \bar{m} \int_0^l \mathbf{N}^T \mathbf{N} dr \tag{11}$$

$$\mathbf{C}^e = \bar{c} \int_0^l \mathbf{N}^T \mathbf{N} dr - \mathbf{F}_1^e \tag{12}$$

$$\mathbf{K}^e = EI \int_0^{l^e} (\mathbf{N}_{,rr})^T \mathbf{N}_{,rr} dr + \bar{k}_w \int_0^{l^e} \mathbf{N}^T \mathbf{N} dr - k_s \int_0^{l^e} \mathbf{N}^T \mathbf{N}_{,rr} dr - \mathbf{F}_2^e \quad (13)$$

$$\mathbf{F}_1^e = 2\bar{m}V \int_0^{l^e} \mathbf{N}^T \mathbf{N}_{,r} dr \quad (14)$$

$$\mathbf{F}_2^e = [\bar{m}a + \bar{c}V] \int_0^{l^e} \mathbf{N}^T \mathbf{N}_{,r} dr - \bar{m}V^2 \int_0^{l^e} \mathbf{N}^T \mathbf{N}_{,rr} dr \quad (15)$$

$$\mathbf{P} = \int_0^{l^e} F_c \mathbf{N}^T dr \quad (16)$$

with $(\cdot)_r$ and $(\cdot)_{rr}$ in turn are first derivative and second derivative of r .

To elements of the beam, the Hermitian interpolation N is written as follows:

$$\mathbf{N}_1^e = \frac{1}{(l^e)^3} [2r^3 - 3r^2l^e + (l^e)^3] \quad (17)$$

$$\mathbf{N}_2^e = \frac{1}{(l^e)^3} [r^3l^e - 2r^2(l^e)^2 + r(l^e)^3] \quad (18)$$

$$\mathbf{N}_3^e = \frac{1}{(l^e)^3} [-2r^3 + 3r^2l^e] \quad (19)$$

$$\mathbf{N}_4^e = \frac{1}{(l^e)^3} [r^3l^e - r^2(l^e)^2] \quad (20)$$

Based on finite element method and using numeral degree of freedom technique, respectively, to matrices of the general coordinates' elements, the moving equation of the whole beam model on the foundation is written as follows:

$$\mathbf{M}\ddot{\mathbf{z}} + (\mathbf{C} - \mathbf{F}_1)\dot{\mathbf{z}} + (\mathbf{K} - \mathbf{F}_2)\mathbf{z} = \mathbf{P} \quad (21)$$

where:

\mathbf{M} , \mathbf{C} , \mathbf{K} , \mathbf{P} , respectively, are global mass, damping and stiffness matrices, and the global load vector;

F_1, F_2 denote those elements which depend on time; F_1 and F_2 are not forces but have the force unit so they can be considered to be pseudo-force

Equation (21) is the main differential equation of the traditional MEM; in Eq. (21), we can see the left side is comprised of elements which change over time, and those elements are the pseudo-force F_1 and F_2 matrices. Therefore, when solving the problem we need to update the global mass, damping and stiffness matrices and this prolongs the processing time.

To fix this limitation of the traditional MEM, we like to move the pseudo-forces from the left side of Eq. (21) to the right side. This idea is called IMEM. After the moving, Eq. (21) is written as follows:

$$M\ddot{z} + C\dot{z} + Kz = P + F_1\dot{z} + F_2z \tag{22}$$

Solving the differential motion, Eq. (22) is put to act upon the help of computer which is based on Newmark algorithm. This algorithm is a calculation program written by MATLAB language, and the reliability as well as the calculation method of the program are put to compare to the results of other authors which are available in the reference.

3 Equation, Figure, and Table

3.1 Verifying the Calculation Program

In this part, the article examines some numerical examples to verify the correctness and the reliability of the MATLAB program. The results are compared to those of other authors.

Here is the verification of the high-speed train moving on beam with hanging mass which is used by Koh et al. [13] Fig. 1. The parameters of the train, the beam, and the foundation are demonstrated in Tables 1 and 2.

In the first example, the displacement of the beam while the train is moving on the beam with constant velocity, without consideration of the second foundation parameter affection (velocity $V = 20$ m/s, roughness amplitude margin $a_t = 0.5$ mm and roughness wavelength $\lambda_t = 0.5$ m) (Fig. 3).

Table 1 Parameters for vehicle

Car Body		Bogie		Wheel and axle	
m_1	3500 kg	m_2	250 kg	m_3	350 kg
k_1	1.41×10^5 N/m	k_2	1.26×10^6 N/m	k_3	8×10^9 N/m
c_1	8.87×10^3 Ns/m	c_2	7.1×10^3 Ns/m	c_3	6.7×10^5 Ns/m

Table 2 Parameters for beam and foundation

Beam		Foundation	
\bar{m}	60 kg/m	\bar{k}_w	1×10^7 N/m ²
E	2×10^{11} N/m ²	c	4900 Ns/m ²
I	3.06×10^{-5} m ⁴		
L	50 m		

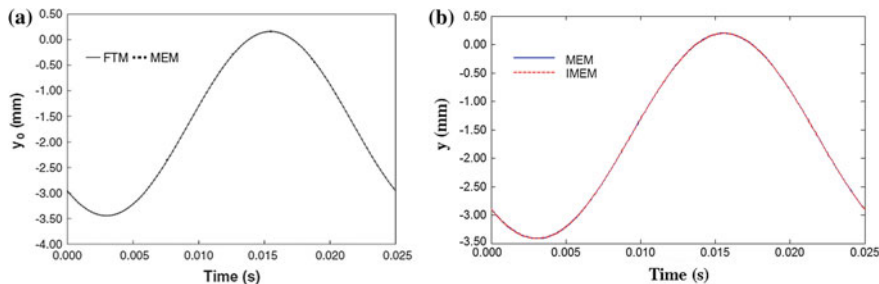


Fig. 3 Beam displacement at the interaction point **a** Koh et al. [13], **b** Article

In the next verification, the displacement of the beam when the train moves on the beam with constant velocity, without consideration of the second foundation parameter affection (first velocity $V = 0$ m/s, then moving with constant acceleration $a_{max} = 10$ m/s², after 2 s it reaches the velocity $V_{max} = 20$ m/s, then it moves with constant deceleration $a_{min} = -10$ m/s², and it stops after 2 s. The total analyzing time is $t = 6$ s, without consideration of foundation roughness amplitude) (Fig. 4).

From these surveyed results, we compare them to those of other authors and it shows that the results from the article are well-matched with others which quote in the references. It proves the calculation program is reliability. Thence, we have the groundwork to continue to analyze the affection of foundation parameters, mass model, the roughness of the beam surface on moving beam response.

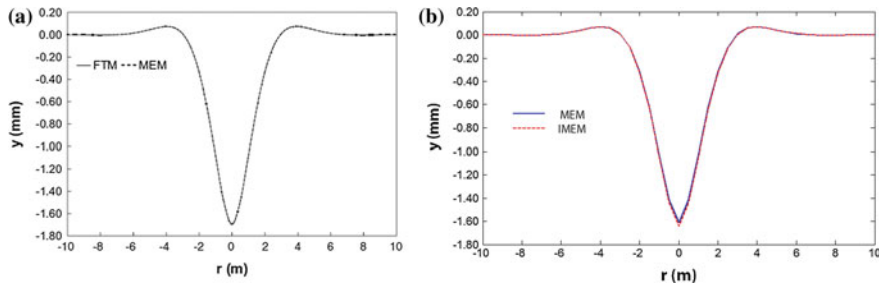


Fig. 4 Beam displacement at the interaction point **a** Koh et al. [13], **b** Article

3.2 Numerical Survey Result

The parameters of over hanging moving mass, beam and foundation of the problem which is showed in Tables 1 and 2. In case 1 and case 2, the second parameter of the foundation changes in turn to $k_s = 0 \text{ N}$; $6 \times 10^5 \text{ N}$; $8 \times 10^6 \text{ N}$; $16 \times 10^6 \text{ N}$ according to Feng and Cook [20] and the load moves on the beam with constant velocity $V = 90 \text{ m/s}$.

- **Case 1:** This problem keeps the roughness wavelength value $\lambda_t = 0.5 \text{ m}$. Changing the roughness amplitude on beam a_t in turn to 0; 0.8; 1.6; 2.4; 3.2; and 4 mm.
- **Case 2:** This problem keeps the roughness amplitude on beam value $a_t = 1.6 \text{ mm}$. Changing the roughness wavelength λ_t in turn to 0.5; 1.0; 1.5; 2.0; 2.5; 3.0; 3.5; and 4.0 m.

Figure 5 indicates the analyzed results of the dynamic response of the beam in case 1. The result shows that when increasing the second parameter of the foundation, then the value of the beam displacement also decreases; the more value of k_s increases, the more value of the beam displacement decreases. Therefore, the second parameter of the foundation is significant; it reduces dynamic response of beam system.

Also in Fig. 5, the analysis shows that when increasing the roughness amplitude on beam, the value of the beam displacement also increases. The more value of a_t increases, the more value of the beam displacement increases. This proves that the beam displacement depends on the roughness amplitude very large on beam. When the roughness amplitude on beam increases, then the beam displacement also increases likely linear with it.

Figure 6 shows the analyzed moving response in case 2. The analysis of Fig. 6 shows that the roughness wavelength on beam λ_t is small between 0.5 and 2 m; if increasing the wavelength, the beam displacement also increases. Nevertheless,

Fig. 5 Maximum displacement of the beam when keeping the value of the roughness wavelength $\lambda_t = 0.5 \text{ m}$, changing the second parameter of the foundation k_s and the roughness amplitude

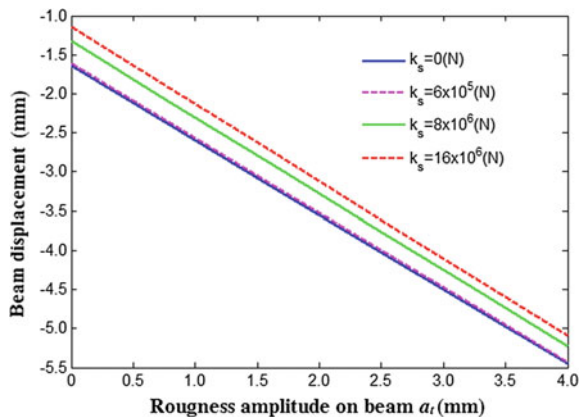
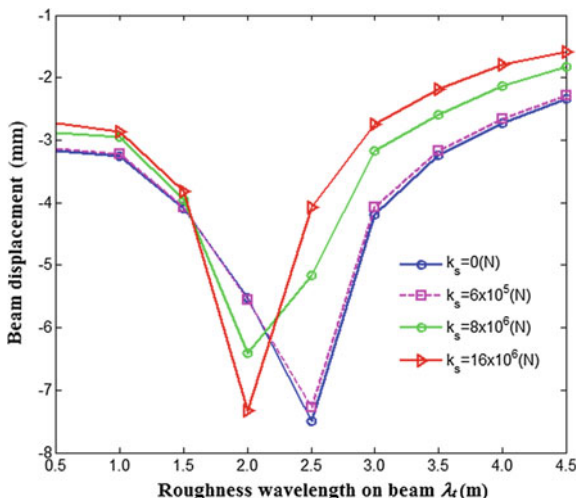


Fig. 6 Maximum beam displacement when keeping the value of the roughness amplitude on beam $a_r = 1.6$ mm, changing the second foundation parameter and the roughness wavelength



when the value of the roughness wavelength increases to a certain point, specifically in case 2, when the wavelength increases over 2.5 m then the beam displacement decreases and is asymptotic to a certain point. When the roughness wavelength on beam λ_r is between 2.0 and 2.5 m, then the beam displacement value increases and reaches the maximum point. Specifically when $k_s = 6 \times 10^6$ N, then the maximum displacement is -7.2728 mm (Table 3) with the wavelength $\lambda_r = 2.5$ m.

- **Case 3:** This problem keeps the value of the second foundation parameter $k_s = 6 \times 10^5$ (N) and the roughness amplitude on beam $a_r = 0.5$ mm. Changing the roughness wavelength λ_r in turn to 0.5; 1.0; 1.5; 2.0; 2.5; 3.0; 3.5; 4.0 m and velocity V changes in turn to 5; 10; 15; 20; 25; 30; 35; 40; 45; 50; 55; 60; 65; 70; 75; 80; 85; 90; 95; 100; 105; 110; 115; 120 (m/s).

By observing Fig. 7, we can tell that to each value of the roughness wavelength, when the velocity increases to a certain point, then the beam displacement reaches the maximum value. When the beam displacement reaches the maximum value and still velocity keeps going up, the beam displacement decreases and is asymptotic to a certain point. On the other hand, when increasing the roughness wavelength on beam, the velocity makes the displacement reach the maximum value and the beam displacement also goes up correspondently.

From the result of Table 4, we can see that to make the beam displacement reach the maximum value, then the ratio of the roughness wavelength and velocity has to be a certain value. This ratio of the roughness wavelength and velocity $T = \lambda_r/V$ is also the beam oscillation. The appearance of the maximum displacement at wavelength from 1.5 to 2.0 m is the consequence of resonance. In a way, the exciting frequency $f_c = 1/T$ will be nearly to the natural frequency $f_n = \omega/2\pi$ (Table 5).

Table 3 Maximum beam displacement when keeping the value of the roughness amplitude on beam $a_r = 1.6$ mm, changing the second foundation parameter and the roughness wavelength (mm)

k_s (N)	Roughness wavelength on beam λ_r (m)									
	0.5	1.0	1.5	2.0	2.5	3.0	3.5	4.0	4.5	
0	-3.1675	-3.2607	-4.0924	-5.5265	-7.4960	-4.1917	-3.2315	-2.7274	-2.3422	
6×10^5	-3.1407	-3.2303	-4.0812	-5.5627	-7.2728	-4.0760	-3.1701	-2.6689	-2.2891	
8×10^6	-2.8864	-2.9422	-3.9535	-6.4122	-5.1626	-3.1793	-2.5893	-2.1353	-1.8190	
16×10^6	-2.7215	-2.8611	-3.8147	-7.3314	-4.0752	-2.7435	-2.1871	-1.7839	-1.5846	

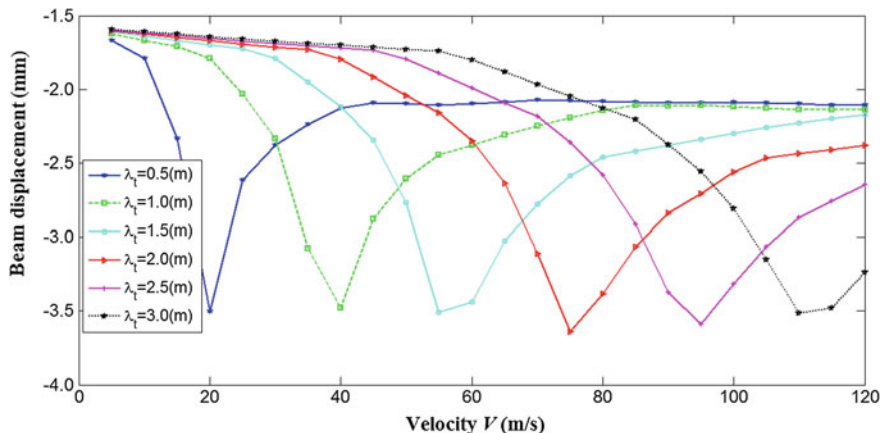


Fig. 7 Maximum beam displacement when keeping the roughness amplitude on beam $a_t = 0.5$ mm, changing velocity and the roughness wavelength

Table 4 Period and frequency of beam (mm)

Roughness wavelength on beam λ_t (m)	Maximum displacement (mm)	Velocity V (m/s)	Period $T = \lambda/V$ (s)	Exciting frequency $f_c = 1/T$ (Hz)
0.5	-3.50179	20	0.0250	40.00
1.0	-3.47803	40	0.0250	40.00
1.5	-3.50986	55	0.0273	36.67
2.0	-3.63765	75	0.0267	37.50
2.5	-3.58805	95	0.0263	38.00
3.0	-3.51318	110	0.0273	36.67

Table 5 Natural frequency of the system in the first five modes

Natural frequency (Hz)	Mode 1	Mode 2	Mode 3	Mode 4	Mode 5
$f_n = \omega/2\pi$	0.955	11.6	38.1	65	65

- **Case 4:** This math remains the roughness wavelength intact on beam $\lambda_t = 0.5$ m, and the second foundation parameter is 6×10^5 N. Changing the roughness amplitude on beam a_t in turn to 0; 0.8; 1.6; 2.4; 3.2; and 4 mm.
- **Case 5:** This math remains the roughness amplitude on beam $a_t = 1.6$ mm, and the second foundation parameter is 6×10^5 N. Changing of the roughness wavelength on beam λ_t in turn to 0.5; 1.0; 1.5; 2.0; 2.5; 3.0; 3.5; and 4.0 m.

In case 4 and case 5, the velocity varies as in Fig. 8. The velocity is divided into three phases (phase 1: increasing; phase 2: constant velocity; phase 3: decreasing). The original velocity of the object is $V = 0$ m/s, then it moves with constant

Fig. 8 Vehicle velocity profile

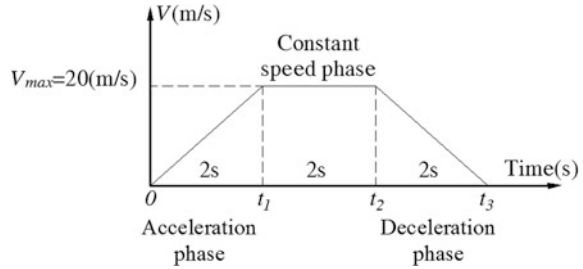
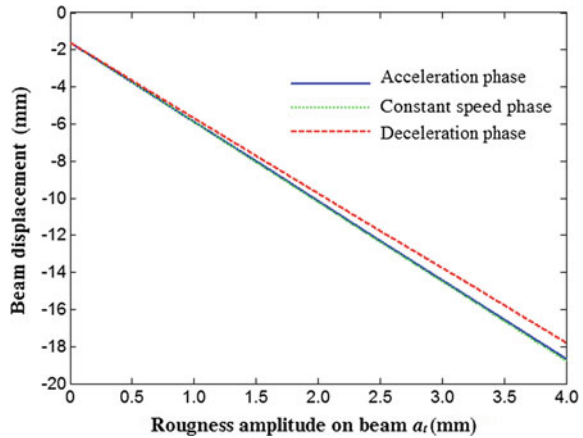


Fig. 9 Maximum beam displacement when keeping the roughness wavelength on beam $\lambda_t = 0.5$ m, changing only the roughness amplitude

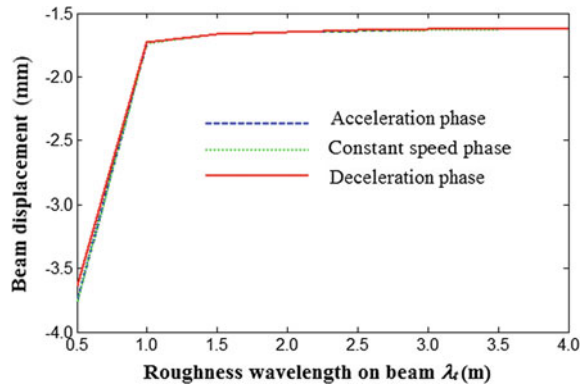


acceleration $a_{max} = 10 \text{ m/s}^2$. After 2 s of acceleration, the object has the constant velocity $V_{max} = 20 \text{ m/s}$ in 2 s and moves with constant deceleration $a_{min} = -10 \text{ m/s}^2$ and stops after 2 s.

Figure 9 shows the value of the beam displacement at each phase of the velocity and each value of the roughness magnitude on beam. The result shows that when increasing the roughness amplitude on beam, the value of the beam displacement increases also. Besides, other phases like acceleration, constant velocity, or deceleration do not make the value of the beam displacement increase, and these values are closely the same. Thence, the beam displacement depends very much on the roughness amplitude on beam. When the roughness amplitude increases, the value of the beam displacement also increases linearly.

Figure 10 shows the value of the beam displacement at each phase of the velocity and each value of the roughness wavelength on beam. We can tell that the bigger value of the roughness wavelength, the smaller the beam displacement of three phases of the velocity. The beam displacement decreases dramatically when the wavelength $\lambda_t = 1.0 \text{ mm}$ and is asymptotic to a certain point. This proves that the beam displacement is also affected by the roughness wavelength on beam.

Fig. 10 Maximum beam displacement when keeping the roughness amplitude $a_r = 1.6$ mm, changing only the roughness wavelength



4 Conclusions

The paper presents the result on dynamic analysis of beams on two-parameter viscoelastic Pasternak foundation subjected to the moving load and considering effects of beam roughness developed with Improved Moving Element Method (IMEM). The result shows that the second foundation parameter has significant effect on dynamic response of beam; when increasing the second foundation parameter, the beam displacement also decreases. The model of two-parameter foundation has the smaller displacement than the traditional viscoelastic foundation ($k_s = 0$).

In addition, the beam roughness also has influence significantly on dynamic response of beam. When the roughness amplitude increases, the beam displacement also increases with nearly linear ratio. Besides, when the roughness wavelength is between $\lambda_r = 0.5\text{--}2$ m, the more roughness wavelength increases, the more beam displacement increases. However, when the roughness wavelength reaches to a certain point, the beam displacement will decrease and be asymptotic to a certain point.

The resonance makes the beam displacement to reach the maximum value. The cause of this resonance depends on many elements such as: the velocity of the mass, the roughness wavelength on beam, and the second foundation parameter. Therefore, it is necessary to consider the combination of all mentioned above elements in the engineering design to avoid this dangerous resonance.

When the load moves with the various accelerations, decelerations, or constant velocity, then the beam displacement depends on the roughness amplitude on beam. The beam displacement increases when the amplitude increases. Moreover, the beam displacement also varies dramatically when the roughness wavelength varies. Thus, in the engineering design, special consideration of dynamic response of moving load resting on beam with various speed is essential and correct to the real demand of the structural beam.

References

1. Winkler E (1867) Die lehre von der elastizitat und festigkeit, Dominicus Prague
2. Flamenco-Borodich MM (1940) Some approximate theories of elastic foundation. *Uchenyie Zapiski Moskovskogo Gosudarstvennogo Universiteta Mekhanika* 46, pp 3–18 (in Russian)
3. Hetényi M (1946) Beams on elastic foundation: theory with applications in the fields of civil and mechanical engineering. University of Michigan Press, Michigan USA
4. Pasternak PL (1954) On a new method of analysis of an elastic foundation by means of two constants. *Gosudarstvennoe Izdatelstvo literaturi po Stroitelstvu Arkhitekture*, Moscow (in Russian)
5. Reissner E (1967) Note on the formulation of the problem of the plate on an elastic foundation. *Acta Mech* 4:88–91
6. Chang-Yong C, Yang Z (2008) Dynamic response of a beam on a Pasternak foundation and under a moving load. *J Chongqing University (English Edition)* 7(4):311–316. ISSN 1671-8224
7. Kumari S, Sahoo PP, Sawant VA (2012) Dynamic response of railway track using two parameters model. *Int J Sci Eng Appl* 1(2). ISSN 2319-7560
8. Luong-Van H, Nguyen-Thoi T, Liu GR, Phung-Van P (2014) A cell-based smoothed finite element method using three-node shear-locking free Mindlin plate element (CS-FEM-MIN3) for dynamic response of laminated composite plates on viscoelastic foundation. *Eng Anal Boundary Elem* 42:8–19
9. Phung-Van P, Nguyen-Thoi T, Luong-Van H, Thai-Hoang C, Nguyen-Xuan H (2014) A cell-based smoothed discrete shear gap method (CS-FEM-DSG3) using layerwise deformation theory for dynamic response of composite plates resting on viscoelastic foundation. *Comput Methods Appl Mech Eng* 272:138–159
10. Phung-Van P, Luong-Van H, Nguyen-Thoi T, Nguyen-Xuan H (2014) A cell-based smoothed discrete shear gap method (CS-FEM-DSG3) based on the CO-type higher-order shear deformation theory for dynamic responses of Mindlin plates on viscoelastic foundations subjected to a moving sprung vehicle. *Int J Numer Methods Eng* 98(13):988–1014
11. Nguyen-Thoi T, Luong-Van H, Phung-Van P, Rabczuk T, Tran-Trung D (2013) Dynamic responses of composite plates on the Pasternak foundation subjected to a moving mass by a cell-based smoothed discrete shear gap (CS-FEM-DSG3) method. *Int J Compos Mater* 3 (A):19–27
12. Lou P, Au FTK (2013) Finite element formulae for internal forces of Bernoulli-Euler beams under moving vehicles. *J Sound Vib* 332:1533–1552
13. Koh CG, Ong JSY, Chua DKH, Feng J (2003) Moving element for train-track dynamics. *Int J Numer Methods Eng* 56:1549–1567
14. Tran MT, Ang KK, Luong VH (2014) Vertical dynamic response of non-uniform motion of high-speed rails. *J Sound Vib*. <https://dx.doi.org/10.2016/j.jsv.2014.05.053>
15. Ang KK, Tran MT, Luong VH (2013) Track vibrations during accelerating and decelerating phases of high-speed rails. In: Thirteenth East Asia-Pacific conference on structural engineering and construction EASEC-13 11 Sapporo Japan
16. Ang KK, Dai J (2013) Response analysis of high-speed rail system accounting for abrupt change of foundation stiffness. *J Sound Vib* 332:2954–2970
17. Ang KK, Dai J, Tran MT, Luong VH (2014) Analysis of high-speed rail accounting for jumping wheel phenomenon. *Int J Comput Methods* 11(3):1343007-1–1343007-12. <https://dx.doi.org/10.1142/S021987621343007X>
18. Tran MT, Ang KK, Luong VH (2016) Vertical dynamic response of high-speed rails during sudden deceleration. *Int J Comput Methods*
19. Do KQ, Luong VH (2010) *Structural dynamics*. Ho Chi Minh City National University Publishing Company
20. Feng Z, Cook R (1983) Beam elements on two-parameter elastic foundations. *J Eng Mech* 109:1390–1402

Part XI
Biological Systems

The Prevention of Pressure Ulcers: Biomechanical Modelization and Simulation of Human Seat Cushion Contributions



T. H. Bui, P. Lestriez, D. Pradon, K. Debray and R. Taiar

Abstract The main cause of pressure ulcers (PUs) is high pressure on the surface of buttock-tissue and support cushion as well as the area inside the bones and muscle tissue. There are also many other factors, including shear stress, friction, temperature and moisture. So far, many studies have used numerical simulations and experiments to find the influence of the stresses and strains, the surface pressures on the formation and development of pressure ulcers. This paper presents a biomechanical modelization and simulation of the interactions between wheelchair seat cushion and human buttock-tissue (HBT) aiming to prevent ulcers. In this paper, we used three-dimensional (3D) finite element model (FEM) of a HBT in contact with a honeycomb seat cushion (HSC) in a sitting position. This cushion is made from thermoplastic polyurethane (TPU) for disabled people who use wheelchairs. Mechanical simulation was performed to find the pressure distribution, the stress and the deformation. Thermal simulation permits to identify the temperature distribution on the surface of HBT and HSC that are the factors can cause PUs. Our results showed that the highest distribution pressure, the von Mises stress, respectively, found corresponds to 175.8 and 36.45 kPa. The highest temperatures obtained in the zone of interaction between the buttock-tissue and HSC correspond to 33.74 °C after 35 min seating. Our study proposes a new methodology for the improvement and validation of FEM to identify the risk of PUs. The results will permit to improve

T. H. Bui (✉) · P. Lestriez · K. Debray · R. Taiar
University of Reims of Champagne-Ardenne (URCA), GRESPI, Reims, France
e-mail: he-thong.bui@etudiant.univ-reims.fr

P. Lestriez
e-mail: philippe.lestriez@univ-reims.fr

K. Debray
e-mail: karl.debray@univ-reims.fr

R. Taiar
e-mail: redha.taiar@univ-reims.fr

D. Pradon
U1179 End: icap UVSQ INSERM CHU Raymond Poincaré APHP, Garches, France
e-mail: didier.pradon@aphp.fr

cushion by collaboration with the manufacturer (optimization of shapes and materials) to create the own cushion model for each patient increasing his daily life.

Keywords Thermal-mechanical · Buttock-tissue · Pressure ulcers (PUs) Wheelchair · Seat cushion · Honeycomb · Thermoplastic polyurethane (TPU) Finite element

1 Introduction

The PUs are common pathologies for paralyzed patients, disabled people who have to sit for a long time on wheelchair [1, 2]. The contact interaction between HBT and seat cushion for a prolonged period can cause some discomfort. This due to the loading stresses applied mainly between the ischial tuberosities and the soft tissue at the seat interface. This application causes the pressure distribution on the surface, the stresses inside buttock-tissue, the shear stress, the friction and the microclimate. These are the main factors causing the pressure ulcers. According to the report of the World Health Organization (WHO) in 2008, there were estimated to be 650 million disabled people around the world and about 10% of them require wheelchairs for their daily life. This number will increase because the world population will age over time [3–5]. Otherwise, the treatment cost of this problem may be up to 12500 € per person [6]. Therefore, changing the design of the product or choosing products with features suitable should be emphasized to achieve this goal [7, 8]. In fact, many studies have focused on stress factors and pressure at the surface caused the PUs [9–15]. These studies used different materials of the cushion to compare the effect of cushions in the context of improved comfort and prevention of PUs. In parallel, these studies were used in 2D and 3D FEM in the aim to determine the stress distribution inside the model created by the ischial tuberosity, muscle tissue and the pressure at the buttock-cushion interface. However, there are very few studies showing the effect of temperature distribution on the surface of the buttock-tissue and seat cushion to PUs [16–20]. Therefore, we cannot see the influence and importance of temperature factors on pressure ulcers. The main aim of this study is to propose a 3D FEM of a HBT in contact with a HSC made from TPU. We study the impact of stress distribution, pressure distribution and thermal distribution at the interface HBT and HSC in the aim to prevent PUs improving the comfort of users.

2 Methodology

2.1 *Buttock-Tissue and Seat Cushion Model*

We selected the buttock-tissue model based on the ISO standards 16840-2:2007 [21], and the “Zygote Human Factors” model was associated with the sitting

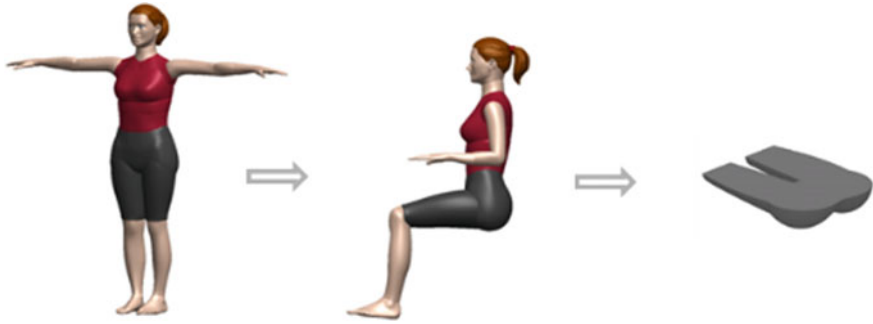


Fig. 1 3D CAD the buttock-tissue model

position [22]. This model was used from the study of Bui et al. [3], which was designed by SolidWorks software as shown in Fig. 1. The total length of the buttock-tissue model was 450 mm for a human.

The HSC used in this study is called “Stimulite[®] Honeycomb Cushion” [23] with the dimensions $L \times W \times H = 460 \text{ mm} \times 410 \text{ mm} \times 70 \text{ mm}$. Figure 2a indicates the structure of the classic type of “Stimulite[®] Honeycomb Cushion” from SUPRACOR Company and distributed by PHYSIPRO. The structure of cushion consists of three layers of perforated honeycomb hexagonal bee and separated by horizontal sheets (Fig. 2b). The alveolar has six faces: 2 double 0.4 mm of thickness and 4 single 0.2 mm of thickness and several transverse holes with a diameter of 1.3 mm (Fig. 2d). The clear blue transparent on top layer (Fig. 2c) is generated to reduce the shear stresses at the interface of buttock-tissue and seat cushion.

Because of the symmetry of this model, so to reduce the time calculated by FEM. In this study, we only created a half buttock-tissue/honeycomb cushion model. Figure 3a shows the half FEM of the buttock-tissue and honeycomb cushion model. In order to increase quality, the mesh elements were created very smoothly and finely compared to other published models [9–13, 23]. The buttock-tissue and honeycomb cushion models were developed using a total number of 10,500,256 elements and 5,084,925 nodes. The type of element used to mesh the different parts

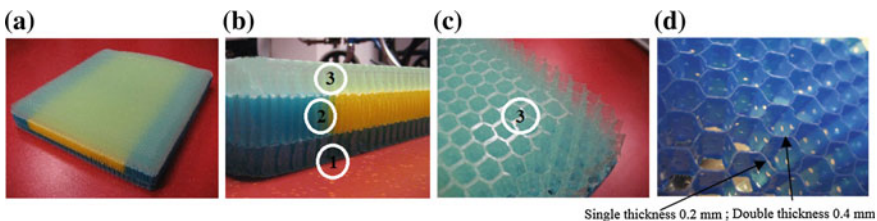


Fig. 2 Structural decomposition of “Stimulite[®] Honeycomb Cushion”. **a** Stimulite[®] Honeycomb Cushion; **b** horizontal sheets separated three layer of cushion; **c** the surface to reduce shear stress at the interface contact; **d** thickness of alveolar

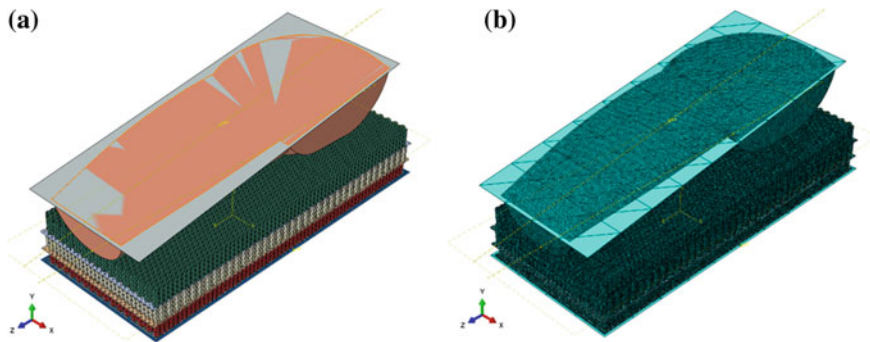


Fig. 3 3D CAD (a) and FEM (b) of a half buttock-tissue and honeycomb cushion

of the geometry is tetrahedral C3D4 with 1,623,344 mesh elements, and the element size is set to 1 mm. In addition, the type of element for honeycomb cushion is triangular S3R with total number of 8,586,042, and the element size is set to 1 mm. The three horizontal sheets are separated to three layers of honeycomb cushion with a triangular S3R (1 mm of size) (Fig. 3b).

2.2 Material Models

It is well known that hyperelastic behaviour of the seat cushion and the HBT materials is nonlinear, isotropic and nearly incompressible. In this paper, a nonlinear Mooney-Rivlin material was applied to the wheelchair seat cushion and the HBT [9–15, 24, 25]. The viscoelastic behaviour of the two models was defined by using a time-based Prony series. The parameter materials of the honeycomb cushion (TPU) were obtained from tensile and compressive tests that were conducted using the INSTRON 33R4204 machine. Figure 4b represents the tensile curve obtained from the tests for the TPU material. Some material parameters are extracted and used for the model according to Kanyanta et al. [24]. The second, static equilibrium equations with large strain were affected in the material model in this FEM. The Mooney-Rivlin hyperelastic model [10, 11, 13–15, 25] was employed for muscles behaviours. The model was based on the strain energy function as indicated in Eq. (1):

$$W = C_{10}(\bar{I}_1 - 3) + C_{01}(\bar{I}_2 - 3) + \frac{2}{D_1}(J - 1)^2 \quad (1)$$

where W is the strain energy per unit of reference volume; J is the Jacobine deformation. In Eq. (1), C_{10} , C_{01} and D_1 are the material-dependent parameters.

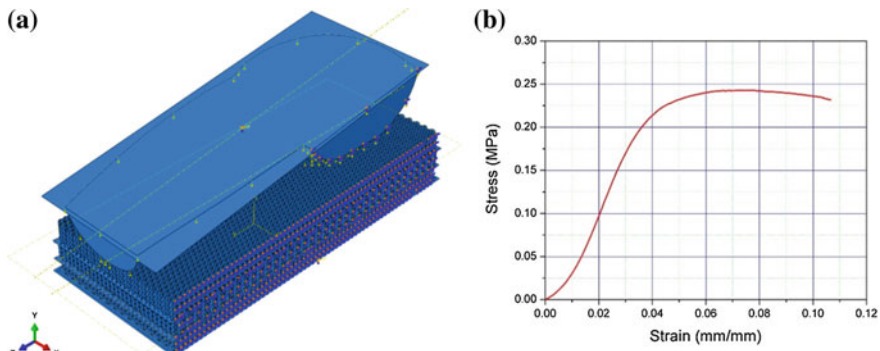


Fig. 4 **a** Loading and boundary conditions on the HBT and HSC model; **b** nonlinear stress–strain curve of HSC material (TPU)

$D_1 = \frac{1-2\nu}{C_{10} + C_{01}}$, where ν is the Poisson’s ratio of the material. \bar{I}_1 and \bar{I}_2 are the first and second deviatoric strain invariants defined as following (2) and (3),

$$\bar{I}_1 = \bar{\lambda}_1^2 + \bar{\lambda}_2^2 + \bar{\lambda}_3^2 \tag{2}$$

$$\bar{I}_2 = \bar{\lambda}_1^{(-2)} + \bar{\lambda}_2^{(-2)} + \bar{\lambda}_3^{(-2)} \tag{3}$$

where the deviatoric stretches are rewritten $\bar{\lambda}_i = J^{-1/3} \lambda_i$; λ_i are the principal stretches. The parameters of buttock-tissue were taken from Dabnichki et al. [25]; Grujicic et al. [13]; Verver et al. [10]. In Eq. (1), C_{10} , C_{01} and D_1 are the material parameters and ν is the Poisson’s ratio ($\nu \cong 0.495$). The Mooney-Rivlin hyperelastic parameters of honeycomb wheelchair seat cushion are as follows: $C_{10} = 1.24$ (MPa), $C_{01} = 0.01$ (MPa), $D_1 = 0.008$ (MPa⁻¹). The Mooney-Rivlin hyperelastic parameters of buttock-tissue are as follows: $C_{10} = 0.00165$ (MPa), $C_{01} = 0.00335$ (MPa), $D_1 = 2$ (MPa⁻¹).

The viscoelastic behaviour of the buttock-tissue is defined by using a time-based Prony series model [14], and the time-dependent shear relaxation modulus $G(t)$ is given by Eq. (4):

$$G(t) = G_0 - \sum_{i=1}^N G_i \left(1 - e^{-t/\tau_i^G}\right) \tag{4}$$

where τ_i^G the relaxation time and N is the order of the Prony series. G_0 and G_i are, respectively, the instantaneous and relative shear modulus. The viscoelastic parameters for the buttock-tissue model were set as $g_1 = 0.5$, $k_1 = 0.5$ and $\tau_1 = 0.8$ s [14, 26].

The viscoelastic parameters of the HSC were determined by plotting the normalized stress with initial stress σ_0 against time. The viscoelastic model was

obtained from relaxation tests by fitting a three-term Prony series (Eq. 5) to the relaxation data as follows [24]:

$$E(t) = 6.5(1 + 0.023e^{-t/12} + 0.08e^{-t/98} + 0.034e^{-t/1600}) \quad (5)$$

3 Mechanical-Thermal Simulation

3.1 Mechanical Simulation

The mechanical simulation was implemented by using an explicit integration law and diagonal element mass matrix. The motion equations of the body were integrated using the following explicit central-difference integration law:

$$\dot{u}_{(i+\frac{1}{2})}^N = \dot{u}_{(i-\frac{1}{2})}^N + \frac{\Delta t_{(i+1)} + \Delta t_i}{2} * \ddot{u}_{(i)}^N \quad (6)$$

and

$$u_{(i+\frac{1}{2})}^N = u_{(i)}^N + \Delta t_{(i+1)} * \dot{u}_{(i+\frac{1}{2})}^N \quad (7)$$

where u^N is a degree of freedom (a displacement or rotation component) and the subscript i refers to the increment number in an explicit dynamics step. The central-difference integration operator is explicit such that the kinematic state is advanced using known values of $\dot{u}_{(i-\frac{1}{2})}^N$ and $\dot{u}_{(i)}^N$ from the previous increment (Abaqus version 6.13, [27]).

The interaction between the HBT and HSC models was analyzed in ABAQUS/explicit 6.13-4 and the penalty contact method with finite sliding. The surface-to-surface contact with a 0.5 coefficient of friction was used to define the contact pair between the HBT and HSC models [13, 14]. The outer surface of the HBT model was defined as the master-surface and the surface of the cushion as the slave-surface. The upper surface of the HBT model was linked with a rigid surface plate by the Tie contact. In order to connect together the three horizontal layers of HSC, the contacts Tie was used (Fig. 4a). We apply 10^{-5} mass scaling coefficient and half buttock-tissue/honeycomb cushion to reduce the computation time.

The loading applied to our model represents a human male weighing 75 kg. Figure 4a shows the loading and boundary conditions between the HBT and HSC. In this model, we applied a mass of 37.5 kg for half a buttock-tissue (representing half the male human body weight) [2]. The bottom surface of the HSC is fixed. The HBT used in our study permits to quantify the impact of the load on the cushion in the Y-axis. A typical computational analysis of the BHT and HSC interactions was carried out on a 64-bit Windows by the Centre of calculation of University Reims Champagne-Ardenne.

3.2 Thermal Simulation

Pennes [28] and Fiala [29] have developed the heat transport mechanism that occurs in living tissue in the so-called bio-heat formulated. This differential equation describes the heat dissipation in homogeneous, infinite tissue volume:

$$k \left(\frac{\partial^2 T}{\partial r^2} + \frac{\omega}{r} \frac{\partial T}{\partial r} \right) + q_m + \beta(T_b - T) = \rho C_v \frac{\partial T}{\partial t} \tag{8}$$

In this equation, k the tissue thermal conductivity [$\text{W m}^{-1} \text{K}^{-1}$]; T the tissue temperature [$^{\circ}\text{C}$]; q_m the metabolic heat flow [W m^{-3}]; for all body elements, r denotes the radial coordinate [m]; ω is a geometry factor; ($\omega = 1$ for polar coordinates and $\omega = 2$ for spherical coordinates); $\beta(T_b - T)$ is blood perfusion, with $\beta = \rho_{bl} \cdot w_{bl} \cdot c_{bl}$ (heat convection term), where ρ_{bl} is density of blood [kg m^{-3}], w_{bl} is blood perfusion rate [$\text{m}^3 \text{s}^{-1} \text{m}^{-3}$], c_{bl} heat capacitance of blood [$\text{J kg}^{-1} \text{K}^{-1}$]; T_b the arterial blood temperature [$^{\circ}\text{C}$]. This combined effect is balanced by the storage of heat within the tissue mass (right-hand side of equation..., where ρ is tissue density [kg m^{-3}], tissue heat capacitance [$\text{J kg}^{-1} \text{K}^{-1}$], t is time [s]).

In our study, we fixed 34°C according to [29] for the modelization of HBT. The synopsis of the heat transfer modelling is presented in Fig. 5.

A finite element method was used to simulate the temperature distribution in the HSC in contact with the HBT as a function of time. The general governing equation can be presented as [16]:

$$\rho C_v \frac{\partial T}{\partial t} = k \nabla^2 T + S \tag{9}$$

where the HSC local temperature, T [$^{\circ}\text{C}$], varies with spatial coordinates and time, t [s]. The thermophysical properties k , ρ , and C_v are the material thermal conductivity [$\text{W m}^{-1} \text{K}^{-1}$], density [kg m^{-3}] and specific heat [$\text{J kg}^{-1} \text{K}^{-1}$], respectively. The source term, S , is the heat generation per unit volume for the nodes. In this works, a symmetric condition is assumed, and the computational domain is limited to the right half of the HBT and the HSC to reduce the calculation time. The HSC was applied in our simulation without cover, and the temperature is considered to be at 20°C , which is the ambient temperature (T_{room}). Equation (9) is the heat exchange equation between two contacts, which means the contact areas between

Fig. 5 Synopsis of the heat transfer modelling

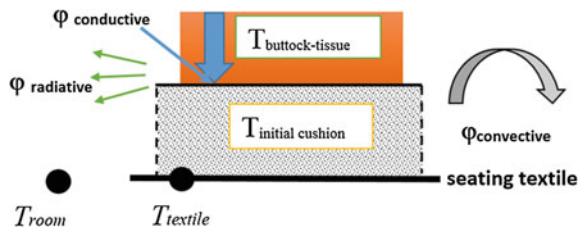


Table 1 Thermal properties of HBT and HSC at room temperature for our simulation

Materials	Thermal conductivity (W C ⁻¹ m ⁻¹)	Specific heat (J kg ⁻¹ C ⁻¹)	Density (kg m ⁻³)
Buttock-tissue	0.33 → 0.54	3430 → 3720	1020–1090
Honeycomb cushion	0.19 → 0.25	1500 → 1800	1120

the HBT and the HSC. For non-contact areas, the heat exchange between the HBT, the HSC and the ambient air occurs by convection and radiation. The effective local heat transfer coefficient can be defined as:

$$\varphi = \varphi_r + \varphi_c = \sigma\epsilon(\bar{T}^4 - T_\infty^4) + \bar{h}_c(\bar{T} - T_\infty) \tag{10}$$

In this study, we used the ABAQUS/Standard 6.13-4 software to perform the thermal simulation for the right half of the HBT and the HSC. The thermal parameters of the buttock-tissue and honeycomb cushion materials in this simulation are shown in Table 1 [30–32].

4 Results and Discussion

4.1 Results of Mechanical Simulation

4.1.1 Contact Pressure Distribution

The maximum contact pressure of 175.8 kPa was concentrated in the HBT shown in Fig. 6. Compared with the results (187.7 kPa) obtained by Grujicic et al. [13], in which subjects were modelled in the same sitting position, our results yield a reduction in contact pressure of approximately 12 kPa. In our study, the total

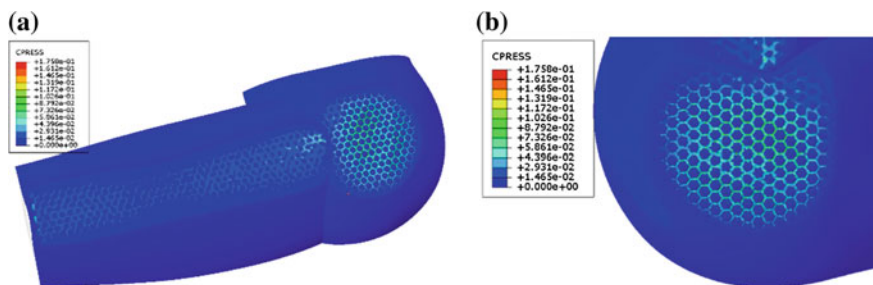


Fig. 6 Contacted pressure distribution over the HBT/HSC interface: **a** global view; **b** enlarge view

contact surface area analyzed is smaller than that studied by Grujicic et al. [13]. With this result, we can see that HSC is more competitive than polyurethane foam cushions for the problem of reducing pressure on the surface HBT/HSC.

4.1.2 The Von Mises Stress

The von Mises stresses of the HBT were determined by FEM. Figure 7 shows the distribution of the von Mises equivalent stress on both the surface and the inside of the buttock-tissue. The maximum value of the von Mises stress on the buttock is 36.44 kPa. These values are smaller than those in the 2D and 3D models found in the literature. In their 2D FEM, Oomens et al. [33] found 180 kPa for the same sitting position analyzed in our study.

In other 3D FEM of Verver et al. [10], Makhsous et al. [11] quantified the impact of skin, fat, muscle and bone on buttock-tissue. For both studies, the authors obtained values of 45–50 kPa and 40–50 kPa, respectively, for sitting positions similar to those analyzed in our study.

4.1.3 Distribution of Contact Shear Stress

Using a constant coefficient of friction in static condition (0.5), Fig. 8 shows the contact shear stress distribution. Our average value is 5.7 kPa is compared to 2 kPa as obtained by Grujicic et al. [13]. The differences in these average values may be explained by the differences in the material used for the two cushions, i.e. in our case, the honeycomb cushion with contacted edge versus the foam polyurethane cushion with flat contact surface used by Grujicic et al.

4.2 Result of Thermal Simulation

Figure 9 shows simulated temperature distribution on the HSC surface after 35 min of sitting. The highest temperature obtained at the HSC surface of our study was

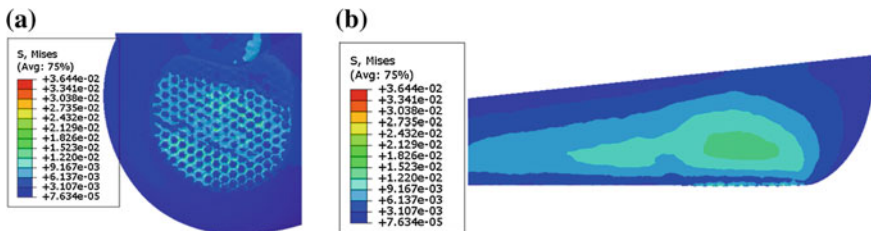


Fig. 7 Von Mises stresses distribution; **a** at the interface buttock-tissue; **b** inside the buttock-tissue

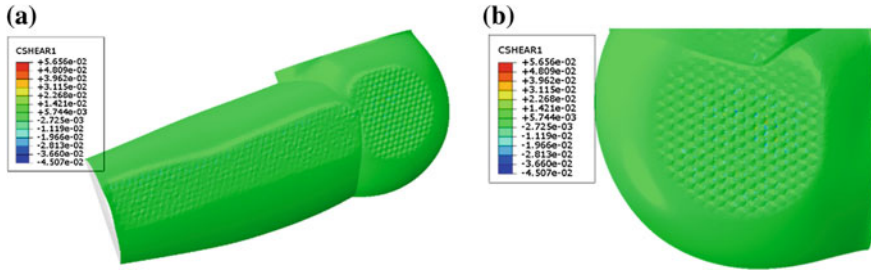


Fig. 8 Contact shear stress distribution over the HBT/HSC interface: **a** global view; **b** enlarged view

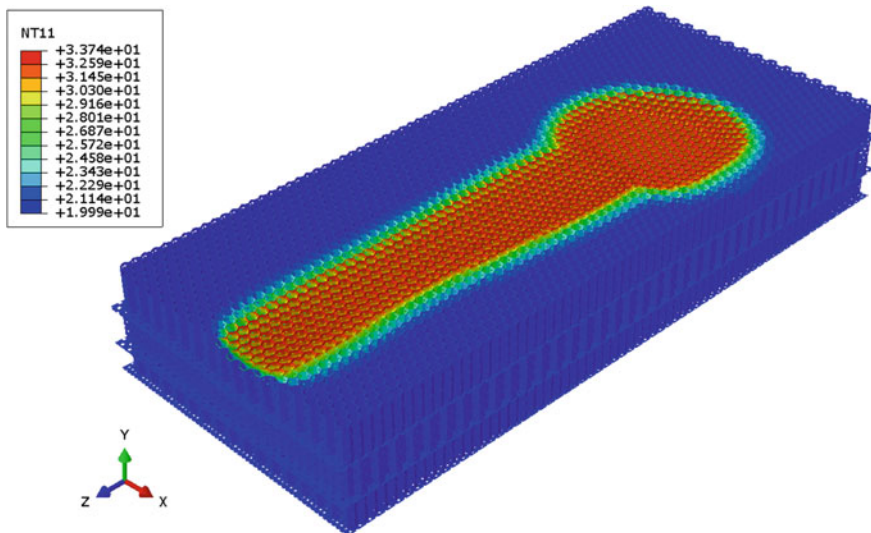


Fig. 9 Temperature distribution on the surface HSC after 35 min of sitting

33.74 °C (Fig. 9). Karimi et al. [16] after 20 min of sitting with the foam polyurethane seat cushion obtained 35.4 °C in their simulation. The HSC appears more efficient, reducing the temperature at the interface HBT and HSC.

Figure 10 shows that almost the largest temperature values are concentrated in the centre of the HBT and the thigh-tissue at large contact position. At other locations on the HSC, these locations are far from the buttock-tissue (no direct contact with the buttock-tissue), which have lower temperature.

Based on the graph in Fig. 11, we can see that the temperature at the surface of HSC increases rapidly during the first period of simulations (about the first 6 min). The temperature value at the HSC surface increases very fast from 20 to 32.7 °C (black spline). This is due to the significant temperature difference between the HBT and HSC. Then the temperature on the HSC continued to increase relative in

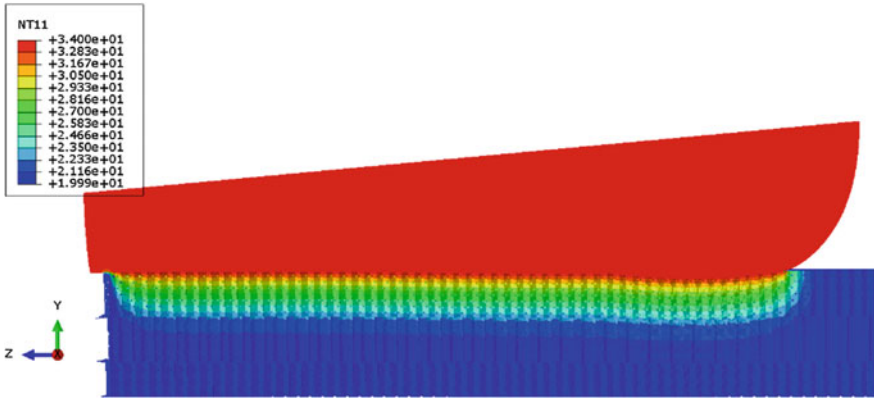


Fig. 10 Temperature distribution in the buttock-tissue and honeycomb cushion after sitting (35 min, cutting model in y-z plan)

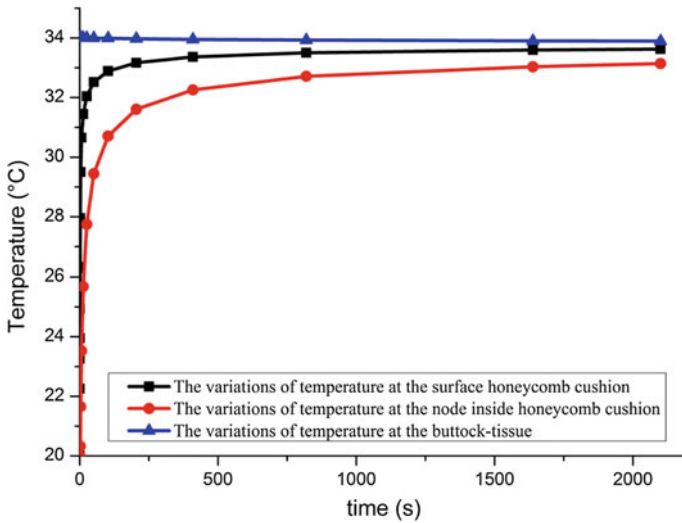


Fig. 11 Variations of temperature in the contact areas

the next period (6–22 min) with temperature values increasing from 32.7 to 33.2 °C. However, the rate of heat transfer at surface of HSC slows down over time after about 6 min initially. During the rest of time, from 22 to 35 min, the temperature increases to the maximum value and then saturates at 33.74 °C.

5 Conclusions

This article used the finite element method to develop a mechanical-thermal simulation of the biomechanical model of HBT and HSC. We studied the influence of the mechanical factors such as the distribution pressure, the von Mises stress, the strain and the temperature distribution at the interface of HBT and the HSC. These factors cause the formation and development of the pressure ulcers. Mechanical simulation for biomechanical model of HBT and the HSC has been realized commonly in literature. However, thermal simulation for biomechanical model of the HBT and the wheelchair seat cushion is relatively new and has not been studied much in the literature before, so this is an originality of our research. Mechanical results obtained showed that our cushion (HSC) is better suited and designed to reduce stress on the HBT and thus prevents the formation of pressure ulcers. The temperature distribution on HSC obtained by thermal simulation permits to evaluate the effect of temperature on seat comfort and provides methods to prevent PUs of patient and wheelchair users. Through our study, the results will be useful for manufacturers to improve cushion design and consequently the daily life of the patient. The predictions based on mechanical-thermal analysis of the interaction between user and the cushion will allow the better advises on the new conception of the product satisfying the comfort of users in order to prevent pressure ulcers.

The next step of this study will be performed experimentations to record the temperature distribution by the infrared camera and the distribution pressure by mapping the pressure at the surface of seat cushion to compare the results obtained by experimentations with the results obtained by numerical simulation to help the selection of appropriate cushion.

References

1. Kosiak M, Kubicek WG, Wilson M, Danz JN, Kottke FJ (1958) Evaluation of pressure as a factor in the production of ischial ulcers. *Arch Phys Med Rehabil* 39(10):623–629
2. Crenshaw RP, Vistnes RP (1989) A decade pressure sore research: 1977–1987. *J Rehabil Res Dev* 26(1):63–74
3. Bui HT, Lestriez P, Pradon D, Debray K (2016) Biomechanical modeling of medical seat cushion and human buttock tissue to prevent pressure ulcers. In: 22nd congress of the European society of biomechanics
4. Bui HT, Pradon D, Lestriez P, Debray K, Taiar R, Guillon B (2017) Influence of different types of wheelchair cushions for pressure ulcers in view of the experimental approach. In: *Proceedings of the IASTED international conference (BioMed 2017)*, pp 164–167
5. OMS (2008) *Guide pour les services de fauteuils roulants manuels dans les régions à faibles revenus*, pp 1–142
6. Bennett G, Dealey C, Posnett J (2004) The cost of pressure ulcers in the UK. *Age Ageing* 33:230–235
7. Ferguson-Pell MW (1990) Seat cushion selection. *J Rehabil Res Dev* 2:49–73

8. Sprigle S, Chung KC, Brubaker CE (1990) Reduction of sitting pressures with custom contoured cushions. *J Rehabil Res Dev* 27(2):135–140
9. Chow WW, Odell EI (1978) Deformations and stresses in soft body tissues of a sitting person. *J Biomech Eng* 100(2):79–87
10. Verver MM, van Hoof J, Oomens CW, Wismans JS, Baaijens FP (2004) A finite element model of the human buttocks for prediction of seat pressure distributions. *Comput Methods Biomech Biomed Eng* 7(4):193–203
11. Makhsous M, Lim D, Hendrix R, Bankard J, Rymer WZ, Lin F (2007) Finite element analysis for evaluation of pressure ulcer on the buttock: development and validation. *IEEE Trans Neural Syst Rehabil Eng* 15(4):517–525
12. Wagnac E, Aubin C, Dansereau J (2008) A new method to generate a patient-specific finite element model of the human buttocks. *IEEE Trans Biomed Eng* 55(2):774–782
13. Grujicic M, Pandurangan B, Arakere G, Bell WC, He T, Xie X (2009) Seat-cushion and soft-tissue material modeling and a finite element investigation of the seating comfort for passenger-vehicle occupants. *Mater Des* 30(10):4273–4285
14. Tang CY, Chan W, Tsui CP (2010) Finite element analysis of contact pressures between seat cushion and human buttock-thigh tissue. *Engineering* 02(09):720–726
15. Mohanty PP, Mahapatra SS (2014) A finite element approach for analyzing the effect of cushion type and thickness on pressure ulcer. *Int J Ind Ergon* 44:499–509
16. Karimi G, Chan EC, Culham JR (2004) Thermal modeling of driver/seat interfaces in automotive applications. Society of Automotive Engineers, Inc., pp 1–7
17. Chan EC, Karimi G, Rose D, Culham JR (2004) Mechanical-thermal simulation of passenger-loaded vehicle seat in severe winter conditions. Society of Automotive Engineers, Inc., pp 1–10
18. Konstantinov M, Wagner C (2014) Numerical simulation of the air flow and thermal comfort in a train cabin. In: Proceedings of the second international conference on railway technology: research, development and maintenance, pp 283–293
19. Konstantinov M, Wagner C (2015) Numerical simulation of the thermal comfort in a train cabin. *Int J Railway Technol* 4(3):69–88
20. Gefen A (2011) How do microclimate factors affect the risk for superficial pressure ulcers: a mathematical modeling study. *J Tissue Viability* 20(3):81–88
21. Norme ISO (2007) Wheelchair seating—Part 2: Determination of physical and mechanical characteristics of devices intended to manage tissue integrity—seat cushions (2007)
22. Zygote Media Group Inc (2012) 3D human model. <http://www.3dscience.com/humanfactors/>. Accessed 20 Dec 2011
23. Physipro Company (2016) Stimulite honeycomb cushion Classic. <http://www.physipro.com/fr/produit/coussin-stimulite-classique/>. Accessed 20 Oct 2016
24. Kanyanta V, Ivankovic A (1994) Mechanical characterisation of polyurethane elastomer for biomedical applications. *J Mech Behav Biomed Mater* 208(1):51–62
25. Dabnichki PA, Crocombe AD (1994) Deformation and stress analysis of supported buttock contact. *Proc Inst Mech Eng* 208(1):9–17
26. Brienza DM, Karg PE, Jo Geyer M, Kelsey S, Treffer E (2001) The relationship between pressure ulcer incidence and buttock-seat cushion interface pressure in at-risk elderly wheelchair users. *Arch Phys Med Rehabil* 82(4):529–533
27. Abaqus version 6.13, 2013. User Documentation
28. Pennes HH (1978) Analysis of tissue and arterial blood temperatures in the resting human forearm. *J Appl Physiol* 1:93–121
29. Fiala D (1998) Dynamic simulation of human heat transfer and thermal comfort. Thesis institute of energy and sustainable development De Montfort University Leicester
30. BASF (2011) Thermoplastic polyurethane elastomers (TPU) Elastollan®—material properties. *Tech Inf* 1–44

31. Calvert J, Duck F, Clift S, Azaime H (2007) Surface heating by transvaginal transducers. *Ultrasound Obstet Gynecol* 29:427–432
32. Shaw A, Pay NM, Preston RC, Bond AD (1999) Proposed standard thermal test object for medical ultrasound. *Ultrasound Med Biol* 25:121–132
33. Oomens CW, Bressers OF, Bosboom EM, Bouten CV, Blader DL (2003) Can loaded interface characteristics influence strain distributions in muscle adjacent to bony prominences? *Comput Methods Biomech Biomed Eng* 6(3):171–180